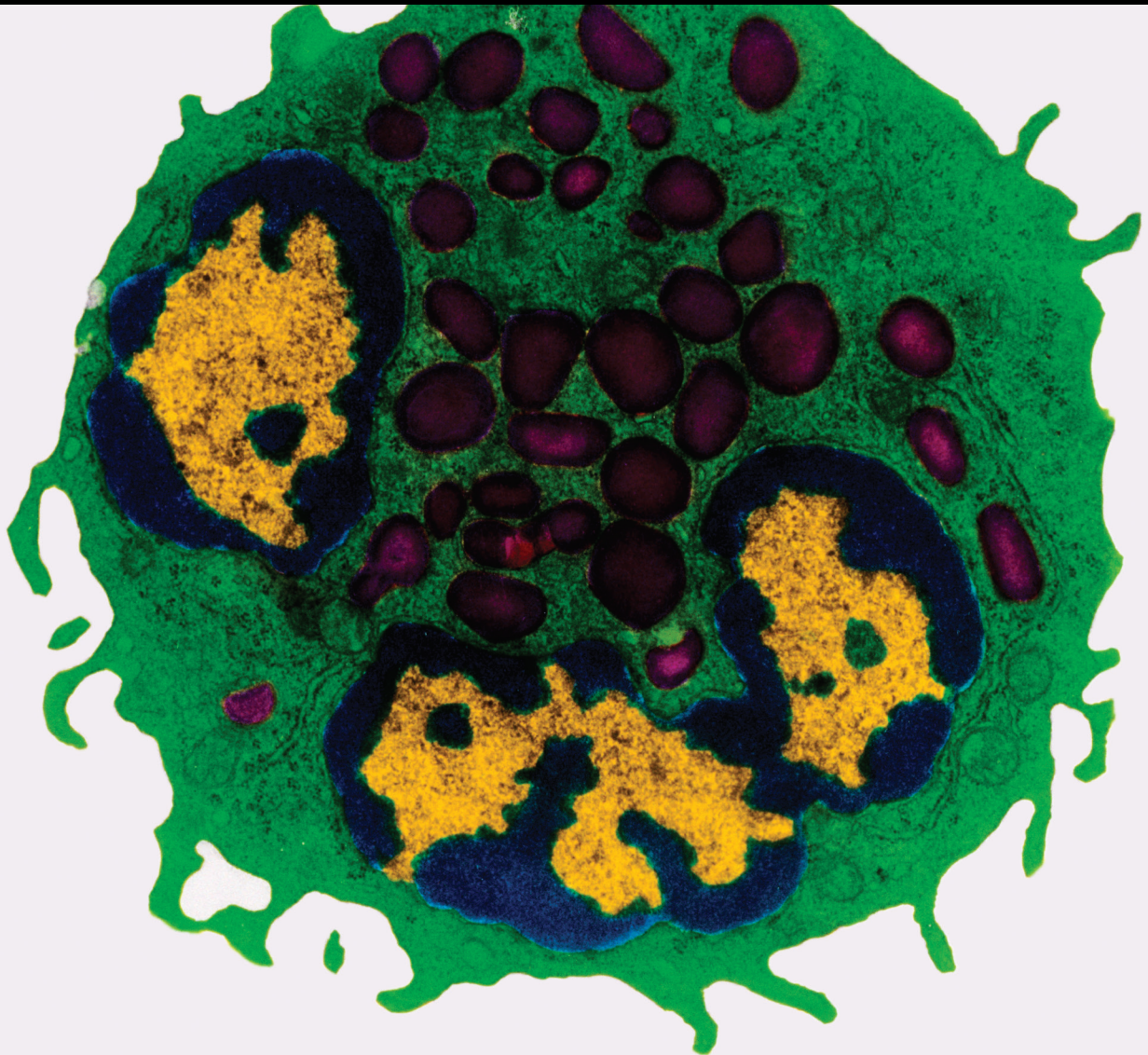


Metabolism of the Host and Microbes to Modulate Immunocytes

Lead Guest Editor: Shuai Chen

Guest Editors: Miaomiao Wu, Mingliang Jin, Xiaolu Jin, Yaoyao Xia, and Xin Zong





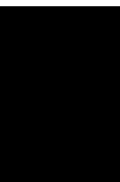
Metabolism of the Host and Microbes to Modulate Immunocytes

Mediators of Inflammation

Metabolism of the Host and Microbes to Modulate Immunocytes

Lead Guest Editor: Shuai Chen


Guest Editors: Miaomiao Wu, Mingliang Jin, Xiaolu
Jin, Yaoyao Xia, and Xin Zong







Copyright © 2021 Hindawi Limited. All rights reserved.

This is a special issue published in “Mediators of Inflammation.” All articles are open access articles distributed under the Creative Commons Attribution License, which permits unrestricted use, distribution, and reproduction in any medium, provided the original work is properly cited.

Chief Editor







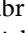
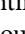
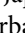
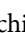
Anshu Agrawal , USA

Associate Editors

Carlo Cervellati , Italy
Elaine Hatanaka , Brazil
Vladimir A. Kostyuk , Belarus
Carla Pagliari , Brazil



Academic Editors

Amedeo Amedei , Italy
Emiliano Antiga , Italy
Tomasz Brzozowski , Poland
Daniela Caccamo , Italy
Luca Cantarini , Italy
Raffaele Capasso , Italy
Calogero Caruso , Italy
Robson Coutinho-Silva , Brazil
Jose Crispin , Mexico
Fulvio D'Acquisto , United Kingdom
Eduardo Dalmarco , Brazil
Agnieszka Dobrzyn, Poland
Ulrich Eisel , The Netherlands
Mirvat El-Sibai , Lebanon
Giacomo Emmi , Italy
Claudia Fabiani , Italy
Fabíola B Filippin Monteiro , Brazil
Antonella Fioravanti , Italy
Tânia Silvia Fröde , Brazil
Julio Galvez , Spain
Mirella Giovarelli , Italy
Denis Girard, Canada
Markus H. Gräler , Germany
Oreste Gualillo , Spain
Qingdong Guan , Canada
Tommaso Iannitti , United Kingdom
Byeong-Churl Jang, Republic of Korea
Yasumasa Kato , Japan
Cheorl-Ho Kim , Republic of Korea
Alex Kleinjan , The Netherlands
Martha Lappas , Australia
Ariadne Malamitsi-Puchner , Greece
Palash Mandal, India
Joilson O. Martins , Brazil
Donna-Marie McCafferty, Canada
Barbro N. Melgert , The Netherlands

Paola Migliorini , Italy
Vinod K. Mishra , USA
Eeva Moilanen , Finland
Elena Niccolai , Italy
Nadra Nilsen , Norway
Sandra Helena Penha Oliveira , Brazil
Michal A. Rahat , Israel
Zoltan Rakonczay Jr. , Hungary
Marcella Reale , Italy
Emanuela Roscetto, Italy
Domenico Sergi , Italy
Mohammad Shadab , USA
Elena Silvestri, Italy
Carla Sipert , Brazil
Helen C. Steel , South Africa
Saravanan Subramanian, USA
Veendamali S. Subramanian , USA
Taina Tervahartiala, Finland
Alessandro Trentini , Italy
Kathy Triantafilou, United Kingdom
Fumio Tsuji , Japan
Maria Letizia Urban, Italy
Giuseppe Valacchi , Italy
Kerstin Wolk , Germany
Soh Yamazaki , Japan
Young-Su Yi , Republic of Korea
Shin-ichi Yokota , Japan
Francesca Zimetti , Italy

Contents

The Role of Oxidative Stress and Antioxidant Balance in Pregnancy

Tarique Hussain , Ghulam Murtaza, Elsayed Metwally, Dildar Hussain Kalhoro, Muhammad Saleem Kalhoro, Baban Ali Rahu, Raja Ghazanfar Ali Sahito, Yulong Yin, Huansheng Yang, Muhammad Ismail Chughtai, and Bie Tan 


Review Article (11 pages), Article ID 9962860, Volume 2021 (2021)

The Key Ingredient Acacetin in Weishu Decoction Alleviates Gastrointestinal Motility Disorder Based on Network Pharmacology Analysis

Xuan Guo , Yin Xu , Hua-liang Tan , Xiao-juan Wang , and Lin Xiao 


Research Article (12 pages), Article ID 5265444, Volume 2021 (2021)

The Mutual Inhibition of FoxO1 and SREBP-1c Regulated the Progression of Hepatoblastoma by Regulating Fatty Acid Metabolism

Yu Hu, Hongyan Zai, Wei Jiang, Zhenglin Ou, Yuanbing Yao, and Qin Zhu 


Research Article (18 pages), Article ID 5754592, Volume 2021 (2021)

p300/Sp1-Mediated High Expression of p16 Promotes Endothelial Progenitor Cell Senescence Leading to the Occurrence of Chronic Obstructive Pulmonary Disease

Zhihui He , Huaihuai Peng, Min Gao, Guibin Liang, Menghao Zeng, and Xuefeng Zhang


Research Article (17 pages), Article ID 5599364, Volume 2021 (2021)

Long Noncoding RNA HCG9 Promotes Osteosarcoma Progression through RAD51 by Acting as a ceRNA of miR-34b-3p

Lu Wang, Shuangqing Li, Lin Qi, and Lin Ling 



Research Article (16 pages), Article ID 9978882, Volume 2021 (2021)

lncRNA PAPPAS1 Induces the Development of Hypertrophic Scar by Upregulating TLR4 through Interacting with TAF15

Pengju Fan , Yongjie Wang, Jingjing Li, and Man Fang


Research Article (23 pages), Article ID 3170261, Volume 2021 (2021)

BMSCs Regulate Astrocytes through TSG-6 to Protect the Blood-Brain Barrier after Subarachnoid Hemorrhage

Yilv Wan , Min Song, Xun Xie, Zhen Chen, Ziyun Gao, Xiang Wu, Rui Huang, and Min Chen 


Research Article (18 pages), Article ID 5522291, Volume 2021 (2021)

Oxidative Stress Level as a Predictor of Anastomotic Leakage after Rectal Surgery

Jiajun Luo, Hongxue Wu, Yu Yang, Yue Jiang, Jingwen Yuan, and Qiang Tong 



Research Article (9 pages), Article ID 9968642, Volume 2021 (2021)

Exosomes Containing LINC00636 Inhibit MAPK1 through the miR-450a-2-3p Overexpression in Human Pericardial Fluid and Improve Cardiac Fibrosis in Patients with Atrial Fibrillation

Langsha Liu, Fanyan Luo, and Kaibo Lei 



Research Article (20 pages), Article ID 9960241, Volume 2021 (2021)

CBP22, a Novel Bacteriocin Isolated from *Clostridium butyricum* ZJU-F1, Protects against LPS-Induced Intestinal Injury through Maintaining the Tight Junction Complex

Tenghao Wang, Jie Fu, Xiao Xiao, Zeqing Lu, Fengqin Wang, Mingliang Jin, Yizhen Wang , and Xin Zong 


Research Article (12 pages), Article ID 8032125, Volume 2021 (2021)

LR12 Promotes Liver Repair by Improving the Resolution of Inflammation and Liver Regeneration in Mice with Thioacetamide- (TAA-) Induced Acute Liver Failure

Yongjuan Wang , Xiaoli Xie, Hongqun Liu, Huimin Liu, and Huiqing Jiang 


Research Article (20 pages), Article ID 2327721, Volume 2021 (2021)

Nontargeted Metabolomic Analysis of Plasma Metabolite Changes in Patients with Adolescent Idiopathic Scoliosis

Lige Xiao, Guanteng Yang, Hongqi Zhang , Jinyang Liu, Chaofeng Guo , and Yang Sun 

Research Article (11 pages), Article ID 5537811, Volume 2021 (2021)

EZH2 Mediates miR-146a-5p/HIF-1 α to Alleviate Inflammation and Glycolysis after Acute Spinal Cord Injury

Shuangfei Ni, Bo Yang, Lei Xia, and Huafeng Zhang 



Research Article (14 pages), Article ID 5591582, Volume 2021 (2021)

An Aptamer-Based Antagonist against the Receptor for Advanced Glycation End-Products (RAGE) Blocks Development of Colorectal Cancer

Jihui Zheng , Wenjing Zhu , Fang He , Zhu Li , Na Cai , and Hong-Hui Wang 



Research Article (8 pages), Article ID 9958051, Volume 2021 (2021)

Catheter-Based Radiofrequency Renal Sympathetic Denervation Decreases Left Ventricular Hypertrophy in Hypertensive Dogs

Shan Tu , Zhi-Jie Shen, Xiao-Yan Wang, Li-Xiong Zeng, and Zhi-Hui Zhang 


Research Article (14 pages), Article ID 9938486, Volume 2021 (2021)

Recombinant Human Thymosin Beta-4 Protects against Mouse Coronavirus Infection

Rui Yu, Yunyun Mao, Kai Li, Yanfang Zhai, Yue Zhang, Shuling Liu, Yuemei Gao, Zhengshan Chen, Yanhong Liu, Ting Fang, Mengsu Zhao, Ruihua Li, Junjie Xu , and Wei Chen 



Research Article (9 pages), Article ID 9979032, Volume 2021 (2021)

Gene Expression Profiling and Biofunction Analysis of HepG2 Cells Targeted by Crocetin

Yi-Ling Wen, Yong Li, Guangcheng Zhu, Zhibing Zheng, Meng Shi, and Si Qin 

Research Article (10 pages), Article ID 5512166, Volume 2021 (2021)

Whole-Transcriptome RNA Sequencing Reveals Significant Differentially Expressed mRNAs, miRNAs, and lncRNAs and Related Regulating Biological Pathways in the Peripheral Blood of COVID-19 Patients

Cai-xia Li , Jian Chen, Shu-kai Lv, Jin-hui Li, Lei-lei Li, and Xiao Hu 

Research Article (22 pages), Article ID 6635925, Volume 2021 (2021)



Contents

The Regulatory Role of α -Ketoglutarate Metabolism in Macrophages

Shaojuan Liu , Jie Yang , and Zhenfang Wu 




Review Article (7 pages), Article ID 5577577, Volume 2021 (2021)

Dihydromyricetin Acts as a Potential Redox Balance Mediator in Cancer Chemoprevention

Liang Chen, Meng Shi, Chenghao Lv, Ying Song, Yuanjie Wu, Suifei Liu, Zhibing Zheng, Xiangyang Lu , and Si Qin 



Review Article (18 pages), Article ID 6692579, Volume 2021 (2021)

The Diagnosis Value of a Novel Model with 5 Circulating miRNAs for Liver Fibrosis in Patients with Chronic Hepatitis B

Qingqing Zhang, Qidi Zhang, Binghang Li, Ying Qu, Zhenghong Li, Lungen Lu , Rongzhou Li , and Xiaobo Cai 


Research Article (11 pages), Article ID 6636947, Volume 2021 (2021)

Phylogenetic Analysis of ALV-J Associated with Immune Responses in Yellow Chicken Flocks in South China

Qihong Zhang , Guodong Mo, Tingting Xie, Zihao Zhang, Huali Fu, Ping Wei, and Xiquan Zhang 






Research Article (13 pages), Article ID 6665871, Volume 2021 (2021)

Yeast Fermentate Prebiotic Ameliorates Allergic Asthma, Associating with Inhibiting Inflammation and Reducing Oxidative Stress Level through Suppressing Autophagy

Subo Gong, Xiaoying Ji, Jing Su, Yina Wang, Xianghong Yan, Guyi Wang, Bin Xiao, Haiyun Dong, Xudong Xiang, and Shaokun Liu 


Research Article (13 pages), Article ID 4080935, Volume 2021 (2021)

Effect of Oral Administration with *Lactobacillus plantarum* CAM6 Strain on Sows during Gestation-Lactation and the Derived Impact on Their Progeny Performance

César Betancur , Yordan Martínez , Guillermo Tellez-Isaias , Rogel Castillo , and Xinghua Ding 




Research Article (8 pages), Article ID 6615960, Volume 2021 (2021)

circRNA circ_102049 Implicates in Pancreatic Ductal Adenocarcinoma Progression through Activating CD80 by Targeting miR-455-3p

Jie Zhu, Yong Zhou, Shanshan Zhu, Fei Li, Jiajia Xu, Liming Zhang, and Hairong Shu 

Research Article (30 pages), Article ID 8819990, Volume 2021 (2021)

Associations among Dietary Omega-3 Polyunsaturated Fatty Acids, the Gut Microbiota, and Intestinal Immunity

Yawei Fu , Yadong Wang , Hu Gao, DongHua Li, RuiRui Jiang, Lingrui Ge, Chao Tong, and Kang Xu 


Review Article (11 pages), Article ID 8879227, Volume 2021 (2021)

Early T-Cell Precursor Leukemia Has a Higher Risk of Induction-Related Infection among T-Cell Acute Lymphoblastic Leukemia in Adult

Kangyu Huang , Min Dai, Qiuli Li, Nannan Liu, Dainan Lin, Qiang Wang, Xuan Zhou, Zhixiang Wang, Ya Gao, Hua Jin, Xiaoli Liu, Qifa Liu , and Hongsheng Zhou 



Research Article (10 pages), Article ID 8867760, Volume 2020 (2020)

Therapeutic Effect of Ginsenoside Rd on Experimental Autoimmune Encephalomyelitis Model Mice: Regulation of Inflammation and Treg/Th17 Cell Balance

Bo Jin, Chixiao Zhang, Yu Geng, and Mei Liu 


Research Article (12 pages), Article ID 8827527, Volume 2020 (2020)

High-Fructose Diet Increases Inflammatory Cytokines and Alters Gut Microbiota Composition in Rats

Yong Wang , Wentao Qi , Ge Song, Shaojie Pang, Zhenzhen Peng, Yong Li, and Panli Wang



Research Article (10 pages), Article ID 6672636, Volume 2020 (2020)

Effects of Dietary Histidine on Growth Performance, Serum Amino Acids, and Intestinal Morphology and Microbiota Communities in Low Protein Diet-Fed Piglets

Meng Kang, Jie Yin , Jie Ma, Xin Wu, Ke Huang, Tiejun Li, and Long Ouyang


Research Article (7 pages), Article ID 1240152, Volume 2020 (2020)

Cangfudaotan Decoction Alleviates Insulin Resistance and Improves Follicular Development in Rats with Polycystic Ovary Syndrome via IGF-1-PI3K/Akt-Bax/Bcl-2 Pathway

Chenye Wang , Caifei Ding, Zhoujia Hua, Chunyue Chen, and Jia Yu 



Research Article (16 pages), Article ID 8865647, Volume 2020 (2020)

The Association of Fecal Microbiota in Ankylosing Spondylitis Cases with C-Reactive Protein and Erythrocyte Sedimentation Rate

Gang Liu, Yonghong Hao, Qiang Yang, and Shucai Deng 



Research Article (8 pages), Article ID 8884324, Volume 2020 (2020)

Alterations in the Blood Parameters and Fecal Microbiota and Metabolites during Pregnant and Lactating Stages in Bama Mini Pigs as a Model

Cui Ma, QianKun Gao, WangHong Zhang, Md. Abul Kalam Azad , and XiangFeng Kong 



Research Article (13 pages), Article ID 8829072, Volume 2020 (2020)

Crude Radix Aconiti Lateralis Preparata (FuZi) with *Glycyrrhiza* Reduces Inflammation and Ventricular Remodeling in Mice through the TLR4/NF- κ B Pathway

Ping Yan, Wen Mao, Lushuai Jin, Mingsun Fang, Xia Liu, Jiali Lang, Lu Jin, Beibei Cao, Qiyang Shou , and Huiying Fu 

Research Article (13 pages), Article ID 5270508, Volume 2020 (2020)



Inhibitory Effects of Apigenin on Tumor Carcinogenesis by Altering the Gut Microbiota

Shichang Bian , Hongjuan Wan, Xinyan Liao, and Weisheng Wang 

Research Article (9 pages), Article ID 7141970, Volume 2020 (2020)

Contents

Essential Oil and Juice from Bergamot and Sweet Orange Improve Acne Vulgaris Caused by Excessive Androgen Secretion

Peng Sun, Liang Zhao , Nanhai Zhang, Chengtao Wang, Wei Wu, Arshad Mehmood, Liebing Zhang, Baoping Ji, and Feng Zhou 



Research Article (10 pages), Article ID 8868107, Volume 2020 (2020)

Metabolic Profiling by UPLC–Orbitrap–MS/MS of Liver from C57BL/6 Mice with DSS-Induced Inflammatory Bowel Disease

Zhongquan Xin, Zhenya Zhai, Hongrong Long, Fan Zhang, Xiaojun Ni, Jinping Deng, Lunzhao Yi , and Baichuan Deng 

Research Article (13 pages), Article ID 6020247, Volume 2020 (2020)



miRNA-10a-5p Alleviates Insulin Resistance and Maintains Diurnal Patterns of Triglycerides and Gut Microbiota in High-Fat Diet-Fed Mice

Yawei Guo , Xiaohui Zhu, Sha Zeng, Mingyi He, Xiurong Xing, and Changyuan Wang 

Research Article (8 pages), Article ID 8192187, Volume 2020 (2020)

Review Article

The Role of Oxidative Stress and Antioxidant Balance in Pregnancy

Tarique Hussain ^{1,2}, **Ghulam Murtaza**,³ **Elsayed Metwally**,⁴ **Dildar Hussain Kalhoro**,⁵ **Muhammad Saleem Kalhoro**,⁶ **Baban Ali Rahu**,³ **Raja Ghazanfar Ali Sahito**,⁷ **Yulong Yin**,⁸ **Huansheng Yang**,⁹ **Muhammad Ismail Chughtai**,² and **Bie Tan** ¹

¹College of Animal Science and Technology, Hunan Agricultural University, Changsha, 410128 Hunan, China

²Animal Science Division, Nuclear Institute for Agriculture and Biology College, Pakistan Institute of Engineering and Applied Sciences (NIAB-C, PIEAS), Faisalabad 38000, Pakistan

³Department of Animal Reproduction, Faculty of Animal Husbandry and Veterinary Sciences, Sindh Agriculture University, Tandojam, Sindh 70050, Pakistan

⁴Department of Cytology & Histology, Faculty of Veterinary Medicine, Suez Canal University, Ismailia, Egypt

⁵Department of Veterinary Microbiology, Faculty of Animal Husbandry and Veterinary Sciences, Sindh Agriculture University, Tandojam, Sindh 70050, Pakistan

⁶Department of Animal Products Technology, Faculty of Animal Husbandry and Veterinary Sciences, Sindh Agriculture University, Tandojam, Sindh 70050, Pakistan

⁷Institute of Neurophysiology, University of Cologne, Cologne 50931, Germany

⁸Institute of Subtropical Agriculture, Chinese Academy of Sciences, Changsha, 410125 Hunan, China

⁹Hunan International Joint Laboratory of Animal Intestinal Ecology and Health, Laboratory of Animal Nutrition and Human Health, College of Life Sciences, Hunan Normal University, Changsha, Hunan 410081, China

Correspondence should be addressed to Tarique Hussain; drtariquerahoo@gmail.com and Bie Tan; bietan@hunau.edu.cn

Received 15 March 2021; Revised 16 August 2021; Accepted 4 September 2021; Published 27 September 2021

Academic Editor: Mingliang Jin

Copyright © 2021 Tarique Hussain et al. This is an open access article distributed under the Creative Commons Attribution License, which permits unrestricted use, distribution, and reproduction in any medium, provided the original work is properly cited.

It has been widely known that oxidative stress disrupts the balance between reactive oxygen species (ROS) and the antioxidant system in the body. During pregnancy, the physiological generation of ROS is involved in a variety of developmental processes ranging from oocyte maturation to luteolysis and embryo implantation. While abnormal overproduction of ROS disrupts these processes resulting in reproductive failure. In addition, excessive oxidative stress impairs maternal and placental functions and eventually results in fetal loss, IUGR, and gestational diabetes mellitus. Although some oxidative stress is inevitable during pregnancy, a balancing act between oxidant and antioxidant production is necessary at different stages of the pregnancy. The review aims to highlight the importance of maintaining oxidative and antioxidant balance throughout pregnancy. Furthermore, we highlight the role of oxidative stress in pregnancy-related diseases.

1. Introduction

Several reproductive problems have been linked to oxidative stress. Oxidative stress occurs when the body's antioxidant system is depleted owing to an excess of reactive oxygen species (ROS). ROS are highly reactive molecules that are unstable and short-lived. These molecules contribute to the control

of signaling pathways, as well as cellular and physiological processes [1]. However, excess ROS may cause cellular toxicity [2]. Animals have an enzymatic antioxidant defense mechanism that suppresses the formation of reactive oxygen species (ROS). It is worth noting that cellular integrity is maintained by a balance of enzymatic and non-enzymatic antioxidant systems. When oxidative stress increases, both

antioxidant systems are depleted resulting in reproductive problems [3, 4]. Enzymatic antioxidants like glutathione peroxidase (GPx) and superoxide dismutase (SOD) are antioxidants to neutralize free radicals. On other hand, the non-enzymatic antioxidants such as vitamin C, vitamin E, plant polyphenol, carotenoids, and glutathione interrupt free radical chain reactions. Importantly, antioxidants may have therapeutic promise in the treatment of reproductive-related problems [5].

ROS has a biological effect on various reproductive processes, such as oocyte maturation, fertilization, embryo development, pregnancy, as well as oocyte maturation and fertility. A number of research studies, including animals and humans, showed that ROS has been implicated with female reproduction, particularly ovaries [6–8], fallopian tubes [9] and embryos [10].

The primary function of the placenta is to exchange nutrients and oxygen between mother and fetus. Therefore, interference in these functions leads to hypoxia due to oxidative stress. The disruption in placental function is due to many factors resulting in pregnancy complications [11]. A large number of studies reported that pregnancy problems have been associated with overwhelming oxidative stress from the placenta and or maternal tissues [12]. Other mechanisms are also implicated in the etiology of these complications; oxidative stress has evolved to regulate the cellular and molecular pathways such as altered angiogenesis and inflammation to mediate disease outcomes [13]. The oxidative scenario develops due to increased ROS and depletion of the antioxidant system [14]. Though the development of abnormal oxidative stress leads to spontaneous abortion, idiopathic recurrent pregnancy loss and embryogenesis defect [2, 15–18].

Oxidative stress has been linked to a number of metabolic processes that affect animal health and performance [19]. The study of oxidative stress has increased as a result of its role in adverse pregnancy outcomes. Oxidative stress exhibits dual functions, it aids in the maintenance of redox balance and it plays a part in female reproductive processes. As a result, oxidative stress may aggravate IUGR, endometriosis, and other reproductive issues. Oxidative stress also regulates signaling networks including Kelch-like ECH-associated protein 1, Nuclear factor erythroid 2-related factor 2 (Keap1-Nrf2), nuclear factor kappa-B (NF- κ B), forkhead transcription factors of the O class (FOXO) and Mitogen-activated protein kinase (MAPK). Lastly, targeting these pathways appears attractive as a potential therapeutic strategy against pregnancy-related anomalies [5].

2. Oxidative Stress and Its Regulatory Mechanism

ROS are oxidative metabolic byproducts that play an important part in cellular activity. They are also implicated in a number of pathological diseases, including *in-vitro* and *in-vivo* pregnancy difficulties [20–25]. The factors responsible for overproduction of ROS are ultraviolet radiation, cigarette smoking, alcohol, non-steroidal anti-inflammatory medication, ischemia-reperfusion injury, chronic infections, and

inflammatory diseases [26, 27]. The enzyme superoxide dismutase converts the superoxide anion radical to hydrogen peroxide and oxygen [28], and catalase eliminates hydrogen peroxide when its quantities in the cell are higher [29]. Glutathione reductase is found throughout the body tissues and operates similarly to GPx. Using several systems; the GSR enzyme reduced oxidized glutathione by utilizing NADPH [30, 31].

The secondary defense is based on the GPx enzyme, which possesses peroxidase activity and may eliminate lipid hydroperoxides irrespective phospholipase A2 [32]. There are also a number of oxido-reductases that catalyse thiol and other protein reduction processes. Protective enzymes against free radicals are produced once the cellular components have been oxidatively damaged. For example, DNA nuclear enzymes are known to protect DNA from oxidative damage induced by free radicals [33]. Vitamin E functions as a cofactor for glutathione peroxidase enzymes, and its presence in all cellular membranes suggests that it can protect lipids from oxidation. The ascorbic acid-GSH redox couple directly reduces the tocopherol radical. While β -carotene functions in concert with vitamin E, which is a strong scavenger of free radicals, but β -carotene only works at low oxygen pressure. Vitamin E, on the other hand, protects β -carotene against oxidative damage [34]. In addition, some antioxidants work as free radical quenchers [35]. Early pregnancy deficiency in antioxidants has been associated with the development of maternal-related disorders such as gestational hypertension, gestational diabetes, and other complications [36]. Therefore, the generation of ROS molecules controls several signaling pathways that govern a variety of cellular functions. The activation of these signals causes a change in cellular function, which has a pathogenic effect on the cell [37].

3. Oxidative Stress Scenarios in Pregnancy

In normal pregnancy, the developing tissues and organs of the fetus require enough nutrition and oxygen. These processes generate ROS in both maternal and fetal tissues that influence fetal growth development. To provide a suitable environment for the fetus and maternal body, the balance between ROS and antioxidants could be maintained [38]. During pregnancy, the body undergoes numerous physiological changes. The evidence of ROS formation in the second trimester of pregnancy was assumed by the researchers. Increased production of ROS occurs due to the enhanced metabolism, high consumption of oxygen and utilization of fatty acids. During third trimester of pregnancy, increase insulin resistance, fat catabolism, and release of free fatty acids resulting in enhanced production of hydrogen peroxide [39]. Placental cells have a lot of mitochondria, which are the main source of pro-oxygenates. The superoxide anion radical produces more radical species and their generation rises as the pregnancy continues.

Several studies have found that oxidative stress is linked to pregnancy complications that may influence fetal development. The major causes are a lack of nutrition and oxygen for developing fetuses, which causes hypoplasia and disrupts

placental function [39, 40]. The difference in total plasma antioxidants status between pregnant and non-pregnant individuals has been observed, implying a low level in the first phase of pregnancy. The total antioxidant capacity of a pregnant woman increases during the second and third trimesters, and by the last week of pregnancy, it has reached the level of a non-pregnant woman. TAC activity increases after the 8th week of pregnancy, and these changes are linked to differences in plasma uric acid levels [41]. Furthermore, reduced TAC levels in pregnancy have been linked to low levels of serum albumin, bilirubin, and vitamin E [42]. As a result, it appears that plasma SOD activity is reduced during pregnancy [43]. The SOD reduction promoted triglycerides, total cholesterol, and low-density lipoprotein (LDL) cholesterol levels in blood plasma. Therefore, SOD refers as indicator of oxidative stress and lipid peroxide activity followed by 25 weeks of pregnancy. As a result, lipid peroxidation levels in the blood are higher in pregnant women, serving as a marker of oxidative stress. Previous studies have found that supplementing pregnant individuals with the dietary vitamins, antioxidants, and minerals enhanced TAC activity [42–44].

4. Oxidative Stress in Ovary, Uterus and Placenta

Almost every stage of pregnancy is affected by ROS. ROS is known to be the important regulator of ovarian cellular activity [45]. The ROS positive impact has been already mentioned. Previous studies showed that the presence of SOD in ovary, copper-zinc SOD (Cu-Zn SOD) in granulosa cells of follicles and manganese superoxide dismutase (MnSOD) in luteal cells of the corpus luteum in rats [46]. The sources of ROS in the follicles are macrophages, leukocytes and cytokines [26]. Ovulation is dependent on concentration of ROS. ROS suppressors have been demonstrated to interfere with the ovulatory process [47]. Follicles development is associated with an increased metabolic function of granulosa cells, particularly excess amount of cytochrome P450 and steroidogenesis [48]. The presence of ROS in pre-ovulatory follicles alters blood flow and finally leads to follicle rupture [49]. Furthermore, FSH stimulates the synthesis of estrogen, while the overexpression of CAT in developing follicles protects them from apoptosis, ensuring that ovarian function is preserved [50]. Depletion of oxygen is required for follicular angiogenesis [6]. The corpus luteum contributes to functional luteolysis by producing ROS. During the luteal phase, both the ROS and antioxidants are linked to progesterone production [51]. The beneficial effects of ROS and antioxidants in female reproductive and pregnancy outcomes are depicted in Table 1.

The developing fetus has a high energy requirement due to the placental hyperactive metabolic rate, resulting in oxidative stress [52]. Of note, that superoxide anions produced by placental mitochondria appear to be the essential source of ROS and lipid peroxidation in the placenta [53]. As the pregnancy progresses, mitochondrial synthesis of lipid peroxides, free radicals, and vitamin E may also increase [54]. The placenta and large blood arteries mature slowly in the

second phase of the pregnancy. After that, maternal blood pumps via interstitial space into the mother's spiral artery [54, 55]. Free radicals are abundant in placental tissues, and oxidation occurs throughout the process. With the help of antioxidant activity, the placenta can slowly adapt to the environment after recovering from stress [40].

SOD activity decreases during the late luteal phase due to increased amounts of lipid peroxide. Importantly, ROS are known to have a role in numerous phases of the endometrial cycle, and may also produce PGF₂ through NF- κ B activation [56]. Estrogen and progesterone levels dropped significantly as a result of lower SOD expression. In a consequence, ROS accumulates in the uterus, leading to implantation failure. The basal level of ROS controls angiogenic activity in the endometrium and results in endometrial regeneration during each cycle. Thus, appropriate ROS concentration is critical for normal homeostasis. However, an increased level of ROS from the placenta has been associated with pregnancy-related disorders [57–59]. The TNF- α cytokine that influences endothelial cell dysfunction and the antioxidant Mn-SOD are both disrupted and have protective effects. The production of cytokines and prostaglandins is increased by ROS-related poor placental function, producing endothelial cell injury and contributing to preeclampsia [60].

5. Regulation of Multiple Signaling Pathways by Oxidative Stress

Oxidative stress has been linked to influence signaling pathways, particularly in reproductive diseases ranging from egg production to ovulation. It alters immune system of the uterus resulting in embryonic failure [61, 62]. Oxidative stress has also been involved in regulating molecular pathways in reproductive disorders such as p38 MAPK, Keap1-Nrf2, the Jun N-terminal kinase (JNK), the FOXO family, and apoptotic pathways. Therefore, the research on this aspect may yield new insights that might influence female reproductive system.

Nrf2 is a signaling molecule that protects cellular function by acting as an antioxidant in response to oxidative stress [63]. Physiologically, Nrf2 binds with Keap1 in the cytoplasm before being degraded by the proteasome [64]. Once the Nrf2 is activated, it translocate into nucleus, where it activates several antioxidant genes [65]. In contrast, activation of antioxidant genes and restoration of vascular redox homeostasis are required when OS is evident suggesting the crucial function of Nrf2 [66]. The deficiency of Nrf2 induced fetal DNA damage and neurological discrepancies and inactivation of Nrf2 were also exhibited inflammation triggered trophoblastic apoptosis. Previous evidence showed that Nrf2 plays an important role in pregnancy and protects the fetus from OS *in-utero* [67]. The maternal immune system is susceptible to Nrf2. Nrf2 is only decreased once the full-term foetus is delivered in a normal pregnancy. When a fetus is infected *in utero*, the Nrf2 expression is favorably reduced [68]. In the case of OS-induced metritis, it is expected that Nrf2 would be considerably decreased, and Keap1 would bind to Nrf2. Similarly, FOXO3 is essential in the interaction between Keap1 and Nrf2. In the absence

TABLE 1: Positive effect of ROS and antioxidant system in various events of female reproduction and pregnancy outcomes.

Oxidant/antioxidant compounds	Functional activity	Species	References
↑ expression of GSTm2	Preparation of uterus for blastocyst implantation	Mouse	[130]
↑ GPX and GSR activities	Regulator of H ₂ O ₂ and cell death in placental progression	Sheep	[131]
Silence the expression of GPX4	Influencing embryonic brain and heart functions	Mouse	[132]
↓ hydrogen peroxide and superoxide radical	Control uterine contractions	Humans	[133]
↑ SOD1, GPX and GST activities in early pregnancy	Rescue Corpus luteum form apoptosis	Sheep	[134]
↑ CAT and GPX and oviduct GSH in estrus cycle	Govern hydrogen peroxide during fertilization	Cow	[135]
↑ expression of SOD1 in early pregnancy	Directions of luteal functions	Human	[136]
↑ CAT and GPX, and GSH in placenta tissues	Regulates hydrogen peroxide and activation of placental differentiation	Human	[137]
↑ CAT, SOD and GPX in placental and fetal tissues	Defense against ROS toxicity in fetoplacental system	Human	[138]
↑ uterine peroxide at blastocyst attachment	Defense to negative effects of hydrogen peroxide actions	Rat	[139]

of FOXO3, Nrf2 is activated by AKT and protects cells against OS [69]. Lastly, we hypothesized that OS causes inflammation in the reproductive system, with FOXO3 playing a role in the interaction between Keap1 and Nrf2, which may be used as a marker for OS insults.

NF- κ B is an inert molecule, its family comprises five transcription factors c-Rel, p50, p52, RelB and RelA (p65) [70]. NF-B is a redox-sensitive transcription factor that is the primary regulator of the inflammatory response [71]. Therefore, the beneficial effects of NF- κ B are evident in embryonic stress that activates NF- κ B and other diverse inflammatory cytokines which persuades apoptosis within placenta [72]. Hence, it was concluded that NF- κ B plays an important role in the cell survival by releasing anti-apoptotic genes. In normal conditions, NF- κ B is bound to inhibitory I κ B proteins and remains inactive in the cytoplasm. The breakdown of I κ B proteins activates NF-B, which subsequently translocate into the nucleus and generates desirable genes, whereas I κ B proteins are mediated by the I κ B kinase (IKK) complex (IKK α and IKK β) [73]. Increased expression of NF- κ B in cultured endometrial stromal cells has been found in reproductive diseases such as endometriosis [74]. Altered production of NF- κ B production has been associated with inflammation. Endometriosis is a condition induced by OS which increases the concentration of TNF- α , resulting in inflammation thereby; NF- κ B is activated. Moreover, IL-1 β activates NF- κ B, which in turn produces inflammatory cytokines [75], comprising macrophage migration inhibitory factor (MIF) in endometrial stromal cells [76] and TNF- α in immortalized epithelial (12Z) cell line [77]. In summary, OS-mediated reproductive disorders are caused by NF- κ B activation.

FOXO1 and FOXO3 have been contributed to OS and pregnancy. The FOXO subfamily of Forkhead transcription factors is a direct downstream target of the PI3K/Akt pathway [78]. The family of FOXO proteins is involved in different biological processes such as proliferation, apoptosis, autophagy, metabolism, inflammation, differentiation and stress tolerance [79]. The FOXC1 displays a pivotal role in

reproduction and also mediates cyclic differentiation and apoptosis in normal endometrium [80]. Recent studies have shown that FOXO1 knockdown disrupts the expression of over 500 genes in decidualized human endometrial stromal cells [81]. Previous research has shown that FOXO transcription factors can control multiple gene responses to change hormone levels [82]. Besides, that FOXO1 is also responsible for the induction of decidual marker genes, including WNT4, prolactin (PRL) and insulin-like growth factor-binding protein 1 (IGFBP1) [83].

Three signaling molecules are triggered by the extracellular milieu, including ERK, which is activated by inflammation and growth factors, and JNK and p38 MAPK, which are mostly activated by stress and inflammation [84]. It has been shown that ERK activation is increased in endometrial tissue, suggesting that ERK may play a role in endometriosis and phosphorylated ERK is increased in primary eutopic epithelial cells [85]. ERK activation can also be influenced by oxidative stress. In response to normal women, hydrogen peroxide causes ERK phosphorylation in endometriotic stromal cells [86].

6. Contribution of Oxidative Stress in Pregnancy Complications

6.1. Intrauterine Growth Restriction. Intrauterine growth restriction (IUGR) is a pregnancy ailment in which an underweight/incomplete fetus develops in the uterus [87]. The causes are multifactorial such as maternal, fetal, placental, infectious, or genetics [88]. About 76% of intrauterine deaths have been associated with IUGR [89]. The most significant cause of IUGR is utero-placental dysfunction occurs due to the congested maternal utero-placental blood flow [90]. Proper functioning of the placenta requires greater energy demand for cell growth, proliferation and metabolic activity which in turn produce oxidative stress. Oxidative stress plays an essential role against various stimuli which influence placental function [91]. Cellular injury occurs as a result of lipid peroxidation and fatty acid oxidation, and

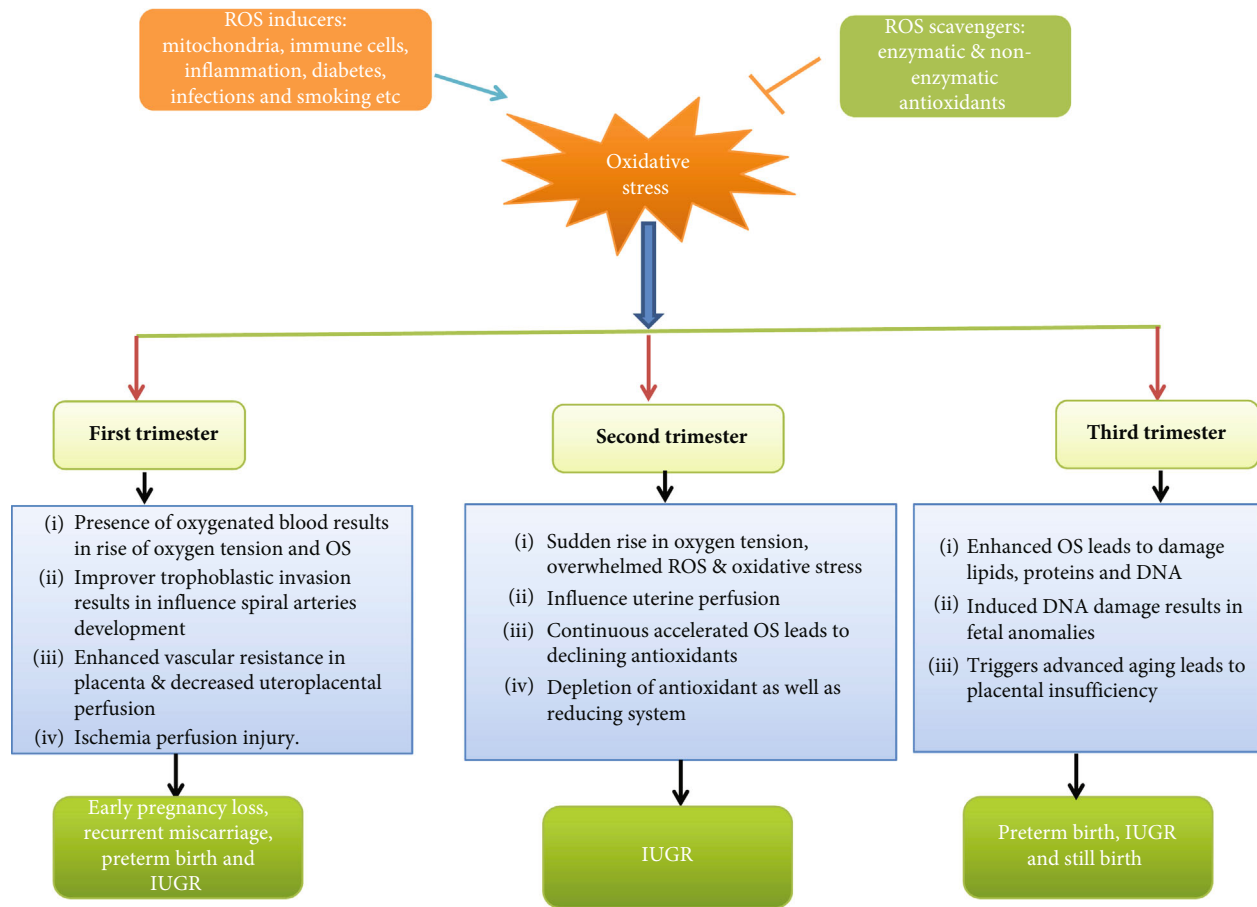


FIGURE 1: The Impact of Oxidative Stress on Pregnancy Outcomes.

it is mostly utilised to identify oxidative stress indicators [92]. Evidence of IUGR in livestock has been raised through environmental factors and affects goats, sheep, pigs and other animals. Of note, that significant evidence of IUGR exists in multi-fetal animals including pigs. It has been documented those animals with this condition have reduced birth weight, postnatal growth, development and liver dysfunction [93]. A detailed description of IUGR occurrences in clinical and health deviations is well been ascribed in the previous studies [94–96]. More evidence is required to be revealed the underlying molecular mechanisms.

6.2. Spontaneous Miscarriage and Recurrent Pregnancy Loss. Spontaneous abortion can be classified as loss of pregnancy before 20 weeks of gestation. The incidence may range from 8-20% in pregnancies and is due to chromosomal aberration, which accounts for 50% of all miscarriages. While, the rest are associated with congenital and uterine malfunctions, infections, maternal diseases and unknown causes [97].

In early pregnancy losses, elevated levels of MDA and lipid peroxides were observed in placental tissues in comparison with controls. Previous studies have shown that overloading of ROS could lead to the premature and sudden formation of maternal placental perfusion [2]. Other evidence reported that oxidative stress damage the trophoblast and ultimately leading to early pregnancy losses. The inci-

dence of oxidative stress occurred due to the depletion of the antioxidants system and thus unable to scavenge free radicals [87, 98]. Although there is diversity in previous studies, it seems to be a relationship between ROS and antioxidants in miscarriage. The abnormal placentation may arise from syncytiotrophoblasts and may be vulnerable to idiopathic recurrent pregnancy loss [97]. Oxidative stress enables the potential to influence pregnancies due to the depletion of antioxidant capacity within the body [99]. The influence of oxidative stress in pregnancy problems is depicted in Figure 1. The issue of recurrent pregnancy losses, research gaps, and their treatment has been thoroughly reviewed [100, 101].

6.3. Gestational Diabetes Mellitus (GDM). GDM is a type of diabetes mellitus in which pregnant women develops glucose intolerance to a different degree [102]. It was reported in 2-5% of pregnancies while; data suggested the incidences increased up to 18% in all pregnancies [103]. GDM develops during the second trimester of pregnancy, causing fetal macrosomia, perinatal mortality, and making mother vulnerable for T2DM [102, 104].

The pregnancy has been linked to an imbalance of pro and anti-inflammatory mediators [105]. The levels of T cells subsets were increased in women with GDM compared to control healthy subjects whereas; T cells expressing CTLA-

4, a downregulation of the immune system which lightly expressed in Tregs were suppressed [106]. Changes in the Treg population suggest that the Treg pool in GDM is becoming less active [76]. Thus, it suggests that the lack of immune down-regulation helps maternal-fetal tolerance. Although, the toll-like receptors TLR-2 and TLR-4 stimulate inflammatory cytokines which were enhanced in peripheral blood mononuclear cells of women with GDM [107]. Previous literature revealed the ambiguous results of TNF- α in GDM condition [79, 82], but more descriptive role of GDM is well-highlighted somewhere else [108]. An evidence of oxidative stress-related problems during pregnancy is well-reviewed by others [12, 109].

7. Antioxidant Approaches in Pregnancy

The detrimental effects of oxidative stress and ROS on female reproduction system have been well illustrated for since long [110]. It was suggested that the generation of ROS is impaired by cytochrome P450 and corpus luteum, which itself is considered a key source. The initiation of oocyte maturation and others processes are mostly affected by different levels of ROS and antioxidants [6]. Endometriosis and unexplained infertility conditions are also linked to the OS [111].

Antioxidant supplementation possess positive effects through a variety of pathways, including direct scavenging of reactive oxygen species (ROS) and damage repair [112]. The protective effects on fertility consisting enhanced blood circulation in endometrium, reduced hyperandrogenism, lowered insulin resistance, and positive impact on prostaglandin synthesis and steroidogenesis [112–114]. A current systematic review indicates the positive impact of antioxidants in female fertility [115]. Antioxidants were also involved in enhancing live birth weight and clinical pregnancy rates. Though, the evidence is poor with a slight increase to high heterogeneity due to the trials on enrolled women offering various kinds of antioxidants. Antioxidants have shown various responses when they are taken alone or in combination exerted a positive effect on pregnancy rate [116]. Moreover, dietary/injectable source of antioxidants during periparturient period provide beneficial effects on pregnancy outcome and growth performance of suckling kids of goats [117, 118].

There is evidence that increased antioxidant levels confront and scavenge ROS in women who have repeated abortions as a result of ROS overload. Previous research has found that women with recurrent abortion have higher levels of lipoperoxides and lower amounts of vitamin A, E, and beta carotene, suggesting the role of ROS. When compared to healthy subject, glutathione activity was low in women who had recurrent abortions [44, 119]. Moreover, selenium concentration from hair samples was also significantly reduced in recurrent abortion than the healthy pregnancies [120]. Increased glucose levels during pregnancy cause teratogenic consequences due to chemical changes and DNA rearrangements. Increased glucose causes the formation of glycation products, which affect genomic function and negatively regulate embryonic development. In diabetic

pregnancy, changes in membrane lipids induce biological prostaglandin events, and an enhanced level of ROS causes dysmorphogenesis in the fetus [121]. A reduced level of lipid peroxidation in women with GDM was reported due to depletion of antioxidants activity. Hydroperoxide production affects prostaglandin synthesis patterns, which may result in morbidity owing to antioxidant depletion [122]. GDM also triggers oxidative stress in fetus, thus the intake of antioxidants during pregnancy is essential factor for improving pregnancy health [123]. Further, a detailed description on the role of antioxidants in pregnancy is well-discussed in the previous studies [2, 44, 124–129].

8. Conclusion

Antioxidant defense has been established to regulate the generation of ROS; however the increased amount of ROS cannot be controlled, resulting in oxidative stress. So, the potential strategies of antioxidant to decrease ROS levels are critical. According to a large number of studies, oxidative stress is the primary contributing factor in a variety of pregnancy complications. Overstimulation of ROS can cause hyperglycemia, IUGR, miscarriage, and spontaneous abortion throughout all stages of pregnancy. Placental oxidative stress is caused by a number of variables, including maternal history, genetics, and environmental factors, and can lead to negative pregnancy outcomes. Future research should focus on improving the breakdown of intracellular ROS and enhancing antioxidant bioavailability. Targeting signaling molecules with natural bioactive compounds will be used to minimize the occurrence of reproductive problems.

Conflicts of Interest

All authors have no any conflict of interest.

Acknowledgments

This project was funded by the National Natural Science Foundation of China (32072745, 31960666) and Innovation Province Project (2019RS3021).

References

- [1] D. Pereira, N. E. de Long, R. C. Wang, F. T. Yazdi, A. C. Holloway, and S. Raha, "Angiogenesis in the placenta: the role of reactive oxygen species signaling," *BioMed Research International*, vol. 2015, Article ID 814543, 12 pages, 2015.
- [2] L. Poston, N. Igosheva, H. D. Mistry et al., "Role of oxidative stress and antioxidant supplementation in pregnancy disorders," *American Journal of Clinical Nutrition*, vol. 94, 6 Suppl, pp. 1980s–1985s, 2011.
- [3] M. T. Lin and M. F. Beal, "Mitochondrial dysfunction and oxidative stress in neurodegenerative diseases," *Nature*, vol. 443, no. 7113, pp. 787–795, 2006.
- [4] N. Khansari, Y. Shakiba, and M. Mahmoudi, "Chronic inflammation and oxidative stress as a major cause of age-related diseases and cancer," *Recent Patents on Inflammation & Allergy Drug Discovery*, vol. 3, no. 1, pp. 73–80, 2009.

- [5] J. Lu, Z. Wang, J. Cao, Y. Chen, and Y. Dong, "A novel and compact review on the role of oxidative stress in female reproduction," *Reproductive Biology and Endocrinology*, vol. 16, no. 1, pp. 1–18, 2018.
- [6] H. R. Behrman, P. H. Kodaman, S. L. Preston, and S. Gao, "Oxidative stress and the ovary," *Journal of the Society of Gynecologic Investigation*, vol. 8, 1_suppl, pp. S40–S42, 2001.
- [7] L. Sabatini, C. Wilson, A. Lower, T. Al-Shawaf, and J. G. Grudzinski, "Superoxide dismutase activity in human follicular fluid after controlled ovarian hyperstimulation in women undergoing in vitro fertilization," *Fertility and Sterility*, vol. 72, no. 6, pp. 1027–1034, 1999.
- [8] M. Jozwik, S. Wolczynski, M. Jozwik, and M. Szamatowicz, "Oxidative stress markers in preovulatory follicular fluid in humans," *Molecular Human Reproduction*, vol. 5, no. 5, pp. 409–413, 1999.
- [9] S. El Moutassim, P. Guerin, and Y. Menezo, "Expression of genes encoding antioxidant enzymes in human and mouse oocytes during the final stages of maturation," *Molecular Human Reproduction*, vol. 5, no. 8, pp. 720–725, 1999.
- [10] P. Guerin, S. El Moutassim, and Y. Menezo, "Oxidative stress and protection against reactive oxygen species in the pre-implantation embryo and its surroundings," *Human Reproduction Update*, vol. 7, no. 2, pp. 175–189, 2001.
- [11] M. H. Schoots, S. L. Gordijn, S. A. Scherjon, H. van Goor, and J. L. Hillebrands, "Oxidative stress in placental pathology," *Placenta*, vol. 69, pp. 153–161, 2018.
- [12] A. C. Pereira and F. Martel, "Oxidative stress in pregnancy and fertility pathologies," *Cell Biology and Toxicology*, vol. 30, no. 5, pp. 301–312, 2014.
- [13] S. J. Holdsworth-Carson, R. Lim, A. Mitton et al., "Peroxisome proliferator-activated receptors are altered in pathologies of the human placenta: gestational diabetes mellitus, intrauterine growth restriction and preeclampsia," *Placenta*, vol. 31, no. 3, pp. 222–229, 2010.
- [14] L. C. Sánchez-Aranguren, C. E. Prada, C. E. Riaño-Medina, and M. Lopez, "Endothelial dysfunction and preeclampsia: role of oxidative stress," *Frontiers in Physiology*, vol. 5, p. 372, 2014.
- [15] G. J. Burton, H. W. Yung, T. Cindrova-Davies, and D. S. Charnock-Jones, "Placental endoplasmic reticulum stress and oxidative stress in the pathophysiology of unexplained intrauterine growth restriction and early onset preeclampsia," *Placenta*, vol. 30, Suppl A, pp. 43–48, 2009.
- [16] L. Myatt, "Review: Reactive oxygen and nitrogen species and functional adaptation of the placenta," *Placenta*, vol. 31, pp. S66–S69, 2010.
- [17] M. Shibata, F. Hakuno, D. Yamanaka et al., "Paraquat-induced Oxidative Stress Represses Phosphatidylinositol 3-Kinase Activities Leading to Impaired Glucose Uptake in 3T3-L1 Adipocytes," *Journal of Biological Chemistry*, vol. 285, no. 27, pp. 20915–20925, 2010.
- [18] M. G. Tuuli, M. S. Longtine, and D. M. Nelson, "Review: Oxygen and trophoblast biology - A source of controversy," *Placenta*, vol. 32, no. 2, pp. S109–S118, 2011.
- [19] P. Celi, A. Di Trana, and S. Claps, "Effects of plane of nutrition on oxidative stress in goats during the peripartum period," *Veterinary Journal*, vol. 184, no. 1, pp. 95–99, 2010.
- [20] T. Hussain, B. Tan, Y. Yin, F. Blachier, M. C. Tossou, and N. Rahu, "Oxidative Stress and Inflammation: What Polyphenols Can Do for Us?," *Oxidative Medicine and Cellular Longevity*, vol. 2016, 9 pages, 2016.
- [21] T. Hussain, B. Tan, G. Liu et al., "Modulatory Mechanism of Polyphenols and Nrf2 Signaling Pathway in LPS Challenged Pregnancy Disorders," *Oxidative Medicine and Cellular Longevity*, vol. 2017, 14 pages, 2017.
- [22] T. Hussain, B. Tan, N. Rahu, D. Hussain Kalhoro, R. Dad, and Y. Yin, "Protective mechanism of Eucommia ulmoides flavone (EUF) on enterocyte damage induced by LPS," *Free Radical Biology and Medicine*, vol. 108, p. S40, 2017.
- [23] D. Yuan, T. Hussain, B. Tan, Y. Liu, P. Ji, and Y. Yin, "The Evaluation of Antioxidant and Anti-Inflammatory Effects of Eucommia ulmoides Flavones Using Diquat-Challenged Piglet Models," *Oxidative Medicine and Cellular Longevity*, vol. 2017, 9 pages, 2017.
- [24] T. Hussain, B. Tan, G. Liu et al., "The regulatory mechanism of Eucommia ulmoides flavone effects on damage repair in enterocytes," *Free Radical Biology and Medicine*, vol. 120, pp. S139–S140, 2018.
- [25] T. Hussain, D. Yuan, B. Tan et al., "Eucommia ulmoides flavones (EU F) abrogated enterocyte damage induced by LPS involved in NF- κ B signaling pathway," *Toxicology In Vitro*, vol. 62, article 104674, 2020.
- [26] J. Fujii, Y. Iuchi, and F. Okada, "Fundamental roles of reactive oxygen species and protective mechanisms in the female reproductive system," *Reproductive Biology and Endocrinology*, vol. 3, no. 1, pp. 1–10, 2005.
- [27] A. Bhattacharyya, R. Chattopadhyay, S. Mitra, and S. E. Crowe, "Oxidative stress: an essential factor in the pathogenesis of gastrointestinal mucosal diseases," *Physiological Reviews*, vol. 94, no. 2, pp. 329–354, 2014.
- [28] L. W. Oberley, "Mechanism of the tumor suppressive effect of MnSOD overexpression," *Biomedicine & Pharmacotherapy*, vol. 59, no. 4, pp. 143–148, 2005.
- [29] E. D. Harris, "Regulation of antioxidant enzymes," *The FASEB Journal*, vol. 6, no. 9, pp. 2675–2683, 1992.
- [30] J. Spallholz, A. Roveri, L. Yan, L. Boylan, C. Kang, and F. Ursini, "Glutathione peroxidase and phospholipid hydroperoxide glutathione peroxidase in tissues of Balb/C mice," *FASEB Journal (Federation of American Societies for Experimental Biology)*, vol. 5, 1991.
- [31] J. Fujii, J.-i. Ito, X. Zhang, and T. Kurahashi, "Unveiling the roles of the glutathione redox system in vivo by analyzing genetically modified mice," *Journal of Clinical Biochemistry and Nutrition*, vol. 49, no. 2, p. 78, 2011.
- [32] A. B. Fisher, "The phospholipase A₂ activity of peroxiredoxin 6 [S]," *Journal of Lipid Research*, vol. 59, no. 7, pp. 1132–1147, 2018.
- [33] E. B. Kurutas, "The importance of antioxidants which play the role in cellular response against oxidative/nitrosative stress: current state," *Nutrition Journal*, vol. 15, no. 1, pp. 1–22, 2015.
- [34] A. Agarwal, S. Gupta, and R. K. Sharma, "Role of oxidative stress in female reproduction," *Reproductive Biology and Endocrinology*, vol. 3, no. 1, pp. 1–21, 2005.
- [35] Y.-Z. Fang, S. Yang, and G. Wu, "Free radicals, antioxidants, and nutrition," *Nutrition*, vol. 18, no. 10, pp. 872–879, 2002.
- [36] D. Ramiro-Cortijo, T. Herrera, P. Rodríguez-Rodríguez et al., "Maternal plasma antioxidant status in the first trimester of pregnancy and development of obstetric complications," *Placenta*, vol. 47, pp. 37–45, 2016.

- [37] M. Schieber and N. S. Chandel, "ROS Function in Redox Signaling and Oxidative Stress," *Current Biology*, vol. 24, no. 10, pp. R453–R462, 2014.
- [38] A. Bąk and K. Roszkowski, "Oxidative stress in pregnant women," *Archives of Perinatal Medicine*, vol. 19, no. 3, pp. 155–155, 2013.
- [39] K. Duhig, L. Chappell, and A. Shennan, "Oxidative stress in pregnancy and reproduction," *Obstetric Medicine*, vol. 9, no. 3, pp. 113–116, 2016.
- [40] Z. Sultana, K. Maiti, J. Aitken, J. Morris, L. Dedman, and R. Smith, "Oxidative stress, placental ageing-related pathologies and adverse pregnancy outcomes," *American Journal of Reproductive Immunology*, vol. 77, no. 5, 2017.
- [41] V. Toescu, S. L. Nuttall, U. Martin, M. J. Kendall, and F. Dunne, "Oxidative stress and normal pregnancy," *Clinical Endocrinology*, vol. 57, no. 5, pp. 609–613, 2002.
- [42] P. A. Dennerly, "Oxidative stress in development: Nature or nurture?," *Free Radical Biology and Medicine*, vol. 49, no. 7, pp. 1147–1151, 2010.
- [43] D. Hernández-García, C. D. Wood, S. Castro-Obregón, and L. Covarrubias, "Reactive oxygen species: A radical role in development?," *Free Radical Biology and Medicine*, vol. 49, no. 2, pp. 130–143, 2010.
- [44] H. D. Mistry and P. J. Williams, "The importance of antioxidant micronutrients in pregnancy," *Oxidative Medicine and Cellular Longevity*, vol. 2011, 2011.
- [45] R. K. Sharma and A. Agarwal, "Role of reactive oxygen species in gynecologic diseases," *Reproductive Medicine and Biology*, vol. 3, no. 4, pp. 177–199, 2004.
- [46] M. Ishikawa, "Oxygen radicals-superoxide dismutase system and reproduction medicine," *Nippon Sanka Fujinka Gakkai Zasshi*, vol. 45, no. 8, pp. 842–848, 1993.
- [47] K. Shkolnik, A. Tadmor, S. Ben-Dor, N. Nevo, D. Galiani, and N. Dekel, "Reactive oxygen species are indispensable in ovulation," *Proceeding National Academy of Sciences, U S A.*, vol. 108, no. 4, pp. 1462–1467, 2011.
- [48] J. S. Richards, "Hormonal control of gene expression in the ovary," *Endocrine Reviews*, vol. 15, no. 6, pp. 725–751, 1994.
- [49] B. du, K. Takahashi, G. M. Ishida, K. Nakahara, H. Saito, and H. Kurachi, "Usefulness of intraovarian artery pulsatility and resistance indices measurement on the day of follicle aspiration for the assessment of oocyte quality," *Fertility and Sterility*, vol. 85, no. 2, pp. 366–370, 2006.
- [50] N. Sugino, "Roles of reactive oxygen species in the corpus luteum," *Animal Sciences Journal.*, vol. 77, no. 6, pp. 556–565, 2006.
- [51] A. Rizzo, M. T. Roscino, F. Binetti, and R. L. Sciorsci, "Roles of reactive oxygen species in female reproduction," *Reproduction in Domestic Animals*, vol. 47, no. 2, pp. 344–352, 2012.
- [52] L. Myatt and X. L. Cui, "Oxidative stress in the placenta," *Histochemistry and Cell Biology*, vol. 122, no. 4, pp. 369–382, 2004.
- [53] Y. Wang and S. W. Walsh, "Placental mitochondria as a source of oxidative stress in pre-eclampsia," *Placenta*, vol. 19, no. 8, pp. 581–586, 1998.
- [54] E. Jauniaux, B. Gulbis, and G. J. Burton, "The human first trimester gestational sac limits rather than facilitates oxygen transfer to the foetus—a review," *Placenta*, vol. 24, Suppl A, pp. S86–S93, 2003.
- [55] K. H. Lim, Y. Zhou, M. Janatpour et al., "Human cytotrophoblast differentiation/invasion is abnormal in pre-eclampsia," *American Journal of Pathology*, vol. 151, pp. 1809–1818, 1997.
- [56] S. Preutthipan, S. H. Chen, J. L. Tilly, K. Kugu, R. R. Lareu, and A. M. Dharmarajan, "Inhibition of nitric oxide synthesis potentiates apoptosis in the rabbit corpus luteum," *Reproductive Biomedicine Online*, vol. 9, no. 3, pp. 264–270, 2004.
- [57] P. Ghafourifar and C. Richter, "Nitric oxide synthase activity in mitochondria," *Federation of European Biochemical Societies Letters*, vol. 418, no. 3, pp. 291–296, 1997.
- [58] R. Menon, S. J. Fortunato, J. Yu et al., "Cigarette smoke induces oxidative stress and apoptosis in normal term fetal membranes," *Placenta*, vol. 32, no. 4, pp. 317–322, 2011.
- [59] R. Smith, K. Maiti, and R. J. Aitken, "Unexplained antepartum stillbirth: a consequence of placental aging?," *Placenta*, vol. 34, no. 4, pp. 310–313, 2013.
- [60] Y. Oner-Iyidogan, H. Kocak, F. Gurdol, D. Korkmaz, and F. Buyru, "Indices of oxidative stress in eutopic and ectopic endometria of women with endometriosis," *Gynecologic and Obstetric Investigation*, vol. 57, no. 4, pp. 214–217, 2004.
- [61] L. O. Perucci, M. D. Corrêa, L. M. Duse, K. B. Gomes, and L. P. Sousa, "Resolution of inflammation pathways in pre-eclampsia—a narrative review," *Immunologic Research*, vol. 65, no. 4, pp. 774–789, 2017.
- [62] F. Wu, F.-J. Tian, and Y. Lin, "Oxidative Stress in Placenta: Health and Diseases," *BioMed Research International*, vol. 2015, 15 pages, 2015.
- [63] K. Itoh, T. Chiba, S. Takahashi et al., "An Nrf2/Small Maf Heterodimer Mediates the Induction of Phase II Detoxifying Enzyme Genes through Antioxidant Response Elements," *Biochemical and Biophysical Research Communications*, vol. 236, no. 2, pp. 313–322, 1997.
- [64] K. Itoh, N. Wakabayashi, Y. Katoh et al., "Keap1 represses nuclear activation of antioxidant responsive elements by Nrf2 through binding to the amino-terminal Neh2 domain," *Genes & Development*, vol. 13, no. 1, pp. 76–86, 1999.
- [65] H.-Y. Cho, S. P. Reddy, A. DeBiase, M. Yamamoto, and S. R. Kleiberger, "Gene expression profiling of NRF2-mediated protection against oxidative injury," *Free Radical Biology and Medicine*, vol. 38, no. 3, pp. 325–343, 2005.
- [66] T. Ishii, K. Itoh, S. Takahashi et al., "Transcription Factor Nrf2 Coordinately Regulates a Group of Oxidative Stress-inducible Genes in Macrophages*," *Journal of Biological Chemistry*, vol. 275, no. 21, pp. 16023–16029, 2000.
- [67] X. Cheng, S. J. Chapple, B. Patel et al., "Gestational diabetes mellitus impairs Nrf2-mediated adaptive antioxidant defenses and redox signaling in fetal endothelial cells in utero," *Diabetes*, vol. 62, no. 12, pp. 4088–4097, 2013.
- [68] R. Lim, G. Barker, and M. Lappas, "The transcription factor Nrf2 is decreased after spontaneous term labour in human fetal membranes where it exerts anti-inflammatory properties," *Placenta*, vol. 36, no. 1, pp. 7–17, 2015.
- [69] L. Guan, L. Zhang, Z. Gong et al., "FoxO3 inactivation promotes human cholangiocarcinoma tumorigenesis and chemoresistance through Keap1-Nrf2 signaling," *Hepatology*, vol. 63, no. 6, pp. 1914–1927, 2016.
- [70] T. Gilmore, "Introduction to NF- κ B: players, pathways, perspectives," *Oncogene*, vol. 25, no. 51, pp. 6680–6684, 2006.
- [71] M. Hayden, A. West, and S. Ghosh, "NF- κ B and the immune response," *Oncogene*, vol. 25, no. 51, pp. 6758–6780, 2006.
- [72] T. Cindrova-Davies, H.-W. Yung, J. Johns et al., "Oxidative Stress, Gene Expression, and Protein Changes Induced in

- the Human Placenta during Labor,” *The American Journal of Pathology*, vol. 171, no. 4, pp. 1168–1179, 2007.
- [73] C. Scheidereit, “I κ B kinase complexes: gateways to NF- κ B activation and transcription,” *Oncogene*, vol. 25, no. 51, pp. 6685–6705, 2006.
- [74] Y. Sakamoto, T. Harada, S. Horie et al., “Tumor necrosis factor- α -induced interleukin-8 (IL-8) expression in endometriotic stromal cells, probably through nuclear factor- κ B activation: gonadotropin-releasing hormone agonist treatment reduced IL-8 expression,” *The Journal of Clinical Endocrinology & Metabolism*, vol. 88, no. 2, pp. 730–735, 2003.
- [75] V. Veillat, C. Herrmann Lavoie, C. N. Metz, T. Roger, Y. Labelle, and A. Akoum, “Involvement of nuclear factor- κ B in macrophage migration inhibitory factor gene transcription up-regulation induced by interleukin-1 β in ectopic endometrial cells,” *Fertility and Sterility*, vol. 91, no. 5, pp. 2148–2156, 2009.
- [76] W. Cao, M. Morin, V. Sengers et al., “Tumour necrosis factor- α up-regulates macrophage migration inhibitory factor expression in endometrial stromal cells via the nuclear transcription factor NF- κ B,” *Human Reproduction*, vol. 21, no. 2, pp. 421–428, 2006.
- [77] E. M. Grund, D. Kagan, C. A. Tran et al., “Tumor necrosis factor- α regulates inflammatory and mesenchymal responses via mitogen-activated protein kinase kinase, p38, and nuclear factor κ B in human endometriotic epithelial cells,” *Molecular Pharmacology*, vol. 73, no. 5, pp. 1394–1404, 2008.
- [78] A. Brunet, A. Bonni, M. J. Zigmund et al., “Akt promotes cell survival by phosphorylating and inhibiting a Forkhead transcription factor,” *Cell*, vol. 96, no. 6, pp. 857–868, 1999.
- [79] K. E. van der Vos and P. J. Coffey, “The extending network of FOXO transcriptional target genes,” *Antioxidants & Redox Signaling*, vol. 14, no. 4, pp. 579–592, 2011.
- [80] T. Goto, M. Takano, A. Albergaria et al., “Mechanism and functional consequences of loss of FOXO1 expression in endometrioid endometrial cancer cells,” *Oncogene*, vol. 27, no. 1, pp. 9–19, 2008.
- [81] T. Kajihara, J. J. Brosens, and O. Ishihara, “The role of FOXO1 in the decidual transformation of the endometrium and early pregnancy,” *Medical Molecular Morphology*, vol. 46, no. 2, pp. 61–68, 2013.
- [82] T. Kajihara, M. Jones, L. Fusi et al., “Differential expression of FOXO1 and FOXO3a confers resistance to oxidative cell death upon endometrial decidualization,” *Molecular Endocrinology*, vol. 20, no. 10, pp. 2444–2455, 2006.
- [83] B. Gellersen and J. Brosens, “Cyclic AMP and progesterone receptor cross-talk in human endometrium: a decidualizing affair,” *The Journal of Endocrinology*, vol. 178, no. 3, pp. 357–372, 2003.
- [84] A. S. Dhillon, S. Hagan, O. Rath, and W. Kolch, “MAP kinase signalling pathways in cancer,” *Oncogene*, vol. 26, no. 22, pp. 3279–3290, 2007.
- [85] S. Matsuzaki and C. Darcha, “Co-operation between the AKT and ERK signaling pathways may support growth of deep endometriosis in a fibrotic microenvironment in vitro,” *Human Reproduction*, vol. 30, no. 7, pp. 1606–1616, 2015.
- [86] S. S. Andrade, A. D. C. Azevedo, I. C. Monasterio et al., “17 β -Estradiol and steady-state concentrations of H₂O₂: antiapoptotic effect in endometrial cells from patients with endometriosis,” *Free Radical Biology and Medicine*, vol. 60, pp. 63–72, 2013.
- [87] G. J. Burton and E. Jauniaux, “Oxidative stress,” *Best Practice & Research Clinical Obstetrics & Gynaecology*, vol. 25, no. 3, pp. 287–299, 2011.
- [88] D. Sharma, S. Shastri, and P. Sharma, “Intrauterine growth restriction: antenatal and postnatal aspects,” *Clinical Medicine Insights: Pediatrics*, vol. 10, article CMPed.S40070, 2016.
- [89] J. F. Frøen, J. O. Gardosi, A. Thurmann, A. Francis, and B. Stray-Pedersen, “Restricted fetal growth in sudden intrauterine unexplained death,” *Acta Obstetrica et Gynecologica Scandinavica*, vol. 83, no. 9, pp. 801–807, 2004.
- [90] U. Krishna and S. Bhalerao, “Placental insufficiency and fetal growth restriction,” *The Journal of Obstetrics and Gynecology of India*, vol. 61, no. 5, pp. 505–511, 2011.
- [91] T.-H. Hung, J. N. Skepper, D. S. Charnock-Jones, and G. J. Burton, “Hypoxia-Reoxygenation,” *Circulation Research*, vol. 90, no. 12, pp. 1274–1281, 2002.
- [92] A. Biri, N. Bozkurt, A. Turp, M. Kavutcu, Ö. Himmetoglu, and I. Durak, “Role of oxidative stress in intrauterine growth restriction,” *Gynecologic and Obstetric Investigation*, vol. 64, no. 4, pp. 187–192, 2007.
- [93] J. Wang, L. Chen, D. Li et al., “Intrauterine growth restriction affects the proteomes of the small intestine, liver, and skeletal muscle in newborn pigs,” *The Journal of Nutrition*, vol. 138, no. 1, pp. 60–66, 2008.
- [94] J. Armengaud, C. Zyzdorczyk, B. Siddeek, A. Peyter, and U. Simeoni, “Intrauterine growth restriction: Clinical consequences on health and disease at adulthood,” *Reproductive Toxicology*, vol. 99, pp. 168–176, 2021.
- [95] C. S. Rashid, A. Bansal, and R. A. Simmons, “Oxidative stress, intrauterine growth restriction, and developmental programming of type 2 diabetes,” *Physiology*, vol. 33, no. 5, pp. 348–359, 2018.
- [96] C. Garcia-Contreras, M. Vazquez-Gomez, Z. Pardo et al., “Polyphenols and IUGR pregnancies: effects of maternal hydroxytyrosol supplementation on hepatic fat accretion and energy and fatty acids profile of fetal tissues,” *Nutrients*, vol. 11, no. 7, p. 1534, 2019.
- [97] A. Agarwal, A. Aponte-Mellado, B. J. Premkumar, A. Shaman, and S. Gupta, “The effects of oxidative stress on female reproduction: a review,” *Reproductive Biology and Endocrinology*, vol. 10, pp. 1–31, 2012.
- [98] E. Jauniaux, B. Gulbis, and G. J. Burton, “Physiological implications of the materno-fetal oxygen gradient in human early pregnancy,” *Reproductive Biomedicine Online*, vol. 7, no. 2, pp. 250–253, 2003.
- [99] D. Benjamin, R. K. Sharma, A. Moazzam, and A. Agarwal, “Methods for the detection of ROS in human sperm samples,” in *Studies on men's health and fertility*, pp. 257–273, Springer, 2012.
- [100] H. El Hachem, V. Crepau, P. May-Panloup, P. Descamps, G. Legendre, and P. E. Bouet, “Recurrent pregnancy loss: current perspectives,” *International Journal of Women's Health*, vol. Volume 9, pp. 331–345, 2017.
- [101] H. A. Homer, “Modern management of recurrent miscarriage,” *Australian and New Zealand Journal of Obstetrics and Gynaecology*, vol. 59, no. 1, pp. 36–44, 2019.
- [102] M. Coughlan, P. Vervaart, M. Permezel, H. Georgiou, and G. Rice, “Altered placental oxidative stress status in gestational diabetes mellitus,” *Placenta*, vol. 25, no. 1, pp. 78–84, 2004.

- [103] D. A. Sacks, D. R. Hadden, M. Maresh et al., "Frequency of gestational diabetes mellitus at collaborating centers based on IADPSG consensus panel-recommended criteria: the hyperglycemia and adverse pregnancy outcome (HAPO) study," *Diabetes Care*, vol. 35, no. 3, pp. 526–528, 2012.
- [104] M. Gauster, G. Desoye, M. Tötsch, and U. Hiden, "The placenta and gestational diabetes mellitus," *Current Diabetes Reports*, vol. 12, no. 1, pp. 16–23, 2012.
- [105] T. Lekva, E. R. Norwitz, P. Aukrust, and T. Ueland, "Impact of systemic inflammation on the progression of gestational diabetes mellitus," *Current Diabetes Reports*, vol. 16, no. 4, p. 26, 2016.
- [106] K. P. T. Pendelowski, R. Mattar, M. R. Torloni, C. P. Gomes, S. M. Alexandre, and S. Daher, "Immunoregulatory molecules in patients with gestational diabetes mellitus," *Endocrine*, vol. 50, no. 1, pp. 99–109, 2015.
- [107] B. G. Xie, S. Jin, and W. J. Zhu, "Expression of toll-like receptor 4 in maternal monocytes of patients with gestational diabetes mellitus," *Experimental and Therapeutic Medicine*, vol. 7, no. 1, pp. 236–240, 2014.
- [108] T. K. Robakis, L. Aasly, K. E. Williams, C. Clark, and N. L. Rasgon, "Roles of inflammation and depression in the development of gestational diabetes," *Current Behavioral Neuroscience Reports*, vol. 4, no. 4, pp. 369–383, 2017.
- [109] M. Lappas, U. Hiden, G. Desoye, J. Froehlich, S. H. D. Mouzon, and A. Jawerbaum, "The role of oxidative stress in the pathophysiology of gestational diabetes mellitus," *Antioxidants & Redox Signaling*, vol. 15, no. 12, pp. 3061–3100, 2011.
- [110] E. H. Ruder, T. J. Hartman, J. Blumberg, and M. B. Goldman, "Oxidative stress and antioxidants: exposure and impact on female fertility," *Human Reproduction Update*, vol. 14, no. 4, pp. 345–357, 2008.
- [111] A. Agarwal, A. Aponte-Mellado, B. J. Premkumar, A. Shaman, and S. Gupta, "The effects of oxidative stress on female reproduction: a review," *Reproductive Biology and Endocrinology*, vol. 10, no. 1, p. 49, 2012.
- [112] I. Mironczuk-Chodakowska, A. M. Witkowska, and M. E. Zujko, "Endogenous non-enzymatic antioxidants in the human body," *Advances in Medical Sciences*, vol. 63, no. 1, pp. 68–78, 2018.
- [113] N. Ledee-Bataille, F. Olivennes, J. L. Lefaix, G. Chaouat, R. Frydman, and S. Delanian, "Combined treatment by pentoxifylline and tocopherol for recipient women with a thin endometrium enrolled in an oocyte donation programme," *Human Reproduction*, vol. 17, no. 5, pp. 1249–1253, 2002.
- [114] R. L. Thomson, S. Spedding, and J. D. Buckley, "Vitamin D in the aetiology and management of polycystic ovary syndrome," *Clinical Endocrinology*, vol. 77, no. 3, pp. 343–350, 2012.
- [115] M. G. Showell, R. Mackenzie-Proctor, V. Jordan, and R. J. Hart, "Antioxidants for female subfertility," *Cochrane Database of Systems Review*, vol. 7, article CD007807, 2017.
- [116] R. M. Smits, R. Mackenzie-Proctor, K. Fleischer, and M. G. Showell, "Antioxidants in fertility: impact on male and female reproductive outcomes," *Fertility and Sterility*, vol. 110, no. 4, pp. 578–580, 2018.
- [117] N. Mahmood, A. Hameed, and T. Hussain, "Vitamin E and Selenium Treatment Alleviates Saline Environment-Induced Oxidative Stress through Enhanced Antioxidants and Growth Performance in Suckling Kids of Beetal Goats," *Oxidative Medicine and Cellular Longevity*, vol. 2020, 16 pages, 2020.
- [118] A. Afzal, T. Hussain, and A. Hameed, "Moringa oleifera supplementation improves antioxidant status and biochemical indices by attenuating early pregnancy stress in Beetal goats," *Frontiers in Nutrition*, vol. 8, p. 444, 2021.
- [119] J. Abdul-Barry, S. A. Al-Rubai, and Q. A. Qasim, "Study of Oxidant-Antioxidant status in recurrent spontaneous abortion," *TQMJ*, vol. 5, pp. 35–46, 2011.
- [120] A. S. al-Kunani, R. Knight, S. J. Haswell, J. W. Thompson, and S. W. Lindow, "The selenium status of women with a history of recurrent miscarriage," *British Journal of Obstetrics and Gynaecology*, vol. 108, no. 10, pp. 1094–1097, 2001.
- [121] E. A. Reece, "Maternal Fuels, Diabetic Embryopathy: Pathomechanisms and Prevention," *Seminars in Reproductive Medicine*, vol. 17, no. 2, pp. 183–194, 1999.
- [122] E. Malvy, R. Thiébaud, C. Marimoutou, F. Dabis, and the Groupe d'Epidémiologie Clinique du Sida en Aquitaine, "'Weight loss and body mass index as predictors of HIV disease progression to AIDS in adults', Aquitaine cohort, France, 1985-1997," *Journal of American College Nutrition*, vol. 20, no. 6, pp. 609–615, 2001.
- [123] A. M. Maged, H. Torky, M. A. Fouad et al., "Role of antioxidants in gestational diabetes mellitus and relation to fetal outcome: a randomized controlled trial," *Journal of Maternal-Fetal & Neonatal Medicine*, vol. 29, no. 24, pp. 4049–4054, 2016.
- [124] B. Nath and H. Roy, "Antioxidants in Female Reproductive Biology," in *Antioxidants-Benefits, Sources, Mechanisms of Action*, IntechOpen, 2021.
- [125] V. H. Parraguez, F. Sales, O. A. Peralta et al., "Maternal Supplementation with Herbal Antioxidants during Pregnancy in Swine," *Antioxidants*, vol. 10, no. 5, p. 658, 2021.
- [126] A. Taravati and F. Tohidi, "Comprehensive analysis of oxidative stress markers and antioxidants status in preeclampsia," *Taiwanese Journal of Obstetrics and Gynecology*, vol. 57, no. 6, pp. 779–790, 2018.
- [127] E. S. Idogun, M. E. Odiogwu, S. M. Momoh, and F. E. Okonofua, "Effect of pregnancy on total antioxidant capacity in Nigerian women," *Pakistan Journal of Medical Sciences*, vol. 24, no. 2, p. 292, 2008.
- [128] C. Ly, J. Yockell-Lelièvre, Z. M. Ferraro, J. T. Arnason, J. Ferrier, and A. Gruslin, "The effects of dietary polyphenols on reproductive health and early development," *Human Reproduction Update*, vol. 21, no. 2, pp. 228–248, 2015.
- [129] K. H. Al-Gubory, P. A. Fowler, and C. Garrel, "The roles of cellular reactive oxygen species, oxidative stress and antioxidants in pregnancy outcomes," *The International Journal of Biochemistry & Cell Biology*, vol. 42, no. 10, pp. 1634–1650, 2010.
- [130] H. Ni, X. J. Yu, H. J. Liu et al., "Progesterone regulation of glutathione S-transferase Mu2 expression in mouse uterine luminal epithelium during preimplantation period," *Fertility and Sterility*, vol. 91, no. 5, pp. 2123–2130, 2009.
- [131] C. Garrel, P. A. Fowler, and K. H. Al-Gubory, "Developmental changes in antioxidant enzymatic defences against oxidative stress in sheep placentomes," *Journal of Endocrinology*, vol. 205, pp. 107–116, 2010.
- [132] A. Borchert, C. C. Wang, C. Ufer, H. Schiebel, N. E. Savaskan, and H. Kuhn, "The Role of Phospholipid Hydroperoxide Glutathione Peroxidase Isoforms in Murine

- Embryogenesis*," *Journal of Biological Chemistry*, vol. 281, no. 28, pp. 19655–19664, 2006.
- [133] A. Y. Warren, B. Matharoo-Ball, R. W. Shaw, and R. N. Khan, "Hydrogen peroxide and superoxide anion modulate pregnant human myometrial contractility," *Reproduction*, vol. 130, no. 4, pp. 539–544, 2005.
- [134] K. H. al-Gubory, P. Bolifraud, G. Germain, A. Nicole, and I. Ceballos-Bicot, "Antioxidant enzymatic defence systems in sheep corpus luteum throughout pregnancy," *Reproduction*, vol. 128, no. 6, pp. 767–774, 2004.
- [135] J. Lapointe and J. F. Bilodeau, "Antioxidant defenses are modulated in the cow oviduct during the estrous cycle," *Biology of Reproduction*, vol. 68, no. 4, pp. 1157–1164, 2003.
- [136] N. Sugino, S. Takiguchi, S. Kashida, A. Karube, Y. Nakamura, and H. Kato, "Superoxide dismutase expression in the human corpus luteum during the menstrual cycle and in early pregnancy," *Molecular Human Reproduction*, vol. 6, no. 1, pp. 19–25, 2000.
- [137] E. Jauniaux, A. L. Watson, J. Hempstock, Y. P. Bao, J. N. Skepper, and G. J. Burton, "Onset of Maternal Arterial Blood Flow and Placental Oxidative Stress: A Possible Factor in Human Early Pregnancy Failure," *American Journal of Pathology*, vol. 157, no. 6, pp. 2111–2122, 2000.
- [138] S. Qanungo and M. Mukherjea, "Ontogenic profile of some antioxidants and lipid peroxidation in human placental and fetal tissues," *Molecular and Cellular Biochemistry*, vol. 215, no. 1/2, pp. 11–19, 2000.
- [139] L. A. Baiza-Gutman, M. M. Flores-Sánchez, M. Díaz-Flores, and J. J. Hicks, "Presence of uterine peroxidase activity in the rat early pregnancy," *International Journal of Biochemistry & Cellular Biology*, vol. 32, no. 2, pp. 255–262, 2000.

Research Article

The Key Ingredient Acacetin in Weishu Decoction Alleviates Gastrointestinal Motility Disorder Based on Network Pharmacology Analysis

Xuan Guo ¹, Yin Xu ^{2,3}, Hua-liang Tan ², Xiao-juan Wang ² and Lin Xiao ²

¹Institute of Traditional Chinese Medicine, Hunan University of Traditional Chinese Medicine, Changsha 410208, China

²Department of Internal Medicine, The First Affiliated Hospital of Hunan University of Traditional Chinese Medicine, Changsha 410007, China

³Hunan University of Chinese medicine, 300 bachelor's road, Yuelu District, Changsha City, Hunan Province, China

Correspondence should be addressed to Yin Xu; zyydxgx@126.com

Received 23 April 2021; Revised 9 August 2021; Accepted 28 August 2021; Published 21 September 2021

Academic Editor: Xin Zong

Copyright © 2021 Xuan Guo et al. This is an open access article distributed under the Creative Commons Attribution License, which permits unrestricted use, distribution, and reproduction in any medium, provided the original work is properly cited.

Background. Gastrointestinal motility disorder is a common gastrointestinal disease, which seriously affects life quality. Traditional Chinese medicine (TCM) has been widely used as an alternative therapy for gastrointestinal motility disorder. Acacetin is a natural flavonoid compound that has antioxidant and anti-inflammatory, antidepressant, and anticancer properties. However, the efficacy of Acacetin in the treatment of gastrointestinal motility disorders has not been studied. Our aim was to investigate the mechanism of Acacetin-alleviated gastrointestinal motility disorder and its efficacy based on network pharmacology. **Methods.** We performed network pharmacology to predict the active components, match Weishu decoction (WSD) targets in gastrointestinal motility disorders, and investigate its potential pharmacological mechanisms. We performed the GO and KEGG enrichment analysis. **In vivo,** we investigated the effects of Acacetin in the gastrointestinal motility disorder model. **Results.** Based on network pharmacological method, the key active ingredient of WSD was identified as Acacetin, and the enrichment signaling pathway was the PI3K-AKT signaling pathway. Acacetin and Mosapride accelerated gastric emptying time, reduced gastric remnant rate, and increased small intestinal propulsion rate. The levels of GAS and MTL were increased after using Acacetin. These results indicated that Acacetin could improve gastrointestinal motility disorders. Among them, high-dose Acacetin showed a better effect. Acacetin could regulate protein and lipid metabolism in mice with gastrointestinal motility disorder. Furthermore, Acacetin could modulate gastrointestinal inflammation and apoptosis. The detection of the PI3K-AKT signaling pathway-related proteins showed that Acacetin improved gastrointestinal motility disorder by inhibiting the activation of the PI3K-AKT signaling pathway. **Conclusion.** The key ingredient Acacetin in WSD could alleviate gastrointestinal motility disorder by inhibiting the activation of the PI3K-AKT signaling pathway based on network pharmacology analysis. The efficacy and safety of Acacetin treatment provide strong experimental support for the clinical treatment of gastrointestinal motility disorder.

1. Introduction

Gastrointestinal motility disorder is a common gastrointestinal disease that seriously affects the quality of life and socioeconomic costs [1]. It is characterized by abnormal motor, sensory, or secretory functions that alter the intestinal function and lead to a significant disease burden [2]. Millions of patients worldwide suffer from gastrointestinal motility disorders, which include debilitating symptoms such as chronic

nausea and vomiting [3]. The most severe gastrointestinal motility disorders may directly lead to intestinal failure [4]. It has been reported that up to 80% of critically ill patients suffer from gastrointestinal motility disorders. In critically ill patients, gastrointestinal dysfunction or gastrointestinal failure is associated with increased morbidity and mortality [5]. In addition to movement disorders, the factors leading to the decreased visceral perceptual threshold are common in the pathogenesis of functional gastrointestinal diseases

[6]. However, the pathogenesis of gastrointestinal motility disorder remains unclear and may be closely associated with gastrointestinal hypersensitivity, impaired food intake regulation, delayed gastric emptying, lipoprotein metabolism, and neuropsychological factors. Although many drugs have been developed to treat gastrointestinal motility disorders, very few drugs are currently available.

Traditional Chinese medicine (TCM) is the precious treasure of the Chinese nation. Thousands of years of practical experience has made significant contributions to preventing and treating human diseases [7]. At present, TCM has been widely used as an alternative therapy for gastrointestinal motility disorders. Weishu decoction (WSD) consists of Radix Bupleurum 10g, Cyperus rotundus 10g, unripe bitter orange 10g, Rhizoma Atractylodes 10g, White Peony 10g, Fructus Toosendan 6g, Rhizoma Corydalis 10g, Inula flowerlog 10g, and Charred medicated leaven 10g, which can alleviate gastrointestinal motility disorder [8]. However, the exact mechanism of the WSD effect on gastrointestinal motility disorder remains unclear.

With the vigorous development of network pharmacology in recent years, a new approach to finding therapeutic drugs has emerged [9]. Network pharmacology is the combined analysis of TCM preparations that provides a powerful tool for establishing a “complex protein/gene-disease” network and revealing the regulation principle of small molecules [10]. Its core theory is a new holistic and systematic “network goal” method [11]. The holistic philosophy of TCM has much in common with the core ideas of emerging network pharmacology and network biology. It can systematically overcome the needs of complex diseases such as cancer [12]. Therefore, this study was based on network pharmacology to study the mechanism of WSD’s key active ingredient on gastrointestinal motility disorder.

2. Material and Methods

2.1. Disease Target Identification and Network Establishment.

The TCMS online database (<https://tcmsp.com/tcmsp.php>) [13] was used to retrieve the ADME parameter information of the components of WSD, and the components with drug-likeness (DL) ≥ 0.18 [14] were included to predict the component targets. The included compounds were identified by the SwissTargetPrediction database (<http://www.swisstargetprediction.ch/>) [15], and the target with probability greater than 0 was finally contained. Taking “Gastrointestinal motility disorders” and “disorders of gastrointestinal motility (DGIM)” as keywords, human genes were searched in the GeneCards database (<https://www.genecards.org/>) [16], NCBI gene database (<https://www.ncbi.nlm.nih.gov/>) [17], and OMIM database (<https://www.omim.org/>) [18]. Among them, GeneCards data filtered the median value of the relevance score to obtain more relevant targets. In R software analysis, all drug-protein targets and disease-related proteins were classified into two independent groups. The screened drug targets and disease targets were input into the Venn 2.1. The common targets of drug diseases were input into the String database (<https://string-db.org/cgi/input.pl>) to construct the protein-protein interaction (PPI)

network [19]. The species was set as “*Homo sapiens*,” and the credibility was set as >0.9 . In order to better understand the complex interaction relationship between components, diseases, and corresponding targets, a component-disease-target network diagram was constructed based on the included components, therapeutic diseases, and targets and was imported into Cytoscape 3.8.0 to draw the network diagram. Then, the topology analysis was carried out by NetworkAnalyzer [20]. Genes with a score greater than average were selected as key targets by degree sorting. In this study, key genes were screened through the MCODE analysis [21].

2.2. *Bioinformatic Annotation.* GO biological process (BP), molecular function (MF), and cell component (CC) enrichment were carried out on the common targets of drug diseases, and the items with corrected $P \leq 0.05$ were screened using the String database. The ClusterProfiler, enrichplot, and ggplot2 packages were installed, and the R 3.6.3 software was used to make histograms and bubble plots. KEGG pathway enrichment analysis was carried out on common targets of drug diseases, and the items with corrected $P \leq 0.05$ were also screened using the String database.

2.3. *Establishment of DGIM Model.* The adult SPF C57BL/6 male mice were raised in a temperature- and humidity-controlled animal facility on a 12-hour light/dark cycle. The mice were randomly divided into 9 groups with 12 mice in each group. They were divided into the control group (CG), the model group (MG), the low-dose Acacetin group (LAG), the middle-dose Acacetin group (MAG), the high-dose Acacetin group (HAG), the Mosapride group (MPG) (positive control). Acacetin was purchased from Selleck Chemicals (#S5318, Houston, Texas, USA), dissolved in dimethyl sulfoxide (DMSO), and stored at -20°C . The model of gastrointestinal motility disorder induced by atropine [22]. Acacetin was orally administered 10, 25, and 50 mg/kg for LAG, MAG, and HAG, respectively [23], and Mosapride was orally administered 1.37 mg/kg for MPG [24]. Distilled water (10 mL/kg) was given to the CG and MG. All treatment groups were treated once a day for 14 days. On the 14th day, after taking the drugs for 1 h, except the CG, the other groups were injected with atropine 1.5 mg/kg. After 30 min, all mice were orally administered 0.5 mL of semisolid paste (0.2% CMC-Na and 5% carbon), and 30 min later, blood was collected.

2.4. *Gastric Remnant Rate and Small Intestinal Propulsion Rate.* The mice were orally administered 0.5 mL of semisolid paste and were killed 30 min later. The difference between total gastric weight and net gastric weight was the residual weight in the stomach, and the percentage of residual weight in the stomach and the weight of semisolid paste was the gastric remnant rate (%). The small intestine of mouse was put on the plane without traction, and the total length from the pylorus to the ileocecal area and the distance from the pylorus to the front end of carbon were measured. The percentage of the advancing length of semisolid paste and the total length of the small intestine was the small intestinal propulsion rate [25].

2.5. Enzyme Linked Immunosorbent Assay (ELISA). ELISA was performed to detect serum gastrin (GAS) and motilin (MTL), serum protein metabolism indexes prealbumin (PAB), ceruloplasmin (CER) and transferrin (TRF), and lipid metabolism indexes triglyceride (TG), low-density lipoprotein cholesterol (LDL-C), high-density lipoprotein cholesterol (HDL-C), total cholesterol (TC), and inflammatory factors TNF- α , IL-1 β , and IL-6 levels. The GAS, MTL, PAB, CER, TRF, TNF- α , IL-1 β , and IL-6 were detected by GAS (#CSB-E12743r, CUSABIO, China), MTL (#CSB-E08208r, CUSABIO, China), PAB (MLBIO, China), CER (MLBIO, China), TRF (#CSB-E12723r, CUSABIO, China), TNF- α (#CSB-E11987r, CUSABIO, China), IL-1 β (#CSB-E08055r, CUSABIO, China), and IL-6 (#CSB-E04640r, CUSABIO, China) ELISA kit according to the instructions. The concentration of GAS, MTL, PAB, CER, TRF, TNF- α , IL-1 β , and IL-6 was calculated using the Bio-Tek microplate analyzer (MB-530, HEAES, China) by forming a standard curve based on the provided values. The concentration of TG, LDL-C, HDL-C, and TC were detected by the TG (#A110-2-1, Nanjing Jiancheng Bioengineering Institute, China), LDL-C (#A113-2-1, Nanjing Jiancheng Bioengineering Institute, China), HDL-C (#A112-2-1, Nanjing Jiancheng Bioengineering Institute, China), and TC (#A111-2-1, Nanjing Jiancheng Bioengineering Institute, China) kit according to the instructions.

2.6. Quantitative Real-Time PCR (qRT-PCR). The relative expression levels of Bcl-2, Bax, Caspase-12, TNF- α , IL-1 β , and IL-6 in the gastric antrum tissues were detected by qRT-PCR. Total RNA was extracted by Trizol methods; RNA was reversely transcribed into cDNAs in accordance with the instruction of a reverse transcription kit (#4368814, Invitrogen, USA). SYBR Green qPCR mix (Invitrogen) was performed to test gene relative expression in ABI 7900 system. The relative level of the gene was calculated by $2^{-\Delta\Delta C_t}$ method with β -actin as the internal gene. The primer sequences used in this study are shown in Table 1.

2.7. Western Blot. RIPA lysis buffer (#P0013B, Beyotime) was applied to extract the total protein from the gastric antrum tissues. The protein was mixed with the SDS-PAGE loading buffer (#MB2479, Meilunbio) for 5 min in boiling water at 100°C. The proteins were separated by gel electrophoresis and transferred to the PVDF membrane. Then, they were sealed with 5% skim milk solution for 2 h at room temperature, and incubated with diluted primary antibodies TNF- α (ab255275, 1: 1000, Abcam, UK), IL-1 β (ab9722, 0.2 μ g/mL, Abcam, UK), IL-6 (ab233706, 1: 1000, Abcam, UK), Bax (ab32503, 1: 5000, Abcam, UK), Caspase-12 (ab62463, 1 μ g/mL, Abcam, UK), Bcl-2 (ab182858, 1: 2000, Abcam, UK), PI3K (ab191606, 1: 5000, Abcam, UK), p-PI3K(ab182651, 1: 800, Abcam, UK), AKT (10176-2-AP, 1: 1000, Proteintech, USA), p-AKT (66444-1-Ig, 1: 5000, Proteintech, USA), and β -actin (66009-1-Ig, 1: 5000, Proteintech, USA) at room temperature for 90 min. The secondary antibody HRP goat anti-mouse IgG (SA00001-1, 1: 5000, Proteintech, USA) or HRP goat anti-Rabbit IgG (SA00001-2, 1: 6000, Proteintech, USA) was incubated with the membrane at room

TABLE 1: The primers used in this study.

Primer ID	5'-3'
TNF- α -F	CCCCTCTATTATAATTGCACCT
TNF- α -R	CTGGTAGTTTAGCTCCGTTT
IL-1 β -F	CAGCAGCATCTCGACAAGAG
IL-1 β -R	AAAGAAGGTGCTTGGGTCCT
IL-6-F	TCACTATGAGGTCTACTCGG
IL-6-R	CATATTGCCAGTTCTTCGTA
Caspase-12-F	ATAAAGAGCCAGATATTCTTCGT
Caspase-12-R	TCACCCCTCTCAGTGGTCA
Bax-F	TTGCTACAGGGTTTCATCCAGG
Bax-R	GCTCCAAGGTCAGCTCAGGT
Bcl-2-F	CTGGTGGACAACATCGCTCT
Bcl-2-R	ATAGTTCCACAAAGGCATCCCA
β -Actin-F	ACATCCGTAAGACCTCTATGCC
β -Actin-R	TACTCCTGCTTGCTGATCCAC

temperature for 90 min. The protein bands were detected by the Chemiscope6100 system (Clinx Co., Ltd, Shanghai, China). The integrated density of protein bands was determined by the Quantity One 4.6.2 software and corrected by subtracting the measured integrated density with the background integrated density. β -Actin was used as the internal reference for detecting relative expression levels.

2.8. Immunohistochemistry (IHC). The expressions of PI3K, p-PI3K, AKT, and p-AKT were detected by IHC in the gastric antrum tissues of different groups. The slices were roasted at 60°C for 12 h. Then, the slices were dewaxed to water and heated to repair the antigen. 1% periodic acid was added, and the endogenous enzyme was inactivated for 10 min at room temperature. The PI3K (ab151549, 1: 100, Abcam, UK), p-PI3K (ab182651, 1: 100, Abcam, UK), AKT (10176-2-AP, 1: 100, Proteintech, USA), and p-AKT (66444-1-Ig, 1: 100, Proteintech, USA) primary antibodies were incubated overnight at 4°C. The secondary antibody was incubated at 37°C for 30 min. DAB was used for color development, hematoxylin was restained for 10 min, washed with distilled water, and PBS returned to blue. All levels of alcohol were dehydrated for 5 min. After removal, it was placed in xylene for 10 min. Then, it was sealed with neutral gum and observed under the microscope. We selected the location of the gastric antrum, taking a 400-fold field of view. Image-pro-plus 6.0 analysis software was chosen for IOD analysis. The average optical density (positive area IOD under the field of view/tissue area under the field of view) was performed to indicate the relative expression of PI3K, p-PI3K, AKT, and p-AKT.

2.9. Statistical Analysis. Statistical analysis was performed using GraphPad 8.0 software, and three independent experimental data were expressed as mean \pm standard deviation (SD). The unpaired *T*-test was used between the two groups conforming to the normal distribution. The one-way

analysis of variance (ANOVA) was conducted among multiple groups, followed by Tukey's post hoc test. $P < 0.05$ was considered statistically significant.

3. Results

3.1. The Assumed Targets of WSD. In this study, the TCMSP online database (<https://tcmsp.com/tcmsp.php>) [13] was used to retrieve the ADME parameter information of the components of WSD, and the components with $DL \geq 0.18$ [14] were included to predict the component targets. The included compounds were identified by the SwissTargetPrediction database (<http://www.swisstargetprediction.ch/>) [15], and the target with probability greater than 0 was finally contained. As shown in Supplementary Table 1, a total of 15 active components were included in WSD. We showed the average physicochemical value of each component, including the molecule weight (MW), the value of partition coefficient between octanol and water (ALogP), hydrogen-bond donors (Hdon), hydrogen-bond acceptors (Hacc), oral bioavailability (OB), blood brain barrier (BBB), DL, and fractional water accessible surface area of all atoms with negative partial charge (FASA-). Supplementary Table 2 showed a total of 460 target compounds in WSD. Taking "Gastrointestinal motility disorders" and "disorders of gastrointestinal motility (DGIM)" as keywords, human genes were searched in the GeneCards database (<https://www.genecards.org/>) [16], NCBI gene database (<https://www.ncbi.nlm.nih.gov/>) [17], and OMIM database (<https://www.omim.org/>) [18]. Among them, the GeneCards data filtered the median value of the relevance score to obtain more relevant targets. After searching, 2691 genes were found in the Genecards database, 3 genes were found in the NCBI database, and 618 targets were found in the OMIM database. After the combined deletion of these three databases, 3216 genes related to gastrointestinal motility disorders were obtained.

3.2. Network Analysis of Targets. In the R software analysis, all drug-protein targets and disease-related proteins were classified into the two independent groups. The screened drug targets and disease targets were input into the Venny 2.1. As shown in Figure 1(a), a total of 228 common targets were obtained from the Venny diagram of the screened drug targets and disease targets. The common targets of drug diseases were input into the String database (<https://string-db.org/cgi/input.pl>) [19] to construct the PPI network. The species was set as "*Homo sapiens*," and the credibility was set as >0.9 . There were 228 nodes and 1017 edges in the PPI network, and the average degree was 8.92. Figure 1(b) showed the PPI network diagram of drug-disease common targets. At the same time, we constructed the component-disease-target network diagram (Figure 1(c)). To better understand the complex interaction relationship between components, diseases, and corresponding targets, a component-disease-target network diagram was imported into the Cytoscape 3.8.0 to draw the network diagram. Then, the topology analysis was carried out by the NetworkAnalyzer [20]. In our study, we found 15 active ingredients. The

higher the degree value was, the more important the component was (Table 2). Among them, Acacetin had the highest degree. Therefore, Acacetin might be the key active ingredient in WSD.

3.3. Predicting Functional Enrichment Analysis for WSD. The R package provided for GO annotation enrichment analysis, including the CC, MF, and BP analyses. GO annotation showed that the drug-disease crossover proteins were mainly related to the cellular response to drug, peptidyl-tyrosine phosphorylation, peptidyl-tyrosine modification of BP, the national cell body, synaptic membrane of CC, the protein serine/threonine kinase activity, and protein tyrosine kinase activity of MF (Figure 2(a)). In addition, KEGG enrichment analysis was closely associated with the PI3K-AKT signaling pathway, MAPK signaling pathway, and proteoglycans in cancer (Figure 2(b)). Then, we drew the network diagram of component-disease-pathway-target to more intuitively show the multicomponent-multitarget action characteristics of active ingredients of TCM in the treatment of gastrointestinal motility disorders. As shown in Figure 3, blue was the compound, including Acacetin, Galangin, dihydrocapsaicin, Matairesinol, albiglorin, and imperatorin. Yellow was the target of TCM, and green was the top 20 pathways with the most significant enrichment. Based on these predicted molecular mechanisms and the network analysis results, we designed *in vivo* experiments to test whether Acacetin could inhibit gastrointestinal inflammation and apoptosis from alleviating gastrointestinal motility disorders.

3.4. Acacetin Improved Gastrointestinal Motility in Mice. By constructing the gastrointestinal motility disorder model, we found that compared with the CG, gastric emptying was delayed, gastric remnant rate was increased, and small intestinal propulsion rate was decreased in the MG. Compared with the MG, Acacetin and Mosapride accelerated gastric emptying time, reduced gastric remnant rate, and increased small intestinal propulsion rate. These results revealed that Acacetin and Mosapride could improve gastrointestinal motility, and high-dose Acacetin had the better effect (Figure 4(a)). The results of ELISA showed that compared with the CG, the contents of MTL and GAS in the MG decreased significantly. Compared with the MG, the levels of GAS and MTL increased after using Acacetin and Mosapride (Figure 4(b)). These results indicated that Acacetin could regulate the contents of GAS and MTL in mice with gastrointestinal motility disorder, and the high-dose Acacetin had the better effect.

3.5. Acacetin Regulated Protein and Lipid Metabolism in Gastrointestinal Motility Disorder Mice. To study whether the alleviating effect of Acacetin on gastrointestinal motility disorder was related to protein and lipid metabolism, we used ELISA to detect indicators related to protein metabolism and lipid metabolism. ELISA results showed that the levels of PAB, CER, and TRF were decreased in the MG compared with the CG. Compared to the MG, PAB, CER, and TRF levels were significantly increased after Acacetin

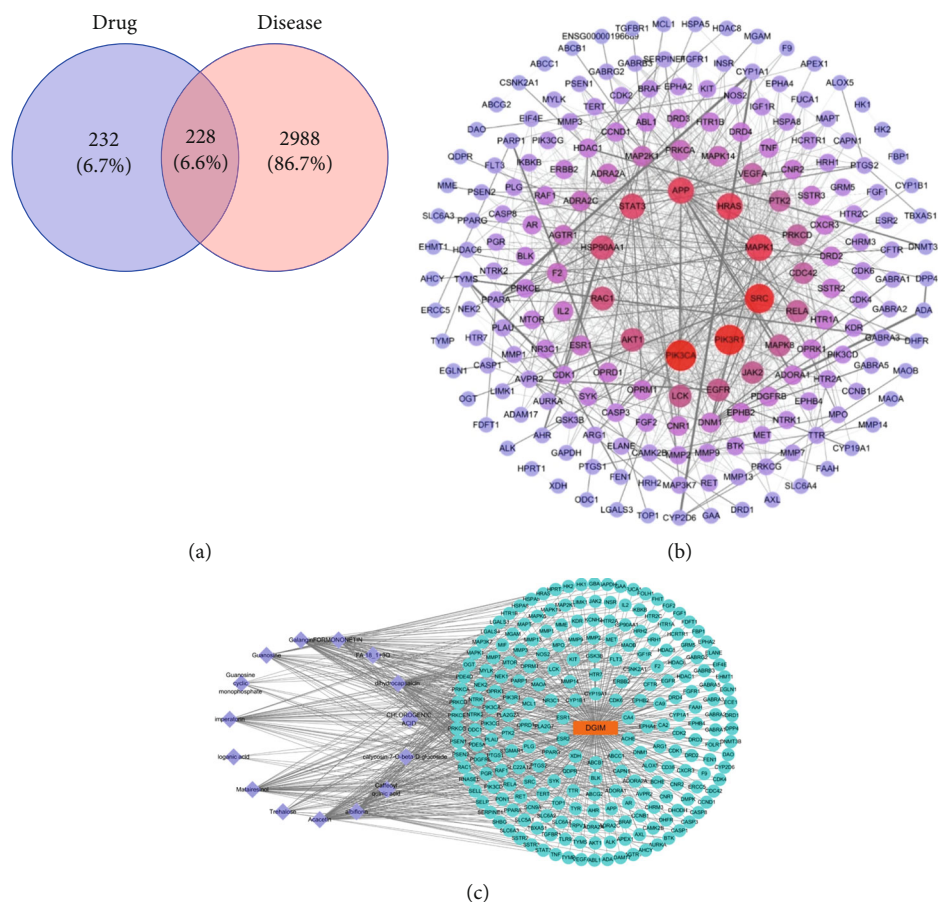


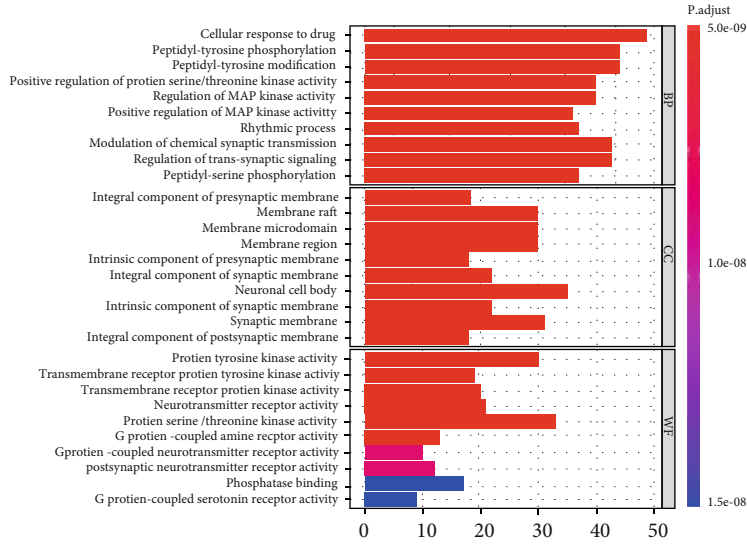
FIGURE 1: Network analysis of targets. (a) Venn diagram of screened drug targets and disease targets. (b) PPI network diagram of common targets for drug diseases. The color and size of the node were adjusted according to the degree value. The larger the color, the deeper the degree value; the thickness of the line, from thick to thin, indicated that the edge betweenness was from large to small. (c) Component-disease-target network diagram. Among them, the lavender circle was the active ingredient, green was the target of drug action on the disease, and orange was the disease.

TABLE 2: The key ingredients in Weishu decoction.

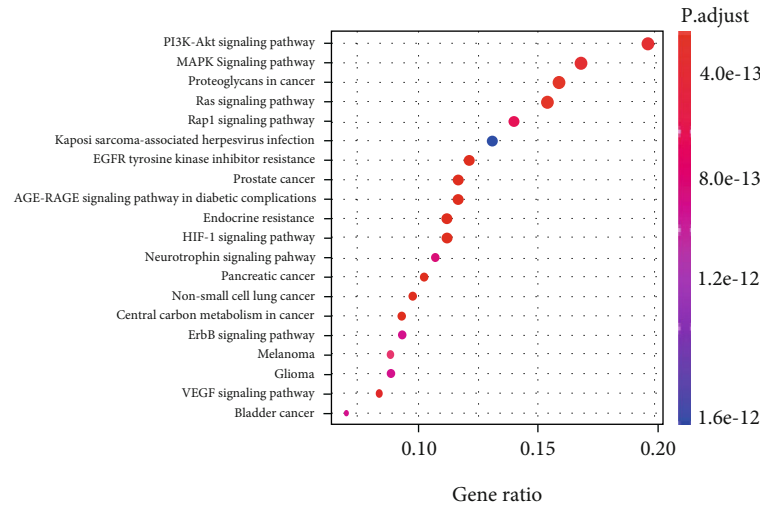
Name	Average shortest path length	Betweenness centrality	Closeness centrality	Degree
Acacetin	2.411523	0.030515	0.414676	64
Galangin	2.427984	0.029059	0.411864	63
Dihydrocapsaicin	2.502058	0.027317	0.399671	56
Matairesinol	2.55144	0.022025	0.391935	51
Albiflorin	2.600823	0.015837	0.384494	42
Imperatorin	2.633745	0.012516	0.379688	38
Formononetin	2.699588	0.008011	0.370427	31
Guanosine	2.716049	0.008303	0.368182	30
Trehalose	2.823045	0.003325	0.354227	20
Chlorogenic acid	2.831276	0.001778	0.353198	17
Guanosine cyclic monophosphate	2.930041	0.000886	0.341292	11
Calycosin-7-O-beta-D-glucoside	2.888889	0.000502	0.346154	8
Loganic acid	2.938272	0.000189	0.340336	5

and Mosapride treatment (Figure 5(a)). Compared with the CG, serum TG level was increased, and LDL-C, HDL-C, and TC levels were significantly decreased in the MG. Com-

pared with the MG, serum TG level was decreased, and LDL-C, HDL-C, and TC levels were increased after Acacetin and Mosapride treatment (Figure 5(b)). These results



(a)



(b)

FIGURE 2: Bioinformatic analyzed of drug-disease intersection targets. (a) Gene ontology annotations. (b) KEGG annotation.

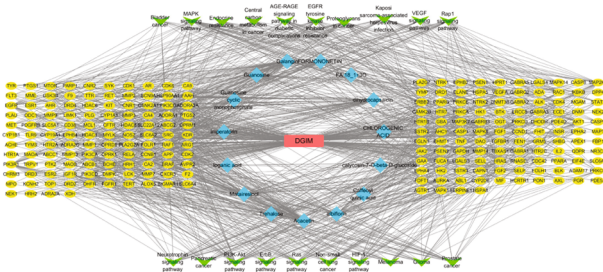


FIGURE 3: Component-disease-pathway-target network. Blue was the compound, yellow was the target of traditional Chinese medicine, and green was the top 20 pathways with the most significant enrichment.

suggested that Acacetin could regulate the protein and lipid metabolism of gastrointestinal motility disorder mice, and the effect of high-dose Acacetin was the best.

3.6. Acacetin Regulated Gastrointestinal Inflammation and Apoptosis. To investigate the effects of Acacetin on gastrointestinal inflammation and apoptosis, we first detected the levels of inflammation-related indicators. Compared with the CG, serum levels of $TNF-\alpha$, $IL-1\beta$, and $IL-6$ were significantly increased in the MG. Compared with the MG, the levels of $TNF-\alpha$, $IL-1\beta$, and $IL-6$ were decreased after Acacetin and Mosapride treatment (Figure 6(a)). The effect of high-dose Acacetin was the best, indicating that Acacetin could inhibit the inflammatory response. Next, we validated the levels of apoptosis-related markers. qRT-PCR and

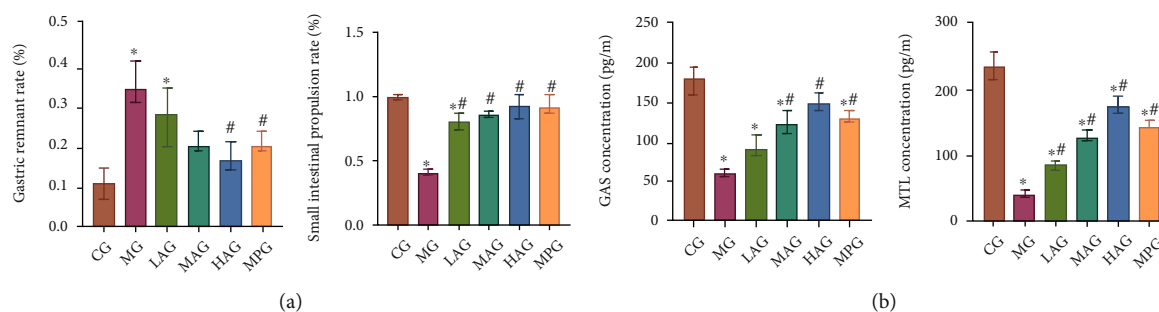


FIGURE 4: Acacetin improved gastrointestinal motility in mice. (a) Comparison of gastric remnant rate and small intestinal propulsion rate in each group. (b) The serum levels of GAS and MTL were detected by ELISA. CG: control group; MG: model group, LAG: low-dose Acacetin group; MAG: middle-dose Acacetin group; HAG: high-dose Acacetin group; MPG: Mosapride group; * $P < 0.05$ vs. CG; # $P < 0.05$ vs. MG.

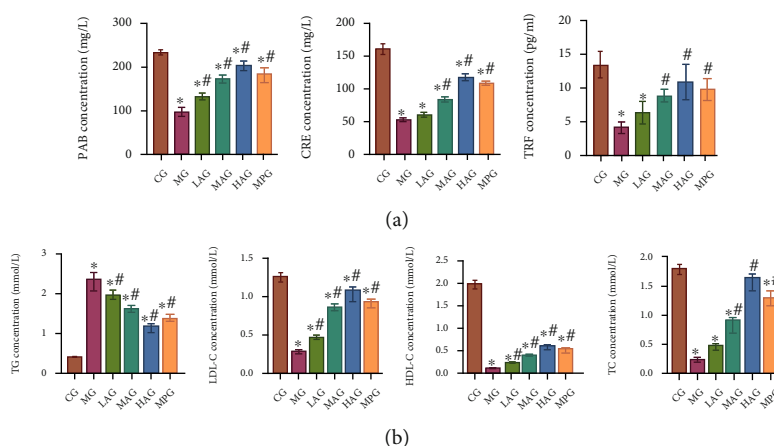


FIGURE 5: Acacetin regulated protein and lipid metabolism in gastrointestinal motility disorder mice. (a) ELISA was used to detect PAB, CER, and TRF levels. (b) The serum levels of TG, LDL-C, HDL-C, and TC were detected by ELISA. CG: control group; MG: model group; LAG: low-dose Acacetin group; MAG: middle-dose Acacetin group; HAG: high-dose Acacetin group; MPG: Mosapride group; * $P < 0.05$ vs. CG; # $P < 0.05$ vs. MG.

Western blot results showed that, compared with the CG, the expression of Bcl-2 was decreased, the expression of Bax and Caspase-12 was increased, and the expression of proinflammatory cytokines TNF- α , IL-1 β , and IL-6 was also increased in the MG. Compared with the MG, the expression of Bcl-2 was increased, the expression of Bax and Caspase-12 was decreased, and the expression of proinflammatory cytokines TNF- α , IL-1 β , and IL-6 was also decreased after the treatment of Acacetin and Mosapride (Figures 6(b) and 6(c)). These results suggested that Acacetin could regulate gastrointestinal inflammation and apoptosis.

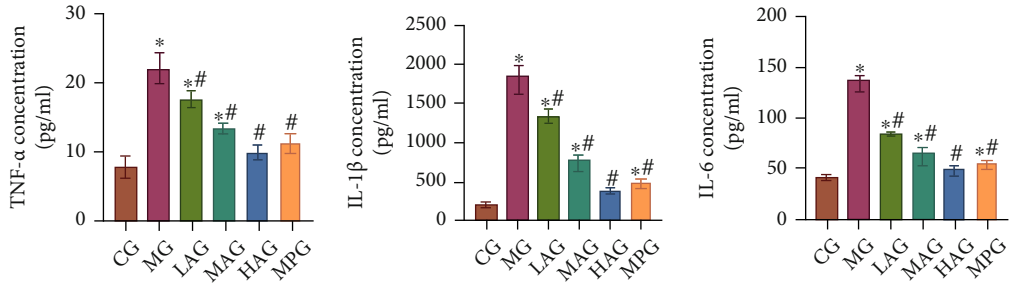
3.7. Acacetin Improved Gastrointestinal Motility by Inhibiting the Activation of the PI3K-AKT Signaling Pathway. Based on the results of KEGG enrichment analysis, we analyzed the role of Acacetin in the regulation of the PI3K-AKT signaling pathway. Western blot and IHC were performed to detect the expression of PI3K-AKT signaling pathway-related proteins PI3K, p-PI3K, AKT, and p-AKT. The results showed that Acacetin and Mosapride improved the expression of p-PI3K and p-AKT. That was, by down-regulating PI3K and AKT, the gastrointestinal motility dis-

orders were improved, and the effect of high-dose Acacetin was better (Figures 7(a) and 7(b)). Overall, these data revealed that high-dose Acacetin could improve gastrointestinal motility disorders by inhibiting the activation of the PI3K-AKT signaling pathway.

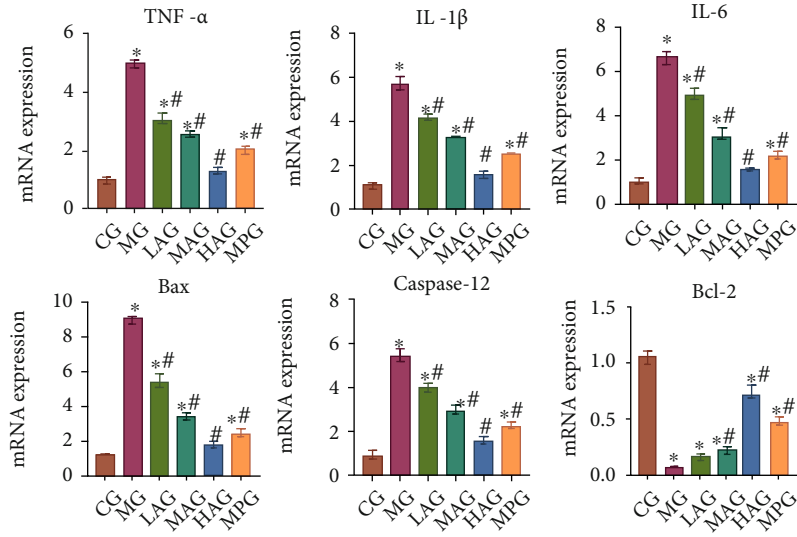
4. Discussion

Gastrointestinal motility disorder is a common gastrointestinal disease that seriously affects life quality. Based on network pharmacological methods, we conducted many experiments. The results showed that high-dose Acacetin could regulate the PI3K-AKT signaling pathway to inhibit gastrointestinal inflammation and apoptosis and regulate protein metabolism and lipid metabolism. It is helpful to regulate the contents of GAS and MTL in mice with gastrointestinal motility disorders and improve gastric emptying ability, which plays an essential role in alleviating gastrointestinal motility disorders.

A variety of hormones play a regulatory role in gastric motility, among which GAS and MTL are the main hormones associated with gastrointestinal motility disorders.



(a)



(b)

FIGURE 6: Continued.

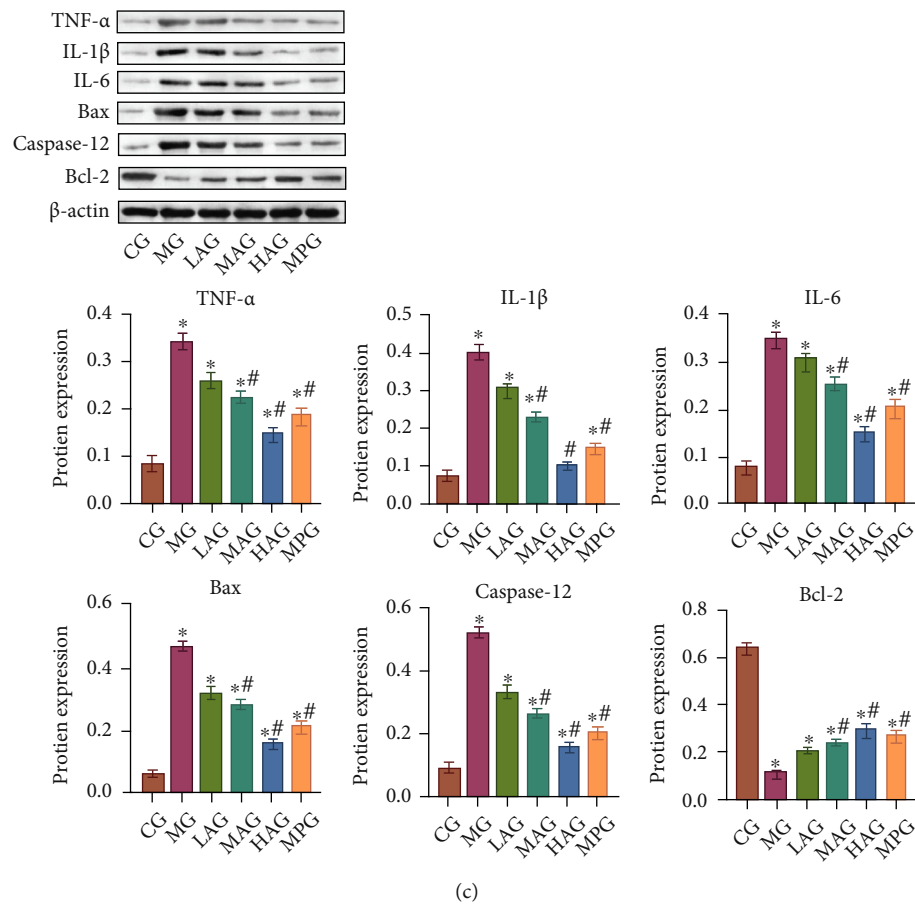


FIGURE 6: Acacatin regulated gastrointestinal inflammation and apoptosis. (a) The levels of TNF- α , IL-1 β , and IL-6 in serum of mice were determined by ELISA. (b) qRT-PCR was performed to detect the mRNA expressions of inflammatory cytokines TNF- α , IL-1 β , and IL-6 and apoptotic proteins Bcl-2, Bax, and Caspase-12. (c) Western blot was used to detect the protein expressions of inflammatory cytokines TNF- α , IL-1 β , and IL-6 and apoptotic proteins Bcl-2, Bax, and Caspase-12. CG: control group; MG: model group, LAG: low-dose Acacatin group; MAG: middle-dose Acacatin group; HAG: high-dose Acacatin group; MPG: Mosapride group; * $P < 0.05$ vs. CG; # $P < 0.05$ vs. MG.

GAS is a crucial gastrointestinal hormone that is mainly secreted by G cells [26]. GAS can biaxially regulate gastric acid secretion to keep the gastric acid level in dynamic balance, and the physiological level of GAS could promote gastric emptying [27]. MTL is a protein encoded by the MLNR gene, which can cause the intense contraction of phase III of interdigestive transitional complex movement, promoting gastrointestinal muscle contraction and accelerating gastric emptying [28]. Studies have found that Salsola Collina, an edible plant, can promote gastric emptiness and intestinal propulsion [29]. In the functional gastrointestinal disease with weight loss, after using mirtazapine, the levels of GAS and MTL will be significantly increased [30]. In this study, the levels of GAS and MTL were increased after Acacatin and Mosapride treatment. It suggested that Acacatin could modulate GAS and MTL levels in gastrointestinal motility disorder mice, and high-dose Acacatin has the best effect.

Serum PAB is an effective tool for evaluating malnourished patients [31]. It has been reported that the level of PAB in the study group was significantly higher than that in the control group when parenteral nutrition was given after the gastric cancer surgery [32]. CER is a kind of ferrous oxidase in mammalian plasma and plays a vital role in the

iron metabolism [33]. TRF is thought to be the “delivery system” for many beneficial and harmful metal ions to enter cells [34]. It has been reported that patients with inflammatory bowel disease have abnormal lipid metabolism compared with healthy people [35]. In Crohn disease patients, lipid profiles, lipoprotein concentration and composition, and oxidation-antioxidant status are disturbed [36]. We speculated that the abnormality of protein and lipid metabolism might be related to gastrointestinal motility disorders. The results showed that after using Acacatin, the levels of PAB, CER, and TRF were significantly increased, the levels of LDL-C, HDL-C, and TC were increased, and TG level was decreased. These results indicated that high-dose Acacatin could regulate protein metabolism and lipid metabolism in gastrointestinal motility disorder mice, and high-dose Acacatin has the best effect. The analysis of the correlation between nutrient metabolic indexes and disease conditions might be helpful to provide better clinical treatment and improve prognosis.

During the occurrence of gastrointestinal motility disorders, cytokines mediating the inflammatory response in the injury area can secrete inflammatory factors. Acacatin has antioxidant and anti-inflammatory effects [37]. In the study

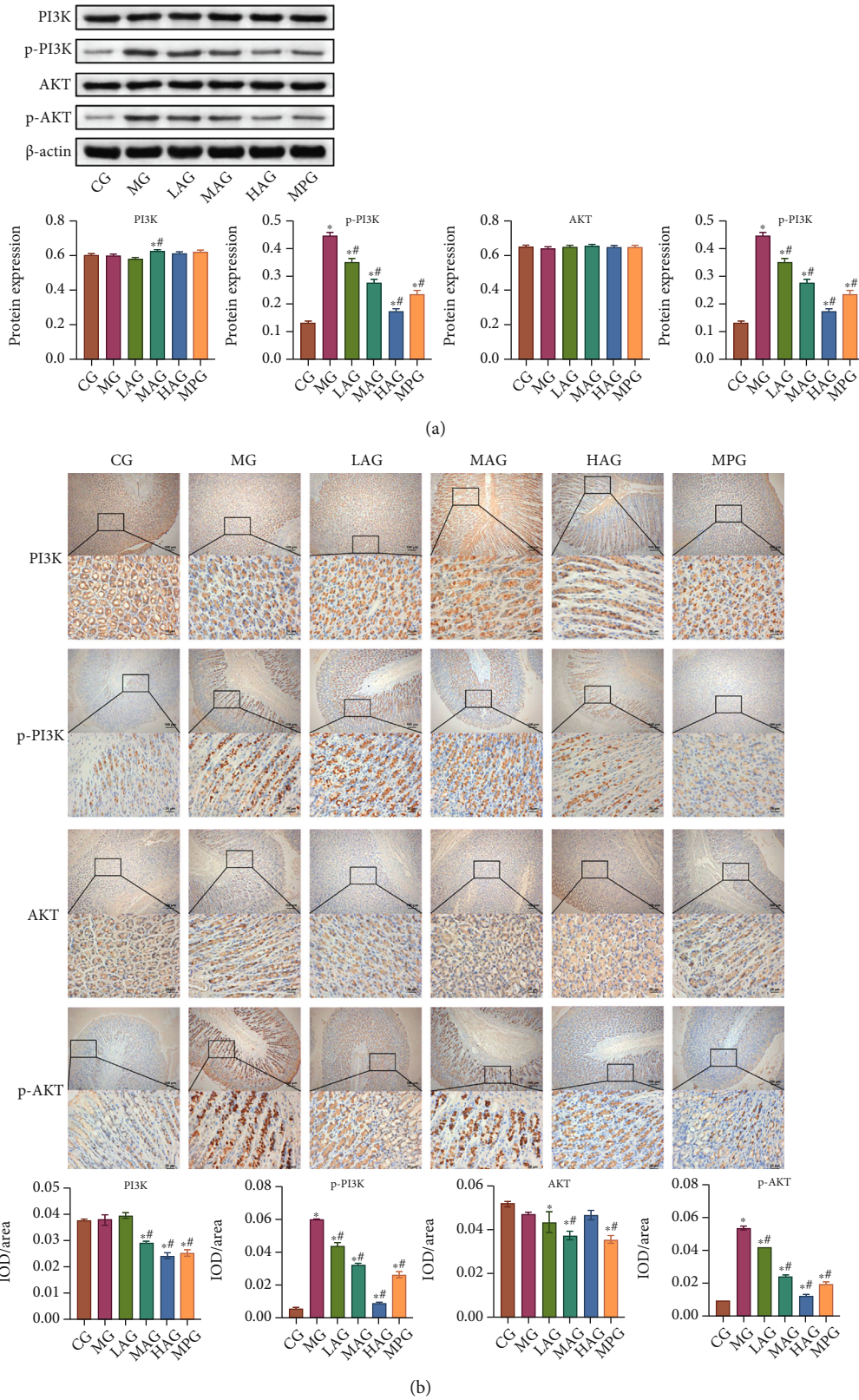


FIGURE 7: Acacetin improved gastrointestinal motility by inhibiting the activation of the PI3K-AKT signaling pathway. (a) The expression of the PI3K-AKT signaling pathway-related proteins PI3K, p-PI3K, AKT, and p-AKT was detected by Western blot. (b) IHC was used to measure the expression of PI3K, p-PI3K, AKT, and p-AKT in gastric antrum tissues. CG: control group; MG: model group; LAG: low-dose Acacetin group; MAG: middle-dose Acacetin group; HAG: high-dose Acacetin group; MPG: Mosapride group; * $P < 0.05$ vs. CG; # $P < 0.05$ vs. MG; scale bar = 25 μ m; the magnification was 400 times; scale bar = 100 μ m; the magnification was 100 times.

of cerebral ischemia-reperfusion injury, the expression of TNF- α , IL-1 β , and IL-6 was significantly decreased after Acacetin treatment compared with the middle cerebral artery occlusion group [38]. Acacetin can inhibit the increase of TNF- α , IL-6, and IL-1 β in the lipopolysaccharide-stimulated human periodontal ligament cells in a dose-dependent manner and inhibit cell apoptosis [39]. In our study, the levels of TNF- α , IL-1 β , and IL-6 were decreased after using Acacetin, while the expression of Bcl-2 was increased, and the expression of Bax and Caspase-12 was decreased. These results suggested that Acacetin could regulate gastrointestinal inflammation and apoptosis, and high-dose Acacetin has the best effect. As a classical signaling pathway, the PI3K-AKT signaling pathway plays a vital role in the diseases. *Caulis Sargentodoxae* could regulate the PI3K-AKT signaling pathway to exert anti-inflammatory effects [40]. PI3K could respond to LPS and TNF- α , activate AKT, and affect NF- κ B to produce antiapoptotic and proinflammatory effects [41]. Our study found that high-dose Acacetin improved gastrointestinal motility disorders by inhibiting the activation of the PI3K-AKT signaling pathway.

However, our study has some limitations. As shown in Table 2, the degree of Acacetin was 64, and the degree of Galangin was 63. The two compounds did not differ obviously in terms of topological parameters. Therefore, we also should experimentally evaluate the therapeutic effect of Galangin. However, due to the limitation of experimental funds, we cannot experimentally evaluate the therapeutic effect of Galangin at present. In the future, we will further investigate the effect of Galangin on gastrointestinal motility disorders and the mechanisms involved and compare the efficacy of Acacetin and Galangin.

In conclusion, our findings suggest that high-dose Acacetin regulates the PI3K-AKT signaling pathway to inhibit gastrointestinal inflammation and apoptosis, regulate protein metabolism and lipid metabolism, and help regulate the levels of GAS and MTL. Acacetin treatment has high efficacy and safety, which could significantly improve the gastrointestinal motility disorder mice, improve the ultrastructure of gastrointestinal tissue, and inhibit the inflammatory response. Our study provides strong experimental support for the clinical treatment of gastrointestinal motility disorders with Acacetin.

Data Availability

All available data information is included in the article.

Conflicts of Interest

All authors claimed that there was no potential conflict of interest between them.

Acknowledgments

The authors would like to thank the First Affiliated Hospital of Hunan University of Traditional Chinese Medicine Laboratory for providing space and materials for their experiments. This study was supported by the National Natural

Science Foundation of China (No. 81904176), Hunan Natural Science Youth Fund (No. 2019JJ50463), and Hunan University of traditional Chinese medicine to build a first-class discipline in China (2018-2020).

Supplementary Materials

Supplementary Materials Supplementary Table 1: a total of 15 active components in Weishu Decoction. Supplementary Table 2: a total of 460 target compounds in Weishu Decoction. (*Supplementary Materials*)

References

- [1] B. E. Lacy and K. Weiser, "Gastrointestinal motility disorders: an update," *Digestive Diseases*, vol. 24, no. 3-4, pp. 228-242, 2006.
- [2] N. Valentin, A. Acosta, and M. Camilleri, "Early investigational therapeutics for gastrointestinal motility disorders: from animal studies to phase II trials," *Expert Opinion on Investigational Drugs*, vol. 24, no. 6, pp. 769-779, 2015.
- [3] D. Foong, J. Zhou, A. Zarrouk, V. Ho, and M. D. O'Connor, "Understanding the biology of human interstitial cells of Cajal in gastrointestinal motility," *International Journal of Molecular Sciences*, vol. 21, no. 12, p. 4540, 2020.
- [4] C. Di Lorenzo and N. N. Youssef, "Diagnosis and management of intestinal motility disorders," *Seminars in Pediatric Surgery*, vol. 19, no. 1, pp. 50-58, 2010.
- [5] C. Madl and U. Madl, "Gastrointestinal motility in critically ill patients," *Medizinische Klinik - Intensivmedizin und Notfallmedizin*, vol. 113, no. 5, pp. 433-442, 2018.
- [6] A. J. Bredenoord and A. J. Smout, "Advances in motility testing—current and novel approaches," *Nature Reviews. Gastroenterology & Hepatology*, vol. 10, no. 8, pp. 463-472, 2013.
- [7] M. Yang, J. L. Chen, L. W. Xu, and G. Ji, "Navigating traditional Chinese medicine network pharmacology and computational tools," *Evidence-Based Complementary and Alternative Medicine*, vol. 2013, pp. 1-731923, 2013.
- [8] X. J. Wang, J. S. Guo, Y. Xu et al., "Effect of Shuwei decoction (舒胃汤) on rats with functional dyspepsia," *Chinese Journal of Integrative Medicine*, 2016.
- [9] Z. Zhou, B. Chen, S. Chen et al., "Applications of network pharmacology in traditional Chinese medicine research," *Evidence-based Complementary and Alternative Medicine*, vol. 2020, 7 pages, 2020.
- [10] R. Zhang, X. Zhu, H. Bai, and K. Ning, "Network pharmacology databases for traditional Chinese medicine: review and assessment," *Frontiers in Pharmacology*, vol. 10, p. 123, 2019.
- [11] X. Wang, Z. Y. Wang, J. H. Zheng, and S. Li, "TCM network pharmacology: a new trend towards combining computational, experimental and clinical approaches," *Chinese Journal of Natural Medicines*, vol. 19, no. 1, pp. 1-11, 2021.
- [12] S. Li and B. Zhang, "Traditional Chinese medicine network pharmacology: theory, methodology and application," *Chinese Journal of Natural Medicines*, vol. 11, no. 2, pp. 110-120, 2013.
- [13] J. Ru, P. Li, J. Wang et al., "TCMSP: a database of systems pharmacology for drug discovery from herbal medicines," *Journal of Cheminformatics*, vol. 6, no. 1, 2014.
- [14] L. Gao, X. D. Wang, Y. Y. Niu et al., "Molecular targets of Chinese herbs: a clinical study of hepatoma based on network pharmacology," *Scientific Reports*, vol. 6, no. 1, 2016.

- [15] D. Gfeller, A. Grosdidier, M. Wirth, A. Daina, O. Michielin, and V. Zoete, "SwissTargetPrediction: a web server for target prediction of bioactive small molecules," *Nucleic Acids Research*, vol. 42, no. W1, pp. W32–W38, 2014.
- [16] M. Safran, I. Dalah, J. Alexander et al., "GeneCards Version 3: the human gene integrator," *Database: the journal of biological databases and curation*, vol. 2010, 2010.
- [17] NCBI Resource Coordinators, "Database resources of the National Center for Biotechnology Information," *Nucleic Acids Research*, vol. 46, no. D1, pp. D8–D13, 2018.
- [18] J. S. Amberger, C. A. Bocchini, F. Schiettecatte, A. F. Scott, and A. Hamosh, "OMIM.org: Online Mendelian Inheritance in Man (OMIM®), an online catalog of human genes and genetic disorders," *Nucleic Acids Research*, vol. 43, no. D1, pp. D789–D798, 2015.
- [19] D. Szklarczyk, A. L. Gable, D. Lyon et al., "STRING v11: protein-protein association networks with increased coverage, supporting functional discovery in genome-wide experimental datasets," *Nucleic Acids Research*, vol. 47, no. D1, pp. D607–D613, 2019.
- [20] N. T. Doncheva, J. H. Morris, J. Gorodkin, and L. J. Jensen, "Cytoscape String App: network analysis and visualization of proteomics data," *Journal of Proteome Research*, vol. 18, no. 2, pp. 623–632, 2019.
- [21] C. Sun, Q. Yuan, D. Wu, X. Meng, and B. Wang, "Identification of core genes and outcome in gastric cancer using bioinformatics analysis," *Oncotarget*, vol. 8, no. 41, pp. 70271–70280, 2017.
- [22] X. Chang, S. Wang, Y. R. Bao, T. J. Li, X. M. Yu, and X. S. Meng, "Multicomponent, multitarget integrated adjustment - metabolomics study of Qizhiweitong particles curing gastrointestinal motility disorders in mice induced by atropine," *Journal of Ethnopharmacology*, vol. 189, pp. 14–21, 2016.
- [23] H. R. Kim, C. G. Park, and J. Y. Jung, "Acacetin (5, 7-dihydroxy-4'-methoxyflavone) exhibits in vitro and in vivo anticancer activity through the suppression of NF- κ B/Akt signaling in prostate cancer cells," *International Journal of Molecular Medicine*, vol. 33, no. 2, pp. 317–324, 2014.
- [24] X. A. Guo, Y. Liu, X. J. Wang, Y. Xu, H. L. Tan, and J. Yin, "Effect of Shuwei decoction on enteric nervous system-interstitial cells of Cajal-smooth muscle network structure injury in deep muscle nerve plexus of functional dyspepsia rats," *Zhongguo Zhong Xi Yi Jie He Za Zhi*, vol. 36, no. 4, pp. 454–459, 2016.
- [25] W. Xu, N. Wang, H. R. Ding et al., "Effects of Pogostemon cablin on gastrointestinal function of rats with syndrome of damp retention in middle-jiao," *Zhongguo Zhong Yao Za Zhi*, vol. 42, no. 23, pp. 4649–4655, 2017.
- [26] D. Fourmy, V. Gigoux, and J. C. Reubi, "Gastrin in gastrointestinal diseases," *Gastroenterology*, vol. 141, no. 3, pp. 814–818.e3, 2011.
- [27] E. Kristensson, M. Sundqvist, R. Håkanson, and E. Lindström, "High gastrin cell activity and low ghrelin cell activity in high-anxiety Wistar Kyoto rats," *The Journal of Endocrinology*, vol. 193, no. 2, pp. 245–250, 2007.
- [28] T. Ohno, E. Mochiki, and H. Kuwano, "The roles of motilin and ghrelin in gastrointestinal motility," *International Journal of Peptide*, vol. 2010, article 820794, pp. 1–6, 2010.
- [29] S. Wang, M. Yan, Y. Guo, R. Sun, H. Jin, and Y. Gong, "In vivo and in vitro effects of Salsola collina on gastrointestinal motility in rats," *Iranian Journal of Basic Medical Sciences*, vol. 23, no. 3, pp. 383–389, 2020.
- [30] S. M. Jiang, L. Jia, J. Liu, M. M. Shi, and M. Z. Xu, "Beneficial effects of antidepressant mirtazapine in functional dyspepsia patients with weight loss," *World Journal of Gastroenterology*, vol. 22, no. 22, pp. 5260–5266, 2016.
- [31] H. F. Zhang, L. Q. Li, Y. L. Ge et al., "Serum prealbumin improves the sensitivity of pneumonia severity index in predicting 30-day mortality of CAP patients," *Clin Lab*, vol. 66, no. 5/2020, 2020.
- [32] Y. Jin, C. Yong, K. Ren, D. Li, and H. Yuan, "Effects of post-surgical parenteral nutrition on patients with gastric cancer," *Cellular Physiology and Biochemistry*, vol. 49, no. 4, pp. 1320–1328, 2018.
- [33] N. E. Hellman and J. D. Gitlin, "CERULOPLASMINMETABOLISM ANDFUNCTION," *Annual Review of Nutrition*, vol. 22, no. 1, pp. 439–458, 2002.
- [34] H. Li and Z. M. Qian, "Transferrin/transferrin receptor-mediated drug delivery," *Medicinal Research Reviews*, vol. 22, no. 3, pp. 225–250, 2002.
- [35] B. Ripollés Piquer, H. Nazih, A. Bourreille et al., "Altered lipid, apolipoprotein, and lipoprotein profiles in inflammatory bowel disease: consequences on the cholesterol efflux capacity of serum using Fu5AH cell system," *Metabolism*, vol. 55, no. 7, pp. 980–988, 2006.
- [36] E. Levy, Y. Rizwan, L. Thibault et al., "Altered lipid profile, lipoprotein composition, and oxidant and antioxidant status in pediatric Crohn disease," *The American Journal of Clinical Nutrition*, vol. 71, no. 3, pp. 807–815, 2000.
- [37] S. Wang, B. Lin, W. Liu et al., "Acacetin induces apoptosis in human osteosarcoma cells by modulation of ROS/JNK activation," *Drug Design, Development and Therapy*, vol. Volume 14, pp. 5077–5085, 2020.
- [38] J. Bu, S. Shi, H. Q. Wang et al., "Acacetin protects against cerebral ischemia-reperfusion injury via the NLRP3 signaling pathway," *Neural Regeneration Research*, vol. 14, no. 4, pp. 605–612, 2019.
- [39] J. Liu, Y. G. Wang, S. Y. Yu, C. E. Li, and S. M. Kang, "Protective effect of acacetin in human periodontal ligament cells via regulation of autophagy and inflammation," *Die Pharmazie*, vol. 75, no. 9, pp. 436–439, 2020.
- [40] B. Liu, X. Zheng, J. Li et al., "Revealing mechanism of Caulis Sargentodoxae for the treatment of ulcerative colitis based on network pharmacology approach," *Bioscience Reports*, vol. 41, no. 1, 2021.
- [41] J. Wei and J. Feng, "Signaling pathways associated with inflammatory bowel disease," *Recent Patents on Inflammation & Allergy Drug Discovery*, vol. 4, no. 2, pp. 105–117, 2010.

Research Article

The Mutual Inhibition of FoxO1 and SREBP-1c Regulated the Progression of Hepatoblastoma by Regulating Fatty Acid Metabolism

Yu Hu, Hongyan Zai, Wei Jiang, Zhenglin Ou, Yuanbing Yao, and Qin Zhu 

Department of General Surgery, Xiangya Hospital, Central South University, Changsha, 410008, China

Correspondence should be addressed to Qin Zhu; zhuqinn08@163.com

Received 22 April 2021; Revised 22 July 2021; Accepted 25 August 2021; Published 8 September 2021

Academic Editor: Shuai Chen

Copyright © 2021 Yu Hu et al. This is an open access article distributed under the Creative Commons Attribution License, which permits unrestricted use, distribution, and reproduction in any medium, provided the original work is properly cited.

Background. Hepatoblastoma (HB) is the most common liver malignancy in pediatrics, but the treatment for this disease is minimal. This study is aimed at exploring the effect of FoxO1 and SREBP-1c on HB and their mechanism. **Methods.** FoxO1, SREBP-1c, FASN, ACLY, ACC, and MAGL expressions in tissue samples were detected by RT-qPCR and WB. IHC was utilized to measure FASN content. Overexpression and knockdown of FoxO1 and sSREBP-1c were performed on Huh-6 cells. Cell proliferation, migration, and invasion were examined by CCK8, scratch, and transwell assay. ELISA was performed to test the ATP, FAO, NEFA, and Acetyl-CoA contents. ChIP was used to detect the interaction between SREBP-1c protein and the FoxO1 gene. In vivo tumorigenesis was conducted on mice. The morphology of tumor tissue sections was observed by HE staining. **Results.** FoxO1 expression was downregulated in HB tissue, while the expressions of SREBP-1c, FASN, ACLY, ACC, and MAGL were upregulated. In Huh-6 cells and mouse tumor tissues, FoxO1 knockdown resulted in increased cell proliferation, migration, and invasion and active fatty acid metabolism. On the contrary, after the knockdown of SREBP-1c, cell proliferation, migration, and invasion were weakened, and fatty acid metabolism was significantly reduced. SREBP-1c interacted with the promoter of the FoxO1 gene. When FoxO1 was knocked down, the tumor tissue was more closely packed. After the knockdown of the SREBP-1c gene, the structure of tumor cells was deformed. **Conclusion.** FoxO1 and SREBP-1c inhibited each other in HB, leading to the increase of intracellular fatty acid metabolism, and ultimately facilitated the development of HB.

1. Introduction

Hepatoblastoma (HB) is a pediatric tumor caused by hepatic progenitors or hepatoblasts. It is the most common liver malignant tumor in pediatrics. Its annual incidence is 1.5 cases per million, accounting for about 1% of all childhood cancers [1]. The primary treatment for HB is surgical resection, but about 60% of the tumors are unresectable at the onset, so the therapeutic effect is minimal [2]. Therefore, there is an urgent need to explore the pathogenesis of HB and develop new therapeutic targets to improve the clinical outcome of HB patients. One of the characteristics of cancer cells is reprogramming fatty acid metabolism [3]. Variation in lipid metabolisms, such as increased fatty acid uptake, de novo lipogenesis, is closely related to the generation of

cancer cells [4]. The expression and activity of enzymes involved in lipid metabolism are significantly increased in many cancer cells, such as fatty acid synthase (FASN) and Acetyl-coenzyme A carboxylase (ACC) [5]. FASN plays a crucial role in lipid metabolism and has become an attractive target in clinical cancer treatment [6]. However, the mechanism of lipid metabolism in HB is still unclear.

The forkhead box-O1 (FoxO1) is a central regulator of metazoan physiology and plays a role in cell cycle, proliferation, apoptosis, autophagy, stress resistance, DNA repair, tumor inhibition, metabolism, and other cellular activities [7]. FoxO1 is tightly regulated by modifying its mRNA and protein, and its expression is regulated by nutritional signals in the environment [8]. Dysfunction of the FoxO1 pathway leads to various metabolic diseases, including diabetes,

obesity, nonalcoholic fatty liver disease, and atherosclerosis [8]. FoxO1 is also thought to inhibit the development of osteosarcoma, but the mechanism of its inhibitory effect is not precise [9]. FoxO1 also plays a vital role in fat metabolism. It is reported that FoxO1 can slow down lipid deposition in the liver caused by stress response [10].

Sterol regulatory element-binding proteins are a class of transcription factors that regulate lipid homeostasis by controlling the synthesis of cholesterol, fatty acids, triglycerides, and phospholipids [11]. Among them, sterol regulatory element-binding protein-1c (SREBP-1c) is derived from the SREBP-1c gene on chromosome 17 and mainly regulates the synthesis of fatty acids and triglycerides [12]. It is an essential link between oncogenic signals and tumor metabolism [13]. Activation of SREBP-1c causes upregulation of FASN, enhances fatty acid metabolism, and theoretically promotes cancer development [14]. Geng et al. believed that SREBP-1c-driven lipid metabolism could be targeted to treat glioblastoma [15]. The regulatory pathway of FoxO1 and SREBP-1c in endometrial cancer was established [16]. FoxO1 inhibited insulin-induced SREBP-1c promoter activity in goat mammary epithelial cells and the transcription of SREBP-1c by the liver X receptor response element and SREBP response element on the SREBP-1c promoter [17]. However, it is still elusive whether FoxO1 and SREBP-1c play a role in regulating fatty acid metabolism in HB.

Derive from the above background, we wanted to explore the effect of FoxO1 and SREBP-1c on HB cells and study the mechanism of fatty acid metabolism in HB. Therefore, we collected clinical samples of HB and paracancerous tissues, purchased various HB cell lines, and conducted in vitro and in vivo experiments. This study contributes to our further understanding of the pathophysiology of HB and is expected to provide a new approach for the clinical treatment of HB patients.

2. Materials and Methods

2.1. Tissues and Cells. Clinical HB and paracancerous tissue samples were collected from Xiangya Hospital and divided into HB and control groups, with 5 samples in each group. The Human Research Ethics Committee of Xiangya Hospital approved this study (No. AF/SQ202104798). HB cells including HepG2 (bio-105877), HB611 (bio-73286), Huh-6 (bio-73060), and human normal liver cell WRL68 (bio-53604) were purchased from Biobw and cultured in DMEM medium (D5796, Sigma) containing 10% fetal bovine serum (#10099141, Gibco) at 37°C and 5% CO₂. In order to investigate the effect of FoxO1, Huh-6 cells were randomly divided into 5 groups (the control, the oe-NC, the oe-FoxO1, the si-NC, and the si-FoxO1 groups). In the second majority of the study, Huh-6 cells were divided into 5 groups (control, si-NC, si-FoxO1, si-SREBP-1c, and si-FoxO1+si-SREBP-1c groups) to study the effect of SREBP-1c.

2.2. Vector Recombination and Cell Transfection. The si-FoxO1 and si-SREBP-1c vectors were obtained by integrating the shRNA sequence targeting human FoxO1 or SREBP-1c into a psi-LVRU6MP lentivirus vector (GeneCo-

poeia). The human FoxO1 cDNA sequence was inserted into the pCDH-CMV-MCS-EF1a vector (Epoch Life Science Inc) to get the oe-FoxO1 vector. The empty psi-LVRU6MP lentivirus vector was used as the si-FoxO1 vector. The empty pCDH-CMV-MCS-EF1a vector was the oe-FoxO1 vector. Then, the constructed vector was transfected into 293 T cells (HEK293T, Procell) to produce lentiviral solutions. These lentiviral solutions were transfected into Huh-6 cells with the assistance of 8 µg/mL of Polybrene (#H9268, Sigma-Aldrich) [18]. Forty-eight hours after transfection [19], the cells were further examined.

2.3. Real-Time Quantitative Polymerase Chain Reaction (RT-qPCR). The trizol method was used to extract total RNA from cells and tissues. cDNA was obtained by reverse transcription using an mRNA reverse transcription kit (#CW2569, Cowin Bio). Primer sequences of FoxO1, SREBP-1c, FASN, ATP-citric acid lyase (ACLY), ACC, monoacylglycerol lipase (MAGL), and β-actin were designed (Table 1). Shanghai Sangon Biotech synthesized the primers. Fluorescent dye was added to prepare the PCR reaction system. DNA amplification was performed by a fluorescent quantitative PCR apparatus (PIKOREAL96, Thermo). The amplification and fusion curves of each gene were obtained by real-time monitoring of fluorescence signals. β-Actin was used as an internal reference. The relative expression of genes was calculated using the 2^{-ΔΔCT} method.

2.4. Western Blot (WB). Total protein of cells and tissues was extracted with RIPA lysate (#P0013B, Beyotime). The mixture was bathed in water for 5 min after the protein supernatant was thoroughly mixed with the loading buffer. Then, the protein samples were isolated on gel and electrophoresis at a constant pressure of 75 V for 130 min. After electrophoresis, the target protein was transferred to the nitrocellulose membrane. The membranes were sealed and then incubated with primary antibodies FASN (1:2000, 10624-1-AP, Proteintech), ACLY (1:10000, 67166-1-Ig, Proteintech), ACC (1:4000, 21923-1-AP, Proteintech), MAGL (1:5000, ab124796, Abcam), and β-actin (1:5000, 60008-1-Ig, Proteintech) for 90 min. After incubation, the membranes were washed with PBST. The membranes and secondary antibody HRP goat anti-mouse IgG (SA00001-1, 1:5000, Proteintech) or HRP goat anti-rabbit IgG (SA00001-2, 1:6000, Proteintech) were then incubated for 90 min. Finally, the strips on the membranes were visualized using SuperECL Plus hypersensitive luminescence solution (K-12045-D50, Advansta). Grayscale values for all stripes were determined by Photoshop 2019. β-Actin was used as an internal parameter. The expression of the protein was expressed by the ratio of the grayscale value of the target protein to that of the reference protein.

2.5. Immunohistochemistry (IHC). IHC detected the expression of FASN in tissues. Paraffin sections of HB and paracancerous tissues were made. After the sections were deparaffinized and rehydrated, they were heated in a microwave oven to repair the antigen. The endoenzymes were inactivated by adding 1% periodate acid to the sections. Then, sections and the anti-FASN antibody (10624-1-AP,

TABLE 1: RT-qPCR primer sequences.

Gene	Sequences (5'-3')	Product length (bp)
<i>FoxO1</i>	F: ACTTCATCTCATTCTCCCTTCTGC R: GCACAACTTACAGCTGGTTTTCAA	199
<i>ACLY</i>	F: CCTCAGCCATCCAGAATCGG R: CTTCAGCCAGGACTTGACCC	194
<i>SREBP-1c</i>	F: GCTCCCTAGGAAGGGCCGTA R: CACTCTTAGTTTTCTCCGTTT	240
<i>FASN</i>	F: CCTGGCTGCCTACTACATCG R: CACATTTCAAAGGCCACGCA	102
<i>ACC</i>	F: CTCTTGGCCTTTTCCCGGTC R: GTTATCCCCAAACCCAGGCA	228
<i>MAGL</i>	F: TCCAGCATGCCAGAGGAAAG R: TGGGACACAAAGATGAGGGC	142
<i>β-Actin</i>	F: ACATCCGTAAAGACCTCTATGCC R: AGCACAGCCTGGATAGCAAC	224

TABLE 2: FoxO1 primer sequences.

Primer	Sequences (5'-3')	Product length (bp)
1	F: CAGAACCCCATGGCTAAGGTC R: ATCTAATCCTGGCTCATTCCT	153
2	F: ACACTGAGGGTCCATCCCA R: AGTTTTACACTGAACTGTGCAT	165
3	F: TGTTAGACTTTGTAGCCGGACAG R: TGGCCGATTCACAGATCAAGA	125
4	F: ACACTGGAAGACCTTTGCCTT R: GAACAGCCCTCCACCTACCTT	108
5	F: GGATTGGGGTACAAGTCCAC R: GGTTTCCTGATGTATTACCCAC	168
6	F: CCCCATATTTCCACGAACTCCA R: AGGACAAATAACAAGCGACCTTC	159

1:100, Proteintech) were incubated overnight at 4°C and then incubated with the second antibody for 30 min the next day. The sections were rinsed with PBS solution and incubated with DAB solution (ZSGB-BIO) for 5 min at room temperature. Sections were re-stained with hematoxylin for 5 min. The sections were treated with alcohol and xylene and sealed with neutral resin. Microscope (BA410T, MOTIC) was used to capture images, and the image analysis software was Image-Pro-Plus. The average IOD was calculated by the ratio of the cumulative optical density of the positive expression site to the sample area in view.

2.6. Cell Counting Kit-8 (CCK8) Assay. The cells were digested with trypsin and resuspended in a DMEM medium. Cells were seeded in a 5×10^3 cells/well density in a 96-well

plate of 100 μ L per well. The plates were placed in an incubator at 37°C and 5% CO₂ for preculture. 10 μ L CCK8 solution (NU679, Dojindo) was added to each well. Cells were further incubated in the incubator for 4 h. Bio-Tek microplate analyzer (MB-530, HEALES) was used to measure the absorbance at 450 nm.

2.7. Scratch Assay. Trypsin was used to digest the cells in the logarithmic growth phase were digested into a single-cell suspension. Cells were seeded into a 6-well culture plate at a density of 5×10^5 cells per well. The cells were cultured at 37°C in a 5% CO₂ incubator for about 24 h until covered with six-well plates. A scratch was made with a pipette tip along the transverse line behind the six-well plates. The plates were washed three times with PBS to remove

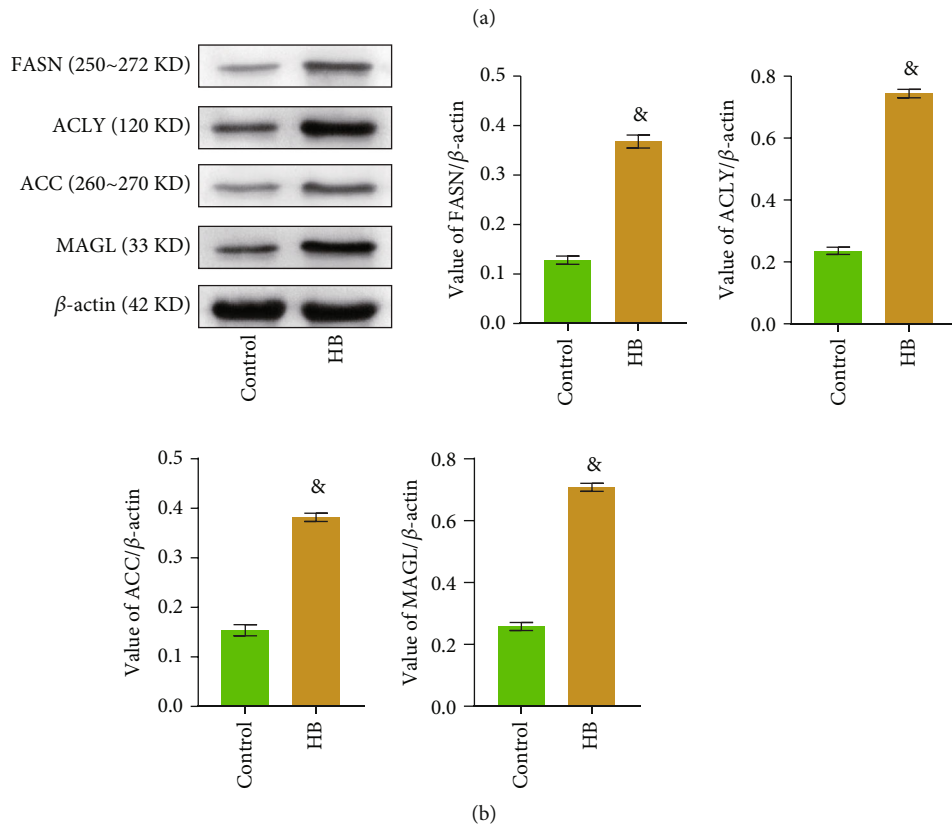
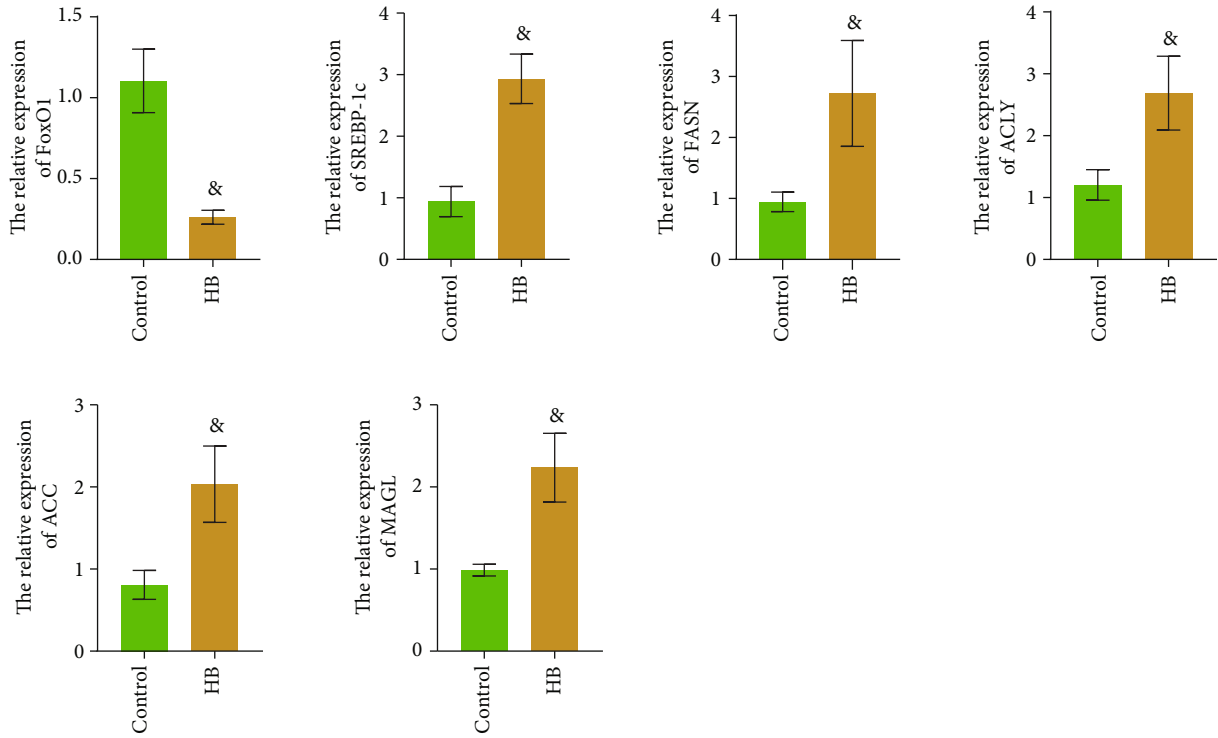


FIGURE 1: Continued.

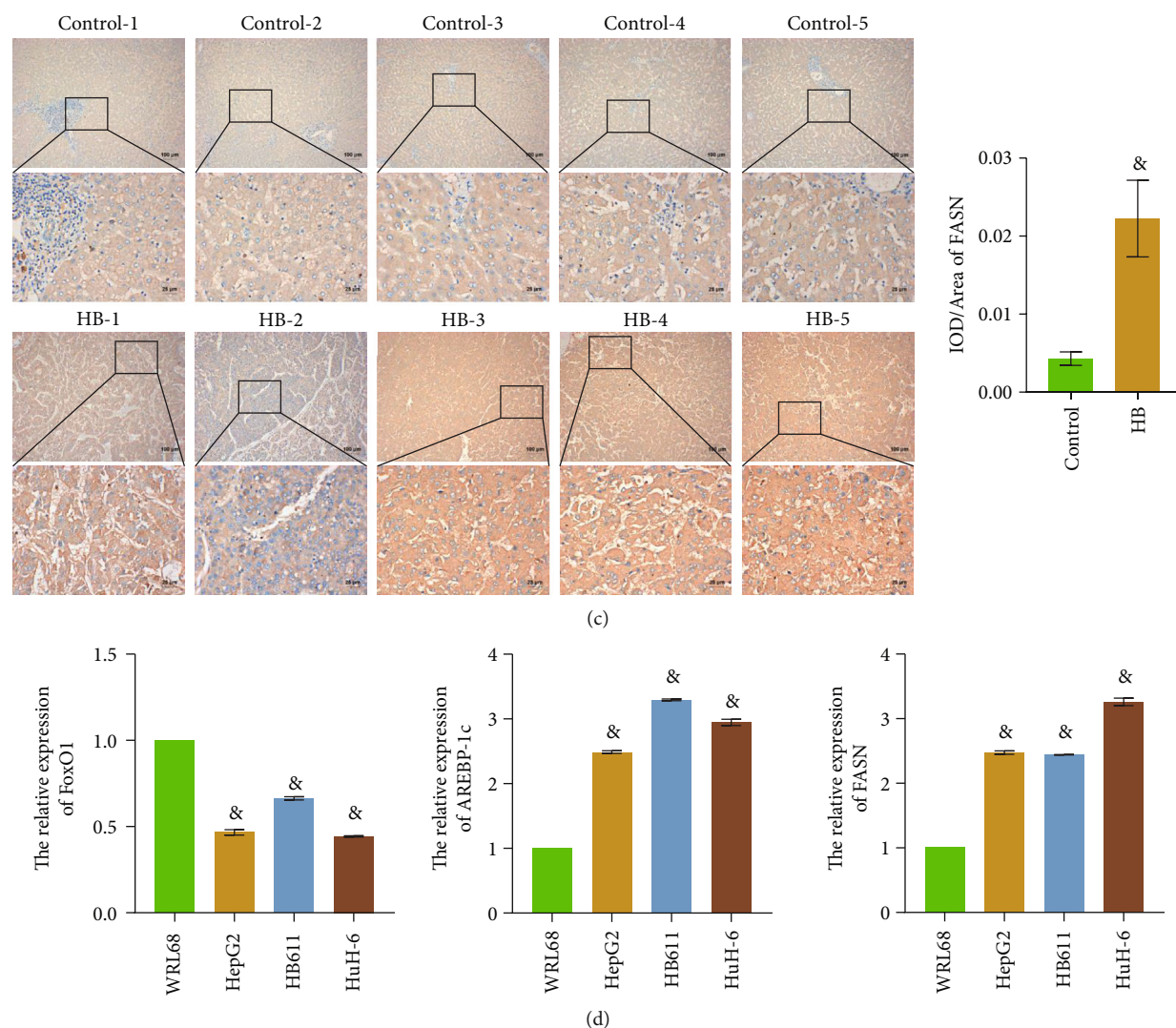


FIGURE 1: FoxO1 expression was downregulated while SREBP-1c and fatty acid metabolism genes were upregulated in HB. (a) The relative expression levels of FoxO1, SREBP-1c, FASN, ACLY, ACC, and MAGL were detected by RT-qPCR. (b) WB was used to measure the expressions of FASN, ACLY, ACC, and MAGL. (c) IHC evaluated the expression levels of FASN. (d) RT-qPCR was performed to examine the relative expressions of FoxO1, SREBP-1c, and FASN. The magnification is 100 or 400 times, and the corresponding scale bar is 100 μm or 25 μm ; $\&P < 0.05$ vs. the control group in (a-c); $\&P < 0.05$ vs. the WRL68 group in (d). All experiments were performed 5 times.

scratched cells. Then, serum-free DMEM medium was added. After being cultured for 0 h, 24 h, and 48 h, the cells were photographed under an inverted biological microscope (DSZ2000X, Cnmicro).

2.8. Transwell Assay. Transwell chamber (#3428, Corning) with a matrix gel (#354262, BD) was used to perform the transwell assay. The cells were digested into single-cell suspension with trypsin and resuspended in serum-free medium to 2×10^6 cells/mL. 100 μL cell suspension was inoculated in the up-compartment, and 500 μL 10% DMEM/F12 medium (D8437, Sigma) was added in the low-compartment. It was incubated in an incubator at 37°C for 48 h. The cells in the up-compartment were rinsed with PBS solution. Cells were fixed with paraformaldehyde

for 20 min, and the membrane was removed. The membrane was stained with 0.1% crystal violet for 5 min. Cells on the outer surface of the upper compartment were observed under an inverted biological microscope. After decolorization by acetic acid immersion, the cells' absorbance at 550 nm was measured with a microplate analyzer [20].

2.9. Fatty Acid Metabolism Detection. Nanjing Jiancheng Bioengineering Institute produced the ATP Assay Kit (#A095-1-1), Nonesterified Free Fatty Acids Assay Kit (#A042-2-1), and Triglyceride (TG) Assay Kit (#A110-1-1). Human Fatty Acid Oxidase (FAO) ELISA Kit (#JL48747) and Human Acetyl-Coenzyme A (Acetyl-CoA) ELISA Kit (#JL32777) were purchased from Jianglaibio (Shanghai, China). These kits were used to test adenosine triphosphate

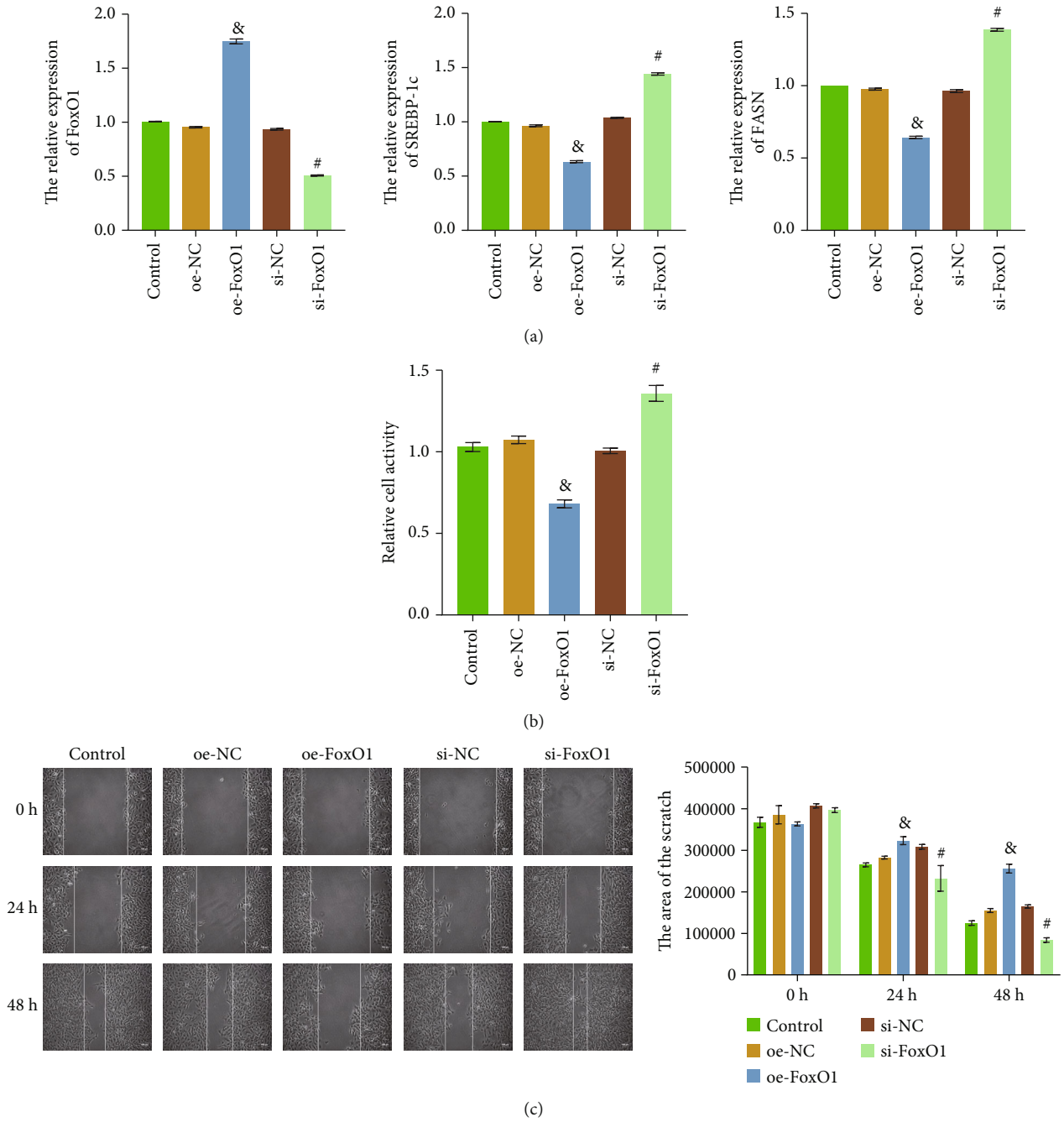
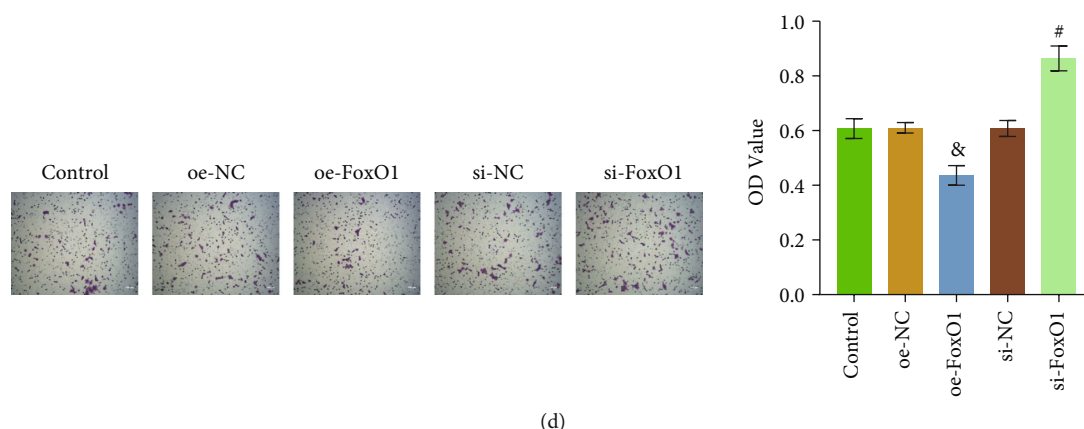


FIGURE 2: Continued.



(d)

FIGURE 2: FoxO1 deficiency led to upregulation of SREBP-1c expression and enhanced proliferation, migration, invasion of HB. (a) RT-qPCR detected the relative expression levels of FoxO1, SREBP-1c, and FASN. (b) CCK8 assay was used to detect cell proliferation. (c) Cell migration was evaluated by scratch assay. (d) Transwell assay was performed to examine cell invasion. The magnification is 100 times, scale bar = 100 μm ; $^{\&}P < 0.05$ vs. the oe-NC group; $^{\#}P < 0.05$ vs. the si-NC group. All experiments were performed 3 times.

(ATP), FAO, TG, nonesterified fatty acid (NEFA), and Acetyl-CoA in cells. Each step strictly follows the instructions of the manual. Finally, the light signal at the specified wavelength was detected with a microplate analyzer [21].

2.10. Chromatin Immunoprecipitation (ChIP). ChIP Kit (ab500, Abcam) was used to detect the direct interaction between SREBP-1c and FoxO1. After the cells were digested with trypsin, the cell suspension was incubated with formaldehyde and glycine to cross-link the target protein and the corresponding genomic DNA. Buffer D and protease inhibitors were added to the cell suspension. The mixture was ultrasonically crushed for 60 s and centrifuged. Agarose gel electrophoresis was performed to analyze the DNA fragment size. Then, immunoprecipitation was performed using agarose beads according to the instructions. Finally, the agarose beads were suspended with DNA purifying slurry to unlock the cross-linking and purify the DNA. Six pairs of primers were designed according to the FoxO1 gene's promoter (Table 2). RT-qPCR amplified DNA, and Fold Enrichment was calculated using the $2^{-\Delta\Delta\text{CT}}$ method.

2.11. In Vivo Tumorigenesis. Eight-week-old female nude mice (BALB/c, nu/nu) were purchased from the Animal Center of Central South University. Mice were randomly divided into 5 groups ($n = 9$): the control, the si-NC, the si-FoxO1, the si-SREBP-1c, and the si-FoxO1+si-SREBP-1c groups. Then, they were kept in captivity free of pathogens and given food and water at will. HepG2 cells were digested with trypsin and resuspended in a sterile salt solution. An equal number of HepG2 cells (2×10^5) was subcutaneously injected into the lower abdomen of nude mice [21]. Tumor volume was measured weekly until the maximum volume was 1000 mm^3 . All mice were sacrificed with the manual cervical dislocation method. Tumor tissues were removed, measured, weighed, and further examined.

2.12. Hematoxylin and Eosin (HE) Staining. The tumor tissues of mice were made into paraffin sections. The sections were baked in the microwave oven at 60°C for 2 h. The sections were then deparaffinized in xylene and placed in 100%, 100%, 95%, 85%, and 75% ethanol for 5 min at each stage. The sections were soaked in distilled water and stained with hematoxylin for 5 min and eosin solution for 3 min. Then, the sections were dehydrated in gradient alcohol and soaked in xylene two times, each 10 min. Finally, they were sealed with neutral gum (Sigma), and photos were taken with an ordinary light microscope (BA210T, Motic).

2.13. Immunofluorescence (IF). A microwave oven was used for baking the paraffin sections of mouse tumor tissues at 60°C for 2 h. The sections were deparaffinized and rehydrated by xylene and multiple concentration ethanol solutions. The slices were immersed in pH 6.0 citrate buffer (Wellbio). The citrate buffer was heated by the microwave oven for 24 min. After the buffer liquid was cooled, the sections were immersed in sodium borohydride solution for 30 min and Sudan Black solution for 5 min. Sections were sealed with 10% normal serum for 60 min. Sections were incubated overnight with primary antibody FASN (1:50, 10624-1-AP, Proteintech) at 4°C . On the second day, sections were incubated with the secondary antibody at 37°C for 90 min. Finally, sections were incubated with DAPI solution (Wellbio) at 37°C for 10 min and rinsed with PBS buffer. Sections were sealed with buffered glycerin and observed under a fluorescence microscope.

2.14. Statistical Analysis. Statistical analysis was performed using SPSS 20.0 (SPSS Inc, USA). Data were presented in the form of mean \pm standard deviation ($\bar{X} \pm \text{SD}$). All experiments were repeated at least three times. The Student t -test was used to analyze the differences between the two groups. Comparisons among multiple groups were conducted by one-way analysis of variance, followed by Tukey's post hoc test. $P < 0.05$ was considered statistically significant.

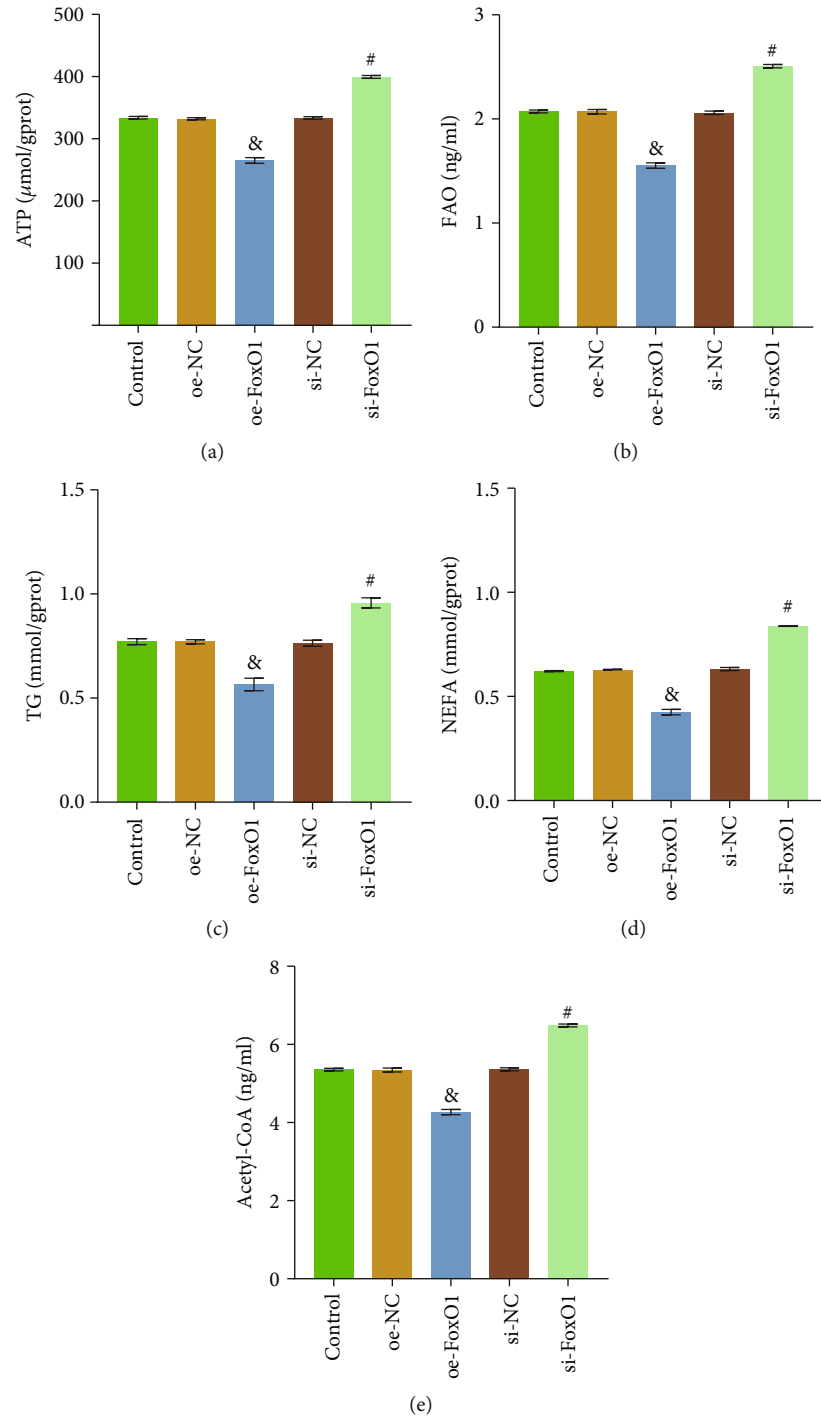


FIGURE 3: FoxO1 deficiency enhanced fatty acid metabolism in HB. (a) ATP Assay Kit was used to detect the concentration of total cellular ATP. (b) Human FAO ELISA Kit was adopted to examine FAO. (c) TG Assay Kit detected TG. (d) NEFA was examined with Nonesterified Free Fatty Acids Assay Kit. (e) Cellular Acetyl-CoA level was evaluated with Human Acetyl-CoA ELISA Kit. ^{⚠} $P < 0.05$ vs. the oe-NC group; [#] $P < 0.05$ vs. the si-NC group. All experiments were performed 3 times.

3. Results

3.1. FoxO1 Expression Was Downregulated while SREBP-1c and Fatty Acid Metabolism Genes Were Upregulated in HB.

In order to explore the changes of fatty acid metabolism in HB, RT-qPCR and WB detected the expressions of FoxO1,

SREBP-1c, FASN, ACLY, ACC, and MAGL in clinical samples. As shown from Figure 1(a), compared with the control group, the FoxO1 expression in the HB group was decreased, and the SREBP-1c expression was significantly increased. At the level of RNA and protein, the expression levels of fatty acid metabolism-related indexes (FASN, ACLY, ACC, and

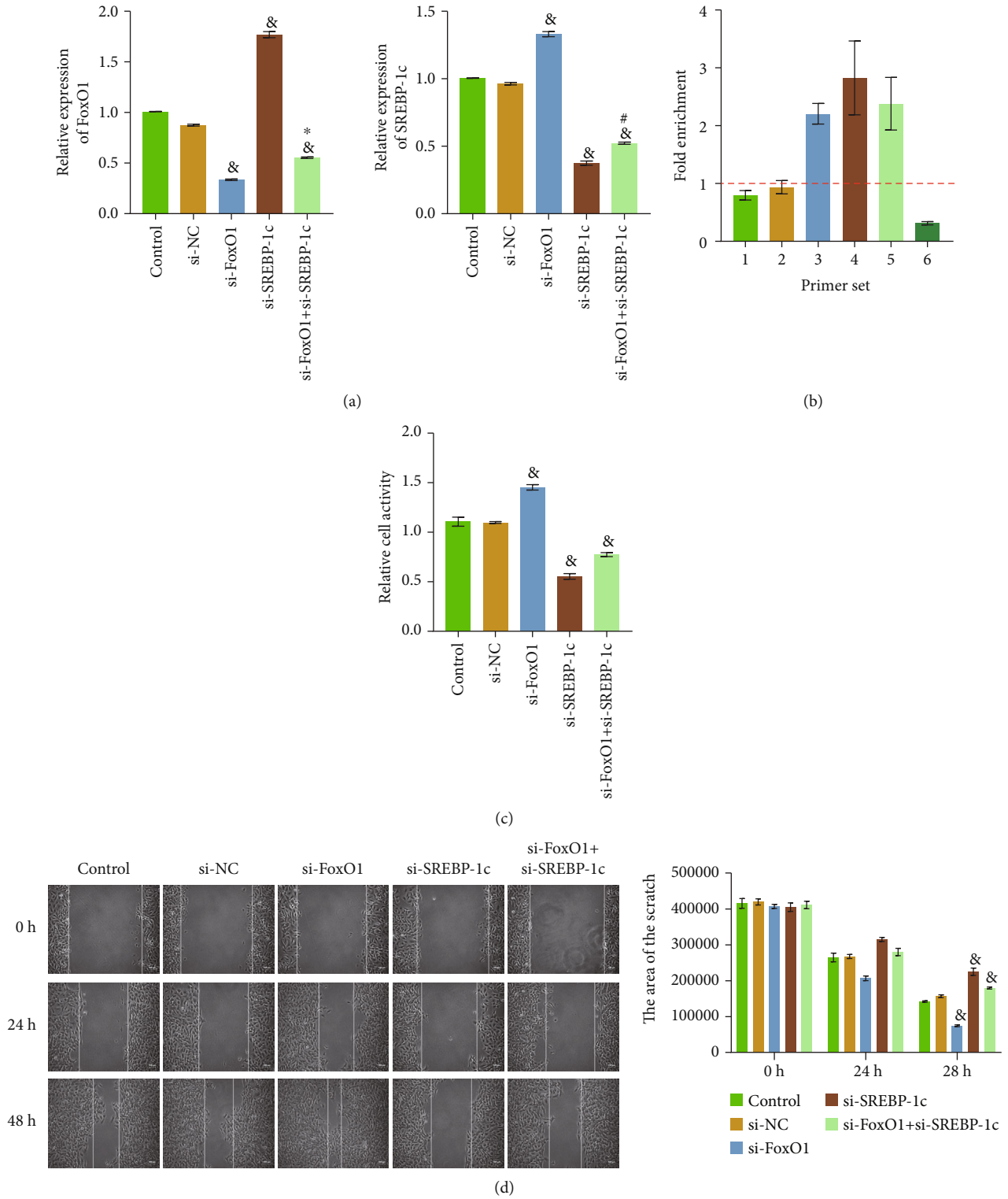


FIGURE 4: Continued.

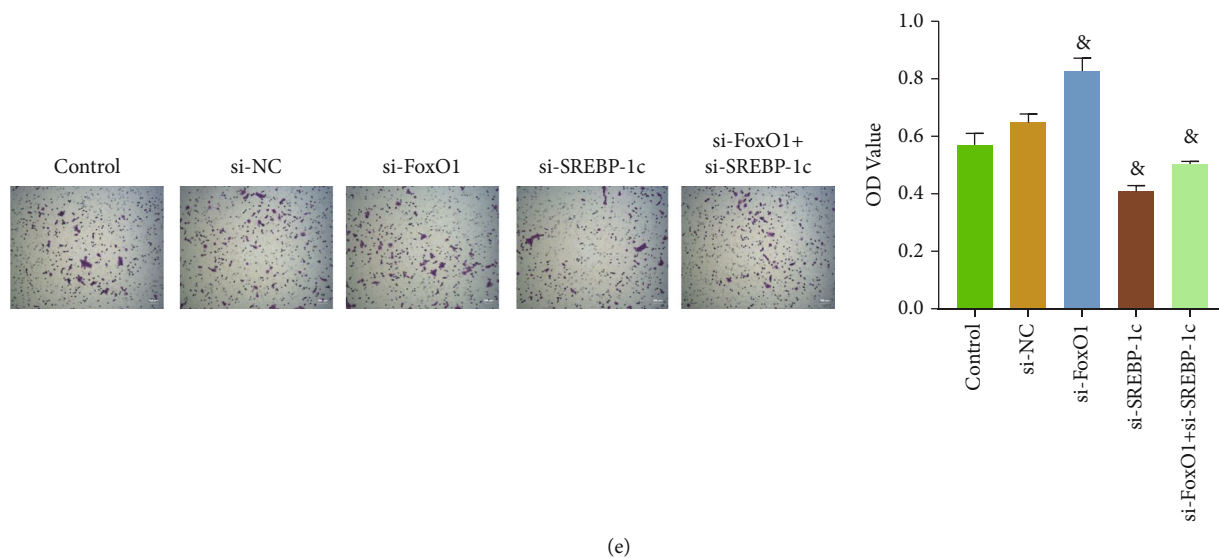


FIGURE 4: FoxO1 and SREBP-1c inhibited each other and regulated Huh-6 cell functions. (a) RT-qPCR detected the relative expression levels of FoxO1 and SREBP-1c. (b) ChIP was performed to detect the direct interaction between the FoxO1 gene and SREBP-1c protein. (c) CCK8 assay was used to detect cell proliferation. (d) Cell migration was evaluated by scratch assay. (e) Transwell assay was performed to examine cell invasion. The magnification is 100 times, scale bar = 100 μm ; [&] $P < 0.05$ vs. the si-NC group, [#] $P < 0.05$ vs. the si-FoxO1 group, and [#] $P < 0.05$ vs. the si-SREBP-1c group. All experiments were performed 3 times.

MAGL) in the HB group were higher than those in the control group (Figures 1(a) and 1(b)). IHC results showed that FASN expression was upregulated in the HB group compared with the control group (Figure 1(c)). As shown in Figure 1(d), among the three kinds of HB, the difference in gene expression between Huh-6 cells and normal liver cells (WRL68) was the most significant, so Huh-6 cells were selected for subsequent experiments.

3.2. FoxO1 Deficiency Led to Upregulation of SREBP-1c Expression and Enhanced Proliferation, Migration, Invasion of HB. In order to determine the effect of FoxO1 on SREBP-1 expression and cell function in HB, Huh-6 cells with FoxO1 overexpression or knockdown were constructed. RT-qPCR detected the expression levels of FoxO1, SREBP-1c, and FASN, and the results suggested that FoxO1 overexpression or knockdown cells were completed (Figure 2(a)). Compared with the oe-NC group, the expression of SREBP-1c and FASN in the oe-FoxO1 group decreased. Compared with the si-NC group, the expression levels of SREBP-1c and FASN in the si-FoxO1 group were increased (Figure 2(a)). As shown in Figures 2(b)–2(d), cell proliferation, migration, and invasion abilities in the oe-FoxO1 group were weaker than those in the oe-NC group. Compared with the si-NC group, cell proliferation, migration, and invasion abilities of the si-FoxO1 group were enhanced. In other words, FoxO1 could inhibit the expression of SREBP-1c and FASN and reduce the proliferation, migration, and invasion abilities of Huh-6 cells.

3.3. FoxO1 Deficiency Enhanced Fatty Acid Metabolism in HB. Intracellular fatty acid metabolism in both overexpression and deletion of FoxO1 was examined to clarify the effect of FoxO1 on fat metabolism in HB. As shown in

Figures 3(a)–3(e), compared with the oe-NC group, ATP, FAO, TG, NEFA, and Acetyl-CoA contents in the oe-FoxO1 group decreased. In the meantime, compared with the si-NC group, the contents of ATP, FAO, TG, NEFA, and Acetyl-CoA in the si-FoxO1 group increased (Figures 3(a)–3(e)). These results suggested that FoxO1 could inhibit the uptake and production of ATP, TG, NEFA, and Acetyl-CoA. It also inhibits the FAO. In other words, FoxO1 inhibited fatty acid metabolism (including anabolism and catabolism) in Huh-6 cells.

3.4. FoxO1 and SREBP-1c Inhibited Each Other and Regulated Huh-6 Cell Functions. It has been previously confirmed that FoxO1 has a regulatory effect on SREBP-1c and HB. To further explore how FoxO1 and SREBP-1c work together, Huh-6 cells that FoxO1 and SREBP-1c knockdown at the same time or SREBP-1c knockdown alone were constructed. Figure 4(a) showed that SREBP-1c could inhibit FoxO1 expression (fold change ≈ 1.65), and FoxO1 also inhibited SREBP-1c expression (fold change ≈ 1.39). We could see that SREBP-1c had a more substantial inhibitory effect on FoxO1 than FoxO1 on SREBP-1c (fold change $\approx 1.65 > 1.39$). Then, ChIP was performed to study whether there was a direct interaction between SREBP-1c and FoxO1 gene. As shown in Figure 4(b), the Fold Enrichment of primers 3, 4, and 5 was greater than 1, indicating that the enrichment capacity of nonspecific adsorption of antibodies was less than the specific action of antibodies. It showed that SREBP-1c directly interacted with sites 3, 4, and 5 of the FoxO1 gene's promoter. Cell function results exhibited that compared with the si-NC group, the cells' proliferation, migration, and invasion abilities in the si-SREBP-1c group were reduced. In contrast, those in the si-FoxO1 group were enhanced (Figures 4(c)–4(e)). When

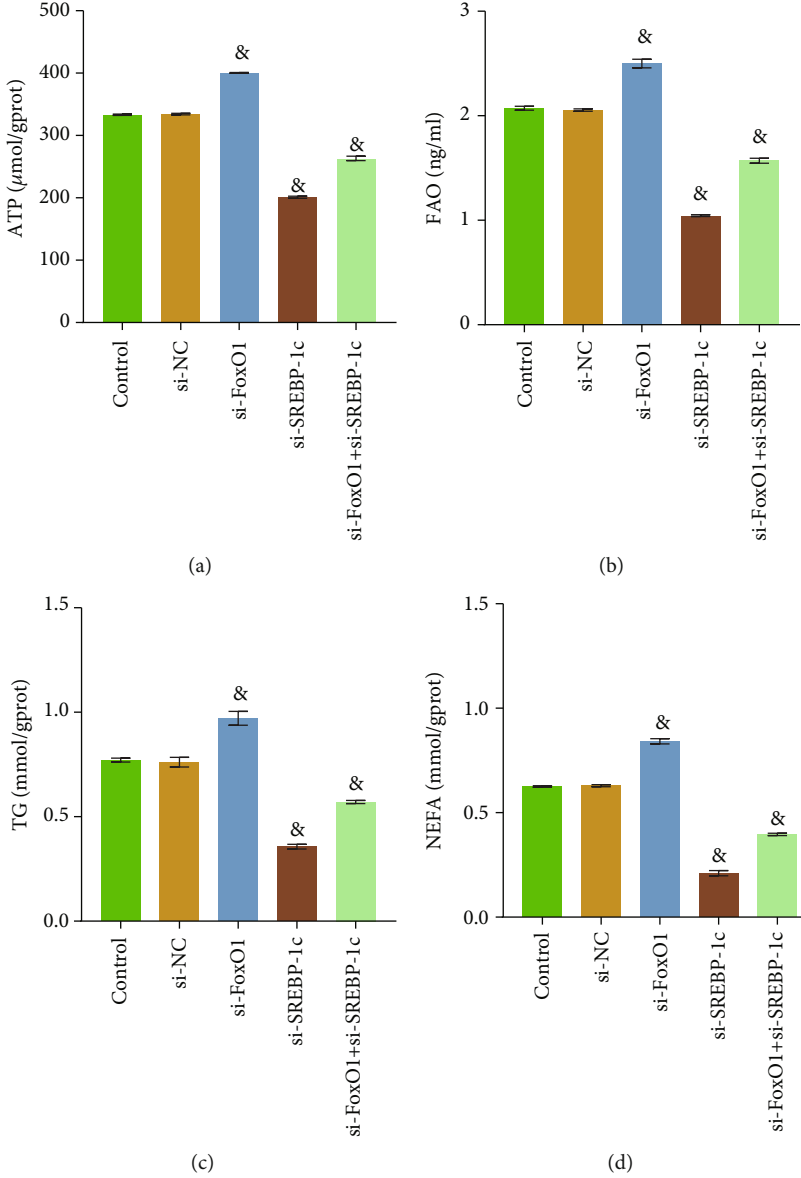


FIGURE 5: Continued.

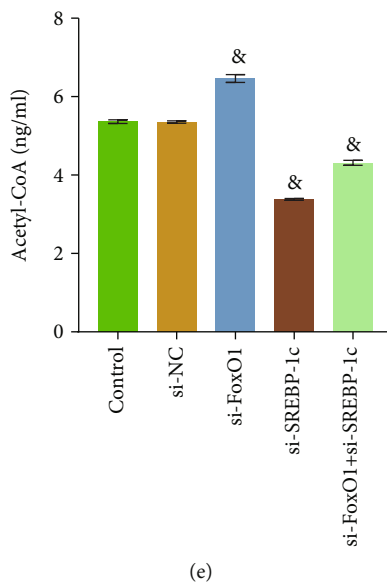


FIGURE 5: Coordinated regulation of FoxO1 and SREBP-1c regulated fatty acid in Huh-6 cells. (a) ATP Assay Kit was used to detect the concentration of total cellular ATP. (b) Human FAO ELISA Kit was adopted to examine FAO. (c) TG Assay Kit detected TG. (d) NEFA was examined with Nonesterified Free Fatty Acids Assay Kit. (e) Cellular Acetyl-CoA level was evaluated with Human Acetyl-CoA ELISA Kit. [&] $P < 0.05$ vs. the si-NC group. All experiments were performed 3 times.

FoxO1 and SREBP-1c were knocked down simultaneously, cells' proliferation, migration, and invasion abilities were reduced. These results suggested that FoxO1 inhibited cell proliferation, migration, and invasion, while SREBP-1c had the opposite effect. Meanwhile, FoxO1 and SREBP-1c inhibit each other, and their net effect in Huh-6 cells was to promote cell proliferation, migration, and invasion.

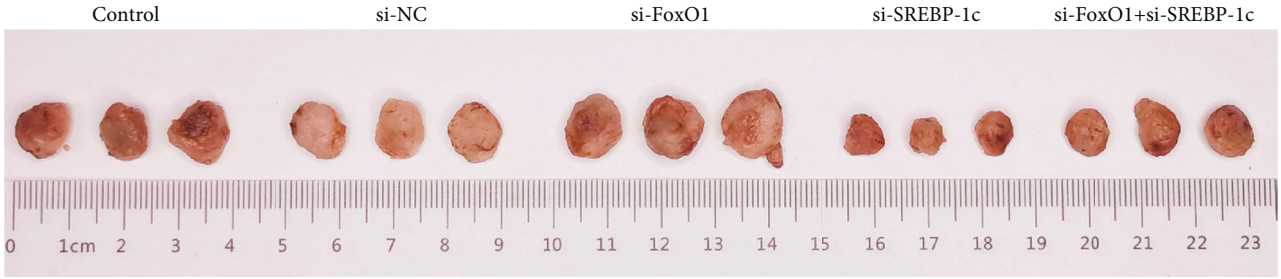
3.5. Coordinated Regulation of FoxO1 and SREBP-1c Regulated Fatty Acid Metabolism in Huh-6 Cells. We have demonstrated that FoxO1 has a regulatory effect on SREBP-1c and fatty acid metabolism in HB cells. To study how FoxO1 and SREBP-1c play roles in regulating fatty acid metabolism, we constructed Huh-6 cells that knocked down both FoxO1 and SREBP-1c or knocked down SREBP-1c alone for the detection of fatty acid metabolism-related indicators. As shown in Figures 5(a)–5(e), compared with the si-NC group, the contents of ATP, FAO, TG, NEFA, and Acetyl-CoA decreased in the si-FoxO1+si-SREBP-1c group and the si-SREBP-1c group, while that increased in the si-FoxO1 group. These results indicated that the net effect of FoxO1 and SREBP-1c was to promote fatty acid metabolism in HB cells.

3.6. Coordinated Regulation of FoxO1 and SREBP-1c Facilitated the Progression of HB by Regulating Fatty Acid Metabolism In Vivo. Previous experiments were all conducted in vitro. Subcutaneous tumor-forming models of nude mice were constructed, and tumor tissues were collected to verify whether the results of the in vivo experiments were consistent with those in vitro. Figure 6(a) showed that the subcutaneous tumorigenesis model of nude mice was successfully constructed. As shown from Figure 6(b), com-

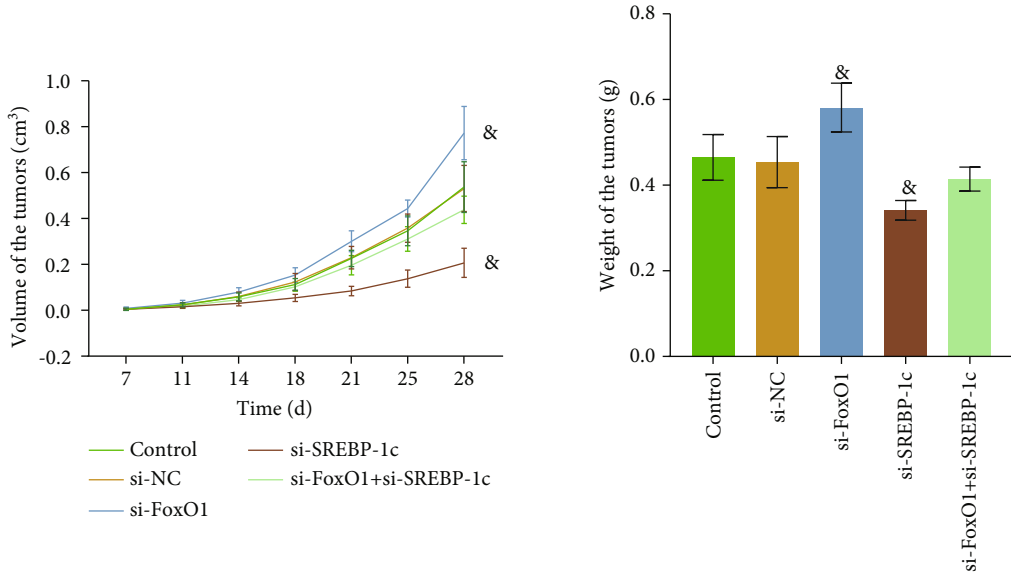
pared with the si-NC group, the tumor volume and weight of the si-FoxO1 group increased significantly, while those of the si-SREBP-1c group decreased. RT-qPCR results demonstrated that knockdown of FoxO1 and SREBP-1c genes was successfully realized in tumor tissues (Figure 6(c)). As shown in Figure 6(d), compared with the si-NC group, the tumor tissue structure and morphology were regular and tightly arranged in the si-FoxO1 group. In si-SREBP-1c and si-FoxO1+si-SREBP-1c groups, the structure of tumor tissues was damaged. Compared with the si-NC group, the expression levels of FASN, ACLY, ACC, and MAGL in the si-FoxO1 group were increased in the si-SREBP-1c and si-FoxO1+si-SREBP-1c groups were decreased (Figures 7(a)–7(c)). Tumor tissue detection results showed that FoxO1 and SREBP-1c inhibited each other, and the net effect of FoxO1 and SREBP-1c facilitated the progression of HB by regulating fatty acid metabolism in vivo.

4. Discussion

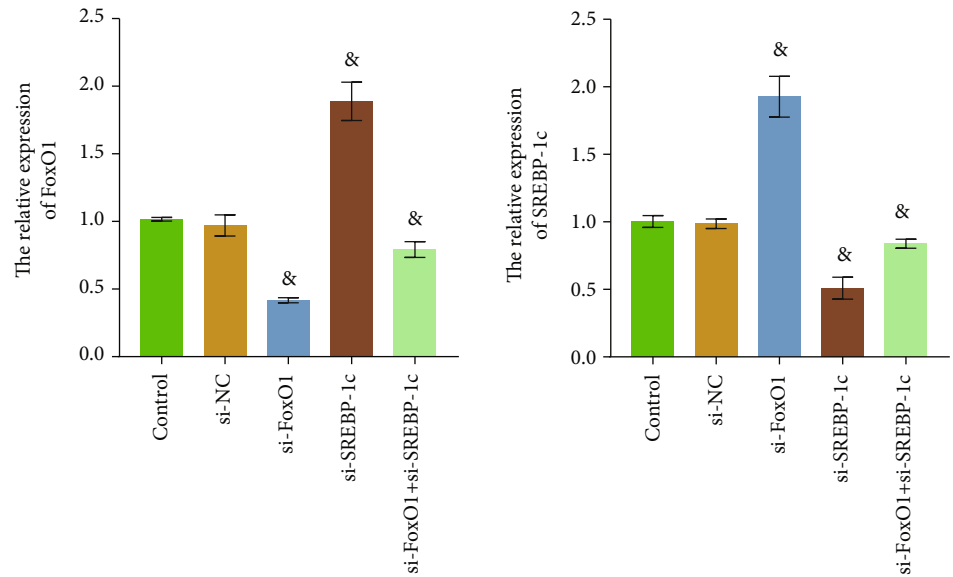
Metabolic reprogramming in cancer cells has been recognized as one of the basic features of cancer [22]. In gastric cancer, SREBP-1c is activated and fatty acid synthesis is significantly increased [23]. Neoadipogenesis and fatty acid β -oxidation are very active in hepatocellular carcinoma [24]. Our analysis of clinical samples indicates that the expression of FoxO1 was downregulated in HB tissues, and the expression of genes of SREBP-1c and key enzymes in fatty acid metabolism were significantly upregulated. Naturally, the activation of SREBP-1c and fatty acid metabolism is preliminarily considered a significant characteristic of HB. FoxO1 degradation promotes cell proliferation in colon cancer [25]. Interestingly, FoxO1 overexpression in esophageal



(a)



(b)



(c)

FIGURE 6: Continued.

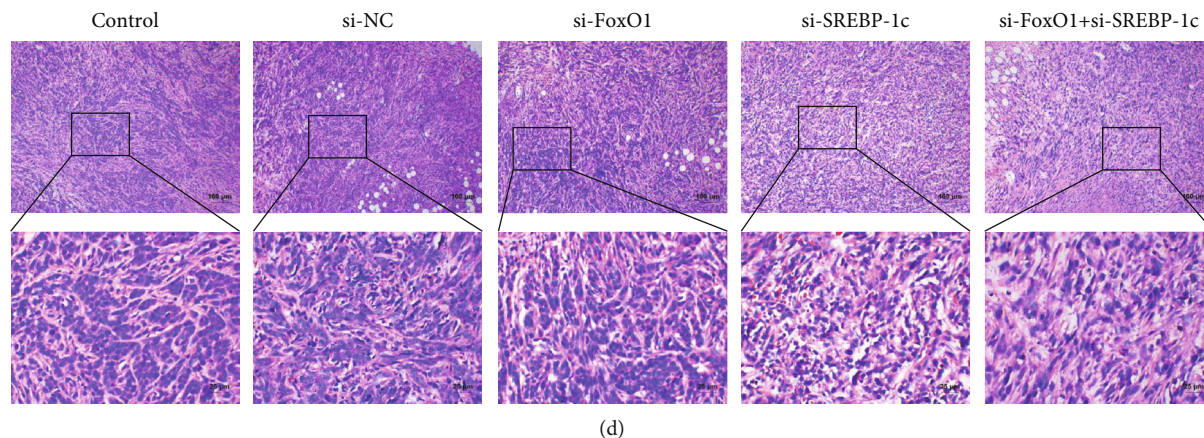


FIGURE 6: Coordinated regulation of FoxO1 and SREBP-1c facilitated the progression of HB in vivo. (a) Photograph of subcutaneous neoplasia in nude mice. (b) Volume and weight of tumor tissues. (c) The relative expression levels of FoxO1 and SREBP-1c were detected by RT-qPCR. (d) HE staining was performed to observe tumor tissues. The magnification is 100 or 400 times, and the corresponding scale bar is 100 μm or 25 μm ; $^*P < 0.05$ vs. the si-NC group. All experiments were performed 3 times.

cancer promotes tumor development by increasing macrophage infiltration [26]. After cervical cancer, the proliferation, migration, and invasion abilities are significantly enhanced [27]. In summary, FoxO1 has various functions and regulates the progression of multiple types of cancer through numerous pathways. In this study, we find that the knockdown of FoxO1 promotes the development of HB. SREBP-1c is a crucial protein in fatty acid metabolism [28]. It activates the transcription of FASN, a major fat-generating gene, which promotes the growth of bladder cancer [29]. In our study, when SREBP-1c was knocked down, the proliferation, migration, invasion, and division abilities of HB cells were reduced, and the fatty acid metabolism level was also significantly decreased.

In the study of diabetic cardiomyopathy, Ying et al. found that FoxO1 has a regulatory effect on fatty acid metabolism [30]. The ATP level of cancer cells is much higher than that of normal differentiated cells to meet the energy needs of growth and proliferation [31]. Usually, differentiated cells rely primarily on mitochondrial oxidative phosphorylation to produce ATP, a process that uses three main biofuels: glucose, glutamine, and fatty acids, while the proliferation of cancer cells depends on the FAO [32]. FAO is significantly enhanced in human glioblastoma, and inhibition of FAO leads to decreased intracellular ATP level and viability [33]. We detected ATP and FAO in HB. Results indicated that the knockdown of FoxO1 could significantly increase FAO in HB and keep ATP at a high level. In other words, FoxO1 deficiency promotes catabolism of fatty acids in HB. Acetyl-CoA is a precursor of fatty acid and cholesterol synthesis [34]. ACLY-dependent Acetyl-CoA production plays a crucial role in the early stages of pancreatic neoplasia [35]. NEFAs are organic compounds with variable linear chain lengths of 6-32 carbons and hydrophilic heads containing a carboxylic acid, promoting colon, lung, skin, and breast cancer [36]. Lipids stored in lung neutrophils are trans-

ported to metastatic tumor cells through the micropinocytosis-lysosome pathway, which enhances the survival and proliferation of tumor cells [37]. Our results showed that FoxO1 knockdown significantly increased Acetyl-CoA, NEFA, and TG levels in HB. In other words, FoxO1 deficiency can promote the anabolism of fatty acids in HB. Epigallocatechin gallate suppresses hepatic cholesterol synthesis by targeting SREBP-2 through SIRT1/FoxO1 signaling pathway [38]. In our study, FoxO1 knockdown accelerated HB cells' energy production, enhanced fatty acid metabolism, and ultimately promoted the development of HB cells. This result is consistent with previous studies.

Many studies have shown that FoxO1 could affect fatty acid metabolism by regulating the expression of SREBP-1c. For example, knockdown of FoxO1 significantly increased SREBP-1c and FASN in hepatitis C virus-infected cells [39]. Deng et al. found that FoxO1 could disrupt the assembly of key components of the SREBP-1c promoter transcription complex and inhibit the activity of the SREBP-1c promoter, thereby inhibiting the expression of SREBP-1c [40]. However, the mechanism by which FoxO1 plays a role in HB remained unclear. Through knockdown and overexpression of FoxO1, our study proved that FoxO1 could also inhibit the expression of SREBP-1c and inhibit fatty acid metabolism in HB. Interestingly, we found that SREBP-1c also had an inhibitory effect on FoxO1 (Figure 4(a)). There were few reports about the inhibitory effect of SREBP-1c on FoxO1, so we performed a ChIP experiment to prove the direct interaction between SREBP-1c and FoxO1. Some studies also supported that SREBP-1c could inhibit the expression of FoxO1 through indirect action. For example, Sajan et al. found that atypical protein kinase C activated by SREBP-1c inactivated FoxO1 via WD40/PROF (a scaffold protein)-associated Akt in diabetes [41]. Therefore, it was essential to determine their net effect on HB growth. We knocked down

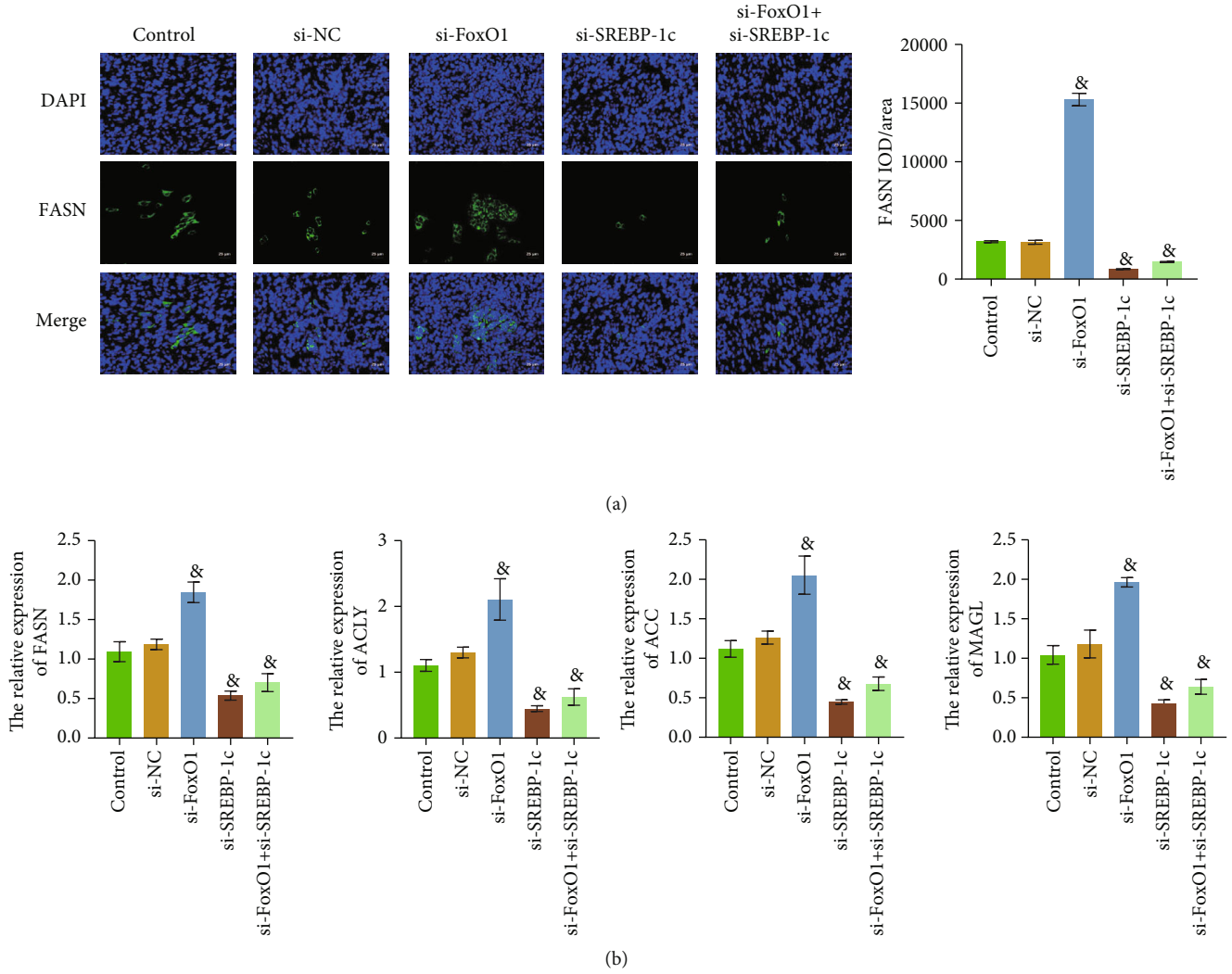


FIGURE 7: Continued.

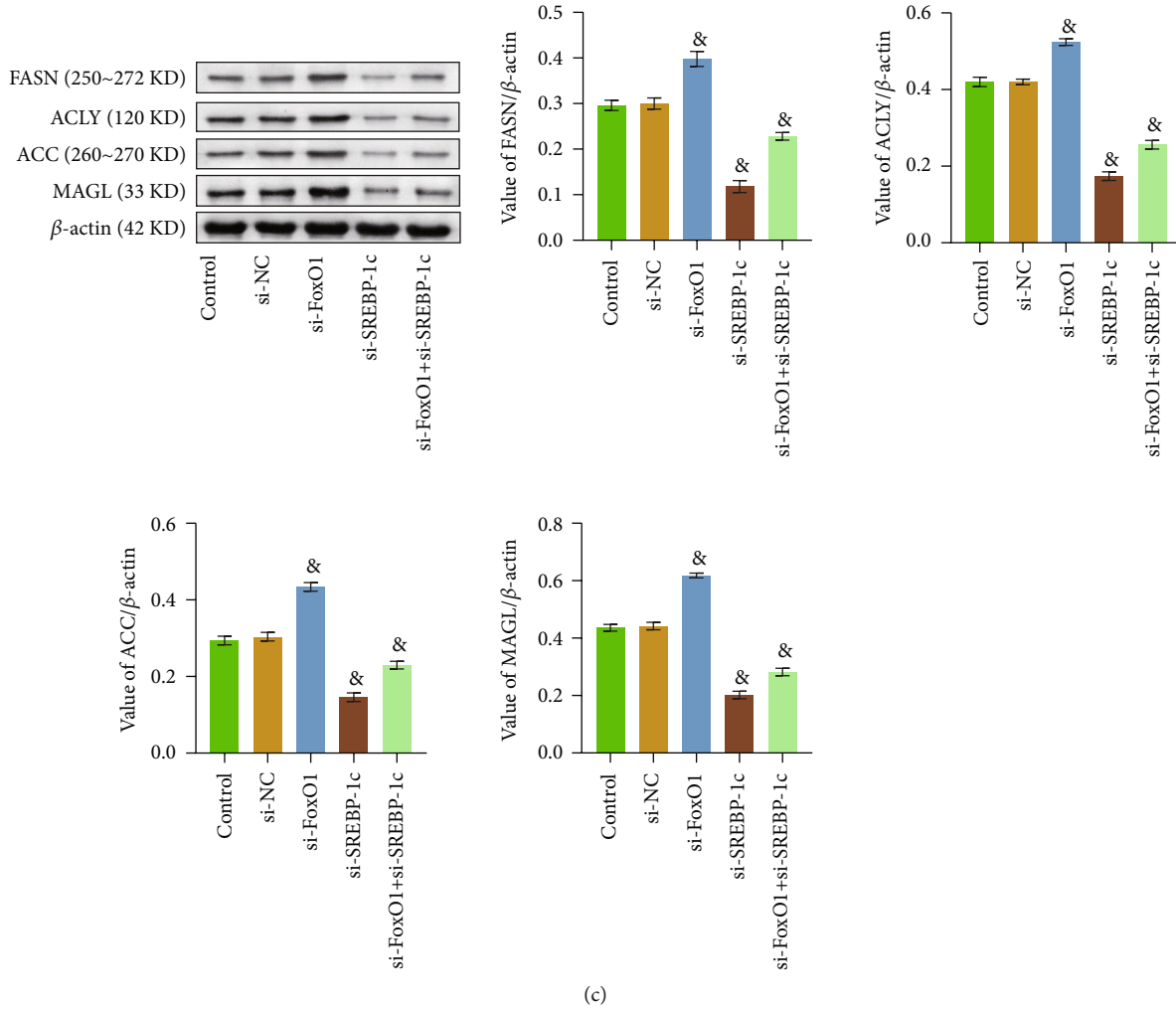


FIGURE 7: Coordinated regulation of FoxO1 and SREBP-1c regulated fatty acid metabolism in vivo. (a) The concentration of FASN was detected by IF. (b) The relative expression levels of FASN, ACLY, ACC, and MAGL were evaluated by RT-qPCR. (c) WB was used to measure the expressions of FASN, ACLY, ACC, and MAGL. The magnification is 400 times, scale bar = 25 μm; *P < 0.05 vs. the si-NC group. All experiments were performed 3 times.

FoxO1 and SREBP-1c simultaneously in Huh-6 cells and found that fatty acid metabolism of Huh-6 cells was inhibited, and cell function and tumor-forming ability were weakened. In other words, coordinated regulation of FoxO1 and SREBP-1c could facilitate the progression of HB by regulating fatty acid metabolism.

In this study, we found mutual inhibition of FoxO1 and SREBP-1c in HB. In addition, SREBP-1c could bind to the promoter of FoxO1 to regulate its transcription. However, the mechanism of how FoxO1 inhibits SREBP-1c expression remains unclear. As mentioned earlier, SPREP-1c also inhibits FoxO1 expression through indirect regulation. In HB, it is still unclear whether direct or indirect regulation plays a dominant role. We were unable to carry out a detailed study on this part because of insufficient experimental funds. In the future, we will conduct a series of molecular biology experiments to refine our research.

5. Conclusion

FoxO1 could slow down the progress of HB by inhibiting the fatty acid metabolism while SREBP-1c promotes it. FoxO1 and SREBP-1c have an inhibitory effect on each other. Coordinated regulation of FoxO1 and SREBP-1c facilitated the progression of HB by regulating fatty acid metabolism in vivo and vitro. These findings provided a theoretical basis for a better understanding of the mechanism of fatty acid metabolism in HB. They helped to develop new targets for the clinical treatment of HB.

Abbreviations

- HB: Hepatoblastoma
- FASN: Fatty acid synthase
- ACC: Acetyl-coenzyme A carboxylase
- FoxO1: Forkhead box-O1

SREBP-1c: Sterol regulatory element-binding protein-1c
 ACLY: ATP-citric acid lyase
 MAGL: Monoacylglycerol lipase
 TG: Triglyceride
 FAO: Fatty acid oxidase
 Acetyl-CoA: Acetyl-coenzyme A
 NEFA: Nonesterified fatty acid.

Data Availability

The data used to support the findings of this study are available from the corresponding authors upon request.

Conflicts of Interest

The authors declare that there is no conflict of interest regarding the publication of this article.

Authors' Contributions

Qin Zhu, Yu Hu, and Hongyan Zai conceptualized the study design. Yu Hu, Hongyan Zai, Wei Jiang, Zhenglin Ou, and Yuanbing Yao collected specimens and experimental data. Hongyan Zai and Wei Jiang did a statistical analysis of the data. Zhenglin Ou and Yuanbing Yao wrote the first draft of the manuscript.

Acknowledgments

This work was supported by Xiangya Hospital.

References

- [1] I. Cristóbal, M. Sanz-Álvarez, M. Luque, C. Caramés, F. Rojo, and J. García-Foncillas, "The role of microRNAs in hepatoblastoma tumors," *Cancers (Basel)*, vol. 11, no. 3, p. 409, 2019.
- [2] S. R. Musick, M. Smith, A. S. Rouster, and H. M. Babiker, *Hepatoblastoma*, in *StatPearls*, StatPearls Publishing Copyright, Treasure Island (FL), 2021.
- [3] N. Koundouros and G. Poulgiannis, "Reprogramming of fatty acid metabolism in cancer," *British Journal of Cancer*, vol. 122, no. 1, pp. 4–22, 2020.
- [4] M. Yi, J. Li, S. Chen et al., "Emerging role of lipid metabolism alterations in cancer stem cells," *Journal of Experimental & Clinical Cancer Research*, vol. 37, no. 1, p. 118, 2018.
- [5] Y. Ma, S. M. Temkin, A. M. Hawkridge et al., "Fatty acid oxidation: an emerging facet of metabolic transformation in cancer," *Cancer Letters*, vol. 435, pp. 92–100, 2018.
- [6] C. W. Fhu and A. Ali, "Fatty acid synthase: an emerging target in cancer," *Molecules*, vol. 25, no. 17, p. 3935, 2020.
- [7] R. K. Yadav, A. S. Chauhan, L. Zhuang, and B. Gan, "FoxO transcription factors in cancer metabolism," *Seminars in Cancer Biology*, vol. 50, pp. 65–76, 2018.
- [8] S. Peng, W. Li, N. Hou, and N. Huang, "A review of FoxO1-regulated metabolic diseases and related drug discoveries," *Cell*, vol. 9, no. 1, 2020.
- [9] H. Guan, P. Tan, L. Xie et al., "FOXO1 inhibits osteosarcoma oncogenesis via Wnt/ β -catenin pathway suppression," *Oncogene*, vol. 4, no. 9, article e166, 2015.
- [10] W. Zhang, S. Patil, B. Chauhan et al., "FoxO1 Regulates Multiple Metabolic Pathways in the Liver," *The Journal of Biological Chemistry*, vol. 281, no. 15, pp. 10105–10117, 2006.
- [11] M. J. Ang, J. Kim, S. Lee et al., "Transcriptome profiling reveals novel candidate genes related to hippocampal dysfunction in SREBP-1c knockout mice," *International Journal of Molecular Sciences*, vol. 21, no. 11, p. 4131, 2020.
- [12] Y. Zhang, C. Li, C. Hu et al., "Lin28 enhances de novo fatty acid synthesis to promote cancer progression via SREBP-1," *EMBO Reports*, vol. 20, no. 10, article e48115, 2019.
- [13] D. Guo, E. H. Bell, P. Mischel, and A. Chakravarti, "Targeting SREBP-1-driven lipid metabolism to treat cancer," *Current Pharmaceutical Design*, vol. 20, no. 15, pp. 2619–2626, 2014.
- [14] M. Teran-Garcia, A. W. Adamson, G. Yu et al., "Polyunsaturated fatty acid suppression of fatty acid synthase (FASN): evidence for dietary modulation of NF-Y binding to the Fasn promoter by SREBP-1c," *The Biochemical Journal*, vol. 402, no. 3, pp. 591–600, 2007.
- [15] F. Geng, X. Cheng, X. Wu et al., "Inhibition of SOAT1 suppresses glioblastoma growth via blocking SREBP-1-mediated lipogenesis," *Clinical Cancer Research*, vol. 22, no. 21, pp. 5337–5348, 2016.
- [16] Y. Wang, L. Zhang, X. Che, W. Li, Z. Liu, and J. Jiang, "Roles of SIRT1/FoxO1/SREBP-1 in the development of progesterin resistance in endometrial cancer," *Archives of Gynecology and Obstetrics*, vol. 298, no. 5, pp. 961–969, 2018.
- [17] Q. He, J. Luo, J. Wu et al., "FoxO1 knockdown promotes fatty acid synthesis via modulating SREBP1 activities in the dairy goat mammary epithelial cells," *Journal of Agricultural and Food Chemistry*, vol. 68, no. 43, pp. 12067–12078, 2020.
- [18] S. E. Woodfield, Y. Shi, R. H. Patel et al., "MDM4 inhibition: a novel therapeutic strategy to reactivate p53 in hepatoblastoma," *Scientific Reports*, vol. 11, no. 1, p. 2967, 2021.
- [19] Z. Luo and P. Cao, "Long noncoding RNA PVT1 promotes hepatoblastoma cell proliferation through activating STAT3," *Cancer Management and Research*, vol. Volume 11, pp. 8517–8527, 2019.
- [20] J. S. Wu, S. R. Sheng, X. H. Liang, and Y. L. Tang, "The role of tumor microenvironment in collective tumor cell invasion," *Future Oncology*, vol. 13, no. 11, pp. 991–1002, 2017.
- [21] D. V. Pham, N. Tilija Pun, and P. H. Park, "Autophagy activation and SREBP-1 induction contribute to fatty acid metabolic reprogramming by leptin in breast cancer cells," *Molecular Oncology*, vol. 15, no. 2, pp. 657–678, 2021.
- [22] M. Sciacovelli and C. Frezza, "Metabolic reprogramming and epithelial-to-mesenchymal transition in cancer," *The FEBS Journal*, vol. 284, no. 19, pp. 3132–3144, 2017.
- [23] Q. Sun, X. Yu, C. Peng et al., "Activation of SREBP-1c alters lipogenesis and promotes tumor growth and metastasis in gastric cancer," *Biomedicine & Pharmacotherapy*, vol. 128, article 110274, 2020.
- [24] J. Li, Q. Huang, X. Long et al., "CD147 reprograms fatty acid metabolism in hepatocellular carcinoma cells through Akt/mTOR/SREBP1c and P38/PPAR α pathways," *Journal of Hepatology*, vol. 63, no. 6, pp. 1378–1389, 2015.
- [25] Y. C. Chae, J. Y. Kim, J. W. Park et al., "FOXO1 degradation via G9a-mediated methylation promotes cell proliferation in colon cancer," *Nucleic Acids Research*, vol. 47, no. 4, pp. 1692–1705, 2019.
- [26] Y. Wang, Z. Lyu, Y. Qin et al., "FOXO1 promotes tumor progression by increased M2 macrophage infiltration in

- esophageal squamous cell carcinoma,” *Theranostics*, vol. 10, no. 25, pp. 11535–11548, 2020.
- [27] Y. Liu, Y. Yang, L. Li et al., “LncRNA SNHG1 enhances cell proliferation, migration, and invasion in cervical cancer,” *Biochemistry and Cell Biology*, vol. 96, no. 1, pp. 38–43, 2018.
- [28] X. Zhu, H. Bian, L. Wang et al., “Berberine attenuates nonalcoholic hepatic steatosis through the AMPK- SREBP-1c-SCD1 pathway,” *Free Radical Biology & Medicine*, vol. 141, pp. 192–204, 2019.
- [29] T. Tao, Q. Su, S. Xu et al., “Down-regulation of PKM2 decreases FASN expression in bladder cancer cells through AKT/mTOR/SREBP-1c axis,” *Journal of Cellular Physiology*, vol. 234, no. 3, pp. 3088–3104, 2019.
- [30] F. Ying, H. Liu, E. H. Ching Tang et al., “Prostaglandin E receptor subtype 4 protects against diabetic cardiomyopathy by modulating cardiac fatty acid metabolism via FOXO1/CD36 signalling,” *Biochemical and Biophysical Research Communications*, vol. 548, pp. 196–203, 2021.
- [31] M. G. Vander Heiden, L. C. Cantley, and C. B. Thompson, “Understanding the Warburg effect: the metabolic requirements of cell proliferation,” *Science*, vol. 324, no. 5930, pp. 1029–1033, 2009.
- [32] A. Carracedo, L. C. Cantley, and P. P. Pandolfi, “Cancer metabolism: fatty acid oxidation in the limelight,” *Nature Reviews Cancer*, vol. 13, no. 4, pp. 227–232, 2013.
- [33] L. S. Pike, A. L. Smift, N. J. Croteau, D. A. Ferrick, and M. Wu, “Inhibition of fatty acid oxidation by etomoxir impairs NADPH production and increases reactive oxygen species resulting in ATP depletion and cell death in human glioblastoma cells,” *Biochimica et Biophysica Acta*, vol. 1807, no. 6, pp. 726–734, 2011.
- [34] A. Vazquez, J. J. Kamphorst, E. K. Markert, Z. T. Schug, S. Tardito, and E. Gottlieb, “Cancer metabolism at a glance,” *Journal of Cell Science*, vol. 129, no. 18, pp. 3367–3373, 2016.
- [35] A. Carrer, S. Trefely, S. Zhao et al., “Acetyl-CoA metabolism supports multistep pancreatic tumorigenesis,” *Cancer Discovery*, vol. 9, no. 3, pp. 416–435, 2019.
- [36] I. S. Senatorov and N. H. Moniri, “The role of free-fatty acid receptor-4 (FFA4) in human cancers and cancer cell lines,” *Biochemical Pharmacology*, vol. 150, pp. 170–180, 2018.
- [37] P. Li, M. Lu, J. Shi et al., “Lung mesenchymal cells elicit lipid storage in neutrophils that fuel breast cancer lung metastasis,” *Nature Immunology*, vol. 21, no. 11, pp. 1444–1455, 2020.
- [38] Y. Li and S. Wu, “Epigallocatechin gallate suppresses hepatic cholesterol synthesis by targeting SREBP-2 through SIRT1/FOXO1 signaling pathway,” *Molecular and Cellular Biochemistry*, vol. 448, no. 1-2, pp. 175–185, 2018.
- [39] S. K. Bose, H. Kim, K. Meyer, N. Wolins, N. O. Davidson, and R. Ray, “Forkhead box transcription factor regulation and lipid accumulation by hepatitis C virus,” *Journal of Virology*, vol. 88, no. 8, pp. 4195–4203, 2014.
- [40] X. Deng, W. Zhang, I. S. O-Sullivan et al., “FoxO1 Inhibits Sterol Regulatory Element-binding Protein-1c (SREBP-1c) Gene Expression via Transcription Factors Sp1 and SREBP-1c,” *The Journal of Biological Chemistry*, vol. 287, no. 24, pp. 20132–20143, 2012.
- [41] M. P. Sajan, M. C. Lee, F. Fougere, J. Sajan, C. Cleland, and R. V. Farese, “Coordinated regulation of hepatic FoxO1, PGC-1 α and SREBP-1c facilitates insulin action and resistance,” *Cellular Signalling*, vol. 43, pp. 62–70, 2018.

Research Article

p300/Sp1-Mediated High Expression of p16 Promotes Endothelial Progenitor Cell Senescence Leading to the Occurrence of Chronic Obstructive Pulmonary Disease

Zhihui He ¹, Huaihuai Peng,² Min Gao,¹ Guibin Liang,² Menghao Zeng,¹ and Xuefeng Zhang¹

¹Department of Critical Care Medicine, The Third Xiangya Hospital, Central South University, Changsha, 410013 Hunan, China

²Department of Critical Care Medicine, The Second Xiangya Hospital, Central South University, Changsha, 410011 Hunan, China

Correspondence should be addressed to Zhihui He; hzh703@csu.edu.cn

Received 19 February 2021; Revised 19 July 2021; Accepted 2 August 2021; Published 20 August 2021

Academic Editor: Xin Zong

Copyright © 2021 Zhihui He et al. This is an open access article distributed under the Creative Commons Attribution License, which permits unrestricted use, distribution, and reproduction in any medium, provided the original work is properly cited.

Objective. Chronic obstructive pulmonary disease (COPD) is a common chronic disease and develops rapidly into a grave public health problem worldwide. However, what exactly causes the occurrence of COPD remains largely unclear. Here, we are trying to explore whether the high expression of p16 mediated by p300/Sp1 can cause chronic obstructive pulmonary disease through promoting the senescence of endothelial progenitor cells (EPCs). **Methods.** Peripheral blood EPCs were isolated from nonsmoking non-COPD, smoking non-COPD, and smoking COPD patients. The expressions of p16, p300, and senescence-related genes were detected by RT-PCR and Western Blot. Then, we knocked down or overexpressed Sp1 and p300 and used the ChIP assay to detect the histone H4 acetylation level in the promoter region of p16, CCK8 to detect cell proliferation, flow cytometry to detect the cell cycle, and β -galactosidase staining to count the proportion of senescent cells. **Results.** The high expression of p16 was found in peripheral blood EPCs of COPD patients; the cigarette smoke extract (CSE) led to the increase of p16. The high expression of p16 in EPCs promoted cell cycle arrest and apoptosis. The CSE-mediated high expression of p16 promoted cell senescence. The expression of p300 was increased in peripheral blood EPCs of COPD patients. Moreover, p300/Sp1 enhanced the histone H4 acetylation level in the promoter region of p16, thereby mediating the senescence of EPCs. And knockdown of p300/Sp1 could rescue CSE-mediated cell senescence. **Conclusion.** p300/Sp1 enhanced the histone H4 acetylation level in the p16 promoter region to mediate the senescence of EPCs.

1. Introduction

Chronic obstructive pulmonary disease (COPD) is a common chronic disease whose prevalence, disability rate, mortality rate, and social burden caused by it have been increasing year by year, developing into a severe public health issue. At present, it is generally believed that smoking is the major cause that induces COPD, while its pathogenesis has not been fully elucidated yet. COPD is considered to be a disease of premature lung failure [1–4]. EPCs are precursor cells of endothelial cells, which are differentiated from mesoderm angioblasts and participate in human embryonic angiogenesis [5, 6]. Due to their differentiation into endothelial cells

and their biological characteristics such as secretion of vasoactive substances, proliferation, homing, and migration, endothelial progenitor cells (EPCs) play a very important role in postnatal angiogenesis, reendothelialization, tissue regeneration, and repair [7–9].

The p16 gene belongs to the INK4 gene family and consists of four members: p16^{INK4A}, p15^{INK4B}, p18^{INK4C}, and p19^{INK4D}, which all have the biological characteristics of cell growth inhibition and tumor suppression [10]. p16 is also the second most common tumor suppressor gene just after p53. It has been widely considered a familial melanoma gene, whose immunohistochemistry has a clearly defined role in certain pathological conditions [11]. Meanwhile, p16 has also

been found to play a critical role in cell senescence. Cell senescence is an irreversible block of cell growth. Biochemical and morphological changes occur during cell senescence, including the formation of unique cell morphology, such as flat cytoplasm [12]. Cell senescence is an irreversible arrest of cell growth accompanied by biochemical and morphological changes, which includes the formation of unique cell morphology, such as flat cytoplasm [13]. p16-mediated senescence leads to chromatin recombination, which is associated with the inhibition of genes regulated by transcription factor E2F1 [13, 14]. Chromatin recombination in oncogene-induced premature senescence is characterized by SAHF (senescence-associated heterochromatin lesions), manifested as dense nuclear DNA and concentrated H3K9 trimethylation [15, 16].

Studies have reported that the quantity reduction and function recession of EPCs in the peripheral blood of COPD patients is highly associated with the severity of the disease [17]. In emphysema animal models, the proliferation, secretion, and adhesion of bone marrow EPCs decreased, with the expression of senescence marker p16 (INK4a) in bone marrow EPCs and lung tissues increasing, while the stem cell antigen 1 (Sca-1) and c-Kit expression decreased [18]; meanwhile, the fact that cigarette smoke extract (CSE) can directly induce the dysfunction of EPCs cultured in vitro and the changes in the expression levels of the above-mentioned gene suggest that EPC senescence and EPC gradual exhaustion exist in smoking-related COPD [18–20]. The COPD mouse model was further transplanted with allogeneic normal EPCs through the trachea, the results of which showed that after EPC transplantation, not only the lung function and emphysema pathological changes of COPD mice were significantly improved, the level and activity of matrix metalloproteinase in bronchoalveolar lavage fluid and the apoptosis of alveolar septum cells decreased, and the total antioxidant capacity increased as well [20–24]. EPCs are a very promising vascular health biomarker with broad application prospects and can be used for the treatment of a series of clinical diseases [25]. Previous studies have revealed that the quantity and function of EPCs in COPD patients might decrease, and increasing p16 expression plays an important role in maintaining characteristic cell cycle arrest [26–28]. In this study, we found high expression of p16 in the peripheral blood EPCs of COPD patients, which would lead to an increase in the transcriptional activity of p16.

Histone posttranslational modification is the main epigenetic mechanism regulating the life process, and histone acetylation is catalyzed by histone acetyltransferase [29]. Histone acetyltransferase (HAT), like p300/CBP, is a key transcriptional coactivator involved in regulating a variety of genes. Activated HAT enables p300/CBP the ability to affect chromatin activity through nucleosome histone modification. Current available data reveal that Sp1 and p300 perform cooperative work in the transcriptional regulation of several genes [30, 31]. Sp1, as a critical transcription factor in mammals, is closely associated with the formation of the Sp1/HAT complex [32, 33]. At the promoter of the eukaryote gene, Sp1 is able to recruit histone acetylase (HAT) and deacetylase (HDAC) concomitantly to regulate the histone acetylation

in a dynamical and rapid way, thereby either to activate or to repress gene expressions [34–36]. Previous literature reported that p300 knockdown could reduce the expression of β -galactosidase (β -Gal) in endothelial cells and ease the senescence-like changes of endothelial cells. However, very limited researches were made upon the p300/Sp1-mediated high expression of p16 in endothelial progenitor cell senescence and the development of chronic obstructive pulmonary disease [37–39]. Therefore, in this study, we conducted a more in-depth study focusing on this regulatory mechanism.

2. Materials and Methods

2.1. Clinical Samples. This study was approved by the Third Xiangya Hospital of Central South University (No. 2018-056). We recruited three groups of subjects consisting of 18 nonsmoking non-COPD, 20 smoking non-COPD, and 20 smoking COPD patients. COPD patients were defined in accordance with the standard of the Global Initiative for Chronic Obstructive Lung Disease criteria (postbronchodilator FEV1/FVC < 0.7). COPD patients were in stable clinical state, with no evidence of respiratory infection or acute exacerbation for at least four weeks. Patients with comorbidities like asthma, interstitial lung disease, heart failure, and/or neuromuscular disease were excluded from this study (for patient information, please check Supplementary Table 1). The smoking history of subjects was determined from the mean number of pack-years of cigarette consumption. Venous blood samples (10 mL) were collected from subjects individually.

2.2. EPC Isolation and Identification. 58 human volunteers' blood samples were successfully collected in this study. As there were 3 groups, for each group, the blood samples were collected from about 20 patients. The blood sample was collected in 4–5 batches for each group, 4 to 5 patients each batch. For each batch of collected blood samples, we mixed the blood and took 20 mL to extract EPCs for experimentation. 20 mL blood samples were diluted in EGM (Lonzo, CC-3156) in 50 mL sterile centrifuge tube (1:1, v/v). The same volume of diluent was added to the upper centrifuge tube containing lymphocyte separation medium (Axis-Shield). The test tube was centrifuged at 2500 rpm for 30 min at room temperature, and then, the intermediate monocyte layer was collected and placed into an empty centrifuge barrel using an aseptic suction. The cells were washed twice with PBS, and the monocytes were collected. 10% FBS or 5% pHPL and 10 U/mL heparin (Trevigen, 3450-048-08) were added to the medium in order to avoid blood platelet coagulation; then, the cells were cultured in 12-well plates coated with rat tail-derived type 1 collagen (Termo, A1048301) with EGM medium. After an overnight incubation, non-adherent cells were collected for replating. Preheated medium was added to dilute cells, and cells were isolated from 3 wells in a 12-well plate and 6 wells in a 24-well plate, performed for three times. Then, the medium was refreshed once a day for the first seven days and once every other day for the next seven days. Later on, the medium

was refreshed once every 2 or 3 days. EPCs were identified through flow cytometry using CD34 (Abcam, ab64480), CD133 (Abcam, ab19898), and VEGFR2 (Abcam, ab39256) antibody. EPCs were detached, centrifuged, and washed twice with phosphate-buffered saline (PBS) and then resuspended in Stain Buffer and counted. The cell suspension was transferred to new 1.5 mL Eppendorf tubes, with roughly 5×10^4 cells in each tube. $5 \mu\text{L}$ of CD34 and CD133 antibodies and isotype controls was added to a $50 \mu\text{L}$ cell suspension based on the concentrations of antibodies recommended in the instructions of flow cytometry. After being mixed evenly, the cell suspension containing antibodies was cultured in a refrigerator at 4°C in full darkness for 30 min, triple washed with precooled Stain Buffer, and centrifuged for 5 min at 400 g. The unbound antibodies were washed away. In the end, cells were resuspended in flow tubes with $500 \mu\text{L}$ Stain Buffer and detected by flow cytometry. The results of flow cytometry were analyzed and processed by using FlowJo 7.6 software.

2.3. Western Blot. The cells were washed three times with precooled PBS, lysed with RIPA lysate, and centrifuged at 12000 rpm for 10 min; then, the supernatant was gathered for detecting protein concentration using a BCA detection reagent (Beijing Kangwei Century Biotechnology Co., Ltd., CW0014). After electrophoresis with voltage altered from 60 V to 120 V, the protein was transferred to the PVDF membrane using wet-to-electric transfer. Following that, the membrane was blocked using 5% skim milk-TBST and cultured overnight at 4°C with primary antibodies as follows: anti-Col1a1 (CST, 84336; 1:1000), MMP3 (Abcam, ab52915; 1:1000), MMP13 (Abcam, ab39012; 1:1000), Pal1 (Abcam, ab7205; 1:1000), and GAPDH (Thermo, AM4300; 1:5000). Subsequently, the membrane was cultured with horseradish peroxidase-labeled goat anti-rabbit IgG (Beijing CoWin Biosciences, China). Afterwards, Tanon™ High-sig ECL Western Blotting Substrate (Shanghai Tanon Co., Ltd., 180-501) was used to develop the film, and the gray value was detected by ImageJ (NIH). Thereafter, the protein level was expressed by the ratio of the gray value of the target bands to that of the internal reference (GAPDH).

2.4. RNA Extraction and RT-PCR. Total RNA was extracted by TRIzol (Thermo Fisher, 15596026) and reverse-transcribed into cDNA by PCR amplification instrument (Bio-Rad). Subsequently, real-time quantitative RT-PCR experiments were conducted using ABI 7500 quantitative PCR instrument (ABI 7500, Thermo Fisher), with reaction conditions set as follows: predenaturation at 95°C for 10 min, 40-cycle denaturation at 95°C for 10 s, annealing at 60°C for 20 s, and extension at 72°C for 34 s. Then, the samples were analyzed using either PCR or quantitative PCR. The primer pairs of p16 were as follows: sense 5'-TTCCTG GACACGCTGGT-3' and antisense 5'-CAATCGGGGAT GTCTGAG-3'. The primer pairs of p300 were as follows: sense 5'-GACCCTCAGCTTTTAGGAATCC-3' and antisense 5'-TGCCGTAGCAACACAGTGTCT-3'. The primer

pairs of β -actin were as follows: sense 5'-TCGTGCGTGAC ATTAAGGAG-3' and antisense 5'-ATGCCAGGGTACAT GGTGGT-3'. The primer pairs of Col1a1 were as follows: sense 5'-GCAGCTGGGTCCTCAGAAT-3' and antisense 5'-CAGTCCCCAGTTCCTC-3'. The primer pairs of MMP3 were as follows: sense 5'-CAGACTTGTCCCGTTT CCAT-3' and antisense 5'-GGTGCTGACTGCATCA AAGA-3'. The primer pairs of MMP13 were as follows: sense 5'-CAGACTTGTCCCGTTTCCAT-3' and antisense 5'-GGTGCTGACTGCATCAAAGA-3'. The primer pairs of Pal1 were as follows: sense 5'-TCTACAACAACGGATT GCCGTCC-3' and antisense 5'-CACGGTGTTCCTCACC GCGTGC-3'. Data were analyzed using the $2^{-\Delta\Delta\text{Ct}}$ method with β -actin acting as the internal control.

2.5. Cell Cycle Analysis by Flow Cytometry. Cells were digested with trypsin, fixed with 70% ethanol, preserved and stored overnight at 4°C , then suspended in $50 \mu\text{L}$ phosphate buffer with $0.5 \mu\text{L}$ and $10 \mu\text{g/mL}$ RNase A and $150 \mu\text{L}$ propidium iodide. Following that, cell DNA content was quantified using FACSCalibur (BD Biosciences, San Jose, CA, USA).

2.6. Chromatin Immunoprecipitation. ChIP protocol has been described previously [40] with antiacetyl H4 (Millipore, 06-866) antibody used. The samples were assessed by either PCR or RT-QPCR.

2.7. Cell Transfection. Before cell transfection, EPCs were seeded into 24-well plates, and 0.5 mL contained approximately 1×10^5 cells. Plasmid transfection was performed using Lipofectamine™ 2000 (Thermo Fisher, 1668030) based on the Lipofectamine 2000 transfection instructions. RNAi Max (Invitrogen, 13778075) was transfected with 50 nmol/L siRNA in serum-free and antibiotic-free medium according to the manufacturer's protocol. The siRNA sequences were as follows: Sp1 siRNA 1: CCUGGAGUGAUGCCUAAUA TT; Sp1 siRNA 2: CCAGCAACAUGGGAAUUAUTT; p300 siRNA 1: GCAGCUCAACCAUCCACUATT; p300 siRNA 2: GCAAACAUCGAGCGGAAUTT; and p16 siRNA: AGAACCAGAGAGGCTCTGA.

The medium was changed to the complete growth condition 6 hours after transfection; then, the cells were harvested 72 hours after transfection.

2.8. Immunofluorescence. The cells were washed twice using PBS (5 min each), fixed with 4% paraformaldehyde for 15 min, incubated with 0.5% Triton/PBS for 6 min, blocked (10% goat serum, 0.05% NaN_3 , 0.2% Triton, and diluted with PBS at 37°C for 30 min), and incubated with primary antibody overnight at 4°C . Following that, the cells were incubated with a fluorescent secondary antibody (Thermo Fisher) in full darkness for 1 hour, stained with DAPI for 5 min and sealed. Finally, a confocal microscope (Leica SP5) was used to take pictures of the cells, or a fluorescence microscope was used to observe the cells.

2.9. β -Gal Staining. Basing on the manufacturer's protocol, cells were stained with SA- β -gal activity using a cell senescence detection kit (Millipore, KAA002). Then, positive staining was quantified using ImageJ and Image Pro Premier software.

2.10. Cell Counting Kit-8 (CCK8) Assay. Each plate was inoculated with cells basing on the experimental group set. The cells in the logarithmic growth phase were made into cell suspension, and the inoculation density was set as 3×10^4 cells/mL, and 100 μ L cell suspension was placed in a 96-well plate with three replicate wells which were inoculated in each group. 100 μ L of culture medium was used as blank control and incubated at 37°C overnight in a 5% CO₂ incubator. A Cell Counting Kit-8 (CCK8) and serum-free DMEM were mixed with a volumetric ratio of 1:10 and added to the test wells at a dose of 100 μ L/well, then incubated at 37°C for 1 h in a 5% CO₂ incubator. The absorbance at 450 nm was measured using a microplate reader, with the plate values recorded.

2.11. Luciferase Experiment. p300 and Sp1 were cotransfected with the luciferase vector driven by a p16 promoter. The 505 bp fragment of p16 was amplified by PCR with p16F 5'-CCAAACAC-CCCGATTCAATTTGGCA-3' and p16R5'-CCGCTGCCTGCTCTACCCCTCTCC-3' primers to produce the luciferase reporter plasmid of p16 promoter. The PCR fragment was cloned into PCR 2.1-TOPO vector, and the sequence was verified. After 48 h of transfection, the Luciferase Reporter Assay System (Thermo) was used for detection, and the specific steps were in accordance with the corresponding kit instructions. The cell culture medium in each hole was discarded, and 100 μ L 1 \times cell lysate was added to each hole. The cell lysate was oscillated on a shaker for 30 min, and the impurities were precipitated by centrifugation (1200 rpm, 1 min). A total of 20 μ L of cell lysate was added to each well of the opaque 96-well plate, and 100 μ L of luciferase detection reagent II (LAR II) and 100 μ L of sea kidney luciferase reagent were added in turn according to the instructions. Tecan Infinite F200/M200 luciferase activity value (*R*) of each well was detected by Tecan Infinite F200/M200 multifunctional microplate reader, and the *F/R* value was used as the relative activity value of each well for statistical analysis.

2.12. Statistical Analysis. All the data were presented as mean \pm standard deviation. The data of two groups were compared with a *T* test, and the data of multiple groups were analyzed using one-way analysis of variance (ANOVA). Data analysis was conducted using SPSS17.0 (SPSS, Inc., Chicago, Illinois, USA) and GraphPad Prism 8.0 (GraphPad Software, San Diego, California, USA). Statistical significance was assumed when $P < 0.05$ while significantly difference was confirmed when $P < 0.01$.

3. Results

3.1. High Expression of p16 Occurred in Peripheral Blood EPCs of COPD Patients. As a fundamental cytokine, p16

can regulate the cell senescence process. In order to explore the expression of p16 in peripheral blood EPCs of nonsmoking non-COPD, smoking non-COPD, and smoking COPD patients, we firstly isolated peripheral blood EPCs of these patients and identified those isolated cells by flow cytometry (Figure 1(a)). Then, we detected the expression of p16 in different groups by RT-PCR and Western Blot, whose results showed that the mRNA and protein levels of p16 were significantly increased in peripheral blood EPCs of COPD patients (Figures 1(b) and 1(c)). Then, we further verified whether CSE would lead to the increase of p16. We cultured EPCs from the peripheral blood of nonsmoking and non-COPD patients with different concentrations of CSE. RT-PCR results showed that the expression of p16 increased gradually with the increase of CSE concentration. Meanwhile, Western Blot results showed that the protein level of p16 increased significantly with the increase of CSE concentration (Figures 1(d) and 1(e)).

3.2. High Expression of p16 in EPCs Inhibited Cell Activity and Promoted Cell Cycle Arrest. We then detected the proliferation of EPCs in nonsmoking non-COPD, smoking non-COPD, and smoking COPD patients. The CCK8 assay showed that the proliferation ability of EPCs in smoking COPD patients decreased markedly (Figure 2(a)). Further, we knocked down p16 in EPCs of smoking COPD patients and found that the low expression of p16 could rescue the decrease of endothelial progenitor cell activity in those patients (Figure 2(b)). While the CSE treatment was conducted, we found during the meantime that knocking down the expression of p16 in EPCs could effectively block the inhibitory effect of CSE on cell proliferation (Figure 2(c)). We further analyzed the cell cycle of EPCs in nonsmoking non-COPD, smoking non-COPD, and smoking COPD patients, the results of which showed that G1/S phase transition arrest occurred in the EPCs of all the smoking COPD patients (Figure 2(d)). Moreover, we knocked down p16 in EPCs of smoking COPD patients, finding that the low expression of p16 could rescue the G1/S phase arrest of EPCs in those patients (Figure 2(e)). At the same time, we knocked down p16 in CSE-treated non-COPD EPC cells, and we found that knocking down p16 could inhibit the G1/S phase arrest caused by CSE (Figure 2(f)).

3.3. CSE-Mediated p16 Overexpression Promoted Cell Senescence. To investigate the effect of the high expression of p16 on senescence of endothelial progenitor cells, we performed β -Gal staining and detected the expression of senescence-related genes. The β -Gal staining experiment revealed that CSE could promote the senescence of EPCs. We also found that knocking down the expression of p16 in EPCs could inhibit the cell senescence caused by CSE (Figure 3(a)). Immunofluorescence staining demonstrated that CSE promoted the high expression of Lamp1, which indicated the increase of lysosomes, the high autophagy of cells, and increasing senescence degree of EPCs, while knocking down p16 would reduce the expression of Lamp1 to a certain degree (Figure 3(b)). Meantime, we also detected the expression of senescence-related genes. Senescence-related

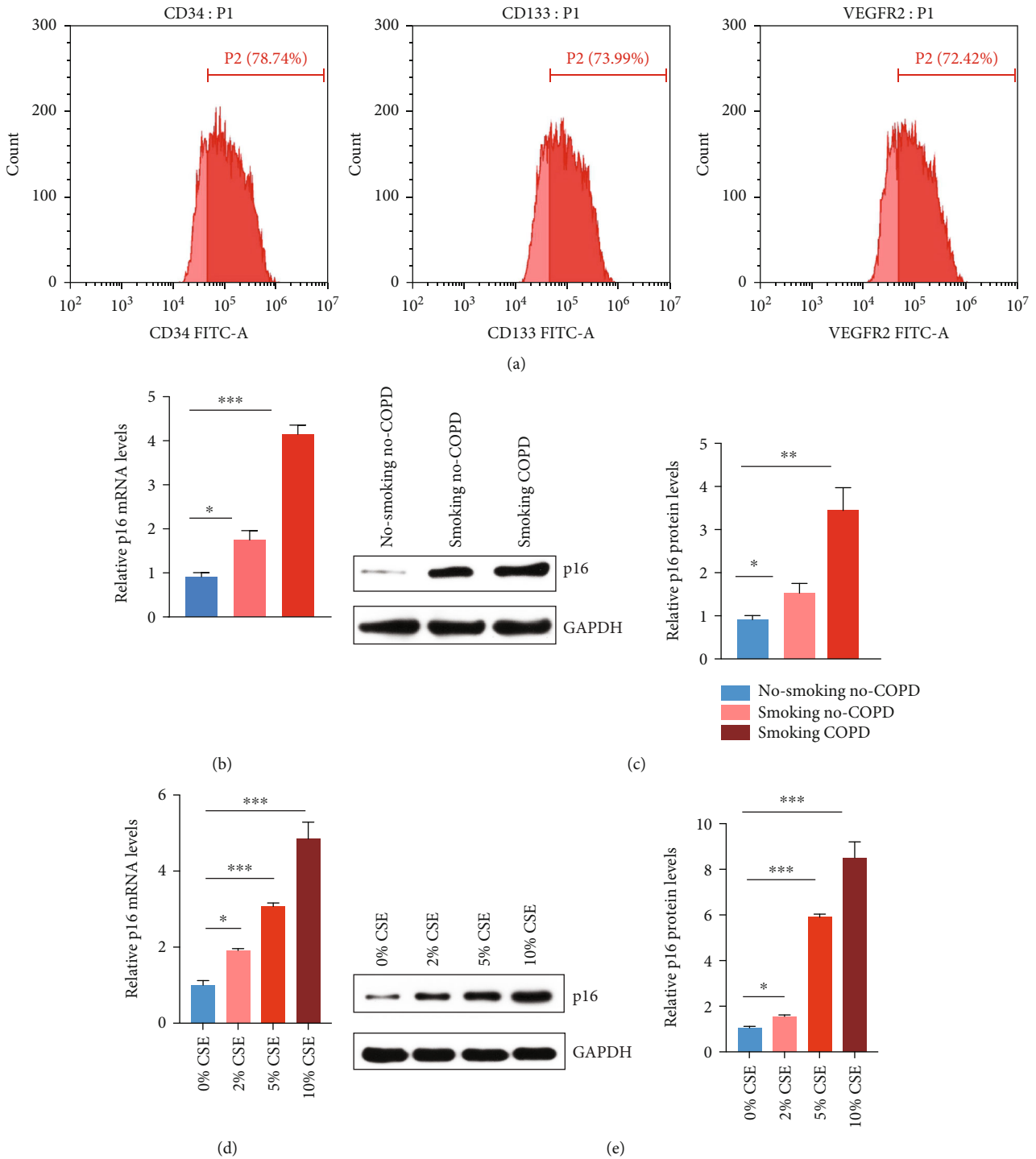


FIGURE 1: High expression of p16 in EPCs of COPD patients. (a) Peripheral blood EPCs were isolated from nonsmoking non-COPD patients. Flow cytometry verified that the isolated cells were peripheral blood endothelial cells. (b) RT-PCR was used to detect the expression of p16 in peripheral blood EPCs of nonsmoking non-COPD, smoking non-COPD, and smoking COPD patients. (c) Western Blot was used to detect the expression of p16 in peripheral blood EPCs of nonsmoking non-COPD, smoking non-COPD, and smoking COPD patients setting each group with 20 samples. (d) Peripheral blood EPCs from nonsmoking non-COPD patients were treated with different concentrations of CSE, and the expression of p16 was detected by RT-PCR. (e) Peripheral blood EPCs from nonsmoking non-COPD patients were treated with different concentrations of CSE, and the expression of p16 was detected by Western Blot. **p* < 0.05, ***p* < 0.01, and ****p* < 0.001.

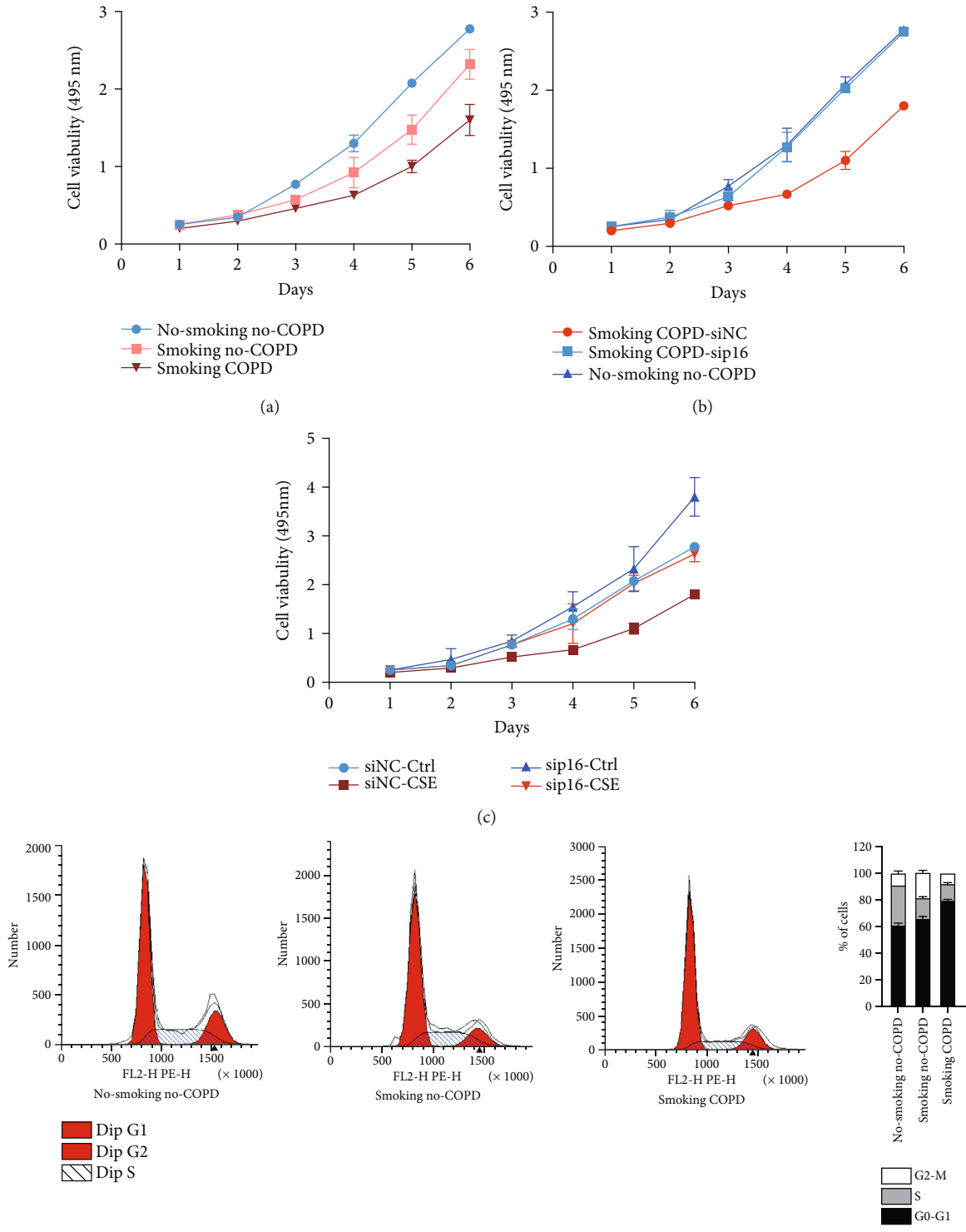


FIGURE 2: Continued.

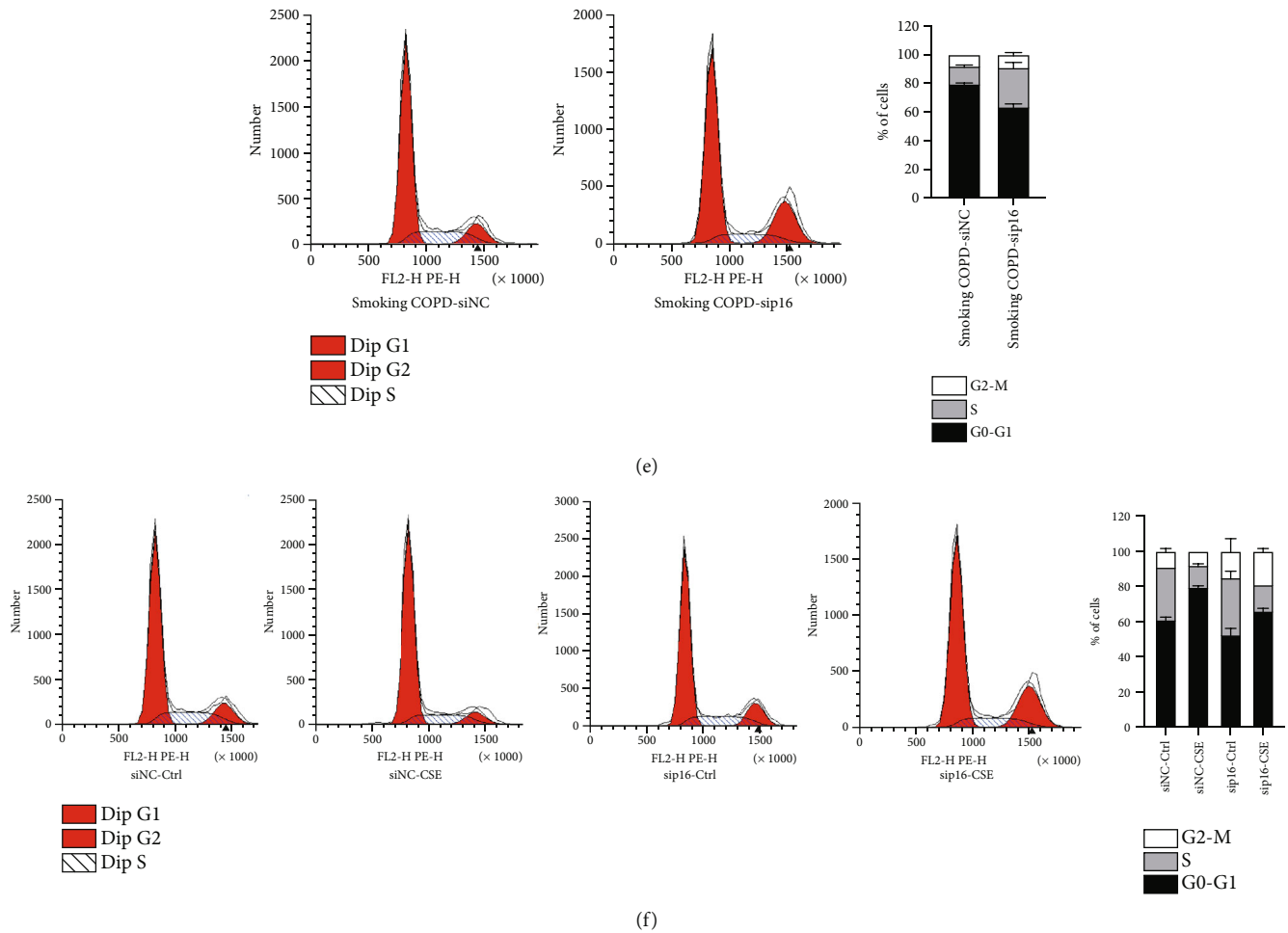


FIGURE 2: High expression of p16 in EPCs promoted cell cycle arrest and apoptosis. (a) Peripheral blood EPCs were isolated from nonsmoking non-COPD, smoking non-COPD, and smoking COPD patients, and cell proliferation was detected by CCK8. (b) Peripheral blood EPCs of smoking COPD patients were isolated, p16 was knocked down by siRNA, and cell proliferation was detected by CCK8. (c) Peripheral blood EPCs from nonsmoking non-COPD were treated with 5% CSE, p16 was knocked down by siRNA, and cell proliferation was detected by CCK8. (d) Peripheral blood EPCs were isolated from nonsmoking non-COPD, smoking non-COPD, and smoking COPD patients, and cell cycle was detected by flow cytometry. (e) Peripheral blood EPCs from smoking COPD patients were isolated, siRNA knocked down p16, and cell cycle was detected by flow cytometry. (f) Peripheral blood EPCs from nonsmoking non-COPD patients were treated with 5% CSE, p16 was knocked down by siRNA, and cell cycle was detected by flow cytometry.

genes *Colla1*, *MMP3*, *MMP13*, and *Pal1* were highly expressed in EPCs treated with CSE, while the expressions of those genes were inhibited with p16 knocked down (Figures 3(c) and 3(d)).

3.4. Increased Expression of p300 Promoted the High Expression of p16. Previous studies reported that p300 could regulate the transcriptional activity of p16, and the high expression of p300 could promote cell cycle arrest [41]. We also discovered that among nonsmoking non-COPD, smoking non-COPD, and smoking COPD patients, the expression of p300 in the peripheral blood progenitor cells of smoking COPD patients was remarkably higher than that of the other two groups (Figure 4(a)). When the cells were treated with CSE and the expression of p300 was knocked down, the expression of p16 was also decreased as revealed by RT-PCR and Western Blot results (Figures 4(b) and 4(c)). When the small molecule inhibitor of p300 (C646) was added to the

EPCs treated with CSE, we found that the decrease of p300 activity could inhibit the expression of p16 to some extent. All those together suggest that in the high expression of p16 mediated by CSE, p300 is very likely to be a potential transcriptional regulator in the upstream of p16.

3.5. p300/Sp1 Regulated p16 Transcriptional Activity. Previous studies suggested that p300 functions as a transcriptional coactivator to regulate many cellular responses such as cell cycle progression and cellular differentiation, and this process relies on the transcriptional factor Sp1. Meanwhile, Sp1 directs the formation of preinitiation complexes to -464 to -452 bp region of the p16 promoter [41, 42]. In order to validate whether this signaling pathway could also regulate the senescence of EPCs mediated by CSE, we firstly overexpressed different amounts of p300 in EPCs and detected the activity of the p16 promoter by luciferase assay. We found that p16 promoter activity increased with the increase of

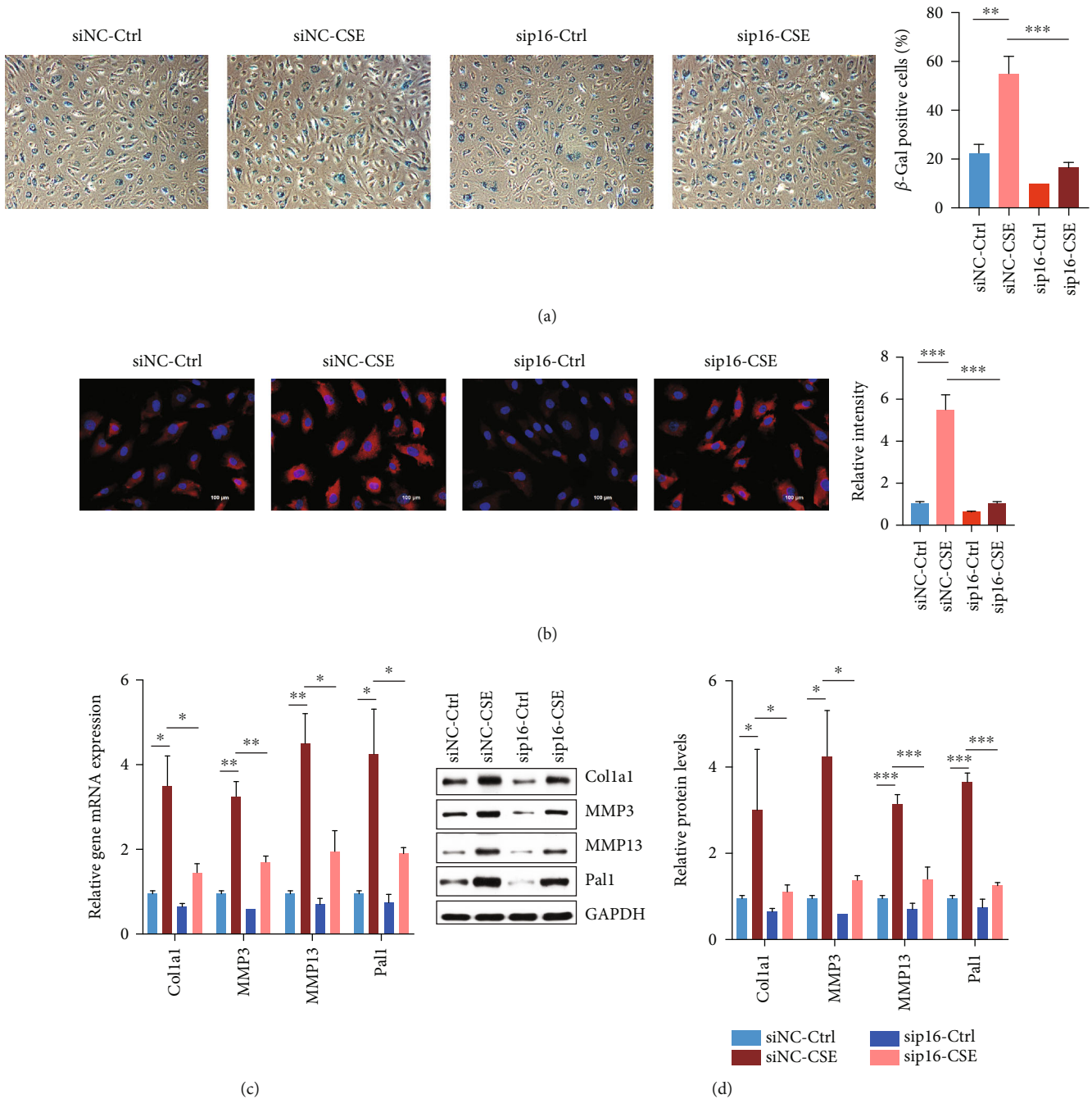


FIGURE 3: CSE-mediated high expression of p16 promoted cell senescence. (a) Peripheral blood EPCs from nonsmoking non-COPD patients were treated with 5% CSE, p16 was knocked down by siRNA, and the proportion of senescence cells was counted by β -galactosidase staining. (b) Peripheral blood EPCs from nonsmoking non-COPD patients were treated with 5% CSE, p16 was knocked down by siRNA, and the expression of Lamp1 was detected by immunofluorescence. (c) Peripheral blood EPCs from nonsmoking non-COPD patients were treated with 5% CSE, p16 was knocked down by siRNA, and the expressions of senescence-related genes Col1a1, MMP3, MMP13, and Pal1 were detected by RT-PCR. (d) Peripheral blood EPCs from nonsmoking non-COPD patients were treated with 5% CSE, p16 was knocked down by siRNA, and the expressions of senescence-related genes Col1a1, MMP3, MMP13, and Pal1 were tested by Western Blot. * $p < 0.05$, ** $p < 0.01$, and *** $p < 0.001$.

p300 expression (Figure 5(a)). Overexpression of Sp1 could also promote the transcriptional activity of the p16 promoter (Figure 5(b)), while knockdown of p300 or Sp1 would inhibit the transcriptional activity of the p16 promoter (Figure 5(c)). We overexpressed or knocked down p300/Sp1 in EPCs and

found that overexpression of p300/Sp1 promoted the high expression of p16 in EPCs, while knockdown of p300/Sp1 inhibited the expression of p16 (Figures 5(d) and 5(e)). ChIP assay displayed that overexpression of p300/Sp1 promoted histone H4 acetylation in the p16 promoter region, while

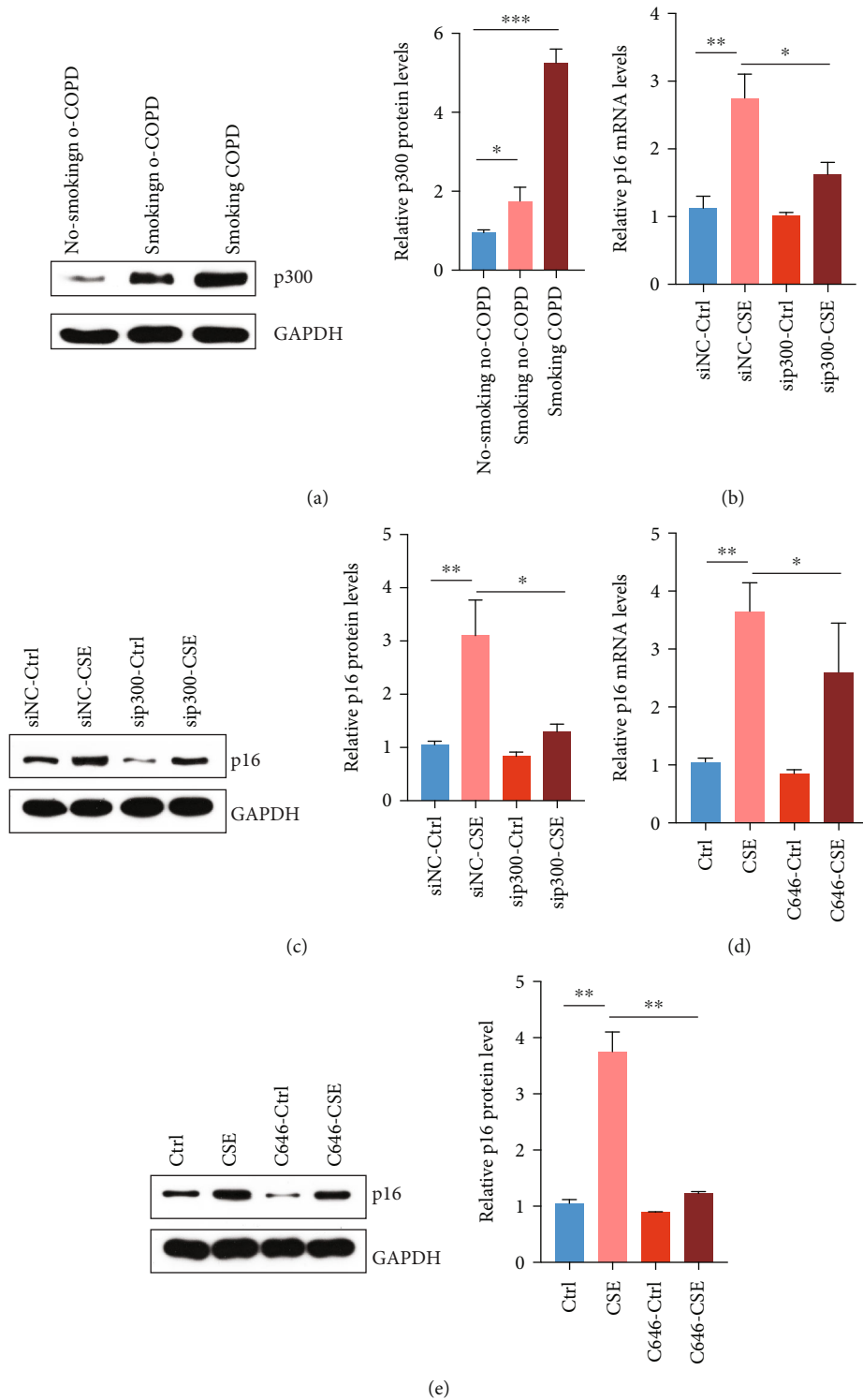
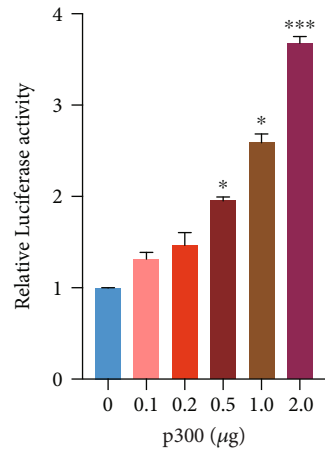
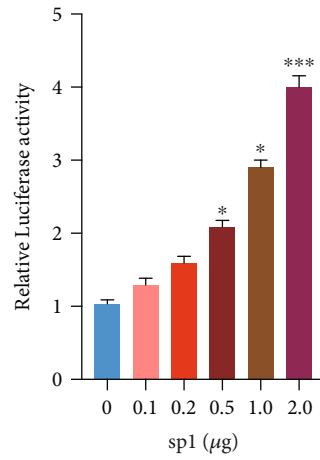


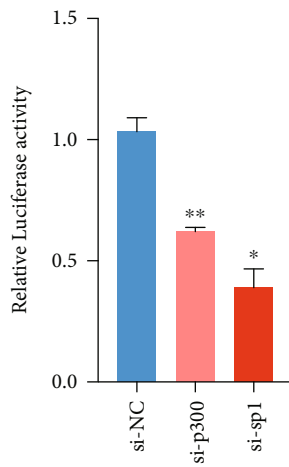
FIGURE 4: Increased p300 mediated the high expression of p16. (a) Western Blot was used to detect the expression of p300 in peripheral blood EPCs of nonsmoking non-COPD, smoking non-COPD, and smoking COPD patients setting each group with 20 samples. (b) Peripheral blood EPCs from nonsmoking non-COPD patients were treated with 5% CSE, p300 was knocked down by siRNA, and the expression of p16 was detected by RT-PCR. (c) Peripheral blood EPCs from nonsmoking non-COPD patients were treated with 5% CSE, p300 was knocked down by siRNA, and the expression of p16 was tested by Western Blot. (d) Peripheral blood EPCs from nonsmoking non-COPD patients were treated with 5% CSE and p300 small molecule inhibitor C646, and the expression of p16 was detected by RT-PCR. (e) Peripheral blood EPCs from nonsmoking non-COPD patients were treated with 5% CSE and p300 small molecule inhibitor C646, and the expression of p16 was tested by Western Blot. * $p < 0.05$, ** $p < 0.01$, and *** $p < 0.001$.



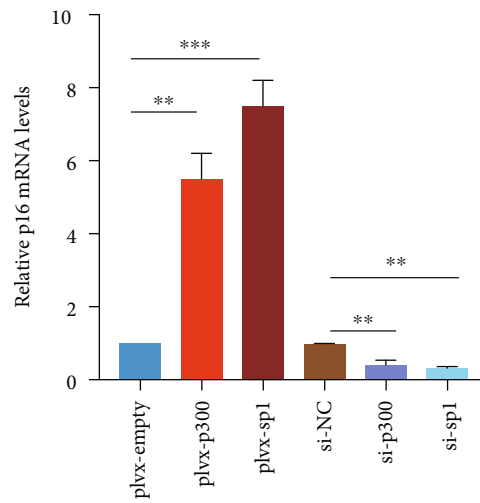
(a)



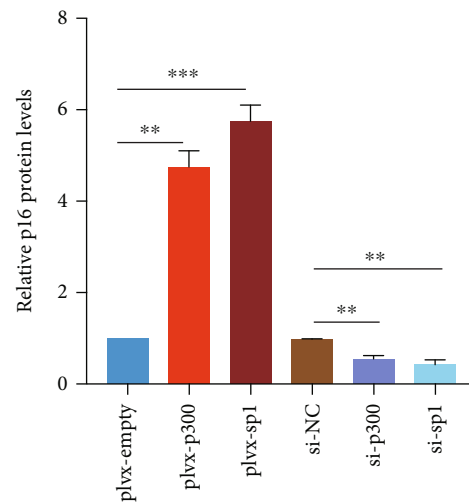
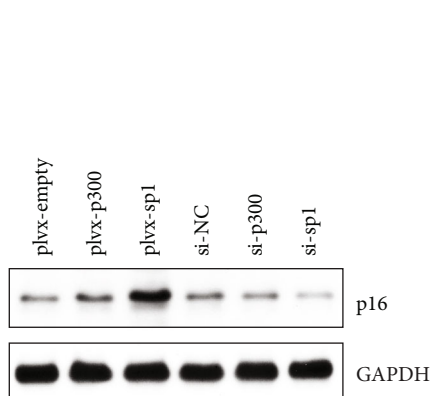
(b)



(c)



(d)



(e)

FIGURE 5: Continued.

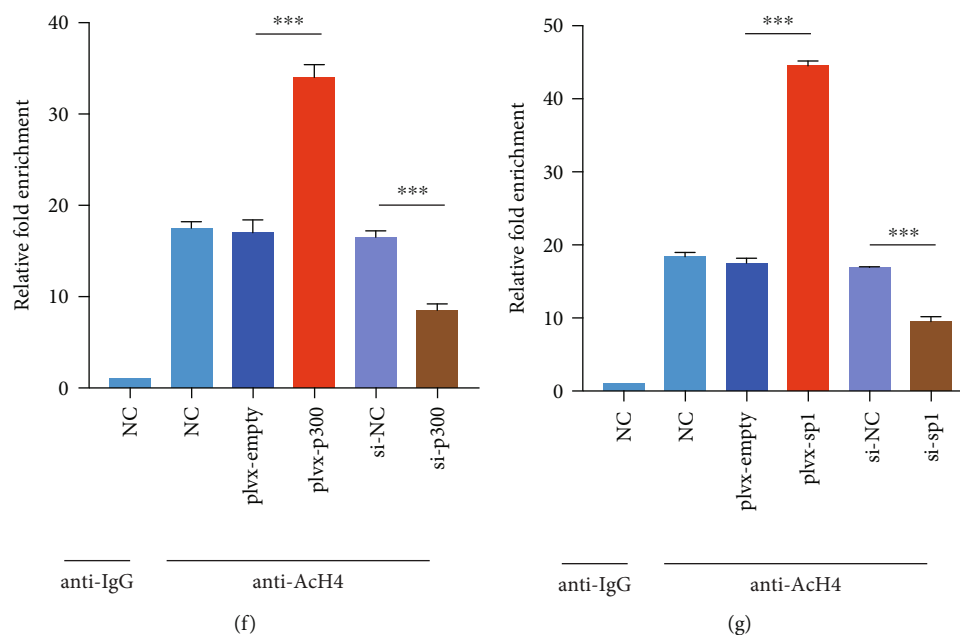


FIGURE 5: p300/Sp1 regulated p16 transcriptional activity. (a) Different amounts of p300 were overexpressed in EPCs, and the activity of the p16 promoter was detected by luciferase. (b) Different amounts of Sp1 were overexpressed in EPCs, and the activity of the p16 promoter was detected by luciferase. (c) p300/Sp1 were knocked down in EPCs, and the activity of the p16 promoter was detected by luciferase. (d) p300/Sp1 were overexpressed or knocked down in EPCs, and the expression of p16 was detected by RT-PCR. (e) p300/Sp1 were overexpressed or/and knocked down in EPCs, and the expression of p16 was tested by Western Blot. (f) p300 was overexpressed or/and knocked down in EPCs, and the level of histone H4 acetylation in the p16 promoter region was detected by ChIP assay. (g) Sp1 was overexpressed or/and knocked down in EPCs, and the level of histone H4 acetylation in the p16 promoter region was detected by the ChIP assay. All the EPCs used in this figure were from nonsmoking non-COPD patients. * $p < 0.05$, ** $p < 0.01$, and *** $p < 0.001$.

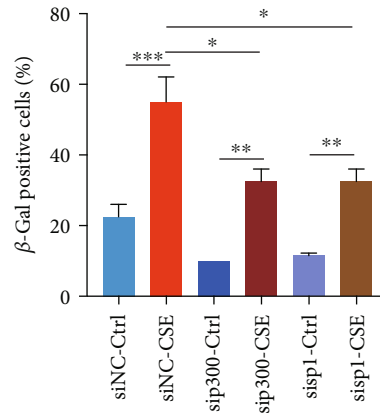
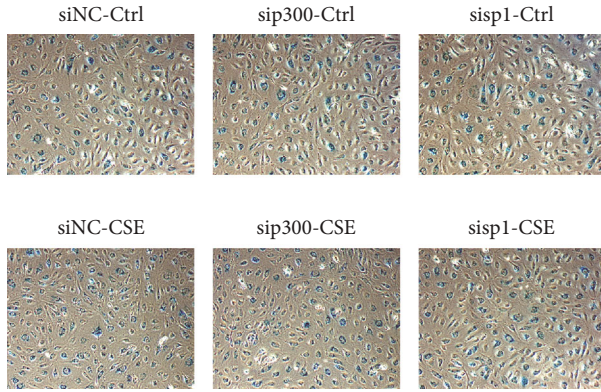
knockdown of these two genes had the opposite effect (Figures 5(f) and 5(g)). The above results indicated that p300/Sp1 were jointly involved in the high expression of p16 in EPCs mediated by CSE.

3.6. Low Expression of p300/Sp1 Inhibited CSE-Mediated Cell Senescence. To further testify that p300/Sp1 regulates the high expression of p16 in EPCs mediated by CSE, we knocked down p300 or Sp1 in EPCs treated with CSEs. Both β -Gal staining and Lamp1 immunofluorescence experiments demonstrated that knocking down p300 or Sp1 could inhibit cell senescence mediated by CSE to a certain extent (Figures 6(a) and 6(b)). Similarly, flow cytometry results also showed that knocking down p300 or Sp1 inhibited the cell cycle arrest of EPCs (Figure 6(c)). At the same time, we also detected the expression of senescence-related genes Col1a1, MMP3, MMP13, and Pal1, finding that knockdown of p300 or Sp1 could also inhibit the CSE-mediated high expression of those senescence genes to a certain degree (Figures 6(d) and 6(e)). Further, we also performed the rescue experiment. We knocked down p300 or Sp1 in CSE-treated EPCs and overexpressed p16. We found that after overexpressing p16, the mRNA and protein levels of senescence-related genes Col1a1, MMP3, MMP13, and Pal1 were significantly increased, indicating that CSE regulated the expression of p16 through p300 or Sp1, thereby causing the senescence of EPCs (Figures 6(f) and 6(g)).

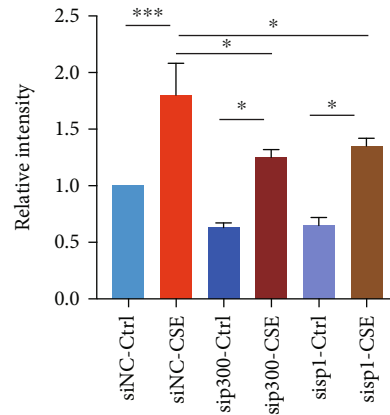
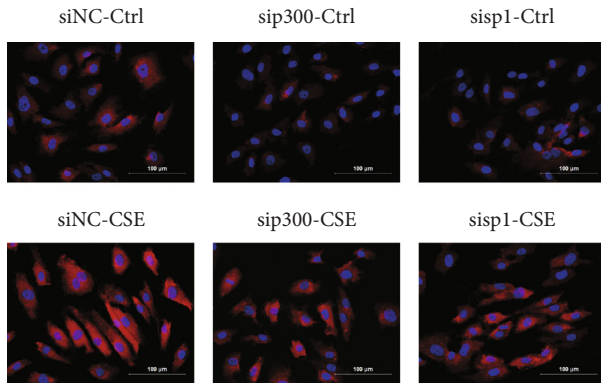
4. Discussion

COPD is the most common respiratory system disease and the fourth leading cause of death all over the world. It is featured by progressive airflow obstruction, which is a response to harmful particles or gases, especially cigarette smoke, and is related to the chronic inflammatory process of airway and lung parenchyma [43]. The pathogenic mechanism of COPD has not been fully uncovered yet. Our study found that p16 expression increased in EPCs of COPD patients, which inhibited cell activity, promoted cell cycle arrest, and enhanced senescence of vascular endothelial cells. Vascular EPCs are important biomarkers of vascular health. Previous studies have indicated that there exists a certain degree of vascular EPC reduction in COPD patients. Our study suggested that decreased EPCs were highly likely to be caused by increased p16 expression induced by smoking. Furthermore, we found that CSE increased the expression of p300/sp1, which in turn mediated the increase of p16 expression in EPCs. Importantly, our study demonstrated that CSE truly promoted the progress of COPD, providing a theoretical basis for explaining the pathogenesis of COPD.

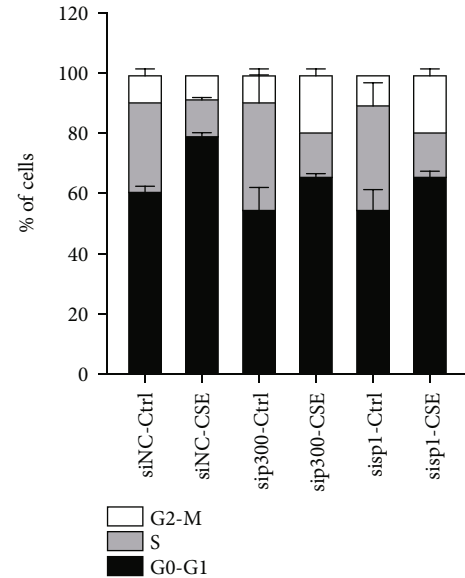
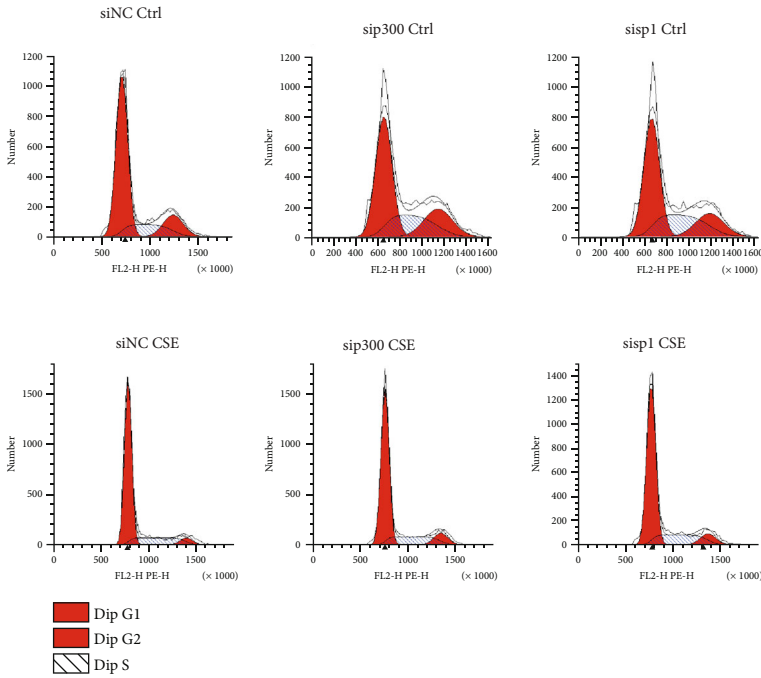
Histone acetyltransferase p300 is a transcription activator, which was originally discovered in the search for the adenovirus carcinogenic transcription factor E1A binding protein, and later, it was demonstrated to have histone acetyltransferase activity [44, 45]. Both the lung tissues of mice exposed to cigarette smoke and the human bronchial



(a)

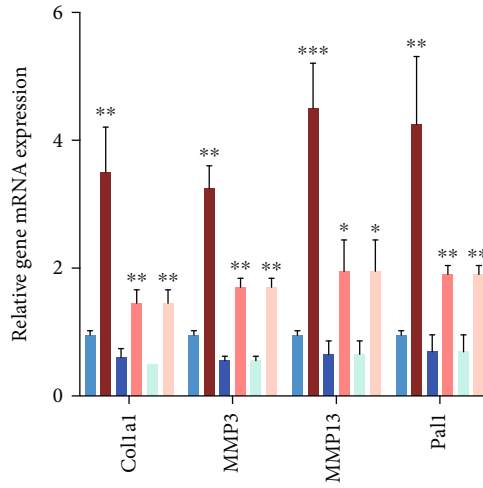


(b)

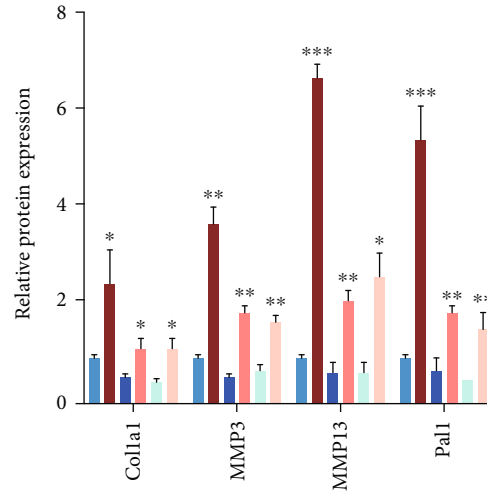
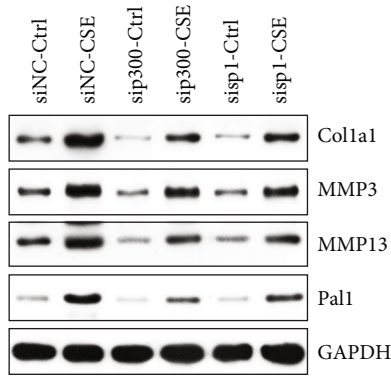


(c)

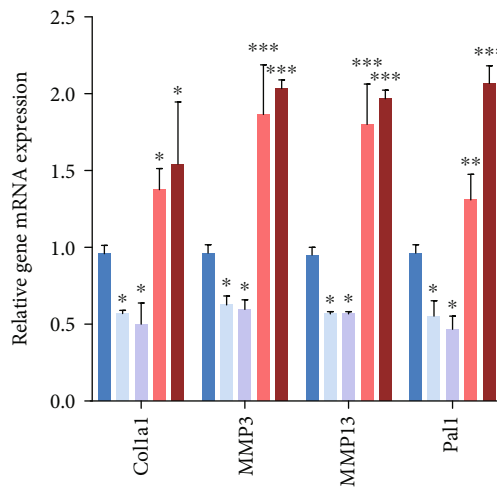
FIGURE 6: Continued.



(d)

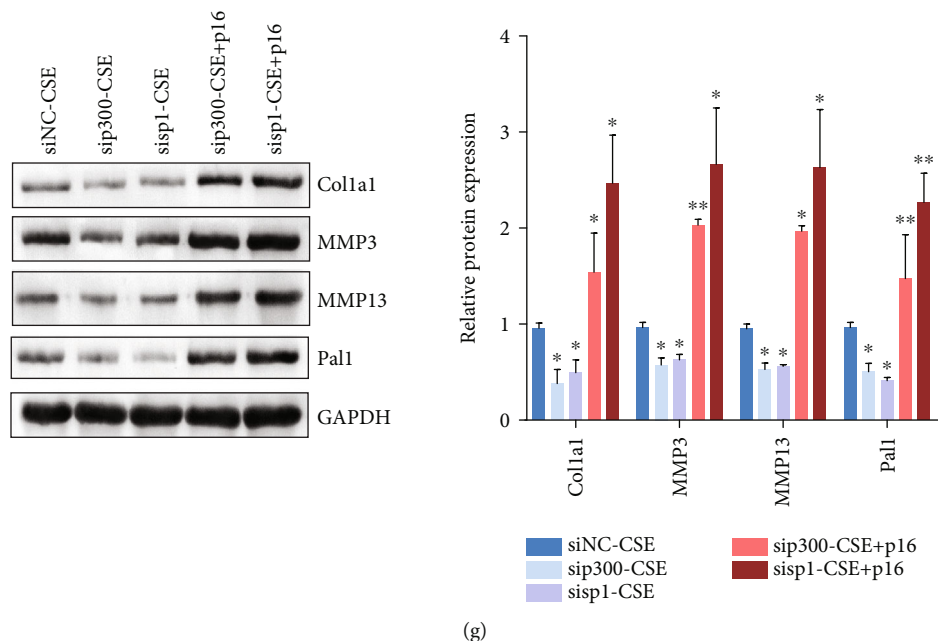


(e)



(f)

FIGURE 6: Continued.



(g)

FIGURE 6: Low expression of p300/Sp1 inhibited CSE-mediated cell senescence. (a) Peripheral blood EPCs were treated with 5% CSE, p300/Sp1 were knocked down by siRNA, and the proportion of senescence cells was counted by β -galactosidase staining. (b) Peripheral blood EPCs were treated with 5% CSE, p300/Sp1 were knocked down by siRNA, and the expression of Lamp1 expression was detected by immunofluorescence. (c) Peripheral blood EPCs were treated with 5% CSE, p300/Sp1 were knocked down by siRNA, and cell cycle distribution was detected by flow cytometry. (d) Peripheral blood EPCs were treated with 5% CSE, p300/Sp1 were knocked down by siRNA, and the expressions of senescence-related genes Col1a1, MMP3, MMP13, and Pal1 were detected by RT-PCR. (e) Peripheral blood EPCs were treated with 5% CSE, p300/Sp1 were knocked down by siRNA, and the expressions of senescence-related genes Col1a1, MMP3, MMP13, and Pal1 were tested by Western Blot. (f) Peripheral blood EPCs were treated with 5% CSE, p300/Sp1 were knocked down by siRNA, p16 was overexpressed, and the expressions of senescence-related genes Col1a1, MMP3, MMP13, and Pal1 were detected by RT-PCR. (g) Peripheral blood EPCs were treated with 5% CSE, p300/Sp1 were knocked down by siRNA, p16 was overexpressed, and the expressions of senescence-related genes Col1a1, MMP3, MMP13, and Pal1 were tested by Western Blot. All the EPCs used in this figure were from nonsmoking non-COPD patients. * $p < 0.05$, ** $p < 0.01$, and *** $p < 0.001$.

epithelial cells induced by CSE display an upregulation of the histone H4K12 acetylation level. Knockdown of p300 can reduce the expression of β -galactosidase and slow down the senescence-like modifications of endothelial cells [46]. In this study, we found that p300 upregulated the expression of p16. The increase of histone acetyltransferase p300 in COPD may be involved in the pathogenesis of COPD by upregulating the acetylation level of histone H4K12, thereby activating the expression of senescence-related factors and promoting the senescence of EPCs. Since p300 is a transcription activator, it is also worth studying whether p300 will activate other transcription factors in addition to p16. Meanwhile, we did not know exactly why there existed a high expression of p300 in peripheral blood EPCs of COPD patients.

Histone modifying enzymes are regulated by the ubiquitin-proteasome degradation pathway. Ubiquitination modification is regarded as the signal of protein degradation [47]. And in cells, the ubiquitin-proteasome pathway is the main pathway for ATP-dependent protein-selective degradation, which mainly functions on some regulatory proteins with short half-life and some structural abnormalities, misconfigurations, or damaged proteins in cells to regulate cell activities [48, 49]. Rom et al. [50] found that cigarette smoking exposure could activate the ubiquitin-proteasome pathway, leading to skeletal muscle protein degradation and cell damage. Jeong et al. [51]

reported that the activated ubiquitin-proteasome pathway in lung cancer cells could result in the degradation of histone acetyltransferase p300. It is also worth studying whether there exists a smoking-induced deubiquitinase activation in the body that could promote the senescence of EPCs to participate in the process of COPD through stabilizing the expression of p300 protein, upregulating the acetylation level of histone H4K12, and activating the transcription of senescence-related factors.

The study limitations mainly lie on the limited patient population covered by the analysis. The COPD patients selected in this study were mainly acute exacerbations including no stable patients. Meanwhile, since we studied endothelial progenitor cells extracted from the peripheral blood of multiple patients and did not specifically compare the activity of p300/p21 in endothelial progenitor cells of patients with grade A-D COPD, our study could not fully represent the entire clinical spectrum of COPD patients.

It has been reported that in patients with early COPD, the number of EPCs increases, and EPCs contribute to the repair and reconstruction of pulmonary vessels, while in patients with late COPD, the number of EPCs in circulation decreases [52–54]. In this study, we did not explore whether the number and function of circulating EPCs in four patients changed. Follow-up studies will explore the above issues more in-depth.

In general, our study found increased expressions of p16 and p300 in peripheral blood EPCs of COPD patients, and CSE would lead to the increase of p16. In addition, p300/Sp1 enhanced the histone H4 acetylation level in the p16 promoter region to mediate the senescence of EPCs.

Data Availability

The data that support the findings of this study are available from the corresponding author upon reasonable request.

Ethical Approval

This study was approved by the Third Xiangya Hospital of Central South University, Changsha, Hunan, China.

Consent

Written informed consent was obtained from all subjects.

Conflicts of Interest

The authors declare that there is no conflict of interest regarding the publication of this article.

Authors' Contributions

Liang G and Peng H conceived the study, performed the experiment and data analysis, and drafted the manuscript. Gao M, Zeng M, and Zhang X performed the experiment and data collection. He Z conceived the study and its design and critically revised the manuscript. Zhihui He performed the study design, data acquisition, statistical analysis, and writing of the manuscript. Huaihui Peng and Min Gao performed the sample collection and contributed to writing the manuscript. Guibin Liang performed the study design, data interpretation, and writing of the manuscript. Menghao Zeng and Xuefeng Zhang performed the data interpretation and writing of the manuscript. All authors read and approved the final manuscript.

Acknowledgments

This study was supported by the Natural Science Foundation of China (81870040).

Supplementary Materials

Supplementary Table 1: detailed demographic and clinical characteristics of patients in this study. (*Supplementary Materials*)

References

- [1] K. F. Rabe and H. Watz, "Chronic obstructive pulmonary disease," *The Lancet*, vol. 389, no. 10082, pp. 1931–1940, 2017.
- [2] S. Majewski and W. J. Piotrowski, "Air pollution-an overlooked risk factor for idiopathic pulmonary fibrosis," *Journal of Clinical Medicine*, vol. 10, no. 1, p. 77, 2021.
- [3] M. G. Matera, M. Cazzola, and C. Page, "Prospects for COPD treatment," *Current Opinion in Pharmacology*, vol. 56, pp. 74–84, 2021.
- [4] P. J. Barnes, "Targeting cellular senescence as a new approach to chronic obstructive pulmonary disease therapy," *Current Opinion in Pharmacology*, vol. 56, pp. 68–73, 2021.
- [5] S. Negri, P. Faris, R. Berra-Romani, G. Guerra, and F. Moccia, "Endothelial transient receptor potential channels and vascular remodeling: extracellular Ca²⁺ entry for angiogenesis, arteriogenesis and vasculogenesis," *Frontiers in Physiology*, vol. 10, 2020.
- [6] R. Miao, V. Y. Lim, N. Kothapalli et al., "Hematopoietic stem cell niches and signals controlling immune cell development and maintenance of immunological memory," *Frontiers in Immunology*, vol. 11, p. 600127, 2020.
- [7] E. B. Peters, "Endothelial progenitor cells for the vascularization of engineered tissues," *Tissue Engineering. Part B, Reviews*, vol. 24, no. 1, pp. 1–24, 2018.
- [8] B. M. Greene and H. R. Taylor, "The status of ivermectin in the treatment of human onchocerciasis," *The American Journal of Tropical Medicine and Hygiene*, vol. 41, no. 4, pp. 460–466, 1989.
- [9] T. Feng, Z. Gao, S. Kou et al., "No evidence for erythromyeloid progenitor-derived vascular endothelial cells in multiple organs," *Circulation Research*, vol. 127, no. 10, pp. 1221–1232, 2020.
- [10] S. He and N. E. Sharpless, "Senescence in health and disease," *Cell*, vol. 169, no. 6, pp. 1000–1011, 2017.
- [11] H. Rayess, M. B. Wang, and E. S. Srivatsan, "Cellular senescence and tumor suppressor gene p16," *International Journal of Cancer*, vol. 130, no. 8, pp. 1715–1725, 2012.
- [12] E. Sikora, A. Bielak-Żmijewska, and G. Mosieniak, "What is and what is not cell senescence," *Postepy Biochemii*, vol. 64, no. 2, pp. 110–118, 2018.
- [13] R. Zhang, M. V. Poustovoitov, X. Ye et al., "Formation of macroH2A-containing senescence-associated heterochromatin foci and senescence driven by ASF1a and HIRA," *Developmental Cell*, vol. 8, no. 1, pp. 19–30, 2005.
- [14] M. Narita, S. Nuñez, E. Heard et al., "Rb-mediated heterochromatin formation and silencing of E2F target genes during cellular senescence," *Cell*, vol. 113, no. 6, pp. 703–716, 2003.
- [15] R. di Micco, G. Sulli, M. Dobreva et al., "Interplay between oncogene-induced DNA damage response and heterochromatin in senescence and cancer," *Nature Cell Biology*, vol. 13, no. 3, pp. 292–302, 2011.
- [16] M. Kosar, J. Bartkova, S. Hubackova, Z. Hodny, J. Lukas, and J. Bartek, "Senescence-associated heterochromatin foci are dispensable for cellular senescence, occur in a cell type- and insult-dependent manner and follow expression of p16^{ink4a}," *Cell Cycle*, vol. 10, no. 3, pp. 457–468, 2011.
- [17] S. Rafii, J. M. Butler, and B. S. Ding, "Angiocrine functions of organ-specific endothelial cells," *Nature*, vol. 529, no. 7586, pp. 316–325, 2016.
- [18] Z. H. He, Y. Chen, P. Chen et al., "5-Aza-2'-deoxycytidine protects against emphysema in mice via suppressing p16^{ink4a} expression in lung tissue," *International Journal of Chronic Obstructive Pulmonary Disease*, vol. Volume 12, pp. 3149–3158, 2017.
- [19] Z. H. He, Y. Chen, P. Chen, S. D. He, J. R. Ye, and D. Liu, "Decitabine enhances stem cell antigen-1 expression in cigarette smoke extract-induced emphysema in animal model,"

- Experimental Biology and Medicine* (Maywood, N.J.), vol. 241, no. 2, pp. 131–139, 2016.
- [20] S. He, Z. He, Y. Chen et al., “C-kit/c-kit ligand interaction of bone marrow endothelial progenitor cells is influenced in a cigarette smoke extract-induced emphysema model,” *Experimental Lung Research*, vol. 39, no. 6, pp. 258–267, 2013.
- [21] D. G. Yang, L. Liu, and X. Y. Zheng, “Cyclin-dependent kinase inhibitor p16^{INK4a} and telomerase may co-modulate endothelial progenitor cells senescence,” *Ageing Research Reviews*, vol. 7, no. 2, pp. 137–146, 2008.
- [22] K. A. Serban and I. Petrache, “Mouse models of COPD,” *Methods in Molecular Biology*, vol. 1809, pp. 379–394, 2018.
- [23] J. Chen, L. Dai, T. Wang, J. He, Y. Wang, and F. Wen, “The elevated CXCL5 levels in circulation are associated with lung function decline in COPD patients and cigarette smoking-induced mouse model of COPD,” *Annals of Medicine*, vol. 51, no. 5-6, pp. 314–329, 2019.
- [24] H. Zhang, D. Sun, D. Li et al., “Long non-coding RNA expression patterns in lung tissues of chronic cigarette smoke induced COPD mouse model,” *Scientific Reports*, vol. 8, no. 1, p. 7609, 2018.
- [25] E. Sala, C. Villena, C. Balaguer et al., “Abnormal levels of circulating endothelial progenitor cells during exacerbations of COPD,” *Lung*, vol. 188, no. 4, pp. 331–338, 2010.
- [26] D. Vagero and R. Olin, “How do we analyse a cohort of healthy workers?,” *Scandinavian Journal of Social Medicine*, vol. 13, no. 4, pp. 165–167, 1985.
- [27] C. Puglia, G. Frasca, T. Musumeci et al., “Curcumin loaded NLC induces histone hypoacetylation in the CNS after intraperitoneal administration in mice,” *European Journal of Pharmacology and Biopharmaceutics*, vol. 81, no. 2, pp. 288–293, 2012.
- [28] I. K. Sundar, M. Z. Nevid, A. E. Friedman, and I. Rahman, “Cigarette smoke induces distinct histone modifications in lung cells: implications for the pathogenesis of COPD and lung cancer,” *Journal of Proteome Research*, vol. 13, no. 2, pp. 982–996, 2014.
- [29] R. Wang, M. Xin, Y. Li, P. Zhang, and M. Zhang, “The functions of histone modification enzymes in cancer,” *Current Protein & Peptide Science*, vol. 17, no. 5, pp. 438–445, 2016.
- [30] M. Singh, A. Bacolla, S. Chaudhary et al., “Histone acetyltransferase MOF orchestrates outcomes at the crossroad of oncogenesis, DNA damage response, proliferation, and stem cell development,” *Molecular and Cellular Biology*, vol. 40, no. 18, 2020.
- [31] K. K. Lee and J. L. Workman, “Histone acetyltransferase complexes: one size doesn’t fit all,” *Nature Reviews. Molecular Cell Biology*, vol. 8, no. 4, pp. 284–295, 2007.
- [32] K. Beishline and J. Azizkhan-Clifford, “Sp1 and the ‘hallmarks of cancer’,” *The FEBS Journal*, vol. 282, no. 2, pp. 224–258, 2015.
- [33] N. Y. Tan and L. M. Khachigian, “Sp1 phosphorylation and its regulation of gene transcription,” *Molecular and Cellular Biology*, vol. 29, no. 10, pp. 2483–2488, 2009.
- [34] T. L. Hilton, Y. Li, E. L. Dunphy, and E. H. Wang, “TAF1 histone acetyltransferase activity in Sp1 activation of the cyclin D1 promoter,” *Molecular and Cellular Biology*, vol. 25, no. 10, pp. 4321–4332, 2005.
- [35] S. Koizume, S. Ito, E. Miyagi et al., “HIF2 α -Sp1 interaction mediates a deacetylation-dependent FVII-gene activation under hypoxic conditions in ovarian cancer cells,” *Nucleic Acids Research*, vol. 40, no. 12, pp. 5389–5401, 2012.
- [36] H. C. Kirch, S. Ruschen, D. Brockmann et al., “Tumor-specific activation of hTERT-derived promoters by tumor suppressive E1A-mutants involves recruitment of p300/CBP/HAT and suppression of HDAC-1 and defines a combined tumor targeting and suppression system,” *Oncogene*, vol. 21, no. 52, pp. 7991–8000, 2002.
- [37] P. Sen, Y. Lan, C. Y. Li et al., “Histone acetyltransferase p300 induces de novo super-enhancers to drive cellular senescence,” *Molecular Cell*, vol. 73, no. 4, pp. 684–698.e8, 2019, e8.
- [38] S. Liu, H. Liu, R. Qin et al., “The cellular senescence of leukemia-initiating cells from acute lymphoblastic leukemia is postponed by β -Arrestin1 binding with P300-Sp1 to regulate hTERT transcription,” *Cell Death & Disease*, vol. 8, no. 4, article e2756, 2017.
- [39] E. Kim, B. E. Zucconi, M. Wu et al., “MITF expression predicts therapeutic vulnerability to p300 inhibition in human melanoma,” *Cancer Research*, vol. 79, no. 10, pp. 2649–2661, 2019.
- [40] F. Lu, X. Cui, S. Zhang, T. Jenuwein, and X. Cao, “Arabidopsis REF6 is a histone H3 lysine 27 demethylase,” *Nature Genetics*, vol. 43, no. 7, pp. 715–719, 2011.
- [41] X. Wang, L. Pan, Y. Feng et al., “p300 plays a role in p16^{INK4a} expression and cell cycle arrest,” *Oncogene*, vol. 27, no. 13, pp. 1894–1904, 2008.
- [42] Y. Huang, J. Wu, R. Li et al., “B-MYB delays cell aging by repressing p16 INK4 α transcription,” *Cellular and Molecular Life Sciences*, vol. 68, no. 5, pp. 893–901, 2011.
- [43] A. Agusti, C. Vogelmeier, and R. Faner, “COPD 2020: changes and challenges,” *American Journal of Physiology. Lung Cellular and Molecular Physiology*, vol. 319, no. 5, pp. L879–L883, 2020.
- [44] E. Froimchuk, Y. Jang, and K. Ge, “Histone H3 lysine 4 methyltransferase KMT2D,” *Gene*, vol. 627, pp. 337–342, 2017.
- [45] N. G. Iyer, H. Ozdag, and C. Caldas, “p300/CBP and cancer,” *Oncogene*, vol. 23, no. 24, pp. 4225–4231, 2004.
- [46] R. Mortuza, S. Chen, B. Feng, S. Sen, and S. Chakrabarti, “High glucose induced alteration of SIRT1 in endothelial cells causes rapid aging in a p300 and FOXO regulated pathway,” *PLoS One*, vol. 8, no. 1, article e54514, 2013.
- [47] M. Uckelmann and T. K. Sixma, “Histone ubiquitination in the DNA damage response,” *DNA Repair (Amst)*, vol. 56, pp. 92–101, 2017.
- [48] C. Zou and R. K. Mallampalli, “Regulation of histone modifying enzymes by the ubiquitin-proteasome system,” *Biochimica et Biophysica Acta*, vol. 1843, no. 4, pp. 694–702, 2014.
- [49] D. Vucic, V. M. Dixit, and I. E. Wertz, “Ubiquitylation in apoptosis: a post-translational modification at the edge of life and death,” *Nature Reviews. Molecular Cell Biology*, vol. 12, no. 7, pp. 439–452, 2011.
- [50] O. Rom, S. Kaisari, D. Aizenbud, and A. Reznick, “Involvement of E3 ubiquitin ligases in cigarette smoke associated muscle catabolism,” *Free Radic Biol Med*, vol. 75, 75, Supplement 1, p. S5, 2014.
- [51] M. J. Jeong, E. J. Kim, E. A. Cho, S. K. Ye, G. H. Kang, and Y. S. Juhn, “cAMP signalling decreases p300 protein levels by promoting its ubiquitin/proteasome dependent degradation via Epac and p38 MAPK in lung cancer cells,” *FEBS Letters*, vol. 587, no. 9, pp. 1373–1378, 2013.
- [52] V. I. Peinado, J. Ramírez, J. Roca, R. Rodríguez-Roisin, and J. A. Barberà, “Identification of vascular progenitor cells in pulmonary arteries of patients with chronic obstructive pulmonary disease,” *American Journal of Respiratory Cell and Molecular Biology*, vol. 34, no. 3, pp. 257–263, 2006.

- [53] P. Palange, U. Testa, A. Huertas et al., "Circulating haemopoietic and endothelial progenitor cells are decreased in COPD," *The European Respiratory Journal*, vol. 27, no. 3, pp. 529–541, 2006.
- [54] A. Huertas, U. Testa, R. Riccioni et al., "Bone marrow-derived progenitors are greatly reduced in patients with severe COPD and low-BMI," *Respiratory Physiology & Neurobiology*, vol. 170, no. 1, pp. 23–31, 2010.

Research Article

Long Noncoding RNA HCG9 Promotes Osteosarcoma Progression through RAD51 by Acting as a ceRNA of miR-34b-3p

Lu Wang, ShuangQing Li, Lin Qi, and Lin Ling 

Department of Orthopedics, The Second Xiangya Hospital, Central South University, Changsha, Hunan 410011, China

Correspondence should be addressed to Lin Ling; linglin0812@csu.edu.cn

Received 19 March 2021; Accepted 20 July 2021; Published 19 August 2021

Academic Editor: Miaomiao Wu

Copyright © 2021 Lu Wang et al. This is an open access article distributed under the Creative Commons Attribution License, which permits unrestricted use, distribution, and reproduction in any medium, provided the original work is properly cited.

Background. Long noncoding RNAs (lncRNAs) have critical regulatory functions in biological and pathological activities during osteosarcoma progression. It is important to elucidate the expression pattern and reveal the underlying mechanisms of the newly identified lncRNAs. **Methods.** Herein, we screened the differentially expressed lncRNAs in osteosarcoma tumors and cell lines using lncRNA microarray. The candidate lncRNA was further verified by qRT-PCR, and the association of gene expression with clinicopathological features was evaluated by Kyoto Encyclopedia of Genes and Genomes (KEGG) pathway analysis. The targeting miRNA was identified using starBase analysis, and the competing endogenous RNA (ceRNA) network was established by STRING. Overexpression and silence of RNA were detected by qRT-PCR. Osteosarcoma cell proliferation was measured with CCK-8 assay, and the migration and invasion were evaluated with Transwell assay. Colony formation assay was observed. Flow cytometry evaluated the cell cycle. Western blot was performed to detect the mitotic markers and apoptosis-related proteins. A nude mouse tumor formation experiment was used to evaluate osteosarcoma progression *in vivo*. Cooverexpressing miR-34b-3p with RAD51 reversed the miR-34b-3p-induced changes in proliferation, the cell cycle, the expression of H2A.X, and that of apoptosis-related proteins. **Results.** HCG9 was identified as osteosarcoma-associated lncRNA. Osteosarcoma tissues and cell lines expressed higher levels of HCG9 as compared to normal tissues and osteoblasts, and high expression of HCG9 was further proved to be related to metastasis and the grade of osteosarcoma in clinical cases. Knockdown of HCG9 inhibited the proliferation, migration, and invasion of osteosarcoma cells. miR-34b-3p was identified as the target of HCG9, and RAD51 acted as a potential target of miR-34b-3p. Cooverexpressing miR-34b-3p with HCG9 partially suppressed the HCG9-stimulated proliferation, migration, and invasion of osteosarcoma cells *in vitro* and delayed the tumor progression *in vivo*. **Conclusion.** We discovered that lncRNA HCG9 promoted the proliferation of osteosarcoma cells via suppressing miR-34b-3p. Our study provides novel biomarkers and potential therapeutic targets for osteosarcoma treatment.

1. Introduction

Osteosarcoma is the most common primary bone malignancy that occurs predominantly in adolescents [1]. Despite the advancement in diagnosis, chemotherapy, and surgical techniques, the prognosis of osteosarcoma remains poor. The long-term survival rate of localized osteosarcoma is 77%, while this disease becomes more lethal when metastasis occurs, with the long-term survival rate dropping to 26% according to the American Cancer Society. Although the underlying molecular mechanism of osteosarcoma remains unclear, extensive efforts have been expanded to explore more targeted and localized treatment for osteosarcoma [2].

With the increasing knowledge of molecular pathogenesis, gene therapy has emerged as a controlled, targeted, and specific treatment for osteosarcoma [3, 4].

Over 90% of the human genome does not encode proteins, recognized as “noncoding RNAs” (ncRNAs) [5]. Long noncoding RNAs (lncRNAs) are a class of ncRNAs that contain over 200 nucleotides. Increasing pieces of evidence have shown that dysregulated lncRNA gene expression is associated with tumor progression [6–8]. The first study on lncRNA in osteosarcoma was performed by Li et al., who identified over 400 upregulated and 798 downregulated lncRNAs in osteosarcoma by lncRNA expression microarray, providing valuable potential biomarkers for osteosarcoma

[9]. Gao and Lian reported that lncRNA MALAT1 was an independent prognostic factor of osteosarcoma [10], and another lncRNA, H19, was also proved to be associated with osteosarcoma progression [11]. HCG9 is also known as the human leukocyte antigen complex group 9 gene, and studies have reported that HCG9 was related to lung squamous cell carcinoma [12] and nasopharyngeal carcinoma [13]. However, the role of HCG9 in osteosarcoma remains unknown.

One of the major functions of lncRNAs is acting as competing endogenous RNAs (ceRNAs) to regulate lncRNA/miRNA/mRNA crosstalk [14]. The ceRNA hypothesis was proposed by Salmena et al. [15]. They hypothesized that lncRNAs are complete for the miRNA binding sites via partial complementarity, which leads to a decreased miRNA activity for mRNA regulation. Since then, many researchers have validated this theory [16]. In osteosarcoma specifically, Pan et al. reported that lncRNA FBXL19-AS1 sponged miR-346 to regulate osteosarcoma cell proliferation [17]. Zheng et al. connected the lncRNA SNHG3/miR-151a-3p/RAB22A functioning axis to regulate osteosarcoma invasion and migration [18]. However, many potential lncRNA/miRNA regulations have not yet to be identified.

In this study, we performed lncRNA microarray analysis and identified HCG9 as one of the differentially expressed lncRNAs in osteosarcoma tissues. To our knowledge, this is the first report to associate HCG9 with osteosarcoma progression. We established a ceRNA network, and the targeting miRNA miR-34b-3p was pinpointed. The interaction between HCG9 and miR-34b-3p was validated with bioinformatic analysis and molecular biological analysis, and we also reported that RAD51 was the potential downstream mRNA targeted by miR-34b-3p. The impact of HCG9 knockdown and overexpression on osteosarcoma cells *in vitro* and tumor progression *in vivo* was evaluated. Our results provided novel biomarkers of osteosarcoma and revealed the theoretical basis of the underlying mechanisms.

2. Materials and Methods

2.1. lncRNA Microarray Chip and Bioinformatic Analysis. lncRNA gene expressions in osteosarcoma tissues and paracarcinoma tissues were analyzed. The GSE21257 dataset from the GEO database (<https://www.ncbi.nlm.nih.gov/gds/>) was used as the reference. Univariate Cox regression analysis was used to identify the differentially expressed lncRNAs. A minimum X -fold change in gene expressions between tumor tissue and normal tissue with $P < 0.05$ was screened. The Cancer Cell Line Encyclopedia database was used as the reference to validate HCG9 expression in cancer cells.

The osteosarcoma survival information was used to generate Kaplan-Meier separate survival analysis and log-rank tests for the correlation between HCG9 expression and survival rates. Kyoto Encyclopedia of Genes and Genomes (KEGG) pathway analysis was conducted to establish the association between HCG9 and clinicopathological features of osteosarcoma.

The ceRNA network was generated by assessing the interaction among proteins with STRING (2017 release) in the standard combined score > 0.4 . The visualization of the

protein-protein interaction (PPI) network was obtained with Cytoscape software (version 3.6.1). Molecular Complex Detection (MCODE, version 1.31) was adopted to identify the significant modules and the top-ranked genes in the PPI network.

2.2. Tissue Collection. A total number of 47 patients who received tumor removal surgeries from the Second Xiangya Hospital were recruited. 15 pairs of osteosarcoma and paracarcinoma tissues were collected from the patients who consented to all the investigations in this study. Patients were all informed and signed written consent before surgery. All procedures and tissue collection protocols were approved by the Institutional Review Board of the Second Xiangya Hospital. Tissue specimens were stored in liquid nitrogen or fixed in 10% formalin before the execution of experiments.

2.3. Cell Culture and Transfection. Osteoblast cell line hFOB1.19 and osteosarcoma cell lines U2OS, MG-63, and MNNG/HOS were all purchased from ATCC (Manassas, VA). Cells were cultured in Dulbecco's Modified Eagle's Medium (DMEM) (Gibco) containing 10% fetal bovine serum in a 5% CO₂ atmosphere at 37°C. For cell transfection, HCG9 overexpressing plasmid, HCG9 small interfering RNAs (siRNAs), and negative controls were purchased from Thermo Fisher Scientific Inc. miR-34b-5p mimics and negative controls were purchased from Qiagen. The transfection was performed using Lipofectamine 2000 (Thermo Fisher Scientific, Waltham, MA) according to the manufacturer's protocol. Cells were harvested for characterization at 48 hours posttransfection.

2.4. Transwell Assay. Cell migration and invasion were both assessed with the Transwell system. For migration assay, 2×10^4 cells were suspended in 100 μ L serum-free DMEM and seeded in the upper chambers of an 8 μ m pore size Transwell plate (Corning, USA). For invasion assay, the upper chamber of an 8 μ m pore size Transwell plate was pre-coated with the Matrigel™ Matrix (BD Biosciences, CA, USA), and 2×10^4 cells were seeded and cultured in serum-free DMEM.

For both assays, a total volume of 500 μ L DMEM containing 10% fetal bovine serum (Gibco) was added to the lower chambers. After 24 h in culture, the migrated and invaded cells at the bottom surface were fixed with 4% paraformaldehyde and stained with 1% crystal violet. The cells were observed with a Zeiss upright microscope. The staining was washed using 33% acetic acid, and the absorption at 590 nm was analyzed with a microplate reader (Thermo Fisher Scientific).

2.5. Cell Counting Kit-8 (CCK-8) Assay. Cell proliferation was evaluated with the CCK-8 assay (Dojindo, Japan). Wild-type control and transfected cells were harvested and seeded into a 96-well plate. Three technical repeats were performed for each group. After cell adherence and 24 h of culture, 10 μ L CCK-8 solution was added to each well and incubated at 37°C for 4 h. Cell proliferation was evaluated with a microplate reader (Bio-Rad Laboratories, Hercules, CA) at 450 nm.

2.6. Colony Formation. Wild-type and transfected cells were seeded in a 6-well plate with a density of 800 cells/well. After 10 days in culture, the cells were fixed with 4% paraformaldehyde and stained with 1% crystal violet. The staining was washed using 33% acetic acid, and the absorption at 590 nm was analyzed with a microplate reader (Thermo Fisher Scientific).

2.7. Quantitative Real-Time Polymerase Chain Reaction (qRT-PCR). Total RNA was isolated from osteosarcoma tumor tissues, paracarcinoma soft tissues, and cell lines using a TRIzol® reagent (Invitrogen, CA, USA). cDNAs were synthesized using a PrimeScript™ RT reagent kit (ComWin Biotech, Beijing, China). Primers of HCG9 and miR-34b-5p were obtained from Thermo Fisher Scientific. The primer sequences are shown in Table 1. PCR was performed with the SYBR Green Master Mix (ComWin Biotech, Beijing, China) using a fluorescent quantitative PCR system (Thermo Fisher Scientific, USA). The relative expression levels were calculated using the $2^{-\Delta\Delta Ct}$ method, and GAPDH and U6 were used as the internal reference for mRNAs and miRNAs, respectively.

2.8. Western Blot. Cells or tissues were lysed in a RIPA lysis buffer (Beyotime Biotechnology, Shanghai, China) for 10 min on ice. The protein concentrations were determined using a BCA Protein Assay Kit. An equal amount of protein was loaded and separated using SDS-polyacrylamide gel electrophoresis. The proteins were then transferred to a nitrocellulose membrane. Membranes were blocked in a 1x PBS buffer containing 5% nonfat milk and 0.1% Tween-20 (PBST) for 1 h at room temperature, then subsequently stained with primary antibodies overnight at 4°C, including β -actin (mouse, 1:5000; cat# 66009-1-Ig; Proteintech, USA), H2A.X (mouse, 1:1000; cat# ab26350; Abcam, UK), RAD51 (rabbit, 1:1000; cat# ab133534; Abcam, UK), p53 (mouse, 5 μ g/mL; cat# ab26; Abcam, UK), Bcl-2 (rabbit, 1:1000; cat# 12789-1-AP; Proteintech, USA), Bax (rabbit, 1:1000; cat# 50599-2-Ig; Proteintech, USA), and Caspase-3 (rabbit, 1:1000; cat# 19677-1-AP; Proteintech, USA). After washing 3 times with PBST, the membranes were incubated with horseradish peroxidase-conjugated goat anti-rabbit (1:6000; cat# SA00001-2; Proteintech, USA) or goat anti-mouse antibodies (1:5000; cat# SA00001-1; Proteintech, USA) for 1.5 h at room temperature. After 1 min incubation with enhanced chemiluminescence (SuperECL Plus, Advanta, USA), the signal intensity was detected by X-ray.

2.9. Cell Cycle Analysis. Cells in different transfection groups were collected and washed with PBS. After fixation with ice-cold 70% (v/v) ethanol for 24 h, the samples were washed again with PBS and then incubated with RNase A (100 μ g/mL) for 30 min. The samples were stained with PI (final concentration 50 μ g/mL) for 30 min, and flow cytometry analysis was conducted to determine the distribution of the cell cycle.

2.10. In Vivo Tumorigenesis. Male BALB/C nude mice (6 weeks of age) were purchased from Hunan SJA Laboratory Animal Co., Ltd. (Changsha, China) and housed in the ani-

TABLE 1: Primer sequences.

Gene	Sequences (5'-3')
HCG9	F: AGTCAGGAGCCCCATAGTCCC R: CCGCTGAGGCAGTCACATCCC
miR-34b-5p	F: CCAATCACTAACTCCACTGCCAT
RAD51	F: GAGCGTTCAACACAGACCAC R: AGTGCATACCTAGATTCTACCAT
β -Actin	F: ACCCTGAAGTACCCCATCGAG R: AGCACAGCCTGGATAGCAAC
U6	F: CTCGCTTCGGCAGCACA R: AACGCTTCACGAATTTGCGT

mal facility at the Second Xiangya Hospital. All experimental protocols were approved by the Institutional Animal Ethics Committee at the Second Xiangya Hospital of Central South University. For tumor formation, 2×10^6 MNNG/HOS cells were suspended in 200 μ L PBS and injected into the subcutaneous area. Lentiviral vectors of HCG9 and miR-34b-3p were constructed by GeneChem (Shanghai, China) and were administered via lateral tail vein injection before tumor cells were injected. Tumor volume was measured with a vernier caliper on days 4, 7, 11, 14, 17, 21, 24, and 28. At 28 days post-surgery, the mice were euthanized and the tumors were dissected for weight measurement.

2.11. Ki67 Staining. Tumor samples were harvested and fixed in 10% formalin overnight at room temperature. Samples were gradually dehydrated in ethanol and embedded in paraffin blocks. Sections of 5 μ m were collected, deparaffinized, and rehydrated. The antigens were retrieved by boiling in a Tris buffer (pH = 6) for 15 min using a steamer. Samples were then blocked in 1% bovine serum albumin solution (Sigma-Aldrich) and stained with the primary Ki67 antibody (rabbit, 1:500; ab15580; Abcam) overnight at 4°C. After washing with PBS, the samples were stained with the horseradish peroxidase (HRP) (goat; cat# ab6721; Abcam, UK) secondary antibody at 1:250 concentration for 1 hour at room temperature. Stained samples were mounted and observed under a Zeiss upright microscope.

2.12. Statistical Analysis. All data were presented as mean \pm standard deviation, and all experiments were repeated independently at least 3 times. Student's *t*-test and one-way ANOVA were used to compare data between two groups and among three groups, respectively, using GraphPad Prism 8.0. $P < 0.05$ was considered statistically significant.

3. Results

3.1. HCG9 Gene Expression Was Elevated in Osteosarcoma Tissues and Cells. We analyzed lncRNA chip data and assessed the correlation with osteosarcoma for each lncRNA using Cox proportional hazards regression. Six genes presented statistically significant expressions ($P < 0.05$) in osteosarcoma tissues versus paracarcinoma tissues and were

screened, which were MALAT1, HCG9, FAM99A, FAM87B, DLEU2, and C8orf49 (Figure 1(a)). Secondary structural identification was performed using AnnoLnc Annotation, and HCG9 was determined as our target for this study (Figure 1(b)). We analyzed HCG9 gene expression in the Cancer Cell Line Encyclopedia (CCLE) database and found that HCG9 gene expression was elevated in various cancer cell lines (Figure 1(c)). Therefore, we further validated HCG9 gene expression in osteosarcoma and paracarcinoma tissues collected from patients. The qRT-PCR result demonstrated that HCG9 gene expression was significantly upregulated in osteosarcoma tumor tissues as compared to paracarcinoma tissues (Figure 1(d)). HCG9 gene expression was also assessed in human fetal osteoblast cell line hFOB1.19 and osteosarcoma cell lines U2OS, MG-63, and MNNG/HOS, and the expression was enhanced in all three osteosarcoma cell lines as compared to hFOB1.19 cells. MNNG/HOS demonstrated the highest HCG9 gene expression. Thus, MNNG/HOS cells were selected for the following experiments in this study (Figure 1(e)). We analyzed the overall survival rate by plotting Kaplan-Meier survival plots and log-rank tests for median dichotomized HCG9 gene expression, and $P < 0.05$ was considered statistically significant. A receiver operating characteristic curve (ROC) was plotted, and the area under the curve (AUC) was analyzed to validate the association between HCG9 gene expression and prognosis (Supplemental Fig. 1). AUC at 2 years had an accuracy of 0.72. The Kaplan-Meier plot showed that the overall survival rate was significantly lower ($P = 0.024$) in the HCG9 high expression group compared with the low expression group (Figure 1(f)), suggesting HCG9 was associated with the prognosis of osteosarcoma patients.

3.2. HCG9 Mediated the Osteosarcoma Cell Proliferation and Apoptosis. We next investigated how HCG9 expression impacted the proliferation and apoptosis of osteosarcoma cells. We established an HCG9 gene knockdown colony (sh-HCG9) and verified the gene expression of HCG9 with qRT-PCR. The HCG9 gene expression was significantly inhibited in the sh-HCG9 cells as compared to the wild-type control cells (Figure 2(a)). sh-HCG9 impaired the invasion and migration ability of MNNG/HOS cells. The number of invasion and migration cells was significantly lower in the sh-HCG9 group as compared to the control group (Figures 2(b) and 2(c)). Knockdown of HCG9 also suppressed MNNG/HOS cell proliferation and colony formation, as the CCK-8 assay result and colony formation result demonstrated significantly lower proliferation rates and colony counts in the sh-HCG9 group as compared to the control group (Figures 2(d) and 2(e)). sh-HCG9 induced cell arrest, as shown in the cell cycle analysis, the G0/G1 phase was significantly enhanced, and the G2/M phase was significantly inhibited in the sh-HCG9 group (Figure 2(f)). sh-HCG9 also promoted proapoptotic protein expression, including Bax, Caspase-3, and p53, and inhibited antiapoptotic protein Bcl-2 (Figure 2(g)). These results suggested that depletion of HCG9 significantly inhibited proliferation and invasion, induced cell arrest, and promoted the apoptotic phenotype of osteosarcoma cells.

3.3. HCG9 Expression Was Associated with Pathological Features of Osteosarcoma Patients. We analyzed the expression matrix of HCG9 and screened HCG9-associated gene expressions ($P < 0.05$). Using KEGG pathway analysis, we discovered that the high expression of HCG9 was correlated with the metastasis of osteosarcoma (Supplemental Fig. 2A). The association between HCG9 and clinicopathological features such as age, gender, metastasis, grade, and pathology state is presented in Supplemental Fig. 2B – 2F. High HCG9 expression was associated with cancer metastasis (Supplemental Fig. 2D) and grade (Supplemental Fig. 2E) but not the other pathological features such as age (Supplemental Fig. 2B) and gender (Supplemental Fig. 2C). We collected 44 osteosarcoma cases from the Second Xiangya Hospital and validated the correlation between HCG9 and clinicopathological features. Pearson's chi-squared test was performed to evaluate the P value. A significant association was identified between HCG9 gene expression and distant metastasis ($P = 0.009$) (Supplemental Fig. 2D) and clinical stage ($P = 0.028$) (Supplemental Fig. 2E). These results demonstrated that HCG9 gene expression was essential in osteosarcoma metastasis and progression clinically.

3.4. HCG9 Negatively Regulated miR-34b-3p to Mediate the Osteosarcoma Cell Proliferation and Apoptosis. We used starBase V2.0 to predict the potential targets of HCG9, and miR-34b-3p was identified as the only target for HCG9. A total number of 104 mRNAs were pinpointed as potential targets for miR-34b-3p; thus, the ceRNA network is established and presented in Figure 3(a). The distribution of targeting mRNAs in the chromosomes was visualized by Cytoscape (Figure 3(b)). The STRING analysis (<http://string-db.org/>) was performed on miRNA-targeted genes, and the PPI network was constructed with 40 nodes and 46 edges. By performing MCODE, two modules were identified (Figure 3(c)). Module 1 included AHCTF1, XPO1, ITGB3BPP, and PPP1CC, which are immune response-associated genes, and module 2 included CDH2, MET, and NOTCH2, which are associated with DNA damage response [19, 20]. Gene ontology (GO), biological process (BP), and KEGG enrichment analyses showed the upregulated genes enriched in the organelle division and cell cycle pathways and the downregulated genes enriched in the miRNA in cancer and Notch signaling pathways (Supplemental Fig. 3). Gene expression of miR-34b-3p was significantly downregulated in osteosarcoma tissues and cell lines as compared to paracarcinoma tissues and osteoblast cell lines, respectively (Figures 3(d) and 3(e)). Knockdown of HCG9 significantly enhanced miR-34b-3p gene expression, suggesting HCG9 negatively regulated miR-34b-3p (Figure 3(f)). Overexpression of miR-34b-3p obviously upregulated the expression level of miR-34b-3p (Figure 3(g)).

To verify the regulatory role of miR-34b-3p in osteosarcoma cell proliferation, migration, and invasion, we established HCG9 and miR-34b-3p overexpressing MNNG/HOS cells. HCG9 overexpression significantly enhanced cell proliferation within 24 h of culture, and cooverexpressing HCG9 and miR-34b-3p partially reversed such effect (Figure 4(a)). HCG9 promoted colony-forming ability, while

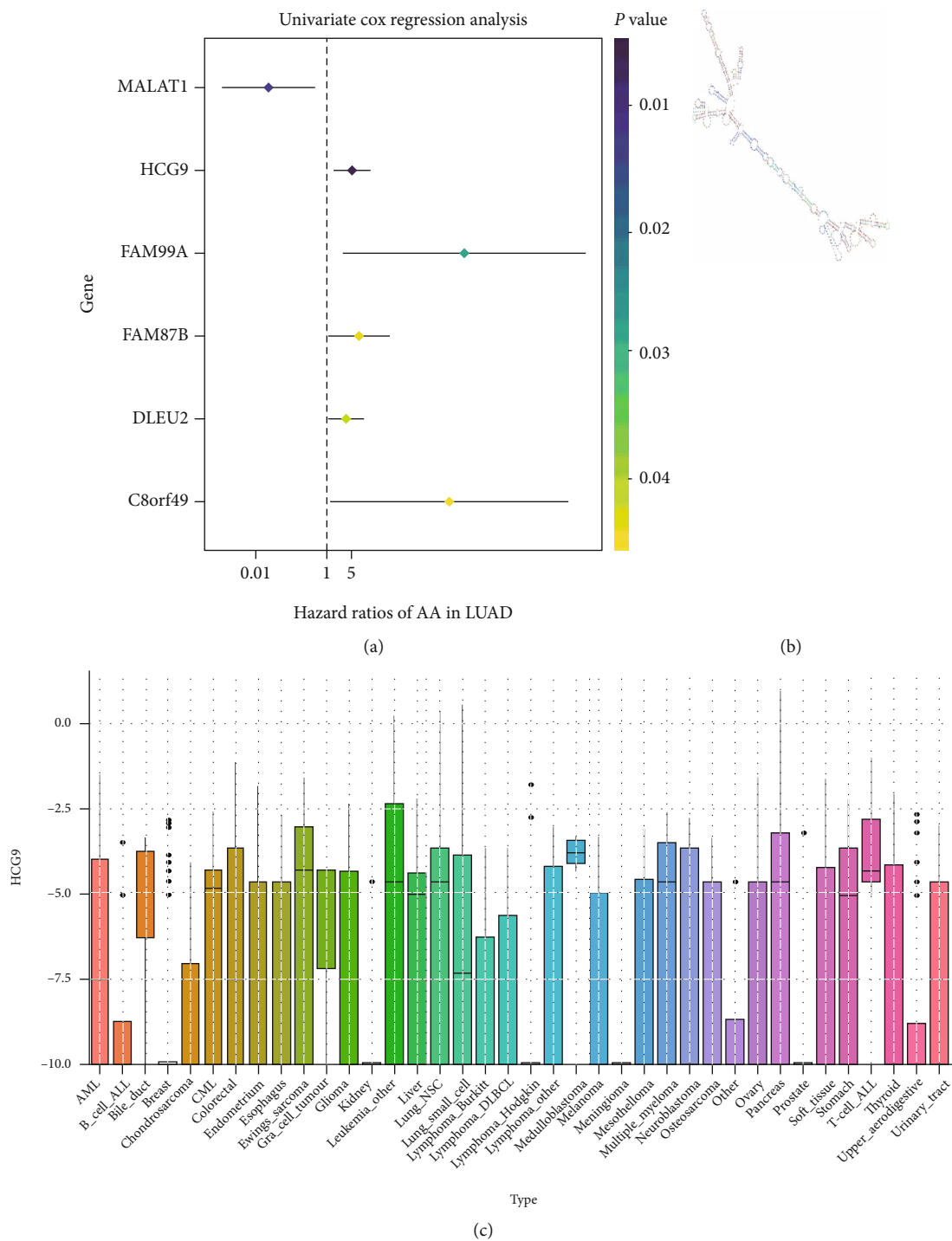


FIGURE 1: Continued.

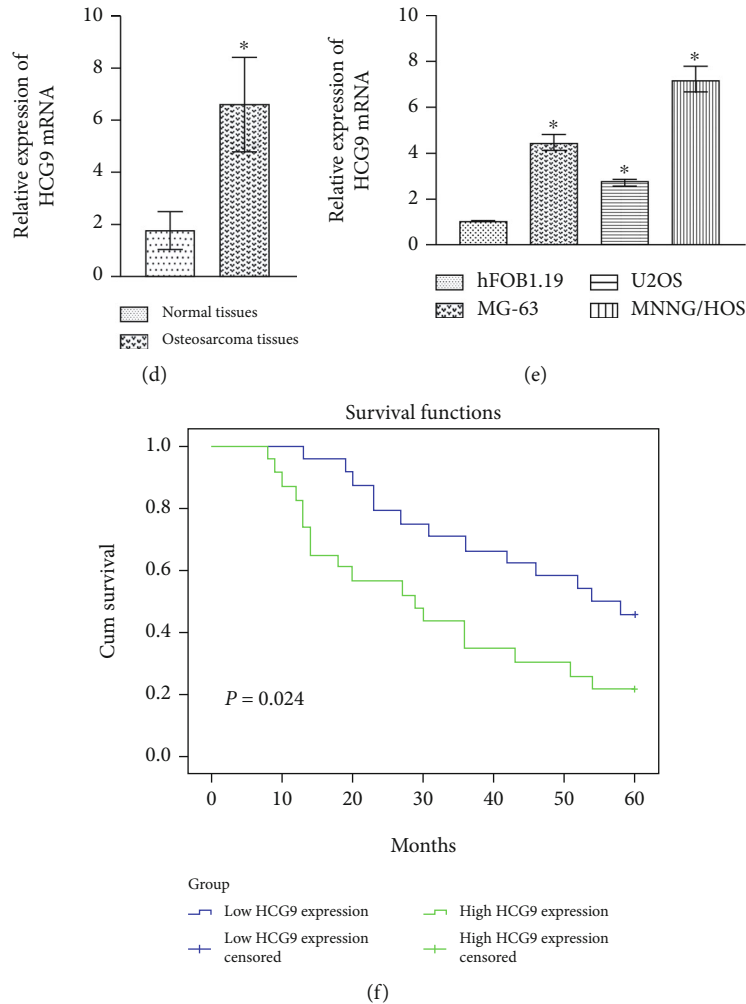


FIGURE 1: HCG9 gene expression was upregulated in osteosarcoma tissues and cells. (a) lncRNA chip data was analyzed using Cox proportional hazards regression based on the GSE21257 database, and 6 genes expressed differently in osteosarcoma tissues were screened. (b) Secondary structure prediction of HCG9 using AnnoLnc Annotation. (c) Analysis of HCG9 gene expression in the CCLE database. (d) HCG9 gene expression in osteosarcoma tumor tissue and paracarcinoma tissue. * $P < 0.05$ vs. the paracarcinoma tissues. (e) HCG9 gene expression in osteoblast and osteosarcoma cell lines. * $P < 0.05$ vs. the hFOB1.19 group. (f) Kaplan-Meier analysis of the associations between the HCG9 expression level and the overall survival of patients with osteosarcoma.

cooverexpressing HCG9 and miR-34b-3p partially reduced the number of colonies as compared to the HCG9 group (Figures 4(b) and 4(c)). Cooverexpressing miR-34b-3p also inhibited MNNG/HOS cell invasion and migration that were stimulated by HCG9 overexpression (Figures 4(d) and 4(e)). The cell cycle and apoptosis-related proteins were also impacted by HCG9 and miR-34b-3p expressions. Overexpressing HCG9 encouraged cell mitosis as flow cytometry results showed that the cell number in the G2/M cycle of the HCG9 group was significantly higher than that of the control group. Cooverexpressing HCG9 and miR-34b-3p abolished such effect (Figure 4(f)). RAD51 is the key enzyme that regulates the cell cycle and preserves the G2/M phase, whereas H2A.X preserves cell cycle arrest. Overexpressing HCG9 promoted RAD51 expression and suppressed H2A.X expression, indicating HCG9 induced mitosis and hyperproliferation of the osteosarcoma cells. Cooverexpressing miR-34b-3p partially reversed such effect (Figure 4(g)). Proapop-

totic proteins Bax, Caspase-3, and p53 were inhibited by HCG9 overexpression and reversed by miR-34b-3p/HCG9 cooverexpression. Antiapoptotic protein Bcl-2 was impacted in the opposite manner (Figure 4(h)). These results suggested that HCG9 enhanced proliferation and suppressed apoptosis of osteosarcoma cells by suppressing miR-34b-3p expression. Overexpressing miR-34b-3p partially reversed HCG9-stimulated hyperproliferation.

3.5. miR-34b-3p Induced Cell Cycle Arrest via Downregulating RAD51. We next evaluated the potential target of miR-34b-3p. RAD51 regulated the cell cycle and DNA damage checkpoint, and these pathways were significantly upregulated in our clinical osteosarcoma tissue samples (Supplemental Fig. 3). The potential binding site between miR-34b-3p and RAD51 was predicted using starBase (Figure 5(a)). We established miR-34b-3p overexpressing and miR-34b-3p/RAD51 cooverexpressing osteosarcoma

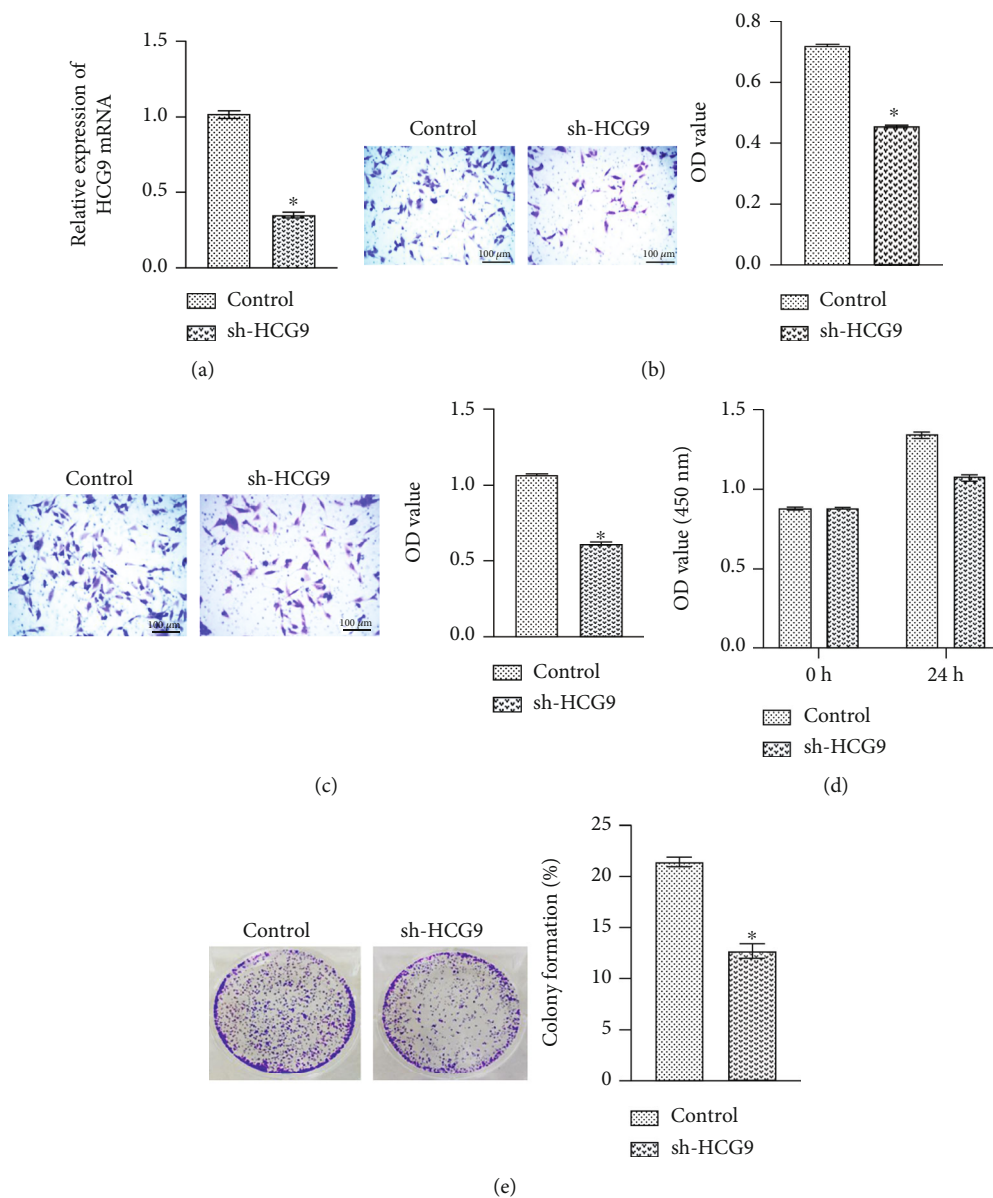


FIGURE 2: Continued.

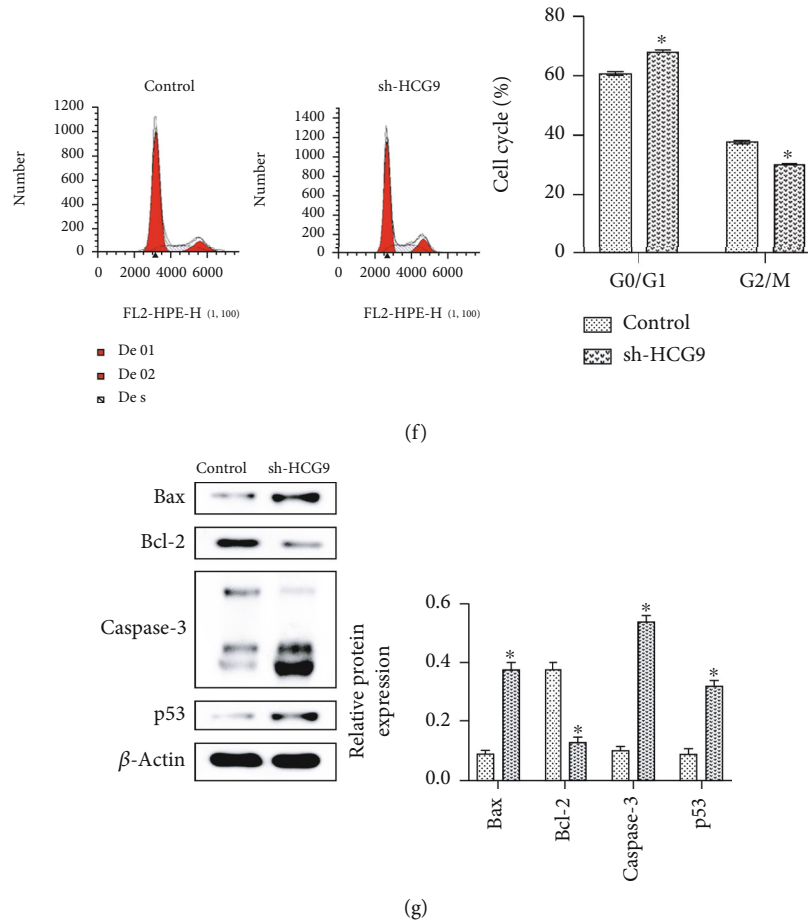


FIGURE 2: Knockdown of HCG9 inhibited MNNG/HOS cell proliferation, migration, and invasion. (a) HCG9 gene expression in the wild-type control and sh-HCG9 groups. (b) Representative images and OD value of invasion in the control and sh-HCG9 cells assessed by Transwell assay. Scale bar: 100 μ m. (c) Representative images and OD value of migration in the control and sh-HCG9 cells assessed by Transwell assay. Scale bar: 100 μ m. (d) CCK-8 assay of cell proliferation in the control and sh-HCG9 groups. (e) Representative images and cell number of colonies formed by the control and sh-HCG9 cells. (f) Cell cycle analysis by flow cytometry. (g) Apoptosis-related protein expressions (Bax, Bcl-2, Caspase-3, and p53) in the control and sh-HCG9 groups. $n = 6$ in each group. * $P < 0.05$ vs. the control group.

cells to evaluate the involvement of RAD51. The expression of miR-34b-3p was significantly upregulated in the miR-34b-3p overexpression group and was partially reversed in the miR-34b-3p/RAD51 cooverexpression group (Figure 5(b)). CCK-8 assay results showed that miR-34b-3p overexpression inhibited cell proliferation as compared to the control group, whereas miR-34b-3p/RAD51 cooverexpression recovered the proliferation of osteosarcoma cells (Figure 5(c)). RAD51 also played a role in the miR-34b-3p-mediated cell cycle, and miR-34b-3p overexpression induced cell cycle arrest, as it reduced the cell number in the G2/M phase as compared to the control group, while miR-34b-3p/RAD51 cooverexpression restored the G2/M phase (Figure 5(d)). RAD51 protein expression was significantly inhibited by miR-34b-3p overexpression and restored by miR-34b-3p/RAD51 cooverexpression. Cell cycle arrest marker H2A.X was impacted oppositely (Figure 5(e)). miR-34b-3p enhanced the expressions of proapoptotic proteins, including Bax, Caspase-3, and p53, and inhibited the expression of antiapoptotic protein Bcl-2. miR-34b-3p/RAD51 cooverexpression partially reversed such effect of miR-34b-3p

(Figure 5(f)). These results indicated that RAD51 could serve as the potential target of miR-34b-3p and played a critical role in the HCG9/miR-34b-3p functioning axis.

3.6. HCG9 Promoted Osteosarcoma Progression while miR-34b-3p Ameliorated HCG9-Stimulated Osteosarcoma Progression In Vivo. We evaluated the role of HCG9 and miR-34b-3p in regulating osteosarcoma progression *in vivo* using a nude mouse model. As compared to the tumor control, HCG9 overexpression significantly aggregated the tumor growth, and coexpressing miR-34b-3p partially attenuated the HCG9-stimulated tumor growth, as evidenced by tumor volume and weight analysis (Figures 6(a) – 6(c)). The immunohistochemistry staining result showed excessive Ki67-positive cells in the HCG9 overexpressing group, and the HCG9/miR-34b-3p cooverexpressing group partially reduced the Ki67-positive cell number (Figure 6(d)), indicating miR-34b-3p mitigated the tumor aggressiveness stimulated by HCG9. Gene expressions of HCG9, miR-34b-3p, and RAD51 were evaluated by qRT-PCR to validate the overexpressing efficiency. HCG9 overexpression suppressed miR-

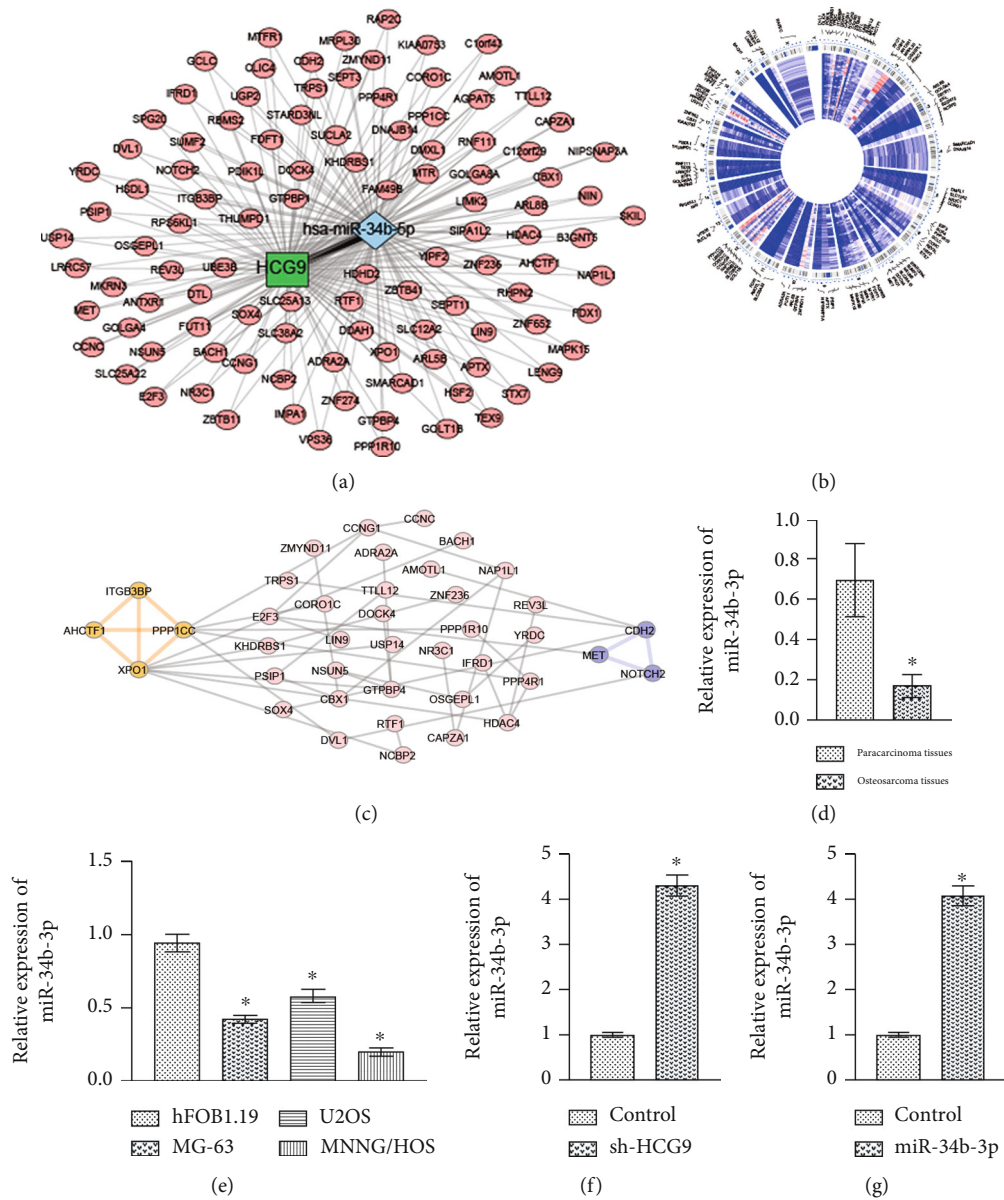


FIGURE 3: HCG9 negatively regulated miR-34b-3p. (a) starBase bioinformatic analysis predicted potential interaction between HCG9 and miR-34b-3p and mRNAs regulated by miR-34b-3p. (b) Cytoscape analysis visualized miR-34b-3p-regulated mRNA distribution in chromosomes. (c) STRING and MCODE analyses identified PPI and two different modules. (d) miR-34b-3p gene expression in osteosarcoma and paracarcinoma tissues evaluated by qRT-PCR. * $P < 0.05$ vs. the paracarcinoma tissues. (e) miR-34b-3p gene expression in osteosarcoma and osteoblast cell lines evaluated by qRT-PCR. * $P < 0.05$ vs. the hFOB1.19 group. (f) miR-34b-3p gene expressions in sh-HCG9 and control osteosarcoma cells evaluated by qRT-PCR. (g) miR-34b-3p gene expressions in miR-34b-3p and control osteosarcoma cells evaluated by qRT-PCR. $n = 6$ in each group. * $P < 0.05$ vs. the control group.

34b-3p and promoted RAD51, whereas cooverexpressing HCG9/miR-34b-3p reversed such effect (Figure 6(e)). Western blot results further confirmed that the protein expression of RAD51 was positively impacted by HCG9 overexpression and reversed by HCG9/miR-34b-3p cooverexpression. H2A.X protein expression was impacted in the opposite manner (Figure 6(f)). HCG9 overexpression induced an antiapoptotic phenotype in the tumor tissue, as it suppressed proapoptotic Bax, Caspase-3, and p53 expressions and promoted antiapoptotic Bcl-2 expression. Cooverexpressing HCG9/miR-34b-3p partially blocked antiapoptotic effect

(Figure 6(g)). The *in vivo* results confirmed that HCG9 aggravated tumor progression and miR-34b-3p reversed such effect.

4. Discussions

Distant metastases are often associated with osteosarcoma after surgery. It is reported that metastases occurred in over 85% of patients who had osteosarcoma [21], and the metastasis drastically aggravated the prognosis of osteosarcoma [22]. Recent studies have suggested that lncRNAs exhibited

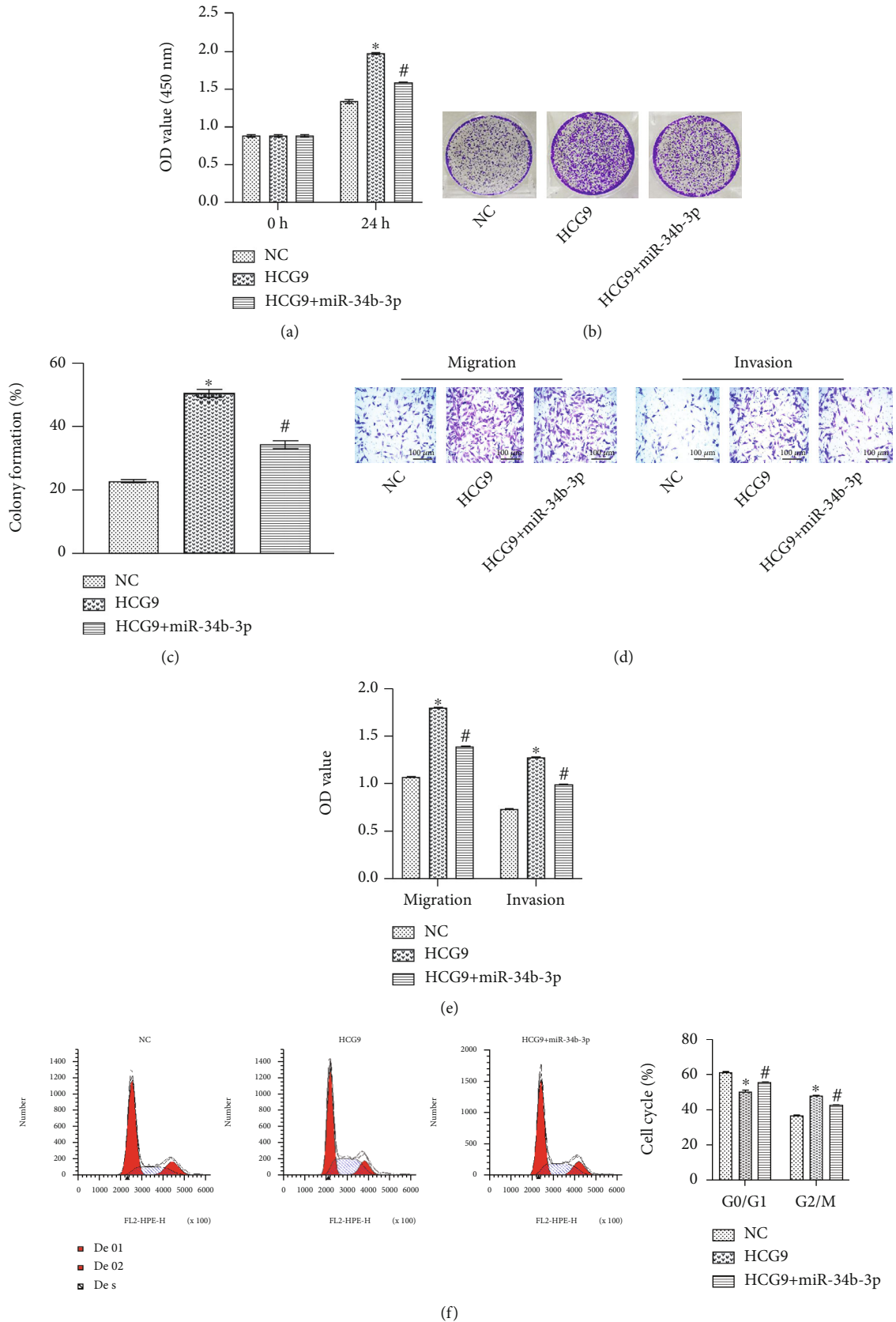


FIGURE 4: Continued.

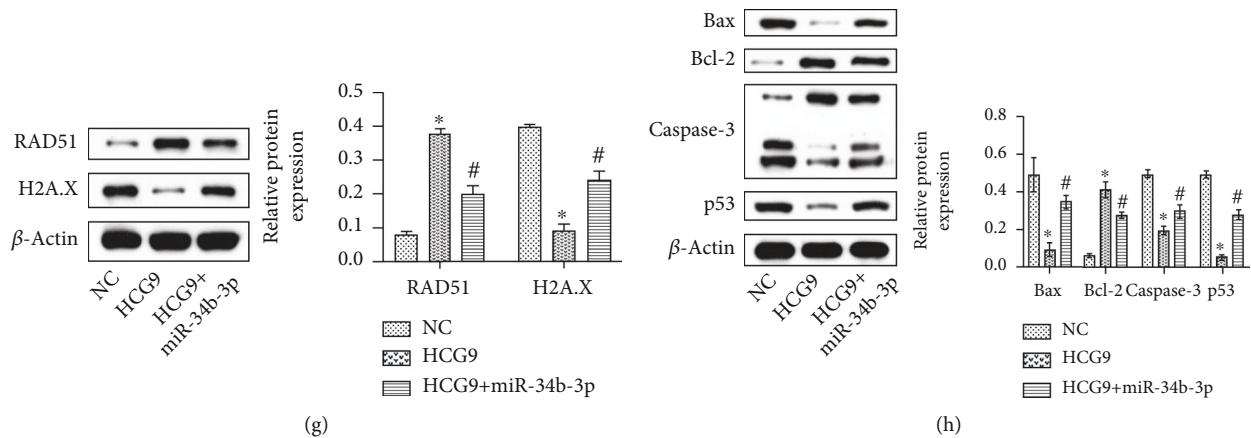


FIGURE 4: miR-34b-3p overexpression attenuated HCG9-stimulated proliferation, migration, and invasion of osteosarcoma cells. (a) CCK-8 assay of cell proliferation in the control, HCG9, and HCG9+miR-34b-3p groups. (b) Colony formation and (c) cell counts in the control, HCG9, and HCG9+miR-34b-3p groups. (d) Representative images and (e) migrated and invaded cell numbers in the control, HCG9, and HCG9+miR-34b-3p groups. (f) Cell cycle analysis of the control, HCG9, and HCG9+miR-34b-3p groups. Scale bar: 100 μ m. (g) Protein expression of RAD51 and H2A.X (h) Apoptosis-related protein expressions (Bax, Bcl-2, Caspase-3, and p53) in the control, HCG9, and HCG9+miR-34b-3p groups. $n = 6$ in each group. * $P < 0.05$ vs. the control group. # $P < 0.05$ vs. the HCG9 group.

important regulatory functions in regulating metastasis of osteosarcoma [23]. In our current study, we developed a genome-wide approach to link lncRNA HCG9 to clinicopathological features of osteosarcoma, especially metastasis. We discovered that high HCG9 was correlated with metastasis and severe cancer grades. The proliferation, migration, and invasion of osteosarcoma cells responded to the alteration of HCG9 gene expression. Using the bioinformatic technique, we established the ceRNA network of HCG9 and the targeting miRNA was determined. To our knowledge, this is the first study that reported the essential regulatory role of HCG9 and its underlying mechanism in osteosarcoma progression.

Dysregulated lncRNA gene expression was commonly found in tumor tissues. For osteosarcoma, in particular, an increasing number of studies have reported various lncRNAs expressed differently in tumor tissues and paracarcinoma tissues [9]. RNA microarray is a powerful tool to screen abnormal lncRNA expressions in tumors and paracarcinoma tissues, providing potential candidates for gene therapy [24]. Over 25,000 lncRNAs were analyzed by microarray, and thousands of osteosarcoma-associated genes were identified [25]. Among these identified lncRNAs, the role of a small number of tumor-suppressive and oncogenic lncRNAs in osteosarcoma has been elucidated. For example, MALAT1 is one of the first identified cancer-associated genes, and it is commonly studied in osteosarcoma. Wang et al. reported that lncRNA MALAT1 was highly expressed in osteosarcoma tumor tissues and promoted tumor metastasis [26]. Other oncogenic lncRNAs such as H19, HULC, SNHG12, and HOTAIR also demonstrated their regulatory functions in promoting cancer cell proliferation, inhibiting apoptosis, and aggravating tumor progression [27–30]. Herein, we screened 6 osteosarcoma-related genes by lncRNA microarray, MALAT1, HCG9, FAM99A, FAM87B, DLEU2, and C8orf49. MALAT1 and DLEU2 have been shown to promote osteosarcoma progression in previous studies [31, 32].

FAM99A, FAM87B, and C8orf49 have not been reported in osteosarcoma studies and are rarely reported in other cancers. Due to the limitation of funds and time, we did not carry out in-depth research on them. In future studies, we will further determine whether they are associated with osteosarcoma. HCG9 has been briefly reported in breast cancer and gastric cancer [33, 34] but never in osteosarcoma. By analyzing CCLE, we found that HCG9 was associated with various cancer progressions. Further bioinformatic analysis showed that high HCG9 expression was associated with osteosarcoma progression. Therefore, we finally chose HCG9 as our research object. Additional validation was conducted by comparing HCG9 expression in clinical osteosarcoma samples with paracarcinoma tissues, and abnormally elevated HCG9 expression was confirmed in tumor samples. Knockdown of HCG9 significantly suppressed osteosarcoma cell proliferation, migration, and invasion, demonstrating an oncogenic role of HCG9. To our knowledge, HCG9 was for the first time reported to be associated with osteosarcoma progression, and our results provided a new biomarker for osteosarcoma diagnosis and treatment.

One of the main functions of lncRNAs was acting as ceRNAs to regulate miRNA expressions. ceRNAs are a novel class of posttranscriptional regulators of gene expressions, which compete for the binding to miRNA/mRNA recognition elements [35]. Establishing a ceRNA network using bioinformatic techniques facilitates elucidating the possible impacts on the major signaling pathways in cancer progression. Huang et al. analyzed the differentially expressed ceRNAs associated with recurrent soft tissue sarcomas based on The Cancer Genome Atlas (TCGA) database, providing comprehensive information for improving personalized management for soft tissue sarcoma [36]. Several identified ceRNA axes in osteosarcoma were studied in detail in *in vitro* and *in vivo* animal models. For instance, Zheng et al. reported that lncRNA SNHG3 is competitively bound to miR-151a-3p to regulate RAB22A activity and mediate

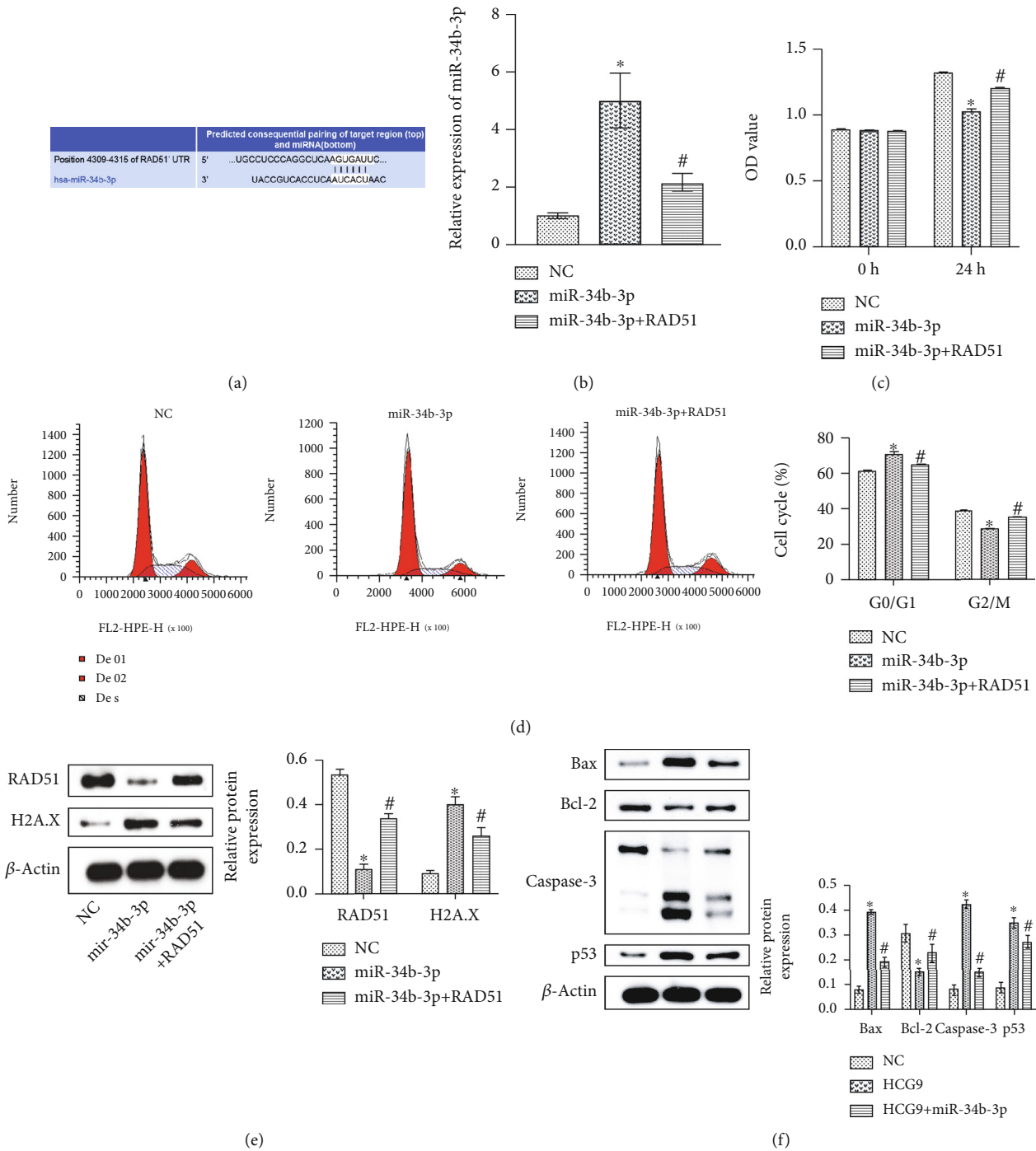


FIGURE 5: miR-34b-3p downregulated RAD51 to inhibit osteosarcoma cell proliferation. (a) Potential binding sites between miR-34b-3p and RAD51. (b) Gene expression of miR-34b-3p. (c) Cell proliferation. (d) Cell cycle analysis. (e) RAD51 and H2A.X protein expression. (f) Apoptosis-related protein expressions (Bax, Bcl-2, Caspase-3, and p53) in the control, miR-34b-3p, and miR-34b-3p+RAD51 groups. * $P < 0.05$ vs. the control group. # $P < 0.05$ vs. the miR-24b-3p group.

osteosarcoma cell invasion and migration [18]. Xie et al. found that TUG1 could potentially bind to miR-9-5p and miR-212-3p to regulate different signaling pathways in osteosarcoma progression [37, 38], revealing the details of two small pieces in the entire puzzle of the ceRNA network. In our current study, miR-34b-3p was predicted by starBase as the only potential target of HCG9. The miR-34 family is commonly downregulated in different cancers [39], includ-

ing ovarian cancer and pancreatic cancer [40, 41]. However, there has been no report of miR-34b-3p in regulating osteosarcoma progression. Herein, we established the ceRNA network that linked HCG9 with miR-34b-3p, and the signaling pathways impacted by these ncRNAs were also elucidated. The ceRNA network and pathway analysis pinpointed 4 DNA damage-related pathways involving the DNA damage checkpoint and mitotic cell cycle, indicating the

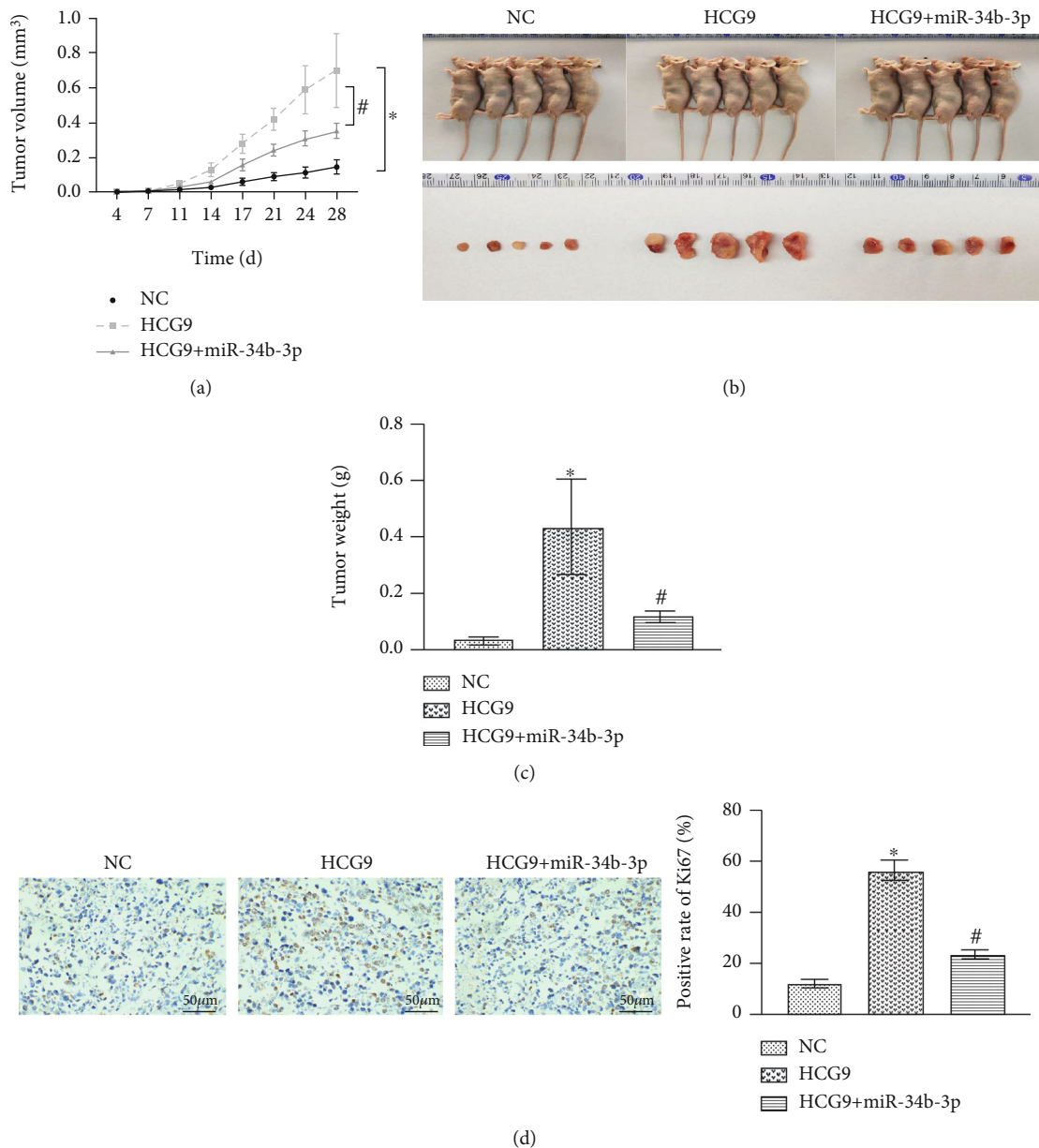


FIGURE 6: Continued.

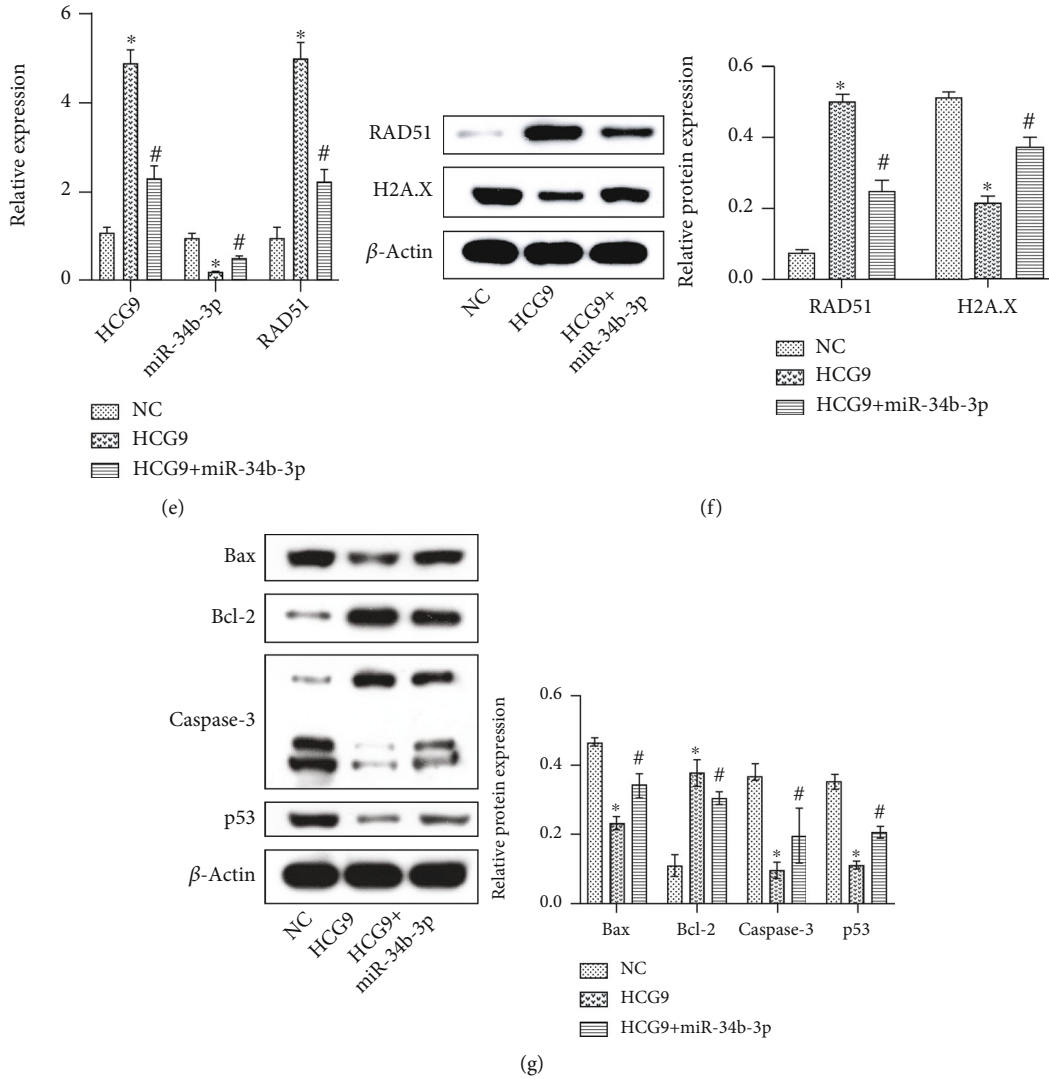


FIGURE 6: miR-34b-3p ameliorated HCG9-stimulated osteosarcoma progression *in vivo*. (a) Quantification of tumor volume. (b) Representative images of tumor growth. (c) Quantification of tumor weight in the control, HCG9, and HCG9+miR-34b-3p groups. (d) Ki67 staining of tumor tissue and the positive rate. Scale bar: 100 μ m. (e) Gene expression of HCG9, miR-34b-3p, and RAD51. (f) Protein expression of RAD51 and H2A.X. (g) Apoptosis-related protein expressions (Bax, Bcl-2, Caspase-3, and p53) in the control, HCG9, and HCG9+miR-34b-3p groups. * $P < 0.05$ vs. the control group. # $P < 0.05$ vs. the HCG9 group.

HCG9/miR-34b-3p axis played a major role in the DNA repair and cell cycle. We identified RAD51, the key enzyme that promoted mitosis, as the potential target of miR-34b-3p and found that miR-34b-3p induced cell cycle arrest by downregulating RAD51, and HCG9 negatively regulated miR-34b-3p. Therefore, positively regulated RAD51 promoted proliferation and inhibited apoptosis of osteosarcoma cells. We did not perform the dual-luciferase report experiment due to time and investigation funds. It is indeed necessary to verify the relationship between miR-34b-3p and RAD51 through the dual-luciferase report experiment. We have planned this verification in future studies.

In summary, our data demonstrated that HCG9 negatively regulated miR-34b-3p, and abnormally low expressions of miR-34b-3p in osteosarcoma tumor tissues supported our hypothesis. By overexpressing miR-34b-3p, the *in vitro* hyperproliferation, migration, and invasion, as

well as *in vivo* tumor growth stimulated by HCG9 overexpression, were mitigated, suggesting a potential protective role of miR-34b-3p in osteosarcoma progression.

5. Conclusion

HCG9 gene expression increased in osteosarcoma tissues and cell lines, and high HCG9 expression was particularly associated with osteosarcoma metastasis. miR-34b-3p served as the target of HCG9, and RAD51 was the potential target of miR-34b-3p. Overexpressing HCG9 promoted osteosarcoma cell proliferation, migration, and invasion *in vitro*, as well as aggravated tumor progression *in vivo*. Cooverexpression of miR-34b-3p and HCG9 was able to attenuate the osteosarcoma progression. Our study provided novel therapeutic targets that will assist osteosarcoma treatment in clinical practice.

Data Availability

The authors confirm that all data underlying the findings are available. All relevant data are within the paper and its supporting information files.

Ethical Approval

The animal study was reviewed and approved by the Laboratory Animal Center, the Second Xiangya Hospital of Central South University (Approval No. 2020408). The disposal of animals during the experiment conforms to the standard of “Guiding Opinions on Treating Experimental Animals” issued by the Ministry of Science and Technology in 2006. All procedures and tissue collection protocols were approved by the Institutional Review Board of the Second Xiangya Hospital.

Consent

Patients were all informed and signed written consent before surgery.

Conflicts of Interest

The authors declare that there is no conflict of interest.

Authors' Contributions

The contributions of the authors involved in this study are as follows: conception and design: Lu Wang; provision of study materials: Shuangqing Li; collection and assembly of data: Lin Qi; data analysis and interpretation: Lin Ling; manuscript writing: all authors; and final approval of manuscript: all authors. All authors have read and approved the final manuscript, and we have taken due care to ensure the integrity of the work.

Acknowledgments

We thank the Second Xiangya Hospital, Central South University, for all the support. This work was supported by the Natural Science Foundation of Hunan Province (No. 2021JJ30939).

Supplementary Materials

Supplemental Fig. 1 (A) ROC plot and (B) AUC analysis of the correlation between HCG9 gene expression and survival rates. Supplemental Fig. 2 (A) Heat map of HCG9 expression and gene expressions. Correlation between HCG9 expression and (B) age, (C) gender, (D) metastasis, (E) grade, and (F) pathology state. Supplemental Fig. 3 GO, BP, and KEGG analyses of the enrichment of mRNAs regulated by the HCG9/miR-34b-3p axis in signaling pathways. (*Supplementary Materials*)

References

- [1] G. Ottaviani and N. Jaffe, “The epidemiology of osteosarcoma,” *Cancer Treatment and Research*, vol. 152, pp. 3–13, 2009.
- [2] W. Zhou, M. Hao, X. Du, K. Chen, G. Wang, and J. Yang, “Advances in targeted therapy for osteosarcoma,” *Discovery medicine*, vol. 17, no. 96, pp. 301–307, 2014.
- [3] M. L. Tan, P. F. Choong, and C. R. Dass, “Osteosarcoma—conventional treatment vs. gene therapy,” *Cancer biology & therapy*, vol. 8, no. 2, pp. 106–117, 2009.
- [4] K. Zhao, S. Y. Yang, J. Geng et al., “Combination of anginex gene therapy and radiation decelerates the growth and pulmonary metastasis of human osteosarcoma xenografts,” *Cancer medicine*, vol. 7, no. 6, pp. 2518–2529, 2018.
- [5] J. X. Yang, R. H. Rastetter, and D. Wilhelm, “Non-coding RNAs: an introduction,” *Advances in Experimental Medicine and Biology*, vol. 886, pp. 13–32, 2016.
- [6] Z. Liu, H. Y. Yan, S. Y. Xia, C. Zhang, and Y. C. Xiu, “Down-regulation of long non-coding RNA TRIM52-AS1 functions as a tumor suppressor in renal cell carcinoma,” *Molecular Medicine Reports*, vol. 13, no. 4, pp. 3206–3212, 2016.
- [7] Y. Zhang, P. Zhang, X. Wan et al., “Downregulation of long non-coding RNA HCG11 predicts a poor prognosis in prostate cancer,” *Biomedicine & Pharmacotherapy*, vol. 83, pp. 936–941, 2016.
- [8] J. Dai, L. J. Xu, G. D. Han et al., “Down-regulation of long non-coding RNA ITGB2-AS1 inhibits osteosarcoma proliferation and metastasis by repressing Wnt/ β -catenin signaling and predicts favourable prognosis,” *Artificial cells, nanomedicine, and biotechnology*, vol. 46, supplement 3, pp. S783–S790, 2018.
- [9] J. P. Li, L.-h. Liu, J. Li et al., “Microarray expression profile of long noncoding RNAs in human osteosarcoma,” *Biochemical and biophysical research communications*, vol. 433, no. 2, pp. 200–206, 2013.
- [10] K. Gao and D. Lian, “Long non-coding RNA MALAT1 is an independent prognostic factor of osteosarcoma,” *European Review for Medical and Pharmacological Sciences*, vol. 20, no. 17, pp. 3561–3565, 2016.
- [11] T. He, D. Xu, T. Sui, J. Zhu, Z. Wei, and Y. Wang, “Association between H19 polymorphisms and osteosarcoma risk,” *European Review for Medical and Pharmacological Sciences*, vol. 21, no. 17, pp. 3775–3780, 2017.
- [12] L. Qi, T. Zhang, Y. Yao et al., “Identification of lncRNAs associated with lung squamous cell carcinoma prognosis in the competitive endogenous RNA network,” *PeerJ*, vol. 7, article e7727, 2019.
- [13] M. L. Chua, J. T. Wee, E. P. Hui, and A. T. Chan, “Nasopharyngeal carcinoma,” *The Lancet*, vol. 387, no. 10022, pp. 1012–1024, 2016.
- [14] G. Hu, F. Niu, B. A. Humburg et al., “Molecular mechanisms of long noncoding RNAs and their role in disease pathogenesis,” *Oncotarget*, vol. 9, no. 26, pp. 18648–18663, 2018.
- [15] L. Salmena, L. Poliseno, Y. Tay, L. Kats, and P. P. Pandolfi, “A *_*ceRNA hypothesis: the Rosetta Stone of a hidden RNA language?,” *Cell*, vol. 146, no. 3, pp. 353–358, 2011.
- [16] L. Wang, K. B. Cho, Y. Li, G. Tao, Z. Xie, and B. Guo, “Long noncoding RNA (lncRNA)-mediated competing endogenous RNA networks provide novel potential biomarkers and therapeutic targets for colorectal cancer,” *International Journal of Molecular Sciences*, vol. 20, no. 22, p. 5758, 2019.
- [17] R. Pan, Z. He, W. Ruan et al., “lncRNA FBXL19-AS1 regulates osteosarcoma cell proliferation, migration and invasion by sponging miR-346,” *OncoTargets and therapy*, vol. Volume 11, pp. 8409–8420, 2018.

- [18] S. Zheng, F. Jiang, D. Ge et al., “LncRNA SNHG3/miRNA-151a-3p/RAB22A axis regulates invasion and migration of osteosarcoma,” *Biomedicine & Pharmacotherapy*, vol. 112, p. 108695, 2019.
- [19] L. Pan, M. E. Lemieux, T. Thomas et al., “IER5, a DNA damage response gene, is required for Notch-mediated induction of squamous cell differentiation,” *eLife*, vol. 9, 2020.
- [20] M. Medová, D. M. Aebersold, and Y. Zimmer, “The molecular crosstalk between the MET receptor tyrosine kinase and the DNA damage response—biological and clinical aspects,” *Cancers*, vol. 6, no. 1, pp. 1–27, 2014.
- [21] Z. Yang, X. Li, Y. Yang, Z. He, X. Qu, and Y. Zhang, “Long noncoding RNAs in the progression, metastasis, and prognosis of osteosarcoma,” *Cell death & disease*, vol. 7, no. 9, pp. e2389–e2389, 2016.
- [22] X. Huang, J. Zhao, J. Bai et al., “Risk and clinicopathological features of osteosarcoma metastasis to the lung: a population-based study,” *Journal of bone oncology*, vol. 16, p. 100230, 2019.
- [23] Z. Li, X. Yu, and J. Shen, “Long non-coding RNAs: emerging players in osteosarcoma,” *Tumor Biology*, vol. 37, no. 3, pp. 2811–2816, 2016.
- [24] K. Zhang, H. Shi, H. Xi et al., “Genome-wide lncRNA microarray profiling identifies novel circulating lncRNAs for detection of gastric cancer,” *Theranostics*, vol. 7, no. 1, pp. 213–227, 2017.
- [25] R. Chen, G. Wang, Y. Zheng, Y. Hua, and Z. Cai, “Long non-coding RNAs in osteosarcoma,” *Oncotarget*, vol. 8, no. 12, pp. 20462–20475, 2017.
- [26] Y. Wang, Y. Zhang, T. Yang et al., “Long non-coding RNA MALAT1 for promoting metastasis and proliferation by acting as a ceRNA of miR-144-3p in osteosarcoma cells,” *Oncotarget*, vol. 8, no. 35, pp. 59417–59434, 2017.
- [27] P. He, Z. Zhang, G. Huang et al., “miR-141 modulates osteoblastic cell proliferation by regulating the target gene of lncRNA H19 and lncRNA H19-derived miR-675,” *American journal of translational research*, vol. 8, no. 4, pp. 1780–1788, 2016.
- [28] V. R. M. Uzan, A. H. Lengert, É. Boldrini et al., “High expression of HULC is associated with poor prognosis in osteosarcoma patients,” *PloS one*, vol. 11, no. 6, p. e0156774, 2016.
- [29] W. Ruan, P. Wang, S. Feng, Y. Xue, and Y. Li, “Long non-coding RNA small nucleolar RNA host gene 12 (SNHG12) promotes cell proliferation and migration by upregulating angiomin gene expression in human osteosarcoma cells,” *Tumor Biology*, vol. 37, no. 3, pp. 4065–4073, 2016.
- [30] B. Wang, Y. Su, Q. Yang et al., “Overexpression of long non-coding RNA HOTAIR promotes tumor growth and metastasis in human osteosarcoma,” *Molecules and Cells*, vol. 38, no. 5, pp. 432–440, 2015.
- [31] D. Ren, H. Zheng, S. Fei, and J. L. Zhao, “MALAT1 induces osteosarcoma progression by targeting miR-206/CDK9 axis,” *Journal of Cellular Physiology*, vol. 234, no. 1, pp. 950–957, 2018.
- [32] W. Liu, P. C. Liu, K. Ma, Y. Y. Wang, Q. B. Chi, and M. Yan, “LncRNA DLEU2 promotes tumour growth by sponging miR-337-3p in human osteosarcoma,” *Cell Biochemistry and Function*, vol. 38, no. 7, pp. 886–894, 2020.
- [33] C. Seidl, M. Port, C. Apostolidis et al., “Differential gene expression triggered by highly cytotoxic α -emitter-immunoconjugates in gastric cancer cells,” *Investigational new drugs*, vol. 28, no. 1, pp. 49–60, 2010.
- [34] H. Chang, H.-C. Jeung, J. J. Jung, T. S. Kim, S. Y. Rha, and H. C. Chung, “Identification of genes associated with chemosensitivity to SAHA/taxane combination treatment in taxane-resistant breast cancer cells,” *Breast cancer research and treatment*, vol. 125, no. 1, pp. 55–63, 2011.
- [35] L. Polisenio and P. P. Pandolfi, “PTEN ceRNA networks in human cancer,” *Methods*, vol. 77, pp. 41–50, 2015.
- [36] R. Huang, T. Meng, R. Chen et al., “The construction and analysis of tumor-infiltrating immune cell and ceRNA networks in recurrent soft tissue sarcoma,” *Aging*, vol. 11, no. 22, pp. 10116–10143, 2019.
- [37] C.-H. Xie, Y.-M. Cao, Y. Huang et al., “Long non-coding RNA TUG1 contributes to tumorigenesis of human osteosarcoma by sponging miR-9-5p and regulating POU2F1 expression,” *Tumor Biology*, vol. 37, no. 11, pp. 15031–15041, 2016.
- [38] C. Xie, B. Chen, B. Wu, J. Guo, and Y. Cao, “LncRNA TUG1 promotes cell proliferation and suppresses apoptosis in osteosarcoma by regulating miR-212-3p/FOXA1 axis,” *Biomedicine & Pharmacotherapy*, vol. 97, pp. 1645–1653, 2018.
- [39] H. Hermeking, “The _miR-34_ family in cancer and apoptosis,” *Cell Death & Differentiation*, vol. 17, no. 2, pp. 193–199, 2010.
- [40] D. C. Corney, C.-I. Hwang, A. Matoso et al., “Frequent down-regulation of miR-34 family in human ovarian cancers,” *Clinical Cancer Research*, vol. 16, no. 4, pp. 1119–1128, 2010.
- [41] Q. Ji, X. Hao, M. Zhang et al., “MicroRNA miR-34 inhibits human pancreatic cancer tumor-initiating cells,” *PLoS One*, vol. 4, no. 8, article e6816, 2009.

Research Article

lncRNA PAPPAS1 Induces the Development of Hypertrophic Scar by Upregulating TLR4 through Interacting with TAF15

Pengju Fan , Yongjie Wang, Jingjing Li, and Man Fang

Department of Burn and Plastic, Xiangya Hospital, Central South University, Changsha, Hunan 410008, China

Correspondence should be addressed to Pengju Fan; fanpj2005@126.com

Received 7 April 2021; Revised 20 May 2021; Accepted 5 June 2021; Published 5 July 2021

Academic Editor: Yaoyao Xia

Copyright © 2021 Pengju Fan et al. This is an open access article distributed under the Creative Commons Attribution License, which permits unrestricted use, distribution, and reproduction in any medium, provided the original work is properly cited.

Hypertrophic scar (HTS) is a complicated pathological process induced mainly by burns and wounds, with abnormal proliferation of fibroblasts and the transformation of fibroblasts to myofibroblasts. PAPPAS1, a differentially expressed long noncoding RNA (lncRNA) in the HTS tissues, attracted our interests in its potential role and mechanism in the development and process of HTS. In the present study, the regulatory effect of lncRNA PAPPAS1 on the Toll-like receptor 4 (TLR4) signal pathway, as well as the molecular mechanism, was investigated. Bioinformatics analysis was utilized to screen the differentially expressed lncRNAs in HTS tissues. PAPPAS1 was significantly upregulated in both HTS tissues and hypertrophic scar fibroblast (HTsFb) cells. The expression levels of TLR4, MyD88, TGF- β 1, collagen I, collagen III, and α -SMA were greatly elevated in HTsFb cells. By knocking down PAPPAS1, the proliferation of HTsFb cells, TLR4, and TGF- β 1 signal pathway and the expression of fibrosis markers both in HTsFb cells and HTS tissues were suppressed. It was accompanied by the alleviated pathological state in the HTS tissues, which were significantly reversed by cotransfecting with the pcDNA3.1-TLR4 vector. Positive correlation and interaction were observed between PAPPAS1 and TAF15 and between TAF15 and the promoter of TLR4, respectively. In conclusion, lncRNA PAPPAS1 might induce the development of HTS by upregulating TLR4 through interacting with TAF15.

1. Introduction

Hypertrophic scar (HTS) is the complication of burns or wounds, which is mainly clinically characterized with local redness, itchy pain, hyperplasia becoming hard, local contracture, articular dyskinesia, and even repeated rupturing or cancerization [1, 2]. Not only the normal physiological function and appearance but also the psychology of the patients are significantly influenced by HTS, which contributes to the impaired social interaction and is generally considered as a public health issue. The pathological characteristics of HTS are the abnormal proliferation of fibroblasts, the transformation of fibroblasts to myofibroblasts, and the excessive accumulation of the extracellular matrix (ECM) [3, 4]. Although multiple hypotheses have been proposed to claim the pathogenesis of HTS, the pathological mechanism of HTS still remains unknown. It is of great significance to explore the possible molecular mechanism underlying HTS for the clinical treatment of HTS.

Epigenetics is a biological research method investigating the changes in phenotype that are not rooted in DNA sequence, including the DNA methylation, histone modification, chromatin remodeling, and noncoding RNA [5]. lncRNAs are noncoding RNAs greater than 200 nucleotides in length, which are originally regarded as the “noise” in the genome transcription without biological functions. However, in recent years, lncRNAs are reported to be involved in multiple cellular biological processes, such as epigenetic, transcriptional, and posttranscriptional regulation of gene expression, the silence of X chromosome, the activation of transcription, and nuclear transmission [6–8]. Accumulative evidences suggested the significant function of lncRNA in the process and development of HTS and fibrosis [9–11]. In our preliminary experiment, we found that lncRNA PAPPAS1 was differentially expressed in the HTS tissues and normal skin tissues based on the bioinformatics analysis. lncRNA PAPPAS1 is a rarely studied lncRNA which was only discussed in adenovirus infection [12], placenta precreta [13],

and osteoporosis [14], with very limited information in its properties. It attracted our interest in its potential role and mechanism in the development and process of HTS.

Toll-like receptors (TLRs) are a couple of transmembrane proteins located on the cytomembrane, which recognize the conservative pathogen-associated molecular patterns (PAMPs). It includes lipopolysaccharide (LPS), bacterial lipoprotein, CpG DNA, virus double-strain RNA, hyaluronic acid, heat shock protein (HSPs), and S100 protein [15]. Multiple internal and external substances, such as taxol, fibulin, hyaluronic acid, oligosaccharide, HSP60, HSP70, fibrinogen, and High-mobility group box 1 (HMGB1), can be recognized by TLR4, making TLR4 a promising target in the field of antiviral, antibacterial, and tissue repairment [16–18]. Seki reported that the fake receptor of transforming growth factor- β (TGF- β), bone morphogenetic protein, and activin membrane-bound inhibitor (BAMBI) could be downregulated by stimulating the TLR4 on the membrane of hepatic stellate cells, which further activates the TGF- β 1 signal pathway and contributes to the liver fibrosis [19].

In the injured skin tissues and lung tissues of scleroderma patients, the abnormal expression of TLR4 activated the Smad signal pathway in the fibroblasts, enhanced the sensitivity of fibroblasts to TGF- β 1, accelerated the synthesis of collagens, and regulated the expression of several genes involved in the tissue remodeling and extracellular matrix homeostasis [20]. Recently, it was reported that the expression level of TLR4 was relatively higher in the HTS tissues than in the normal skin tissues [21]. The development and process of HTS could be accelerated by activating TLR4 through upregulating TGF- β 1, connective tissue growth factor, collagen I, and collagen III [22–24], which was consistent with the data achieved in our previous researches [25, 26]. However, the upstream mechanism of TLR4 in the pathogenesis of HTS still remains unknown.

In our preliminary experiments, we found that PAPPAS1 could bind with TLR4 in the HTS tissues, which further encouraged us to explore the roles and effect of PAPPAS1 and its possible target of TLR4 in the development of HTS. In the present study, the differentially expressed lncRNA in the HTS tissues and normal skin tissues will be screened and the potential biological function of PAPPAS1 in the development and process of HTS will be explored by investigating the correlation between PAPPAS1 and TLR4.

2. Materials and Methods

2.1. Bioinformatics Analysis on the HTS Tissues and Normal Skin Tissues. The data of lncRNA and mRNA expression was obtained from the Gene Expression Omnibus (GEO) database repository, the publicly available genomics database from the National Center for Biotechnology Information (NCBI). Dataset GSE151153 has 3 HTS samples and 3 normal samples. Dataset GSE158155 has 24 HTS samples and 4 normal samples. Dataset GSE151153 and dataset GSE158155 were standardized by the RMA algorithm using the limma package in the R computing environment, respectively. Next, differential analysis ($|\log_{2}FC| > 2$, adjusted p value < 0.05) were identified severally. The volcano map was

displayed. The correlation analysis on coexpression patterns of differentially expressed lncRNA and mRNA was performed by the pheatmap package, and a heat map was drawn. Gene Ontology (Go) and Kyoto Encyclopedia of Genes and Genomes (KEGG) enrichment analyses were performed on the differentially expressed mRNA of GSE158155 using the function of clusterProfiler in R, and the significant pathways were shown, respectively (adjusted p value < 0.05).

2.2. Animals, Cells, and Treatments. 48 BALB/c nude mice (6 weeks old, 20–23 g each) were randomly divided into 6 groups, half male and half female in each group. Mice were purchased from Beijing Vital River Laboratory Animal Technology Co. Ltd. The environmental temperature was maintained at 24–26°C, and the relative humidity was maintained at 50%–60%. All mice were freely ingested water and food. Normal human skin fibroblasts (NsFb) were obtained from Wuhan University Cell Bank, and human HTsFb cells were purchased from Shanghai Bailey Biotechnology Co. Ltd. They were incubated in the completed DMEM medium containing 10% fetal bovine serum (FBS) at 37°C with 5% CO₂.

2.3. Transfection. The HTsFb cells were collected and incubated in 6-well plates. Short hairpin RNAs (shRNAs) against lncRNA PAPPAS1 (sh-PAPPAS1#1 and sh-PAPPAS1#2) were utilized to reduce the PAPPAS1. The corresponding negative control was sh-NC (sh-NC). The expression level of lncRNA PAPPAS1 was promoted by transfecting with the pcDNA3.1-PAPPAS1 vector. PcDNA3.1-NC was used as negative control. And TLR4 was upregulated by transfecting with the pcDNA3.1-TLR4 vector (2.5 μ g). The negative control of the two overexpression plasmids was pcDNA3.1-NC. TAF15 was downregulated by transfecting with sh-TAF15 and upregulated by transfecting with over-TAF15. Their negative controls were sh-NC and over-NC, respectively. All the vectors (2.5 μ g) were transfected into the HTsFb cells accompanied with lipofectamine 3000 (5 μ L, Invitrogen, CA, USA), followed by being harvested at 37°C with 5% CO₂ after 48 hours of incubation. All the plasmids were synthesized by HonorGene (Changsha, China).

2.4. Lentiviral Transfection. Sh-NC, sh-PAPPAS1#1, sh-PAPPAS1#2, pcDNA3.1-NC, and pcDNA3.1-TLR4 were inserted into lentiviral vector pLVX-IRES-tdTomato. The constructed plasmid and packaging plasmid were cotransfected into HTsFb cells. The virus particles were harvested by ultracentrifugation 48 hours after transfection. Finally, the prepared virus particles were injected into the mice.

2.5. Quantitative Real-Time PCR (qRT-PCR). At the end of the experiment, cells and tissues of different treatment groups were collected to extract total RNA by TRIzol reagent (Thermo Fisher, no. 15596026). Subsequently, 2 μ L of total RNA with a HiFiScript cDNA Synthesis Kit (CWbiotech, no. CW2569) was used to synthesize cDNA. The primers for PAPPAS1, GAPDH, U6, TAF15, TLR4, and β -actin were designed by using Primer5 software after searching

TABLE 1: Primers for genes involved in qRT-PCR.

Gene	Primer
PAPPA-AS1 RT	Forward 5'-AGCCTCTTTGCCTAATATCCTT-3' Reverse 5'-GCCACAGAAGAACCTTACCAG-3'
GAPDH RT	Forward 5'-ACAGCCTCAAGATCATCAGC-3' Reverse 5'-GGTCATGAGTCCTTCCACGAT-3'
U6 RT	Forward 5'-CTCGCTTCGGCAGCACA-3' Reverse 5'-AACGCTTACGAATTTGCGT-3'
TAF15 RT	Forward 5'-ACAAGGACACAGGAAAGCCAAA-3' Reverse 5'-AATTCAGGTCTTCTAGTGGCAA-3'
TLR4 RT	Forward 5'-AGACACTTTATTTCAGAGCCGTTG-3' Reverse 5'-AAGGCGATACAATTCCACC-3'
β -Actin RT	Forward 5'-ACCCTGAAGTACCCCATCGAG-3' Reverse 5'-AGCACAGCCTGGATAGCAAC-3'

the target gene mRNA sequences on NCBI. The primers for qRT-PCR were listed in Table 1:

We used UltraSYBR Mixture (CWbiotech, no. CW2601) for qRT-PCR, according to the manufacturer's instructions, at 95°C for 10 minutes and the 40 cycles at 95°C for 15 seconds and 60°C for 30 seconds. $2^{-\Delta\Delta Ct}$ method was used to compare the relative expression of genes.

2.6. Western Blotting Assay. Cells were collected and lysed in RIPA lysis buffer (Cell Signaling Technology, Boston, USA). 15% SDS-PAGE was used to segregate the proteins. Subsequently, the isolated proteins were transfer to the PVDF membranes (Cell Signaling Technology, Boston, USA) by semidry transfer. 5–10% BSA solution was added and hatched for 1–2 h. Then, the membranes were incubated with primary antibody against TLR4, MyD88, collagen I, collagen III, TGF- β , α -SMA, or β -actin (1 : 1,000, Abcam, Massachusetts, USA) at 25°C for 2 h. After being washed over, horseradish peroxidase-conjugated secondary antibody (1 : 3,000, Abcam, Massachusetts, USA) was used to incubate with the membranes at 25°C. One to two hours later, blots were incubated with the ECL reagents (Amersham, UK) and exposed under Amersham Imager 600 (GE).

2.7. Subcellular Fractionation Assay. We extracted and purified cytoplasmic and nuclear RNAs of the cells through PARIS™ Kit (Invitrogen) according to the manufacturer's instructions. PCR was used to detect RNA content in cytoplasm and nucleus. U6 was used as a nuclear RNA marker and GAPDH as a soluble cytoplasmic marker. The CT value refers to the number of cycles when the fluorescence signal in each reaction tube reaches the set threshold. We used the Ct value to measure the content of PAPPA-AS1; the higher the Ct value, the lower the content of PAPPA-AS1.

2.8. Fluorescence In Situ Hybridization (FISH) Assay. FISH assay was used to detect the localization of PAPPA-AS1 in cells as previously described [27]. PBS was used to wash the

cells grown on the slides. 4% paraformaldehyde was used to fix the slides. The images were captured by a confocal microscope.

2.9. The Establishment of the HTS Model in Nude Mice. HTS tissues were obtained from clinical HTS patients at least 6 months since the initial injury. Excrescent subcutaneous fat was removed from the human HTS tissues, followed by being cut into 2.0 cm \times 1.5 cm slides. The nude mice were made to inhale with 3% isoflurane (tsbiochem, no. T19651) for anesthesia via a nose cone, and a 2.0 cm \times 1.5 cm incision on the back of the mouse was clipped out, followed by transplanting the human HTS tissues onto the wounding part and being wrapped. Suture was taken out 15 days postsurgery and the mice with necrotic HTS tissues were excluded from the experiments. All mice were killed by intravenous injection of 150 mg/kg barbiturate. Death was determined by observing the heartbeat and breathing. This experiment has been approved by Xiangya Hospital of Central South University animal experiment ethics committee (no. 2019sydw0009) and Xiangya Hospital of Central South University medical ethics committee (no. 202004121).

2.10. Immunofluorescence (IF) Staining. Briefly, after modeling, mice were perfused with cold PBS and then injected with 4% formalin for 24 hours. The isolated HTS tissues were soaked with 4% formalin at 4°C, followed by dehydrating for 7 days using 30% sucrose. Subsequently, the tissues were mounted in OCT and kept in the fridge. 4% paraformaldehyde was used to fix the cells grown on the slides. Primary antibodies rabbit anti-collagen I, anti-collagen III, or anti- α -SMA (1 : 200) were used to incubated with the cells or slices prepared by cryosections at a 10 μ m thickness. The secondary antibodies conjugated with FITC and DAPI (nuclear marker, color blue) were then incubated for fluorescence staining. The pictures were taken with a fluorescence microscope.

2.11. H&E Staining. HTS tissues were isolated from the wounding site of each animal, followed by being washed over by PBS for several hours. After being dehydrated with 70%, 80%, and 90% ethanol solution successively, the tissues were incubated with equal quality of ethanol and xylene. Following being incubated for 15 min, equal quality of xylene was used to mix with the tissues for 15 min. The step was repeated until the tissue looked transparent. Then, the samples were embedded in paraffin, sectioned, and stained with hematoxylin and eosin. The images were caught by an inverted microscope (Olympus, Tokyo, Japan).

2.12. Cell Viability Assay. The cell viability was determined by the MTT assay. The cells were collected and incubated in the 96-well plates containing DMEM medium for 24 hours, followed by changing the medium with newly prepared medium containing MTT solution to be incubated for 2 hours at 37°C. Following removing the medium, the MTT solution was dissolved by DMSO at 37°C for 15 min; the absorbance of which was detected at 490 nm according to the protocol described previously [28]. The OD values of each group were recorded to evaluate the cell viability of each group.

2.13. Chromatin Immunoprecipitation (ChIP) Assays. The correlation between TAF15 and the promoter region of TLR4 was evaluated by ChIP assay using an EZMagna ChIP kit (Millipore, Billerica, USA). Briefly, the cells were incubated with 1% formaldehyde for 10 min, followed by being terminated with 125 nM glycine. Subsequently, the DNA fragments were extracted from the collected cells at a length between 200 and 1000 bp, followed by being incubated with the specific antibodies at 4°C overnight. Then, DNA enrichment was achieved by adding the Dynabeads Protein G (Thermo Fisher Scientific, Waltham, USA) and incubated for 2 hours. QRT-PCR was used to detect the precipitated DNA and IgG was taken as a negative control in the system.

2.14. RNA Pull-Down Assay. The cells were lysed with buffer containing Tris-HCl, EDTA, NaCl, NP-40, protease inhibitor, phosphatase inhibitor, and RNase inhibitor. Followed by centrifugation, the supernatant was collected. A Biotin RNA Labeling Mix kit (Roche, Rotkreuz, Switzerland) was used to biotinylate the extracted RNA, which was then transcribed in vitro. Subsequently, the DNase I (Thermo Fisher Scientific, Waltham, USA) and Sephadex G-50 Quick Spin Columns (Sigma, Missouri, USA) were used to mix with the labeled RNA, which was incubated with the cell supernatant at 4°C for 2 hours. Subsequently, the mixture was incubated with Dynabeads™ MyOne™ Streptavidin T1 (Invitrogen, California, USA) at 4°C for 1 hour. Following being washed over, the SDS-PAGE and Coomassie blue staining were used to detect the proteins with lncRNA PAPPAS1. The protein bands were evaluated by the LC-MS/MS mass spectrometry.

2.15. Luciferase Reporter Assay. The suspected binding sites of TAF15 in the TLR4 promoter region was cloned into the firefly luciferase in the pGL3 vector (Invitrogen, California, USA). The HTsFb cells were transfected with the plasmids

and the TAF15 expressed vector (TAF15 construct) or the negative control (empty vector), which were coinoculated with the lipofectamine 3000 (Invitrogen, California, USA) according to the protocol of the manufacturer. Following incubating for 48 hours, the relative luciferase activity was evaluated by the dual-luciferase reporter assay system (Promega, Madison, WI).

2.16. RNA Immunoprecipitation (RIP) Assay. The correlation between TLR4 and TAF15 was verified using the EZMagna RIP Kit (Millipore, Massachusetts, USA) according to the manufacturer's instructions. Briefly, the HTsFb cells were lysed with RIP lysis buffer at 4°C half an hour, followed by being incubated with RIP buffer containing magnetic beads, which were conjugated to the antibodies against Ago2 (CST, Boston, USA) or anti-rabbit IgG (negative control, CST, Boston, USA). The precipitated RNAs were analyzed by the RT-qPCR technology and the total RNA was taken as input controls.

2.17. Statistical Analysis. All the data in the present study were shown as mean ± SD. GraphPad Prism 8 was used for data analysis. Student's *t*-test was used between the two groups conforming to the normal distribution. Comparisons among multiple groups were conducted by one-way analysis of variance (ANOVA), followed by Tukey's post hoc test. *p* < 0.05 was considered statistically significant.

3. Results

3.1. lncRNA PAPPAS1 Was Screened through Bioinformatics Analysis. The GEO dataset was used to screen differentially expressed lncRNA and mRNA in the clinical HTS tissues and the normal skin tissues. As shown in Figure 1(a), lncRNA PAPPAS1 was upregulated overtly in the HTS tissues compared with in the normal skin tissues (logFC = 4.46, *p* value < 0.05). Approximately 464 mRNAs were screened out (Figure 1(b)). Among them, 385 and 79 mRNAs were remarkably downregulated and upregulated, respectively, in contrast to the normal skin tissues. In particular, the expression of TLR4, MyD88, and TGF was all significantly upregulated and the multiples of expression difference were 3.26, 2.39, and 2.87 (*p* value < 0.05). The correlation of top 30 upregulated lncRNAs and related mRNA was shown in Figure 1(c). Among them, the expression of lncRNA PAPPAS1 was significantly correlated with TLR4, MyD88, and TGF and the expression correlation was greater than 0.5. We selected the evidently upregulated mRNAs for functional enrichment analysis. The results of Go enrichment analysis showed that the mRNAs played important roles in various biological processes, including the secondary metabolite biosynthetic process, melanin biosynthetic process, melanin metabolic process, extracellular matrix, collagen-containing extracellular matrix, melanosome membrane, extracellular matrix structural constituent, extracellular matrix structural constituent conferring tensile strength, and heparin binding (Figure 1(d)). The results of KEGG analysis suggested the mRNAs were mainly associated with the PI3K-Akt

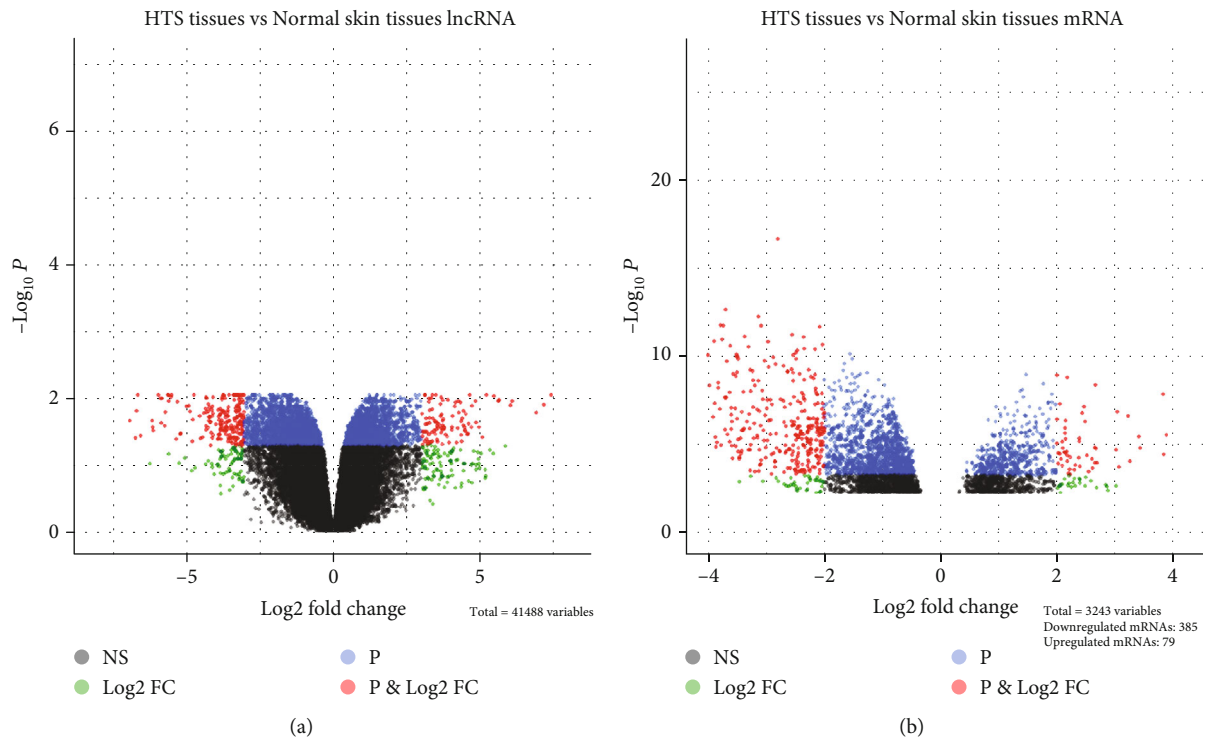
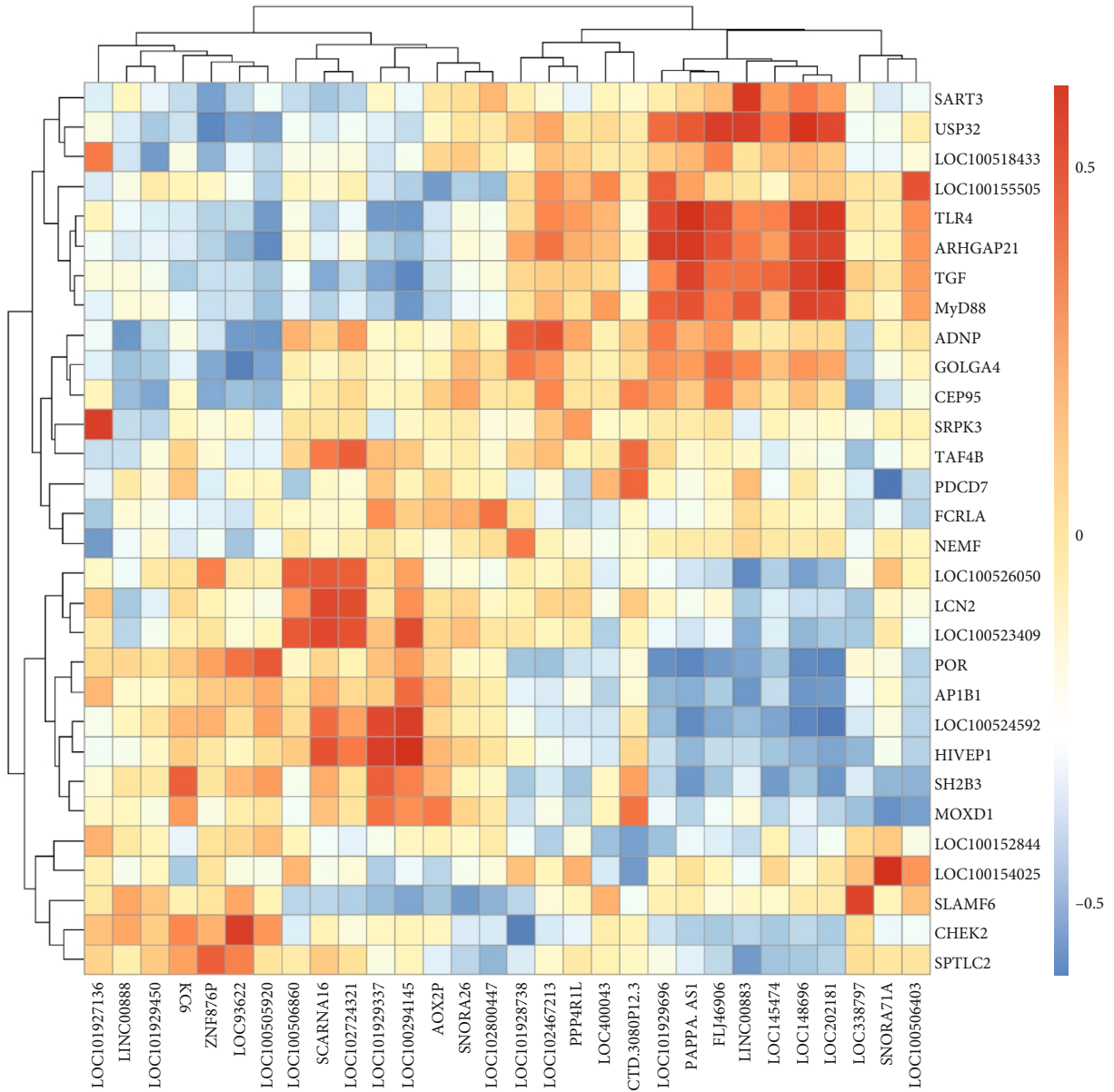
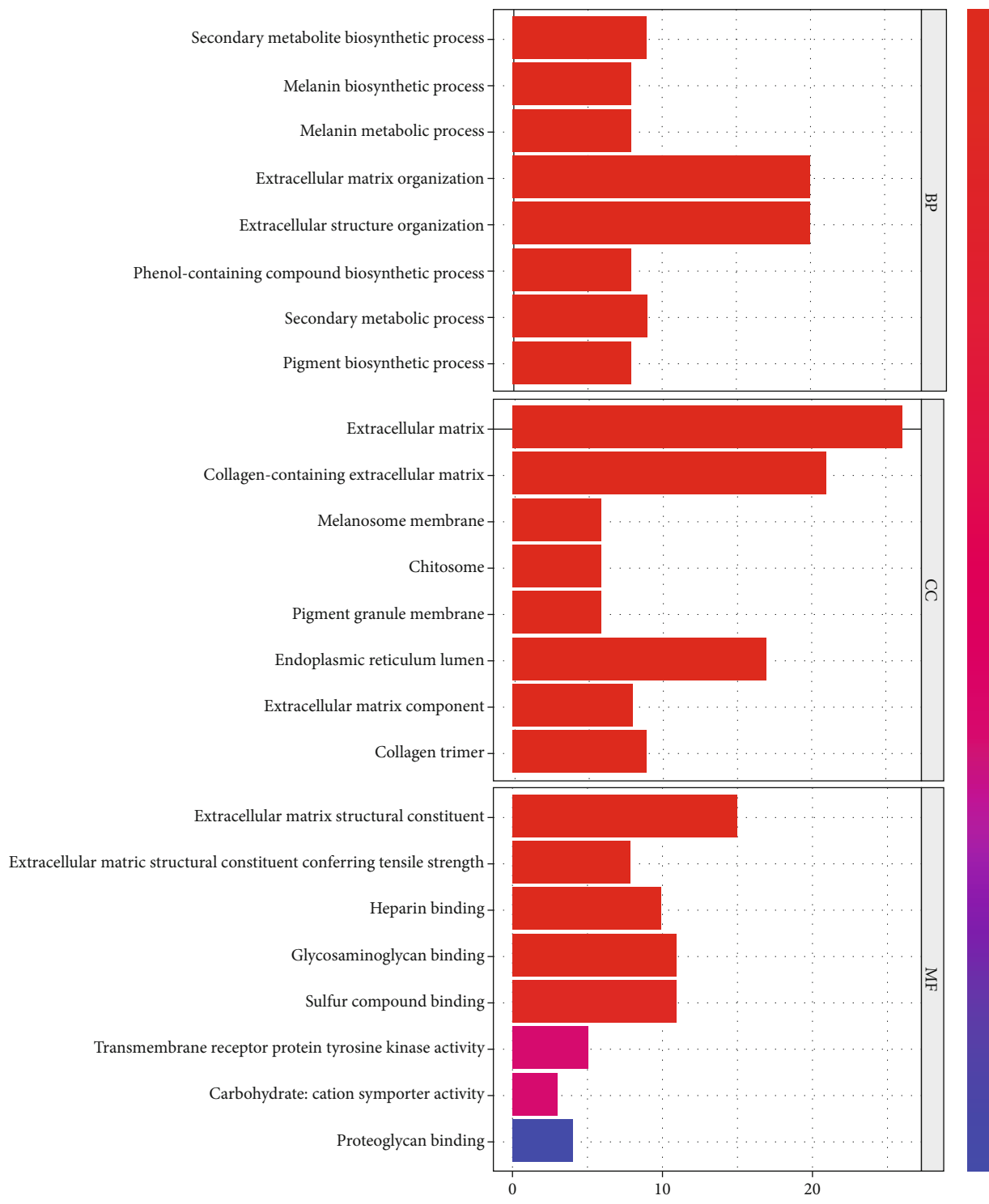


FIGURE 1: Continued.



(c)

FIGURE 1: Continued.



(d)

FIGURE 1: Continued.

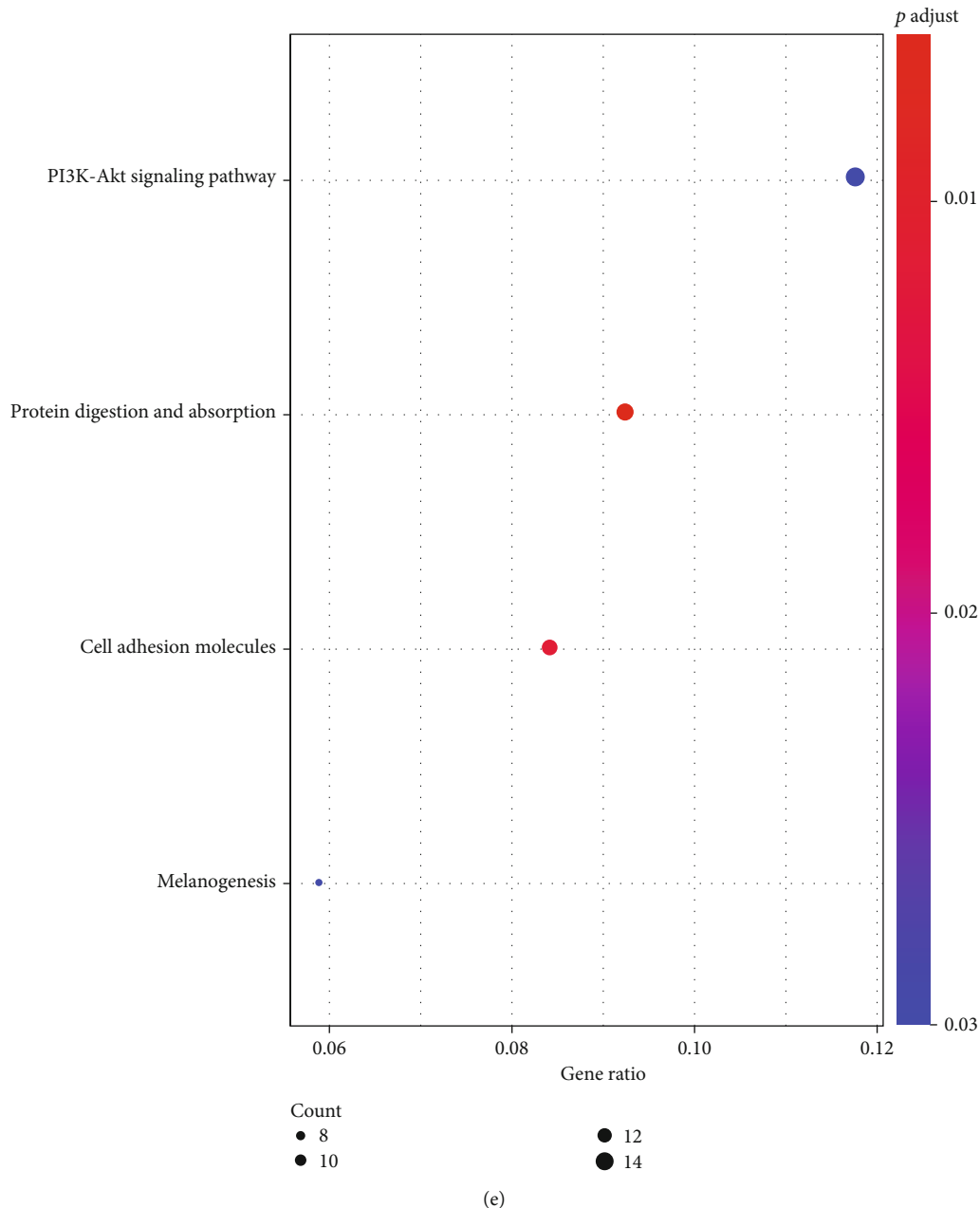


FIGURE 1: lncRNA PAPP A-AS1 was screened through bioinformatics analysis. (a) Volcano plot of the differentially expressed lncRNAs between HTS and normal skin tissues. (b) Volcano plot of the differentially expressed mRNAs between HTS and normal skin tissues. (c) Correlation clustering heat map of lncRNA and mRNA expression matrix. (d, e) The pathway regulated by mRNA of GO and KEGG enrichment analysis was conducted in HTS tissue.

signaling pathway, protein digestion and absorption, and cell adhesion molecules (Figure 1(e)). Therefore, we speculated that the development of HTS was related to the abnormal activation of lncRNA PAPP A-AS1 and the TLR4/MyD88/TGF signaling pathway.

3.2. lncRNA PAPP A-AS1 Was Significantly Upregulated in Clinical HTS Tissues and HTsFb Cells. To verify the relative expression level of these lncRNAs in HTS and pick out the most significant one, the expression of these lncRNAs in the NsFb and HTsFb cells was evaluated. As shown in

Figure 2(a), approximately 3-fold expressional change on lncRNA PAPP A-AS1 was observed in HTsFb cells, compared to NsFb cells (** $p < 0.01$ vs. NsFb), which was the lncRNA with the most significance. To evaluate the state of the TLR4 downstream signal pathway, the expression level of related proteins was determined in both the NsFb and HTsFb cells. As shown in Figures 2(b) and 2(c), we found that TLR4, MyD88, collagen I, collagen III, TGF- β 1, and α -SMA were significantly upregulated in the HTsFb cells, compared to NsFb cells (** $p < 0.01$ vs. NsFb).

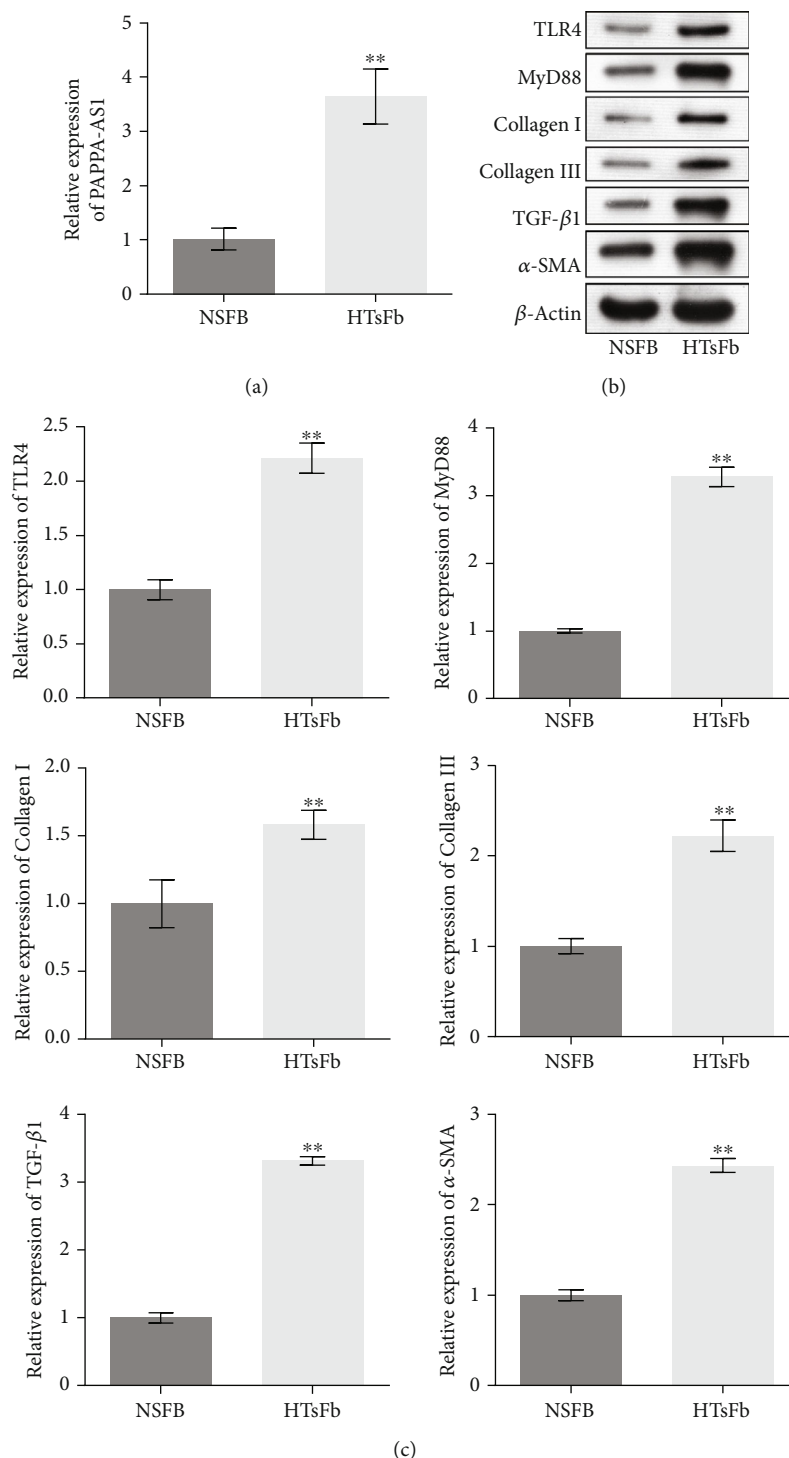


FIGURE 2: lncRNA PAPPAS1 was significantly upregulated in clinical HTS tissues and HTsFb cells. (a) qRT-PCR was used to detect the expression of PAPPAS1 in the NsFb and HTsFb cells. (b, c) The expression levels of TLR4, MyD88, collagen I, collagen III, TGF-β1, and α-SMA were evaluated by Western blot. NSFB group: normally cultured NSFB cells; HTsFb group: normally cultured HTsFb cells (** $p < 0.01$ vs. NsFb).

3.3. Knocking Down PAPPAS1 Suppressed the Proliferation of HTsFb Cells by Inhibiting the TLR4/MyD88 and TGF-β1 Signal Pathways In Vitro. To evaluate the function of PAPPAS1 in HTsFb cells, the PAPPAS1 knockdown HTsFb cells were established by short hairpin RNA (shRNA)

technology. As shown in Figure 3(a), the expression of PAPPAS1 was significantly suppressed in the sh-PAPPAS1#1 or sh-PAPPAS1#2 group, compared with the sh-NC group (** $p < 0.01$ vs. sh-NC). We further detected the proliferation ability of transfected cells. As shown in

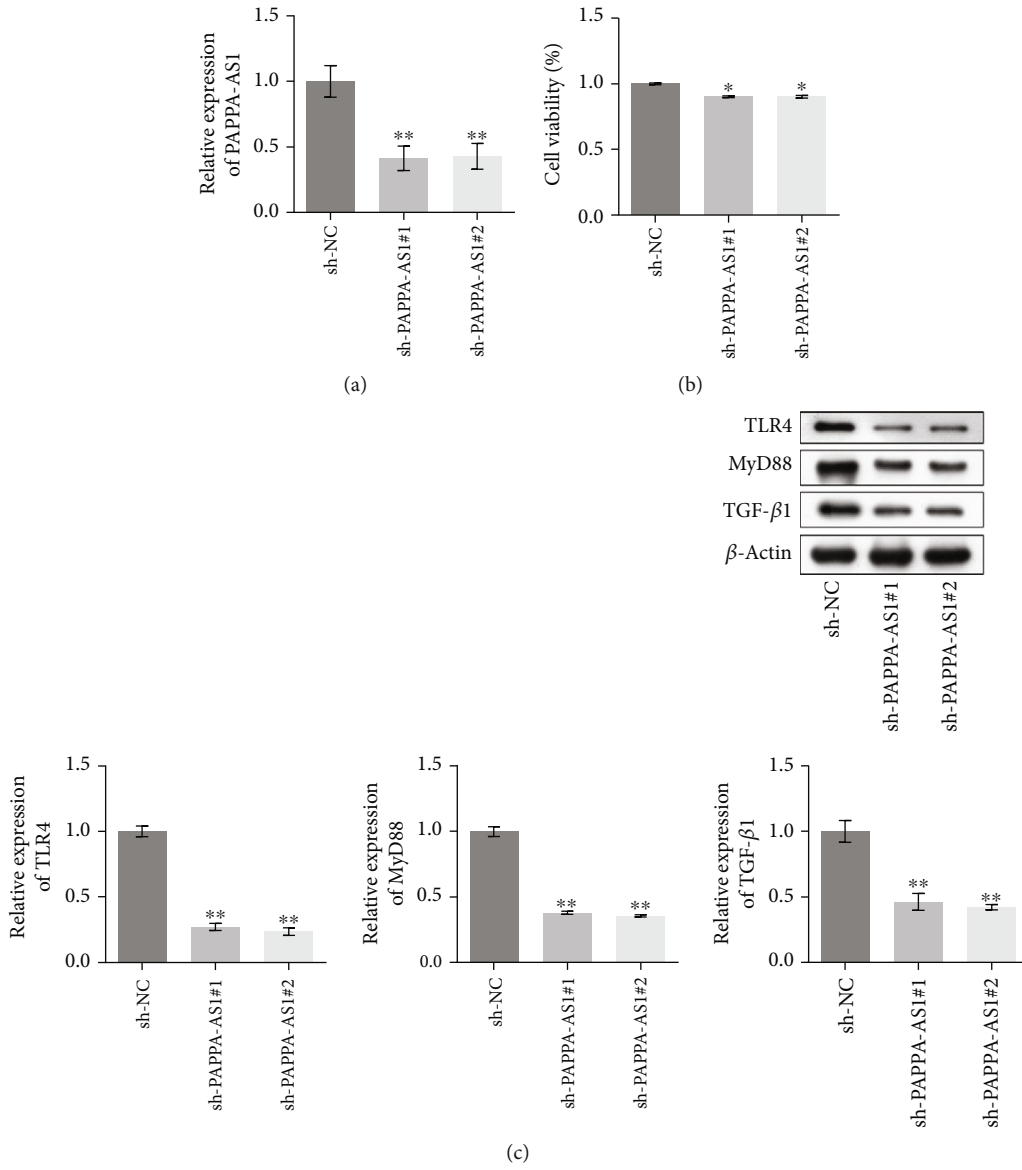


FIGURE 3: Continued.

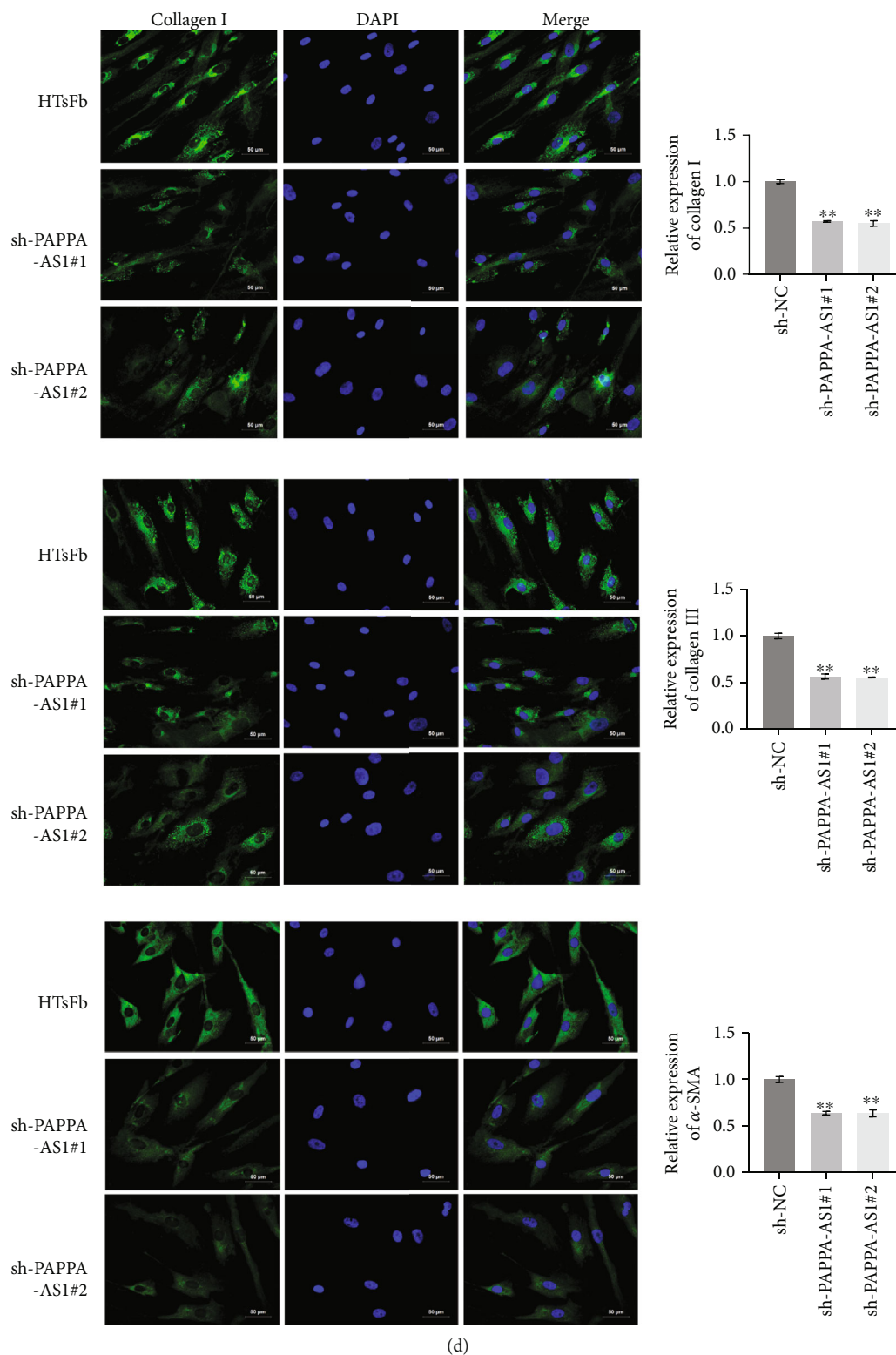


FIGURE 3: Knocking down PAPPA-AS1 suppressed the proliferation of HTsFb cells by inhibiting the TLR4/MyD88 and TGF- β 1 signal pathways. (a) QRT-PCR was used to detect the expression of PAPPA-AS1. (b) MTT assay was used to check the cell proliferation ability. (c) The expression levels of TLR4, MyD88, and TGF- β 1 were evaluated by Western blot. (d) The expression levels of collagen I, collagen III, and α -SMA were evaluated by IF staining. sh-NC group: HTsFb cells were transfected with sh-NC plasmid; sh-PAPPA-AS1#1 group: HTsFb cells were transfected with sh-PAPPA-AS1#1 plasmid; sh-PAPPA-AS1#2 group: HTsFb cells were transfected with sh-PAPPA-AS1#2 plasmid (* $p < 0.05$ vs. sh-NC, ** $p < 0.01$ vs. sh-NC).

Figure 3(b), the OD value in the sh-PAPPA-AS1#1 or sh-PAPPA-AS1#2 group was significantly lower, compared with the sh-NC group (** $p < 0.01$ vs. sh-NC), indicating an inhibitory effect on HTsFb cell proliferation ability by knocking down PAPPA-AS1. In addition, by transfecting the HTsFb cells with sh-PAPPA-AS1#1 or sh-PAPPA-AS1#2, the expression levels of TLR4, MyD88, and TGF- β 1 (Figure 3(c)) in the HTsFb cells were significantly suppressed (** $p < 0.01$ vs. sh-NC). Figure 3(d) showed the fluorescence intensities of fibrosis markers, collagen I, collagen III, and α -SMA, in the treated HTsFb cells. We found that the fluorescence intensities of collagen I, collagen III, and α -SMA decreased greatly in the sh-PAPPA-AS1#1 or sh-PAPPA-AS1#2 group, compared with the sh-NC group.

3.4. Knocking Down PAPPA-AS1 Alleviated the Fibrosis State of HTS Mice In Vivo. To evaluate the effect of lncRNA PAPPA-AS1, we inserted the shRNAs into the lentiviral particles, which were further injected into the HTS tissues. As shown in Figure 4(a), compared with sh-NC, the number of fibroblasts, the number of capillaries, and epithelial thickness were decreased in the sh-PAPPA-AS1#1 and sh-PAPPA-AS1#2 groups. In addition, the expression levels of TLR4, MyD88, and TGF- β 1 (Figure 4(b)) in the HTS tissues were significantly suppressed in the sh-PAPPA-AS1#1 or sh-PAPPA-AS1#2 group, compared with the sh-NC group (** $p < 0.01$ vs. sh-NC). Figure 4(c) showed the fluorescence intensities of collagen I, collagen III, and α -SMA in the HTS tissues of each group. The fluorescence intensities of collagen I, collagen III, and α -SMA were suppressed greatly in the sh-PAPPA-AS1#1 or sh-PAPPA-AS1#2 group, compared with the sh-NC group.

3.5. lncRNA PAPPA-AS1 Interacted with TAF15 and Upregulated Its Expression in the HTsFb Cells In Vitro. To explore the mechanism underlying the regulatory effect of lncRNA PAPPA-AS1 on the TLR4/MyD88 and TGF- β 1 signal pathways, we explored the interaction of lncRNA PAPPA-AS1 with an RNA-binding protein (RBP), TAF15. As shown in Figures 5(a) and 5(b), we found that lncRNA PAPPA-AS1 was located both in the nucleus and cytoplasm of the HTsFb cells. The results of RIP assay were shown in Figure 5(c). Taking SNRNP70 as a positive control, compared to IgG, lncRNA PAPPA-AS1 was significantly highly expressed in the TAF15 group. To further confirm the interaction between lncRNA PAPPA-AS1 and TAF15, we performed the RNA pull-down assay. As shown in Figure 5(d), the results showed that lncRNA PAPPA-AS1 interacted with TAF15, indicating an obvious interaction between lncRNA PAPPA-AS1 and TAF15 (** $p < 0.01$ vs. IgG).

3.6. lncRNA PAPPA-AS1 Induced the Transcription of TLR4 by Recruiting TAF15 to the TLR4 Promoter In Vivo and Vitro. As the knockdown efficacy was nearly equal between sh-PAPPA-AS1#1 and sh-PAPPA-AS1#2, one of the shRNAs was chosen for the subsequent experiments (sh-PAPPA-AS1#1). In addition, PAPPA-AS1-overexpressed HTsFb cells were established by transfecting the cells with the pcDNA3.1-PAPPA-AS1 vector. It showed that the trans-

fections of the overexpression of PAPPA-AS1 were successful (Figure 6(a)). As shown in Figure 6(b), compared to sh-NC + pcDNA-3.1-NC, TAF15 was significantly downregulated in the sh-PAPPA-AS1#1 group and upregulated in the over-PAPPA-AS1 group, indicating a positive correlation between the expression of PAPPA-AS1 and TAF15. As shown in the aforementioned results, the TLR4 signal pathway was regulated by lncRNA PAPPA-AS1, which might be related to the development of HTS. We further investigated the expression levels of TLR4 and TAF15 in the normal skin tissues and the scar tissues. Both TLR4 and TAF15 were found to be significantly upregulated in the scar tissues (Figure 6(c), ** $p < 0.01$ vs. normal tissues). In addition, a positive correlation between the expression levels of TLR4 and TAF15 in the scar tissues was observed (Figure 6(d)). To explore the relationship between TLR4 and TAF15, the TAF15 knockdown and TAF15-overexpressed HTsFb cells were established. As shown in Figure 6(e), the expression level of TAF15 was significantly suppressed in the sh-TAF15 group and elevated in the over-TAF15 group. In addition, TLR4 was downregulated in the sh-TAF15 group and upregulated in the over-TAF15 group (** $p < 0.01$ vs. control). ChIP assay (Figure 6(f)) revealed that TAF15 interacted with the promoter of TLR4 (** $p < 0.01$ vs. IgG). As shown in Figure 6(g), significant luciferase activity was observed in the TAF15-transfected cells, further verifying the interaction between TAF15 and TLR4 (** $p < 0.01$ vs. NC).

3.7. PAPPA-AS1 Promoted the Proliferation of HTsFb Cells by Regulating the TAF15/TLR4 Axis In Vitro. After confirming the interaction between lncRNA PAPPA-AS1 and TAF15, as well as TAF15 and TLR4, we further verify whether the regulatory effect of PAPPA-AS1 on the proliferation was related to the impact of PAPPA-AS1 on TLR4 expression. In order to verify the success of TLR4 overexpression, we carried out qRT-PCR detection. Figure 7(a) showed that the expression of TLR4 in HTsFb cells increased after transfection of pcDNA-TLR4. The PAPPA-AS1 knockdown HTsFb cells, and the PAPPA-AS1 knockdown and TLR4-overexpressed HTsFb cells were established. As shown in Figure 7(b), the suppressed cell viability of HTsFb cells in the sh-PAPPA-AS1#1 group was significantly elevated in the sh-PAPPA-AS1#1 + TLR4 group (** $p < 0.01$ vs. sh-NC, ## $p < 0.01$ vs. sh-PAPPA-AS1#1). In addition, the downregulated TLR4, MyD88, and TGF- β 1 induced by the knockdown of PAPPA-AS1 were greatly reversed in the sh-PAPPA-AS1#1 + pcDNA-TLR4 group (Figure 7(c), ** $p < 0.01$ vs. sh-NC, ## $p < 0.01$ vs. sh-PAPPA-AS1#1). As shown in Figure 7(d), compared with sh-NC group, fluorescence intensities of collagen I, collagen III, and α -SMA were suppressed greatly in the sh-PAPPA-AS1#1 group, which was significantly elevated in the sh-PAPPA-AS1#1 + pcDNA-TLR4 group.

3.8. PAPPA-AS1 Impacted the Fibrosis State of HTS Mice by Regulating the TAF15/TLR4 Axis In Vivo. To verify the underlying mechanism on the function of PAPPA-AS1 in the development of HTS, sh-PAPPA-AS1#1 and sh-PAPPA-AS1#1 combined with the pcDNA3.1-TLR4 vector

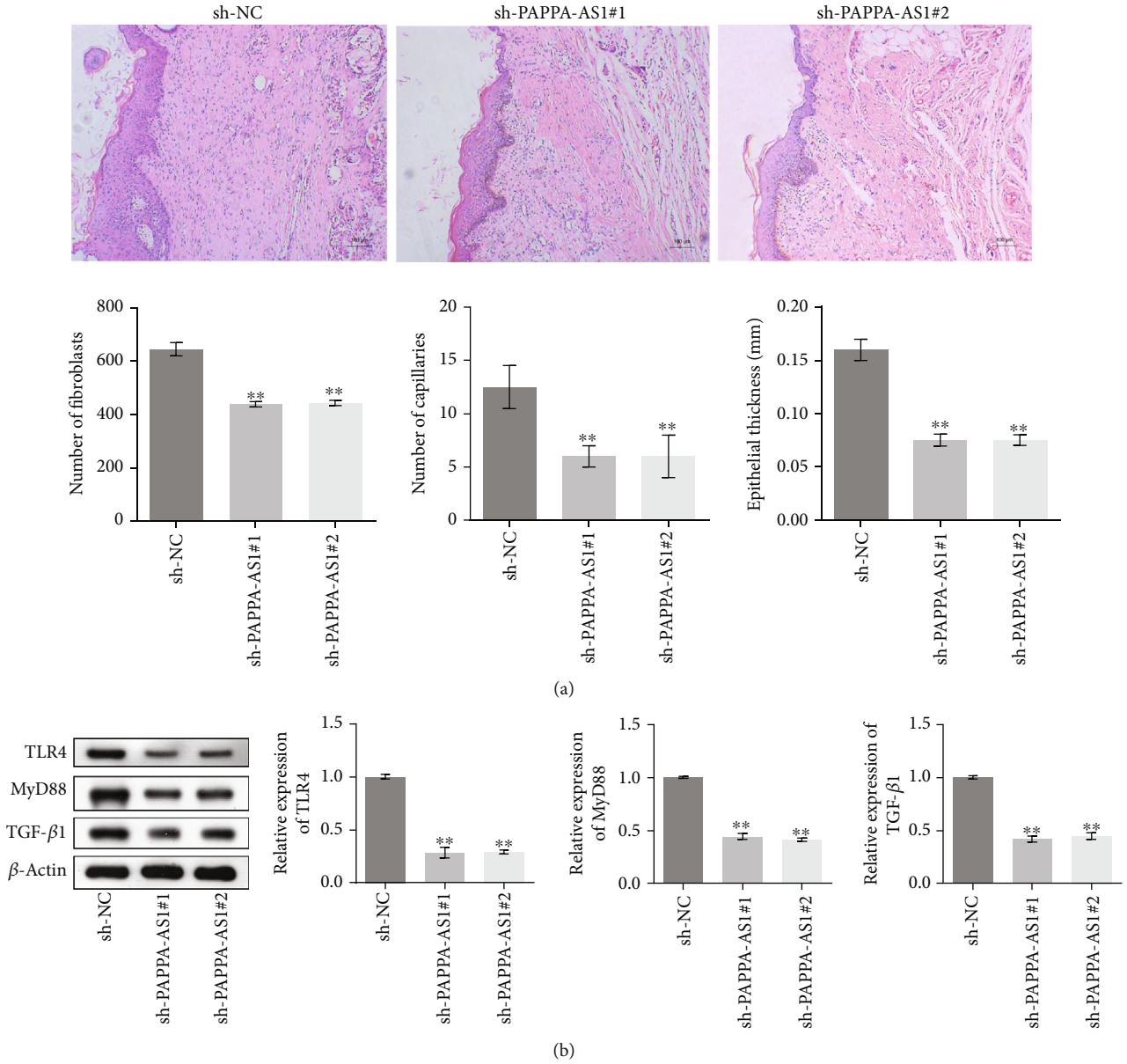
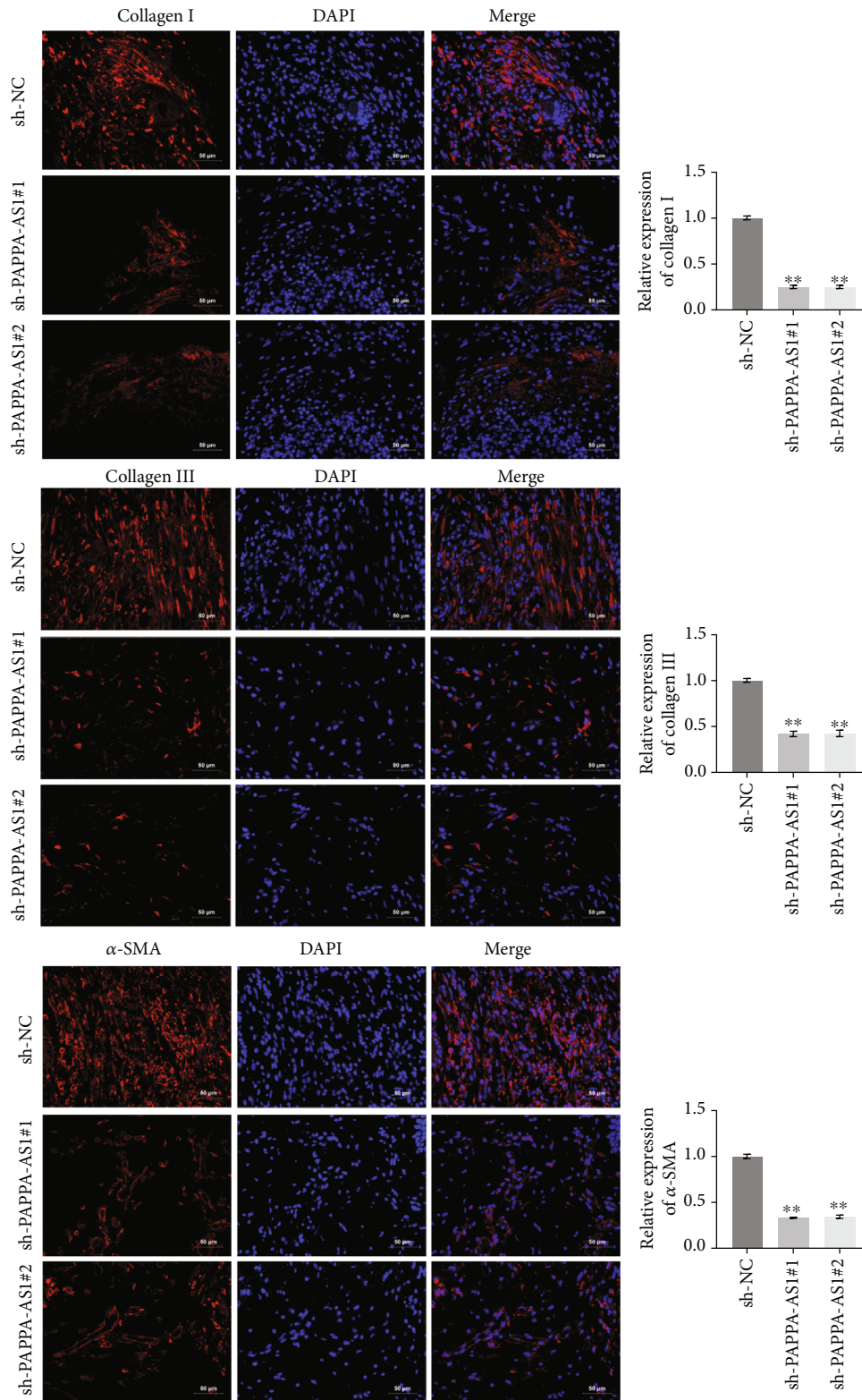


FIGURE 4: Continued.



(c)

FIGURE 4: Knocking down PAPP-AS1 alleviated the fibrosis state of HTS mice. (a) HE staining was used to evaluate the pathological state of HTS tissues, and the number of fibroblasts, number of capillaries, and epithelial thickness were counted (** $p < 0.01$ vs. sh-NC). (b) The expression levels of TLR4, MyD88, and TGF- β 1 in the HTS tissues were evaluated by Western blot (** $p < 0.01$ vs. sh-NC). (c) The expression levels of collagen I, collagen III, and α -SMA in the HTS tissues were evaluated by IF staining. sh-NC group: mice were injected with sh-NC lentivirus; sh-PAPPA-AS1#1 group: mice were injected with sh-PAPPA-AS1#1 lentivirus; sh-PAPPA-AS1#2 group: mice were injected with sh-PAPPA-AS1#2 lentivirus.

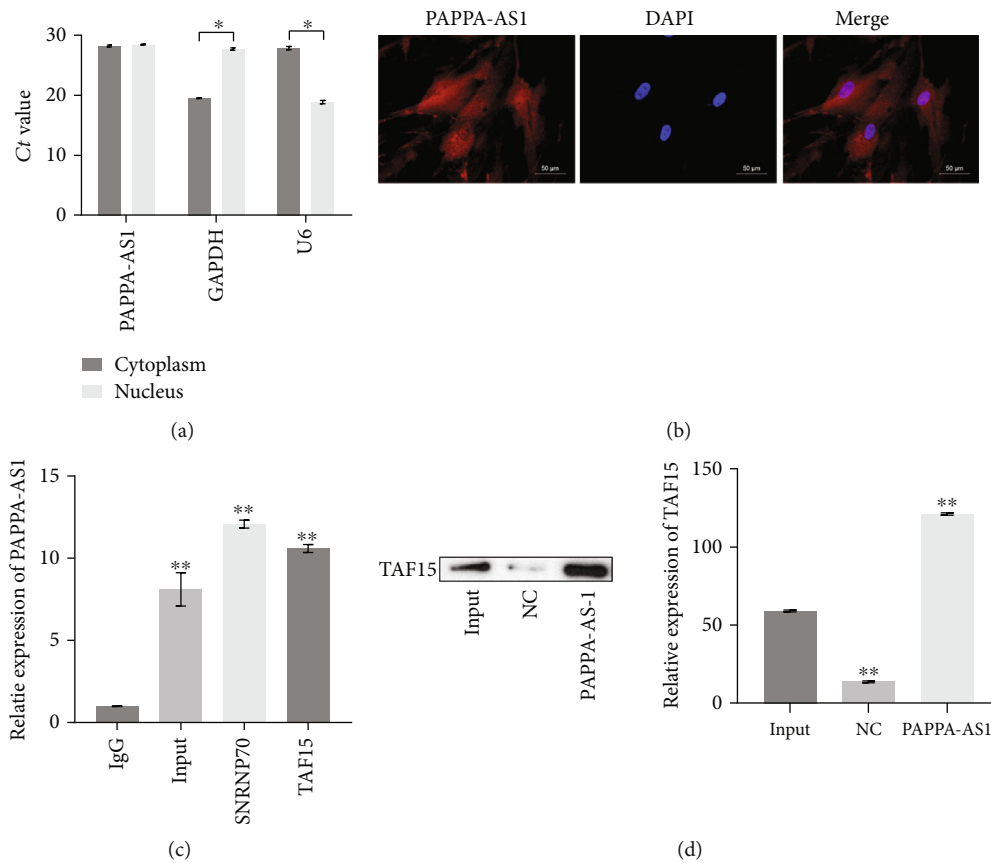


FIGURE 5: lncRNA PAPP-AS1 interacted with TAF15 and upregulated its expression in the HTsFb cells. (a) Subcellular fractionation assay was used to determine the expression of PAPP-AS1 in the cytoplasm and nucleus ($*p < 0.05$ vs. cytoplasm). (b) The expression of PAPP-AS1 in the cytoplasm and nucleus was verified by RNA FISH assay. (c, d) The interaction between PAPP-AS1 and TAF15 was detected by RIP assay and RNA pull-down assay ($**p < 0.01$ vs. IgG).

were inserted into the lentiviral particles, which were further injected into the HTS tissues of the animals. The results in Figure 7(a) show that the expression of TLR4 in the pcDNA-TLR4 group was higher than that in the pcDNA-NC group. It was suggested that pcDNA-TLR4 played an important role. As shown in Figure 8(b), compared with the sh-NC group, the number of fibroblasts and the number of capillaries were reduced in the sh-PAPP-AS1#1 group, which were reversed in the sh-PAPP-AS1#1 + pcDNA-TLR4 group, and so as the epithelial thickness. The inhibited expression levels of TLR4, MyD88, and TGF- β 1 in the HTS tissues (Figure 8(c)) induced by knockdown of PAPP-AS1 were significantly elevated in the sh-PAPP-AS1#1 + pcDNA-TLR4 group ($**p < 0.01$ vs. sh-NC and $##p < 0.01$ vs. sh-PAPP-AS1#1). In addition, the decreased fluorescence intensities of collagen I, collagen III, and α -SMA in the HTS tissues induced by knockdown of PAPP-AS1 were significantly elevated in the sh-PAPP-AS1#1 + pcDNA-TLR4 group (Figure 8(d)).

4. Discussion

lncRNA has been reported to be involved in multiple types of diseases by regulating the expression of key proteins, including malignant tumors [29, 30], fibrosis [31, 32], and autoim-

mune diseases [33, 34]. Jiang and Guo found that THBS1 induced the growth of hypertrophic scar fibroblasts [35]. HTS is a complicated pathological process with multiple cellular signal pathways and abnormally expressed proteins involved; the development and process of which are recently reported to be related to the differentially expressed lncRNA [36]. Ma and Liu claimed that lncRNA FAM225B promoted the progression of HTS [37]. However, the underlying mechanism is still unknown. In the present study, the differentially expressed lncRNAs between normal skin tissues and HTS tissues were screened using a lncRNA array. lncRNA PAPP-AS1 was picked out due to its high expression level in the HTsFb cells compared to NsFb. Fibroblasts are reported to be the main participants in the process and development of HTS by secreting collagens; the excessive proliferation of which is regarded as the main inducer for the formation of HTS [38, 39]. Therefore, in the present study, HTsFb cells were taken as the study objects. By knocking down the expression level of lncRNA PAPP-AS1 in the HTsFb cells, the proliferation ability of HTsFb cells and the expression level of fibrosis markers were significantly suppressed, indicating a potential correlation between lncRNA PAPP-AS1 and the fibrosis process of HTsFb cells. In addition, the *in vivo* experiments confirmed that the pathological state of HTS tissues was alleviated and the expression level of fibrosis

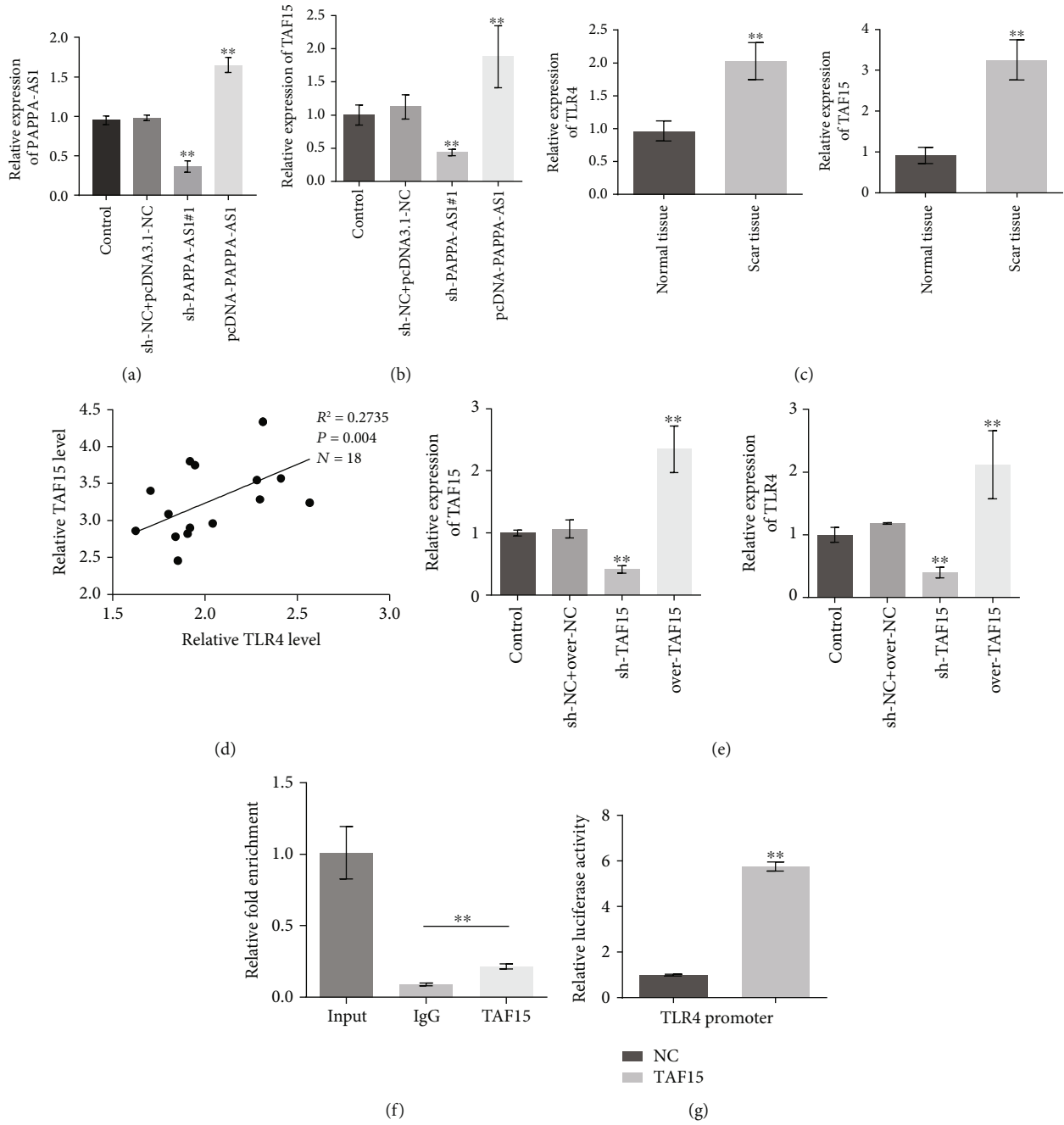


FIGURE 6: lncRNA PAPPAs-AS1 induced the transcription of TLR4 by recruiting TAF15 to the TLR4 promoter. (a) The relative expression of PAPPAs-AS1 was detected by qRT-PCR. (b) qRT-PCR was used to detect the expression of TAF15 (** $p < 0.01$ vs. sh-NC + pcDNA3.1-NC). (c) The expression levels of TAF15 and TLR4 in the tissues were evaluated by RT-qPCR (** $p < 0.01$ vs. normal tissues). (d) The correlation between the expression of TAF15 and TLR4 in the HTs tissues was evaluated. (e) RT-qPCR was used to detect the expression of TAF15 and TLR4 in the treated HTsFb cells (** $p < 0.01$ vs. sh-NC + over-NC). (f) ChIP assay evaluated the interaction between TAF15 and the promoter of TLR4 (** $p < 0.01$ vs. IgG). (g) The interaction between TAF15 and the promoter of TLR4 was verified by luciferase assay. Control group: normally cultured HTsFb cells; sh-NC + pcDNA3.1-NC group: HTsFb cells were transfected with sh-NC plasmid and pcDNA3.1-NC plasmid simultaneously; sh-PAPPAs-AS1#1 group: HTsFb cells were transfected with sh-PAPPAs-AS1#1 plasmid; pcDNA3.1-PAPPAs-AS1 group: HTsFb cells were transfected with pcDNA3.1-PAPPAs-AS1 plasmid; normal skin tissue group: human normal skin tissue; scar tissue: human scar tissue; sh-NC + over-NC group: HTsFb cells were transfected with sh-NC plasmid and over-NC plasmid simultaneously; sh-TAF15 group: HTsFb cells were transfected with sh-TAF15 plasmid; over-TAF15 group: HTsFb cells were transfected with over-TAF15 plasmid. (** $p < 0.01$ vs. NC).

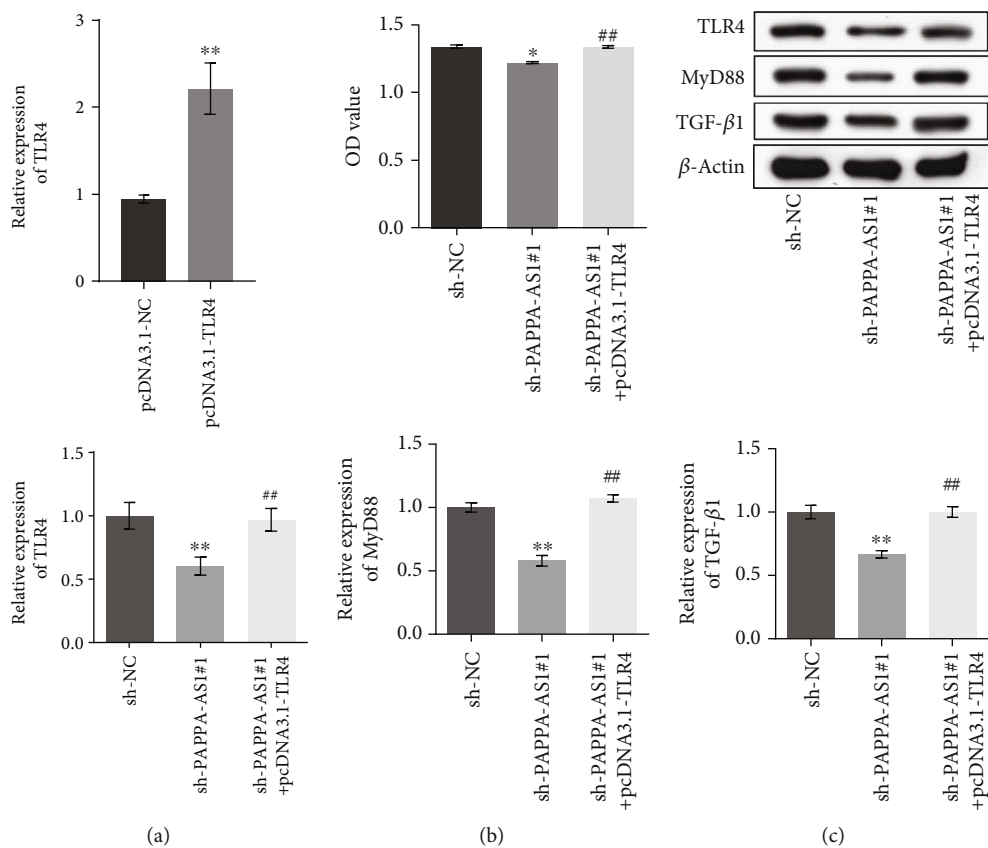
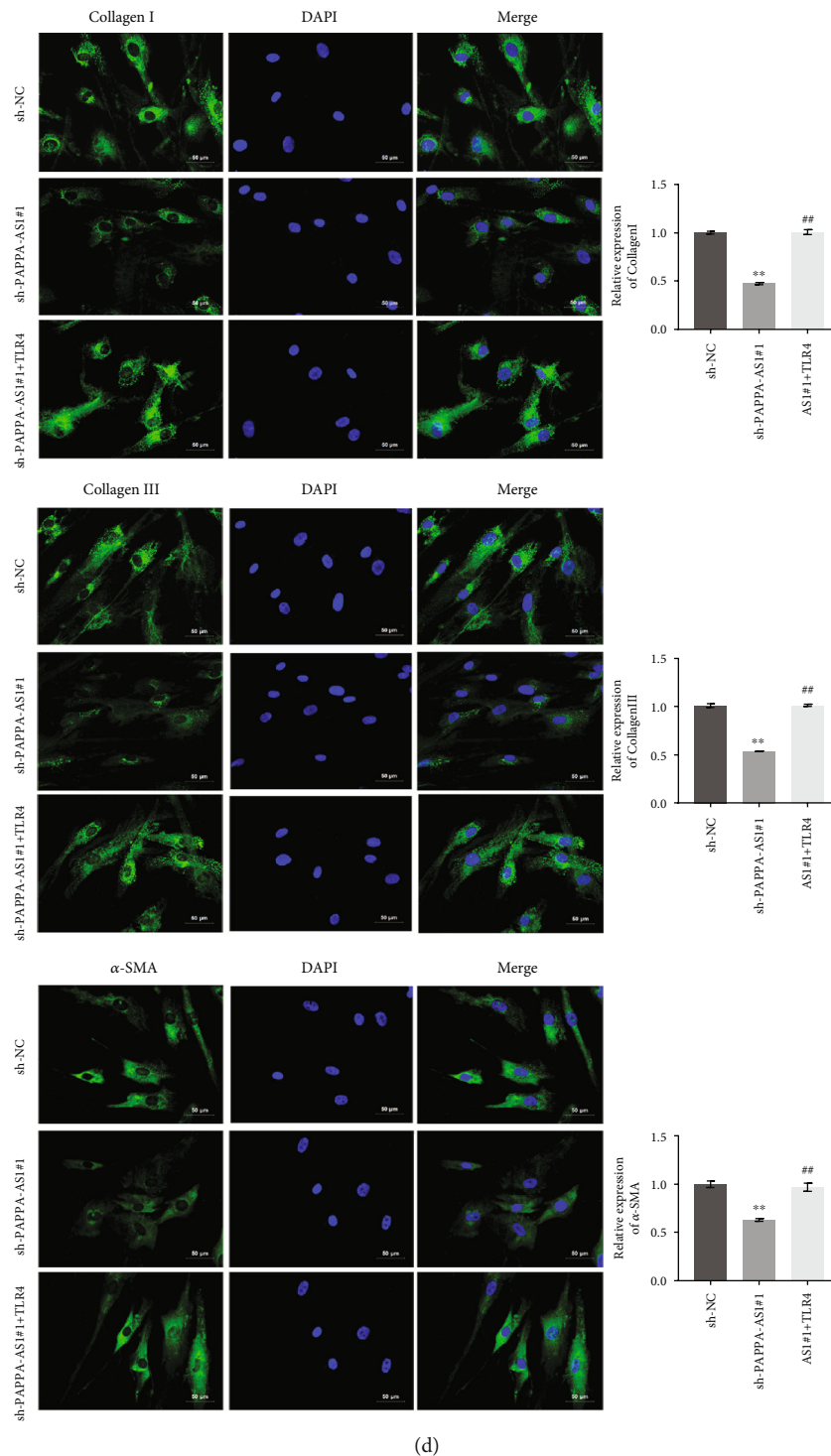
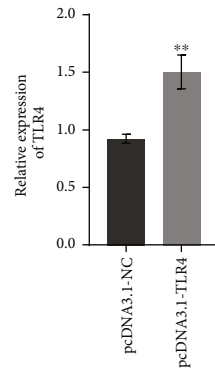


FIGURE 7: Continued.

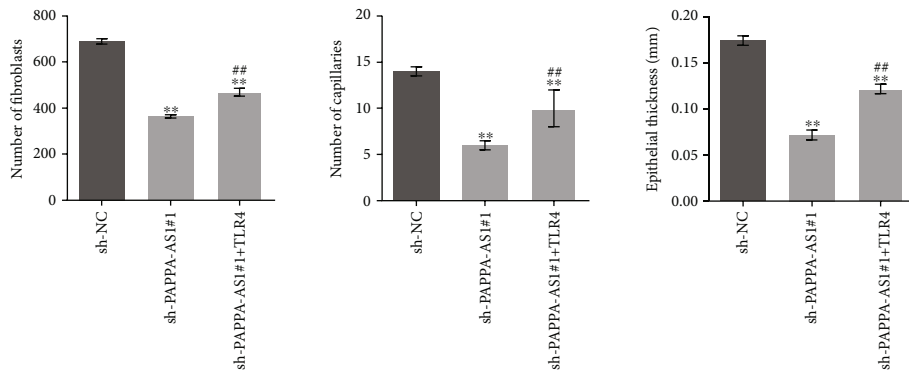
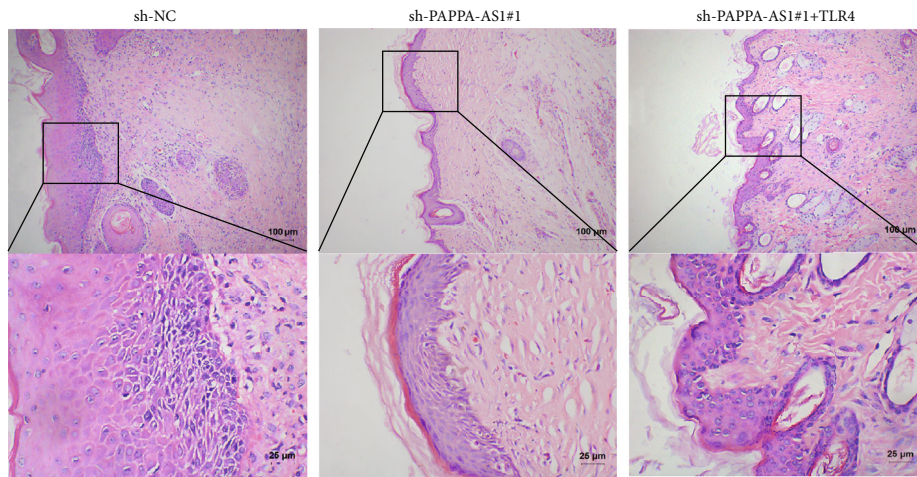


(d)

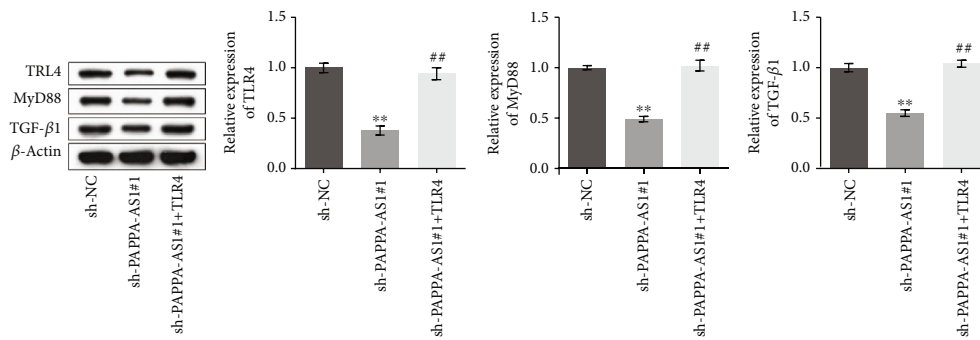
FIGURE 7: PAPPA-AS1 promoted the proliferation of HTsFb cells by regulating the TAF15/TLR4 axis. (a) The relative expression of TLR4 was detected by qRT-PCR. (b) MTT assay was used to detect the proliferation of the treated HTsFb cells ($*p < 0.05$, vs. sh-NC; $##p < 0.01$ vs. sh-PAPPA-AS1#1). (c) The expression levels of TLR4, MyD88, and TGF- β 1 were evaluated by Western blot. (d) The expression levels of collagen I, collagen III, and α -SMA were evaluated by IF staining. pcDNA3.1-NC group: HTsFb cells were transfected with pcDNA3.1-NC plasmid; pcDNA3.1-TLR4 group: HTsFb cells were transfected with pcDNA3.1-TLR4 plasmid; sh-NC group: HTsFb cells were transfected with sh-NC plasmid; sh-PAPPA-AS1#1 group: HTsFb cells were transfected with sh-PAPPA-AS1#1 plasmid; sh-PAPPA-AS1#1 + pcDNA3.1-TLR4 group: HTsFb cells were transfected with sh-PAPPA-AS1#1 and pcDNA3.1-TLR4 plasmid simultaneously ($**p < 0.01$ vs. sh-NC, $##p < 0.01$ vs. sh-PAPPA-AS1#1).



(a)

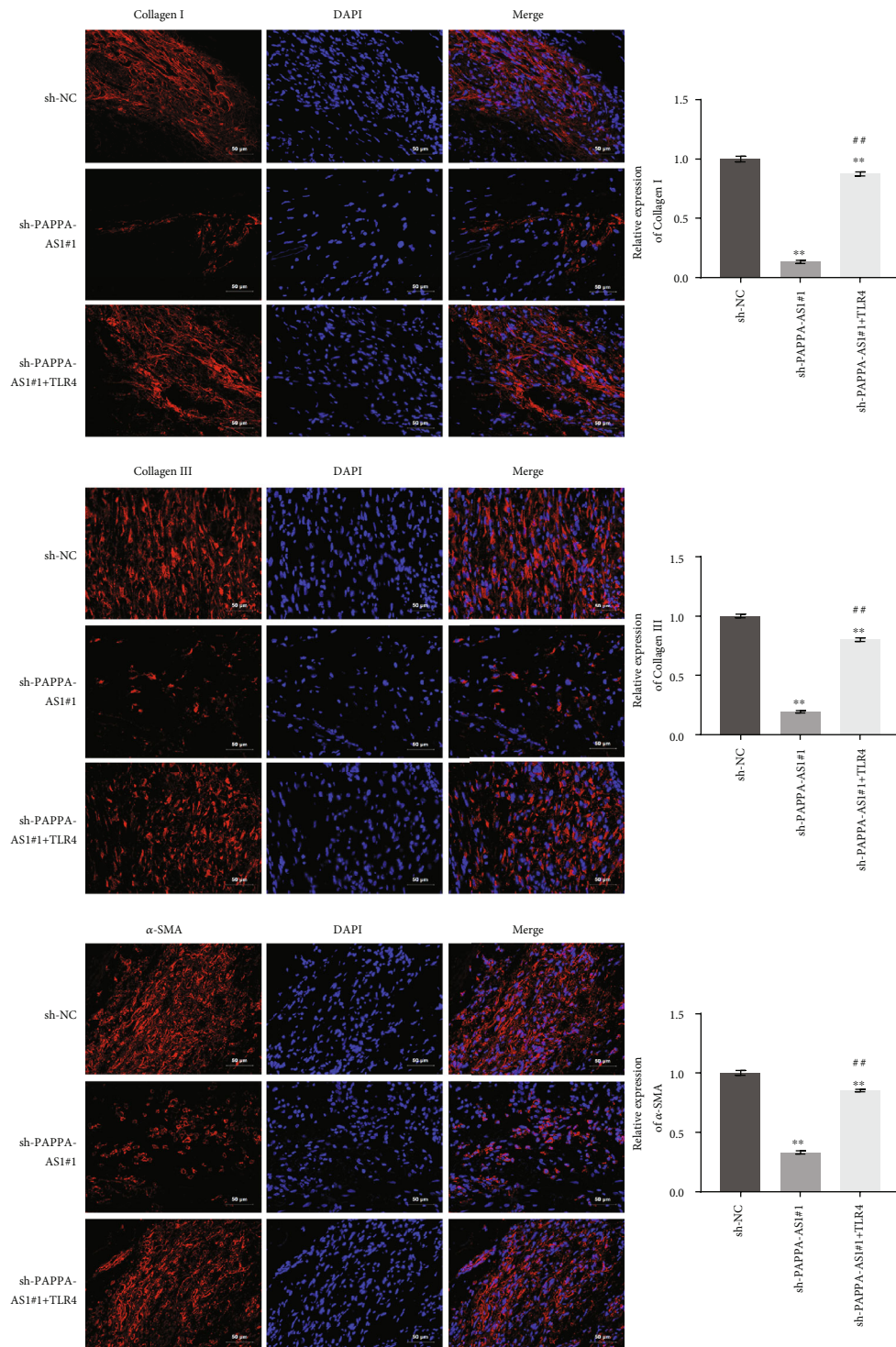


(b)



(c)

FIGURE 8: Continued.



(d)

FIGURE 8: PAPPA-AS1 impacted the fibrosis state of HTS mice by regulating the TAF15/TLR4 axis. (a) The relative expression of TLR4 was detected by qRT-PCR. (b) HE staining was used to evaluate the pathological state of HTS tissues. (c) The expression levels of TLR4, MyD88, and TGF- β 1 in the HTS tissues were evaluated by Western blot (** $p < 0.01$ vs. sh-NC, ## $p < 0.01$ vs. sh-PAPPA-AS1#1). (d) The expression levels of collagen I, collagen III, and α -SMA in the HTS tissues were evaluated by IF staining. pcDNA3.1-NC group: mice were injected with pcDNA3.1-NC lentivirus; pcDNA3.1-TLR4 group: mice were injected with pcDNA3.1-TLR4 lentivirus; sh-NC group: mice were injected with sh-NC lentivirus; sh-PAPPA-AS1#1 group: mice were injected with sh-PAPPA-AS1#1 lentivirus; sh-PAPPA-AS1#1 + pcDNA3.1-TLR4 group: mice were injected with sh-PAPPA-AS1#1 and pcDNA3.1-TLR4 lentivirus simultaneously.

markers was inhibited by injecting the lentiviral particles containing the shRNA against lncRNA PAPPAS1. Taken these preliminary data together, we suspected that the development of HTS was possibly related to the upregulation of lncRNA PAPPAS1. But we still do not know what kinds of molecules induced lncRNA PAPPAS1 constitutively in HTsFb. In the future, we will use bioinformatics methods to explore and predict the molecules acting on PAPPAS1 and provide more possibilities for better HTS treatment.

The TLR4/MyD88 signal pathway is a classic inflammatory signal pathway, which is reported to exert an important role in the development and process of fibrosis [40]. By regulating the NF- κ B signal pathway, the TLR4/MyD88 signal triggers the excessive production of inflammatory factors to induce and aggravate the pathological state of fibrosis [41, 42]. In addition, the TGF- β 1 signal pathway can be activated by the stimulation on the TLR4/MyD88 axis [19], which is regarded as an important growth factor in fibrogenesis. By inducing the formation of ECM and preventing ECM from being degraded, the production of fibrogenic myofibroblasts will be inhibited by TGF- β 1 [43]. In addition, the regulatory effect of TGF- β 1 on fibrogenic activities was related to the activation of Smad signaling pathways through impacting the type I receptor-mediated phosphorylation of Smad2 and Smad3 [44]. Suppressing TGF- β 1 has been proved to alleviate fibrosis in multiple animal models [45, 46]. In the present study, we found that both the TLR4/MyD88 signal pathway and the TGF- β 1 signal pathway were significantly activated in the HTsFb cells, which were reversed by knocking down the expression level of lncRNA PAPPAS1, indicating that lncRNA PAPPAS1 might induce the process of HTS by suppressing the TLR4/MyD88 signal pathway and TGF- β 1 signal pathway. However, there may be other molecules in the TLR4/MyD88 pathway and we still cannot conclude that it is entirely the role of TLR4. TLR4 may play more complex functions in scars, which requires a more comprehensive research to explore. Therefore, we will carry out thorough analysis and complete experiments to explore the role of various molecules in the TLR4/MyD88 pathway on HTS in our future work. We will also combine the current work to compare the difference between TLR4 alone and its collaboration function with PAPPAS1.

To further investigate the molecular mechanism, we focused on the RNA-binding protein, TATA-box binding protein-associated factor 15 (TAF15), which belongs to the FET family [47]. The FET family is widely expressed in different tissues, and the structure of the family members is highly similar to each other, which is reported to be involved in such biological processes as transcription, splicing, miRNA formation, RNA transport, and maintenance of genomic integrity [48]. Recently, TAF15 is widely reported to interact with lncRNA to regulate the transcription and translation of target genes. Pan et al. [49] claims that in the process of colon cancer, lncRNA TRPM2-AS interacts with TAF15 to stabilize the mRNA of transient receptor potential melastatin 2 (TRPM2), which induces the development of colon cancer. The expression level of LINC010148 can be elevated by USF1, and LINC010148 interacts with TAF15 to bind to the promoter of YAP1, which further triggers the development of squa-

mous carcinoma [50]. In the present study, the interaction between lncRNA PAPPAS1 and TAF15 was confirmed by RNA pull-down and RIP assay. In addition, the binding between TAF15 and the promoter of TLR4 was confirmed by ChIP and luciferase assay. We further verified that lncRNA PAPPAS1 regulated the TLR4/MyD88 signal pathway and TGF- β 1 signal pathway in the HTsFb cells by interacting with TAF15 to upregulate the expression level of TLR4, which was further proved in the HTS nude mouse model.

However, there was still limitation in the present study. For example, we verified the function of the lncRNA PAPPAS1/TAF15/TLR4 axis by transfecting both sh-PAPPAS1#1 and pcDNA3.1-TLR4 into HTsFb cells or HTS tissues, which abolished the effects of sh-PAPPAS1#1. No direct evidence was provided to claim the involvement of TAF15. In our future work, upregulating TAF15 in the sh-PAPPAS1#1-transfected HTsFb cells or HTS tissues will be performed to directly verify the involvement of TAF15. In addition, in the present study, the xenograft HTS tissues from the clinic were transplanted onto the nude mice to establish the animal model, which was independent and only provided the prospective data. In our further work, other HTS animal models, such as a HTS rabbit model and transgenic animals, will be used to evaluate the biofunction of lncRNA PAPPAS1 and the potential underlying mechanism in the development and process of HTS.

5. Conclusion

Through our experiments and analysis, we demonstrated that lncRNA PAPPAS1 might induce the development of HTS by upregulating TLR4 through interacting with TAF15.

Data Availability

The datasets used or analyzed during the current study are available from the corresponding author on reasonable request.

Conflicts of Interest

The authors declare no conflict of interests.

Authors' Contributions

Pengju Fan did the following: conceptualization, methodology, software, data curation, and writing—original draft preparation. Yongjie Wang did the following: visualization, investigation, and supervision. Jingjing Li did the following: software and validation. Man Fang did the following: writing—reviewing and editing.

Acknowledgments

The authors would like to thank the Department of Burn and Plastic, Xiangya Hospital, and Central South University for all the support.

References

- [1] F. B. Rabello, C. D. Souza, and J. A. Farina Jr, "Update on hypertrophic scar treatment," *Clinics*, vol. 69, no. 8, pp. 565–573, 2014.
- [2] J. Song, X. Li, and J. Li, "Emerging evidence for the roles of peptide in hypertrophic scar," *Life Sciences*, vol. 241, p. 117174, 2020.
- [3] S. Chawla and S. Ghosh, "Regulation of fibrotic changes by the synergistic effects of cytokines, dimensionality and matrix: towards the development of an in vitro human dermal hypertrophic scar model," *Acta Biomaterialia*, vol. 69, pp. 131–145, 2018.
- [4] X. Fang, X. Hu, Z. Zheng et al., "Smad interacting protein 1 influences transforming growth factor-beta1/Smad signaling in extracellular matrix protein production and hypertrophic scar formation," *Journal of Molecular Histology*, vol. 50, no. 6, pp. 503–514, 2019.
- [5] Z. H. Harvey, Y. Chen, and D. F. Jarosz, "Protein-based inheritance: epigenetics beyond the chromosome," *Molecular Cell*, vol. 69, no. 2, pp. 195–202, 2018.
- [6] R.-W. Yao, Y. Wang, and L.-L. Chen, "Cellular functions of long noncoding RNAs," *Nature Cell Biology*, vol. 21, no. 5, pp. 542–551, 2019.
- [7] M. Sarfi, M. Abbastabar, and E. Khalili, "Long noncoding RNAs biomarker-based cancer assessment," *Journal of Cellular Physiology*, vol. 234, no. 10, pp. 16971–16986, 2019.
- [8] L. Lorenzi, F. Avila Cobos, A. Decock et al., "Long noncoding RNA expression profiling in cancer: challenges and opportunities," *Genes Chromosomes & Cancer*, vol. 58, no. 4, pp. 191–199, 2019.
- [9] J. Li, L. Chen, C. Cao et al., "The long non-coding RNA LncRNA8975-1 is upregulated in hypertrophic scar fibroblasts and controls collagen expression," *Cellular Physiology and Biochemistry: International Journal of Experimental Cellular Physiology, Biochemistry, and Pharmacology*, vol. 40, no. 1–2, pp. 326–334, 2016.
- [10] Q. Nong, S. Li, Y. Wu, and D. Liu, "LncRNA COL1A2-AS1 inhibits the scar fibroblasts proliferation via regulating miR-21/Smad7 pathway," *Biochemical and Biophysical Research Communications*, vol. 495, no. 1, pp. 319–324, 2018.
- [11] L. Tu, Q. Huang, S. Fu, and D. Liu, "Aberrantly expressed long noncoding RNAs in hypertrophic scar fibroblasts in vitro: a microarray study," *International Journal of Molecular Medicine*, vol. 41, no. 4, pp. 1917–1930, 2018.
- [12] H. Zhao, M. Chen, S. B. Lind, and U. Pettersson, "Distinct temporal changes in host cell lncRNA expression during the course of an adenovirus infection," *Virology*, vol. 492, pp. 242–250, 2016.
- [13] Q. Jiang, L. Dai, N. Chen et al., "Integrative analysis provides multi-omics evidence for the pathogenesis of placenta percreta," *Journal of Cellular and Molecular Medicine*, vol. 24, no. 23, pp. 13837–13852, 2020.
- [14] A. del Real, L. López-Delgado, C. Sañudo et al., "Long noncoding RNAs as bone marrow stem cell regulators in osteoporosis," *DNA and Cell Biology*, vol. 39, no. 9, pp. 1691–1699, 2020.
- [15] H. Tsukamoto, S. Takeuchi, K. Kubota et al., "Lipopolysaccharide (LPS)-binding protein stimulates CD14-dependent Toll-like receptor 4 internalization and LPS-induced TBK1-IKKe-IRF3 axis activation," *The Journal of Biological Chemistry*, vol. 293, no. 26, pp. 10186–10201, 2018.
- [16] K. Ohashi, V. Burkart, S. Flohe, and H. Kolb, "Cutting edge: heat shock protein 60 is a putative endogenous ligand of the toll-like receptor-4 complex," *Journal of Immunology*, vol. 164, no. 2, pp. 558–561, 2000.
- [17] M. J. Portou, R. Yu, D. Baker, S. Xu, D. Abraham, and J. Tsui, "Hyperglycaemia and ischaemia impair wound healing via Toll-like receptor 4 pathway activation in vitro and in an experimental murine model," *European Journal of Vascular and Endovascular Surgery*, vol. 59, no. 1, pp. 117–127, 2020.
- [18] F. M. Davis, A. Kimball, A. den Dekker et al., "Histone methylation directs myeloid TLR4 expression and regulates wound healing following cutaneous tissue injury," *Journal of Immunology*, vol. 202, no. 6, pp. 1777–1785, 2019.
- [19] E. Seki, S. de Minicis, C. H. Österreicher et al., "TLR4 enhances TGF- β signaling and hepatic fibrosis," *Nature Medicine*, vol. 13, no. 11, pp. 1324–1332, 2007.
- [20] S. Bhattacharyya, K. Kelley, D. S. Melichian et al., "Toll-like receptor 4 signaling augments transforming growth factor- β responses: a novel mechanism for maintaining and amplifying fibrosis in scleroderma," *American Journal of Pathology*, vol. 182, no. 1, pp. 192–205, 2013.
- [21] J. Wang, K. Hori, J. Ding et al., "Toll-like receptors expressed by dermal fibroblasts contribute to hypertrophic scarring," *Journal of Cellular Physiology*, vol. 226, no. 5, pp. 1265–1273, 2011.
- [22] J. Chen, B. Zeng, H. Yao, and J. Xu, "The effect of TLR4/7 on the TGF- β -induced Smad signal transduction pathway in human keloid," *Burns*, vol. 39, no. 3, pp. 465–472, 2013.
- [23] R. Lei, J. Li, F. Liu et al., "HIF-1 alpha promotes the keloid development through the activation of TGF-beta/Smad and TLR4/MyD88/NF-kappa B pathways," *Cell Cycle*, vol. 18, no. 23, pp. 3239–3250, 2019.
- [24] F. Segreto, G. F. Marangi, P. Gigliofiorito, F. Briganti, and P. Persichetti, "HSP90 and TLR4 interplay in keloids," *Plastic and Reconstructive Surgery*, vol. 137, no. 2, pp. 480E–481E, 2016.
- [25] P.-J. Fan, X.-H. Yang, M.-Z. Xiao, J.-H. Long, and S.-R. Lei, "Toll like receptor-4 involved in the mechanism of hyperplastic scarring via TGF- β ," *Progress in Biochemistry and Biophysics*, vol. 38, no. 9, pp. 842–849, 2011.
- [26] S. C. Pengju Fan, Z. Li, X. Yang, S. Lei, and W. Tan, "Gallic acid inhibits LPS induced hypertrophic scar inflammation via Toll-like receptor 4/nuclear factor- κ B/peroxisome proliferator-activated receptor γ signaling," *International Journal of Clinical and Experimental Medicine*, vol. 11, 2018.
- [27] Y. P. Hu, Y. P. Jin, X. S. Wu et al., "LncRNA-HGBC stabilized by HuR promotes gallbladder cancer progression by regulating miR-502-3p/SET/AKT axis," *Molecular Cancer*, vol. 18, no. 1, p. 167, 2019.
- [28] N. J. R. Blackburn, B. Vulesevic, B. McNeill et al., "Methylglyoxal-derived advanced glycation end products contribute to negative cardiac remodeling and dysfunction post-myocardial infarction," *Basic Research in Cardiology*, vol. 112, no. 5, 2017.
- [29] J. Li, Z. Li, W. Zheng et al., "LncRNA-ATB: an indispensable cancer-related long noncoding RNA," *Cell proliferation*, vol. 50, no. 6, 2017.
- [30] J. Wang, Z. Su, S. Lu et al., "LncRNA HOXA-AS2 and its molecular mechanisms in human cancer," *Clinica Chimica Acta; International Journal of Clinical Chemistry*, vol. 485, pp. 229–233, 2018.
- [31] K. Hao, W. Lei, H. Wu et al., "LncRNA-Safe contributes to cardiac fibrosis through Safe-Sfrp2-HuR complex in mouse

- myocardial infarction,” *Theranostics*, vol. 9, no. 24, pp. 7282–7297, 2019.
- [32] H. Peng, L. Y. Wan, J. J. Liang, Y. Q. Zhang, W. B. Ai, and J. F. Wu, “The roles of lncRNA in hepatic fibrosis,” *Cell & Bioscience*, vol. 8, no. 1, 2018.
- [33] X. Bi, X. H. Guo, B. Y. Mo et al., “LncRNA PICSAR promotes cell proliferation, migration and invasion of fibroblast-like synoviocytes by sponging miRNA-4701-5p in rheumatoid arthritis,” *eBioMedicine*, vol. 50, pp. 408–420, 2019.
- [34] F. Xu, L. Jin, Y. Jin, Z. Nie, and H. Zheng, “Long noncoding RNAs in autoimmune diseases,” *Journal of Biomedical Materials Research Part A*, vol. 107, no. 2, pp. 468–475, 2019.
- [35] D. Jiang, B. Guo, F. Lin, Q. Hui, and K. Tao, “Effect of THBS1 on the biological function of hypertrophic scar fibroblasts,” *BioMed Research International*, vol. 2020, Article ID 8605407, 8 pages, 2020.
- [36] L. Chen, J. Li, Q. Li et al., “Non-coding RNAs: the new insight on hypertrophic scar,” *Journal of Cellular Biochemistry*, vol. 118, no. 8, pp. 1965–1968, 2017.
- [37] X. Ma and L. Liu, “Knockdown of FAM225B inhibits the progression of the hypertrophic scar following glaucoma surgery by inhibiting autophagy,” *Molecular Medicine Reports*, vol. 23, no. 3, 2021.
- [38] G. S. Park, M. K. An, J. H. Yoon et al., “Botulinum toxin type a suppresses pro-fibrotic effects via the JNK signaling pathway in hypertrophic scar fibroblasts,” *Archives of Dermatological Research*, vol. 311, no. 10, pp. 807–814, 2019.
- [39] J. Zhao, J. Yu, Y. Xu et al., “Epidermal HMGB1 activates dermal fibroblasts and causes hypertrophic scar formation in reduced hydration,” *The Journal of Investigative Dermatology*, vol. 138, no. 11, pp. 2322–2332, 2018.
- [40] H. H. Kang, I. K. Kim, H. I. Lee et al., “Chronic intermittent hypoxia induces liver fibrosis in mice with diet-induced obesity via TLR4/MyD88/MAPK/NF- κ B signaling pathways,” *Biochemical and Biophysical Research Communications*, vol. 490, no. 2, pp. 349–355, 2017.
- [41] P. Liu, F. Li, M. Qiu, and L. He, “Expression and cellular distribution of TLR4, MyD88, and NF- κ B in diabetic renal tubulointerstitial fibrosis, *in vitro* and *in vivo*,” *Diabetes Research and Clinical Practice*, vol. 105, no. 2, pp. 206–216, 2014.
- [42] Q. Shao, C. Jiang, Y. Xia et al., “Dioscin ameliorates peritoneal fibrosis by inhibiting epithelial-to-mesenchymal transition of human peritoneal mesothelial cells via the TLR4/MyD88/NF- κ B signaling pathway,” *International Journal of Clinical and Experimental Pathology*, vol. 12, no. 3, pp. 867–875, 2019.
- [43] A. M. Gressner and R. Weiskirchen, “Modern pathogenetic concepts of liver fibrosis suggest stellate cells and TGF- β as major players and therapeutic targets,” *Journal of Cellular and Molecular Medicine*, vol. 10, no. 1, pp. 76–99, 2006.
- [44] S. Dooley, B. Delvoux, M. Streckert et al., “Transforming growth factor beta signal transduction in hepatic stellate cells via Smad2/3 phosphorylation, a pathway that is abrogated during *in vitro* progression to myofibroblasts. TGF β signal transduction during transdifferentiation of hepatic stellate cells,” *FEBS Letters*, vol. 502, no. 1-2, pp. 4–10, 2001.
- [45] S. Xavier, E. Piek, M. Fujii et al., “Amelioration of radiation-induced fibrosis,” *The Journal of Biological Chemistry*, vol. 279, no. 15, pp. 15167–15176, 2004.
- [46] X. Yang, J. J. Letterio, R. J. Lechleider et al., “Targeted disruption of SMAD3 results in impaired mucosal immunity and diminished T cell responsiveness to TGF- β ,” *The EMBO Journal*, vol. 18, no. 5, pp. 1280–1291, 1999.
- [47] M. Neumann, E. Bentmann, D. Dormann et al., “FET proteins TAF15 and EWS are selective markers that distinguish FTLD with FUS pathology from amyotrophic lateral sclerosis with FUS mutations,” *Brain: A Journal of Neurology*, vol. 134, no. 9, pp. 2595–2609, 2011.
- [48] K. K. C. Li, B. L. Chau, and K. A. W. Lee, “Differential interaction of PRMT1 with RGG-boxes of the FET family proteins EWS and TAF15,” *Protein Science*, vol. 27, no. 3, pp. 633–642, 2018.
- [49] L. Pan, Y. Li, L. Jin, J. Li, and A. Xu, “TRPM2-AS promotes cancer cell proliferation through control of TAF15,” *The International Journal of Biochemistry & Cell Biology*, vol. 120, p. 105683, 2020.
- [50] L. Chen, Q. Chen, S. Kuang et al., “USF1-induced upregulation of LINC01048 promotes cell proliferation and apoptosis in cutaneous squamous cell carcinoma by binding to TAF15 to transcriptionally activate YAP1,” *Cell Death & Disease*, vol. 10, no. 4, p. 296, 2019.

Research Article

BMSCs Regulate Astrocytes through TSG-6 to Protect the Blood-Brain Barrier after Subarachnoid Hemorrhage

Yilv Wan ¹, Min Song,² Xun Xie,² Zhen Chen,³ Ziyun Gao,³ Xiang Wu,³ Rui Huang,³ and Min Chen ³

¹Department of Neurosurgery, The First Affiliated Hospital of Nanchang University, Nanchang, Jiangxi 330000, China

²The Second Clinical Medical College of Nanchang University, Nanchang, Jiangxi 330000, China

³Department of Neurosurgery, The Second Affiliated Hospital of Nanchang University, Nanchang, Jiangxi 330000, China

Correspondence should be addressed to Min Chen; chen85min@126.com

Received 19 February 2021; Revised 12 May 2021; Accepted 2 June 2021; Published 30 June 2021

Academic Editor: Miaomiao Wu

Copyright © 2021 Yilv Wan et al. This is an open access article distributed under the Creative Commons Attribution License, which permits unrestricted use, distribution, and reproduction in any medium, provided the original work is properly cited.

Background. In patients with subarachnoid hemorrhage (SAH), the damage of the blood-brain barrier (BBB) can be life-threatening. Mesenchymal stem cells are widely used in clinical research due to their pleiotropic properties. This study is aimed at exploring the effect of BMSCs regulating astrocytes on the BBB after SAH. **Methods.** The SAH model was established by perforating the blood vessels. BMSCs were transfected with TSG-6 inhibitor plasmid and cocultured with astrocytes. Intravenous transplantation of BMSCs was utilized to treat SAH rats. We performed ELISA, neurological scoring, Evans blue staining, NO measurement, immunofluorescence, BBB permeability, Western blot, HE staining, Nissl staining, and immunohistochemistry to evaluate the effect of BMSCs on astrocytes and BBB. **Results.** SAH rats showed BBB injury, increased BBB permeability, and brain histological damage. BMSCs will secrete TSG-6 after being activated by TNF- α . Under the influence of TSG-6, the NF- κ B and MAPK signaling pathways of astrocytes were inhibited. The expression of iNOS was reduced, while occludin, claudin 3, and ZO-1 expression was increased. The production of harmful substances NO and ONOO⁻ decreased. The level of inflammatory factors decreased. The apoptosis of astrocytes was weakened. TSG-6 secreted by BMSCs can relieve inflammation caused by SAH injury. The increase in BBB permeability of SAH rats was further reduced and the risk of rebleeding was reduced. **Conclusion.** BMSCs can regulate the activation of astrocytes through secreting TSG-6 in vivo and in vitro to protect BBB.

1. Introduction

Subarachnoid hemorrhage (SAH) is a devastating form of stroke that leads to incurable outcomes [1, 2]. When SAH occurs, a variety of pathophysiological reactions starts immediately. Early brain injury (EBI) refers to direct brain damage and secondary pathophysiological reactions within 72 hours after SAH occurs, including increased intracranial pressure and decreased cerebral blood flow, and the resulting local cerebral ischemia [3]. These changes immediately lead to neuronal cell death, blood-brain barrier (BBB) permeability changes, and brain edema [4–6]. In the basic structure that retains the normal function of the BBB, cytoplasmic adhesion proteins and transmembrane proteins together form its tight junction structure. Among them, cytoplasmic adhesion pro-

teins include several subtypes of zonula occludens-1 (ZO-1), ZO-2, and ZO-3, which form the basis of tight junctions. Transmembrane proteins are comprised of occludin, claudin, junctional adhesion molecules (JAM), and tricellulin [7, 8]. Therefore, it can be determined whether the BBB is damaged by detecting cytoplasmic adhesion proteins and transmembrane proteins.

Astrocytes play an important role in maintaining the integrity of the BBB [9]. Astrocytes can produce large amounts of NO through inducible nitric oxide synthase (iNOS) under the action of some stimulating factors. NO combines with superoxide anion (O²⁻) to produce a metabolite called peroxynitrite (ONOO⁻). ONOO⁻ is not only a potent biological oxidant but also a very toxic and destructive product [10]. Our previous work confirmed that it can reduce

the destruction of BBB and the degree of cerebral edema after cerebral hemorrhage by inhibiting the production of iNOS and ONOO⁻, but whether the target involves astrocytes is not unknown. Since astrocytes may have a close relationship with the amount of ONOO⁻ production in the state of 3neuroinflammation, bone marrow mesenchymal stem cells (BMSCs) were used to study the protective effect of BBB after SAH and astrocytes were used as the research target.

BMSCs are a group of adult stem cells with biological characteristics, multidifferentiation potential, and self-replication [11]. The recent literature review has noted that in SAH animal experiments, intravenous transplantation of BMSCs can improve the neurological function of SAH animals. The related mechanism may be linked to reducing neuronal apoptosis, reducing inflammation, and improving the microstructure of brain tissue. However, specific targets of BMSCs and the mechanisms involved need to be further studied [12]. More and more studies have confirmed that paracrine action played an important role in the treatment of BMSCs. Factors related to the paracrine action of BMSCs include interleukin 10 (IL-10), indoleamine 2,3-dioxygenase (indoleamine 2,3-dioxygenase), and tumor necrosis factor-induced protein 6 (TNF- α -induced protein 6 (TSG-6)) [13, 14]. TSG-6 has become an important anti-inflammatory factor for studying the paracrine effects of BMSCs [13, 15].

With the deepening of research on TSG-6, the downstream signaling pathways regulated by TSG-6 are gradually discovered by researchers. Choi has pointed out that TSG-6 had a bearing on the downstream nuclear factor kappa B (NF- κ B) signaling pathway [14]. In addition, related studies have believed that inhibiting the downstream NF- κ B signaling pathway was an important way for TSG-6 to exert its biological characteristics [16, 17]. The NF- κ B family includes transcription factors such as p65, which are involved in cell apoptosis and inflammation [18]. As another important pathway in the nervous system, mitogen-activated protein kinase (MAPK) is a set of proteases that can be stimulated by different cells and plays a role in regulating inflammation, oxidative stress, etc. [19]. The MAPK family includes p38MAPK, JNK, and ERK1/2. Among them, p38MAPK and JNK mainly play a role in inflammation and apoptosis, while ERK1/2 plays a role in proliferation and differentiation [20]. Although the results of previous studies supported that BMSCs can reduce brain edema after cerebral hemorrhage and protect BBB through TSG-6, there is no relevant research on whether BMSCs can decrease BBB damage through TSG-6 in SAH. In addition, since astrocytes play an important part in the neuroinflammatory process and maintaining the integrity of the BBB, whether TSG-6 regulates astrocyte targets through related signaling pathways needs further verification. Through the research of this subject, we can clarify the role of BMSCs in regulating target cells through TSG-6, to provide new ideas and basis for BMSCs in the research and treatment of SAH.

2. Results

2.1. Characteristic of SAH Modeling. We established a rat model of SAH to observe the pathological changes of SAH. No rat died in the sham group (0 of 8 rats). Approximately,

13.51% of the rats (37 of 5) classified into the SAH group died within 24 hours after SAH induction. To observe whether the SAH model was successful, we performed the neurobehavioral score of mNSS on the rats. As found in Figure 1(a), the score of the sham group was significantly lower than that of the SAH group. After modeling, rats in the SAH group had walking instability, limb hemiplegia, and poor response to external stimuli. Subsequently, the brains of the two groups of rats were taken out. In Figure 1(b), we observed that the ventral surface of the rats in the sham group was smooth. No bleeding was seen, and the general structure of the brain tissues was not significantly changed. However, the SAH group rats showed obvious blood accumulation on the surface of the temporal cortex and no obvious changes in the gross structure of brain tissue. To further determine whether the model was successful, the degree of brain histological injury was observed by HE (Figure 1(c)) and Nissl staining (Figure 1(d)). HE staining showed histological damage in both the prefrontal lobe and hippocampus in the SAH group compared with the sham group. Nissl bodies were reduced and neurons were damaged in the prefrontal cortex and hippocampus in the SAH group compared with the sham group. Results of HE and Nissl staining showed that the neurologic scores obtained in this model were reliable and positively correlated with the histology/pathologic changes of the SAH brain. To further examine whether astrocytes were affected by the breakdown of the BBB, immunohistochemistry was used to measure the markers of activated astrocytes GFAP+. Figure 1(e) revealed that GFAP+ positive was increased in the SAH group. The above suggested the success of SAH modeling. It was primarily manifested in the destruction of BBB and the activation of astrocytes.

2.2. BMSCs Secreted TSG-6 to Protect Activated Astrocytes. To determine the effect of BMSCs on astrocytes in a SAH model, we conducted a series of in vitro experiments. In Figure 2(a), qRT-PCR was used to measure the expression of TSG-6. It was found that when TNF- α stimulated BMSC activation, the expression of TSG-6 increased. To study whether TSG-6 expression affected activated astrocytes, we silenced the TSG-6 gene of BMSC cells. Figure 2(b) indicated that after silencing the TSG-6 gene, the expression level of TSG-6 decreased. It provided direct evidence that the silent TSG-6 was successfully constructed. Figures 2(c) and 2(d) data revealed that after BMSCs were stimulated by TNF- α to secrete TSG-6, TSG-6 promoted astrocyte occludin, claudin 3, and ZO-1 expression in both mRNA and protein levels, while iNOS was reduced. In the case of silencing TSG-6 in BMSCs, the expression levels of astrocyte occludin, claudin 3, and ZO-1 were reduced but iNOS was increased. Figure 2(e) showed that BMSCs stimulated by TNF- α to secrete TSG-6 decreased astrocyte apoptosis while silencing of TSG-6 in BMSC promoted astrocyte apoptosis. Figure 2(f) displayed that BMSCs stimulated by TNF- α to secrete TSG-6 increased the invasion ability of astrocytes while the invasion ability of astrocytes was reduced after silencing of TSG-6 in BMSCs. In summary, these findings suggested that TSG-6 secreted by BMSCs could increase the production of tight junction proteins in astrocytes, with increased invasion and less apoptosis.

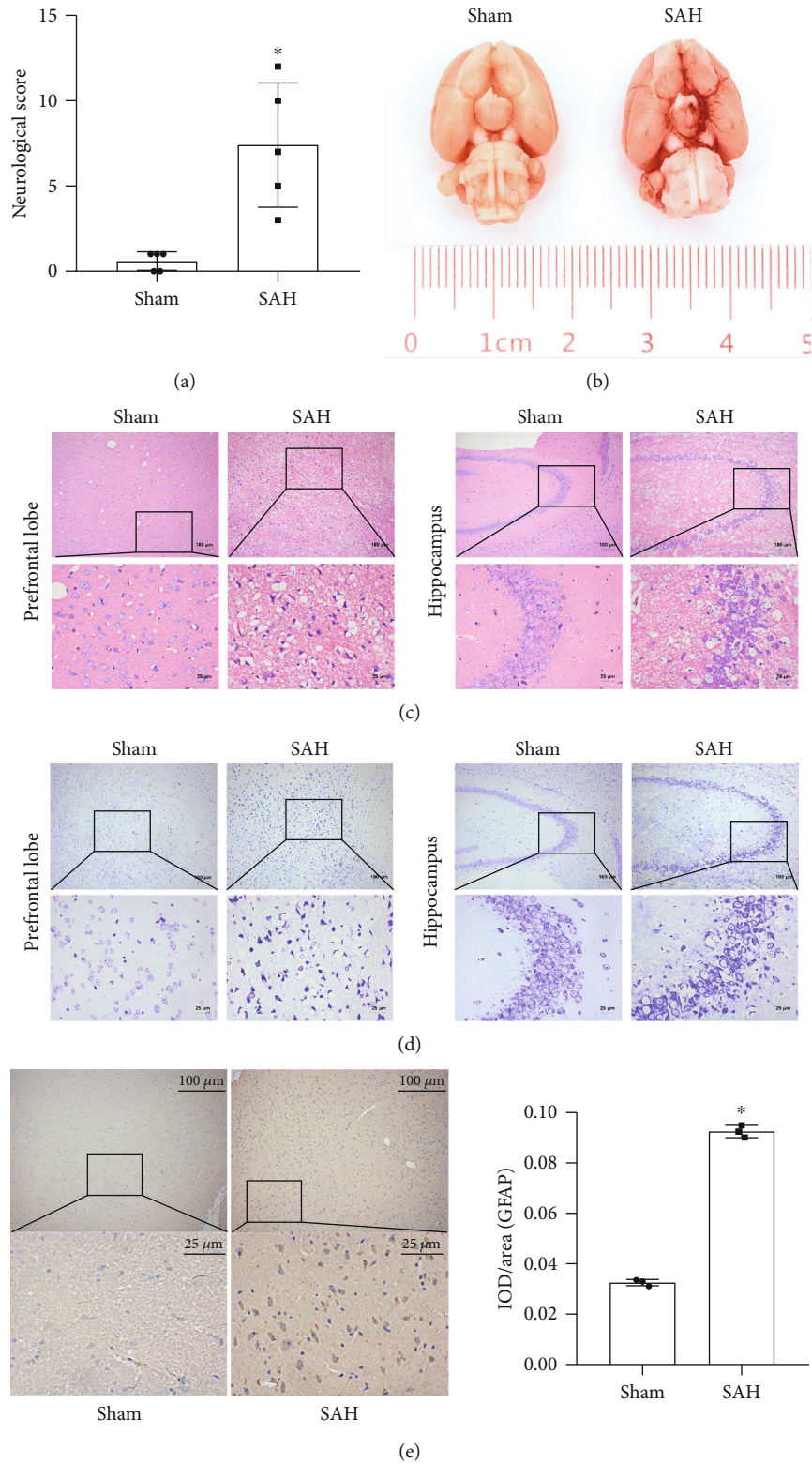


FIGURE 1: Pathological features of the SAH model. (a) Quantitative analysis of neurological scores. (b) Representative brains from the sham and SAH groups. (c) HE staining. (d) Nissl staining. (e) Immunohistochemical was used to detect of positive expression of activated astrocyte marker GFAP+. *Compared with the sham group, $P < 0.05$. The above results were all measurement data, expressed as mean \pm SD, and an unpaired t -test was used between the two groups.

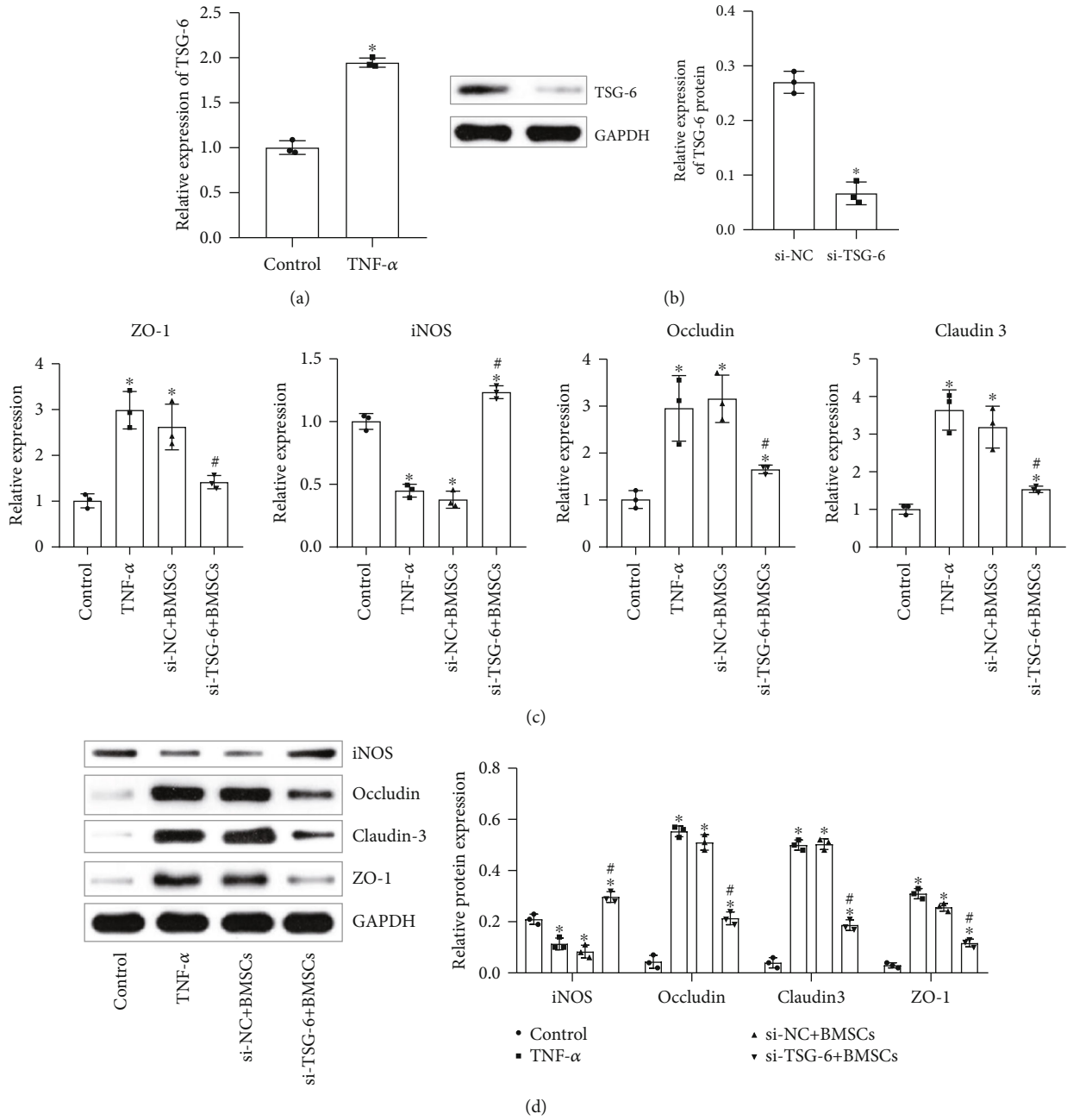
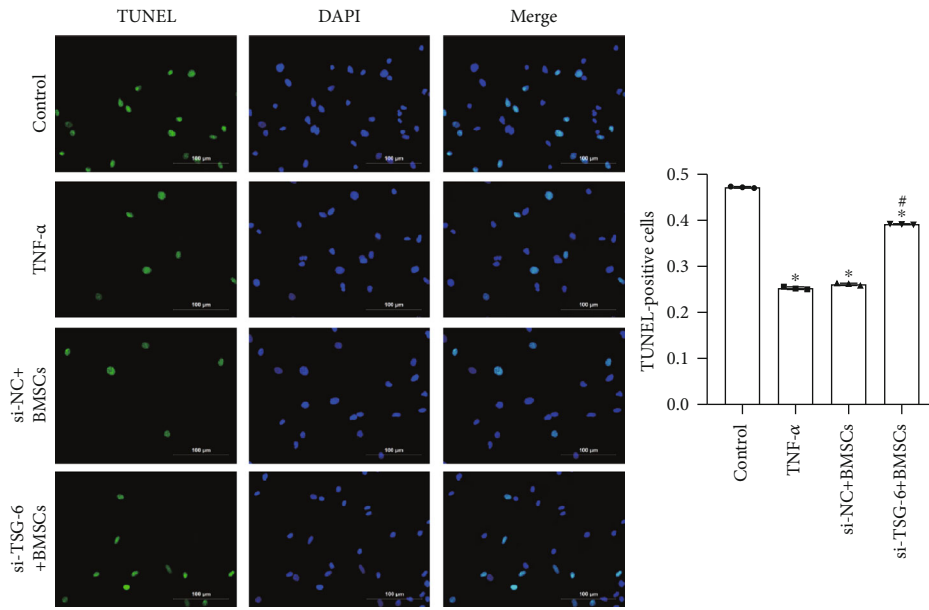
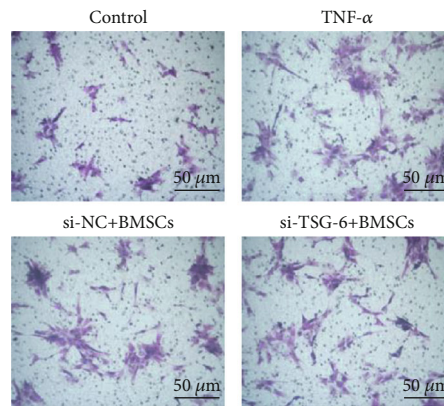


FIGURE 2: Continued.



(e)



(f)

FIGURE 2: The effect of TSG-6 secreted by BMSCs on activated astrocytes. (a) qRT-PCR was utilized to detect TSG-6 expression in BMSC cells. (b) Western blot analysis of the expression of TSG-6 in BMSC cells. (c) qRT-PCR was utilized to test the expression levels of occludin, claudin 3, ZO-1, and iNOS in activated astrocytes. (d) Western blot was used to measure the protein expression levels of occludin, claudin 3, ZO-1, and iNOS in astrocytes. (e) TUNEL assay was used to detect astrocyte apoptosis (scale bar, 100 μm). (f) Invasion of astrocytes was examined by transwell assay (scale bar, 50 μm). BMSCs (medium containing BMSCs (TNF- α activation group)), si-NC+BMSCs (medium containing BMSCs (NC siRNA + TNF- α activation group)), and si-TSG-6+BMSCs (medium containing BMSCs (siRNA-TSG-6 + TNF- α activation group)). *Compared with the control group, $P < 0.05$; #compared with the si-NC+BMSC group, $P < 0.05$. The above experimental results were all measurement data. Data were expressed as the mean \pm SD. One-way ANOVA and Tukey's test were used only for the data comparison between multiple groups.

2.3. BMSCs Regulated the NF- κ B/MAPK Signaling Pathway through TSG-6. We further investigated whether TSG-6 activated the NF- κ B/MAPK pathway in astrocytes. We used qRT-PCR and Western blot to measure the expression of the NF- κ B and MAPK signaling pathway genes. The data results in Figure 3 showed that compared with that in the control group, the expression of mRNAs related to the NF- κ B signaling pathway (NF- κ B) and MAPK signaling pathway (p38, JNK, ERK1, and ERK2) in the TNF- α group was inhibited. Compared with the si-NC + BMSC group, the expression of the NF- κ B signaling pathway (NF- κ B) and MAPK signaling pathway (p38, JNK, ERK1, and ERK2) in the si-TSG-6 + BMSC group was considerably increased. The above results demonstrated that TSG-6 secreted by BMSCs could inhibit the NF- κ B/MAPK signaling pathway in astrocytes.

2.4. Astrocytes Were Protected by Inhibition of NF- κ B. The above experimental results suggested that TSG-6 secreted by BMSCs can inhibit the expression of the NF- κ B signaling pathway. We further studied the effect of the NF- κ B signaling pathway on activating astrocytes. First, we used the NF- κ B blocker to silence the expression of NF- κ B in astrocytes. Figure 4(a) demonstrated that the expression of NF- κ B in the si-NF- κ B group decreased, indicating that the si-NF- κ B group was successfully constructed. Data in Figures 4(b)–4(d) showed that compared with the si-NC group, the levels of related inflammatory factors IL-6, IL-1 β , IFN- γ , TGF- β 1, and iNOS in the si-NF- κ B group decreased. This indicated that si-NF- κ B reduced the inflammatory response in astrocytes. Figure 4(e) showed that si-NF- κ B increased occludin, claudin 3, and ZO-1 expression in astrocytes. We further detected astrocyte apoptosis. Figure 4(e) showed that si-NF- κ B inhibited astrocyte apoptosis. Therefore, inhibition of the NF- κ B signaling pathway was an effective way to protect astrocytes against injury. We speculated that TSG-6 secreted by BMSCs may protect activated astrocytes by inhibiting the expression of the NF- κ B signaling pathway.

2.5. Inhibition of the MAPK Signaling Pathway Protected Astrocytes. To learn the influence of the MAPK signaling pathway on astrocytes, we primarily used MAPK blockers to silence the expression of MAPK in astrocytes. The result of Figure 5(a) revealed that the expression of p38 decreased, indicating that the si-MAPK group was successfully constructed. Figures 5(b)–5(f) showed that after inhibiting the expression of MAPK, the levels of related inflammatory factors IL-6, IL-1 β , IFN- γ , TGF- β 1, and iNOS secreted by astrocytes decreased. Moreover, the fluorescence intensity of occludin, claudin 3, and ZO-1 increased. Finally, the flow cytometry results indicated that astrocyte apoptosis was reduced in the si-MAPK group compared with the si-NC group. In short, inhibiting the MAPK signaling pathway could also protect activated astrocytes. We suspected that TSG-6 secreted by BMSCs may protect astrocytes by inhibiting the expression of the MAPK signaling pathway.

2.6. BMSCs Regulated Astrocytes through TSG-6 to Protect the BBB after SAH. To further study whether TSG can protect the BBB, we conducted animal experiments to explore.

Figure 6(a) examined that the SAH model resulted in decreased TSG-6 and increased iNOS expression in brain tissue, while activated BMSCs promoted TSG-6 and reduced iNOS protein expression. Silencing of TSG-6 in BMSCs can decrease TSG-6 and promote iNOS protein expression. Compared with the si-NC + BMSC group, the expression of p38, JNK, p-JNK, ERK, p-ERK, p65, and p-p65 was increased in the si-TSG-6 + BMSC group. The data in Figure 6(b) showed that inhibition of TSG-6 can promote the expression of genes associated with the NF- κ B/MAPK signaling pathway. Compared with the si-NC + BMSC group, the levels of IFN- γ , IL-6, IL-1 β , and TGF- β 1 in the si-TSG-6 + BMSC group were increased. It was found in Figure 6(c) that the inflammatory response of astrocytes is enhanced after blocking the expression of TSG-6 in BMSCs. In Figure 6(d), Evans blue staining was used to measure the permeability of the BBB. The results demonstrated that silencing of TSG-6 in BMSCs can enhance the permeability of the BBB, which caused harmful substances to enter the neurons of the brain tissue. Figures 6(e) and 6(f) identified that TSG-6 secreted by BMSCs can reduce the formation of NO and ONOO⁻ in SAH rats which is a direct result of BBB destruction. In Figure 6(g), the immunofluorescence results showed that TSG-6 secreted by BMSCs downregulated the expression of GFAP and iNOS in SAH rats, while the expression of GFAP and iNOS was upregulated in the si-TSG-6 + BMSC group compared with the si-NC + BMSC group. The above indicated that TSG-6 secreted by BMSCs could inhibit inflammation and decrease BBB damage in SAH rats through the NF- κ B/MAPK signaling pathway.

3. Material and Methods

3.1. Animals. We purchased 45 SPF (specific pathogen-free) SD rats with a weight of 200 ± 20 g and 6–8 weeks old from Hunan Slack Jingda Experimental Animal Co. Ltd. The disposal of animals during the experiment complied with the “Guiding Opinions on Treating Experiment Animals” issued by the Ministry of Science and Technology in 2006. Eight of them were selected as the sham group, and the remaining 37 were used to construct the SAH model.

3.2. SAH Model. The SAH model was established by perforating the blood vessels. The animals were anesthetized by intraperitoneal injection of 1% (*w/v*) sodium pentobarbital (35 μ mg/kg). The bifurcation of the right common carotid artery was exposed. The external carotid artery was separated. The blood flow was blocked with a vascular clamp. Blunt 3-0 single-stranded nylon sutures were inserted into the internal carotid artery from the bifurcation of the common carotid artery 18–20 mm to cause the artery to rupture. The suture was maintained for about 15 s and then pulled out. Then, the wound was closed. The procedure of the sham group was as of the SAH group, except that the blood vessel was not punctured. 37 animals were used for modeling, of which 5 died. The modeling success rate was calculated by the number of animals successfully modeled/total number of animals (the modeling success rate = $32/37 * 100\%$).

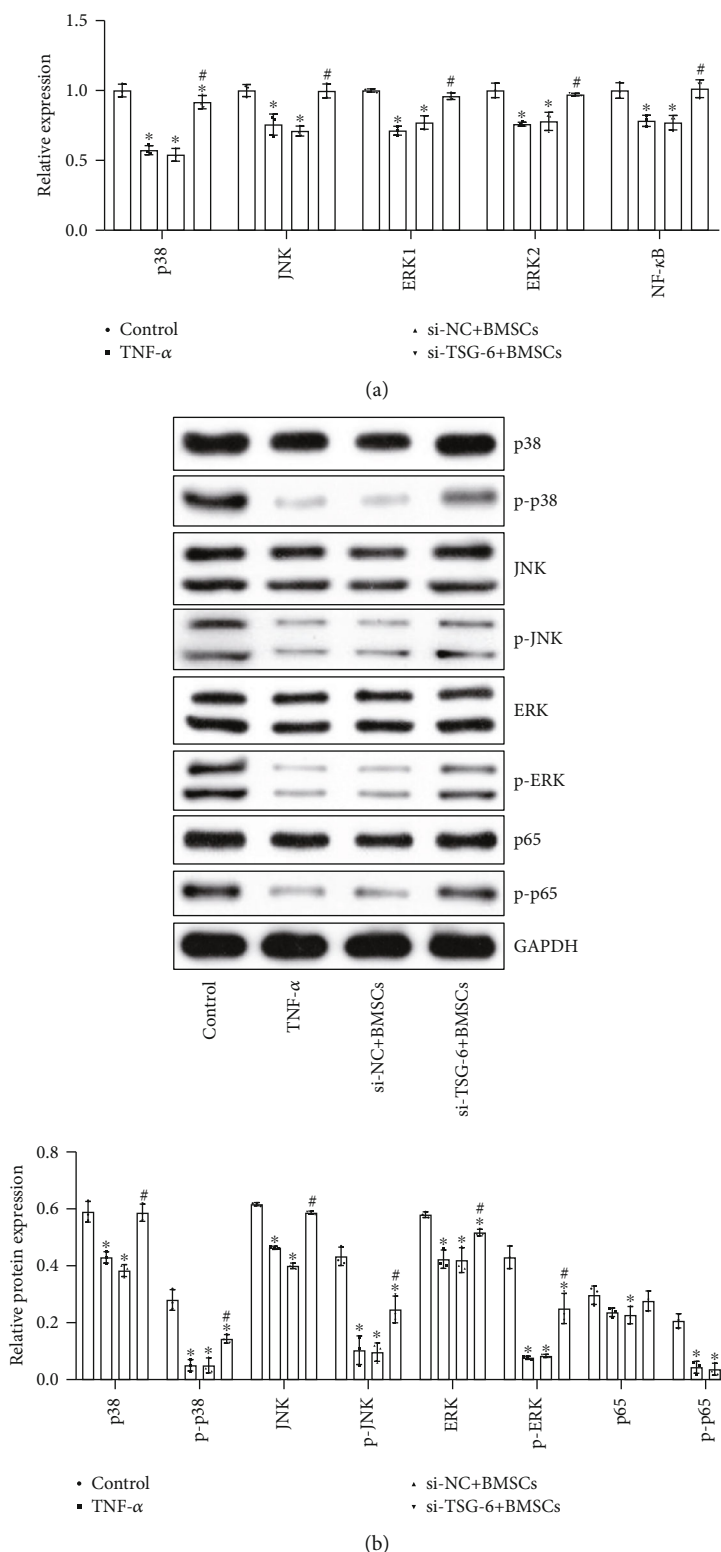


FIGURE 3: TSG-6 secreted by BMSCs inhibited the activation of the NF-κB/MAPK signaling pathway. (a) qRT-PCR measured the expression of the NF-κB/MAPK signaling pathway. (b) Western blot observed the protein expression of the NF-κB/MAPK signaling pathway. BMSCs (medium containing BMSCs (TNF-α activation group)), si-NC + BMSCs (medium containing BMSCs (NC siRNA + TNF-α activation group)), and si-TSG-6 + BMSCs (medium containing BMSCs (siRNA-TSG-6 + TNF-α activation group)). *Compared with the control group, $P < 0.05$; # compared with the si-NC + BMSC group, $P < 0.05$. The above experimental results were all measurement data. Data were expressed as the mean \pm SD. One-way ANOVA and Tukey's test were used only for the data comparison between multiple groups.

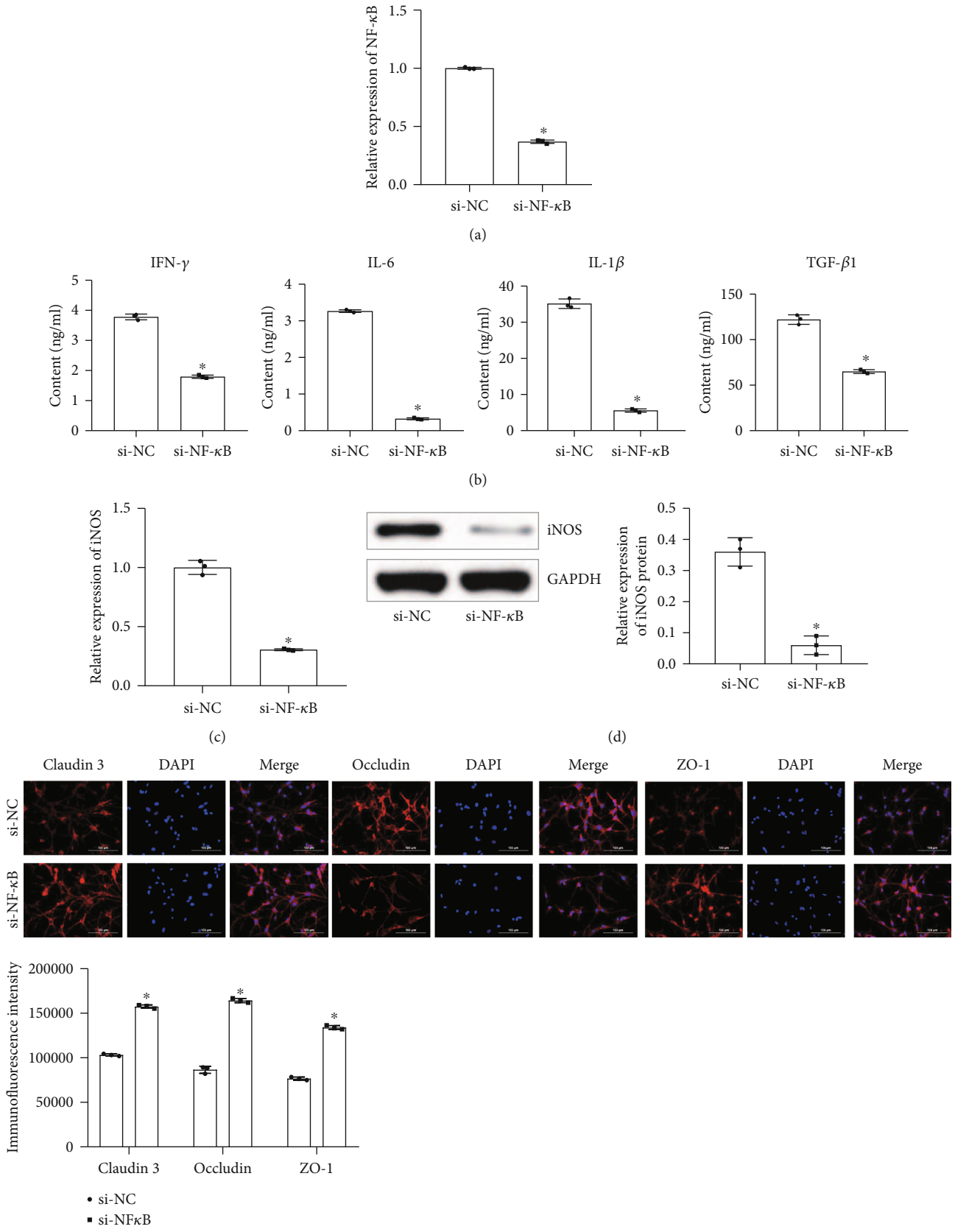


FIGURE 4: Continued.

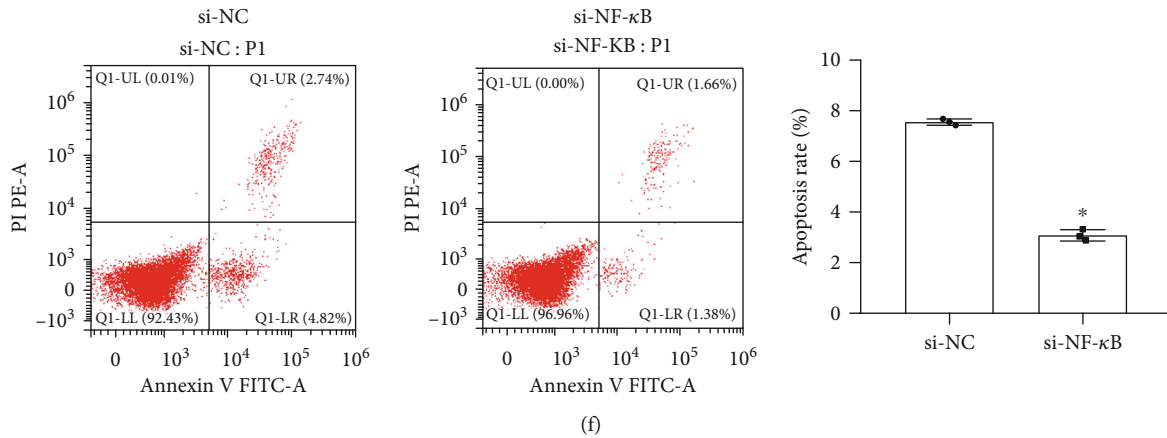


FIGURE 4: Astrocytes were protected by inhibition of NF- κ B. (a) qRT-PCR tested the expression of NF- κ B. (b) ELISA was used to measure the content of IFN- γ , IL-6, IL-1 β , and TGF- β 1 in astrocytes. (c) qRT-PCR detected the expression of iNOS. (d) Western blot measured the protein expression of iNOS. (e) Fluorescence intensity of claudin 3, occludin, and ZO-1 was detected by immunofluorescence (scale bar, 100 μ m). (f) Flow cytometry was used to measure the apoptosis rate of astrocytes. * Compared with the si-NC group, $P < 0.05$. The above experimental results were all measurement data. Data are expressed as the mean \pm SD. The unpaired t -test was used between the two groups.

3.3. Cell Culture. Human bone marrow mesenchymal stem cells (hBMSCs) and astrocytes were purchased from HonorGene (Changsha Aibiwei Biotechnology Co. Ltd.). 2×10^5 astrocytes/well were activated by lipopolysaccharide (LPS) and placed in the lower transwell compartment. BMSCs were cultured in the human mesenchymal stem cell culture medium (Cyagen Biosciences Inc., Guangzhou, China) at 37°C and 5% CO₂. When the third-generation BMSC reached 80% fusion, which was inoculated in a 24-well culture plate at 1.0×10^5 cells/well, 2 mL of complete medium was added to each well. BMSCs are activated by TNF- α . TSG-6 siRNA and NC siRNA were taken out and frozen on ice. Two centrifuge tubes were taken, and each tube was added with a 95 μ L serum-free medium, and then, 100 μ g TSG-6 siRNA and 5 μ L Lip 2000 were added into the centrifuge tubes, respectively. NC siRNA was also added to the corresponding centrifuge tubes in this way. TSG-6 siRNA and NC siRNA were transfected into BMSCs activated by TNF- α . The cells were then cultured at 37°C for 24 hours. Subsequently, BMSCs of one of the above treatments were placed in the upper compartment and cocultured with astrocytes at 37°C for 24 h. According to the composition contained in the medium of the upper chamber, they were divided into control (medium-control group), BMSCs (medium containing BMSCs (TNF- α activation group)), si-NC + BMSCs (medium containing BMSCs (NC siRNA + TNF- α activation group)), and si-TSG-6 + BMSCs (medium containing BMSCs (siRNA-TSG-6 + TNF- α activation group)).

3.4. BMSC Intervention In Vivo. 3×10^6 cells (including BMSCs, si-NC + BMSCs, and si-TSG-6 + BMSCs) in what was the same treatment as in the cell experiment were suspended in 1 mL of PBS within 1 hour after successful induction of SAH and then slowly injected through the femoral vein for 5 minutes. The needle was pulled out. The femoral vein was ligated. In the SAH group, rats were intravenously injected with the same amount of PBS without BMSCs. Then,

the 32 successfully modeled animals were divided into 5 groups, 8 in each group: the SAH group, BMSC group, si-NC + BMSC group, and si-TSG-6 + BMSC group.

3.5. Assessment of Neurological Injury. The modified neurological severity score (mNSS) includes a series of comprehensive tests to evaluate motor (muscle state, abnormal movement), sensory (visual, tactile, and proprioceptive), and reflex capabilities. A point was awarded for a specific task or tested reflexes that were not performing. Therefore, the higher the score, the more serious the injury (normal score: 0; maximum score: 18). After successful modeling, mNSS was evaluated to determine the severity of the injury.

3.6. Enzyme-Linked Immunosorbent Assay (ELISA). After the specimens were placed at room temperature for 2 hours, they were centrifuged at 2–8°C at 1000 g for 15 minutes and the supernatant was taken for testing. The kit was as follows: IL-1 β (China, CSB-E04640R), IL-6 (China, CSB-E08055R), IFN- γ (China, CSB-E04579R), and TGF- β 1 (China, CSB-E04727R) were purchased from Cusabio Biotech Co. Ltd. ONOO⁻ (China, JL21035) was purchased from Jianglaibio Co. Ltd. Horseradish peroxidase-labeled avidin solution 100 μ L was added to each well and incubated at 37°C for 1 hour. Substrate solution (90 μ L) was added to each well in order, and color was developed at 37°C for 15–30 minutes. 50 μ L of termination solution was added to each well in sequence to terminate the reaction. Within 5 minutes after the end of the reaction, the optical density (OD value) of each well was measured sequentially under an enzyme standard instrument (China, MB-530) at the wavelength of 450 nm.

3.7. Quantitative Real-Time PCR (qRT-PCR). The total RNA from tissue and cell samples was extracted using a TRIzol kit (15596026, Thermo, USA). In the next step, the extracted total RNA was reversely transcribed into cDNA according to the instruction of a reverse transcription kit (CW2569, CWBIO, China). Subsequently, real-time PCR was performed on a

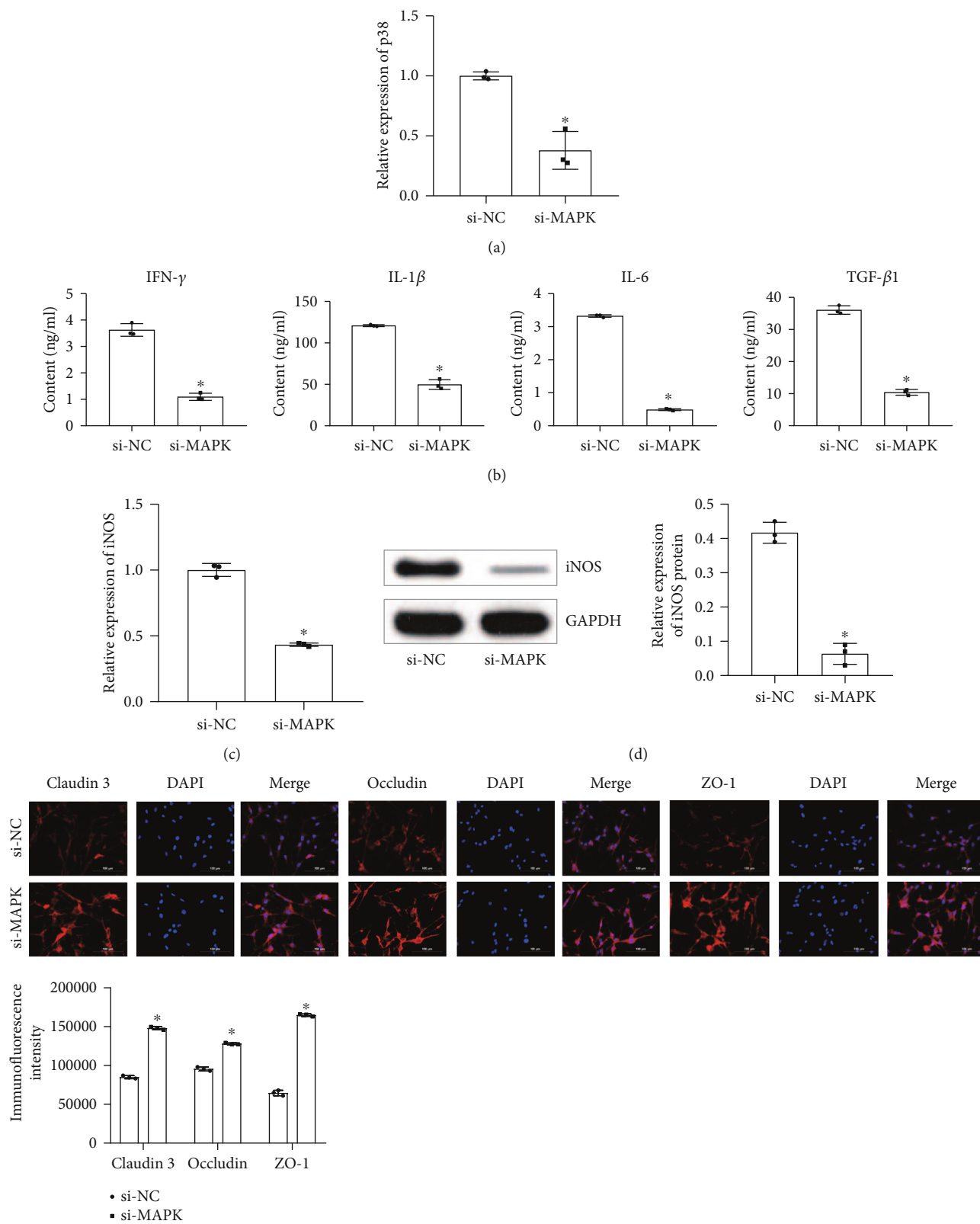


FIGURE 5: Continued.

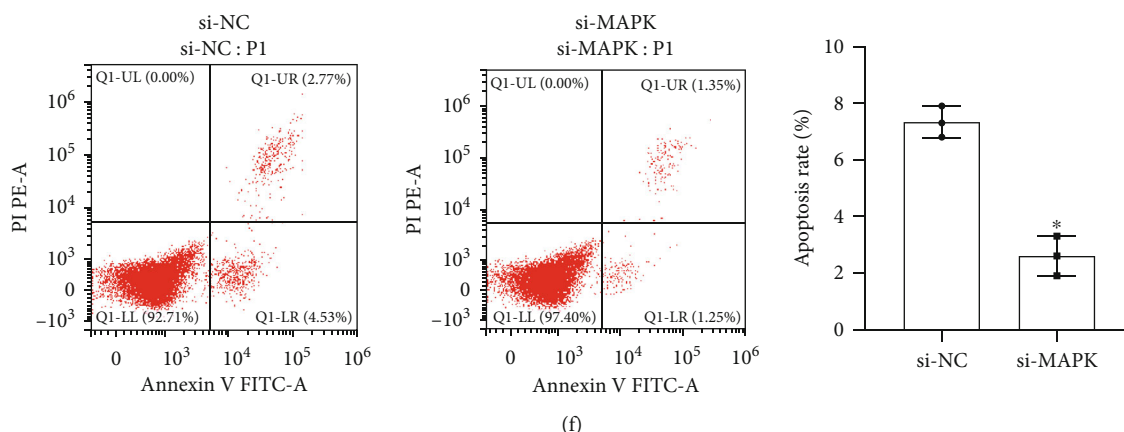


FIGURE 5: Inhibition of the MAPK signaling pathway to regulate astrocytes. (a) qRT-PCR detected p38 expression. (b) ELISA to measure the contents of IFN- γ , IL-1 β , IL-6, and TGF- β 1. (c) qRT-PCR examined the expression of iNOS. (d) Western Blot examined the protein expression of iNOS. (e) Immunofluorescence detection of occludin, claudin 3, and ZO-1 fluorescence intensity (scale bar, 100 μ m). (f) Flow cytometry was used to measure the apoptosis rate of astrocytes. *Compared with the si-NC group, $P < 0.05$. The above experimental results were all measurement data. Data are expressed as the mean \pm SD. The unpaired t -test was used between the two groups.

fluorescence quantitative RCP instrument (QuantStudio 1, Thermo, USA) using an UltraSYBR Mixture (CW2601, CWBIO, China). The internal reference was β -actin, and the primer sequence was found in Table 1. With 2 μ g cDNA as the template, the relative quantitative method ($2^{-\Delta\Delta Ct}$ method) was used to calculate the relative transcription level of the target gene: $\Delta\Delta Ct = \Delta$ experimental group $- \Delta$ control group, $\Delta Ct = Ct(\text{target gene}) - Ct(\beta - \text{actin})$. The experiment was repeated three times.

3.8. Western Blot. The RIPA kit (R0010, Solarbio, China) was used to extract the total protein of tissue and cell samples. The BCA method was used to determine the protein concentration. The protein was separated by 10% SDS-PAGE electrophoresis and transferred to the NC membrane by electrotransfer. The membrane was blocked with 5% skimmed milk for 2 h at room temperature and incubated with the primary antibody overnight at 4°C. For primary antibodies, we used rabbit anti-TSG-6 (0.1 μ g/mL, ab204049, Abcam), rabbit anti-iNOS (1:500, ab3523, Abcam), rabbit anti-ZO-1 (1:4000, 21773-1-AP, Proteintech), rabbit anti-occludin (1:1000, 27260-1-AP, Proteintech), rabbit anti-claudin 3 (1:500, 16456-1-AP, Proteintech), rabbit anti-p38 (1:1000, 14064-1-AP, Proteintech), rabbit anti-p-p38 (1:1000, ab4822, Abcam), rabbit anti-JNK (1:1000, ab179461, Abcam), rabbit anti-p-JNK (1:5000, ab124956, Abcam), rabbit anti-p65 (1:800, 10745-1-AP, Proteintech), rabbit anti-p-p65 (1:800, ab97726, Abcam), rabbit anti-ERK (1:2000, 16443-1-AP, Proteintech), rabbit anti-p-ERK (1:5000, ab201015, Abcam), and rabbit anti-GAPDH (1:5000, 10494-1-AP, Proteintech). The membrane was rinsed 3 times with TBST for 10 minutes each time and then incubated with HRP goat anti-rabbit IgG (1:5000, SA00001-2, Proteintech, USA). The membrane was immersed in Super ECL Plus (K-12045-D50, Advansta, USA) for luminescence development. GAPDH was used as an internal reference. The target band was analyzed by ImageJ software.

3.9. Transwell Assay. MSC cells were cultured in DMEM containing 10% FBS with 1% double resistance and NESS in an incubator at 37°C, 5% CO₂, and saturated humidity. Logarithmically grown cells were placed in a six-well plate and treated in groups after adherence to the wall. Matrigel was diluted with 100 μ L cold, serum-free MEM medium for each well, and the final concentration was 200 μ g per well. Matrigel was incubated at 37°C for 30 minutes and the supernatant was sucked out. 500 μ L complete medium of 10% FBS was placed in the lower compartment at 37°C for 48 h. The upper chamber was taken out and put into a new well containing PBS. The upper chamber was washed with PBS 3 times, and the upper chamber cells were wiped clean with a cotton ball. The cell was fixed with 4% paraformaldehyde for 20 minutes. 0.1% crystal violet was dyed for 5 min and washed 5 times. The film was given to the slide and photographs were taken under the microscope. The chamber was taken out and soaked in 10% acetic acid for decolorization. At 550 nm, the absorbance (OD) value was determined by a microplate reader.

3.10. Flow Cytometry. The cells were washed with PBS twice and centrifuged at 2000 rpm for 5 min each. About 1–5 \times 10⁵ cells were collected. 500 μ L binding buffer was in addition to suspend cells. After Annexin V-FITC (5 μ L) was added, 5 μ L propidium iodide was added and mixed. The reaction lasted for 5–15 min at room temperature and away from light. The results were noted and detected by flow cytometry within 1 h.

3.11. TUNEL. The cell climbing piece was fixed with 4% paraformaldehyde for 30 minutes. Proteinase K working fluid was prepared. 100 μ L 1 \times equilibrium buffer was added to each sample and incubated at room temperature for 10–30 min. 50 μ L TdT incubation buffer was added to the cell climbing piece. The DAPI (Wellbio, China) working fluid was dyed at 37°C for 10 min. The cell climbing piece was washed with

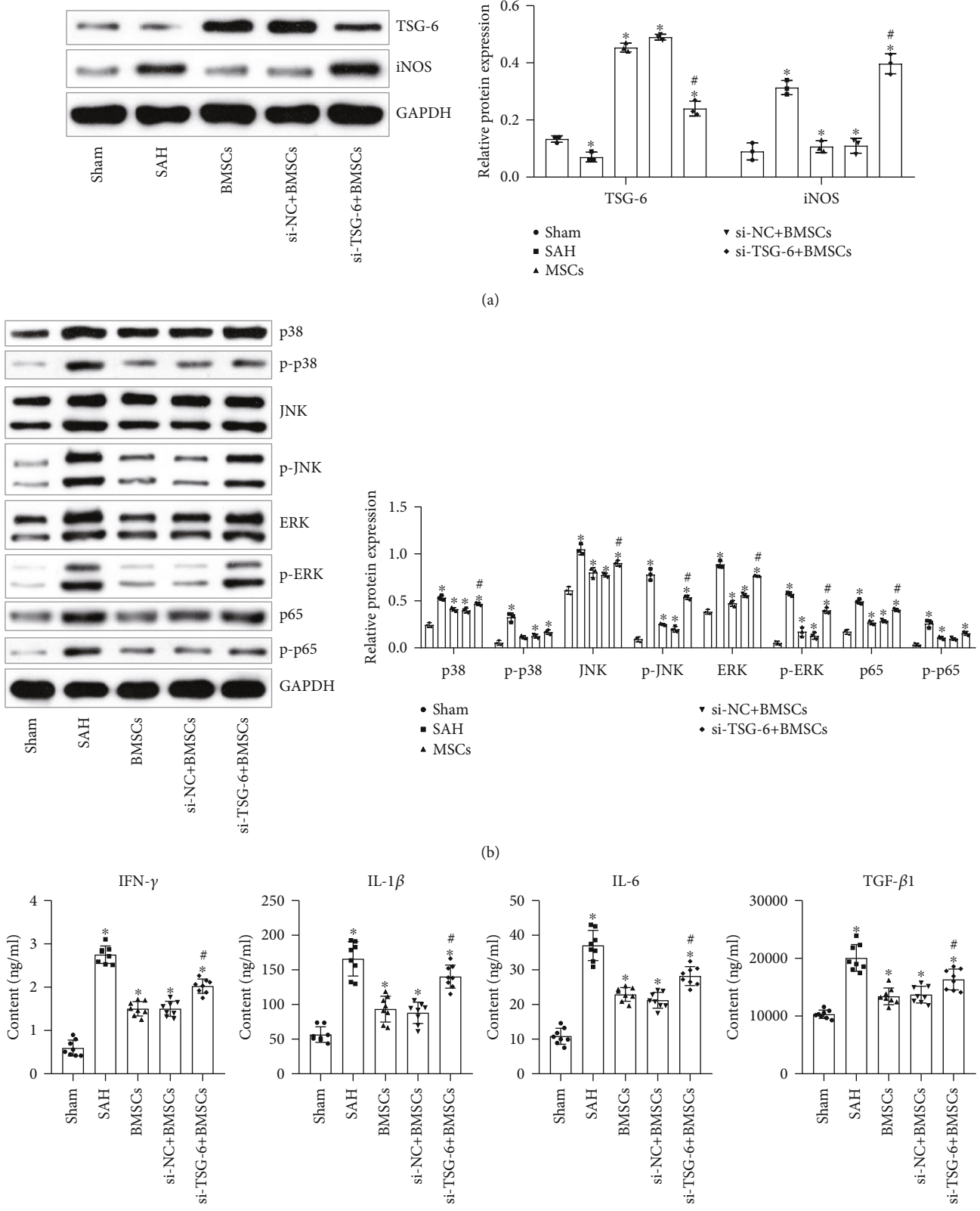
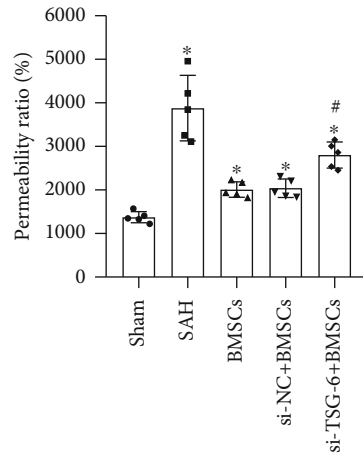
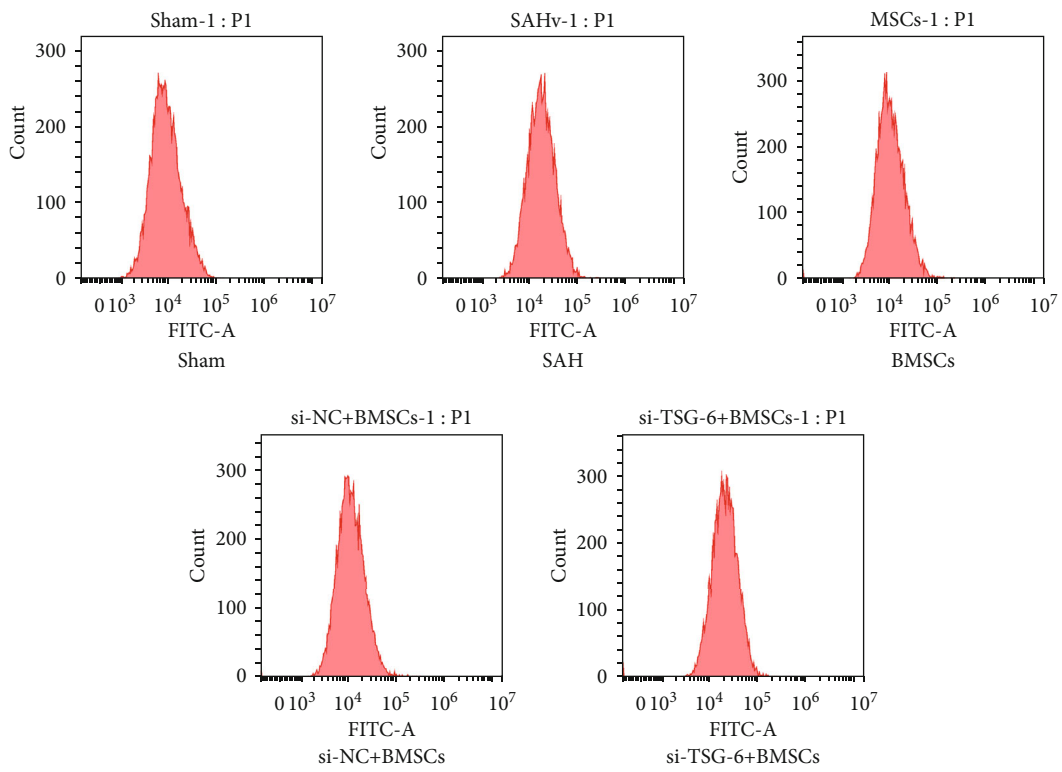


FIGURE 6: Continued.



(d)



(e)

FIGURE 6: Continued.

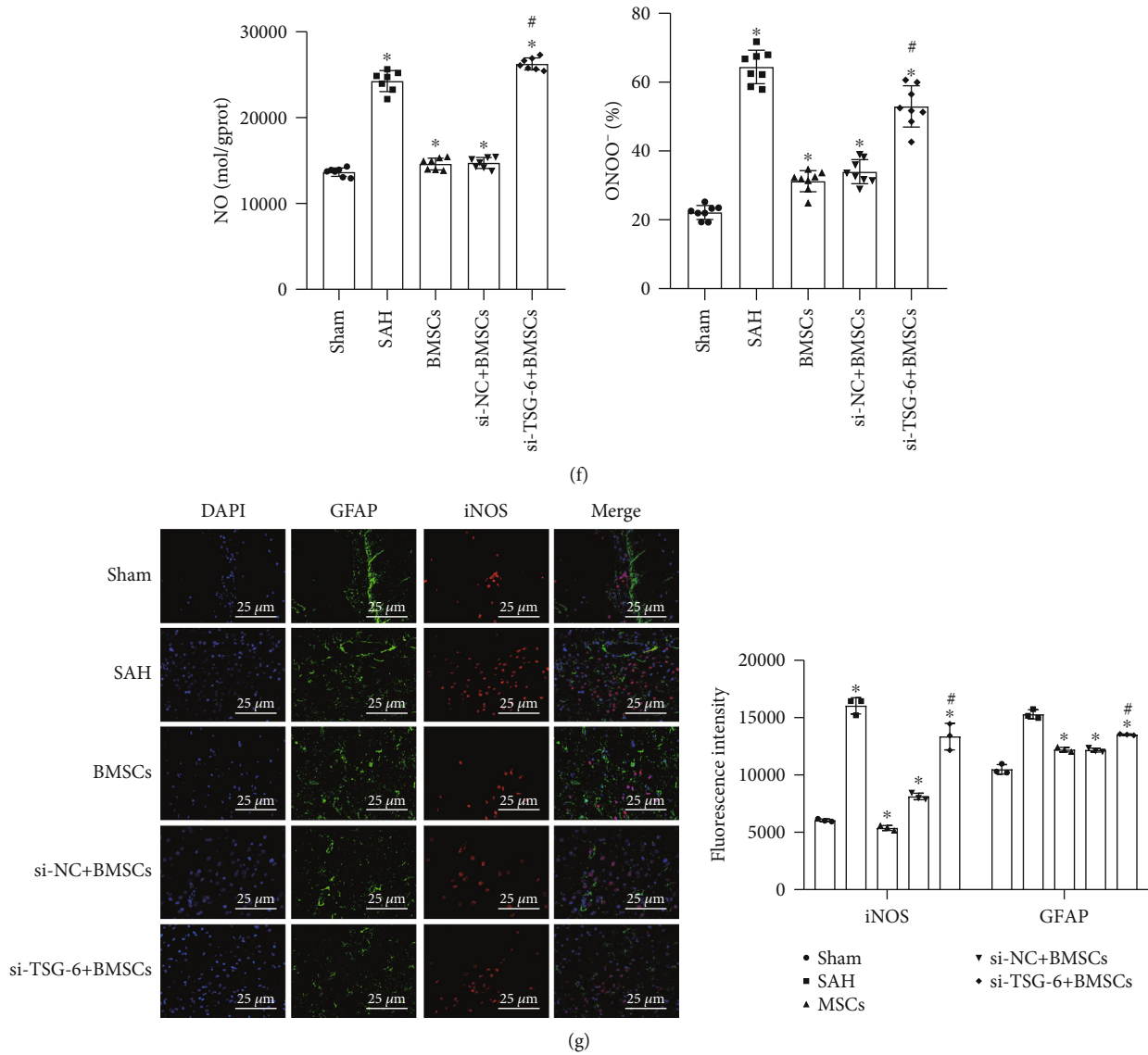


FIGURE 6: BMSCs regulate astrocytes through TSG-6 to treat rats suffering from SAH. (a) The expression of TSG-6 and iNOS was measured by qRT-PCR and Western blot. (b) qRT-PCR and Western blot were used to measure the expression level of the NF- κ B/MAPK signaling pathway. (c) ELISA was used to test the level of inflammatory factors secreted by activated astrocytes. (d) Evans blue detected changes in BBB permeability. (e) NO fluorescent probe analyzed the amount of NO production in the cell. (f) Determination of the ONOO⁻ level in rat serum by ELISA. (g) Double immunofluorescence staining was used to measure the expression of iNOS (red) and GFAP (green). BMSCs (medium containing BMSCs (TNF- α activation group)), si-NC+BMSCs (medium containing BMSCs (NC siRNA + TNF- α activation group)), and si-TSG-6+BMSCs (medium containing BMSCs (siRNA-TSG-6 + TNF- α activation group)). * Compared with the sham group, $P < 0.05$; # compared with the si-NC+BMSC group, $P < 0.05$. The above experimental results were all measurement data. Data are expressed as the mean \pm SD. One-way ANOVA and Tukey's test were used for the data comparison between multiple groups.

PBS 5 min 3 times. The samples were stored in the dark and observed under a fluorescence microscope (BA410T, Motic, China).

3.12. Immunohistochemistry (IHC). The slices were baked at 60°C for 12 h. The slices were dewaxed and heated to repair the antigen. An appropriately diluted primary antibody GFAP (556330, BD Pharmingen) was added overnight at 4°C. 50–100 μ L anti-mouse IgG-HRP (Bio-Rad, Hercules, CA) was added and incubated at 37°C for 30 min and then

washed with PBS for 5 min 3 times. Diaminobenzidine (DAB, ZSGB-BIO, China) was used to be a chromogen. The samples were placed in xylene for 10 min 2 times. The neutral gum was sealed and enforced under a microscope.

3.13. Immunofluorescence (IF). We took out the cell climbing piece and washed it with PBS 2–3 times. 0.3% Triton was added at 37°C for 30 minutes. The slices were baked at 60°C for 12 h. The slices were dewaxed and heated to repair the antigen. The slices were incubated with 5% BSA at 37°C for

TABLE 1: Primer sequences.

Gene	Sequences (5'-3')
TSG-6	F: TCTTTACAGACCCGAAGCG R: TCTTCCTACAAAGCCGTGGAC
iNOS	F: AGGCACAAGACTCTGACACCC R: CGCACTTCTGTCTCTCCAAACCC
Occludin	F: CCCAGACCACTATGAAACCGACT R: CAGCCATGTACTCTTCGCTCT
Claudin 3	F: AAGATGTACGACTCGCTGCT R: CTGCCAGTAGGATAGACACCAC
p38	F: AGCTTACCGATGACCAGTT R: CACGTAGCCGGTCATTTTCGTC
JNK	F: ACGAGTTTTATGATGACGCCTT R: CCACAGACCATAAATCCACGTT
ERK1	F: GCTGCTGTGTCTTTATCTATCCC R: CTCCACCCCTCTGTAGCAC
ERK2	F: TCATTTCGCTGCAAGATGGAC R: TAAATCCCAGGCAGTGAGCAT
RELA	F: CACCAAAGACCCACCTCACCG R: CTTGCTCCAGGTCTCGCTTC
ZO-1	F: CCTAATAAGAACAGAGCCGAGCA R: GCAACATCAGCAATCGGTCCA
β -Actin	F: ACATCCGTAAAGACCTCTATGCC R: TACTCCTGCTTGCTGATCCAC

60 minutes. Primary antibody claudin 3 (1:50, 16456-1-AP, Proteintech), occludin (1:50, 27260-1-AP, Proteintech), and ZO-1 (1:200, 21773-1-AP, Proteintech) were added to the cell climbing pieces at 4°C overnight. 50–100 μ L anti-rabbit IgG-labeled fluorescent antibodies (1:200, SA00013-4, Proteintech) were added to the cell climbing pieces and incubated at 37°C for 90 min. Primary antibody GFAP (1:1000, ab279290, Proteintech) and iNOS (1:500, ab3523, Proteintech) were added to the slices at 4°C overnight. 50–100 μ L anti-mouse (1:200, SA00013-5, Proteintech) and rabbit (1:200, SA00013-4, Proteintech) IgG-labeled fluorescent antibodies were added to the cell climbing pieces and incubated at 37°C for 90 min. DAPI solution was used to stain the nucleus at 37°C for 10 min, and PBS was used to wash the cell climbing piece for 5 min 3 times. Buffer glycerin was used to seal the cell climbing piece. The samples were stored in the dark and observed under a fluorescence microscope (BA210T, Motic, China).

3.14. Evans Blue Dye Assays. Rats were injected intravenously with 8 mL/kg 0.6% NaF 2 hours after successful modeling. After 30 minutes, the rats were perfused with 10 mL normal saline. The cerebral hemispheres were homogenized with 30% trichloroacetic acid and centrifuged at 10000 g for 5 minutes. From the supernatant, the concentration of NaF was measured with a fluorometer under excitation at 460 nm and emission at 515 nm through a standard curve. The permeability ratio was calculated by dividing the NaF (pg/mg) of the study case/the NaF of the normal control.

3.15. Assay of Intracellular NO Production. Cells were resuspended with diluted DAF-FM DA at a concentration of 1×10^6 /mL. The cells were incubated in a 37°C cell incubator for 20 minutes, and mixed upside down every 5 minutes to make the probe fully contact with the cells. The cells were washed three times with PBS (pH 7.4) to sufficiently remove DAF-FM DA that did not enter the cells. Fluorescence intensity was measured by a flow meter under 495 nm excitation wavelength and 515 nm emission wavelength.

3.16. HE Staining. The brain tissue was fixed with 4% paraformaldehyde at room temperature for 24 h. The samples were dehydrated in gradient ethanol and embedded into a wax block. Each sample was cut into 2–3 μ m slices. The slices were baked at 62°C for 2–6 h, then dewaxed, and rehydrated. The cytoplasm was stained with different degrees of red and or pink, in sharp contrast with the blue nucleus. The slices were observed under a microscope (BA210T, Motic, Singapore).

3.17. Nissl Staining. The brain tissue was fixed with 4% paraformaldehyde at room temperature for 24 h. The samples were dehydrated in gradient ethanol and embedded into a wax block. Each sample was cut into 2–3 μ m slices. The slices were baked at 62°C for 2–6 h, then dewaxed, and rehydrated. The slices were added with Nissl staining solution and incubated for 5 min. The slices were added with Nissl differentiation solution until nuclei and particles were clear. The slices were observed under a microscope (BA210T, Motic, Singapore).

3.18. Statistical Analysis. All Data were analyzed by Graph-Pad Prism 8.0 software (GraphPad Software, San Diego, California, USA). The unpaired *t*-test was used between the two groups conforming to the normal distribution. Comparisons among multiple groups were conducted by one-way analysis of variance (ANOVA), followed by Tukey's post hoc test. A value of $P < 0.05$ was considered to be statistically significant.

4. Discussion

The purpose of this study was to determine whether TSG-6 secreted by BMSCs could protect the BBB after SAH by regulating the NF- κ B/MAPK signaling pathway. To this end, we discussed in vitro and in vivo levels. In vitro experiments showed that TSG-6 secreted by BMSCs upregulated the expression of ZO-1, occludin, and claudin 3, downregulated the expression of iNOS and cell apoptosis, promoted cell invasion, and inhibited the NF- κ B/MAPK signaling pathway in astrocytes. Silencing TSG-6 in BMSCs canceled this effect in astrocytes. Further inhibition of the NF- κ B/MAPK signaling pathway showed that the inflammatory response of astrocytes was decreased, the expressions of ZO-1, occludin, and claudin 3 were upregulated and apoptosis was inhibited. In addition, in vivo studies confirmed that transplanted BMSCs can effectively protect BBB by secreting TSG-6.

Currently, early brain injury (EBI) and delayed cerebral ischemia (DCI) are the main manifestations of SAH in two stages. Neuroprotection and antivasospasm are the most studied directions in many studies [21, 22]. Once the intracranial aneurysm ruptures, SAH is usually catastrophic because there is no effective treatment for the combined

brain injury [23]. In most countries, nimodipine is the only drug approved for the treatment of SAH because no other intervention has been shown to work [24]. Therefore, there is an urgent need to study potential molecular targets of SAH to optimize therapeutic efficacy. In recent years, the research on BMSC transplantation is very hot. Predecessors verified the effectiveness and safety of BMSCs in the treatment of traumatic brain injury in mice [25]. We targeted astrocytes, which are closely related to the BBB, to treat SAH by intravenous transplantation of BMSCs. The endovascular perforation model of SAH is indeed not reproducible. In recent years, the endovascular perforation model duplicated the early pathophysiology of SAH. It has been widely used to study the early brain injury after SAH [26–29]. The endovascular perforation model has been proposed for clinical trial [30]. Therefore, in this project, we constructed an endovascular perforation rat model to study the effects of BMSCs on astrocytes and BBB after SAH through secreting TSG-6. After BMSCs activated by TNF- α were transplanted through the vein, BMSCs secreted a large amount of TSG-6. We found that TSG-6 could regulate the activation of astrocytes, protect BBB, and effectively treat SAH.

BBB destruction and neuroinflammation are the main pathological changes of brain injury, which lead to poor prognosis after SAH [31]. Studies have confirmed that TSG-6 is a powerful anti-inflammatory factor. Its powerful anti-inflammatory effects mainly include inhibition of proteases in the inflammatory network, binding to corresponding hydrophobic acid fragments and blocking the proinflammatory effects of the bound and inhibiting neutrophils to migrate to the center of inflammation [32]. Studies have also established a rat brain trauma model to confirm that a large amount of paracrine TSG-6 after intravenous transplantation of BMSCs can improve the neurological dysfunction of rats [33]. Previous studies mainly revealed that exogenous TSG-6 exhibited anti-inflammatory properties. We conducted experiments on this basis, and the results were in line. The focus of our research was placed on targeting TSG-6 to regulate astrocytes in the SAH rat model. Our data showed that the expression of TSG-6 in brain tissue was decreased after SAH. TSG-6 secreted by BMSCs promoted the expression of ZO-1, occludin, and claudin 3 in astrocytes, decreased the expression of iNOS and apoptosis level, promoted cell invasion, protected BBB, and alleviated early brain injury. Astrocyte injury and early brain injury were aggravated to some extent after TSG-6 was silenced in BMSCs. These results indicated that the neuroprotective effect of BMSCs was related to phenotypic regulation of astrocyte translocation through TSG-6. But the way of action was not clear yet, which is the content of our next research. Considering the limited budget and space, we did not evaluate neurobehavior dysfunction after treatment of BMSC and si-TSG-6 + BMSC in this project. In future research, we will further improve. It is necessary to indicate where the BMSCs go in the brain and whether they can release TSG-6 in the SAH brain. It can further confirm in vivo whether BMSCs act on astrocytes in the brain and whether TSG-6 was secreted by BMSCs to protect BBB after SAH. We hypothesized that BMSCs protected BBB by secreting TSG-6 in some form. In

the next project, we will explore this conjecture through fluorescence labeling in vivo and in vitro. Results need to be confirmed by using the TSG-6 KO mice to exclude the effect of endogenous TSG-6. Due to limited funding and inadequate animal handling facilities, TSG-6 KO was not used in this study to exclude endogenous TSG-6 interference. We will improve in the following study. This project lays a solid foundation for the following research.

Many important molecules participate in the destruction of the BBB through various independent or related signal transduction pathways. NF- κ B is a key transcription factor regulating the expression of various proinflammatory genes [34]. To elucidate the molecular mechanism of TSG-6 anti-inflammatory function, we first evaluated its effect on NF- κ B activity. The results revealed that TSG-6 secreted by BMSCs inhibited the expression of p65 and p-p65 in LPS-activated astrocytes and the inflammatory response was alleviated. Silencing TSG-6 in BMSCs had the opposite effect. In addition to the NF- κ B pathway, it has also been observed that MAPK can mediate the expression of GFAP and various astrocyte regulatory molecules in vivo and in vitro [35]. The MAPK pathway may be triggered by oxidative stress, which may hinder the recovery of the BBB. This may be linked to the increase in the concentration of proinflammatory cytokines and mediators (IFN- γ , IL-6, and IL-1 β). Our results showed that TSG-6 secreted by BMSCs inhibited LPS-activated astrocytes p-38, p-p38, JNK, p-JNK, ERK, and p-ERK levels and reduced the inflammatory response. Silencing TSG-6 in BMSCs promoted the expression of p-38, p-p38, JNK, p-JNK, ERK, p-ERK, and inflammatory response. The results in vivo were consistent with those in cells. We hypothesized that TSG-6 secreted by BMSCs protected astrocytes and BBB by inhibiting the NF- κ B/MAPK signaling pathway. To test this conjecture, we further inhibited the NF- κ B/MAPK signaling pathway in astrocytes. We found that the inflammatory response of astrocytes was reduced. The expressions of ZO-1, occludin, and claudin 3 were upregulated. Apoptosis was inhibited. Considering the limitations of space and budget, we did not perform inhibition of the NF- κ B/MAPK signaling pathway in vivo to observe the effect of transplanted BMSCs on BBB of SAH rats by secreting TSG-6. Due to the small sample size, we did not carry out the analysis of sample size estimation, which needs to be further improved. In future projects, we will further explore the potential mechanism by which transplanted BMSCs protect BBB in SAH rats by secreting TSG-6. We are also interested in whether inflammatory factors affect the BBB in a concentration-dependent manner, and we have further research ideas on the peculiar ways of their regulation. In our future research, we will pay more attention to the treatment of SAH by clinical vein transplantation of BMSCs.

5. Conclusion

In conclusion, our data demonstrated that TSG-6 secreted by BMSCs could play endogenous brain protection after SAH. In vitro, we demonstrated that TSG-6 secreted from BMSCs can induce astrocytes to anti-inflammatory through the

NF- κ B/MAPK pathway. In vivo, we demonstrated that BMSCs regulated the activation of astrocytes through secreting TSG-6 to protect BBB after SAH. Our findings may provide new ideas and basis for BMSCs in the research and treatment of SAH.

Data Availability

The data used to support to the findings of this study are available from the corresponding author upon request.

Ethical Approval

This study was approved by the animal experiment ethics committee of the First Affiliated Hospital of Nanchang University and the Second Affiliated Hospital of Nanchang University and conducted in strict accordance with the national institutes of health guidelines for the care and use of experimental animals.

Conflicts of Interest

The authors declare that they have no competing interests.

Authors' Contributions

Yilv Wan performed the experiment, analyzed the data, and wrote the original draft; Min Song, Xun Xie, Zhen Chen, Ziyun Gao, Xiang Wu, and Rui Huang performed the experiment; Min Chen guided the experiment, reviewed, and edited the manuscript.

Acknowledgments

This work was supported by the National Natural Science Foundation of China (no. 81760224) and the youth foundation of the Second Affiliated Hospital of Nanchang University (2019YNQN12014).

References

- [1] G. Hou and H. Chen, "MEL ameliorates post-SAH cerebral vasospasm by affecting the expression of eNOS and HIF1 α via H19/miR-138/eNOS/NO and H19/miR-675/HIF1 α ," *Molecular Therapy - Nucleic Acids*, vol. 19, pp. 523–532, 2019.
- [2] A. K. Petridis, M. A. Kamp, J. F. Cornelius et al., "Aneurysmal subarachnoid hemorrhage," *Dtsch Arztebl In*, vol. 114, no. 13, pp. 226–236, 2017.
- [3] J. DjelilovicVranic, V. BasicKes, M. TiricCampara, E. Djozic, and J. Kulenovic, "Follow-up of vasospasm by transcranial doppler sonography (TCD) in subarachnoid hemorrhage (SAH)," *Acta Informatica Medica*, vol. 25, no. 1, pp. 14–18, 2017.
- [4] J. Ivanidze, R. A. Ferraro, A. E. Giambrone, A. Z. Segal, A. Gupta, and P. C. Sanelli, "Blood-brain barrier permeability in aneurysmal subarachnoid hemorrhage: correlation with clinical outcomes," *American Journal of Roentgenology*, vol. 211, no. 4, pp. 891–895, 2018.
- [5] F. Nakano, L. Liu, F. Kawakita et al., "Morphological characteristics of neuronal death after experimental subarachnoid hemorrhage in mice using double Immunoenzymatic technique," *The Journal of Histochemistry and Cytochemistry*, vol. 67, no. 12, pp. 919–930, 2019.
- [6] H. Suzuki, M. Fujimoto, F. Kawakita et al., "Tenascin-C in brain injuries and edema after subarachnoid hemorrhage: findings from basic and clinical studies," *Journal of Neuroscience Research*, vol. 98, no. 1, pp. 42–56, 2020.
- [7] H. Wang, T. Li, L. Zhao et al., "Dynamic effects of Ioversol on the permeability of the blood-brain barrier and the expression of ZO-1/occludin in rats," *Journal of Molecular Neuroscience*, vol. 68, no. 2, pp. 295–303, 2019.
- [8] S. Bhowmick, V. D'Mello, D. Caruso, A. Wallerstein, and P. M. Abdul-Muneer, "Impairment of pericyte-endothelium cross-talk leads to blood-brain barrier dysfunction following traumatic brain injury," *Experimental Neurology*, vol. 317, pp. 260–270, 2019.
- [9] P. Giannoni, J. Badaut, C. Dargazanli et al., "The pericyte-glia interface at the blood-brain barrier," *Clinical Science*, vol. 132, no. 3, pp. 361–374, 2018.
- [10] H. Chen, B. Guan, X. Chen et al., "Baicalin attenuates blood-brain barrier disruption and hemorrhagic transformation and improves neurological outcome in ischemic stroke rats with delayed t-PA treatment: involvement of ONOO⁻-MMP-9 pathway," *Translational Stroke Research*, vol. 9, no. 5, pp. 515–529, 2018.
- [11] Y. Li, F. Yang, M. Gao et al., "miR-149-3p regulates the switch between adipogenic and osteogenic differentiation of BMSCs by targeting FTO," *Molecular Therapy - Nucleic Acids*, vol. 17, pp. 590–600, 2019.
- [12] L. Xiong, L. Sun, Y. Zhang, J. Peng, J. Yan, and X. Liu, "Exosomes from bone marrow mesenchymal stem cells can alleviate early brain injury after subarachnoid hemorrhage through miRNA129-5p-HMGB1 pathway," *Stem Cells and Development*, vol. 29, no. 4, pp. 212–221, 2020.
- [13] S. J. Lee, J. Kim, W. H. Choi, S. R. Park, B. H. Choi, and B. H. Min, "Immunophenotype and immune-modulatory activities of human fetal cartilage-derived progenitor cells," *Cell Transplantation*, vol. 28, no. 7, pp. 932–942, 2019.
- [14] H. Choi, R. H. Lee, N. Bazhanov, J. Y. Oh, and D. J. Prockop, "Anti-inflammatory protein TSG-6 secreted by activated MSCs attenuates zymosan-induced mouse peritonitis by decreasing TLR2/NF- κ B signaling in resident macrophages," *Blood*, vol. 118, no. 2, pp. 330–338, 2011.
- [15] W.-J. Song, Q. Li, M. O. Ryu et al., "TSG-6 released from intraperitoneally injected canine adipose tissue-derived mesenchymal stem cells ameliorate inflammatory bowel disease by inducing M2 macrophage switch in mice," *Stem Cell Research & Therapy*, vol. 9, no. 1, p. 91, 2018.
- [16] R. Zhang, Y. Liu, K. Yan et al., "Anti-inflammatory and immunomodulatory mechanisms of mesenchymal stem cell transplantation in experimental traumatic brain injury," *Journal of Neuroinflammation*, vol. 10, no. 1, 2013.
- [17] Y. Liu, R. Zhang, K. Yan et al., "Mesenchymal stem cells inhibit lipopolysaccharide-induced inflammatory responses of BV2 microglial cells through TSG-6," *Journal of Neuroinflammation*, vol. 11, no. 1, p. 135, 2014.
- [18] W. Qin, J. Li, R. Zhu et al., "Melatonin protects blood-brain barrier integrity and permeability by inhibiting matrix metalloproteinase-9 via the NOTCH3/NF- κ B pathway," *Ageing*, vol. 11, no. 23, pp. 11391–11415, 2019.
- [19] J.-L. Lai, Y.-H. Liu, C. Liu et al., "Indirubin inhibits LPS-induced inflammation via TLR4 abrogation mediated by the

- NF- κ B and MAPK signaling pathways,” *Inflammation*, vol. 40, no. 1, pp. 1–12, 2017.
- [20] M. Chen, L. Lai, X. Li et al., “Baicalein attenuates neurological deficits and preserves blood-brain barrier integrity in a rat model of intracerebral hemorrhage,” *Neurochemical Research*, vol. 41, no. 11, pp. 3095–3102, 2016.
- [21] R. L. Macdonald, “Delayed neurological deterioration after subarachnoid haemorrhage,” *Nature Reviews Neurology*, vol. 10, no. 1, pp. 44–58, 2014.
- [22] S. Chen, H. Feng, P. Sherchan et al., “Controversies and evolving new mechanisms in subarachnoid hemorrhage,” *Progress in Neurobiology*, vol. 115, pp. 64–91, 2014.
- [23] A. L. de Oliveira Manoel, A. Goffi, T. R. Marotta, T. A. Schweizer, S. Abrahamson, and R. L. Macdonald, “The critical care management of poor-grade subarachnoid haemorrhage,” *Critical Care*, vol. 20, no. 1, 2016.
- [24] S. N. Neifert, E. K. Chapman, M. L. Martini et al., “Aneurysmal subarachnoid hemorrhage: the last decade,” *Translational Stroke Research*, vol. 12, no. 3, pp. 428–446, 2021.
- [25] W. Li, F. Yang, J. Gao, Y. Tang, J. Wang, and Y. Pan, “Over-expression of TRPC6 via CRISPR based synergistic activation mediator in BMSCs ameliorates brain injury in a rat model of cerebral ischemia/reperfusion,” *Neuroscience*, vol. 415, pp. 147–160, 2019.
- [26] J. Mo, B. Enkhjargal, Z. D. Travis et al., “AVE 0991 attenuates oxidative stress and neuronal apoptosis via Mas/PKA/CREB/UCP-2 pathway after subarachnoid hemorrhage in rats,” *Redox Biology*, vol. 20, pp. 75–86, 2019.
- [27] T. Zhang, P. Wu, E. Budbazar et al., “Mitophagy reduces oxidative stress via Keap1 (Kelch-like epichlorohydrin-associated protein 1)/Nrf2 (nuclear factor-E2-related factor 2)/PHB2 (Prohibitin 2) pathway after subarachnoid hemorrhage in rats,” *Stroke*, vol. 50, no. 4, pp. 978–988, 2019.
- [28] X. Hu, J. Yan, L. Huang et al., “INT-777 attenuates NLRP3-ASC inflammasome-mediated neuroinflammation via TGR5/cAMP/PKA signaling pathway after subarachnoid hemorrhage in rats,” *Brain, Behavior, and Immunity*, vol. 91, pp. 587–600, 2021.
- [29] F. A. Sehba, “Rat endovascular perforation model,” *Translational Stroke Research*, vol. 5, no. 6, pp. 660–668, 2014.
- [30] S. Chen, Q. Ma, P. R. Krafft et al., “P2X7R/cryopyrin inflammasome axis inhibition reduces neuroinflammation after SAH,” *Neurobiology of Disease*, vol. 58, pp. 296–307, 2013.
- [31] J. Pang, Y. Chen, L. Kuai et al., “Inhibition of blood-brain barrier disruption by an apolipoprotein E-mimetic peptide ameliorates early brain injury in experimental subarachnoid hemorrhage,” *Translational Stroke Research*, vol. 8, no. 3, pp. 257–272, 2017.
- [32] C. M. Milner and A. J. Day, “TSG-6: a multifunctional protein associated with inflammation,” *Journal of Cell Science*, vol. 116, no. 10, pp. 1863–1873, 2003.
- [33] A. J. Day and C. M. Milner, “TSG-6: a multifunctional protein with anti-inflammatory and tissue-protective properties,” *Matrix Biology*, vol. 78–79, pp. 60–83, 2019.
- [34] S. Park, J. J. Choi, B. K. Park, S. J. Yoon, J. E. Choi, and M. Jin, “Pheophytin *a* and chlorophyll *a* suppress neuroinflammatory responses in lipopolysaccharide and interferon- γ -stimulated BV2 microglia,” *Life Sciences*, vol. 103, no. 2, pp. 59–67, 2014.
- [35] B. Bellaver, D. G. Souza, L. D. Bobermin, D. O. Souza, C. A. Gonçalves, and A. Quincozes-Santos, “Resveratrol protects hippocampal astrocytes against LPS-induced neurotoxicity through HO-1, p38 and ERK pathways,” *Neurochemical Research*, vol. 40, no. 8, pp. 1600–1608, 2015.

Research Article

Oxidative Stress Level as a Predictor of Anastomotic Leakage after Rectal Surgery

Jiajun Luo, Hongxue Wu, Yu Yang, Yue Jiang, Jingwen Yuan, and Qiang Tong 

Department of Gastrointestinal Surgery I Section, Renmin Hospital of Wuhan University, Wuhan 430060, China

Correspondence should be addressed to Qiang Tong; qiangtong@whu.edu.cn

Received 4 April 2021; Accepted 4 June 2021; Published 29 June 2021

Academic Editor: Mingliang Jin

Copyright © 2021 Jiajun Luo et al. This is an open access article distributed under the Creative Commons Attribution License, which permits unrestricted use, distribution, and reproduction in any medium, provided the original work is properly cited.

Background. Early diagnosis of anastomotic leakage (AL) after rectal surgery can reduce the adverse effects of AL, thereby reducing morbidity and mortality. Currently, there are no accepted indicators or effective scoring systems that can clearly identify patients at risk of anastomotic leakage. **Methods.** A prospective study with assessment of the diagnostic accuracy of oxidative stress level (CAT, SOD, MDA) in serum and drain fluid compared to white blood cell count (WBC), C-reactive protein (CRP), and neutrophil percentage (NEUT) in prediction of AL in patients undergoing elective rectal surgery with anastomosis. **Results.** Most of the oxidative stress indicators we detected are of considerable significance in the diagnosis of anastomotic leakage. The level of MDA on postoperative day (POD)3 (areas under the curve (AUC): 0.831) and POD5 (AUC: 0.837) in the serum and on POD3 (AUC: 0.845) in the drain fluid showed the same excellent diagnostic accuracy as the level of CRP on the POD3 (AUC: 0.847) and POD5 (AUC: 0.896). **Conclusions.** The overall level of oxidative stress in serum and drain fluid is a reliable indicator for the early diagnosis of anastomotic leakage after rectal surgery. More specifically, among the redox indicators analyzed, MDA has almost the same predictive value as CRP, which provides another useful biomarker for the early diagnosis of anastomotic leakage.

1. Introduction

Colorectal cancer (CRC) is the third most commonly diagnosed malignancy and the fourth leading cause of cancer-related deaths in the world [1]. It is widely accepted that colorectal cancer continues to be a severe problem. Colorectal surgery is long established as the mainstay treatment for colorectal cancer [2]. Rectal cancer accounts for about 67% of colorectal cancers and has a higher incidence of postoperative anastomotic leakage (AL) than colon surgery [3]. AL occurs in 4%–33% [4] of patients and is a major complication after restorative resection for rectal cancer that may adversely impact morbidity, mortality, and functional outcomes [5, 6]. Despite efforts to reduce AL occurrence, the incidence of AL has remained relatively unchanged over the last several years [7].

The ongoing occurrence of AL is due to many factors including those pertaining to surgical technique such as blood supply, tension, suture type, or device deployment, as well as, patient-related factors such as frailty, poor nutritional status, or chemoradiotherapy [8]. AL is clearly associated

with the healing process following surgery of the gut. Reactive oxygen species (ROS) and oxidative stress have long been recognized as key components in wound healing [9]. Furthermore, data have shown that the production of specific ROS and the activation of specific formyl peptide receptors (FPRs) regulate intestinal wound healing [10]. Low concentrations of ROS production are necessary to ward off invading microorganisms and are crucial for cell survival signaling, but excessive ROS or impaired ROS detoxification causes oxidative damage, which may lead to AL [11].

At present, the surgeons' clinical risk assessment has a low predictive value for AL in rectal surgery [12]. Early diagnosis of AL is important to allow for alternative treatments to prevent morbidity and mortality. Many scholars have made great efforts to find early AL diagnostic markers. Previous studies have reported that C-reactive protein (CRP) [13–16], procalcitonin (PCT) [14], cytokines [17], lactate [18], and amylase [19] could help in the early diagnosis of AL, but limitations remain. Considering the important role of ROS in intestinal healing, we believe that the detection of ROS and oxidative stress levels could be a complementary

TABLE 1: Characteristics of rectal cancer (RC) patients.

Parameter	AL (<i>n</i> = 16)	Without AL (<i>n</i> = 254)	<i>P</i> value
Gender, M (%)	12 (75.0)	150 (59.1)	0.294
Age, mean ± s (years)	61.3 ± 10.3	62.7 ± 7.1	0.608
Comorbidities, <i>n</i> (%)			
Metabolic	3 (18.8)	13 (5.1)	0.060
Cardiovascular	6 (37.5)	52 (20.5)	0.120
ASA score, <i>n</i> (%)			0.544
1-2	12 (75.0)	172 (67.7)	
3	4 (25.0)	82 (32.3)	
Neo-adjuvant CRT, <i>n</i> (%)	5 (31.3)	26 (10.2)	0.010
Stage, TNM, <i>n</i> (%)			0.070
I	1 (6.2)	76 (29.9)	
II	7 (43.8)	54 (21.3)	
III	8 (50.0)	114 (44.9)	
IV	0 (0)	10 (3.9)	

TABLE 2: Comparison of CRP/WBC/NEUT on POD3 and POD5 in patients with and without anastomotic leak.

Parameter (mean ± SD)	AL (<i>n</i> = 16)	Without AL (<i>n</i> = 254)	<i>P</i> value
CPR _{POD3}	109.8 ± 39.8	65.2 ± 22.3	<0.001
WBC _{POD3}	9.492 ± 4.063	8.703 ± 3.086	0.332
NEUT _{POD3}	84.02 ± 5.847	78.05 ± 5.368	<0.001
CPR _{POD5}	111.2 ± 53.2	43.5 ± 18.4	<0.001
WBC _{POD5}	11.054 ± 3.844	7.723 ± 2.477	<0.001
NEUT _{POD5}	82.72 ± 10.96	74.01 ± 8.798	<0.001

CRP: C-reactive protein; NEUT: neutrophil percentage; WBC: white blood cells; POD: postoperative day.

method for the early diagnosis of AL. In this study, the levels of three redox indicators, catalase (CAT), malondialdehyde (MDA), and superoxide dismutase (SOD) will be determined in patients' serum and drain fluid and assessed for correlation with AL. We will also measure C-reactive protein (CRP) along with quantification of white blood cells (WBC) and neutrophil percentage (NEUT) for comparison to determine its diagnostic accuracy.

2. Materials and Methods

2.1. Patients. All patients were diagnosed with rectal cancer and underwent elective rectal surgery with primary anastomosis. The exclusion criteria included patients under 18 years of age, emergency operations, advanced cancers that were not amenable to curative resection, immunosuppression, and patients with severe infections or an American Society of Anesthesiologists (ASA) physical status ≥ 4 . Pre-operative workup included a physical examination, colonoscopy, computed tomography (CT), and chest X-ray or chest CT. The decision to perform laparoscopic or open surgery is based on the patient's condition and willingness. The diagnosis of AL is based on intestinal contents in the peritoneal drainage fluid and oral contrast agent exudation during fluo-

roscopy or CT examination. The present study was designed as a prospective observational pilot study. Written informed consent was obtained from all patients prior to enrolment. This study was approved by the Ethics Committee of Renmin Hospital of Wuhan University.

2.2. Analytical Methods. Blood samples were collected from patients on postoperative day (POD)3 and POD5. Blood was drawn by venipuncture, allowed to clot for 30 minutes, and then centrifuged (10 min, 1000×g). Serum was collected and kept frozen at -80° until examination. Drain fluid were collected on POD3 and POD5 and kept frozen at -80° until examination. The quantification of the WBC and NEUT was performed with a hematology analyzer. The C-reactive protein (CRP) concentration in serum was determined by the turbidimetric method with a CRP test. Catalase (CAT), malondialdehyde (MDA), and superoxide dismutase (SOD) levels in serum and drain fluid were determined using commercially available kits (Nanjing Jiancheng Bioengineering Institute, Nanjing, China).

2.3. Statistical Analysis. Statistical analyses were performed using SPSS Statistics 22.0 software. *P* values < 0.05 were considered statistically significant. The χ^2 test for independence

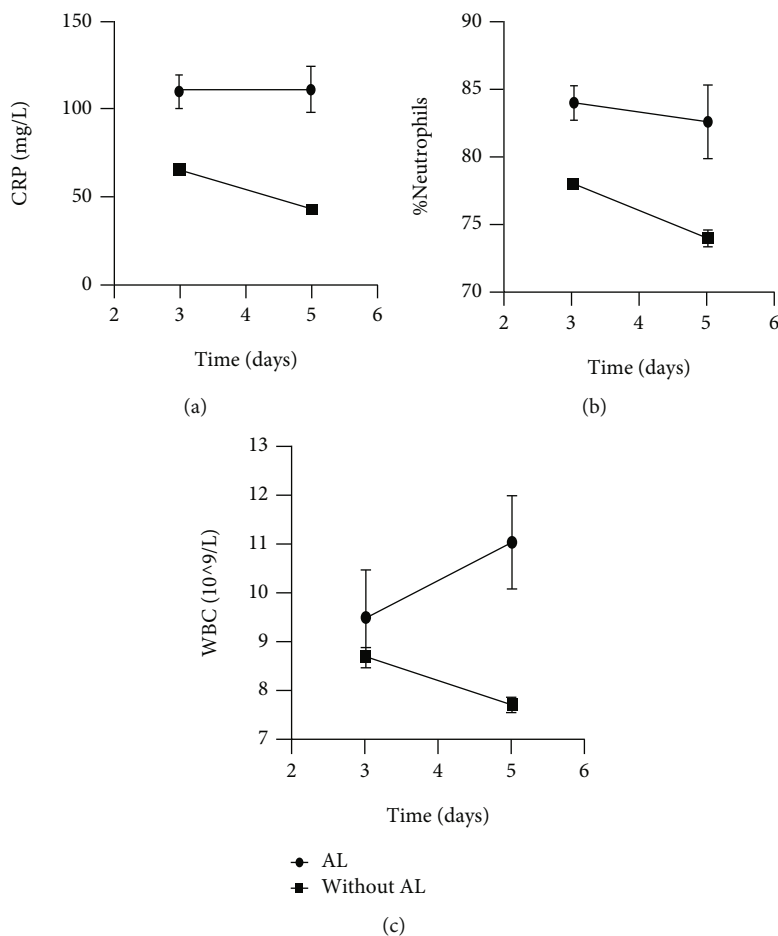


FIGURE 1: Mean levels of CRP (a), NEUT (b), and WBC (c) and relative error bars on POD3 and POD5.

TABLE 3: Comparison of CAT/MDA/SOD (serum) on POD3 and POD5 in patients with and without anastomotic leak.

Parameter (mean ± SD)	AL (n = 16)	Without AL (n = 254)	P value
CAT _{POD3}	45.82±27.20	86.23±52.01	0.023
MDA _{POD3}	1.629±1.119	0.531±0.309	<0.001
SOD _{POD3}	0.394±0.503	0.409±0.394	0.885
CAT _{POD5}	32.82±17.21	57.63±52.26	0.060
MDA _{POD5}	1.912±1.211	0.419±0.233	<0.001
SOD _{POD5}	0.302±0.218	0.408±0.127	0.002

CAT: catalase; SOD: superoxide dismutase; MDA: malondialdehyde; POD: postoperative day.

in a contingency table and Fisher’s exact test were used. The diagnostic accuracy of tests was quantified using the area (AUC) under the receiver operating characteristic (ROC) curve.

3. Results

A total of 270 patients with rectal cancer undergoing elective rectal surgery were enrolled in this study. Of these, 14 patients underwent open rectal resection and 256 underwent laparoscopy surgery. Characteristics of patients are shown in

Table 1. A total of 31 (11.5%) patients underwent neoadjuvant treatment. Sixteen (5.93%) patients developed AL. AL was diagnosed between postoperative days 4 and 10. During statistical analyses of AL vs. non-AL, no differences in demographic data except neoadjuvant treatment were observed.

Serum levels of CRP, WBC, and NEUT on POD3 and POD5 are illustrated in Table 2, and their changes are shown in Figure 1. The levels of all three serum factors were higher in the AL group than in the non-AL group and were statistically significant except WBC (POD3). The trends for CRP, WBC, and NEUT in the AL group were basically the same

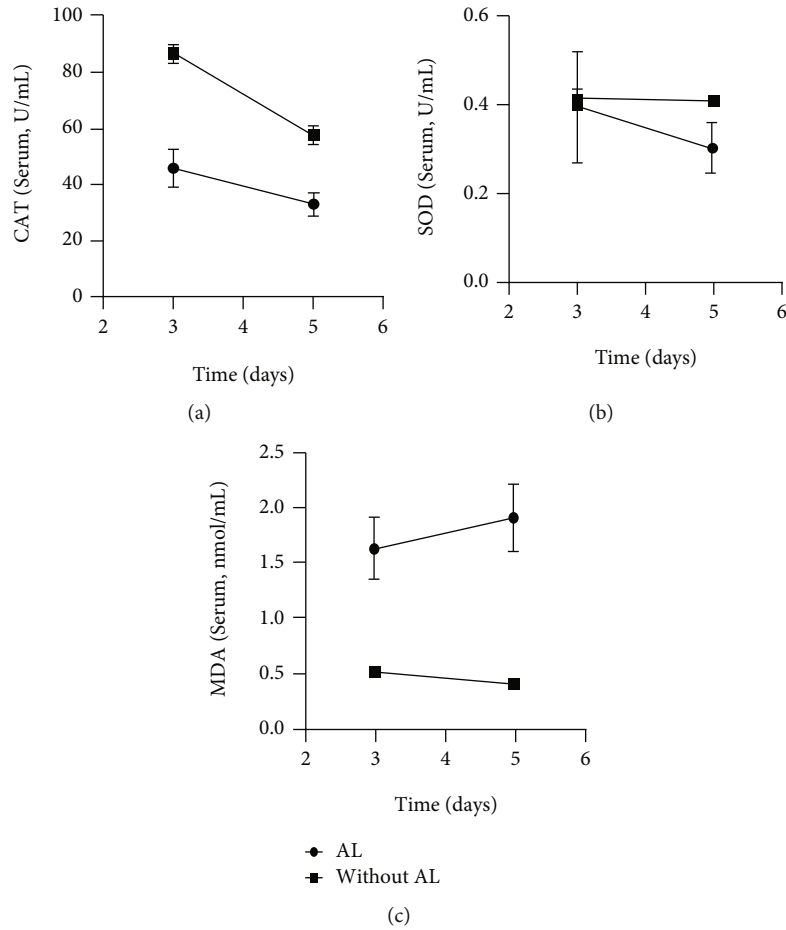


FIGURE 2: Mean levels of CAT (a), SOD (b), and MDA (c) and relative error bars on POD3 and POD5 in serum.

TABLE 4: Comparison of CAT/MDA/SOD (drain fluid) on POD3 and POD5 in patients with and without anastomotic leak.

Parameter (mean \pm SD)	AL ($n = 16$)	Without AL ($n = 254$)	P value
CAT _{POD3}	59.62 \pm 48.50	90.06 \pm 58.46	0.043
MDA _{POD3}	0.906 \pm 0.652	0.219 \pm 0.205	<0.001
SOD _{POD3}	0.358 \pm 0.112	0.536 \pm 0.237	0.003
CAT _{POD5}	49.18 \pm 35.68	116.5 \pm 50.91	<0.001
MDA _{POD5}	1.387 \pm 0.556	1.294 \pm 0.406	0.840
SOD _{POD5}	0.332 \pm 0.055	0.369 \pm 0.096	0.014

CAT: catalase; SOD: superoxide dismutase; MDA: malondialdehyde; POD: postoperative day.

and increased overall with a slight decrease from POD3 to POD5, while all factors in the non-AL group were lower in comparison.

Serum levels of CAT, MDA, and SOD on POD3 and POD5 are illustrated in Table 3, and their changes are shown in Figure 2. The levels of CAT (POD3) and SOD (POD5) in the AL group were significantly lower than those in the non-AL group while the levels of MDA in the AL group were sig-

nificantly higher than those in the non-AL group. Within the AL group between POD3 and POD5, CAT and SOD were decreased and MDA was increased, while in the non-AL group both CAT and MDA were decreased and SOD remained essentially unchanged.

Drain fluid levels of CAT, MDA, and SOD on POD3 and POD5 are illustrated in Table 4, and their changes are shown in Figure 3. The differences in their levels in drainage fluid are similar to those in serum and are statistically significant except for MDA (POD5). Within the AL group between POD3 and POD5, CAT and SOD were decreased and MDA was increased, while in the non-AL group both CAT and MDA were increased and SOD decreased.

All the above indicators with statistically significant differences are drawn with ROC curves (Figures 4–6). The AUC ROC for CRP (POD3), NEUT (POD3), CRP (POD5), NEUT (POD5), and WBC (POD5) are 0.847, 0.779, 0.896, 0.719, and 0.766, respectively. The AUC ROC for CAT (POD3), MDA (POD3), SOD (POD5), and MDA (POD5) in serum are 0.759, 0.831, 0.769, and 0.837, respectively. The AUC ROC for CAT (POD3), MDA (POD3), SOD (POD3), CAT (POD5), and SOD (POD5) in drain fluid are 0.676, 0.845, 0.738, 0.836, and 0.635, respectively.

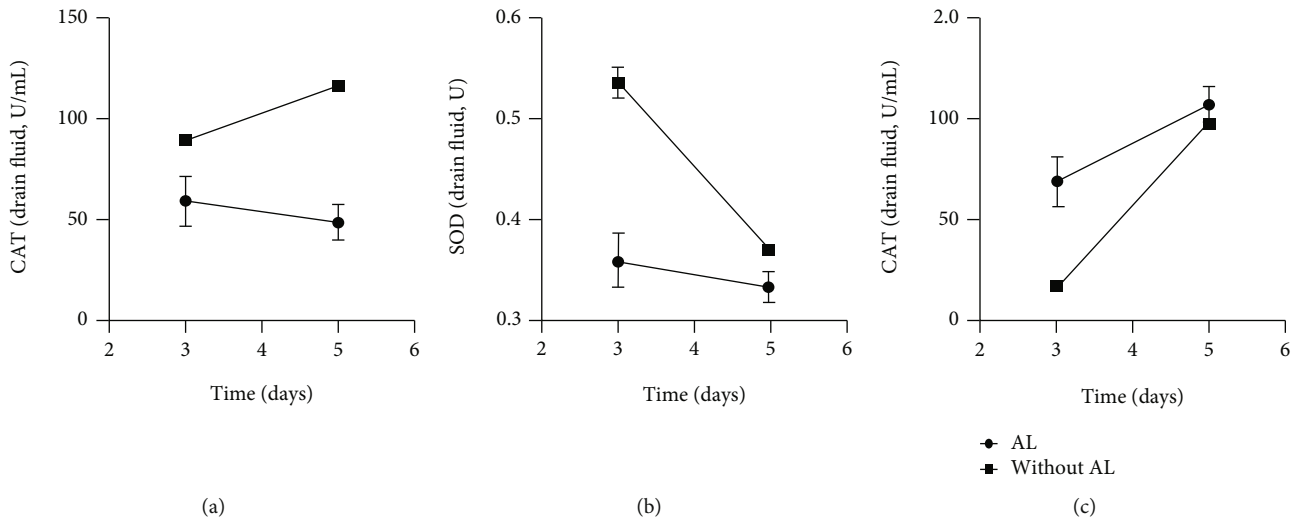


FIGURE 3: Mean levels of CAT (a), SOD (b), and MDA (c) and relative error bars on POD3 and POD5 in drain fluid.

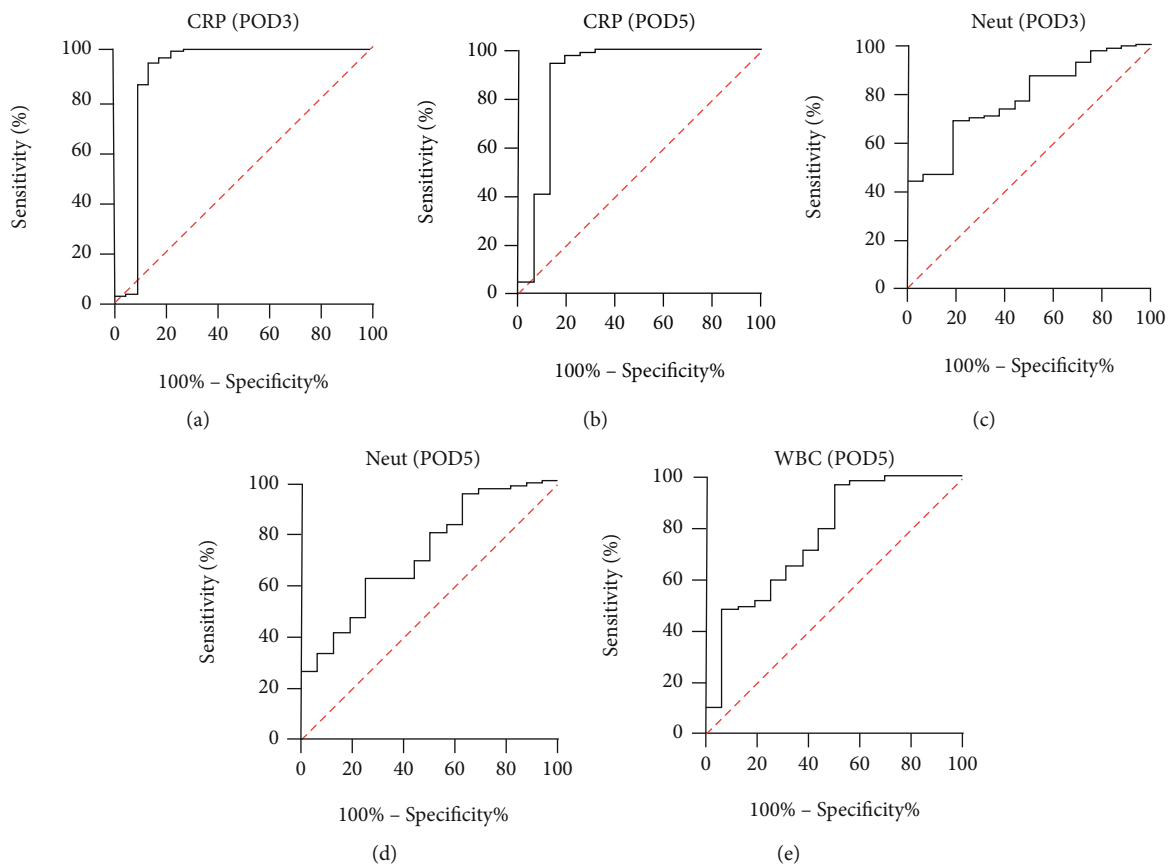


FIGURE 4: ROC curve analysis on POD3 for CRP (a) and Neut (c) and on POD5 for CRP (b), Neut (d), and WBC (e).

4. Discussion

For patients with rectal cancer, surgery is the main treatment method. The surgical method of rectal cancer has gradually developed from the initial partial resection to the expanded radical resection, and recently, it has been moving in the

direction of precise and minimally invasive. The surgical method of rectal cancer is constantly being developed and improved. Laparoscopic rectal surgery has become the trend of modern colorectal surgery. Robotic rectal surgery has also been gradually implemented, and the concept of TaTME has also been proposed. With the deepening of the surgeon's

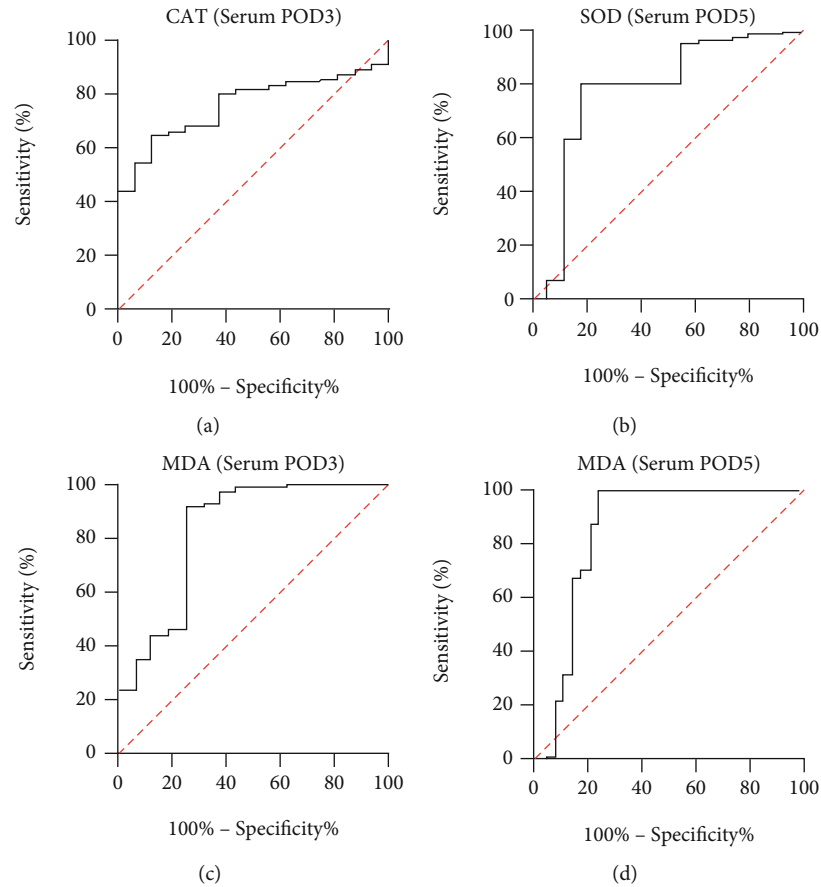


FIGURE 5: ROC curve analysis on POD3 in serum for CAT (a) and MDA (c) and on POD5 for SOD (b) and MDA (d).

understanding of perineum anatomy [20], the probability of complications of nerves and surrounding organs after rectal surgery is decreasing, but the incidence of anastomotic leakage does not seem to be significantly reduced. Compared with open surgery, the incidence of anastomotic leakage is similar in laparoscopic surgery and robotic surgery [21–23]. Early detection of anastomotic leakage is still an urgent problem.

At present, the most widely studied biomarker for prediction of AL is CRP [13, 14, 24–37]. NEUT and WBC counts are also candidate indicators; however, their value in prediction of AL is still controversial [38]. In our research, we first detected three indicators: CRP, NEUT, and WBC on POD3 and POD5, and CRP levels show a predictive effect as reported in the literature (AUC: CRP on POD3 = 0.847, CRP on POD5 = 0.896).

Whether in the serum or in the drain fluid, the oxidative stress indicators (CAT, MDA, and SOD) we have detected showed a diagnostic value for AL. The level of MDA exhibited the same superior diagnostic accuracy as the level of CRP (AUC: MDA (serum) on POD3 = 0.831, MDA (serum) on POD5 = 0.837, and MDA (drain fluid) on POD3 = 0.845).

It is well established that one of the main causes of AL is a decrease in anastomotic perfusion [39]. Studies have shown that tissue ischemia or necrosis often causes

inflammation and oxidative stress, which further damages tissues [40]. The level of oxidative stress may reflect the degree of tissue ischemia. Another factor that is closely related to the healing of anastomosis is the deposition and metabolism of collagen [41]. Matrix metalloproteinases (MMPs) mediate collagen degradation, thereby increasing the risk of AL [42]. It is reported in the literature that oxidative stress injury can upregulate MMP expression, and the level of oxidative stress may reflect the level of MMP expression.

CAT, SOD, and MDA are commonly used oxidative stress indicators. In our study, we observed that compared with those of the non-AL leakage group, the levels of SOD and CAT in the serum and drain fluid of the AL group were significantly reduced, while the level of MDA was significantly increased. Our study found these indicators have a similar AL predictive effect as CRP. SOD and CAT are antioxidant enzymes, which constitute the primary cellular antioxidant defenses [43]. Studies have reported that the rise of SOD, CAT, and other antioxidant enzymes is an indication of tissue repair [44]. MDA has been used as a biomarker of oxidative stress. An increase of MDA reflects the enhancement of lipid peroxidation and tissue damage [45]. We hypothesize that the antioxidant system of patients with anastomosis is impaired, which leads to poor healing of anastomotic tissue.

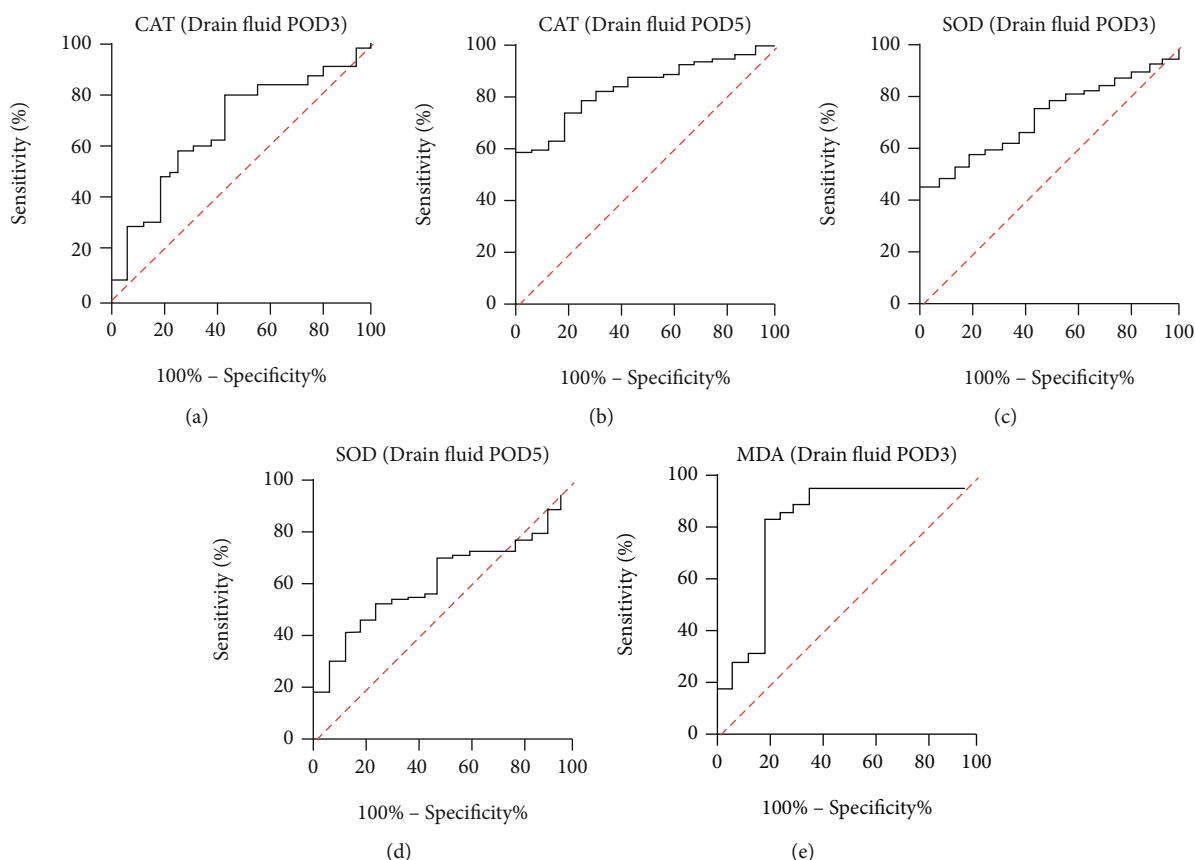


FIGURE 6: ROC curve analysis on POD3 in drain fluid for CAT (a), SOD (c), and MDA (e) and on POD5 for CAT (b) and SOD (d).

5. Conclusions

In conclusion, the oxidative stress indicators we tested show great potential for the early diagnosis of AL in serum and drain fluid. Our research reveals that the level of MDA in serum or drain fluid has good diagnostic accuracy for AL. The oxidative stress level is expected to become a useful predictor of AL in the future.

Data Availability

The datasets used and analyzed during the current study are available from the corresponding author on reasonable request.

Conflicts of Interest

The authors declare that they have no conflicts of interest.

Authors' Contributions

Qiang Tong designed the study, interpreted the results, and wrote the manuscript. Jiajun Luo, Hongxue Wu, Yu Yang, Yue Jiang, and Jingwen Yuan performed the experiments. All authors read and approved the final manuscript. Jiajun Luo and Hongxue Wu contributed equally to this work.

Acknowledgments

This work was supported by the National Natural Science Foundation of China (No. 81172186 (QT)), by the Natural Science Foundation of Hubei Province (No. 2018CFB504 (QT)), by the Guidance Foundation of Renmin Hospital of Wuhan University (No. RMYD2018M67 (QT)), and by Hubei Province Health and Family Planning Scientific Research Project (No. WJ2019M200 (HXW)).

References

- [1] M. Arnold, M. S. Sierra, M. Laversanne, I. Soerjomataram, A. Jemal, and F. Bray, "Global patterns and trends in colorectal cancer incidence and mortality," *Gut*, vol. 66, no. 4, pp. 683–691, 2017.
- [2] M. Rentsch, T. Schiergens, A. Khandoga, and J. Werner, "Surgery for colorectal cancer - trends, developments, and future perspectives," *Visceral Medicine*, vol. 32, no. 3, pp. 184–191, 2016.
- [3] N. C. Buchs, P. Gervaz, M. Secic, P. Bucher, B. Mugnier-Konrad, and P. Morel, "Incidence, consequences, and risk factors for anastomotic dehiscence after colorectal surgery: a prospective monocentric study," *International Journal of Colorectal Disease*, vol. 23, no. 3, pp. 265–270, 2008.
- [4] C. L. Sparreboom, Z. Q. Wu, J. F. Ji, and J. F. Lange, "Integrated approach to colorectal anastomotic leakage: communication, infection and healing disturbances," *World Journal of Gastroenterology*, vol. 22, no. 32, pp. 7226–7235, 2016.

- [5] Z. R. Lu, N. Rajendran, A. C. Lynch, A. G. Heriot, and S. K. Warriar, "Anastomotic leaks after restorative resections for rectal cancer compromise cancer outcomes and survival," *Diseases of the Colon & Rectum*, vol. 59, no. 3, pp. 236–244, 2016.
- [6] F. E. Turrentine, C. E. Denlinger, V. B. Simpson et al., "Morbidity, mortality, cost, and survival estimates of gastrointestinal anastomotic leaks," *Journal of the American College of Surgeons*, vol. 220, no. 2, pp. 195–206, 2015.
- [7] J. Meyer, S. Naiken, N. Christou et al., "Reducing anastomotic leak in colorectal surgery: the old dogmas and the new challenges," *World Journal of Gastroenterology*, vol. 25, no. 34, pp. 5017–5025, 2019.
- [8] K. Guyton and J. C. Alverdy, "The gut microbiota and gastrointestinal surgery," *Nature Reviews. Gastroenterology & Hepatology*, vol. 14, no. 1, pp. 43–54, 2017.
- [9] R. Bachmann, D. Leonard, N. Delzenne, A. Kartheuser, and P. D. Cani, "Novel insight into the role of microbiota in colorectal surgery," *Gut*, vol. 66, no. 4, pp. 738–749, 2017.
- [10] J. V. Cordeiro and A. Jacinto, "The role of transcription-independent damage signals in the initiation of epithelial wound healing," *Nature Reviews. Molecular Cell Biology*, vol. 14, no. 4, pp. 249–262, 2013.
- [11] M. Cano Sanchez, S. Lancel, E. Boulanger, and R. Neviere, "Targeting oxidative stress and mitochondrial dysfunction in the treatment of impaired wound healing: a systematic review," *Antioxidants*, vol. 7, no. 8, p. 98, 2018.
- [12] A. Karliczek, N. J. Harlaar, C. J. Zeebregts, T. Wiggers, P. C. Baas, and G. M. van Dam, "Surgeons lack predictive accuracy for anastomotic leakage in gastrointestinal surgery," *International Journal of Colorectal Disease*, vol. 24, no. 5, pp. 569–576, 2009.
- [13] E. Asti, G. Bonitta, M. Melloni et al., "Utility of C-reactive protein as predictive biomarker of anastomotic leak after minimally invasive esophagectomy," *Langenbeck's Archives of Surgery*, vol. 403, no. 2, pp. 235–244, 2018.
- [14] J. L. Muñoz, M. O. Alvarez, V. Cuquerella et al., "Procalcitonin and C-reactive protein as early markers of anastomotic leak after laparoscopic colorectal surgery within an enhanced recovery after surgery (ERAS) program," *Surgical Endoscopy*, vol. 32, no. 9, pp. 4003–4010, 2018.
- [15] O. Benoit, M. Faron, N. Margot et al., "C-Reactive protein values after colorectal resection: can we discharge a patient with a C-reactive protein value >100? A retrospective cohort study," *Diseases of the Colon and Rectum*, vol. 62, no. 1, pp. 88–96, 2019.
- [16] B. A. Messias, R. V. Botelho, S. S. Saad, E. R. Mocchetti, K. C. Turke, and J. Waisberg, "Serum C-reactive protein is a useful marker to exclude anastomotic leakage after colorectal surgery," *Scientific Reports*, vol. 10, no. 1, p. 1687, 2020.
- [17] M. Zawadzki, M. Krzystek-Korpacka, A. Gamian, and W. Witkiewicz, "Serum cytokines in early prediction of anastomotic leakage following low anterior resection," *Wideochir Inne Tech Maloinwazyjne*, vol. 13, no. 1, pp. 33–43, 2018.
- [18] B. Ip, K. T. Ng, S. Packer, S. Paterson-Brown, and G. W. Couper, "High serum lactate as an adjunct in the early prediction of anastomotic leak following oesophagectomy," *International Journal of Surgery*, vol. 46, pp. 7–10, 2017.
- [19] D. A. Clark, T. Cuda, A. Riddell, G. Radford-Smith, and M. Solomon, "Drain fluid amylase as a sensitive biomarker for the early detection of anastomotic leakage in ileal pouch surgery," *Colorectal Disease*, vol. 21, no. 4, pp. 460–464, 2019.
- [20] C. Oikonomou, S. Gourgiotis, R. Cirocchi et al., "Re-exploring the pelvic neuroanatomy from a new perspective and a potential guidance for TaTME: a "bottom-up" approach," *Updates in Surgery*, vol. 73, no. 2, pp. 503–512, 2021.
- [21] S. Di Saverio, W. Stupalkowska, A. Hussein, N. Fearnhead, and J. Wheeler, "Laparoscopic ultralow anterior resection with intracorporeal coloanal stapled anastomosis for low rectal cancer – is robotic surgery or transanal total mesorectal excision always needed to achieve a good oncological and sphincter-sparing dissection – a video vignette," *Colorectal Disease*, vol. 21, no. 7, pp. 848–849, 2019.
- [22] C. Staudacher, A. Vignali, D. P. Saverio, O. Elena, and T. Andrea, "Laparoscopic vs. open total mesorectal excision in unselected patients with rectal cancer: impact on early outcome," *Diseases of the Colon and Rectum*, vol. 50, no. 9, pp. 1324–1331, 2007.
- [23] P. Gavriliadis, J. Wheeler, A. Spinelli, N. de'Angelis, C. Simopoulos, and S. di Saverio, "Robotic vs laparoscopic total mesorectal excision for rectal cancers: has a paradigm change occurred? A systematic review by updated meta-analysis," *Colorectal Disease*, vol. 22, no. 11, pp. 1506–1517, 2020.
- [24] A. B. Almeida, G. Faria, H. Moreira, J. Pinto-de-Sousa, P. Correia-da-Silva, and J. C. Maia, "Elevated serum C-reactive protein as a predictive factor for anastomotic leakage in colorectal surgery," *International Journal of Surgery*, vol. 10, no. 2, pp. 87–91, 2012.
- [25] M. Benedetti, P. Ciano, I. Pergolini et al., "Early diagnosis of anastomotic leakage after colorectal surgery by the Dutch leakage score, serum procalcitonin and serum C-reactive protein: study protocol of a prospective multicentre observational study by the Italian ColoRectal Anastomotic Leakage (iC)," *Il Giornale di Chirurgia*, vol. 40, no. 1, pp. 20–25, 2019.
- [26] Y. M. Ho, J. Laycock, A. Kirubakaran, L. Hussain, and J. Clark, "Systematic use of the serum C-reactive protein concentration and computed tomography for the detection of intestinal anastomotic leaks," *ANZ Journal of Surgery*, vol. 90, no. 1-2, pp. 109–112, 2020.
- [27] N. Lagoutte, O. Facy, A. Ravoire et al., "C-reactive protein and procalcitonin for the early detection of anastomotic leakage after elective colorectal surgery: Pilot study in 100 patients," *Journal of Visceral Surgery*, vol. 149, no. 5, pp. e345–e349, 2012.
- [28] J. Lu, L. Zheng, R. Li et al., "Diagnostic value of dynamic monitoring of C-reactive protein in drain drainage to predict early anastomotic leakage after colorectal cancer surgery," *Zhonghua Wei Chang Wai Ke Za Zhi*, vol. 20, no. 9, pp. 1055–1059, 2017.
- [29] P. Matthiessen, M. Henriksson, O. Hallböök, E. Grunditz, B. Norén, and G. Arbmán, "Increase of serum C-reactive protein is an early indicator of subsequent symptomatic anastomotic leakage after anterior resection," *Colorectal Disease*, vol. 10, no. 1, pp. 75–80, 2008.
- [30] I. Mintziras, E. Maurer, V. Kanngiesser, and D. K. Bartsch, "C-reactive protein and drain amylase accurately predict clinically relevant pancreatic fistula after partial pancreaticoduodenectomy," *International Journal of Surgery*, vol. 76, pp. 53–58, 2020.
- [31] P. Ortega-Deballon, F. Radais, O. Facy et al., "C-Reactive protein is an early predictor of septic complications after elective colorectal surgery," *World Journal of Surgery*, vol. 34, no. 4, pp. 808–814, 2010.

- [32] J. J. Platt, M. L. Ramanathan, R. A. Crosbie et al., "C-reactive protein as a predictor of postoperative infective complications after curative resection in patients with colorectal cancer," *Annals of Surgical Oncology*, vol. 19, no. 13, pp. 4168–4177, 2012.
- [33] I. S. Reynolds, M. R. Boland, F. Reilly et al., "C-reactive protein as a predictor of anastomotic leak in the first week after anterior resection for rectal cancer," *Colorectal Disease*, vol. 19, no. 9, pp. 812–818, 2017.
- [34] P. P. Singh, I. S. Zeng, S. Srinivasa, D. P. Lemanu, A. B. Connolly, and A. G. Hill, "Systematic review and meta-analysis of use of serum C-reactive protein levels to predict anastomotic leak after colorectal surgery," *The British Journal of Surgery*, vol. 101, no. 4, pp. 339–346, 2014.
- [35] S. R. Smith, P. Pockney, R. Holmes et al., "Biomarkers and anastomotic leakage in colorectal surgery: C-reactive protein trajectory is the gold standard," *ANZ Journal of Surgery*, vol. 88, no. 5, pp. 440–444, 2018.
- [36] P. Waterland, J. Ng, A. Jones et al., "Using CRP to predict anastomotic leakage after open and laparoscopic colorectal surgery: is there a difference?," *International Journal of Colorectal Disease*, vol. 31, no. 4, pp. 861–868, 2016.
- [37] T. Welsch, S. A. Müller, A. Ulrich et al., "C-reactive protein as early predictor for infectious postoperative complications in rectal surgery," *International Journal of Colorectal Disease*, vol. 22, no. 12, pp. 1499–1507, 2007.
- [38] A. T. Stearns, F. Liccardo, K. N. Tan et al., "Physiological changes after colorectal surgery suggest that anastomotic leakage is an early event: a retrospective cohort study," *Colorectal Disease*, vol. 21, no. 3, pp. 297–306, 2019.
- [39] C. Zhang, L. Chen, M. Cui et al., "Short- and long-term outcomes of rectal cancer patients with high or improved low ligation of the inferior mesenteric artery," *Scientific Reports*, vol. 10, no. 1, article 15339, 2020.
- [40] P. H. Sung, K. C. Lin, H. T. Chai et al., "Losing regulation of the extracellular matrix is strongly predictive of unfavorable prognostic outcome after acute myocardial infarction," *International Journal of Molecular Sciences*, vol. 21, no. 17, article 6219, 2020.
- [41] X. H. Wang, J. S. Ni, N. L. Cao et al., "In vivo evaluation of Mg-6Zn and titanium alloys on collagen metabolism in the healing of intestinal anastomosis," *Scientific Reports*, vol. 7, no. 1, article 44919, 2017.
- [42] P. M. Krarup, M. Eld, K. Heinemeier, L. N. Jorgensen, M. B. Hansen, and M. S. Ågren, "Expression and inhibition of matrix metalloproteinase (MMP)-8, MMP-9 and MMP-12 in early colonic anastomotic repair," *International Journal of Colorectal Disease*, vol. 28, no. 8, pp. 1151–1159, 2013.
- [43] B. Qian, J. Li, K. Guo et al., "Antioxidant biocompatible composite collagen dressing for diabetic wound healing in rat model," *Regenerative Biomaterials*, vol. 8, no. 2, article rbab003, 2021.
- [44] R. Melekoglu, O. Ciftci, S. Eraslan, A. Cetin, and N. Basak, "Beneficial effects of curcumin and capsaicin on cyclophosphamide-induced premature ovarian failure in a rat model," *Journal of Ovarian Research*, vol. 11, no. 1, p. 33, 2018.
- [45] M. I. Ezzat, M. M. Okba, S. H. Ahmed et al., "In-depth hepatoprotective mechanistic study of *Phyllanthus niruri*: in vitro and in vivo studies and its chemical characterization," *PLoS One*, vol. 15, no. 1, article e0226185, 2020.

Research Article

Exosomes Containing LINC00636 Inhibit MAPK1 through the miR-450a-2-3p Overexpression in Human Pericardial Fluid and Improve Cardiac Fibrosis in Patients with Atrial Fibrillation

Langsha Liu, Fanyan Luo, and Kaibo Lei 

Department of Cardiac Surgery, Xiangya Hospital, Central South University, Changsha, China

Correspondence should be addressed to Kaibo Lei; 402511@csu.edu.cn

Received 26 March 2021; Revised 13 May 2021; Accepted 29 May 2021; Published 28 June 2021

Academic Editor: Shuai Chen

Copyright © 2021 Langsha Liu et al. This is an open access article distributed under the Creative Commons Attribution License, which permits unrestricted use, distribution, and reproduction in any medium, provided the original work is properly cited.

The purpose of this study was to investigate the regulatory mechanism of miR-450a-2-3p in myocardial fibrosis in patients with atrial fibrillation. For this purpose, the expression profile of GSE55296 was extracted from the GEO database, and differentially expressed lncRNAs were identified. Gene ontology analysis of the target genes of miR-450a-2-3p indicated that there was a regulatory relationship between LINC00636 and miR-450a-2-3p. Further, the expression levels of the analyzed RNAs were confirmed by RT-qPCR. TGF- β 1-induced cardiac fibroblasts (CFs) and human umbilical vein endothelial cells (HUVECs) were used to establish a myocardial fibrosis model and endothelium-mesenchymal transformation (EMT) model *in vivo*. We hypothesized that exosomes containing LINC00636 regulate the expression of miR-450a-2-3p. LINC00636 was positively correlated with the expression of miR-450a-2-3p. The overexpression of miR-450a-2-3p suppressed the MAPK1 expression in CFs, thereby inhibiting the expression of α -SMA, COL1, and COL3 and preventing CF proliferation. In HUVECs, the miR-450a-2-3p overexpression upregulated the expression of VE-Cadherin (VE-Cad) and platelet endothelial cell adhesion molecule-1 (PECAM-1/CD31) by inhibiting the mitogen-activated protein kinase 1 (MAPK1) expression, whereas the expression levels of vimentin, COL1, and COL3 decreased. These results indicate that LINC00636, which is present in human pericardial fluid, is an antifibrotic molecule that inhibits MAPK1 through the miR-450a-2-3p overexpression and improves cardiac fibrosis in patients with atrial fibrillation.

1. Introduction

Atrial fibrillation (AF) is one of the most common sustained supraventricular arrhythmias that increase the risk of stroke [1]. The underlying mechanism is thought to be associated with electrical and structural atrial remodeling, which lead to cardiac fibrosis [2, 3]. The activation and proliferation of cardiac fibroblasts (CFs), which produce excessive extracellular matrix (ECM) components, such as collagen-1 (COL1) and collagen-3 (COL3), play a pivotal role in fibrogenesis in patients with AF [4]. Furthermore, CFs can differentiate into myofibroblasts, the cells that present a 2-fold higher ability to synthesize collagen, including alpha smooth muscle actin (α -SMA) [5]. Although in physiological conditions cardiac fibrosis is low, differentiation of monocytes, endothelial cells, bone marrow circulating progenitor cells, and peripheral cells

in pathological conditions increase cardiac fibrosis [6–8]. Consequently, endothelial-mesenchymal transition (EMT) in endothelial cells is closely related to cardiac fibrosis. However, the molecular mechanisms of cardiac fibrosis and EMT in AF are largely unclear.

Long noncoding RNAs (lncRNAs) are a subclass of transcripts longer than 200 bp without identifiable open reading frames or protein-coding capacity that are derived from intergenic regions (the antisense strand of a given gene) of the genome, introns of protein-coding genes, or through alternative splicing [9]. Recent research has shown that the lncRNA LINC00636 affects the proliferation, apoptosis, migration, and invasion of cervical cancer cells [10]. However, the influence of LINC00636 on CFs has not yet been studied. Our previous comprehensive bioinformatic analysis validated with RT-qPCR showed that miR-450a-2-3p was

downregulated in CFs exposed to transforming growth factor (TGF)- β 1 and human umbilical vein endothelial cells (HUVECs) and may act as microRNAs (miRNAs) that inhibit fibrosis [11]. miRNAs are capable of regulating the gene expression; they reduce the gene expression by degrading or functionally inhibiting target mRNAs after transcription [12]. MiRNAs produced from parental cells in bioactive forms are not destroyed in biological fluids, thereby exhibiting great potential as disease biomarkers [13]. Hence, the components of the pericardial fluid (PF) that surround the heart, epicardial adipose tissues, and large vascular roots that carry blood to the heart may reflect the myocardial protein expression profile. Recent research has shown that miRNAs can promote angiogenesis of endothelial cells through exosomes in human PF [14]. However, their role in the atrial remodeling of exosomes in AF is not well characterized.

Bioinformatic analysis suggested that the miR-450a-2-3p/MAPK1 pathway affects cardiac fibrosis. Based on this result, we focused on upstream target molecules of the miR-450a-2-3p/MAPK1 pathway and performed functional phenotype verification at the cellular level. Specifically, we focused on the effects of LINC00636 downregulation in CFs and hypothesized that LINC00636 mediates miR-450a-2-3p to affect the CF cellular activity. Furthermore, we demonstrated that MAPK1 acts as a downstream target of miR-450a-2-3p and functions as a fibrogenic gene in fibrosis progression. Collectively, the goal of this study was to discover and identify a cardiac fibrosis-associated lncRNA and its molecular mechanism using bioinformatic analyses. Our findings may help identify the possible mechanisms of AF and contribute to the development of more promising therapeutic targets.

2. Material and Methods

2.1. Collection and Treatment of PF Samples. The study was conducted in accordance with the Declaration of Helsinki, as revised in 2013. All protocols were approved by the Ethics Committee of Xiangya Hospital Central South University (201803209), and informed consent was obtained from all participants. We isolated exosomes present in the PF of nAF for subsequent experiments. In addition, total RNA was extracted from the PF exosomes of patients with nAF ($n = 12$) or AF ($n = 12$).

2.2. Bioinformatic Analyses. For our study, we selected Gene Expression Omnibus (GEO, <http://www.ncbi.nlm.nih.gov/geo/>), which is a publicly accessible database containing gene/microarray profiles. The gene expression profile GSE55296 was extracted from the GEO database. Using software *R* and the *ggplot2* (3.3.0) package, we generated volcano plots and boxplots of the selected gene expression profile. The lncRNA-to-miRNA prediction was performed using lncBase (http://carolina.imis.athena-innovation.gr/diana_tools/web/index.php?r=lncbasev). Using the *igraph* package in *R*, we created a network map. Finally, we created an enrichment map using the *clusterProfiler_3.11.0* package in *R*.

2.3. Isolation and Extraction of Exosomes from PF. PF exosomes were isolated using THE ExoQuick kit (System Biosci-

ences, PA, USA) according to manufacturer's instructions. Briefly, after centrifugation of PF at $3,000 \times g$ for 15 min, the pellet containing cell debris was discarded, and the supernatant was transferred to a sterile container. An appropriate volume of ExoQuick-exosome precipitate solution was added to the PF. The ExoQuick/PF mixture was centrifuged again at $1,500 \times g$ for 30 min, and the supernatant was removed using suction. The remaining pellet, containing exosomes, was resuspended in PBS.

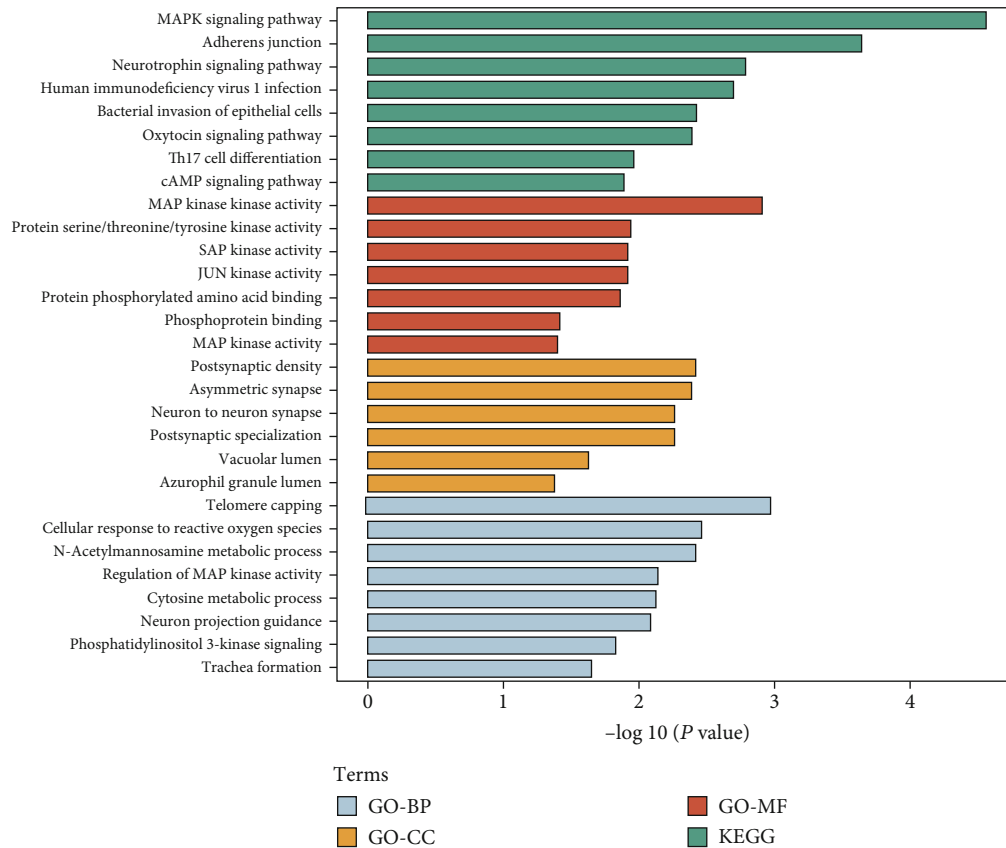
2.4. Transmission Electron Microscopy (TEM). Phosphotungstic acid (approximately 1%) was prepared in a phosphate buffer. The suspension sample ($10 \mu\text{L}$) was dropped onto a coated copper mesh, which was subsequently incubated in an oven at 37°C . A filter paper cut into shapes with sharp corners was used to absorb the staining solution. Thereafter, phosphotungstic acid staining solution ($10 \mu\text{L}$) was dropped on the copper mesh with the prepared sample using sample gun. After 1–2 min, excess phosphotungstic acid was washed off. Transmission electron microscopy (TEM) was performed using a HT-7800 microscope (Hitachi, Japan) to observe and capture images of the exosome morphology.

2.5. Fluorescent Imaging of Exosome Uptake. A total of $50 \mu\text{L}$ of sample containing exosomes isolated from the human PF were diluted with Diluent C to a final volume of $250 \mu\text{L}$ and labeled with $1.5 \mu\text{L}$ of PKH26 dye. Then, $150 \mu\text{L}$ of exosome samples was incubated with CFs or HUVECs overnight at 4°C . After washing, the cells were stained with 1 ml of $1 \mu\text{g/ml}$ DAPI, and pictures were captured using a Motic inverted fluorescence microscope.

2.6. Cell Culture and Treatment. Both HUVECs and rat primary CFs used in this study were purchased from ScienCell (CA, USA). After 3–8 generations, the cells were selected for experimental verification. HUVECs were cultured in Dulbecco's Modified Eagle's Medium (DMEM) containing 10% fetal bovine serum (FBS) and 1% penicillin-streptomycin. CF cultures were supplemented with 1% fibroblast growth supplement-2 (ScienCell, CA, USA).

The cells were digested with 0.25% trypsin (Beyotime Biotechnology, Shanghai, China) (containing 0.02% EDTA) at 37°C for 5 min followed by centrifugation at 1,000 rpm and then seeded into 6-well plates. A total of $20 \mu\text{L}$ of Lipo2000 (Invitrogen, CA, USA) diluted in 1 ml of serum-free DMEM was mixed with $10 \mu\text{L}$ each of mimic, mimic-control, inhibitor, and inhibitor-control (Honorgene, Changsha, China) diluted in $250 \mu\text{L}$ of serum-free DMEM for 20 min. The transfection medium was replaced with DMEM containing FBS after 6 h. After 24 h, the cells were incubated with 50 ng/ml of recombinant human TGF- β 1 for 24 h.

2.7. RNA Extraction and Quantitative Real-Time Analysis (RT-qPCR). Total RNA was extracted according to the manufacturer's instructions. Briefly, 1 ml of TRIzol (Thermo Fisher Scientific, MA, USA) was added per 10 cm^2 of the plate surface area. mRNAs were reverse transcribed using a reverse transcription kit (Cowin, Beijing, China). RT-qPCR was performed using an UltraSYBR mixture (Cowin, Beijing, China). The relative expression of genes was calculated using the



(e)

FIGURE 1: LncRNAs and their potential target genes in AF and SR patients. (a) Volcano plot of differentially expressed lncRNAs. Red and blue dots represent the high and low differential expression of lncRNAs, respectively. (b) Box plot of the LINC00636 expression in the two groups. (c) Map of binding sites between LINC00636 and miR-450a-2-3p. (d) Network map for LINC00636-related genes and miR-450a-2-3p. (e) GO and KEGG pathway enrichment analyses.

$2^{-\Delta\Delta CT}$. The miRNA expression of samples was normalized with that of U6 small nuclear RNA, and the mRNA expression of samples was normalized with that of β -actin. All primers used in this study were commercially obtained from Sangon (Shanghai, China) and are shown in Supplementary Table 1.

2.8. Western Blot Analysis of Protein Expression Levels. Cells or exosomes were lysed in RIPA buffer (Beyotime Biotechnology, Shanghai, China). After centrifugation at $12,000 \times g$ for 15 min at 4°C , the supernatant was collected. Protein concentration was determined using the bicinchoninic acid assay using a commercial kit (Cwbio, Beijing, China). Next, 160 μL of protein was separated using a 40 μL 5 \times loading buffer and then transferred to a nitrocellulose filter membrane. The membrane was incubated in 5% bovine serum albumin (BSA) at 4°C for 1.5 h and incubated overnight with primary antibody at 4°C . The primary antibodies used for western blotting were as follows: β -actin (1:5000; Proteintech, IL, USA), CD9 (1:2,000; Proteintech, IL, USA), CD63 (1:1000; Proteintech, IL, USA), Tsg101 (1:5000; Abcam, Cambridge, United Kingdom), α -SMA (1:1000; Proteintech, IL, USA), COL1 (1:1000; Bioss, Beijing, China), COL3 (1:500; Proteintech, IL, USA), MAPK1 (1:1000; Proteintech, IL,

USA), VE-Cad (1:1000; CST, MA, USA), PECAM-1/CD31 (1:2000; Proteintech, IL, USA), and vimentin (1:2000; Proteintech, IL, USA). After overnight incubation with the primary antibody, the membrane was incubated with the corresponding secondary antibodies (HRP goat anti-mouse IgG, 1:5000; HRP goat anti-rabbit IgG, 1:6000; Proteintech, IL, USA) at 25°C for 90 min. Detection was performed using an enhanced chemiluminescence (ECL) system (Advansta, CA, USA). Relative protein expression levels were analyzed using the Quantity One v4.6.2 software.

2.9. Immunofluorescence (IF). After rinsing with PBS three times, the cells were fixed with 4% paraformaldehyde (#28908, ThermoFisher, China) for 30 min. Next, the cells were infiltrated with 0.3% Triton X-100 for 30 min. After 60 min of blocking with 5% BSA, the cells were incubated overnight at 4°C with primary antibodies against BSA. The primary antibodies used for IF were α -SMA (1:50; BOSTER, CA, USA), vimentin (1:50; Proteintech, IL, USA), and VE-Cad (1:50; CST, MA, USA). The cells were subsequently incubated at 37°C for 90 min with the corresponding secondary antibodies: CoraLite594-conjugated goat anti-mouse IgG (H+L) (1:200; Proteintech, IL, USA) and CoraLite594-conjugated goat anti-rabbit IgG (H+L) (1:200; Proteintech,

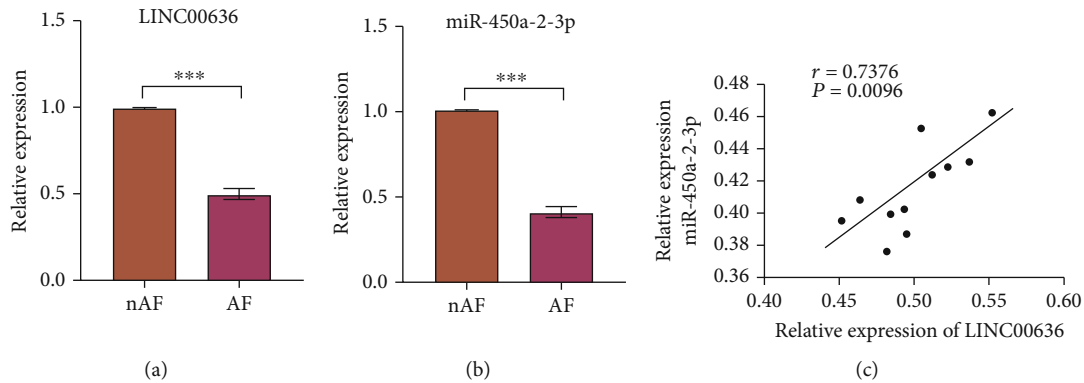


FIGURE 2: The expression of RNAs in human pericardial exosomes. (a, b) The expression levels of LINC00636 and miR-450a-2-3p determined using RT-qPCR. (c) LINC00636 expression levels are positively correlated with those of miR-450a-2-3p. Data is expressed as mean \pm standard deviation calculated from three independent experiments. *** $P < 0.001$.

IL, USA). Cells were then stained with DAPI for 10 min. A MotiC image system was used for the observation and acquisition of images. Fluorescence intensity was analyzed using ImageJ.

2.10. Dual-Luciferase Reporter Gene Assay. To determine the direct target of miR-450a-2-3p, 293 T cells that were cotransfected with miR-450a-2-3p mimic or NC-mimic and the 3' UTR of MAPK1 or the mutant 3' UTR of MAPK1 were cultured in 24-well plates for 48 h. The binding site of miR-450a-2-3p in the MAPK1 3' UTR was mutated, and the activity of luciferase from *Renilla reniformis* or *Photinus pyralis* was measured.

2.11. Cell Proliferation Assay. Cell Counting Kit-8 (Dojindo, Japan) was used to evaluate cell proliferation according to manufacturer's instructions. Briefly, CFs were inoculated into 96-well plates with recombinant human TGF- β 1 and miR-450a-2-3p mimic or miR-450a-2-3p inhibitor and their respective controls. The cellular proliferation rate was measured at 4 h using a microplate spectrophotometer (Huisong, Shenzhen, China) at a wavelength of 450 nm.

2.12. Scratch Assay. Transfected HUVECs that proliferated to form a full layer were rinsed with sterile PBS. The cell scratch was made using a sterile pipette tip in the cell monolayer along the surface of the culture dish. Cell migration to the scratch area was measured immediately after creating a scratch and 6 h later. The cell area was quantified using ImageJ v1.53e (Media Cybernetics, Inc., Rockville, MD, USA). The migration rate of HUVECs was defined as migration area/original scratch area \times 100%.

2.13. Statistical Analysis. Two-tailed Student's *t*-test was used to compare the two different conditions. In cases in which the data did not follow a normal distribution, the Mann-Whitney test was used. The experimental comparisons of three or more experimental groups were performed using Tukey's multicomparison test or one-way ANOVA with Dunnett's posthoc test. Correlation between indicators was analyzed using Pearson. All data were expressed as the mean \pm SEM. GraphPad Prism 8.0 software (GraphPad Software, San

Diego, CA, USA) was used for statistical analysis. $P < 0.05$ was considered statistically significant.

3. Results

3.1. Potential Functional Significance of LINC00636/miR-450a-2-3p/MAPK1 in AF. We performed genetic screening using the GSE55296 dataset, which consists of hundreds of lncRNAs with markedly different expression levels between the two groups as shown in the volcano plot (Figure 1(a)), among which the lncRNAs, namely, AC022532.1, LINC00636, and SNHG16, were downregulated (Figure 1(b)). According to Linbase bioinformatic prediction, miR-450a-2-3p is a potential target gene of LINC00636 (Figure 1(c)). To preliminarily explore the potential functions of the dysregulated lncRNAs in AF, a functional enrichment analysis of the target genes of LINC00636 was performed based on GO terms. The mRNA targets of miR-450a-2-3p included a variety of genes, such as apoptosis-related genes MAPK1, BCL11A, and CBX8 (Figure 1(d)). Similar results were observed in the GO analysis of LINC00636. GO functional annotation was performed on the potential target genes at the three levels: biological process (BP), cellular component (CC), and molecular function (MF). The cAMP signaling pathway, Th17 cell differentiation, and MAPK1 were found to be closely related to these genes (Figure 1(e)).

3.2. Verification of the lncRNA Expression in Clinical Samples. To confirm the reliability of HTS results, exosomes derived from the PF of 12 nAF subjects and 12 AF patients were collected for RT-qPCR validation of LINC00636 and miR-450a-2-3p expression levels. As shown in Figure 2, the relative expression of LINC00636 in PF exosomes was reduced in the AF group compared to that in the nAF group, which was consistent with the HTS results. The expression of miR-450a-2-3p in the AF group was also lower than that in the nAF group. According to Pearson's analysis, the LINC00636 expression level was positively correlated with that of miR-450a-2-3p, which suggests a positive effect on AF.

3.3. Isolation and Characterization of Exosomes Derived from the PF and the Uptake of Exosomes by CFs. We

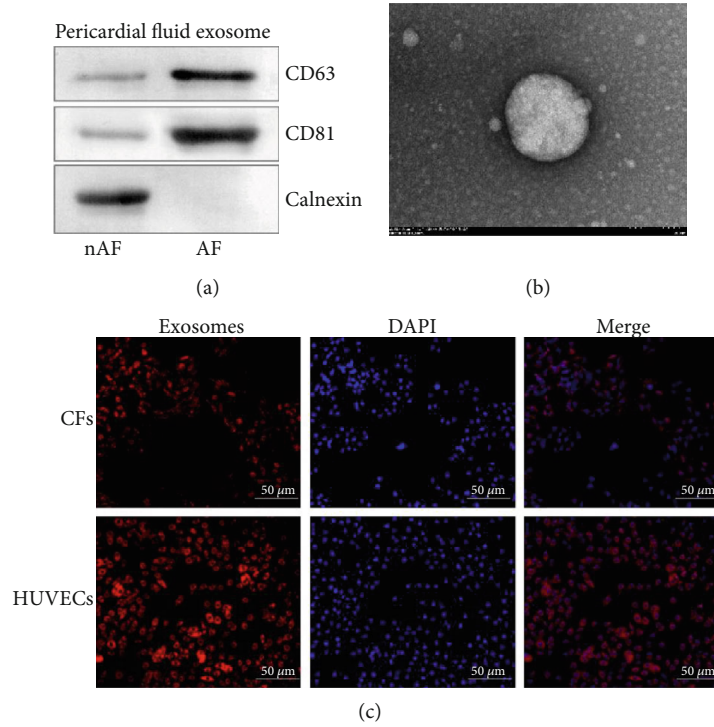


FIGURE 3: Characterization and the uptake of exosomes. (a) Biological markers of PF-derived exosomes were detected by western blot. (b) Images of exosomes acquired by TEM. (c) Uptake of PF-derived exosomes in CFs and HUVECs.

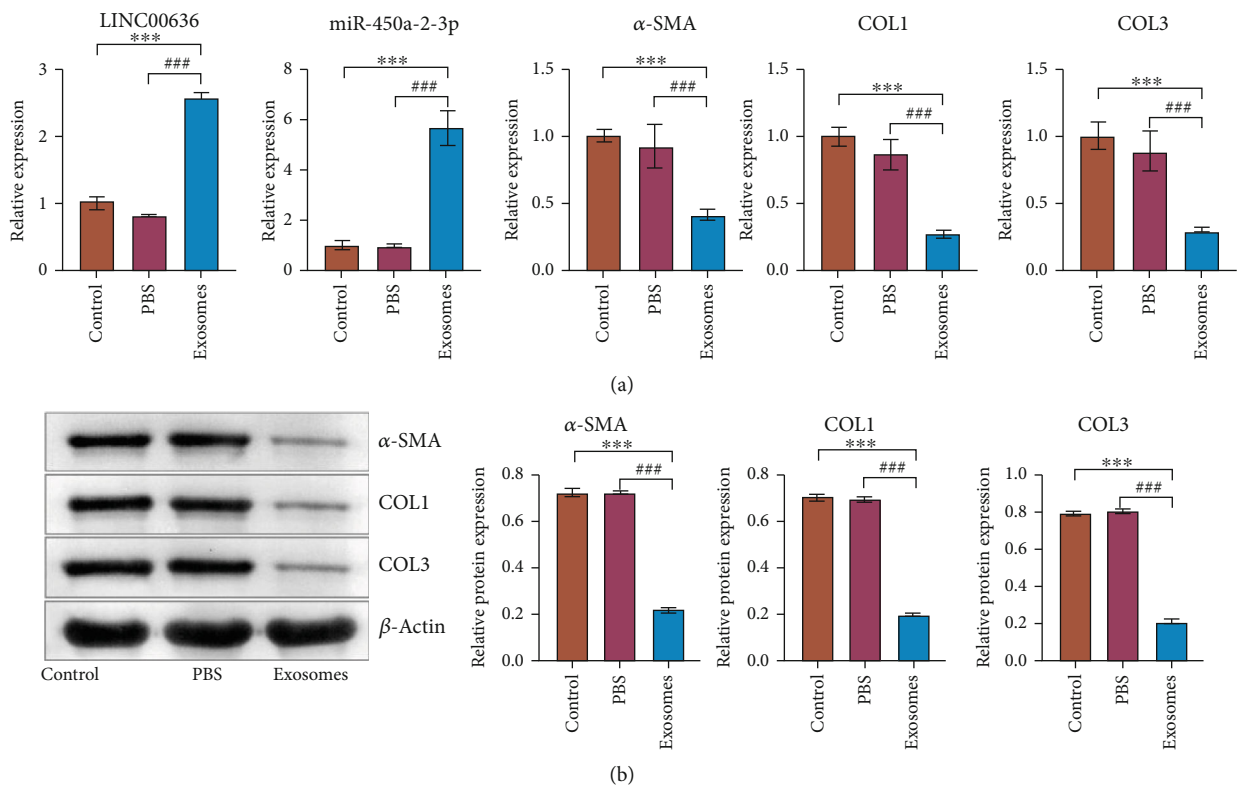


FIGURE 4: Exosomes containing LINC00636 could regulate miR-450a-2-3p and affects CFs. (a) Gene expression levels were detected by RT-qPCR. (b) α-SMA, COL1, and COL3 protein levels were detected by western blot. *** indicates significant differences with the control group, $P < 0.001$; ### indicates significant differences with the PBS group, $P < 0.001$.

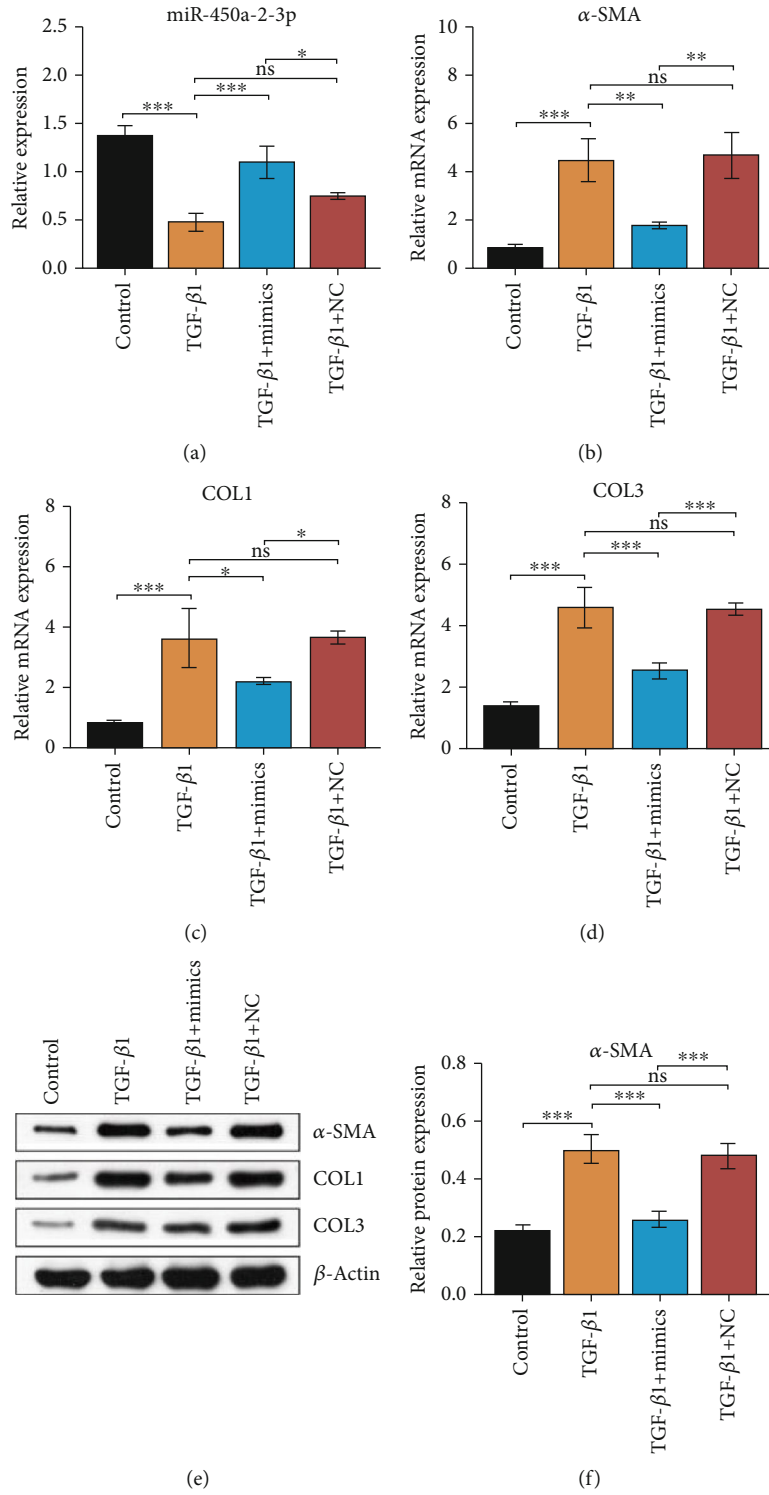


FIGURE 5: Continued.

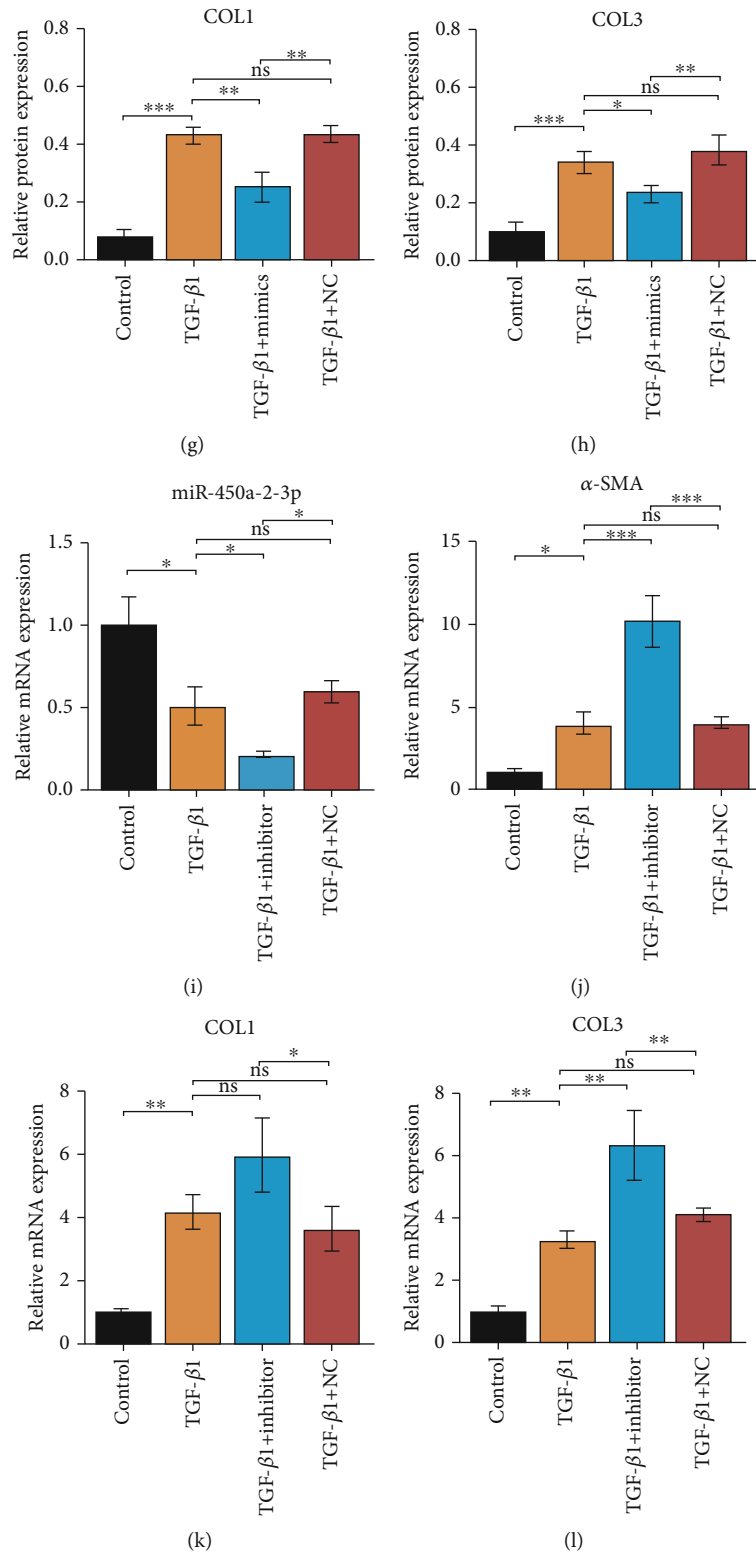


FIGURE 5: Continued.

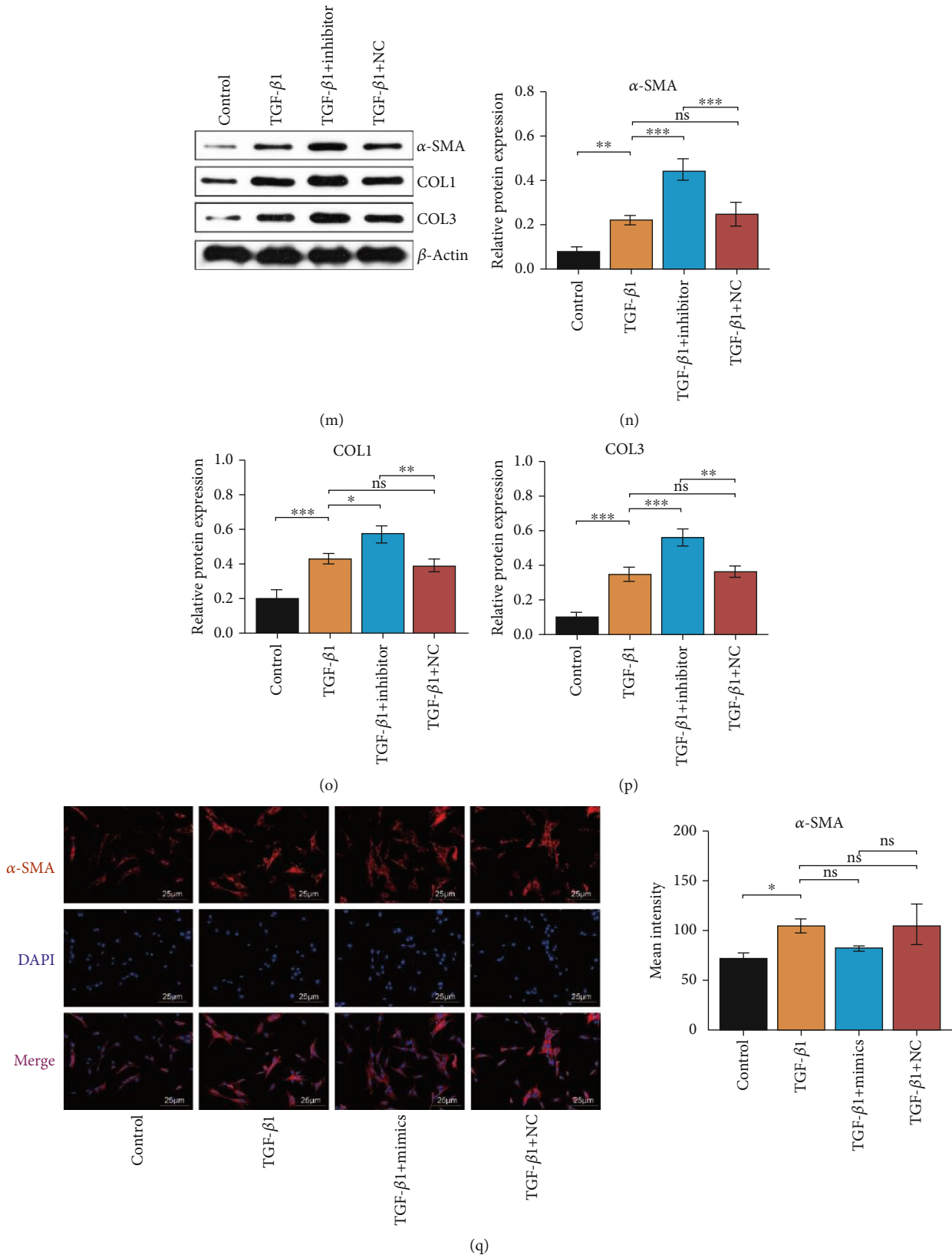


FIGURE 5: Continued.

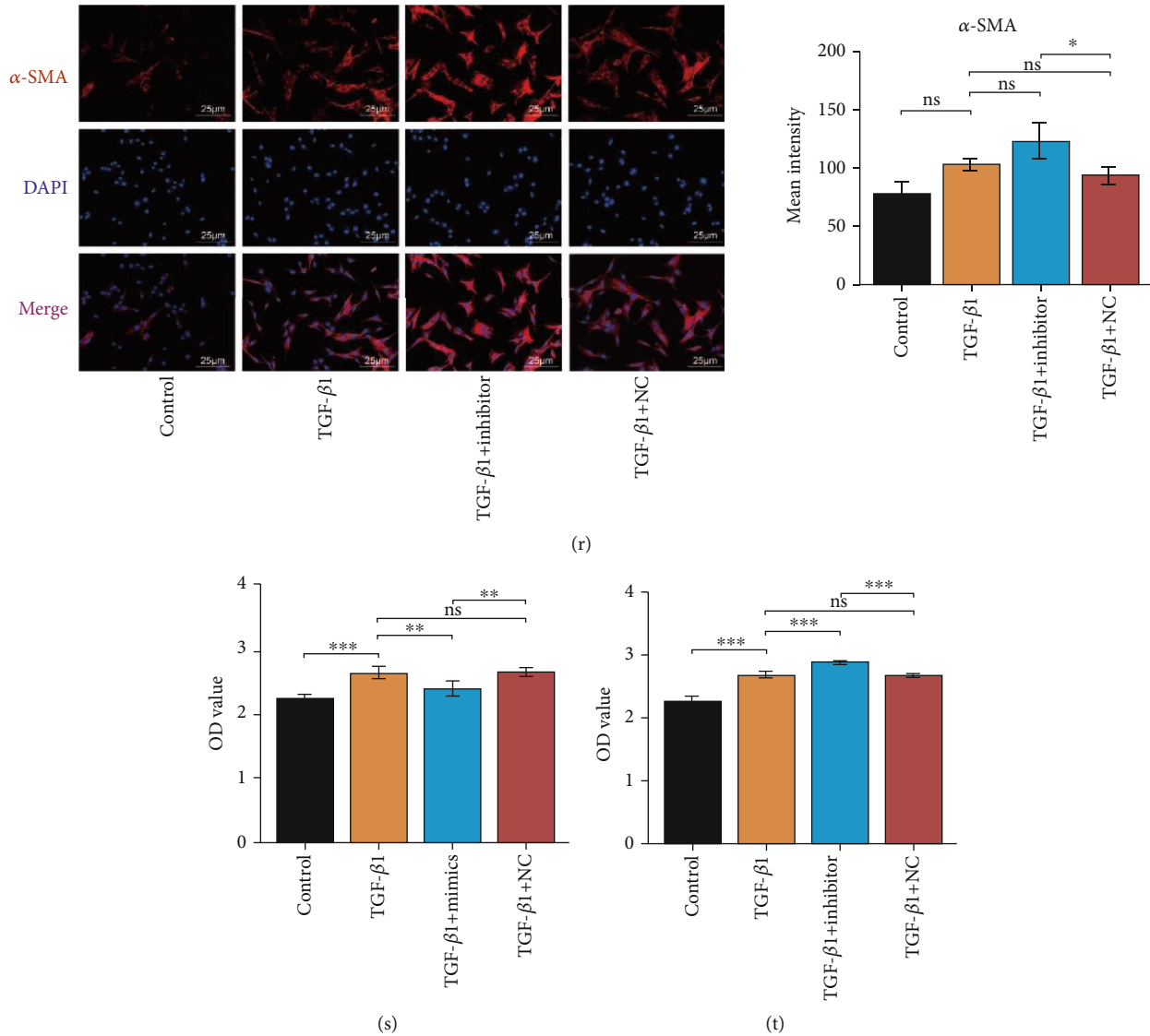


FIGURE 5: miR-450a-2-3p decreases TGF- β -induced activation and proliferation of CFs. miR-450a-2-3p, α -SMA, COL1, and COL3 mRNA expression in CFs transfected with mimics (a)–(d) and inhibitor (i)–(l) was detected using RT-qPCR. The protein levels of α -SMA, COL1, and COL3 in CFs transfected with mimics (e)–(h) and inhibitor (m)–(p) were determined using western blotting. The expression level of the miRNAs analyzed was normalized to the expression level of U6, and the expression level of mRNAs and proteins was normalized to the expression level of β -actin. Representative images of immunofluorescence staining for α -SMA in CFs transfected with mimics and inhibitor (r) (200 \times magnification) showed the antifibrotic effect of miR-450a-2-3p. CF proliferation measured by the CCK-8 assay after mimics (s) and inhibitor (t) treatment. Data is presented as the mean \pm SEM of three independent experiments. * $P < 0.05$, ** $P < 0.01$, *** $P < 0.001$, **** $P < 0.0001$.

hypothesized that lncRNAs carried by PF-derived exosomes may play a partial role in cardiomyocyte fibrosis. Therefore, we first isolated exosomes in the PF of the nAF and AF groups and confirmed their identity by analyzing the protein levels of several exosome markers using western blot (Figure 3(a)). A diagram of the isolated exosomes is shown in Figure 3(b). CFs and HUVECs stained with DAPI solution exhibited efficient uptake of exosomes as indicated by the internalization of PKH26-labeled exosomes (Figure 3(c)).

3.4. I LINC00636 Containing Exosomes Regulates miR-450a-2-3p and Affects CFs. To explore the effect of exosomes on

CFs, we cocultured CFs and exosomes isolated from the PF of nAF patients. The expression level of LINC00636 in CFs was determined using RT-qPCR. Compared with the control and PBS groups, LINC00636 was highly expressed in the cells that had been incubated exosomes. Furthermore, miR-450a-2-3p was highly expressed in cells incubated with exosomes in than in the control group. LINC00636 may mediate miR-450a-2-3p expression levels, impacting the degree of fibrosis in CFs. Further, the expression levels of α -SMA, COL1, and COL3 were decreased at mRNA and protein levels (Figure 4). These results further suggest that exosomal LINC00636 may mediate miR-450a-2-3p expression to affect the degree of fibrosis in CFs.

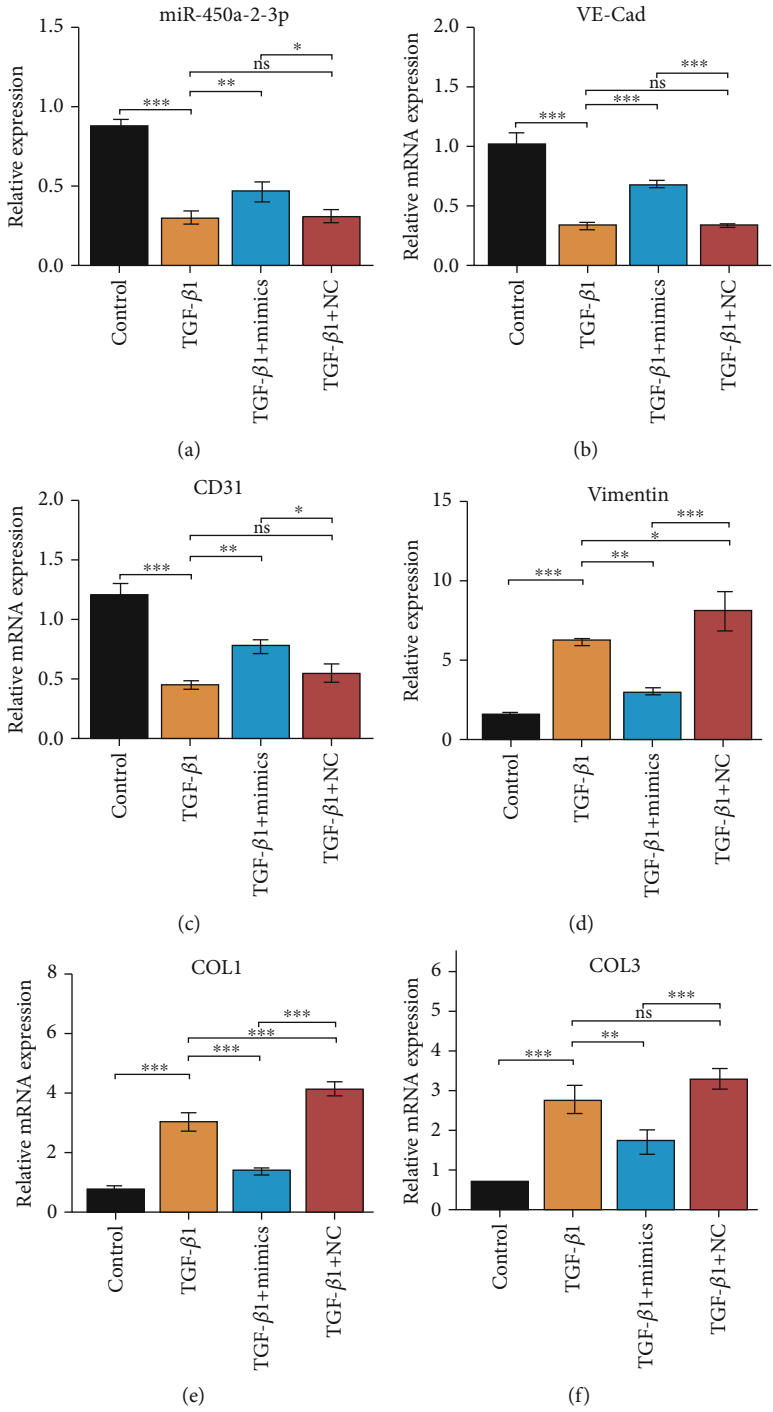


FIGURE 6: Continued.

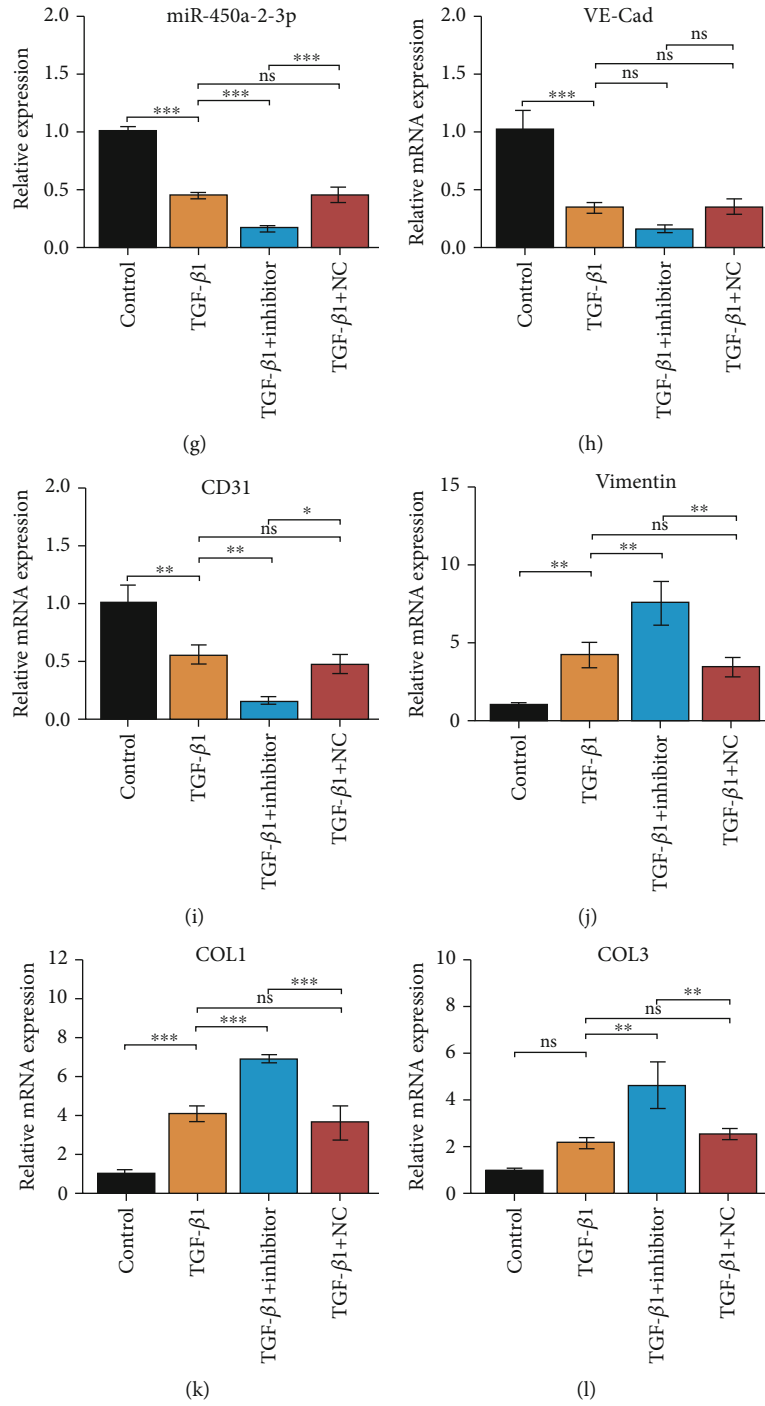


FIGURE 6: Continued.

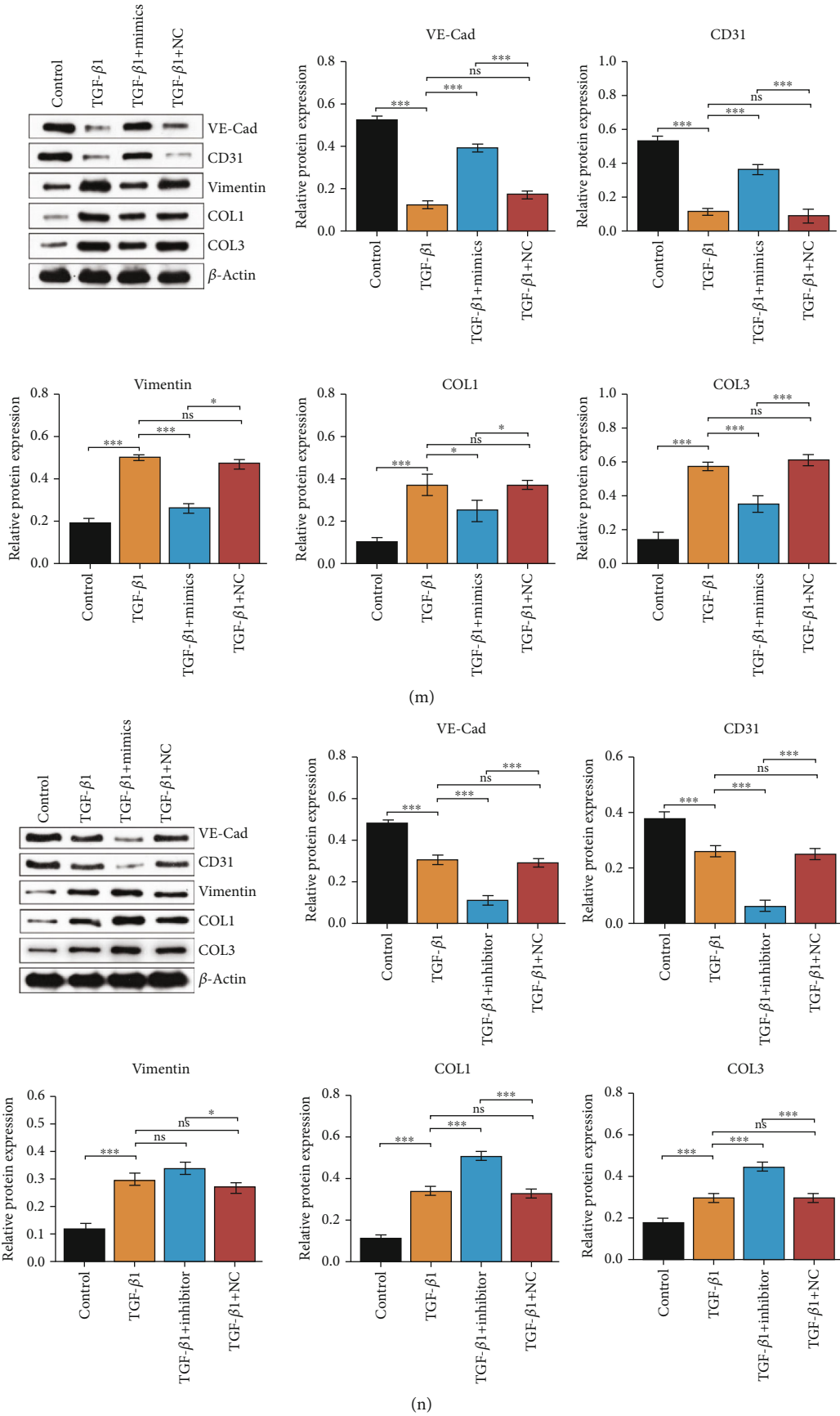
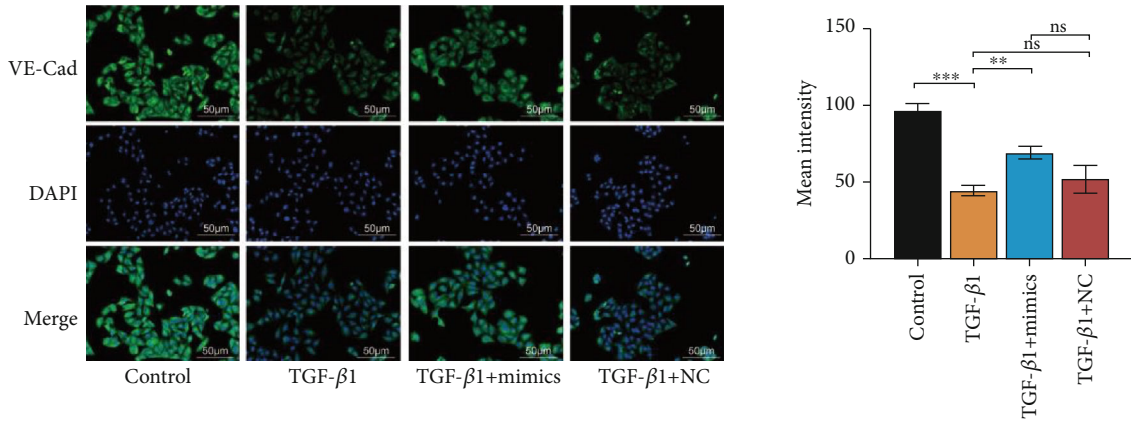
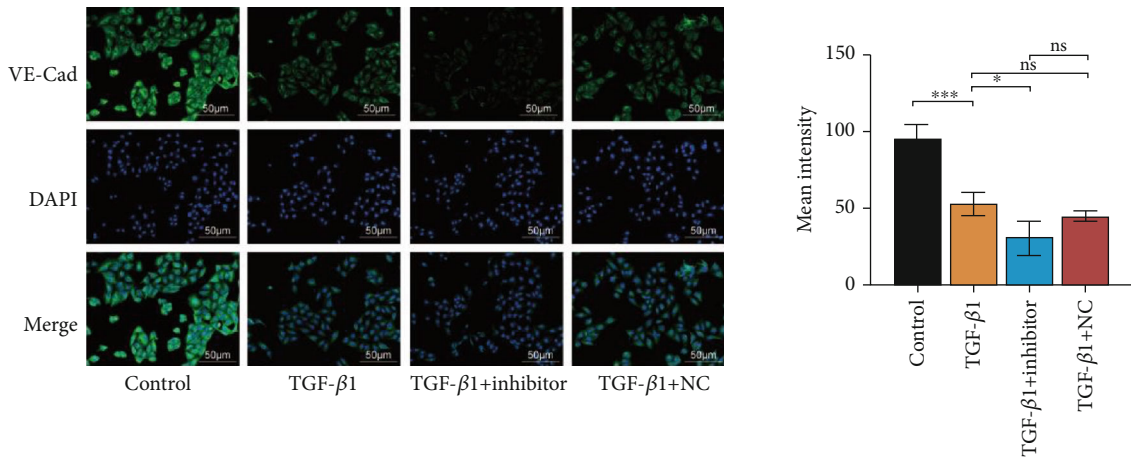


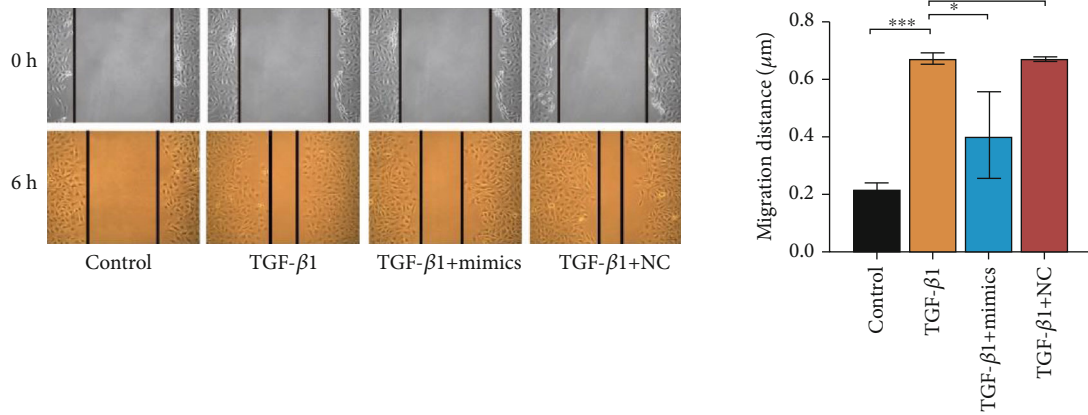
FIGURE 6: Continued.



(o)

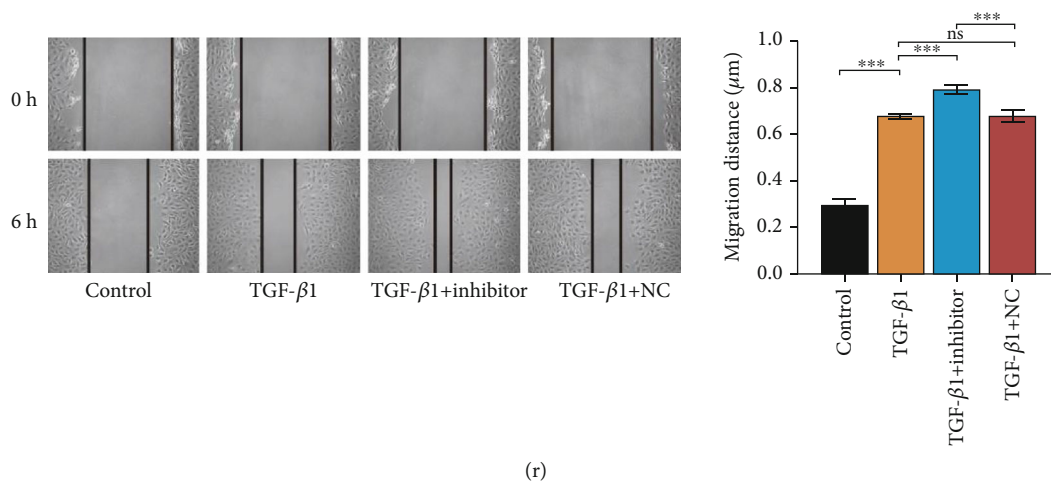


(p)



(q)

FIGURE 6: Continued.



(r)

FIGURE 6: miR-450a-2-3p inhibits TGF- β 1-induced EMT of HUVECs induced by TGF- β 1. miR-450a-2-3p, VE-Cad, CD31, vimentin, COL1, and COL3 mRNA levels in HUVECs transfected with mimics (a)–(f) and inhibitor (g)–(l) were determined via RT-qPCR. The protein levels of VE-Cad, CD31, vimentin, COL1, and COL3 in CFs transfected with mimics (m) and inhibitor (n) were examined using western blot. Expression levels of miRNAs were normalized to that of U6, and the expression levels of mRNAs and proteins were normalized to that of actin. Representative images of VE-Cad immunofluorescence staining in HUVECs transfected with mimics (o) and inhibitor (p) ($\times 200$ magnification) showed the antifibrotic effect of miR-450a-2-3p. Representative images of the scratch assay of mimic- (q) and inhibitor-transfected (r) HUVECs ($\times 100$ magnification). Data is presented as the mean \pm SEM of three independent experiments. * $P < 0.05$, ** $P < 0.01$, *** $P < 0.001$, **** $P < 0.0001$.

3.5. MiR-450a-2-3p Inhibits TGF- β 1-Induced Activation of CFs. To investigate the role of miR-450a-2-3p in the activation of CFs, TGF- β 1-induced CFs were transfected with miR-450a-2-3p-mimic, control mimic, miR-450a-2-3p inhibitor, and control inhibitor. We measured the expression level of miR-450a-2-3p in untreated CFs and TGF- β 1-treated CFs by RT-qPCR. Compared with the control condition, the miR-450a-2-3p expression was significantly downregulated in CFs treated with TGF- β . After transfection, the level of miR-450a-2-3p was higher in the mimic condition and lower in the inhibitor condition than in the TGF- β 1-treated CFs, confirming that the transfection of mimic and inhibitor was successful (Figures 5(a) and 5(i)). The overexpression of miR-450a-2-3p attenuated TGF- β 1-induced upregulation of α -SMA, COL1, and COL3 at transcription (Figures 5(b)–5(d)) and protein (Figures 5(e)–5(h)) levels. Conversely, the expression of α -SMA, COL1, and COL3 in TGF- β 1-induced CFs was further promoted when the miR-450a-2-3p expression was inhibited at both mRNA and protein levels (Figures 5(j)–5(p)). Similarly, the IF results demonstrated that the miR-450a-2-3p mimic significantly inhibited the α -SMA overexpression in TGF- β 1-induced CFs (Figure 5(q)), whereas the opposite was observed in the miR-450a-2-3p inhibitor group (Figure 5(r)). Based on the CCK8 assay, TGF- β 1 stimulation promoted the proliferation of CFs, but this effect was reversed by miR-450a-2-3p mimic treatment (Figure 5(s)). In contrast, when transfected with miR-450a-2-3p inhibitor, proliferation of TGF- β 1-induced CFs was further increased (Figure 5(t)). Together, these results suggest that miR-450a-2-3p inhibits the TGF- β 1-induced activation of CFs.

3.6. MiR-450a-2-3p Downregulates the TGF- β 1-Induced EMT of HUVECs. To investigate whether miR-450a-2-3p

can continuously inhibit EMT in HUVECs, we transfected TGF- β 1-induced HUVECs with miR-450a-2-3p mimic, miR-450a-2-3p inhibitor, and their negative control and detected miR-450a-2-3p expression levels in HUVECs from the different treatment groups. TGF- β 1 stimulation significantly reduced the expression of miR-450a-2-3p. However, this inhibition was partially abolished by the miR-450a-2-3p mimic, whereas it was intensified by the miR-450a-2-3p inhibitor (Figure 6(a)).

The protein expression levels of VE-CAD and PECAM-1/CD31 were decreased when the cells were stimulated with TGF- β 1, whereas the expression levels of vimentin, COL1, and COL3 increased. MiR-450a-2-3p mimics reversed the changes observed in the expression levels of these genes (Figures 6(b)–6(g)). In the miR-450a-2-3p inhibitor group, the expression levels of VE-Cad and PECAM-1/CD31 were inhibited, and the expression of vimentin, COL1, and COL3 was significantly enhanced (Figures 6(h)–6(l)). The changes in the expression level of these proteins were consistent with the changes detected at the mRNA level (Figures 6(m) and 6(n)).

The immunofluorescence assay of VE-Cad further validated these results (Figures 6(o) and 6(p)). Enhanced endothelial cell migration is one of the characteristics of EMT. Scratch experiments showed that TGF- β 1 accelerated HUVEC migration, an effect that was blocked by the miR-450a-2-3p mimic (Figure 6(q)), whereas miR-450a-2-3p inhibitor substantially facilitated HUVEC migration (Figure 6(r)). These results suggested that miR-450a-2-3p plays an antifibrotic role by suppressing EMT in HUVECs.

3.7. MAPK1 Is the Target of miR-450a-2-3p. To investigate the underlying mechanism of miR-450a-2-3p in CFs and HUVECs during cardiac remodeling, we assessed the mRNA

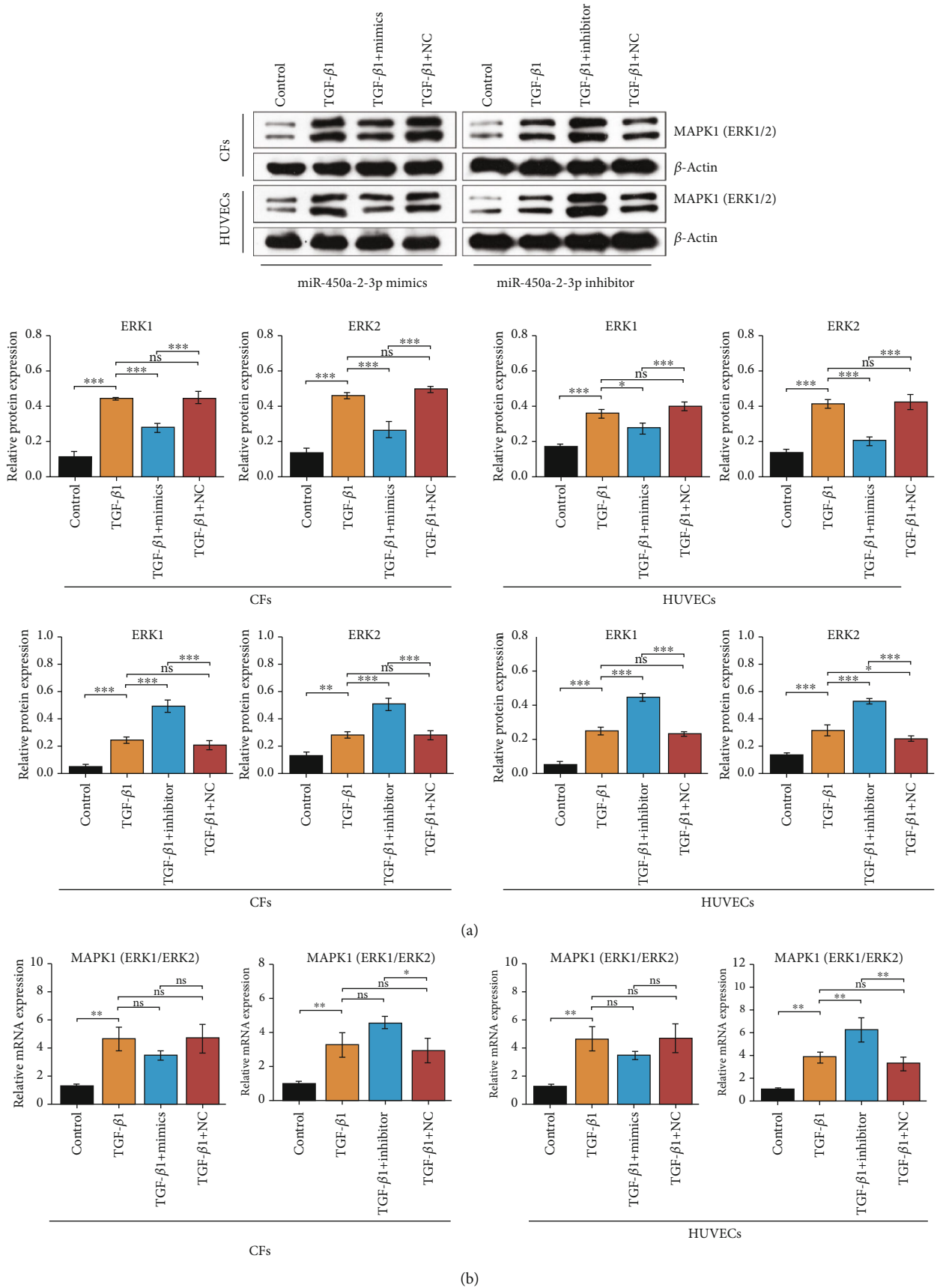


FIGURE 7: Continued.

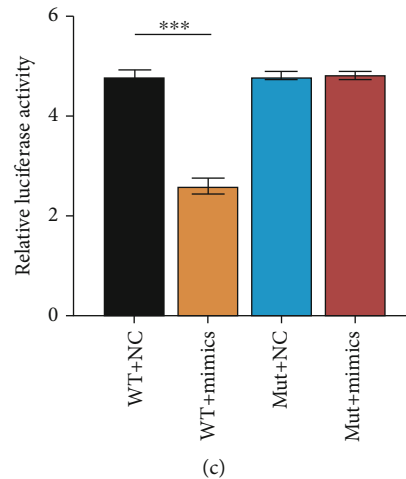


FIGURE 7: miR-450a-2-3p targets ERK1/2 (MAPK1). Protein (a) and mRNA (b) levels of ERK1/2 in CFs and HUVECS transfected with mimics or inhibitor were measured using western blot or RT-qPCR, respectively. The expression levels of mRNA and proteins were normalized to that of actin. (c) Relative luciferase activity of WT or mutant MAPK1 3'-UTR reporter cotransfected with miR-450a-2-3p mimics. Data is presented as the mean \pm SEM of three independent experiments. * $P < 0.05$, ** $P < 0.01$, *** $P < 0.001$, **** $P < 0.0001$.

and protein levels of endogenous MAPK1 in CFs and HUVECs. Transfection with miR-450a-2-3p-mimics significantly reduced the endogenous MAPK1 expression at both mRNA and protein levels, whereas transfection with miR-450a-2-3p inhibitor markedly augmented MAPK1 mRNA and protein expression levels (Figures 7(a) and 7(b)).

To further verify whether there is a targeting relationship between miR-450a-2-3p and MAPK1, luciferase reporter plasmids with the 3'UTR or 3'UTR-mut of MAPK1 were constructed. Cotransfection with miR-450a-2-3p and the wild-type 3'UTR of MAPK1 dramatically inhibited relative luciferase activity. Furthermore, transfection with miR-450a-2-3p had little influence on the relative luciferase activity of the mutant MAPK1 3'UTR (Figure 7(c)). These results demonstrate that MAPK1 is a direct target of miR-450a-2-3p.

3.8. Overexpression of MAPK1 Neutralizes the Effect of miR-450a-2-3p. We next investigated whether MAPK1 is required for the miR-450a-2-3p activity. CCK8 data showed that the overexpression of MAPK1 eliminated the inhibitory effect of miR-450a-2-3p on CF (Figure 8(a)). In addition, the scratch assay showed that the inhibitory effect of miR-450a-2-3p mimic on HUVEC migration was markedly abolished by MAPK1 (Figure 8(b)). These findings suggest that miR-450a-2-3p is dependent on MAPK1 to regulate CF proliferation and EMT in HUVECs.

4. Discussion

Atrial structural remodeling is closely associated with cardiac fibrosis, which is considered to be fundamental to the occurrence and progression of AF. The abnormal expression of the ECM in CFs, the most common cell type in the heart, plays a deleterious role in cardiac fibrosis [15]. So far, there are still only a few effective therapeutic strategies for cardiac fibrosis due to the great difficulty of reversing cardiac fibrosis [16].

Hence, researching potential targets to inhibit myocardial fibrosis is essential to develop new strategies to prevent and cure atrial fibrillation.

To date, an overwhelming majority of lncRNAs have not been well characterized. However, lncRNAs have been shown to be involved in almost every facet of gene regulation, including epigenetic regulation, imprinting, nuclear and cytoplasmic trafficking, transcription, and mRNA splicing. Thus, lncRNAs are involved in many diverse biological processes, including cell cycle, cell proliferation, apoptosis, and differentiation [10]. After we discovered the presence of LINC00636 in pericardial fluid, we further found that LINC00636 could mediate the effect of miR-450a-2-3p on CFs. We have not verified whether there is a direct targeted regulation of the two ncRNAs. In recent years, studies have shown that lncRNAs can adsorb miRNAs. Since there are no lncRNAs that target the promotion of miRNA expression, we speculate that there may be an unknown pathway between LINC00636 and miR-450a-2-3p, which we seek to investigate to in our future research.

miRNAs, which are endogenous small noncoding RNAs, play important roles in regulating cardiac remodeling. For example, miR-30/133 regulates myocardial fibrosis by suppressing the expression of connective tissue growth factor in left ventricular hypertrophy [17]. In this study, the miR-450a-2-3p expression in CFs and HUVECs was downregulated under the induction of TGF- β 1, which may be an important factor in the progression of fibrosis. However, when the miR-450a-2-3p expression was upregulated, the TGF- β 1-induced overexpression of COL1, COL3, and α -SMA was inhibited, suggesting the inhibition of CF activation. On the other hand, when miR-450a-2-3p was upregulated in TGF- β 1-stimulated HUVECs, VE-Cad, PECAM-1/CD31, vimentin, COL1, and COL3 were upregulated, indicating that miR-450a-2-3p suppressed TGF- β 1-induced EMT in HUVECs. TGF- β 1 is one of the most effective factors in

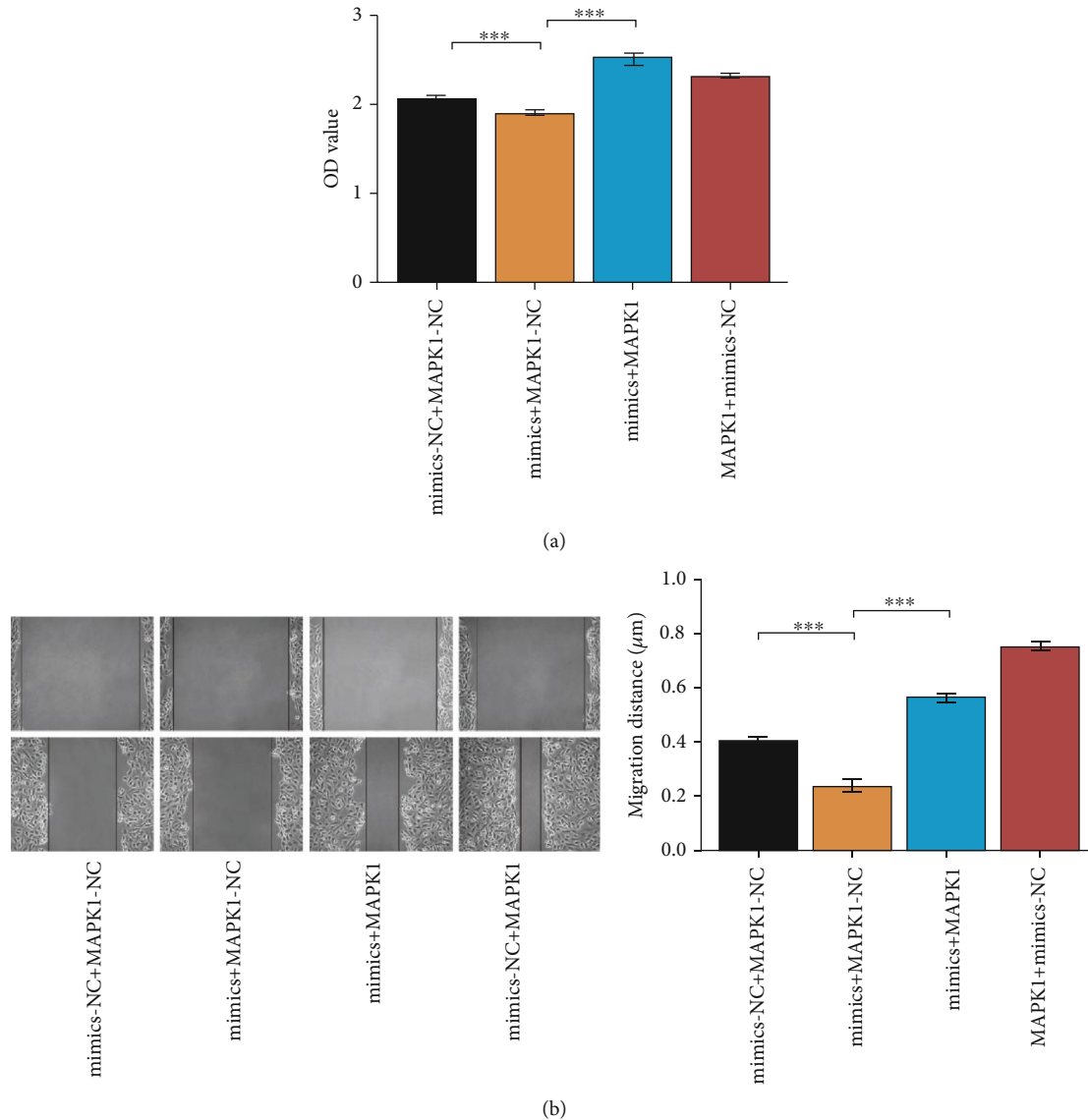


FIGURE 8: MAPK1 neutralizes the antifibrogenic effect by miR-450a-2-3p. (a) The proliferation of CFs was quantified by the CCK8 assay. CFs were transfected with mixture of miR-450a-2-3p mimics or NC (10 μ L) and MAPK1 overexpression plasmid or empty vector (2.5 μ g) for 48 h. (b) The scratch test was used to characterize the EMT in HUVECs. HUVECs were treated with blend of miR-450a-2-3p mimics or NC (10 μ L) and MAPK1 overexpression plasmid or empty vector (2.5 μ g) for 24 h. Data is presented as the mean \pm SEM of three independent experiments. * $P < 0.05$, ** $P < 0.01$, *** $P < 0.001$, **** $P < 0.0001$.

inducing cardiac fibrosis among various regulatory stimuli of AF [18, 19]. TGF- β 1 signaling involves at least two independent pathways, typical Smad-dependent pathway [20] and Smad-independent or certain atypical pathways [21, 22]. Studies have shown that endothelin 1 (ET-1) and TGF- β 1 jointly promote myofibroblast differentiation [23]. This may be related to the ability of ET-1 to induce ECM production in fibroblasts and differentiation of myofibroblasts [24]. Similarly, AngII induces the production of ET-1 through MAPK1 and reactive oxygen species, thereby promoting fibroblast activation and fibrosis [25]. Additionally, TGF- β 1-induced production of MAPK1 is required for the expression of CTGF, which is a key marker of myofibroblast differentia-

tion [26, 27]. In essence, the TGF- β 1/MAPK1 pathway may play a key role in atrial fibrosis [28].

MAPK1, a member of the MAPK family, has been reported to be involved in a variety of biological processes, such as myocardial fibrosis [22–30]. In an AF dog model, TRPC3 was found to regulate the proliferation of myocardial fibrosis by affecting Ca^{2+} influx through the MAPK1/miRNA-26/NFAT pathway, thereby increasing the expression of TRPC3 in the myocardium [30]. Some miRNAs play a role in pathological processes by regulating MAPK1. For instance, Thum et al. found that miR-21 regulates the MAPK1 signaling pathway, affecting the growth of CFs and the secretion of related cytokines, thereby affecting the

process of interstitial fibrosis [29]. We confirmed the relationship between miR-450a-2-3p and MAPK1 through bioinformatic prediction analyses and dual luciferase assay. Furthermore, CCK8 and scratch assays showed that the MAPK1 overexpression could counteract the effect of miR-450a-2-3p. These results suggested that both the effects of miR-450a-2-3p on CF proliferation and EMT in HUVECs were affected by MAPK1.

In conclusion, exosomal LINC00636 may mediate the effect of miR-450a-2-3p through the MAPK1 pathway on the viability of CFs, which might be used to treat myocardial fibrosis. Exosomes containing LINC00636 in human pericardial fluid promoted the expression of miR-450a-2-3p to inhibit MAPK1 and improve cardiac fibrosis in patients with atrial fibrillation.

Data Availability

The original data is GSE55296 of the GEO database.

Ethical Approval

The authors are accountable for all aspects of the work in ensuring that questions related to the accuracy or integrity of any part of the work are appropriately investigated and resolved. The study was conducted in accordance with the Declaration of Helsinki (revised in 2013). The study was approved by the Ethics Committee of Xiangya Hospital Central South University (201803209), and informed consent was obtained from all the participants.

Conflicts of Interest

The authors declare that they have no competing interests.

Authors' Contributions

Langsha Liu conceived and design experiments. Kaibo Lei and Fanyan Luo performed the experiments. Kaibo Lei and Langsha Liu wrote the paper. All authors have read and agreed to the published version of the manuscript.

Acknowledgments

This work was supported by the National Natural Science Foundation of China (to Fanyan Luo; no. 81873494) and the Hunan Natural Science Foundation (to Fanyan Luo; no. 2018JJ2665).

Supplementary Materials

All primer sequences were used in the study. (*Supplementary Materials*)

References

[1] S. S. Chugh, R. Havmoeller, K. Narayanan et al., "Worldwide epidemiology of atrial fibrillation: a Global Burden of Disease 2010 Study," *Circulation*, vol. 129, no. 8, pp. 837–847, 2014.

[2] B. Burstein and S. Nattel, "Atrial fibrosis: mechanisms and clinical relevance in atrial fibrillation," *Journal of the American College of Cardiology*, vol. 51, no. 8, pp. 802–809, 2008.

[3] H. Cochet, A. Mouries, H. Nivet et al., "Age, atrial fibrillation, and structural heart disease are the main determinants of left atrial fibrosis detected by delayed-enhanced magnetic resonance imaging in a general cardiology population," *Journal of Cardiovascular Electrophysiology*, vol. 26, no. 5, pp. 484–492, 2015.

[4] B. H. Smaill, "Fibrosis, myofibroblasts, and atrial fibrillation," *Circulation. Arrhythmia and Electrophysiology*, vol. 8, no. 2, pp. 256–257, 2015.

[5] J. Baum and H. S. Duffy, "Fibroblasts and myofibroblasts: what are we talking about?," *Journal of Cardiovascular Pharmacology*, vol. 57, no. 4, pp. 376–379, 2011.

[6] E. M. Zeisberg and R. Kalluri, "Origins of cardiac fibroblasts," *Circulation Research*, vol. 107, no. 11, pp. 1304–1312, 2010.

[7] J. D. Lajiness and S. J. Conway, "The dynamic role of cardiac fibroblasts in development and disease," *Journal of Cardiovascular Translational Research*, vol. 5, no. 6, pp. 739–748, 2012.

[8] P. Snider, K. N. Standley, J. Wang, M. Azhar, T. Doetschman, and S. J. Conway, "Origin of cardiac fibroblasts and the role of periostin," *Circulation Research*, vol. 105, no. 10, pp. 934–947, 2009.

[9] G. St Laurent, C. Wahlestedt, and P. Kapranov, "The landscape of long noncoding RNA classification," *Trends in Genetics*, vol. 31, no. 5, pp. 239–251, 2015.

[10] Y. Zhong, Q. Lu, W. Qiu, and Y. Luo, "LINC00636 promotes lymph node metastasis and cervical cancer through targeting NM23," *Bioscience Reports*, vol. 40, no. 10, 2020.

[11] L. Liu and Y. Chen, "Identification of microRNAs enriched in exosomes in human pericardial fluid of patients with atrial fibrillation based on bioinformatic analysis," *Journal of Thoracic Disease*, vol. 12, no. 10, pp. 5617–5627, 2020.

[12] G. Condorelli, M. V. Latronico, and E. Cavarretta, "microRNAs in cardiovascular diseases: current knowledge and the road ahead," *Journal of the American College of Cardiology*, vol. 63, no. 21, pp. 2177–2187, 2014.

[13] X. Chen, Y. Ba, L. Ma et al., "Characterization of microRNAs in serum: a novel class of biomarkers for diagnosis of cancer and other diseases," *Cell Research*, vol. 18, no. 10, pp. 997–1006, 2008.

[14] C. Beltrami, M. Besnier, S. Shantikumar et al., "Human pericardial fluid contains exosomes enriched with cardiovascular-expressed microRNAs and promotes therapeutic angiogenesis," *Molecular Therapy*, vol. 25, no. 3, pp. 679–693, 2017.

[15] C. A. Souders, S. L. Bowers, and T. A. Baudino, "Cardiac fibroblast: the renaissance cell," *Circulation Research*, vol. 105, no. 12, pp. 1164–1176, 2009.

[16] Q. Wang, Y. Yu, P. Zhang et al., "The crucial role of activin a/ALK4 pathway in the pathogenesis of Ang-II-induced atrial fibrosis and vulnerability to atrial fibrillation," *Basic Research in Cardiology*, vol. 112, no. 4, p. 47, 2017.

[17] R. F. Duisters, A. J. Tijssen, B. Schroen et al., "miR-133 and miR-30 regulate connective tissue growth factor: implications for a role of microRNAs in myocardial matrix remodeling," *Circulation Research*, vol. 104, no. 2, pp. 170–178, 2009.

[18] R. Khan and R. Sheppard, "Fibrosis in heart disease: understanding the role of transforming growth factor-beta in cardiomyopathy, valvular disease and arrhythmia," *Immunology*, vol. 118, no. 1, pp. 10–24, 2006.

- [19] A. Leask, "Potential therapeutic targets for cardiac fibrosis: TGFbeta, angiotensin, endothelin, CCN2, and PDGF, partners in fibroblast activation," *Circulation Research*, vol. 106, no. 11, pp. 1675–1680, 2010.
- [20] R. M. Greene, P. Nugent, P. Mukhopadhyay, D. R. Warner, and M. M. Pisano, "Intracellular dynamics of Smad-mediated TGFbeta signaling," *Journal of Cellular Physiology*, vol. 197, no. 2, pp. 261–271, 2003.
- [21] L. Hecker, R. Vittal, T. Jones et al., "NADPH oxidase-4 mediates myofibroblast activation and fibrogenic responses to lung injury," *Nature Medicine*, vol. 15, no. 9, pp. 1077–1081, 2009.
- [22] J. Davis, A. R. Burr, G. F. Davis, L. Birnbaumer, and J. D. Molkentin, "A TRPC6-dependent pathway for myofibroblast trans-differentiation and wound healing in vivo," *Developmental Cell*, vol. 23, no. 4, pp. 705–715, 2012.
- [23] X. Shi-wen, L. Kennedy, E. A. Renzoni et al., "Endothelin is a downstream mediator of profibrotic responses to transforming growth factor beta in human lung fibroblasts," *Arthritis and Rheumatism*, vol. 56, no. 12, pp. 4189–4194, 2007.
- [24] A. Leask, "Targeting the TGFβ, endothelin-1 and CCN2 axis to combat fibrosis in scleroderma," *Cellular Signalling*, vol. 20, no. 8, pp. 1409–1414, 2008.
- [25] P. Shephard, B. Hinz, S. Smola-Hess, J. J. Meister, T. Krieg, and H. Smola, "Dissecting the roles of endothelin, TGF-β and GM-CSF on myofibroblast differentiation by keratinocytes," *Thrombosis and Haemostasis*, vol. 92, no. 8, pp. 262–274, 2004.
- [26] A. Leask, A. Holmes, C. M. Black, and D. J. Abraham, "Connective tissue growth factor gene regulation," *The Journal of Biological Chemistry*, vol. 278, no. 15, pp. 13008–13015, 2003.
- [27] S. Xie, M. B. Sukkar, R. Issa, U. Oltmanns, A. G. Nicholson, and K. F. Chung, "Regulation of TGF-β1-induced connective tissue growth factor expression in airway smooth muscle cells," *American Journal of Physiology. Lung Cellular and Molecular Physiology*, vol. 288, no. 1, pp. L68–L76, 2005.
- [28] L. Han and J. Li, "Canonical transient receptor potential 3 channels in atrial fibrillation," *European Journal of Pharmacology*, vol. 837, pp. 1–7, 2018.
- [29] T. Thum, C. Gross, J. Fiedler et al., "MicroRNA-21 contributes to myocardial disease by stimulating MAP kinase signalling in fibroblasts," *Nature*, vol. 456, no. 7224, pp. 980–984, 2008.
- [30] M. Harada, X. Luo, X. Y. Qi et al., "Transient receptor potential canonical-3 channel-dependent fibroblast regulation in atrial fibrillation," *Circulation*, vol. 126, no. 17, pp. 2051–2064, 2012.

Research Article

CBP22, a Novel Bacteriocin Isolated from *Clostridium butyricum* ZJU-F1, Protects against LPS-Induced Intestinal Injury through Maintaining the Tight Junction Complex

Tenghao Wang,^{1,2,3} Jie Fu,¹ Xiao Xiao,¹ Zeqing Lu,¹ Fengqin Wang,^{1,2} Mingliang Jin,^{1,2} Yizhen Wang ¹ and Xin Zong ¹

¹Key Laboratory of Molecular Animal Nutrition, Ministry of Education, College of Animal Sciences, Zhejiang University, Hangzhou, China

²Key Laboratory of Animal Nutrition and Feed Science in Eastern China, Ministry of Agriculture, Hangzhou, Zhejiang Province, China

³Zhejiang Qinglian Food Co., Ltd., Jiaxing, China

Correspondence should be addressed to Yizhen Wang; yzwang321@zju.edu.cn and Xin Zong; zongxin@zju.edu.cn

Received 5 July 2020; Revised 14 September 2020; Accepted 10 May 2021; Published 1 June 2021

Academic Editor: Tomasz Brzozowski

Copyright © 2021 Tenghao Wang et al. This is an open access article distributed under the Creative Commons Attribution License, which permits unrestricted use, distribution, and reproduction in any medium, provided the original work is properly cited.

A novel bacteriocin secreted by *Clostridium butyricum* ZJU-F1 was isolated using ammonium sulfate fractionation, cation exchange chromatography, affinity chromatography, and reverse-phase high-performance liquid chromatography (RP-HPLC). The bacteriocin, named CBP22, contained 22 amino acids with the sequence PSAWQITKCAGSIAWALGSGIF. Analysis of its structure and physicochemical properties indicated that CBP22 had a molecular weight of 2264.63 Da and a +1 net charge. CBP22 showed activity against *E. coli* K88, *E. coli* ATCC25922, and *S. aureus* ATCC26923. The effects and potential mechanisms of bacteriocin CBP22 on the innate immune response were investigated with a lipopolysaccharide- (LPS-) induced mouse model. The results showed that pretreatment with CBP22 prevented LPS-induced impairment in epithelial tissues and significantly reduced serum levels of IgG, IgA, IgM, TNF- α , and sIgA. Moreover, CBP22 treatment increased the expression of the zonula occludens and reduced permeability as well as apoptosis in the jejunum in LPS-treated mice. In summary, CBP22 inhibits the intestinal injury and prevents the gut barrier dysfunction induced by LPS, suggesting the potential use of CBP22 for treating intestinal damage.

1. Introduction

Prebiotics, first identified in 1905, have been used to manipulate microorganisms in the host to improve measurable health outcomes [1]. The probiotic *Clostridium butyricum* (*C. butyricum*) has been widely reported to have beneficial effects on hosts, including the prevention of bacterial and viral infections, immunoregulation, alleviation of acute pancreatitis and liver damage, and the reduction of lipogenesis, as well as having antitumor effects. We previously isolated the *C. butyricum* ZJU-F1 strain from the feces of a healthy pig and preserved it in the China General Microbiological Culture Collection Centre (CGMCC No. 8939, Shanghai, China). Our previous studies have shown that *C. butyricum*

ZJU-F1 can alleviate growth retardation and intestinal barrier dysfunction caused by weaning [2]. However, the specific components of *C. butyricum* that are responsible for the beneficial biological functions are, as yet, unclear.

Much of our knowledge of the mechanisms of probiotics is based on bacteriocins. Bacteriocins are a class of bioactive polypeptides or proteins that are encoded by specific bacterial genes and synthesized in the ribosome. During the last decade, bacteriocins have been widely studied in the field of food preservation and alternative antibiotics. A growing number of studies have shown that bacteriocins have multiple biological functions, including antiviral activities, anti-infection of the gastrointestinal tract, spermicidal activities, and anticancer activity [3–6]. For example, plantaricin, a

bacteriocin secreted by *Lactobacillus plantarum*, potentially benefits diet-induced obese mice via fortifying tight junctions between intestinal epithelial cells [7]. Bacteriocin Lmo2776 of *Listeria monocytogenes* can target the commensal *Prevotella copri* and modulate intestinal infection [8].

To date, three bacteriocins of *C. butyricum*, butyricin 7423, butyricin M588, and perfringocin 1105, with molecular weights of 32.5 kDa, 8 kDa, and 76.0 kDa, respectively, have been characterized [9, 10]. Sequence analysis of a bacteriocinogenic plasmid of *C. butyricum* found that butyricin M588 with 83 amino acids is encoded by the gene ORF3 and has high antibacterial activity against *Clostridium beijerinckii* and *C. pasteurianum* [10]. Butyricin 7423 alters the permeability of *C. pasteurianum* cell membranes, allowing the release of metabolites and ions [11]. It has been reported that the growth performance improvement of *C. butyricum* was associated with reducing or preventing the barrier damage caused by ETEC K88 in piglets and broiler chickens [12–14]. Mechanistically, studies have shown that *C. butyricum* regulation of immune response is through the TLR2-mediated MyD88-independent signaling pathway [15, 16]. However, the potential biological functions and mechanisms of action of bacteriocins secreted by *C. butyricum* in intestinal health have not yet been elucidated.

The intestine contains the largest number of immune cells of any tissue in the body to maintain tolerance and promote immune responses against a variety of clinically important pathogens [17, 18]. Irritable bowel syndrome (IBS), characterized by irregular bowel habits, affects 10% of the world's population in the 21st century, but its aetiology remains largely undetermined [19, 20]. Studies have shown that intestinal infection, inflammation, and imbalance of intestinal microbiota can lead to IBS [21–23]. Several recent studies have shown a lower microbial diversity and a higher instability in the intestines of patients with IBS [20, 22]. Moreover, studies reported an increase in relative abundance of *Firmicutes*, mainly *Clostridium* cluster XIVa and *Ruminococcaceae*, together with a reduction in the relative abundance of *Bacteroidetes* in the intestines of patients with IBS [22, 24–26]. Our previous study suggested that maintaining tight junction complexes could modulate the inflammatory response to protect intestinal health [27]. Intestinal dysfunction plays a crucial role in the occurrence of systemic inflammation, suggesting that the intestine is the “engine” of systemic inflammation [28]. The intestinal mucosa forms a physical metabolic barrier, restricting the spread of pathogens, toxins, and allergens from the intestinal lumen to the circulatory system. The integrity of the intestinal barrier requires an accurate and delicate balance between proliferation and apoptosis [29, 30], the expression of tight junction proteins, such as ZO-1, ZO-2, occludin, and claudin-1 [31], and signaling molecules such as mucins, cytokines, Toll-like receptors, and chemokines [32].

In this study, we isolated and characterized the bacteriocin CBP22 from *Clostridium butyricum* ZJU-F1. The effects and potential mechanisms of bacteriocin CBP22 on the intestinal immune response were investigated by assessing alterations in the intestinal barrier with a lipopolysaccharide (LPS-) induced intestinal injury mouse model. Taken

together, we identified a new bacteriocin CBP22 and present evidence of its functions and mechanisms of action in immunomodulation.

2. Materials and Methods

2.1. Reagents. *Clostridium butyricum* ZJU-F1 came from our laboratory. *Staphylococcus aureus* ATCC5923, *Escherichia coli* ATCC25922, *Escherichia coli* K88, *Escherichia coli* K12, *Pseudomonas aeruginosa* CMCC27853, *Enterococcus faecalis* EC533, and *Enterococcus faecalis* EC618 were purchased from the China General Microbiological Culture Collection Center. RCM media and Mueller-Hinton (MH) broth were purchased from Hopebio (Qingdao, China). Lipopolysaccharide (LPS) O111:B4 and 4 kDa fluorescein isothiocyanate-conjugated dextran (FD4) were purchased from Sigma-Aldrich.

2.2. Bacteriocin Purification. After culturing ZJU-F1 in RCM medium at 37°C and 225 rpm until the $OD_{600} = 0.8$, the supernatant was isolated. Tris-HCl (20 mM, pH = 8.0) was slowly added to the supernatant, followed by a very slow addition of ammonium sulfate at 4°C. After stirring for 2 h, the precipitate was collected by centrifugation (15,000 rpm, 10 min) and resuspended in binding buffer (20 mM Tris-HCl, 500 mM NaCl, 20 mM imidazole, 10 mM 2-mercaptoethanol, pH 8.0) and then dialyzed against the same buffer at 4°C for 12 h. Using the method of Luan et al. [33], the dialyzed preliminary extract was applied to a cation exchange column (GE Healthcare, Chicago, IL, USA) and was eluted by application of a salt gradient from 0 to 50% (*w/v*) NaCl in 20 mM Tris-HCl and 10 mM 2-mercaptoethanol (pH 8.0). All peaks were pooled and analyzed by sodium dodecyl sulfate-polyacrylamide gel electrophoresis (SDS-PAGE) and then dialyzed in binding buffer at 4°C for 12 h. The dialyzed mixture was then applied to a Ni-NTA resin column (1 ml) equilibrated with binding buffer, followed by a step gradient with elution buffer. Peaks were again analyzed by SDS-PAGE and collected separately before concentrating to 10 mg/ml. Each fraction was tested for antibacterial activity, and the fractions with antibacterial activity were further separated by reverse-phase high-performance liquid chromatography (RP-HPLC) [34]. The samples were dissolved in solvent A (5% acetonitrile containing 0.1% (*v/v*) TFA) and then applied to RP-HPLC. The separation was performed using a linear gradient from 15% to 45% solvent B (0.1% (*v/v*) TFA in 95% acetonitrile) for 40 min at a flow rate of 2.0 ml/min, measured at 215 nm. In short, the principle of eluting proteins with Ni NTA column was that the Ni NTA column contains agarose microspheres. Under the action of agarose chelating medium, the microspheres chelate with Ni^{2+} , and the chelated Ni^{2+} can interact with the imidazole rings on His, Cys, or Trp, so as to achieve protein separation. Then, the sequences of purified proteins were determined by the Edman degradation method. The bacteriocin was synthesized by chemical synthesis based on the amino acid sequence, which was used for subsequent experiments *in vitro* and *in vivo*.

2.3. Antimicrobial Assays. The minimal inhibitory concentrations (MICs) were determined according to a modified

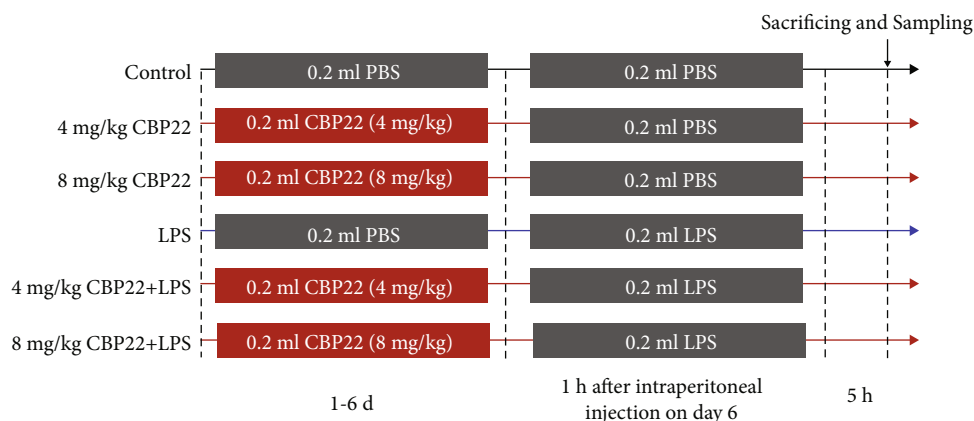


FIGURE 1: Experimental design and scheme of animal treatments.

version of the National Committee for Clinical Laboratory Standards broth microdilution method [35]. Microorganisms to be tested were grown to log phase in MH broth and transferred to fresh MH broth to a final concentration of 1×10^5 CFU/ml. The concentrations of bacteriocin were diluted by twofold serial dilutions to 2.5, 5, 10, 20, 40, 80, 160, 320, 640, 1280, and 2560 $\mu\text{g/ml}$. Bacterial solutions (90 ml) and bacteriocin (10 μl) of different concentrations were added into a 96-well plate. The positive and negative controls were 100 μl bacterial solution and 100 μl MH broth, respectively. The MICs were measured after incubation for 24 h at 37°C. Each experiment was performed in triplicate.

2.4. Analysis of Structure and Physicochemical Properties. The Edman degradation method was used to determine the N-terminal amino acid sequence of the purified peptide according to the instructions of Applied Biosystems Company's gas-phase protein sequencer. The helical wheel plots, secondary structures, and physicochemical properties were predicted and analyzed by the online resources HeliQuest (<https://heliquest.ipmc.cnrs.fr/>) [36] and the Zhang laboratory at the University of Michigan (<https://zhanglab.cmb.med.umich.edu/>) [37].

2.5. Hemolysis Assay. The hemolysis test was carried out using the method described by Gao et al. [35]. Briefly, fresh anticoagulated pig blood was collected from a healthy donor (Hangzhou, China) in a polycarbonate tube containing heparin. The blood was washed twice with PBS and then diluted to 1% in PBS with or without 10% fetal bovine serum. CBP22 was serially diluted with 0.01% acetic acid to 0 $\mu\text{g/ml}$ to 256 $\mu\text{g/ml}$. Different concentrations (10 μl) of CBP22 were incubated with erythrocytes (90 μl) at 37°C for 2 h in a 96-well plate. After centrifugation, the supernatants were transferred to a new 96-well plate to measure the absorbance at 405 nm. The negative and positive controls were erythrocytes incubated in 10 μl 0.01% acetic acid and 1% Triton X-100, respectively. Hemolysis (%) was calculated as follows:

$$\text{Hemolysis}(\%) = \frac{A_{\text{antimicrobial peptide}} - A_{0.01\% \text{ acetic acid}}}{A_{1\% \text{ Triton X-100}} - A_{0.01\% \text{ acetic acid}}} * 100. \quad (1)$$

2.6. Animals and Experimental Design. Sixty ICR male mice, aged 4-6 weeks, purchased from Shanghai SLAC Laboratory Animal Central, were used. The mice were raised in plastic cages under standard conditions (12 h light-dark cycle, 22-25°C, humidity 50-70%) and with free access to food and water. All animal experiments were carried out under the Animal Care and Use Committee of Zhejiang University.

As shown in Figure 1, the mice were randomly divided into six groups of 10 each. On day 6, mice in the LPS and CBP22+LPS groups were intraperitoneally injected with LPS (10 mg/kg, 200 μl each mouse) 1 h after CBP22 or PBS treatment; the other groups were injected with an equal volume of PBS. The mice were sacrificed, and blood samples were collected by cardiac puncture 5 h after LPS stimulation. In addition, both LPS and CBP22 were dissolved in PBS before administration.

2.7. Intestinal Histomorphology. The jejunum samples of mice were fixed in 4% paraformaldehyde for 24 h and then embedded in paraffin blocks. Sections of 5 μm thickness were cut and stained with hematoxylin and eosin (H&E), and images were acquired through a Leica DM3000 Microsystem (Leica, Germany). The villus height and crypt depth were measured using a Leica microscope (DM3000; Leica, Wetzlar, Germany) equipped with a CCD camera (DFC420; Leica). All programs were executed three times, and the data presented is the average of the three replicates. The degree of small intestinal injury was evaluated by Chiu's score classification [38] as follows: grade zero, normal mucosal villi; grade one, well-structured villi but subepithelial spaces; grade two, elevated villous epithelium with increasing subepithelial spaces; grade three, some cast-off villous epithelium; grade four, structural destruction of villi resulting in shedding and telangiectasia; and grade five, destruction of all the mucosa, hemorrhage, and ulceration.

2.8. Intestinal Permeability. The assessment of intestinal permeability is based on the measurement of FD4 in serum. Mice that had been intraperitoneally injected with LPS or PBS were given FD4 by oral gavage (20 mg/kg body weight) after 1 h. The blood collected at the time of sacrifice was centrifuged at 12,000 rpm at 4°C for 5 minutes. The concentration of FD4 in the serum was determined by measuring

TABLE 1: Specific primers used for real-time PCR.

Primer	Sequence (5'–3')	Length (bp)	T _m (°C)	
ZO-1	F	TCATCCCAAATAAGAACAGAGC	198	60
	R	GAAGAACAACCCTTTCATAAGC		
ZO-2	F	GCTTTGGTGTGGACCAAGAT	269	60
	R	TCCATTATGGGTTTGCATGA		
Claudin-1	F	GCTGGGTTTCATCCTGGCTTCT	110	60
	R	CCTGAGCGGTCACGATGTTGTC		
Occludin	F	AAGCAAGTGAAGGGATCTGC	204	60
	R	GGGGTTATGGTCCAAAGTCA		
TNF- α	F	GCATGGTGGTGGTTGTTTCTGACGAT	99	60
	R	GCTTCTGTTGGACACCTGGAGACA		
GAPDH	F	CAACGGCACAGTCAAGGCTGAGA	112	60
	R	CTCAGCACCAGCATCACCCCAT		

fluorescence using a SpectraMax M5 plate reader (Molecular Devices, San Jose, CA, USA) with an excitation wavelength of 485 nm and an emission wavelength of 535 nm.

2.9. TUNEL Staining. The TUNEL assay was used to identify jejunal epithelial cell apoptosis. The Leica DM3000 microscope system was used to analyze labeled cells. At least five views of each image from the different groups were taken with the background light kept constant between images. Five random duplications from each group were analyzed, the ratio of apoptotic to nonapoptotic cells was calculated according to the positive brown coloration, and the average values were calculated. The apoptosis index (AI) was calculated according to the following formula:

$$AI = \frac{\text{the number of apoptosis cells (AC)}}{\text{AC} + \text{the number of intact cells (IC)}} * 100\%. \quad (2)$$

2.10. Measurement of Immunoglobulins and TNF- α in Serum. The serum levels of immunoglobulins (IgG, IgA, and IgM) and TNF- α were determined using an enzyme-linked immunosorbent assay (ELISA) kit (Multisciences, Hangzhou, China) according to the manufacturer's protocol.

2.11. Determination of Intestinal sIgA Concentrations. The expression level of sIgA in ileal tissue was determined by a double-antibody sandwich ELISA, as previously described [39] using an ELISA kit purchased from Multisciences (Hangzhou, China). The ileal protein concentrations were measured by the BCA kit (KeyGEN, China), and the concentrations of sIgA were expressed as μg sIgA/mg protein.

2.12. Real-Time PCR. Total RNA was extracted from the jejunum using the TRIzol reagent according to the manufacturer's instructions. The RNA was reverse-transcribed into cDNA using a cDNA Reverse Transcription Kit. The sequences of the gene-specific primers were determined from previous publications [40] and were synthesized and purchased from Sangon Biotech (Shanghai, China). The primer

sequences and their T_m values and sizes are listed in Table 1. Amplification and detection were carried out using the SYBR Premix Ex Taq Kit (Takara Clontech, Otsu, Japan) in the ABI StepOnePlus Real-time PCR system (Applied Biosystems, Foster City, CA, USA). All the samples were analyzed in triplicate, and negative controls were included to check for the nonspecific amplification of primers.

2.13. Statistical Analysis. All statistical analyses were performed using SPSS software (Version 20.0, IBM Corp., Armonk, NY, USA), and all data were expressed as the means \pm standard error (SEM). Significant differences between the control and experimental groups were determined by a one-way ANOVA with Duncan's multiple range test. Statistically, a *P* value of less than 0.05 was considered significant.

3. Results

3.1. Isolation, Purification, and Identification of CBP22. The bacteriocin in the supernatant of ZJU-F1 was preliminarily extracted by ammonium sulfate precipitation and then separated and purified by cation exchange column chromatography, yielding three fractions (Figure 2(a)). The three fractions were separated and collected by affinity chromatography (Figure 2(b)). We then tested the antibacterial activity of the three fractions and found that only the second fraction showed antibacterial activity against *E. coli* and *S. aureus*. Thus, the second fraction was freeze-dried and concentrated, followed by purification on RP-HPLC. SDS-PAGE analysis showed that the molecular weight of the second fraction was about 3 kDa. Sequencing showed that the bacteriocin was a 22-amino acid peptide with the sequence PSAWQITK-CAGSIAWALGSGIF; the peptide was, therefore, named *Clostridium butyricum* peptide 22 (CBP22).

To further investigate the physicochemical properties of CBP22, we used helical wheel plots and secondary structure prediction by online analysis tools (Figures 2(c) and 2(d)). The results indicated that the isoelectric point of CBP22

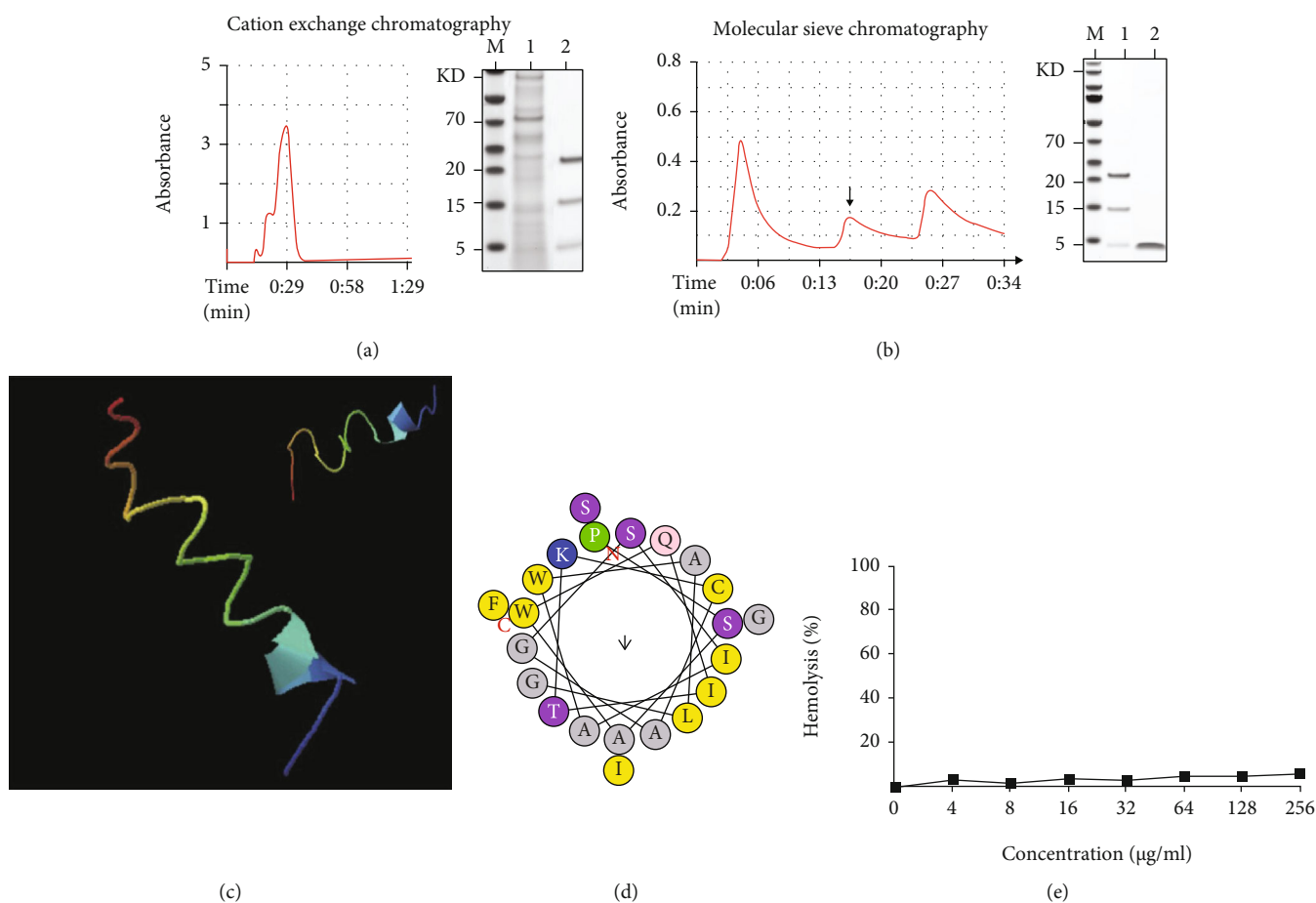


FIGURE 2: Isolation and identification of CBP22. (a) Cation exchange chromatography of the supernatant from *C. butyricum* culture medium at a wavelength of 215 nm and SDS-PAGE analysis. M: mark; lane 1: before purification; lane 2: after purification. (b) Affinity chromatography of products from (a) at a wavelength of 215 nm and SDS-PAGE analysis. M: mark; lane 1: before purification; lane 2: after purification. (c) Secondary structure prediction of CBP22. (d) Helical wheel plots of CBP22. (e) Hemolytic activity of CBP22 against porcine red blood cells. The hemoglobin release was monitored at 576 nm. The data are expressed as the mean \pm SEM, $n = 3$ biological replicates; bars with different small capital letters are statistically different from one another.

was 8.64 and the molecular weight was 2264.64 Da, with a net charge of +1 and hydrophobicity of 0.719 and a hydrophobic moment of 0.134.

3.2. Antibacterial Activity of CBP22. To evaluate the antibacterial activity of CBP22, the minimal inhibitory concentration (MIC) of the bacteriocin CBP22 against pathogenic bacteria was determined. As Table 2 shows, the CBP22 exhibited moderate activity against *E. coli* K88 with a MIC of 32 $\mu\text{g/ml}$ and showed low activity against *E. coli* ATCC25922 and *S. aureus* ATCC26923, with MICs of 128 and 64 $\mu\text{g/ml}$, respectively.

3.3. Hemolytic Activity. The hemolytic activity of the CBP22 against human erythrocytes was determined as a measure of toxicity to mammalian cells. The results showed that CBP22 had a low lethality to erythrocytes between 0 and 256 $\mu\text{g/ml}$. Fewer than 10% of erythrocytes were killed even at 256 $\mu\text{g/ml}$ (Figure 2(e)). These results indicated that CBP22 is safe to eukaryotes.

TABLE 2: Antibacterial activity of CBP22 measured by MIC.

Bacterial species	MIC ($\mu\text{g/ml}$)
Gram-negative bacteria	
<i>E. coli</i> K88	32
<i>E. coli</i> ATCC25922	128
<i>E. coli</i> K12	>256
<i>P. aeruginosa</i> CMCC27853	>256
Gram-positive bacteria	
<i>S. aureus</i> ATCC26923	64
<i>E. faecium</i> EC533	>256
<i>E. faecalis</i> EC618	>256

3.4. Intestinal Morphology. To further investigate the effects of CBP22 on intestinal health, we induced a mouse model with LPS stimulation. As shown in Figure 3(a), H&E staining of jejunal specimens from the control and CBP22-treated groups showed integrated villi and compactly arrayed

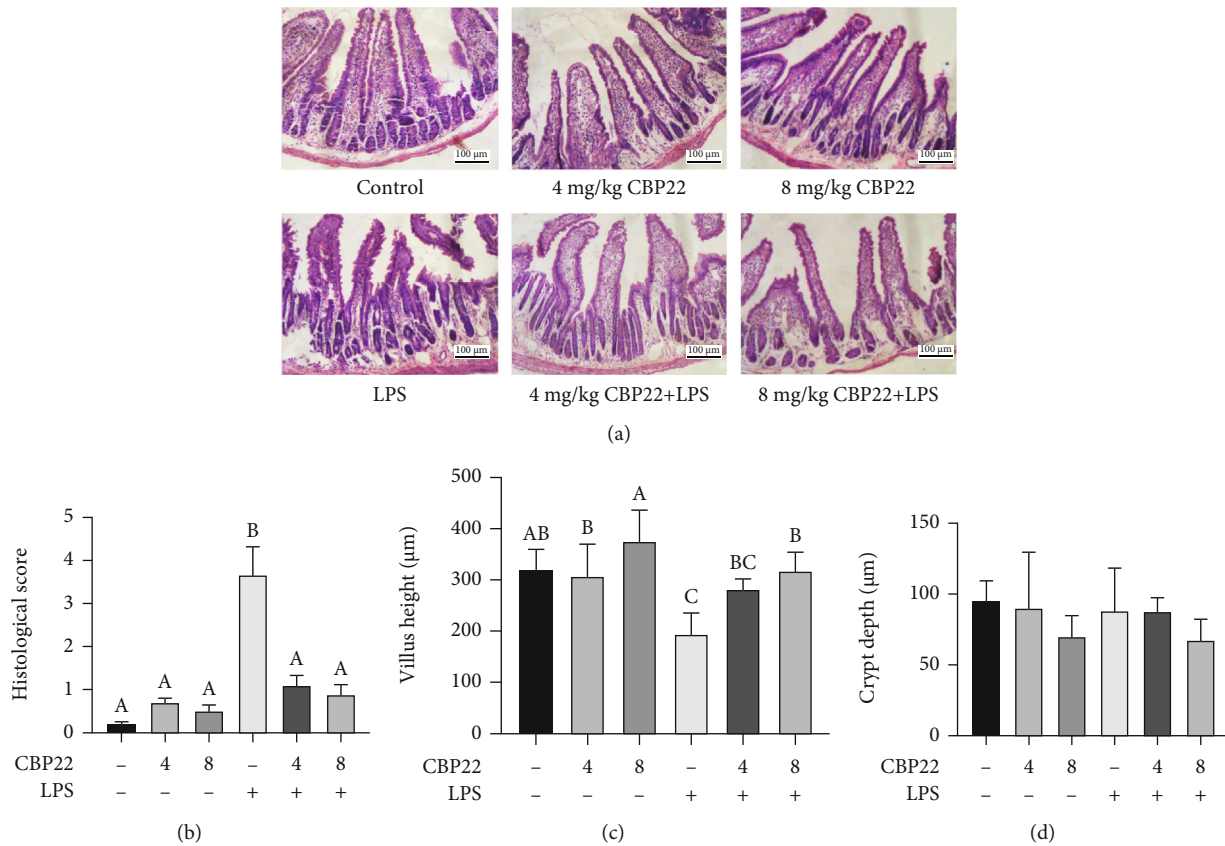


FIGURE 3: The protective effects of CBP22 on jejunal morphology in mice treated with LPS. (a) H&E staining of the jejunal mucosa, scale bar = 100 μm. (b) Mucosal damage grading. (c) Villus heights in the jejunum. (d) Crypt depths in the jejunum. The data are expressed as the mean ± SEM, $n = 10$ biological replicates; bars with different small capital letters are statistically different from one another.

epithelium. On the contrary, the intestinal epithelia of the jejunum in LPS-treated mice showed marked injury with epithelial exfoliation, discontinuous brush borders, and blunt villi. However, the jejunal villi of mice pretreated with 4 mg/kg and 8 mg/kg CBP22 were relatively intact, which suggested that CBP22 significantly alleviated the injury caused by LPS to the villi. Based on the score of small intestinal mucosal injury, we found that pretreatment with CBP22 prevented intestinal mucosal injury induced by LPS (Figure 3(b)).

As Figures 3(c) and 3(d) show, compared with the control group, the jejunal villus height and crypt depth in mice treated with 4 mg/kg and 8 mg/kg CBP22 were not significantly different while high concentrations of CBP22 caused a trend of increasing villus height and decreasing crypt depth. However, the villus height in the LPS group was reduced without significant alteration of the crypt depth. CBP22 pretreatment significantly alleviated the villus shortening caused by LPS with an improvement of 27.6% after treatment with 8 mg/kg CBP22 but with no effect on the crypt depth. These results suggest that CBP22 can protect the intestinal villi of mice from LPS damage.

3.5. Intestinal Epithelial Cell Apoptosis. Tissue TUNEL staining was conducted to analyze the levels of apoptosis in the jejunum. The brown and blue staining represented the apo-

ptotic and normal nuclei, respectively. In contrast to the control group, the apoptosis index of the 4 mg/kg and 8 mg/kg CBP22 treatments showed no significant difference, but LPS-treated mice showed a significantly increased jejunal apoptosis index. Compared with LPS-treated mice, in the mice pretreated with 4 mg/kg and 8 mg/kg CBP22 followed by treatment with LPS, the apoptosis index was significantly decreased by 82.65% and 86.81%, respectively (Figures 4(a) and 4(b)).

3.6. Serum Levels of IgA, IgG, IgM, and TNF-α. To determine the effects of CBP22 on the LPS-induced immune response, the levels of immunoglobulins and cytokines were measured. LPS treatment resulted in a marked increase in serum levels of IgA, IgG, and IgM compared with the control. CBP22 pretreatment significantly alleviated the elevation of serum immunoglobulins induced by LPS (Figures 5(a)–5(c)).

As shown in Figure 5(d), the serum TNF-α concentration of mice in the 4 mg/kg and 8 mg/kg CBP22 groups was slightly elevated but not significantly so. LPS treatment resulted in a 3.85-fold increase in serum TNF-α concentration relative to the control group (104.31 ± 11.63 pg/ml vs. 27.10 ± 7.14 pg/ml). CBP22 pretreatment significantly reduced TNF-α secretion induced by LPS to the same level as the control group.

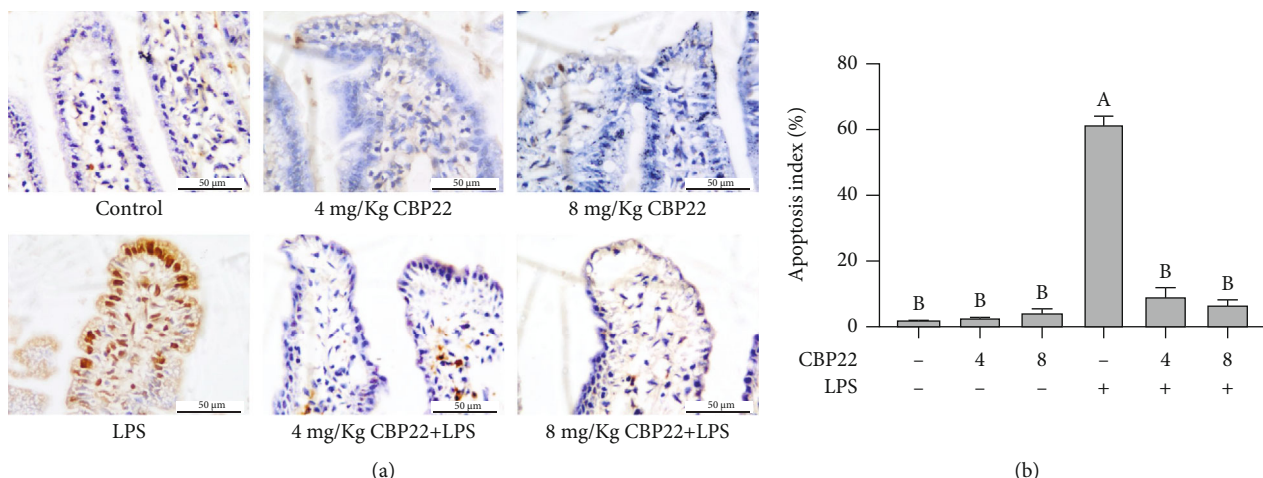


FIGURE 4: The effect of CBP22 on jejunum cell apoptosis in mice. (a) TUNEL staining of jejunal epithelial tissues, brown signals, scale bar = 50 μ m. (b) Apoptosis index of jejunal epithelial cells. The data are expressed as the mean \pm SEM, $n = 10$ biological replicates; bars with different small capital letters are statistically different from one another.

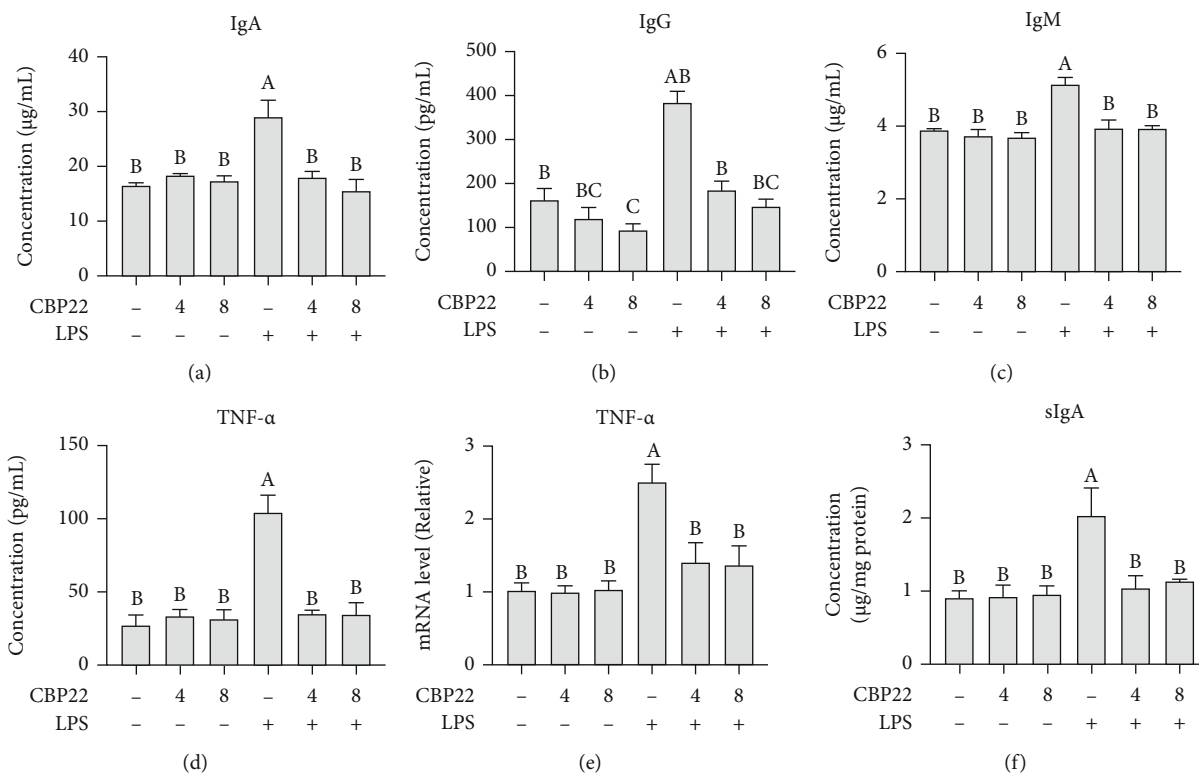


FIGURE 5: Effects of CBP22 on immune function in LPS-stimulated mice. (a–d) The concentration of IgA (a), IgG (b), IgM (c), and TNF- α (d) in serum. (e) Real-time PCR analysis of TNF- α mRNA expression in the jejunum. (f) Concentration of sIgA in the ileum. The q-PCR results are presented relative to those of GAPDH. The data are expressed as the mean \pm SEM, $n = 10$ biological replicates; bars with different small capital letters are statistically different from one another.

3.7. *Intestinal sIgA and TNF- α Level.* To further confirm the effects of CBP22 on the immune response, the TNF- α mRNA expression in the jejunum was determined. Similar to the results in the serum, there was no significant difference between TNF- α mRNA in the jejunum of mice treated with 4 mg/kg and 8 mg/kg CBP22. The expression of TNF- α

mRNA in the jejunum of LPS-treated mice was significantly increased, but pretreatment with 4 mg/kg and 8 mg/kg CBP22 followed by LPS resulted in significantly lower levels than those of the LPS group (Figure 5(e)).

The results of the ileal sIgA levels are shown in Figure 5(f). In comparison with the control mice, there

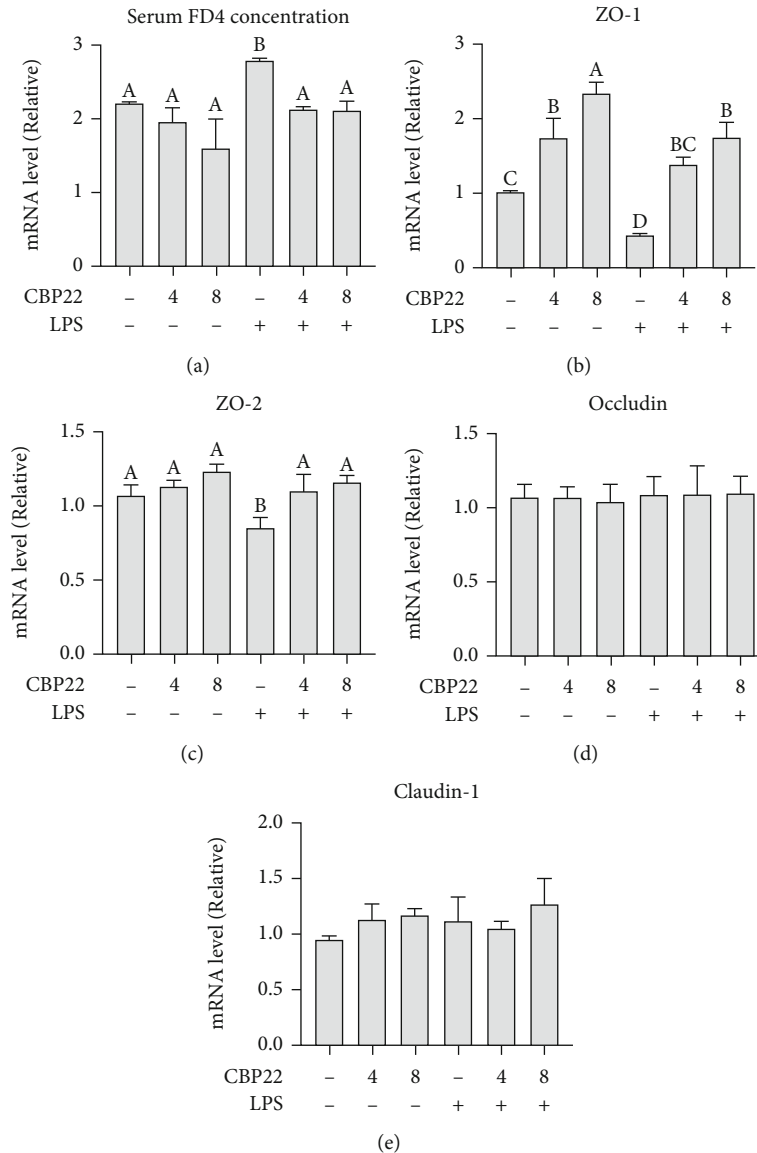


FIGURE 6: The protective effects of CBP22 on the intestinal barrier. (a) Intestinal permeability is determined by serum FD4 concentration. (b–d) RT-PCR analysis. The mRNA expression of tight junctions and results are presented relative to those of GAPDH, (b) ZO-1, (c) ZO-2, (d) occludin, and (e) claudin-1. The data are expressed as the mean \pm SEM, $n = 10$ biological replicates; bars with different small capital letters are statistically different from one another.

was no significant difference in the level of sIgA in the terminal ileum of mice treated with 4 mg/kg and 8 mg/kg CBP22. However, LPS treatment resulted in a 123.08% increase in the sIgA level relative to the control group. Pretreatment with 4 mg/kg and 8 mg/kg CBP22 significantly decreased secretion of sIgA by 40.39% and 43.84%, respectively, with no difference from the control group.

3.8. Intestinal Permeability. As the gut barrier function can regulate immune function, we assessed the intestinal permeability in each group. As shown in Figure 6(a), after intraperitoneal injection with LPS, the intestinal permeability to FD4 was significantly increased indicating that the barrier function was impaired. Pretreatment of LPS-administered mice

with 4 mg/kg and 8 mg/kg CBP22 significantly reduced the FD4 concentration in the serum indicating that CBP22 can protect the mouse intestinal barrier function against LPS challenge. However, there was no significant difference between CBP22 treatment alone and the control groups.

3.9. Intestinal Tight Junction Expression. To further investigate the role of CBP22 in intestinal barrier function, tight junction markers, such as claudin-1, occludin, ZO-1, and ZO-2, were measured. The mRNA expression levels of ZO-1 in the jejunum of mice treated with 4 mg/kg and 8 mg/kg CBP22 alone increased significantly in a dose-dependent manner (Figure 6(b)). LPS markedly reduced the mRNA expression of ZO-1 and ZO-2 by 57% and 15%, respectively,

but did not affect claudin-1 and occludin expression compared with the control group. As expected, CBP22 pretreatment completely and significantly abrogated the LPS-induced reduction in ZO-1 and ZO-2 mRNA (Figures 6(b)–6(d)).

4. Discussion

In this study, we describe the isolation of a novel bacteriocin from *C. butyricum* ZJU-F1 named CBP22 with a molecular weight of 2264.63 Da. We then demonstrated the role and potential mechanism of action of CBP22 effect on intestinal injury using an LPS-induced mouse model.

In recent years, studies found that many bacteriocins, such as SA2715 [41], MQ1 [42], and Nisin [43], have great potential as natural preservatives in food. In addition, bacteriocin is also widely used in oral care, skincare, vaginal care, and anticancer drugs [43–46]. In contrast to the other three known bacteriocins of *C. butyricum*, the molecular weight of CBP22 was relatively small, only 2264.35 Da, which is conducive to industrial production and a wide application in preservatives in the food and the care of oral, skin, and vaginal [43, 47]. In general, bacteriocins have a high toxicity. Hemolysis is an important indicator to evaluate the safety of bacteriocin. If the hemolysis rate is less than 5%, the bacteriocin is considered to have no hemolysis [48]. Our results showed that CBP22 had a very low hemolytic activity with less than 5%, indicating its potential safety. Moreover, our results found that CBP22 showed antibacterial activity against *E. coli* and *S. aureus* while not affecting *P. aeruginosa*, *E. faecium*, or *E. faecalis*, indicating that CBP22 may be a bacteriocin with narrow-spectrum antibacterial activity. Meanwhile, the physicochemical properties of CBP22 showed that it had one positive charge, which may be the reason for its weak antibacterial activity [49]. If CBP22 is used as the model to design derivative peptides, by changing one or more amino acids to increase the charge number and hydrophobic moment, a derivative peptide with high antibacterial activity and narrower antibacterial spectrum can be found, which will be conducive to the development of antibacterial specific and efficient bacteriocin.

In addition to antibacterial activity, the immune regulatory function of bacteriocins has attracted increasing attention. LPS is commonly used to induce acute immune responses in mammals, destroying the self-renewal of the intestinal villi and resulting in a high cell apoptosis index. The intestinal mucosa is the major site of nutrient absorption and digestion [50]. Intestinal diseases can directly destroy the ability to absorb and digest nutrients and may even cause inflammatory-related diseases that affect the whole body. It has been reported that bacteriocins and antimicrobial peptide can regulate tissue half-life and clearance of neutrophils by suppressing apoptosis [51]. Our results have shown that CBP22 alleviated intestinal damage caused by LPS and confirmed marked injury and a high cell apoptosis index for the jejunal intestinal epithelia of LPS-treated mice using H&E staining. As expected, all of these effects were significantly inhibited by CBP22 injection.

Bacteriocins modulate the immune response through regulating inflammation, inducing chemotaxis, initiating

specific immunity, directly enhancing the ability of the body to fight infection, and specifically activating immune cells [4, 44]. About bacteriocin regulation of intestinal immunity, the study found that a *Listeria monocytogenes* bacteriocin could target the commensal *Prevotella copri* and modulate intestinal infection [8]. Besides, it has also been found that gassericin A, a bacteriocin, secreted by intestinal microorganisms, bound KRT19 protein to the plasma membrane of intestinal epithelial cell, and activates intracellular mTOR-mediated phosphodiesterase activity, resulting in the downregulation of cAMP and cGMP levels, thereby reducing the incidence of diarrhea in early-weaned piglets [52]. IgG, IgM, and IgA, important effector molecules in humoral immunity, can neutralize the toxicity of bacterial toxins, enhance the phagocytosis of mononuclear macrophages, and bind viral antigens to regulate immunity [53, 54]. Consistent with previous studies [55], our data showed that LPS significantly increased the levels of IgA, IgG, and IgM in mouse serum. Although CBP22 treatment alone did not affect the serum immunoglobulin levels, pretreatment with CBP22 could reduce the elevated immunoglobulin levels induced by LPS. These results suggested that CBP22 can activate the nonspecific immunity of mice to neutralize and eliminate LPS. sIgA, a major component of the mucosal defense system, can inhibit the adhesion of intestinal epithelial pathogenic microorganisms and the proliferation of viruses. Our results showed that sIgA concentration was dramatically increased after intraperitoneal LPS injection but pretreatment with CBP22 decreased the sIgA concentration in the ileum, indicating that CBP22 may inhibit this extreme immune response to protect the health of the mouse. Besides, after intraperitoneal LPS injection, the serum levels of TNF- α and the gene expression of TNF- α in the small intestine increased rapidly, possibly because LPS activated inflammatory signaling pathways such as NF- κ B and MAPK, thereby activating the expression of downstream proinflammatory factors [56]. Our results suggested that pretreatment with CBP22 can significantly reduce the TNF- α level in serum and the TNF- α mRNA level in the small intestine, which may be because CBP22 alleviates inflammation by inhibiting I κ B degradation and NF- κ B activation [57].

The pathogenesis of sepsis has been attributed, at least in part, to the loss of intestinal epithelial barrier [58]. As the first line of defense, the barrier plays a vital role in maintaining intestinal health, preventing the uptake of pathogenic microorganisms, bacterial endotoxins, antigens, and toxic macromolecules from the lumen to the gut [59]. *Lactobacillus plantarum* bacteriocin improved the gut and body of diet-induced obese mice by maintaining the integrity of the epithelial barrier [7]. Mechanistically, bacteriocin secreted by probiotic lactobacilli was involved in the maintenance of the mucosal barrier, mainly through MAPK-dependent mechanisms [60]. To investigate the potential mechanism of CBP22 on immune function, we evaluated the effect of CBP22 on intestinal epithelial barrier function in mice. Healthy intestinal tissue was less permeable to FD4 to the blood, which was released into the blood only when intestinal mucosal barrier was damaged, so their levels could directly reflect the degree of damage to the intestinal epithelial

mucosa and permeability [61]. We found that CBP22 reduced the level of FD4, indicating that CBP22 alleviated LPS-induced permeability. Tight junction proteins, such as ZO-1, ZO-2, occludin, and claudin-1, are important factors regulating intestinal permeability and are the major barrier components. Our results showed that LPS downregulated the gene expression of the tight junction proteins ZO-1 and ZO-2 resulting in deterioration of the gut structure. These results further confirmed the conclusion that CBP22 may regulate intestinal injury by maintaining the barrier function.

In conclusion, we isolated and characterized a novel bacteriocin CBP22 from *C. butyricum*. Based on the analysis of its structure, physicochemical properties, antibacterial activity, and safety, we present evidence supporting the role of CBP22 as a potential regulator of intestinal injury and explore its mechanisms of action through enhancing the intestinal barrier function.

Data Availability

The data of qRT-PCR, Western blot, and ELISA used to support the findings of this study are available from the corresponding authors upon request.

Ethical Approval

The study was approved by the Animal Care and Use Committee of Zhejiang University (protocol code ZJU20160396 and protocol data 2016-03-04).

Conflicts of Interest

All authors declare that they have no conflict of interest.

Authors' Contributions

Tenghao Wang and Jie Fu have contributed equally and share first authorship.

Acknowledgments

We would like to thank the Wang lab members for the helpful discussion. This work was funded by the National Natural Science Foundation of China (Grant Nos. 32002185 and 31630075), the Zhejiang Provincial Natural Science Foundation of China (Grant No. LQ21C170002), and the China Postdoctoral Science Foundation (Grant No. 2020M671741).

References

- [1] B. P. Abraham and E. M. M. Quigley, "Probiotics in inflammatory bowel disease," *Gastroenterology Clinics of North America*, vol. 46, no. 4, pp. 769–782, 2017.
- [2] X. Zong, T. H. Wang, Z. Q. Lu, D. G. Song, J. Zhao, and Y. Z. Wang, "Effects of *Clostridium butyricum* or in combination with *Bacillus licheniformis* on the growth performance, blood indexes, and intestinal barrier function of weanling piglets," *Livestock Science*, vol. 220, pp. 137–142, 2019.
- [3] V. M. Quintana, N. I. Torres, M. B. Wachsman, P. J. Sinko, V. Castilla, and M. Chikindas, "Antiherpes simplex virus type 2 activity of the antimicrobial peptide subtilisin," *Journal of Applied Microbiology*, vol. 117, no. 5, pp. 1253–1259, 2014.
- [4] J. J. Quereda, O. Dussurget, M.-A. Nahori et al., "Bacteriocin from epidemic *Listeria* strains alters the host intestinal microbiota to favor infection," *Proceedings of the National Academy of Sciences*, vol. 113, no. 20, pp. 5706–5711, 2016.
- [5] K. E. Sutyak, R. A. Anderson, S. E. Dover et al., "Spermicidal activity of the safe natural antimicrobial peptide subtilisin," *Infectious Diseases in Obstetrics and Gynecology*, vol. 2008, Article ID 540758, 6 pages, 2008.
- [6] S. Ahmadi, M. Ghollasi, and H. M. Hosseini, "The apoptotic impact of nisin as a potent bacteriocin on the colon cancer cells," *Microbial Pathogenesis*, vol. 111, pp. 193–197, 2017.
- [7] D. D. Heeney, Z. Zhai, Z. Bendiks et al., "Lactobacillus plantarum bacteriocin is associated with intestinal and systemic improvements in diet-induced obese mice and maintains epithelial barrier integrity in vitro," *Gut Microbes*, vol. 10, no. 3, pp. 382–397, 2019.
- [8] N. Rollhion, B. Chassaing, M.-A. Nahori et al., "A *Listeria monocytogenes* Bacteriocin Can Target the Commensal *Prevotella copri* and Modulate Intestinal Infection," *Cell Host Microbe*, vol. 26, no. 5, pp. 691–701.e5, 2019.
- [9] D. J. Clarke, R. M. Robson, and J. G. Morris, "Purification of two *Clostridium* bacteriocins by procedures appropriate to hydrophobic proteins," *Antimicrob Agents Chemother*, vol. 7, no. 3, pp. 256–264, 1975.
- [10] S. Nakanishi and M. Tanaka, "Sequence analysis of a bacteriocinogenic plasmid of *Clostridium butyricum* and expression of the bacteriocin gene in *Escherichia coli*," *Anaerobe*, vol. 16, no. 3, pp. 253–257, 2010.
- [11] D. J. Clarke, C. D. Morley, D. B. Kell, and J. G. Morris, "On the mode of action of the bacteriocin butyricin 7423. Effects on membrane potential and potassium-ion accumulation in *Clostridium pasteurianum*," *European Journal of Biochemistry*, vol. 127, no. 1, pp. 105–116, 1982.
- [12] H. H. Li, Y. P. Li, Q. Zhu, J. Y. Qiao, and W. J. Wang, "Dietary supplementation with *Clostridium butyricum* helps to improve the intestinal barrier function of weaned piglets challenged with enterotoxigenic *Escherichia coli* K88," *Journal of Applied Microbiology*, vol. 125, no. 4, pp. 964–975, 2018.
- [13] J. Fu, T. Wang, X. Xiao et al., "*Clostridium butyricum* ZJU-F1 benefits the intestinal barrier function and immune response associated with its modulation of gut microbiota in weaned piglets," *Cells*, vol. 10, no. 3, p. 527, 2021.
- [14] L. Zhang, L. Zhang, X. Zhan et al., "Effects of dietary supplementation of probiotic, *Clostridium butyricum*, on growth performance, immune response, intestinal barrier function, and digestive enzyme activity in broiler chickens challenged with *Escherichia coli* K88," *Journal of Animal Science and Biotechnology*, vol. 7, no. 1, p. 3, 2016.
- [15] Q. Gao, L. Qi, T. Wu, and J. Wang, "*Clostridium butyricum* activates TLR2-mediated MyD88-independent signaling pathway in HT-29 cells," *Molecular and Cellular Biochemistry*, vol. 361, no. 1-2, pp. 31–37, 2012.
- [16] S. J. Sui, Z. B. Tian, Q. C. Wang et al., "*Clostridium butyricum* promotes intestinal motility by regulation of TLR2 in interstitial cells of Cajal," *European Review for Medical and Pharmacological Sciences*, vol. 22, no. 14, pp. 4730–4738, 2018.
- [17] A. M. Mowat and W. W. Agace, "Regional specialization within the intestinal immune system," *Nature Reviews Immunology*, vol. 14, no. 10, pp. 667–685, 2014.

- [18] X. Zong, J. Fu, B. Xu, Y. Wang, and M. Jin, "Interplay between gut microbiota and antimicrobial peptides," *Animal Nutrition*, vol. 6, no. 4, pp. 389–396, 2020.
- [19] L. Zhao, W. Yang, Y. Chen et al., "A Clostridia-rich microbiota enhances bile acid excretion in diarrhea-predominant irritable bowel syndrome," *The Journal of Clinical Investigation*, vol. 130, no. 1, pp. 438–450, 2020.
- [20] P. Enck, Q. Aziz, G. Barbara et al., "Irritable bowel syndrome," *Nature Reviews Disease Primers*, vol. 2, no. 1, article 16014, 2016.
- [21] M. Simrén, G. Barbara, H. J. Flint et al., "Intestinal microbiota in functional bowel disorders: a Rome foundation report," *Gut*, vol. 62, no. 1, pp. 159–176, 2013.
- [22] M. Rajilić-Stojanović, D. M. Jonkers, A. Salonen et al., "Intestinal microbiota and diet in IBS: causes, consequences, or epiphenomena?," *American Journal of Gastroenterology*, vol. 110, no. 2, pp. 278–287, 2015.
- [23] S. C. Bischoff, G. Barbara, W. Buurman et al., "Intestinal permeability—a new target for disease prevention and therapy," *BMC Gastroenterology*, vol. 14, no. 1, p. 189, 2014.
- [24] A. Salonen, W. M. de Vos, and A. Palva, "Gastrointestinal microbiota in irritable bowel syndrome: present state and perspectives," *Microbiology (Reading)*, vol. 156, no. 11, pp. 3205–3215, 2010.
- [25] I. B. Jeffery, P. W. O'Toole, L. Öhman et al., "An irritable bowel syndrome subtype defined by species-specific alterations in faecal microbiota," *Gut*, vol. 61, pp. 997–1006, 2012.
- [26] L. Krogus-Kurikka, A. Lyra, E. Malinen et al., "Microbial community analysis reveals high level phylogenetic alterations in the overall gastrointestinal microbiota of diarrhoea-predominant irritable bowel syndrome sufferers," *BMC Gastroenterology*, vol. 9, no. 1, p. 95, 2009.
- [27] X. Zong, W. Hu, D. Song et al., "Porcine lactoferrin-derived peptide LFP-20 protects intestinal barrier by maintaining tight junction complex and modulating inflammatory response," *Biochemical Pharmacology*, vol. 104, pp. 74–82, 2016.
- [28] H. T. Hassoun, B. C. Kone, D. W. Mercer, F. G. Moody, N. W. Weisbrodt, and F. A. Moore, "Post-injury multiple organ failure: the role of the gut," *Shock*, vol. 15, pp. 1–10, 2001.
- [29] P. A. Hall, P. J. Coates, B. Ansari, and D. Hopwood, "Regulation of cell number in the mammalian gastrointestinal tract: the importance of apoptosis," *Journal of Cell Science*, vol. 107, Part 12, pp. 3569–3577, 1994.
- [30] A. J. M. Watson, S. Chu, L. Sieck et al., "Epithelial barrier function in vivo is sustained despite gaps in epithelial layers," *Gastroenterology*, vol. 129, pp. 902–912, 2005.
- [31] Q. Li, Q. Zhang, C. Wang, X. Liu, N. Li, and J. Li, "Disruption of tight junctions during polymicrobial sepsis in vivo," *The Journal of Pathology*, vol. 218, no. 2, pp. 210–221, 2009.
- [32] C. Arce, M. Ramírez-Boo, C. Lucena, and J. J. Garrido, "Innate immune activation of swine intestinal epithelial cell lines (IPEC-J2 and IPI-2I) in response to LPS from *Salmonella typhimurium*," *Comparative Immunology, Microbiology and Infectious Diseases*, vol. 33, pp. 161–174, 2010.
- [33] C. Luan, H. W. Zhang, D. G. Song, Y. G. Xie, J. Feng, and Y. Z. Wang, "Expressing antimicrobial peptide cathelicidin-BF in *Bacillus subtilis* using SUMO technology," *Applied Microbiology and Biotechnology*, vol. 98, pp. 3651–3658, 2014.
- [34] R. Song, R.-B. Wei, H.-Y. Luo, and D.-F. Wang, "Isolation and characterization of an antibacterial peptide fraction from the pepsin hydrolysate of half-fin anchovy (*Setipinna taty*)," *Molecules*, vol. 17, pp. 2980–2991, 2012.
- [35] W. Gao, L. Xing, P. Qu et al., "Identification of a novel cathelicidin antimicrobial peptide from ducks and determination of its functional activity and antibacterial mechanism," *Scientific Reports*, vol. 5, pp. 17260–17260, 2015.
- [36] R. Gautier, D. Douguet, B. Antonny, and G. Drin, "HELI-QUEST: a web server to screen sequences with specific alpha-helical properties," *Bioinformatics*, vol. 24, no. 18, pp. 2101–2102, 2008.
- [37] J. Yang, R. Yan, A. Roy, D. Xu, J. Poisson, and Y. Zhang, "The I-TASSER Suite: protein structure and function prediction," *Nature Methods*, vol. 12, no. 1, pp. 7–8, 2015.
- [38] C. J. Chiu, A. H. McArdle, R. Brown, H. J. Scott, and F. N. Gurd, "Intestinal mucosal lesion in low-flow states," *Archives of Surgery*, vol. 101, pp. 478–483, 1970.
- [39] J. Snel, M. H. Bakker, and P. J. Heidt, "Quantification of antigen-specific immunoglobulin A after oral booster immunization with ovalbumin in mice mono-associated with segmented filamentous bacteria or *Clostridium innocuum*," *Immunology Letters*, vol. 58, pp. 25–28, 1997.
- [40] X. Zong, J. Zhao, H. Wang et al., "Mettl3 deficiency sustains long-chain fatty acid absorption through suppressing Traf6-dependent inflammation response," *Journal of Immunology*, vol. 202, no. 2, pp. 567–578, 2019.
- [41] S. B. Wayah and K. Philip, "Characterization, yield optimization, scale up and biopreservative potential of fermentin SA715, a novel bacteriocin from *Lactobacillus fermentum* GA715 of goat milk origin," *Microbial Cell Factories*, vol. 17, pp. 125–125, 2018.
- [42] S. B. Wayah and K. Philip, "Pentocin MQ1: a novel, broad-spectrum, pore-forming bacteriocin from *Lactobacillus pentosus* CS2 with quorum sensing regulatory mechanism and biopreservative potential," *Frontiers in Microbiology*, vol. 9, pp. 564–564, 2018.
- [43] V. Juturu and J. C. Wu, "Microbial production of bacteriocins: latest research development and applications," *Biotechnology Advances*, vol. 36, pp. 2187–2200, 2018.
- [44] P. Baidara, S. Korpole, and V. Grover, "Bacteriocins: perspective for the development of novel anticancer drugs," *Applied Microbiology and Biotechnology*, vol. 102, pp. 10393–10408, 2018.
- [45] P. D. Cotter, C. Hill, and R. P. Ross, "Bacteriocins: developing innate immunity for food," *Nature Reviews Microbiology*, vol. 3, pp. 777–788, 2005.
- [46] P. M. O'Connor, T. M. Kuniyoshi, R. P. S. Oliveira, C. Hill, R. P. Ross, and P. D. Cotter, "Antimicrobials for food and feed; a bacteriocin perspective," *Current Opinion in Biotechnology*, vol. 61, pp. 160–167, 2020.
- [47] K. Kimura and S. Yokoyama, "Trends in the application of *Bacillus* in fermented foods," *Current Opinion in Biotechnology*, vol. 56, pp. 36–42, 2019.
- [48] F. E. Lopez, P. A. Vincent, A. M. Zenoff, R. A. Salomón, and R. N. Fariás, "Efficacy of microcin J25 in biomatrices and in a mouse model of *Salmonella* infection," *Journal of Antimicrobial Chemotherapy*, vol. 59, pp. 676–680, 2007.
- [49] M. Zasloff, "Antimicrobial peptides of multicellular organisms," *Nature*, vol. 415, no. 6870, pp. 389–395, 2002.
- [50] L. Gu, N. Li, J. Gong, Q. Li, W. Zhu, and J. Li, "Berberine ameliorates intestinal epithelial tight-junction damage and down-regulates myosin light chain kinase pathways in a mouse model of endotoxemia," *The Journal of Infectious Diseases*, vol. 203, no. 11, pp. 1602–1612, 2011.

- [51] A. M. van der Does, P. S. Hiemstra, and N. Mookherjee, "Anti-microbial host defence peptides: immunomodulatory functions and translational prospects," *Advances in Experimental Medicine and Biology*, vol. 1117, pp. 149–171, 2019.
- [52] J. Hu, L. Ma, Y. Nie et al., "A microbiota-derived bacteriocin targets the host to confer diarrhea resistance in early-weaned piglets," *Cell Host Microbe*, vol. 24, pp. 817–832.e818, 2018.
- [53] A. J. Macpherson, B. Yilmaz, J. P. Limenitakis, and S. C. Ganal-Vonarburg, "IgA function in relation to the intestinal microbiota," *Annual Review of Immunology*, vol. 36, pp. 359–381, 2018.
- [54] H. W. Schroeder Jr. and L. Cavacini, "Structure and function of immunoglobulins," *The Journal of Allergy and Clinical Immunology*, vol. 125, pp. S41–S52, 2010.
- [55] P. Li, Y. Yao, Y. Ma, and Y. Chen, "miR-150 attenuates LPS-induced acute lung injury via targeting AKT3," *International Immunopharmacology*, vol. 75, article 105794, 2019.
- [56] S. Copeland, H. S. Warren, S. F. Lowry, S. E. Calvano, and D. Remick, "Acute inflammatory response to endotoxin in mice and humans," *Clinical Diagnostic Laboratory Immunology*, vol. 12, pp. 60–67, 2005.
- [57] Y. Gao, S. Lecker, M. J. Post et al., "Inhibition of ubiquitin-proteasome pathway-mediated I κ B α degradation by a naturally occurring antibacterial peptide," *Journal of Clinical Investigation*, vol. 106, pp. 439–448, 2000.
- [58] J. Ho, H. Chan, Y. Liang et al., "Cathelicidin preserves intestinal barrier function in polymicrobial sepsis," *Critical Care*, vol. 24, no. 1, pp. 47–47, 2020.
- [59] J. R. Turner, "Intestinal mucosal barrier function in health and disease," *Nature Reviews Immunology*, vol. 9, pp. 799–809, 2009.
- [60] L. M. T. Dicks, L. Dreyer, C. Smith, and A. D. van Staden, "A review: the fate of bacteriocins in the human gastro-intestinal tract: do they cross the gut-blood barrier?," *Frontiers in Microbiology*, vol. 9, pp. 2297–2297, 2018.
- [61] L. Zhao, L. Luo, W. Jia et al., "Serum diamine oxidase as a hemorrhagic shock biomarker in a rabbit model," *PLoS One*, vol. 9, article e102285, 2014.

Research Article

LR12 Promotes Liver Repair by Improving the Resolution of Inflammation and Liver Regeneration in Mice with Thioacetamide- (TAA-) Induced Acute Liver Failure

Yongjuan Wang ¹, Xiaoli Xie,¹ Hongqun Liu,^{1,2} Huimin Liu,¹ and Huiqing Jiang ¹

¹Department of Gastroenterology, The Second Hospital of Hebei Medical University, Hebei Key Laboratory of Gastroenterology, Hebei Institute of Gastroenterology, Hebei Clinical Research Center for Digestive Diseases, China

²Liver Unit, Cumming School of Medicine, University of Calgary, Calgary, Canada

Correspondence should be addressed to Huiqing Jiang; jianghuiqing1959@sina.com

Received 15 April 2021; Accepted 12 May 2021; Published 29 May 2021

Academic Editor: Miaomiao Wu

Copyright © 2021 Yongjuan Wang et al. This is an open access article distributed under the Creative Commons Attribution License, which permits unrestricted use, distribution, and reproduction in any medium, provided the original work is properly cited.

Background. Triggering receptor expressed on myeloid cells-1 (TREM-1) controls the mobilization of inflammatory cells in response to injury and consequently enhances liver damage. LR12 is a TREM-1 inhibitory peptide. However, the role of LR12 in acute liver failure (ALF) has remained elusive. This study was aimed at indicating whether LR12 could promote liver repair in mice with thioacetamide- (TAA-) induced ALF. **Methods.** BALB/c mice were intraperitoneally injected with TAA, followed by intravenous injection of LR12. Damage and regeneration of the liver were assessed. LO2 cells and macrophages were used to assess the therapeutic effects of LR12. **Results.** Mice treated with TAA for 24 h developed ALF, while liver inflammation was alleviated after LR12 treatment. Moreover, LR12 promoted hepatocyte regeneration in mice with TAA-induced ALF. *In vitro*, the supernatant from TAA+LR12-treated macrophages promoted the proliferation of LO2 cells. Cytokine protein microarray analysis suggested that LR12 promoted the secretion of C-C chemokine ligand 20 (CCL20) from macrophages. Besides, neutralization of CCL20 blocked the effects of LR12, thus inhibited the proliferation of LO2 cells *in vitro*, aggregated the liver inflammation, and restrained hepatocyte regeneration in ALF mice *in vivo*. Furthermore, we also found that LR12 activated the p38 mitogen-activated protein kinase (MAPK) pathway in hepatocytes through promoting the secretion of CCL20 from macrophages. **Conclusions.** LR12 could improve the resolution of inflammation and liver regeneration in mice with TAA-induced ALF by promoting the secretion of CCL20 from macrophages and activating the p38 MAPK pathway. Therefore, LR12 could be an attractive therapeutic target for the treatment of ALF.

1. Introduction

Acute liver failure (ALF) is a highly unpredictable disease that can evolve into a fatal consequence within few days or weeks. Although it can be induced by a variety of factors [1–6], it is characterized by similar clinical features, including acute deterioration of liver function, extensive necrosis of hepatocytes, and multiple organ failure. To our knowledge, ALF seriously threatens human health because of the high mortality rate and the lack of an effective medication [7, 8]. Liver transplantation is the most effective treatment for ALF [9, 10]. However, its application has been restricted by

a serious shortage of donor organs and high expenses. Therefore, novel effective therapies are urgently required.

Hepatic necrosis leads to the recruitment of a large number of inflammatory cells in the liver, which further triggers the systemic inflammatory response syndrome, and may be the main pathological mechanism of ALF [11, 12]. Therefore, inhibition of inflammatory response is essential for the treatment of ALF. Triggering receptor expressed on myeloid cell-1 (TREM-1) is mainly expressed on macrophages, neutrophils, and monocytes and may act as a cell surface receptor, transcribing proinflammatory cytokines and interacting with toll-like receptors (TLRs) [13, 14]. Recently, studies

have shown that TREM-1 promotes liver inflammation, and deletion of TREM-1 reduces liver injury and inflammatory cell infiltration [15, 16]. Small molecules and peptides, such as LP17 and LR12, can inhibit TREM-1. As a conserved motif from a TREM-like transcript, LR12 (LQEEDAGEYGC) reduces the inflammatory response caused by lipopolysaccharide (LPS), prevents connective tissue disorders, and even improves the survival rate [17]. Additionally, LR12 inhibits the amplification loop of the inflammatory process mediated by TREM-1, while it does not eliminate the inflammatory response [18]. The safety and pharmacokinetics of LR12 (<http://www.inotrem.com>; MOTREM™, INN: nangibotide, CAS number 2014384-91-7) are being evaluated in a first-in-man study. However, its role in the treatment of ALF has remained elusive.

Previous studies have demonstrated that liver regeneration is a critical determinant of survival in animal models of ALF [19, 20]. Agents enhancing liver regeneration hold a great therapeutic potential for ALF. A study has shown that blockade of TREM-1 potentiates cellular proliferation in an experimental model of ischemic stroke, resulting in functional improvement [21]. The present study was aimed at indicating whether LR12 could alleviate liver inflammation and promote liver regeneration in thioacetamide- (TAA-) induced ALF in mice.

2. Materials and Methods

2.1. Animal Models. Male Balb/c mice (age, 6-8 weeks old) were attained from Beijing Vital River Laboratory Animal Technology Co., Ltd. (Beijing, China) and fed with food and water ad libitum under 12:12 h light-dark cycles. The random assigning of mice into four groups was undertaken as follows: control, TAA model, LR12, and TAA+LR12 ($n = 6/\text{group}$). PBS was infused into mice in the control group; TAA (1200 mg/kg, Beijing Solarbio Science & Technology Co., Ltd., Beijing, China) was intraperitoneally (i.p.) injected in the TAA model group; LR12 (5 mg/kg, Beijing SBS Genetech Co., Ltd., Beijing, China) was intravenously administered in the LR12 group; and TAA (1200 mg/kg) was i.p. injected, followed by intravenous injection of LR12 (5 mg/kg) 1 h later in the TAA+LR12 group. The mice utilized for survival analysis were randomly allocated into two groups: TAA model and TAA+LR12 ($n = 9/\text{group}$). The mice used for administration of the anti-C-C chemokine ligand 20 (CCL20) antibody were randomly assigned into two groups: TAA+LR12+rat IgG (1 mg/kg/day, i.p.; R&D Systems, Minneapolis, MN, USA) and TAA+LR12+anti-CCL20 (1 mg/kg/day, i.p.; R&D Systems) ($n = 4/\text{group}$).

All animal experiments were carried out according to the requirements of the Ethics Committee of the Second Hospital of Hebei Medical University (Shijiazhuang, China; approval no. 2021-AE004).

2.2. Cell Lines and Cultivation. The human hepatic LO2 cells and human monocytic THP-1 cells were achieved from Shanghai Institutes for Biological Sciences of Chinese Academy of Sciences (Shanghai, China). Cultivation of LO2 and THP-1 cells into a Roswell Park Memorial Institute-

(RPMI-) 1640 medium was conducted with the addition of 10% fetal bovine serum (FBS) (Gibco, Carlsbad, CA, USA). Differentiation of THP-1 monocytes into macrophages was undertaken after stimulating with 100 nM phorbol 12-myristate 13-acetate (PMA) for 72 h. Then, the cells were cultured in the RPMI-1640 medium for 72 h. LO2 cells were assigned into four groups: control, 0.5 mM, 1 mM, and 2 mM group. LO2 or THP-1 cells were divided at random into four groups: control, TAA model, LR12, and TAA+LR12. The control group received PBS; the TAA model group was stimulated with TAA (1 mM); the LR12 group received LR12 (10 ng/mL); and the TAA+LR12 group was administered with TAA (1 mM) and LR12 (10 ng/mL). LO2 cells for CCL20 (100 ng/mL) treatment were allocated into four groups: control, TAA model, CCL20, and TAA+CCL20. LO2 cells for anti-CCL20 treatment were allocated at random into two groups: TAA+LR12 and TAA+LR12+anti-CCL20 (5 mM). A humidified atmosphere (5% CO₂, 37°C) was utilized for the cultivation of cell lines.

2.3. Isolation and Culture of Primary Hepatocytes and Macrophages. It was attempted to perfuse the liver with ethylenediaminetetraacetic acid (EDTA, 37°C, 5 min), as well as digest it with the assistance of 0.1% pronase E (37°C, 2 min) and 0.032% collagenase IV (37°C, 5 min). After the collagenase perfusion, the digested liver was removed and manually disrupted with ophthalmic scissors in a DMEM containing 10% FBS and 1% penicillin-streptomycin. The tissue was then filtered through a 70 μm nylon mesh. It was attempted to undertake centrifugation (150 g, 4°C, 10 min). The pellet was enriched with hepatocytes. The supernatant (enriched with macrophages) was transferred into a clean EP tube, centrifugation was performed (150 g, 4°C, 10 min), the pellet was suspended with 3 mL DMEM, and 30% percoll (4 mL) was added into the DMEM. After centrifugation (500 g, 5 min), the middle layer enriched with macrophages was collected, mixed with 4 mL DMEM, and centrifuged. The pellet enriched with hepatocytes was suspended with DMEM (6 mL), 50% percoll (5 mL) was added into the DMEM, and centrifugation was followed (150 g, 5 min). After that, the pellet (enriched with hepatocytes) was suspended with William's E medium and cultured at the same environment as macrophages. Primary hepatocytes and macrophages were divided at random into four groups: control, TAA model, LR12, and TAA+LR12.

2.4. Blood Chemistry and Liver Histology. The levels of alanine aminotransferase (ALT) and aspartate aminotransferase (AST) in serum were detected using kits that could be attained from the Nanjing Jincheng Bioengineering Institute (Nanjing, China). We employed hematoxylin and eosin (H&E) to stain slides (5 μm), and the visualization was undertaken via a light microscope (Olympus, Japan).

2.5. Confocal Laser Scanning Microscopy (CLSM). CLSM was carried out as per standard protocol. Primary antibodies were as follows: anti-cytokeratin 18 (CK-18) (Proteintech Group, Chicago, IL, USA), antiproliferating cell nuclear antigen (PCNA) (Proteintech Group), anti-F4/80 (Santa Cruz

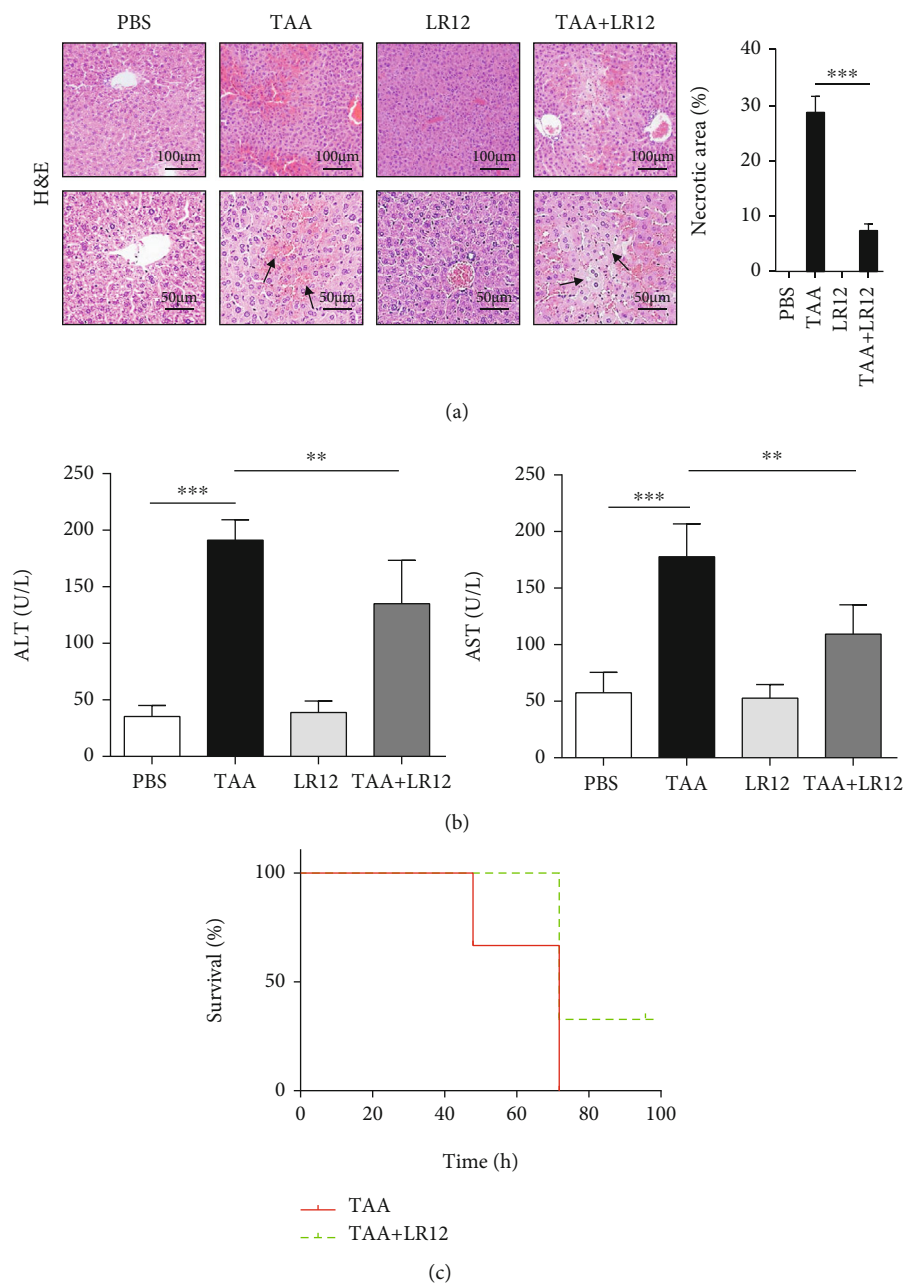
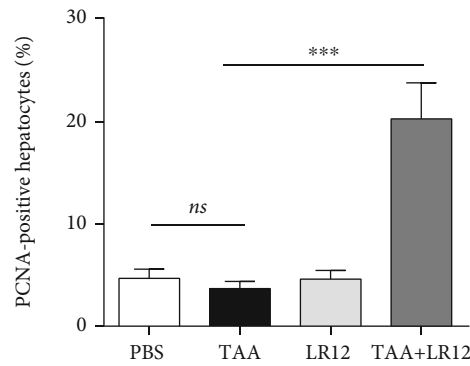
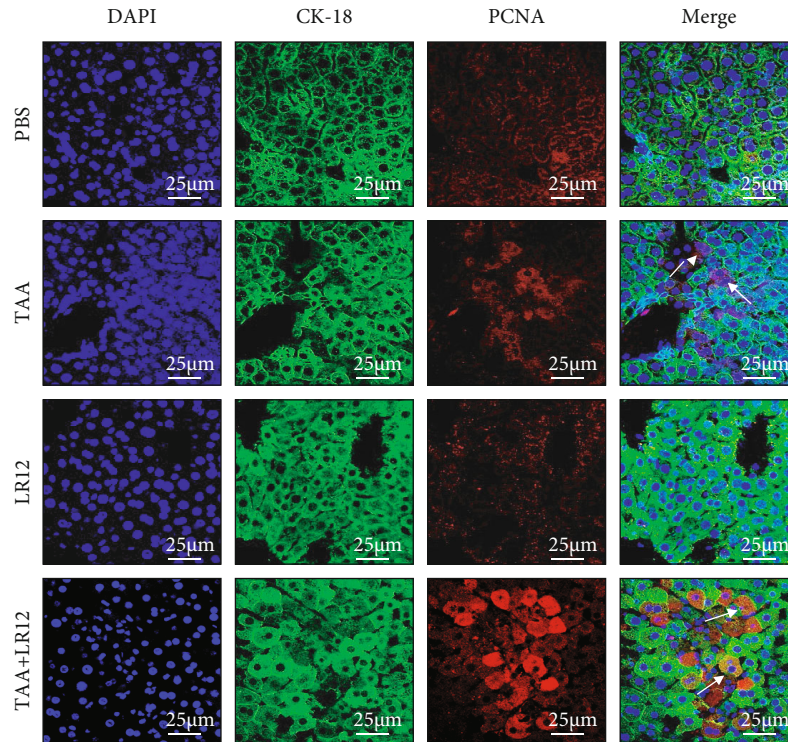
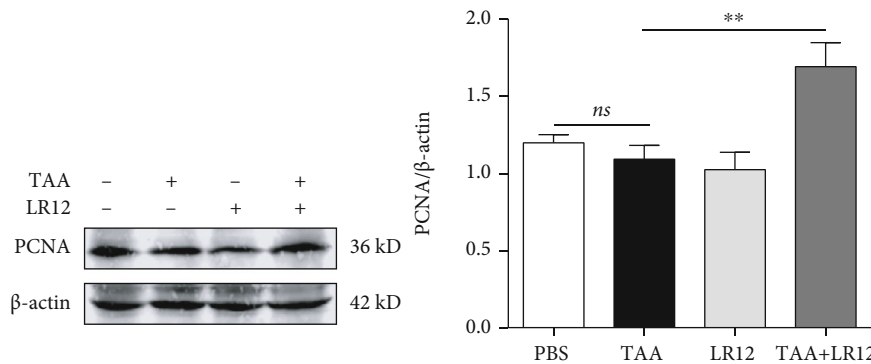


FIGURE 1: Continued.



(d)



(e)

FIGURE 1: Injection of LR12 reduced the liver inflammation and stimulated liver regeneration following TAA-induced ALF in mice. (a) H&E staining (magnification, 200x and 400x) showing inflammatory cell infiltration and necrotic area (%) in the liver. (b) Serum levels of alanine aminotransferase (ALT) and aspartate aminotransferase (AST). (c) Survival curve from mice with TAA-induced ALF ($n = 9/\text{group}$). (d) CLSM showing CK18 and PCNA staining in the liver. (e) Western blotting detected PCNA expression in the liver tissue. Data were presented as the mean \pm standard deviation (SD) ($n = 6$). * $P < 0.05$, ** $P < 0.01$, and *** $P < 0.001$ versus control group.

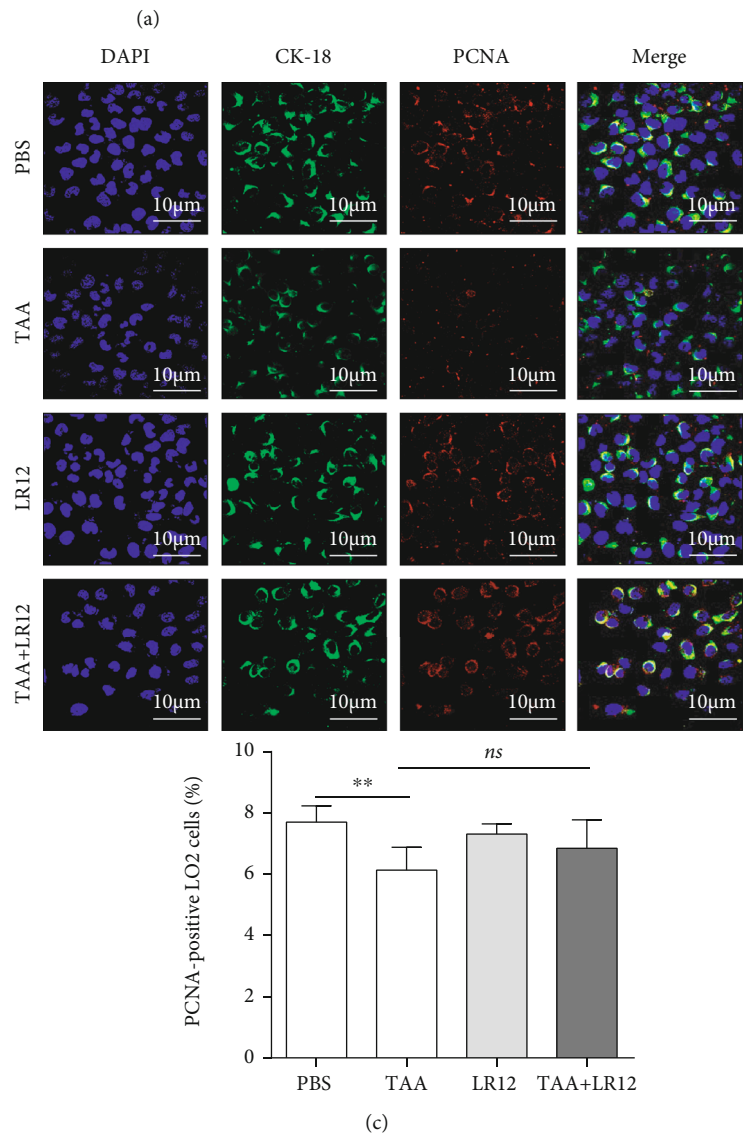
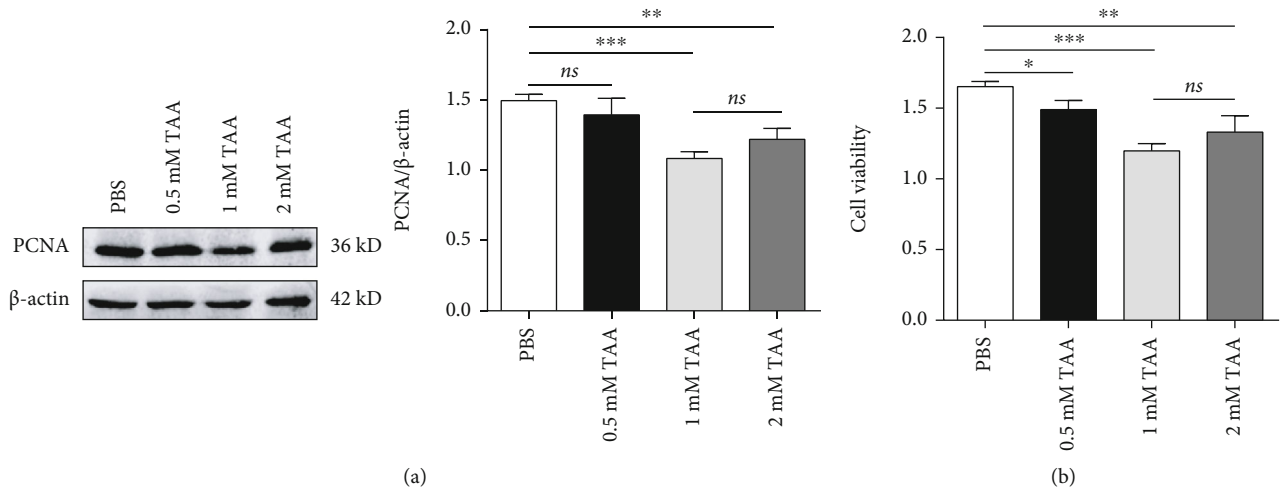


FIGURE 2: Continued.

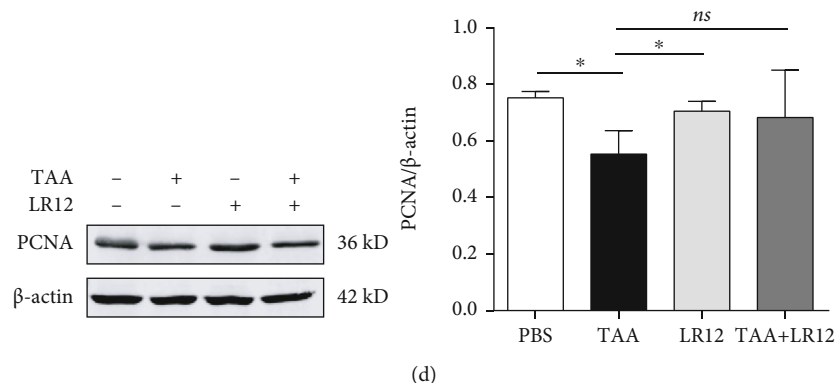


FIGURE 2: TAA induced hepatic injury *in vitro* and LR12 did not directly promote the proliferation of hepatocytes. (a) Western blot analysis of PCNA in LO2 cells stimulated with different concentrations of TAA (0.5, 1, and 2 mM). (b) CCK-8 assay of viability of LO2 cells. (c) CLSM showing CK18 and PCNA staining in LO2 cells. (d) Western blot analysis of PCNA expression in LO2 cells stimulated with TAA (1 mM) and/or LR12 (10 ng/mL). Data were presented as the mean \pm standard deviation (SD). * $P < 0.05$, ** $P < 0.01$, and *** $P < 0.001$ versus control group.

Biotechnology, Dallas, TX, USA), and anti-CCL20 (Affinity Biosciences, Cincinnati, OH, USA). We also utilized the ImageJ software (National Institutes of Health, Bethesda, MD, USA) to perform analyses.

2.6. Western Blotting. We further attempted to homogenize liver samples and cells in radioimmunoprecipitation assay (RIPA) buffer. Western blotting was undertaken as per standard protocol. Primary antibodies were as follows: PCNA (1 : 1000), p-p38 (1 : 500; Abways Co., Ltd., Shanghai, China), p38 (1 : 500; Abways), glyceraldehyde 3-phosphate dehydrogenase (GAPDH) (1 : 1000; Abcam, Cambridge, UK), and beta-actin (1 : 1000). Visualization of protein bands was undertaken via the ECL system and imaged using the Odyssey Infrared Imaging System (LI-COR, Lincoln, NB, USA), which was standardized to beta-actin or GAPDH as internal controls.

2.7. Cell Counting Kit-8 (CCK-8) Assay. Evaluation of cell survival rates was carried out using the CCK-8 assay (Key-Gen Biotechnology Co., Ltd., Nanjing, Jiangsu, China). Seeding of $\sim 10^4$ cells into 96-well plates was conducted. After 24 h of culture, different doses of TAA and LR12 (10 ng/ml) or supernatant from macrophages treated with TAA+LR12 were added separately. Incubation of each well was undertaken with the assistance of $10 \mu\text{g}$ CCK-8 in the dark (2 h). We also could measure absorbance (490 nm) via a multifunction microplate reader (BioTek, Montpellier, VT, USA).

2.8. Flow Cytometry (FCM). Seeding of 1×10^6 LO2 cells into 6-well plates was conducted. Supernatants from macrophages treated with TAA or TAA+LR12 were added into LO2 cells. After 24 h of culture, LO2 cells were digested with trypsin and centrifuged at $1000 \times g$ for 5 min. Cells were washed with PBS and fixed with 70% ethanol at 4°C overnight. Cells were then centrifuged at $1000 \times g$ for 5 min and rewashed with PBS. After gentle mixing with PI (Beyotime, Shanghai, China), mixed cells were filtered and incubated in the dark at 37°C for 30 min before analysis with a flow cyt-

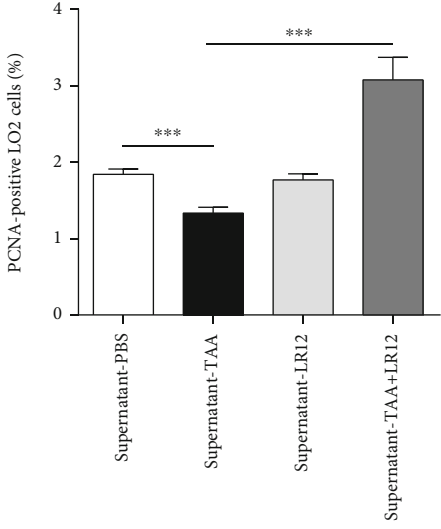
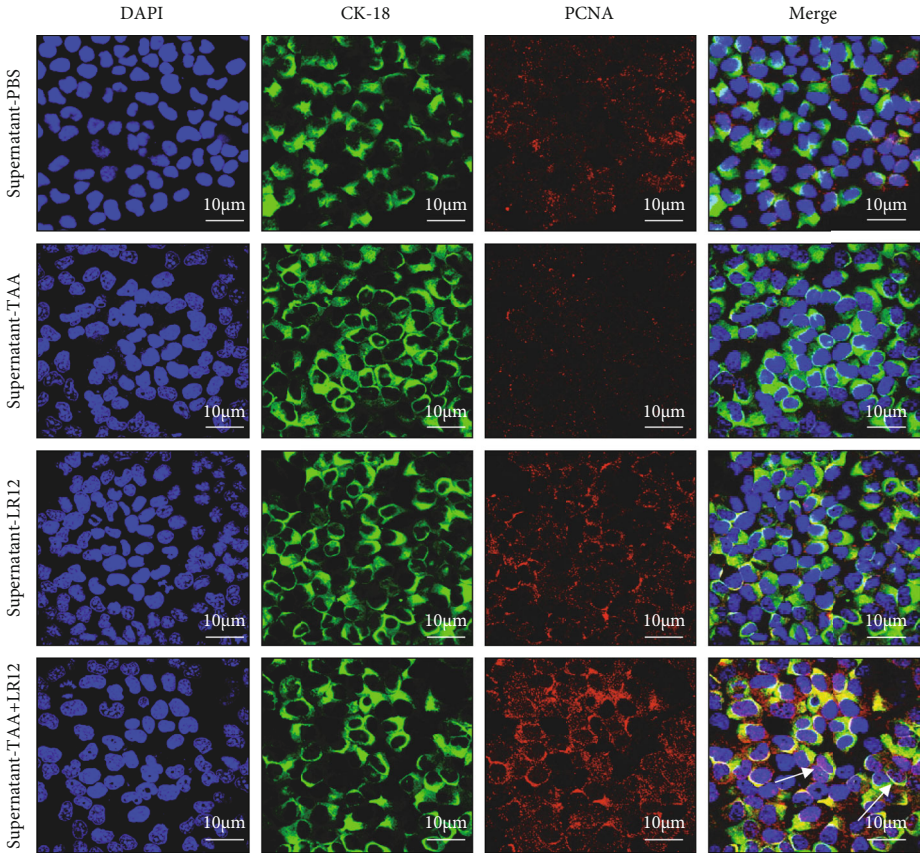
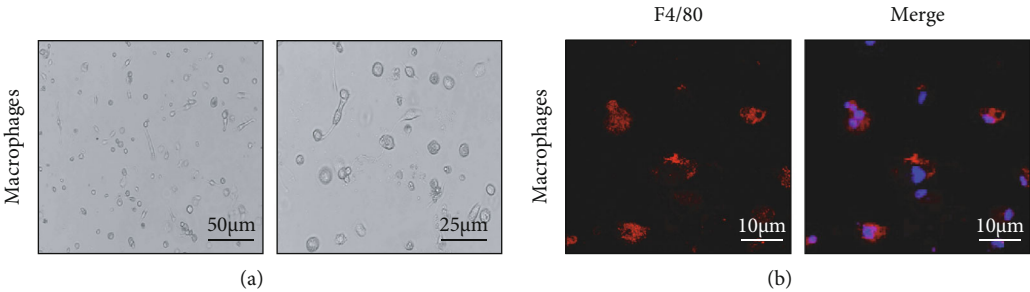
ometer (BD Biosciences, Franklin Lake, New Jersey, USA). PI fluorescence was detected at 488 nm.

2.9. Cytokine Protein Microarray. The supernatants from the four groups (control, TAA model, LR12, and TAA+LR12) were collected. The RayBio Human Cytokine Antibody Array Kit (QAH-TH17-1-1 microarray; RayBiotech, Norcross, GA, USA) was utilized to identify the cytokines based on instructions provided by the manufacturer. The images were analyzed via the RayBio ScanAnalyzer software (RayBiotech).

2.10. Enzyme-Linked Immunosorbent Assay (ELISA). The concentration of CCL20 was determined by using the 70-EK1211-24 kit (MultiSciences Co., Ltd., Hangzhou, China) based on instructions provided by the manufacturer. We also measured the optical density through an enzyme-labelling reader (450 nm) with a 570 nm wavelength correction reading. The concentrations of the unknown reagents were measured as well.

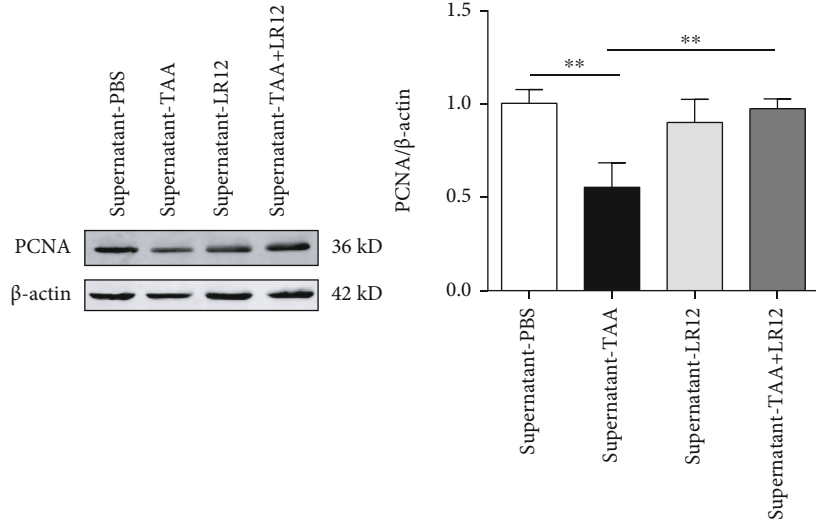
2.11. Quantitative Reverse Transcription Polymerase Chain Reaction (RT-qPCR). The isolation of total RNA from cells was undertaken with the RNeasy Mini Kit (Qiagen, Hilden, Germany). The synthesis of first-strand cDNA from $2 \mu\text{g}$ RNA was carried out via the iScript cDNA Synthesis Kit (Bio-Rad Laboratories, Inc., Hercules, CA, USA). RT-qPCR was applied in triplicate using the SYBR Green Real-Time PCR Master Mix System. Normalization of gene expression data was performed with the assistance of GAPDH. The following sequences of primers were used for RT-qPCR: for hCCL20: 5'-3' "TTGCTCCTGGCTGCTTTGATGT" and 3'-5' "GTTTTGGATTTGCGCACACAGAC," and for hGAPDH: 5'-3' "CAACGGATTGGTTCGTATTGG" and 3'-5' "GCAACAATATCCACTTTACCAGAGTTAA." The changes of gene expression data were calculated by the $2^{-\Delta\Delta\text{CT}}$ method.

2.12. Statistical Analysis. We employed the SPSS 25.0 software (IBM, Armonk, NY, USA) to conduct statistical

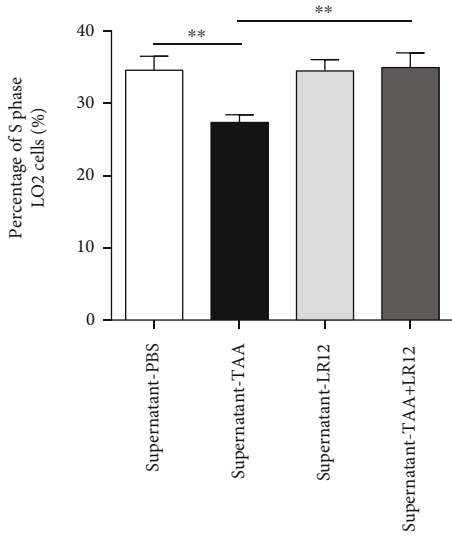
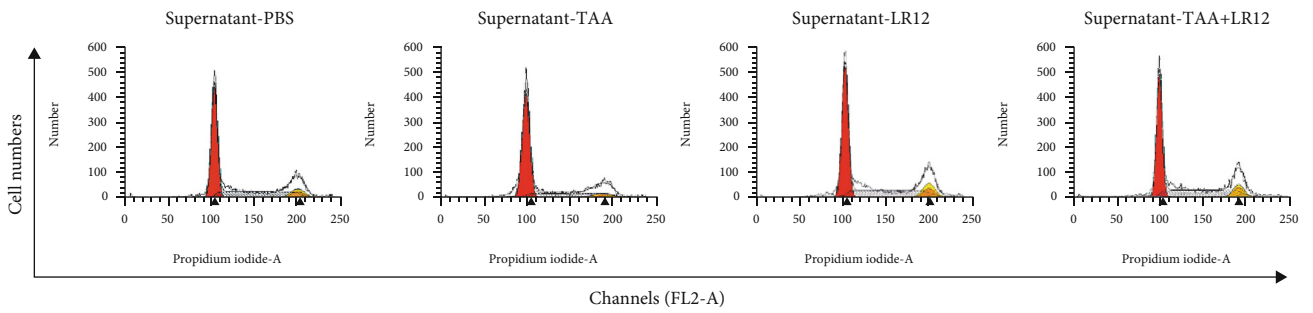


(c)

FIGURE 3: Continued.



(d)



(e)

FIGURE 3: Continued.

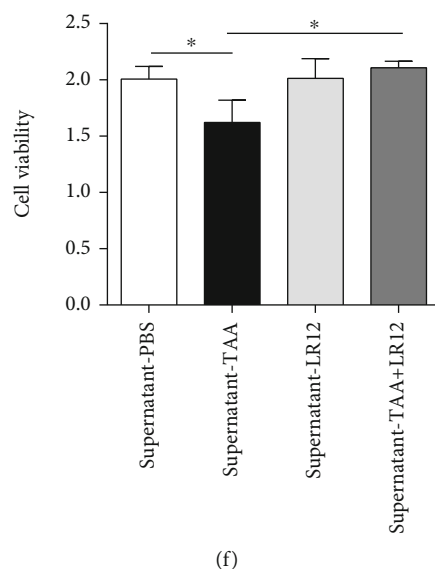


FIGURE 3: LR12 promoted hepatocyte proliferation via macrophages in LO2 cells. (a) THP-1 cells were successfully differentiated into macrophages by PMA (100 ng/mL). (b) Immunofluorescence images of F4/80 staining and DAPI in macrophages. (c) CLSM showing CK18 and PCNA staining in LO2 cells stimulated with the macrophage supernatant. (d) Western blot analysis of PCNA in LO2 cells stimulated with the macrophage supernatant. (e) The LO2 cell cycle detected by flow cytometric analysis. (f) CCK-8 assay analysis of LO2 cell viability. Data were presented as the mean \pm standard deviation (SD). * $P < 0.05$, ** $P < 0.01$, and *** $P < 0.001$ versus control group.

analyses. We also attempted to present data in the form of mean \pm standard deviation (SD). We utilized one-way analysis of variance (ANOVA) for comparing data among multiple groups. We set the significance level to $P < 0.05$.

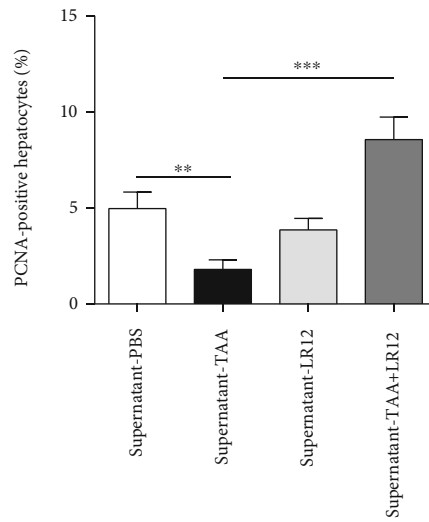
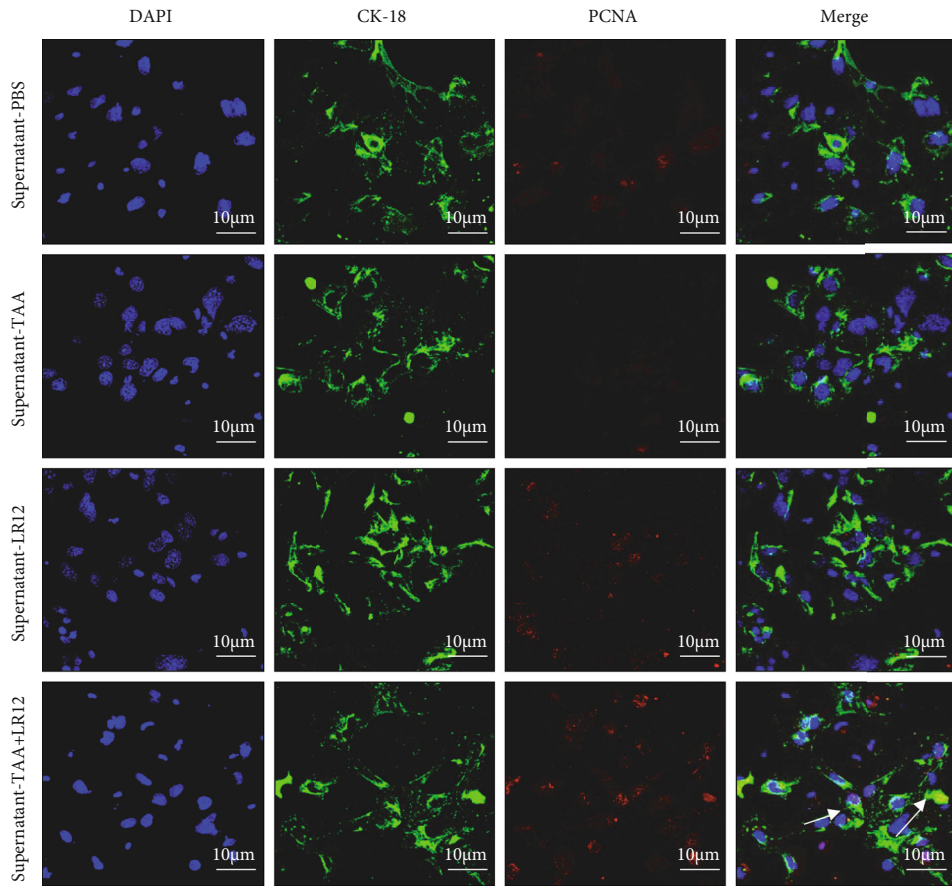
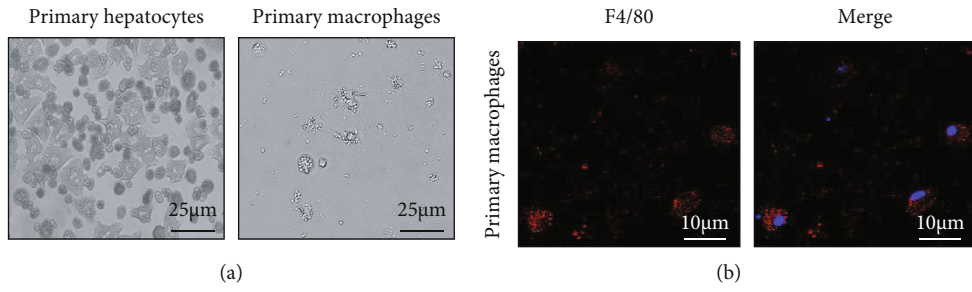
3. Results

3.1. LR12 Attenuated Liver Injury and Promoted Liver Regeneration in Mice with TAA-Mediated ALF. There were no significant inflammatory cell infiltration and hepatic necrosis in the liver in control and LR12 groups. Compared with the control group, hepatic necrosis was evident in the liver in mice with TAA-induced ALF, accompanied by inflammatory cell infiltration (Figure 1(a)). After LR12 treatment for 24 h, the necrosis and inflammation in the liver were significantly reduced (Figure 1(a)). Additionally, the serum levels of ALT and AST in the TAA model group were markedly elevated compared to those in the control group. However, they were significantly downregulated in the TAA+LR12 group (Figure 1(b)). Most importantly, we tested the mortality of mice at time points of 48, 72, and 96 h, and the findings revealed that LR12 prolonged the survival time of mice compared with the TAA model group (Figure 1(c)). CLSM indicated that compared to the TAA model group, PCNA-positive hepatocytes in the liver in the TAA+LR12 group were significantly upregulated, which were mainly located in a central venous catheter (Figure 1(d)), and this result was in line with the outcome of Western blotting (Figure 1(e)).

3.2. LR12 Did Not Promote Proliferation by Directly Acting on Hepatocytes. Firstly, we established a model of hepatic injury in LO2 cells *in vitro* that could be treated with diverse concentrations of TAA (0, 0.5, 1, and 2 mM), and the outcomes

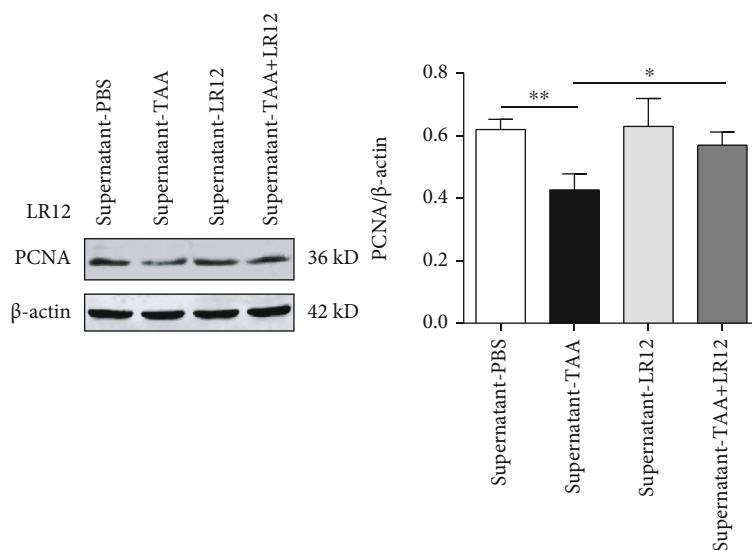
of Western blotting uncovered that PCNA expression was downregulated in both 1 mM and 2 mM groups (Figure 2(a)). Besides, the CCK-8 assay demonstrated that the proliferation of LO2 cells was notably attenuated in the three mentioned concentrations (Figure 2(b)). Although there was a mild increase in both PCNA and CCK-8 viability of LO2 cells in the 2 mM group, no significant difference was found in comparison with that in the 1 mM group (Figures 2(a) and 2(b)). In order to indicate whether LR12 could directly promote the proliferation of hepatocytes, we used 1 mM TAA to induce hepatic injury and then treated LO2 cells with LR12 (10 ng/mL). The results of Western blotting and CLSM unveiled that PCNA expression was not elevated in LO2 cells in the TAA+LR12 group (Figures 2(c) and 2(d)), which confirmed that LR12 did not promote proliferation by directly acting on hepatocytes.

3.3. LR12 Promoted the Proliferation of Hepatocytes by Acting on Macrophages. To better understand the mechanisms of LR12 promoting the proliferation of hepatocytes, we attempted to determine whether it could act on macrophages. Firstly, we differentiated THP-1 cells into macrophage-like cells. Our results showed that PMA (100 ng/mL) successfully induced the adhesion of THP-1 cells (Figure 3(a)). In addition, immunofluorescence staining revealed that the adherent THP-1 cells were F4/80-positive cells (Figure 3(b)). We treated LO2 cells with TAA (1 mM) for 24 h and then treated macrophages with TAA (1 mM) combined with LR12 (10 ng/mL, 24 h), and we subsequently transferred the supernatant of macrophages into LO2 cells (24 h). CLSM and Western blotting uncovered that PCNA expression in LO2 cells treated with the supernatant from TAA-treated macrophages was downregulated; besides, the supernatant from TAA+LR12-treated macrophages



(c)

FIGURE 4: Continued.



(d)

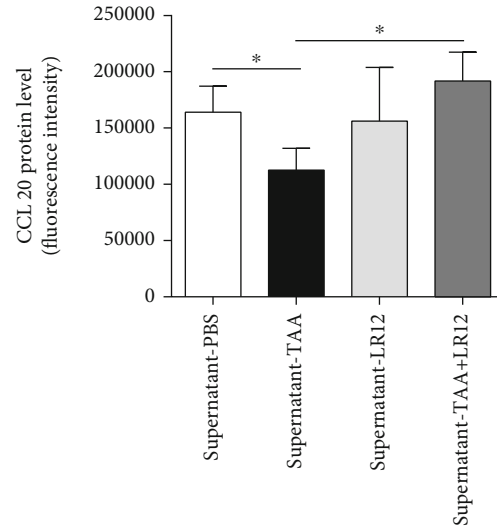
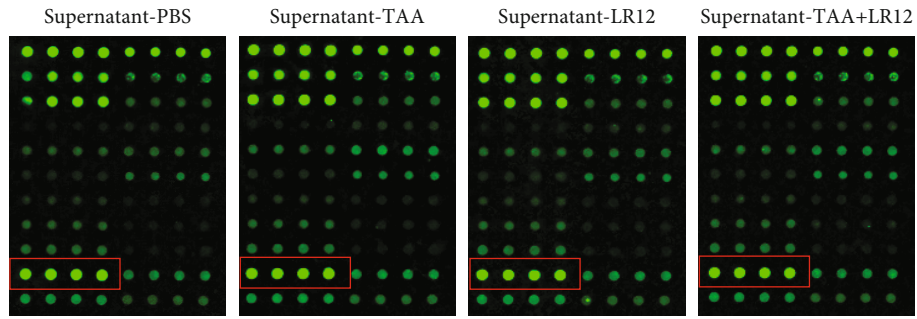
FIGURE 4: LR12 promoted primary hepatocyte proliferation via macrophages. (a) Primary hepatocytes and macrophages were extracted. (b) Immunofluorescence images of F4/80 staining and DAPI in primary macrophages. (c) CLSM showing CK18 and PCNA staining in primary hepatocytes stimulated with the primary macrophage supernatant. (d) Western blot analysis of PCNA in primary hepatocytes stimulated with the primary macrophage supernatant. Data were presented as the mean \pm standard deviation (SD). * $P < 0.05$, ** $P < 0.01$, and *** $P < 0.001$ versus control group.

significantly upregulated PCNA expression in LO2 cells (Figures 3(c) and 3(d)). In addition, FCM demonstrated that the supernatant from TAA+LR12-treated macrophages induced a higher number of LO2 cells in the S phase (Figure 3(e)). The CCK-8 assay indicated that the proliferation of LO2 cells was significantly elevated by the supernatant from TAA+LR12-treated macrophages (Figure 3(f)). The testing of primary hepatocytes and macrophages revealed similar results as LO2 cells and THP-1-induced macrophages (Figure 4).

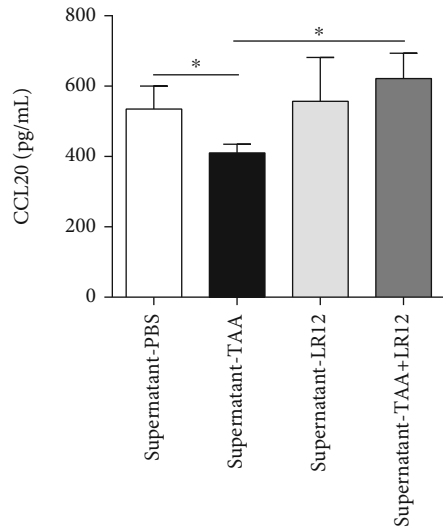
3.4. LR12 Induced Regeneration of Hepatocytes by Promoting the Secretion of CCL20. The results of cytokine protein microarray revealed that the protein level of CCL20 in the supernatant from TAA-treated macrophages was downregulated (Figure 5(a)). However, the protein level of CCL20 was significantly upregulated in the supernatant from TAA+LR12-treated macrophages (Figure 5(a)). ELISA also revealed that the protein level of CCL20 was downregulated in the supernatant from TAA-treated macrophages, while it was upregulated in the supernatant from TAA+LR12-treated macrophages (Figure 5(b)). We also found that the CCL20 mRNA level was markedly downregulated in TAA-treated macrophages compared to the control group, while it was upregulated in TAA+LR12-treated macrophages (Figure 5(c)). In addition, CLSM indicated that compared to the TAA model group, CCL20 expression in F4/80-positive cells was upregulated in mice treated with TAA+LR12 (Figure 5(d)). Furthermore, CCL20 (100 ng/mL) upregulated the PCNA expression in TAA-treated LO2 cells *in vitro* (Figure 5(e)).

3.5. CCL20 Neutralization Aggravated the Severity of TAA-Induced ALF and Inhibited Liver Regeneration. Western blotting indicated that compared to TAA+LR12-treated LO2 cells, anti-CCL20 hAbs (5 mM) blocked the effects of LR12 on macrophages and downregulated PCNA expression in LO2 cells *in vitro* (Figure 6(a)). Anti-CCL20 mAbs (1 mg/kg) also significantly aggravated the severity of hepatic necrosis and increased the serum levels of ALT and AST in the TAA+LR12 group (Figures 6(b) and 6(c)). In addition, CLSM showed that neutralization of CCL20 inhibited PCNA expression in hepatocytes, while it upregulated PCNA expression in inflammatory cells (Figure 6(d)). This finding was also approved by Western blotting (Figure 6(e)).

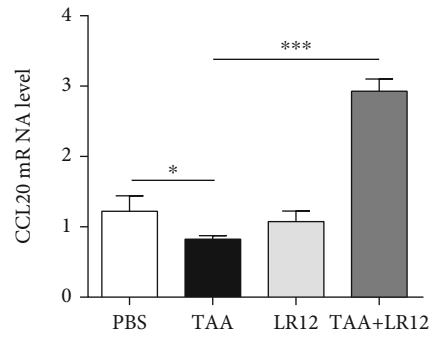
3.6. LR12 Activated the p38 Mitogen-Activated Protein Kinase (MAPK) Signaling Pathway by Promoting CCL20 Secretion from Macrophages. The phosphorylation level of p38 (p-p38) MAPK expression was downregulated in the TAA group, and LR12 treatment led to a noticeable increase in p-p38 MAPK (Figure 7(a)). We further extracted primary hepatocytes after treatment with LR12 in mice with TAA-induced ALF. Our findings unveiled that p-p38 MAPK level was markedly elevated in the TAA+LR12 treatment group (Figure 7(b)). In addition, anti-CCL20 hAbs downregulated the protein level of p-p38 MAPK in the TAA+LR12 group *in vitro* (Figure 7(c)). CLSM showed that LR12 enhanced translocation of p38 MAPK from the cytoplasm to the hepatocyte nuclei in mice, while anti-CCL20 mAbs inhibited the accumulation of p38 MAPK in hepatocyte nuclei and upregulated the protein level of p38 MAPK in the inflammatory cells in LR12-treated ALF mice (Figure 7(d)).



(a)



(b)



(c)

FIGURE 5: Continued.

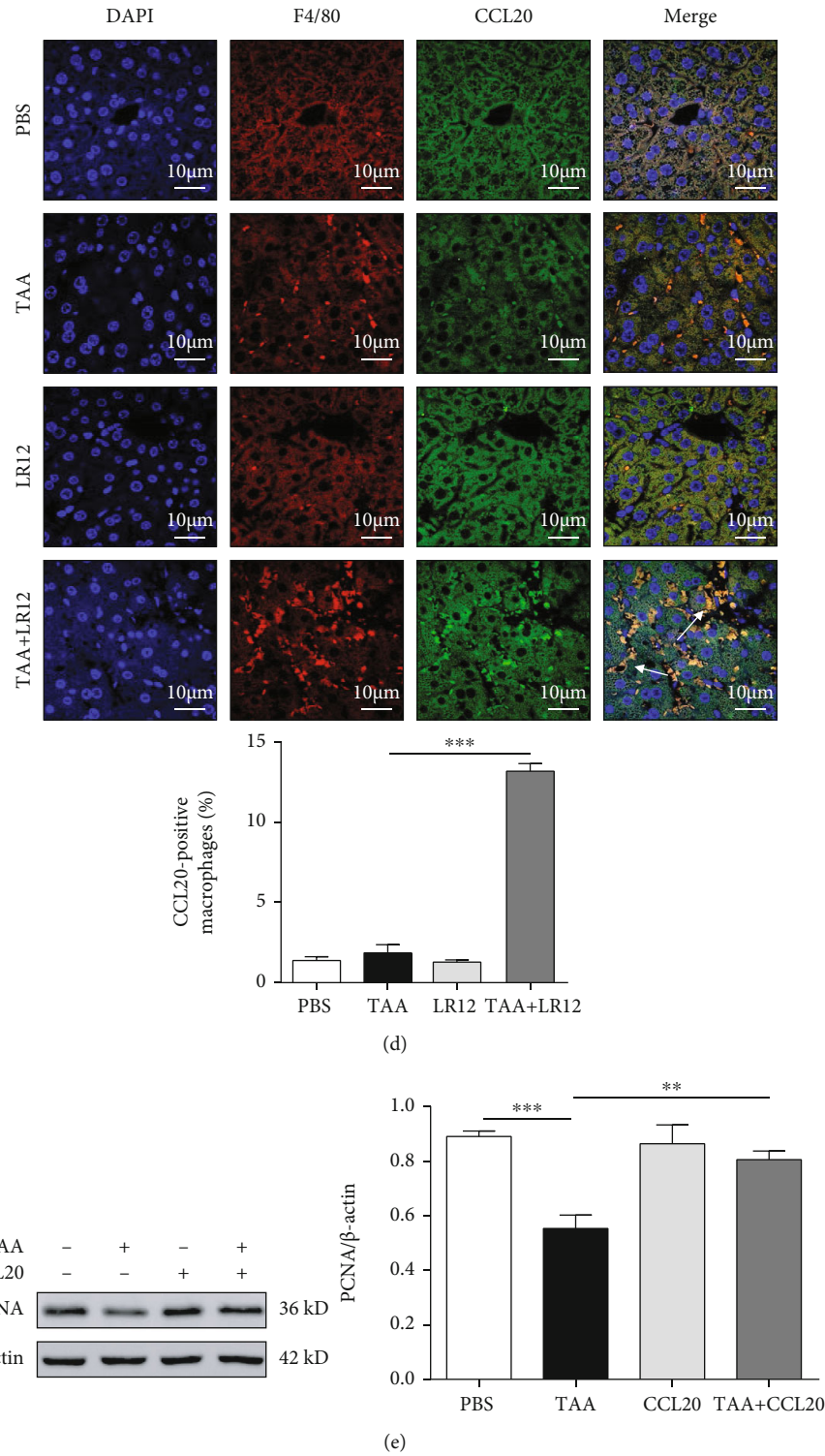
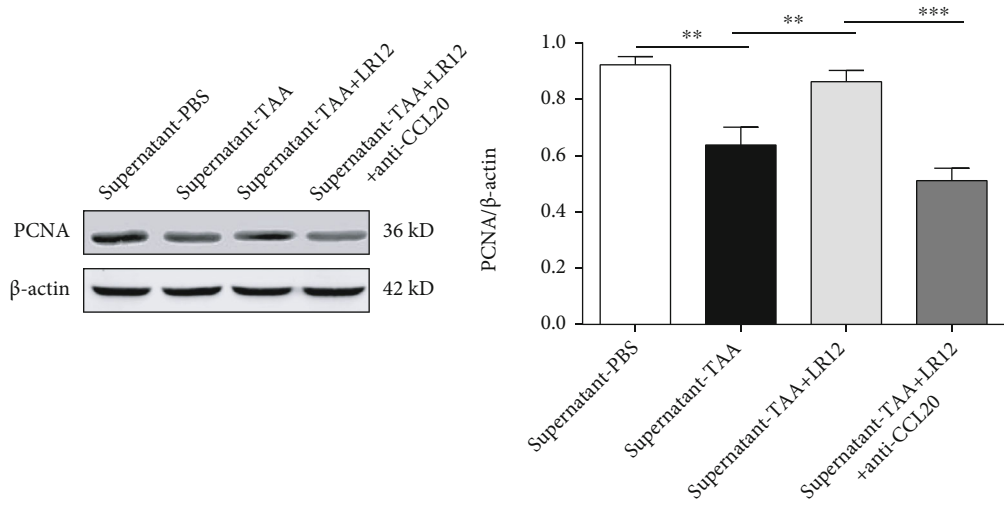
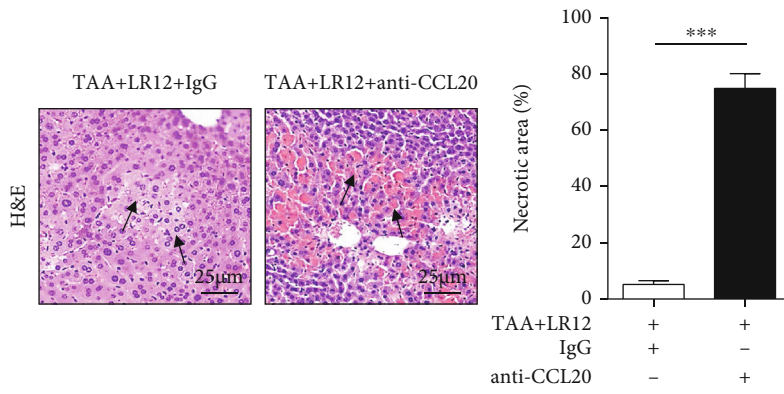


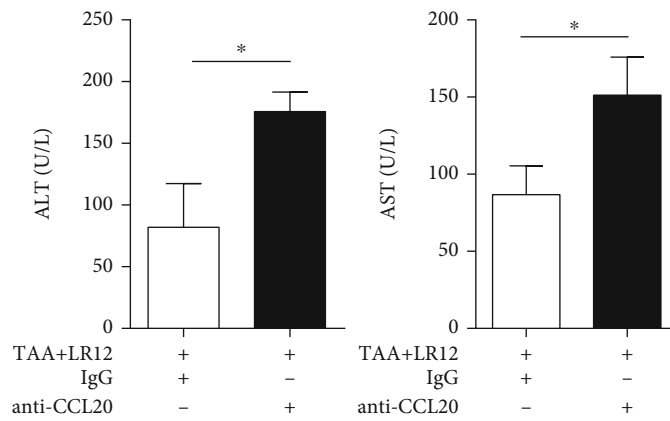
FIGURE 5: LR12 promoted hepatocyte regeneration via CCL20 secreted by macrophages. (a) The cytokine protein microarray of the supernatant from macrophages. (b) ELISA of CCL20 in the supernatant from macrophages. (c) The mRNA level of CCL20 in macrophages. (d) CLSM showing F4/80 and CCL20 staining in the liver tissues. (e) Western blot analysis of PCNA in LO2 cells stimulated with CCL20. Data were presented as the mean \pm standard deviation (SD). * $P < 0.05$, ** $P < 0.01$, and *** $P < 0.001$ versus control group.



(a)



(b)



(c)

FIGURE 6: Continued.

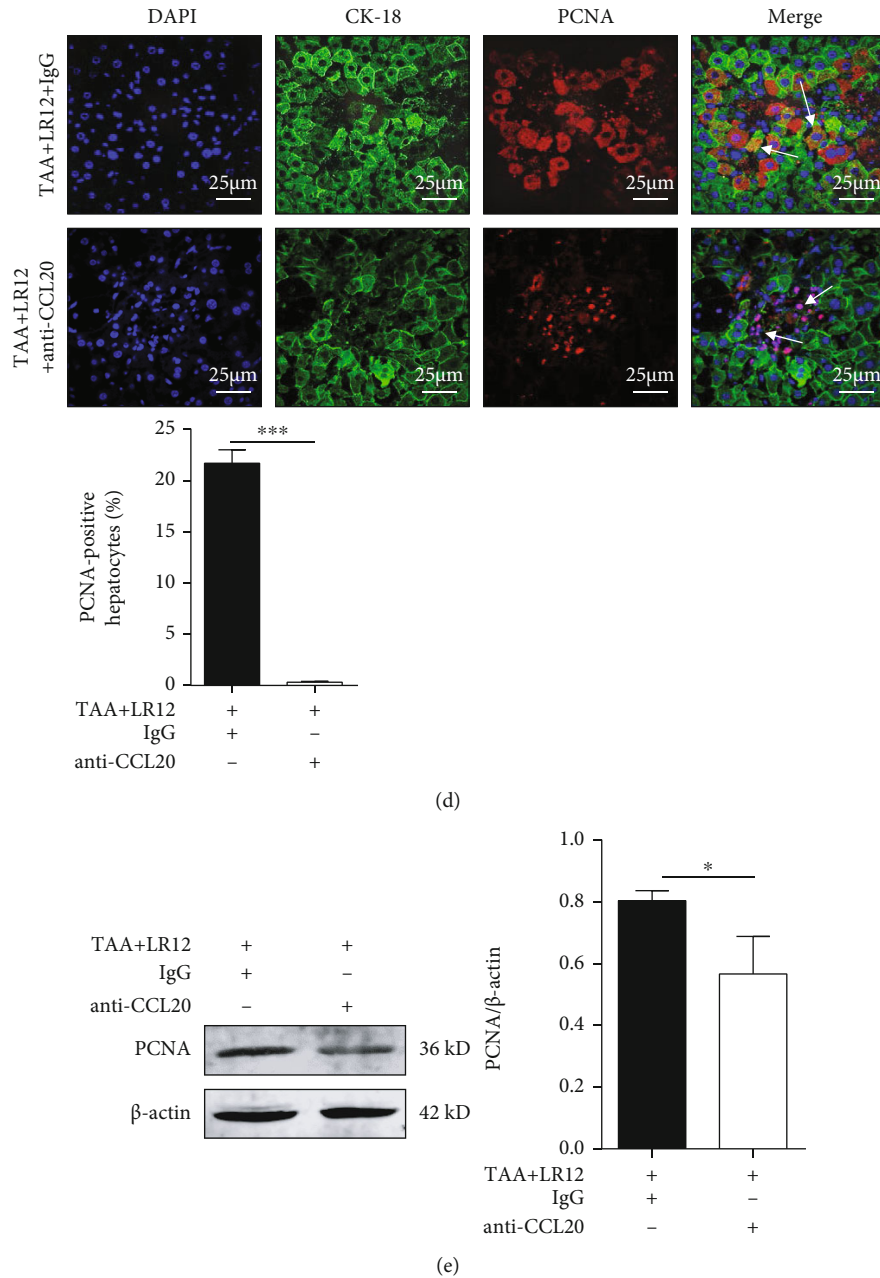


FIGURE 6: CCL20 neutralization aggravated the severity of TAA-induced ALF and inhibited liver regeneration. (a) Western blot analysis of PCNA in LO2 cells stimulated with TAA+LR12 or/and anti-CCL20 hAbs. (b) H&E staining (magnification, 400x) of the liver tissues in mice treated with TAA+LR12 and normal rat IgG or anti-CCL20 mAbs. (c) The levels of alanine aminotransferase (ALT) and aspartate aminotransferase (AST) in serum. (d) CLSM showing CK18 and PCNA staining in the liver tissues in mice treated with TAA+LR12 and normal rat IgG or anti-CCL20 mAbs. (e) Western blot analysis of PCNA in the liver tissues. Data were presented as the mean \pm standard deviation (SD). * $P < 0.05$, ** $P < 0.01$, and *** $P < 0.001$ versus control group.

4. Discussion

At present, this is the first study concentrated on the role of LR12 in the promotion of liver regeneration on TAA-induced ALF in mice via macrophages. The anti-CCL20 antibody blocked the effects of LR12 on hepatocyte proliferation. In addition, the present research indicated that LR12 activated the p38 MAPK pathway in hepatocytes via CCL20 secreted by macrophages (Figure 8).

TREM-1 is known to amplify inflammatory responses. Recently, evidences showed that it played an important role in sterile inflammatory diseases. Nguyen-Lefebvre et al. reported that TREM-1 promoted liver injury induced by carbon tetrachloride (CCl_4) administration [15]. Rao et al. demonstrated that inhibition of TREM-1 attenuated lipid accumulation and inflammation in the nonalcoholic fatty liver disease [16]. Another research showed that TREM-1 inhibitors could prevent excessive inflammation and

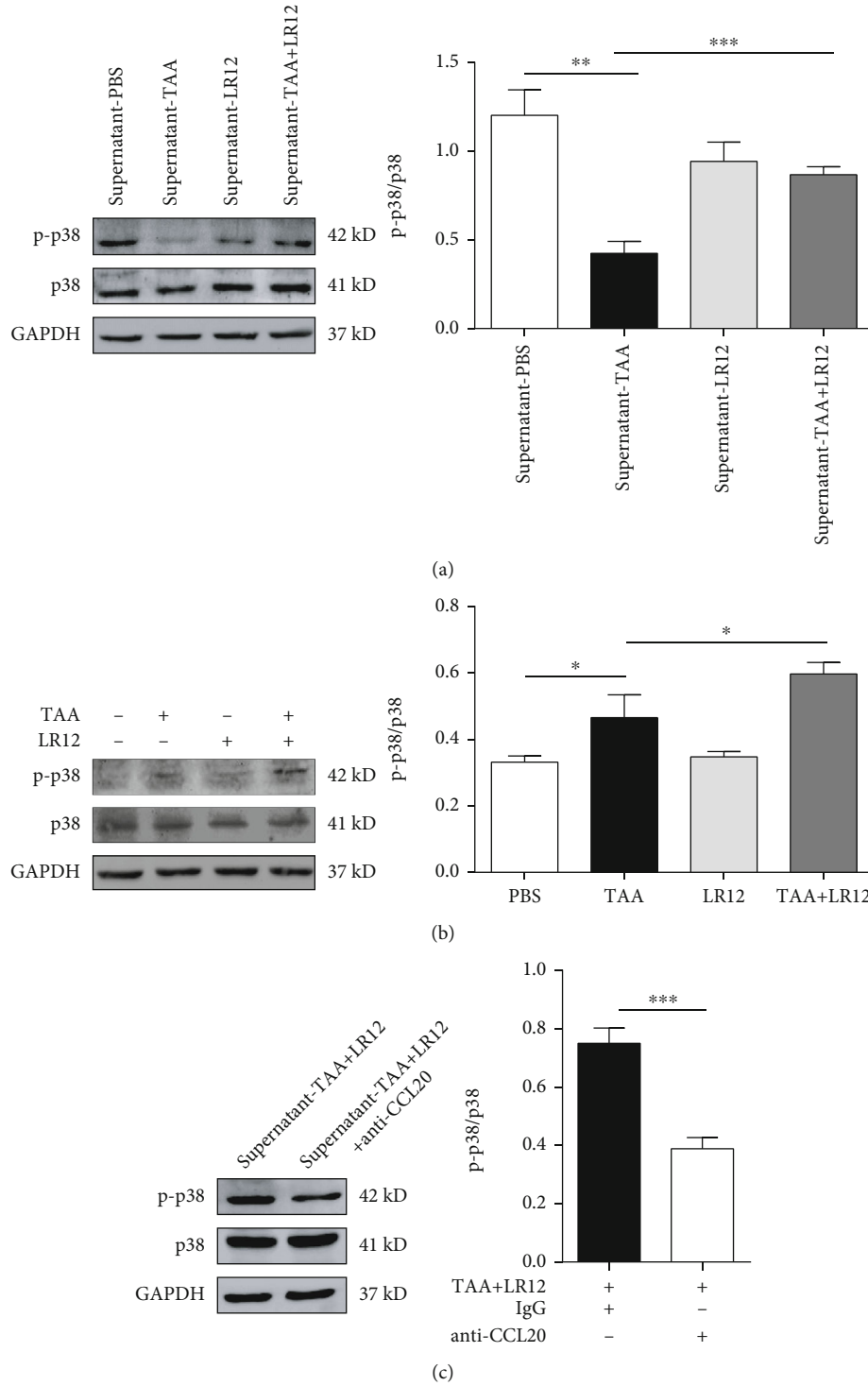


FIGURE 7: Continued.

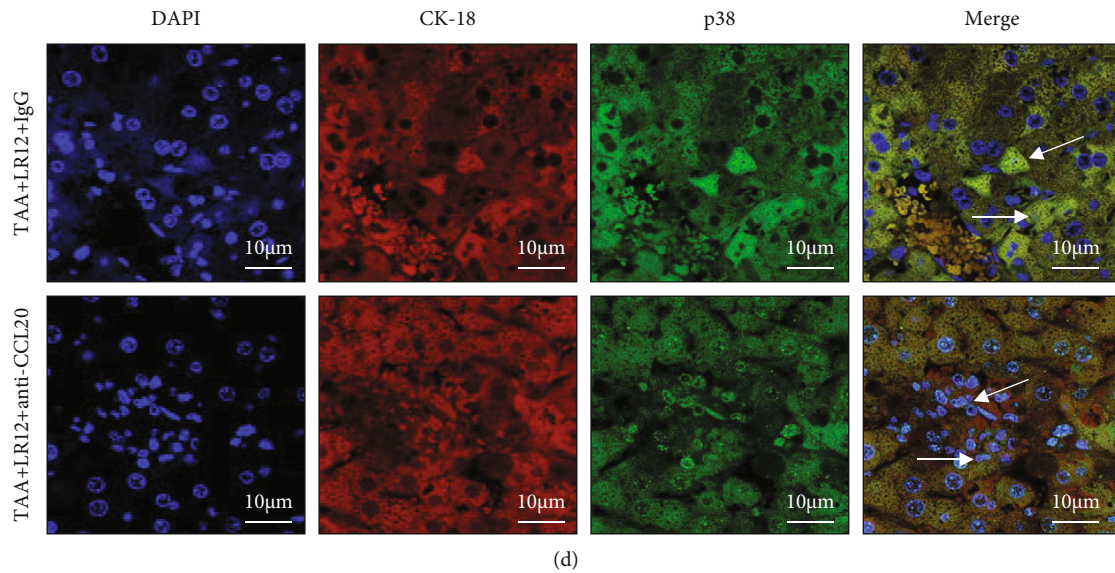


FIGURE 7: LR12 activated the p38 MAPK pathway by promoting the secretion of CCL20 from macrophages. (a) Western blot analysis of p-p38 in LO2 cells stimulated with the supernatant from macrophages. (b) Western blot analysis of p-p38 in primary hepatocytes. (c) Western blot analysis of p-p38 in LO2 cells stimulated with TAA+LR12 or/and anti-CCL20 hAbs. (d) CLSM showing CK18 and p38 staining in the liver tissues. Data were presented as the mean ± standard deviation (SD). * $P < 0.05$, ** $P < 0.01$, and *** $P < 0.001$ versus control group.

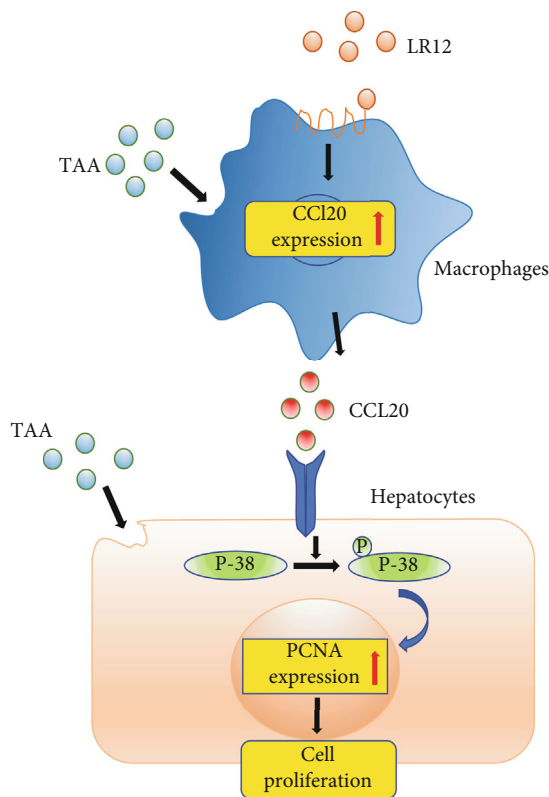


FIGURE 8: LR12 could promote regeneration of hepatocytes.

decrease the severity of the diseases and mortality. LR12 could reduce the severity of sepsis and acute myocardial infarction [22]. Consistent with previous studies, the present study revealed that LR12 reduced the liver inflammation and hepatic necrosis in mice with TAA-induced ALF. Most

importantly, LR12 could improve the survival rate of ALF mice.

To date, a limited number of researches have been concentrated on the relationship between TREM-1 and tissue regeneration. Xu et al. showed that blockade of TREM-1 potentiated synaptic plasticity and cellular proliferation in the hippocampus in an experimental model of ischemic stroke, which resulted in a long-term functional improvement [21]. In the current research, we found that LR12 could elevate PCNA expression and thus could promote regeneration of damaged hepatocytes in mice with TAA-induced ALF. To our knowledge, regenerative nodules are commonly observed in chronic liver injury, such as cirrhosis, which can be formed by local proliferation of hepatocytes and deposition of the extracellular matrix [23]. In our study, we found that the regenerated hepatocytes were located in the area of hepatic necrosis, and the structure of hepatic lobules in the TAA+LR12 group was normal, without deposition of the extracellular matrix in the central vein, which was different from the regenerative nodules in the cirrhotic liver.

In order to better study the mechanism of LR12 promoting hepatocyte regeneration, we established a cell model of TAA-induced hepatic injury *in vitro*, and we found that TAA could inhibit the PCNA expression and cell viability in LO2 cells. However, our results showed that LR12 could not directly promote the regeneration of hepatocytes in TAA-induced hepatic injury *in vitro*. The liver contains an abundant population of tissue-resident macrophages, namely, Kupffer cells (KCs), accounting for 80-90% of the body's macrophages [24]. Due to their broad diversity and plasticity, KCs play dual roles in different stages of ALF [25]. In the early phase of ALF, hepatocyte-mediated release of alarmins triggers the activation of KCs to produce a large amount of proinflammatory cytokines, thereby aggravating tissue damage [24]. However, in the resolution/tissue repair

phase of ALF, KCs undergo functional reprogramming toward a prorestorative phenotype, favoring wound healing and tissue recovery [26–28]. Lewis and Veldhuizen found that macrophages may hold a therapeutic value for acetaminophen- (APAP-) induced ALF to facilitate resolution of necrosis and promote liver regeneration [29]. Golbar et al. showed that the depletion of hepatic KCs by chlorophosphonic acid liposomes could significantly aggravate TAA-induced ALF in rats [30]. In the current study, we treated LO2 cells with the supernatant from macrophages stimulated with TAA or TAA+LR12, and we found that LR12 could increase the expression of PCNA in LO2 cells, which indicated that LR12 promoted liver regeneration through macrophages in TAA-induced hepatic injury *in vitro*. Additionally, our results indicated that the expression of PCNA was the highest in the TAA+LR12 group in mice with TAA-induced ALF, while a significantly higher expression of PCNA was not observed in the TAA+LR12 group *in vitro*. This may be related to the fact that hepatocytes are in a state of temporary nonproliferation *in vivo*; thus, the expression of PCNA was not significantly increased in the control or LR12 group in mice. However, LO2 cells are immortalized cell lines, with a strong proliferation ability under normal conditions.

Macrophages and macrophage-related factors have been reported to play a substantial role in the liver regeneration. A previous research demonstrated that perfluorooctane sulfonate could induce the activation of KCs in hepatocyte proliferation through the nuclear factor kappa B (NF- κ B)/tumor necrosis factor- α (TNF- α)/IL-6 signaling pathway [31]. The results of the current research unveiled that the levels of cytokines (e.g., TNF- α , IL-6, and transforming growth factor- β (TGF- β)) did not increase significantly. However, we found that CCL20 expression was upregulated after LR12 treatment. CCL20, as a second-generation chemokine, may act as both homeostatic and inflammatory chemokines under different conditions. It was originally identified in the liver [32]. The role of CCL20 in injury and regeneration of the liver remains controversial. Affo et al. reported that CCL20 played an important role in inducing the direct damage to the liver cells and/or participates in the LPS cascade, leading to the liver injury [33]. However, many scholars pointed out that the liver-homing capacity of CCL20 may also mediate tissue protection, repair, and regeneration. Rao et al. demonstrated that γ DT cells regulated liver regeneration by producing IL-22 and IL-17, which could not only accelerate the direct mitosis of hepatocytes but also promote the regeneration of leukocytes in the liver [34]. Scheiermann et al. reported that utilization of the IL-36 receptor antagonist weakened the CCL20 expression and impaired liver regeneration in APAP-induced liver injury in mice [35]. Our findings demonstrated that CCL20 upregulated PCNA expression in TAA-induced hepatic injury in Lo-2 cells *in vitro*, which indicated that CCL20 might promote liver regeneration in mice with TAA-induced ALF. Recently, Gonzalez-Guerrero et al. showed that neutralization of CCL20 in acute kidney injury might aggravate kidney injury and was associated with a reduced cell proliferation [36]. In the present study, we found that neutralization of CCL20

blocked the effects of LR12 on macrophages and inhibited the proliferation of hepatocytes *in vitro*. We also noted that neutralization of CCL20 increased the liver inflammation and liver necrosis in the TAA+LR12 group. Importantly, we observed that neutralization of CCL20 inhibited the effects of LR12 and downregulated the expression of PCNA in hepatocytes in mice with TAA-induced ALF. Hence, it could be concluded that LR12 promoted hepatocyte regeneration by stimulating macrophages to secrete CCL20.

To date, the role of the p38 MAPK pathway in the injury and regeneration of the liver has remained elusive. Heinrichsdorff et al. reported that the p38 MAPK pathway inhibited the activation of JNK, thereby preventing liver failure that might be caused by LPS or TNF- α [37]. Zhang et al. declared that IL-18 promoted the proliferation of liver cells in rat through the p38 MAPK signaling pathway [38]. However, Campbell et al. concluded that the p-p38 MAPK pathway was not necessary for DNA replication during liver regeneration after partial hepatectomy [39]. Tormos et al. demonstrated that p38 played a dual role in the proliferation of hepatocytes [40]. The present research uncovered that LR12 induced p-p38 MAPK expression in hepatocytes in TAA-induced ALF. However, neutralization of CCL20 inhibited p-p38 MAPK expression in LO2 cells. Therefore, our findings suggested that LR12 promoted liver regeneration via CCL20, as well as activating the p38 MAPK pathway.

In summary, we first addressed the role of LR12 in TAA-induced ALF in mice. Furthermore, LR12 could promote liver regeneration, mainly by promoting macrophages to secrete CCL20 and activating the p38 MAPK pathway. Therefore, our results indicated that LR12 could be an attractive therapeutic target for the treatment of ALF.

Abbreviations

ALF:	Acute liver failure
ALT:	Alanine aminotransferase
AST:	Aspartate aminotransferase
APAP:	Acetaminophen
CCL20:	C-C chemokine ligand 20
CLSM:	Confocal laser scanning microscopy
CCl ₄ :	Carbon tetrachloride
CK18:	Cytokeratin 18
CCK-8:	Cell Counting Kit-8.
ELISA:	Enzyme-linked immunosorbent assay
EDTA:	Ethylenediaminetetraacetic acid
FCM:	Flow cytometry
GAPDH:	Glyceraldehyde 3-phosphate dehydrogenase
H&E:	Hematoxylin and eosin
KCs:	Kupffer cells
LPS:	Lipopolysaccharide
MAPK:	Mitogen-activated protein kinase
NF- κ B:	Nuclear factor kappa B
PMA:	Phorbol 12-myristate 13-acetate
PCNA:	Proliferating cell nuclear antigen
RIPA:	Radioimmunoprecipitation assay
RT-qPCR:	Quantitative reverse transcription polymerase chain reaction
SD:	Standard deviation

TAA: Thioacetamide
 TREM-1: Triggering receptor expressed on the myeloid cell-1
 TLRs: Toll-like receptors
 TNF- α : Tumor necrosis factor-alpha
 TGF- β : Transforming growth factor- β .

Data Availability

The data in this study is available upon reasonable request to the correspondence author.

Conflicts of Interest

The authors declare no conflict of interests.

Authors' Contributions

Yongjuan Wang, Xiaoli Xie, and Huiqing Jiang conceived and designed the experiments. Yongjuan Wang performed the research. Huimin Liu conducted the data analysis. Yongjuan Wang wrote the first-draft manuscript, and Hongqun Liu and Huiqing Jiang revised the manuscript.

Acknowledgments

The current research was supported by the National Natural Science Foundation of China (Grant Nos. 81770601, 81602529, and 81702324), the Natural Science Foundation of Hebei Province (Grant Nos. H2018206176 and H2017206141), and the Hebei Graduate Innovation Funding Project (Grant No. CXZZBS2018076).

References

- [1] T. S. Hong, C. Grassberger, B. Y. Yeap et al., "Pretreatment plasma HGF as potential biomarker for susceptibility to radiation-induced liver dysfunction after radiotherapy," *NPJ Precision Oncology*, vol. 2, no. 1, p. 22, 2018.
- [2] G. Ostapowicz, R. J. Fontana, F. V. Schiødt et al., "Results of a prospective study of acute liver failure at 17 tertiary care centers in the United States," *Annals of Internal Medicine*, vol. 137, no. 12, pp. 947–954, 2002.
- [3] G. Ferrere, L. Wrzosek, F. Cailleux et al., "Fecal microbiota manipulation prevents dysbiosis and alcohol-induced liver injury in mice," *Journal of Hepatology*, vol. 66, no. 4, pp. 806–815, 2017.
- [4] A. Wasley, A. Fiore, and B. P. Bell, "Hepatitis A in the era of vaccination," *Epidemiologic Reviews*, vol. 28, no. 1, pp. 101–111, 2006.
- [5] M. S. Khuroo and S. Kamili, "Aetiology and prognostic factors in acute liver failure in India," *Journal of Viral Hepatitis*, vol. 10, no. 3, pp. 224–231, 2003.
- [6] O. E. Anastasiou, B. Dogan-Cavus, O. Kucukoglu et al., "Corticosteroid therapy improves the outcome of autoimmune hepatitis-induced acute liver failure," *Digestion*, vol. 98, no. 2, pp. 104–111, 2018.
- [7] W. Bernal and J. Wendon, "Acute liver failure," *The New England Journal of Medicine*, vol. 369, no. 26, pp. 2525–2534, 2013.
- [8] W. Bernal, G. Auzinger, A. Dhawan, and J. Wendon, "Acute liver failure," *The Lancet*, vol. 376, no. 9736, pp. 190–201, 2010.
- [9] W. Bernal, T. J. S. Cross, G. Auzinger et al., "Outcome after wait-listing for emergency liver transplantation in acute liver failure: a single centre experience," *Journal of Hepatology*, vol. 50, no. 2, pp. 306–313, 2009.
- [10] G. Germani, E. Theocharidou, R. Adam et al., "Liver transplantation for acute liver failure in Europe: outcomes over 20 years from the ELTR database," *Journal of Hepatology*, vol. 57, no. 2, pp. 288–296, 2012.
- [11] N. Rolando, J. Wade, M. Davalos, J. Wendon, J. Philpott-Howard, and R. Williams, "The systemic inflammatory response syndrome in acute liver failure," *Hepatology*, vol. 32, no. 4, pp. 734–739, 2000.
- [12] L. E. Schmidt and F. S. Larsen, "Prognostic implications of hyperlactatemia, multiple organ failure, and systemic inflammatory response syndrome in patients with acetaminophen-induced acute liver failure," *Critical Care Medicine*, vol. 34, no. 2, pp. 337–343, 2006.
- [13] A. Tammaro, M. Derive, S. Gibot, J. C. Leemans, S. Florquin, and M. C. Dessing, "TREM-1 and its potential ligands in non-infectious diseases: from biology to clinical perspectives," *Pharmacology & Therapeutics*, vol. 177, pp. 81–95, 2017.
- [14] H. Zheng, C. A. Heiderscheidt, M. Joo et al., "MYD88-dependent and -independent activation of TREM-1 via specific TLR ligands," *European Journal of Immunology*, vol. 40, no. 1, pp. 162–171, 2010.
- [15] A. T. Nguyen-Lefebvre, A. Ajith, V. Portik-Dobos et al., "The innate immune receptor TREM-1 promotes liver injury and fibrosis," *The Journal of Clinical Investigation*, vol. 128, no. 11, pp. 4870–4883, 2018.
- [16] S. Rao, J. Huang, Z. Shen, C. Xiang, M. Zhang, and X. Lu, "Inhibition of TREM-1 attenuates inflammation and lipid accumulation in diet-induced nonalcoholic fatty liver disease," *Journal of Cellular Biochemistry*, vol. 120, no. 7, pp. 11867–11877, 2019.
- [17] T. Liu, Y. Zhou, P. Li et al., "Blocking triggering receptor expressed on myeloid cells-1 attenuates lipopolysaccharide-induced acute lung injury via inhibiting NLRP3 inflammasome activation," *Scientific Reports*, vol. 6, no. 1, p. 39473, 2016.
- [18] J. Joffre, S. Potteaux, L. Zeboudj et al., "Genetic and pharmacological inhibition of TREM-1 limits the development of experimental atherosclerosis," *Journal of the American College of Cardiology*, vol. 68, no. 25, pp. 2776–2793, 2016.
- [19] B. Bhushan and U. Apte, "Liver regeneration after acetaminophen hepatotoxicity: mechanisms and therapeutic opportunities," *The American Journal of Pathology*, vol. 189, no. 4, pp. 719–729, 2019.
- [20] S. Mukherjee, K. Chellappa, A. Moffitt et al., "Nicotinamide adenine dinucleotide biosynthesis promotes liver regeneration," *Hepatology*, vol. 65, no. 2, pp. 616–630, 2017.
- [21] P. Xu, X. Zhang, Q. Liu et al., "Microglial TREM-1 receptor mediates neuroinflammatory injury via interaction with SYK in experimental ischemic stroke," *Cell Death & Disease*, vol. 10, no. 8, p. 555, 2019.
- [22] A. Boufenzar, J. Lemarié, T. Simon et al., "TREM-1 mediates inflammatory injury and cardiac remodeling following myocardial infarction," *Circulation Research*, vol. 116, no. 11, pp. 1772–1782, 2015.

- [23] D. Schuppan and N. H. Afdhal, "Liver cirrhosis," *The Lancet*, vol. 371, no. 9615, pp. 838–851, 2008.
- [24] F. Heymann and F. Tacke, "Immunology in the liver – from homeostasis to disease," *Nature Reviews. Gastroenterology & Hepatology*, vol. 13, no. 2, pp. 88–110, 2016.
- [25] E. Triantafyllou, K. J. Woollard, M. J. W. McPhail, C. G. Antoniades, and L. A. Possamai, "The role of monocytes and macrophages in acute and acute-on-chronic liver failure," *Frontiers in Immunology*, vol. 9, p. 2948, 2018.
- [26] E. Triantafyllou, O. T. Pop, L. A. Possamai et al., "MerTK expressing hepatic macrophages promote the resolution of inflammation in acute liver failure," *Gut*, vol. 67, no. 2, pp. 333–347, 2018.
- [27] C. G. Antoniades, A. Quaglia, L. S. Taams et al., "Source and characterization of hepatic macrophages in acetaminophen-induced acute liver failure in humans," *Hepatology*, vol. 56, no. 2, pp. 735–746, 2012.
- [28] P. S. Lewis, L. Campana, N. Aleksieva et al., "Alternatively activated macrophages promote resolution of necrosis following acute liver injury," *Journal of Hepatology*, vol. 73, no. 2, pp. 349–360, 2020.
- [29] B. Song, C. Zhang, W. Hu et al., "Nano-designed carbon monoxide donor SMA/CORM2 exhibits protective effect against acetaminophen induced liver injury through macrophage reprogramming and promoting liver regeneration," *Journal of Controlled Release*, vol. 331, pp. 350–363, 2021.
- [30] H. M. Golbar, T. Izawa, K. K. Wijesundera et al., "Depletion of hepatic macrophages aggravates liver lesions induced in rats by thioacetamide (TAA)," *Toxicologic Pathology*, vol. 44, no. 2, pp. 246–258, 2016.
- [31] R. Han, F. Zhang, C. Wan, L. Liu, Q. Zhong, and W. Ding, "Effect of perfluorooctane sulphonate-induced Kupffer cell activation on hepatocyte proliferation through the NF- κ B/TNF- α /IL-6-dependent pathway," *Chemosphere*, vol. 200, pp. 283–294, 2018.
- [32] A. Zlotnik and O. Yoshie, "Chemokines: a new classification system and their role in immunity," *Immunity*, vol. 12, no. 2, pp. 121–127, 2000.
- [33] S. Affò, O. Morales-Ibanez, D. Rodrigo-Torres et al., "CCL20 mediates lipopolysaccharide induced liver injury and is a potential driver of inflammation and fibrosis in alcoholic hepatitis," *Gut*, vol. 63, no. 11, pp. 1782–1792, 2014.
- [34] R. Rao, C. S. Graffeo, R. Gulati et al., "Interleukin 17-producing $\gamma\delta$ T cells promote hepatic regeneration in mice," *Gastroenterology*, vol. 147, no. 2, pp. 473–484.e2, 2014.
- [35] P. Scheiermann, M. Bachmann, L. Härdle et al., "Application of IL-36 receptor antagonist weakens CCL20 expression and impairs recovery in the late phase of murine acetaminophen-induced liver injury," *Scientific Reports*, vol. 5, no. 1, p. 8521, 2015.
- [36] C. González-Guerrero, J. L. Morgado-Pascual, P. Cannata-Ortiz et al., "CCL20 blockade increases the severity of nephrotoxic folic acid-induced acute kidney injury," *The Journal of Pathology*, vol. 246, no. 2, pp. 191–204, 2018.
- [37] J. Heinrichsdorff, T. Luedde, E. Perdiguero, A. R. Nebreda, and M. Pasparakis, "p38 α MAPK inhibits JNK activation and collaborates with I κ B kinase 2 to prevent endotoxin-induced liver failure," *EMBO Reports*, vol. 9, no. 10, pp. 1048–1054, 2008.
- [38] J. Zhang, C. Ma, Y. Liu, G. Yang, Y. Jiang, and C. Xu, "Interleukin 18 accelerates the hepatic cell proliferation in rat liver regeneration after partial hepatectomy," *Gene*, vol. 537, no. 2, pp. 230–237, 2014.
- [39] J. S. Campbell, G. M. Argast, S. Y. Yuen, B. Hayes, and N. Fausto, "Inactivation of p38 MAPK during liver regeneration," *The International Journal of Biochemistry & Cell Biology*, vol. 43, no. 2, pp. 180–188, 2011.
- [40] A. M. Tormos, R. Taléns-Visconti, A. R. Nebreda, and J. Sastre, "p38 MAPK: a dual role in hepatocyte proliferation through reactive oxygen species," *Free Radical Research*, vol. 47, no. 11, pp. 905–916, 2013.

Research Article

Nontargeted Metabolomic Analysis of Plasma Metabolite Changes in Patients with Adolescent Idiopathic Scoliosis

Lige Xiao,^{1,2} Guanteng Yang,^{1,2} Hongqi Zhang ^{1,2} Jinyang Liu,^{1,2} Chaofeng Guo ^{1,2} and Yang Sun ^{1,2}

¹Department of Spine Surgery and Orthopaedics, Xiangya Hospital, Central South University, Changsha, China

²National Clinical Research Center for Geriatric Disorders, Xiangya Hospital, Central South University, Changsha, China

Correspondence should be addressed to Chaofeng Guo; 343942471@qq.com and Yang Sun; sy_sunrise@csu.edu.cn

Received 23 February 2021; Revised 20 April 2021; Accepted 27 April 2021; Published 26 May 2021

Academic Editor: Shuai Chen

Copyright © 2021 Lige Xiao et al. This is an open access article distributed under the Creative Commons Attribution License, which permits unrestricted use, distribution, and reproduction in any medium, provided the original work is properly cited.

Objective. Adolescent idiopathic scoliosis (AIS) is a relatively common spinal rotation deformity, and the pathogenesis of AIS is accompanied by metabolic dysfunction and changes in biochemical factors. In this study, plasma metabolite changes in AIS patients were analyzed based on nontargeted metabolomics to provide new insights for clarifying functional metabolic abnormalities in AIS patients. **Methods.** Clinical indexes and blood samples were collected from 12 healthy subjects and 16 AIS patients. Metabolomics was used to analyze the changes in metabolites in plasma samples. The correlation between plasma metabolites and clinical indexes was analyzed by the Spearman rank correlation coefficient. **Results.** Analysis of clinical data showed that the body weight, body mass index (BMI), and bone mineral density (BMD) index of the AIS group significantly decreased, while the blood phosphorus and Cobb angles increased significantly. Metabolomic analysis showed significant changes in 72 differential metabolites in the plasma of the AIS group, mainly including organooxygen compounds, carboxylic acids and derivatives, fatty acyls, steroids and steroid derivatives, and keto acids and derivatives. The Kyoto Encyclopedia of Genes and Genomes (KEGG) pathway showed that arginine biosynthesis, D-glutamine and D-glutamate metabolism, alanine, aspartate and glutamate metabolism, and citrate cycle (TCA cycle) were significantly enriched in the AIS and healthy groups. Spearman rank correlation coefficient analysis showed that the plasma metabolites C00026 (oxoglutarate), C00062 (L-arginine, arginine), C01042 (N-acetylaspartate), and C00158 (citrate) were significantly correlated with clinical indexes in AIS patients. In the healthy group, the plasma metabolites C00122 (fumarate), C00025 (glutamate and L-glutamic acid) and C00149 (malate, L-malic acid) were significantly correlated with clinical indexes, while C00624 (N-acetylglutamate) was not significantly correlated with the clinical indexes. **Conclusion.** The occurrence of AIS led to changes in clinical indexes and plasma metabolites. Plasma biomarkers and functional metabolic pathways were correlated with clinical indexes, which might provide new insights for the diagnosis and treatment of AIS.

1. Introduction

Adolescent idiopathic scoliosis (AIS) is the most common spinal rotation deformity, affecting approximately 1-4% of adolescents worldwide [1]. Early diagnosis could increase the possibility of successful conservative treatment, thus reducing surgical intervention. AIS has a poor prognosis and a high mortality rate and can easily increase the risk of respiratory failure and cardiovascular disease [2]. The Abnormal neuromuscular system and calcium metabolism, as well as genetic and mechanical factors, might play a role

in the pathogenesis of AIS. The physiological secondary effects of severe scoliosis were associated with restrictive lung disease, but the degree of deformity in most patients was not sufficient to affect their cardiopulmonary function. The clinical symptoms and pathological changes of AIS indicated that before abnormal growth of the spine, patients had metabolic dysfunction, and blood biochemical factors were involved in its pathogenesis, but the etiology of AIS was still unknown [3]. Metabolomics is a research method used to quantitatively analyze all metabolites in organisms and to search for the relative relationships between metabolites

and physiological and pathological changes. It is an integral part of system biology [4–6]. Metabolomics had been widely used in the screening and diagnosis of disease biomarkers, which might be helpful for the early screening and treatment of AIS.

Ultra-performance liquid chromatography (UPLC) combined with quadrupole time-of-flight mass spectrometry (TOFMS) has been used to investigate the serum metabolic status between 30 AIS patients and 31 healthy controls. The metabolic profile of AIS patients usually deviated from that of healthy controls, and seven differential metabolites were identified as candidate diagnostic biomarkers, including PC (20:4), 2-hexanoylcarnitine, β -D-glucopyranosuronic acid, DG (38:9), MG (20:3), LysoPC (18:2), and LysoPC (16:0). These candidate metabolites indicated that lipid metabolism in AIS was blocked, including glycerophospholipid, glyceride, and fatty acid metabolism [7]. The increased expression of triglyceride lipase and hormone sensitive lipase in the adipose tissue further confirmed the increased lipid metabolism of AIS [8]. A domestic research team used metabolomics to analyze the changes in the gut microbiota metabolites of postmenopausal osteoporosis patients and identified the gut microbiota metabolites related to bone mineral density (BMD) and bone transformation markers, indicating that the changes in gut microbiota metabolites in postmenopausal osteoporosis patients were related to the decrease in BMD or bone metabolism indexes [9]. These studies demonstrated that serum differential metabolites found in AIS could be used as potential diagnostic biomarkers, and that lipid metabolism played a role in the pathogenesis of AIS.

In addition, most AIS patients have abnormal changes in estrogen and estrogen receptors, including increased serum estrogen concentrations, abnormal cellular responses to estrogen, older menarche age, and estrogen receptor gene polymorphisms, which are closely related to the susceptibility of AIS, the severity of the curve, and the progression of scoliosis [10, 11]. Plasma, the extracellular fluid of blood cells, is an important part of the internal environment of the body and plays an important role in communication between the internal and external environment of the body. In a recent study, Shen et al. found that the fecal microbial composition of AIS patients was different from that of healthy controls. Through proteomic analysis of the correlation between gut microbiota and plasma protein, it was confirmed that fecal *Prevotella* was positively correlated with host plasma FN1 and negatively correlated with host VDAC1 and AHNK [12]. The composition of plasma could be changed by the metabolic activity of the body and the external environment, but under normal circumstances, the body kept the composition of plasma relatively constant through various regulatory functions [13]. When the body is sick, the changes in some components in plasma might exceed the normal range. Therefore, the determination of plasma components might provide a basis for the diagnosis and treatment of AIS.

At present, there is no research on the plasma biomolecular metabolites of AIS patients. This study intends to use metabolomics to perform nontargeted broad screening of metabolites and analyze the differences in plasma metabolites between AIS patients and healthy subjects to elucidate the

metabolic characteristics of AIS and provide a theoretical basis for the early screening of AIS.

2. Materials and Methods

2.1. Study Subjects. We studied subjects aged 12–18 years who were diagnosed with AIS from Hunan Province, China. Subjects completed a questionnaire about age, race, medication history, and medical history. The study excluded patients with other types of scoliosis caused by congenital or postural or neuromuscular factors and did not recruit subjects with acute infectious diseases, severe allergies, gastrointestinal diseases, and abnormal liver and kidney functions within the first month. None of the subjects underwent any surgery or rehabilitation. Height, weight, and body mass index (BMI) of all subjects were recorded.

2.2. Sample Preparation. The blood of all participants was centrifuged at 1150 g at 4°C for 10 minutes in a centrifuge tube coated with heparin. The supernatant was then aliquoted (100 μ L) into a labeled test tube and stored at -80°C before preparation for metabolomics analysis.

2.3. LC-MS/MS Analysis and Annotation. Samples (100 μ L) were mixed with 300 μ L of methanol and 20 μ L of internal standard, vortexed for 30 s, extracted by ultrasonication in an ice water bath for 5 min, and stored at -20°C for 2 h. The mixture was centrifuged at 4°C (13,000 rpm, 15 min), and 200 μ L of supernatant was put into a 2 mL injection bottle for LC-MS/MS analysis. Baseline filtering, peak identification, integration, retention time correction, peak alignment, and normalization were performed on the original data obtained after mass spectrometry, and finally, a data matrix of retention time, mass/charge ratio, and peak intensity was obtained. Raw data were obtained for quality control, and bioinformatic analysis was performed.

MetaboAnalyst (<https://www.metaboanalyst.ca/>) was used for bioinformatic analysis. MetaboAnalyst is a comprehensive platform dedicated to metabolomic data analysis. There is a wide array of commonly used statistical and machine learning methods. In this study, the bioinformatic analyses, including univariate fold change, *t*-test, volcano plot, multivariate principal component analysis (PCA), partial least squares-discriminant analysis (PLS-DA), heatmap, and correlation analysis were applied. PCA is an unsupervised multidimensional statistical analysis method that can reflect the overall metabolic differences between samples in each group and the degree of variability between samples within the group [14]. PLS-DA is a multivariate statistical analysis method with supervised pattern recognition that groups multidimensional data according to the different factors that need to be searched before compression, so that the variables most relevant to the factors used for grouping could be found, and the influence of some other factors could be reduced [15]. The Kyoto Encyclopedia of Genes and Genomes (KEGG) pathway database was used to perform metabolic pathway enrichment analysis [16].

2.4. Correlation Analysis. The Spearman rank correlation coefficient and heatmap were generated to analyze the

correlation between different metabolites and clinical indexes by Graph Prism 8.0 software.

2.5. Statistical Analysis. Statistical analysis of the data was performed using Graph Prism 8.0 and R software 3.1.0. The comparison between the two groups used Student's *t*-test or the Wilcoxon signed rank test, depending on whether the variable was normally distributed. $P < 0.05$ indicated that the difference was statistically significant.

3. Results

3.1. Characteristics of the Participants Involved in This Study.

In this study, 12 healthy subjects and 16 AIS patients were collected, and their clinical data were statistically analyzed. Compared with the healthy group, the body weight and BMI of the AIS group significantly decreased, and the Cobb angle degree increased significantly. BMD measurements found that AIS patients had a significantly lower BMD index in the lumbar and femoral areas. Blood analysis showed that serum calcium and magnesium levels did not change significantly compared with the healthy group, while serum phosphorus levels increased significantly. The statistical analysis results of the clinical data are shown in Table 1. The above results indicate that the clinical indexes of AIS patients change to different degrees, which are closely related to the health of AIS patients.

3.2. Plasma Metabolism Profiles in AIS and Healthy Subjects.

To study the changes in metabolic phenotypes, plasma samples of healthy subjects and AIS patients were collected, and endogenous small molecules with relative molecular weights less than 1000 in plasma were widely screened by nontargeted metabolomics. Qualitative metabolites were based on public databases and self-built software databases. The normalized data matrix was used for multivariate statistical analysis, and PCA (Figure 1(a)) and partial least squares regression analysis (Figure 1(b)) were performed on all samples and quality control samples. PCA showed that the principal component 1 (PC1) index was 14%, and the PC2 index was 10%. PLS-DA analysis showed that the index of the variable factor was 12.5%. PCA and PLS-DA analysis showed uniform dispersion of quality control and grouped samples, which indicated that the stability and reliability of instrumental analysis were excellent and could be used for further analysis. A heatmap showed the top 100 metabolites obtained by nontargeted screening in the healthy group and AIS groups. It showed that the healthy group and AIS group were enriched with dominant metabolites (Figure 1(c)). These results suggested that the occurrence of AIS might lead to an abnormal plasma metabolome or AIS-related metabolic dysfunction.

3.3. Different Plasma Metabolism Profiles between AIS and Healthy Subjects.

To further analyze the differences in plasma metabolites between healthy subjects and AIS patients, we combined the VIP value of multivariate statistical analysis of OPLS-DA and the *P* value of the univariate statistical analysis *t*-test to screen the significantly different metabolites between different comparison groups. The threshold of sig-

nificant difference was $VIP \geq 1$ and *t*-test $P < 0.05$ [17]. After data normalization, cluster analysis and heatmaps were drawn to show the accumulation of different metabolites in the comparison groups [18]. A heatmap showed the top 50 metabolites significantly enriched in the AIS group and the healthy group (Figure 2(a)). The fold change diagram further showed the plasma fold changes of 72 different metabolites between the healthy group and the AIS group (Figure 2(b)). Volcano plots showed that 27 kinds of plasma differential metabolites were significantly increased, and 45 kinds were significantly decreased in the AIS group, and the absolute value of $\log_2(FC)$ was ≥ 0.5869 , $P < 0.05$ (Figure 2(c)).

Based on the Human Metabolome Database (<https://hmdb.ca/>), the differential metabolites in plasma were classified and summarized [19, 20]. Among them, the concentration of phenols anthranilate in the plasma metabolite class level of AIS patients increased. The concentration of methyl nicotinate in plasma pyridines and derivatives increased. The concentration of ribitol, L-arabitol, D-arabitol, D-xylitol, N-acetylgalactosamine, isopropanolamine, and trimethylamine N-oxide in plasma organooxygen compounds increased. The concentration of imidazopyrimidine hypoxanthine increased. The concentration of 4-acetamidobutanoate, N-acetylasparagine, L-arginine, arginine, N-acetylaspartate, homocitrulline, citrate, phosphocreatine, and dimethylmalonic acid in plasma carboxylic acids and derivatives increased. The plasma fatty acyl sebaccate and nervonate concentrations increased. Plasma steroids and steroid derivatives taurodeoxycholic acid and taurocholic acid concentrations increased. The plasma keto acids and derivative oxoglutarate concentration increased. In addition, the unclassified maleamate, trigonelline, and monoethylmalonate concentrations increased. These results indicated that plasma metabolites were significantly altered in AIS patients, accompanied by the activation of metabolic pathways related to phenols, organic oxides, fatty acids, amino acids, and bile salts.

3.4. Metabolic Pathway Analysis between AIS and Healthy Subjects.

To explore the functional changes caused by the changes in plasma metabolites in AIS patients, based on raw metabolomic data, signaling pathway function prediction analysis was carried out through the KEGG pathway database (<https://www.kegg.jp/kegg/pathway.html>). The KEGG pathway analysis showed the top 25 enriched signaling pathways in the AIS group and healthy group (Figure 3). There were significant changes in the L1 level metabolism functional pathway in the plasma of AIS patients. In the L2 level of amino acid metabolism, the L3 level of arginine biosynthesis was enriched in 14 plasma metabolites ($P = 0.000144$), of which C00026 (oxoglutarate) and C00062 (L-arginine, arginine) were significantly enriched in AIS patients, and C00624 (N-acetylglutamate), C00025 (glutamate, L-glutamic acid), and C00122 (fumarate) were significantly enriched in healthy subjects. At the L2 level of metabolism of other amino acids, the L3 level of D-glutamine and D-glutamate metabolism was enriched in 6 plasma metabolites ($P = 0.000118$), of which C00026 (oxoglutarate) was significantly enriched in AIS patients, and

TABLE 1: Clinical information of the participants.

Participants	Control ($n = 12$)	AIS ($n = 16$)	P value
Age (years)	16.41 \pm 3.20	15.12 \pm 1.70	0.180
Gender (male/female)	6/6	6/10	0.508
Height (m)	1.70 \pm 0.08	1.65 \pm 0.08	0.169
Weight (kg)	73.18 \pm 15.10	48.00 \pm 10.44	<0.001
BMI (kg/m ²)	25.36 \pm 5.41	17.39 \pm 2.73	<0.001
Cobb angles (°)		45.56 \pm 12.78	<0.001
Bone density			
Waist T	-0.60 \pm 1.23	-2.70 \pm 1.03	<0.001
Waist Z	0.20 \pm 1.04	-1.90 \pm 1.13	<0.001
Thigh T	-0.64 \pm 1.46	-2.75 \pm 0.94	<0.001
Thigh Z	-0.18 \pm 1.34	-2.15 \pm 1.08	<0.001
Blood calcium (mmol/L)	2.32 \pm 0.21	2.47 \pm 0.35	0.213
Blood phosphate (mmol/L)	1.31 \pm 0.14	1.58 \pm 0.15	<0.001
Blood magnesium (mmol/L)	0.85 \pm 0.07	0.95 \pm 0.40	0.432

C00025 (glutamate, L-glutamic acid) was significantly enriched in healthy subjects. In the L2 level of amino acid metabolism, the L3 level of alanine, aspartate, and glutamate metabolism were enriched in 28 plasma metabolites ($P = 0.000454$), of which C00026 (oxoglutarate), C01042 (N-acetylaspartate), and C00158 (citrate) were significantly enriched in AIS patients, and C00025 (glutamate, L-glutamic acid) and C00122 (fumarate) were significantly enriched in healthy subjects. In the L2 level of carbohydrate metabolism, the L3 level of citrate cycle (TCA cycle) was enriched in 20 plasma metabolites ($P = 0.0448$), of which C00026 (oxoglutarate) and C00158 (citrate) were significantly enriched in AIS patients, and C00122 (fumarate) and C00149 (malate, L-malic acid) were significantly enriched in healthy subjects. The above results indicated that the significant accumulation and depletion of plasma metabolites in AIS patients were related to the functional metabolic preference for amino acid metabolism and energy cycling pathways.

3.5. Correlation between Plasma Metabolites and the Clinical Index. Based on the clinical index characteristics of AIS patients and the plasma metabolomic analysis, we found that compared with healthy subjects, the clinical index of AIS patients showed serious adverse changes, and the types and functions of plasma metabolites of AIS patients were significantly changed. To further explore the changes between the plasma differential metabolites and the clinical index of AIS patients, the Spearman rank correlation coefficient was used to calculate the relationship between 72 plasma differential metabolites and the clinical index of AIS patients. Among them, 57 plasma differential metabolites were significantly correlated with the clinical index of patients (Figure 4). A heatmap showed that plasma metabolite C00026 (oxoglutarate) was negatively correlated with weight ($r = -0.40$, $P = 0.031$), BMI ($r = -0.41$, $P = 0.029$), and BMD (thigh T , $r = -0.42$, $P = 0.024$ and thigh Z , $r = -0.38$, $P = 0.041$) in AIS

patients. C00062 (L-arginine) was significantly negatively correlated with weight ($r = -0.51$, $P = 0.005$), BMI ($r = -0.50$, $P = 0.005$), and BMD (waist T , $r = -0.39$, $P = 0.038$ and thigh T , $r = -0.39$, $P = 0.036$) but positively correlated with Cobb angles ($r = 0.48$, $P = 0.009$). C00062 (arginine) was significantly negatively correlated with weight ($r = -0.49$, $P = 0.007$), BMI ($r = -0.49$, $P = 0.007$), and BMD (waist T , $r = -0.38$, $P = 0.043$ and thigh T , $r = -0.38$, $P = 0.042$) and positively correlated with Cobb angles ($r = 0.46$, $P = 0.012$). C01042 (N-acetylaspartate) was significantly negatively correlated with weight ($r = -0.53$, $P = 0.003$), BMI ($r = -0.41$, $P = 0.026$), and BMD (waist T , $r = -0.59$, $P < 0.001$; waist Z , $r = -0.53$, $P = 0.003$; thigh T , $r = -0.62$, $P < 0.001$ and thigh Z , $r = -0.59$, $P < 0.001$), while positively correlated with blood phosphate ($r = 0.43$, $P = 0.019$) and Cobb angles ($r = 0.71$, $P < 0.001$). C00158 (citrate) was negatively correlated with weight ($r = -0.37$, $P = 0.049$) and BMI ($r = -0.40$, $P = 0.032$) and positively correlated with blood phosphate ($r = 0.44$, $P = 0.018$).

The plasma metabolite C00122 (fumarate) was significantly positively correlated with weight ($r = 0.44$, $P = 0.017$) and negatively correlated with Cobb angles ($r = -0.45$, $P = 0.015$) in healthy subjects. C00025 (glutamate and L-glutamic acid) was positively correlated with weight ($r = 0.50$, $P = 0.005$), BMI ($r = 0.51$, $P = 0.005$), and BMD (waist T , $r = 0.38$, $P = 0.041$ and waist Z , $r = 0.40$, $P = 0.034$), while negatively correlated with blood phosphate ($r = -0.54$, $P = 0.002$) and Cobb angles ($r = -0.51$, $P = 0.005$). C00149 (malate, L-malic acid) was positively correlated with weight ($r = 0.43$, $P = 0.020$), BMI ($r = 0.41$, $P = 0.029$), and BMD (waist T , $r = 0.42$, $P = 0.024$ and waist Z , $r = 0.40$, $P = 0.030$) and negatively correlated with blood phosphate ($r = -0.49$, $P = 0.007$) and Cobb angles ($r = -0.54$, $P = 0.002$). In addition, there was no significant correlation between clinical height index and the differentially enriched plasma metabolites in the AIS and healthy groups. There was no significant correlation between plasma metabolite C00624 (N-

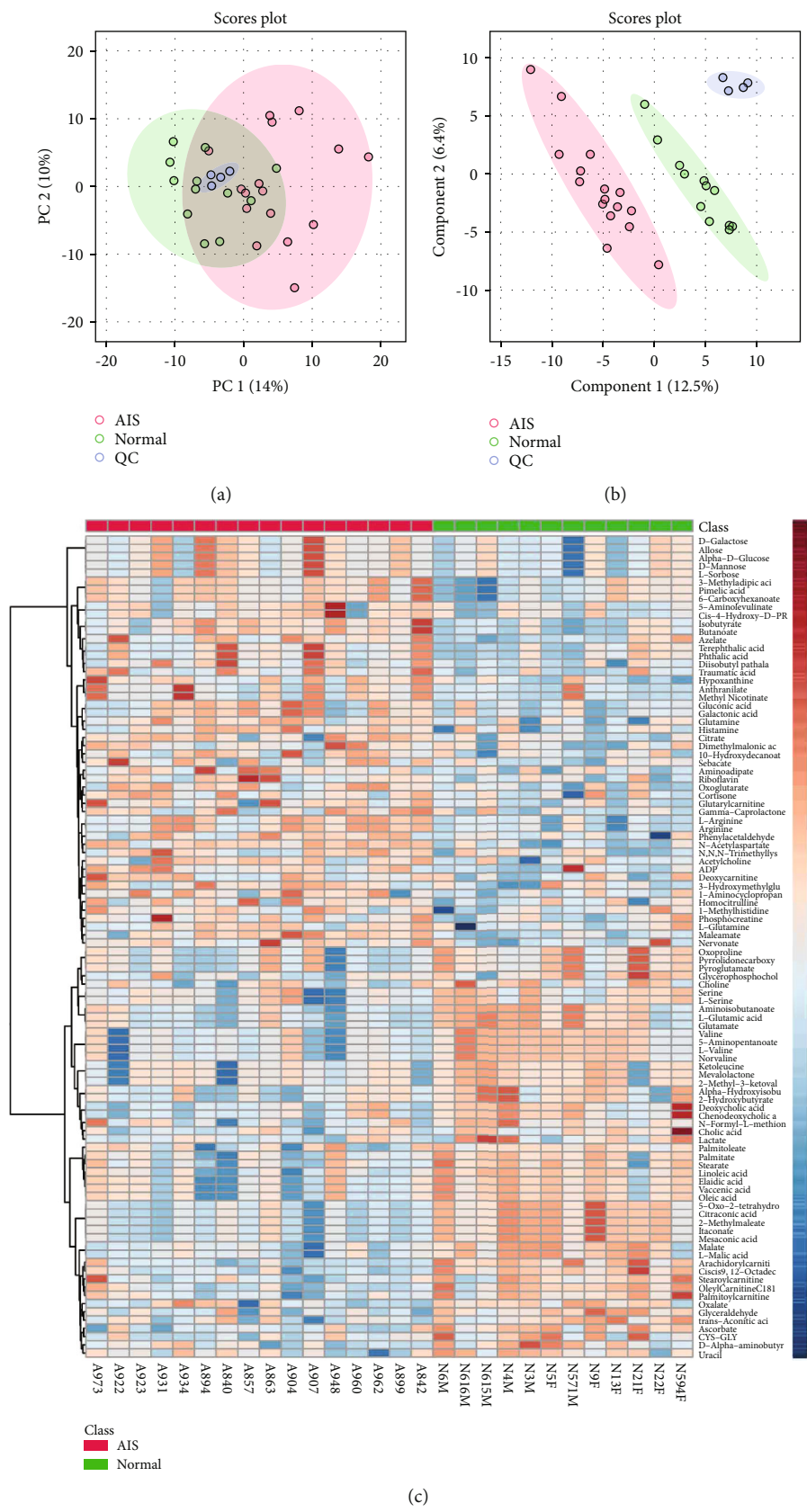


FIGURE 1: The analysis of plasma metabolite profiles. (a) PCA was used to analyze the degree of dispersion of samples in the quality control and healthy and AIS groups. (b) PLS-DA was used to analyze the degree of dispersion of samples in the quality control and healthy and AIS groups. (c) Heatmap shows the distribution of the top 100 metabolites among different samples.

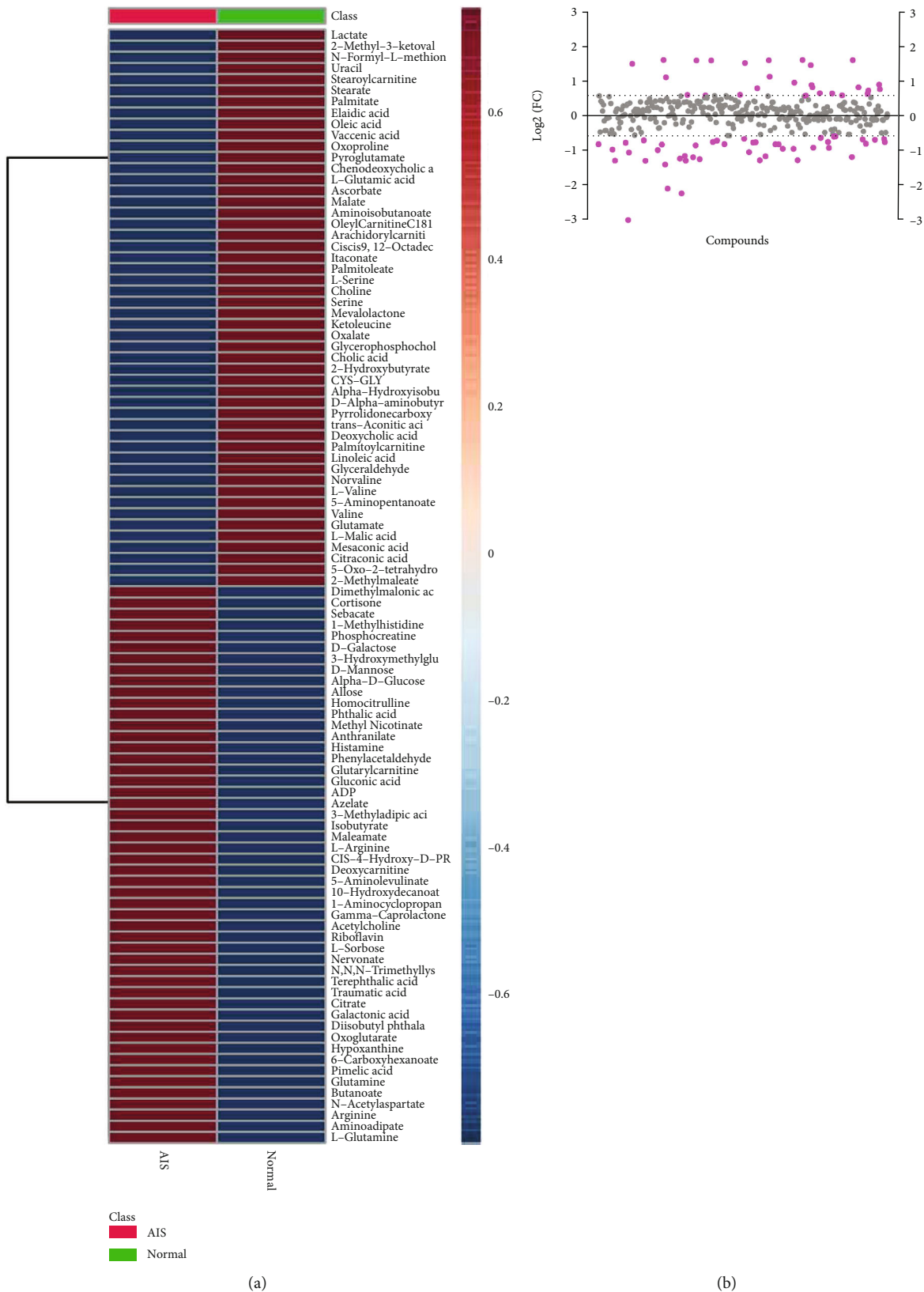


FIGURE 2: Continued.

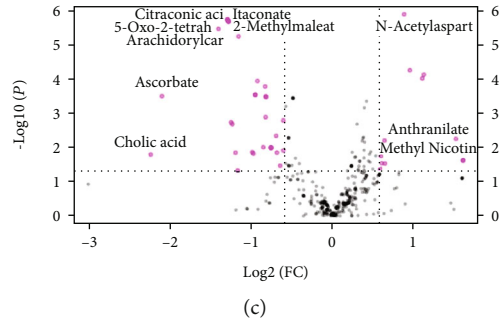


FIGURE 2: Analysis of the different metabolites. (a) Heatmap shows the difference in the top 50 metabolites between the healthy group and the AIS group. (b) Fold change diagram shows the fold change of different metabolites. (c) Volcano plot shows the changes in different metabolites.

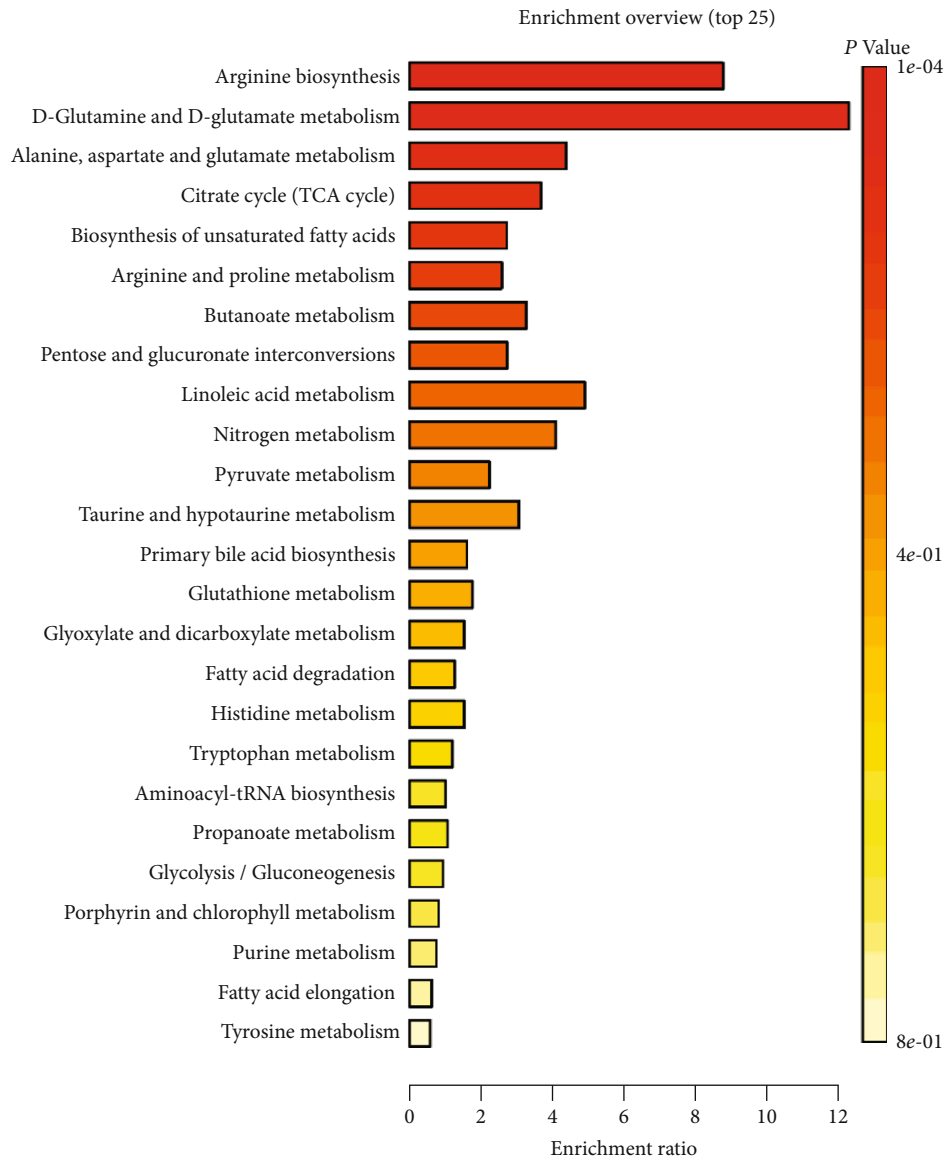


FIGURE 3: KEGG pathway analysis of metabolites.

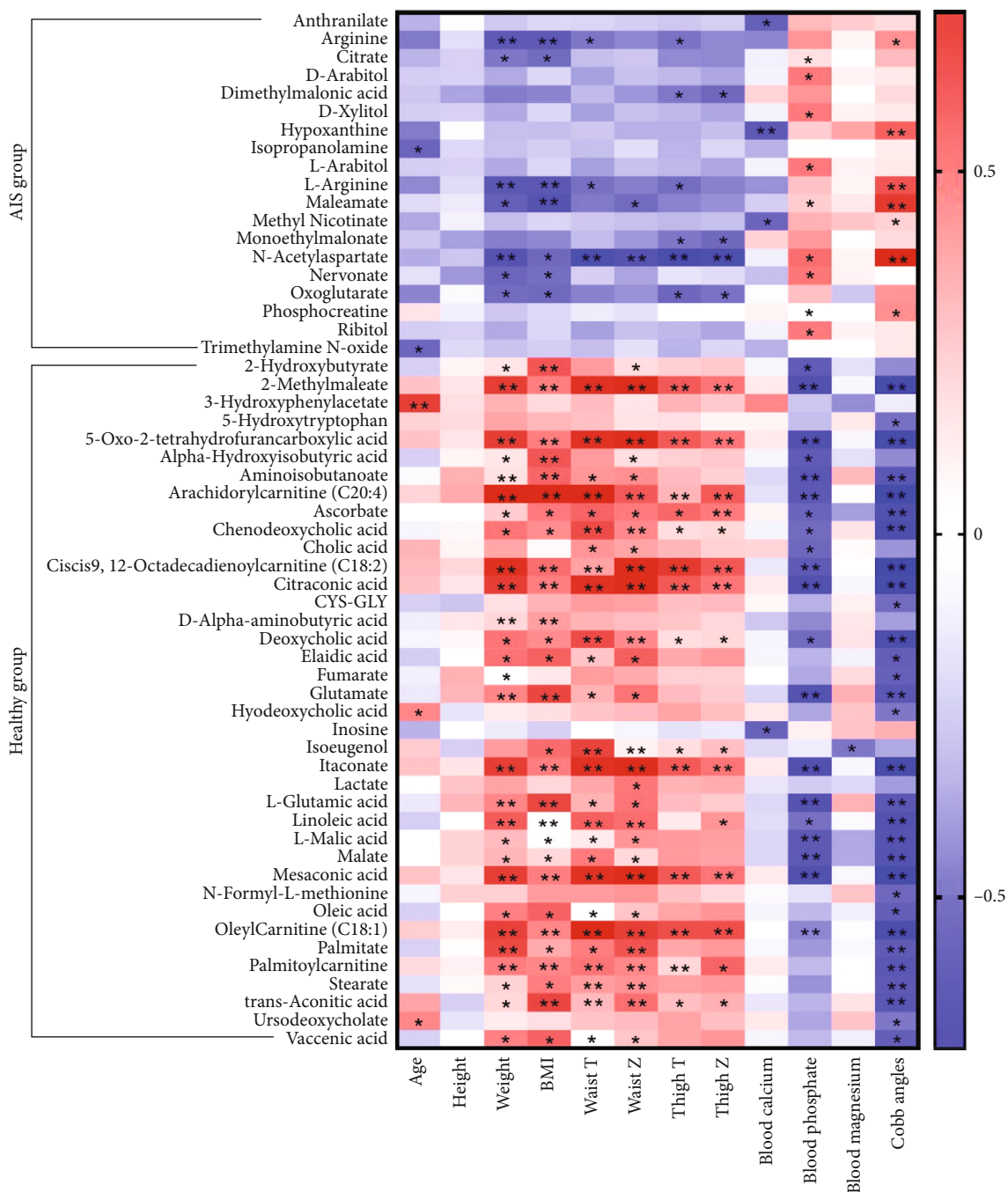


FIGURE 4: Correlation analysis of metabolites and clinical indexes.

acetylglutamate) and the clinical index in healthy subjects. These results suggested that the significantly enriched and depleted metabolites in the plasma of AIS patients and clinical indexes might be used as AIS-related biomarkers for early screening.

4. Discussion

Early screening of AIS is still a major challenge in clinical diagnosis. In this study, metabolomics was used to deeply analyze the differences in plasma metabolites of AIS patients

for the first time. Plasma organooxygen compounds, carboxylic acids, and derivatives were significantly enriched in AIS patients, and 57 metabolites were significantly correlated with clinical indexes. We found that plasma C00026 (oxoglutarate) was significantly enriched in AIS patients, and it was significantly negatively correlated with weight, BMI, and BMD (thigh T and thigh Z). Oxoglutarate, also known as α -ketoglutarate, AKG, or 2-oxoglutarate, was classified as a γ -keto acid or a γ -keto acid derivative. α -Ketoglutarate is a key molecule in the tricarboxylic acid (TCA) cycle and plays a fundamental role in determining the overall rate of this

important metabolic process [21, 22]. In the TCA cycle, AKG is decarboxylated to succinyl coenzyme A and carbon dioxide by AKG dehydrogenase, which is the key control point of the TCA cycle. AKG is a nitrogen scavenger and a source of glutamic acid and glutamine, which can stimulate protein synthesis and inhibit protein degradation in muscles. AKG could reduce protein catabolism and increase protein synthesis, thereby enhancing the formation of the musculoskeletal tissue [21]. Interestingly, enteral feeding of AKG supplements could significantly increase circulating plasma levels of hormones such as insulin, growth hormone, and insulin-like growth factor 1 [21, 23]. Recent studies have shown that α -ketoglutarate promotes the differentiation of TH1 cells with the consumption of glutamine, which is beneficial to the differentiation of Tregs [24]. The enrichment of oxoglutarate in the plasma of AIS patients indicated increased demand for bone tissue formation, the disorder of hormone, and energy metabolism related to growth and metabolism in adolescents. Therefore, the regulation of plasma oxoglutarate might help promote the recovery of AIS.

C00062 (arginine) is an essential amino acid with physiological activity in the L-type strain. L-Arginine is an amino acid with multiple functions in the body that helps to process ammonia that is used to make compounds such as nitric oxide, creatine, L-glutamic acid, and L-proline and can be converted into glucose and glycogen when needed. At a high dose, L-arginine also stimulates the release of growth hormone and prolactin. Arginine is a known inducer of mTOR and is responsible for inducing protein synthesis through the mTOR pathway. The inhibition of mTOR by rapamycin partially reduces arginine-induced protein synthesis [25]. Catabolic diseases such as sepsis, injury, and cancer could lead to increased utilization of arginine, and the utilization of arginine might exceed normal body production, resulting in arginine consumption. Arginine also activated the AMPK pathway and stimulates skeletal muscle fatty acid oxidation and muscle glucose uptake, thereby increasing insulin secretion by pancreatic β cells [26]. This study found that plasma C00062 (L-arginine, arginine) was significantly enriched in AIS patients, and it was significantly negatively correlated with weight, BMI, and BMD (waist T and thigh T) and significantly positively correlated with Cobb angles. The massive enrichment of L-arginine and arginine in the plasma of AIS patients might be the metabolic dysfunction caused by AIS, and the reasonable regulation of plasma arginine metabolism might help the recovery and treatment of AIS.

C01042 (N-acetylaspartate) is a derivative of aspartic acid that is synthesized by aspartic acid and acetyl coenzyme A in neurons. Various functions of N-acetylaspartate are still under investigation, but the main proposed functions include acting as a neuroosmotic agent and participating in fluid balance in the brain, acting as a source of lipid acetate for the synthesis of myelin in oligodendrocytes, used as a precursor for the synthesis of the important dipeptide neurotransmitter N-acetylaspartyl glutamate (NAAG), and playing a potential role in the energy production of neuronal mitochondria [27, 28]. However, when N-acetylaspartate was present at a sufficiently high level, it could have a variety of adverse effects on many organ systems. Abnormally high levels of N-

acetylaspartate in blood (organic acidemia), urine (organic aciduria), brain, and other tissues could cause general metabolic acidosis [29]. Adults with acidosis or acidemia are prone to headache, confusion, tiredness, tremor, lethargy, and flapping tremor. C01042 (N-acetylaspartate) was significantly enriched in the plasma of AIS patients, which might be related to the spinal injury caused by the AIS endangering spinal nervous system.

The plasma metabolites C00122 (fumarate), C00025 (glutamate and L-glutamic acid), and C00149 (malate, L-malic acid) were significantly enriched in healthy subjects and were closely correlated with clinical indexes. C00149 (malate, L-malic acid) is an organic dicarboxylic acid with a sour taste. Malic acid and fumarate are intermediate products of the TCA cycle [30, 31]. Under aerobic conditions, the oxidation of malic acid to oxaloacetic acid can provide a reduced mitochondrial equivalent through the redox shuttle between malic acid and aspartic acid. Under anaerobic conditions, the accumulation of excess reduction equivalents inhibits glycolysis, and the simultaneous reduction of malic acid to succinate and oxidation to oxaloacetic acid could remove the accumulated reduction equivalents, which leads to malic acid reversing the inhibition of hypoxia on glycolysis and energy production. C00122 (fumarate) is a dicarboxylic acid that has recently been identified as a metabolite or an endogenous carcinogenic metabolite. High levels of this organic acid can be found in tumors or biological fluids around tumors. Its carcinogenic effect seemed to be due to its ability to inhibit prolyl hydroxylase [32]. C00025 (glutamate and L-glutamic acid) is one of the 20 kinds of proteogenic amino acids. Glutamate is the most abundant fast excitatory neurotransmitter in the mammalian nervous system. Glutamate induced excitotoxicity was part of the ischemic cascade and is associated with stroke, amyotrophic lateral sclerosis, systemic lupus erythematosus, and Alzheimer's disease [33]. The depletion of the plasma metabolites C00122 (fumarate), C00025 (glutamate and L-glutamic acid), and C00149 (malate, L-malic acid) in AIS patients might be related to energy metabolism and spinal injury.

The study limitations mainly lie in the limited patient population covered by the analysis. The AIS patients selected in this study had mainly severe scoliosis with Cobb angles of $45.56 \pm 12.78^\circ$. Meanwhile, since we studied the plasma metabolomics of multiple patients and did not specifically compare the gender and clinical classification of patients with King, Lenke, or PUMC (Peking Union Medical College) in AIS, our study may not fully represent the entire clinical spectrum of AIS patients. It has been reported that the Carter effect exists in AIS, and the incidence of AIS in women is 2-10 times higher than that in men [34-37]. In this study, we did not explore whether the gender or clinical classification affected the plasma metabolomics of AIS patients. In-depth follow-up studies will explore the above issue further.

In summary, this study used metabolomics to open the black box of plasma metabolomics in AIS patients. Based on the differential analysis of biomarkers, 72 small molecule metabolites were changed. Among them, the plasma metabolites C00026 (oxoglutarate), C00062 (L-arginine, arginine), C01042 (N-acetylaspartate), and C00158 (citrate) were

significantly enriched in AIS patients. The plasma metabolites C00122 (fumarate), C00025 (glutamate and L-glutamic acid), C00149 (malate, L-malic acid), and C00624 (N-acetylglutamate) were significantly depleted. These eight AIS-related plasma biomarkers have significant effects on the functional metabolism of the following four signaling pathways: arginine biosynthesis, D-glutamine and D-glutamate metabolism, alanine, aspartate and glutamate metabolism, and citrate cycle (TCA cycle). Based on clinical index correlation analysis, it was found that these eight AIS-related plasma biomarkers were clearly correlated with clinical indexes, BMD, and Cobb angles or could be used as new targets for clinical screening and treatment of AIS.

5. Conclusion

The occurrence of AIS led to significant changes in clinical indexes, BMD, Cobb angles, and plasma metabolites. Changes in blood metabolism functional pathways were closely related to AIS-related plasma biomarkers. Plasma biomarkers and their functional metabolism might provide new insights for the screening and treatment of AIS.

Data Availability

The data used to support the findings of this study are available from the corresponding author upon request.

Ethical Approval

This study was specifically approved by the Medical Ethics Committee of Xiangya Hospital of Central South University (202004137), Changsha, Hunan, China, and conducted in strict accordance with the institutes of health guidelines for the care and use of experimental animals. Written informed consent was obtained from all participants.

Conflicts of Interest

The authors declare no competing interests.

Authors' Contributions

Yang Sun and Chaofeng Guo designed the research. Lige Xiao and Guanteng Yang performed the research. Hongqi Zhang and Jinyang Liu analyzed the data. All authors contributed to the writing and revisions. All authors reviewed the manuscript. Lige Xiao and Guanteng Yang are co-first authors.

Acknowledgments

The authors would like to thank the Medical Ethics Committee of Xiangya Hospital of Central South University and Natural Science Foundation of Hunan, Independent Exploration, and Innovation Project for Postgraduate Student of CSU for their Funding support. This study was supported by the Natural Science Foundation of Hunan, China (2020JJ5919), Independent Exploration and Innovation Project for Postgraduate Student of CSU, China (2020zzts264),

and Natural Science Foundation of Hunan, China (2019JJ40523), (2019JJ80014), and (2018JJ6060).

References

- [1] L. A. Rinsky and J. G. Gamble, "Adolescent Idiopathic Scoliosis," *Western journal of medicine*, vol. 369, no. 16, pp. 1558–1560, 2013.
- [2] S. L. Weinstein, L. A. Dolan, K. F. Spratt, K. K. Peterson, M. J. Spoonamore, and I. V. Ponseti, "Health and function of patients with untreated idiopathic scoliosis: a 50-year natural history study," *Jama the Journal of the American Medical Association*, vol. 289, no. 20, pp. 2644–2645, 2003.
- [3] W. J. Wang, H. Y. Yeung, W. C.-W. Chu et al., "Top theories for the etiopathogenesis of adolescent idiopathic scoliosis," *Journal of Pediatric Orthopaedics*, vol. 31, 1 Supplement, pp. S14–S27, 2011.
- [4] M. Liu, X. Liu, H. Wang et al., "Metabolomics study on the effects of Buchang Naoxintong capsules for treating cerebral ischemia in rats using UPLC-Q/TOF-MS," *Journal of Ethnopharmacology*, vol. 180, pp. 1–11, 2016.
- [5] M. C. Chambers, B. Maclean, R. Burke et al., "A cross-platform toolkit for mass spectrometry and proteomics," *Nature Biotechnology*, vol. 30, no. 10, pp. 918–920, 2012.
- [6] C. Kuhl, R. Tautenhahn, C. Böttcher, T. R. Larson, and S. Neumann, "CAMERA: an integrated strategy for compound spectra extraction and annotation of liquid chromatography-mass spectrometry data sets," *Analytical Chemistry*, vol. 84, no. 1, pp. 283–289, 2012.
- [7] Z. J. Sun, H. M. Jia, G. X. Qiu et al., "Identification of candidate diagnostic biomarkers for adolescent idiopathic scoliosis using UPLC/QTOF-MS analysis: a first report of lipid metabolism profiles," *Scientific Reports*, vol. 6, no. 1, p. 22274, 2016.
- [8] Y. C. Chen, J. Greenbaum, H. Shen, and H. W. Deng, "Association between gut microbiota and bone health: potential mechanisms and prospective," *The Journal of Clinical Endocrinology and Metabolism*, vol. 102, no. 10, pp. 3635–3646, 2017.
- [9] J. He, S. Xu, B. Zhang et al., "Gut microbiota and metabolite alterations associated with reduced bone mineral density or bone metabolic indexes in postmenopausal osteoporosis," *Aging*, vol. 12, no. 9, pp. 8583–8604, 2020.
- [10] C. Zhou, H. Wang, Y. Zou, and H. Fang, "Research progress of role of estrogen and estrogen receptor on onset and progression of adolescent idiopathic scoliosis," *Zhongguo Xiu Fu Chong Jian Wai Ke Za Zhi*, vol. 29, no. 11, pp. 1441–1445, 2015.
- [11] G. Liu, Y. Hao, Q. Yang, and S. Deng, "The association of fecal microbiota in ankylosing spondylitis cases with C-reactive protein and erythrocyte sedimentation rate," *Mediators of Inflammation*, vol. 2020, Article ID 8884324, 2020.
- [12] N. Shen, N. Chen, X. Zhou et al., "Alterations of the gut microbiome and plasma proteome in Chinese patients with adolescent idiopathic scoliosis," *Bone*, vol. 120, pp. 364–370, 2019.
- [13] S. Lucas, Y. Omata, J. Hofmann et al., "Short-chain fatty acids regulate systemic bone mass and protect from pathological bone loss," *Nature Communications*, vol. 9, no. 1, p. 55, 2018.
- [14] B. D. Wang, K. Ceniccola, S. J. Hwang, R. Andrawis, and N. H. Lee, "Alternative splicing promotes tumour aggressiveness and drug resistance in African American prostate cancer," *Nature Communications*, vol. 8, no. 1, p. 15921, 2017.

- [15] Y. Yu, P. Wang, R. Yu, J. Lu, and K. Zhou, "Long-Term Exposure of Psoralen and Isopsoralen Induced Hepatotoxicity and Serum Metabolites Profiles Changes in Female Rats," *Metabolites*, vol. 9, no. 11, p. 263, 2019.
- [16] K. Minoru, F. Miho, T. Mao, S. Yokoi, and M. Kanae, "KEGG: new perspectives on genomes, pathways, diseases and drugs," *Nucleic Acids Research*, vol. D1, pp. D353–DD61, 2017.
- [17] "Chemical fingerprint analysis for discovering markers and identifying *Saussurea involucrea* by HPLC coupled with OPLS-DA," *Journal of Analytical Methods in Chemistry*, vol. 2020, Article ID 7560710, 2020.
- [18] C. Durón, "Heatmap centrality: a new measure to identify super-spreader nodes in scale-free networks," *PLoS One*, vol. 15, no. 7, article e0235690, 2020.
- [19] D. S. Wishart, "Metabolomic Data Exploration and Analysis with the Human Metabolome Database," in *Computational Methods and Data Analysis for Metabolomics*, pp. 165–184, 2020.
- [20] D. S. Wishart, D. Tzur, C. Knox et al., "HMDB: the human metabolome database," *Nucleic Acids Research*, vol. 35, no. - Database, pp. D521–D526, 2007.
- [21] N. Wu, M. Yang, U. Gaur, H. Xu, and D. Li, "Alpha-ketoglutarate: physiological functions and applications," *Biomolecules & Therapeutics*, vol. 24, no. 1, pp. 1–8, 2016.
- [22] R. M. Chin, X. Fu, M. Y. Pai et al., "The metabolite α -ketoglutarate extends lifespan by inhibiting ATP synthase and TOR," *Nature*, vol. 510, no. 7505, pp. 397–401, 2014.
- [23] V. F. Wendisch, "Microbial production of amino acid-related compounds," *Advances in Biochemical Engineering/Biotechnology*, vol. 159, pp. 255–269, 2017.
- [24] D. Klysz, X. Tai, P. A. Robert et al., "Glutamine-dependent α -ketoglutarate production regulates the balance between T helper 1 cell and regulatory T cell generation," *Science Signaling*, vol. 8, no. 396, p. ra97, 2015.
- [25] C. Bauchart-Thevret, L. Cui, G. Wu, and D. G. Burrin, "Arginine-induced stimulation of protein synthesis and survival in IPEC-J2 cells is mediated by mTOR but not nitric oxide," *Ajp Endocrinology & Metabolism*, vol. 299, no. 6, pp. E899–E909, 2010.
- [26] K. C. Linden, G. D. Wadley, A. P. Garnham, and G. K. McConnell, "Effect of l-arginine infusion on glucose disposal during exercise in humans," *Medicine and Science in Sports and Exercise*, vol. 43, no. 9, pp. 1626–1634, 2011.
- [27] B. Campi, S. Codini, G. Daniele, A. Marvelli, and A. Saba, "Plasma N-acetylaspartate: development and validation of a quantitative assay based on HPLC-MS-MS and sample derivatization," *Clinica Chimica Acta*, vol. 508, pp. 146–153, 2020.
- [28] G. Daniele, B. Campi, A. Saba, S. Codini, and E. Ferrannini, "Plasma N-Acetylaspartate is related to age, obesity, and glucose metabolism: effects of antidiabetic treatment and bariatric surgery," *Frontiers in Endocrinology*, vol. 11, 2020.
- [29] M. Gotoh, S. E. C. Davies, and T. P. Obrenovitch, "Brain tissue acidosis: effects on the extracellular concentration of N-acetylaspartate," *Journal of Neurochemistry*, vol. 69, no. 2, pp. 655–661, 2010.
- [30] Q. Feng, Y. Li, Y. Yang, and J. Feng, "Urine metabolomics analysis in patients with normoalbuminuric diabetic kidney disease," *Frontiers in Physiology*, vol. 11, p. 578799, 2020.
- [31] X. Tang, J. Liu, W. Dong et al., "The cardioprotective effects of citric acid and L-malic acid on myocardial ischemia/reperfusion injury," *Evidence-based Complementary & Alternative Medicine (eCAM)*, vol. 2013, pp. 1–11, 2013.
- [32] C. Schmidt, M. Sciacovelli, and C. Frezza, "Fumarate hydratase in cancer: a multifaceted tumour suppressor," *Seminars in Cell and Developmental Biology*, vol. 98, 2019.
- [33] Z. Cieslarova, F. S. Lopes, C. L. do Lago, M. C. França, and A. V. C. Simionato, "Capillary electrophoresis tandem mass spectrometry determination of glutamic acid and homocysteine's metabolites: Potential biomarkers of amyotrophic lateral sclerosis," *Talanta*, vol. 170, pp. 63–68, 2017.
- [34] L. M. Kruse, J. G. Buchan, C. A. Gurnett, and M. B. Dobbs, "Polygenic threshold model with sex dimorphism in adolescent idiopathic scoliosis: the Carter effect," *The Journal of Bone and Joint Surgery. American Volume*, vol. 94, no. 16, pp. 1485–1491, 2012.
- [35] M. Wiernicka, T. Kotwicki, E. Kamińska et al., "Postural stability in adolescent girls with progressive idiopathic scoliosis," *BioMed Research International*, vol. 2019, Article ID 7103546, 2019.
- [36] I. Kou, N. Otomo, K. Takeda et al., "Genome-wide association study identifies 14 previously unreported susceptibility loci for adolescent idiopathic scoliosis in Japanese," *Nature Communications*, vol. 10, no. 1, p. 3685, 2019.
- [37] S. Kawasaki, H. Shigematsu, M. Tanaka, Y. Suga, Y. Yamamoto, and Y. Tanaka, "Is brace treatment unnecessary for cases of adolescent idiopathic scoliosis above Risser sign 3?," *Journal of Orthopaedic Science*, vol. 25, no. 6, pp. 975–979, 2020.

Research Article

EZH2 Mediates miR-146a-5p/HIF-1 α to Alleviate Inflammation and Glycolysis after Acute Spinal Cord Injury

Shuangfei Ni,¹ Bo Yang,² Lei Xia,¹ and Huafeng Zhang¹ 

¹Orthopaedics, The First Affiliated Hospital of Zhengzhou University, Zhengzhou City, Henan Province, China

²Neurosurgery, The First Affiliated Hospital of Zhengzhou University, China

Correspondence should be addressed to Huafeng Zhang; fcczhanghf@zzu.edu.cn

Received 14 January 2021; Accepted 27 April 2021; Published 20 May 2021

Academic Editor: Yaoyao Xia

Copyright © 2021 Shuangfei Ni et al. This is an open access article distributed under the Creative Commons Attribution License, which permits unrestricted use, distribution, and reproduction in any medium, provided the original work is properly cited.

Acute spinal cord injury (ASCI) is a severe traumatic disease of the central nervous system, the underlying mechanism of which is unclear. This study was intended to study the role of EZH2 and miR-146a-5p/HIF-1 α in inflammation and glycolysis after ASCI, providing reference and basis for the clinical treatment and prognosis of ASCI injury. We used lipopolysaccharide (LPS) to induce inflammation of microglia, and we constructed the ASCI animal model. qRT-PCR detected the relative expression levels of EZH2, HIF-1 α , miR-146a-5p, IL-6, TNF- α , IL-17, PKM2, GLUT1, and HK2 in cells and tissues. Western blot was performed to detect the expression levels of EZH2, HIF-1 α , H3K27me3, IL-6, TNF- α , IL-17, PKM2, GLUT1, and HK2. ChIP verified the enrichment of H3K27me3 in the miR-146a-5p promoter region. Bioinformatics predicted the binding sites of HIF-1 α and miR-146a-5p, and dual-luciferase reporter assay verified the binding of HIF-1 α and miR-146a-5p. ELISA detects the levels of inflammatory factors IL-6, TNF- α , and IL-17 in the cerebrospinal fluid of rats. The GC-TOFMS was used to detect the changes of glycolytic metabolites in the cerebrospinal fluid of rats. EZH2 could mediate inflammation and glycolysis of microglia. EZH2 regulates inflammation and glycolysis through HIF-1 α . EZH2 indirectly regulated the HIF-1 α expression by mediating miR-146a-5p. EZH2 mediates miR-146a-5p/HIF-1 α to alleviate inflammation and glycolysis in ASCI rats. In the present study, our results demonstrated that EZH2 could mediate miR-146a-5p/HIF-1 α to alleviate the inflammation and glycolysis after ASCI. Therefore, EZH2/miR-146a-5p/HIF-1 α might be a novel potential target for treating ASCI.

1. Introduction

Acute spinal cord injury (ASCI) is a severe traumatic disease of the central nervous system (CNS) [1]. Spinal cord tissues respond to injury after ASCI, and the gene expression profile of cells changes, which affects the repair of injury after ASCI, and epigenetic regulation plays an important role. Enhancer of zeste homology 2 (EZH2) is located on the human chromosome 7q35. EZH2 mainly catalyzes the histone H3 lysine 27 trimethylation (H3K27me3), which mediates the change of chromatin structure, closes transcription factor binding sites, inhibits the transcription of target genes, and participates in many physiological or pathological processes [2]. Studies have shown that nerve damage dramatically increases the number of microglia expressing EZH2 [3]. Therefore, it is an effective strategy to improve the functional recovery after

ASCI by exploring the means of regulating the orderly response of cell genes, thus promoting angiogenesis.

Hypoxia inducible factor 1 (HIF-1) is a heterodimer, which is composed of HIF-1 α and HIF-1 β . The expression of HIF-1 α is regulated by cell oxygen concentration and plays a very important role in immune response [4]. HIF-1 α expression increases early after ASCI and plays a protective role in nerve recovery [5]. Hypoxia could enhance HIF-1 α expression in microglia and promote microglia migration [6]. Studies have found that under high glucose-stimulated human peritoneal mesothelial cells, EZH2 could increase the trimethylation of H3K4 on the HIF-1 α promoter and directly activate the transcription of HIF-1 α [7]. It is reported that HIF-1 is the main regulator of glycolysis [8]. Spinal cord injury (SCI) can lead to rapid muscle atrophy and oxidative-glycolytic fiber-type transformation. Acute disruption of

skeletal muscle glucose uptake 7 days after ASCI leads to decreased pyruvate and lactate levels [9]. However, there are few studies on the inflammation and glycolysis mediated by EZH2 and HIF-1 α after ASCI.

MicroRNA (miRNA), as a highly conserved short non-coding RNA, plays an important role in a lot of biological functions (tissue development, organogenesis, and metabolism) [10]. Many studies have reported that a large number of miRNAs are dysregulated after ASCI, indicating that miRNAs might be involved in the regulation of ASCI [11, 12]. As an important type of miRNA, miR-146a participates in regulating immune and inflammation processes [13]. It has been shown that miR-146a-5p can alleviate neuropathic pain in the spinal cord [14, 15]. Studies also reported that miR-146a-5p is downregulated after ASCI [16], and studies have also verified that miR-125b-5p/miR-146a-5p targeting the expression of HIF-1/SP1-dependent ROBO4 may delay the progression of diabetic retinopathy [17]. However, little research has been done on the regulatory relationship between HIF-1 α and miR-146a-5p in ASCI.

Therefore, the present study focused on the regulatory mechanisms of EZH2 and miR-146a-5p/HIF-1 α in inflammation and glycolysis after ASCI. Through the above studies, we intend to elucidate the possibility of EZH2-miR-146a-5p/HIF-1 α as a new target for treating ASCI and other inflammation-related CNS injuries, so as to provide reference and basis for the clinical treatment and prognosis of ASCI injury.

2. Material and Methods

2.1. Cell Culture and Transfection. Microglia were purchased from HonorGene (Changsha, China). Microglia were cultured in DMEM (#41500034, GIBCO, China) medium containing 10% FBS (#10099141, GIBCO, China), placed at 37°C, and cultivated in a humidity chamber with 5% CO₂. Lipopolysaccharide (LPS) induces inflammation of microglia [18], which is divided into two groups: Control group and LPS group (given with a final concentration of 1.0 μ g/mL LPS) [19, 20]. The short hairpin targeting EZH2 (sh-EZH2) and sh-NC were synthesized by Sangon Biotech (Shanghai, China) for knockdown EZH2 expression. To overexpress HIF-1 α , HIF-1 α sequences were ligated with the LV003 vector.

2.2. Establishment of the ASCI Model. Forty-eight SD rats (200-250 g) were randomly divided into a Sham group, ASCI group, ASCI+NC-EZH2 group, and ASCI+sh-EZH2 group. The latter three groups were collectively referred to as the model group, with 12 rats in each group. The method of constructing the ASCI animal model was as follows: after conventional anesthesia, rats were placed in the prone position and skin preparation, disinfection, and sheet laying were carried out. Then, a longitudinal incision was made with the spinous process of thoracic 10 as the center. The skin, subcutaneous, and muscle were cut in turn, and the vertebral plate was removed to expose the spinal cord. The modified Allen's strike method [21] was used to establish an incomplete spinal cord contusion model (the strike force was 8 g

\times 25 mm). Hemorrhage and swelling of the spinal cord tissue and spastic twitching of the lower limbs of the rats indicate that the animal model was successfully constructed. After washing the wound, we closed the incision layer by layer. Penicillin 2WU/Bid was routinely injected intramuscularly to prevent infection. After the operation, we massaged the bladder regularly to help urinate, 2-4 times a day, until the rats could urinate spontaneously. In the Sham group, the wound was closed immediately after the vertebral plate resection, and the spinal cord was not exposed to any mechanical injury. 5 min after the rat model was established, sh-EZH2 was transfected into the rat. After 72 h of the animal model, the rats were sacrificed and the blood and cerebrospinal fluid collected.

2.3. Basso-Beattie-Bresnahan (BBB) Score Assessed Hindlimb Function in Rats. The rats were all subjected to behavioral tests for the recovery of hindlimb function at 12, 24, and 48 h before injury and after treatment, with BBB score as an indicator [22]. We observed the motion of the ankle joint of the hindlimbs, landing of the sole and instep of the foot, stability of the trunk, and position of the tail.

2.4. Quantitative Real-Time PCR (qRT-PCR). qRT-PCR was used to test the relative expression levels of EZH2, HIF-1 α , miR-146a-5p, IL-6, TNF- α , IL-17, PKM2, GLUT1, and HK2 in cells and tissues. In short, total RNA was extracted by TRIzol method, and RNA was reversely transcribed into cDNAs in accordance with the instruction of a reverse transcription kit (CW2569, CWBIO, China). The relative expression of genes was tested by SYBR Green qPCR mix (Invitrogen) on an ABI 7900 system. The internal reference gene was β -actin, and the $2^{-\Delta\Delta C_t}$ method was used to calculate the relative transcription level of the target gene. The primer sequences used in this study are shown in Table 1.

2.5. Western Blot. The protein was extracted from tissues and cells with a RIPA lysis buffer (#P0013B, Beyotime Biotechnology) and mixed with a SDS-PAGE loading buffer (#MB2479, Meilunbio). The mixture was heated in boiling water at 100°C for 5 min. The membrane was blocked with 5% skim milk for 2 h at room temperature and incubated with the primary antibody EZH2 (#21800-1-AP, dilution 1:1500, Proteintech), HIF-1 α (#ab1, dilution 1:400, Abcam), H3K27me3 (#ab9050, dilution 1:1000, Abcam), IL-6 (#bs-0782R, dilution 1:1000, Bioworld), TNF- α (#ab6671, dilution 1:1000, Abcam), IL-17 (#ab79056, dilution 1:1000, Abcam), PKM2 (#15822-1-AP, dilution 1:2000, Proteintech), GLUT1 (#21829-1-AP, dilution 1:1000, Proteintech), HK2 (#ab209847, dilution 1:1500, Abcam), and β -actin (#66009-1-Ig, dilution 1:2000, Proteintech) at 4°C. Rinse three times with TBST and incubate with secondary antibodies. The protein bands were detected by the ChemiScope 6100 system (Clinux Co., Ltd., Shanghai, China); the internal reference for expression levels was β -actin.

2.6. Chromatin Immunoprecipitation (ChIP). We used a ChIP kit to verify the enrichment of H3K27me3 in the miR-146a-5p promoter region. Cells were fixed with 1% formalin for 10 minutes, and the DNA was randomly

TABLE 1: The primer sequences used in this study.

Primer ID	5'-3'
EZH2-F	TCTCACCAGCTGCAAAGTGT
EZH2-R	AGAGGAGTTGTGTTTTCCCACT
HIF-1 α -F	ACGATTGTGAAGTTAATGCTCCC
HIF-1 α -R	AACCAACAGAAACGAAACCCC
IL-6-F	TCACTATGAGGTCTACTCGG
IL-6-R	CATATTGCCAGTTCTTCGTA
TNF- α -F	CCCCTCTATTATAATTGCACCT
TNF- α -R	CTGGTAGTTTAGCTCCGTTT
IL-17-F	CGTTTCCTCTATTGTCCGCCAT
IL-17-R	TGGAAGGCAGACAATTCTAACCC
PKM2-F	GTGCCGCTGGACATTGACTC
PKM2-R	ATTCAGCCGAGCCACATTCATCC
GLUT1-F	GCTGTGGCTGGCTTCTCTAACTG
GLUT1-R	AGCAGCACCGTGAAGATGATGAAG
HK2-F	CCTGGTTTCAAAGCGGTCG
HK2-R	AGTCGGGGTCGAGTAGAGAAA
miR-146a-5p-R	GCTGTCAACGATACGCTACGTAAC
miR-146a-5p-F	AAGTTCAGTTCTTTGTGCGACGTA
5S-F	GCCTACAGCCATACCACCCGGAA
5S-R	CCTACAGCACCCGGTATCCCA
β -Actin-F	ACATCCGTAAGACCTCTATGCC
β -Actin-R	TACTCCTGCTTGCTGATCCAC

fragmented to 200-800 bp by ultrasound, and the DNA was immunoprecipitated with a specific antibody against the target protein of H3K27me3 (#ab32106, dilution 1:1000, Abcam). Then, we use 100 μ L H₂O for purification and elution of ChIP DNA, and qRT-PCR detected 2.5 μ L ChIP-DNA [7]. Different primers were used to detect the enrichment of H3K27me3 in the miR-146a-5p promoter region. Primer sequences used are shown in Table 1.

2.7. Bioinformatics Prediction and Dual-Luciferase Assay. We used starBase to predict the binding site of HIF-1 α and miR-146a-5p. To verify the binding of HIF-1 α to miR-146a-5p, wild-type (WT) or mutant (MUT) HIF-1 α fragments were constructed and inserted into a pmirGLO Vector (Promega). We use the Lipofectamine 3000 reagent (Thermo Fisher Scientific) with transfected recombinant vectors into MG. NC and miR-145-5p mimics were simultaneously introduced into the cells as specified. Then, we measured the luciferase activity [23].

2.8. ELISA. The cerebrospinal fluid of rats was tested for inflammatory factors. The inflammatory factors IL-6, TNF- α , and IL-17 were detected with a quantitative IL-6, TNF- α , and IL-17 ELISA kit according to the manufacturer's instructions. The concentration of IL-6, TNF- α , and IL-17 in cerebrospinal fluid was calculated by the American DYNATECH MR 7000 microplate reader to form a standard curve with the provided values, and the results were expressed in pg/mL.

2.9. Metabolomics Analysis. Gas Chromatography Time-of-Flight Mass Spectrometry (GC-TOFMS) was used to detect glycolytic metabolite Glucose-6-Phosphate (G6P), Fructose-6-Phosphate (F6P), SUCCINATE, and MALATE changes in the cerebrospinal fluid of rats, and they were divided into four groups: sham, ASCI, ASCI+NaCl, and ASCI+GSK126 (EZH2 inhibitor).

2.10. Statistical Analysis. The statistical analysis of the data was performed using GraphPad 8.0. Three independent experimental data were expressed as mean \pm standard deviation (SD). Differences between two or more groups were analyzed using Student's *t*-test or using one-way ANOVA. *P* < 0.05 was considered statistically significant.

3. Results

3.1. The Inflammation, Glycolysis, and HIF-1 α in Microglia Treated with LPS Were Associated with Upregulated EZH2. In order to study the inflammation, glycolysis, and relationship between HIF-1 α and EZH2 in microglia treated with LPS, qRT-PCR and Western blot were performed to detect EZH2; HIF-1 α ; inflammatory factors IL-6, TNF- α , and IL-17; and glycolysis-related gene PKM2, GLUT1, and HK2 expression levels in the Control and LPS groups. qRT-PCR and Western blot showed that compared with the Control group, EZH2 and HIF-1 α expression in the LPS group was increased (fold change \approx 2; **P* < 0.05 vs. Control group; Figures 1(a), 1(b), and 1(e)). The expression of inflammatory factors IL-6, TNF- α , and IL-17 and glycolysis-related genes PKM2, GLUT1, and HK2 also increased in the LPS group (fold change \approx 1.5 ~ 3; **P* < 0.05 vs. Control group; Figures 1(c)–1(e)), which indicated that HIF-1 α inflammation and glycolysis in microglia treated with LPS were associated with upregulated EZH2.

3.2. The Inflammation and Glycolysis in Microglia Were Mediated by EZH2. To investigate whether EZH2 is related to the inflammation and glycolysis of microglia, we knocked down EZH2 in microglia. As shown in Figures 2(a) and 2(b), qRT-PCR and Western blot results show the knockdown efficiency of EZH2 in microglia (fold change \approx 0.5; **P* < 0.05 vs. sh-NC group). Compared with the Control group and the sh-NC group, HIF-1 α ; inflammatory factors IL-6, TNF- α , and IL-17; and glycolysis-related gene PKM2, GLUT1, and HK2 expressions decreased in the sh-EZH2 group (fold change \approx 0.5; **P* < 0.05 vs. Control group; Figure 2(c)), indicating that EZH2 could mediate inflammation and glycolysis of microglia.

3.3. EZH2 Regulated Inflammation and Glycolysis through HIF-1 α . To study the relationship between EZH2 and HIF-1 α in inflammation and glycolysis, we performed interference with EZH2 and overexpression of HIF-1 in microglia. As shown in Figures 3(a) and 3(b), the results of qRT-PCR and Western blot showed the overexpression efficiency of HIF-1 α in microglia (fold change \approx 2; **P* < 0.05 vs. oe-NC group). The qRT-PCR and Western blot results showed that compared with the Control group and the oe-NC group, the expression levels of inflammatory factors IL-6, TNF- α , and

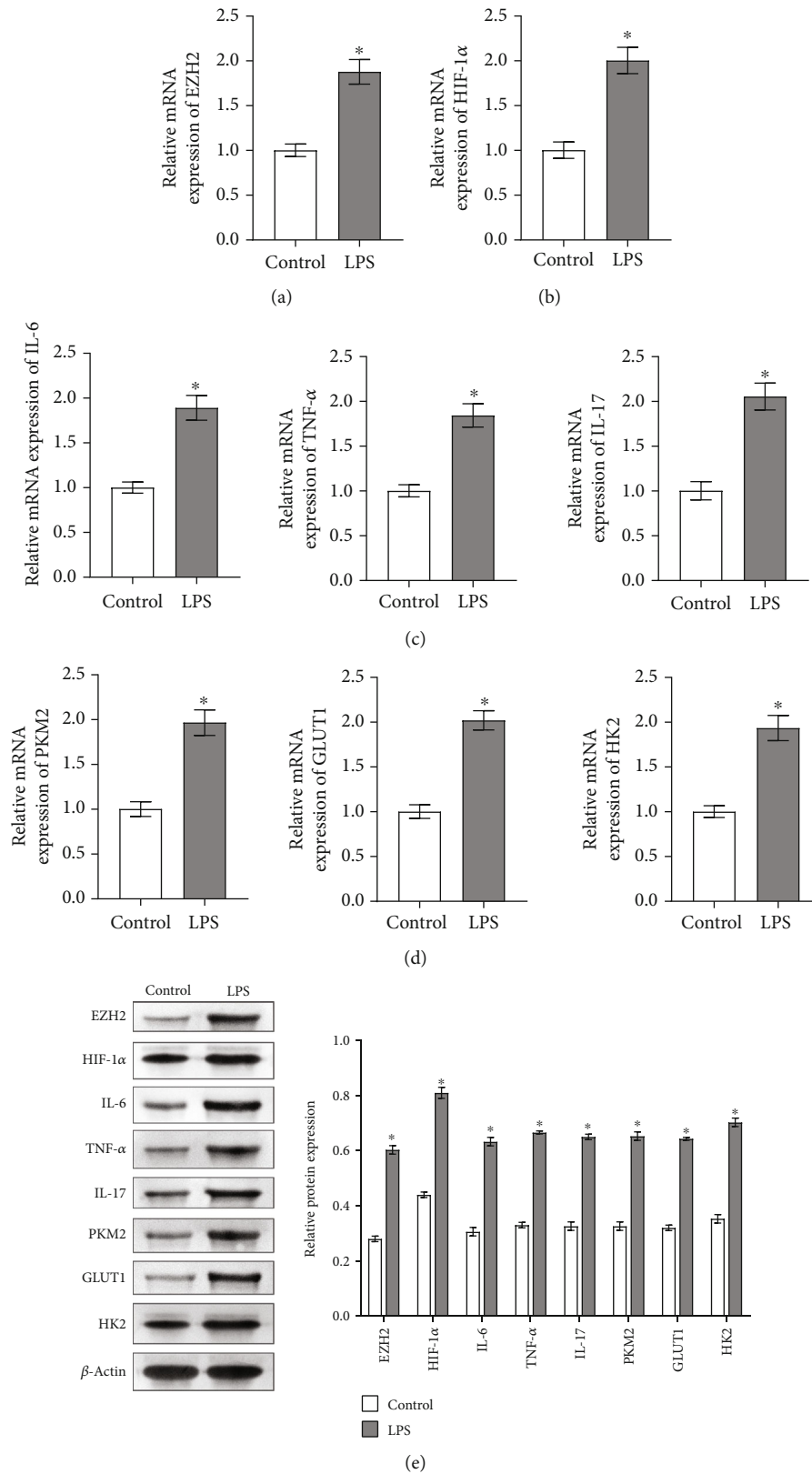


FIGURE 1: The inflammation, glycolysis, and HIF-1 α in microglia treated with LPS were associated with upregulated EZH2. In the control group and LPS group. (a) qRT-PCR detected EZH2 expression. (b) qRT-PCR was performed to detect the expression of HIF-1 α . (c) The expressions of inflammatory factors IL-6, TNF- α , and IL-17 were detected by qRT-PCR. (d) qRT-PCR detected glycolysis-related gene PKM2, GLUT1, and HK2 expressions. (e) Western blot analysis of the expression of EZH2; HIF-1 α ; inflammatory factors IL-6, TNF- α , and IL-17; and glycolysis-related genes PKM2, GLUT1, and HK2. * $P < 0.05$ vs. Control group.

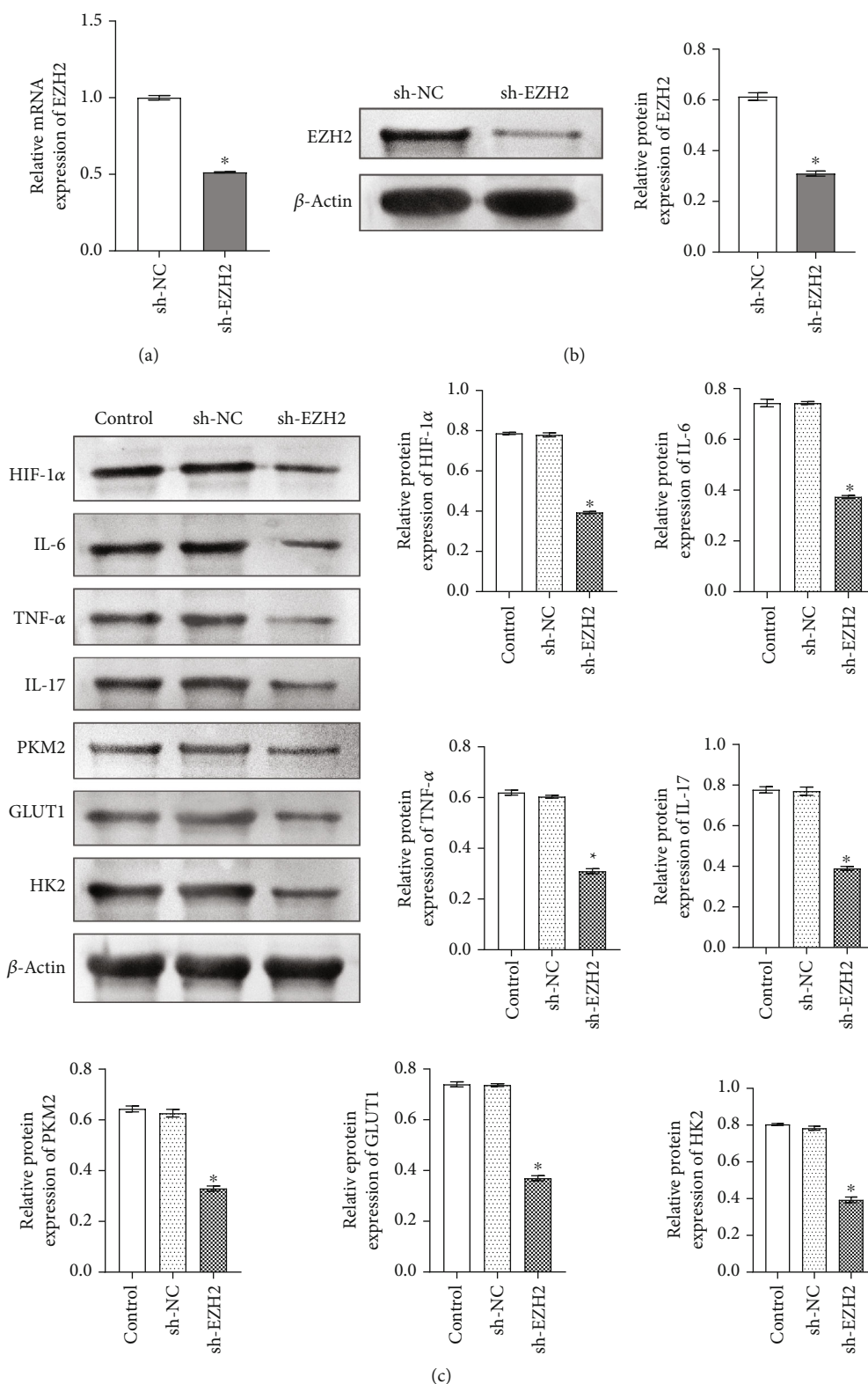


FIGURE 2: The inflammation and glycolysis in microglia were mediated by EZH2. (a, b) qRT-PCR and Western blot detected the knockdown efficiency of EZH2 in MG, respectively. * $P < 0.05$ vs. sh-NC group. (c) Western blot was performed to detect HIF-1 α ; inflammatory factors IL-6, TNF- α , and IL-17; and glycolysis-related gene PKM2, GLUT1, and HK2 expressions in the Control group, sh-NC group, and sh-EZH2 group. * $P < 0.05$ vs. Control group.

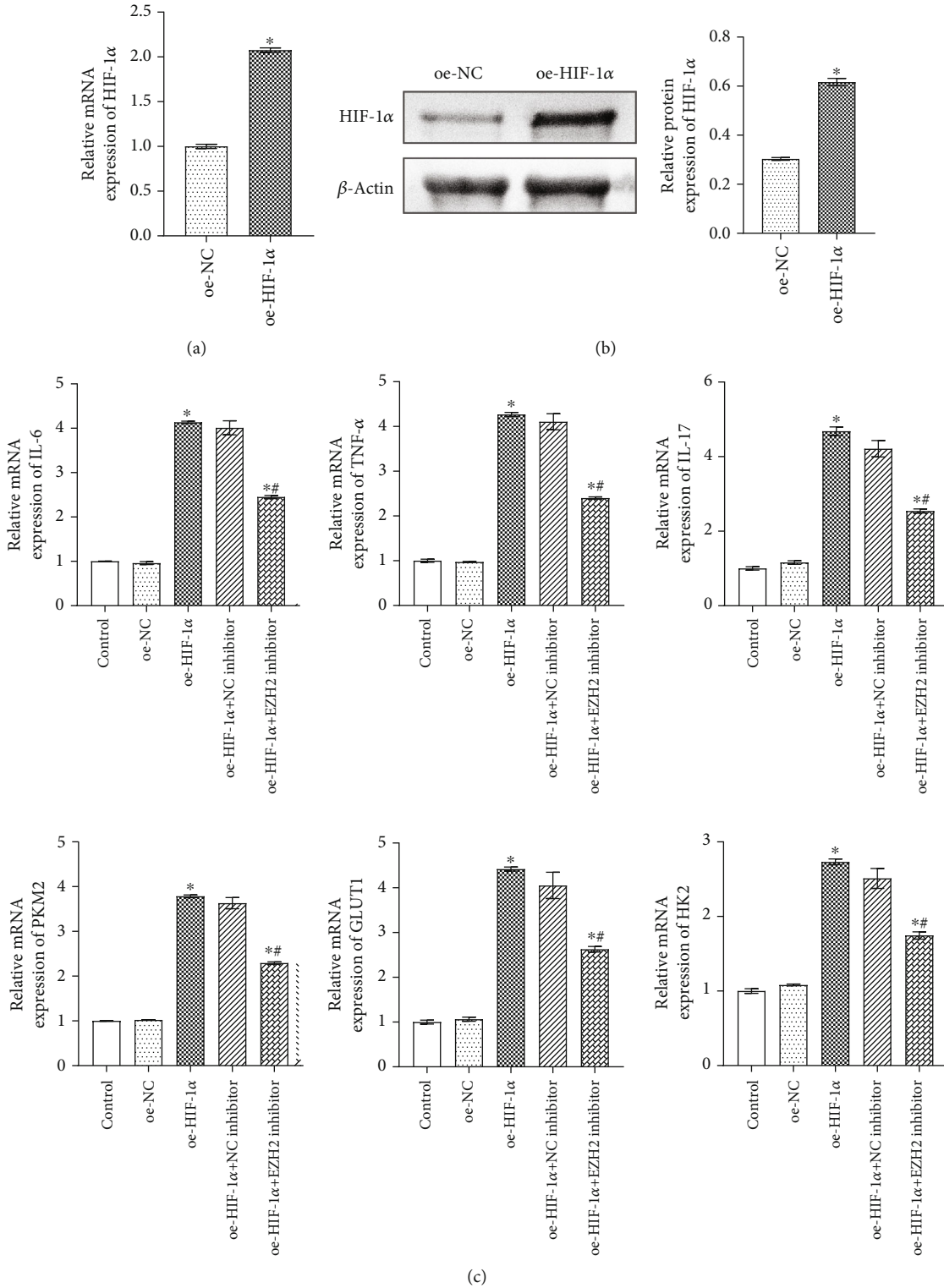


FIGURE 3: Continued.

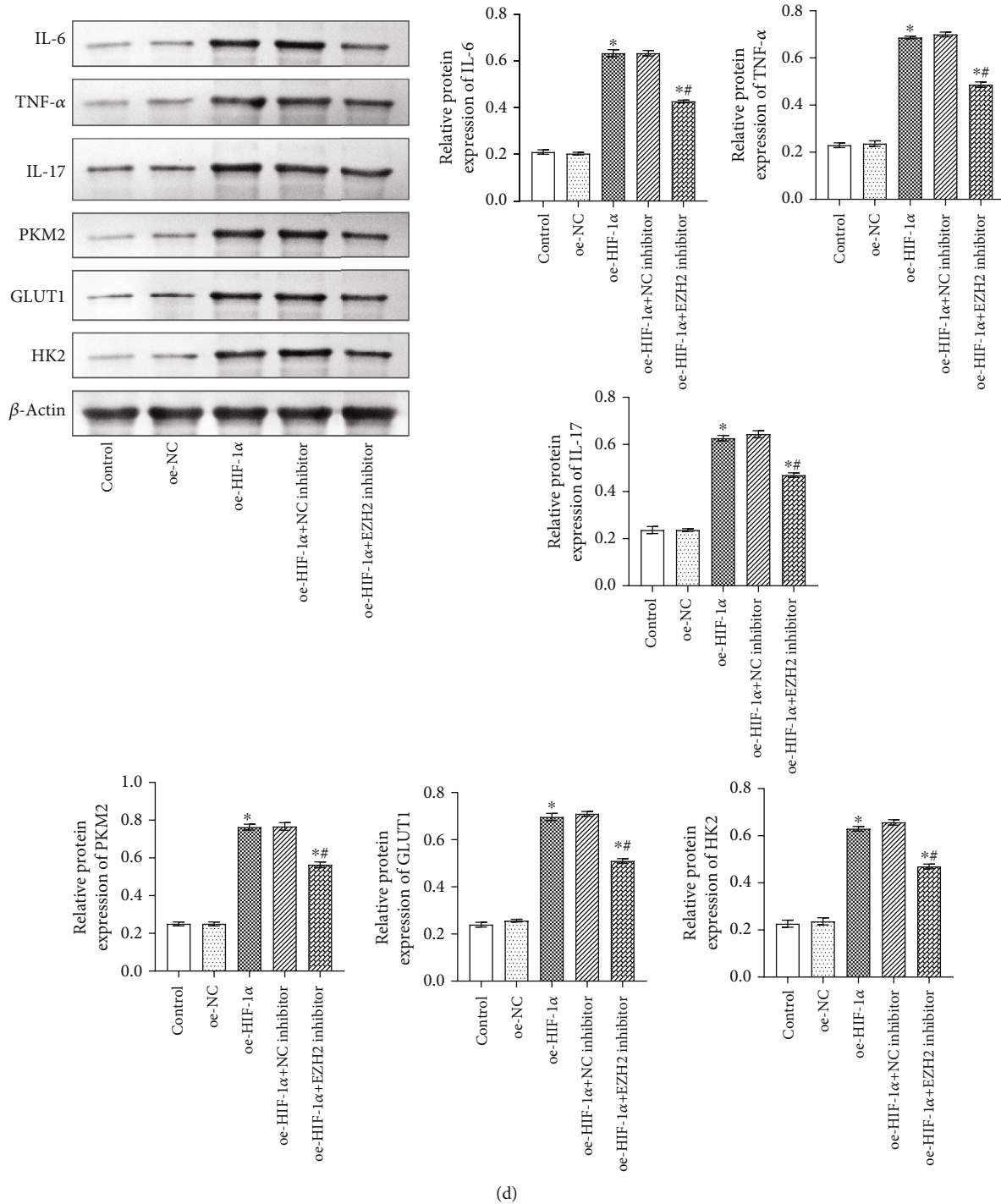


FIGURE 3: EZH2 regulated inflammation and glycolysis through HIF-1 α . (a, b) qRT-PCR and Western blot were performed to detect the overexpression of HIF-1 α in microglia, respectively. * $P < 0.05$ vs oe-NC group. (c) qRT-PCR were used to detect inflammatory factors IL-6, TNF- α , and IL-17 and glycolysis-related gene PKM2, GLUT1, and HK2 expressions. * $P < 0.05$ vs Control group; # $P < 0.05$ vs oe-HIF-1 α group. (d) Western blot detected inflammatory factors IL-6, TNF- α , and IL-17 and glycolysis-related gene PKM2, GLUT1, and HK2 expressions. * $P < 0.05$ vs. Control group; # $P < 0.05$ vs. oe-HIF-1 α group.

IL-17 and glycolysis-related genes PKM2, GLUT1, and HK2 were increased in the oe-HIF-1 α group, while decreased in the oe-HIF-1 α +EZH2 inhibitor group (fold change $\approx 1.5 \sim 4.5$; * $P < 0.05$ vs. Control group; # $P < 0.05$ vs. oe-HIF-1 α group; Figures 3(c) and 3(d)). These results indicate that EZH2 regulated inflammation and glycolysis through HIF-1 α .

3.4. EZH2 Indirectly Regulated the HIF-1 α Expression by Mediating miR-146a-5p. To explore the relationship between H3K27me3 and miR-146a-5p, we first performed Western blot and qRT-PCR verification in microglia treated by LPS. The Western blot results showed that H3K27me3 was upregulated in the LPS group compared with the Control group

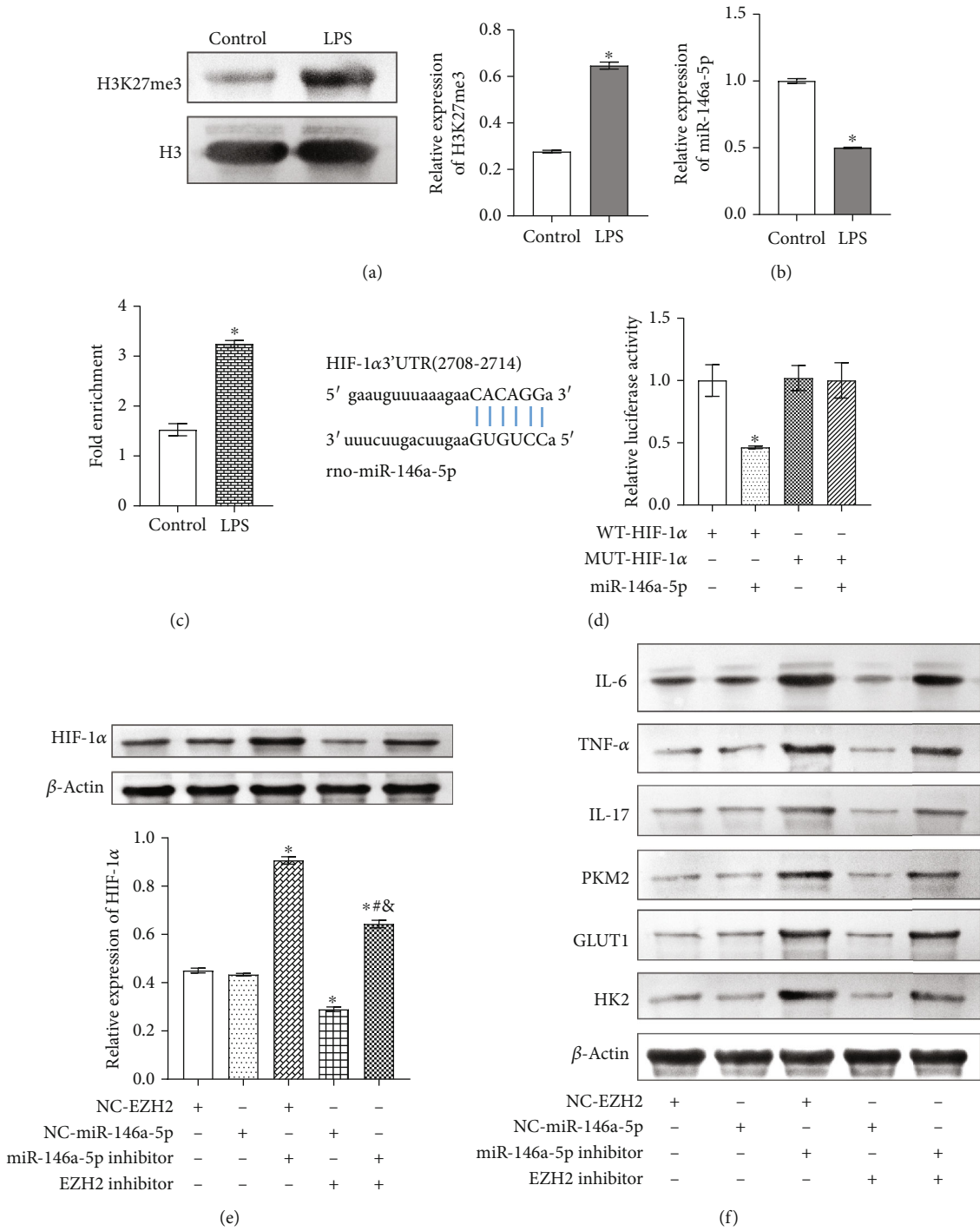


FIGURE 4: Continued.

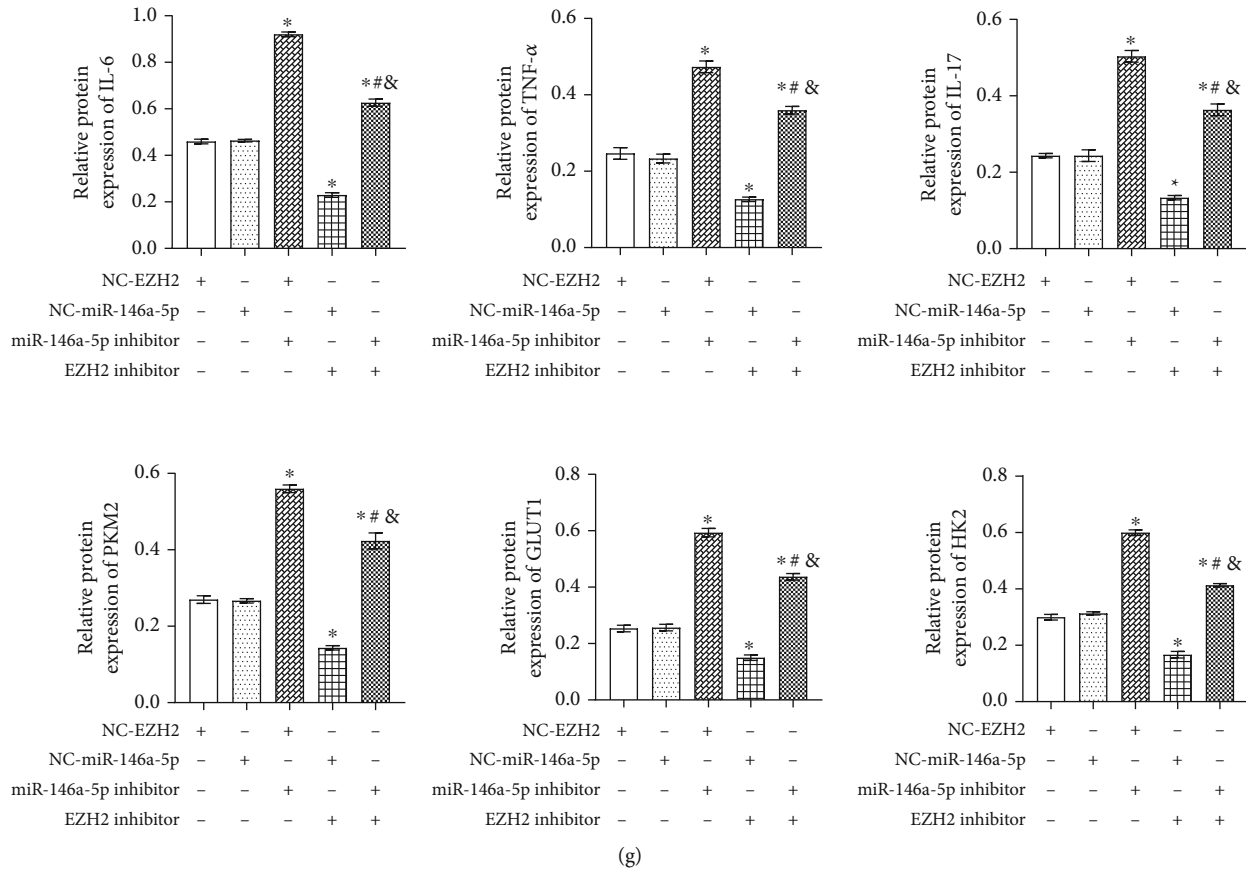


FIGURE 4: EZH2 indirectly regulated the HIF-1 α expression by mediating miR-146a-5p. (a) Western blot detected the expression of H3K27me3 in the Control group and LPS group. $*P < 0.05$ vs. Control group. (b) qRT-PCR detected miR-146a-5p expression in the Control group and LPS group. $*P < 0.05$ vs. Control group. (c) ChIP was used to analyze the enrichment of H3K27me3 in the miR-146a-5p promoter region. $*P < 0.05$ vs. Control group. (d) starBase predicted the binding sites of HIF-1 α and miR-146a-5p, and dual-luciferase report assay verified the binding of HIF-1 α and miR-146a-5p. $*P < 0.05$ vs. WT-HIF-1 α group. (e) Western blot detected the expression of HIF-1 α in the NC-EZH2 group, NC-miR-146a-5p group, miR-146a-5p inhibitor group, EZH2 inhibitor+NC-miR-146a-5p group, and EZH2 inhibitor+miR-146a-5p inhibitor group. $*P < 0.05$ vs. NC-EZH2 group; $*P < 0.05$ vs. NC-EZH2+miR-146a-5p inhibitor group; $^{\&}P < 0.05$ vs. NC-miR-146a-5p+EZH2 inhibitor. (f) Western blot detected inflammatory factors IL-6, TNF- α , and IL-17 and glycolysis-related gene PKM2, GLUT1, and HK2 expressions. (g) Inflammatory factors IL-6, TNF- α , and IL-17 and glycolysis-related gene PKM2, GLUT1, and HK2 expressions. $*P < 0.05$ vs. NC-EZH2 group; $*P < 0.05$ vs. NC-EZH2+miR-146a-5p inhibitor group; $^{\&}P < 0.05$ vs. NC-miR-146a-5p+EZH2 inhibitor.

(fold change ≈ 3 ; $*P < 0.05$ vs Control group; Figure 4(a)). qRT-PCR results suggested that miR-146a-5p was downregulated in the LPS group compared with the Control group (fold change ≈ 0.5 ; $*P < 0.05$ vs Control group; Figure 4(b)). Subsequently, ChIP verified the enrichment of H3K27me3 in the miR-146a-5p promoter region, and the results showed that H3K27me3 occurred in miR-146a-5p (fold change ≈ 2 ; $*P < 0.05$ vs Control group; Figure 4(c)). To investigate the targeting relationship between miR-146a-5p and HIF-1 α , starBase confirmed the binding sites of miR-146a-5p and HIF-1 α . Dual-luciferase report assay showed that the luciferase activity of WT HIF-1 α was significantly decreased after transfection of miR-145-5p mimics (fold change ≈ 0.5 ; $*P < 0.05$ vs WT-HIF-1 α group; Figure 4(d)). These results suggested that miR-146a-5p binds to HIF-1 α .

Furthermore, we used EZH2 and miR-146a-5p inhibitors to study whether EZH2 could regulate HIF-1 α expression through miR-146a-5p. As shown in Figures 4(e)–4(g), com-

pared with the NC-EZH2 group and the NC-miR-146a-5p group, HIF-1; inflammatory factors IL-6, TNF- α , and IL-17; and glycolysis-related gene PKM2, GLUT1, and HK2 expressions were upregulated in the miR-146a-5p inhibitor group and EZH2 inhibitor+miR-146a-5p inhibitor group, but downregulated in the EZH2 inhibitor+NC-miR-146a-5p group (fold change $\approx 0.5 \sim 2.5$; $*P < 0.05$ vs. NC-EZH2 group; $^{\#}P < 0.05$ vs. NC-EZH2+miR-146a-5p inhibitor group; $^{\&}P < 0.05$ vs. NC-miR-146a-5p+EZH2 inhibitor), which confirmed that EZH2 indirectly regulated the HIF-1 α expression by mediating miR-146a-5p.

3.5. EZH2 Mediates miR-146a-5p/HIF-1 α to Alleviate Inflammation and Glycolysis in ASCI Rats. We have demonstrated that EZH2 indirectly regulated the HIF-1 α expression by mediating miR-146a-5p at the cellular level. To study the relationship between EZH2 and miR-146a-5p/HIF-1 α in vivo, we constructed the ASCI animal model. The qRT-

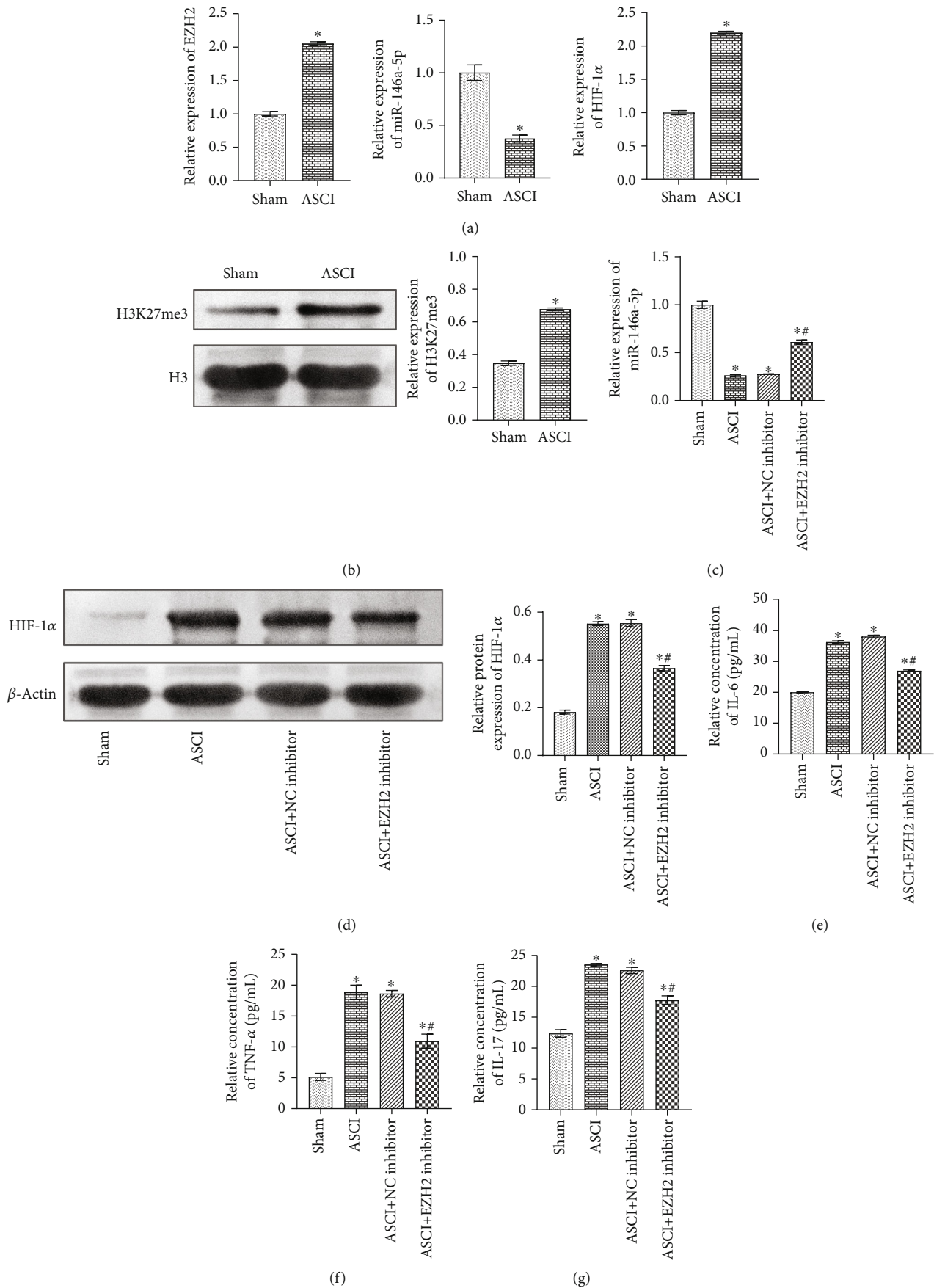


FIGURE 5: Continued.

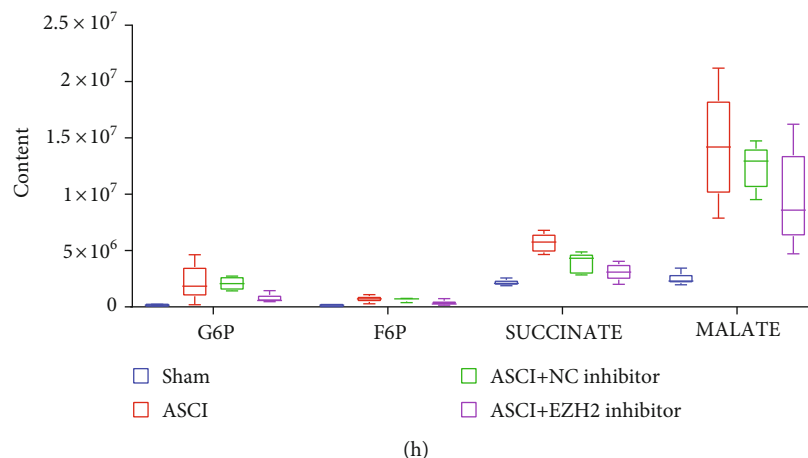


FIGURE 5: EZH2 mediates miR-146a-5p/HIF-1 α to alleviate inflammation and glycolysis in ASCI rats. (a) qRT-PCR detected EZH2, miR-146a-5p, and HIF-1 α expressions in the Sham group and ASCI group. (b) Western blot detected the expression of H3K27me3 in the Sham group and ASCI group. (c) qRT-PCR was performed to detect miR-146a-5p expression. (d) Western blot detected the expression of HIF-1 α . (e–g) ELISA was performed to detect inflammatory factor IL-6, TNF- α , and IL-17 levels in the cerebrospinal fluid of rats. (h) Metabolomics detected the relative levels of glycolytic metabolites G6P, F6P, SUCCINATE, and MALATE. * $P < 0.05$ vs. Sham group; # $P < 0.05$ vs. ASCI group.

PCR results indicated that, compared with the Sham group, EZH2 and HIF-1 α expression levels in the ASCI group were increased, while the expression levels of miR-146a-5p were decreased (fold change $\approx 0.3 \sim 2.5$; * $P < 0.05$ vs Sham group; Figure 5(a)). Western blot results showed that compared with the Sham group, H3K27me3 expression was upregulated in the ASCI group (fold change ≈ 2 ; * $P < 0.05$ vs. Sham group; Figure 5(b)).

Subsequently, we investigated the regulatory effects of EZH2 and miR-146a-5p/HIF-1 α on inflammation and glycolysis in the Sham group, ASCI group, ASCI+NC inhibitor group, and ASCI+EZH2 inhibitor group. The qRT-PCR results showed that miR-146a-5p expression in the ASCI group was decreased compared with that in the Sham group. Compared with the ASCI group and the ASCI+NC inhibitor group, miR-146a-5p expression in the ASCI+EZH2 inhibitor group was increased, which indicated that downregulation of EZH2 promoted the expression of miR-146a-5p in ASCI rats (fold change $\approx 0.3 \sim 0.7$; * $P < 0.05$ vs. Sham group; # $P < 0.05$ vs. ASCI group; Figure 5(c)). The Western blot results showed that compared with the Sham group, HIF-1 α expression was increased in the ASCI group. Compared with the ASCI group and the ASCI+NC inhibitor group, HIF-1 α expression in the ASCI+EZH2 inhibitor group was decreased, which showed that downregulation of EZH2 inhibits HIF-1 α expression in ASCI rats (fold change $\approx 0.5 \sim 3$; * $P < 0.05$ vs. Sham group; # $P < 0.05$ vs. ASCI group; Figure 5(d)).

ELISA detected the levels of IL-6, TNF- α , and IL-17 in the cerebrospinal fluid of rats in each group. It was observed that EZH2 could inhibit the levels of IL-6, TNF- α , and IL-17 in the ASCI group (fold change $\approx 0.5 \sim 4$; * $P < 0.05$ vs. Sham group; # $P < 0.05$ vs. ASCI group; Figures 5(e)–5(g)). As shown in Figure 5(h), metabolomics results indicated that adding EZH2 inhibitor GSK126 inhibits the relative levels of glycolytic metabolites G6P, F6P, SUCCINATE, and

MALATE in the ASCI group. Supplementary Figure 1 shows the relationship diagram where EZH2 mediates miR-146a-5p/HIF-1 α to alleviate inflammation and glycolysis. The above results suggest that EZH2 mediates miR-146a-5p/HIF-1 α to relieve inflammation and glycolysis in ASCI.

4. Discussion

ASCI has a high rate of disability and mortality. For ASCI patients with incomplete spinal cord injury, early reasonable diagnosis and treatment measures can promote nerve recovery to a certain extent and improve the prognosis of patients [24]. Studies have shown that immune inflammation and glycolysis play an important role in the progression of ASCI [25, 26]. But the specific mechanism has not been explored clearly. In the present study, we studied the relationship between inflammation, glycolysis, HIF-1 α , and EZH2 in microglia treated with LPS and in the ASCI animal model. The results showed that EZH2 mediates miR-146a-5p/HIF-1 α to alleviate inflammation and glycolysis.

In the early stage of SCI, the cytokines mediating inflammation at the site of injury could secrete related inflammatory factors. These inflammatory factors then accumulate and invade the SCI injury site, eventually leading to a secondary inflammation that aggravates the occurrence of injury, including TNF- α and IL-6 [27]. TNF- α is an important inflammatory mediator and pathogenic factor, which can promote cells and tissues in the CNS to produce other inflammatory mediators together with leukocytes and participate in the inflammatory response [28]. In the early stage of SCI, the increase of IL-6 can cause inflammation and edema in the injured area, aggravate the infiltration of inflammatory cells, and inhibit the recovery of nerve function [29, 30]. Studies have shown that IL-17 can stimulate astrocytes to release chemokines, causing the infiltration of peripheral neutrophils into the CNS and aggravating the inflammatory

response [31]. We found that knockdown of EZH2 could effectively inhibit the synthesis and release of TNF- α , IL-6, and IL-17.

The main function of EZH2 is to methylate H3K27me3 by transferring the methyl from the cofactor S-adenosine L-methionine (SAM), but H3K27me3 is associated with gene transcription inhibition, so EZH2 cannot directly act on HIF-1 α through H3K27me3. We hypothesized that EZH2 may indirectly regulate HIF-1 α expression by mediating the methylation of miRNA upstream of HIF-1 α . It was found that after interference with EZH2 and overexpression of HIF-1 α , the release of inflammatory factors TNF- α , IL-6, and IL-17 is reduced, thus alleviating the damage of inflammatory response caused by ASCI, which indicates that EZH2 can regulate the inflammation through HIF-1 α . Studies have suggested that miR-146a-5p is downregulated after the occurrence of ASCI [16], and studies have also verified that miR-146a-5p has a targeting relationship with HIF-1 α [17]. We confirmed that EZH2 could indirectly regulate HIF-1 α expression by mediating miR-146a-5p after addition of EZH2 and miR-146a-5p inhibitors.

Increased glycolysis has also been found in a variety of neurological diseases, such as cerebral ischemia, neurodegenerative diseases, traumatic brain injury, and SCI [26, 32–34]. Previous studies have shown that increased glycolysis may provide a potential source of energy for the CNS, which can rescue nerve cells [35]. HIF-1 is a key factor in glycolysis, which stimulates the expression of glycolysis transporters and enzymes supporting high glycolysis rates [34]. The effective self-activation of HIF-1 is achieved via its interaction with glycolytic pathways [8]. Under hypoxia, HIF-1, which is stable in cancer cells, promotes glycolytic activity through upregulating GLUT1 and PKM2 expression [36]. The upregulation of PKM2 in turn promotes the transactivation of HIF-1, and the glycolysis product lactic acid further stabilizes HIF-1, therefore forming a self-enhancing feedback loop for HIF-1 activity [34]. PKM2 has been reported to be a key determinant of LPS activating macrophages and promoting inflammatory responses [37]. Inhibition of HIF-1 promotes apoptosis through HK2-dependent mechanisms and reduces systemic vascular remodeling disease [38]. Previous studies have found that EZH2 could promote tumorigenesis and malignant progression via activating glycolysis of EAF2-HIF-1 α signaling transduction [39]. We found that after interference with EZH2 and overexpression of HIF-1 α , glycolysis-related gene PKM2, GLUT1, and HK2 expressions decreased, indicating that EZH2 could regulate glycolysis through HIF-1 α . In the ASCI animal model, we also found that EZH2 regulates glycolysis by mediating miR-146a-5p/HIF-1 α . In summary, we found that EZH2 mediates miR-146a-5p/HIF-1 α to alleviate the inflammation and glycolysis after ASCI. However, this study is only a preliminary study. Although our research can illustrate the purpose of the study, our Western blot experimental results also have some imperfections. For example, the double banding of H3 and IL-6 in Figure 4 may be caused by the high concentration of the primary or secondary antibody, the nonspecific reaction of the polyclonal anti-

body itself, the weak specificity of the antibody, or the long compression time of the membrane. In addition, further experiments will be conducted in the future to study the role of epigenetic regulation in ASCI.

5. Conclusion

Our research results demonstrated that EZH2 mediates miR-146a-5p/HIF-1 α to alleviate the inflammation and glycolysis after ASCI. Our study provides reference and basis for the clinical treatment and prognosis of ASCI in the future and provides a new target for the treatment of ASCI.

Abbreviations

ASCI:	Acute spinal cord injury
LPS:	Lipopolysaccharide
qRT-PCR:	Quantitative real-time PCR
CNS:	Central nervous system
EZH2:	Enhancer of zeste homology 2
PRC2:	Polycomb repressive complex 2
H3K27me3:	Histone H3 lysine 27 trimethylation
HIF-1:	Hypoxia inducible factor 1
SCI:	Spinal cord injury
miRNA:	MicroRNA
BBB:	Basso-Beattie-Bresnahan
ChIP:	Chromatin immunoprecipitation
WT:	Wild type
MUT:	Mutant
GC-TOFMS:	Gas chromatography time-of-flight mass spectrometry
G6P:	Glucose-6-phosphate
F6P:	Fructose-6-phosphate
SD:	Standard deviation
SAM:	S-Adenosine L-methionine.

Data Availability

All data and figures used to support the findings of this study are included within the article.

Conflicts of Interest

The authors declare that they have no conflicts of interest with the contents of this article.

Acknowledgments

The authors should thank the First Affiliated Hospital of Zhengzhou University for their technical support. This work was supported by the National Natural Science Foundation of China (Grant Nos. 82002353, 81902215, and U2004113), China Postdoctoral Science Foundation (Grant No. 2020M682360), and He'nan Postdoctoral Scientific Research Foundation (Grant No. 252419).

Supplementary Materials

Supplementary Figure 1: the relationship diagram about EZH2 mediates miR-146a-5p/HIF-1 α to alleviate inflammation and glycolysis. (*Supplementary Materials*)

References

- [1] Z. M. Gong, Z. Y. Tang, and X. L. Sun, "miR-411 suppresses acute spinal cord injury via downregulation of Fas ligand in rats," *Biochemical and Biophysical Research Communications*, vol. 501, no. 2, pp. 501–506, 2018.
- [2] X. Wang, Y. Wang, L. Li et al., "A lncRNA coordinates with Ezh2 to inhibit HIF-1 α transcription and suppress cancer cell adaptation to hypoxia," *Oncogene*, vol. 39, no. 9, pp. 1860–1874, 2020.
- [3] R. Yadav and H. R. Weng, "EZH2 regulates spinal neuroinflammation in rats with neuropathic pain," *Neuroscience*, vol. 349, pp. 106–117, 2017.
- [4] M. Yee Koh, "HIF-1 regulation: not so easy come, easy go," *Trends in Biochemical Sciences*, vol. 33, no. 11, pp. 526–534, 2008.
- [5] Y. Li, W. Han, Y. Wu et al., "Stabilization of hypoxia inducible factor-1 α by dimethylxalylglycine promotes recovery from acute spinal cord injury by inhibiting neural apoptosis and enhancing axon regeneration," *Journal of Neurotrauma*, vol. 36, no. 24, pp. 3394–3409, 2019.
- [6] X. Wang, C. Li, Y. Chen et al., "Hypoxia enhances CXCR4 expression favoring microglia migration via HIF-1 α activation," *Biochemical and Biophysical Research Communications*, vol. 371, no. 2, pp. 283–288, 2008.
- [7] Q. Wang, L. Xu, X. Zhang, D. Liu, and R. Wang, "GSK343, an inhibitor of EZH2, mitigates fibrosis and inflammation mediated by HIF-1 α in human peritoneal mesothelial cells treated with high glucose," *European Journal of Pharmacology*, vol. 880, p. 173076, 2020.
- [8] D. Jia, M. Lu, K. H. Jung et al., "Elucidating cancer metabolic plasticity by coupling gene regulation with metabolic pathways," *Proceedings of the National Academy of Sciences of the United States of America*, vol. 116, no. 9, pp. 3909–3918, 2019.
- [9] Z. A. Graham, J. A. Siedlik, L. Harlow et al., "Key glycolytic metabolites in paralyzed skeletal muscle are altered seven days after spinal cord injury in mice," *Journal of Neurotrauma*, vol. 36, no. 18, pp. 2722–2731, 2019.
- [10] X. Yu, H. Zheng, M. T. Chan, and W. K. K. Wu, "MicroRNAs: new players in cataract," *American Journal of Translational Research*, vol. 9, no. 9, pp. 3896–3903, 2017.
- [11] N. K. Liu, X. F. Wang, Q. B. Lu, and X. M. Xu, "Altered microRNA expression following traumatic spinal cord injury," *Experimental Neurology*, vol. 219, no. 2, pp. 424–429, 2009.
- [12] J. Li, J. Huang, L. Dai et al., "miR-146a, an IL-1 β responsive miRNA, induces vascular endothelial growth factor and chondrocyte apoptosis by targeting Smad4," *Arthritis Research & Therapy*, vol. 14, no. 2, p. R75, 2012.
- [13] H. Kong, F. Yin, F. He et al., "The effect of miR-132, miR-146a, and miR-155 on MRP8/TLR4-induced astrocyte-related inflammation," *Journal of Molecular Neuroscience*, vol. 57, no. 1, pp. 28–37, 2015.
- [14] Y. Lu, D. L. Cao, B. C. Jiang, T. Yang, and Y. J. Gao, "MicroRNA-146a-5p attenuates neuropathic pain via suppressing TRAF6 signaling in the spinal cord," *Brain, Behavior, and Immunity*, vol. 49, pp. 119–129, 2015.
- [15] X. Li, J. S. Kroin, R. Kc et al., "Altered spinal microRNA-146a and the microRNA-183 cluster contribute to osteoarthritic pain in knee joints," *Journal of Bone and Mineral Research*, vol. 28, no. 12, pp. 2512–2522, 2013.
- [16] Y. He, B. Lv, Y. Huan et al., "Zhenbao pill protects against acute spinal cord injury via miR-146a-5p regulating the expression of GPR17," *Bioscience Reports*, vol. 38, no. 1, 2018.
- [17] Q. Gong, J. Xie, Y. Li, Y. Liu, and G. Su, "Enhanced ROBO4 is mediated by up-regulation of HIF-1 α /SP1 or reduction in miR-125b-5p/miR-146a-5p in diabetic retinopathy," *Journal of Cellular and Molecular Medicine*, vol. 23, no. 7, pp. 4723–4737, 2019.
- [18] M. Zhang, L. Wang, S. Huang, and X. He, "MicroRNA-223 targets NLRP3 to relieve inflammation and alleviate spinal cord injury," *Life Sciences*, vol. 254, p. 117796, 2020.
- [19] M. Erschbamer, K. Pernold, and L. Olson, "Inhibiting epidermal growth factor receptor improves structural, locomotor, sensory, and bladder recovery from experimental spinal cord injury," *The Journal of Neuroscience*, vol. 27, no. 24, pp. 6428–6435, 2007.
- [20] Y. Cao, G. Li, Y. F. Wang et al., "Neuroprotective effect of baicalin on compression spinal cord injury in rats," *Brain Research*, vol. 1357, pp. 115–123, 2010.
- [21] A. R. Allen, "Surgery of experimental lesion of spinal cord equivalent to crush injury of fracture dislocation of spinal COLUMN," *Journal of the American Medical Association*, vol. LVII, no. 11, pp. 878–880, 1911.
- [22] D. M. Basso, M. S. Beattie, and J. C. Bresnahan, "A sensitive and reliable locomotor rating scale for open field testing in rats," *Journal of Neurotrauma*, vol. 12, no. 1, pp. 1–21, 1995.
- [23] S. Li, M. Zeng, L. Yang et al., "Hsa_circ_0008934 promotes the proliferation and migration of osteosarcoma cells by targeting miR-145-5p to enhance E2F3 expression," *The International Journal of Biochemistry & Cell Biology*, vol. 127, article 105826, 2020.
- [24] K. A. Lyon and J. H. Huang, "An improved way to predict neurologic recovery in acute spinal cord injury," *Neurology*, vol. 89, no. 16, pp. 1654–1655, 2017.
- [25] Y. H. Wang, J. Chen, J. Zhou, F. Nong, J. H. Lv, and J. Liu, "Reduced inflammatory cell recruitment and tissue damage in spinal cord injury by acellular spinal cord scaffold seeded with mesenchymal stem cells," *Experimental and Therapeutic Medicine*, vol. 13, no. 1, pp. 203–207, 2017.
- [26] H. Murai, C. Itoh, N. Wagai, T. Nakamura, A. Yamaura, and H. Makino, "Local spinal cord glucose utilization and extracellular potassium activity changes after spinal cord injury in rats," *Nō to Shinkei*, vol. 43, no. 4, pp. 337–342, 1991.
- [27] Y. L. Lee, K. Shih, P. Bao, R. S. Ghirnikar, and L. F. Eng, "Cytokine chemokine expression in contused rat spinal cord," *Neurochemistry International*, vol. 36, no. 4–5, pp. 417–425, 2000.
- [28] C. Ferrarese, P. Mascarucci, C. Zoia et al., "Increased cytokine release from peripheral blood cells after acute stroke," *Journal of Cerebral Blood Flow and Metabolism*, vol. 19, no. 9, pp. 1004–1009, 1999.
- [29] K. Yamauchi, K. Osuka, M. Takayasu et al., "Activation of JAK/STAT signalling in neurons following spinal cord injury in mice," *Journal of Neurochemistry*, vol. 96, no. 4, pp. 1060–1070, 2006.
- [30] A. T. Stammers, J. Liu, and B. K. Kwon, "Expression of inflammatory cytokines following acute spinal cord injury in a rodent

- model,” *Journal of Neuroence Research*, vol. 90, no. 4, pp. 782–790, 2012.
- [31] J. M. Rodgers, L. Zhou, and S. D. Miller, “Act1, scene brain: astrocytes play a lead role,” *Immunity*, vol. 32, no. 3, pp. 302–304, 2010.
- [32] Y. Lv, B. Zhang, C. Zhai et al., “PFKFB3-mediated glycolysis is involved in reactive astrocyte proliferation after oxygen-glucose deprivation/reperfusion and is regulated by Cdh1,” *Neurochemistry International*, vol. 91, pp. 26–33, 2015.
- [33] W. Fu, D. Shi, D. Westaway, and J. H. Jhamandas, “Bioenergetic mechanisms in astrocytes may contribute to amyloid plaque deposition and toxicity,” *The Journal of Biological Chemistry*, vol. 290, no. 20, pp. 12504–12513, 2015.
- [34] C. J. de Saedeleer, T. Copetti, P. E. Porporato, J. Verrax, O. Feron, and P. Sonveaux, “Lactate activates HIF-1 in oxidative but not in Warburg-phenotype human tumor cells,” *PLoS One*, vol. 7, no. 10, article e46571, 2012.
- [35] K. L. Carpenter, I. Jalloh, and P. J. Hutchinson, “Glycolysis and the significance of lactate in traumatic brain injury,” *Frontiers in Neuroscience*, vol. 9, p. 112, 2015.
- [36] W. Luo, H. Hu, R. Chang et al., “Pyruvate kinase M2 is a PHD3-stimulated coactivator for hypoxia-inducible factor 1,” *Cell*, vol. 145, no. 5, pp. 732–744, 2011.
- [37] E. M. Palsson-McDermott, A. M. Curtis, G. Goel et al., “Pyruvate kinase M2 regulates Hif-1 α activity and IL-1 β induction and is a critical determinant of the Warburg effect in LPS-activated macrophages,” *Cell Metabolism*, vol. 21, no. 1, pp. 65–80, 2015.
- [38] C. M. Lambert, M. Roy, G. A. Robitaille, D. E. Richard, and S. Bonnet, “HIF-1 inhibition decreases systemic vascular remodelling diseases by promoting apoptosis through a hexokinase 2-dependent mechanism,” *Cardiovascular Research*, vol. 88, no. 1, pp. 196–204, 2010.
- [39] B. Pang, X. R. Zheng, J. X. Tian et al., “EZH2 promotes metabolic reprogramming in glioblastomas through epigenetic repression of EAF2-HIF1 α signaling,” *Oncotarget*, vol. 7, no. 29, pp. 45134–45143, 2016.

Research Article

An Aptamer-Based Antagonist against the Receptor for Advanced Glycation End-Products (RAGE) Blocks Development of Colorectal Cancer

Jihui Zheng ¹, Wenjing Zhu ¹, Fang He ¹, Zhu Li ², Na Cai ² and Hong-Hui Wang ¹

¹College of Biology, Hunan University, Changsha, China

²CellWay Bio, Changsha, China

Correspondence should be addressed to Na Cai; cainaya@hotmail.com and Hong-Hui Wang; wanghonghui@hnu.edu.cn

Received 3 March 2021; Accepted 23 April 2021; Published 5 May 2021

Academic Editor: Shuai Chen

Copyright © 2021 Jihui Zheng et al. This is an open access article distributed under the Creative Commons Attribution License, which permits unrestricted use, distribution, and reproduction in any medium, provided the original work is properly cited.

Tumor angiogenesis plays a crucial role in colorectal cancer development. Dysregulation of the receptor for the advanced glycation end-products (RAGE) transmembrane signaling mediates inflammation, resulting in various cancers. However, the mechanism of the RAGE signaling pathway in modulating development of colorectal cancer has not been explored. In this study, an aptamer-based RAGE antagonist (Apt-RAGE) was used to inhibit interaction between RAGE and S100B, thus blocking downstream NF κ B-mediated signal transduction. *In vitro* results showed that Apt-RAGE effectively inhibited S100B-dependent and S100B-independent RAGE/NF κ B activation in colorectal HCT116 cancer cells, thus decreasing proliferation and migration of cells. Notably, expression and secretion of VEGF-A were inhibited, implying that Apt-RAGE can be used as an antiangiogenesis agent in tumor therapy. Moreover, Apt-RAGE inhibited tumor growth and microvasculature formation in colorectal tumor-bearing mice. Inhibition of angiogenesis by Apt-RAGE was positively correlated with suppression of the RAGE/NF κ B/VEGF-A signaling. The findings of this study show that Apt-RAGE antagonist is a potential therapeutic agent for treatment of colorectal cancer.

1. Introduction

Colorectal cancer is a multifactorial disease that affects over four million people worldwide [1]. Previous studies report that the development of colorectal cancer is highly correlated with tumor angiogenesis [2] which is implicated in the pathological process of many critical diseases [3]. Inhibition of angiogenesis is associated with alleviation of cancer progression and metastasis [4, 5]. New blood vessels formed during angiogenesis may contribute to inflammation-associated carcinogenesis, inducing tumor progression and tumor metastasis [6, 7]. Unregulated release of different inflammatory mediators in the tumor microenvironment (TME) activates growth, proliferation, and migration of colorectal cancer cells [8]. In addition, inflammation mediators in TME induce abnormal angiogenesis by increasing secretion of vascular endothelial growth factor (VEGF). Moreover, the receptor for advanced glycation end-products (RAGE)

is positively correlated with increased vessel density and progression of colorectal cancer, implying that the RAGE signaling pathway participates in VEGF-mediated angiogenesis [9].

RAGE is a type I transmembrane receptor present in diverse cell types and functions as a pattern-recognition receptor [10]. Interaction of RAGE with its various ligands (including AGE, HMGB1, and S100B) promotes cancer cell growth, invasion, and angiogenesis [3]. The S100 protein ligand activates the RAGE signaling thus promoting survival and proliferation of cancer cells [11]. In addition, overexpression of RAGE promotes colon cancer malignancy by accelerating proliferation and migration of cancer cells through activation of nuclear factor-kappa B- (NF κ B-) mediated transcription leading to inflammation-associated carcinogenesis [12–14]. Furthermore, S100B plays an essential role in colon carcinogenesis by promoting NF κ B-mediated transcription through the RAGE signaling, affecting various phenotypes

of cancer such as proliferation, metastasis, and angiogenesis [15]. Therefore, studies should explore novel specific therapeutic agents targeting S100B/RAGE/NF κ B axis to block development of colorectal cancer.

Cell surface receptor targeting strategies have explored aptamers as novel candidates for targeted cancer therapy. Aptamers have various advantages over protein-based drugs, such as antibodies or peptides [16]. Aptamers are short and single-stranded oligonucleotides and have been reported to be antagonists against various target proteins through phylogenetic and exponential enrichment (SELEX) analysis [17]. Aptamers are chemical antibodies with three-dimensional structures; therefore, they have excellent thermal stability and high affinity and specificity for the homologous protein targets and display good biocompatibility [18, 19]. Therefore, in this study, we developed an aptamer-based strategy for use as a molecular inhibitor of RAGE/NF κ B/VEGF-A axis for suppression of inflammatory-induced angiogenesis associated with colorectal cancer progression.

The aim of this study was to design an aptamer against RAGE as a new antagonist to selectively inhibit RAGE/NF κ B signaling transductions. Analysis showed that the aptamer-based antagonist inhibited proliferation and migration of colorectal cancer cells induced by S100B. In addition, it decreased synthesis and secretion of VEGF-A protein, which is implicated in tumor angiogenesis. The *in vivo* results indicated that the aptamer of RAGE exhibited excellent inhibition activity on development of colorectal tumors, by suppressing angiogenesis and microvasculature formation in xenograft nude mice. The findings of this study, therefore, show that the novel aptamer against RAGE is a potential therapeutic agent for treatment of colorectal cancer.

2. Material and Methods

2.1. Reagents. The fetal bovine serum (FBS) was purchased from Biological Co., Ltd.; penicillin-streptomycin (100x), 0.25% trypsin-EDTA (1x), serum-free cryopreservation fluid, 3-(4,5-dimethyl-2-thiazolyl)-2,5-diphenyl-2-H-tetrazolium bromide (CCK-8), ECL luminescent agents, color pre-dyed protein marker, and antibody diluent were purchased from New Cell & Molecular Biotech Co., Ltd.; recombinant protein S100B (*E. coli*, N-6His) was purchased from Novoprotein Scientific Inc. RIPA lysis buffer was purchased from Beyotime Biotechnology. Phosphatase inhibitors and protease inhibitors were from Bimake; nitrocellulose membrane was purchased from Merck Millipore Company; antibodies against phosphorylated NF κ B p65 (Ser 536), phosphorylated Akt (Ser 473), and phosphorylated ERK1/2 (Thr202/Tyr204) were purchased from Cell Signaling Technology (Beverly, Massachusetts, USA). The polyclonal antibodies for VEGF-A, RAGE, and CD31 were from Santa Cruz Biotechnology (Santa Cruz). The primary monoclonal antibody against α -tubulin was purchased from CellWay technology (CellWay Bio). The secondary antibodies including HRP-conjugated goat anti-mouse IgG (H&L) and HRP-conjugated goat anti-rabbit IgG (H&L) were from Invitrogen. PrimeScript™ RT reagent kit (perfect real time), Takara RR037A kit, EasyGeno rapid recombinant clone kit, endotoxin-free plasmid extrac-

tion kit, and DNA gel recovery kit were obtained from Tiangen.

2.2. Cell Culture. HCT116 cell, a colon cancer cell line, was cultured in Dulbecco's modified Eagle's medium (DMEM) with 10% FBS and 1% penicillin/streptomycin. All cells were incubated in a humidified atmosphere at 37°C with 5% CO₂.

2.3. Preparation of Apt-RAGE. The aptamer against RAGE (Apt-RAGE) was adopted based on the systematic evolution of ligands by exponential enrichment (SELEX) previously. [20] Sequences of Apt-RAGE and the control DNA aptamer (Ctrl-aptamer) are as follows. Apt-RAGE: 5'-CCTGATATG GTGTACCCGCCCTTAGTATTGGTGTCTAC-3' and Ctrl-aptamer: 5'-TTCGGCCTGGGGGCGGCCAGTTCG GGTCCAGTCGCGGGAG-3'.

2.4. Molecular Cloning. The cloning primers (Supplemental Table 1) were designed according to the CDS sequence of the gene *AGER* (Homo sapiens gene of *rage*). The cDNA fragment of the RAGE was amplified by PCR and cloned into the plasmid of pcDNA 3.1 vector. The plasmids of pcDNA 3.1 RAGE were isolated and identified by Sanger sequencing (Tsingke Biotech Co., Ltd.).

2.5. Plasmid Transfection. Cells were inoculated and transfected into a 6-well plate culture dish (Wuxi NEST Biotechnology Co., Ltd.) with about 2×10^5 cells per well on the day before transfection, and the cell density could reach about 70-80% on the next day. The mixture of Lipo8000™ Transfection reagent and plasmids was dripped into the cells in the six-well plate. After 6 hours, the culture medium was changed for 48 h culturing.

2.6. Western Blotting. Cells were seeded in a 6-well plate culture dish (NEST Biotech Co., Ltd.). Before treatment, the cells were starved for 24 h by incubation with the DMEM containing 0.2% FBS. Subsequently, the cells were pretreated with Ctrl-aptamer or Apt-RAGE for one hour, then treated with S100B for 30 min in the incubator, and then lysed with RIPA lysis buffer. The cell lysates were centrifuged at 14000 rcf for 10 min at 4°C and separated by 10% SDS-PAGE electrophoresis followed by transferring to a nitrocellulose membrane by semidry electrophoretic transfer unit. Each membrane was blocked with 5% skim milk in PBST (1x PBS with 0.1% Tween-20) at room temperature for 1.5 h and incubated with different primary antibodies (1:1000 dilution) overnight at 4°C. Subsequently, the membranes were incubated with horseradish peroxidase-conjugated secondary antibodies at room temperature for 1 h. Finally, the membranes were reacted with ECL substrate solution (NCM Biotech Co., Ltd.) and the chemiluminescent images were acquired and analyzed using Bio-Imaging Systems (MicroChem4.2).

2.7. Cell Viability Assay. The CCK8 assay was carried out to determine relative cell viability. [21] HCT116 cells were seeded at 5×10^3 cells/well on a 96-well plate culture dish (Wuxi NEST Biotechnology Co., Ltd.) and allowed to adhere for 24 h at 37°C in 5% CO₂. The cells were pretreated with

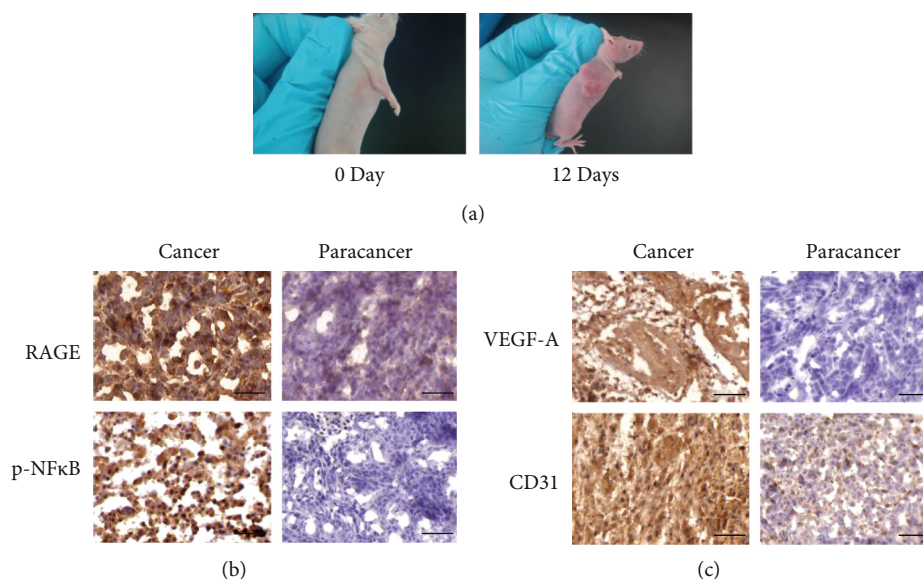


FIGURE 1: Association of RAGE expression with tumor angiogenesis in colorectal cancer development. (a) HCT116 cells were intradermally injected into the upper flank of 6-week female nude mice to establish colorectal cancer xenograft model. (b) Immunohistochemical analysis of cancer tissues and the paracancer tissues from nude mice using antibodies against RAGE and p-NFκB. Scale bar: 50 μm. (c) Immunohistochemical analysis of cancer tissues and the paracancer tissues from nude mice using antibodies against VEGF-A and CD31. Scale bar: 50 μm.

Apt-RAGE (100 nM) and then treated with S100B (2 μg/mL), S100B within the fresh medium for 24 h, 48 h, or 72 h. After the incubation, cells within the 96-well plate were incubated with CCK8 solution for 1–3 h at 37°C in 5% CO₂, followed by measurement using a GENios Microplate Reader (TECAN) at the absorbance at 450 nm.

2.8. Wound Healing Assay. 3×10^4 HCT116 cells were seeded into a 12-well plate culture dish (Wuxi NEST Biotechnology Co., Ltd.) for 90% confluence and scratched using a 200 μL tip. After scratching, the cells were washed with PBS twice, and then the medium containing Apt-RAGE (100 nM) was added. After 1 h, S100B was added to the culture medium. Under an inverted microscope, the scratched cells were photographed after 0 h, 24 h, and 48 h. The wound closure rate was calculated as follows: Migration rate (%) = (Scratch distance at 0 h – Scratch distance at indicated time)/Scratch distance at 0 h × 100.

2.9. Transwell Assay. The migration ability of HCT116 cells was assessed by using Transwell chamber (BD Biosciences, San Diego, CA). 500 μL of complete medium containing 10% FBS was supplemented into the lower chamber (the bottom of a 24-well plate), then the medium containing Apt-RAGE (100 nM) or Ctrl-aptamer. Next, 5×10^4 cells/well were added into the upper chamber. S100B was added into the lower chamber. After 24 h incubation, the migrated cells were stained with crystal violet. Five random fields at 200x magnification were used for cell counting for each membrane.

2.10. Measurement of VEGF-A by ELISA. ELISA was performed to determine VEGF-A production according to the

user's manual of a Human VEGF-A ELISA kit (ABclonal Technology).

2.11. Xenograft Studies. The animal experiments were approved by the ethical committee of College of Biology, Hunan University, China, and performed according to the *Guide for the Care and Use of Laboratory Animals* of the National Institutes of Health. The HCT116 cells (2×10^6 cells) were intradermally injected into the upper flank of female 6-week nude mice ($n = 20$). 2 days posttumor inoculation, Apt-RAGE (38.4 pmol/day/g body weight, $n = 5$) or vehicle ($n = 5$) was injected adjacent to the tumor daily for 12 days. The volume of tumors and body weight were measured daily. The tumor volume (mm³) = [(width)/2 × length/2] mm³. At 12 days posttumor inoculation, mice were humanely sacrificed by isoflurane inhalation, and the HCT116 tumor section was excised for immunohistochemical staining.

2.12. Immunohistochemical Staining. Harvested tumors and paracancerous tissue were embedded in the optimal cutting temperature compound (OCT, Tissue-Tek, Sakura), stored at –80°C. Immunohistochemistry was carried out using a two-step ELISA Kit (mouse/rabbit-enhanced polymer system) (ZSGB-BIO). Primary antibodies include RAGE (1 : 50 dilution), VEGF-A (1 : 50 dilution), p-NFκB (1 : 50 dilution), and CD31 (1 : 50 dilution). The specimens were stained using the DAB kit (ZSGB-BIO) and then imaged using a digital slicing system (Pannoramic MIDI).

2.13. Statistical Analysis. All values were presented as the means ± SEM. Statistical significance was evaluated using the Student *t*-test for paired comparison (GraphPad Prism 6); * $p < 0.05$ and ** $p < 0.01$ were considered to be significant.

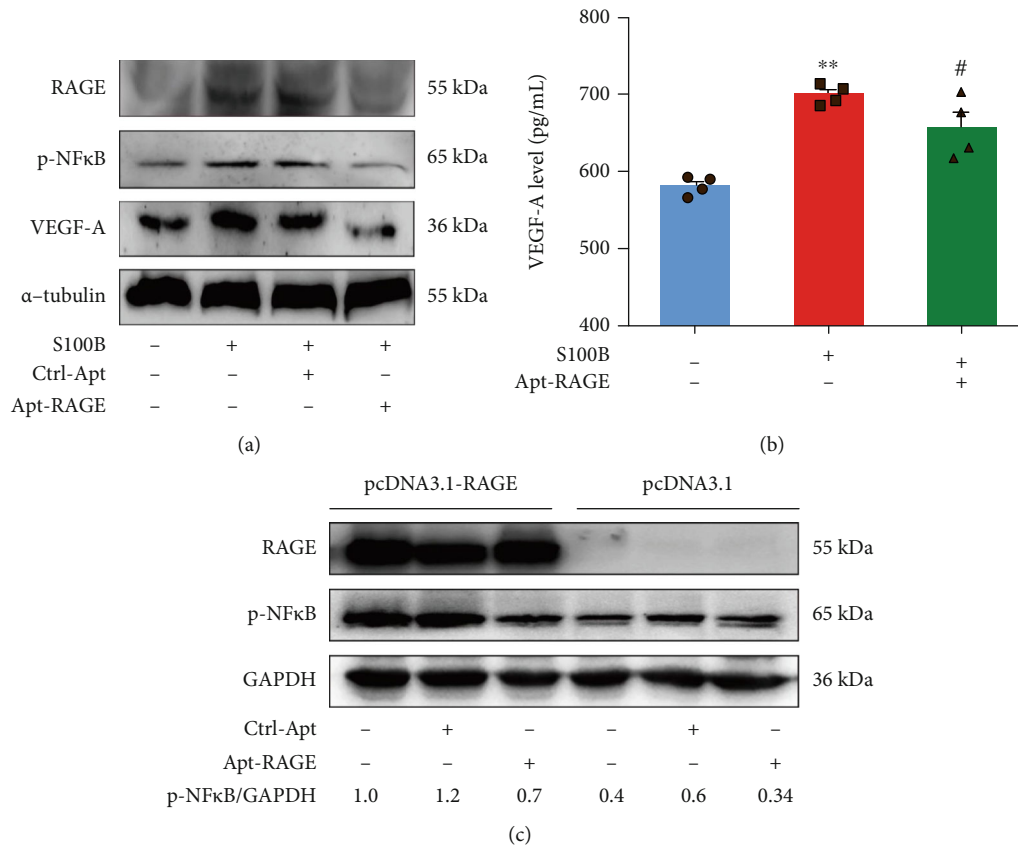


FIGURE 2: Inhibitory effect of Apt-RAGE on S100B-induced synthesis and secretion of VEGF-A protein. (a) HCT116 cells were starved and pretreated with 100 nM Apt-RAGE or Ctrl-Apt for 90 min in the presence of S100B (2 μg/mL). Phosphorylation of NFκB, VEGF-A, and RAGE was examined using western blotting. (b) ELISA assay was used to determine VEGF-A release in the culture medium treated with S100B (2 μg/mL) in the presence or absence of Apt-RAGE (100 nM) or Ctrl-Apt (100 nM). Data are presented as the means ± SEM, ** $p < 0.01$ vs. untreated control and # $p < 0.05$ in Apt-RAGE vs. S100B. (c) Apt-RAGE inhibited S100B-independent phosphorylation of NFκB in RAGE-overexpressed cells. HCT116 cells transfected with pcDNA3.1-RAGE or pcDNA3.1 for 48 h and incubation with Apt-RAGE (100 nM) for 20 min. Phosphorylation of NFκB and the expression of VEGF-A and RAGE were examined using western blotting.

3. Results

3.1. RAGE Expression Correlates with Microvasculature Formation in Colorectal Cancer. Tumor-associated angiogenesis is associated with tumor growth and development *in vivo* [22]. A colorectal tumor-bearing nude mouse model was established to explore the role of RAGE in tumor-associated angiogenesis (Figure 1(a)). Expression of RAGE and phosphorylation of NFκB were analyzed through immunohistochemistry staining of tumor specimens prepared post 12 days after tumor inoculation days. Analysis of staining results showed increase in expression level of RAGE protein and significant phosphorylation of NFκB in colorectal tumor tissue compared with those in paracancer normal tissue (Figure 1(b)). Notably, CD31-positive blood vessels formed adjacent to tumor tissues, and a significant increase in the level of VEGF-A was observed compared with those in the adjacent normal tissue (Figure 1(c)). These findings imply that development of colorectal cancer may be mediated by RAGE/NFκB/VEGF-A axis, which plays a role in promoting tumor angiogenesis.

3.2. Apt-RAGE Blocks the NFκB Signaling Pathway and VEGF-A Secretion. The role of RAGE signaling in tumorigenesis was explored using *in vitro* cultured colorectal cells. S100B, a ligand of RAGE and a known mediator of inflammation, significantly induced phosphorylation of NFκB and expression of VEGF-A (Figure 2(a)). It has been previously reported that the RAGE-NFκB signaling plays an essential role in VEGF-A secretion [23]. In this study, we explored the relationship between S100B and VEGF-A secretion using HCT116 cells. ELISA analysis showed that S100B enhanced VEGF-A secretion in the culture medium (Figure 2(d)), implying that VEGF-A secretion is mediated by induction of the RAGE/NFκB signaling pathway by S100B. We proposed that the aptamer-based RAGE antagonist (Apt-RAGE) may inhibit the interaction between RAGE and S100B to block downstream NFκB-mediated signal transduction. The aptamer against RAGE was previously screened and was used to block the RAGE-RAGE signaling, which efficiently attenuated the development experimental diabetic nephropathy [20]. We characterized the stability of Apt-RAGE in 10% serum and found that the Apt-RAGE remained stable

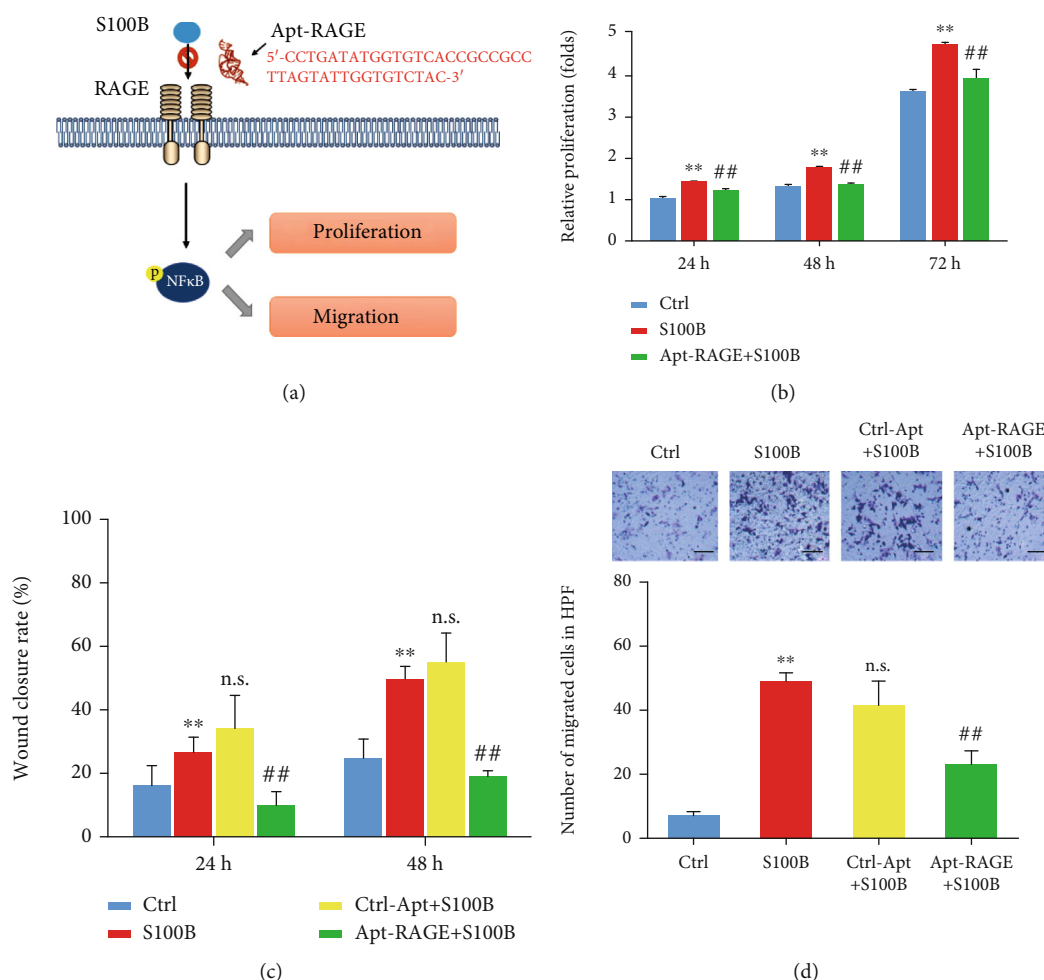


FIGURE 3: Apt-RAGE inhibited proliferation and migration of colorectal cancer cells. (a) Schematic illustration of Apt-RAGE effect on proliferation and migration of cancer cells. (b) Effect of Apt-RAGE (100 nM) on proliferation of HCT116 cells promoted by S100B (2 μg/mL) was detected by CCK8 cell counting kit at 24 h, 48 h, and 72 h. Data are presented as the means ± SEM, * $p < 0.01$ vs. untreated control and $^{\#}p < 0.05$ vs. S100B. (c) Quantitation of the effect of Apt-RAGE (100 nM) on migration induced by S100B (2 μg/mL) in wound healing assay at 24 h or 48 h. * $p < 0.01$ vs. untreated group and $^{\#}p < 0.01$ vs. S100B-treated group. n.s. indicates that the difference is not significant compared with the S100B-treated group. (d) Quantitative analysis of the effect of Apt-RAGE (100 nM) on directional migration induced by S100B (2 μg/mL) evaluated using Transwell assay. Upper panel: representative image of the membrane with migrated cells, scale bar: 200 μm. Lower panel: analysis of migrated cells using Transwell assay. Data are presented as the means ± SEM, ** $p < 0.01$ vs. untreated control, $^{\#}p < 0.01$ vs. S100B-treated group. n.s. indicates that the difference is not significant compared with the S100B-treated group.

without degradation in 5 hours, which could be enough for cell experiment and in vivo study (Figure S1). Based on the Mfold software simulation, two predicted secondary structures were generated by free energy minimization using the RNA folding algorithm (Figure S2). The calculated free energy for each aptamer is $\Delta GA = -2.07$ kcal/mol and $\Delta GB = -1.39$ kcal/mol. Notably, pretreatment of HCT116 cells with 100 nM Apt-RAGE significantly inhibited S100B-induced phosphorylation of NFκB and increased in VEGF-A protein level compared with the Ctrl-Apt-treated group (Figure 2(a)). We also examined other signaling pathways and found that Apt-RAGE failed to affect the Akt and ERK signaling, suggesting the specificity of the Apt-RAGE to block the RAGE/NFκB signaling (Figure S3). Furthermore, we confirmed that Apt-RAGE suppressed

secretion of VEGF-A in culture medium (Figure 2(b)). These findings imply that Apt-RAGE inhibits VEGF-A release by inhibiting the RAGE/NFκB signaling pathway.

A previous study reports that overexpression of RAGE affects downstream signaling thus promoting proliferation of hepatic cancer cells in a ligand-independent manner [24]. To explore the effect of high overexpression of RAGE on the NFκB signaling in colorectal cancer cells, HCT116 cells were transfected with pcDNA-3.1-RAGE to overexpress human RAGE protein. Overexpression of RAGE significantly increased phosphorylation of NFκB in pcDNA 3.1 RAGE-transfected cells compared with the control cells transfected with an empty vector (pcDNA 3.1) lacking RAGE (Figure 2(c)). Analysis showed that Apt-RAGE significantly inhibited phosphorylation of NFκB in HCT116 cells

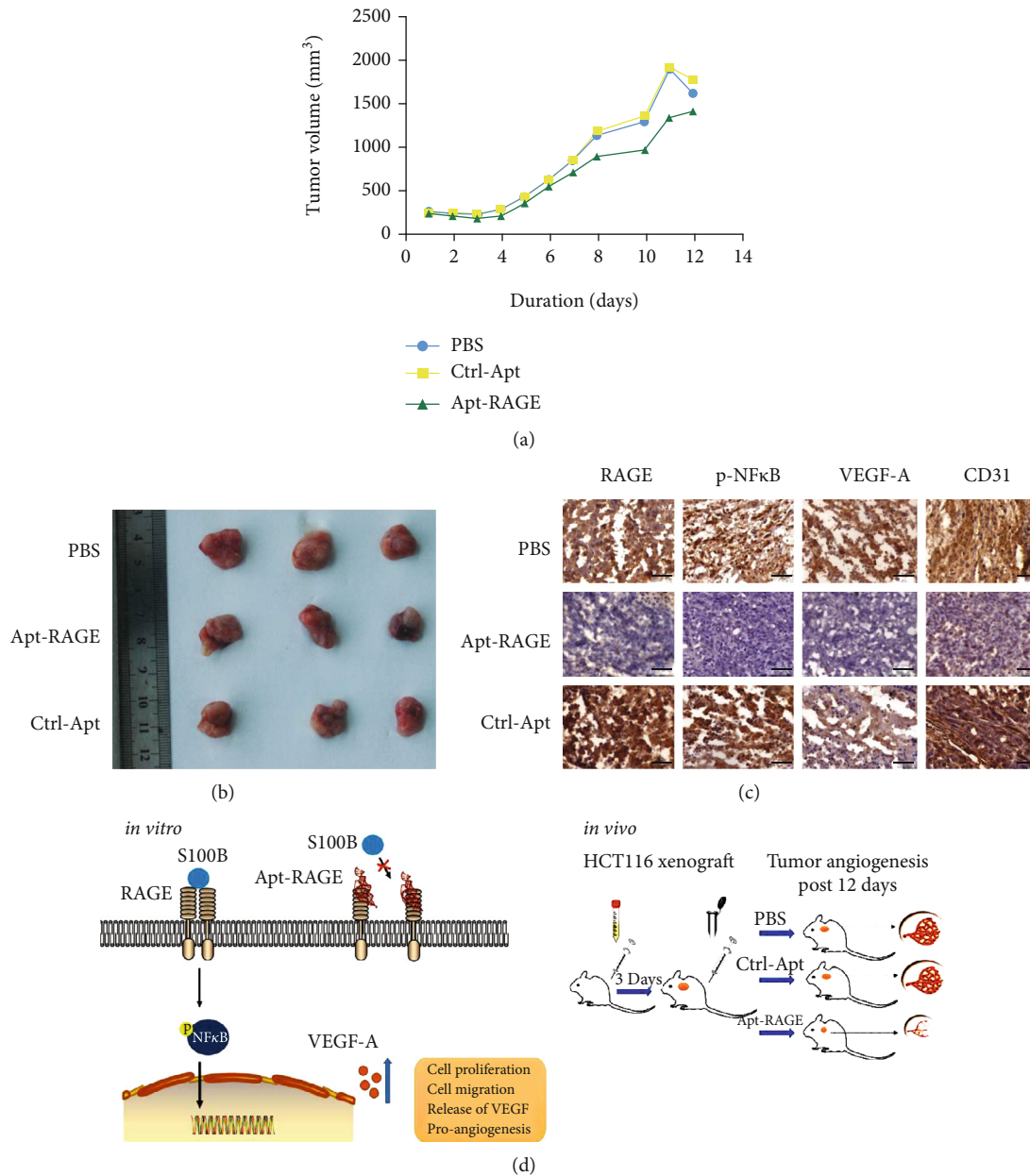


FIGURE 4: Effects of Apt-RAGE on angiogenesis of HCT116 cells xenograft nude mice. (a) The average volume of tumors treated with PBS ($n = 5$), Ctrl-Apt ($n = 5$), or Apt-RAGE ($n = 5$). Tumor volume was measured until the end of the experiments. (b) Images of representative tumors. (c) IHC staining was performed with RAGE, p-NFκB, VEGF, or CD31 on the frozen sections. Scale bar: 50 μm. (d) Schematic illustration of the role of Apt-RAGE to inhibit *in vivo* tumor angiogenesis (right) by blocking the S100B/RAGE/NFκB/VEGF-A signaling pathway (left).

with overexpressed RAGE (Figure 2(c)). This finding indicates that Apt-RAGE can be used as a potent antagonist for RAGE protein to inhibit the S100B-dependent and S100B-independent RAGE/NFκB signaling.

3.3. Apt-RAGE Inhibits S100B-Induced Proliferation and Migration. Further, we explored the role of S100B on proliferation and migration of colorectal cancer cells (Figure 3(a)). Analysis showed that S100B significantly increased proliferation of HCT116 cells (2 μg/mL) compared with that of controls (Figure 3(b)). Pretreatment with 100 nM Apt-RAGE

significantly reduced proliferation of HCT116 cells (Figure 3(b)). To explore the effect of S100B on cell migration, a wound scratch assay was performed on a 2D interface. Analysis showed a significant increase in cell migration rate after treatment with S100B in a time-dependent manner compared with control cells (Figure 3(c), Figure S4). However, pretreatment with Apt-RAGE (100 nM) significantly reduced S100B-induced wound closure of HCT116 cells. Further, Transwell assay was performed to investigate the effect of Apt-RAGE on S100B-induced cell migration using a 3D interface. Analysis showed that Apt-RAGE significantly

decreased the number of migrated cells compared with that of the S100B-treated group (Figure 3(d)). These findings show that Apt-RAGE effectively inhibits S100B-induced proliferation and migration of colorectal cancer cells.

3.4. Apt-RAGE Retards Development of Colorectal Cancer by Modulating Angiogenesis *In Vivo*. To investigate the effects of Apt-RAGE aptamer as an antagonistic agent *in vivo*, a colorectal tumor xenograft model was constructed. In summary, HCT116 cells were injected subcutaneously in mice to induce tumors. The tumor-bearing mice were administered with Apt-RAGE or Ctrl-aptamer daily for 12 days. The tumor volume from the mice treated with the Apt-RAGE was significantly smaller compared with that of the control group (Figure 4(a)). In the first four days, the tumor growth in the experimental group was similar to the control group, whereas growth gradually decreased from day five, compared with the PBS group and the Ctrl-aptamer group (Figure 4(b)). Analysis showed that Apt-RAGE significantly inhibited tumor growth. Furthermore, immunohistochemical analysis was performed showing that Apt-RAGE inhibited the RAGE level and phosphorylation of NF κ B, resulting in low VEGF-A levels compared with levels in the control group (Figure 4(c)). These findings indicate that Apt-RAGE inhibits tumor angiogenesis by blocking RAGE/NF κ B signal transduction.

4. Discussion

Development of colorectal cancer is associated with aberrant RAGE activation through angiogenesis-promoting TME inflammation. Therefore, RAGE is a potential therapeutic target for colorectal cancer treatment [9, 15]. RAGE binds to multiple ligands, including advanced glycation end-products (AGEs) and S100 proteins. After binding these ligands, it activates the downstream NF κ B pathway which is implicated in regulation of cell proliferation, survival, differentiation, and autophagy [25, 26]. In the present study, RAGE expression level was determined and the association with microvessel density in colorectal cancer tissue specimens was explored. The findings of this study showed that colorectal cancer tissues express high RAGE protein levels, which are positively correlated with increased microvessel density. In addition, phosphorylation NF κ B pattern was positively correlated with expression levels of VEGF and CD31 proteins in colorectal cancer tissue specimens.

S100B is used as a diagnostic marker for inflammatory malignant tumors. The S100B-induced signaling is positively correlated with development of various tumors [27, 28]. Moreover, VEGF-A promotes tumor angiogenesis during development of colorectal cancer [15]. This study explored the role of the S100B/RAGE signaling on cell viability, migration, and angiogenesis and progression of colorectal cancer. The findings of this study show that increased S100B protein levels are correlated with significant increase in proliferation and migration of human colon cancer cell *in vitro*. In addition, S100B activity significantly increased VEGF-A secretion from cultured cells. Apt-RAGE inhibited the RAGE signaling in colorectal cancer cells, thus inhibiting activation of NF κ B,

tumor cell proliferation, migration, and release of VEGF-A. A previous study reported that RAGE is highly expressed in hepatoma cancer cells and is implicated in promoting proliferation of hepatoma cancer cells [24]. Similarly, the findings of this study showed that RAGE overexpression induces phosphorylation of NF κ B in the absence of S100B. Notably, analysis showed that Apt-RAGE inhibits S100B-independent NF κ B activation through inhibition of RAGE expression. Furthermore, the findings of this study indicate that Apt-RAGE inhibits S100B-RAGE-mediated angiogenesis by inhibiting S100B-induced activation of NF κ B. The inhibitory effect of Apt-RAGE on *in vitro* tumor angiogenesis was confirmed *in vivo* (Figure 4). *In vivo* experiments showed that Apt-RAGE inhibits phosphorylation of NF κ B and expression of VEGF, thus decreasing microvasculature which was analyzed through CD31-positive staining of the vascular endothelium in colorectal tumor specimens.

In conclusion, the findings of this study show that Apt-RAGE, an antagonist for RAGE, significantly inhibits synthesis and secretion of VEGF-A protein by inhibiting the NF κ B pathway in human colon cancer cells. Therefore, inhibition of Apt-RAGE on VEGF-A-mediated angiogenesis significantly decreases formation of microvasculature around tumors in xenograft model. In addition, Apt-RAGE inhibited S100B-dependent activation of proliferation and migration of colorectal cancer cells, which are critical events for cancer cells to adapt to the TME during tumor progression (Figure 4(d)). To the best of our knowledge, this is first study to report that Apt-RAGE inhibits proangiogenic and proliferative features of colorectal cancer cells. These results provide a basis for selective targeting of S100B/RAGE signaling using aptamer which is a novel approach to develop novel nucleic acid drugs for colon cancer therapy.

Data Availability

The quantification data used to support the findings of this study are included within the article.

Conflicts of Interest

The authors declare no competing financial interests.

Acknowledgments

This work was supported by the Natural Science Foundation of Hunan Province (Grant No. 2020JJ4383), the Innovation-Oriented Advanced Technology and Industrial Technology Program Project of Hunan Province (Grant No. 2020SK2017), and the Changsha Municipal Natural Science Foundation (Grant No. kq2014043).

Supplementary Materials

Supplemental Table 1: primer sequences for plasmid construction. Figure S1: the characterization of Apt-RAGE. (A) The molecular size of Apt-RAGE (Apt-RAGE) and Ctrl-aptamer (Ctrl-Apt). (B) The serum stability of Apt-RAGE. Figure S2: schematic representations of the secondary

structures of the Apt-RAGE. Predicted secondary structures were generated by free energy minimization using the RNA folding algorithm Mfold (calculated free energy for each aptamer: $\Delta GA = -2.07$ kcal/mol and $\Delta GB = -1.39$ kcal/mol. Figure S3: effect of Apt-RAGE on the AKT and ERK signaling pathway in cultured HCT116 cells. Figure S4: effect of Apt-RAGE (100 nM) on the migration induced by S100B (2 $\mu\text{g}/\text{mL}$) was detected by wound healing assay at 24 h or 48 h. Scale bar: 50 μm . (Supplementary Materials)

References

- [1] C. Lucas, N. Barnich, and H. Nguyen, "Microbiota, inflammation and colorectal cancer," *International Journal of Molecular Sciences*, vol. 18, no. 6, p. 1310, 2017.
- [2] K. A. Rmali, M. C. A. Puntis, and W. G. Jiang, "Tumour-associated angiogenesis in human colorectal cancer," *Colorectal Disease*, vol. 9, no. 1, pp. 3–14, 2007.
- [3] M. B. Majnooni, S. Fakhri, A. Smeriglio et al., "Antiangiogenic effects of coumarins against cancer: from chemistry to medicine," *Molecules*, vol. 24, no. 23, p. 4278, 2019.
- [4] Z. Li, W. Yan-qing, Y. Xiao et al., "Exosomes secreted by chemoresistant ovarian cancer cells promote angiogenesis," *J. Ovarian. Res.*, vol. 14, no. 1, p. 7, 2021.
- [5] K. Ganesh and J. Massagué, "Targeting metastatic cancer," *Nature Medicine*, vol. 27, no. 1, pp. 34–44, 2021.
- [6] L. Rodriguez-Caso, A. Reyes-Palomares, F. Sanchez-Jimenez, A. R. Quesada, and M. A. Medina, "What is known on angiogenesis-related rare diseases? A systematic review of literature," *Journal of Cellular and Molecular Medicine*, vol. 16, no. 12, pp. 2872–2893, 2012.
- [7] K. Cole, K. Pravoverov, and J. E. Talmadge, "Role of myeloid-derived suppressor cells in metastasis," *Cancer and Metastasis Reviews*, 2021.
- [8] V. Catalano, A. Turdo, S. Di Franco, F. Dieli, M. Todaro, and G. Stassi, "Tumor and its microenvironment: a synergistic interplay," *Seminars in Cancer Biology*, vol. 23, no. 6, pp. 522–532, 2013.
- [9] H. Liang, Y. Zhong, S. Zhou, and L. Peng, "Knockdown of RAGE expression inhibits colorectal cancer cell invasion and suppresses angiogenesis in vitro and in vivo," *Cancer Letters*, vol. 313, no. 1, pp. 91–98, 2011.
- [10] P. Swami, S. Thiagarajan, A. Vidger, V. S. K. Indurthi, S. W. Vetter, and E. Leclerc, "RAGE up-regulation differently affects cell proliferation and migration in pancreatic cancer cells," *International Journal of Molecular Sciences*, vol. 21, no. 20, p. 7723, 2020.
- [11] M. T. T. Win, Y. Yamamoto, S. Munesue et al., "Regulation of RAGE for attenuating progression of diabetic vascular complications," *Experimental Diabetes Research*, vol. 2012, Article ID 894605, 8 pages, 2012.
- [12] M. K. Fuentes, S. S. Nigavekar, T. Arumugam et al., "RAGE activation by S100P in colon cancer stimulates growth, migration, and cell signaling pathways," *Diseases of the Colon and Rectum*, vol. 50, no. 8, pp. 1230–1240, 2007.
- [13] C. Cirillo, G. Sarnelli, G. Esposito, F. Turco, L. Steardo, and R. Cuomo, "S100B protein in the gut: the evidence for enteroglia-sustained intestinal inflammation," *World Journal of Gastroenterology*, vol. 17, no. 10, pp. 1261–1266, 2011.
- [14] P. Moravkova, D. Kohoutova, S. Rejchrt, J. Cyrany, and J. Bures, "Role of S100 proteins in colorectal carcinogenesis," *Gastroenterology Research and Practice*, vol. 2016, Article ID 2632703, 7 pages, 2016.
- [15] L. Seguella, R. Capuano, M. Pesce et al., "S100B protein stimulates proliferation and angiogenic mediators release through RAGE/pAkt/mTOR pathway in human colon adenocarcinoma Caco-2 cells," *International Journal of Molecular Sciences*, vol. 20, no. 13, p. 3240, 2019.
- [16] G. Zhu and X. Chen, "Aptamer-based targeted therapy," *Advanced Drug Delivery Reviews*, vol. 134, pp. 65–78, 2018.
- [17] M. Song, G. Li, Q. Zhang, J. Liu, and Q. Huang, "De novo post-SELEX optimization of a G-quadruplex DNA aptamer binding to marine toxin gonyautoxin 1/4," *Computational and Structural Biotechnology Journal*, vol. 18, pp. 3425–3433, 2020.
- [18] H. Sun and Y. Zu, "A highlight of recent advances in aptamer technology and its application," *Molecules*, vol. 20, no. 7, pp. 11959–11980, 2015.
- [19] N. Nakamura, T. Matsui, Y. Ishibashi et al., "RAGE-aptamer attenuates the growth and liver metastasis of malignant melanoma in nude mice," *Molecular Medicine*, vol. 23, no. 1, pp. 295–306, 2017.
- [20] T. Matsui, Y. Higashimoto, Y. Nishino, N. Nakamura, K. Fukami, and S. I. Yamagishi, "RAGE-aptamer blocks the development and progression of experimental diabetic nephropathy," *Diabetes*, vol. 66, no. 6, pp. 1683–1695, 2017.
- [21] R. Li and Y.-H. Gan, "Inhibiting HDAC1 enhances the anti-cancer effects of statins through downregulation of GGTase- β expression," *International Journal of Molecular Sciences*, vol. 18, no. 5, p. 1010, 2017.
- [22] A. Ojima, T. Matsui, S. Maeda et al., "DNA aptamer raised against advanced glycation end products inhibits melanoma growth in nude mice," *Laboratory Investigation*, vol. 94, no. 4, pp. 422–429, 2014.
- [23] J. N. Tsoporis, S. Izhar, G. Proteau, G. Slaughter, and T. G. Parker, "S100B-RAGE dependent VEGF secretion by cardiac myocytes induces myofibroblast proliferation," *Journal of Molecular and Cellular Cardiology*, vol. 52, no. 2, pp. 464–473, 2012.
- [24] J. Li, P. W. Wu, Y. Zhou et al., "RAGE induces hepatocellular carcinoma proliferation and sorafenib resistance by modulating autophagy," *Cell Death & Disease*, vol. 9, no. 2, p. 225, 2018.
- [25] X. Chen, L. Zhang, I. Y. Zhang et al., "RAGE expression in tumor-associated macrophages promotes angiogenesis in glioma," *Cancer Research*, vol. 74, no. 24, pp. 7285–7297, 2014.
- [26] C. Adamopoulos, C. Piperi, A. N. Gargalionis et al., "Advanced glycation end products upregulate lysyl oxidase and endothelin-1 in human aortic endothelial cells via parallel activation of ERK1/2-NF- κ B and JNK-AP-1 signaling pathways," *Cellular and Molecular Life Sciences*, vol. 73, no. 8, pp. 1685–1698, 2016.
- [27] A. R. Bresnick, D. J. Weber, and D. B. Zimmer, "S100 proteins in cancer," *Nature Reviews. Cancer*, vol. 15, no. 2, pp. 96–109, 2015.
- [28] L. Seguella, F. Rinaldi, C. Marianecchi et al., "Pentamidine thwarts S100B effects in human colon carcinoma biopsies favouring wtp53 rescue," *Journal of Cellular and Molecular Medicine*, vol. 24, no. 5, pp. 3053–3063, 2020.

Research Article

Catheter-Based Radiofrequency Renal Sympathetic Denervation Decreases Left Ventricular Hypertrophy in Hypertensive Dogs

Shan Tu , Zhi-Jie Shen, Xiao-Yan Wang, Li-Xiong Zeng, and Zhi-Hui Zhang 

Department of Cardiology, The Third Xiangya Hospital of Central South University, Changsha, 410006 Hunan Province, China

Correspondence should be addressed to Zhi-Hui Zhang; zhangzhihui0869@126.com

Received 18 March 2021; Revised 6 April 2021; Accepted 10 April 2021; Published 26 April 2021

Academic Editor: Yaoyao Xia

Copyright © 2021 Shan Tu et al. This is an open access article distributed under the Creative Commons Attribution License, which permits unrestricted use, distribution, and reproduction in any medium, provided the original work is properly cited.

This study explored the effects of renal sympathetic denervation (RDN) on hyperlipidity-induced cardiac hypertrophy in beagle dogs. Sixty beagles were randomly assigned to the control group, RDN group, or sham-operated group. The control group was fed with a basal diet, while the other two groups were given a high-fat diet to induce model hypertension. The RDN group underwent an RDN procedure, and the sham-operated group underwent only renal arteriography. At 1, 3, and 6 months after the RDN procedure, the diastolic blood pressure (DBP) and systolic blood pressure (SBP) levels were markedly decreased in the RDN group relative to the sham group ($P < 0.05$). After 6 months, serum norepinephrine (NE) and angiotensin II (AngII), as well as left ventricular levels, in the RDN group were statistically lower than those in the sham group ($P < 0.05$). Also, the left ventricular mass (LVM) and left ventricular mass index (LVMI) were significantly decreased, while the E/A peak ratio was drastically elevated ($P < 0.05$). Pathological examination showed that the degree of left ventricular hypertrophy and fibrosis in the RDN group was statistically decreased relative to those of the sham group and that the collagen volume fraction (CVF) and perivascular circumferential collagen area (PVCA) were also significantly reduced ($P < 0.05$). Renal sympathetic denervation not only effectively reduced blood pressure levels in hypertensive dogs but also reduced left ventricular hypertrophy and myocardial fibrosis and improved left ventricular diastolic function. The underlying mechanisms may involve a reduction of NE and AngII levels in the circulation and myocardial tissues, which would lead to the delayed occurrence of left ventricular remodeling.

1. Introduction

The rapid emergence and serious consequence of hypertension are now considered one of the major threats to the quality of human life. Hypertension is not only a risk factor for myocardial infarction, coronary artery disease, and stroke but also the most common cause of death [1, 2]. Refractory hypertension is a vital risk factor for the occurrence of cardiovascular events. Patients with hypertension experience changes in left ventricular hypertrophy (LVH) and myocardial fibrosis, even before the incidence of clinical events [3].

Structural cardiac changes are often accompanied by impaired left ventricular function, such as abnormal left ventricular relaxation and increased left ventricular diastolic filling pressure. Studies have shown that diastolic dysfunction may occur in hypertensive subjects with a normal left ventricular mass (LVM) [4, 5]. Left ventricular hypertrophy and diastolic dysfunction are closely related to death and

disability rates for cardiovascular diseases [6, 7]. Studies have found that the reversal of LVH improves the prognosis of cardiovascular diseases and that LVH is independent of other risk factors. Therefore, LVH is recommended as an intermediate treatment endpoint [8].

As a novel technology for treating refractory hypertension, catheter-based radiofrequency renal sympathetic denervation (RDN) decreases the activity of the afferent and efferent renal sympathetic nerve fibers through catheter ablation at the vascular intima, thereby effectively lowering diastolic blood pressure (DBP) and systolic blood pressure (SBP) in cases of refractory hypertension and reducing the heart rate of patients with refractory hypertension [9–11]. In addition, Mahfoud et al. demonstrated that catheter-based RDN significantly decreased the level of BP and left ventricular mass index (LVMI), resulting in improved ejection fraction (EF) and circumferential strain in subjects with resistant hypertension [12]. In subjects for whom the office-

based blood pressure exhibits a slight decrease of less than 10 mmHg at 6 months after the RDN procedure, RDN reduces LVM. The above effects of RDN may be independent of effects such as decreased blood pressure and the lowering of the heart rate [13, 14].

Due to the limitations of RDN, such as unclear mechanisms of action, imperfect surgical methodology, and non-ideal surgical instruments, there is a great deal of scientific controversy regarding RDN. The effects of RDN on the structure and function of the left ventricular and the vital factors associated with the long-term prognosis of patients with hypertension require further investigation. In this study, we explored the changes in blood pressure level, the severity of LVH, and the diastolic function of the left ventricular in hypertensive dogs treated with RDN.

2. Materials and Methods

2.1. Experimental Animals. Sixty beagles, half of which were males and half of which were females, were bought from the Shanghai Laboratory Animal Center. All the dogs were 10–12 months of age and belonged to the same strain. Dogs were housed individually in separate cages at the Xiangya Animal Facility of Central South University. Then, after adaptive feeding for 7 days, the dogs underwent bilateral renal arteriography to determine their renal arterial anatomy. All experimental protocols were approved by the Animal Care and Use Committee of the Third Xiangya Hospital of Central South University and performed in accordance to the guidelines of Animal Care and Use Committee of the Third Xiangya Hospital of Central South University.

2.2. Establishment of the Hypertension Model. The sixty beagles were randomly assigned to the control group, the RDN group, or the sham-operated group ($n = 20$, individually). In the control group, the animals were given a diet formulated for adult dogs (250 g of food per dog per day). The RDN group and the sham-operated group were fed with a high-fat diet for 90 days (adult dog food [150 g/day] + lard [0.4 kg/day]). The edible lard was bought from the market (Green Island [Sichuan] Food Co., Ltd.). To stimulate the dogs' appetites, an appropriate amount of salt and canned dog food was added to the diets of both groups. The dogs were fed regularly once per day between 9:00 and 10:00 a.m. and were given a dog calcium supplement (1 tablet) every other day. After 3 months of high-fat feeding, one beagle in the RDN group and one in the sham-operated group had blood pressure levels that did not meet the criteria for hypertension, indicating a failure to establish the hypertension model. Therefore, the corresponding data were excluded. After the RDN procedure, the dogs in the RDN group and the sham-operated group were given a high-fat diet to maintain a constant body mass.

2.3. Monitoring Body Weight, Blood Pressure Level, and Heart Rate. All dogs were weighed regularly at 9:00 a.m. under fasting conditions using electronic scales. Using a noninvasive animal blood pressure meter (Beijing Ruanlong Biotechnology Co., Ltd.), the blood pressure level in the tail arterial of

the beagles was measured while the dogs were fully awake. Beagles were restrained in animal holders. Once a beagle became completely calm, cuffs were placed on the roots of the dogs' tails. After setting up the correct parameters, the blood pressure monitors automatically read the SBP level, DBP level, and heart rate value. Each dog was measured six times. Data that deviated from the expected standard error were excluded, and the means of the remaining data were calculated. Before the experiment, blood pressure levels and heart rates of the beagles were recorded twice per week. The preparation of the hypertension model began once the blood pressure and heart rate data became stable, which were used as the baselines. The blood pressure level and heart rate were detected at the following time points: before the protocol of the hypertension model and then at 2 weeks, 4 weeks, 6 weeks, and 12 weeks. The RDN group was subjected to the RDN procedure. The blood pressures and heart rates of all dogs were measured at 1, 3, and 6 months after the RDN treatment.

2.4. Echocardiography. Color Doppler echocardiography was conducted on the anesthetized experimental dogs prior to renal arteriography using the Toshiba 880 cardiac ultrasound machine. Echocardiography was performed at baseline, before the RDN procedure, and after the RDN procedure by the same cardiac sonographer. The end-diastolic diameter of the interventricular septum (IVSd), left ventricular end-diastolic diameter (LVEDD), and left ventricular posterior wall dimension (LVPWd) were detected using M-type ultrasound. The LVM was calculated using the Devereux equation. In addition, the left atrial diameter, ejection fraction (EF) value, and peak E/A ratio were determined.

2.5. Examination of the Biochemical Indices. The experimental dogs were restrained in holders. Blood samples were collected from the small saphenous vein located on the lateral side of the hind limbs of the dogs in the morning under fasting conditions. Samples were processed and tested in accordance with the corresponding requirements. The kidney tissues were collected at 6 months after the RDN procedure. The following biochemical indices were examined: serum creatinine (measured using the chemiluminescence method), cystatin C (using the immune transmission turbidity method), kidney norepinephrine (NE, using high-performance liquid chromatography [HPLC]), and angiotensin II (AngII) (using enzyme-linked immunosorbent assay [ELISA] and radioimmunoassay).

2.6. RDN Procedure. The RDN group underwent the RDN procedure, and the sham-operated group received only renal arteriography. Beagles were fasted before the procedure. The skin of the back and the bilateral femoral artery area was prepared. Each beagle was anesthetized via an intramuscular injection of 15 mg/kg ketamine, followed by the inhalation of 5% isoflurane for 3 min. After oral tracheal intubation, the inhalation isoflurane concentration was changed to 2% until 10 min before surgery. After anesthesia, the animals were immobilized in the supine position. Ablation electrodes were placed on the back of the dogs and connected to a

radiofrequency ablation device (IBI, St. Jude Medical, Inc., USA). The temperature was maintained at around 55°C, and the ablation power was set at 10 W. The area of the right femoral artery was cleaned with conventional disinfection techniques. Then, the right femoral artery was punctured, and an 8F arterial sheath was inserted into the femoral artery. One hundred U/kg heparin was injected along the sheath. Subsequently, a guiding catheter was inserted into the arterial sheath while the blood pressure level was monitored. Afterward, renal arteriography was conducted, and the renal artery was located. A standard 5F radiofrequency ablation catheter was then inserted in the arterial sheath (IBI radiofrequency ablation catheter, St. Jude Medical, Inc., USA). Four spots on each side of the inner wall of the renal artery were selected as the ablation sites, and sequential point-by-point ablation was performed in the order of lower wall, anterior wall, posterior wall, and upper wall [15]. Each site was ablated continuously for 120 s. After successful bilateral renal artery ablation, renal arteriography was performed once again to determine whether renal artery dissection or stenosis had occurred. Finally, the sheath was removed. Sterile gauze was pressed against the puncture site for 45 min to stop the bleeding. The right hind limb was then bandaged. Penicillin was administered via intramuscular injection to prevent infection. At 1, 3, and 6 months after the RDN procedure, the dogs were reexamined and subjected to renal arteriography.

2.7. Euthanasia and Tissue Collection. Six months after the RDN procedure, the animals were sacrificed via an intravenous injection of 10 ml saturated KCl after being anesthetized by the inhalation of isoflurane (5%) for 10 min. The hearts were collected, and the NE and AngII content in the left ventricular was determined. In addition, the left ventricular tissues were fixed and used for hematoxylin and eosin (HE) staining and Masson's trichrome staining. Subsequently, the pathological structural changes in the left ventricular tissues were analyzed via microscopy and electron microscopy. The cardiac tissues stained with Masson's trichrome were further analyzed using a light microscopy and image analysis system to determine the myocardial collagen volume fraction (CVF) and myocardial perivascular circumferential collagen area (PVCA). The CVF was calculated with the following formula: $CVF = \text{collagen area} / \text{total area of each microscopic field of view}$. Five randomly selected fields of view were analyzed, and the cardiac CVF was expressed as the mean CVF of the five fields. The PVCA was calculated using the following formula: $PVCA = \text{area of collagen surrounding the arterioles in the ventricular wall} / \text{arterial lumen area}$. In each sample, four arterioles in the ventricular wall were selected, and the cross section of the arterioles was analyzed. The mean PVCA was considered the final cardiac PVCA.

2.8. Statistical Analysis. The data analysis was conducted using SPSS 19.0 software. Most data were shown as the means \pm standard deviations (SD), whereas the count data were presented as the incidence rate or constitute ratio. All data were analyzed with a normality test and homogeneity-of-variance test. If the data were normally distributed and

met the assumption of homogeneity of variances, the comparison of the means between the two groups was performed with Student's *t*-test, and the comparison between multiple groups was conducted using a one-way analysis of variance (ANOVA). If the data failed to show homogeneity of variance, the comparison between the two groups was analyzed with the Mann-Whitney test, whereas the comparison between multiple groups was analyzed with the Kruskal-Wallis test. The comparison of the heart rate was performed with Fisher's exact test. A *P* value of less than 0.05 was considered statistically significant.

3. Results

3.1. Safety of the RDN Procedure. No deaths occurred in the experiment; ten dogs had hematomas at the puncture sites. After reapplying pressure and bandages, the dogs suffered no sequelae. During the ablation procedure, five dogs experienced renal artery spasm. These dogs were given nitroglycerin injections. Approximately 10 min after the injection, renal artery spasm was alleviated. Renal angiography was conducted immediately after the RDN procedure. No renal artery dissection or thrombosis was detected. The dogs were reexamined at 1, 3, and 6 months after the RDN procedure, and renal arteriography showed no evidence of renal artery stenosis.

3.2. Changes in Body Weight, Heart Rate, Blood Lipid Level, Renal Function, and Blood Pressure in the Experimental Dogs (Table 1, Figure 1). As shown in Table 1, no statistical differences were found in baseline body weight, heart rate, blood lipid level, creatinine level, cystatin C level, or blood pressure level between the three groups ($P > 0.05$). After the establishment of the hypertension model (before the RDN procedure), the body weight, low-density lipoprotein (LDL) level, total cholesterol (TC) level, triglyceride (TG) level, SBP level, and DBP level were significantly increased in the animals of the RDN group and the sham-operated group relative to the baselines and those of the control group ($P < 0.05$). Meanwhile, no statistical differences were detected in the above indicators between the RDN group and sham-operated group ($P > 0.05$). Heart rate was slightly increased in the RDN group and the sham-operated group after the establishment of the model relative to the baseline and the control group ($P > 0.05$). The body weights of animals in the RDN group and the sham-operated group also were not significantly increased after the RDN procedure relative before the RDN procedure ($P > 0.05$). Heart rate was slightly decreased in the dogs in the RDN group at 1, 3, and 6 months after the RDN procedure. However, no statistical differences were detected in heart rates before and after the RDN procedure ($P > 0.05$). At 1, 3, and 6 months after the RDN procedure, the heart rate was slightly raised in the RDN group and the sham-operated group relative to the control group ($P > 0.05$). The creatinine and cystatin C levels in the animals of the RDN group were slightly different from those before the RDN procedure at 1, 3, and 6 months after the RDN procedure. In addition, there were no significant differences in creatinine and cystatin C levels between the RDN group

TABLE 1: Changes in body weight, heart rate, blood pressure, blood lipid levels, and renal function in experimental dogs (control group ($n = 20$), sham-operated group ($n = 19$), and RDN group ($n = 19$, $\bar{x} \pm S$)).

Group	BW (kg)	HR (times/min)	SBP (mmHg)	DBP (mmHg)	TC (mmol/l)	TG (mmol/l)	LDL (mmol/l)	Cr (mg/dl)	CC (mmol/l)
Control group									
Baseline	12.3 ± 1.9	132.7 ± 23.9	125.7 ± 6.0	73.6 ± 6.0	5.12 ± 0.82	0.44 ± 0.12	0.11 ± 0.03	55.83 ± 10.08	0.21 ± 0.03
Preprocedure	13.1 ± 1.2	124.3 ± 6.0	129.7 ± 6.8	75.3 ± 10.6	4.80 ± 0.57	0.47 ± 0.20	0.09 ± 0.03	52.83 ± 15.22	0.20 ± 0.03
1 month	13.2 ± 1.1	122.9 ± 17.61	130.8 ± 6.5	77.3 ± 13.4				50.33 ± 7.58	0.16 ± 0.04
3 months	13.3 ± 1.0	125.4 ± 18.26	130.8 ± 6.5	81.6 ± 4.6				48.00 ± 8.22	0.17 ± 0.03
6 months	13.3 ± 0.8	124.3 ± 21.57	127.8 ± 3.6	78.2 ± 7.4	4.95 ± 0.47	0.49 ± 0.14	0.10 ± 0.04	54.00 ± 2.28	0.18 ± 0.03
Sham-operated group									
Baseline	12.3 ± 0.5	129.6 ± 11.7	124.7 ± 8.2	76.4 ± 8.4	5.41 ± 0.81	0.46 ± 0.09	0.10 ± 0.02	57.75 ± 6.75	0.21 ± 0.03
Preprocedure	17.5 ± 2.7 ^{ab}	141.3 ± 13.5	151.6 ± 12.3 ^{ab}	95.1 ± 9.2 ^{ab}	7.73 ± 1.20 ^{ab}	0.56 ± 0.18 ^{ab}	0.21 ± 0.08 ^{ab}	52.37 ± 9.05	0.20 ± 0.05
1 month	17.6 ± 2.9 ^{ab}	136.5 ± 8.72	153.7 ± 13.7 ^{ab}	93.2 ± 12.1 ^{ab}				51.50 ± 7.91	0.18 ± 0.05
3 months	18.3 ± 1.8 ^{ab}	140.5 ± 17.17	152.5 ± 12.6 ^{ab}	91.6 ± 9.7 ^{ab}				53.25 ± 5.57	0.19 ± 0.04
6 months	18.5 ± 1.9 ^{ab}	143.9 ± 18.01	155.8 ± 8.5 ^{ab}	95.8 ± 16.0 ^{ab}	7.95 ± 1.14 ^{ab}	0.61 ± 0.15 ^{ab}	0.20 ± 0.05 ^{ab}	54.25 ± 3.69	0.20 ± 0.03
RDN group									
Baseline	11.8 ± 0.8	131.5 ± 10.7	123.7 ± 10	77.1 ± 9.6	5.41 ± 0.81	0.50 ± 0.13	0.12 ± 0.05	53.33 ± 12.32	0.21 ± 0.05
Preprocedure	17.6 ± 2.0 ^{ab}	143.7 ± 14.2	153.1 ± 9.5 ^{ab}	92.5 ± 7.6 ^{ab}	7.84 ± 0.88 ^{ab}	0.56 ± 0.12 ^{ab}	0.23 ± 0.06 ^{ab}	47.22 ± 12.39	0.21 ± 0.05
1 month	17.7 ± 2.1 ^{ab}	133.3 ± 12.76	134.6 ± 8.4 ^{cd}	82.9 ± 7.0 ^{cd}				46.22 ± 6.94	0.16 ± 0.04
3 months	17.9 ± 2.4 ^{ab}	131.4 ± 15.08	131.4 ± 10.4 ^{cd}	82.9 ± 7.0 ^{cd}				47.00 ± 7.48	0.17 ± 0.03
6 months	18.6 ± 2.3 ^{ab}	131.2 ± 22.18	129.6 ± 8.4 ^{cd}	79.4 ± 5.3 ^{cd}	7.23 ± 1.27 ^{ab}	0.56 ± 0.13 ^{ab}	0.18 ± 0.07 ^{ab}	50.44 ± 4.58	0.18 ± 0.03

^aCompared with baseline, $P < 0.05$. ^bCompared with the control group, $P < 0.05$. ^cCompared with the sham-operated group, $P < 0.05$. ^dCompared with preprocedure, $P < 0.05$. BW: body weight; HR: heart rate; SBP: systolic blood pressure; DBP: diastolic blood pressure; TC: total cholesterol; TG: triglycerides; LDL: low-density lipoprotein; Cr: creatinine; CC: cystatin C.

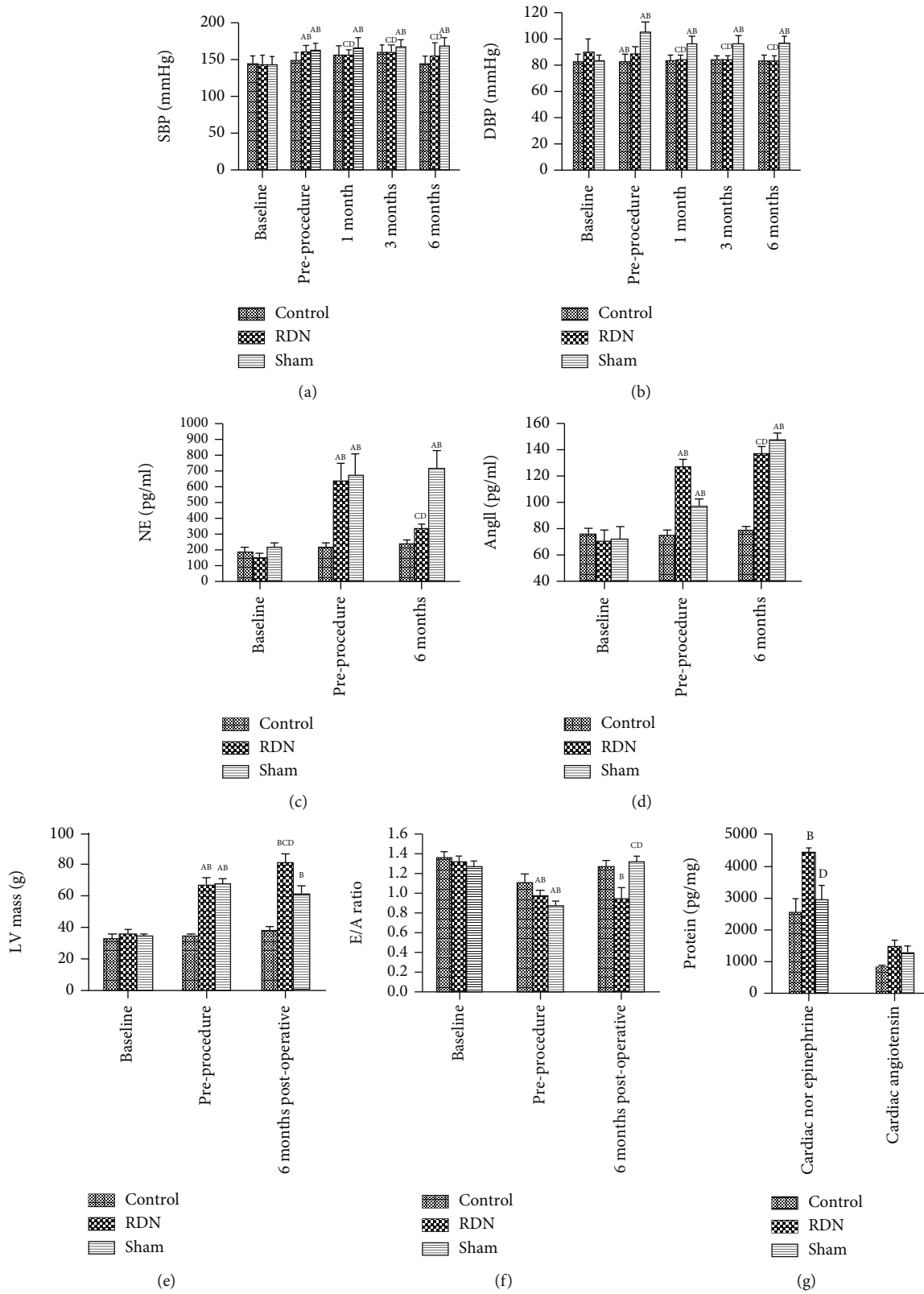


FIGURE 1: Changes in blood pressure, left ventricular mass (LVM), peak E/A ratio, norepinephrine (NE), and angiotensin II (AngII) in experimental dogs. ^ACompared with baseline, $P < 0.05$. ^BCompared with the control group, $P < 0.05$. ^CCompared with the sham group, $P < 0.05$. ^DCompared with preprocedure, $P < 0.05$.

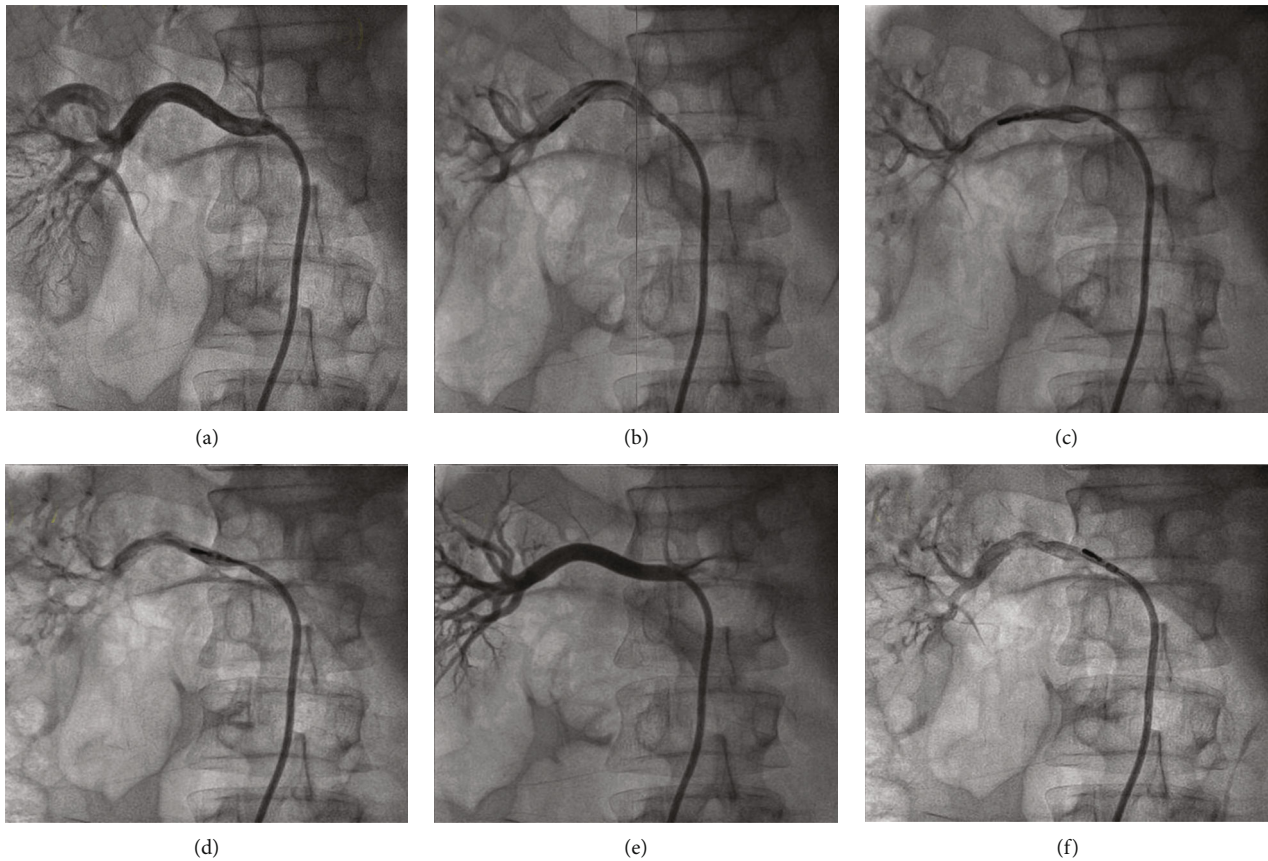


FIGURE 2: RDN procedure: (a) right renal arteriography before ablation; (b) ablation of lower wall of the right renal artery; (c) ablation of anterior wall of the right renal artery; (d) ablation of posterior wall of the right renal artery; (e) ablation of upper wall of the right renal artery; (f) right renal arteriography after ablation.

and sham-operated group or between the RDN group and the control group at the same time points after the RDN procedure ($P > 0.05$).

The SBP and DBP levels were markedly decreased in the RDN group at 1, 3, and 6 months after the RDN procedure. At each time point after the RDN procedure, the SBP and DBP levels were decreased in the RDN group relative to those of the sham-operated group ($P < 0.05$). After the RDN procedure, the RDN group had similar blood pressure as compared to that in the control group. The difference in blood pressure level was not significant ($P > 0.05$). No statistical changes were detected in the levels of SBP and DBP in the sham-operated group at various time points after the procedure ($P > 0.05$) (Table 1, Figure 2).

3.3. Changes in Kidney NE and AngII in the Experimental Dogs. As shown in Table 2 and Figure 1, no statistical differences were found in the levels of kidney NE and AngII between the control group, RDN group, and sham-operated group ($P > 0.05$). After the establishment of the hypertension model, the levels of kidney NE and AngII were drastically increased in the RDN group and sham-operated group in comparison with the baselines and the control group (all $P < 0.05$). No statistical differences were found in the serum kidney NE and AngII levels between the RDN group and

the sham-operated group ($P > 0.05$). Compared with baseline, the level of serum AngII was slightly elevated in the control group after the establishment of the model ($P > 0.05$). After 6 months of the RDN procedure, the serum levels of NE and AngII were markedly decreased in the RDN group relative to the NE and AngII levels before the procedure and in the sham-operated group after the procedure ($P < 0.05$). After 6 months of the RDN procedure, the levels of NE and AngII in the left ventricular myocardial tissues were drastically decreased in the RDN group relative to the sham-operated group, whereas the AngII level was higher in the RDN group relative to the control group (all $P < 0.05$). In addition, the sham-operated group had significantly higher levels of NE and AngII in the left ventricular myocardial tissues relative to the control group ($P < 0.05$).

3.4. Echocardiographic Evaluation of Structural Cardiac Changes in the Experimental Dogs. As shown in Table 3, no statistical differences were detected in baseline LVM, LVMI, and peak E/A ratio ($P > 0.05$) between the three groups. After the establishment of the model, the LVM and LVMI were drastically increased, while the peak E/A ratio was statistically reduced, in the RDN group and the sham-operated group relative to the baselines and the control group ($P < 0.05$). At 6 months after the RDN procedure, LVM

TABLE 2: Changes in levels of norepinephrine (NE) and angiotensin II (AngII) in experimental dogs (control group ($n = 20$), sham-operated group ($n = 19$), and RDN group ($n = 19$, $\bar{x} \pm S$)).

Group	NE (pg/ml)	AngII (pg/ml)	Myocardial NE (pg/mg)	Myocardial AngII (pg/mg)
Control group				
Baseline	123.36 \pm 80.16	66.48 \pm 5.19		
Preprocedure	141.13 \pm 52.17	67.84 \pm 8.03		
6 months	180.82 \pm 77.03	69.33 \pm 2.58	1953.5 \pm 606.7	963.0 \pm 192.2
Sham-operated group				
Baseline	140.16 \pm 70.63	63.40 \pm 8.80		
Preprocedure	553.2 \pm 202.90 ^{ab}	130.40 \pm 8.3 ^{ab}		
6 months	609.20 \pm 144.36 ^{ab}	136.20 \pm 6.27 ^{ab}	4343.6 \pm 346.4 ^b	1217.1 \pm 186.9 ^b
RDN group				
Baseline	106.12 \pm 52.01	63.31 \pm 7.19		
Preprocedure	531.07 \pm 159.58 ^{ab}	122.74 \pm 10.78 ^{ab}		
6 months	299.45 \pm 97.08 ^{acd}	88.49 \pm 5.69 ^{acd}	2272.9 \pm 774.0 ^c	1077.8 \pm 196.0 ^c

^aCompared with baseline, $P < 0.05$. ^bCompared with the control group, $P < 0.05$. ^cCompared with the sham-operated group, $P < 0.05$. ^dCompared with preprocedure, $P < 0.05$.

and LVMI were statistically lower in the RDN group relative to the sham-operated group ($P < 0.05$), whereas the peak E/A ratio was drastically increased in the RDN group relative to the sham-operated group ($P < 0.05$).

3.5. Pathological Changes in the Left Ventricular Myocardium of the Experimental Dogs. The left ventricular myocardium was subjected to H&E staining, and the results showed that the size and the cross-sectional area of the cardiomyocytes were statistically smaller in the RDN group relative to the sham-operated group (Figure 3). In addition, the cardiomyocytes in the RDN group were arranged in a more orderly manner. Electron microscopy revealed that the myocardial myofilaments were intact in the RDN group. Only a portion of the myofilaments in the cardiomyocytes were dissolved and ruptured. A fraction of the mitochondria and cells became swollen. By contrast, multifocal dissolution and fragmentation of the myofilaments were found in the sham-operated group. In the sham-operated group, mitochondrial and cellular swelling was evident, and the numbers of mitochondria and cells were statistically reduced. Masson's trichrome staining revealed that a small number of collagen fibers were deposited in the myocardial stroma and perivascular area in the RDN group, whereas a large number of collagen fibers were produced in the sham-operated group. As shown in Table 4, the Masson staining of the myocardium demonstrated that CVF was statistically increased in the sham-operated group and the RDN group relative to the control group ($P < 0.05$). In contrast, the CVF was statistically decreased in the RDN group relative to the sham-operated group ($4.32 \pm 1.33\%$ vs. $12.65 \pm 1.67\%$, $P < 0.05$). The PVCA was statistically increased in the sham-operated group relative to the control group ($P < 0.05$). No statistical differences in PVCA were detected between the RDN group and the control group ($P > 0.05$). In addition, PVCA was markedly decreased in the RDN group relative to the sham-operated group (0.85 ± 0.16 vs. 1.11 ± 0.19 , $P < 0.05$).

4. Discussion

In the present study, we found that an RDN procedure not only effectively decreased the blood pressure levels in hypertensive dogs induced via a high-fat diet but also reduced left ventricular hypertrophy and myocardial fibrosis and improved the left ventricular diastolic function. The functional improvement (diastolic function) of RDN has potential implications for heart failure, which is another area of clinical interest as a potential application for RDN [16].

A high-fat diet is now widely used to establish models of hypertension [17]. Specifically, neurohormonal and hemodynamic changes in the high-fat diet-induced hypertension model are virtually the same as the pathophysiological changes in human hypertension. Moreover, the high-fat diet-induced model is more likely to display LVH in the early stages of model development. According to previous studies, the construction of the hypertension model is considered successful if blood pressure levels in the dogs are measured at 17 ± 2 mmHg over the baseline after high-fat feeding [18]. In our research, after 3 months of high-fat feeding, the dogs exhibited statistically increased body weight and TC and LDL levels relative to the control group. The SBP level increased by more than 20 mmHg in 90.9% (20/22) of dogs fed with the high-fat diet, indicating the successful establishment of a hypertension model. The amplitude of the blood pressure increase was slightly higher than those reported in previous reports [18, 19]. Heart rates were also slightly elevated in dogs fed with the high-fat diet ($P > 0.05$).

Multiple studies on hypertension have demonstrated that increased sympathetic nerve activity plays a critical role in the pathological mechanisms of refractory hypertension. The RDN procedure developed in recent years ablates the afferent and efferent sympathetic nervous fibers located in the adventitia of the renal arteries through radiofrequency catheters, which blocks the pathways activated by renal sympathetic nerves, reduces the activity of sympathetic nerves, and eventually controls blood pressure. However, there is

TABLE 3: Echocardiographic evaluation of structural cardiac changes in experimental dogs (control group ($n = 20$), sham-operated group ($n = 19$), and RDN group ($n = 19$, $\bar{x} \pm S$)).

Group	LVEDD (mm)	IVST (mm)	LVPW (mm)	LVM (g)	LVMI (g/kg)	LVEF (%)	Peak E (cm/s)	Peak A (cm/s)	Peak E/A	LAD (mm)
Control group										
Baseline	25.7 ± 1.0	6.33 ± 0.5	6.0 (5.0-7.0)	30.7 ± 3.4	2.49 ± 0.1	61.2 ± 2.2	0.68 ± 0.2	0.52 ± 0.1	1.32 ± 0.1	19.8 ± 1.8
Preprocedure	25.3 ± 1.4	6.17 ± 0.4	6.0 (6.0-7.0)	30.9 ± 2.8	2.48 ± 0.2	60.3 ± 5.9	0.74 ± 0.1	0.63 ± 0.1	1.17 ± 0.3	21.0 ± 1.6
6 months	25.6 ± 1.5	6.0 ± 0.6	6.0 (6.0-7.0)	32.2 ± 2.8	2.35 ± 0.1	62.8 ± 5.0	0.79 ± 0.1	0.66 ± 0.1	1.20 ± 0.1	20.6 ± 1.5
Sham-operated group										
Baseline	25.6 ± 1.0	6.50 ± 0.5	6.0 (6.0-7.0)	31.9 ± 4.2	2.57 ± 0.3	61.6 ± 1.9	0.68 ± 0.1	0.51 ± 0.1	1.31 ± 0.1	19.5 ± 1.1
Preprocedure	28.6 ± 1.3 ^{ad}	9.88 ± 0.6 ^{ad}	8.0 (7.0-8.0) ^{ad}	62.8 ± 5.9 ^{ad}	3.62 ± 0.4 ^{ad}	64.2 ± 3.6	0.54 ± 0.1 ^{ad}	0.59 ± 0.1	0.91 ± 0.1 ^{ad}	20.5 ± 1.3
6 months	28.1 ± 1.1 ^{ad}	10.0 ± 0.6 ^{ad}	8.0 (7.0-9.0) ^{ad}	65.1 ± 4.3 ^{ad}	3.63 ± 0.6 ^{ad}	61.8 ± 4.1	0.48 ± 0.1 ^{ad}	0.55 ± 0.1 ^{ad}	0.87 ± 0.4 ^{ad}	25.3 ± 1.6 ^{ad}
RDN group										
Baseline	25.1 ± 1.0	6.64 ± 0.5	6.0 (5.0-7.0)	32.0 ± 4.5	2.69 ± 0.2	62.0 ± 1.9	0.68 ± 0.1	0.51 ± 0.1	1.27 ± 0.1	19.8 ± 1.4
Preprocedure	29.1 ± 1.0 ^{ad}	10.0 ± 0.7 ^{ad}	7.0 (7.0-8.0) ^{ad}	62.3 ± 5.2 ^{ad}	3.57 ± 0.5 ^{ad}	62.0 ± 2.2	0.48 ± 0.1 ^{ad}	0.57 ± 0.1	0.83 ± 0.1 ^{ad}	20.5 ± 1.2
6 months	29.7 ± 1.9 ^{ad}	8.6 ± 0.8 ^{bc}	6.1 (6.0-7.0) ^{bc}	52.2 ± 4.4 ^{bc}	2.82 ± 0.1 ^{bc}	62.3 ± 3.1	0.70 ± 0.1 ^{bc}	0.56 ± 0.1	1.25 ± 0.1 ^{bc}	21.1 ± 1.2

^aCompared with baseline, $P < 0.05$. ^bCompared with preprocedure, $P < 0.05$. ^cCompared with the sham-operated group, $P < 0.05$. ^dCompared with the control group, $P < 0.05$. LVEDD: left ventricular end-diastolic diameter; IVST: interventricular septal thickness; LVPW: left ventricular posterior wall; LVM: left ventricular mass; LVMI: left ventricular mass index; LVEF: left ventricular ejection fraction; peak E: early peak diastolic velocity; peak A: peak atrial velocity; peak E/A: the ratio of peak E to peak A; LAD: left atrial diameter.

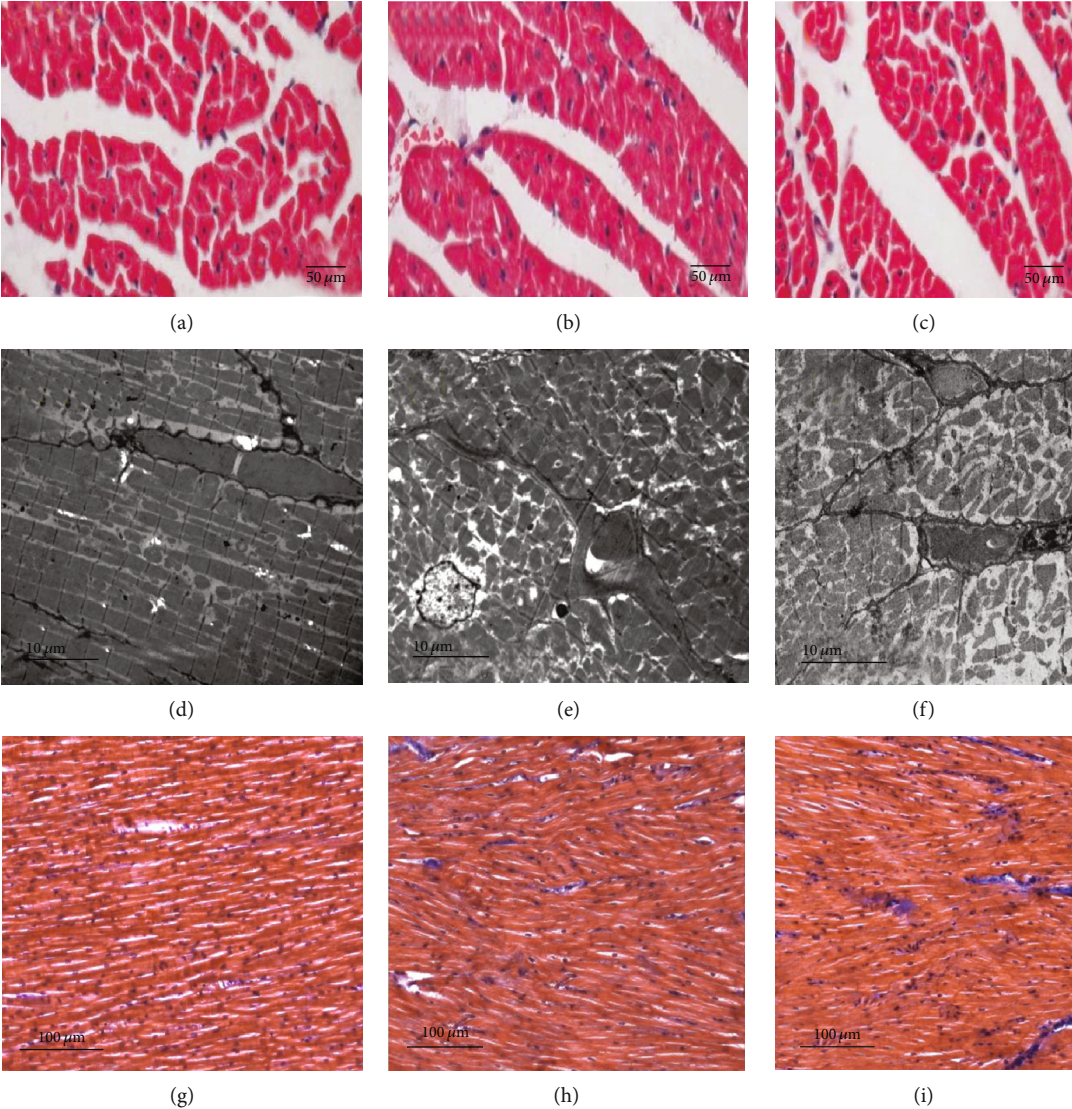


FIGURE 3: Continued.

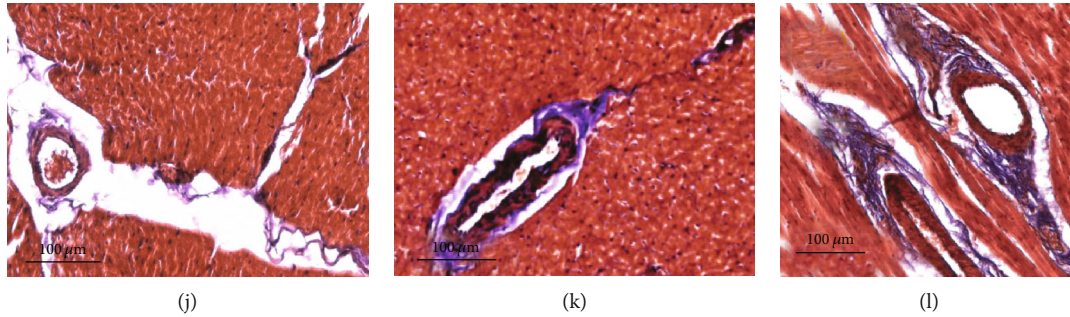


FIGURE 3: Pathological changes in the left ventricular myocardium of experimental dogs. (a–c) HE staining of myocardial tissue (light microscopy, 400x): (a) normal myocardial tissue in the control group, (b) the RDN group, and (c) the sham-operated group. The size and cross-sectional area of cardiomyocytes were statistically smaller in the RDN group than in the sham-operated group. Additionally, cardiomyocytes in the RDN group were arranged in a more orderly manner, similar to the control group. (d–f) Electron microscopy images of myocardial tissue (12000x): (d) the control group, (e) the RDN group: a portion of cardiomyocyte myofilaments was dissolved and ruptured, and a fraction of the mitochondria became swollen, and (f) the sham-operated group: multifocal dissolution and fragmentation of the myofilaments were apparent, mitochondrial and cellular swelling was evident, and the numbers of the mitochondria and cells were markedly reduced. (g–i) Masson's trichrome staining of myocardial tissue (light microscopy, 400x): (g) the control group, (h) the RDN group: a small number of collagen fibers were deposited in the myocardial stroma, and (i) the sham-operated group: large numbers of collagen fibers were produced in the myocardial stroma (red indicates cardiomyocytes, blue indicates collagen fibers, and red arrow points to collagen fiber). (j–l) Masson's trichrome staining of myocardial tissue (light microscopy, 400x): (j) the control group, (k) the RDN group: a small number of collagen fibers were deposited in the perivascular area, and (l) the sham-operated group: large numbers of collagen fibers were produced in the perivascular area (red indicates cardiomyocytes, blue indicates collagen fibers, and red arrow points to collagen fiber).

TABLE 4: Changes in collagen volume fraction (CVF) and perivascular circumferential collagen area (PVCA) in the left ventricular myocardium in experimental dogs ($\bar{x} \pm S$).

Group	Parameters	
	CVF (%)	PVCA
Control ($n = 10$)	2.241 ± 0.67	0.67 ± 0.11
Surgically treated ($n = 10$)	4.32 ± 1.33^a	0.85 ± 0.16
Sham-operated ($n = 10$)	12.65 ± 1.67^{ab}	1.11 ± 0.19^{ab}

^aCompared with the control group, $P < 0.05$. ^bCompared with the RDN group, $P < 0.05$.

considerable controversy regarding the clinical efficacy of RDN. The reported clinical efficacy of RDN varies greatly between studies [9, 20]. Specifically, in the SYMPPLICITY HTN-3 trial, the 6-month follow-up results failed to meet the primary endpoint of effectively reducing blood pressure levels [20]. However, some researchers have supported the notion that experimental results may be influenced by a multiplicity of practice-specific factors, such as a short learning curve and follow-up time, as well as defects in the design of surgical instruments [9, 20]. Therefore, as a new technology, RDN requires further exploration and improvement. In this study, the blood pressure levels of the experimental animals were strictly monitored. The SBP and DBP levels were statistically decreased in the RDN group at 1, 3, and 6 months after the RDN procedure as compared with the SBP and DBP levels before RDN and in the sham-operated group at the same time points ($P < 0.05$). At 6 months after RDN, dogs in the RDN group maintained near-normal blood pressure levels. By contrast, the blood pressure levels were statistically increased in the sham-operated group relative to the control

group. The results indicated that RDN had a statistical anti-hypertensive effect that was stable and long lasting. The results were similar to that of Dijk et al., and in spontaneous hypertension rats, the progressions of renal injury, cardiac remodeling, and increased blood pressure were regulated by renal sympathetic activities because they were inhibited by the RDN procedure [21]. Selejan et al. showed that sympathetic activity suppressed sRAGE/RAGE balance through the sympathetic modulation accomplished by the RDN procedure and thus prevented RAGE-induced cardiac lesions in subjects with hypertension and metabolic syndrome [22]. However, unlike the existing literature, this study uses Beagle dogs as target animals to further verify the application of RDN in a large-animal model. Comparing the body weights before and after the RDN procedure, the RDN group and the sham-operated group exhibited insignificantly increased body weights after RDN treatment ($P > 0.05$). The results may be related to the continued high-fat feeding after RDN. No statistical difference was found in body weights between the RDN group and sham-operated group at 6 months after RDN. Therefore, the effect of body weight on blood pressure can be excluded. We also compared heart rates before and after the RDN procedure and found that heart rate was reduced in the RDN group at various time points after RDN. In addition, the heart rate was slightly lower in the RDN group relative to the sham-operated group. Standard radiofrequency catheters were used in the present study. No substantial differences exist between the catheters used in the present study and Simplicity catheters (Medtronic, Inc.) in terms of catheter material, radiofrequency energy source, and mode of ablation. The main differences lie in the length of the ablation electrode at the head portion of the catheter and the shape of the distal end of the catheter. The length

of the ablation electrode on the standard radiofrequency catheter was 4 mm, which ensures an increase in the contact area with the renal artery, as well as the ablation and injury of additional renal sympathetic nerves. The employment of the standard radiofrequency catheter is conducive to controlling the ablation temperature, reducing renal artery intimal injury, and increasing the safety of the procedure. The safety and effectiveness of the standard radiofrequency catheters have been confirmed by our previous investigation and studies conducted by other researchers [15, 23, 24].

During the RDN procedure, the ablation power was set to 10 W, which was higher than the power recommended for Simplicity catheters. The pathological results of our previous animal study showed that the application of an ablation power of 8 W induced minimal renal nerve damage and a poor antihypertensive effect (data not shown). The reason for the phenomenon may be that the length of the ablation electrode on the standard radiofrequency catheter was 4 mm. The standard radiofrequency catheter offered a larger effective ablation area and dissipated heat more quickly. Therefore, a power increase is necessary to effectively damage the renal sympathetic nerves in the adventitia of the renal arteries. A better ablation catheter should be designed to increase the effect of RDN. In the present study, ten beagles developed subcutaneous hematomas after the RDN procedure, which was related to the extensive femoral artery injury caused by the 8F arterial sheath, which had a large diameter, and inadequate hemostatic press after RDN. However, after reapplying the hemostatic bandage, the dogs all recovered within 1 week. At 1, 3, and 6 months after the RDN procedure, the experimental dogs were reexamined and subjected to renal arteriography. Long-term complications, such as renal artery stenosis, renal artery dissection, and aneurysm, were not detected. These findings were consistent with the results of RDN-related clinical trials and supported the safety of RDN [9, 20].

The major left ventricular structural and functional changes caused by hypertension are LVH and myocardial fibrosis. Evidence shows that an increase in the LVM precedes the onset of overt hypertension [25, 26]. Left ventricular hypertrophy can be diagnosed via an electrocardiogram (ECG) or color Doppler echocardiography [25, 26]. Electrocardiogram diagnoses mild LVH at a rate that is 7-35% lower than echocardiography and diagnoses moderate-to-severe LVH at rates 10-50% lower than echocardiography [25]. At present, LVH is defined as an increase in LVM, which can be expressed as ventricular wall thickening, cardiac chamber enlargement, or both. Hypertension induces an increase in LVM mainly through a chronic increase in left ventricular afterload, neuroendocrine activation, and genetic factors. The pathophysiological mechanisms of LVH involve a statistical increase in the number and size of sarcomeres in every cardiomyocyte. In addition, hypertension may lead to myocardial interstitial fibrosis [27]. Both LVH and myocardial fibrosis increase left ventricular stiffness, resulting in left ventricular diastolic dysfunction. The present study showed that LVM and LVMI were statistically increased, while peak E/A ratio was markedly reduced, in the RDN group and sham-operated group after the establishment of the model relative to baseline and the control group, indicating that

LVH and diastolic dysfunction occurred early in dogs with hypertension. However, at 6 months after the RDN procedure, the LVM and LVMI were statistically decreased in the RDN group relative to the sham-operated group, whereas the peak E/A ratio was drastically increased, which was consistent with the results of Jiang et al. [28]. The results indicated that RDN alleviated LVH and improved diastolic function. In their study, the RDN procedure was performed in spontaneous hypertension rats, and the results showed that blood pressure and LVMI were statistically reduced after the surgery. The results indicated that RDN alleviated LVH and improved diastolic function. In addition, H&E staining of the left ventricular myocardium showed that the size and cross-sectional area of the cardiomyocytes were statistically smaller in the RDN group relative to the sham-operated group. The results further confirmed that the RDN procedure alleviated LVH from the histopathological perspective.

Myocardial fibrosis refers to the excess accumulation of collagen fibers, the statistical elevation of collagen concentration, or a change in the collagenous components of the normal tissue structure of the myocardium. In clinical practice, collagen-specific staining is often performed on endomyocardial biopsy or autopsy tissues, and the CVF and PVCA are often calculated to evaluate the proportion and extent of interstitial fibrosis and perivascular fibrosis [29]. In the present study, the Masson staining of the myocardium showed that myocardial fibrosis occurred in both the RDN group and the sham-operated group. However, CVF and PVCA were statistically lower in the RDN group relative to the sham-operated group ($P < 0.05$). The results further demonstrated that the RDN procedure alleviated left ventricular myocardial fibrosis from a histopathological perspective.

A great deal of studies have shown that AngII plays a vital role in the development of LVH in patients with hypertension [30, 31]. Research has revealed that, in transgenic rats exhibiting the overexpression of the angiotensinogen gene, the contributing role of AngII in the development of myocardial hypertrophy appears to be independent of hypertension [32]. However, it is unclear whether the renin-angiotensin-aldosterone system (RAAS) regulates the production of Ang II through *in situ* renin release or the uptake of circulating renin [33]. Regression analysis has shown that plasma AngII is statistically correlated with LVM and that this correlation is independent of blood pressure and body size [34, 35]. The direct role of increased levels of NE on the human heart beyond systemic BP changes in humans has been shown most convincingly with a radiotracer dilution methodology in hypertensive subjects [36]. The RAAS is also closely related to myocardial fibrosis. AngII promotes the synthesis of stromal collagen by cardiac fibroblasts. The mechanism by which AngII induces myocardial fibrosis involves the binding of AngII to Ang II type 1 (AT1) receptor. The binding of AngII to the AT1 receptor activates extracellular signal-regulated kinase (ERK) through tyrosine kinase pathways; induces fibroblast proliferation; and activates the expression of collagen, fibrin, and integrin genes, thereby inducing myocardial fibrosis [37].

The present study showed that, after the successful establishment of the hypertension model, the serum NE and AngII levels were statistically higher in the RDN group and sham-operated group relative to the control group. The results indicated that the increased activities of the sympathetic nerves and RAAS represented an important mechanism underlying high-fat diet-induced hypertension. After the RDN procedure, the serum level of NE and AngII was markedly reduced in the RDN group relative to the sham-operated group, indicating that RDN successfully reduced the activity of sympathetic nerves and the RAAS. Specifically, we examined, for the first time, local NE and AngII levels in myocardial tissues at 6 months after RDN and found that the local NE and AngII levels in the left ventricular myocardium were significantly reduced in the RDN group relative to the sham-operated group. The results indicated that RDN reduced the level of NE and AngII in the circulation and myocardial tissues by decreasing the activity of the sympathetic nerves and RAAS, thereby reducing the direct injury to cardiomyocytes, mediated by NE and AngII. In addition to lowering blood pressure, reducing NE and AngII levels may represent another important mechanism by which RDN protects left ventricular structure and function. Research shows that Ang II can increase the activities of the sympathetic nervous system at various levels by facilitating NE release [38, 39]. Chen et al. also showed that RDN alleviates the onset of heart failure by downregulating angiotensin levels [40]. A study of an animal model of abdominal aortic coarctation revealed that blood pressure is not affected after sympathectomy, whereas LVH is statistically deduced, indicating that the anti-LVH effect of sympathectomy is independent of blood pressure [41]. Current clinical research data also suggest that RDN reduces LVH and improves diastolic function, independent of the blood pressure-lowering effect [13]. Therefore, we have reason to believe that RDN alleviates LVH and fibrosis by reducing NE and AngII levels in the circulation and myocardial tissues and that the above effects on the part of RDN are also independent of its blood pressure-lowering effect. The present study provides important large-animal experiment-derived preclinical evidence for RDN application to treat hypertension complicated by left ventricular remodeling.

One limitation of this study was the small sample size. Due to the sample size, we were not able to sacrifice the animals at 1 month and 3 months after the RDN procedure to examine structural changes in cardiac tissues. Therefore, it is impossible to compare the cardiac structure at the above time points with that at 6 months after RDN. In addition, the present study failed to further investigate the relationship between NE/AngII levels and hypertension-induced cardiac damage from the prospective of molecular mechanisms. In addition, the NE content in the denervated kidneys was not measured to assess the difference between the denervated kidney and the sham-operated group or the effect of RDN on glucose and other glucose metabolism parameters. The above issues will be addressed in our future studies. We will attempt to further clarify the potential mechanisms of action of RDN, develop and improve this novel treatment method, and provide new ideas about clinical applications of RDN.

Abbreviations

AngII:	Angiotensin II
CVF:	Collagen volume fraction
DBP:	Diastolic blood pressure
EF:	Ejection fraction
HE staining:	Hematoxylin-eosin staining
IVSTd:	Interventricular septal depth
LAD:	Left atrial diameter
LVEDD:	Left ventricular end-diastolic diameter
LVEF:	Left ventricular ejection fraction
LVH:	Left ventricular hypertrophy
LVM:	Left ventricular mass
LVMI:	Left ventricular mass index
LVSD:	Left ventricular end-systolic diameter
LVPWT:	Left ventricular posterior wall depth
NE:	Norepinephrine
SBP:	Systolic blood pressure
RAAS:	Renin-angiotensin-aldosterone system
RDN:	Renal sympathetic denervation
PVCA:	Perivascular collagen area.

Data Availability

All data generated or analyzed during this study are included in this article. The datasets used and/or analyzed during the current study are available from the corresponding author on reasonable request.

Ethical Approval

All experimental protocols were approved by the Institutional Animal Care and Use Committee of the Third Xiangya Hospital of Central South University and were performed according to the National Institutes of Health's *Guide for the Care and Use of Laboratory Animals* and the guidelines of the Animal Welfare Act.

Consent

Consent is not applicable. This article does not contain any studies with human participants performed by any of the authors.

Conflicts of Interest

The authors have no conflicts of interest to declare.

Authors' Contributions

Shan Tu is responsible for the conception and study design. Zhi-Jie Shen is responsible for the data acquisition. Xiao-Yan Wang is responsible for the data analysis. Li-Xiong Zeng is responsible for the manuscript drafting. Zhi-Hui Zhang is responsible for the manuscript revising. All authors have read and approved the final version of this manuscript to be published.

Acknowledgments

This study was funded by the Key Science and Technology Project of the Science and Technology Department of Hunan Province of China (2012WK2002).

References

- [1] Collaborators GBDHL, "Hearing loss prevalence and years lived with disability, 1990-2019: findings from the Global Burden of Disease Study 2019," *The Lancet*, vol. 397, no. 10278, pp. 996-1009, 2021.
- [2] I.-M. Lee, E. J. Shiroma, F. Lobelo, P. Puska, S. N. Blair, and P. T. Katzmarzyk, "Effect of physical inactivity on major non-communicable diseases worldwide: an analysis of burden of disease and life expectancy," *Lancet*, vol. 380, no. 9838, pp. 219-229, 2012.
- [3] F. H. Messerli, S. F. Rimoldi, and S. Bangalore, "The transition from hypertension to heart failure: contemporary update," *JACC: Heart Failure*, vol. 5, no. 8, pp. 543-551, 2017.
- [4] L. Thapa, S. Shrestha, R. Kandu et al., "Prevalence of stroke and stroke risk factors in a south-western community of Nepal," *Journal of Stroke and Cerebrovascular Diseases*, vol. 30, no. 5, 2021.
- [5] L. Thapa, S. Shrestha, R. Kandu et al., "Influence of dietary iron intake restriction on the development of hypertension in weanling prehypertensive rats," *Heart and Vessels*, vol. 33, no. 7, pp. 820-825, 2021.
- [6] X. Li, Q. Lu, Y. Qiu et al., "Direct cardiac actions of the sodium glucose co-transporter 2 inhibitor empagliflozin improve myocardial oxidative phosphorylation and attenuate pressure-overload heart failure," *Journal of the American Heart Association*, vol. 10, no. 6, article e018298, 2021.
- [7] P. L. Myhre, S. Selvaraj, and S. D. Solomon, "Management of hypertension in heart failure with preserved ejection fraction," *Current Opinion in Cardiology*, 2021.
- [8] A. R. De Caterina and A. M. Leone, "Why β -blockers should not be used as first choice in uncomplicated hypertension," *The American Journal of Cardiology*, vol. 105, no. 10, pp. 1433-1438, 2010.
- [9] H. Krum, M. P. Schlaich, P. A. Sobotka et al., "Percutaneous renal denervation in patients with treatment-resistant hypertension: final 3-year report of the Symplicity HTN-1 study," *The Lancet*, vol. 383, no. 9917, pp. 622-629, 2014.
- [10] M. Qiu, Q. Shan, C. Chen et al., "Renal sympathetic denervation improves rate control in patients with symptomatic persistent atrial fibrillation and hypertension," *Acta Cardiologica*, vol. 71, no. 1, pp. 67-73, 2016.
- [11] C. Ukena, F. Mahfoud, A. Spies et al., "Effects of renal sympathetic denervation on heart rate and atrioventricular conduction in patients with resistant hypertension," *International Journal of Cardiology*, vol. 167, no. 6, pp. 2846-2851, 2013.
- [12] F. Mahfoud, D. Urban, D. Teller et al., "Effect of renal denervation on left ventricular mass and function in patients with resistant hypertension: data from a multi-centre cardiovascular magnetic resonance imaging trial," *European Heart Journal*, vol. 35, no. 33, pp. 2224-2231, 2014.
- [13] S. H. Schirmer, M. M. Y. A. Sayed, J.-C. Reil et al., "Improvements in left ventricular hypertrophy and diastolic function following renal denervation: effects beyond blood pressure and heart rate reduction," *Journal of the American College of Cardiology*, vol. 63, no. 18, pp. 1916-1923, 2014.
- [14] M. C. Brandt, F. Mahfoud, S. Reda et al., "Renal sympathetic denervation reduces left ventricular hypertrophy and improves cardiac function in patients with resistant hypertension," *Journal of the American College of Cardiology*, vol. 59, no. 10, pp. 901-909, 2012.
- [15] J. R. Henegar, Y. Zhang, C. Hata, I. Narciso, M. E. Hall, and J. E. Hall, "Catheter-based radiofrequency renal denervation: location effects on renal norepinephrine," *American Journal of Hypertension*, vol. 28, no. 7, pp. 909-914, 2015.
- [16] I. Hopper, E. Gronda, U. C. Hoppe et al., "Sympathetic response and outcomes following renal denervation in patients with chronic heart failure: 12-month outcomes from the Symplicity HF feasibility study," *Journal of Cardiac Failure*, vol. 23, no. 9, pp. 702-707, 2017.
- [17] A. P. Rocchini, J. Q. Yang, M. J. Smith, and M. A. Supiano, "Serial changes in norepinephrine kinetics associated with feeding dogs a high-fat diet," *Journal of Clinical Hypertension*, vol. 12, no. 2, pp. 117-124, 2010.
- [18] T. E. Lohmeier, R. Iliescu, B. Liu, J. R. Henegar, C. Maric-Bilkan, and E. D. Irwin, "Systemic and renal-specific sympathoinhibition in obesity hypertension," *Hypertension*, vol. 59, no. 2, pp. 331-338, 2012.
- [19] G. Domingos-Souza, F. M. Santos-Almeida, C. A. Meschiari et al., "The ability of baroreflex activation to improve blood pressure and resistance vessel function in spontaneously hypertensive rats is dependent on stimulation parameters," *Hypertension Research*, 2021.
- [20] D. L. Bhatt, D. E. Kandzari, W. W. O'Neill et al., "A controlled trial of renal denervation for resistant hypertension," *The New England Journal of Medicine*, vol. 370, no. 15, pp. 1393-1401, 2014.
- [21] C. G. M. van Dijk, N. R. Oosterhuis, Y. J. Xu et al., "Distinct endothelial cell responses in the heart and kidney microvasculature characterize the progression of heart failure with preserved ejection fraction in the obese ZSF1 rat with cardiorenal metabolic syndrome," *Circulation. Heart Failure*, vol. 9, no. 4, article e002760, 2016.
- [22] S.-R. Selejan, D. Linz, A.-M. Tatu et al., "Sympathoadrenergic suppression improves heart function by upregulating the ratio of sRAGE/RAGE in hypertension with metabolic syndrome," *Journal of Molecular and Cellular Cardiology*, vol. 122, pp. 34-46, 2018.
- [23] J. Hawson, J. A. Harmer, M. Cowan et al., "Renal denervation for the management of refractory ventricular arrhythmias: a systematic review," *JACC: Clinical Electrophysiology*, vol. 7, no. 1, pp. 100-108, 2021.
- [24] M. Böhm, K. Kario, D. E. Kandzari et al., "Efficacy of catheter-based renal denervation in the absence of antihypertensive medications (SPYRAL HTN-OFF MED Pivotal): a multicentre, randomised, sham-controlled trial," *The Lancet*, vol. 395, no. 10234, pp. 1444-1451, 2020.
- [25] M. Yildiz, A. A. Oktay, M. H. Stewart, R. V. Milani, H. O. Ventura, and C. J. Lavie, "Left ventricular hypertrophy and hypertension," *Progress in Cardiovascular Diseases*, vol. 63, no. 1, pp. 10-21, 2020.
- [26] D. Lovic, P. Narayan, A. Pittaras, C. Faselis, M. Dumas, and P. Kokkinos, "Left ventricular hypertrophy in athletes and hypertensive patients," *Journal of Clinical Hypertension*, vol. 19, no. 4, pp. 413-417, 2017.

- [27] H. Lee, K. N. Kershaw, M. T. Hicken et al., "Cardiovascular disease among Black Americans: comparisons between the U.S. Virgin Islands and the 50 U.S. states," *Public Health Reports*, vol. 128, no. 3, pp. 170–178, 2013.
- [28] W. Jiang, L. Tan, Y. Guo, X. Li, X. Tang, and K. Yang, "Effect of renal denervation procedure on left ventricular hypertrophy of hypertensive rats and its mechanisms," *Acta Cirúrgica Brasileira*, vol. 27, no. 11, pp. 815–820, 2012.
- [29] R. Eiros, G. Romero-González, J. J. Gavira et al., "Does chronic kidney disease facilitate malignant myocardial fibrosis in heart failure with preserved ejection fraction of hypertensive origin?," *Journal of Clinical Medicine*, vol. 9, no. 2, p. 404, 2020.
- [30] J. Díez, "Diagnosis and treatment of myocardial fibrosis in hypertensive heart disease," *Circulation Journal*, vol. 72, Supplement A, pp. A8–12, 2008.
- [31] J. Díez, B. Lopez, A. Gonzalez, and R. Querejeta, "Clinical aspects of hypertensive myocardial fibrosis," *Current Opinion in Cardiology*, vol. 16, no. 6, pp. 328–335, 2001.
- [32] F. Z. Marques, E. Nelson, P.-Y. Chu et al., "High-fiber diet and acetate supplementation change the gut microbiota and prevent the development of hypertension and heart failure in hypertensive mice," *Circulation*, vol. 135, no. 10, pp. 964–977, 2017.
- [33] A. Nishiyama and H. Kobori, "Independent regulation of renin-angiotensin-aldosterone system in the kidney," *Clinical and Experimental Nephrology*, vol. 22, no. 6, pp. 1231–1239, 2018.
- [34] C. R. Gingles, R. Symon, S. J. Gandy et al., "Allopurinol treatment adversely impacts left ventricular mass regression in patients with well-controlled hypertension," *Journal of Hypertension*, vol. 37, no. 12, pp. 2481–2489, 2019.
- [35] H. Lee, Y.-H. Kong, K.-H. Kim, J. Huh, I.-S. Kang, and J. Song, "Left ventricular hypertrophy and diastolic function in children and adolescents with essential hypertension," *Clinical Hypertension*, vol. 21, no. 1, p. 21, 2015.
- [36] M. P. Schlaich, D. M. Kaye, E. Lambert, M. Sommerville, F. Socratous, and M. D. Esler, "Relation between cardiac sympathetic activity and hypertensive left ventricular hypertrophy," *Circulation*, vol. 108, no. 5, pp. 560–565, 2003.
- [37] J. Galatioto, C. I. Caescu, J. Hansen et al., "Cell type-specific contributions of the angiotensin II type 1a receptor to aorta homeostasis and aneurysmal disease-brief report," *Arteriosclerosis, Thrombosis, and Vascular Biology*, vol. 38, no. 3, pp. 588–591, 2018.
- [38] C. L. McGowan, C. F. Notarius, A. McReynolds et al., "Effect of angiotensin AT1 receptor blockade on sympathetic responses to handgrip in healthy men," *American Journal of Hypertension*, vol. 24, no. 5, pp. 537–543, 2011.
- [39] J. Struck, P. Muck, D. Trübger et al., "Effects of selective angiotensin II receptor blockade on sympathetic nerve activity in primary hypertensive subjects," *Journal of Hypertension*, vol. 20, no. 6, pp. 1143–1149, 2002.
- [40] W.-J. Chen, H. Liu, Z.-H. Wang et al., "The impact of renal denervation on the progression of heart failure in a canine model induced by right ventricular rapid pacing," *Frontiers in Physiology*, vol. 10, 2020.
- [41] J. R. Wright, A. a. E. Shurrab, A. Cooper, P. R. Kalra, R. N. Foley, and P. A. Kalra, "Left ventricular morphology and function in patients with atherosclerotic renovascular disease," *Journal of the American Society of Nephrology*, vol. 16, no. 9, pp. 2746–2753, 2005.

Research Article

Recombinant Human Thymosin Beta-4 Protects against Mouse Coronavirus Infection

Rui Yu, Yunyun Mao, Kai Li, Yanfang Zhai, Yue Zhang, Shuling Liu, Yuemei Gao, Zhengshan Chen, Yanhong Liu, Ting Fang, Mengsu Zhao, Ruihua Li, Junjie Xu , and Wei Chen 

Beijing Institute of Biotechnology, Beijing 100071, China

Correspondence should be addressed to Junjie Xu; xujunjie@sina.com and Wei Chen; cw0226@foxmail.com

Received 12 March 2021; Revised 25 March 2021; Accepted 31 March 2021; Published 21 April 2021

Academic Editor: Yaoyao Xia

Copyright © 2021 Rui Yu et al. This is an open access article distributed under the Creative Commons Attribution License, which permits unrestricted use, distribution, and reproduction in any medium, provided the original work is properly cited.

Coronaviruses (CoVs) are enveloped and harbor an unusually large (30–32 kb) positive-strand linear RNA genome. Highly pathogenic coronaviruses cause severe acute respiratory syndrome (SARS) (SARS-CoV and SARS-CoV-2) and Middle East respiratory syndrome (MERS) (MERS-CoV) in humans. The coronavirus mouse hepatitis virus (MHV) infects mice and serves as an ideal model of viral pathogenesis, mainly because experiments can be conducted using animal-biosafety level-2 (A-BSL2) containment. Human thymosin beta-4 (T β 4), a 43-residue peptide with an acetylated N-terminus, is widely expressed in human tissues. T β 4 regulates actin polymerization and functions as an anti-inflammatory molecule and an antioxidant as well as a promoter of wound healing and angiogenesis. These activities led us to test whether T β 4 serves to treat coronavirus infections of humans. To test this possibility, here, we established a BALB/c mouse model of coronavirus infection using mouse CoV MHV-A59 to evaluate the potential protective effect of recombinant human T β 4 (rhT β 4). Such a system can be employed under A-BSL2 containment instead of A-BSL3 that is required to study coronaviruses infectious for humans. We found that rhT β 4 significantly increased the survival rate of mice infected with MHV-A59 through inhibiting virus replication, balancing the host's immune response, alleviating pathological damage, and promoting repair of the liver. These results will serve as the basis for further application of rhT β 4 to the treatment of human CoV diseases such as COVID-19.

1. Introduction

Coronaviruses (CoVs) that cause severe acute respiratory syndrome (SARS), such as SARS-CoV/SARS-CoV-2, and Middle East respiratory syndrome (MERS), such as MERS-CoV, are members of a large family of enveloped, single-stranded, positive-strand RNA viruses. Coronaviruses infect vertebrates and may cause acute respiratory distress syndrome (ARDS) with high morbidity and mortality rates, depending on species [1, 2].

The novel coronavirus pneumonia (COVID-19) outbreak and subsequent global pandemic caused by SARS-CoV-2 commenced around the end of 2019. When this manuscript was submitted for publication, there were more than 100 million cases and more than 2 million deaths worldwide. SARS-CoV-2, which is the seventh known coronavirus that

infects humans, enters the respiratory system through the upper respiratory tract and eventually infects alveolar cells [3]. The virus continuously proliferates, destroys the alveoli, and enters the capillaries. As blood circulates, the “battlefield” is further expanded, causing pathologies such as conjunctivitis, pneumonia, diarrhea, anosmia, abnormal liver function, renal failure, and heart damage that culminates in severe disease [4].

Mouse coronaviruses, also known as mouse hepatitis viruses (MHVs), are histologically classified as respiratory strains such as MHV-1, MHV-2, MHV-3, MHV-A59, and MHV-JHM as well as enterophilic strains such as MHV-y and MHV-R1. The respiratory strain MHV-A59 used here, as well as SARS-CoV and SARS-CoV-2, are β -coronaviruses. MHV-A59 can spread to numerous target organs after replicating in nasal epithelial cells. MHV is an excellent model for

studying the pathogenesis, tropism, and virulence, as well as the host's antiviral immune response. Further, MHV serves as a model for SARS-CoV infection. Moreover, MHV readily infects mice but not humans, and experiments can be conducted using animal-biosafety level-2 (A-BSL2) containment instead of A-BSL3 that is required for handling SARS-CoV and SARS-CoV-2 [5].

Thymosin beta-4 (T β 4), an N-acetylated 43-amino acid residue peptide (molecular mass, 4960.5 Da; isoelectric point, 4.6) [6], is widely distributed among tissues of mammals and other vertebrates [7]. T β 4 possesses numerous biological activities such as inhibiting inflammation [8–13], preventing infection of wounds [14], inhibiting apoptosis [15–17] and scar formation [9, 15, 18], promoting cell migration and angiogenesis [19–21], accelerating collagen deposition, and upregulating the production of laminin-5 [22–27]. Nonclinical and clinical studies show the clinical importance of T β 4 for treating dry eye, cardiac failure [19, 28], lung fibrosis [29, 30], septic shock [8], liver injury [31], and acute ischemic kidney injury [32, 33]. T β 4 facilitates cardioprotection and regeneration of the ischemic heart by promoting the survival of cardiomyocytes through modulating the inflammatory environment and promoting neovascularization [28]. T β 4 possesses antioxidant, anti-inflammatory, and antifibrotic potential as demonstrated by studies of a mouse model of chronic liver injury [31]. In a rat model of ischemic acute kidney injury, the beneficial therapeutic effects of T β 4 are mediated through inhibition of extracellular matrix remodeling and apoptosis, as well as modulation of renal redox status and inflammation [33].

The multiple activities of T β 4 may be useful for treating coronavirus infection. Specifically, T β 4 may exert its biological activities at the molecular, cellular, and tissue levels to inhibit the “cytokine storm” caused by coronaviruses. Further, T β 4 may play an important role in reconstituting the immune response, inhibiting inflammation, reducing lung injury, ameliorating pulmonary fibrosis, and reducing systemic sequelae of coronavirus pneumonia.

As proof of principle, here, we used recombinant human T β 4 (rhT β 4) to evaluate the protective effect of rhT β 4 in a mouse model of MHV-A59 infection. Compared with chemically synthesized T β 4, rhT β 4 has numerous advantages such as uniform quality, unlimited scale of production, relatively low production costs, and minimal adverse environmental effects. The results provide an experimental basis for applying rhT β 4 to the treatment of human CoV infection.

2. Materials and Methods

2.1. Virus, Cells, Mice, and rhT β 4. MHV-A59 was acquired from Guangdong Laboratory Animals Monitoring Institute of China. DBT cells were provided by the Chinese Experimental Animal Resources Research Institute for Food and Drug Control. Uninfected and MHV-A59-infected cells were passaged and preserved in our laboratory. Female SPF BALB/c mice (18–20 g) were purchased from Beijing Vital River Laboratory Animal Technology Co., Ltd. All animal experiments were performed according to protocols approved by the Institutional Animal Care and Use Committee of Beijing Institu-

tion of Biotechnology (Identification code: IACUC-DWZX-2020-041; date of approval: 30 April 2020). Virus production and all animal experiments were performed in an A-BSL2 laboratory, and rhT β 4 was expressed and purified using our patented technology (Chinese invention patent No: ZL200910135972.0 and ZL201910498316.0) [34].

2.2. Reagents and Kits. The culture medium DMEM and fetal bovine serum (FBS) are products of Gibco. A Bio-Plex Pro Mouse Cytokine 23-plex Assay Kit (M60009RDPD) was purchased from Bio-Rad Laboratories, Inc. A Mouse C-Reactive Protein ELISA Kit (ab222511) was purchased from Abcam. An MHV-Ab ELISA Kit (DG30747M) was purchased from Beijing Winter Song Boye Biotechnology Co. Ltd, China. An RNeasy Plus Mini Kit (74136), a QuantiTect Reverse Transcription Kit (205311), and a QuantiTect Probe PCR Kit (204343) were purchased from QIAGEN. Paraformaldehyde (4%) was purchased from Beijing Solarbio Technology Co. Ltd, China. RNAsore reagent was purchased from TIANGEN Biotech (Beijing) Co. Ltd, China. The preparation of sections for histopathological analysis and hematoxylin-eosin (HE) staining of mouse organs was performed by Beijing Soonbio Technology Co., Ltd, China.

2.3. Virus Propagation and Titer Determination. DBT cells were cultured at 37°C in an atmosphere containing 5% CO₂ in DMEM containing 5% FBS in culture flasks filled to 90% capacity. The virus growth medium was then replaced with DMEM containing 2% FBS, and MHV-A59 (multiplicity of infection = 10) was added. The cells were monitored each day. When >75% of the cells exhibited cytopathic effects, the culture flask was frozen at –80°C and thawed. The supernatant was collected and centrifuged for 5 min at 1000 × g to remove cells. The supernatants were frozen and stored at –80°C. The TCID₅₀ of the virus was calculated using the method of Reed-Muench [35].

2.4. Infection of Mice and Administration of rhT β 4. SPF BALB/mice ($n = 24$) were randomly divided into the groups as follows: sham, placebo, and rhT β 4. Each of the eight mice in the sham group was intraperitoneally injected with 0.1 mL of normal saline (NS) daily from days 0 to 10 (Figure 1). The eight mice in the placebo group were each intraperitoneally injected with 2×10^3 TCID₅₀ of MHV-A59 on day 0, and 0.1 mL NS was intraperitoneally injected into each mouse once daily from days 1 to 10. The mice in the rhT β 4 group were intraperitoneally injected with 2×10^3 TCID₅₀ of MHV-A59 per mouse on day 0, and 300 μ g of rhT β 4 in 0.1 mL NS was intraperitoneally injected per mouse daily from days 1 to 10. The mice in each group were observed until day 14.

These experiments were then repeated with the same groups and dosing schedule, and the number of mice was increased to 12 in each group for next analysis.

The surviving mice were weighed on days 0, 2, 5, 8, and 14. Food consumption of each group was monitored by weighing the food on days 3, 6, 10, and 14. Blood was collected from the tail vein of surviving mice, and the serum was separated on days 1, 3, and 14. On days 3 and 14, 3 mice in each group were killed, and the liver, lung, and kidney

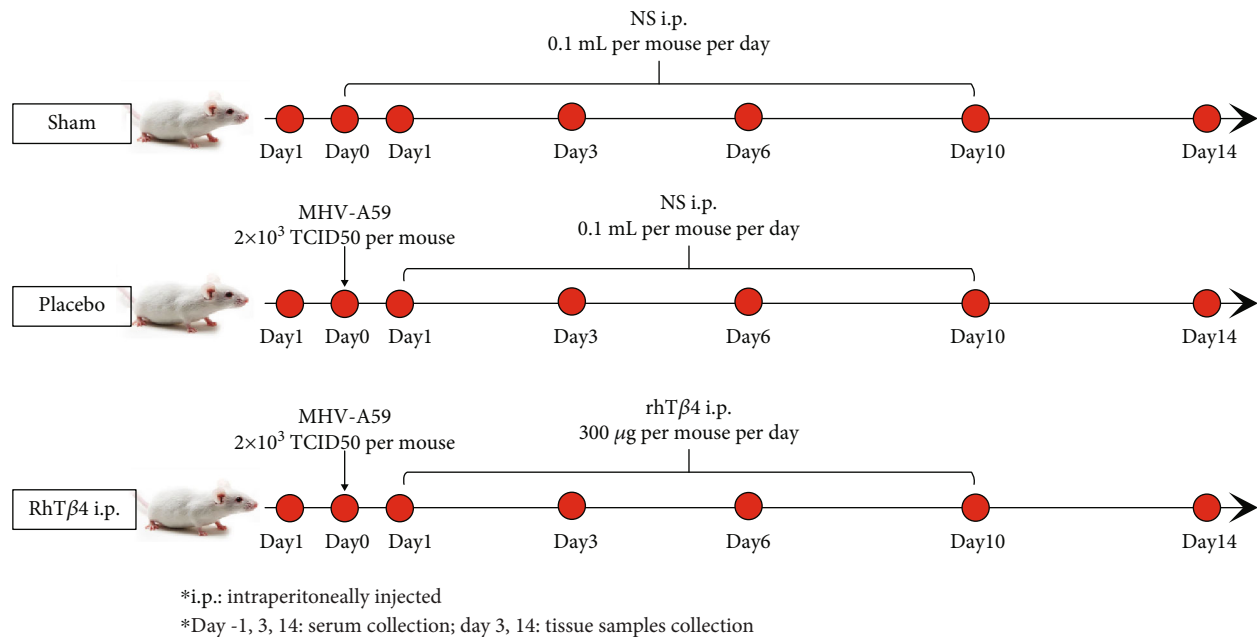


FIGURE 1: Process of mice experiment. Each of the mice in the sham group was intraperitoneally injected with 0.1 mL of normal saline (NS) daily from days 0 to 10. The mice in the placebo group were each intraperitoneally injected with 2×10^3 TCID₅₀ of MHV-A59 on day 0, and 0.1 mL NS was intraperitoneally injected into each mouse once daily from days 1 to 10. The mice in the rhTβ4 group were intraperitoneally injected with 2×10^3 TCID₅₀ of MHV-A59 per mouse on day 0, and 300 μg of rhTβ4 in 0.1 mL NS was intraperitoneally injected per mouse daily from days 1 to 10. The mice in each group were observed until day 14.

tissues were collected. The tissues were stored in 4% paraformaldehyde or in RNastore reagent. Two mice in the placebo group survived, and their data on day 14 were combined.

2.5. Analysis of Anti-MHV Antibodies. The tail vein blood of the surviving mice in each group was collected on day 14 into serum separator tubes. The blood was allowed to clot for 2 h at room temperature before centrifugation for 20 min at approximately $1000 \times g$. The freshly prepared serum was immediately assayed using the MHV-Ab ELISA Kit. A standard curve was generated using six concentrations of the standard, and the concentration of the anti-MHV antibodies was evaluated.

2.6. Quantitative Real-Time Polymerase Chain Reaction (qPCR) Analysis of Viral RNA in Mouse Tissues. The qPCR assays employed a TaqMan probe to quantify MHV-A59 RNA in liver, lung, and kidney tissues of mice 3 and 14 days postinfection. The sequences of the primers and TaqMan probe were designed according to the MHV-A59 sequence (GenBank No. FJ6742245) as follows: MHV-F: 5' -ggaactctcgttgggcattact-3'; MHV-R: 5' -tatgttgtaaaatgataatcttgggt-3'; MHV-probe: FAM-acatgctacggctcgttaaccgaactgt-BHQ1. A 130-bp DNA fragment which contained the T7 promoter sequence and a specific sequence from MHV-A59, was cloned into the pCloneEZ-TOPO-NRS-Amp vector (Taihe Biotechnology, Beijing, China) as a positive control. The copy numbers of the plasmid containing the 130bp insert were estimated to serve as standards.

Tissue RNAs prepared using a RNeasy Plus Mini Kit were reverse transcribed with a QuantiTect Reverse Transcription Kit and quantitated according to the protocol supplied with the QuantiTect Probe PCR Kit. TaqMan reaction

mixtures (20 μL) contained 10 μL of 2× Master Mix, 400 nM MHV-F or MHV-R primer, 200 nM MHV probe, and 2 μL of cDNA template. After initial denaturation at 95°C for 10 min, 40 amplification cycles were performed, which included melting and annealing steps at 95°C, 15 s and 60°C and 60 s, respectively. Amplification, detection, and data analysis were performed using an ABI 7500 Real-Time PCR system (Applied Biosystems, USA).

2.7. Cytokine Assays. Cytokines in mouse sera were detected using a Bio-Plex Pro Mouse Cytokine 23-plex Assay Kit according to the protocol provided by the manufacturer. Data were acquired using a Bio-Plex 200 System (Bio-Rad, USA). The cytokines tested were as follows: IL-1α, IL-1β, IL-2, IL-3, IL-4, IL-5, IL-6, IL-9, IL-10, IL-12 p40, IL-12 p70, IL-13, IL-17A, eotaxin, G-CSF, GM-CSF, IFN-γ, KC, MCP-1 (MCAF), MIP-1α, MIP-1β, RANTES, and TNF-α.

2.8. C-Reactive Protein (CRP) Assay. The CRP concentrations in mouse sera were measured using a Mouse C-Reactive Protein ELISA Kit according to the protocol provided by the manufacturer. The quantity of CRP was interpolated from a standard curve.

2.9. Hematoxylin-Eosin (HE) Staining. Liver, lung, and kidney tissues were harvested on days 3 and 14 postinfection and stored in 4% paraformaldehyde. Pathological injury and inflammation in the HE-stained samples were observed and recorded.

2.10. Statistical Analysis. Data represent the average ± SD of each treatment group. The significance of the differences of

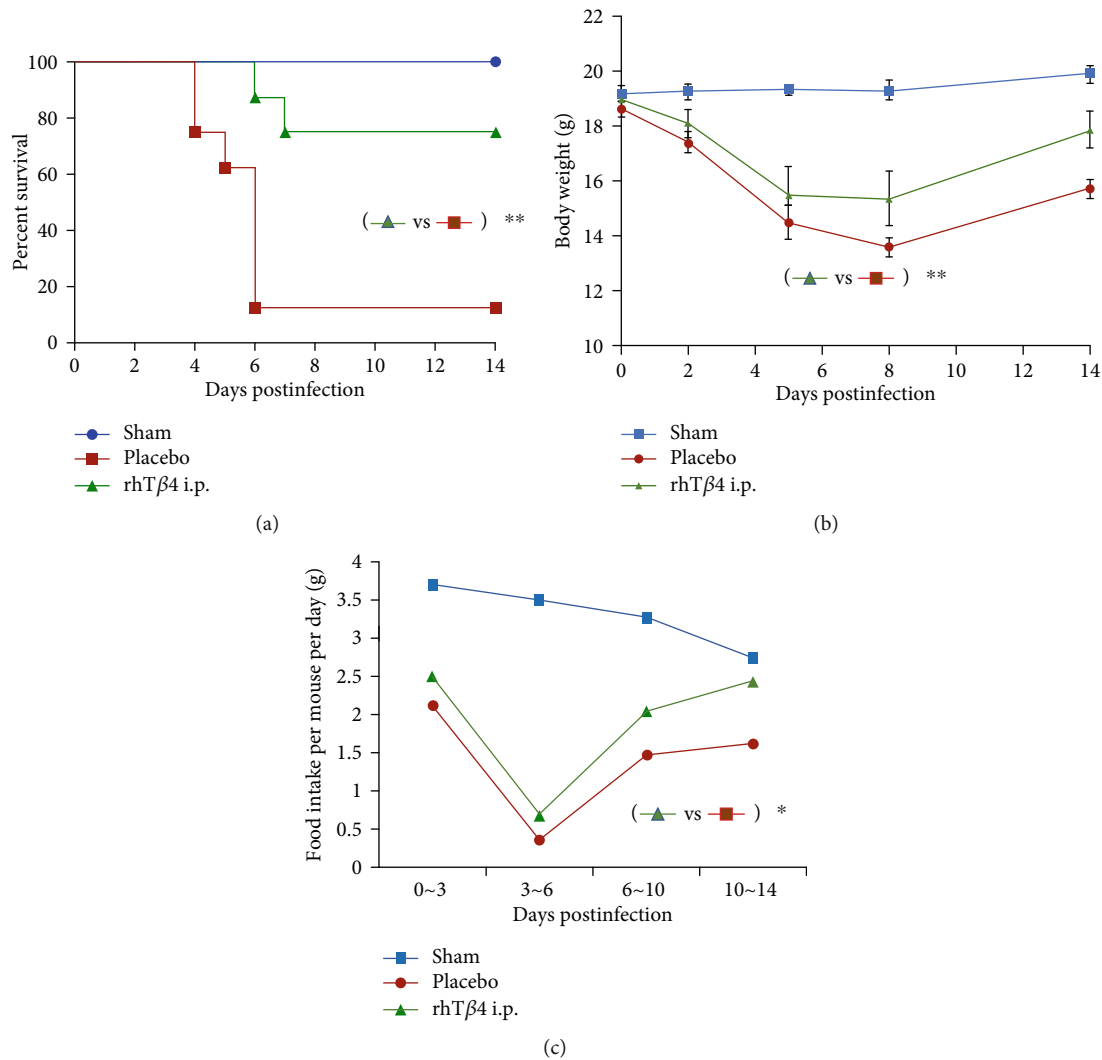


FIGURE 2: Protection of rhTβ4 i.p in BALB/c mice by infection of MHV-A59. (a) The survival rate of mice in group sham, placebo, and rhTβ4 i.p ($n = 8$ per group). Log-rank (Mantel-Cox) test was used to analyze the statistical difference between groups. $**P < 0.01$. (b) Change of body weights was monitored at 2, 5, 8, and 14 d.p.i. Two-way ANOVA was used to compare two group data. $**P < 0.01$. (c) Food intake of the survived mice in each group was calculated during 0~3, 3~6, 6~10, and 10~14 d.p.i. Two-way ANOVA was used to compared two group data. $*P < 0.05$.

survival rates between groups was analyzed using a log-rank (Mantel-Cox) test. A Student unpaired t -test was used to determine the significance of the difference between two independent datasets, two-way ANOVA was used to determine the significance of the difference between two groups, and $P < 0.05$ represents a significant difference.

3. Results

3.1. Effects of rhTβ4 on Mice Infected with MHV-A59. Mice in the placebo group began to show typical signs of illness from day 2 postinfection, including difficulty walking, hunched posture, and erect and piled up hair. These mice began to die from day 4 postinfection, while mice in the rhTβ4 group began to die on day 6 postinfection. The survival rates of mice in the placebo and rhTβ4 groups were 12.5% and 75%, respectively ($P < 0.01$) (Figure 2(a)).

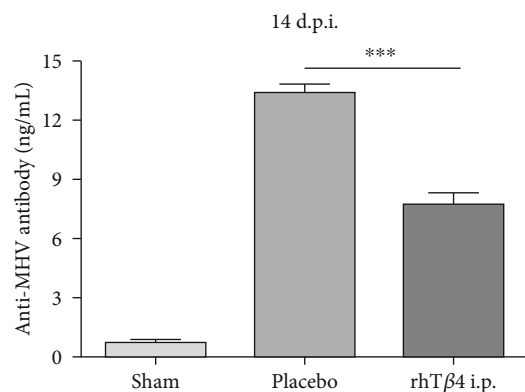


FIGURE 3: Anti-MHV antibody concentrations in serum at 14 d.p.i. The MHV antibodies in mice serum of group sham ($n = 13$), placebo ($n = 2$), AND rhTβ4 ($n = 11$) were quantified by ELISA. The unpaired t -test was used to compare two group data. $***P < 0.001$.

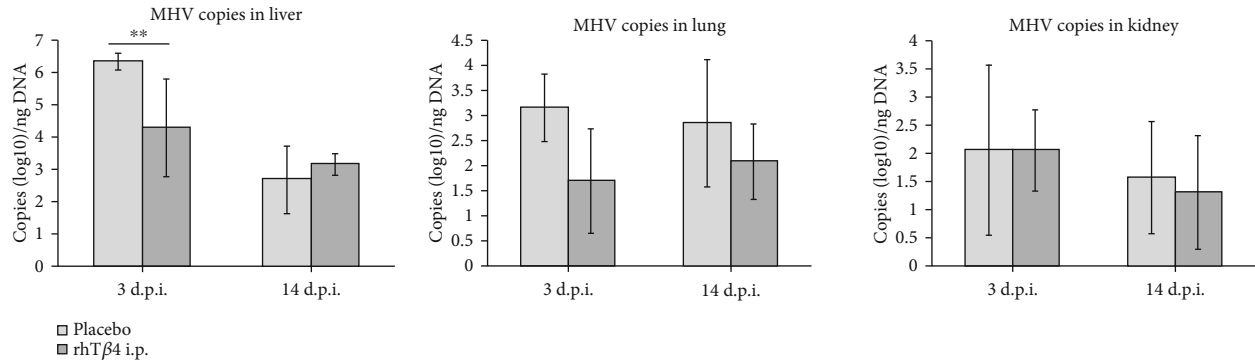


FIGURE 4: The virus RNA copies of MHV-A59 in the liver, lung, and kidney of mice. The MHV RNA copies in mice tissues of group placebo and rhTβ4 were quantified real-time qPCR. The unpaired *t*-test was used to compare two group data. ** $P < 0.01$.

TABLE 1: Comparison of cytokine levels in each group.

Days post infection	Compared to group sham	Group	
		Placebo	rhTβ4
3 d.p.i.	Significantly higher	IL-1α, IL-1β, IL-3, IL-4, IL-5, IL-6, IL-10, IL-12p40, IL-12p70, IL-13, Eotaxin, G-CSF, GM-CSF, KC, MCP-1(MCAF), MIP-1α, MIP-1β, RANTES, TNF-α	IL-1α, IL-1β, IL-3, IL-4, IL-5, IL-6, IL-10, IL-12p40, IL-12p70, IL-13, Eotaxin, G-CSF, GM-CSF, KC, MCP-1(MCAF), MIP-β, RANTES, TNF-α
	Significantly lower	/	/
	No significantly different	IL-2, IL-9, IL-17A, IFN-γ	IL-2, IL-9, IL-17A, IFN-γ, MIP-1α
	Significantly higher	/	/
	Significantly lower	IL-3, IL-6, IL-9, IL-12p70, IL-13, Eotaxin, GM-CFS, IFN-γ, MCP-1(MCAF), RANTES, TNF-α	/
14 d.p.i.	No significantly different	IL-1α, IL-1β, IL-2, IL-4, IL-5, IL-10, IL-12p40, IL=17A, G-CSF, KC, MIP-1α, MIP-1β	IL-1α, IL-1β, IL-2, IL-3, IL-4, IL-5, IL-6, IL-9, IL-10, IL-12p40, IL-12p70, IL-13, IL=17A, Eotaxin, G-CSF, GM-CSF, IFN-γ, KC, MCP-1(MCAF), MIP-1α, MIP-1β, RANTES, TNF-α

Mice in the placebo and rhTβ4 groups lost appetite, and their body weights started decreasing on day 2 postinfection, compared with those of the mice in the sham group (Figure 2(b)). The weight loss of mice in the rhTβ4 group was lower compared with that of the placebo group ($P < 0.05$) and gradually increased starting from day 8 postinfection. Food consumption of mice in the placebo and the rhTβ4 groups significantly decreased after challenge. The lowest food consumption occurred from days 3 to 6 postinfection and then gradually increased (Figure 2(c)).

3.2. Anti-MHV Antibody Concentrations. MHV specific antibodies were detected in the sera of survivors on day 14 postinfection. MHV-A59 challenge elicited titers of specific antibodies in the placebo and rhTβ4 groups. The anti-MHV antibody concentrations in group rhTβ4 were significantly lower compared with those of the placebo group ($P < 0.001$) (Figure 3).

3.3. Viral RNA Copy Numbers in Tissues. The number of MHV-A59 RNA copies in the liver was the highest, followed by the lung and kidney. On day 3 postinfection, the viral RNA copies of liver tissues in the rhTβ4 group were significantly

lower compared with those of the placebo group ($P < 0.01$), and there was no significant difference between viral RNA copy numbers in the tissues of these group on day 14 after challenge. Further, these values did not significantly differ between the rhTβ4 placebo groups (Figure 4).

3.4. Cytokine and CRP Levels. As shown in Table 1, on day 3 postinfection, the concentrations of 18 of 23 cytokines in the sera of both the placebo and rhTβ4 groups were significantly increased vs normal values ($P < 0.05$). The levels of the four cytokines were not significantly different. On day 14 postinfection, the levels of the 23 cytokines in the rhTβ4 group returned to normal, while the concentrations of 11 cytokines in the placebo group were significantly lower compared with normal values ($P < 0.05$). There was no significant change in the CRP concentration of each group during the experiment (Figure 5). These results indicate that MHV-A59 significantly inhibited the immune response of mice in the late stage of virus infection and during convalescence. However, rhTβ4 effectively balanced the levels of proinflammatory and anti-inflammatory cytokines to maintain physiological immune homeostasis.

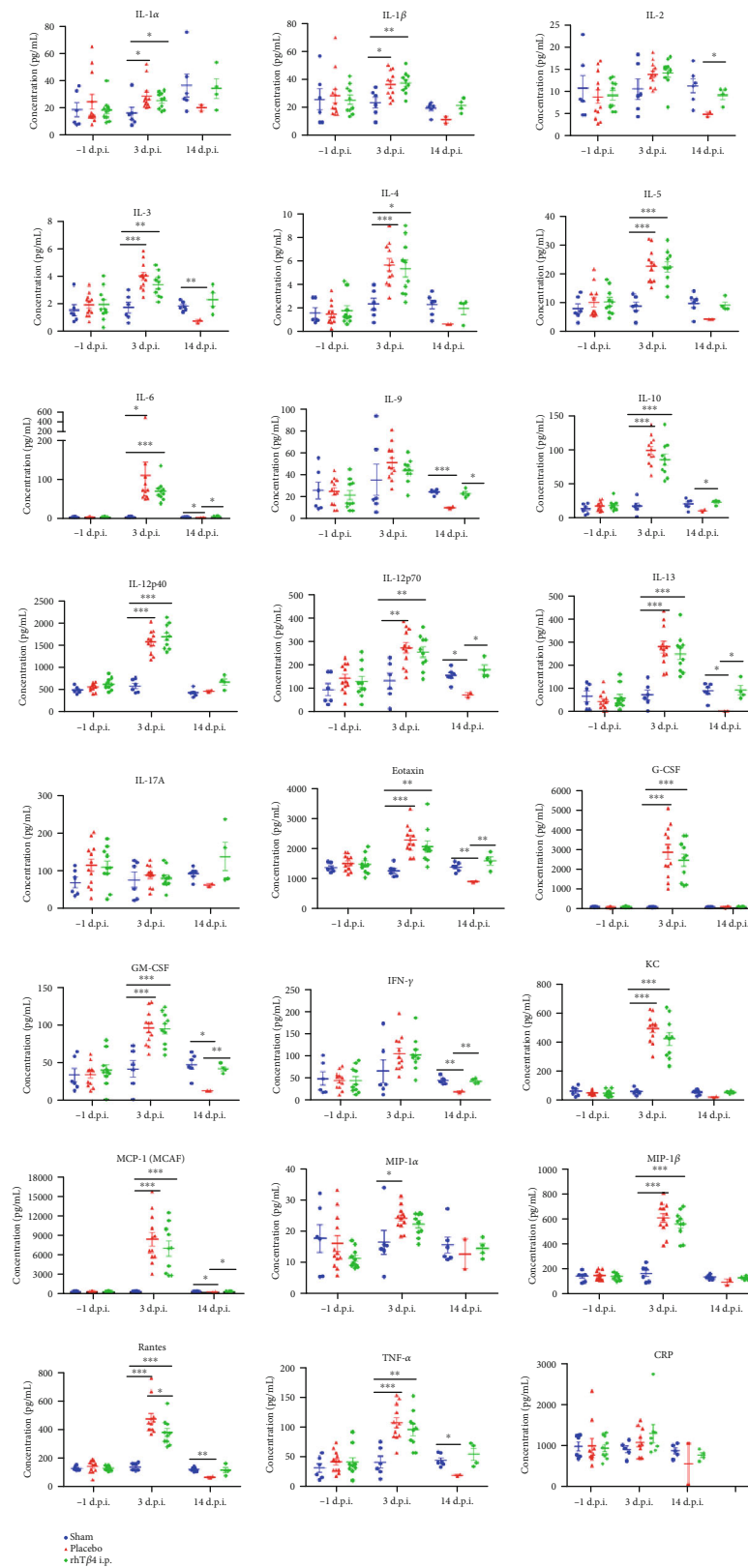


FIGURE 5: The cytokines and CRP concentrations in the mice serum. Cytokines in mouse sera were detected using a Bio-Plex Pro Mouse Cytokine 23-plex Assay Kit. The CRP concentrations in mouse sera were measured using a Mouse C-Reactive Protein ELISA Kit. The unpaired *t*-test was used to compare two group data. * $P < 0.05$, ** $P < 0.01$, and *** $P < 0.001$.

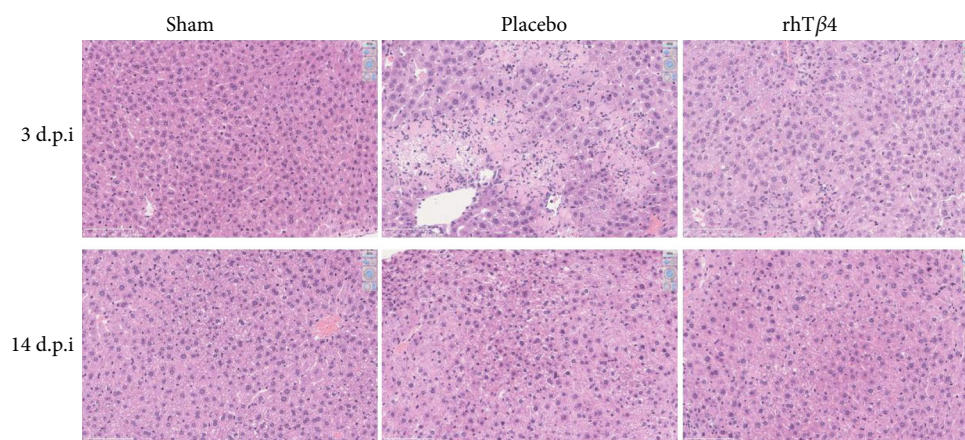


FIGURE 6: Pathological section of mice livers. Liver tissues were removed from the mice at 3 d.p.i. or 14 d.p.i., fixed with 4% paraformaldehyde for examination. The samples were dehydrated, embedded, and sliced for HE staining, and the pathologies of the livers were evaluated under microscope (Nikon Ci-S, Japan). The magnification of the pictures shown is $\times 40$.

3.5. Protection from Tissue Injury. There was no significant injury to the lungs or kidneys of the placebo and rhT $\beta 4$ groups. In contrast, MHV-A59 caused severe liver injury. For example, day 3 postinfection of mice in the placebo group caused hepatocyte necrosis, watery degeneration, inflammatory cell infiltration (including granulocytes and mononuclear cells), and bleeding in some necrotic areas of the liver. The rhT $\beta 4$ group exhibited hepatocyte necrosis, watery degeneration, and minimal infiltration by inflammatory cells of the liver. Compared with mice in the placebo group, the rate and degrees of inflammatory cell infiltration of mice in the rhT $\beta 4$ group decreased by day 14 postinfection, and hepatocyte necrosis was repaired in mice in the placebo group; although, there was watery degeneration and inflammatory cell infiltration (the number of Kupffer cells increased) and minimal hepatocyte regeneration. The rhT $\beta 4$ group exhibited hepatocyte regeneration (binucleate and macronuclear regenerated hepatocytes). Compared with the placebo group, the livers of the rhT $\beta 4$ group underwent injury repair, and hepatocyte proliferation was detected (Figure 6).

4. Discussion

Here, we show that MHV can be used as a model to screen for drugs that inhibit CoV infection under A-BLS2 containment. In contrast, studies of CoVs that are pathogenic for humans such as CoV-2 require A-BLS3 containment and the use of transgenic mice that express the CoV-2 receptor, human angiotensin-converting enzyme 2 [36].

The anti-inflammatory activities of T $\beta 4$ suggested to us that it may serve to treat coronavirus infections of humans. Further, Han et al. found an association between reductions in serum levels T $\beta 4$ and the severity of liver failure caused by chronic HBV infection [37], and Shahabuddin et al. found that chronic infection with HIV-1 reduces the level of T $\beta 4$ in infected cells [38].

Here, we show that rhT $\beta 4$ increased the survival rate of mice infected with MHV-A59, significantly reduced viral titers in the liver during the early stage of infection, protected the liver from severe injury, and promoted hepatocyte regen-

eration and tissue repair. There was no significant difference in the numbers of virus RNA copies of tissues between the placebo and rhT $\beta 4$ groups during the later stage of infection. However, the anti-MHV-specific antibody titers of the rhT $\beta 4$ group were significantly lower compared with those of the placebo group 14 days postinfection. This may be explained by the discordance between viral RNA copy numbers and the number of infectious viruses.

T helper cells (Th) play an important role in regulating the immune system. Th1 cells inhibit virus infection leading to inflammation or delayed type hypersensitivity through the secretion of cytokines such as IL-1, IFN- γ , and TNF- β . Th2 cells produce numerous cytokines (e.g., IL-4, IL-5, IL-6, IL-10, and IL-13) that induce B cells to mount a humoral immune response [39]. Th cells produce proinflammatory (e.g., TNF - α , IL-2, IL-6, IL-8, IL-12, IL-17, IL-23, IFN γ , and MIF) and anti-inflammatory cytokines (e.g., IL-4, IL-13, IL-10, TGF - β , and IL-1R α). Under normal physiological conditions, Th1 and Th2 cells maintain a balanced state of mutual inhibition and proliferation. The dynamic balance of proinflammatory and anti-inflammatory cytokines determines the development and outcome of inflammation. An imbalance in cytokine activities leads to pathology. Three days after MHV-A59 infection, the concentrations of anti-inflammatory and proinflammatory cytokines significantly increased, and all the physical characteristics of the mice, histopathology, cytokine assays suggested that the mice infected with MHV-A59 were in the “cytokine storm” state. The mice in the placebo group began to recover 14 days postinfection, as indicated by increased body weight and food consumption. However, the levels of 11 cytokines in the placebo group were significantly lower compared with their normal values, indicating that the virus significantly inhibited the activities of Th1 and Th2 cells to suppress the antiviral immune response. However, the level of each of the 23 cytokines produced by rhT $\beta 4$ -treated mice returned to normal 14 days after challenge. These results show that rhT $\beta 4$ effectively balanced the activities of Th1 and Th2 cells as well as the concentrations of proinflammatory and anti-inflammatory cytokines to restore normal immune homeostasis.

Only two survived mice data were detected in the placebo group at 14 d.p.i., which is a small shortcoming of this study. Although we had tried different challenge doses of MHV-A59, no more mice in the placebo group could survive under the condition that the survival rate was statistically different, unless the sample size was particularly large. We will further increase the number of mice to acquire more data in the next study.

5. Conclusion

MHV-A59 can be used as a model virus to study CoVs under conditions of A-BSL2 containment. As proof of principle, we show here that although rhT β 4 was not virucidal, it protected mice from virus challenge by balancing the immune response, promoting the regeneration of damaged cells, and repairing tissue damage, leading to rapid mitigation of the pathological consequences of CoV infection.

Data Availability

The data used to support the findings of this study are available from the corresponding author upon request.

Additional Points

Highlights. This was the first report of recombinant human thymosin beta-4 (rhT β 4) in the treatment of mouse coronavirus infection, which showed that rhT β 4 significantly increased the survival rate of mice infected with MHV-A59 through inhibiting virus replication, balancing the host's immune response, alleviating pathological damage, and promoting repair of the liver. These results will serve as the basis for further application of rhT β 4 to the treatment of human CoV diseases such as COVID-19.

Conflicts of Interest

The authors declare that they have no conflicts of interest with the contents of this article.

Authors' Contributions

Rui Yu, Junjie Xu, and Wei Chen conceptualized and designed the study. Rui Yu, Yunyun Mao, Kai Li, Yanfang Zhai, Yue Zhang, Shuling Liu, Yuemei Gao, Yanhong Liu, Ting Fang, and Mengsu Zhao performed the experiments. Zhengshan Chen and Ruihua Li analyzed the data. Junjie Xu drafted the article and revised it critically for the important intellectual content. Wei Chen finally approved of the version to be submitted.


References

- [1] S. R. Weiss and S. Navas-Martin, "Coronavirus pathogenesis and the emerging pathogen severe acute respiratory syndrome coronavirus," *Microbiology and Molecular Biology Reviews*, vol. 69, no. 4, pp. 635–664, 2005.
- [2] D. Schoeman and B. C. Fielding, "Coronavirus envelope protein: current knowledge," *Virology Journal*, vol. 16, no. 1, p. 69, 2019.
- [3] Y. A. Malik, "Properties of coronavirus and SARS-CoV-2," *The Malaysian Journal of Pathology*, vol. 42, no. 1, pp. 3–11, 2020.
- [4] X. Yang, Y. Yu, J. Xu et al., "Clinical course and outcomes of critically ill patients with SARS-CoV-2 pneumonia in Wuhan, China: a single-centered, retrospective, observational study," *The Lancet Respiratory Medicine*, vol. 8, no. 5, pp. 475–481, 2020.
- [5] R. W. Körner, M. Majjouti, M. A. A. Alcazar, and E. Mahabir, "Of mice and men: the coronavirus MHV and mouse models as a translational approach to understand SARS-CoV-2," *Viruses*, vol. 12, no. 8, p. 880, 2020.
- [6] E. Hannappel, "Thymosin β 4 and its posttranslational modifications," *Annals of the New York Academy of Sciences*, vol. 1194, no. 1, pp. 27–35, 2010.
- [7] S. K. Hu, T. L. Low, and A. L. Goldstein, "Modulation of terminal deoxynucleotidyl transferase activity by thymosin," *Molecular and Cellular Biochemistry*, vol. 41, pp. 49–58, 1981.
- [8] M. Badamchian, M. O. Fagarasan, R. L. Danner, A. F. Suffredini, H. Damavandy, and A. L. Goldstein, "Thymosin β 4 reduces lethality and down-regulates inflammatory mediators in endotoxin-induced septic shock," *International Immunopharmacology*, vol. 3, no. 8, pp. 1225–1233, 2003.
- [9] M. A. Cavasin, "Therapeutic potential of thymosin-beta4 and its derivative N-acetyl-seryl-aspartyl-lysyl-proline (ac-SDKP) in cardiac healing after infarction," *American Journal of Cardiovascular Drugs*, vol. 6, no. 5, pp. 305–311, 2006.
- [10] G. Sosne, E. A. Szliter, R. Barrett, K. A. Kernacki, H. Kleinman, and L. D. Hazlett, "Thymosin beta 4 promotes corneal wound healing and decreases inflammation in vivo following alkali injury," *Experimental Eye Research*, vol. 74, no. 2, pp. 293–299, 2002.
- [11] G. Sosne, P. Qiu, P. L. Christopherson, and M. K. Wheeler, "Thymosin beta 4 suppression of corneal NF κ B: A potential anti-inflammatory pathway," *Experimental Eye Research*, vol. 84, no. 4, pp. 663–669, 2007.
- [12] G. Sosne, P. L. Christopherson, R. P. Barrett, and R. Fridman, "Thymosin- β 4 modulates corneal matrix metalloproteinase levels and polymorphonuclear cell infiltration after alkali injury," *Investigative Ophthalmology & Visual Science*, vol. 46, no. 7, pp. 2388–2395, 2005.
- [13] J. D. Young, A. J. Lawrence, A. G. MacLean et al., "Thymosin β 4 sulfoxide is an anti-inflammatory agent generated by monocytes in the presence of glucocorticoids," *Nature Medicine*, vol. 5, no. 12, pp. 1424–1427, 1999.
- [14] L. C. Huang, D. Jean, R. J. Proske, R. Y. Reins, and A. M. McDermott, "Ocular surface expression and in vitro activity of antimicrobial peptides," *Current Eye Research*, vol. 32, no. 7–8, pp. 595–609, 2007.
- [15] I. Bock-Marquette, A. Saxena, M. D. White, J. Michael DiMaio, and D. Srivastava, "Thymosin β 4 activates integrin-linked kinase and promotes cardiac cell migration, survival and cardiac repair," *Nature*, vol. 432, no. 7016, pp. 466–472, 2004.
- [16] J. H. Ho, K. C. Tseng, W. H. Ma, K. H. Chen, O. K. S. Lee, and Y. Su, "Thymosin beta-4 upregulates anti-oxidative enzymes and protects human cornea epithelial cells against oxidative damage," *The British Journal of Ophthalmology*, vol. 92, no. 7, pp. 992–997, 2008.

- [17] J. H. Ho, C. H. Chuang, C. Y. Ho, Y. R. V. Shih, O. K. S. Lee, and Y. Su, "Internalization is essential for the antiapoptotic effects of exogenous thymosin β -4 on human corneal epithelial cells," *Investigative Ophthalmology & Visual Science*, vol. 48, no. 1, pp. 27–33, 2007.
- [18] H. P. Ehrlich and S. W. Hazard III, "Thymosin β 4 enhances repair by organizing connective tissue and preventing the appearance of myofibroblasts," *Annals of the New York Academy of Sciences*, vol. 1194, no. 1, pp. 118–124, 2010.
- [19] N. Smart, C. A. Risebro, A. A. D. Melville et al., "Thymosin β 4 induces adult epicardial progenitor mobilization and neovascularization," *Nature*, vol. 445, no. 7124, pp. 177–182, 2007.
- [20] K. M. Malinda, A. L. Goldstein, and H. K. Kueinman, "Thymosin beta 4 stimulates directional migration of human umbilical vein endothelial cells," *The FASEB Journal*, vol. 11, no. 6, pp. 474–481, 1997.
- [21] D. S. Grant, J. L. Kinsella, M. C. Kibbey et al., "Matrigel induces thymosin beta 4 gene in differentiating endothelial cells," *Journal of Cell Science*, vol. 108, Part 12, pp. 3685–3694, 1995.
- [22] G. Sosne, A. Siddiqi, and M. Kurpakus-Wheater, "Thymosin- β 4 inhibits corneal epithelial cell apoptosis after ethanol exposure in vitro," *Investigative Ophthalmology & Visual Science*, vol. 45, no. 4, pp. 1095–1100, 2004.
- [23] P. Qiu, M. Kurpakus-Wheater, and G. Sosne, "Matrix metalloproteinase activity is necessary for thymosin beta 4 promotion of epithelial cell migration," *Journal of Cellular Physiology*, vol. 212, no. 1, pp. 165–173, 2007.
- [24] P. Roy, Z. Rajfur, D. Jones, G. Marriott, L. Loew, and K. Jacobson, "Local photorelease of caged thymosin β 4 in locomoting keratocytes causes cell turning," *The Journal of Cell Biology*, vol. 153, no. 5, pp. 1035–1048, 2001.
- [25] G. Sosne, S. Hafeez, A. L. Greenberry, and M. Kurpakus-Wheater, "Thymosin beta4 promotes human conjunctival epithelial cell migration," *Current Eye Research*, vol. 24, no. 4, pp. 268–273, 2002.
- [26] G. Sosne, L. Xu, L. Prach et al., "Thymosin beta 4 stimulates laminin-5 production independent of TGF- β ," *Experimental Cell Research*, vol. 293, no. 1, pp. 175–183, 2004.
- [27] G. Sosne, P. Qiu, A. L. Goldstein, and M. Wheeler, "Biological activities of thymosin beta4 defined by active sites in short peptide sequences," *The FASEB Journal*, vol. 24, no. 7, pp. 2144–2151, 2010.
- [28] S. Bollini, P. R. Riley, and N. Smart, "Thymosin β 4: multiple functions in protection, repair and regeneration of the mammalian heart," *Expert Opinion on Biological Therapy*, vol. 15, Supplement 1, pp. 163–174, 2015.
- [29] E. Conte, T. Genovese, E. Gili et al., "Thymosin β 4 protects C57BL/6 mice from bleomycin-induced damage in the lung," *European Journal of Clinical Investigation*, vol. 43, no. 3, pp. 309–315, 2013.
- [30] E. Conte, T. Genovese, E. Gili et al., "Protective effects of thymosin β 4 in a mouse model of lung fibrosis," *Annals of the New York Academy of Sciences*, vol. 1269, no. 1, pp. 69–73, 2012.
- [31] R. Shah, K. Reyes-Gordillo, Y. Cheng, R. Varatharajalu, J. Ibrahim, and M. R. Lakshman, "Thymosin β 4 prevents oxidative stress, inflammation, and fibrosis in ethanol- and LPS-induced liver injury in mice," *Oxidative Medicine and Cellular Longevity*, vol. 2018, Article ID 9630175, 12 pages, 2018.
- [32] E. Vasilopoulou, P. J. D. Winyard, P. R. Riley, and D. A. Long, "The role of thymosin- β 4 in kidney disease," *Expert Opinion on Biological Therapy*, vol. 15, Supplement 1, pp. 187–190, 2015.
- [33] U. Aksu, O. M. Yaman, I. Guner et al., "The protective effects of Thymosin- β -4 in a rat model of ischemic acute kidney injury," *Journal of Investigative Surgery*, vol. 8, pp. 1–9, 2019.
- [34] R. Yu, S. Cao, Y. Liu et al., "Highly effective biosynthesis of N-acetylated human thymosin β 4 (T β 4) in *Escherichia coli*," *Artificial Cells, Nanomedicine, and Biotechnology*, vol. 46, Supplement 3, pp. S95–S104, 2018.
- [35] D. L. Krah, "A simplified multiwell plate assay for the measurement of hepatitis a virus infectivity," *Biologicals*, vol. 19, no. 3, pp. 223–227, 1991.
- [36] L. Bao, W. Deng, B. Huang et al., "The pathogenicity of SARS-CoV-2 in hACE2 transgenic mice," *Nature*, vol. 583, no. 7818, pp. 830–833, 2020.
- [37] T. Han, Y. Liu, H. Liu et al., "Serum thymosin beta4 levels in patients with hepatitis B virus-related liver failure," *World Journal of Gastroenterology*, vol. 16, no. 5, pp. 625–630, 2010.
- [38] M. Shahabuddin, G. McKinley, M. J. Potash, and D. J. Volsky, "Modulation of cellular gene expression of HIV type 1 infection as determined by subtractive hybridization cloning: downregulation of thymosin beta 4 in vitro and in vivo," *AIDS Research and Human Retroviruses*, vol. 10, no. 11, pp. 1525–1529, 1994.
- [39] P. Kidd, "Th1/Th2 balance: the hypothesis, its limitations, and implications for health and disease," *Alternative Medicine Review*, vol. 8, no. 3, pp. 223–246, 2003.

Research Article

Gene Expression Profiling and Biofunction Analysis of HepG2 Cells Targeted by Crocetin

Yi-Ling Wen,¹ Yong Li,¹ Guangcheng Zhu,¹ Zhibing Zheng,¹ Meng Shi,¹ and Si Qin^{1,2} 

¹Lab of Food Function and Nutrigenomics, College of Food Science and Technology, Hunan Agricultural University, Changsha 410128, China

²Department of Biochemical Science and Technology, Faculty of Agriculture, Kagoshima University, Korimoto 1-21-24, Kagoshima 890-0065, Japan

Correspondence should be addressed to Si Qin; qinsiman@hunau.edu.cn

Received 11 February 2021; Revised 3 March 2021; Accepted 17 March 2021; Published 2 April 2021

Academic Editor: Xin Zong

Copyright © 2021 Yi-Ling Wen et al. This is an open access article distributed under the Creative Commons Attribution License, which permits unrestricted use, distribution, and reproduction in any medium, provided the original work is properly cited.

Crocetin is a carotenoid extracted from *Gardenia jasminoides*, one of the most popular traditional Chinese medicines, which has been used in the prevention and treatment of various diseases. The present study is aimed at clarifying the effect of crocetin on gene expression profiling of HepG2 cells by RNA-sequence assay and further investigating the molecular mechanism underlying the multiple biofunctions of crocetin based on bioinformatics analysis and molecular evidence. Among a total 23K differential genes identified, crocetin treatment upregulated the signals of 491 genes (2.14% of total gene probes) and downregulated the signals of 283 genes (1.24% of total gene probes) by ≥ 2 -fold. The Gene Ontology analysis enriched these genes mainly on cell proliferation and apoptosis (BRD4 and DAXX); lipid formation (EHMT2); cell response to growth factor stimulation (CYP24A1 and GCNT2); and growth factor binding (ABCB1 and ABCG1), metabolism, and signal transduction processes. The KEGG pathway analysis revealed that crocetin has the potential to regulate transcriptional misregulation, ABC transporters, bile secretion, alcoholism, systemic lupus erythematosus (SLE), and other pathways, of which SLE was the most significantly disturbed pathway. The PPI network was constructed by using the STRING online protein interaction database and Cytoscape software, and 21 core proteins were obtained. RT-qPCR datasets serve as the solid evidence that verified the accuracy of transcriptome sequencing results with the same change trend. This study provides first-hand data for comprehensively understanding crocetin targeting on hepatic metabolism and its multiple biofunctions.

1. Introduction

Crocetin (*Gardenia jasminoides*) is a carotenoid originally extracted from a medicinal and edible resource and is one of the most popular traditional Chinese medicines. Crocetin has been used in the prevention and treatment of various diseases with health-promoting effects such as antioxidation, antitumor, anticardiovascular illness, anti-inflammation, hepatoprotection, and neuroprotection [1]. These therapeutic effects are achieved with different mechanisms. Accumulated data showed that crocetin could scavenge free radicals by inhibiting lipid peroxidation and increasing the activity of antioxidant enzymes including GST, GSH-Px, catalase, glutathione peroxidase (GPx), and superoxide dismutase

(SOD) [2, 3]. Tumor invasion was suppressed by crocetin through reducing MMP expression and tumor proliferation by inducing cell cycle arrest, and enhancing apoptosis by activating caspase 3 [4, 5]. Cardiovascular disorders such as hypertension, thrombosis formation, and myocardial infarction (MI) could be potentially prevented or treated by crocetin. Moreover, crocetin effectively prevented inflammatory markers such as NF- κ B, TNF- α , IL-1 β , IL-6, and IL-8 and inhibited iNOS/COX-2 activity and induction of NO/PGE2 [6–8]. The main mechanisms of the protective effects of crocetin in liver and nerve damage are mediated by the restoration of antioxidant enzyme activity and inhibition of the superoxide anion and/or free radical [9–11]. The nutritional value and therapeutic potential of crocetin have been

gradually revealed, and it is therefore necessary to comprehensively and deeply analyze the molecular mechanism of the action of crocetin, and then fully reveal its functional activity.

Nutrigenomics is an emerging research field that studies the genomic changes caused by diet, covering the interaction of health, diet, and genomics. The human diet is composed of a complex mixture of substances and biological activity. It is functionally divided into three aspects: some can directly affect gene expression, some can modulate transcription factor activity after metabolism, while some can induce transcription after stimulating the signal transduction cascade [12]. Transcriptome refers to the sum of RNA transcribed by cells, tissues, or organisms at a certain developmental stage or under physiological conditions, mainly composed of messenger RNA (mRNA), noncoding RNA (ncRNA), and microRNA (miRNA). Transcriptomics is a discipline that systematically studies the global transcription map of the whole genome and reveals the network of molecular mechanisms of complex biological processes and trait regulation. A variety of techniques, including EST sequence construction and study, gene microarray, gene expression series analysis (SAGE), large-scale parallel sequencing (MPSS), and RNA-seq, have been developed to study the transcriptome. RNA-seq technology is established on the basis of EST technology and gene microarray. It is different from the gene expression microarray method in the sense that RNA-seq can not only detect transcripts corresponding to the existing genome sequence, but it can also find and quantify new transcripts, which have more advantages in the study of selective splicing events, new genes and transcripts, and fusion transcripts. RNA-seq has become the most popular method for transcriptome studies due to its low cost, its high throughput, and its applicability to species with no genomic background.

Recently, in the field of nutrition, there have been many studies on organisms, cells, or tissues under different nutritional states based on RNA-seq technology. Studies have reported that dietary composition can affect gene expression, thus affecting biological processes and pathways. Therefore, changing the dietary composition and proportion of farm animals could improve the nutritional value of meat products [13–15]. Suarez-Vega et al. [16] used the RNA-seq technique to study the MED-related mammary responses induced by CLA in breast milk, and compared the transcriptome data of mammary cells in ewes with the CLA-induced MFD group, the non-MED group, and the FO-MFD group, and identified the core genes involved in the downregulation of fatty acid synthesis in CLA-MFD and FO-MFD. Today, RNA-seq remains the preferred method of analysis for transcriptomes, and nutritionists are able to use transcriptome data to develop a framework for improving dietary composition and novel functional foods as a way to promote human health.

To study the effect of crocetin on the whole genome expression profile of human hepatocytes, RNA-seq technology was performed in HepG2 cells with or without crocetin treatment. The GO and KEGG pathway analysis has been applied to investigate the multiple biofunctions of crocetin.

RT-qPCR was further used to verify the gene expression data. This study demonstrated the potential of using of crocetin as a functional ingredient applicable in medicine and food.

2. Materials and Methods

2.1. Materials, Cell Culture, and Cytotoxicity. Crocetin was provided by Tairui Biotechnology Co., Ltd. (Nanyang, Henan, China). LPS (*Escherichia coli* serotype 055:B5) was from Sigma-Aldrich (St. Louis, USA). Human hepatoblastoma HepG2 cells were purchased from ATCC (Rockville, USA) and cultured at 37°C in a 5% CO₂ atmosphere in Dulbecco's modified Eagle's medium (DMEM; Gibco BRL, Gaithersburg, USA) containing 10% FBS. Fetal bovine serum (FBS) was from Biological Industries (Kibbutz Beit Haemek, Israel). 3-(4,5-Dimethylthiazol-2-yl)-2,5-diphenyl tetrazolium bromide (MTT) was purchased from Sigma-Aldrich (St. Louis, USA). MTT assay was used to check the cytotoxicity of crocetin. Briefly, HepG2 cells were seeded into a 96-well plate at a density of 10⁴ cells per well and preincubated at 37°C in 5% CO₂ for 24 h. The cells were treated with a series of crocetin concentrations (0, 10 μM, 20 μM, and 40 μM) for another 24 h, then MTT (final concentration 0.5 mg/ml) was added to the plate and incubated for 4 h in the dark. Acidic isopropanol (0.04–0.1 M HCl in isopropanol) was added to dissolve the formazan crystals, and the optical density (OD) was measured at 570 nm with a microplate reader (Thermo Fisher Scientific, Waltham, USA). Cell viability was measured by comparing the OD of crocetin-treated cells with that of untreated cells.

2.2. RNA Extraction and Construction of cDNA Library. HepG2 cells were precultured for 24 h and then were treated with 20 μM crocetin dissolved in 0.1% DMSO for 8 h. Total RNA was extracted using the Isogen RNA kit (Nippon Gene Co., Tokyo, Japan) according to the manufacturer's protocol. The concentration and quality of RNA were assessed by a NanoDrop Spectrophotometer and an Agilent 2200 Bioanalyzer following the manufacturer's protocol. The cDNA of the purified mRNA was transformed and amplified by PCR technology, and the PCR products were purified by AMPure XP beads to complete the construction of the cDNA library. After the library construction was completed, the library was initially quantified (Qubit 2.0), then the insert fragment size of the library was detected using Agilent 2100, and the qualified cDNA libraries were sequenced on an Illumina HiSeq 2500 platform for high-throughput sequencing.

2.3. Bioinformatics Analysis. The R language package DESeq2 was used to screen differentially expressed genes. The significant difference standard for differentially expressed genes in this study is $|\log_2 \text{fold change}| > 0$ and $p \text{ value} < 0.05$, where the fold change value of the gene is the difference fold change, and the higher the value, the greater the difference in the expression of the gene between the two groups; the p value is the probability of hypothesis testing in the statistical model, and the smaller the p value, the greater the difference in expression between samples. DAVID is an online, web-based bioinformatics network analysis platform, which can

TABLE 1: The primers used for real-time PCR.

Oligonucleotide	Sequence (5'-3')
FGFBP1-F	CTTCACAGCAAAGTGGTCTCA
FGFBP1-R	GACACAGGAAAATTCATGGTCCA
GCNT2-F	TGTTCTGGCTCTATGCCAAA
GCNT2-R	TTAGCAAACAGGCTTGGTGAAT
GPR35-F	GGGAGGACCGTCTGCACAAA
GPR35-R	CCCAGGTGGCTGAATCTGGTG
TNFRSF21-F	GCCAGTGAGAGGGAGGTTGC
TNFRSF21-R	TCCAGCTGGGTGGTGTCTTC
TGFB1-F	GCGTCTGCTGAGGCTCAAGT
TGFB1-R	GCCGGTAGTGAACCCGTTGAT
TCF19-F	GGGGCGGTGATCTCTACAC
TCF19-R	GGGAGTCGGACATTATTGACCA
PCGF2-F	GCGAGGTCTTGAGCAGGAG
PCGF2-R	GGCGATGTCCATGAGGGTGT
GAPDH-F	CATGGCACCGTCAAGGCTGA
GAPDH-R	ACGTACTCAGCGCCAGCATC
ATG2A-F	CTCGCCTCCTCCAGATCAA
ATG2A-R	GGGCATCCTGGTCCACATTG
FOSL1-F	CAGGCGGAGACTGACAAACTG
FOSL1-R	TCCTTCCGGGATTTTGCAGAT
SOCSS-F	GTGCCACAGAAATCCCTCAAA
SOCSS-R	TCTCTTCGTGCAAGTCTTGTC

realize fast, accurate, and comprehensive functional annotation analysis of large-scale gene or protein lists. GO and KEGG analysis methods are used to perform functional analysis on the differentially expressed genes, and to screen out differentially expressed genes enriched in pathways related to crocetin treatment.

2.4. Construction of Protein Interaction Networks. Functions and interactions between proteins were analyzed by the protein-protein interaction (PPI) system. The STRING database is the largest repository of its kind, retrieving millions of discoveries from full-text literature and is updated weekly. Using the Cytoscape software to construct the PPI network, setting the protein-protein interaction score greater than 0.7 has statistical significance. CytoHubba and MCODE were used to determine the core proteins in the complex protein interaction network, and clustering was used to construct functional modules.

2.5. Real-Time PCR. The genes with obvious differential expression were selected, respectively, and the corresponding sequence files were obtained, and the amplification primers of each gene were designed across exons using the Primer 5 software. The primer sequences were designed and applied for gene expression identification as shown in Table 1. Subsequently, these genes were verified by real-time fluorescent quantitative PCR (RT-qPCR). According to manufacturer's manual, the DyNAmo™ SYBR® Green 2-Step qRT-PCR Kit (Finnzymes Oy, Espoo, Finland) was used for reverse

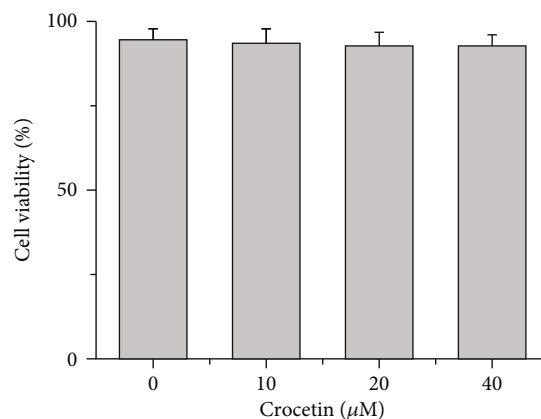


FIGURE 1: The cytotoxicity assay of HepG2 cells treated by crocetin (* $p < 0.05$).

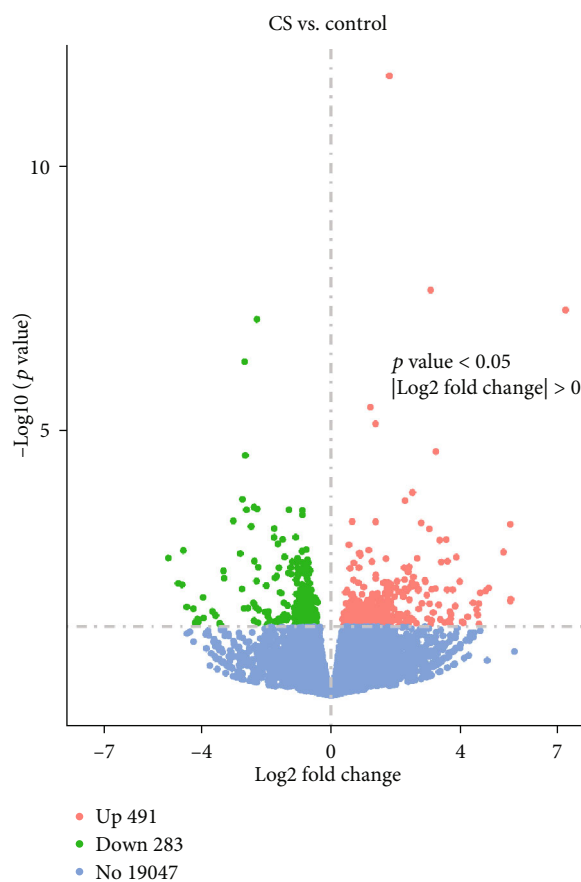


FIGURE 2: Volcano map of differentially expressed genes.

transcription and real-time PCR operations. Specifically, Oligo dT was used to reverse transcribe RNA (200 ng) into cDNA. M-MuLV RNase was applied at 37°C for 30 minutes, and then the reaction was terminated at 85°C for 5 minutes. PCR was determined according to the sequence of each primer with the T_m value. Each PCR contains 250 ng reverse transcript, 75 ng primer, and 10 μ l master mix. The thermal cycling conditions are maintained at 95°C for 15 min, and then at 94°C for 55

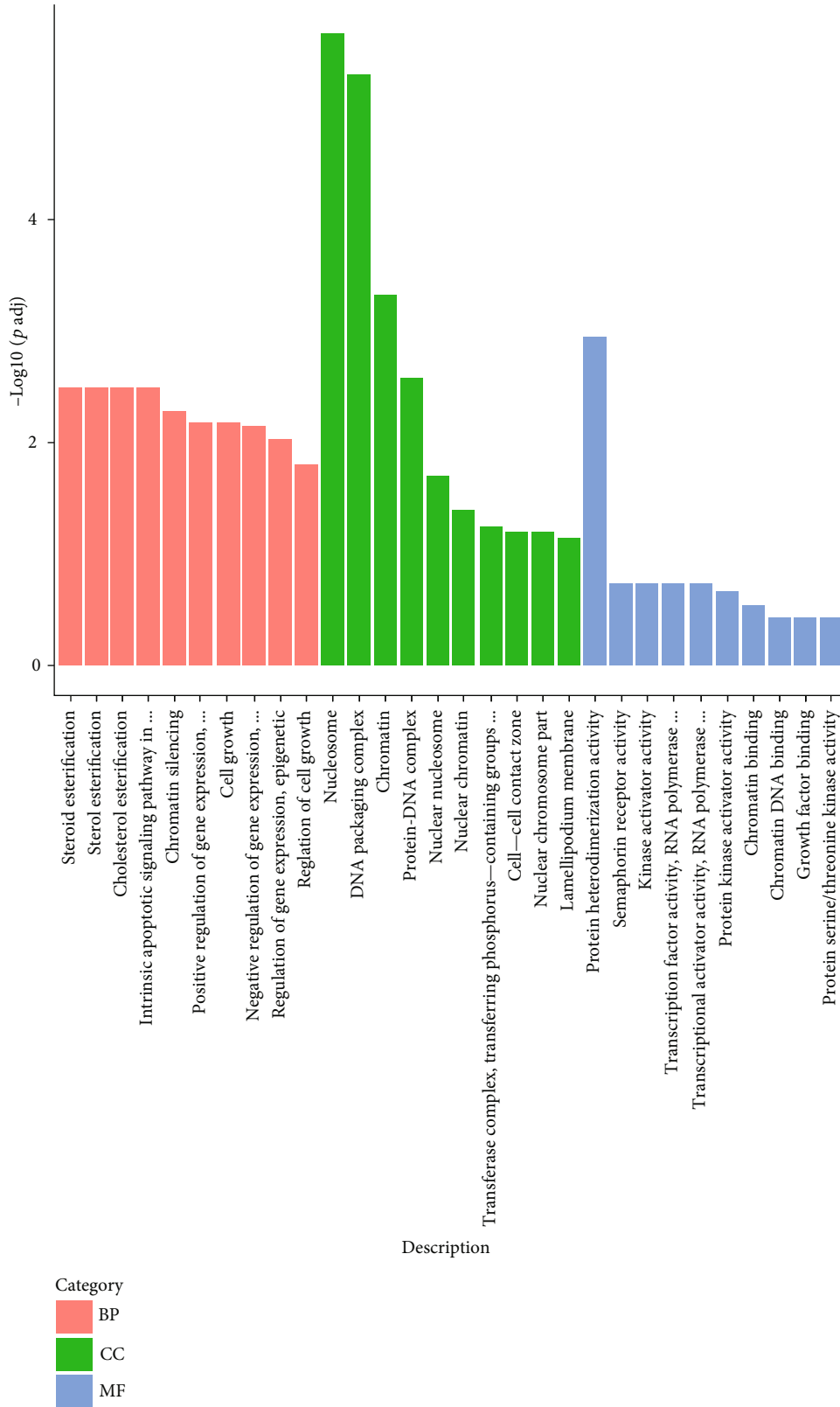


FIGURE 3: GO analysis of differentially expressed genes. GO analysis includes biological process (BP) (red), cell component (CC) (green), and molecular function (MF) (blue).

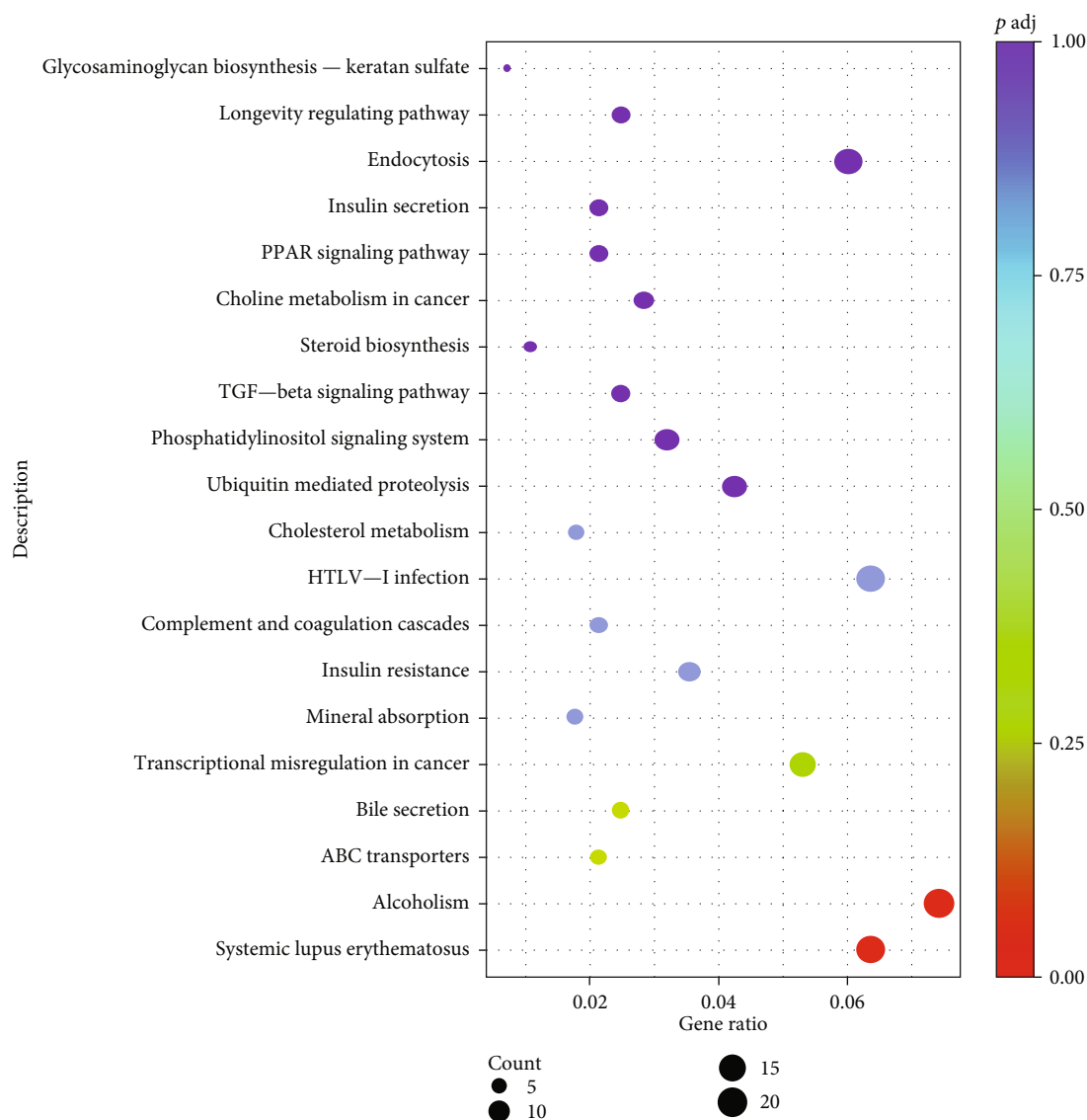


FIGURE 4: KEGG analysis of differentially expressed genes.

cycles of 30 s, with a T_m value of 30 s (melting temperature) and 30 sec at 72°C in a Rotor-Gene-3000AKAA (Corbett Research Pty., NSW, Australia).

2.6. Statistical Analysis. All the experimental data were expressed as mean \pm SD. Statistical significance was analyzed by Student's t -test and ANOVA. A statistical probability of $p < 0.05$ was considered statistically significant.

3. Results

3.1. Gene Expression Profiling. HepG2 cells were treated with diverse concentrations of crocetin, and the cytotoxicity was detected using a CCK-8 kit according the manufacturer's instructions. As shown in Figure 1, compared with the blank group, when the concentration of crocetin reached 40 μM , the number of living cells had no significant change with the survival rate of cells above 90%, indicating that there

was no toxicity to the cells under the concentration of crocetin in the range of 0–40 μM .

Among the total 45K genes, crocetin can affect the expressions of 19,821 genes among the 22,580 annotated genes in HepG2 cells; the disturbed fold of each gene is listed in Supplementary Table 1. As shown in Figure 2, the volcano map reflects the expression status of all the genes, in which green and red represent the downregulated and upregulated genes, respectively, and blue represents the genes with no differentially expressed genes. The total number of differential genes obtained from the experimental group and the control group was 774, among which 491 were upregulated genes and 283 were downregulated genes. The volcano map comparison showed that our method had sufficient coverage to detect differences in gene expression in the CS group relative to the control group.

Among the differentially expressed genes after crocetin treatment, the differentially expressed multiple of 6 genes was greater than or equal to 5, among which 5 genes were

upregulated and 1 gene was downregulated. The differential expression multiple of 19 genes was greater than or equal to 4, among which 11 genes were upregulated and 8 genes were downregulated. There were 39 genes with differential expression ratios greater than or equal to 3, among which 28 genes were upregulated and 11 genes were downregulated. The differential expression ratio of 71 genes was greater than or equal to 2, among which 49 genes were upregulated and 22 genes were downregulated. In general, from the cells treated with crocetin, there were 135 genes (0.68%, 135 : 19821) with a differential expression ratio higher than or equal to 2 times.

3.2. Gene Ontology and KEGG Pathway Analysis. As shown in Figure 3, after CS treatment (control vs. CS), nucleosome and DNA packaging complex-related components were the most significantly disturbed in the cell component group (CC in green), and chromatin and protein-DNA complex-related processes were the most enriched differential genes; the numbers of differential genes were 44 and 22, respectively. From the molecular function group (MF in blue), the most significantly disturbed was the activity of the protein heterodimer, in which the number of differentially enriched genes was 42. The most significantly disturbed in the biological process group (BP in red) was sterol esterification, in which the numbers of differentially enriched genes related to cell growth and gene epigenetic regulation were 40 and 34, respectively.

In order to further understand the functions and pathways of differential genes, the software Clusterprofiler was used to conduct KEGG pathway enrichment analysis of differential gene sets, and the top 20 pathways with the highest enrichment significance were selected for mapping. As shown in Figure 4, after CS treatment, 283 differential genes were compared with 251 KEGG pathways, which were related to transcriptional misregulation, ABC transporters, bile secretion, alcoholism, systemic lupus erythematosus, and other pathways. Among them, systemic lupus erythematosus (SLE) was the most significantly disturbed pathway, which is the first time it was implied that the crocetin has a potent and promising effect on this serious autoimmune disease.

3.3. PPI Network Analysis and Core Disturbed Gene Screening. The PPI network belongs to a scale-free network, which is not uniform. Among the PPI networks, most of the nodes have only one or two connections while a few nodes have lots of connections, ensuring that the system is fully connected. Nodes with a high number of connections, in this network, become hubs, which play an irreplaceable role in biological evolution and in maintaining the stability of the interaction network. These nodes normally have very key biological functions and participate in important life activities. The results show that the more interactions a protein interacts with, the more important is its role for the survival of the cell.

In order to understand the function of crocetin-induced differentially expressed genes and screen out Hub genes/proteins, the STRING database was used to analyze the interactions on the PPI network relationship. The list of

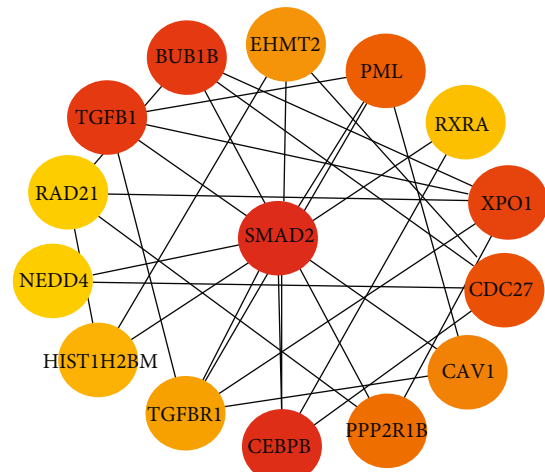


FIGURE 5: The 15 genes with the highest parameter values obtained by calculation are used as hub genes. The color change of the node indicates the increase or decrease of the parameter value.

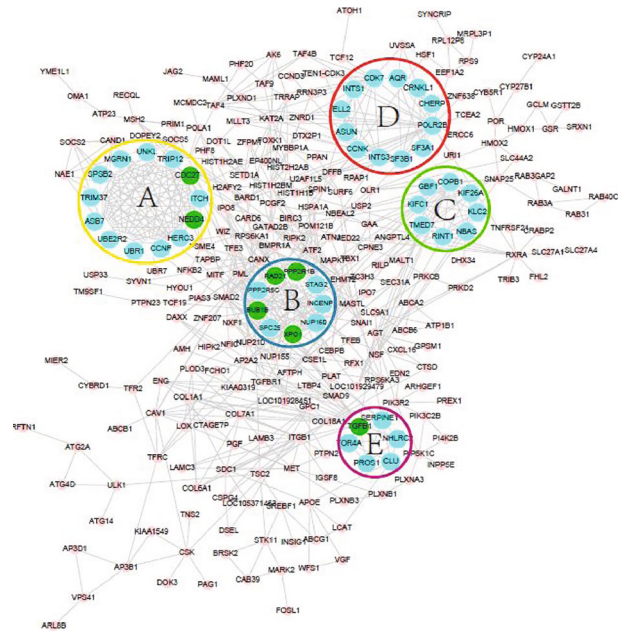


FIGURE 6: The five most important modules in the PPI network. According to the standard with a K-core greater than 6, the five important clusters obtained from formic acid in the PPI network are labeled A, B, C, D, and E, respectively, and are considered to be the topological center of the PPI network. The nodes marked in red represent the upregulated genes participating in the 5 subnetworks (none), and the nodes marked in green represent the downregulated genes.

differentially expressed genes was imported into the STRING database, and the data obtained from experiments, literatures, and high-throughput evidences were combined, and then the protein interaction data set encoded by the differentially expressed genes was downloaded. In the PPI network of differentially expressed genes treated with crocetin, 359 differentially expressed genes that encoded proteins were

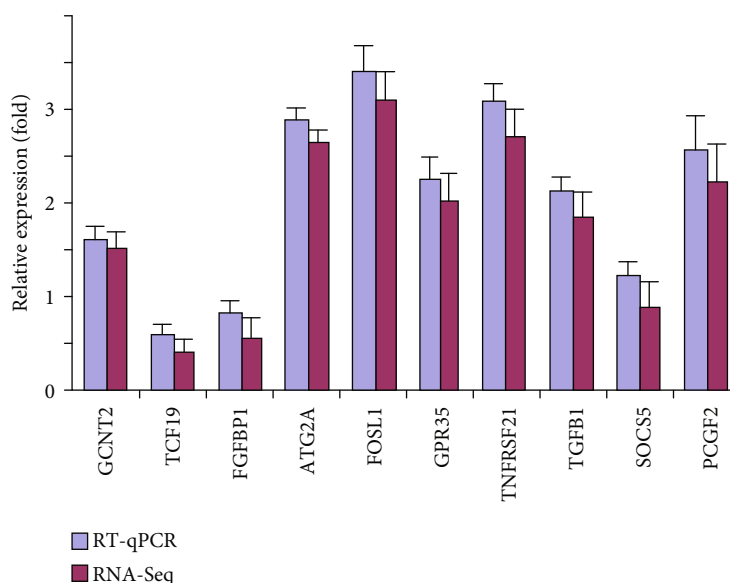


FIGURE 7: Comparison of differential gene expressions obtained by real-time PCR and RNA-seq sequencing results. Error bars show standard deviation.

screened with relatively close interactions, including 359 protein nodes and 761 correlations.

However, it is difficult to visually identify the key nodes in the network due to the scale-free network nature of most biological data networks. CytoHubba plug-ins in the Cytoscape software were then used to calculate the Hub genes/proteins in the network diagram. According to the order of parameter and radiality from high to low as the standard, a total of 15 core proteins were screened, which includes the SMAD family variant 2 (SMAD2), CCAAT enhancer binding protein beta (CEBPB), conversion factor 1 (TGFB1), mitotic checkpoint serine/threonine protein kinase B (BUB1B), output 1 (XPO1), cell division cycle protein 27 (CDC27), early young granulocyte leukemia variant 1 (PML) transcription, protein phosphatase 2 support subunits X5 (PPP2R1B), cellular protein 1 (CAV1), autosomal histone lysine methylation transferase (EHMT2) 2, transforming growth factor beta receptor 1 (TGFBR1), histone (Hist1H2BM), retinol X receptor α (RXRA), adhesive protein complex (Rad21), and E3 ubiquitin protein ligase (Nedd4) (Figure 5). SMAD proteins encoded by their respective genes are signal transducers and transcriptional modulators that mediate multiple signaling pathways [17, 18]. This protein mediates the signal of the transforming growth factor- (TGF-) beta, and thus regulates multiple cellular processes, such as cell proliferation, apoptosis, and differentiation [19, 20]. SMAD proteins are recruited to the TGF-beta receptors through its interaction with the SMAD anchor for receptor activation (SARA) protein, and further phosphorylated by the TGF-beta receptors [21].

For further understanding the important module of PPI, the Cytoscape MCODE software was used to screen out fine modules with K-core values greater than 6, and mark the above 15 hub genes in each module; we can see that the 15 hub genes were mostly in the five important modules selected as shown in Figure 6.

3.4. Regulation of the Expressions of Typical Genes by Crocetin Treatment. Drug metabolic enzymes are composed of phase I and phase II metabolic enzymes and phase III transporters, which play an important role in the metabolism, digestion, and detoxification of foreign substances and drugs. The biological functions of crocetin in the human body, such as anti-cancer, antioxidant, and anti-inflammatory, have been found, but its effect on liver cells, especially on hepatic drug metabolism enzymes and transporters, are still unclear. In the present study, genes with a differential expression ratio greater than or equal to 1.5 were selected as significantly different genes. Among the total 445 metabolic enzyme genes, 28 genes were disturbed by crocetin, with 20 genes upregulated and 8 genes downregulated. For instance, *GCNT2*, *ABCB1*, *ABCG1*, *ABCA2*, *CYP24A1*, *CYP27B1*, and *AHRR* are significantly upregulated genes by crocetin treatment, which implied that crocetin stimulated the expressions of hepatic metabolic enzymes.

In order to know the effect of crocetin on inflammation in the liver cells, several typical inflammatory differentially expressed genes were selected for analysis, and it was found that 199 genes in the total 455 inflammatory genes were significantly disturbed by crocetin treatment, with 158 upregulated genes and 41 downregulated genes. Among them, *GRP35*, *AGT*, *PDE5A*, *MMP28*, *IFIT2*, *TCF19*, *FGFBP1*, *SOCS5*, *TGFBI*, *PCGF2*, *FGFRL1*, *TNFRSF21*, and *VGF* are the most significantly downregulated genes by crocetin treatment, which revealed that crocetin is a potent and promising anti-inflammatory substance. Besides, glycolipid metabolism and other biofunction genes were also selected for analysis, and it was found that many glycolipid metabolism-related genes, 48 from the total of 445 genes, such as *EHMT2*, *AGT*, *RYR3*, *HBPI*, *GCNT2*, *BMT2*, *HSF1*, *NSF*, *TSC2*, *SP2*, *FA2H*, *CAD*, and *APOE*, were the most disturbed genes by crocetin treatment, which indicated that crocetin may exert its multiple biofunction by regulating glycolipid metabolism.

Finally, to verify the accuracy of the transcriptome data, several typical genes are selected by RT-qPCR verification. As shown in Figure 7, the RT-qPCR data showed the same trends with the results of transcriptome, suggesting that RNA-sequencing is believable.

4. Discussion and Conclusion

The present study investigated the effect of crocetin on gene expression profiling of HepG2 cells by RNA-sequence assay and further analyzed the molecular mechanism underlying its multiple biofunction based on bioinformatics analysis and molecular evidence. The 774 differentially expressed genes in the transcription process were annotated by GO and KEGG analysis. In the three categories of the GO analysis catalog, the differentially expressed genes were mainly concentrated in nucleosomes, protein-DNA complexes, transcription factors, lipids, transferases, transcription factors, and other processes in the CC group. When treated with MF, different genes were mainly concentrated in the activities of signal transduction receptors, transcription factors, protein kinases, growth factors, transformation factors, etc. Differential genes were mainly concentrated in the MP group such as esterification, apoptosis, chromatin or gene silencing, and cell response to growth factor stimulation.

Through the PPI network analysis of the interaction between the coding proteins of different genes, the interaction between multiple differentially expressed genes was enriched. Further, 15 core proteins in the network were screened by the Cytoscape software, among which the differentially expressed genes corresponding to the core proteins of PPP2R1b, Rad21, Sub1b, XPO1, and TGFB1 were significantly downregulated. Among them, PPP2R1B is a tumor suppressor gene that encodes the β subtype of the serine/threonine-specific protein phosphatase 2A (PP2A-A β) A subunit, which is inactivated in cancer patients [22]. RAD21 is involved in the regulation of the normal cell cycle, DNA, DSB repair, and apoptosis pathways. In addition, the germline heterozygous or homozygous missense mutations of RAD21 are related to human genetic diseases [23]. XPO1 is an export receptor responsible for the nuclear-cytoplasmic transport of hundreds of proteins and various RNAs. XPO1 is often overexpressed and/or mutated in human cancers, and acts as a carcinogenic driver. Therefore, inhibiting XPO1-mediated nuclear export is a unique treatment strategy [24]. Subsequently, the PPI network of the modules was screened, and 5 important modules were obtained; most of these core proteins were in these 5 important modules.

To be noted, it was found that among the total drug metabolism enzymes (445 genes), 28 genes were significantly disturbed by crocetin treatment, with 20 genes upregulated and 8 genes downregulated, indicating that crocetin could positively influence the processes related to drug metabolism enzymes in human liver cells. Among them, *GCNT2* [25], *ABCBI* [26, 27], *ABCG1* [28, 29], *ABCA2* [30], *CYP24A1* [31, 32], *CYP27B1* [33], and *AHRR* [34] were the core genes of drug metabolism enzymes, which were worthy of further verification. Abnormal cellu-

lar proliferation and apoptosis are typical features of tumor cells, and genetic variations in the study pathway enrichment are mainly involved in transcription, intrinsic apoptotic signaling pathways, gene silencing, miRNA regulation gene silencing, and cell cycle regulation. Of these, 62 and 35 genes directly regulated the cell proliferation and apoptosis processes, respectively, and it is speculated that saffron acid could promote cell proliferation and apoptosis. In particular, *BRD4* [35, 36], *FAM83H* [37, 38], and *FOXK1* [39–42] are reported to be involved in the cell proliferation process of human pancreatic cancer and lung cancer, respectively, while *DAX* [43], *PML* [44], and *ULK1* [45] are reported to be involved in the cell apoptosis process of breast cancer, leukemia, and smooth muscle cells, respectively.

The above results indicate that crocetin is mostly positively associated with drug metabolism enzymes, transporters, inflammatory factors, and glucose and lipid metabolism, as well as cell proliferation and apoptosis processes in HepG2 cells. And the core genes were further detected by an RT-PCR experiment, which was consistent with the results of transcriptome sequencing, indicating that the results of transcriptome sequencing were real and reliable.

To conclude, our transcriptome data revealed gene expression profiles of crocetin in HepG2 cells for the first time. Signaling pathway analysis further demonstrated that systemic lupus erythematosus is involved in crocetin-induced expressions of most hepatic drug metabolizing enzyme genes. These results provide a comprehensive data for understanding the hepatic metabolism, the bioactive role, and the molecular mechanisms of crocetin.

Data Availability

The transcriptome data used to support the findings of this study are included within the supplementary information file.

Conflicts of Interest

We have no direct or indirect commercial financial incentive associated with publishing this article.

Authors' Contributions

Yi-Ling Wen and Yong Li contributed equally to this work.

Acknowledgments

This work was partially supported by grants from the National Key Research and Development Program of China (2019YFC1604903), the Natural Science Foundation of Hunan Province (2019JJ40132), and the Double First-Class Construction Project of Hunan Agricultural University (SYL201802025) to Si Qin.

Supplementary Materials

Supplementary description: raw data of the transcriptome assay in HepG2 cells. (*Supplementary Materials*)

References

- [1] A. R. Khorasany and H. Hosseinzadeh, "Therapeutic effects of saffron (*Crocus sativus* L.) in digestive disorders: a review," *Iranian Journal of Basic Medical Sciences*, vol. 19, no. 5, pp. 455–469, 2016.
- [2] A. S. Ahmad, M. A. Ansari, M. Ahmad et al., "Neuroprotection by crocetin in a hemi-parkinsonian rat model," *Pharmacology, Biochemistry, and Behavior*, vol. 81, no. 4, pp. 805–813, 2005.
- [3] M. B. Khan, M. N. Hoda, T. Ishrat et al., "Neuroprotective efficacy of *Nardostachys jatamansi* and crocetin in conjunction with selenium in cognitive impairment," *Neurological Sciences*, vol. 33, no. 5, pp. 1011–1020, 2012.
- [4] D. Chryssanthi, P. Dedes, N. Karamanos, P. Cordopatis, and F. Lamari, "Crocetin inhibits invasiveness of MDA-MB-231 breast cancer cells via downregulation of matrix metalloproteinases," *Planta Medica*, vol. 77, no. 2, pp. 146–151, 2011.
- [5] K. He, P. Si, H. Wang et al., "Crocetin induces apoptosis of BGC-823 human gastric cancer cells," *Molecular Medicine Reports*, vol. 9, no. 2, pp. 521–526, 2014.
- [6] J. Yan, Z. Qian, L. Sheng et al., "Effect of crocetin on blood pressure restoration and synthesis of inflammatory mediators in heart after hemorrhagic shock in anesthetized rats," *Shock*, vol. 33, no. 1, pp. 83–87, 2010.
- [7] B. Chen, Z. H. Hou, Z. Dong, and C. D. Li, "Crocetin downregulates the proinflammatory cytokines in methylcholanthrene-induced rodent tumor model and inhibits COX-2 expression in cervical cancer cells," *BioMed Research International*, vol. 2015, Article ID 829513, 5 pages, 2015.
- [8] K. N. Nam, Y. M. Park, H. J. Jung et al., "Anti-inflammatory effects of crocin and crocetin in rat brain microglial cells," *European Journal of Pharmacology*, vol. 648, no. 1–3, pp. 110–116, 2010.
- [9] M. Hashemi and H. Hosseinzadeh, "A comprehensive review on biological activities and toxicology of crocetin," *Food and Chemical Toxicology*, vol. 130, pp. 44–60, 2019.
- [10] S. Higashino, Y. Sasaki, J. C. Giddings et al., "Crocetin, a Carotenoid from *Gardenia jasminoides* Ellis, protects against hypertension and cerebral thrombogenesis in stroke-prone spontaneously hypertensive rats," *Phytotherapy Research*, vol. 28, no. 9, pp. 1315–1319, 2014.
- [11] P. Chen, Y. Chen, Y. Wang et al., "Comparative evaluation of hepatoprotective activities of geniposide, crocins and crocetin by CCl₄-induced liver injury in mice," *Biomolecules & Therapeutics*, vol. 24, no. 2, pp. 156–162, 2016.
- [12] C. Carlberg, "Nutrigenomics of Vitamin D," *Nutrients*, vol. 11, no. 3, p. 676, 2019.
- [13] M. S. Ferreira, L. A. Tomaz, M. B. Niehues et al., "The inclusion of de-oiled wet distillers grains in feedlot diets reduces the expression of lipogenic genes and fat content in Longissimus muscle from F1 Angus-Nellore cattle," *PeerJ*, vol. 7, article e7699, 2019.
- [14] M. Yu, Z. Li, W. Chen, T. Rong, G. Wang, and X. Ma, "*Hermetia illucens* larvae as a potential dietary protein source altered the microbiota and modulated mucosal immune status in the colon of finishing pigs," *Journal of Animal Science and Biotechnology*, vol. 10, no. 4, article 50, 2019.
- [15] M. Yu, Z. Li, W. Chen, G. Wang, Y. Cui, and X. Ma, "Dietary supplementation with citrus extract altered the intestinal microbiota and microbial metabolite profiles and enhanced the mucosal immune homeostasis in yellow-feathered broilers," *Frontiers in Microbiology*, vol. 10, article 2662, 2019.
- [16] A. Suárez-Vega, B. Gutiérrez-Gil, P. G. Toral, G. Hervás, J. J. Arranz, and P. Frutos, "Conjugated linoleic acid (CLA)-induced milk fat depression: application of RNA-Seq technology to elucidate mammary gene regulation in dairy ewes," *Scientific Reports*, vol. 9, article 4473, 2019.
- [17] S. Zagabathina, R. Ramadoss, A. H. Harini Priya, and R. Krishnan, "Comparative evaluation of SMAD-2 expression in oral submucous fibrosis and reactive oral lesions," *Asian Pacific Journal of Cancer Prevention*, vol. 21, no. 2, pp. 399–403, 2020.
- [18] D. Kamato, M. Burch, Y. Zhou et al., "Individual Smad2 linker region phosphorylation sites determine the expression of proteoglycan and glycosaminoglycan synthesizing genes," *Cellular Signalling*, vol. 53, pp. 365–373, 2018.
- [19] C. R. Gignoux, D. G. Torgerson, M. Pino-Yanes et al., "An admixture mapping meta-analysis implicates genetic variation at 18q21 with asthma susceptibility in Latinos," *Journal of Allergy and Clinical Immunology*, vol. 142, no. 2, pp. 957–969, 2018.
- [20] J. L. Granadillo, W. K. Chung, L. Hecht et al., "Variable cardiovascular phenotypes associated with SMAD2 pathogenic variants," *Human Mutation*, vol. 39, no. 12, pp. 1875–1884, 2018.
- [21] E. Cannaearts, M. Kempers, A. Maugeri et al., "Novel pathogenic SMAD2 variants in five families with arterial aneurysm and dissection: further delineation of the phenotype," *Journal of Medical Genetics*, vol. 56, no. 4, 2018.
- [22] M. Tamaki, T. Goi, Y. Hirono, K. Katayama, and A. Yamaguchi, "PPP2R1B gene alterations inhibit interaction of PP2A-A β and PP2A-C proteins in colorectal cancers," *Oncology Reports*, vol. 11, pp. 655–659, 2004.
- [23] H. Cheng, N. Zhang, and D. J. G. Pati, "Cohesin subunit RAD21: from biology to disease," *Gene*, vol. 758, article 144966, 2020.
- [24] N. G. Azizian and Y. Li, "XPO1-dependent nuclear export as a target for cancer therapy," *Journal of Hematology & Oncology*, vol. 13, no. 1, 2020.
- [25] C. Li and Q. Wu, "Adaptive evolution of multiple-variable exons and structural diversity of drug-metabolizing enzymes," *BMC Evolutionary Biology*, vol. 7, no. 1, p. 69, 2007.
- [26] A. van Helvoort, A. J. Smith, H. Sprong et al., "MDR1 P-glycoprotein is a lipid translocase of broad specificity, while MDR3 P-glycoprotein specifically translocates phosphatidylcholine," *Cell*, vol. 87, no. 3, pp. 507–517, 1996.
- [27] K. Choi, C. J. Chen, M. Krieger, and I. B. Roninson, "An altered pattern of cross-resistance in multidrug-resistant human cells results from spontaneous mutations in the mdr1 (P-glycoprotein) gene," *Cell*, vol. 53, no. 4, pp. 519–529, 1988.
- [28] E. A. Roundhill, S. Jabri, and S. A. Burchill, "ABCG1 and Pgp identify drug resistant, self-renewing osteosarcoma cells," *Cancer Letters*, vol. 453, pp. 142–157, 2019.
- [29] T. Engel, F. Kannenberg, M. Fobker et al., "Expression of ATP binding cassette-transporter ABCG1 prevents cell death by transporting cytotoxic 7 β -hydroxycholesterol," *FEBS Letters*, vol. 581, no. 8, pp. 1673–1680, 2007.

- [30] J. Mack, D. Townsend, V. Beljanski, and K. Tew, "The ABCA2 transporter: intracellular roles in trafficking and metabolism of LDL-derived cholesterol and sterol-related compounds," *Current Drug Metabolism*, vol. 8, no. 1, pp. 47–57, 2007.
- [31] K. Yasuda, E. Tohyama, M. Takano et al., "Metabolism of 2 α -[2-(tetrazol-2-yl)ethyl]-1 α ,25-dihydroxyvitamin D(3) by CYP24A1 and biological activity of its 24R-hydroxylated metabolite," *The Journal of Steroid Biochemistry and Molecular Biology*, vol. 178, pp. 333–339, 2018.
- [32] E. W. Tieu, E. K. Y. Tang, and R. C. Tuckey, "Kinetic analysis of human CYP24A1 metabolism of vitamin D via the C24-oxidation pathway," *FEBS Journal*, vol. 281, no. 14, pp. 3280–3296, 2014.
- [33] M. B. Meyer and J. W. Pike, "Mechanistic homeostasis of vitamin D metabolism in the kidney through reciprocal modulation of Cyp27b1 and Cyp24a1 expression," *The Journal of Steroid Biochemistry and Molecular Biology*, vol. 196, p. 105500, 2020.
- [34] T. Haarmann-Stemmann and J. Abel, "The arylhydrocarbon receptor repressor (AhRR): structure, expression, and function," *Biological Chemistry*, vol. 387, no. 9, pp. 1195–1199, 2006.
- [35] Y. F. Tan, M. Wang, Z. Y. Chen, L. Wang, and X. H. Liu, "Inhibition of BRD4 prevents proliferation and epithelial-mesenchymal transition in renal cell carcinoma via NLRP3 inflammasome-induced pyroptosis," *Cell Death & Disease*, vol. 11, no. 4, p. 239, 2020.
- [36] M. Yin, Y. Guo, R. Hu et al., "Potent BRD4 inhibitor suppresses cancer cell-macrophage interaction," *Nature Communications*, vol. 11, no. 1, p. 1833, 2020.
- [37] Y. K. Ma, T. H. Shen, and X. Y. Yang, "Upregulation of lncRNA FAM83H-AS1 in hepatocellular carcinoma promotes cell proliferation, migration and invasion by Wnt/ β -catenin pathway," *European Review for Medical and Pharmacological Sciences*, vol. 23, no. 18, pp. 7855–7862, 2019.
- [38] H. Shan, Y. Yang, X. Zhu, X. Han, P. Zhang, and X. Zhang, "FAM83H-AS1 is associated with clinical progression and modulates cell proliferation, migration, and invasion in bladder cancer," *Journal of Cellular Biochemistry*, vol. 120, no. 3, pp. 4687–4693, 2019.
- [39] J. Li, S. Huang, Y. Zhang, W. Zhuo, B. Tong, and F. Cai, "LINC00460 enhances bladder carcinoma cell proliferation and migration by modulating miR-612/FOXK1 axis," *Pharmacology*, vol. 106, pp. 79–90, 2020.
- [40] L. Li, M. Gong, Y. Zhao, X. Zhao, and Q. Li, "FOXK1 facilitates cell proliferation through regulating the expression of p21, and promotes metastasis in ovarian cancer," *Oncotarget*, vol. 8, no. 41, pp. 70441–70451, 2017.
- [41] M. Wencong, W. Jinghan, Y. Yong et al., "FOXK1 promotes proliferation and metastasis of gallbladder cancer by activating AKT/mTOR signaling pathway," *Frontiers in Oncology*, vol. 10, p. 545, 2020.
- [42] H. Xu, S. Huang, X. Zhu, W. Zhang, and X. Zhang, "FOXK1 promotes glioblastoma proliferation and metastasis through activation of Snail transcription," *Experimental and Therapeutic Medicine*, vol. 15, no. 3, pp. 3108–3116, 2018.
- [43] M. Lanzino, P. Maris, R. Sirianni et al., "DAX-1, as an androgen-target gene, inhibits aromatase expression: a novel mechanism blocking estrogen-dependent breast cancer cell proliferation," *Cell Death & Disease*, vol. 4, no. 7, article e724, 2013.
- [44] L. Zhang, Q. S. Chen, P. P. Xu et al., "Catechins induced acute promyelocytic leukemia cell apoptosis and triggered PML-RAR α oncoprotein degradation," *Journal of Hematology & Oncology*, vol. 7, no. 1, p. 75, 2014.
- [45] D. Gui, Z. Cui, L. Zhang et al., "Salidroside attenuates hypoxia-induced pulmonary arterial smooth muscle cell proliferation and apoptosis resistance by upregulating autophagy through the AMPK-mTOR-ULK1 pathway," *BMC Pulmonary Medicine*, vol. 17, no. 1, p. 191, 2017.

Research Article

Whole-Transcriptome RNA Sequencing Reveals Significant Differentially Expressed mRNAs, miRNAs, and lncRNAs and Related Regulating Biological Pathways in the Peripheral Blood of COVID-19 Patients

Cai-xia Li ^{1,2}, Jian Chen,¹ Shu-kai Lv,¹ Jin-hui Li,¹ Lei-lei Li,¹ and Xiao Hu ¹

¹The Fourth Affiliated Hospital Zhejiang University School of Medicine, Yiwu, Zhejiang, China

²The First Affiliated Hospital Zhejiang University School of Medicine, Hangzhou, Zhejiang, China

Correspondence should be addressed to Xiao Hu; huxiao700@zju.edu.cn

Received 3 November 2020; Revised 20 February 2021; Accepted 27 February 2021; Published 2 April 2021

Academic Editor: Yaoyao Xia

Copyright © 2021 Cai-xia Li et al. This is an open access article distributed under the Creative Commons Attribution License, which permits unrestricted use, distribution, and reproduction in any medium, provided the original work is properly cited.

Severe acute respiratory syndrome coronavirus 2 (SARS-CoV-2) was initially identified in China and currently worldwide dispersed, resulting in the coronavirus disease 2019 (COVID-19) pandemic. Notably, COVID-19 is characterized by systemic inflammation. However, the potential mechanisms of the “cytokine storm” of COVID-19 are still limited. In this study, fourteen peripheral blood samples from COVID-19 patients ($n = 10$) and healthy donors ($n = 4$) were collected to perform the whole-transcriptome sequencing. Lung tissues of COVID-19 patients (70%) presenting with ground-glass opacity. Also, the leukocytes and lymphocytes were significantly decreased in COVID-19 compared with the control group ($p < 0.05$). In total, 25,482 differentially expressed messenger RNAs (DE mRNA), 23 differentially expressed microRNAs (DE miRNA), and 410 differentially expressed long noncoding RNAs (DE lncRNAs) were identified in the COVID-19 samples compared to the healthy controls. Gene Ontology (GO) analysis showed that the upregulated DE mRNAs were mainly involved in antigen processing and presentation of endogenous antigen, positive regulation of T cell mediated cytotoxicity, and positive regulation of gamma-delta T cell activation. The downregulated DE mRNAs were mainly concentrated in the glycogen biosynthetic process. We also established the protein-protein interaction (PPI) networks of up/downregulated DE mRNAs and identified 4 modules. Functional enrichment analyses indicated that these module targets were associated with positive regulation of cytokine production, cytokine-mediated signaling pathway, leukocyte differentiation, and migration. A total of 6 hub genes were selected in the PPI module networks including AKT1, TNFRSF1B, FCGR2A, CXCL8, STAT3, and TLR2. Moreover, a competing endogenous RNA network showed the interactions between lncRNAs, mRNAs, and miRNAs. Our results highlight the potential pathogenesis of excessive cytokine production such as MSTRG.119845.30/hsa-miR-20a-5p/TNFRSF1B, MSTRG.119845.30/hsa-miR-29b-2-5p/FCGR2A, and MSTRG.106112.2/hsa-miR-6501-5p/STAT3 axis, which may also play an important role in the development of ground-glass opacity in COVID-19 patients. This study gives new insights into inflammation regulatory mechanisms of coding and noncoding RNAs in COVID-19, which may provide novel diagnostic biomarkers and therapeutic avenues for COVID-19 patients.

1. Introduction

Severe acute respiratory syndrome coronavirus 2 (SARS-CoV-2) is a novel lineage B betacoronavirus that causes zoonotic diseases and was first reported in Wuhan, China, in December 2019 [1, 2]. The pandemic caused by SARS-CoV-2 was named as coronavirus disease 2019 (COVID-

19) by the World Health Organization (WHO) and rapidly spreads around the world [3]. As of February 20, 2021, a total of 111,234,365 coronaviruses confirmed cases and 2,462,703 deaths have been reported all around the world, the USA being on top so far [4].

Previous studies have reported that the COVID-19 patients suffered from asymptomatic or mild respiratory

infection to acute respiratory distress syndrome (ARDS) or multiorgan failure, and this disease was more likely to occur in elderly people with a weak immune function [1, 5, 6]. Most patients have a cough, fever, shortness of breath, and fatigue [7]. Also, the majority of patients with COVID-19 have a pleasing prognosis, but there were still ARDS and multiorgan dysfunction that occurred rapidly, resulting in death within a short time [7, 8]. Therefore, understanding the genomic landscape of serum of COVID-19 patients will help in improving the treatment avenues and diagnosis strategies.

Clinically significantly, SARS-CoV-2 infection rapidly results in severe pneumonia symptoms and complications, and the host immune response against SARS-CoV-2 infection remains largely unknown. The viral RNAs are recognized by toll-like receptors (TLRs), NOD-like receptors (NLRs), and RIG-I-like receptors (RLRs), and the innate immune systems activating the T CD8+ cells, natural killer cells, and macrophages to eliminate the viruses [9, 10]. Unfortunately, the SARS-CoV and Middle East respiratory syndrome coronavirus (MERS-CoV) have evolved strategies to avoid immune responses, which usually trigger excessive inflammatory host responses [11]. It has been reported that the dysregulated production of inflammatory cytokines, known as the “cytokine storm,” in serum was associated with pulmonary inflammation and severe lung histopathology changes in SARS-CoV [12] and MERS-CoV infection [13]. Besides, it is noteworthy that the interstitial mononuclear inflammatory infiltrates in lung tissues were remarkably observed in the COVID-19 biopsy samples through clinical pathological analysis [14]. A study by Xiong et al. demonstrated that excessive cytokine release such as CCL2/MCP-1, CXCL10/IP-10, CCL3/MIP-1A, and CCL4/MIP1B is playing critical roles in COVID-19 pathogenesis [10]. However, the underlying mechanisms involved in the abnormal inflammatory responses under SARS-CoV-2 infection remain to be investigated. Hence, it is important to explore the aberrant expression of genes that are associated with the initiation and development of COVID-19.

Noncoding RNAs (ncRNAs) are a class of crucial regulatory potentials both in transcription and posttranscription and are divided into long ncRNAs (lncRNAs) and short ncRNAs [15, 16]. MicroRNAs (miRNAs), a kind of single-stranded RNA of 18~24 nucleotides in length, participate in messenger RNA (mRNAs) degradation or translational inhibition by binding to the 3' UTR of their target sites [17]. lncRNAs are a special type of ncRNAs with lengths exceeding 200 nucleotides and are also divided into exonic, intronic, intergenic, and overlapping lncRNA based on its locations relative to the corresponding transcripts [18]. A competing endogenous RNA (ceRNA) hypothesis has been firstly proposed by Salmena et al. in 2011 [19] that the lncRNAs can function as a miRNA sponge by complementary base pairing with targeted miRNA using miRNA response elements (MREs) and thus participated in the development and progression of diseases. For the ceRNA patterns, miRNAs also act as the critical communication bridges between the coding and noncoding RNAs. Moreover, recent reports have summarized that miRNAs and lncRNAs have diagnostic and therapeutic potential in inflammatory diseases [20] and

infectious diseases [21, 22]. Therefore, it is essential to further investigate the network regulatory crosstalk across coding and noncoding RNAs induced by miRNAs, which may contribute to discovering the promising drug targets for COVID-19 treatment from a holistic attitude.

With great advances in high-throughput RNA sequencing (RNAseq) technologies, transcriptomic analyses of peripheral blood samples of patients with virus infection are enable us to analyze the differentially expressed genes (DEGs) that associated with the host immune and/or inflammation response and gene interaction regulatory networks [10, 23]. Interestingly, integrated mRNA, miRNA, and lncRNA sequencing analysis will further increase understanding of the biological functions and the corresponding signaling pathways of DEGs in different diseases. However, relevant researches to discuss the global gene expression profile of COVID-19 are greatly limited. In the current study, whole-transcriptome RNAseq was performed in peripheral blood collected from human COVID-19 patients and healthy donors to illustrate the transcriptomic landscape at mRNAs, miRNAs, and lncRNAs levels. Finally, we successfully constructed a lncRNA-miRNA-mRNA network to research preliminarily the potential molecular mechanisms underlying in response to inflammatory host responses in COVID-19. Figure 1 shows the workflow of the whole-transcriptome RNA sequencing study of peripheral blood samples of COVID-19 patients.

2. Materials and Methods

2.1. Patients. The peripheral blood samples were obtained from 10 COVID-19 patients (named as X1~X10, respectively) and 4 healthy donors (named as X11~X14, respectively) at the Fourth Affiliated Hospital, College of Medicine, Zhejiang University from February to March 2020. Besides, the clinical data of these COVID-19 patients was recorded that ranged for various parameters to increase the understanding of COVID-19.

The study was approved by the Ethics Committee of the Fourth Affiliated Hospital, College of Medicine, Zhejiang University, and registered at the Chinese Clinical Trial Registry (ChiCTR2000030305, <http://www.medresman.org.cn/login.aspx>). All patients provided written informed consent, and the patients tested positive for SARS-CoV-2 RNA in pharyngeal swab specimens by real-time reverse transcription-polymerase chain reaction (RT-PCR).

2.2. RNA Extraction, Quality Control, Library Construction, and Sequencing. The whole blood (2 mL) was extracted from all donors by using BD PAXgene blood RNA tubes (BD, cat. no. 762165). The blood was then mixed up and down 8-10 times. After that, the PAXgene tubes were incubated at room temperature for at least 2 h to ensure that the blood cells were completely dissolved. Next, the total RNA was extracted using the TRIzol reagent (Invitrogen, USA) following the manufacturer's protocol. Subsequently, the quantity and quality of total RNA were assessed using a NanoDrop 2000 Spectrophotometer (Thermo Fisher Scientific, USA) and Agilent 2100 bioanalyzer (Agilent

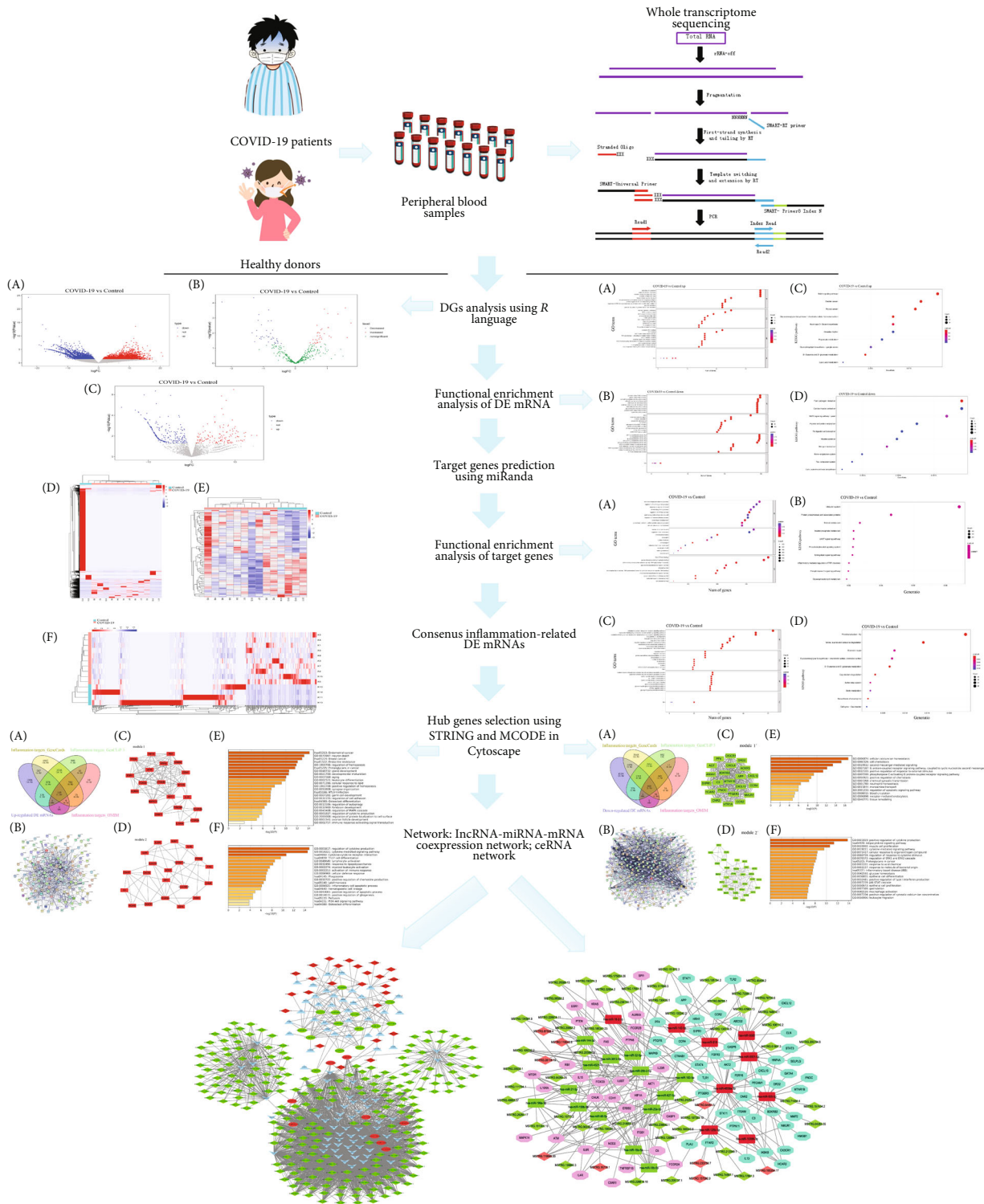


FIGURE 1: The workflow of the Whole-transcriptome RNA sequencing analysis of peripheral blood samples of COVID-19 patients.

Technologies, USA). The sequencing libraries were created with a TruSeq Stranded Total RNA Library Prep Kit (Illumina, USA) according to the manufacturer’s protocol. The libraries were sequenced on an Illumina HiSeq X Ten platform at katimesbio CO., LTD (Hangzhou, China) generating 150 bp paired-end reads.

2.3. Preprocessing of Raw Reads. The quality of the raw reads was estimated using fastp software [24] to remove the low-quality reads and the adaptors. Also, reads that were shorter than 18 nt and those that mapped to rRNA were discarded. Next, the remaining clean reads were genome-mapped using spliced mapping in the Hisat2 package [25].

2.4. Identification of miRNA and lncRNA. miRNAs were initially identified with miRdeep2 software (<https://github.com/rajewsky-lab/mirdeep2>) [26]. For lncRNAs, we screened transcripts longer than 200 bp containing two or more exons from the alignment and chose the transcripts with noncoding ability using the EggNOG (version 5.0.0), Coding-Non-Coding index (CNCI, version 2.0), Pfam Scan (version 1.6), and Coding Potential Calculator 2.0 (CPC2).

2.5. Screening of DE mRNAs, DE miRNAs, and DE lncRNAs. The expression level of each mRNA and lncRNAs was calculated according to the fragments per kilobase of the transcript per million mapped read (FPKM) method. And the expression level of each miRNA was analyzed with the reads per million (RPM) method. Differential expression analysis of mRNA, miRNAs, and lncRNAs was performed with the DESeq R package (version 3.11, <https://bioconductor.org/packages/release/bioc/html/DESeq2.html>). Transcripts with a p value < 0.05 and $|\log_2^{\text{foldchange(FC)}}| > 1$ were considered as DE mRNAs, DE miRNAs, and DE lncRNAs. And the hierarchical clustering analysis was drawn on the DE mRNAs, DE miRNAs, and DE lncRNAs by using the heatmap R package (<http://www.bioconductor.org/packages/release/bioc/html/heatmaps.html>).

2.6. Target Gene Prediction and Functional Enrichment Analysis. To investigate the function of DE miRNAs and DE lncRNAs, we predicted the target genes of all DE miRNAs, as well as the lncRNA *cis*-target genes. Briefly, the miRanda (<http://www.microrna.org/microrna/getDownloads.do>) was used to predict the target genes of DE miRNAs. *Cis*-regulation was used to predict lncRNA targets, and then coding genes in 100 kb upstream and downstream were selected in this study. Furthermore, Gene Ontology (GO) and Kyoto Encyclopedia of Genes and Genomes (KEGG) pathway analysis were performed for these up and downregulated DE mRNAs, DE miRNA targets, and DE lncRNA targets by R package clusterProfiler (<http://bioconductor.org/packages/release/bioc/html/clusterProfiler.html>) [27].

2.7. Preparation of Inflammation-Related Targets. The putative inflammation-related target genes were collected from the following database. GeneCards (<https://www.genecards.org/>) provides comprehensive transcriptomic information on the annotated and predicted human genes [28]; The GenCLIP 3 (<http://ci.smu.edu.cn/genclip3/analysis.php>), multifunctional text-mining tools with the integration of Sphinx with MySQL to quickly retrieve function-related genes from more literature sources [29], and Online Mendelian Inheritance in Man® (OMIM®, <https://omim.org/>), an online catalog of human genes and genetic disorders [30]. Therefore, we retrieved these three databases with the keywords “inflammatory response” to identify the targets associated with inflammation.

2.8. Construction of Inflammation-Related DE mRNA PPI Network and Module Selection. The identified inflammation-related targets were integrated with up/downregulated DE mRNA, respectively, to obtain the potential

inflammation-related DE mRNAs in COVID-19. To explore the interaction of inflammation-related up/downregulated DE mRNAs, a protein-protein interaction (PPI) network was established according to the Search Tool for the Retrieval of the Interacting Genes (STRING, <http://string.embl.de/>) database [31]. Species are set as “Homo sapiens,” and the interactions with a combined score > 0.4 were selected as significant. Then, the PPI networks of inflammation-related up/downregulated DE mRNAs were visualized by Cytoscape v3.6.1 software (<https://cytoscape.org/>), respectively. Besides, the Molecular Complex Detection (MCODE) was used to screen modules of PPI networks with degree cutoff = 2, node score cutoff = 0.2, $k - \text{core} = 2$, and max.depth = 100 [32]. Furthermore, the GO annotation and KEGG pathway analyses in the modules were performed by using the Metascape online tool (<http://metascape.org/gp/index.html#/main/step1>) [33].

2.9. Coexpression Correlation Analysis. To illustrate the coexpression correlation between DE lncRNAs and module targets in PPI networks, the Pearson correlation coefficients of each DE lncRNAs and module targets were calculated by using their expression matrix data. Pearson’s correlation coefficient > 0.9 and p value < 0.05 were considered as the cutoff criterion.

2.10. Construction of the ceRNA Network. To investigate the possible interaction of module targets, DE miRNAs, and DE lncRNAs, a ceRNA network was constructed in this study. The DE lncRNA-miRNA regulatory relationships of DE miRNAs were predicted using the miRDB (<http://mirdb.org/>), an online database for miRNA target prediction and functional annotations [34]. Then, the predicted DE lncRNA-miRNA regulatory relationships were integrated with DE miRNAs to acquire the DE lncRNA-DE miRNA regulation relationship. We integrated the DE lncRNA-module target coexpression relationship and the DE miRNA-module target regulatory relationships; then, the lncRNA-miRNA-mRNA coexpression network was constructed by Cytoscape. Based on the mechanism of ceRNA and the lncRNA-miRNA-mRNA coexpression network, we drew attention to screening lncRNAs that can sponge DE miRNAs. Meanwhile, the ceRNA regulatory network was constructed.

2.11. Statistical Analysis. Results were expressed as the mean \pm standard deviation. Statistical analysis was performed using one-way analysis of variance (ANOVA) and Tukey’s post hoc test. A p value < 0.05 was considered significant.

3. Results

3.1. Baseline Characteristics of 10 COVID-19 Patients. By 31st March 2020, 10 admitted hospital patients were identified as laboratory-confirmed SARS-CoV-2 infection in Yiwu (Zhejiang, China) in the current study (Table 1). The COVID-19 patients were aged 22–73 years, and 6 patients (60%) were female. Fever (50%), cough (60%), and sputum production (30%) were the most common symptoms. According to chest computed tomography findings, 7 patients (70%) presenting with ground-glass opacity. In blood tests, the leukocytes were

TABLE 1: Clinical characteristics of subjects with COVID-19 and health donors.

Characteristic	Control ($n = 4$)	Patients ($n = 10$)
Age, y, mean \pm SD	34.75 \pm 11.84	44.90 \pm 19.94
Men, no. (%)	1 (25)	4 (40)
Women, no. (%)	3 (75)	6 (60)
Signs and symptoms		
Fever		5 (50)
Cough		6 (60)
Sputum production		3 (30)
Sore throat		1 (10)
Stuffy nose		2 (10)
Gastrointestinal (GI) symptom		
Abdominal pain		1 (10)
Chest computed tomography		
Right ground-glass opacity		2 (20)
Right lung infiltrates		2 (20)
Left ground-glass opacity		3 (30)
Bilateral lung ground glass opacity		2 (20)
Bilateral lung infiltrates		1 (10)
Blood count, $\times 10^9/L$, mean \pm SD		
Leukocyte	7.40 \pm 1.4	5.19 \pm 1.7*
Lymphocyte	37.35 \pm 4.29	24.02 \pm 8.58*
Inflammatory indicators, mean \pm SD		
C-reactive protein, mg/L	1.00 \pm 0.75	12.61 \pm 16.61
Tumor necrosis factor α (TNF- α), pg/mL	10.35 \pm 2.40	44.98 \pm 47.67
Interleukin-6, pg/mL	3.24 \pm 2.82	15.09 \pm 20.81

Abbreviations: COVID-19: coronavirus disease 2019; * $p < 0.05$.

significantly decreased in COVID-19 patients, while the lymphocytes were below the levels of healthy donors. Compared to healthy controls, there were no differences in inflammatory indicators of COVID-19 patients in this study.

3.2. Identification of Differentially Expressed Genes. To explore the potential mechanism of “cytokine storm” in COVID-19 patients, we performed the whole transcriptome sequencing to identify the DEGs in the peripheral blood samples. EggNOG, Pfam, CNCI, and CPC2 were used to screen out transcripts with coding potential in this study. The significant differences in DE mRNA, DE miRNA, and DE lncRNA expression between the COVID-19 patients and control groups were represented by volcano plot (Figure 2). Based on the screening criteria, a total of 25,482 DE mRNA were identified, of which 21,340 were downregulated and 4,142 were upregulated (Figure 2(a) and Table S1); 23 DE miRNA were determined to have a fold change ≥ 2.0 and $p < 0.05$, of which 9 were upregulated and 14 were downregulated (Figure 2(b) and Table S2); additionally, we obtained 410 DE lncRNAs including 129 upregulated and 281 downregulated (Figure 2(c) and Table S3). Differentially expressed mRNA, miRNA, and lncRNAs were hierarchically clustered, as shown in Figures 2(d)–(f),

from which we found that the COVID-19 samples can be observably separated from the control samples, suggesting that the differential expression analysis of RNA sequencing data was adequately trustworthy.

3.3. Functional Analysis of Up/Downregulated DE mRNAs. We performed functional annotation and KEGG enrichment analysis on the up/downregulated DE mRNAs, respectively. Figure 3 displays only the top 10 biological processes (BP), cellular component (CC), and molecular function (MF) terms enriched by up/downregulated DE mRNAs. GO enrichment analysis indicated that upregulated DE mRNAs were significantly concentrated in detection of bacterium, detection of external biotic stimulus, antigen processing and presentation of endogenous antigen, positive regulation of T cell mediated cytotoxicity, and positive regulation of gamma-delta T cell activation in BP, azurophil granule membrane and MHC protein complex in CC, telomeric DNA binding, and TAP binding in MF (Figure 3(a)). Also, results of GO analysis showed that the downregulated DE mRNAs were significantly enriched in glycogen biosynthetic process, glucan biosynthetic process, and cell wall macromolecule metabolic process in BP, nucleolus organizer region and nucleolar chromatin in CC, UDP-glucosyltransferase

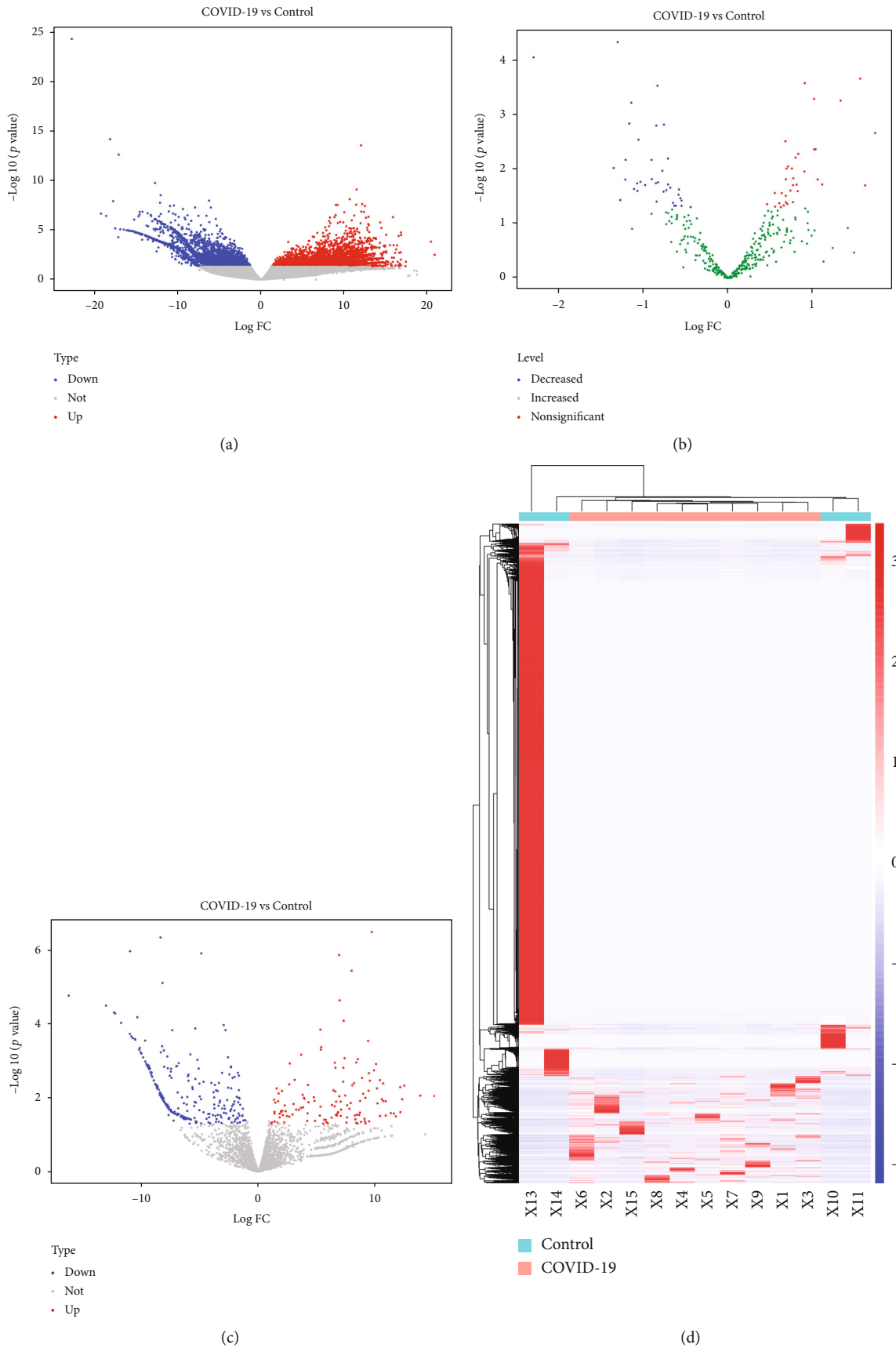
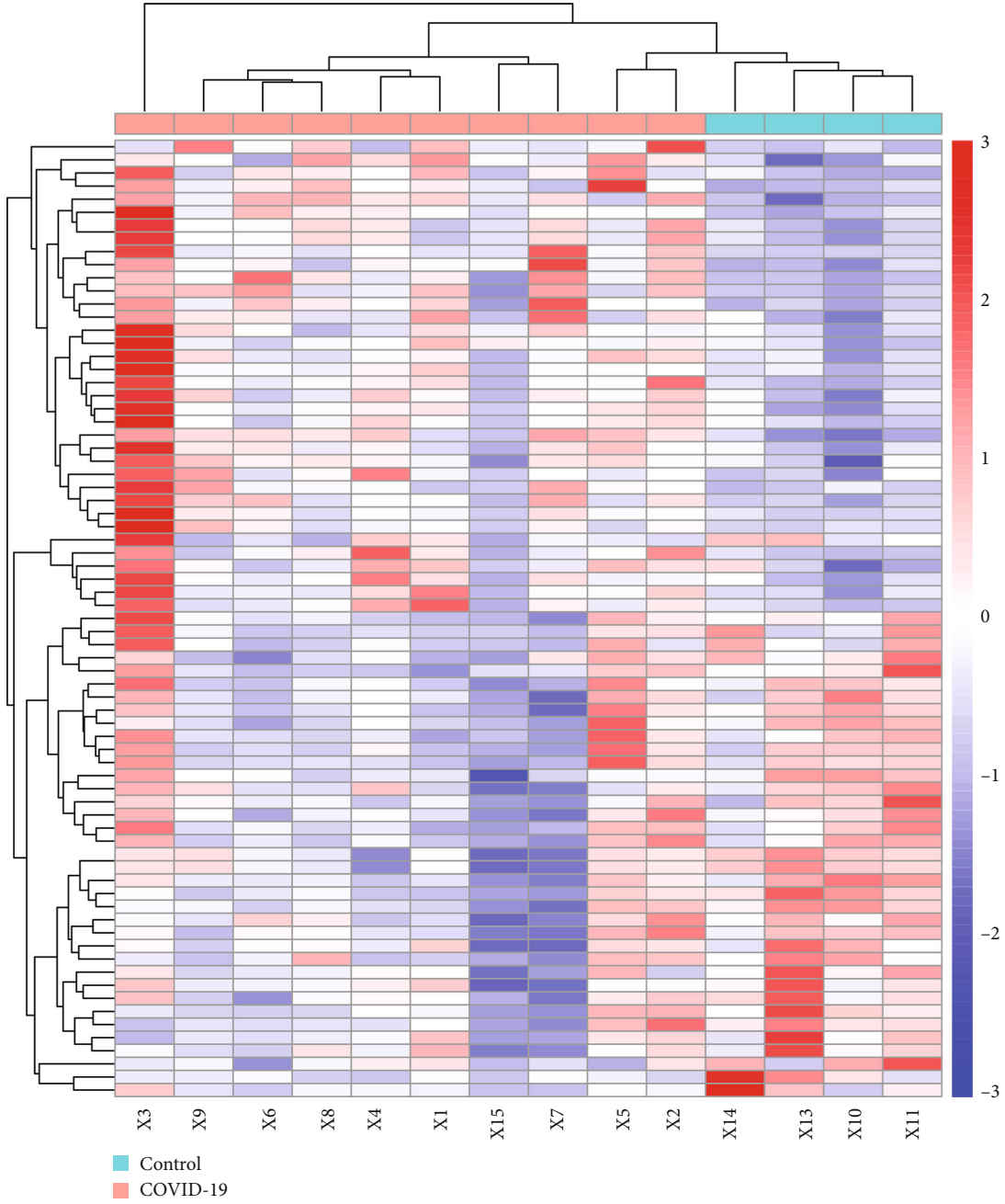
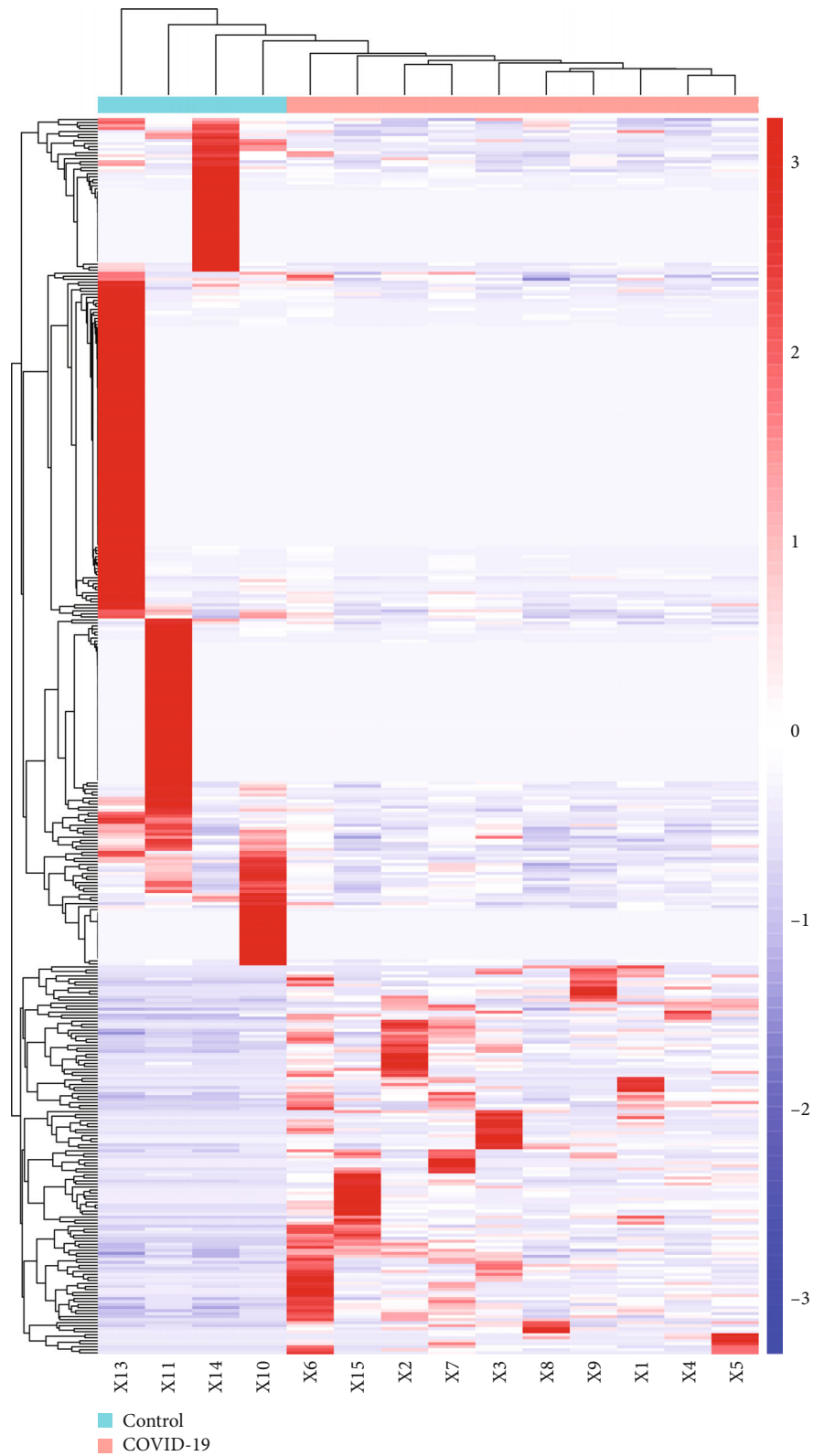


FIGURE 2: Continued.

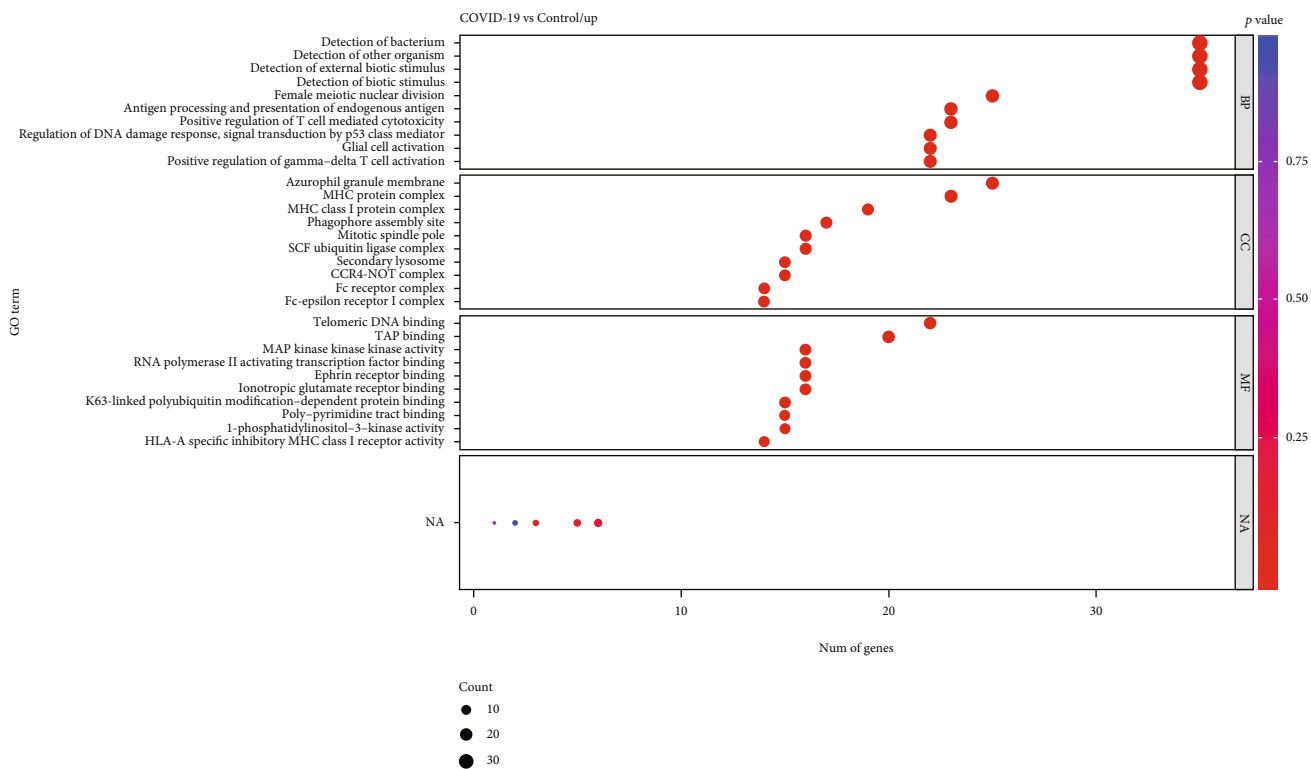


(e)
FIGURE 2: Continued.

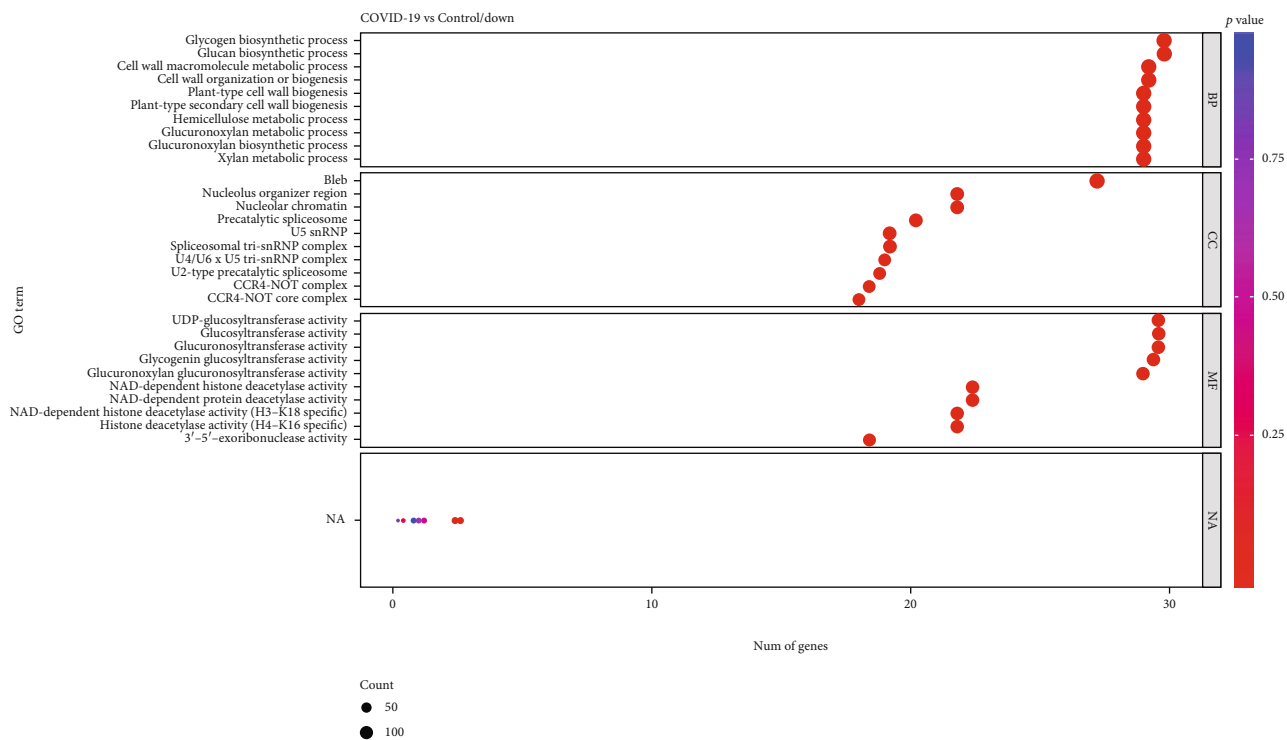


(f)

FIGURE 2: Volcano plots and heatmaps of differentially expressed genes (DEGs). Volcano plots showing significantly different expressions of mRNAs (a), miRNAs (b), and lncRNAs (c) between the COVID-19 and control groups. Red points: upregulated DEGs; blue points: downregulated DEGs; gray and green points: the genes with no obvious difference in expression levels. Heatmaps of DE mRNAs (d), DE miRNAs (e), and DE lncRNAs (f). Red represents upregulation, and blue represents downregulation.



(a)



(b)

FIGURE 3: Continued.

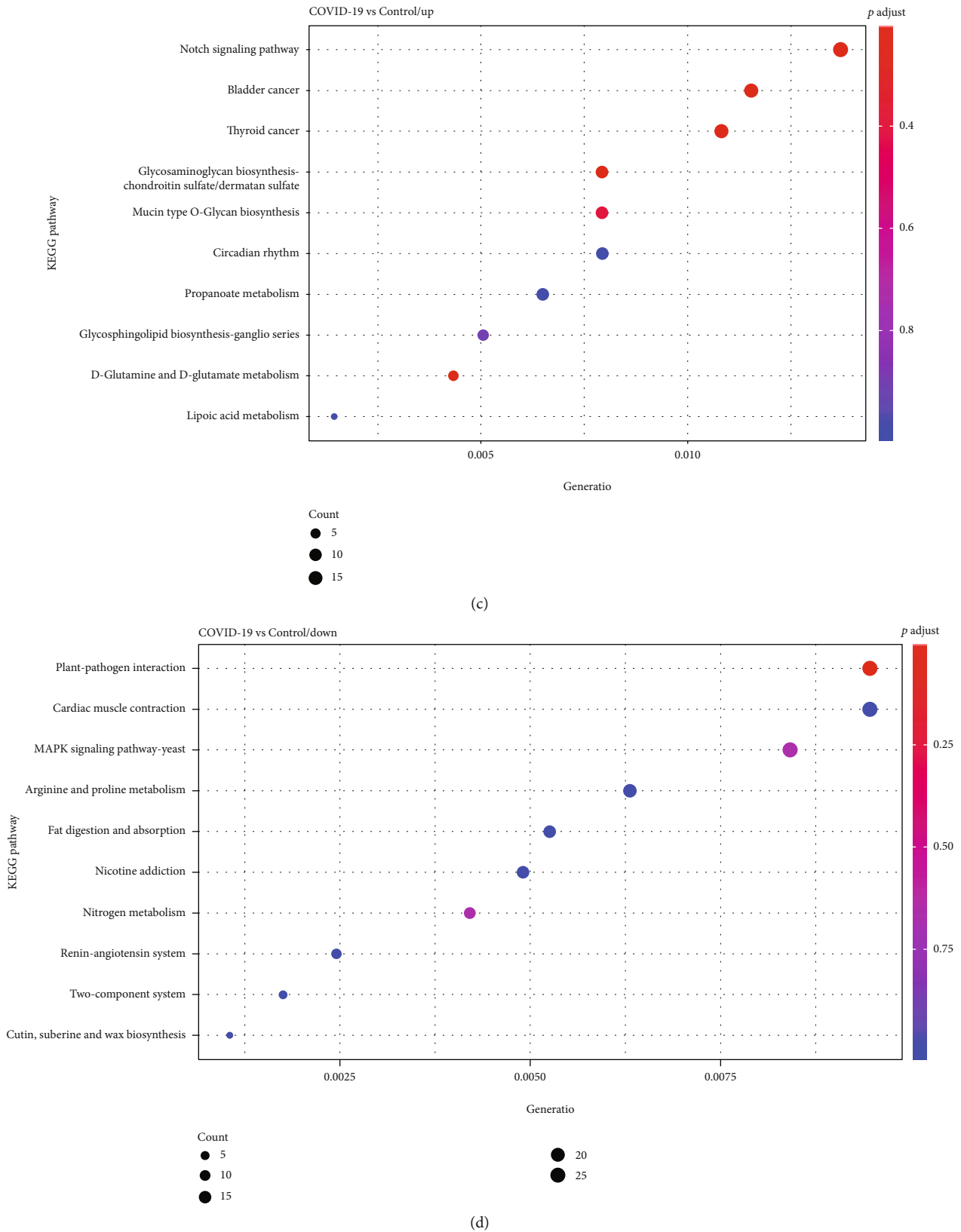
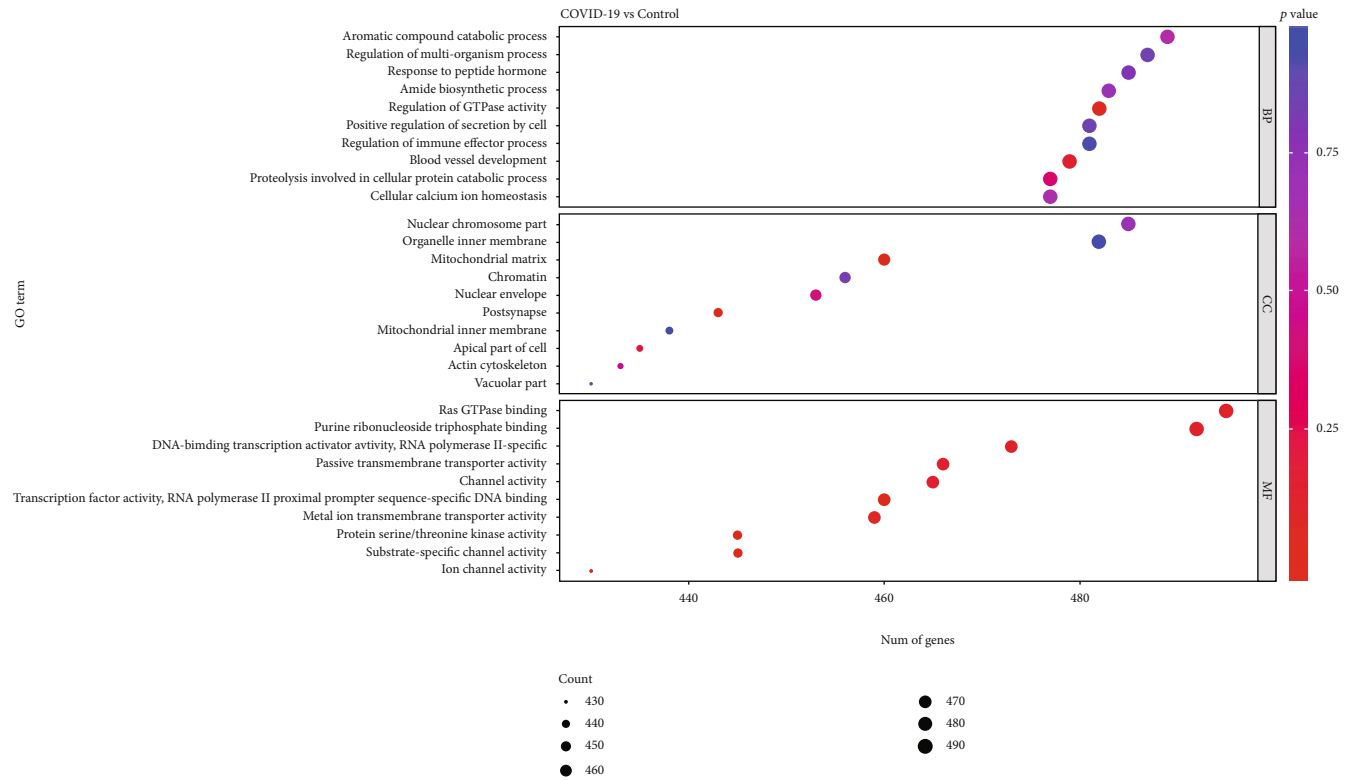
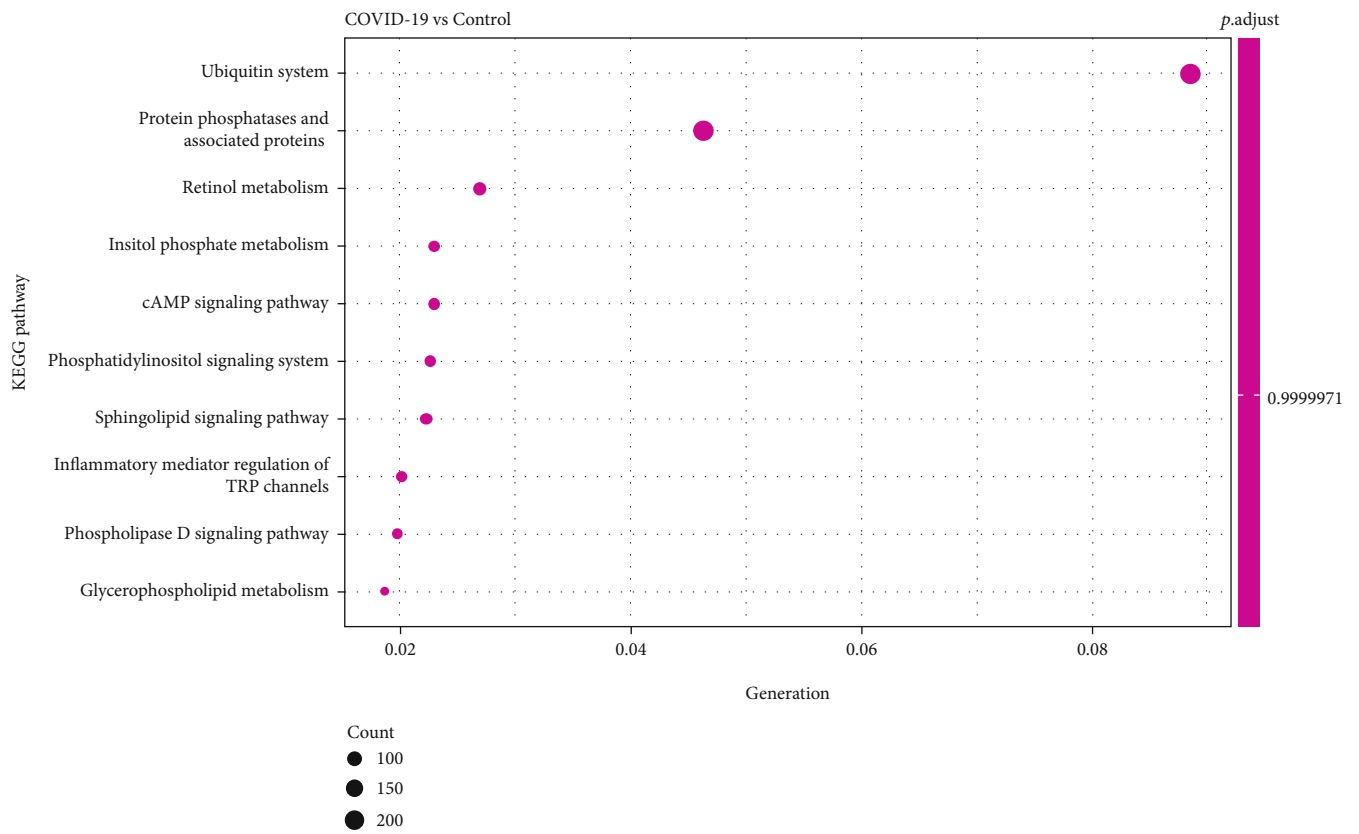


FIGURE 3: Go terms and KEGG pathway enrichment of up/downregulated DE mRNAs in peripheral blood samples of COVID-19 patients. GO term functional enrichment with 3 categories (BP, MF, CC) for upregulated DE mRNAs (a) and downregulated DE mRNAs (b). Top 10 pathways enriched by upregulated DE mRNAs (c) and downregulated DE mRNAs (d).

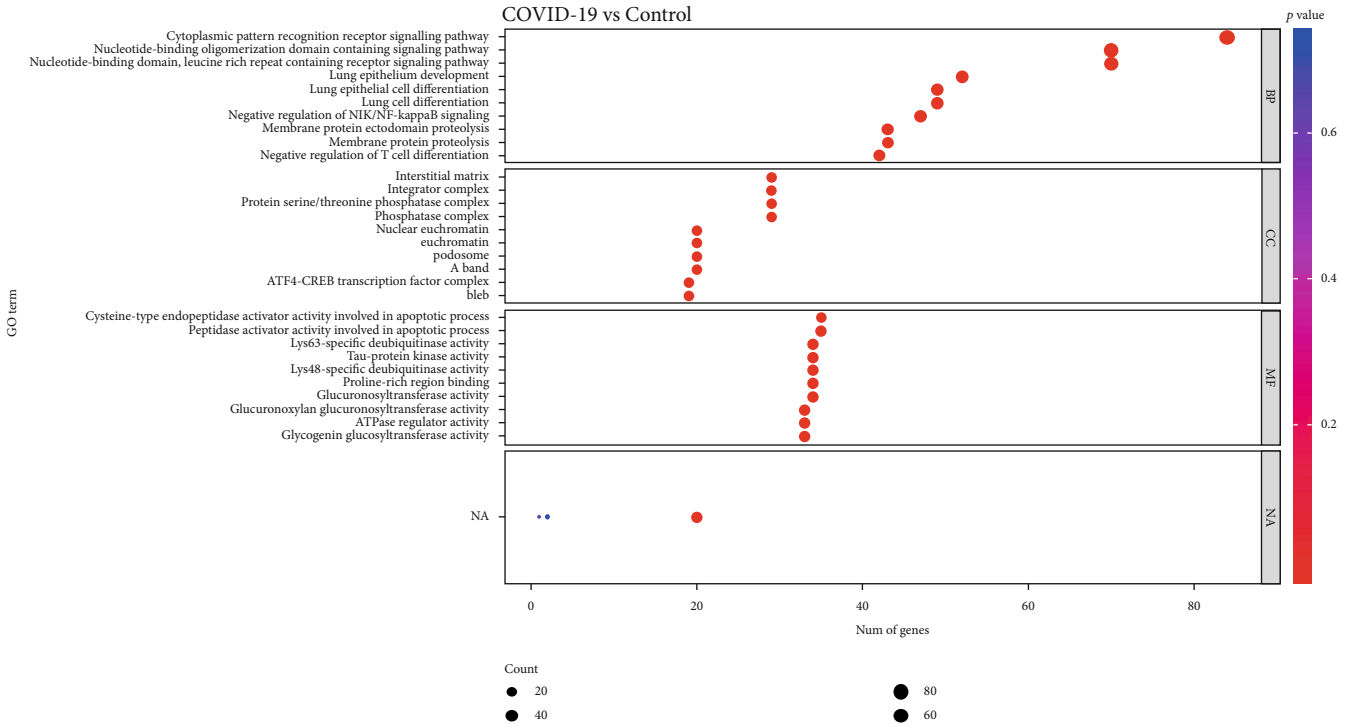


(a)

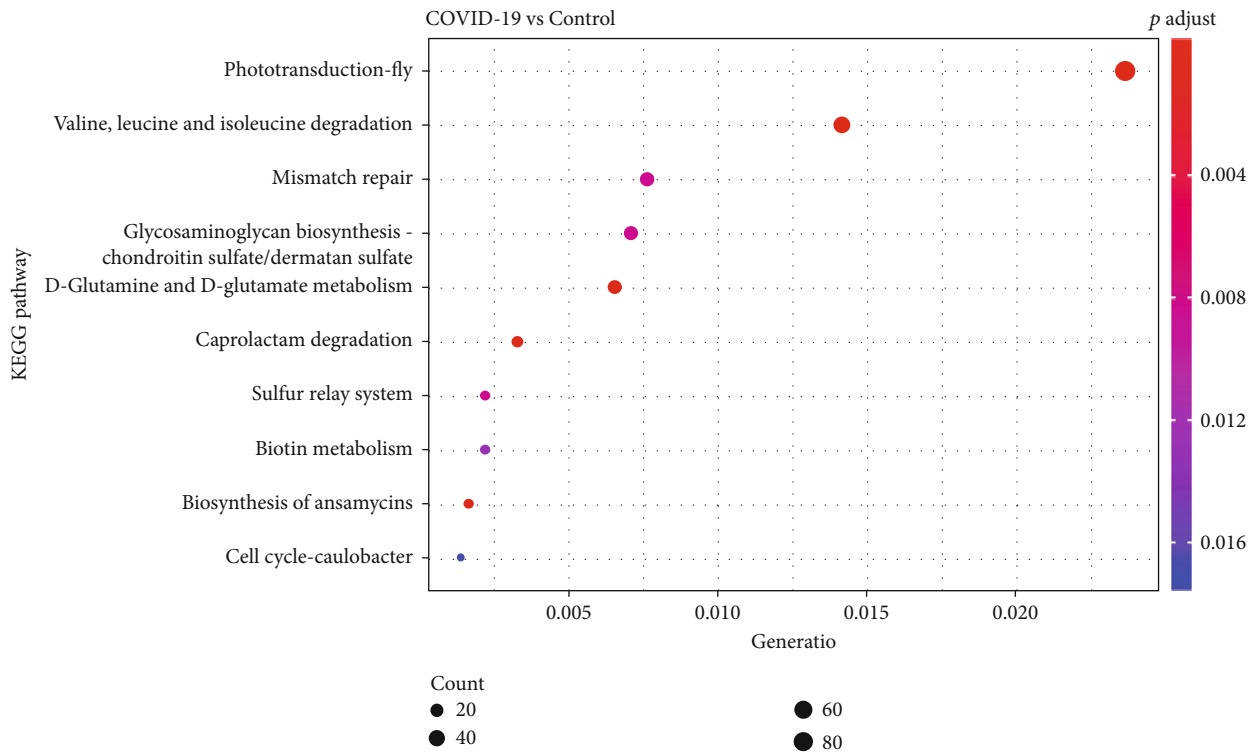


(b)

FIGURE 4: Continued.



(c)



(d)

FIGURE 4: Functional enrichment analyses for target genes of DE miRNA and DE lncRNAs. Bubble plot shows GO (a) and KEGG terms (b) enriched in target genes of DE miRNA. Bubble plot shows GO (c) and KEGG terms (d) enriched in genes regulated by DE lncRNAs.

activity, and NAD-dependent histone deacetylase activity in MF (Figure 3(b)). Besides, the results of the pathway analysis showed that the upregulated DE mRNAs were significantly enriched in the Notch signaling pathway

(Figure 3(c)). Moreover, the downregulated DE mRNAs were significantly associated with plant-pathogen interaction, cardiac muscle contraction, and MAPK signaling pathways (Figure 3(d)).

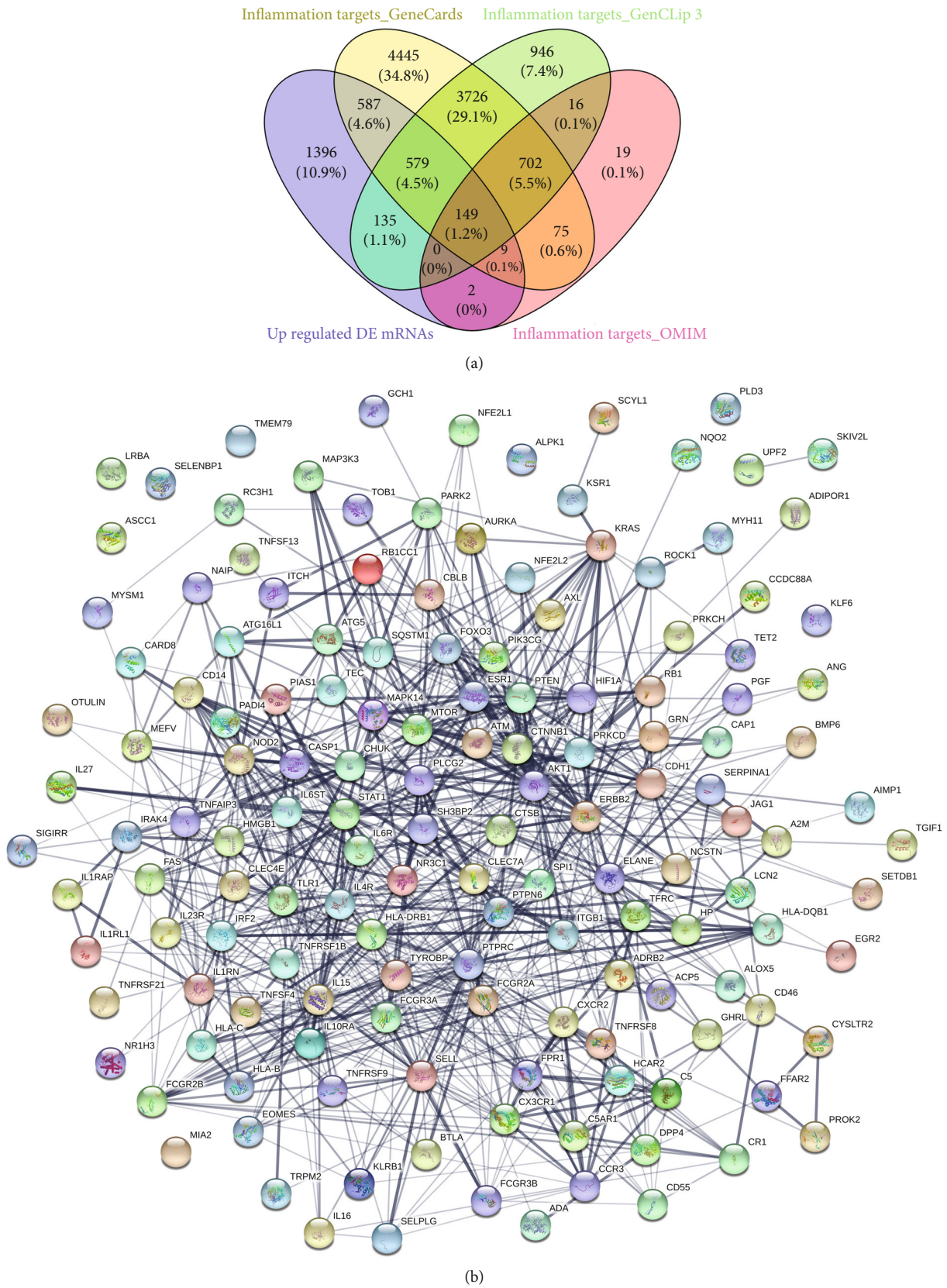
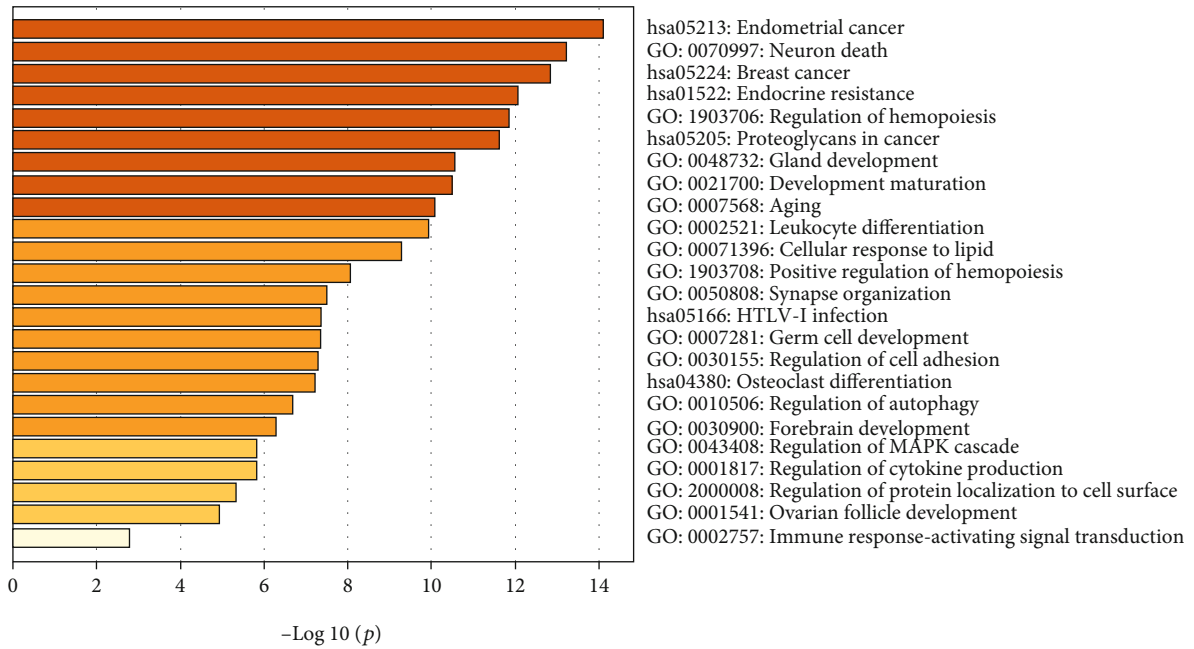
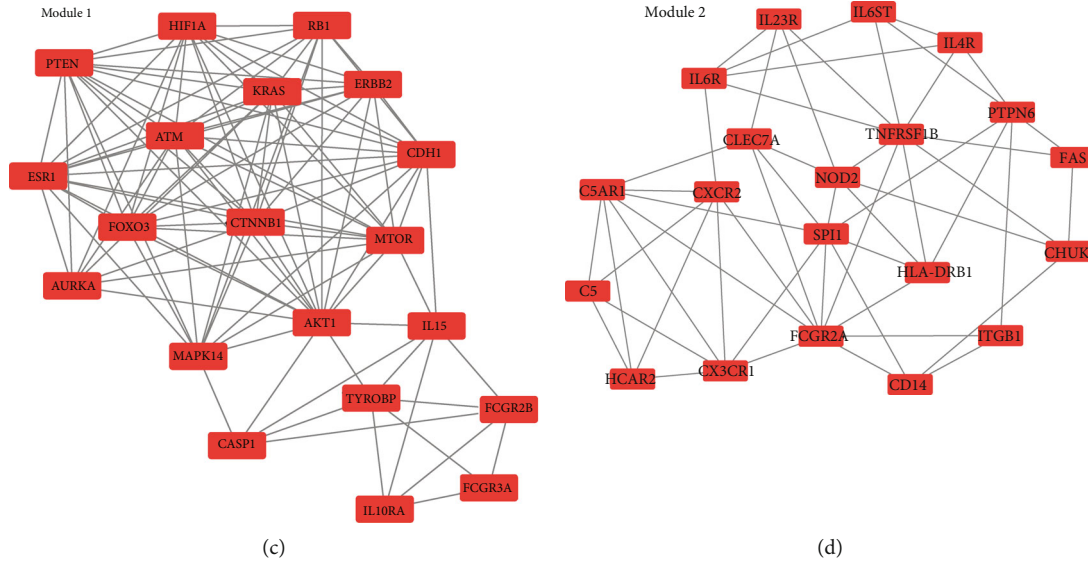


FIGURE 5: Continued.



(e)
FIGURE 5: Continued.

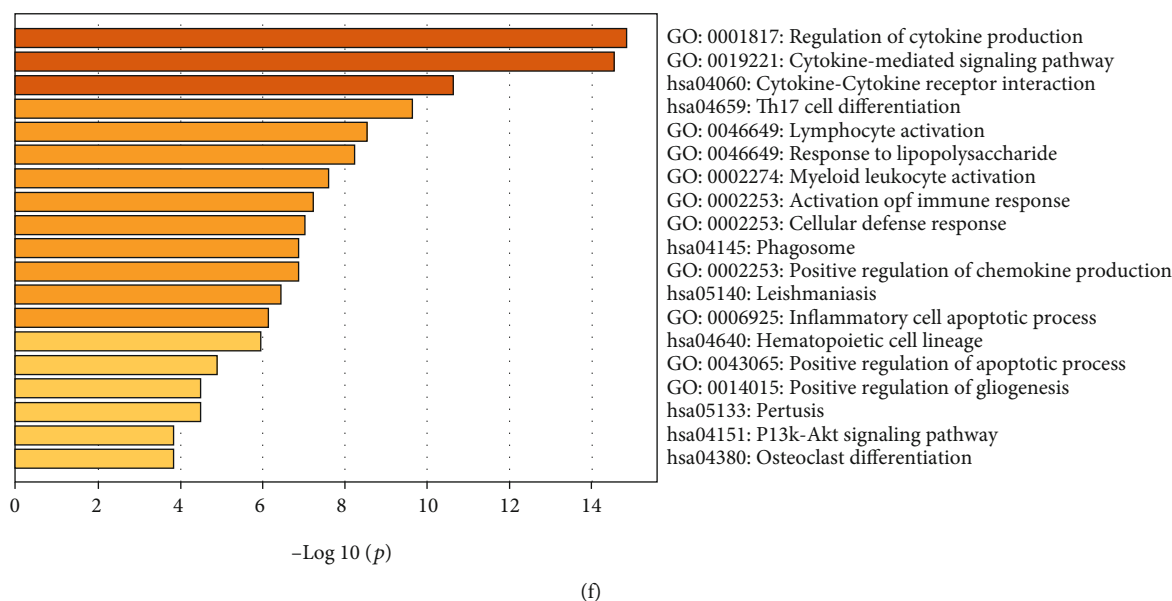


FIGURE 5: Two modules obtained from upregulated-PPI network and its functional enrichment analysis. (a) 149 upregulated inflammation-related DE mRNAs in COVID-19 were collected with Venn analysis. (b) PPI network of upregulated inflammation-related DE mRNAs. (c, d) Significant clustered modules from the PPI network. Red rectangles represent upregulated genes. The GO-BP terms and KEGG pathways enrichment analysis for module 1 (e) and module 2 (f), respectively, using the Metascape database.

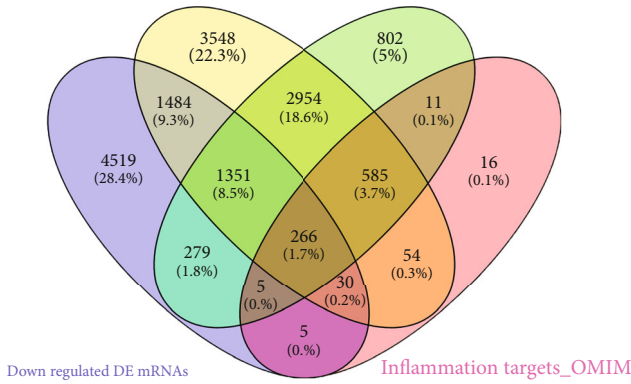
3.4. GO and KEGG Analysis of miRNA-/lncRNA-Related Target Genes. To investigate the biological significance of miRNA-/lncRNA-related target genes, GO and KEGG enrichment analysis was performed by R package clusterProfiler. GO enrichment analysis for miRNA-related genes indicated that they were mainly enriched in aromatic compound catabolic process, regulation of immune effector process in BP, nuclear chromosome part in CC, and Ras GTPase binding in MF (Figure 4(a)). Interestingly, our current study showed found miRNA-related genes are related to the ubiquitin system, inflammatory mediator regulation of TRP channels, etc. (Figure 4(b)). Moreover, the results showed that those genes related to lncRNAs were significantly enriched in the cytoplasmic pattern recognition receptor signaling pathway, lung cell differentiation, negative regulation of NIK/NF- κ B signaling, and negative regulation of T cell differentiation in BP, protein serine/threonine phosphatase complex in CC, and cysteine-type endopeptidase activator activity involved in the apoptotic process in MF (Figure 4(c)). And the lncRNA-related target genes were associated with phototransduction-fly and valine, leucine, and isoleucine degradation pathways (Figure 4(d)).

3.5. PPI Network Analysis. In the current study, the identified inflammation-related targets were collected from the GeneCards, GenCLIP 3, and OMIM databases, respectively. Next, we integrated the upregulated DE mRNAs and the inflammation-related targets, and the results are presented in Figure 5(a) which shown that a total of 149 upregulated inflammation-related DE mRNAs in COVID-19 were obtained. We established the PPI network of the 149 upregulated DE mRNAs associated with the inflammation response according to the interactions predicted by the STRING database. A total of 847 edges and 140 nodes were included

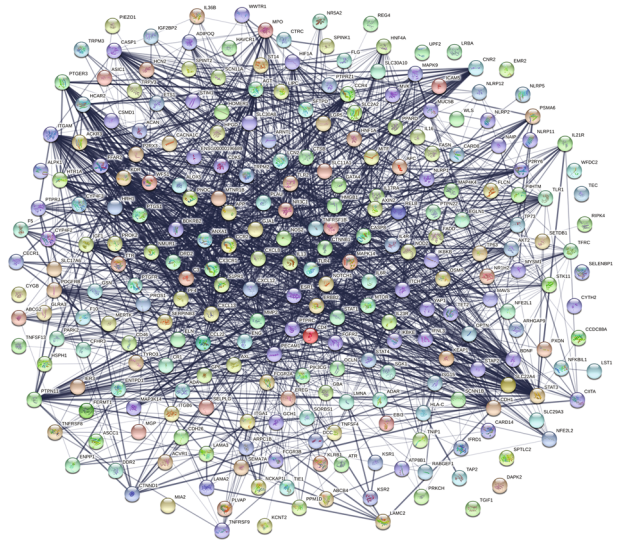
(Figure 5(b)). The nodes with a high degree value can be treated as the hub genes of the network. The PPI network of the inflammation-related upregulated DE mRNAs was divided into two modules (Figures 5(c) and 5(d)). AKT serine/threonine kinase 1 (AKT1, degree = 16) was the core of module 1 (score = 10.526), which included 100 edges and 20 nodes. TNF receptor superfamily member 1B (TNFRSF1B, degree = 9) and Fc fragment of IgG receptor IIa (FCGR2A, degree = 9) were the hub genes of module 2 (score = 5.579), which included 53 edges and 20 nodes. Moreover, target genes in module 1 and module 2 were performed for BP and KEGG pathway enrichment analysis. Enrichment analyses for module 1 demonstrated that the BP and pathways are mainly associated with GO:0070997~neuron death, GO:1903706~regulation of hemopoiesis, GO:0002521~leukocyte differentiation, GO:0002757~immune response-activating signal transduction, hsa05213~endometrial cancer, hsa01522~endocrine resistance, and hsa05166~human T cell leukemia virus type I (HTLV-I) infection (Figure 5(e)). Notably, we found that the genes of module 2 were especially involved in GO:0001817~regulation of cytokine production, hsa04060~cytokine-cytokine receptor interaction, GO:0046649~lymphocyte activation, and GO:0006925~inflammatory cell apoptotic process (Figure 5(f)), indicating that SARS-CoV-2 infection caused active inflammatory responses that resulted in pneumonia in human beings.

Similarly, we also integrated the downregulated DE mRNAs and the inflammation-related targets. Subsequently, the 266 downregulated inflammation-related DE mRNAs were analyzed through the STRING database and Cytoscape software (Figure 6(a)), which formed a PPI network that contains 254 nodes and 1948 edges (Figure 6(b)). The MCODE approach in Cytoscape was used to identify modules in the

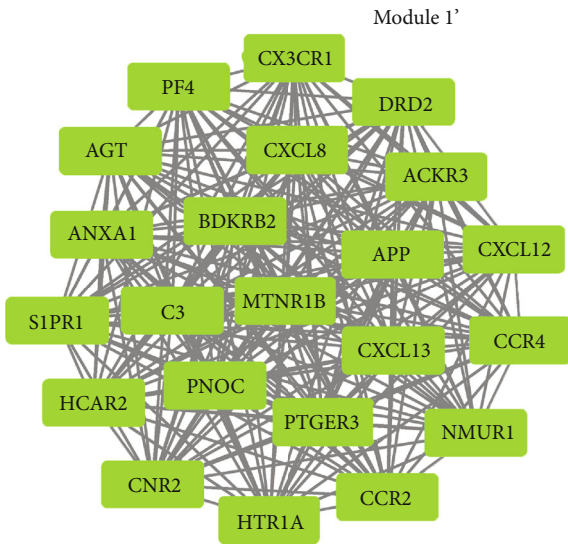
Inflammation targets_GeneCards Inflammation targets_GenCLiP 3



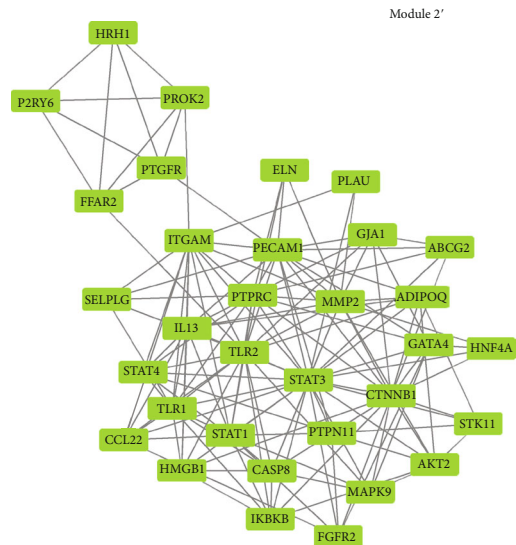
(a)



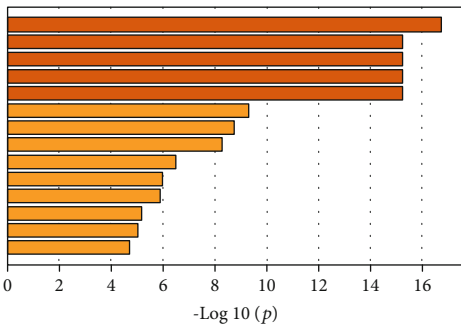
(b)



(c)



(d)



GO: 0006874: Cellular calcium homeostasis
 GO: 0060326: Cell chemotaxis
 GO: 0019932: Second-messenger-mediated signaling
 GO: 0007187: G protein-coupled receptor signaling pathway, coupled to cyclic nucleotide second messenger
 GO: 0032103: Positive regulation of response to external stimulus
 GO: 0007200: Phospholipase C-activating G protein-coupled receptor signaling pathway
 GO: 0050921: Positive regulation of chemotaxis
 GO: 0007268: Chemical synaptic transmission
 GO: 0001780: Neutrophil homeostasis
 GO: 0015844: Monoamine transport
 GO: 2001233: Regulation of apoptotic signaling pathway
 GO: 0008015: Blood circulation
 GO: 0006898: Receptor-mediated endocytosis
 GO: 0048771: Tissue remodeling

(e)

FIGURE 6: Continued.

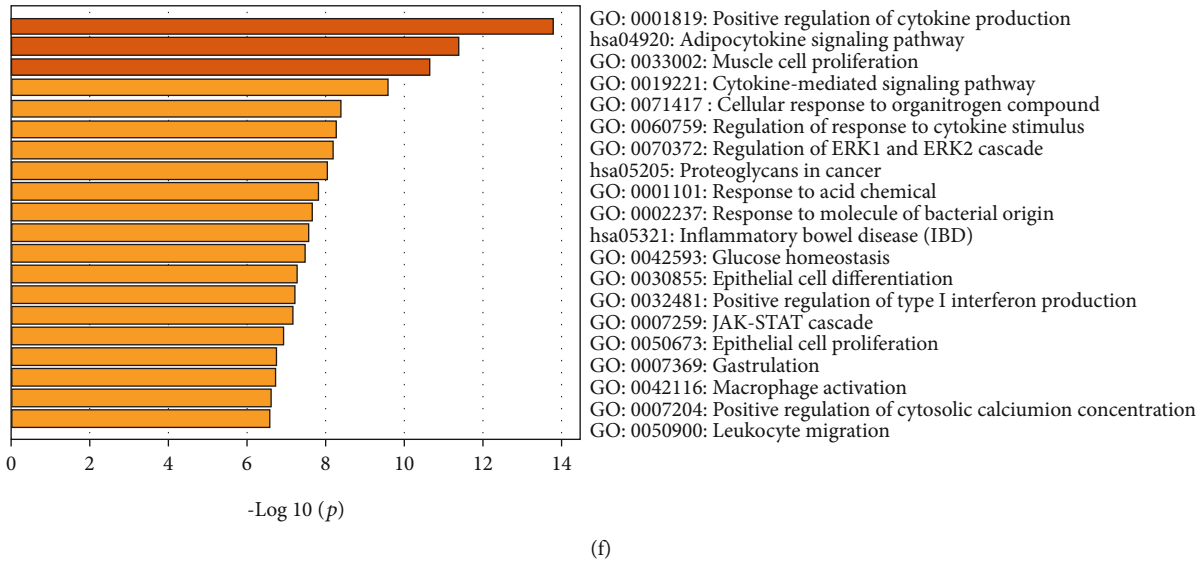


FIGURE 6: Two modules obtained from the downregulated PPI network and its functional enrichment analysis. (a) 266 downregulated inflammation-related DE mRNAs in COVID-19 were collected with Venn analysis. (b) PPI network of downregulated inflammation-related DE mRNAs. (c, d) Significant clustered modules from the PPI network. Green rectangles represent downregulated genes. The GO-BP terms and KEGG pathways enrichment analysis for module 1' (e) and module 2' (f), respectively, using the Metascape database.

PPI network of downregulated inflammation-related DE mRNAs. Then, two modules in the downregulated PPI network were established with the k -core = 2. Module 1' (score = 22) containing 22 nodes and 231 edges was identified, and these nodes had the highest node degree (degree = 21) (Figure 6(c)). According to the degree of the total downregulated PPI network, C-X-C motif chemokine ligand 8 (CXCL8) was selected as the core of module 1. Signal transducer and activator of transcription 3 (STAT3) and toll-like receptor 2 (TLR2) were the hub genes of module 2 (score = 10.588), which included 131 edges and 32 nodes (Figure 6(d)). Also, we performed functional enrichment analyses for these dysregulated genes from the module 1' and module 2, respectively. Many terms of different BP were clustered for module 1', including GO: 0006874~cellular calcium ion homeostasis, GO: 0060326~cell chemotaxis, and GO: 0019932~second-messenger-mediated signaling (Figure 6(e)). To our great interest, multiple GO and KEGG terms were enriched for module 2 that potentially associated with the cytokine storm in COVID-19, for example, "GO: 0001819~positive regulation of cytokine production," "GO: 0019221~cytokine-mediated signaling pathway," "GO: 0042116~macrophage activation", and "GO: 0050900~leukocyte migration" (Figure 6(f)). All molecular aspects including biological processes and signaling pathways point to the cytokine production and cytokine-mediated signaling pathway, suggesting the worth of the considerable potential value of inflammation-related hub genes in the progression of COVID-19.

3.6. Construction of the ceRNA Network. Based on the DE lncRNA-module target coexpression relationship and the DE miRNA-module target regulatory relationships, the lncRNA-miRNA-mRNA coexpression network was constructed. In total, 3,570 lncRNA-miRNA-mRNA interactions

were finally obtained (Figure 7), including 258 DE lncRNAs, 9 upregulated and 14 downregulated DE miRNAs, and 40 upregulated and 55 downregulated module targets. Further, according to the lncRNA-miRNA-mRNA coexpression network and the DE lncRNA-DE miRNA regulation relationship, the ceRNA network was also established (Figure 8). Finally, we found that MSTRG.119845.30/hsa-miR-20a-5p/TNFRSF1B, MSTRG.119845.30/hsa-miR-29b-2-5p/FCGR2A, MSTRG.106112.2/MSTRG.151872.3/MSTRG.51997.3/hsa-miR-6501-5p/STAT3, and MSTRG.106112.2/MSTRG.151872.3/MSTRG.51997.3/hsa-miR-6501-5p/TLR2, MSTRG.105154.2/MSTRG.130010.5/MSTRG.175653.26/MSTRG.228818.11/MSTRG.102242.2/hsa-miR-142-5p/TLR2, MSTRG.157434.2/MSTRG.71484.4/hsa-miR-505-5p/TLR2 axes and a lncRNA could sponge several miRNAs, and a miRNA could also interact with multiple mRNAs. These results highlighted the important role of lncRNAs in pathogenesis of COVID-19 by interacting with miRNAs.

4. Discussion

As is widely known, the SARS-CoV-2, a novel coronavirus, is probably originated from zoonotic coronaviruses, which causes serious pneumonia and lung failure to threaten global public health [35]. Currently, numerous diagnostic kits to test for COVID-19 are optional, and several promising antiviral agents against SARS-CoV-2, such as favipiravir, remdesivir, lopinavir, and ritonavir, have shown clinical effectiveness [36]. Although there have been made significant advances in the development of vaccines and drugs against COVID-19, the underlying mechanisms of the pathogenesis of SARS-CoV-2-associated pneumonia in human beings remain incompletely understood. In our study, leukocytes and lymphocytes were significantly decreased in COVID-19 patients. Hence, it is important to explore the mechanisms

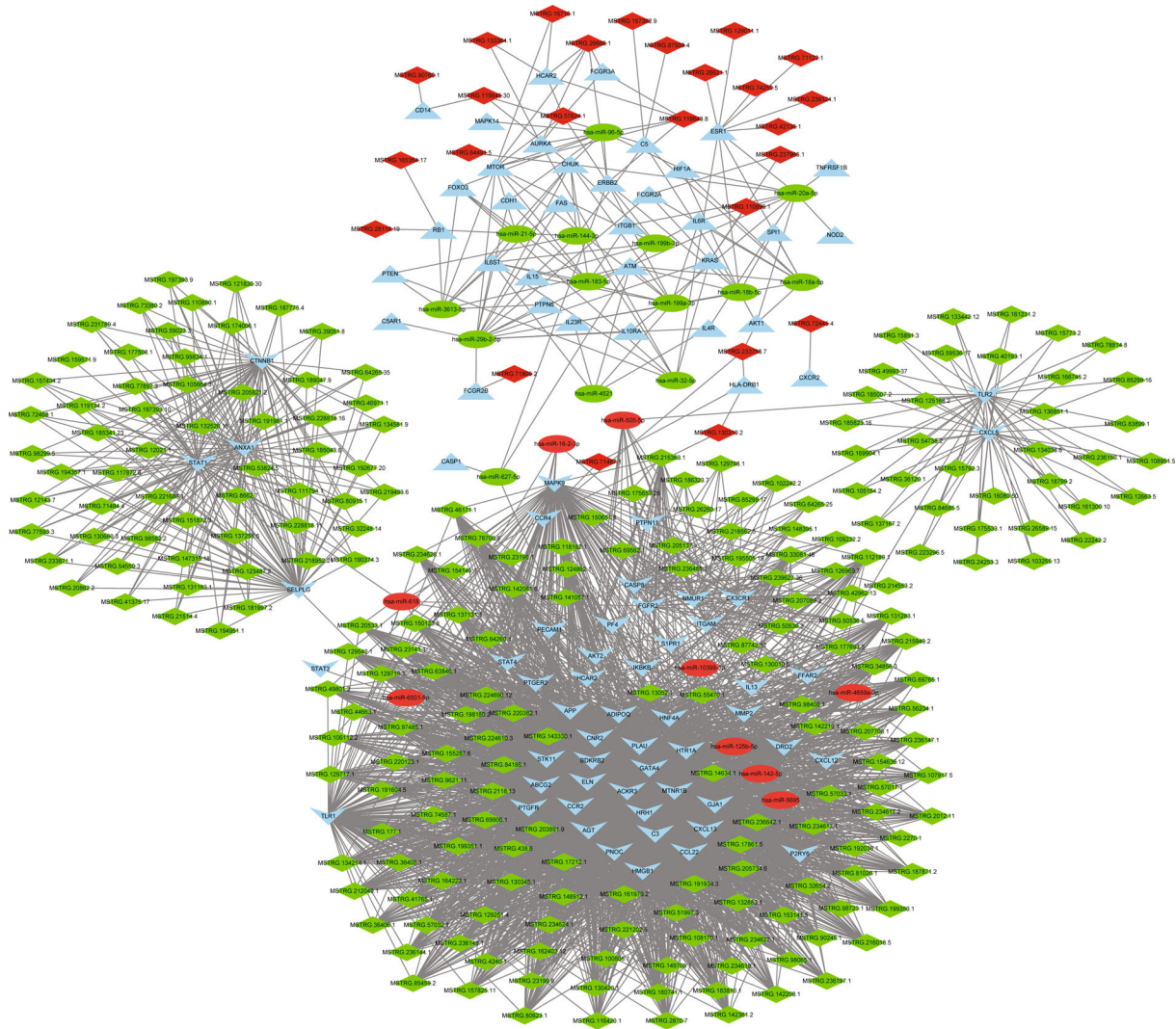


FIGURE 7: The lncRNA-miRNA-mRNA coexpression network. The downward “v” triangle represents the downregulated DE mRNAs, the upward triangle represents the upregulated DE mRNAs, the red ellipse represents the upregulated DE miRNAs, the green ellipse represents the downregulated DE miRNAs, red diamond indicates upregulated DE lncRNAs, and green diamond indicates downregulated DE lncRNAs.

and identify the biomarkers associated with the development of COVID-19.

Several studies have shown that massive alterations in the host transcriptome have been caused to aid in helping the viral survival and replication by regulating the immune and inflammation response under viral infection [10, 37]. With the development of high throughput sequencing, the intension of the transcriptome has been enlarged to contain many types of transcripts, including mRNAs and ncRNAs. In this study, we simultaneously detected mRNAs, miRNAs, and lncRNAs in peripheral blood from COVID-19 patients and healthy donors by using whole transcriptome sequencing. We found that 25,482 DE mRNA, 23 DE miRNA, and 410 DE lncRNAs when peripheral blood samples of COVID-19 patients were compared to control, respectively. Then, the DE mRNAs were used to be enriched into GO terms and KEGG pathways. As expected, results showed that these DEGs were associated with the detection of bacterium, posi-

tive regulation of T cell mediated cytotoxicity, positive regulation of gamma-delta T cell activation, glycogen biosynthetic process, Notch signaling pathway, and MAPK signaling pathways. Additionally, functional analysis on the targets of DE miRNA and DE lncRNAs was also involved in the regulation of immune effector process, inflammatory mediator regulation of TRP channels, lung cell differentiation, negative regulation of NIK/NF-kappaB signaling, and negative regulation of T cell differentiation, which all play significant roles in depressing viral infection.

The inflammatory response has been thought to be a hallmark of SARS and MERS disease with an increased level of IL-6, IL-8, CXCL10, CCL2, and CCL3 [38, 39]. A recent study demonstrated that COVID-19 severe patients had a low level of counts of T cells and a high level of IL-2, IL-6, IFN- γ , and IL-10 compared with the mild patients [40], similar to the results in SARS and MERS. Meanwhile, Xu et al. found mild fibrosis and moderate inflammation in the lung

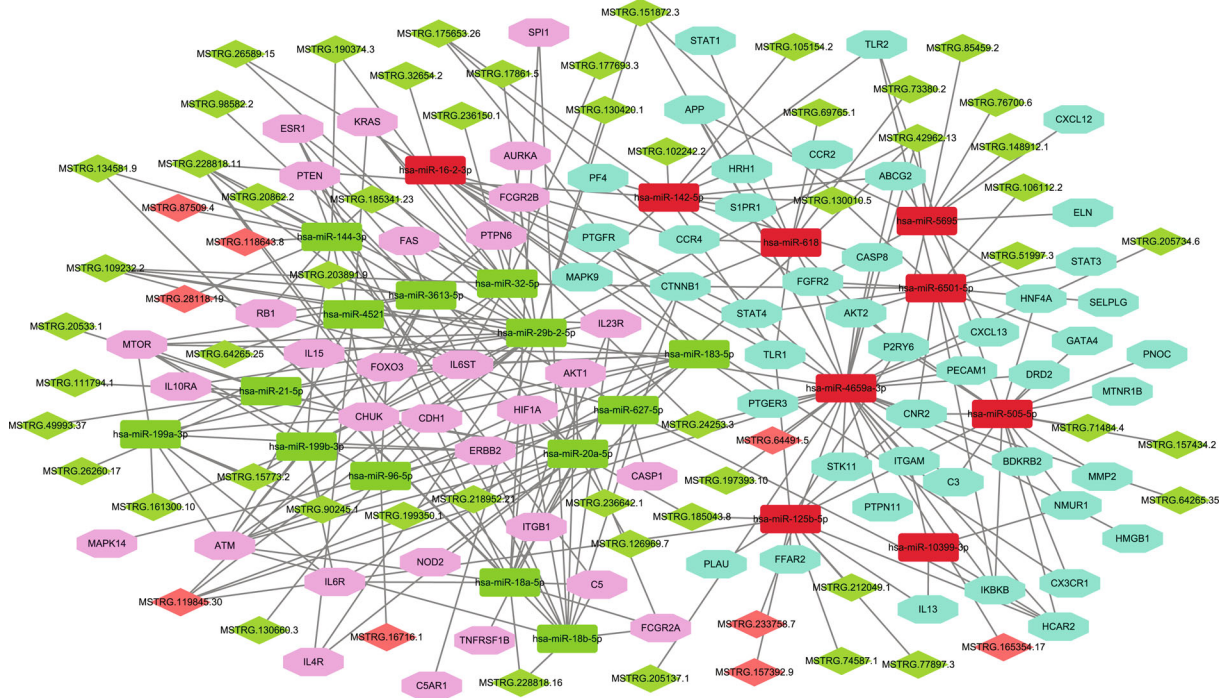


FIGURE 8: The competing endogenous RNA (ceRNA) network of COVID-19. Pink octagon indicates the upregulated DE mRNAs, light blue octagon indicates the downregulated DE mRNAs, red rectangle indicates upregulated DE miRNAs, green rectangle indicates downregulated DE miRNAs, red diamond indicates upregulated DE lncRNAs, and green diamond indicates downregulated DE lncRNAs.

biopsy of COVID-19 patients [14]. Therefore, further highlighting of detailed mechanisms and potential targets in this process would be to establish a foundation for future investigation. In this study, we integrated the up/downregulated DE mRNA with inflammation-related target genes, respectively. We performed GO and KEGG pathway analysis to explore the biological functions and potential pathways on module targets of PPI networks. GO analyses indicated that they were enriched in leukocyte differentiation, immune response-activating signal transduction, and positive regulation of cytokine production. KEGG analyses indicated that these genes associated with inflammation in COVID-19 were enriched in cytokine-cytokine receptor interaction and T17 cell differentiation. Taken together, these important biological processes and pathways of module targets played important roles in the inflammatory process of COVID-19, which strengthened our understanding of the underlying mechanism of “cytokine storm” in COVID-19 and may provide novel therapeutic targets for COVID-19.

We also performed the network topology analysis for module genes. Then, a total of 6 hub targets were identified in the modules including AKT1, TNFRSF1B, FCGR2A, CXCL8, STAT3, and TLR2. Recently, a study revealed a prominent alteration of Akt/mTOR/HIF-1 signaling at the proteotranscriptomic levels in SARS-CoV-2 infected Huh7 cells [41]. The activation of the Akt/mTOR pathway might enable SARS-CoV-2 infection by blocking autophagy and apoptosis [42]. Moreover, a high level of IL-6 can activate mTOR in a STAT3-dependent or independent manner [43, 44]. Accumulating evidence indicates that TNF receptor (TNFR) family member, TNFRSF1B (TNFR2), which is sus-

tained T cell responses, plays important role in protective immunity, inflammatory, and autoimmune diseases [45, 46]. Fc gamma receptors (FcγRs) have an important function in humoral immune responses. Also, rijkers et al. reported that B lymphocyte growth and differentiation factors, including IL-6, IL-10, and TNFRSF1B are associated with increased susceptibility for pneumonia [47]. CXCL8 (also referred to as IL-8), circulating chemokine, is associated with inflammation and immune cell trafficking in the context of viral infections [48]. TLR2 is well-studied toll-like receptors that identify both structural and nonstructural proteins of the virus, as well as cytokine production and inflammation [49]. And the study by Lester et al. shows TLR agonists can help to initiate an immune response and actively take part in viral clearance [50]. Taken together, the above hub targets were significantly related to the immune and inflammatory process of COVID-19.

Increasing evidence indicates that lncRNAs can influence miRNA activity as endogenous sponges to affect mRNA, act as ceRNAs, to regulate a series of biological processes. In the current study, according to the circRNA-miRNA-mRNA coexpression network and the ceRNA network, we observed that MSTRG.119845.30 was identified to bind hsa-miR-20a-5p; MSTRG.119845.30 was identified to hsa-miR-29b-2-5p; MSTRG.106112.2, MSTRG.151872.3, and MSTRG.51997.3 were identified to bind hsa-miR-6501-5p; MSTRG.105154.2, MSTRG.130010.5, MSTRG.175653.26, MSTRG.228818.11, and MSTRG.102242.2 were identified to bind hsa-miR-142-5p; MSTRG.157434.2 and MSTRG.71484.4 were identified to bind hsa-miR-505-5p competitively with its binding sites. None of these DE lncRNAs and DE miRNAs have been

reported to be functional during COVID-19, which provided useful noncoding target candidates for further work on COVID-19 pathogenesis.

5. Conclusion

In summary, this study investigated the underlying mechanism of “cytokine storm” in COVID-19 patients using whole-transcriptome sequencing. We identified 95 module targets involved in the positive regulation of cytokine production, including AKT1, TNFRSF1B, FCGR2A, CXCL8, STAT3, and TLR2. In addition, we identified several differentially expressed miRNAs and lncRNAs in peripheral blood samples of COVID-19 patients that were closely related to the regulation of the immune effector process and negative regulation of NIK/NF-kappaB signaling. On the basis of the codifferently expressed lncRNAs and mRNA transcripts, we constructed a ceRNA regulatory network that contained 95 DE mRNAs, 23 DE miRNAs, and 258 DE lncRNAs. Within the network, we suspected that the 6 ceRNA subnetworks (i.e., MSTRG.119845.30/hsa-miR-20a-5p/TNFRSF1B, MSTRG.119845.30/hsa-miR-29b-2-5p/FCGR2A, and MSTRG.106112.2/hsa-miR-6501-5p/STAT3) may play a crucial role in the development of COVID-19. These DEGs contribute to an increased understanding of the genomic landscape of SARS-CoV-2 infection and may be confirmed as promising diagnostic biomarkers and therapeutic strategies for COVID-19 patients. However, there are some limitations to this study. First, the DE mRNAs, DE miRNAs, and DE lncRNAs were identified based on the small sample data. In the future, the precise changes of these DEGs should be confirmed based on large clinical samples. Second, further experimental validation with corresponding COVID-19 model *in vitro* and *in vivo* should be made to identify the specific roles of these DEGs.

Abbreviations

SARS-CoV-2:	Severe acute respiratory syndrome coronavirus 2
COVID-19:	Coronavirus disease 2019
DE mRNA:	Differentially expressed messenger RNAs
DE miRNA:	Differentially expressed microRNAs
DE lncRNAs:	Differentially expressed long noncoding RNAs
Go:	Gene ontology
PPI:	Protein-protein interaction
WHO:	World Health Organization
ARDS:	Acute respiratory distress syndrome
TLRs:	Toll-like receptors
NLRs:	NOD-like receptors
RLRs:	RIG-I-like receptors
MERS-CoV:	Middle East respiratory syndrome coronavirus
ncRNAs:	Noncoding RNAs
ceRNA:	Endogenous RNA
MREs:	miRNA response elements
RNAseq:	RNA sequencing
DEGs:	Differentially expressed genes

CNCI:	Coding-noncoding index
CPC2:	Coding potential calculator 2.0
FPKM:	Fragments per kilobase of transcript per million mapped reads
RPM:	Reads per million
KEGG:	Kyoto Encyclopedia of Genes and Genomes
STRING:	Search Tool for the Retrieval of Interacting Genes
MCODE:	Molecular complex detection
BP:	Biological process
CC:	Cellular component
MF:	Molecular function
AKT1:	AKT serine/threonine kinase 1
TNFRSF1B:	TNF receptor superfamily member 1B
FCGR2A:	Fc fragment of IgG receptor IIa
HTLV-I:	Human T cell leukemia virus type I
CXCL8:	C-X-C motif chemokine ligand 8
STAT3:	Signal transducer and activator of transcription 3
TLR2:	Toll-like receptor 2
FcγRs:	Fc gamma receptors.

Data Availability

All supporting data of this study can be found within the manuscript and its supplementary files and available from the corresponding author upon request.

Ethical Approval

The study was approved by the Ethics Committee of the Fourth Affiliated Hospital, College of Medicine, Zhejiang University, and registered at the Chinese Clinical Trial Registry (ChiCTR2000030305).

Disclosure

The funders did not have any role or influence in the study design, execution, analyses, interpretation of the data, or writing of the manuscript.

Conflicts of Interest

The authors declare no competing interests.

Authors' Contributions

CXL, JC, and XH conceptualized the study design. CXL, JC, SK Lv, JHL, LLL, and XH recruited the patients, collected specimens, and collected demographic and clinical data. CXL and JC analyzed the sequencing data and interpreted the results. CXL wrote the initial drafts of the manuscript. CXL, JC, and XH revised the manuscript. All authors read and approved the final manuscript. Cai-xia Li and Jian Chen contributed equally to this work.

Acknowledgments

This study was supported by Jinhua Science and Technology Bureau New Crown Research Key Project in Zhejiang

Province (Grant No. 2020XG-30) and the Natural Science Foundation of China of Zhejiang Province (Grant No. LY20H180013).

Supplementary Materials

Table S1: the differentially expressed mRNAs of peripheral blood samples in COVID-19 patients. Table S2: the differentially expressed miRNA of peripheral blood samples in COVID-19 patients. Table S3: the differentially expressed lncRNAs of peripheral blood samples in COVID-19 patients. (*Supplementary Materials*)

References

- [1] C. Huang, Y. Wang, X. Li et al., "Clinical features of patients infected with 2019 novel coronavirus in Wuhan, China," *Lancet*, vol. 395, no. 10223, pp. 497–506, 2020.
- [2] Q. Ye, B. Wang, and J. Mao, "The pathogenesis and treatment of the 'cytokine Storm' in COVID-19," *The Journal of Infection*, vol. 80, no. 6, pp. 607–613, 2020.
- [3] J. Nkengasong, "China's response to a novel coronavirus stands in stark contrast to the 2002 SARS outbreak response," *Nature Medicine*, vol. 26, no. 3, pp. 310–311, 2020.
- [4] Worldometer COVID-19 Coronavirus Pandemic, 2021, <https://www.worldometers.info/coronavirus/>.
- [5] C. Qin, L. Zhou, Z. Hu et al., "Dysregulation of immune response in patients with coronavirus 2019 (COVID-19) in Wuhan, China," *Clinical Infectious Diseases*, vol. 71, no. 15, pp. 762–768, 2020.
- [6] W. J. Guan, Z. Y. Ni, Y. Hu et al., "Clinical characteristics of coronavirus disease 2019 in China," *The New England Journal of Medicine*, vol. 382, no. 18, pp. 1708–1720, 2020.
- [7] T. Singhal, "A review of coronavirus disease-2019 (COVID-19)," *Indian Journal of Pediatrics*, vol. 87, no. 4, pp. 281–286, 2020.
- [8] S. P. Adhikari, S. Meng, Y. J. Wu et al., "Epidemiology, causes, clinical manifestation and diagnosis, prevention and control of coronavirus disease (COVID-19) during the early outbreak period: a scoping review," *Infectious Diseases of Poverty*, vol. 9, no. 1, p. 29, 2020.
- [9] T. Nelemans and M. Kikkert, "Viral innate immune evasion and the pathogenesis of emerging RNA virus infections," *Viruses*, vol. 11, no. 10, p. 961, 2019.
- [10] Y. Xiong, Y. Liu, L. Cao et al., "Transcriptomic characteristics of bronchoalveolar lavage fluid and peripheral blood mononuclear cells in COVID-19 patients," *Emerging Microbes & Infections*, vol. 9, no. 1, pp. 761–770, 2020.
- [11] Y. Chen, Q. Liu, and D. Guo, "Emerging coronaviruses: genome structure, replication, and pathogenesis," *Journal of Medical Virology*, vol. 92, no. 4, pp. 418–423, 2020.
- [12] C. K. Wong, C. W. K. Lam, A. K. L. Wu et al., "Plasma inflammatory cytokines and chemokines in severe acute respiratory syndrome," *Clinical and Experimental Immunology*, vol. 136, no. 1, pp. 95–103, 2004.
- [13] A. R. Fehr, R. Channappanavar, and S. Perlman, "Middle East respiratory syndrome: emergence of a pathogenic human coronavirus," *Annual Review of Medicine*, vol. 68, no. 1, pp. 387–399, 2017.
- [14] Z. Xu, L. Shi, Y. Wang et al., "Pathological findings of COVID-19 associated with acute respiratory distress syndrome," *The Lancet Respiratory Medicine*, vol. 8, no. 4, pp. 420–422, 2020.
- [15] T. Brandenburger, A. Salgado Somoza, Y. Devaux, and J. M. Lorenzen, "Noncoding RNAs in acute kidney injury," *Kidney International*, vol. 94, no. 5, pp. 870–881, 2018.
- [16] L. Tang, P. Li, and L. Li, "Whole transcriptome expression profiles in placenta samples from women with gestational diabetes mellitus," *Journal of Diabetes Investigation*, vol. 11, no. 5, pp. 1307–1317, 2020.
- [17] B. Liu, J. Li, and M. J. Cairns, "Identifying miRNAs, targets and functions," *Briefings in Bioinformatics*, vol. 15, no. 1, pp. 1–19, 2014.
- [18] T. Derrien, R. Johnson, G. Bussotti et al., "The GENCODE v7 catalog of human long noncoding RNAs: analysis of their gene structure, evolution, and expression," *Genome Research*, vol. 22, no. 9, pp. 1775–1789, 2012.
- [19] L. Salmena, L. Poliseno, Y. Tay, L. Kats, and P. P. Pandolfi, "A ceRNA hypothesis: the Rosetta stone of a hidden RNA language?," *Cell*, vol. 146, no. 3, pp. 353–358, 2011.
- [20] Q. Lu, R. Wu, M. Zhao, A. Garcia-Gomez, and E. Ballestar, "miRNAs as therapeutic targets in inflammatory disease," *Trends in Pharmacological Sciences*, vol. 40, no. 11, pp. 853–865, 2019.
- [21] X. Zhang, F. Huang, D. Yang, T. Peng, and G. Lu, "Identification of miRNA-mRNA Crosstalk in Respiratory Syncytial Virus- (RSV-) Associated Pediatric Pneumonia through Integrated miRNAome and Transcriptome Analysis," *Mediators of Inflammation*, vol. 2020, Article ID 8919534, 13 pages, 2020.
- [22] L. N. Schulte, W. Bertrams, C. Stielow, and B. Schmeck, "ncRNAs in Inflammatory and Infectious Diseases," *Methods in Molecular Biology*, vol. 1912, pp. 3–32, 2019.
- [23] G. Monaco, B. Lee, W. Xu et al., "RNA-Seq signatures normalized by mRNA abundance allow absolute deconvolution of human immune cell types," *Cell Reports*, vol. 26, no. 6, pp. 1627–1640.e7, 2019.
- [24] S. Chen, Y. Zhou, Y. Chen, and J. Gu, "Fastp: an ultra-fast all-in-one FASTQ preprocessor," *Bioinformatics*, vol. 34, no. 17, pp. i884–i890, 2018.
- [25] D. Kim, B. Langmead, and S. L. Salzberg, "HISAT: a fast spliced aligner with low memory requirements," *Nature Methods*, vol. 12, no. 4, pp. 357–360, 2015.
- [26] M. R. Friedländer, S. D. Mackowiak, N. Li, W. Chen, and N. Rajewsky, "miRDeep2 accurately identifies known and hundreds of novel microRNA genes in seven animal clades," *Nucleic Acids Research*, vol. 40, no. 1, pp. 37–52, 2012.
- [27] G. Yu, L. G. Wang, Y. Han, and Q. Y. He, "clusterProfiler: an R package for comparing biological themes among gene clusters," *OMICS*, vol. 16, no. 5, pp. 284–287, 2012.
- [28] G. Stelzer, N. Rosen, I. Plaschkes et al., "The GeneCards suite: from gene data mining to disease genome sequence analyses," *Current Protocols in Bioinformatics*, vol. 54, no. 1, pp. 1.30.1–1.30.33, 2016.
- [29] J. H. Wang, L. F. Zhao, H. F. Wang et al., "GenCLiP 3: mining human genes' functions and regulatory networks from PubMed based on co-occurrences and natural language processing," *Bioinformatics*, vol. 36, no. 6, pp. 1973–1975, 2019.
- [30] J. S. Amberger, C. A. Bocchini, F. Schiettecatte, A. F. Scott, and A. Hamosh, "OMIM.org: Online Mendelian Inheritance in Man (OMIM®), an online catalog of human genes and genetic

- disorders," *Nucleic Acids Research*, vol. 43, no. D1, pp. D789–D798, 2015.
- [31] D. Szklarczyk, J. H. Morris, H. Cook et al., "The STRING database in 2017: quality-controlled protein-protein association networks, made broadly accessible," *Nucleic Acids Research*, vol. 45, no. D1, pp. D362–D368, 2017.
- [32] G. D. Bader and C. W. Hogue, "An automated method for finding molecular complexes in large protein interaction networks," *BMC Bioinformatics*, vol. 4, no. 1, p. 2, 2003.
- [33] Y. Zhou, B. Zhou, L. Pache et al., "Metascape provides a biologist-oriented resource for the analysis of systems-level datasets," *Nature Communications*, vol. 10, no. 1, p. 1523, 2019.
- [34] Y. Chen and X. Wang, "miRDB: an online database for prediction of functional microRNA targets," *Nucleic Acids Research*, vol. 48, no. D1, pp. D127–D131, 2020.
- [35] H. Li, S. M. Liu, X. H. Yu, S. L. Tang, and C. K. Tang, "Coronavirus disease 2019 (COVID-19): current status and future perspectives," *International Journal of Antimicrobial Agents*, vol. 55, no. 5, article 105951, 2020.
- [36] D. G. Ahn, H. J. Shin, M. H. Kim et al., "Current status of epidemiology, diagnosis, therapeutics, and vaccines for novel coronavirus disease 2019 (COVID-19)," *Journal of Microbiology and Biotechnology*, vol. 30, no. 3, pp. 313–324, 2020.
- [37] S. K. Thaker, J. Ch'ng, and H. R. Christofk, "Viral hijacking of cellular metabolism," *BMC Biology*, vol. 17, no. 1, p. 59, 2019.
- [38] C. K. Min, S. Cheon, N. Y. Ha et al., "Comparative and kinetic analysis of viral shedding and immunological responses in MERS patients representing a broad spectrum of disease severity," *Scientific Reports*, vol. 6, no. 1, article 25359, 2016.
- [39] T. Okabayashi, H. Kariwa, S. Yokota et al., "Cytokine regulation in SARS coronavirus infection compared to other respiratory virus infections," *Journal of Medical Virology*, vol. 78, no. 4, pp. 417–424, 2006.
- [40] J. Liu, S. Li, J. Liu et al., "Longitudinal characteristics of lymphocyte responses and cytokine profiles in the peripheral blood of SARS-CoV-2 infected patients," *eBioMedicine*, vol. 55, article 102763, 2020.
- [41] S. Appelberg, S. Gupta, S. Svensson Akusjärvi et al., "Dysregulation in Akt/mTOR/HIF-1 signaling identified by proteo-transcriptomics of SARS-CoV-2 infected cells," *Emerging Microbes & Infections*, vol. 9, no. 1, pp. 1748–1760, 2020.
- [42] V. Le Sage, A. Cinti, R. Amorim, and A. J. Mouland, "Adapting the stress response: viral subversion of the mTOR signaling pathway," *Viruses*, vol. 8, no. 6, p. 152, 2016.
- [43] J. Pinno, H. Bongartz, O. Klepsch et al., "Interleukin-6 influences stress-signalling by reducing the expression of the mTOR-inhibitor REDD1 in a STAT3-dependent manner," *Cellular Signalling*, vol. 28, no. 8, pp. 907–916, 2016.
- [44] S. Mokuda, T. Tokunaga, J. Masumoto, and E. Sugiyama, "Angiotensin-converting enzyme 2, a SARS-CoV-2 receptor, is upregulated by interleukin 6 through STAT3 signaling in synovial tissues," *The Journal of Rheumatology*, vol. 47, no. 10, pp. 1593–1595, 2020.
- [45] T. So and N. Ishii, "The TNF-TNFR family of co-signal molecules," *Advances in Experimental Medicine and Biology*, vol. 1189, pp. 53–84, 2019.
- [46] E. Denisenko, R. Guler, M. Mhlanga, H. Suzuki, F. Brombacher, and S. Schmeier, "Transcriptionally induced enhancers in the macrophage immune response to mycobacterium tuberculosis infection," *BMC Genomics*, vol. 20, no. 1, p. 71, 2019.
- [47] G. T. Rijkers, L. Holzer, and T. Dusselier, "Genetics in community-acquired pneumonia," *Current Opinion in Pulmonary Medicine*, vol. 25, no. 3, pp. 323–329, 2019.
- [48] F. Coperchini, L. Chiovato, L. Croce, F. Magri, and M. Rotondi, "The cytokine storm in COVID-19: an overview of the involvement of the chemokine/chemokine-receptor system," *Cytokine & Growth Factor Reviews*, vol. 53, pp. 25–32, 2020.
- [49] A. Naz, F. Shahid, T. T. Butt, F. M. Awan, A. Ali, and A. Malik, "Designing multi-epitope vaccines to combat emerging coronavirus disease 2019 (COVID-19) by employing Immunoinformatics approach," *Frontiers in Immunology*, vol. 11, p. 1663, 2020.
- [50] S. N. Lester and K. Li, "Toll-like receptors in antiviral innate immunity," *Journal of Molecular Biology*, vol. 426, no. 6, pp. 1246–1264, 2014.

Review Article

The Regulatory Role of α -Ketoglutarate Metabolism in Macrophages

Shaojuan Liu , Jie Yang , and Zhenfang Wu 

College of Animal Science and National Engineering Research Center for Breeding Swine Industry, South China Agricultural University, Guangzhou, Guangdong 510642, China

Correspondence should be addressed to Jie Yang; jieyang2012@hotmail.com and Zhenfang Wu; wzffemail@163.com

Received 13 January 2021; Revised 2 March 2021; Accepted 10 March 2021; Published 30 March 2021

Academic Editor: Xin Zong

Copyright © 2021 Shaojuan Liu et al. This is an open access article distributed under the Creative Commons Attribution License, which permits unrestricted use, distribution, and reproduction in any medium, provided the original work is properly cited.

Macrophages are multifunctional immune cells whose functions depend on polarizable phenotypes and the microenvironment. Macrophages have two phenotypes, including the M1 proinflammatory phenotype and the M2 anti-inflammatory phenotype, which play important roles in many inflammatory responses and diseases. α -Ketoglutarate is a key metabolite of the TCA cycle and can regulate the phenotype of macrophage polarization to exert anti-inflammatory effects in many inflammation-related diseases. In this review, we primarily elucidate the metabolism, regulatory mechanism, and perspectives of α -ketoglutarate on macrophages. The regulation of macrophage polarization by α -ketoglutarate may provide a promising target for the prevention and therapy of inflammatory diseases and is beneficial to animal health.

1. Introduction

Macrophages are an important part of the immune system and play vital roles in host defense and inflammation. Macrophages originate from monocytes released by the bone marrow, and they can migrate to different organs under natural or pathological conditions to form macrophages [1]. Under different pathological conditions, macrophages are polarized into two inflammatory phenotypes: the M1 proinflammatory phenotype and the M2 anti-inflammatory phenotype. The M1 phenotype is classically activated macrophages induced by various proinflammatory factors, such as lipopolysaccharide (LPS), interferon- γ (INF- γ), and tumor necrosis factor- α (TNF- α) [2–4]. M1 macrophages can excrete multiple proinflammatory cytokines such as interleukin-1 (IL-1), interleukin-12 (IL-12), and interleukin-23 (IL-23), and they can eliminate pathogens and activate adaptive immunity [5]. Conversely, M2 macrophages are alternatively activated macrophages induced by anti-inflammatory factors such as interleukin-4 (IL-4), glucocorticoids, and granulocyte colony factor (G-CSF) [6]. M2 macrophages exhibit anti-inflammatory effects in response to inflammation and produce many anti-inflammatory cytokines such as interleukin-10 (IL-

10), transforming growth factor- β (TGF- β), and interleukin-4 (IL-4) [7–9], which could promote wound repair, fibrosis, and bone reconstruction [10]. The polarizable phenotype of M1 and M2 macrophages is a dynamic process that depends on the microenvironment and is regulated by a variety of intracellular signaling molecules and pathways. Macrophages are characterized by heterogeneity and plasticity and exhibit different functions due to signals in the local microenvironment. The functions of macrophages are affected by metabolites, inflammatory signals, oxygen tension, and cytokines [11–13]. Additionally, many signaling pathways can also regulate the polarization of macrophages, such as the Janus kinase/signal transducers and activators of transcription (JAK/STAT) signaling pathway, phosphatidylinositol 3'-kinase (PI3K)/Akt signaling pathway, c-Jun N-terminal protein kinase (JNK) signaling pathway, notch signaling pathway, and nuclear factor kappa-light-chain-enhancer of B cell (NF- κ B) signaling pathway [14–17]. Of note, cellular metabolism could bidirectionally regulate the functional response of macrophages, and the microenvironment composition of cellular metabolism plays a vital role in macrophage functions; in turn, cellular metabolites alter tissue homeostasis [18]. Furthermore, the balance between the M1 and M2 phenotypes plays

an important role in the occurrence and development of diseases such as tuberculosis, tumors, and atherosclerosis and contributes to maintaining host homeostasis [19–21].

The metabolic characteristics of macrophages are different in the M1 and M2 phenotypes. The metabolism of M1 macrophages is characterized by strengthening the pentose phosphate pathway (PPP), increasing fatty acid oxidation (FAO), and improving anaerobic glycolysis while reducing the oxidative phosphorylation (OXPHOS) process and suppressing the tricarboxylic acid (TCA) cycle [22–24]. In contrast, M2 macrophage metabolism is mainly dependent on FAO and OXPHOS approaches to exert anti-inflammatory effects and repair tissue damage while decreasing glycolysis and the PPP process [25, 26]. All of these approaches could provide energy for macrophage metabolism and functional responses. Moreover, many studies have suggested that some amino acid metabolites play important roles in the prevention and treatment of certain inflammation-related diseases by inducing the polarization of macrophages and regulating macrophage functions. For example, glutamine metabolism could modulate macrophage polarization to prevent obesity and diabetes [27]. Likewise, inhibition of the accumulation and inflammatory signaling pathway of succinate could suppress M1 polarization to exert anti-inflammatory effects [13]. Notably, as an important metabolite of the TCA cycle and a precursor of glutamate and glutamine, α -ketoglutarate serves as an energy source and plays an important role in immunity, bone development, intestinal health, and the oxidative system [28–30]. Moreover, α -ketoglutarate suppresses M1 macrophage activation but promotes M2 macrophage activation to exhibit anti-inflammatory effects by mediating metabolic and epigenetic reprogramming [31]. In this review, we emphasize the regulatory role of α -ketoglutarate in macrophage polarization and provide a reference for the prevention and treatment of inflammatory diseases.

2. α -Ketoglutarate Metabolism in Macrophages

α -Ketoglutarate is a key intermediate in the TCA cycle and is generated from isocitrate by the oxidative decarboxylation of isocitrate dehydrogenase (IDH) and glutamate by the oxidative deamination of glutamate dehydrogenase (GDH). Then, α -ketoglutarate is metabolized into succinyl-CoA, catalyzed by α -ketoglutarate dehydrogenase (α -KGDH). Additionally, glutamine can be converted into α -ketoglutarate under the catalysis of GDH and glutaminase (GLS) via glutaminolysis. Using multiple reaction monitoring (MRM) to detect the targeted ^{13}C -metabolic flux profiling of glucose and its intermediate metabolites in macrophages, glucose was shown to enter the cytoplasm and activate the TCA cycle and glycolysis with increasing intracellular and extracellular metabolites and selected enzyme levels in HIV-1 viral protein R- (Vpr-) induced macrophages [32]. It was observed that α -ketoglutarate was metabolized into glutamate and increased intracellular and extracellular glutamate release, which was further converted into glutamine in HIV-1-infected macrophages; in turn, glutamine metabolism promoted the accumulation of extracellular glutamate and α -ketoglutarate. Moreover, IDH2, as a crucial enzyme in the TCA cycle, catalyzes isocitrate

into α -ketoglutarate. In LPS-induced lung inflammation, IDH2 could regulate α -ketoglutarate production to modulate the proinflammatory response mediated by NF- κ B [33]. Similarly, GDH-mediated α -ketoglutarate can produce energy in the TCA cycle but also inhibit activation of the inhibitor of nuclear factor kappa-B kinase β (IKK β), thus suppressing NF- κ B activation [34].

Collectively, α -ketoglutarate is derived from the oxidative decarboxylation of isocitrate in the TCA cycle and is produced from glutamine and glutamate metabolism or external sources, which play an important role in the polarization of macrophages by providing an energy source for damaged tissues (Figure 1). For example, glutamine metabolism increases the accumulation of α -ketoglutarate and glucose flux in the extracellular milieu of HIV-1-infected macrophages and HIV-1 Vpr-overexpressing macrophages via the glycolytic pathway and TCA cycle, indicating that α -ketoglutarate may be an energy resource for alleviating macrophage damage [32]. In addition, the isotope tracing method was used to investigate the pathways of glutamine metabolism in white spot syndrome virus (WSSV), and glutamine was found to be catabolized to glutamate by GLS and further converted to α -ketoglutarate by GDH to replenish the TCA cycle by the α -KGDH-mediated oxidative pathway and IDH-mediated reductive pathway [35]. Likewise, in HIV-1-infected or LPS-treated macrophages, α -ketoglutarate produced from glutamine metabolism by glutaminase 1 could promote extracellular vesicle release and regulate the inflammatory process [36].

3. α -Ketoglutarate Modulates Macrophage Polarization

α -Ketoglutarate can provide ATP for cell biological processes by activating the mammalian target of rapamycin complex (mTOR) signaling pathway and suppressing glutamine degradation in macrophage polarization [37, 38]. α -Ketoglutarate, as a product of glutamine metabolism, such as the glutamine-glutamate- α KG (Gln-Glu- α -KG) pathway, oxidative glutamine metabolism, and reductive carboxylation mediated by α -KGDH, IDH1, and IDH2, could refuel the TCA cycle and connect with the aerobic glycolysis and lipogenesis pathways in common with the PI3K-Akt-mTOR pathway. In M1-polarized MH-S cells, α -ketoglutarate notably decreased the protein expression of p70 ribosomal protein S6 kinase (P-p70S6K) in LPS-treated groups, but there was no evident change when α -ketoglutarate was added to LPS-rapamycin-treated groups. This result is consistent with the inhibition of LDH and the improvement of ATP production by α -ketoglutarate. Therefore, α -ketoglutarate may serve as an energy source to suppress the inflammatory response and then inhibit M1 macrophage activation induced by LPS [39]. Moreover, α -ketoglutarate could modulate the marker gene expression of M1 and M2 macrophages to alleviate inflammation (Figure 2). α -Ketoglutarate significantly decreased the serum levels of inflammatory cytokines (IL-6 and IL-12) and the expression of IL-1 β , IL-6, and TNF- α , which are M1-specific markers, in lung tissues after 3 h LPS treatment, while it increased the

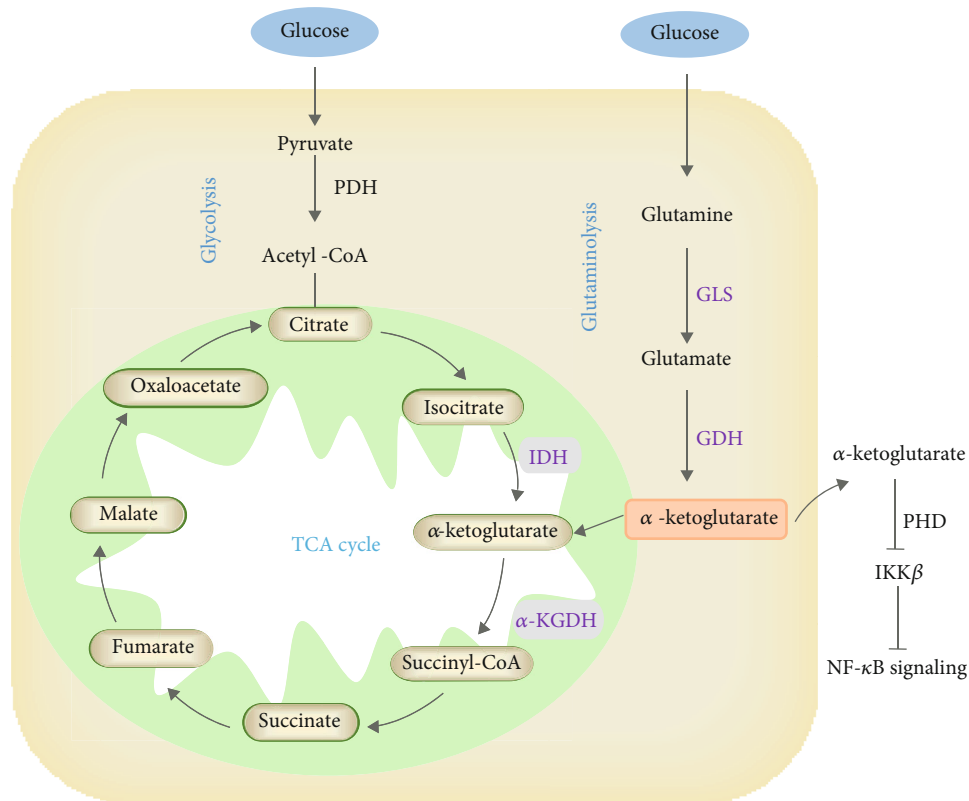


FIGURE 1: α -Ketoglutarate metabolism in macrophages. α -Ketoglutarate is generated from isocitrate by the oxidative decarboxylation of IDH in the TCA cycle or glucose via glycolysis. Additionally, glutamine could be converted into α -ketoglutarate under the catalysis of GDH and GLS via glutaminolysis. Then, α -ketoglutarate is metabolized into succinyl-CoA catalyzed by α -KGDH in the TCA cycle. In addition, GDH-mediated α -ketoglutarate can inhibit IKK β activation and block NF- κ B activation.

anti-inflammatory expression of Arg1 and Mrc1, which are M2 marker genes. Similarly, α -ketoglutarate significantly facilitated peroxisome proliferator-activated receptor γ (PPAR γ) activation and the expression of Arg1 to promote M2 polarization compared to the IL-4-treated group of M2-polarized MH-S cells. In addition, α -ketoglutarate lowered the expression of M1 marker genes, increased the expression of M2 marker genes and IL-10, and suppressed NF- κ B signaling in LPS-induced rats [40]. Furthermore, α -ketoglutarate generated by glutaminolysis can act as a checkpoint to regulate M2 metabolic reprogramming and the participation of FAO in M2 macrophages. Supplementation with dimethyl- α -ketoglutarate (DM- α KG) could promote M2 activation through the α KG-Jmjd3 pathway by suppressing the demethylation of trimethylated histone H3 K27 (H3K27me3) and IL-4-induced genes. Notably, succinate, downstream of α -ketoglutarate, has been reported to increase the expression of the proinflammatory cytokine IL-1 β mediated by HIF-1 α in M1 macrophages, while the α -ketoglutarate/succinate ratio is subject to M1 and M2 macrophage polarization.

α -Ketoglutarate modulates the balance between M1 and M2 macrophage polarization by many means to relieve inflammation. In LPS-induced acute lung injury/acute respiratory distress syndrome (ALI/ARDS), α -ketoglutarate could inhibit M1 polarization by suppressing the mTORC1/p70S6K pathway and promote the M2 phenotype

by enhancing PPAR γ nuclear translocation, which is conducive to preventing inflammatory diseases [39]. The addition of DM- α KG, a cell-permeable analog of α -ketoglutarate, restores the expression of the M2-specific gene Arg 1 and the ratio of α -ketoglutarate/succinate to promote M2 polarization in *P. gingivalis*-treated mouse bone marrow-derived macrophages (BMDMs) [41]. Cheng et al. suggested that DM- α KG produced by glutaminolysis could switch the polarization of M1 macrophages to M2 macrophages in Kupffer cells, which exerts anti-inflammatory effects by inhibiting NF- κ B activity and increasing the phosphorylation of glycogen synthase kinase 3 β (p-GSK3 β) and the expression of suppressor of cytokine signaling 1 (SOCS1) during the prevention and alleviation of hepatic ischemia-reperfusion injury (IRI) [40].

Metabolic and epigenetic remodeling play crucial roles in regulating macrophage reprogramming and phenotypic polarization. In IL-4- or LPS-treated BMDMs, α -ketoglutarate metabolized by glutamine and the Jmjd3-dependent pathway modulates M2 metabolic reprogramming, which serves as a regulator to participate in FAO and manipulates the ratio of α -ketoglutarate/succinate [31]. α -Ketoglutarate inhibits M1 polarization by intervening in the NF- κ B pathway to enhance prolyl hydroxylase (PHD) activity to suppress IKK β activation. Glutaminolysis-derived α -ketoglutarate is conducive to improving endotoxin tolerance in macrophages by modulating NF- κ B signaling and the Jmjd3-dependent

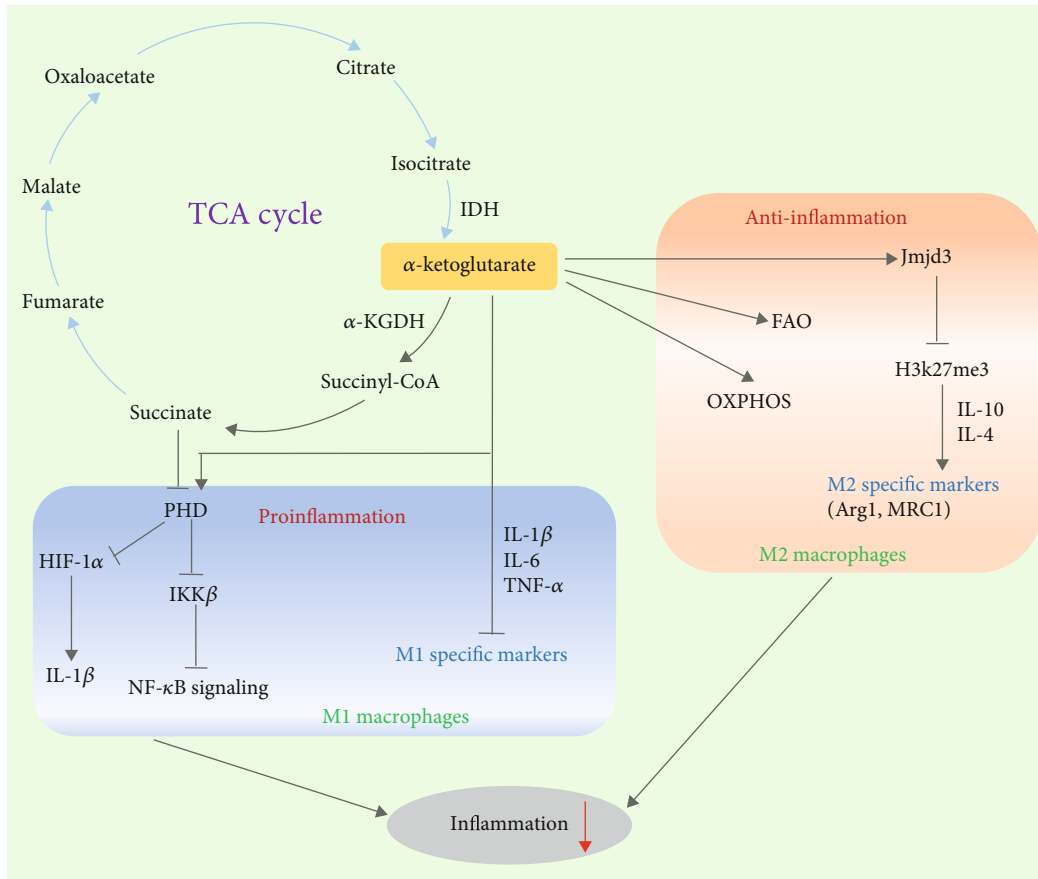


FIGURE 2: The regulatory mechanism of α -ketoglutarate on M1 and M2 polarization. In M1 macrophages, α -ketoglutarate inhibits M1 polarization by enhancing PHD activity to suppress $\text{IKK}\beta$ activation and the $\text{NF-}\kappa\text{B}$ pathway and inhibiting HIF-1 α and IL-1 β expression mediated downstream of succinate in the TCA cycle. In M2 macrophages, α -ketoglutarate generated by glutaminolysis is a checkpoint that regulates M2 metabolic reprogramming and the participation of FAO and OXPHOS in M2 macrophages. Additionally, α -ketoglutarate promotes M2 activation through the α -ketoglutarate-Jmjd3 pathway by suppressing H3K27me3 and increasing the expression of M2-specific markers.

pathway [31]. Mechanistically, melatonin increases α -ketoglutarate levels to promote M2 macrophage polarization and enhance TET-mediated DNA demethylation by increasing exosome secretion through the $\text{STAT3/NF-}\kappa\text{B}$ signaling pathway in mouse adipocytes, which is beneficial to prevent and treat inflammatory diseases [31]. Additionally, the generation of α -ketoglutarate enhanced by Rspodin3-induced metabolism assists in catalyzing DNA hydroxymethylation via ten-eleven translocators (TETs) in lung injury, which acts as a cofactor for epigenetic reprogramming in macrophages to prevent inflammatory lung injury [42].

4. Regulatory Effects of α -Ketoglutarate on Inflammation-Related Diseases in Macrophages

As described above, macrophages have two polarized phenotypes, including the proinflammatory phenotype of M1 macrophages and the anti-inflammatory phenotype of M2 macrophages under different environmental stimuli, and they exhibit different physiological functions. M1 macrophages have a bactericidal function, secrete proinflammatory

factors and regulatory factors, and engage in complement-mediated phagocytosis, which is part of the first line of innate immune system defense: phagocytosis, elimination of foreign pathogens, and activation of the T cell adaptive immune response [43]. However, excessive proinflammatory M1 induces an inflammatory response and has a role in many inflammatory diseases, such as atherosclerosis and severe acute pancreatitis. Studies have shown that a large number of proinflammatory mediators produced by M1 macrophages could aggravate lung injury and accelerate airway remodeling, resulting in the aggravation of asthma [44]. M2 macrophages could promote wound healing and fibrosis, repair tissue, and facilitate tumor growth [20, 45, 46]. Recent studies have suggested that certain metabolites can regulate the activity of epigenetic enzymes to modulate the polarization of macrophages through epigenetic mechanisms to affect the occurrence and development of inflammation-related diseases.

The intermediate metabolites of the TCA cycle could serve as energy sources to mediate the polarization of macrophages through epigenetic mechanisms and prevent certain metabolic diseases. α -Ketoglutarate is an important short-chain carboxylic acid molecule and a key intermediate in

the TCA cycle that connects the key nodes of carbon-nitrogen metabolism in cells and provides carbon source materials and energy for cell growth and proliferation. Previous studies indicated that α -ketoglutarate could regulate the occurrence and development of certain inflammatory diseases by manipulating the polarization of macrophages. It has been reported that the administration of α -ketoglutarate could enhance beige/brown adipogenesis to reverse obesity by strengthening DNA demethylation [47, 48]. Similarly, a study found that melatonin could regulate the levels of cellular and exosomal α -ketoglutarate to enhance the polarization of M2 macrophages and TET-mediated DNA demethylation as a result of alleviating adipose inflammation in mice [49]. In addition, the number of M1 macrophages is increased, the levels of α -ketoglutarate and glutamine are decreased, and an accumulation of succinate has been observed in obesity and diabetes [27]. Therefore, α -ketoglutarate may be a promising target to prevent and treat obesity or diabetes. In LPS-induced lung injury, α -ketoglutarate could effectively promote the polarization of M2 macrophages and decrease inflammation to ameliorate lung damage via PPAR γ nuclear translocation and the mTORC1/p70S6K pathway [39]. Likewise, DM- α KG could inhibit NF- κ B activity and the secretion of proinflammatory cytokines by maintaining a higher ratio of M2/M1 polarization to relieve liver injury [40]. Thus, α -ketoglutarate may be a potential target on macrophages for the prevention and treatment of inflammation-related diseases.

5. Conclusion and Perspectives

Collectively, α -ketoglutarate is a key metabolite of the TCA cycle, which is metabolized in many ways, such as through the TCA cycle, glutaminolysis, and external sources. α -Ketoglutarate could serve as a cofactor to modulate the polarization of M1 and M2 macrophages and alleviate the inflammatory response and inflammation-related diseases. However, the current research results are not sufficient to fully explain the regulatory mechanism of α -ketoglutarate on macrophage polarization, and there is a need to further investigate its potential effects on macrophages. Of note, we summarized many studies on α -ketoglutarate and observed that most of them are related to intestinal function. Interestingly, many studies have demonstrated that intestinal macrophages are the first line of intestinal mucosal immunity and that they play a crucial role in intestinal homeostasis and numerous gastrointestinal diseases [50, 51]. Thus, we propose that the effects of α -ketoglutarate and their mechanisms on intestinal macrophages are worth investigating. Furthermore, we also discovered that macrophage polarization is associated with aging [52, 53]. α -Ketoglutarate can extend lifespan and postpone aging by regulating cell energy metabolism [54–56]. For instance, it was reported that α -ketoglutarate could ameliorate age-related osteoporosis by regulating histone methylation, reducing the expression of H3K9m9e3 and H3K27me3, and increasing BMP signaling and Nanog [57]. Mechanistically, α -ketoglutarate mainly serves as an energy regulator by modulating ATP synthesis, limiting the energy utilization efficiency of nutrients, and maintaining a restricted diet state of organisms to ameliorate aging and

age-related diseases through the mTOR pathway and AMPK signaling, and it is regarded as a potential antiaging agent [55, 58, 59]. Notably, a recent study indicated that the mechanism of extending longevity by α -ketoglutarate is related to a reduction of systemic inflammation and the elevation of IL-10 in aged female mice [54]. Therefore, in view of the above studies, we speculate whether α -ketoglutarate could extend lifespan and ameliorate aging or age-associated diseases by regulating the polarization of macrophages. However, it is not clear if the effect of α -ketoglutarate on longevity is applicable to humans, and the necessary levels of α -ketoglutarate to extend lifespan have not been quantified in animals, but these are areas worthy of further exploration.

Conflicts of Interest

The authors declare that there are no conflicts of interest regarding the publication of this paper.

Authors' Contributions

S.L. conceived and drafted this manuscript, and J.Y. and Z.W. revised this manuscript. All authors reviewed and approved the final manuscript.

Acknowledgments

This work was supported by the Guangdong Provincial Promotion Project on Preservation and Utilization of Local Breed of Livestock and Poultry and the Local Innovative and Research Teams Project of Guangdong Province (2019BT02N630).

References

- [1] D. Kurotaki, H. Sasaki, and T. Tamura, "Transcriptional control of monocyte and macrophage development," *International Immunology*, vol. 29, no. 3, pp. 97–107, 2017.
- [2] A. Dufour, C. L. Bellac, U. Eckhard et al., "C-terminal truncation of IFN- γ inhibits proinflammatory macrophage responses and is deficient in autoimmune disease," *Nature Communications*, vol. 9, no. 1, p. 2416, 2018.
- [3] X. Su, Y. Yu, Y. Zhong et al., "Interferon- γ regulates cellular metabolism and mRNA translation to potentiate macrophage activation," *Nature Immunology*, vol. 16, no. 8, pp. 838–849, 2015.
- [4] M. Orecchioni, Y. Ghosheh, A. B. Pramod, and K. Ley, "Macrophage polarization: different gene signatures in M1(LPS+) vs. classically and M2(LPS-) vs. alternatively activated macrophages," *Frontiers in Immunology*, vol. 10, p. 1084, 2019.
- [5] S. Gordon and F. O. Martinez, "Alternative activation of macrophages: mechanism and functions," *Immunity*, vol. 32, no. 5, pp. 593–604, 2010.
- [6] R. Shrivastava and N. Shukla, "Attributes of alternatively activated (M2) macrophages," *Life Sciences*, vol. 224, pp. 222–231, 2019.
- [7] A. D. Foey, "Macrophages—masters of immune activation, suppression and deviation," in *Immune Response Activation*, pp. 121–149, 2014.

- [8] L. Zhu, Q. Zhao, T. Yang, W. Ding, and Y. Zhao, "Cellular metabolism and macrophage functional polarization," *International Reviews of Immunology*, vol. 34, no. 1, pp. 82–100, 2015.
- [9] M. Jung, Y. Ma, R. P. Iyer et al., "IL-10 improves cardiac remodeling after myocardial infarction by stimulating M2 macrophage polarization and fibroblast activation," *Basic Research in Cardiology*, vol. 112, no. 3, p. 33, 2017.
- [10] N. Chanchareonsook, R. Junker, L. Jongpaiboonkit, and J. A. Jansen, "Tissue-engineered mandibular bone reconstruction for continuity defects: a systematic approach to the literature," *Tissue Engineering. Part B, Reviews*, vol. 20, no. 2, pp. 147–162, 2014.
- [11] L. A. O'Neill, "A critical role for citrate metabolism in LPS signalling," *Biochemical Journal*, vol. 438, no. 3, pp. e5–e6, 2011.
- [12] E. M. Palsson-McDermott, A. M. Curtis, G. Goel et al., "Pyruvate kinase M2 regulates Hif-1 α activity and IL-1 β induction and is a critical determinant of the warburg effect in LPS-activated macrophages," *Cell Metabolism*, vol. 21, no. 1, pp. 65–80, 2015.
- [13] G. M. Tannahill, A. M. Curtis, J. Adamik et al., "Succinate is an inflammatory signal that induces IL-1 β through HIF-1 α ," *Nature*, vol. 496, no. 7444, pp. 238–242, 2013.
- [14] H. Oh, S.-H. Park, M.-K. Kang et al., "Asaronic acid attenuates macrophage activation toward M1 phenotype through inhibition of NF- κ B pathway and JAK-STAT signaling in glucose-loaded murine macrophages," *Journal of Agricultural and Food Chemistry*, vol. 67, no. 36, pp. 10069–10078, 2019.
- [15] J. Wang, L. Xie, S. Wang, J. Lin, J. Liang, and J. Xu, "Azithromycin promotes alternatively activated macrophage phenotype in systematic lupus erythematosus via PI3K/Akt signaling pathway," *Cell Death & Disease*, vol. 9, no. 11, p. 1080, 2018.
- [16] J. Hao, Y. Hu, Y. Li, Q. Zhou, and X. Lv, "Involvement of JNK signaling in IL4-induced M2 macrophage polarization," *Experimental Cell Research*, vol. 357, no. 2, pp. 155–162, 2017.
- [17] Y. Lin, J. L. Zhao, Q. J. Zheng et al., "Notch signaling modulates macrophage polarization and phagocytosis through direct suppression of signal regulatory protein α expression," *Frontiers in Immunology*, vol. 9, p. 1744, 2018.
- [18] J. T. Pesce, T. R. Ramalingam, M. M. Mentink-Kane et al., "Arginase-1-expressing macrophages suppress Th2 cytokine-driven inflammation and fibrosis," *PLoS Pathogens*, vol. 5, no. 4, article e1000371, 2009.
- [19] T. A. Wynn, A. Chawla, and J. W. Pollard, "Macrophage biology in development, homeostasis and disease," *Nature*, vol. 496, no. 7446, pp. 445–455, 2013.
- [20] M. Tariq, J. Zhang, G. Liang, L. Ding, Q. He, and B. Yang, "Macrophage polarization: anti-cancer strategies to target tumor-associated macrophage in breast cancer," *Journal of Cellular Biochemistry*, vol. 118, no. 9, pp. 2484–2501, 2017.
- [21] Z. Hmama, S. Peña-Díaz, S. Joseph, and Y. Av-Gay, "Immuno-oesivation and immunosuppression of the macrophage by Mycobacterium tuberculosis," *Immunological Reviews*, vol. 264, no. 1, pp. 220–232, 2015.
- [22] A. Haschemi, P. Kosma, L. Gille et al., "The sedoheptulose kinase CARKL directs macrophage polarization through control of glucose metabolism," *Cell Metabolism*, vol. 15, no. 6, pp. 813–826, 2012.
- [23] D. Namgaladze and B. Brüne, "Fatty acid oxidation is dispensable for human macrophage IL-4-induced polarization," *Biochimica et Biophysica Acta*, vol. 1841, no. 9, pp. 1329–1335, 2014.
- [24] V. Cruzat, M. Macedo Rogero, K. Noel Keane, R. Curi, and P. Newsholme, "Glutamine: metabolism and immune function, supplementation and clinical translation," *Nutrients*, vol. 10, no. 11, p. 23, 2018.
- [25] Z. Tan, N. Xie, H. Cui et al., "Pyruvate dehydrogenase kinase 1 participates in macrophage polarization via regulating glucose metabolism," *The Journal of Immunology*, vol. 194, no. 12, pp. 6082–6089, 2015.
- [26] M. Nomura, J. Liu, I. I. Rovira et al., "Fatty acid oxidation in macrophage polarization," *Nature Immunology*, vol. 17, no. 3, pp. 216–217, 2016.
- [27] W. Ren, Y. Xia, S. Chen et al., "Glutamine metabolism in macrophages: a novel target for obesity/type 2 diabetes," *Advances in Nutrition*, vol. 10, no. 2, pp. 321–330, 2019.
- [28] R. P. Radzki, M. Bienko, and S. G. Pierzynowski, "Anti-osteopenic effect of alpha-ketoglutarate sodium salt in ovariectomized rats," *Journal of Bone and Mineral Metabolism*, vol. 30, no. 6, pp. 651–659, 2012.
- [29] Y. Hou, L. Wang, B. Ding et al., "Dietary α -ketoglutarate supplementation ameliorates intestinal injury in lipopolysaccharide-challenged piglets," *Amino Acids*, vol. 39, no. 2, pp. 555–564, 2010.
- [30] A. R. Mullen, Z. Hu, X. Shi et al., "Oxidation of alpha-ketoglutarate is required for reductive carboxylation in cancer cells with mitochondrial defects," *Cell Reports*, vol. 7, no. 5, pp. 1679–1690, 2014.
- [31] P. S. Liu, H. Wang, X. Li et al., " α -Ketoglutarate orchestrates macrophage activation through metabolic and epigenetic reprogramming," *Nature Immunology*, vol. 18, no. 9, pp. 985–994, 2017.
- [32] P. K. Datta, S. Deshmane, K. Khalili et al., "Glutamate metabolism in HIV-1 infected macrophages: role of HIV-1 Vpr," *Cell Cycle*, vol. 15, no. 17, pp. 2288–2298, 2016.
- [33] J. H. Park, H. J. Ku, J. H. Lee, and J.-W. Park, "Disruption of IDH2 attenuates lipopolysaccharide-induced inflammation and lung injury in an α -ketoglutarate-dependent manner," *Biochemical and Biophysical Research Communications*, vol. 503, no. 2, pp. 798–802, 2018.
- [34] G. Di Conza, C. H. Tsai, and P. C. Ho, "Fifty shades of α -ketoglutarate on cellular programming," *Molecular Cell*, vol. 76, no. 1, pp. 1–3, 2019.
- [35] S. T. He, D. Y. Lee, C. Y. Tung, C. Y. Li, and H. C. Wang, "Glutamine metabolism in both the oxidative and reductive directions is triggered in shrimp immune cells (hemocytes) at the WSSV genome replication stage to benefit virus replication," *Frontiers in Immunology*, vol. 10, p. 2102, 2019.
- [36] B. Wu, J. Liu, R. Zhao et al., "Glutaminase 1 regulates the release of extracellular vesicles during neuroinflammation through key metabolic intermediate alpha-ketoglutarate," *Journal of Neuroinflammation*, vol. 15, no. 1, p. 79, 2018.
- [37] L. Wang, D. Yi, Y. Hou et al., "Dietary supplementation with α -ketoglutarate activates mTOR signaling and enhances energy status in skeletal muscle of lipopolysaccharide-challenged piglets," *The Journal of Nutrition*, vol. 146, no. 8, pp. 1514–1520, 2016.
- [38] K. Yao, Y. Yin, X. Li et al., "Alpha-ketoglutarate inhibits glutamine degradation and enhances protein synthesis in intestinal porcine epithelial cells," *Amino Acids*, vol. 42, no. 6, pp. 2491–2500, 2012.
- [39] M. Liu, Y. Chen, S. Wang et al., " α -Ketoglutarate modulates macrophage polarization through regulation of PPAR γ

- transcription and MTORC1/P70S6K pathway to ameliorate ALL/ARDS,” *Shock*, vol. 53, no. 1, pp. 103–113, 2020.
- [40] M. X. Cheng, D. Cao, Y. Chen, J. Z. Li, B. Tu, and J. P. Gong, “ α -Ketoglutarate attenuates ischemia-reperfusion injury of liver graft in rats,” *Biomedicine & Pharmacotherapy*, vol. 111, pp. 1141–1146, 2019.
- [41] S. Yu, L. Ding, D. Liang, and L. Luo, “Porphyromonas gingivalis inhibits M2 activation of macrophages by suppressing α -ketoglutarate production in mice,” *Molecular Oral Microbiology*, vol. 33, no. 5, pp. 388–395, 2018.
- [42] B. Zhou, L. Magana, Z. Hong et al., “The angiocrine Rspodin3 instructs interstitial macrophage transition via metabolic-epigenetic reprogramming and resolves inflammatory injury,” *Nature Immunology*, vol. 21, no. 11, pp. 1430–1443, 2020.
- [43] A. Shapouri-Moghaddam, S. Mohammadian, H. Vazini et al., “Macrophage plasticity, polarization, and function in health and disease,” *Journal of Cellular Physiology*, vol. 233, no. 9, pp. 6425–6440, 2018.
- [44] Y.-K. Kim, S.-Y. Oh, S. G. Jeon et al., “Airway exposure levels of lipopolysaccharide determine type 1 versus type 2 experimental asthma,” *The Journal of Immunology*, vol. 178, no. 8, pp. 5375–5382, 2007.
- [45] T. A. Wynn and K. M. Vannella, “Macrophages in tissue repair, regeneration, and fibrosis,” *Immunity*, vol. 44, no. 3, pp. 450–462, 2016.
- [46] N. Nath and K. Kashfi, “Tumor associated macrophages and ‘NO’,” *Biochemical Pharmacology*, vol. 176, article 113899, 2020.
- [47] Q. Tian, J. Zhao, Q. Yang et al., “Dietary alpha-ketoglutarate promotes beige adipogenesis and prevents obesity in middle-aged mice,” *Aging Cell*, vol. 19, no. 1, article e13059, 2020.
- [48] H. S. Kang, J. H. Lee, K. J. Oh et al., “IDH1-dependent α -KG regulates brown fat differentiation and function by modulating histone methylation,” *Metabolism*, vol. 105, article 154173, 2020.
- [49] Z. Liu, L. Gan, T. Zhang, Q. Ren, and C. Sun, “Melatonin alleviates adipose inflammation through elevating α -ketoglutarate and diverting adipose-derived exosomes to macrophages in mice,” *Journal of Pineal Research*, vol. 64, no. 1, 2018.
- [50] M. F. Viola and G. Boeckxstaens, “Intestinal resident macrophages: multitaskers of the gut,” *Neurogastroenterology & Motility*, vol. 32, no. 8, article e13843, 2020.
- [51] S. De Schepper, S. Verheijden, J. Aguilera-Lizarraga et al., “Self-maintaining gut macrophages are essential for intestinal homeostasis,” *Cell*, vol. 175, no. 2, pp. 400–415.e13, 2018.
- [52] C. Jackaman, F. Tomay, L. Duong et al., “Aging and cancer: the role of macrophages and neutrophils,” *Ageing Research Reviews*, vol. 36, pp. 105–116, 2017.
- [53] M. Y. Hu, Y. Y. Lin, B. J. Zhang, D. L. Lu, Z. Q. Lu, and W. Cai, “Update of inflammasome activation in microglia/macrophage in aging and aging-related disease,” *CNS Neuroscience & Therapeutics*, vol. 25, no. 12, pp. 1299–1307, 2019.
- [54] A. A. Shahmirzadi, D. Edgar, C.-Y. Liao et al., “Alpha-ketoglutarate, an endogenous metabolite, extends lifespan and compresses morbidity in aging mice,” *Cell Metabolism*, vol. 32, no. 3, pp. 447–456.e6, 2020.
- [55] M. M. Bayliak and V. I. Lushchak, “Pleiotropic effects of alpha-ketoglutarate as a potential anti-ageing agent,” *Ageing Research Reviews*, vol. 66, article 101237, 2020.
- [56] T. W. Rhoads and R. M. Anderson, “Alpha-ketoglutarate, the metabolite that regulates aging in mice,” *Cell Metabolism*, vol. 32, no. 3, pp. 323–325, 2020.
- [57] Y. Wang, P. Deng, Y. Liu et al., “Alpha-ketoglutarate ameliorates age-related osteoporosis via regulating histone methylations,” *Nature Communications*, vol. 11, no. 1, article 5596, 2020.
- [58] Y. Su, T. Wang, N. Wu et al., “Alpha-ketoglutarate extends Drosophila lifespan by inhibiting mTOR and activating AMPK,” *Aging (Albany NY)*, vol. 11, no. 12, pp. 4183–4197, 2019.
- [59] R. M. Chin, X. Fu, M. Y. Pai et al., “The metabolite α -ketoglutarate extends lifespan by inhibiting ATP synthase and TOR,” *Nature*, vol. 510, no. 7505, pp. 397–401, 2014.

Review Article

Dihydromyricetin Acts as a Potential Redox Balance Mediator in Cancer Chemoprevention

Liang Chen,^{1,2} Meng Shi,² Chenghao Lv,^{1,2} Ying Song,^{1,2} Yuanjie Wu,³ Suifei Liu,⁴ Zhibing Zheng,² Xiangyang Lu ¹ and Si Qin ^{1,2}

¹College of Bioscience and Biotechnology, Hunan Agricultural University, Changsha 410128, China

²College of Food Science and Technology, Hunan Agricultural University, Changsha 410128, China

³Hunan Tea Group Co., Ltd., Changsha 410128, China

⁴Jiangxi Agricultural Engineering College, Yichun 331200, China

Correspondence should be addressed to Xiangyang Lu; xiangyangcn@163.com and Si Qin; qinsiman@hunau.edu.cn

Received 28 December 2020; Revised 11 February 2021; Accepted 27 February 2021; Published 12 March 2021

Academic Editor: Yaoyao Xia

Copyright © 2021 Liang Chen et al. This is an open access article distributed under the Creative Commons Attribution License, which permits unrestricted use, distribution, and reproduction in any medium, provided the original work is properly cited.

Dihydromyricetin (DHM) is a flavonoid extracted from the leaves and stems of the edible plant *Ampelopsis grossedentata* that has been used for Chinese Traditional Medicine. It has attracted considerable attention from consumers due to its beneficial properties including anticancer, antioxidative, and anti-inflammatory activities. Continuous oxidative stress caused by intracellular redox imbalance can lead to chronic inflammation, which is intimately associated with the initiation, promotion, and progression of cancer. DHM is considered a potential redox regulator for chronic disease prevention, and its biological activities are abundantly evaluated by using diverse cell and animal models. However, clinical investigations are still scanty. This review summarizes the current potential chemopreventive effects of DHM, including its properties such as anticancer, antioxidative, and anti-inflammatory activities, and further discusses the underlying molecular mechanisms of DHM in cancer chemoprevention by targeting redox balance and influencing the gut microbiota.

1. Introduction

Ampelopsis grossedentata (*A. grossedentata*) is a medicinal and edible plant widely used in China as a Traditional Chinese Medicine for the treatment of cough, fever, vomiting, hepatitis, colds, chronic nephritis, polyorexia, and sore throat. Tender stems and leaves of *A. grossedentata* are commonly consumed as vine tea in China for centuries due to its health benefiting effects. Dihydromyricetin (3,5,7,3',4',5'-hexahydroxy-2,3-dihydroflavonol (DHM)) (Figure 1), also known as ampelopsin, is a major flavonoid extracted from the leaves and stems of *A. grossedentata*. The content of DHM in *A. grossedentata* ranges from 30% to 40% (dry weight), which is considered to have the highest flavonoid content in natural plants [1]. Several scientific investigations reported that DHM possesses various biological activities

such as anti-inflammatory [2, 3], antioxidative [4, 5], anti-cancer [6, 7], antidiabetic [8–10], antiatherosclerosis [11, 12], and cardioprotective effects [13, 14]. The biological properties and the underlying mechanisms of DHM were investigated mostly by *in vitro* cell cultures and *in vivo* animal models. In addition, DHM was reported as toxicologically safe and could effectively reverse multidrug resistance [15–19]. Hence, DHM is a promising bioactive compound for developing healthy/functional foods.

Despite these health-promoting effects, DHM has very poor water-solubility and aqueous stability. The solubility characteristics of DHM in cold water, hot water, and ethanol were 0.2–0.32 mg/mL at 25°C, 20 mg/mL at 80°C, and 170 mg/mL at 25°C, respectively [20]. DHM is more stable in acidic conditions (pH range of 1.0–5.0) than in an alkaline environment. Under alkaline conditions, especially at a pH

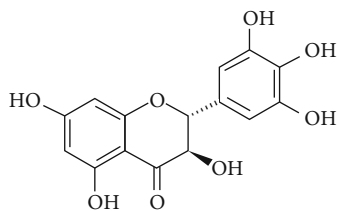


FIGURE 1: Chemical structure of dihydromyricetin (DHM).

range from 6.0 to 8.0, DHM was prone to oxidation and degraded dramatically [21]. Similarly, the stability of DHM is affected by the pH rather than the digestive enzymes including pepsin and pancreatin under the *in vitro* digestion system [21]. At a concentration of 20 $\mu\text{g}/\text{mL}$, DHM was stable at room temperature after 12 h and at -20°C for 10 d, but only 45.42% was retained after 3 h in simulated intestinal fluid at 37°C [21]. The plasma DHM concentration reached maximum (159 $\mu\text{g}/\text{L}$) at 1.5 h postadministration when DHM powder was given at a dosage of 115 mg/kg body weight in rabbits, indicating a low bioavailability of DHM [18]. Efflux transporters, multidrug resistance protein 2, and breast cancer resistance protein also played an important role in DHM uptake and transport processes [22]. A research group had investigated the distribution, excretion, and metabolic profile of DHM and found that most unconverted DHM forms were excreted in feces [23]. Eight metabolites of DHM in urine and feces were found to be linked with reduction, methylation, dehydroxylation, glucuronidation, and sulfation metabolic pathways [23]. These problems together resulted in its low membrane permeability ($P_{\text{eff}} = (1.84 \pm 0.37) \times 10^{-6} \text{ cm/s}$) and compromised bioavailability [18]. However, the amount of DHM from the daily intake of *Ampelopsis grossedentata* that can possibly exert its bioactivity had been investigated in clinical trials. For instance, the administration of DHM at 970 mg/day was reported to effectively ameliorate the glycemic control in type 2 diabetes mellitus in a previous study [18]. In a double-blind clinical trial, daily uptake of 600 mg of DHM exerted anti-inflammatory effects on patients with nonalcoholic fatty liver disease [18].

Through identification and quantification methods, the transport mechanisms and protective effects of DHM in metabolic diseases have recently been reviewed [18, 24]; however, the anti-inflammatory, antioxidative, and anticancer effects and their underlying molecular mechanisms have not been fully documented. This study is aimed at giving an overview of the anti-inflammatory, antioxidative, and anticancer effects of DHM, as well as recent findings regarding its underlying molecular mechanisms including redox balance and the role of gut microbiota.

2. Dihydromyricetin Exerts Its Chemopreventive Potential against Cancer

Cancer is a public health problem and the leading cause of morbidity and mortality worldwide. The redox imbalance

involving persistent chronic inflammation and reduced antioxidant capacity are the critical pathological causes of cancer. Presently, chemoprevention is a major approach to prevent the growth of cancer cells. However, high cost and side effects associated with chemotherapy have prompted scientists to search for safe alternative natural compounds for cancer therapy [25]. Flavonoids are plant phytochemicals, and several epidemiological studies have reported that flavonoid intake may prevent a variety of cancers such as lung, breast, prostate, pancreas, and colon cancers [26].

DHM, a flavonoid from the edible plant *Ampelopsis grossedentata*, exhibited anticancer activity against a variety of cancer cells in various cultured cancer cells and animal models transplanted with cancer cells, as shown in Table 1. The most widely used cell lines for the determination of anticancer effects of DHM were HepG2 and SK-Hep-1 (human hepatocellular carcinoma), MCF-7 and MDA-MB-231 (human breast cancer), PC-3 (human prostate cancer), A549 and H1975 (human non-small-cell lung cancer), U251 and A172 (human glioma), SKOV3 (human ovarian cancer), SGC7901 and SGC7901/5-FU (human gastric carcinoma), and JAR (human choriocarcinoma) [27–39]. Different cancer cell lines were used by various researchers as each cell line has a different origin, tumor characteristics, and signaling pathways. In addition, animals such as mice and rats with transplanted cancer cells have also been used as *in vivo* models for investigation of antitumor activity of DHM [31, 37, 40, 41].

DHM effectively showed anticancer activity in a variety of cancers such as breast cancer, hepatocellular carcinoma, melanoma, ovarian cancer, lung cancer, cervical carcinoma, glioma, and osteosarcoma [32, 33, 42–46]. Among the treatments for different cancer cells, DHM has a broad dosage from 1 to 1000 μM with a duration from 6 to 72 h, presenting cell proliferation inhibition and apoptosis-inducing effects (Table 1). The concentration of DHM used in various studies shifts dramatically, which might be due to the differences in cell lines, DHM purity, and cell treatment conditions. The functional mechanisms and major pathways are also listed in Table 1. DHM inhibited the proliferation of HepG2 cells via G2/M phase cell cycle arrest through the Chk1/Chk2/Cdc25C signaling pathway; induced the apoptosis of HepG2 cells that target ROS-related, Akt/Bad, ERK1/2, AMPK, and PI3K/PDK1/Akt signaling pathways; enhanced the levels of DR4, DR5, Bax, Bad, and caspase 3; and reduced the expression of Bcl-2 protein and mTOR [30, 32, 47, 48]. The suppressing effect of DHM on the MDA-MB-231 breast cancer cell line was reported through ROS generation, ER stress pathway, and inhibition of mTOR [28, 31]. DHM treatment dose-dependently inhibited the growth of HeLa cells by inducing apoptosis through activation of caspases 9 and 3 and increasing the ratio of Bax protein to Bcl-2 [44]. In A549 human adenocarcinoma lung epithelial cells, DHM decreased XIAP and survivin expression levels and cleaved poly(ADP-ribose) polymerase. DHM stimulated apoptosis via a p53-mediated pathway in ovarian cancer cells A2780 and SKOV3 [46]. DHM was also reported to inhibit human melanoma SK-MEL-28 cells by inducing apoptosis; arresting cell cycle at the G1/S phases; increasing the production of p53

TABLE 1: The chemopreventive effect and potential mechanism of dihydromyricetin in cancer.

Origin	Cell lines/animals/human	Treatment methods	Mode of administration	Dose and duration time	Mechanism of action/activities/effects showed	Reference
DHM prepared from <i>A. grossedentata</i> with a purity of 98%	Osteosarcoma cells	Cell cycle and apoptosis analysis		15, 30, and 60 μM for 24 or 48 h	(1) Exhibited anticancer activity through increased p21 expression and G2-M cell cycle arrest, caused DNA damage, activated ATM-CHK2-H2AX signaling pathways, and induced apoptosis in osteosarcoma cells (2) Antitumor could be due to the activation of AMPK and p38MAPK pathways	Zhiqiang et al. (2014)
Ampelopsin $\geq 98\%$	Non-small-cell lung cancer (NSCLC) cells	Cell death analysis		20 μM for 48-72 h	DHM in combination with erlotinib induced cell death via the NOX2-ROS-Bim pathway in NSCLC cells	Seung-Woo et al. (2017)
Ampelopsins A and C isolated from the roots of <i>V. thunbergii</i> with a purity of 98.5 and 99.0%, respectively	MDA-MB-231 breast cancer cells	Metastasis analysis		Ampelopsin A (10–50 μM) and Ampelopsin C (1–5 μM) for 24–72 h	Inhibited metastasis of MDA-MB-231 cells by downregulating the AxL, TYRO3, and FYN expressions	Cheng et al. (2019)
Ampelopsin $\geq 98\%$	MCF-7 and MDA-MB-231 breast cancer cells	Cell viability and increased apoptosis analysis		60 μM for 24 h	DHM inhibited cell viability and increased apoptosis in MCF-7 and MDA-MB-231 breast cancer cells through ROS generation and ER stress pathway	Yong et al. (2014)
Ampelopsin (purity not provided)	HepG2 cells	Apoptosis analysis		0, 12.5, 25, 50, 100, 150, and 200 $\mu\text{g}/\text{mL}$ for 12, 24, and 36 h	(1) Induced apoptosis of HepG2 cells (2) Enhanced the levels of death receptor 4 (DR4) and death receptor 5 (DR5) and reduced the expression of Bcl-2 protein	Shimei et al. (2015)
Ampelopsin $\geq 98\%$	A549 human adenocarcinoma lung epithelial cells	Apoptosis analysis		0, 10, 20, or 30 μM for 48 h	(1) Induced apoptosis in A549 cells (2) Reduced Bcl 2 and increased Bax levels (3) Cleaved PARP and reduced XIAP and survivin expression levels (4) Cleaved poly(ADP-ribose) polymerase expression	Xin-mei et al. (2015)
DHM $\geq 98\%$	Mouse hepatocellular carcinoma cells (Hepal-6)	Cell viability and apoptosis analysis		10, 50, or 100 μM for 6 h, 12 h, and 24 h	DHM inhibited cell viability and induced apoptosis by downregulating ROS production via the TGF β /Smad3 signaling pathway in Hepal 6 cells	Bin et al. (2015)
AMP extracted from <i>A. megalophylla</i> (purity not provided)	HeLa cells	Apoptosis analysis		0, 30, 40, 50, 60, or 70 μM for 8 h or 12 h	Induced apoptosis in HeLa cells through activation of caspases 9 and 3	Peipei et al. (2017)

TABLE 1: Continued.

Origin	Cell lines/animals/human	Treatment methods	Mode of administration	Dose and duration time	Mechanism of action/activities/effects showed	Reference
DHM \geq 98%	Hepatoma cell lines SK-Hep-1 and MHCC97L	Growth inhibition assays		0, 10, 50, and 100 μ mol/L for 24 h	DHM inhibited the migration and invasion of hepatoma cells via reducing the phosphorylation levels of p38, ERK1/2, and JNK (1) Inhibition of the Akt/Bad signaling pathway (2) Upregulated the levels of mitochondrial proapoptotic proteins Bax and Bad	Qing-Yu et al. (2014)
DHM with a purity of 95%	HepG2 cells	Apoptosis analysis		0, 10, 20, and 30 μ M for 24 h	(3) Inhibited the expression of the antiapoptotic protein Bcl-2 and enhanced the cleavage and activation of caspase 3 (4) Degradation of poly(ADP-ribose) polymerase (1) DHM inhibited cell proliferation (SK-MEL-28) cells through cell cycle arrest at the G1/S phase (2) Increased the production of p53 and p21 and downregulated the Cdc25A, Cdc2, and P-Cdc2 proteins	Zhuangwei et al. (2017)
DHM \geq 98%	Human melanoma SK-MEL-28 cells	Cell cycle and apoptosis analysis		0, 50, and 100 μ M for 24, 48, or 72 h	(3) Induced apoptosis through enhancing the expression levels of Bax proteins and decreasing the protein levels of IKK- α , NF- κ B (p65), and P-p38 DHM inhibited AGS cell proliferation and induced cell cytotoxicity through the regulation of expression of apoptotic genes such as p53 and B-cell lymphoma-2	Guofang et al. (2014)
DHM \geq 98%	AGS human gastric cancer cells	Cytotoxicity assays		25, 50, and 100 μ M for 48 or 72 h	DHM-induced autophagy inhibited cell proliferation through suppressing the activation of mTOR and regulating upstream signaling pathways such as ERK1/2, AMPK, and PI3K/PDK1/Akt pathways	Ji et al. (2015)
DHM \geq 98%	HepG2 cells	Cell growth inhibition assays		5, 10, 25, and 50 μ M for 6, 12, 24, and 48 h	Inhibited proliferation of JAr cells by inducing apoptosis through increasing protein expression level of BCL-2 associated X, and associated protein, and decreased the levels of BCL-2 and procaspase 3	Juan et al. (2014)
DHM > 9%	Human choriocarcinoma cell line (JAr cells)	Apoptosis assays		0, 40, 60, and 100 mg/L for 48 h		Yanzhen et al. (2018)

TABLE 1: Continued.

Origin	Cell lines/animals/human	Treatment methods	Mode of administration	Dose and duration time	Mechanism of action/activities/effects showed	Reference
DHM (purity not provided)	Human ovarian cancer A2780 and SKOV3 cells	Apoptosis assays		25, 50, and 100 μ M for 24 or 48 h	DHM inhibited the ovarian cancer cells and induced cell apoptosis through p53-mediated downregulation of survivin	Yingqi et al. (2017)
DHM \geq 98%	HepG2, QGY7701, QGY7703, Huh 7, QSG7701, MHCC97L and H, and SK-Hep-1 cells	Cell proliferation and apoptosis assays		0, 50, and 100 μ M for 24, or 48 h	(1) DHM inhibited cell proliferation and induced cell apoptosis in hepatocellular carcinoma cells (2) Apoptosis was induced through upregulating p53 expression, and the upregulation of p53 increased the levels of cleaved-caspase 3 protein	Jie et al. (2014)
DHM \geq 98%	SK-MEL-28 human melanoma cells	Apoptosis		25, 50, and, 100 μ M for 24 h	Enhanced cell death and apoptosis by regulating the NF- κ B signaling pathway	Ding-Zhou et al. (2017)
DHM \geq 98%	Hepatocellular carcinoma cells	Apoptosis		25-200 μ M for 12 or 24 h	DHM with Nedaplatin (NDP) inhibited growth and induced apoptosis through the activation of the p53/Bcl-2 signaling pathways	Lianggui et al. (2015)
DHM \geq 98%	A549 lung carcinoma cells and fibroblasts	Growth inhibition assays		0, 1, 5, and 10 μ M for 48 h	DHM inhibited the growth of fibroblasts in the lung cancer cells via the activation of Erk1/2 and Akt signaling pathways	Kai-jie et al. (2017)
DHM \geq 98%	Hepatocellular cancer cells (HepG2 and Hep3B)	Growth inhibition and cell cycle assays		2, 10, 50, 100, and 200 μ M for 48 h	Inhibited proliferation of the cells via G2/M phase cell cycle arrest through the Chk1/Chk2/Cdc25C signaling pathway	Haili et al. (2013)
DHM > 99%	Human choriocarcinoma JAR cells	Growth inhibition and cell cycle assays		0, 40, 60, and 100 mg/L for 48 h	DHM inhibited the proliferation of JAR cells through cell cycle arrest via the downregulation of cyclin A1, cyclin D1, SMAD3, and SMAD4 expression levels	Yanzhen et al. (2020)
DHM > 98%	Human ovarian cancer SKOV3 cells	Cell migration, invasion, and apoptosis assays		80 and 120 μ M for 48 h	(1) Exhibited anticancer activity by reducing cell migration and invasion (2) Induced cell apoptosis via upregulation of cleaved-caspase 3 and the Bax/Bcl-2 ratio (3) Inhibited GRASP65 expression and the regulation of the JNK/ERK pathway	Fengjie et al. (2019)
DHM 98%	Human non-small-cell lung cancer	Cytotoxic and apoptosis assays		0, 50, 75, and 100 μ M for 24 h	Exhibited cytotoxic effect by inducing apoptosis through Bcl-w suppression-	Shang-Jyh et al. (2017)

TABLE 1: Continued.

Origin	Cell lines/animals/human	Treatment methods	Mode of administration	Dose and duration time	Mechanism of action/activities/effects showed	Reference
	(A549 and H1975) cell lines				mediated mitochondrial membrane depolarization, caspase 9/7/3 activation, and poly(ADP-ribose) polymerase (PARP) cleavage in A549 and H1975 cells	
DHM (purity not provided)	Human gastric carcinoma cells (SGC7901 and SGC7901/5-FU)	Proliferation inhibition assays		1.25 and 2.5 $\mu\text{g}/\text{mL}$ for 48 h	Inhibited proliferation of both SGC7901 and SGC7901/5-FU cells through the downregulation of the MDRI expression	Mingcai et al. (2020)
DHM \geq 98%	Human hepatocarcinoma (HepG2) cells	Apoptosis assays		10, 50, and 100 μM for 24 h	DHM-induced apoptosis of human hepatocellular carcinoma cells through a ROS-related pathway	Bin et al. (2014)
Ampelopsin (purity not provided)	Breast cancer MDA-MB-231 cells and rats	MNU-induced breast cancer in rats	Orally fed	10, 25, 50 μM for 48 h and 50 and 100 mg/kg BW for 18 weeks	Inhibited the cancer cells effectively in vitro and in vivo through effectively suppressing mammalian target of rapamycin (mTOR) activity in breast cancer	Chang et al. (2014)
Ampelopsis isolated from <i>A. grossedentata</i> with 80%	PC-3 human prostate cancer cells and mice prostate cancer model	Cell migration, invasion, growth inhibition, and apoptosis assays	Oral gavage	0, 25, and 50 μM for 48 h. 150 and 300 mg/kg BW for 8 weeks	(1) Inhibited the migration and invasion of PC-3 cells in vitro (2) Decreased the growth of PC-3 tumors and lymph node and lung metastases in a dose-dependent manner in mice (3) Exhibited anticancer activity via induction of apoptosis, reduction of prostate tumor angiogenesis, and reduction of CXCR4 expression	Feng et al. (2012)
Ampelopsin-sodium (purity not provided)	BALB/c mice	Mice implanted with human bladder carcinoma EJ cells and murine sarcoma 180 cells	IP/IV/II administration	160, 200, and 260 mg/kg BW for 2-3 weeks	DHM considerably inhibited the proliferation of EJ and sarcoma 180 cells both in vivo and in vitro	Baolai et al. (2012)
Ampelopsin \geq 98%	Human glioma cell lines U251 and A172, and male BALB/c-nu mice xenograft model	Apoptosis and tumor growth inhibition	Intraperitoneal administration	25, 50, 100 μM for 24 h and 50 and 100 mg/kg BW for 30 days	(1) Induced apoptosis by arresting at G1 and S phases and autophagy through potentiating ROS generation and JNK activation in human glioma cells (2) DHM activated caspase 8, caspase 9, and caspase 3 contributing to PARP cleavage	Zhigang et al. (2019)

TABLE 1: Continued.

Origin	Cell lines/animals/human	Treatment methods	Mode of administration	Dose and duration time	Mechanism of action/activities/effects showed	Reference
DHM 98%	Colo-205 cells and xenograft tumor transplant mice	Cell growth inhibition assays	Intragastric administration	25, 50, and 100 mg/kg BW for 21 days	(3) Reduced tumor growth of human glioma xenograft in mice Inhibited the proliferation and growth of Colo-205 colon cancer cells considerably <i>in vivo</i> and <i>in vitro</i> via suppression of the expression and secretion of Sema4D	Jun et al. (2019)

and p21 proteins; enhancing the expression levels of Bax proteins; and decreasing the protein levels of IKK- α , NF- κ B (p65), and P-p38 [49]. In addition, DHM suppressed the glioma cell growth through enhancing apoptosis; arresting the cell cycle at the G1 and S phases; and activating caspase 8, caspase 9, and caspase 3 [37]. DHM exhibited anticancer activity in osteosarcoma cells through G2-M cell cycle arrest, DNA damage prevention, stimulation of the ATM-CHK2-H2AX signaling pathways, and enhancing p21 expression [50]. Zuo et al. reported that DHM suppressed the growth of human choriocarcinoma JAR cells by inducing cell cycle arrest and reducing the expression levels of cyclin A1, cyclin D1, SMAD3, and SMAD4. DHM function on other cancer cells is likely to share similar pathways. However, few studies have investigated the cytotoxic effects of DHM on normal cells. The anticancer effects should selectively inhibit the growth of the cancerous cells without damaging the normal cells. The lack of cytotoxic data on normal cells could potentially limit the use of DHM as an anticancer agent.

Several studies evaluated the anticancer effects of DHM in combination with anticancer drugs in order to overcome the drug resistance of cancerous cells. DHM in combination with nedaplatin (anticancer drug) showed a synergistic effect on the inhibition of the growth of hepatocellular carcinoma cells SMMC7721 and QGY7701, and induced apoptosis through the activation of the p53/Bcl-2 signaling pathways [51]. Also, DHM in combination with erlotinib significantly induced the caspase-dependent cell death in NSCLC due to a synergistic effect [43]. More importantly, interactions between DHM and other drugs and their toxicological properties need to be substantially evaluated before use as anticancer drugs since DHM has the potential to show synergy effects with drugs.

Apart from cultured cancer cell lines, many researchers determined the antitumor potential of DHM in various animal models bearing transplanted cancer cells. PC-3 tumor growth was significantly reduced by 49.2% through the administration of DHM at 300 mg/kg BW in mice [27]. It was found that tumor size was significantly reduced in mice treated with DHM compared to the controls in athymic mice xenografted with MDA-MB-231 cells [31], in a nude mice xenograft model bearing the human osteosarcoma cell line U2OS/MTX, in a mice xenograft model bearing the human

osteosarcoma cell line U2OS/MTX [50], and in xenograft BALB/c-nu mice transplanted with the human glioma cell line U251. Though there are some reports on the antitumor effects of DHM, there are some limitations that could hinder the advancement of DHM as an anticancer agent for human use. On the one hand, the molecular mechanism and major pathways still remain unclear. It is important to reveal the mechanism with consistency among cell models, animal models, and clinical studies. Therefore, more research is needed in animals and humans to generate reliable and consistent scientific evidence regarding the anticancer effects of DHM.

3. Antioxidant Capacity Is the Main Reason for the Anticancer Property of DHM

Aerobic cellular respiration generates free radicals and reactive oxygen species (ROS). The in-built antioxidant defense system protects the body from the harmful effects of free radicals. The imbalance between free radicals and the antioxidant defense system results in oxidative stress. The free radicals and ROS contain unpaired electrons in the outer shell, resulting in their instability. These unstable free radicals are highly reactive; attract electrons from other molecules; and cause oxidative damage to proteins, lipids, carbohydrates, and nucleic acids [52]. The oxidative damage inflicted upon macromolecules results in oxidative stress, which has been found to be highly associated with cancer [53].

Plant-derived flavonoids have been shown to inhibit free radicals and oxidative stress [54]. Recently, there have been many studies reporting on the antioxidant capacity of DHM. The evaluation methods, antioxidant properties, and mechanisms of DHM are shown in Table 2. Several *in vitro*, cell culture, and *in vivo* (animals) models are commonly used for the determination of the antioxidant activity of DHM, of which the most commonly used are the *in vitro* methods including free radical scavenging methods such as DPPH, ABTS, oxygen radical absorption capacity (ORAC), H₂O₂ radical scavenging power, and Fe²⁺ chelating method and ferric reducing antioxidant power (FRAP) [5, 55–58]. Several studies documented the *in vitro* free radical scavenging activity of DHM. The IC₅₀ values measured by DPPH, ABTS,

TABLE 2: Antioxidant activities and mechanisms of the action of DHM.

Origin	In vitro/cell culture	Methods of antioxidant activities measure	Dose and duration time	Results	Reference
DHM \geq 99.5%	RAW264.7 cells	Lipopolysaccharide-(LPS-) induced oxidative stress	DHM treated at 0 to 50 $\mu\text{g}/\text{mL}$ for 2 hours	DHM reduced LPS-induced oxidative stress through inhibiting the production of reactive oxygen species (ROS) and enhanced the antioxidant system by activating superoxide dismutase (SOD) and the Nrf2/HO-1 pathway	Xuejun et al. (2018)
DHM \geq 98%	HepG2 cells	Reactive oxygen species (ROS)	DHM at 10, 50, or 100 μM for 6 h, 12 h, and 24 h	DHM reduced ROS accumulation in a concentration-dependent manner in HepG2 cells	Bin et al. (2014)
Ampelopsin purity 95%	In vitro assays	DPPH, ABTS, H_2O_2 , and O_2 radical methods	37°C for 15, 20, and 60 minutes	DHM inhibited free radicals. EC_{50} values of DHM for scavenging DPPH, ABTS, H_2O_2 , and O_2 radicals were 8.18, 5.32, 7.95, and 7.79 ($\mu\text{g}/\text{mL}$), respectively	Xiang et al. (2017)
Ampelopsin 98%	PC12 cells	Reactive oxygen species	Ampelopsin at 50 and 100 μM for 1 h	DHM inhibited reactive oxygen species in 6-OHDA stimulated PC12 cells in concentration-dependent manner	Xianjuan et al. (2015)
Ampelopsin \geq 98%	Glomerular mesangial cells (MCs)	ROS and ROS enzymes	DHM at 0, 10, 20, and 40 μM for 24 h	DHM inhibited the intracellular ROS production and expression levels of ROS-producing enzymes NADPH oxidase 2 (NOX2) and NOX4 and mediated the antioxidative effects through the activation of Nrf2/HO-1 pathway	Chunping et al. (2020)
Ampelopsin > 98%	In vitro assays	Hydroxyl and superoxide radical methods	Ampelopsin 10 to 100 μM for 60 min and 25°C for 20 min	Ampelopsin eliminated $\cdot\text{OH}$ and $\text{O}_2^{\cdot-}$ in a concentration-dependent manner; the EC_{50} values were $29.4 \pm 4.1 \mu\text{M}$ and $88.9 \pm 9.4 \mu\text{M}$	Jiantao et al. (2008)
Ampelopsin > 98%	PC12 cells	Reactive oxygen species	Ampelopsin at 1, 5, and 15 mg/mL for 1 h	Inhibited the formation of reactive oxygen species (ROS) and enhanced the cellular antioxidant defense through activation of the ERK and Akt signaling pathways in PC12 cells	Xianjuan et al. (2011)
DHM 64.7%	In vitro assay	DPPH	DHM at 2, 4, 6, 8, 10, and 12 ppm for 30 min	DHM extract inhibited DPPH radicals with IC_{50} value of 3.9 ppm	Liyun et al. (2015)
DHM \geq 98%	In vitro assays	DPPH and ORAC	DHM at 12.5, 25, 50, 100, 200, and 400 $\mu\text{g}/\text{mL}$ for 30 min	DHM dose-dependently inhibited the DPPH and ORAC radicals	Kun et al. (2019)
DHM \geq 98%	HepG2 cells	Nrf2/Keap1 pathway	40 μM for 3-12 h	Exhibited antioxidant activity by activating the cellular Nrf2/Keap1 pathway	Kun et al. (2019)
Not provided	(HEI-OC) 1 auditory cells	ROS	DHM at 10, 100, and 1000 μM for 24 h	DHM inhibited ROS accumulation in HEI-OC cells	Hezhou et al. (2020)
DHM > 98%	B16F10 mouse melanoma cells	Reactive oxygen species	1, 25, and 50 μM for 24 h	DHM reduced intracellular reactive oxygen species and reactive species (RS) levels	Huey-Chun et al. (2016)
DHM > 98%	Rat cardiac fibroblasts	Ang II-induced oxidative stress	0–320 μM for 4 h or 80 μM for 0–24 h	DHM inhibited cellular reactive oxygen species production and MDA level, and enhanced the SOD activity and total antioxidant capacity (T-AOC)	Qiuyi et al. (2017)
DHM \geq 98%	In vitro assays	DPPH and ABTS	100 mg/mL for 6 min or 30 min	Cookies fortified with DHM significantly enhanced the DPPH and ABTS radical scavenging activities	Jing et al. (2018)
DHM 97%	PC12 cells				

TABLE 2: Continued.

Origin	In vitro/cell culture	Methods of antioxidant activities measure	Dose and duration time	Results	Reference
		Methylglyoxal-(MG-) induced oxidative stress in PC12 cells	20 and 10 mol/L for 24 h	Inhibited the intracellular ROS and modulating AMPK/GLUT4 signaling pathway in PC12 cells	Baoping et al. (2014)
DHM 95%	In vitro assay	DPPH	0 to 50 $\mu\text{g}/\text{mL}$ for 30 min	DHM and lecithin complex inhibited DPPH radicals with IC_{50} value of 22.60 $\mu\text{g}/\text{mL}$	Benguo et al. (2009)
DHM > 98%	Rat cardiomyocytes	Ang II-stimulated reactive oxygen species in cardiomyocytes	20, 40, 80, and 160 μM for 8 h, 12 h, 24 h, or 48 h	DHM reduced ROS generation in Ang II-stimulated cardiomyocytes by increasing total antioxidative capacity through upregulating expression of SOD and thioredoxin	Guoliang et al. (2015)
DHM (purity not provided)	HUVECs	Sodium nitroprusside- (SNP-) induced oxidative damage	300 $\mu\text{mol}/\text{L}$ for 2 hours	DHM reduced ROS overproduction, decreased MDA level and increased SOD activity and showed antioxidant activity in HUVECs by activating the PI3K/Akt/FoxO3a signaling pathway	Xiaoying et al. (2019)
DHM 99%	Human umbilical vein endothelial cells (HUVECs)	H_2O_2 -induced oxidative stress	37.5-300 μM for 2 h	DHM inhibited intracellular ROS overproduction in HUVECs cells	Xiaolong et al. (2015)
Ampelopsin \geq 95%	PK-15 cells	H_2O_2 -induced oxidative stress in PK-15	0, 15, 30, and 60 $\mu\text{g}/\text{mL}$ for 1 h	Significantly decreased MDA production in H_2O_2 -induced PK-15 cells	Tan et al. (2010)
DHM 98%	Colo-205 cells	Reactive oxygen species and MDA	8, 16, and 32 μM for 2 h	Inhibited reactive oxygen species and malondialdehyde levels	Jun et al. (2019)
Ampelopsin 98%	In vitro assay	DPPH method	0.1 to 0.4 $\mu\text{g}/\text{mL}$ for 60 min	DHM inhibited DPPH radicals with IC_{50} value of 0.235 $\mu\text{g}/\text{mL}$	Wenzhen et al. (2014)
DHM 98%	In vitro assays	DPPH, ABTS, O_2 radical, and Fe^{2+} chelating method	2 to 20 $\mu\text{g}/\text{mL}$ for 30 min	Eliminated ABTS, DPPH free radicals, reduced Cu^{2+} , and chelated Fe^{2+}	Xican et al. (2016)
DHM \geq 98%	C57BL/6J mice	Streptozotocin-induced oxidative stress model	DHM at 100 mg/kg/day for 14 weeks	DHM decreased MDA and increased the SOD and GSH-Px	Bin et al. (2017a)
DHM (purity not provided)	Male C57BL/6 mice	Transverse aortic constriction induced oxidative stress in mice	DHM (250 mg/kg/day) for 2 weeks	DHM administration reduced reactive oxygen species and malondialdehyde level, and increased total antioxidant capacity and SOD activity in mice	Yun et al. (2018)
DHM > 98.0%	Chickens	LPS-induced oxidative stress in chickens	0.025%, 0.05%, and 0.1% for 14 days	DHM increased SOD and GSH-Px activity and GSH in chicken plasma and ileum	Yicong et al. (2020)
DHM (purity not provided)	ICR mice	Sleep deprivation induced oxidative stress	100, 50, and 25 mg/kg/day for 14 days	DHM increased SOD activity and reduced MDA level	Hongxiang et al. (2019)
DHM (purity not provided)	Rat	DPPH radical scavenging activity of rat serum	100 mg/kg/BW	DHM increased the antioxidative capacity of rat serum against DPPH radicals	Xiao et al. (2014)
Ampelopsin 95%	Piglets	LPS-induced oxidative stress in piglets	2.5, 5, and 10 $\mu\text{g}/\text{mL}$ for 30 min	Decreased the MDA and protein carbonyl levels in LPS-treated piglets	Xiang et al. (2014)

H_2O_2 , and O_2 radicals were 3.24-22.6, 3.1-5.32, 7.95, and 7.79 $\mu\text{g}/\text{mL}$, respectively (Table 2) [5, 17, 59, 60].

DHM has been shown to protect oxidative stress in various cell culture models with a concentration below 1000 μM ,

as shown in Table 2. Cell lines such as human hepatoma cells (HepG2), human umbilical vein endothelial cells (HUVECs), human colon cancer (Colo-205) cells, porcine kidney epithelial cells (PK-15), PC12 cells, murine macrophage

(RAW264.7) cells, glomerular mesangial cells (MCs), and HEI-OC1 auditory cells have been successfully used to determine the protective effects of DHM in oxidative stress, and oxidative stress is generally created in cell lines by using H_2O_2 free radicals, LPS, methylglyoxal, and sodium nitroprusside [4, 41, 47, 55, 61–67].

Oxidative stress-induced mice, rat, chicken, and piglet models have also been used by many researchers to investigate the protective role of DHM in oxidative stress. The dose used in animal studies was 25 to 250 mg/kg BW, and the duration was between 2 and 3 months. In animal studies, superoxide dismutase (SOD), glutathione peroxidase (GSH-Px), glutathione (GSH), and malondialdehyde (MDA) are commonly measured oxidative stress parameters to estimate the antioxidant capacity of DHM [13, 68–70]. The major antioxidant effects of DHM through the Nrf2/HO-1 pathway, the Nrf2/Keap1 pathway, and the ERK and Akt pathways [5, 62, 66, 71], with an increase of DHM, significantly decreased the ROS levels in human umbilical vein endothelial cells (HUVECs) [71]. DHM exhibited an antioxidative power by activating superoxide dismutase (SOD) and the Nrf2/HO-1 signaling pathway or the Nrf2/Keap1 pathway [5, 64]. Recently, Dong et al. found that DHM exhibited antioxidative effects through the inhibition of intracellular ROS production and expression levels of ROS producing the enzymes NADPH oxidase 2 (NOX2) and NOX4, the suppression of MDA levels, the enhancement of SOD, and the activation of the Nrf2/HO-1 signaling pathway [66]. In another study, Zhang et al. determined the protective effects of DHM on HUVECs against sodium nitroprusside- (SNP-) induced oxidative damage and reported that DHM reduced ROS production and MDA levels, and increased SOD activity by activating the PI3K/Akt/FoxO3a signaling pathways in HUVECs [65]. DHM was also reported to inhibit the oxidative stress in HEI-OC1 auditory cells through the suppression of ROS accumulation [67]. DHM inhibited the activity of phase I enzymes, including cytochrome P450 (CYP), and phase II enzymes, including sulfotransferases (SULTs) and N/O-acetyltransferases (NAT1 and NAT2) [72, 73]. Oxidative stress has been involved in several neurodegenerative diseases such as Parkinson's disease, Alzheimer's disease (AD), and Huntington's disease [62]. Several researchers investigated the neuroprotective effect of DHM in oxidative stress-induced PC12 neuronal-like cells. They also investigated the neuroprotective role of DHM in neuronal-like PC12 cells against H_2O_2 -induced oxidative stress and reported that DHM treatment at 1, 5, and 15 mg/mL for 1 h inhibited the formation of ROS and increased the cellular antioxidant defense through activation of the ERK and Akt signaling pathways in PC12 cells [62]. Jiang et al. found that DHM reduced the oxidative stress in PC12 cells by inhibiting the intracellular ROS production and by modulating the AMPK/GLUT4 signaling pathways [63].

The oxidative stress protection capacity of DHM was also evaluated in several animal models. DHM showed the highest radical scavenging activity (42.26%) of serum at 4 h after DHM administration in rats [57]. Li et al. induced oxidative stress in the brains of ICR mice by sleep deprivation and found that DHM administration significantly reduced oxida-

tive stress by increasing SOD activity and reducing the MDA level in the hippocampus of sleep-deprived mice [69]. Similarly, for streptozotocin-induced or transverse aortic constriction surgery-induced oxidative stress in mice as well as high-fat diet-induced oxidative stress in rats, DHM decreased MDA and increased SOD, GSH, and GSH-Px [13, 74, 75]. When induced by LPS to cause oxidative stress, DHM increased total antioxidant capacity and reduced the MDA levels in piglets, and increased SOD and GSH-Px activity and GSH in chicken plasma and ileum [55, 70]. The scientific evidence from *in vitro*, cell culture, and animal studies clearly indicate that DHM could prevent the free radicals, oxidative stress, and related markers. However, scientific data related to the antioxidant capacity of DHM in humans is scanty. Therefore, more clinical investigations are needed to improve the therapeutic applications of DHM as a natural antioxidant.

4. Anti-Inflammatory Capacity Is Fundamental and Is the Immediate Reason for Its Anticancer Efficacy

Inflammation is a complex and normal response of the immune system to external stimuli such as pathogens, toxins, chemical agents, infection, and tissue injury. When inflammatory cells (e.g., macrophages) are activated by stimuli (e.g., LPS and IFN- γ), inflammatory mediators such as IL-1 β , IL-6, TNF- α , NO, and PGE2 are excessively produced through the activation of common inflammatory signaling pathways such as the NF- κ B, MAPK, and JAK-STAT pathways [76]. The overproduction of inflammatory mediators (IL-1 β , IL-6, TNF- α , NO, and PGE2) has been associated with several diseases such as diabetes, cancer, asthma, metabolic syndrome, arthritis, cardiovascular diseases, and inflammatory bowel diseases [77]. Recently, there has been growing interest in nutraceuticals and functional foods derived from plant sources. Flavonoids are polyphenolic compounds largely present in vegetables, fruits, legumes, and tea. Flavonoids such as quercetin, cyanidin, luteolin, anthocyanidin, catechin, and epicatechin have shown to contain anti-inflammatory properties [78]. DHM has been extensively studied by many researchers for its anti-inflammatory activities using various cell cultures, animal models, and human studies. Several researchers used different inflammatory models (neuroinflammation, arthritis inflammation, and lung inflammation) to investigate the anti-inflammatory potential of DHM. Table 3 shows the various models used and the molecular mechanisms of the anti-inflammatory property of DHM.

The most widely used model for the investigation of the anti-inflammatory activity of plant-derived compounds is the macrophage that is stimulated by LPS. Macrophages play an important role in inflammation. The murine RAW264.7 macrophage cell line is the most commonly used cell culture model for the determination of the anti-inflammatory activity of food-derived compounds. Macrophages stimulated by the Toll-like receptor ligand LPS produce various inflammatory markers such as TNF- α , IL-6, IL-1 β , NO, transcription

TABLE 3: Anti-inflammatory activities and mechanisms of the action of DHM.

Treatment methods	Mode of administration	Dose and duration time	Mechanism of action/activities/effects showed	Reference
LPS-induced inflammation		50, 100, and 150 $\mu\text{g}/\text{mL}$ for 2 h	Shown anti-inflammatory activity by inhibiting interconnected ROS/Akt/IKK/NF- κB signaling pathways. Significantly inhibited the release of nitric oxide (NO) and proinflammatory cytokines such as IL-1 β , IL-6, and TNF- α in a dose-dependent manner	Shimei et al. (2012)
LPS-induced inflammation in RAW264.7 cells		0.4, 0.8, 1.5, 3, 6.2, 12.5, 25, 50, and 100 μM for 24 h	Shown anti-inflammatory effects through the inhibition of the release of nitric oxide (NO) in RAW macrophages	Yuemei et al. (2019)
A549 cells were stimulated with TLR3 agonist poly(I:C)		25, 50, and 100 μM for 3 days	Attenuated inflammation through TLR3 pathway	Yuanxin et al. (2020)
TNF- α -induced inflammation in HUVECs		5, 10, 25, 50, 75, and 100 μM for 24 h	Attenuated endothelial dysfunction induced by TNF- α in a miR-21-dependent manner	Dafeng et al. (2018)
TNF- α -induced inflammation		50–200 μM for 24 hours	Shown anti-inflammatory activity via suppression of TNF- α -induced NF- κB activation	Nina et al. (2016)
LPS-induced cardiomyocyte inflammation		25, 50, and 100 μM for 12 h	Exhibited anti-inflammatory activity in cardiomyocytes by reducing TNF- α and IL-6 levels via inhibition of the TLR4/NF- κB signaling pathways	Meng-qiao et al. (2017)
LPS-induced inflammation in BV-2 cells		10, 25, and 50 μM for 24 h	DHM significantly reduced LPS-induced NO, IL-6, and TNF- α production and levels of iNOS and COX-2 in BV-2 cells	Yafei et al. (2017)
LPS-induced inflammation in BV-2 cells		20, 40, 80, or 100 mg/L for 48 h	DHM exhibited the anti-inflammatory effect on LPS-induced BV-2 microglial cells through the TLR4/NF- κB signaling pathway and suppressed the levels of IL-6, IL-1 β , and TNF- α , and inhibited the protein expression of iNOS and COX-2	Nianshui et al. (2019)
TPA-induced acute inflammation/LPS-induced RAW 264.7 macrophage cells	Topical application	2.3 and 4.6 mg per ear for 5 h/37.5, 75, 150, and 300 μM for 2 h	Shown anti-inflammatory activity through suppressing the activation of NF- κB and the phosphorylation of p38 and JNK. Inhibited the levels of proinflammatory cytokines such as TNF- α , IL-1 β , and IL-6 as well as increased the level of the anti-inflammatory cytokine IL-10 in LPS-treated mice. Reduced the protein expression of iNOS, TNF- α , and COX-2 in RAW cells	Hou et al. (2015)
LPS-induced inflammation	Amp was dissolved in dimethylsulfoxide (DMSO), and dilutions were made in DMEM	0.5 $\mu\text{g}/\text{mL}$ for 24 h	Reduced the phosphorylation levels of JAK2-STAT3 and STAT3 nuclear translocation and suppressed LPS-induced activation of the I κB /NF- κB inflammation pathway. Decreased the production of NO and PGE2 and suppressed the expression of iNOS and COX-2 and reduced proinflammatory cytokines such as IL-1 β , IL-6, and TNF- α	Leihua et al. (2017)
Ovalbumin- (OVA-) induced inflammation in C57BL/6 mouse	Administered intraperitoneally	10 mg/kg BW for 14 days	DHM exhibited anti-inflammatory activity by reducing the levels of IL-4, IL-5, and IL-13 in the bronchoalveolar lavage fluid in an OVA-induced asthma model	Bin et al. (2017)
Doxorubicin- (DOX-) induced cardiotoxicity rat	Administered intragastrically		DHM protected against DOX-induced cardiotoxicity by inhibiting NLRP3	

TABLE 3: Continued.

Treatment methods	Mode of administration	Dose and duration time	Mechanism of action/activities/effects showed	Reference
model and DOX-induced H9C2 cells		100 mg/kg/day or 200 mg/kg/day for 6 weeks	inflammasome activation via stimulation of the SIRT1 pathway and suppressed IL-1 β and IL-18 release, and upregulated SIRT1 protein levels in vivo and in vitro	Zhenzhu et al. (2020)
Cecal ligation and puncture- (CLP-) induced lung injury model	Orally administered	50, 100, 150 mg/kg/day for 3 days	DHM treatment significantly inhibited the CLP-induced NLRP3 inflammasome pathway, IL-1 β , and IL-18	Yu-Chang et al. (2019)
LPS-mediated inflammation	Diet supplemented with ampelopsin	100 and 400 mg/kg BW for 28 days	Showed the anti-inflammatory activity through the reduction of activation of AKT and STAT3 phosphorylation and suppressed the DNA-binding activity of NF- κ B. Decreased the proinflammatory mediators such as TNF- α , IL-1 β , IL-6, and COX-2	Xiang et al. (2017)
Double-blind clinical trial	Orally administered	Four 150 mg capsules daily for 12 weeks	Exhibited anti-inflammatory activity by decreasing the serum levels of TNF- α , cytokeratin-18 fragment, and fibroblast growth factor 21	Shihui et al. (2015)
APP/PS1 double transgenic mice	Injected intraperitoneally	1 mg/kg BW for 2 and 4 weeks	DHM reduced activation of NLRP3 inflammasomes and reduced expression of NLRP3 inflammasome components and decreased IL-1 β in transgenic mice	Jie et al. (2018)
Collagen-induced inflammation	Intraperitoneally	5, 25, and 50 mg/kg BW every other day for 5 weeks	Alleviated inflammation in rats by attenuating IL-1 β production via suppression of NF- κ B signaling	Jing et al. (2019)
Lead- (Pb-) stimulated inflammation	Oral gavage administration	125 and 250 mg/kg/BW for 3 months	Inhibited Pb-induced inflammation by regulating the AMPK, A β , TLR4, MyD88, p38, and GSK-3 β pathways	Chan-Min et al. (2018)
Caerulein-induced inflammation in mice and BMDMs	Intraperitoneally	Single dose of 25/100 mg/kg	Inhibited production of proinflammatory cytokines IL-1 β , TNF- α , and IL-17 in mice and BMDMs	Rongrong et al. (2018)
LPS-induced inflammation in chickens	Feeding in the diet	0.025, 0.05, and 0.1 mg/kg for 14 days	DHM reduced inflammation by inhibiting NLRP3 inflammasome and TLR4/NF- κ B signaling pathway in ileum in chickens	Yicong et al. (2020)
Mice transplanted with Colo-205 cells	Intragastric administration	25, 50, and 100 mg/kg for 21 days	Decreased the levels of IL-1 β , IL-6, IL-8, and TNF- α as well as reduced the expression of COX-2 and iNOS	Jun et al. 2019
LPS-induced inflammation in lung tissue	Oral gavage administration	500 mg/kg BW for 4 days	Exhibited anti-inflammatory effects by inhibiting the MAPK signaling pathway as well as TNF- α , IL-1 β , and IL-6 levels	Bo et al. (2018)
A rat model of inflammation induced by collagen	Intraperitoneally	5, 25, and 50 mg/kg for 5 weeks	Exhibited anti-inflammatory effects by inhibiting NF- κ B signaling pathway	Jing et al. (2020)
Carrageenan-induced paw edema in rat and LPS-induced inflammation in RAW264.7 model	Intraperitoneal injection	50, 100, and 250 mg/kg for 7 days	DHM significantly reduced rat paw edema induced by carrageenan and noticeably inhibited NO secretion, iNOS, and COX-2 protein expression and decreased p65 phosphorylation via suppression of IKK- β activity and IKK- α / β phosphorylation	Rui et al. (2016)
Complete Freund's Adjuvant- (CFA-) induced inflammation in rheumatoid arthritis model	Gavage administration	20 and 50 mg/kg per day for 25 days	DHM inhibited the expressions of proinflammatory cytokines IL-1 β , IL-6, TNF- α , and COX-2 via activating the Nrf2 pathway	Jianguo et al. (2018)
Streptozotocin-induced diabetic inflammation	Intragastrically given Incorporated in the diet	100 mg/kg/day for 14 weeks	DHM reduced the levels of proinflammatory factors such as IL-6 and TNF- α	Bin et al. (2017a)

TABLE 3: Continued.

Treatment methods	Mode of administration	Dose and duration time	Mechanism of action/activities/effects showed	Reference
Alcohol-induced inflammation in C57BL/6 mice		75 and 150 mg/kg BW for 6 weeks	DHM considerably alleviated the hepatic IL-1 β and IL-6 levels	Ping et al. (2017)

factor NF- κ B, and prostaglandin-E2 that regulate the inflammatory responses. Numerous studies reported that DHM showed anti-inflammatory activity through different molecular mechanisms such as suppression of proinflammatory cytokines (IL-1 β , IL-6, IL-8, and TNF- α), activation of the production of an anti-inflammatory cytokine (IL-10), inhibition of MAPKs, suppression of the production of prostaglandins and nitric oxide, and inhibition of the transcription factor NF- κ B [3, 4, 79, 80].

The inflammatory response of the brain or the spinal cord is known as neuroinflammation, and it has an important role in the development of depression by producing cytokines, chemokines, and ROS [26]. Microglial cells are macrophages in the central nervous system and are commonly used as a model to investigate the protective effects of DHM in neuroinflammation. Several researchers evaluated the anti-inflammatory capacity of DHM in neuroinflammation using microglial cells and mice models. Weng et al. investigated the neuroinflammation protection capacity of DHM using murine BV-2 microglial cells activated by LPS and reported that DHM inhibited neuroinflammation by suppressing the I κ B/NF- κ B inflammation pathway as well as decreasing STAT3 nuclear translocation and the phosphorylation levels of JAK2-STAT3. Additionally, the authors demonstrated that DHM treatment significantly inhibited the production of inflammatory mediators IL-1 β , IL-6, TNF- α , nitric oxide (NO), prostaglandin E2 (PGE2), and the enzymes inducible nitric oxide synthase (iNOS) and cyclooxygenase-2 (COX-2) in LPS-induced microglial cells. DHM treatment at 10 and 20 mg/kg/day for 3 days showed an antidepressant-like activity by significantly inhibiting TNF- α and IL-6 gene expressions and protein levels in a mice model of LPS-induced neuroinflammation [81]. DHM at 1 mg/kg BW for 4 weeks significantly inhibited the neuroinflammation of APP/PS1 double transgenic mice by decreasing IL-1 β via reduction of the activation of NLRP3 inflammasomes [82]. In a lead- (Pb-) induced inflammation model in mice, Pb combined with DHM administration at a dose of 125 and 250 mg/kg/BW significantly inhibited TNF- α and IL-1 β and the nuclear translocation of NF- κ B p65 via regulating the AMPK, A β , TLR4, MyD88, p38, and GSK-3 β signaling pathways. DHM exhibited an anti-inflammatory effect on LPS-induced BV-2 microglial cells by suppressing the proinflammatory markers IL-6, IL-1 β , TNF- α , iNOS, and COX-2 through reducing the activation of the TLR4/NF- κ B signaling pathway. These studies proved that DHM possess neuroinflammation protection activity through the inhibition of inflammatory mediators.

The anti-inflammatory effects of DHM were investigated with the administration of a DHM dosage from 0.025 to 500 mg/kg BW within 2 weeks to 14 weeks. Xu et al. studied

the anti-inflammatory capacity of DHM in an ovalbumin- (OVA-) induced mice C57BL/6 model of asthma and demonstrated that DHM treatment significantly decreased the levels of IL-4, IL-5, and IL-13 in the bronchoalveolar lavage fluid compared to the control group [83]. DHM treatment significantly suppressed IL-1 β and IL-18 production by inhibiting the NLRP3 inflammasome through the activation of the SIRT1 signaling pathway in a doxorubicin- (DOX-) induced rat model and in DOX-treated H9C2 cells [84]. DHM was found to reduce the inflammation in CIA rats by attenuating IL-1 β production through the suppression of the NF- κ B signaling pathway [85]. Chu et al. reported that DHM significantly reduced the inflammation in a rat model of rheumatoid arthritis by inhibiting the levels of inflammatory mediators IL-1 β , IL-6, TNF- α , and COX-2 via activating the Nrf2 pathway [86]. Chang et al. investigated the protective role of DHM in ileum inflammation, induced by LPS, in chickens and found that DHM treatment decreased IL-1 β and IL-18 expression through the inhibition of the TLR4/NF- κ B signaling pathways. DHM significantly decreased the proinflammatory cytokines TNF- α , IL-1 β , and IL-6 and the COX-2 gene expressions and increased the production of IL-10 in the liver of piglets injected with LPS [21]. Additionally, the authors demonstrated that DHM supplementation in LPS-treated piglets decreased the activation of AKT and STAT3 phosphorylation and reduced the DNA-binding activity of NF- κ B [21].

More importantly, the anti-inflammatory activity of DHM was also determined in humans. Chen et al. conducted a randomized double-blind controlled clinical trial with sixty adult nonalcoholic fatty liver disease patients, and the DHM was administered (150 mg capsules) twice daily for 12 weeks [87]. The authors found that DHM exhibited an anti-inflammatory activity in humans by decreasing the serum levels of TNF- α , cytokeratin-18 fragment, and fibroblast growth factor 21.

Although sufficient evidence is available from cell culture and animal experiments, the results from clinical studies are meager. Therefore, it is suggested that more studies are needed in humans to further confirm the anti-inflammatory activity of DHM. More results from human studies would provide strong scientific evidence for using DHM as a therapeutic agent to treat inflammation and its related diseases.

5. Gut Microbiota Is a Potential Interface for the Regulation of Redox Balance for Cancer Prevention

The interface of gut microbiota is very important for cancer chemoprevention of DHM, and the interaction between

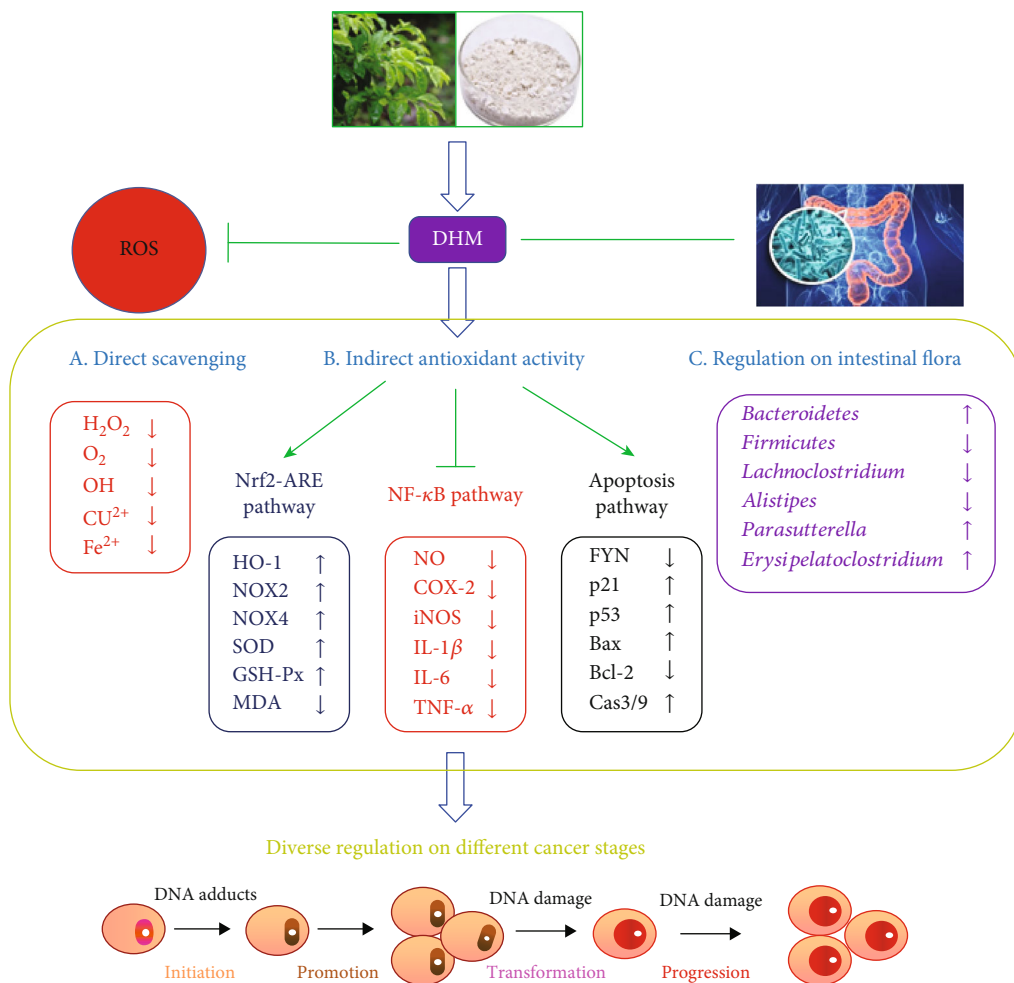


FIGURE 2: Molecular mechanism diagram of the inhibitory effect of DHM on cancer.

DHM and gut microbiota is the key stage for its mechanism study. DHM is a flavonoid with poor oral bioavailability *in vivo* because of its rare absorption in the gastrointestinal tract (GI). Due to the low bioavailability, the vast majority of DHM persists in the colon where it is exposed to the gut microbiota, which markedly alters the richness and diversity of the gut microbiota and modulates the gut microbiota composition [88]. Previous studies indicated that DHM could be distributed widely in different organs such as the liver, kidney, lung, brain, and heart, whereas most of them were eliminated in feces, which indicated that DHM is predominantly distributed in the intestinal tract, and closely interacts with the gut microbiota [89].

It is reported that DHM treatment could obviously change the relative abundances of gut microbiota at different levels [90]. DHM is able to dramatically increase the abundance of *Bacteroidetes* but decrease the abundance of *Firmicutes*, which was related to obesity intervention in humans. In brief, decreasing the ratio of *Firmicutes* to *Bacteroidetes* was demonstrated to control body weight via modulatory glucose and lipid metabolism. Besides, DHM supplement can decrease the abundances of *Lachnospirillum*, *Alistipes*, *Ruminococcaceae* UCG-010, *Allobaculum*, *Ruminiclostridium* 9, *Rikenellaceae* RC9, *Ruminococcaceae* UCG-005,

Anaerotruncus, *Defluviitaleaceae* UCG-011, [*Eubacterium*] *ventriosum*, *Christensenellaceae* R-7, and *Odoribacter*, whereas it can increase the abundances of *Parasutterella*, *Erysipelatoclostridium*, and *Parabacteroides* [91]. Thus, a lot of evidences suggested that DHM supplement could intervene against chronic diseases, such as obesity, diabetes, and cancers, via modulating the gut microbiota composition [92].

Moreover, the interaction between DHM and gut microbiota is reported to be associated with cancer. DHM was reported to promote the CPT-11 effect both in the mouse model of AOM/DSS cancer; tumors were sensitive to 100 mg/kg DHM chemotherapy under 100 mg/kg or 200 mg/kg CPT-11 (irinotecan). DHM-driven CPT-11 chemotherapy induced enhanced IgG levels and the reduction of *Fusobacterium* abundance in the gut [91]. Besides, the intestinal tract is the most important target organ for DHM intervention associated with the chemotherapeutic efficacy and reduced risk of the side effects of cancer treatment via the regulation of immune responses and the shaping of gut microbiota [92].

On the other hand, DHM was reported to be biotransformed into other metabolites by gut microbiota *via* methylation, reduction, dehydroxylation, glucuronidation, and sulfation pathways which may be closely related to the

regulation of redox balance [93]. Therefore, gut microbiota is a potential important interface for regulating the redox balance for providing more therapeutic schedules on various other human diseases.

6. Conclusions and Perspectives

DHM originated from a natural plant in China and has received increasing attention due to its pharmacological activities. In this review, the physicochemical properties of DHM have been mentioned. Its antioxidant, anti-inflammatory, and anticancer activities and related molecular mechanisms have been further reviewed. The molecular mechanism diagram of the inhibitory effect of DHM on cancer has been summarized as shown in Figure 2. In brief, DHM exerts its anticancer activity via direct scavenging of ROS, regulating intestinal microbiota, and indirectly modulating the cellular signaling pathway, including the activation of the Nrf2-ARE pathway, the inhibition of the NF- κ B pathway, and the induction of the apoptosis pathway.

Substantial scientific evidence about the functional properties of DHM is available from cell culture and animal studies. DHM exhibited bioactivities by modulating several molecular pathways. However, the mechanism of pharmacological action, distribution, and metabolism are still not well investigated *in vivo* in animals, and what is more, the evidence from clinical studies is meager. The novel targets of the signaling transduction of DHM still require more work. Furthermore, more studies are needed in humans in order to improve the applications of DHM in food and pharmaceutical industries. The future *in vivo* researches by multiomics technologies are required to understand the safety, bioavailability, and metabolism mechanism of DHM targeting on oxidative stress, inflammation, and cancer, especially to reveal the reciprocal interaction among DHM, cells/organs, and gut microbiota. This could pave ways for the industry applications of DHM as a functional food/healthy food/therapeutic agent.

Abbreviations

AAPH:	2,2'-Azobis (2-amidinopropane) dihydrochloride
ABTS:	3-Ethylbenzothiazoline-6-sulphonic acid
BAD:	Bcl-2-associated death promoter
BAX:	BCL-2-associated X protein
COX-2:	Cyclooxygenase 2
DHM:	Dihydromyricetin
DPPH:	1,1-Diphenyl-2-picrylhydrazyl radical 2,2-diphenyl-1-(2,4,6-trinitrophenyl) hydrazyl
GSH:	Glutathione
H ₂ O ₂ :	Hydrogen peroxide
HCC:	Hepatocellular carcinoma
HUVECs:	Human umbilical vein endothelial cells
iNOS:	Inducible nitric oxide synthase
IL:	Interleukin
IC ₅₀ :	Half-maximal inhibitory concentration
LPO:	Lipid peroxidation
LPS:	Lipopolysaccharide

MDA:	Malondialdehyde
MIC:	Minimum inhibitory concentration
MAPKs:	Mitogen-activated protein kinases
MNU:	1-Methyl-1-nitrosourea
NF- κ B:	Nuclear factor- κ -gene binding
Nrf2:	Nuclear factor erythroid 2-related factor 2
O ₂ ^{•-} :	Superoxide anion
ORAC:	Oxygen radical absorption capacity
OH [•] :	Hydroxyl radicals
ROS:	Reactive oxygen species
SOD:	Superoxide dismutase
STAT3:	Transduction and transcription 3
TNF- α :	Tumor necrosis factor-alpha
TLRs:	Toll-like receptors.

Conflicts of Interest

The authors declare that they have no conflicts of interest.

References

- [1] W. Gao, S.-U. Lee, J. Li, and J.-W. Lee, "Development of improved process with treatment of cellulase for isolation of ampelopsin from dried fruits of *Ampelopsis grossedentata*," *BioResources*, vol. 11, no. 1, pp. 2712–2722, 2015.
- [2] L. Weng, H. Zhang, X. Li et al., "Ampelopsin attenuates lipopolysaccharide-induced inflammatory response through the inhibition of the NF- κ B and JAK2/STAT3 signaling pathways in microglia," *International Immunopharmacology*, vol. 44, pp. 1–8, 2017.
- [3] N. Jing and X. Li, "Dihydromyricetin attenuates inflammation through TLR4/NF-kappaB pathway," *Open Medicine*, vol. 14, no. 1, pp. 719–725, 2019.
- [4] X. Hou, Q. Tong, W. Wang, W. Xiong, C. Shi, and J. Fang, "Dihydromyricetin protects endothelial cells from hydrogen peroxide-induced oxidative stress damage by regulating mitochondrial pathways," *Life Sciences*, vol. 130, pp. 38–46, 2015.
- [5] K. Xie, X. He, K. Chen, J. Chen, K. Sakao, and D.-X. Hou, "Antioxidant properties of a traditional vine tea, *Ampelopsis grossedentata*," *Antioxidants*, vol. 8, no. 8, p. 295, 2019.
- [6] J. Liu, Y. Shu, Q. Zhang et al., "Dihydromyricetin induces apoptosis and inhibits proliferation in hepatocellular carcinoma cells," *Oncology Letters*, vol. 8, no. 4, pp. 1645–1651, 2014.
- [7] Y. Sun, W. Liu, C. Wang et al., "Combination of dihydromyricetin and ondansetron strengthens antiproliferative efficiency of adriamycin in K562/ADR through downregulation of SORCIN: a new strategy of inhibiting P-glycoprotein," *Journal of Cellular Physiology*, vol. 234, no. 4, pp. 3685–3696, 2019.
- [8] L. Chen, M. Yao, X. Fan et al., "Dihydromyricetin attenuates streptozotocin-induced liver injury and inflammation in rats via regulation of NF- κ B and AMPK signaling pathway," *eFood*, vol. 1, no. 2, pp. 188–195, 2020.
- [9] J. He, J. Zhang, L. Dong et al., "Dihydromyricetin attenuates metabolic syndrome and improves insulin sensitivity by upregulating insulin receptor substrate-1 (Y612) tyrosine phosphorylation in db/db mice," *Diabetes, Metabolic Syndrome and Obesity: Targets and Therapy*, vol. 12, pp. 2237–2249, 2019.
- [10] L. Ran, X. L. Wang, H. D. Lang et al., "Ampelopsis grossedentata supplementation effectively ameliorates the glycemic

- control in patients with type 2 diabetes mellitus," *European Journal of Clinical Nutrition*, vol. 73, no. 5, pp. 776–782, 2019.
- [11] T. T. Liu, Y. Zeng, K. Tang, X. M. Chen, W. Zhang, and X. Le Xu, "Dihydromyricetin ameliorates atherosclerosis in LDL receptor deficient mice," *Atherosclerosis*, vol. 262, pp. 39–50, 2017.
 - [12] Y. Zeng, Y. Peng, K. Tang et al., "Dihydromyricetin ameliorates foam cell formation via LXRA- ABCA1/ABCG1-dependent cholesterol efflux in macrophages," *Biomedicine & Pharmacotherapy*, vol. 101, pp. 543–552, 2018.
 - [13] Y. Chen, H.-Q. Luo, L.-L. Sun et al., "Dihydromyricetin attenuates myocardial hypertrophy induced by transverse aortic constriction via oxidative stress inhibition and SIRT3 pathway enhancement," *International Journal of Molecular Sciences*, vol. 19, no. 9, article 2592, 2018.
 - [14] L. Wei, X. Sun, X. Qi, Y. Zhang, Y. Li, and Y. Xu, "Dihydromyricetin ameliorates cardiac ischemia/reperfusion injury through Sirt3 activation," *BioMed Research International*, vol. 2019, Article ID 6803943, 9 pages, 2019.
 - [15] Z. Zhong, G. Zhou, and X. Chen, "The rat chronic toxicity test of total flavone of *Ampelopsis grossedentata* from Guangxi," *Lishizhen Medicine & Materia Medical Research*, vol. 14, no. 4, pp. 193–195, 2003.
 - [16] J. J. Xu, M. J. Yao, and M. C. Wu, "Study on biological efficacy of dihydromyricetin," *Food Science*, vol. 29, pp. 622–625, 2008.
 - [17] L. Zhao, A. Wang, B. Liu, G. Li, Z. Zhang, and S. Chen, "Anti-oxidant and cytotoxic activity of dihydromyricetin from *Ampelopsis grossedentata* leaves," *Agro Food Industry Hi-Tech*, vol. 20, no. 3, pp. 14–17, 2009.
 - [18] D. Liu, Y. Mao, L. Ding, and X.-A. Zeng, "Dihydromyricetin: a review on identification and quantification methods, biological activities, chemical stability, metabolism and approaches to enhance its bioavailability," *Trends in Food Science & Technology*, vol. 91, pp. 586–597, 2019.
 - [19] M. Wu, M. Jiang, T. Dong et al., "Reversal effect of dihydromyricetin on multiple drug resistance in SGC7901/5-FU cells," *Asian Pacific Journal of Cancer Prevention*, vol. 21, no. 5, pp. 1269–1274, 2020.
 - [20] R. Wang, J. Pi, X. Su et al., "Dihydromyricetin suppresses inflammatory responses in vitro and in vivo through inhibition of IKK β activity in macrophages," *Scanning*, vol. 38, no. 6, p. 912, 2016.
 - [21] X. Hou, T. Wang, H. Ahmad, and Z. Xu, "Ameliorative effect of ampelopsin on LPS-induced acute phase response in piglets," *Journal of Functional Foods*, vol. 35, pp. 489–498, 2017.
 - [22] D. Xiang, L. Fan, X. L. Hou et al., "Uptake and transport mechanism of dihydromyricetin across human intestinal Caco-2 cells," *Journal of Food Science*, vol. 83, no. 7, pp. 1941–1947, 2018.
 - [23] H. Li, Q. Li, Z. Liu et al., "The versatile effects of dihydromyricetin in health," *Evidence-based Complementary and Alternative Medicine*, vol. 2017, Article ID 1053617, 10 pages, 2017.
 - [24] H. Tong, X. Zhang, L. Tan, R. Jin, S. Huang, and X. Li, "Multitarget and promising role of dihydromyricetin in the treatment of metabolic diseases," *European Journal of Pharmacology*, vol. 870, article 172888, 2020.
 - [25] K. Nurgali, R. T. Jagoe, and R. Abalo, "Adverse effects of cancer chemotherapy: Anything new to improve tolerance and reduce sequelae?," *Frontiers in Pharmacology*, vol. 9, p. 245, 2018.
 - [26] D. F. Romagnolo and O. I. Selmin, "Flavonoids and cancer prevention: a review of the evidence," *Journal of Nutrition in Gerontology and Geriatrics*, vol. 31, no. 3, pp. 206–238, 2012.
 - [27] F. Ni, Y. Gong, L. Li, H. M. Abdolmaleky, and J.-R. Zhou, "Flavonoid ampelopsin inhibits the growth and metastasis of prostate cancer in vitro and in mice," *PLoS One*, vol. 7, no. 6, article e38802, 2012.
 - [28] Y. Zhou, F. Shu, X. Liang et al., "Ampelopsin induces cell growth inhibition and apoptosis in breast cancer cells through ROS generation and endoplasmic reticulum stress pathway," *PLoS One*, vol. 9, no. 2, article e89021, 2014.
 - [29] Q. Y. Zhang, R. Li, G. F. Zeng et al., "Dihydromyricetin inhibits migration and invasion of hepatoma cells through regulation of MMP-9 expression," *World Journal of Gastroenterology*, vol. 20, no. 29, pp. 10082–10093, 2014.
 - [30] J. Xia, S. Guo, T. Fang et al., "Dihydromyricetin induces autophagy in HepG2 cells involved in inhibition of mTOR and regulating its upstream pathways," *Food and Chemical Toxicology*, vol. 66, pp. 7–13, 2014.
 - [31] H. Chang, X. Peng, Q. Bai et al., "Ampelopsin suppresses breast carcinogenesis by inhibiting the mTOR signalling pathway," *Carcinogenesis*, vol. 35, no. 8, pp. 1847–1854, 2014.
 - [32] S. Qi, X. Kou, J. Lv, Z. Qi, and L. Yan, "Ampelopsin induces apoptosis in HepG2 human hepatoma cell line through extrinsic and intrinsic pathways: involvement of P38 and ERK," *Environmental Toxicology and Pharmacology*, vol. 40, no. 3, pp. 847–854, 2015.
 - [33] X.-M. Chen, X.-B. Xie, Q. Zhao et al., "Ampelopsin induces apoptosis by regulating multiple c-Myc/S-phase kinase-associated protein 2/F-box and WD repeat-containing protein 7/histone deacetylase 2 pathways in human lung adenocarcinoma cells," *Molecular Medicine Reports*, vol. 11, no. 1, pp. 105–112, 2015.
 - [34] S.-J. Kao, W.-J. Lee, J.-H. Chang et al., "Suppression of reactive oxygen species-mediated ERK and JNK activation sensitizes dihydromyricetin-induced mitochondrial apoptosis in human non-small cell lung cancer," *Environmental Toxicology*, vol. 32, no. 4, pp. 1426–1438, 2017.
 - [35] Z. Zhang, H. Zhang, S. Chen et al., "Dihydromyricetin induces mitochondria-mediated apoptosis in HepG2 cells through down-regulation of the Akt/Bad pathway," *Nutrition Research*, vol. 38, pp. 27–33, 2017.
 - [36] Y. Zuo, Q. Xu, Y. Lu et al., "Dihydromyricetin induces apoptosis in a human choriocarcinoma cell line," *Oncology Letters*, vol. 16, no. 4, pp. 4229–4234, 2018.
 - [37] Z. Guo, H. Guozhang, H. Wang, Z. Li, and N. Liu, "Ampelopsin inhibits human glioma through inducing apoptosis and autophagy dependent on ROS generation and JNK pathway," *Biomedicine & Pharmacotherapy*, vol. 116, article 108524, 2019.
 - [38] F. Wang, X. Chen, D. Yuan, Y. Yi, and Y. Luo, "Golgi reassembly and stacking protein 65 downregulation is required for the anti-cancer effect of dihydromyricetin on human ovarian cancer cells," *PLoS One*, vol. 14, no. 11, article e0225450, 2019.
 - [39] Y. Zuo, Y. Lu, Q. Xu et al., "Inhibitory effect of dihydromyricetin on the proliferation of JAR cells and its mechanism of action," *Oncology Letters*, vol. 20, no. 1, pp. 357–363, 2020.
 - [40] B. Zhang, S. Dong, X. Cen et al., "Ampelopsin sodium exhibits antitumor effects against bladder carcinoma in orthotopic xenograft models," *Anti-Cancer Drugs*, vol. 23, no. 6, pp. 590–596, 2012.

- [41] J. Liang, J. Wu, F. Wang, P. Zhang, and X. Zhang, "Semaphorin 4D is required for the induction of antioxidant stress and anti-inflammatory effects of dihydromyricetin in colon cancer," *International Immunopharmacology*, vol. 67, pp. 220–230, 2019.
- [42] Z. Zhao, J.-q. Yin, M.-s. Wu et al., "Dihydromyricetin activates AMP-activated protein kinase and P38MAPK exerting antitumor potential in osteosarcoma," *Cancer Prevention Research*, vol. 7, no. 9, pp. 927–938, 2014.
- [43] S.-W. Hong, N.-S. Park, M. H. Noh et al., "Combination treatment with erlotinib and ampelopsin overcomes erlotinib resistance in NSCLC cells via the Nox2-ROS-Bim pathway," *Lung Cancer*, vol. 106, pp. 115–124, 2017.
- [44] P. Cheng, C. Gui, J. Huang et al., "Molecular mechanisms of ampelopsin from *Ampelopsis megalophylla* induces apoptosis in HeLa cells," *Oncology Letters*, vol. 14, no. 3, pp. 2691–2698, 2017.
- [45] D.-Z. Zhou, H. Y. Sun, J. Q. Yue, Y. Peng, Y. M. Chen, and Z. J. Zhong, "Dihydromyricetin induces apoptosis and cytoprotective autophagy through ROS-NF- κ B signalling in human melanoma cells," *Free Radical Research*, vol. 51, no. 5, pp. 517–528, 2017.
- [46] Y. Xu, S. Wang, H. F. Chan et al., "Dihydromyricetin induces apoptosis and reverses drug resistance in ovarian cancer cells by p53-mediated downregulation of survivin," *Scientific Reports*, vol. 7, no. 1, article 46060, 2017.
- [47] B. Liu, X. Tan, J. Liang et al., "A reduction in reactive oxygen species contributes to dihydromyricetin-induced apoptosis in human hepatocellular carcinoma cells," *Scientific Reports*, vol. 4, no. 1, pp. 1–8, 2014.
- [48] H. Huang, M. Hu, R. Zhao, P. Li, and M. Li, "Dihydromyricetin suppresses the proliferation of hepatocellular carcinoma cells by inducing G2/M arrest through the Chk1/Chk2/Cdc25C pathway," *Oncology Reports*, vol. 30, no. 5, pp. 2467–2475, 2013.
- [49] G. Zeng, J. Liu, H. Chen et al., "Dihydromyricetin induces cell cycle arrest and apoptosis in melanoma SK-MEL-28 cells," *Oncology Reports*, vol. 31, no. 6, pp. 2713–2719, 2014.
- [50] Z. Zhao, J. Q. Yin, M. S. Wu et al., "Dihydromyricetin activates AMP-activated protein kinase and P38MAPK exerting antitumor potential in osteosarcoma," *Cancer Prevention Research*, vol. 7, no. 9, pp. 927–938, 2014.
- [51] L. Jiang, Q. Zhang, H. Ren et al., "Dihydromyricetin enhances the chemo-sensitivity of nedaplatin via regulation of the p53/Bcl-2 pathway in hepatocellular carcinoma cells," *PLoS One*, vol. 10, no. 4, article e0124994, 2015.
- [52] E. Birben, U. M. Sahiner, C. Sackesen, S. Erzurum, and O. Kalayci, "Oxidative stress and antioxidant defense," *World Allergy Organization Journal*, vol. 5, no. 1, pp. 9–19, 2012.
- [53] I. Liguori, G. Russo, F. Curcio et al., "Oxidative stress, aging, and diseases," *Clinical Interventions in Aging*, vol. 13, pp. 757–772, 2018.
- [54] A. N. Panche, A. D. Diwan, and S. R. Chandra, "Flavonoids: an overview," *Journal of Nutritional Science*, vol. 5, 2016.
- [55] X. Hou, J. Zhang, H. Ahmad, H. Zhang, Z. Xu, and T. Wang, "Evaluation of antioxidant activities of ampelopsin and its protective effect in lipopolysaccharide-induced oxidative stress piglets," *PLoS One*, vol. 9, no. 9, article e108314, 2014.
- [56] W. Liao, Z. Ning, L. Ma et al., "Recrystallization of dihydromyricetin from *Ampelopsis grossedentata* and its anti-oxidant activity evaluation," *Rejuvenation Research*, vol. 17, no. 5, pp. 422–429, 2014.
- [57] X. J. Zheng, H. Xiao, Z. Zeng et al., "Composition and serum antioxidation of the main flavonoids from fermented vine tea (*Ampelopsis grossedentata*)," *Journal of Functional Foods*, vol. 9, pp. 290–294, 2014.
- [58] X. Li, J. Liu, J. Lin et al., "Protective effects of dihydromyricetin against \cdot OH-induced mesenchymal stem cells damage and mechanistic chemistry," *Molecules*, vol. 21, no. 5, p. 604, 2016.
- [59] J. Ye, Y. Guan, S. Zeng, and D. Liu, "Ampelopsin prevents apoptosis induced by H₂O₂ in MT-4 lymphocytes," *Planta Medica*, vol. 74, no. 3, pp. 252–257, 2008.
- [60] Y. Wu, Y. Xiao, Y. Yue, K. Zhong, Y. Zhao, and H. Gao, "A deep insight into mechanism for inclusion of 2R, 3R-dihydromyricetin with cyclodextrins and the effect of complexation on antioxidant and lipid-lowering activities," *Food Hydrocolloids*, vol. 103, article 105718, 2020.
- [61] G.-Y. Tan, M.-H. Zhang, J.-H. Feng, A.-Y. Han, S.-S. Zheng, and P. Xie, "Effects of pretreatment by the flavanol ampelopsin on porcine kidney epithelial cell injury induced by hydrogen peroxide," *Agricultural Sciences in China*, vol. 9, no. 4, pp. 598–604, 2010.
- [62] X. Kou and N. Chen, "Pharmacological potential of ampelopsin in Rattan tea," *Food Science and Human Wellness*, vol. 1, no. 1, pp. 14–18, 2012.
- [63] B. Jiang, L. Le, H. Pan, K. Hu, L. Xu, and P. Xiao, "Dihydromyricetin ameliorates the oxidative stress response induced by methylglyoxal via the AMPK/GLUT4 signaling pathway in PC12 cells," *Brain Research Bulletin*, vol. 109, pp. 117–126, 2014.
- [64] X. Zhang, X. Li, J. Fang et al., "(2R,3R)Dihydromyricetin inhibits osteoclastogenesis and bone loss through scavenging LPS-induced oxidative stress and NF- κ B and MAPKs pathways activating," *Journal of Cellular Biochemistry*, vol. 119, no. 11, pp. 8981–8995, 2018.
- [65] X. Zhang, L. Wang, L. Peng et al., "Dihydromyricetin protects HUVECs of oxidative damage induced by sodium nitroprusside through activating PI3K/Akt/FoxO3a signalling pathway," *Journal of Cellular and Molecular Medicine*, vol. 23, no. 7, pp. 4829–4838, 2019.
- [66] C. Dong, G. Wu, H. Li, Y. Qiao, and S. Gao, "Ampelopsin inhibits high glucose-induced extracellular matrix accumulation and oxidative stress in mesangial cells through activating the Nrf2/HO-1 pathway," *Phytotherapy Research*, vol. 34, no. 8, pp. 2044–2052, 2020.
- [67] H. Han, Y. Dong, and X. Ma, "Dihydromyricetin protects against gentamicin-induced ototoxicity via PGC-1 α /SIRT3 signaling in vitro," *Frontiers in Cell and Developmental Biology*, vol. 8, p. 702, 2020.
- [68] B. Wu, J. Lin, J. Luo et al., "Dihydromyricetin Protects against Diabetic Cardiomyopathy in Streptozotocin-Induced Diabetic Mice," *BioMed Research International*, vol. 2017, Article ID 3764370, 13 pages, 2017.
- [69] H. Li, F. Yu, X. Sun, L. Xu, J. Miu, and P. Xiao, "Dihydromyricetin ameliorates memory impairment induced by acute sleep deprivation," *European Journal of Pharmacology*, vol. 853, pp. 220–228, 2019.
- [70] Y. Chang, L. Yuan, J. Liu et al., "Dihydromyricetin attenuates *Escherichia coli* lipopolysaccharide-induced ileum injury in chickens by inhibiting NLRP3 inflammasome and TLR4/NF- κ B signalling pathway," *Veterinary Research*, vol. 51, no. 1, p. 72, 2020.
- [71] X. Liang, T. Zhang, L. Shi et al., "Ampelopsin protects endothelial cells from hyperglycemia-induced oxidative damage

- by inducing autophagy via the AMPK signaling pathway," *Bio-Factors*, vol. 41, no. 6, pp. 463–475, 2015.
- [72] L. Liu, S. Sun, H. Rui, and X. Li, "In vitro inhibitory effects of dihydromyricetin on human liver cytochrome P450 enzymes," *Pharmaceutical Biology*, vol. 55, no. 1, pp. 1868–1874, 2017.
- [73] M. Bebová, Z. Boštíková, M. Moserová et al., "Modulation of xenobiotic conjugation enzymes by dihydromyricetin in rats," *Monatshefte für Chemie - Chemical Monthly*, vol. 148, no. 11, pp. 2003–2009, 2017.
- [74] L. Guo, H. Zhang, and X. Yan, "Protective effect of dihydromyricetin reverts fatty liver through nuclear factor- κ B/p53/B-cell lymphoma 2-associated X protein signaling pathways in a rat model," *Molecular Medicine Reports*, vol. 19, no. 3, pp. 1638–1644, 2019.
- [75] F. Wu, Y. Li, H. Song et al., "Preventive effect of dihydromyricetin against cisplatin-induced nephrotoxicity in vitro and in vivo," *Evidence-based Complementary and Alternative Medicine*, vol. 2016, Article ID 7937385, 9 pages, 2016.
- [76] L. Chen, H. Deng, H. Cui et al., "Inflammatory responses and inflammation-associated diseases in organs," *Oncotarget*, vol. 9, no. 6, pp. 7204–7218, 2018.
- [77] J. Zhong and G. Shi, "Editorial: Regulation of inflammation in chronic disease," *Frontiers in Immunology*, vol. 10, p. 737, 2019.
- [78] S. J. Maleki, J. F. Crespo, and B. Cabanillas, "Anti-inflammatory effects of flavonoids," *Food Chemistry*, vol. 299, article 125124, 2019.
- [79] B. Wang, Y. Xiao, X. Yang et al., "Protective effect of dihydromyricetin on LPS-induced acute lung injury," *Journal of Leukocyte Biology*, vol. 103, no. 6, pp. 1241–1249, 2018.
- [80] J. Wu, K.-J. Fan, Q.-S. Wang, B.-X. Xu, Q. Cai, and T.-Y. Wang, "DMY protects the knee joints of rats with collagen-induced arthritis by inhibition of NF- κ B signaling and osteoclastic bone resorption," *Food & Function*, vol. 11, no. 7, pp. 6251–6264, 2020.
- [81] Z. Ren, P. Yan, L. Zhu et al., "Dihydromyricetin exerts a rapid antidepressant-like effect in association with enhancement of BDNF expression and inhibition of neuroinflammation," *Psychopharmacology*, vol. 235, no. 1, pp. 233–244, 2018.
- [82] J. Feng, J.-. X. Wang, Y.-. H. Du et al., "Dihydromyricetin inhibits microglial activation and neuroinflammation by suppressing NLRP 3 inflammasome activation in APP/PS 1 transgenic mice," *CNS Neuroscience & Therapeutics*, vol. 24, no. 12, pp. 1207–1218, 2018.
- [83] B. Xu, S. Huang, C. Wang, H. Zhang, S. Fang, and Y. Zhang, "Anti-inflammatory effects of dihydromyricetin in a mouse model of asthma," *Molecular Medicine Reports*, vol. 15, no. 6, pp. 3674–3680, 2017.
- [84] Z. Sun, W. Lu, N. Lin et al., "Dihydromyricetin alleviates doxorubicin-induced cardiotoxicity by inhibiting NLRP3 inflammasome through activation of SIRT1," *Biochemical Pharmacology*, vol. 175, article 113888, 2020.
- [85] J. Wu, F.-T. Zhao, K.-J. Fan et al., "Dihydromyricetin inhibits inflammation of fibroblast-like synoviocytes through regulation of nuclear factor- κ B signaling in rats with collagen-induced arthritis," *Journal of Pharmacology and Experimental Therapeutics*, vol. 368, no. 2, pp. 218–228, 2019.
- [86] J. Chu, X. Wang, H. Bi, L. Li, M. Ren, and J. Wang, "Dihydromyricetin relieves rheumatoid arthritis symptoms and suppresses expression of pro-inflammatory cytokines via the activation of Nrf2 pathway in rheumatoid arthritis model," *International Immunopharmacology*, vol. 59, pp. 174–180, 2018.
- [87] S. Chen, X. Zhao, J. Wan et al., "Dihydromyricetin improves glucose and lipid metabolism and exerts anti-inflammatory effects in nonalcoholic fatty liver disease: A randomized controlled trial," *Pharmacological Research*, vol. 99, pp. 74–81, 2015.
- [88] J. van Duynhoven, E. E. Vaughan, D. M. Jacobs et al., "Metabolic fate of polyphenols in the human superorganism," *Proceedings of the National Academy of Sciences*, vol. 108, Supplement 1, pp. 4531–4538, 2011.
- [89] Q. Tong, X. Hou, J. Fang et al., "Determination of dihydromyricetin in rat plasma by LC-MS/MS and its application to a pharmacokinetic study," *Journal of Pharmaceutical and Biomedical Analysis*, vol. 114, pp. 455–461, 2015.
- [90] R. Liu, J. Hong, X. Xu et al., "Gut microbiome and serum metabolome alterations in obesity and after weight-loss intervention," *Nature Medicine*, vol. 23, no. 7, pp. 859–868, 2017.
- [91] X.-H. Zhu, H.-D. Lang, X.-L. Wang et al., "Synergy between dihydromyricetin intervention and irinotecan chemotherapy delays the progression of colon cancer in mouse models," *Food & Function*, vol. 10, no. 4, pp. 2040–2049, 2019.
- [92] N. Iida, A. Dzutsev, C. A. Stewart et al., "Commensal bacteria control cancer response to therapy by modulating the tumor microenvironment," *Science*, vol. 342, no. 6161, pp. 967–970, 2013.
- [93] L. Fan, X. Zhao, Q. Tong et al., "Interactions of dihydromyricetin, a flavonoid from vine tea (*Ampelopsis grossedentata*) with gut microbiota," *Journal of Food Science*, vol. 83, no. 5, pp. 1444–1453, 2018.

Research Article

The Diagnosis Value of a Novel Model with 5 Circulating miRNAs for Liver Fibrosis in Patients with Chronic Hepatitis B

Qingqing Zhang,¹ Qidi Zhang,² Binghang Li,² Ying Qu,² Zhenghong Li,² Lungen Lu^{1,2},
Rongzhou Li¹ and Xiaobo Cai²

¹Department of Gastroenterology, Ruian People's Hospital, Wenzhou, Zhejiang Province 325200, China

²Department of Gastroenterology, Shanghai General Hospital, Shanghai Jiao Tong University School of Medicine, Shanghai 200080, China

Correspondence should be addressed to Lungen Lu; lungenlu1965@163.com, Rongzhou Li; lirongzhou@163.com, and Xiaobo Cai; caixiaobo197908@163.com

Received 26 November 2020; Revised 14 January 2021; Accepted 19 January 2021; Published 1 March 2021

Academic Editor: Xiaolu Jin

Copyright © 2021 Qingqing Zhang et al. This is an open access article distributed under the Creative Commons Attribution License, which permits unrestricted use, distribution, and reproduction in any medium, provided the original work is properly cited.

Background and Aim. miRNAs play an important role in the development of human fibrosis. However, miRNA expression profiles during different stages of chronic hepatitis B (CHB) are not well defined. In this study, we aimed to further validate the features of 5 miRNA candidates from our previous study during different fibrotic stages and the value of diagnosis for liver fibrosis. **Methods.** Differential expression of five selected miRNAs (hsa-mir-1225-3p, hsa-mir-1238, hsa-miR-3162-3P, hsa-miR-4721, and hsa-miR-H7) was verified by qRT-PCR in the plasma of 83 patients and 20 healthy controls. The relative expression of these miRNAs was analyzed in different groups to screen target miRNA. A logistic regression analysis was performed to assess factors associated with fibrosis progression. The receiver operating characteristic (ROC) curve and discriminant analyses validated the ability of these predicted variables to discriminate the nonsignificant liver fibrosis group from the significant liver fibrosis group. Furthermore, the established models were compared with other prediction models to evaluate the diagnostic efficiency. **Results.** These five tested miRNAs all had signature correlations with hepatic fibrotic level ($p < 0.05$), and the upregulation trends were consistent with miRNA microarray analysis previously. The multivariate logistic regression analysis identified that a model of five miRNAs (miR-5) had a high diagnostic accuracy in discrimination of different stages of liver fibrosis. The ROC showed that the miR-5 has excellent value in diagnosis of fibrosis, even better than the Forns score, FIB-4, S index, and APRI. GO functions of different miRNAs mainly involved in various biological processes were markedly involved in HBV and revealed signaling pathways dysregulated in liver fibrosis of CHB patients. **Conclusions.** It was validated that the combination of these five miRNAs was a new set of promising molecular diagnostic markers for liver fibrosis. The diagnosis model (miR-5) can distinguish significant and nonsignificant liver fibrosis with high sensitivity and specificity.

1. Introduction

Hepatitis B virus (HBV) infection has been demonstrated as the major cause of chronic liver diseases which affects about 370 million people in the world [1]. Despite effective vaccination that has resulted in a decrease in acute HBV incidences in many countries, persistent infection of HBV remains a principal challenge [2, 3]. Therefore, it is very important to have an accurate method to diagnose and evaluate chronic hepatitis B-

(CHB-) related liver inflammation and fibrosis safely and conveniently [4]. Biopsy was an invasive method with good diagnostic performance with potential risk of various complications, and it is therefore difficult to be performed routinely [5]. However, the values of noninvasive methods such as image examination and blood tests, including fibrosis-related factors, HBV DNA levels, the presence of HBV antigens 2-4, and aminotransferases (ALT, AST), are limited in distinguishing patients with different fibrotic stages [6-8].

miRNAs are a class of small noncoding RNAs with ~22 nucleotides that regulate 20~80% of the host genes [9, 10]. A lot of studies have proven that different miRNA expressions are associated with liver fibrosis [11–13]. Wang et al. [14] found that miR-122, miR-194/192, miR-223, miR-21, miR155, and miR-29 were specifically expressed or enriched in several types of hepatic cells or in circulation, playing important roles in the pathogenesis of liver diseases. However, it is difficult to distinguish different stages of CHB by miRNA expression profiles. In our previous study, we found that different expressions of serum/plasma miRNAs are closely associated with hepatic fibrosis staging [15]. We identified 140 detectable miRNAs with fold change of expression ≥ 2 and p value < 0.01 in the different groups (Figure 1). We also found that the expressions of hsa-miR-1225-3p, hsv1-miR-H7-3p, hsa-miR-1238-3p, hsa-miR-3162-3p, and hsa-miR-4721 were significantly different between the nonsignificant liver fibrosis group and significant liver fibrosis group. Nevertheless, further investigations are required to explore the diagnostic effects of these 5 miRNA expression profiles.

In this study, these 5 miRNAs were selected as candidates according to our previous study and evaluated in patients with different stages of liver fibrosis. The diagnostic efficiency of our model was also compared with those of other prediction models such as aspartate aminotransferase-to-platelet ratio index (APRI), Forns score, fibrosis index based on the 4 factors (FIB-4), and Spearman correlation (S index). Furthermore, we analyzed the biological function of these miRNAs through bioinformatics analysis. We aim to explore the potential possibility of applying the model including these miRNAs as a stable, reliable, and easy modality for non-invasive diagnosis of hepatic fibrosis.

2. Patients and Methods

2.1. Patients. The CHB liver fibrosis patient cohort was obtained from Shanghai General Hospital and Chinese PLA No. 85 Hospital from July 2012 to December 2014, and 203 CHB patients were enrolled. The inclusion criteria were based on the diagnostic standards of the CHB set by the Chinese Medical Association: serum HBeAg positive/negative, HBsAg positive, HBV DNA positive, anti-HBe positive or negative, ALT persistent or recurrent abnormality, and histopathological evidence of liver injury. Exclusion criteria were concurrent infection with HIV, HCV, or HDV; alcohol daily intake over 30 g; history of liver transplantation; and liver malignancy, drug-induced liver diseases, autoimmune liver diseases, or other types of liver injury. Liver biopsy pathological examination was performed in all the included patients, and the fibrosis stage was evaluated according to the Scheuer pathological classification system [16]. The component of staging (S) was given in a numerical value ranging from 0 to 4 and used to describe disease progression of chronic HBV infection. S0 represents the absence of fibrosis; S1 represents enlarged, fibrotic portal tracts; S2 represents periportal or portal-portal septa, but intact architecture; S3 represents fibrosis with architectural distortion, but no obvious cirrhosis; and S4 represents definite cirrhosis. The patients with cirrhosis were also divided

into Child-Pugh level A (liver compensated cirrhosis) or Child-Pugh level B and Child-Pugh level C (decompensated cirrhosis). Another 20 normal participants aged from 30 to 50 years were enrolled as the control group. Healthy controls were recruited randomly from individuals who had no clinical symptoms of infectious diseases after regular physical examination, and HCV patients enrolled in this study were confirmed to have no other infectious diseases, such as HBV, HIV, and HSV, and have no drug treatment and also have no obvious hepatic steatosis, hepatic fibrosis, and hepatic tumors. This study was approved by the Ethical Committee of Rui'an People's Hospital and Shanghai Jiao Tong University Affiliated First People's Hospital, and all the participants voluntarily joined this study and provided tissue specimens with informed consent. Whole blood and biochemical assessment, coagulation function, HBV quantification, and HBV-DNA quantification were performed. Plasma samples were isolated within 1 h after receiving whole blood and then immediately stored at -80°C for standby use.

2.2. Taqman PCR Analysis. Total RNA was isolated from patients' plasma using mirVana™ PARIS™ (Ambion, America) following the manufacturer's instructions. The relative expression of miRNA was detected by Taqman PCR. The RNA concentration was checked by using a NanoDrop spectrophotometer and was purified with the QIAGEN Rneasy Mini Kit. After that, total RNA was converted to cDNA using Stem-loop RT primer and TaqMan reverse transcription kit in $15\ \mu\text{L}$ reaction. The PCR was using microRNA assays and PCR Master Mix and run using the Life ViiA™ 7 System thermal cycler with the following settings: 95°C for 10 min and 40 cycles of 10 s at 95°C and 30 s at 60°C . The qPCR data were expressed as minus delta Ct using spike-in control as the reference gene. This experiment adopts the external standard method, and cel-miR-39 was selected as the external reference gene in this experiment.

2.3. Assessment of Diagnostic Effectiveness. Diagnostic models of hsa-mir-1225-3p, hsa-mir-1238, hsa-miR-3162-3P, hsa-miR-4721, and hsa-miR-H7 were established, and the diagnostic efficacy was assessed. The receiver operating characteristic curve (ROC curve) of the subjects was established to evaluate the diagnostic efficacy of the individual miRNA, and the area under the curve (AUROC) was calculated by using SPSS 19.0. As a result, the sensitivity and specificity of the differential miRNA and diagnostic models were assessed by the ROC curve and AUROC. At the same time, the diagnostic value of the model was assessed by the ROC curve, and AUROC was compared with the Forns index, APRI, FIB-4 score, and S index of the diagnostic model. The Spearman correlation analysis was used to analyze the correlation between two variables.

2.4. Prediction of Target Genes. In order to predict the relative target genes roundly, TargetScan (<http://www.targetscan.org/>), miRanda (<http://www.microma.org/>), and RNA22 (<http://cbcsrv.watson.ibm.com/rna22.html>) were applied to predict the target genes of different miRNAs. In order to

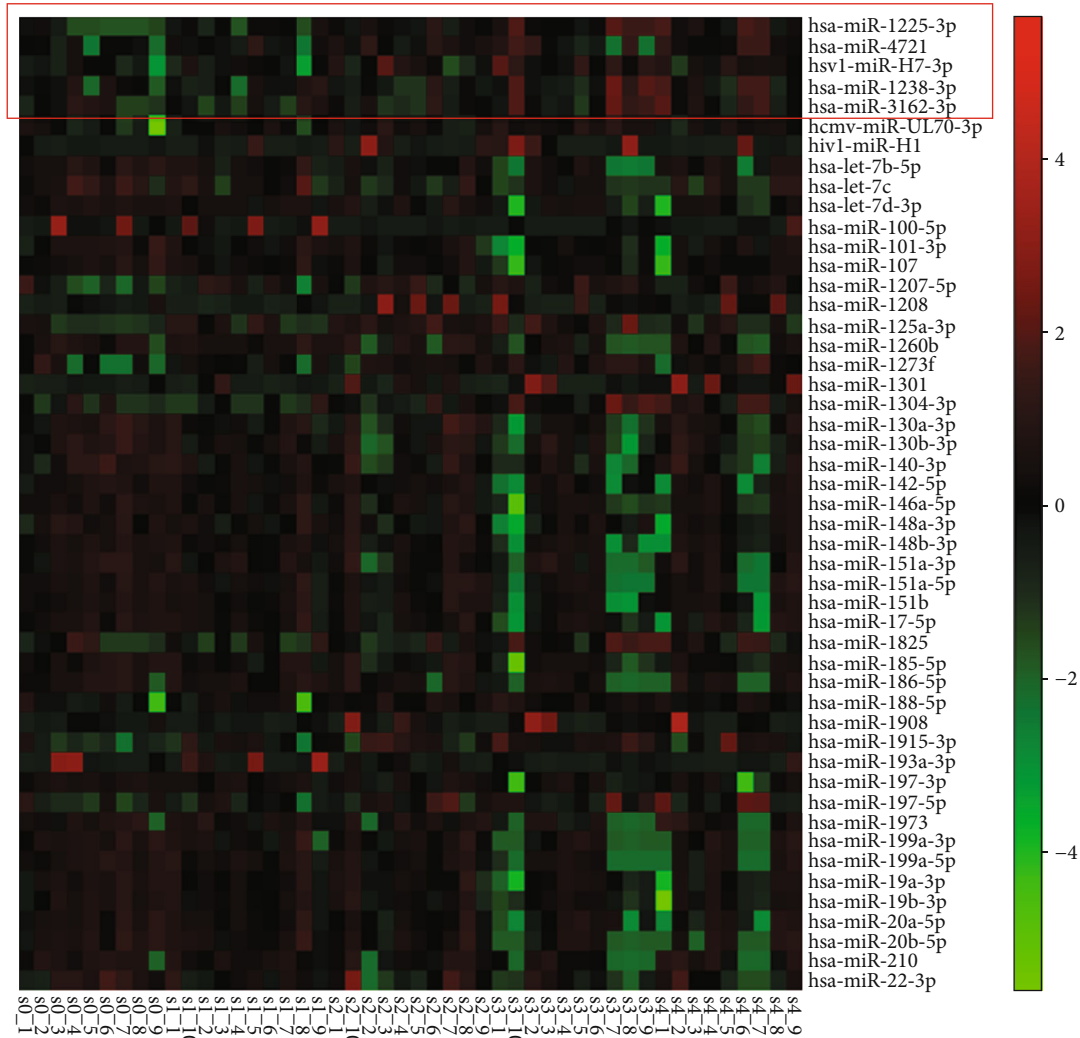


FIGURE 1: Heatmap of top 50 of 140 different miRNAs in patients with hepatitis B virus infection and hepatic fibrosis.

reduce the false-positive rate, the genes which were predicted by three software were taken as candidate target genes.

2.5. Gene Ontology (GO) Analysis. In order to detect the target genes of those miRNAs with different expression levels and to evaluate their function, GO annotation was applied to the target gene according to the GO database (<http://www.geneontology.org/>).

2.6. Statistical Analysis. The statistical analyses were performed using SPSS 19.0 (IBM, Armonk, NY, USA). Data are presented as the means \pm SE. The group *t*-test was used for the data which are consistent with normal distribution, and the Wilcoxon nonparametric test was used for the nonnormal distribution data. *p* values < 0.05 were considered significant. The ROC curve and AUROC analysis were performed using SPSS 19.0 as well. Logistic regression indicates a linear combination of miRNAs. ROC curves and AUROC were used to assess the sensitivity and specificity of miRNA biomarkers and construct the diagnostic models based on the predicted probability. The GO values involved with these genes were

determined, and the Fisher exact test and χ^2 test were used to determine the significance level and error rate of each GO value to enable screening of the significant GO terms reflected by the target gene. *p* < 0.01 was considered to indicate a statistically significant difference. In order to determine the cell pathways affected by the target gene with differential miRNA expression, the Fisher exact test and χ^2 square test were used to determine the significance of the pathways, in which the target gene is involved, based on the Kyoto Encyclopedia of Genes and Genomes (KEGG) database. *p* < 0.05 was considered to indicate a statistically significant difference.

3. Results

3.1. Clinical Characteristics of the Subjects for Hub miRNA Validation. Eighty-three patients with chronic HBV were divided into S0 (10), S1 (15), S2 (13), S3 (10), S4 (10), compensated cirrhosis (13), and decompensated cirrhosis groups (12) according to the Scheuer and Child-Pugh scoring system. Table 1 shows the demographic and clinical characteristics of all subjects included in the study. At this moment,

TABLE 1: Clinical characteristics of the 83 participators ($\bar{x} \pm s$).

Clinical characteristics	Control group (n = 20)	S0 group (n = 10)	S1 group (n = 15)	S2 group (n = 13)	S3 group (n = 10)	S4 group (n = 10)	CC group (n = 13)	DC group (n = 12)
Male/female	10/10	6/4	10/5	8/5	6/4	7/3	9/4	8/4
Age (years old)	38.8 ± 9.8	40.7 ± 14.9	33.8 ± 9.4	38.0 ± 8.4	39.4 ± 13.2	50.1 ± 12.6	51.3 ± 13.1	50.2 ± 17.4
Blood cell counts (10 ⁹ /L)	7.3 ± 2.1	5.9 ± 0.6	5.8 ± 1.0	5.8 ± 3.4	4.3 ± 1.2	5.8 ± 3.4	5.0 ± 1.8	4.2 ± 1.8
Hemoglobin (g/L)	140 ± 12	151 ± 15	148 ± 23	144 ± 16	136 ± 32	144 ± 19	130 ± 31	90 ± 19
Blood platelet (10 ⁹ /L)	175 ± 57	173 ± 12.8	175 ± 12.1	158 ± 24.1	121.3 ± 15.4	154.3 ± 20.1	105.3 ± 16.7	70.2 ± 17.8
ALT (U/L)	26.3 ± 9.3	79.5 ± 42.0	95.3 ± 33.3	124.1 ± 29.0	91.7 ± 17.5	57.1 ± 14.3	91.8 ± 15.2	30.8 ± 10.1
AST (U/L)	23.5 ± 7.1	65.2 ± 23.8	69.4 ± 11.2	91.6 ± 21.5	92.75 ± 19.9	46.4 ± 19.7	67.2 ± 17.2	56.1 ± 12.6
γ-GT (U/L)	31.2 ± 5.7	37.0 ± 18.1	50.8 ± 38.4	76.9 ± 25.8	58.8 ± 28.3	63.2 ± 29.1	61.1 ± 19.2	37.9 ± 13.4
ALP (U/L)	68.0 ± 11.0	69.2 ± 24.4	79.8 ± 22.5	125.5 ± 46.8	94.6 ± 27.9	87.9 ± 11.6	83.6 ± 13.2	100 ± 15.5
T-Bil (μmol/L)	13.6 ± 5.3	27.9 ± 7.41	22.2 ± 8.04	26.9 ± 3.2	19.1 ± 2.3	12.9 ± 4.4	23.3 ± 8.3	68.6 ± 12.3
D-Bil (μmol/L)	5.0 ± 1.2	15.2 ± 5.0	6.5 ± 2.2	11.6 ± 6.1	8.2 ± 3.7	3.6 ± 1.1	7.5 ± 3.3	47.9 ± 9.1
TP (g/L)	74.6 ± 8.3	67.6 ± 8.8	68.6 ± 8.3	72.4 ± 6.2	68.7 ± 8.0	66.8 ± 7.5	66.3 ± 9.6	53.2 ± 5.8
ALB (g/L)	44.5 ± 3.2	40.7 ± 3.7	40.2 ± 4.7	41.5 ± 3.6	39.0 ± 5.1	39.1 ± 5.1	30.3 ± 8.6	22.3 ± 9.4
TC (U/L)	3.3 ± 0.4	4.4 ± 1.0	3.2 ± 0.3	3.6 ± 0.4	3.8 ± 1.1	3.6 ± 0.8	4.8 ± 1.2	3.4 ± 0.2
TG (U/L)	0.6 ± 0.1	1.0 ± 0.4	1.0 ± 0.1	1.7 ± 0.4	1.2 ± 0.4	1.1 ± 0.4	1.4 ± 0.2	1.3 ± 0.3
AFP	12 ± 1.2	18.7 ± 32.1	6.2 ± 4.1	8.0 ± 13.4	28.8 ± 34.8	99.2 ± 12.1	104.2 ± 11.1	31.5 ± 11.2
INR	0.8 ± 0.01	0.97 ± 0.09	1.0 ± 0.03	1.1 ± 0.08	1.05 ± 0.07	1.6 ± 0.06	1.7 ± 0.02	1.8 ± 0.08
HBV-DNA (10 ⁷ U/L)	—	4.5 ± 1.1	13.1 ± 2.7	5.2 ± 2.1	3.1 ± 1.1	1.3 ± 0.2	0.9 ± 0.2	0.6 ± 0.3
HBeAg-positive rate (%)	—	30%	80%	58%	60%	40%	38%	33%

CC: compensated cirrhosis; DC: decompensated cirrhosis; CHB: chronic hepatitis B.

CHB liver fibrosis patients were classified into two groups: nonsignificant liver fibrosis group and significant liver fibrosis group. The nonsignificant liver fibrosis group consisted of 10 S0 and 15 S1 cases, while the significant liver fibrosis group consisted of 13 S2, 10 S3, and 10 S4 cases. Blood platelet differed significantly between the nonsignificant liver fibrosis group and significant liver fibrosis group ($p < 0.05$, Table 2). In order to know the difference of routine clinical indices between liver fibrosis patients and cirrhosis patients, the subjects were divided into the liver fibrosis group (consisting of S0-S3) and cirrhosis group (consisting of S4, compensated cirrhosis, and decompensated cirrhosis groups). And there were statistically different laboratory results for age, hemoglobin, blood cell counts, blood platelet, AST, TG, TC, AFP, INR, and HBeAg-positive rate between the two groups ($p < 0.05$, Table 3). In addition, there were significant differences of AST, ALP, ALB, INR, T-Bil, and D-Bil between compensated cirrhosis patients ($p < 0.05$, Table 4).

3.2. mRNA Expression Validation of Hub miRNAs in Participators. According to our previous study, 5 miRNAs include hsa-mir-1225-3p, hsa-mir-1238, hsa-miR-3162-3P, hsa-miR-4721, and hsa-miR-H7 which were chosen for further investigation. The expression of the 5 miRNAs was analyzed between the different groups. As shown in Figure 2(a), the

expression level of the 5 miRNAs was significantly different between the nonsignificant liver fibrosis group and significant liver fibrosis group ($p < 0.05$). At the same time, the expressions of hsa-mir-1225-3p, hsa-mir-1238, hsa-miR-3162-3p, hsa-miR-4721, and hsa-miR-H7 were upregulated more than 2-fold in the mild-severe fibrosis group (S0-1) and significant liver fibrosis group (S2-4). The trend of miRNA expression is consistent with the chip results, although the upregulation extent is not completely consistent with the chip results, and the results showed great reliability and credibility (Figures 2(b) and 3). Furthermore, single target miRNA of hsa-mir-1225-3p, hsa-mir-1238, hsa-miR-3162-3P, hsa-miR-4721, and hsa-miR-H7 cannot distinguish liver fibrosis (S0-3) from cirrhosis and compensated cirrhosis from decompensated cirrhosis (Table 5).

3.3. Diagnosis Value of Hub miRNAs for CHB Liver Fibrosis and Diagnostic Model Establishment. To explore the diagnostic potential of verified miRNAs for liver fibrosis in CHB patients, ROC curves were constructed. When the target miRNAs were used to diagnose significant hepatic fibrosis, the AUROC for hsa-miR-3162, hsa-miR-1225, hsa-miR-1238, hsa-miR-4721, and hsa-miR-H7 were as follows: 0.899 (95% CI: 0.803-0.995), 0.852 (95% CI: 0.737-0.967), 0.656 (95% CI: 0.521-0.803), 0.650 (95% CI: 0.508-0.792), and 0.650 (95% CI: 0.506-0.794), respectively. The results

TABLE 2: Clinical characteristics of the CHB nonsignificant liver fibrosis group (S0-1) and significant liver fibrosis (S2-4) cases ($\bar{x} \pm s$).

Clinical characteristics	S0-1	S2-4	p
Male/female	16/9	21/12	1.0
Age (years old)	35.4 \pm 14	42 \pm 12	0.064
Blood cell counts ($10^9/L$)	5.8 \pm 0.9	5 \pm 0.4	0.118
Hemoglobin (g/L)	149 \pm 22	142 \pm 23	0.224
Blood platelet ($10^9/L$)	173 \pm 20	145 \pm 17	0.04
ALT (U/L)	60.1 \pm 12.3	94 \pm 11.2	0.107
AST (U/L)	51.2 \pm 7.4	78 \pm 6.3	0.109
γ -GT (U/L)	45.2 \pm 13.9	67 \pm 15	0.123
ALP (U/L)	73.4 \pm 7.7	104 \pm 14.1	0.09
T-Bil (μ mol/L)	22.2 \pm 8.9	32.2 \pm 7.2	0.761
D-Bil (μ mol/L)	8.3 \pm 5.4	15.3 \pm 3.9	0.807
TP (g/L)	64.8 \pm 13	69.6 \pm 7.3	0.148
ALB (g/L)	36.8 \pm 16.2	32 \pm 5.9	0.291
TC (U/L)	4.3 \pm 0.7	4.4 \pm 1.3	0.889
TG (U/L)	1.47 \pm 0.7	1.1 \pm 0.3	0.065
AFP	10.8 \pm 1.7	41.9 \pm 8.3	0.08
INR	0.9 \pm 0.3	1.1 \pm 0.02	0.233
HBV-DNA (10^7 U/L)	9.8 \pm 0.9	4.8 \pm 0.6	0.743
HBeAg-positive rate (%)	60%	72%	0.399

TABLE 3: Clinical characteristics of the CHB liver fibrosis and liver cirrhosis group cases ($\bar{x} \pm s$).

Clinical data	Liver fibrosis group	Liver cirrhosis group	p
Male/female	21/11	30/18	0.815
Age (years old)	38 \pm 12	52 \pm 11	0.0001
Blood cell counts ($10^9/L$)	5.6 \pm 2.0	4.6 \pm 1.6	0.025
Hemoglobin (g/L)	145 \pm 23	124 \pm 28	0.001
Blood platelet ($10^9/L$)	155 \pm 12	112 \pm 15.5	0.002
ALT (U/L)	84 \pm 16.3	60 \pm 21.2	0.285
AST (U/L)	71 \pm 21	39 \pm 11.2	0.023
γ -GT (U/L)	54 \pm 12.1	53 \pm 31.2	0.926
ALP (U/L)	90 \pm 32.1	90 \pm 17.3	0.985
T-Bil (μ mol/L)	22 \pm 12.1	35 \pm 13.2	0.160
D-Bil (μ mol/L)	9.9 \pm 1.8	19.1 \pm 9.5	0.177
TP (g/L)	68 \pm 13	65 \pm 8.3	0.244
ALB (g/L)	39 \pm 9.6	35 \pm 6.7	0.104
TC (U/L)	4.5 \pm 1.1	3.7 \pm 0.8	0.004
TG (U/L)	1.3 \pm 0.6	0.9 \pm 0.3	0.003
AFP	14 \pm 11.1	45 \pm 8.5	0.029
INR	1 \pm 0.2	1.4 \pm 0.6	0.001
HBV-DNA (10^7 U/L)	8.7 \pm 0.6	6.3 \pm 0.7	0.932
HBeAg-positive rate (%)*	95%	45%	0.0001

TABLE 4: Clinical characteristics of the CHB liver cirrhosis CC and DC group cases ($\bar{x} \pm s$).

Clinical data	CC group	DC group	p
Male/female	16/7	8/4	0.071
Age (years old)	50.8 \pm 13.11	54.4 \pm 7.39	0.388
Blood cell counts ($10^9/L$)	4.8 \pm 1.57	4.2 \pm 1.87	0.430
Hemoglobin (g/L)	135 \pm 27	107 \pm 19	0.005
Blood platelet ($10^9/L$)	126 \pm 26	85 \pm 11	0.109
ALT (U/L)	76 \pm 9.7	30 \pm 9.4	0.181
AST (U/L)	58 \pm 13	3.7 \pm 0.64	0.0001
γ -GT (U/L)	62 \pm 12	37 \pm 7.5	0.086
ALP (U/L)	85 \pm 12.6	100 \pm 34.2	0.405
T-Bil (μ mol/L)	18 \pm 8.5	68 \pm 7.5	0.043
D-Bil (μ mol/L)	5.8 \pm 3.3	44 \pm 7.9	0.031
TP (g/L)	66 \pm 8.6	62 \pm 7.3	0.164
ALB (g/L)	37 \pm 7.3	32 \pm 4.4	0.050
TC (U/L)	3.8 \pm 1.0	3.7 \pm 0.6	0.775
TG (U/L)	1.0 \pm 0.3	0.72 \pm 0.24	0.001
AFP	52 \pm 12	31 \pm 9.3	0.459
INR	1.17 \pm 0.21	1.91 \pm 0.87	0.015
HBV-DNA (10^7 U/L)	9.8 \pm 0.9	5.3 \pm 0.7	0.782
HBeAg-positive rate (%)*	60%	33%	0.164

showed that miRNA-3162 and miRNA-1225 had relatively higher accuracy in indicating hepatic fibrosis than hsa-miR-1238, hsa-miR-H7, and hsa-miR-4721 (Figures 4(a)–4(e), Table 6). And then, two forecasting models of miR-5 (hsa-miR-3162, hsa-miR-1225, hsa-miR-1238, hsa-miR-4721, and hsa-miR-H7) and miR-2 (miRNA-3162 and miRNA-1225) were obtained from logistic regression analysis to predict significant hepatic fibrosis (S2-S4). The miR-5 and miR-2 were $\text{miR-5} = 1.115 * \text{miR1225} + 0.157 * \text{miR1238} + 6.256 * \text{miR3162} + 0.072 * \text{miR4721} - 0.831 * \text{miRH7} - 2.729$ and $\text{miR-2} = 0.483 * \text{miR1225} + 7.066 * \text{miR1238} - 2.276$, respectively. To evaluate whether miR-5 and miR-2 can be used as potential diagnostic models for significant hepatic fibrosis, ROC curve analyses were performed. The value of AUROC for miR-5 and miR-2 was 0.909 and 0.895, respectively, and revealed that miR-5 was superior to miR-2 in discriminating the significant hepatic fibrosis group (S2-S4) from the nonsignificant liver fibrosis group (S0-S1) (Figure 4(f), Table 6).

3.4. Comparison of Diagnostic Efficiency between miR-5 and Other Diagnostic Models. Noninvasive diagnosis indices or predictive models for hepatic fibrosis, including the Forns index, APRI, and FIB-4, are all established based on CHB. To analyze the correlation between each diagnostic model and liver fibrosis, the correlation coefficients (r) of the five miRNAs and five diagnostic models were evaluated by the Spearman correlation. The r values of miRNA-1225, miRNA-3162, miRNA-H7 and miR-5 were 0.267, 0.270, 0.295, and 0.632, respectively ($F < 0.05$). There was no

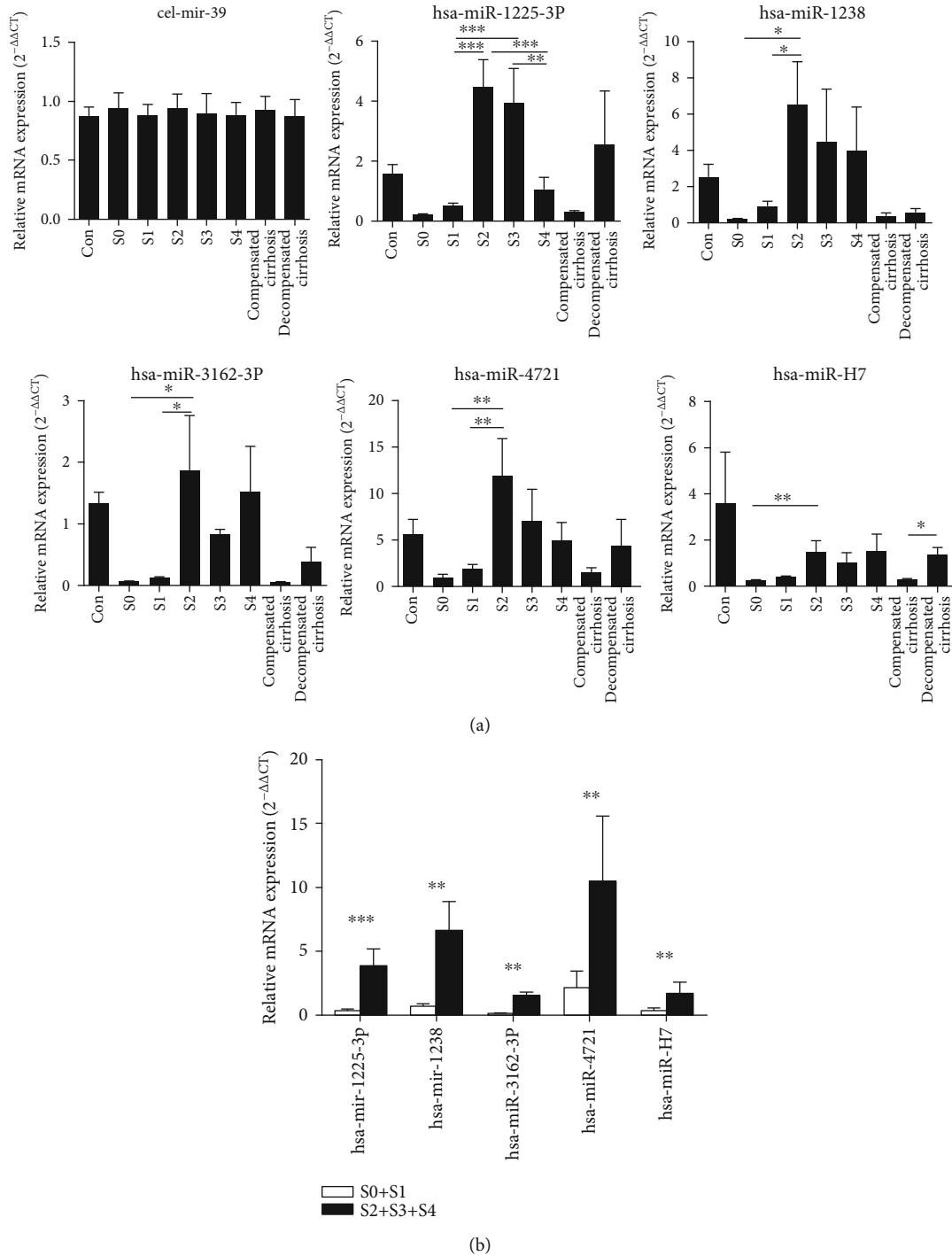


FIGURE 2: Relative mRNA expression level of different plasma microRNAs in cases of the chronic hepatitis B group and control group. (a) mRNA expression of hsa-miR-1225-3p, hsa-miR-1238, hsa-miR-3162-3P, hsa-miR-4721, hsa-miR-H7, and cel-mir-39 in normal control; CHB liver fibrosis S0 patients, S1 patients, S2 patients, S3 patients, and S4 patients; and CHB compensated cirrhosis patients and CHB decompensated cirrhosis patients. (b) mRNA expression of hsa-miR-1225-3p, hsa-miR-1238, hsa-miR-3162-3P, hsa-miR-4721, hsa-miR-H7, and cel-mir-39 in the CHB nonsignificant liver fibrosis group (S0-1) and significant liver fibrosis group (S2-4).

statistical significance for miRNA-1238, miRNA-4721, and APRI for liver fibrosis stages in these subjects. In the prediction of significant hepatic fibrosis (S2-S4), the value of AUROC for these miRNAs and diagnostic models is shown in Figure 4(f); the diagnostic models of miR-5, miRNA-3162, miRNA-1225, and Forns index had high diagnostic

value; and miR-5 had the highest AUROC and the highest diagnostic efficiency.

To further evaluate the diagnostic efficacy of the model miR-5 for significant liver fibrosis (S2-S4), the AUROC of these diagnostic models and five miRNAs were analyzed by using the MedCalc software. The result showed that the

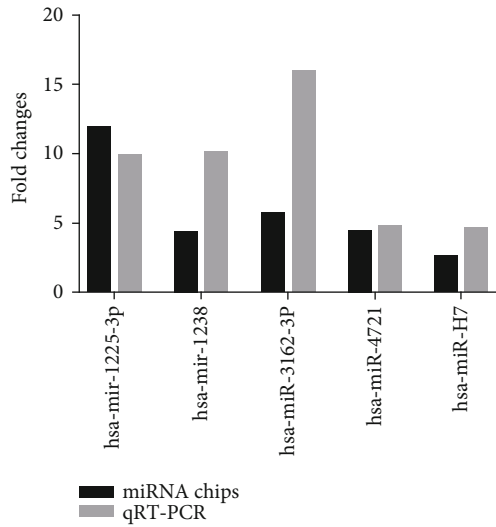


FIGURE 3: The fold changes of miRNA expression in the CHB nonsignificant liver fibrosis group and significant liver fibrosis group and their comparison in miRNA chips.

TABLE 5: p values of miRNA expression in the CHB liver fibrosis group, liver cirrhosis group, compensated cirrhosis group, and decompensated cirrhosis group.

miRNA	S0-S3 vs. liver cirrhosis		CC vs. DC	
	t	p	t	p
hsa-mir-1225-3p	1.277	0.205	-1.066	0.309
hsa-mir-1238	1.284	0.203	0.892	0.379
hsa-miR-3162-3P	0.386	0.701	0.602	0.551
hsa-miR-4721	1.112	0.269	-0.459	0.649
hsa-miR-H7	-0.712	0.478	-0.966	0.341

diagnostic efficacy of miR-5 was significantly better than that of the Forns index, APRI, FIB-4 score, S index, miRNA-H7, miRNA-4721, and miRNA-1238 ($p < 0.05$). At the same time, at a cut-off value of 0.37 for miR-5, the sensitivity was 90.6% and the specificity was 96% in discriminating significant liver fibrosis (Table 7).

3.5. Bioinformatics Analysis. GO functional analysis of 105 differential miRNAs (Table 3) revealed that various biological processes were markedly involved in HBV-related liver fibrosis including biopolymer metabolic processes, signal transduction, protein metabolism, and lipid metabolism. And the same result was obtained from the GO functional analysis of 5 differential miRNAs. The biological processes which were identified to have significant involvement of the differently expressed target gene included molecule functional activation, transmembrane transport, phosphotransferase activity upgrade, binding with protein, purine nucleotide metabolism upgrade, peptidase activation, oxidoreductase activation, binding with L-amino acid peptidase, and cytokine activation.

Pathway significance concentration analysis revealed that the differentially expressed genes were involved in 100 significant signal transduction pathways, including TGF- β /Smad, Wnt, MAPK, Jak/STAT, and VEGF, which have a significant impact on hepatic fibrosis (Figure 5).

4. Discussion

Early diagnosis and sustained follow-up of liver fibrosis are essential for the prevention of liver cirrhosis and end-stage hepatic disease [17]. Liver biopsy is an invasive procedure associated with complications and limitations such as intraobserver and interobserver variation, sampling error, and variability [18]. Therefore, many studies and great interest have been dedicated to the development of noninvasive tests to substitute liver biopsy for fibrosis assessment and follow-up [19, 20]. There are lots of noninvasive diagnosis indices and predictive models for hepatic fibrosis based on chronic hepatitis C (CHC) and alcoholic liver diseases, such as the Forns index [21], FibroTest [22], and APRI [23, 24]. However, a specific noninvasive predictive model for chronic HBV infection and hepatic fibrosis has not yet been developed.

miRNAs with high stability are good noninvasive diagnostic and prognostic markers to predict and monitor a disease in circulation [25]. Circulating miRNAs as diagnostic markers for different cancers were extensively studied in recent years. It has been verified that miRNAs play critical functional roles in HBV-driven hepatocellular carcinoma (HCC) [26–28]. However, there are controversies about the origin of circulating miRNAs and lack of specificity to reflect the disease biology. miR-144 is such a marker which has been identified as a circulating biomarker for different cancers such as hepatocellular carcinoma, renal cell carcinoma, and oral squamous cell carcinoma [29], whereas 6 serum miRNAs (miR-21, miR-199a-5p, miR-200c, miR-31, let-7a, and let-7d) have been identified as biomarkers for idiopathic pulmonary fibrosis, which still needs further validation [30, 31]. However, miRNAs for distinguishing different stages of liver fibrosis have not been well studied. During different statuses of CHB, the profiling of miRNA is also important for understanding the mechanisms of HBV-driven disease progression [2].

In our previous study, there were significant correlations between the levels of five miRNAs (hsa-mir-1225-3p, hsa-mir-1238, hsa-miR-3162-3P, hsa-miR-4721, and hsa-miR-H7) and CHB with different liver fibrosis stages [15]. In this study, we further identified these 5 miRNAs with distinct expression profiles in CHB patients with liver fibrosis. Statistical results showed that the level of clinical indicators did not correlate with the liver biopsy result well. The levels of target miRNAs were significantly different between the non-significant and significant liver fibrosis groups. The diagnosis effectiveness of the identified miRNAs in distinguishing fibrosis stages in CHB patients was determined by ROC curve analysis, whereas most of the previous studies have compared only healthy controls with CHB patients [32]. In this study, 2 logistic diagnosis models (miR-5 and miR-2) with different miRNAs were established, and our results demonstrate that miR-5 performed better than other diagnosis indices and predictive

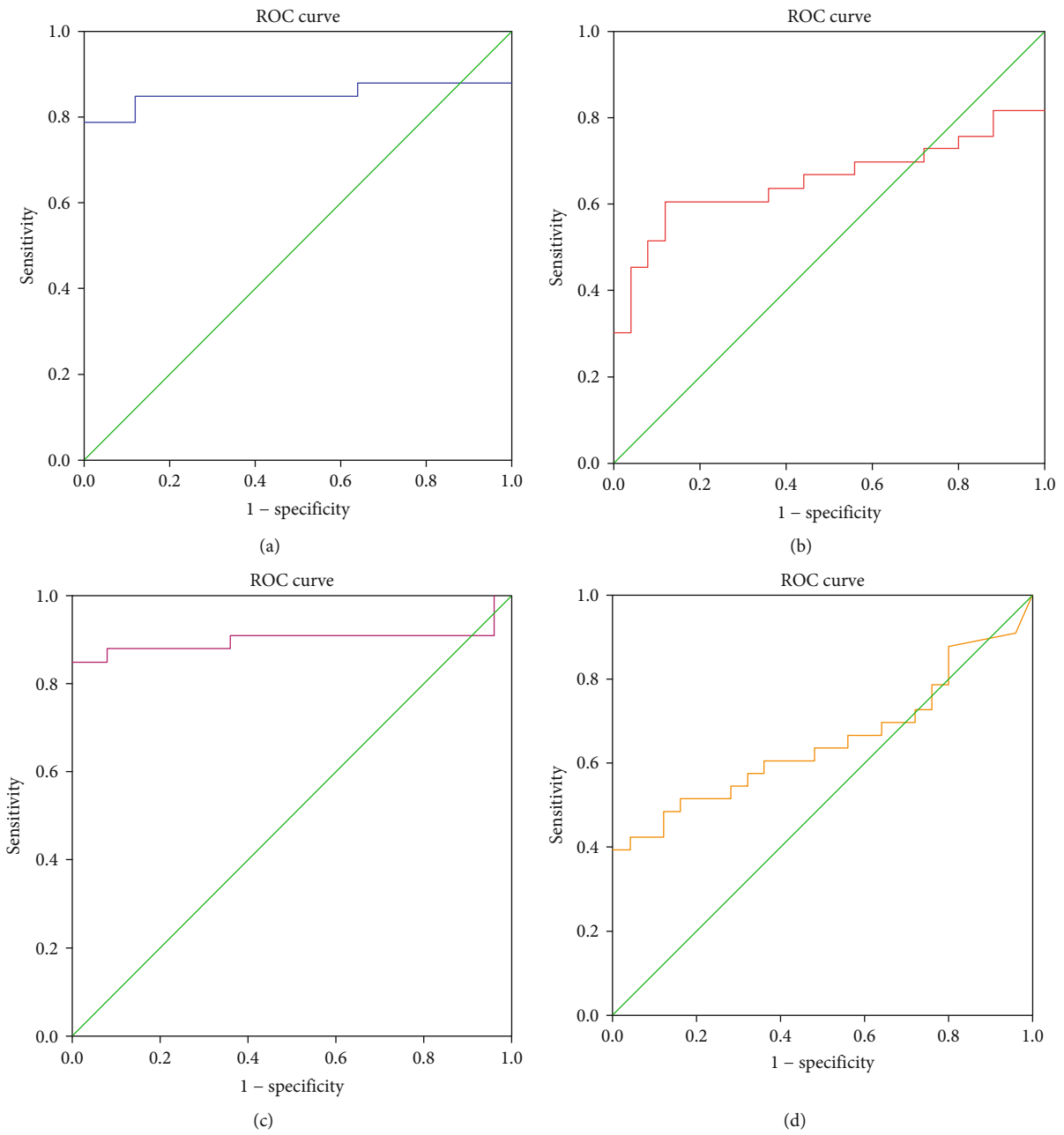


FIGURE 4: Continued.

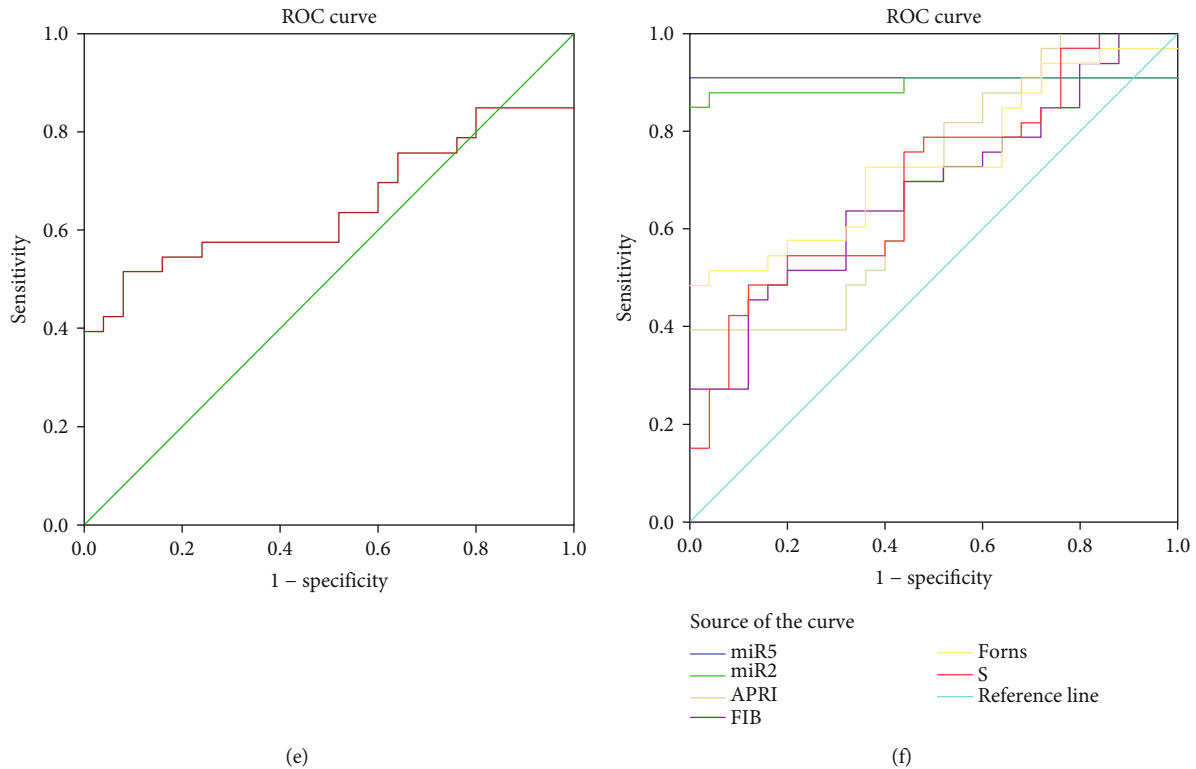


FIGURE 4: ROC curve analysis. ROC curve of hsa-mir-1225-3p (a), hsa-mir-1238 (b), hsa-miR-3162-3P (c), hsa-miR-4721 (d), and hsa-miR-H7 (e) in predicting significant liver fibrosis (S2-4). (f) ROC curve of diagnostic models miR-5, miR-2, APRI, FIB-4, Forns, and S in predicting significant liver fibrosis (S2-4).

TABLE 6: Analysis of the AUROC between the miRNA-5 diagnosis model and other diagnosis models.

Variable	Area	SE	<i>p</i> value	Sensitivity (%)	Specificity (%)	95% CI	
						Lower	Upper
miR-5	0.909	0.050	<0.001	90.9	100	0.811	1.000
miRNA-3162	0.899	0.049	<0.001	84.8	100	0.803	0.995
miR-2	0.895	0.051	<0.001	84.8	100	0.794	0.995
miRNA-1225	0.852	0.059	<0.001	78.8	100	0.737	0.967
S	0.697	0.069	0.011	48.5	88	0.562	0.832
APRI	0.696	0.069	0.011	81.8	48	0.560	0.832
miRNA-1238	0.662	0.072	0.036	60.6	80	0.521	0.803
Forns	0.737	0.065	0.002	48.5	100	0.610	0.864
miRNA-4721	0.650	0.073	0.052	39.4	100	0.508	0.792
miRNA-H7	0.650	0.073	0.052	51.5	92	0.506	0.794
FIB-4	0.679	0.070	0.021	45.5	88	0.542	0.815

models (Forns index, S index, FIB-4, and individual miRNAs) in distinguishing different liver fibrosis stages.

CHB patients could develop hepatic decompensation and related complications [33]. To evaluate the relationship between the miRNA markers and the compensatory capability of liver function, we examined the levels of the miRNAs in compensated or decompensated cirrhosis patients. We found that the 5 miRNAs were upregulated as deterioration of liver compensatory ability and significantly different between the two groups. Therefore, these miRNAs can be used to evaluate

liver decompensation in addition to diagnosing the stage of liver fibrosis. At the same time, the optimum cut-off level of 0.37 of miR-5 was also determined for the diagnosis of liver fibrosis in CHB patients with the sensitivity of 90.6% and specificity of 96% in discriminating different stages of CHB fibrosis.

Genome informatics analysis also indicates that liver fibrosis is related to the GO functions of these differential miRNAs associated with biological processes, such as bio-polymers, signal transduction, protein metabolism, and lipid

TABLE 7: Clinical characteristics of the 57 chronic hepatitis B patients for miRNA chip analysis ($\bar{x} \pm s$).

Group	Critical value		Se	Spe	PPV	NPV	J	LR+	LR-	AUROC
	<0.37	≥0.37								
S0-1	29	1	90.6%	96%	96.6%	88.8%	0.866	22.65	0.097	0.909
S2-4	3	24								

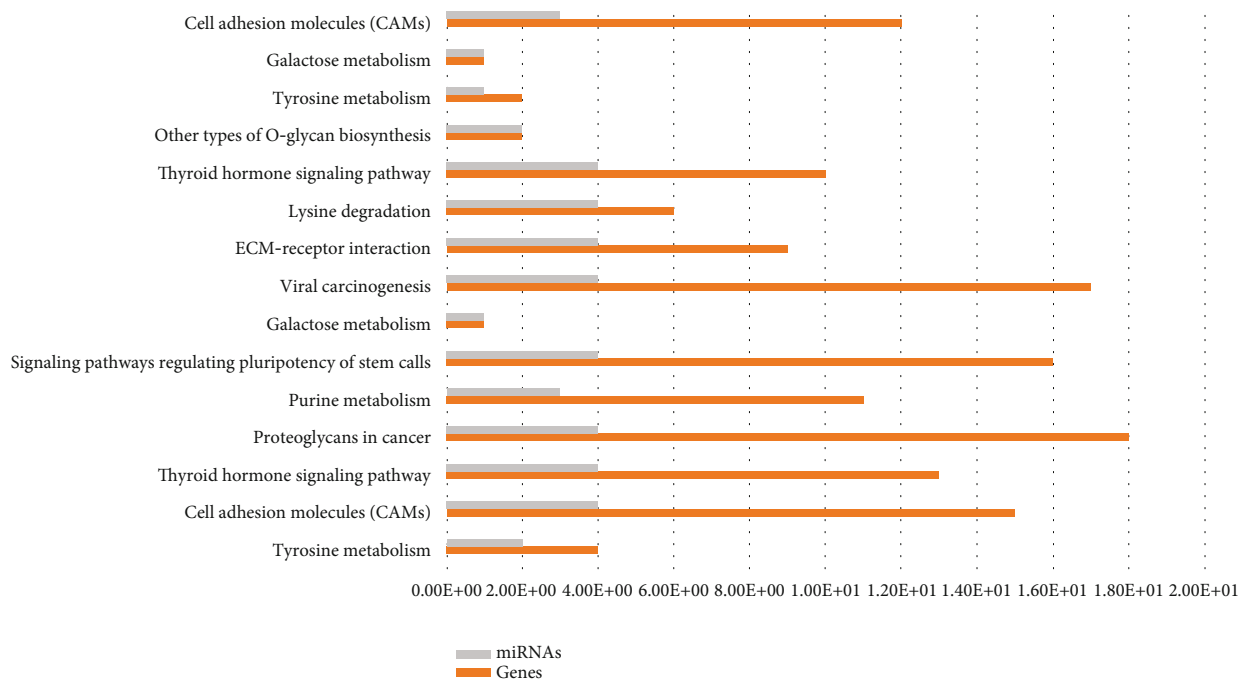


FIGURE 5: Functional enrichment KEGG pathway analysis of miRNAs.

metabolism. The pathway significance analysis revealed more than 100 pathways, which were significantly dysregulated in human CHB-related liver fibrosis. All of these genomic phenomena will help us to explore the potential pathogenesis of this disease.

In conclusion, our study emphasizes the importance of an integrated approach to identify a useful circulating biomarker for the diagnosis of the disease. A comparatively larger sample size might improve the strength of the study, but our findings elucidate a correlation of these disease-specific hepatic miRNAs as biomarkers in detecting human CHB liver fibrosis. Further analysis of the expression profiles of the miRNAs in different stages of liver fibrosis revealed that these miRNAs were differently expressed in certain stages of fibrosis. All these findings would benefit our understanding of the expression profiles of circulating miRNAs in different stages of HBV-driven disease and the development of novel noninvasive diagnostic tools for the identification of fibrosis in CHB patients. In addition, other categorization factors such as inflammation and qualification of viral load will be explored in the further study.

Data Availability

The data used to support the findings of this study are included within the article.

Conflicts of Interest

All authors declare that they have no conflict of interest.

Authors' Contributions

ZQQ, ZQD, LLG, LRZ, and CXB conceived the study design and supervised the scientific work. ZQQ, ZQD, and LBH performed the experiments. ZQQ, QY, and LZH analyzed the data and prepared the figures and tables. ZQQ, ZQD, and LBH wrote the manuscript. LLG, LRZ, and CXB revised the manuscript. All authors contributed to and approved the final manuscript.

Acknowledgments

This study was funded by the National Science and Technology Major Projects of China (2017ZX10202203-007-005), National Science and Technology Major Special Project for Drug Development (2018ZX09201016), and Wenzhou Science and Technology Project (Y20190526).

References

[1] A. Schweitzer, J. Horn, R. T. Mikolajczyk, G. Krause, and J. J. Ott, "Estimations of worldwide prevalence of chronic hepatitis B virus infection: a systematic review of data published

- between 1965 and 2013,” *The Lancet*, vol. 386, no. 10003, pp. 1546–1555, 2015.
- [2] B.-X. Jin, Y.-H. Zhang, W.-J. Jin et al., “MicroRNA panels as disease biomarkers distinguishing hepatitis b virus infection caused hepatitis and liver cirrhosis,” *Scientific Reports*, vol. 5, no. 1, article 15026, 2015.
- [3] H.-T. Zhu, R.-B. Liu, Y.-Y. Liang et al., “Serum microRNA profiles as diagnostic biomarkers for HBV-positive hepatocellular carcinoma,” *Liver International*, vol. 37, no. 6, pp. 888–896, 2017.
- [4] Y. Wen, S.-F. Peng, L. Fu et al., “Serum levels of miRNA in patients with hepatitis B virus-associated acute-on- chronic liver failure,” *Hepatobiliary & Pancreatic Diseases International*, vol. 17, no. 2, pp. 126–132, 2018.
- [5] A. Sinigaglia, E. Lavezzo, M. Trevisan et al., “Changes in microRNA expression during disease progression in patients with chronic viral hepatitis,” *Liver International*, vol. 35, no. 4, pp. 1324–1333, 2015.
- [6] A. Valsamakis, “Molecular testing in the diagnosis and management of chronic hepatitis B,” *Clinical Microbiology Reviews*, vol. 20, no. 3, pp. 426–439, 2007.
- [7] C. L. Zhu, W. T. Li, Y. Li, and R. T. Gao, “Serum levels of tissue inhibitor of metalloproteinase-1 are correlated with liver fibrosis in patients with chronic hepatitis B,” *Journal of Digestive Diseases*, vol. 13, no. 11, pp. 558–563, 2012.
- [8] P. A. Schmeltzer and J. A. Talwalkar, “Noninvasive tools to assess hepatic fibrosis: ready for prime time?,” *Gastroenterology Clinics of North America*, vol. 40, no. 3, pp. 507–521, 2011.
- [9] K. Yu, Q. Li, and N. Li, “MicroRNA profile in peripheral blood mononuclear cells from hepatitis B virus infected patients,” *Annals of Hepatology*, vol. 17, no. 6, pp. 1012–1020, 2018.
- [10] M. El-Hefny, S. Fouad, T. Hussein et al., “Circulating miRNAs as predictive biomarkers for liver disease progression of chronic hepatitis C (genotype-4) Egyptian patients,” *Journal of Medical Virology*, vol. 91, no. 1, pp. 93–101, 2019.
- [11] S. Roy, F. Benz, T. Luedde, and C. Roderburg, “The role of miRNAs in the regulation of inflammatory processes during hepatofibrogenesis,” *Hepatobiliary Surgery and Nutrition*, vol. 4, no. 1, pp. 24–33, 2015.
- [12] J. Lambrecht, S. Verhulst, H. Reynaert, and L. A. van Grunsven, “The miRFIB-score: a serological miRNA-based scoring algorithm for the diagnosis of significant liver fibrosis,” *Cell*, vol. 8, no. 9, p. 1003, 2019.
- [13] A. Abdel-Al, E. El-Ahwany, M. Zoheiry et al., “Mirna-221 and mirna-222 are promising biomarkers for progression of liver fibrosis in hcv egyptian patients,” *Virus Research*, vol. 253, pp. 135–139, 2018.
- [14] X. Wang, Y. He, B. Mackowiak, and B. Gao, “MicroRNAs as regulators, biomarkers and therapeutic targets in liver diseases,” *Gut*, vol. 322526, 2020.
- [15] Q. Zhang, M. Xu, Y. Qu et al., “Analysis of the differential expression of circulating microRNAs during the progression of hepatic fibrosis in patients with chronic hepatitis B virus infection,” *Molecular Medicine Reports*, vol. 12, no. 4, pp. 5647–5654, 2015.
- [16] J. H. Lefkowitz, “Liver biopsy assessment in chronic hepatitis,” *Archives of Medical Research*, vol. 38, no. 6, pp. 634–643, 2007.
- [17] A. Ghosh, A. Ghosh, S. Datta et al., “Hepatic mir-126 is a potential plasma biomarker for detection of hepatitis b virus infected hepatocellular carcinoma,” *International Journal of Cancer*, vol. 138, pp. 2732–2744, 2016.
- [18] P. K. Mada, M. E. Malus, D. A. S. Koppel et al., “Predicting liver fibrosis in the hepatitis C population: concordance analysis between noninvasive scoring systems and percutaneous liver biopsy,” *Cureus*, vol. 12, no. 9, article e10376, 2020.
- [19] M. Qiao, J. H. Yang, Y. Zhu, C. H. Ren, and J. P. Hu, “GC-MS analysis and anti-hepatic fibrosis effect of volatile oil from celery seed by different extraction methods,” *Chinese Journal of Modern Applied Pharmacy*, vol. 36, no. 21, pp. 2625–2632, 2019.
- [20] C. Hayes and K. Chayama, “MicroRNAs as biomarkers for liver disease and hepatocellular carcinoma,” *International Journal of Molecular Sciences*, vol. 17, no. 3, p. 280, 2016.
- [21] P. S. Mitchell, R. K. Parkin, E. M. Kroh et al., “Circulating microRNAs as stable blood-based markers for cancer detection,” *Proceedings of the National Academy of Sciences of the United States of America*, vol. 105, no. 30, pp. 10513–10518, 2008.
- [22] X. Chen, Y. Ba, L. Ma et al., “Characterization of microRNAs in serum: a novel class of biomarkers for diagnosis of cancer and other diseases,” *Cell Research*, vol. 18, no. 10, pp. 997–1006, 2008.
- [23] Z. H. Lin, Y. N. Xin, Q. J. Dong et al., “Performance of the aspartate aminotransferase-to-platelet ratio index for the staging of hepatitis C-related fibrosis: an updated meta-analysis,” *Hepatology*, vol. 53, no. 3, pp. 726–736, 2011.
- [24] C. T. Wai, J. K. Greenon, R. J. Fontana et al., “A simple non-invasive index can predict both significant fibrosis and cirrhosis in patients with chronic hepatitis C,” *Hepatology*, vol. 38, no. 2, pp. 518–526, 2003.
- [25] S. Bao, J. Zheng, N. Li et al., “Serum microRNA levels as a non-invasive diagnostic biomarker for the early diagnosis of hepatitis b virus-related liver fibrosis,” *Gut and Liver*, vol. 11, no. 6, pp. 860–869, 2017.
- [26] Y.-J. Chen, J.-M. Zhu, H. Wu et al., “Circulating microRNAs as a fingerprint for liver cirrhosis,” *PLoS One*, vol. 8, no. 6, article e66577, 2013.
- [27] K. R. Van Keuren-Jensen, I. Malenica, A. L. Courtright et al., “microRNA changes in liver tissue associated with fibrosis progression in patients with hepatitis C,” *Liver International*, vol. 36, no. 3, pp. 334–343, 2016.
- [28] E. El-Ahwany, F. Nagy, M. Zoheiry et al., “Circulating miRNAs as predictor markers for activation of hepatic stellate cells and progression of HCV-induced liver fibrosis,” *Electronic Physician*, vol. 8, no. 1, pp. 1804–1810, 2016.
- [29] M. Zhou, Y. Wu, H. Li, and X. Zha, “MicroRNA-144: a novel biological marker and potential therapeutic target in human solid cancers,” *Journal of Cancer*, vol. 11, no. 22, pp. 6716–6726, 2020.
- [30] G. Yang, L. Yang, W. Wang, J. Wang, J. Wang, and Z. Xu, “Discovery and validation of extracellular/circulating microRNAs during idiopathic pulmonary fibrosis disease progression,” *Gene*, vol. 562, no. 1, pp. 138–144, 2015.
- [31] C. H. Lee, J. H. Kim, and S. W. Lee, “The role of microRNA in pathogenesis and as markers of HCV chronic infection,” *Current Drug Targets*, vol. 18, no. 7, pp. 756–765, 2017.
- [32] P. Qi, S.-q. Cheng, H. Wang, N. Li, Y.-f. Chen, and C.-f. Gao, “Serum microRNAs as biomarkers for hepatocellular carcinoma in Chinese patients with chronic hepatitis B virus infection,” *PLoS One*, vol. 6, no. 12, article e28486, 2011.
- [33] R. Chen, J. C. Wu, T. Liu, Y. Qu, L. G. Lu, and M. Y. Xu, “MicroRNA profile analysis in the liver fibrotic tissues of chronic hepatitis b patients,” *Journal of Digestive Diseases*, vol. 18, no. 2, pp. 115–124, 2017.

Research Article

Phylogenetic Analysis of ALV-J Associated with Immune Responses in Yellow Chicken Flocks in South China

Qihong Zhang ^{1,2}, Guodong Mo,^{1,2} Tingting Xie,^{1,2} Zihao Zhang,^{1,2} Huali Fu,^{1,2} Ping Wei,³ and Xiquan Zhang ^{1,2}

¹Guangdong Provincial Key Laboratory of Agro-Animal Genomics and Molecular Breeding, College of Animal Science, South China Agricultural University, Guangzhou 510642, China

²Key Lab of Chicken Genetics, Breeding and Reproduction, Ministry of Agriculture, Guangzhou 510642, China

³College of Animal Science and Technology, Guangxi University, Nanning 530004, China

Correspondence should be addressed to Xiquan Zhang; xqzhang@scau.edu.cn

Received 8 December 2020; Revised 23 December 2020; Accepted 22 January 2021; Published 9 February 2021

Academic Editor: Shuai Chen

Copyright © 2021 Qihong Zhang et al. This is an open access article distributed under the Creative Commons Attribution License, which permits unrestricted use, distribution, and reproduction in any medium, provided the original work is properly cited.

The aim of this study was to better understand the sequence characteristics and immune responses in avian leukosis virus subgroup J (ALV-J) infected yellow chicken flocks in South China. We isolated four strains of ALV-J virus from these flocks, which were then identified by several methods, including subtype-specific polymerase chain reaction (PCR), enzyme-linked immunosorbent assay (ELISA), and immunofluorescence assay (IFA). All four viruses were sequenced for their complete genomes and named GD19GZ01, GD19GZ02, GD19GZ03, and GD19GZ04. In comparison with the reference sequence, the homology analysis showed that the *gag* and *pol* genes were relatively conserved, whereas *env* contained much variation. Both GD19GZ01 and GD19GZ02 almost entirely lacked the rTM region and E element, while the latter was retained in GD19GZ03 and GD19GZ04. Moreover, the virus replication levels in GD19GZ03 and GD19GZ04 were much higher than those in GD19GZ01 and GD19GZ02. And three virus recombination events in GD19GZ01 and GD19GZ02 were revealed by the results of PDR5 and SimPlot software analysis. Additionally, we found that some interferon-stimulating genes (*CH25H*, *MX*, *PKR*, *OAS*, and *ZAP*) and inflammatory mediators (*IL-4*, *IL-6*, *IL-10*, *IL-12*, *IL-18*, and *TNF- α*) were significantly upregulated in the immune system organs of clinical chickens. Taken together, these findings clarify and reveal the sequence characteristics and trends in the variation of ALV-J infection in yellow chicken flocks of South China.

1. Introduction

Avian leukosis virus (ALV) is a type of avian retrovirus that belongs to the genus *Alpharetrovirus* of the Retroviridae family. According to the molecular biological characteristics of serum neutralization testing, host range, and envelope glycoproteins, the ALVs can be divided into 10 subgroups corresponding to A~J [1, 2]. The ALV-J is an exogenous virus, notable for its extremely high pathogenicity and infectivity, and it is far more harmful to chickens than are the other subgroups [3]. In China, the first record of poultry broilers found infected with ALV-J was in 1991. In recent years, the host range of ALV-J has expanded to the commercial egg layers and the breeds of China [4]. Studies have shown that ALV-J could induce different types of tumors in the liver, spleen,

kidney, heart, bursa, thymus, and ovaries of chickens, such as hemangioma (He) and myeloma (ML) [5, 6]. Importantly, immunosuppression and immune tolerance are induced by ALV-J in infected birds, and this will significantly reduce the effectiveness of various vaccines, which could make birds more susceptible to secondary infections by other viruses or bacteria [7, 8]. Furthermore, ALV-J could coinfect host birds along with other ALV subgroups or even other viruses [10–13]. Due its RNA dimer structure and reverse transcriptase activity, as a retrovirus, ALV-J has a high frequency of mutation events, and it is prone to mutation or recombination.

The yellow chicken breeding industry is a crucial component of the larger poultry industry in South China. Yet, since many small farms still do not strictly screen and eradicate ALVs, coupled to the lack of effective vaccines or therapeutic

drugs, the yellow chicken industry has been continuously threatened by ALV-J outbreaks in South China in recent years [9, 10]. In this study, four strains of the ALV-J virus were isolated from the egg-type yellow chicken at a local farm in South China. We cloned and sequenced the full-length ALV-J virus genomes and analyzed their molecular characteristics. Interestingly, whole-genome analysis of the virus sequence revealed the four strains belonged to the ALV J subgroup, but their molecular sequence characteristics and virus replication levels *in vitro* were significantly different. The results of this study enable a better understanding of the clinical symptoms and molecular characteristics of the virus sequence of ALV-J infections in chicken flocks of South China. This provides important timely data for clarifying the evolution and variation trends of ALV-J.

2. Materials and Methods

2.1. Sick Chicken Samples. A group of parental yellow chickens of the egg-type in a local farm in South China showed telltale symptoms of infection, such as a pale cockscomb, listlessness, a thin body, cluttered feathers, and obvious hemangiomas on their skin and digits. To understand the epidemiology ALVs' infection in yellow chickens, a total of 198 birds (40 weeks old) from that farm were analyzed. In short, anticoagulated blood samples were collected aseptically from each yellow chicken, whose blood was centrifuged to obtain plasma for the virus isolation. According to the previously described method [11], the single-layer DF-1 cells were infected with plasma, after which the cell supernatant was detected by an enzyme-linked immunosorbent assay (Avian Leukosis Virus Antibody Test Kit, IDEXX, USA). Positive individuals were dissected, and their tumor samples were collected aseptically, including the liver, spleen, and kidney, among others, which were fixed with 10% neutral formalin buffer or stored at -80°C till their later use.

2.2. Histopathology. Fresh tissues (liver, spleen, kidney) were collected, fixed with 10% neutral formalin buffer, then dehydrated, embedded in paraffin, sliced, and then stained with hematoxylin and eosin (HE) [12]. The prepared section samples were observed under a light microscope (ECLIPSE 80i Nikon, Japan) for histopathology.

2.3. Detection of ALVs. The peripheral blood was collected aseptically in an anticoagulation tube, of which 200 μl of blood per chicken was taken for its DNA extraction, performed with the NRBC Blood DNA Kit (Omega, USA). This extracted blood DNA was used as the substrate for PCR. A previous methodology was referred to and followed to synthesize specific primers used for each subgroup of ALVs, which also included specific primers for the Marek's disease virus (MDV) and reticuloendothelial hyperplasia virus (REV) [13, 14]. The PCR reaction conditions were as follows: 95°C for 5 min, 95°C for 30 s, then 50°C to 60°C for 30 s, 72°C for 45 s (32 cycles), ending with 72°C for 5 min (Table 1). The ensuing PCR products were detected on a 1% agarose gel (containing 0.5 $\mu\text{g}/\text{ml}$ ethylene bromide).

2.4. Virus Isolation. Since DF-1 cells were only sensitive to exogenous virus particles, the interference of endogenous virus replication could be ruled out [15]. The remaining anticoagulated blood in the preceding step (section above "Detection of ALVs") was centrifuged at 1200 rpm and 4°C for 15 min. The resulting plasma was separated and stored at -80°C . According to a previously described method [9], the plasma samples were inoculated into a 24-well plate containing a DF-1 cell suspension (approximately 1.75×10^5 cells/well), and the plate then placed at 37°C in the presence of 5% CO_2 . After 24 h, the culture solution was removed and replaced with fresh cell maintenance solution (1% Foetal Bovine Serum (FBS), 100 U/ml penicillin, and 100 U/ml streptomycin). These cells were maintained at 37°C under 5% CO_2 for 5–7 days with daily monitoring. Supernatants and precipitated substrates were centrifuged and harvested after the cells had been frozen and thawed three times. According to the manufacturer's instructions, the supernatants were tested for ALV-specific antibodies (namely p27) by ELISA (IDEXX, USA). Then, according to the manufacturer's instructions, the precipitated substrates underwent DNA extraction, using the Tissue DNA Kit (Omega, USA), followed by the full-length amplification of the proviral genome by the PCR.

2.5. Proviral Genome Full-Length Amplification. According to the conserved region of the ALV-J original strain HPRS-103, four pairs of specific primers were designed [11], enabling the full-length viral genome to be amplified in segments. The gel-purified PCR product was ligated into a pMD18-T (Takara Biotechnology, Japan) cloning vector and transformed into DH5 α *Escherichia coli* competent cells. After the transformation's completion, the bacterial solution was evenly spread on an agar plate containing ampicillin and incubated at 37°C for 12–16 h. Finally, the recombinant plasmid harboring the target DNA fragment detected by the PCR was sent to TSINGKE Biotech (Beijing, China) for sequencing. Three independent cloned plasmids were used in each group. The primer sequences are listed in Table 1.

2.6. Sequence Alignments and Analysis. All sequences were aligned and analyzed using DNASTar version 7.1. All the ALVs' strain reference sequences are from the National Center for Biotechnology Information (NCBI) GenBank database (their accession numbers can be found in Table 2). Phylogenetic analysis was performed using MEGA-X by applying neighbor-joining and maximum parsimony methods with 1000 bootstrap replicates [16]. The transcriptional regulatory elements of U3 in the ALV-J structure were analyzed using the online service system of NSITE (from Soft Berry).

2.7. Immunofluorescence Assay (IFA). Those samples that tested positive for infection by ELISA were also tested by IFA. Briefly, the plasma was used to inoculate a monolayered 24-well plate. After incubation for 2 h, the supernatant was removed, and a 1% FBS cell maintenance solution was added to prolong the culture for 4–5 days. After fixing and sealing the cells, the ALV-specific monoclonal antibody JE9 (kindly

TABLE 1: The primers used to detect the ALVs and to amplify the full-length proviral genome of ALV-J isolates.

Primer ^a	Sequence (5'–3')	Annealing temperature (°C)	Size of PCR products (bp)
MDV-F	GGATGAGGTGACTAAGAAAG	59	560
MDV-R	CGAACCAAAGGTAACACACG		
REV-F	GCCTTAGCCGCCATTGTA	53	383
REV-R	CCAGCCTACACCACGAACA		
ALV-A-F	GGATGAGGTGACTAAGAAAG	50	692
ALV-A-R	AGAGAAAGAGGGGTGTCTAAGGAG		
ALV-B-F	GGATGAGGTGACTAAGAAAG	50	847
ALV-B-R	TGGACCAATTCTGACTCATT		
ALV-C-F	GGATGAGGTGACTAAGAAAG	50	860
ALV-C-F	GAGGCCAGTACCTCCCACG		
ALV-D-F	GGATGAGGTGACTAAGAAAG	50	797
ALV-D-F	ATCCATACGCACCACAGTATTCG		
ALV-J-H5	GGATGAGGTGACTAAGAAAG	55	545
ALV-J-H7	CGAACCAAAGGTAACACACG		
F: J-1F	TGTAGTGTTATGCAATACTCTT	52	2100
F: J-1R	CGACCCAGTTTGTCCATCCCTC		
F: J-2F	AGCACCTCCACGCTGACCAC	59	2100
F: J-2R	GGTGGTCGGTAACCCTCACTTTCA		
F: J-3F	GACCCTGCCCTGCCTCTGGAA	59	1800
F: J-3R	CGACGAAATAATAACCACGCACA		
F: J-4F	GCGTGGTTATTATTTCCGTCGTCC	59	2400
F: J-4R	TGAAGCCTTCGCTTCATGCAGGT		

provided by Dr. Aijian Qin, Yangzhou University, Yangzhou, China) as the primary antibody and FITC-labeled antimouse IgG (Bioss, Beijing, China) were used. Cell morphology was observed under a fluorescence microscope, with images recorded using NIS-Elements BR analysis software (Nikon, Japan).

2.8. RNA Isolation and qPCR. Total RNA was extracted using TRIzol reagent (Invitrogen) from tissues or cells and reversed-transcribed with a PrimeScript RT reagent kit with gDNA Eraser (Takara Biotechnology, Japan) according to the manufacturer's instructions. qPCR was performed on a Biorad CFX96 Real-Time Detection System using iTaq™ Universal SYBR® Green Supermix Kit reagents (Biorad, CA, USA). The $2^{-\Delta\Delta Ct}$ method was used to calculate relative expression changes. The primer sequences are listed in Table 3.

For the comparison experiment of virus replication in vitro, samples with a viral load of 10^4 TCID₅₀/0.1 ml were used to inoculate DF-1 cells, and the supernatant and cells were collected at 1, 3, 5, and 7 dpi. The virus copy number was calculated by the absolute quantitative method.

2.9. Statistical Analyses. The data between two groups were analyzed by unpaired *t*-test if the data were in Gaussian distribution and had equal variance, or by unpaired *t*-test with Welch's correction if the data were in Gaussian distribution but with unequal variance, or by nonparametric test (Mann–Whitney *U* test) if the data were not normally dis-

tributed (Prism 8.0). Data were represented as means \pm SD/SEM. Differences with $P < 0.05$ were considered significant: * $P < 0.05$, ** $P < 0.01$, *** $P < 0.001$. Differences within groups are marked with letters (A, a, B, b). The same letter means $P < 0.05$, between different uppercase or lowercase letters means $P < 0.01$, and between uppercase and lowercase letters means $P < 0.001$.

3. Results

3.1. Clinical Features and Histopathology of Sick Chickens. In this study, our experimental animals came from a group of egg-type chickens that were 40-week-old, which exhibited a pale cockscomb, bodyweight loss, mental depression, and decreased productivity. After detecting the ALVs' specificity antibody p27, it was found that a total of 15.7% (31/198) of the sampled chickens were positive for infection and the mortality rate was 3.5% (7/198). In particular, we found that the joints and diameter of the toes of these sick chickens were swollen, with blood blisters and ruptures evident, and signs of bleeding and hemangioma on their skin (Supplementary Figure 1A-1C). The pathological anatomy analysis revealed that the liver was abnormally swollen and almost occupied the entire abdominal cavity, with diffuse tumor nodules of different sizes on the liver surface that were either spherical or flat in shape. Also observed was a diffuse, bright red flower speckled texture as well as a solid texture on the liver. Moreover, there were also sick chickens whose liver edges appeared off-white, with mottled off-white nodules

TABLE 2: The ALV-J reference strains used in this study.

ALV strains	Country	Year	Host	Tumor phenotype	Subgroup	Accession number
RAV-1	USA	1980	Commercial chicken	LL	A	MF926337
2015012	China	2015	N/A	N/A	A	KY612442
SDAU09C2	China	2009	N/A	N/A	B	HM446005
FJ15TH0	China	2016	Hetian chicken	LL	B	KX839489
DL00766	China	2018	Hy-line variety brown	N/A	B & E	MH454773
RAV0	USA	1980	Commercial layer chicken	LL	E	MF817822
AF227	USA	2010	Commercial broiler	LL	E	MF817820
AF229	USA	2010	Commercial broiler chicken	LL	E	MF817821
JS11C1	China	2012	Chinese indigenous chicken	N/A	K	KF746200
JS13LY19	China	2018	Chicken	N/A	K	MG770235
HPRS-103	UK	1989	Parental meat-type chicken	ML	J	Z46390
SCAU-HN06	China	2007	Commercial layer chicken	He	J	HQ900844
PDRC-59831	USA	2007	Broiler	He and ML	J	KP284572
TW-3593	China Taiwan	2008	Taiwan country chickens	N/A	N/A	HM582658
HLJ09MDJ-1	China	2009	Layer chicken	He	J	JN624880
JL093-1	China	2009	Layer hens	He	J	JN624878
JL09L01	China	2009	Commercial egg-type chickens	He and ML	J	HQ148555
YZ9902	China	2010	White meat-type chicken	He	J	HM235670
GD1109	China	2011	Commercial layer chicken	He and ML	J	JX254901
GDKP1202	China	2012	Local commercial broilers	ML	J	JX453210
GifN_001	Japan	2015	N/A	N/A	N/A	MK757486
M180	China	2016	Late-feathering Chinese yellow chicken	N/A	J	KX611834
K243	China	2016	Fast-feathering Chinese yellow chicken	N/A	J	KX611833
GDHN-YM1	China	2018	Commercial layer chicken	He	J	MK683478
GDHN-YM2	China	2018	Commercial layer chicken	He	J	MK683479
SDAU1703	China	2018	Hy-line chicken	He	J	KY980659

ML: myeloid leukaemia; He: hemangioma; LL: lymphoid leukaemia; N/A: data not available.

TABLE 3: The primers used for the qPCR.

Primer ^a	Sequence (5'-3')	Accession no.
<i>GAPDH-F</i>	GAACATCATCCCAGCGTCCA	NM_204305.1
<i>GAPDH-R</i>	CGGCAGGTCAGGTCAACAAC	
<i>CH25H-F</i>	AATCCAGCCGCAGAGCTATC	NM_001277354.1
<i>CH25H-R</i>	CAGCTCTGGAGCTATCACCG	
<i>OSA-F</i>	CAGCGCCTGTACACCGAG	NM_205041.1
<i>OSA-R</i>	GGTTCTCCAGCTCCTTGGTC	
<i>PKR-F</i>	CCTCTGCTGGCCTTACTGTCA	NM_204487.1
<i>PKR-R</i>	AAGAGAGGCAGAAGGAATAATTTGCC	
<i>ZAP-F</i>	TTGATTCGGCGCCTCTCTAC	NM_001012938.1
<i>ZAP-R</i>	ACTGGCCGTGGTCATTCTTC	
<i>MX-F</i>	TTGTCTGGTGTGCTCTTCCT	NM_204609.1
<i>MX-R</i>	GCTGTATTTCTGTGTGCGGTA	

visible in the cross-section, characterized by a soft texture. Other internal organs also betrayed varying degrees of disease (Supplementary Figure 1D-1F). Histopathologically, in normal liver tissues, the morphology of healthy liver lobules could be distinguished. But after the ALV-J

infection, many small round tumor cells infiltrated the liver lobules in the liver tissue of the sickened chickens (Figure 1(a)). Normal spleen tissue was alternately composed of red pulp and white pulp, yet AVL-J infection damaged the structure of the spleen and widened the

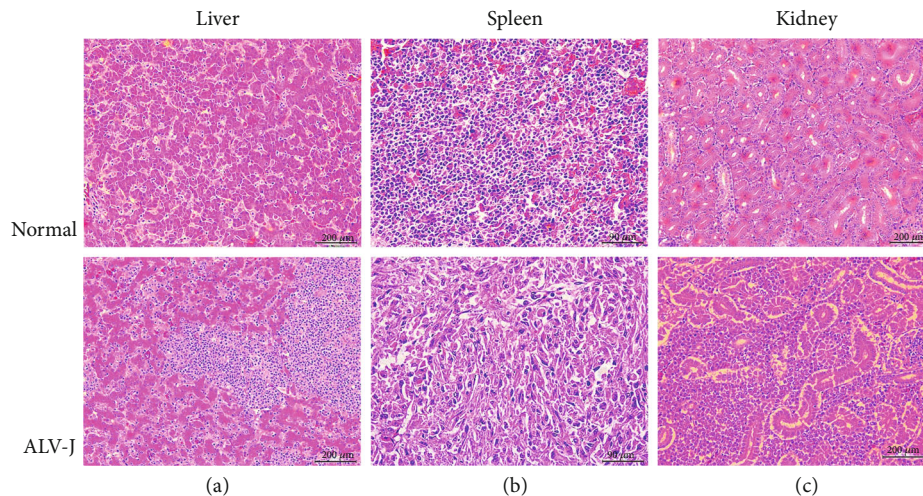


FIGURE 1: Histopathological changes in the clinical samples (hematoxylin and eosin staining). Comparisons between the normal group and ALV-J infection for (a) liver (bar = 200 μ M), (b) spleen (bar = 90 μ M), and (c) kidney (bar = 200 μ M) morphology of the chickens.

intercellular space (Figure 1(b)). Similarly, numerous inflammatory cells infiltrated the kidney, which squeezed and deformed this organ's tubules (Figure 1(c)).

3.2. Identification and Isolation of Virus. Among the 31 positive chickens, we selected the four samples with the highest ELISA value for virus identification and isolation (s/p value of p27). We synthesized specific primers for different subgroups of ALV, which also included those for MDV and REV. The four samples tested positive when using the ALV-J specific primers H5/H7, with a specific band evident at 545 bp, while the other subgroup primers had negative results (Figure 2(a)). Similarly, the ALV-J specific monoclonal antibody JE9 was used for the IFA experiments; this showed positive results as revealed by the strong green fluorescence (Figures 2(c)–2(f)). Therefore, the virus carried by these four samples was ALV-J. We then performed a full-length amplification of the provirus genome and successfully isolated four strains of ALV-J (Figure 2(b)), here named GD19GZ01 through GD19GZ04, respectively. Among them, the fluorescence intensity of GD19GZ03 and GD19GZ04 was higher than that of GD19GZ01 and GD19GZ02 (Figures 2(d)–2(g)).

3.3. Sequence Analysis Results of the Four Isolates Compared with Reference Strains. After alignment with the sequence characteristics of the original ALV-J strain HPRS-103 (GenBank accession number: Z46390), the full-length proviral genomes of GD19GZ01 to GD19GZ04 were obtained, which were 7479–7626 nucleotides (nt) in size, respectively. They all had the classic structure of a retrovirus, featuring the Long Terminal Repeated- (LTR-) leader-*gag-pol-env*-LTR, but they did not contain a viral oncogene, thus indicating that the four isolates belonged to the chronic tumor-causing avian leukemia virus. The four isolates shared 85.1%–98.0% nucleotide identity when compared with the reference strains. The detailed results of these pairwise comparisons are presented in Table 4.

Compared with the classic strain HPRS-103, the main reason for the difference in length between the four isolates was the redundant nonfunctional TM (rTM) region and downstream E element. Both GD19GZ01 and GD19GZ02 lacked the rTM region and E element almost entirely; however, GD19GZ03 and GD19GZ04 lacked the rTM region but retained the E element (Supplementary Figure 2A–2B). Notably, GD19GZ01 and GD19GZ02 each had 11-bp deletions in their 5'U3 and 3'UTR regions (between the bases 95–107 and 613–7625, following the HPRS-103 numbering scheme, same below). GD19GZ01 also had 9 bp insertion on the *env* gene (between bases 6187–6188). The four isolates had different degrees of insertions and deletions in their 5'U3, *env*, and 3'UTR regions, when compared with the original strain HPRS103 (Figure 3(a)).

In terms of the coding region, when compared to the reference strains, the *gag* and *pol* genes of the four strains were relatively conserved, sharing a 94.5%–99.1% nucleotide identity and 95.7%–99.6% amino acid identity, respectively. Yet the *env* gene, which could encode envelope proteins, was the most variable; with it, the four isolates shared only a 56.1%–97.0% nucleotide identity and a 47.1%–95.2% amino acid identity, being able to encode 575, 570, 571, and 568 amino acids in the *env* gene, respectively (Table 4).

The transcriptional regulatory elements of the four isolates in the U3 region were relatively conserved, namely with respect to 1 CAAT, E2BP, NFAP-1, AIB REP1, TATA Box, 2 CarG, Y, and PRE Box. Due to the 43rd base mutation (T/A), the GD19GZ01 virus strain had lost its CAAT Box (Figure 3(b)).

3.4. Phylogenetic Analysis of the Four Isolates. The phylogenetic analysis of the 26 reference sequences and four isolates revealed that the latter formed the same cluster as other isolates in South China in recent years. In this respect, GD19GZ01 through GD19GZ04 have the highest consistency with GDHN-YM2, GDHN-YM1, K243, and M180, respectively. There were also obvious regional differences

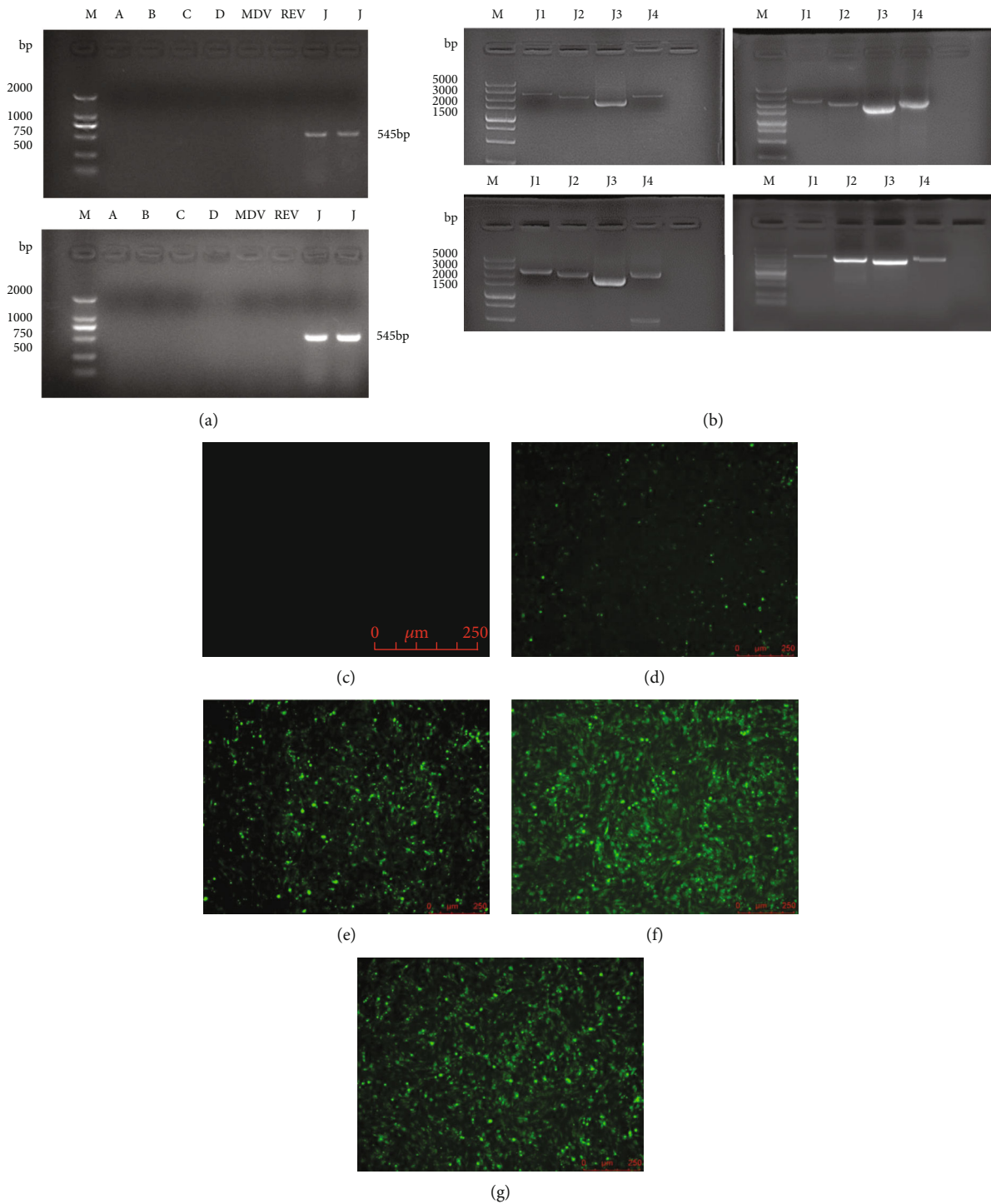


FIGURE 2: Identification of the four virus strains by PCR reaction and IFA response. In panel (a) are the PCR products that were electrophoresed on an agarose gel, and the four viruses at 545 bp, showing the specific bands. (b) Agarose electrophoresis results of the full-length ALV-J genome amplified from the four strains of viruses. (c) Uninfected DF-1 cells as a negative control, at 100 \times . (d-g) GD19GZ01 through GD19GZ04 strains inoculated into the DF-1 cells, respectively; the IFA response indicating specific green fluorescence, at 100 \times . The numbers in the upper column of the gel chart are for the following: M is the marker, A to D are the ALV-A- to ALV-D-specific primers, J is the ALV-J specific primers for H5/H7, and J1 to J4 represent the four segments of the full length of the ALV-J genome. bp: base pairs. The numbers on the left indicate the lengths of the molecular weight standards.

TABLE 4: The nucleotide and amino acid identity shared between GD19GZ01 and the other reference strains.

ALV strains	Nucleotide sequences (%)				Amino acid sequences (%)			
	Whole genome	LTR	Gag	Pol	Env	Gag	Pol	Env
GD19GZ02	97.8	93.7	98.1	98.8	96.0	97.7	99.4	92.6
GD19GZ03	95.8	93.0	96.3	97.3	94.0	97.4	98.4	91.4
GD19GZ04	96.3	97.4	96.5	98.0	95.3	97.4	98.6	92.2
RAV-1	85.6	86.5	96.2	97.1	56.5	97.0	97.7	47.8
2015012	86.8	93.9	95.2	97.1	57.4	96.7	98.3	48.2
SDAU09C2	86.0	95.0	96.6	96.8	57.2	97.7	98.6	48.8
FJ15TH0	86.0	90.7	95.3	97.7	57.6	97.0	98.5	48.8
DL00766	85.1	65.7	96.2	98.5	56.7	97.6	99.0	47.2
RAV0	85.1	63.5	96.7	98.3	56.5	97.4	98.7	48.3
AF227	85.2	64.6	96.6	98.5	56.6	97.9	98.7	48.3
AF229	85.2	64.6	96.7	98.5	56.6	97.9	98.7	48.1
JS11C1	85.2	79.7	94.6	97.9	57.7	96.2	98.4	47.9
JS13LY19	85.3	63.8	96.7	98.3	57.2	98.0	98.6	47.6
HPRS-103	94.7	92.7	96.0	97.3	93.7	96.7	98.6	90.5
SCAU-HN06	95.2	89.5	95.3	97.8	93.7	96.9	99.0	91.9
PDRC-59831	94.7	90.4	94.9	96.8	93.3	96.2	98.3	88.9
TW-3593	85.2	66.1	96.4	98.1	57.0	97.6	98.7	47.6
HLJ09MDJ-1	95.4	86.9	96.3	97.4	95.0	96.7	98.5	92.0
JL093-1	95.4	87.2	96.3	97.5	94.6	96.9	98.5	92.4
JL09L01	94.6	90.4	96.8	97.1	90.0	97.4	97.5	87.7
YZ9902	94.3	92.3	95.0	97.0	93.7	95.9	98.4	89.4
GD1109	95.3	90.4	95.3	98.0	94.9	97.0	98.7	92.3
GDKP1202	95.9	93.0	96.6	96.8	95.1	98.1	98.9	92.8
GifN_001	85.6	89.9	95.3	97.7	56.7	97.0	98.5	49.5
M180	96.2	94.6	96.5	97.4	95.1	97.6	98.9	91.7
K243	95.9	94.2	96.2	97.4	94.0	97.2	98.7	90.4
GDHN-YM1	97.1	97.4	97.4	97.8	95.5	97.3	99.0	93.5
GDHN-YM2	98.0	99.0	97.5	98.7	96.8	97.6	99.3	93.7
SDAU1703	94.9	89.5	96.3	97.3	93.0	96.9	98.5	90.5

among the same subgroups, and the sequence identity of strains from the same region was relatively high (Figure 4).

3.5. All Positions of the Three Recombinants Were between the Gag and Pol Genes. Several potential recombination events were detected by PDR5, but only three of them were accepted as being robust. The recombination sequence of event 1 was for GD19GZ01, and its parental sequences were M180 (ALV-J) and AF227 (ALV-E); that of event 2 was for GD19GZ02 and its parental sequences were GDHN-YM1 (ALV-J) and AF227 (ALV-E), and that of event 3 was GD19GZ02 and its parental sequences were GDHN-YM1 (ALV-J) and SD07LK1 (ALV-J) (Figures 5(a) and 5(b)). All positions of

the three recombinants were between the *gag* and *pol* genes. The *P* values for the six algorithm results (from PDR5 software) are in Supplementary Table 1.

3.6. Differential Expression of Innate Immune Genes and Inflammatory Cytokines in Different Organs of the ALV-J Infection. Interferon resists virus invasion by inducing the production of interferon-stimulating genes (ISGs), and this is an important line of defense for the innate immune response [17]. These ISGs, such as *CH25H*, *MX*, *PKR*, *OAS*, and *ZAP*, have been proven to block virus invasion in different ways to protect cells from infection [18–22]. Therefore, we analyzed the transcriptional levels of related ISGs in different immune organs in the sick chickens. The gene expression for *CH25H*, *MX*, *OAS*, and *ZAP* was significantly upregulated in the cecal tonsils, kidneys, and livers of the four sick chickens (Figure 6(a)). At the same time, we further explored the expression levels of inflammatory cytokines in the immune organs of the same four sick chickens. In their cecal tonsils, *IL-4* and *IL-6* show a trend of downward regulation, whereas the *IL-10* and proinflammatory cytokines *IL-12*, *IL-18*, and *TNF- α* were significantly upregulated. In the spleen, except for *IL-4*, the other five inflammatory cytokines were significantly upregulated. In the liver, the genes for *IL-4*, *IL6*, *IL12*, and *IL-18* were differentially expressed and upregulated, while both *IL-10* and *TNF- α* were downregulated (Figure 6(b)).

The DF-1 cells were infected with a viral load of 10^4 TCID₅₀/0.1 ml, after which the level of viral RNA synthesis and viral particle content were detected at different time points. The qPCR results indicated that GD19GZ02 and GD19GZ03 underwent higher levels of replication at 1 dpi (days postinoculation) than the other two strains, a difference that was an extremely significant difference. However, the virus replication levels of GD19GZ03 and GD19GZ04 became the highest at 3, 5, and 7 dpi. The results of ELISA and qPCR were basically the same. It is worth noting that GD19GZ04 had a low level of virus replication early on, at 1 dpi, but later on, the virus was clearly capable of a higher level of replication. At any time period, the virus replication level of GD19GZ01 was the lowest among the four isolates (Figure 6(c)).

4. Discussion

Since ALVs were included in the “National animal disease prevention and control for the medium and long term planning,” through strict selection measures, the prevention and control of ALVs have made great progress [23]. Although ALVs have been completely eradicated in other countries, there are still reports of ALVs’ outbreak in China among scattered farms and a variety of chicken species [24, 25]. The yellow chicken breeding industry, a pivotal part of the poultry industry in South China, has been continuously attacked by ALV-J in recent years. Similarly, the yellow feather broiler breeders have faced grave problems due to ALV-J infections [26]. Therefore, it is necessary to learn more of the pathogenesis and molecular sequence characteristics of ALV-J infection in yellow chicken flocks in South China.

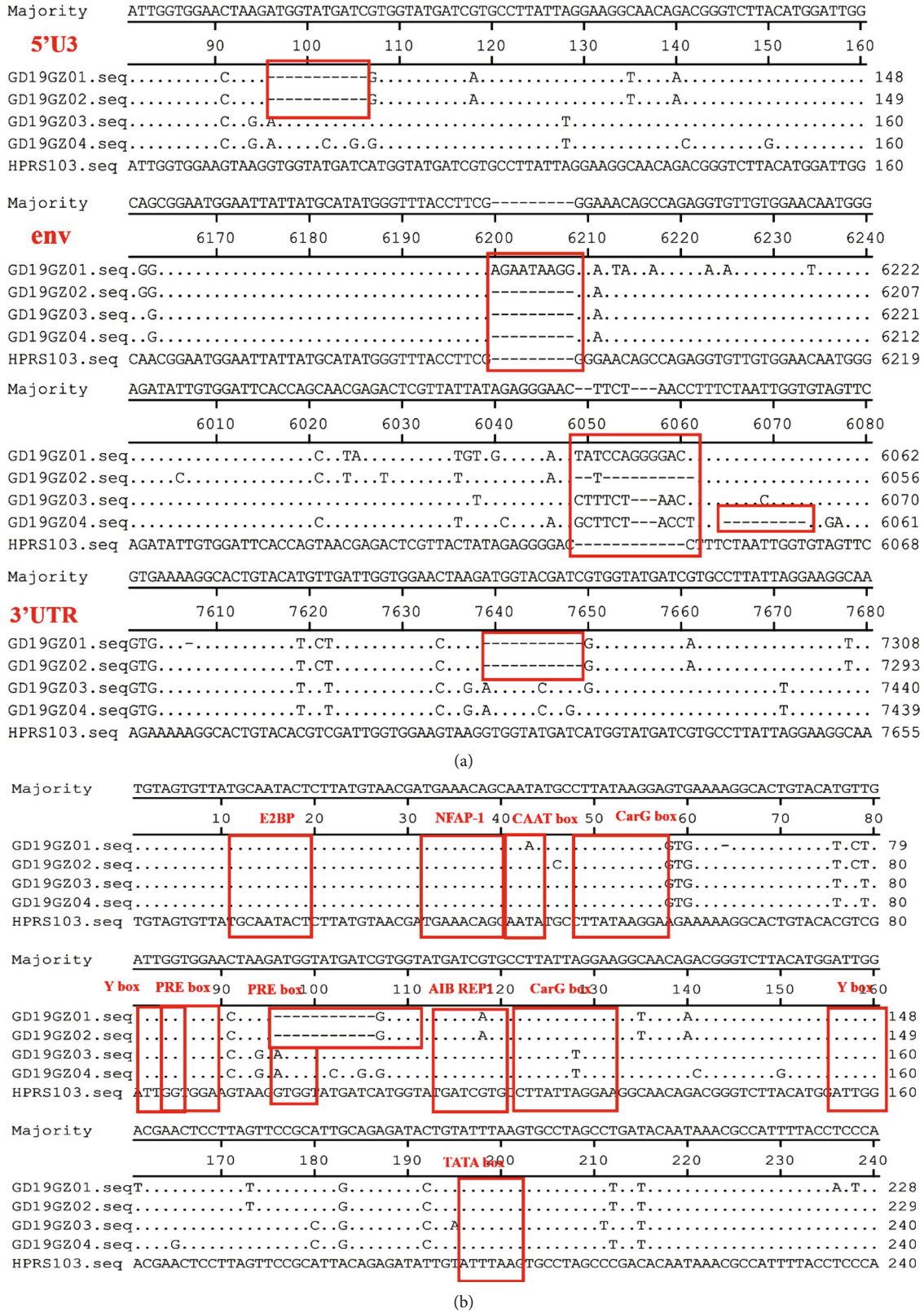


FIGURE 3: Sequence analysis results of the proviral genome. (a) The four isolates have different degrees of insertions and deletions in their 5' U3, env, and 3' UTR regions when compared with those of the original strain HPRS-103. (b) Transcriptional regulatory elements in the 5' U3 region of the four isolates. The dots (.) indicate identical residues, while the letters indicate the base substitutions. The dashes (-) indicate gaps in the alignment. Locations of deletions or insertions are boxed and marked.



FIGURE 4: Phylogenetic relationships of the four isolates to the reference strains, based on the proviral genome sequence. The red background indicates the four isolates and the green background indicates the reference strains that retained the E element. The blue circle indicates hemangioma (He), pink stars indicate myeloma (ML), brown triangles indicate lymphoma leukosis (LL).

In this study, four strains of ALV-J were isolated from the flocks of yellow chickens in South China, and their similarity, phylogenetic analysis, and sequence features were evaluated. GD19GZ01 and GD19GZ02 almost completely lacked the rTM region and E element region, while GD19GZ03 and GD19GZ04 each retained their E element. The four isolates were isolated from the same flock of yellow chickens, but their structural characteristics differed significantly, further highlighting the complexity of the ALV infection in these chicken flocks.

Among the 26 virus reference sequences that we selected, 50% (13/26) of those virus isolates featured an E element deletion. Coincidentally, the number of strains lacking the rTM region was also 50%, so whether it was an isolate that caused either hemangioma (He) or myeloma (ML), the rTM region might still be lost. This suggests that losing the rTM region was probably not related to the type of tumor elicited in the host. Nevertheless, only 15.3% (4/26) of the isolates simultaneously lacked both the rTM region and E element; evidently, then, the deletion of these two regions at once is a relatively rare phenomenon. The specific function of the E element remains unclear, however. Some researchers believe that despite not being essential for tumorigenesis induction by viruses, the E element nonetheless contributes

to oncogenicity in certain genetic lines of chicken [27]. In the comparison with virus replication levels in vitro, we found that GD19GZ02, GD19GZ03, and GD19GZ04 were under the same conditions of the transcriptional regulatory elements in the U3 region, but the in vitro replication levels of GD19GZ03 and GD19GZ04, which retained the E element, were significantly higher than those of GD19GZ01 and GD19GZ02 that lacked it. So, for GD19GZ01, its loss of a transcriptional regulatory element (CAAT box) might explain why it had the lowest level of viral replication at any time. Unfortunately, we have not verified in vivo whether strains that retain the E element are more tumorigenic.

The unique pathogenicity of ALV-J is considered to be closely related to its special *env* gene, which encodes two proteins, GP85 and GP37, of which the former is highly variable while the latter is relatively conserved [28, 29]. In our study, the *env* gene's variation in the four isolates was relatively large, and its consistency with the other reference strains was only 56.1%–97%. Most of these mutations occurred in the hypervariable region hr1, hr2, and the variable region vr3 of GP85.

Chicken type-I interferons (I-IFN) play a dominant role in the chicken immune system and mediate the first line of defense against viral pathogens infecting the avian species

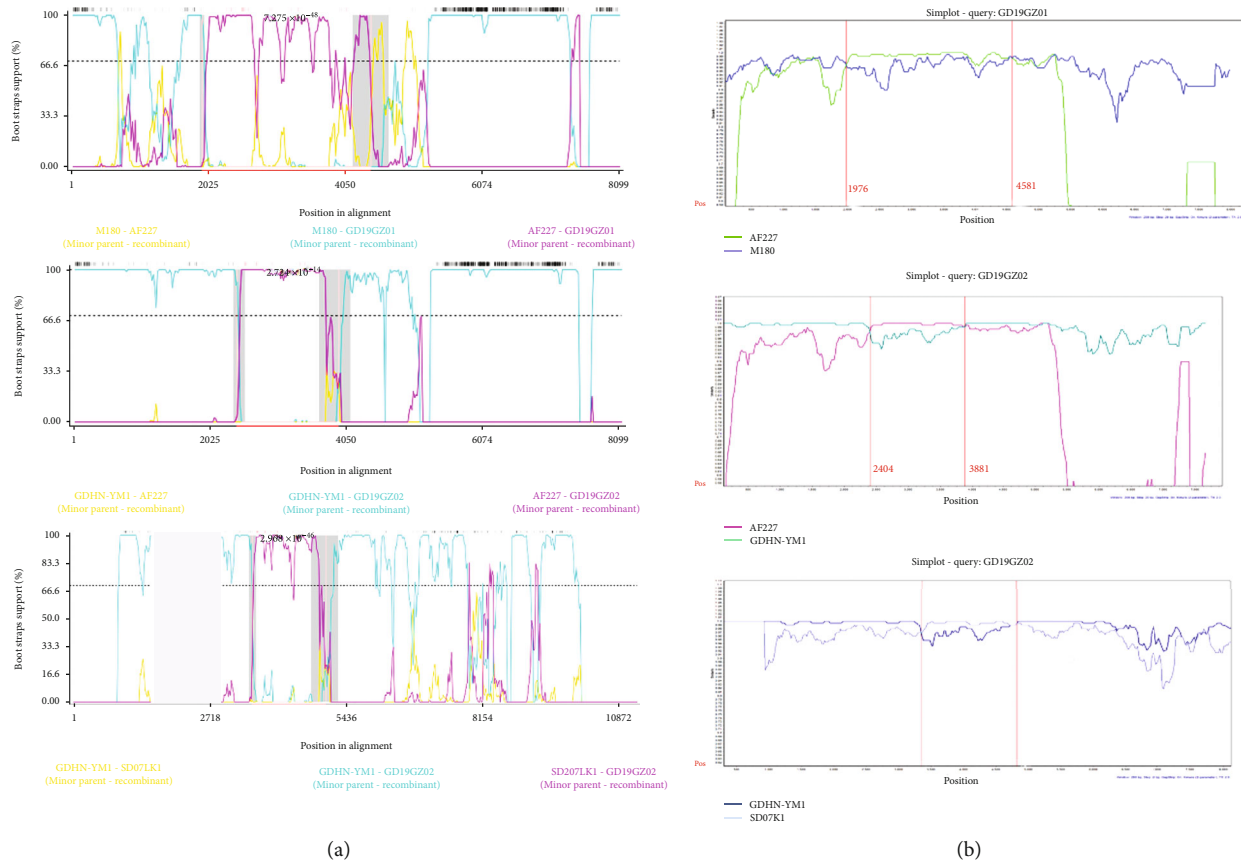


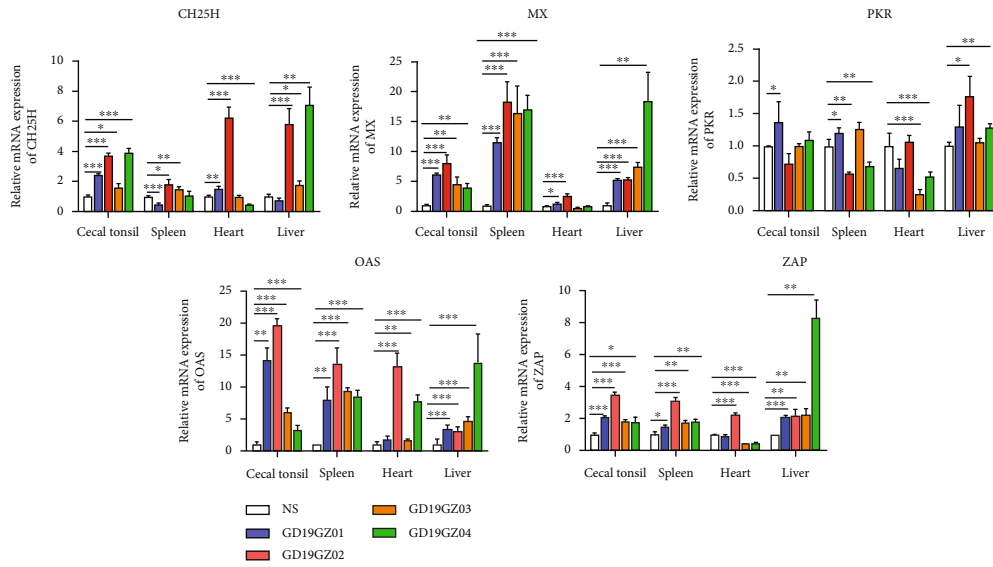
FIGURE 5: Determination of reorganization events. (a) The PDR5 analyzed the recombination events of the virus isolates. The bootscan was based on the pairwise distance model, with a window size of 200, a step size of 50, and 1000 bootstrap replicates generated by the RDP5. (b) The SimPlot analysis graph of reorganized breakpoints. These were based on a 200-bp window; each step is 20 bp for comparison (100 self-expanding, setting a 90% consistent tree, neighbor-joining method, Kimura two-parameter model).

[30]. When IFNs bind to their specific receptors, a cascade of signals is activated that results in the induction of several ISGs, thus establishing the antiviral state in the infected cells [31]. Therefore, we analyzed the expression levels of some ISGs in the immune organs of four sick chickens. These results indicated that *CH25H*, *MX*, *OAS*, and *ZAP* were all significantly upregulated in multiple immune organs (Figure 6(a)). Among them, *CH25H* was proven to inhibit the replication of ALV-J by producing 25HC [18]. However, the immunogenic features of most ISGs are still unknown. Exploring the antiviral potential of ISGs is recommended, since they could serve as valuable targets for therapeutic use against ALV-J and also as potential candidates for vaccine development; this is one of several strategies to deal with ALV-J.

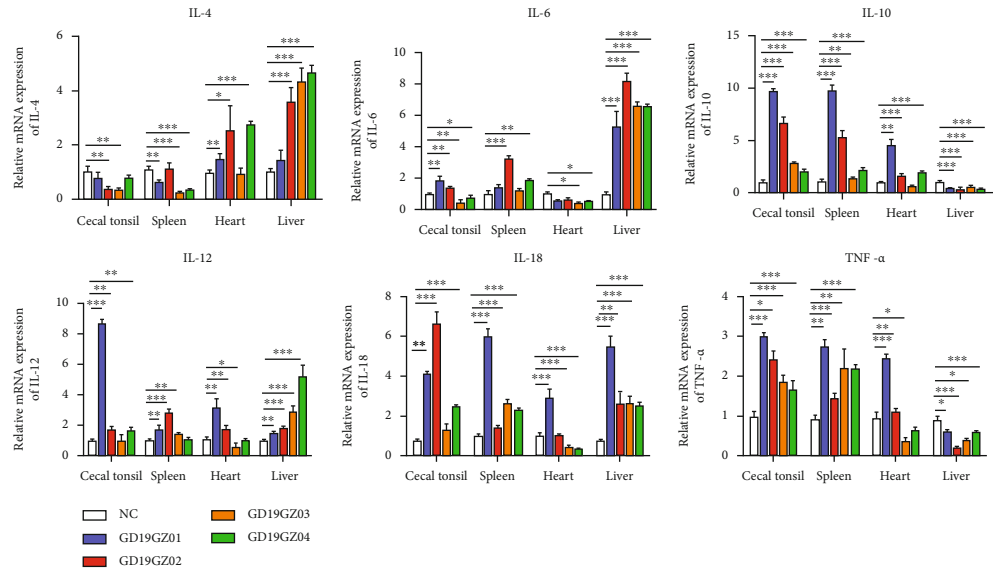
A dynamic and ever-shifting equilibrium exists between proinflammatory cytokines and anti-inflammatory components of the immune system [30]. Accordingly, to investigate deviations from that, we analyzed the expression levels of cytokines in the immune organs of four sick chickens under long-term invasion by ALV-J. The anti-inflammatory cytokines *IL-4* and *IL-6* were significantly upregulated in the liver, and both are known to have marked inhibitory effects on the expression and release of proinflammatory cytokines [32]. Therefore, the release of *TNF- α* was inhibited in the liver.

Although *IL-10* was downregulated in the liver of chickens, it was significantly upregulated in the cecal tonsils, spleen, and heart (Figure 6(b)). The invasion of ALV-J caused a strong inflammatory response in the immune organs of yellow chickens, as evinced by proinflammatory cytokines *IL-12*, *IL-18*, and *TNF- α* that were all significantly upregulated in most of their immune organs. It is worth mentioning that the expression of anti-inflammatory cytokines and proinflammatory cytokines increased abnormally in GD19GZ01. Despite complexities inherent in inflammatory cytokines, therapeutic interventions with specific cytokine inhibitors or anti-inflammatory cytokines have already been shown to confer significant clinical benefits in humans [33]. However, our current knowledge of the immune response caused by ALV-J invading yellow chickens is incomplete, so further research on this aspect is needed.

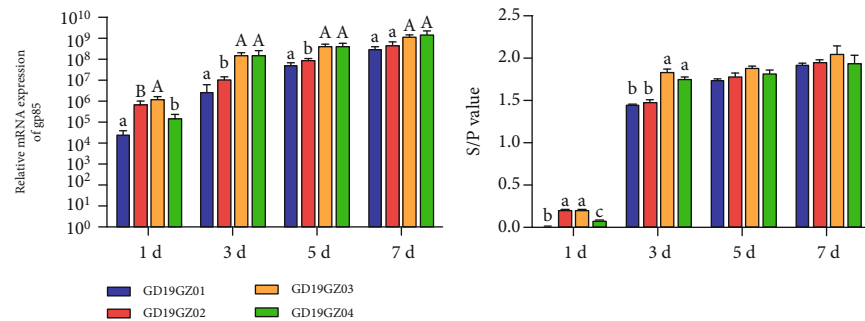
Finally, we used software to detect the occurrence of three viral recombination events on GD19GZ01 and GD19GZ02, all of which were found between the *gag* and *pol* genes. In recombination events 1 and 2, the recombination fragment is composed of an exogenous retrovirus and an endogenous retrovirus. Actually, in the early days, there was a view that ALV-J is a virus obtained by mutual recombination of exogenous retrovirus and endogenous retrovirus [34]. It was worth noting that of all 143 isolates in the NCBI database



(a)



(b)



(c)

FIGURE 6: Expression of the innate immune genes and inflammatory cytokines in different organs of sick chickens and comparison of virus replication in vitro. The expression levels (a) of ISGs and (b) proinflammatory cytokines and anti-inflammatory cytokines in the immune organs. (c) Viral synthesis levels of the four isolates, as determined by qPCR and ELISA assays (the s/p value indicates the viral load). The data shown are the means \pm SEM. The differences with $P < 0.05$ were considered significant. * $P < 0.05$, ** $P < 0.01$, *** $P < 0.001$ (a, b). Differences within groups are marked with letters (A, a, B, b). The same letter means $P < 0.05$, between different uppercase or lowercase letters means $P < 0.01$, and between uppercase and lowercase letters means $P < 0.001$ (c).

(updated August 1, 2020), a total of 316 recombination events were detected. ALVs' recombination not only occurs between different subgroups but also between ALVs and other viruses [35, 36]. The occurrence of recombination events means that viruses continue to evolve under selective pressure, and the final result may be the emergence of new subgroups.

In summary, we isolated four ALV-J from yellow chickens on a farm in South China and performed detailed sequence analyses of them. The results further demonstrate the complexity of ALVS infection in chicken flocks in different regions. Our findings thus help to reveal the clinical symptoms and sequence characteristics of ALV-J infection in yellow chickens in South China and, more generally, they provide valuable data for elucidating the evolution and variation trends of ALVs.

Data Availability

The data supporting the results of our study can be found within this manuscript.

Ethical Approval

All animal research projects were sanctioned by the South China Agriculture University Institutional Animal Care and Use Committee. All animal procedures were performed according to the regulations and guidelines established by this committee and international standards for animal welfare.

Conflicts of Interest

The authors declare no conflict of interest.

Authors' Contributions

Qihong Zhang and Guodong Mo contributed equally to this work.

Acknowledgments

Q.Z. conceived and performed the experiments, analyzed the data, and wrote the manuscript. G.M. and T.X. conceived the experiments, provided the samples, and revised the manuscript. Z.Z. and H.F. analyzed data and assisted in the cell culture work. P.W. made suggestions and revised the manuscript. X.Z. revised and approved the final manuscript. All authors read and approved the final manuscript. This work was supported by the National Natural Science Foundation of China (grant numbers 31801030, 31571269) and the China Agriculture Research System (grant number CARS-41-G03).

Supplementary Materials

Supplementary Table 1. The *P* values of the isolate recombination events are based on the six algorithms of PDR. At least five algorithms with *P* values $<1 \times 10^{-10}$ were required to accept a robust event. Supplementary Figure 1. Clinical

symptoms of sick chicken infected with ALV-J. (A) Swollen toe joints and bleeding. (B) Blood blisters present in the diameter joints. (C) Hemangiomas on the skin. (D) An abnormally enlarged liver almost filling the entire abdominal cavity. (E) A liver cross-section showing grayish white nodules. (F) Kidney swollen with gray-white nodules. Supplementary Figure 2. Comparison of the four isolates to the original strain HPRS-103 with respect to their rTM and E element regions. (A) The four isolates completely lacked a redundant nonfunctional TM (rTM) region. (B) GD19GZ01 and GD19GZ02 almost completely lacked the E element, while GD19GZ03 and GD19GZ04 retained it. The dots (.) indicate identical residues, while the letters indicate base substitutions. The dashes (-) indicate gaps in the alignment. Locations of deletions or insertions are boxed and marked. (*Supplementary Materials*)

References

- [1] R. J. O. Barnard, D. Elleder, and J. A. T. Young, "Avian sarcoma and leukosis virus-receptor interactions: from classical genetics to novel insights into virus-cell membrane fusion," *Virology*, vol. 344, no. 1, pp. 25–29, 2006.
- [2] L. N. Payne, A. M. Gillespie, and K. Howes, "Myeloid leukemogenicity and transmission of the HPRS-103 strain of avian leukosis virus," *Leukemia*, vol. 6, no. 11, pp. 1167–1176, 1992.
- [3] Y. Gao, L. Qin, W. Pan et al., "Avian leukosis virus subgroup J in layer chickens, China," *Emerging Infectious Diseases*, vol. 16, no. 10, pp. 1637–1638, 2010.
- [4] S. Sun and Z. Cui, "Epidemiological and pathological studies of subgroup J avian leukosis virus infections in Chinese local "yellow" chickens," *Avian Pathology Journal of the W.v.p.a.*, vol. 36, no. 3, pp. 221–226, 2007.
- [5] C. Abolnik and D. B. Wandrag, "Avian gyrovirus 2 and avirulent Newcastle disease virus coinfection in a chicken flock with neurologic symptoms and high mortalities," *Avian Diseases*, vol. 58, no. 1, pp. 90–94, 2014.
- [6] M. Feng, M. Dai, T. Xie, Z. Li, M. Shi, and X. Zhang, "Innate immune responses in ALV-J infected chicks and chickens with hemangioma in vivo," *Frontiers in Microbiology*, vol. 7, p. 786, 2016.
- [7] S. He, G. Zheng, D. Zhou, G. Li, and Z. Cheng, "Clonal anergy of CD117+chB6+ B cell progenitors induced by avian leukosis virus subgroup J is associated with immunological tolerance," *Retrovirology*, vol. 16, no. 1, p. 1, 2019.
- [8] P. Wang, L. Lin, M. Shi et al., "Vertical transmission of ALV from ALV-J positive parents caused severe immunosuppression and significantly reduced marek's disease vaccine efficacy in three-yellow chickens," *Veterinary Microbiology*, vol. 244, p. 108683, 2020.
- [9] F. Min, T. Yan, M. Dai et al., "Endogenous retrovirus ev21 dose not recombine with ALV-J and induces the expression of ISGs in the host," *Frontiers in Cellular & Infection Microbiology*, vol. 6, p. 140, 2016.
- [10] S. Qi, L. Yang, W. Li et al., "Molecular characteristics of avian leukosis viruses isolated from indigenous chicken breeds in China," *Poultry Science*, vol. 97, pp. 2917–2925, 2018.
- [11] Y. Li, X. Liu, H. Liu et al., "Isolation, identification, and phylogenetic analysis of two avian leukosis virus subgroup J strains

- associated with hemangioma and myeloid leukosis," *Veterinary Microbiology*, vol. 166, no. 3-4, pp. 356-364, 2013.
- [12] Z. CHENG, J. LIU, Z. CUI, and L. ZHANG, "Tumors associated with avian leukosis virus subgroup J in layer hens during 2007 to 2009 in China," *The Journal of Veterinary Medical Science*, vol. 72, no. 8, pp. 1027-1033, 2010.
- [13] H. Lai, H. Zhang, Z. Ning et al., "Isolation and characterization of emerging subgroup J avian leukosis virus associated with hemangioma in egg-type chickens," *Veterinary Microbiology*, vol. 151, no. 3-4, pp. 275-283, 2011.
- [14] P. Wang, M. Shi, C. He et al., "A novel recombinant avian leukosis virus isolated from gamecocks induced pathogenicity in Three-Yellow chickens: a potential infection source of avian leukosis virus to the commercial chickens," *Poultry science*, vol. 98, no. 12, pp. 6497-6504, 2019.
- [15] R. Maas, D. V. Zoelen, H. Oei, and I. Claassen, "Replacement of primary chicken embryonic fibroblasts (CEF) by the DF-1 cell line for detection of avian leukosis viruses," *Biologicals*, vol. 34, no. 3, pp. 177-181, 2006.
- [16] W. Pan, Y. Gao, L. Qin et al., "Genetic diversity and phylogenetic analysis of glycoprotein GP85 of ALV-J isolates from Mainland China between 1999 and 2010: Coexistence of two extremely different subgroups in layers: coexistence of two extremely different subgroups in layers," *Veterinary Microbiology*, vol. 156, no. 1-2, pp. 205-212, 2012.
- [17] M. U. Goraya, F. Zaighum, N. Sajjad, F. R. Anjum, and S. U. Rahman, "Web of interferon stimulated antiviral factors to control the influenza A viruses replication," *Microbial pathogenesis*, vol. 139, 2019.
- [18] T. Xie, M. Feng, M. Dai, G. Mo, and X. Zhang, "Cholesterol-25-hydroxylase is a chicken ISG that restricts ALV-J infection by producing 25-hydroxycholesterol," *Viruses*, vol. 11, no. 6, p. 498, 2019.
- [19] F. N. Mpenda, C. T. Keambou, M. Kyallo, R. Pelle, and J. Buza, "Polymorphisms of the chicken mx gene promoter and association with chicken embryos' susceptibility to virulent newcastle disease virus challenge," *BioMed Research International*, vol. 2019, Article ID 1486072, 6 pages, 2019.
- [20] O. Schulz, A. Pichlmair, J. Rehwinkel et al., "Protein kinase R contributes to immunity against specific viruses by regulating interferon mRNA integrity," *Cell Host & Microbe*, vol. 7, no. 5, pp. 354-361, 2010.
- [21] R. H. Silverman, "Viral encounters with 2',5'-oligoadenylate synthetase and RNase L during the interferon antiviral response," *Journal of Virology*, vol. 81, no. 23, pp. 12720-12729, 2007.
- [22] Y. Zhu, G. Chen, F. Lv et al., "Zinc-finger antiviral protein inhibits HIV-1 infection by selectively targeting multiply spliced viral mRNAs for degradation," *Proceedings of the National Academy of Sciences of the United States of America*, vol. 108, no. 38, pp. 15834-15839, 2011.
- [23] F. Meng, Q. Li, Y. Zhang, Z. Cui, S. Chang, and P. Zhao, "Isolation and characterization of subgroup J Avian Leukosis virus associated with hemangioma in commercial Hy-Line chickens," *Poultry science*, vol. 97, no. 8, pp. 2667-2674, 2018.
- [24] Q. Zhang, D. Zhao, H. Guo, and Z. Cui, "Isolation and identification of a subgroup A avian leukosis virus from imported meat-type grand-parent chickens," *Virologica Sinica*, vol. 25, no. 2, pp. 130-136, 2010.
- [25] D. M. Zhao, Q. C. Zhang, and Z. Z. Cui, "Isolation and identification of a subgroup B avian leukosis virus from chickens of Chinese native breed Luhua," *Bing Du Xue Bao*, vol. 26, no. 1, pp. 53-57, 2010.
- [26] W. Bo, L. I. Qing-yuan, L. Shao-qiong, Z. Yong-guang, C. Zhi-zhong, and S. H. Sun, "Evaluation on ALV Infection in Fertilized Eggs from A Wan-nan Yellow-feather Parent Broiler Breeder Flock," *Chinese Journal of Animal and Veterinary Sciences*, vol. 42, pp. 224-227, 2011.
- [27] P. M. Chesters, L. P. Smith, and V. Nair, "E (XSR) element contributes to the oncogenicity of Avian leukosis virus (subgroup J)," *The Journal of General Virology*, vol. 87, no. 9, pp. 2685-2692, 2006.
- [28] P. M. Chesters, K. Howes, L. Petherbridge, S. Evans, L. N. Payne, and K. Venugopal, "The viral envelope is a major determinant for the induction of lymphoid and myeloid tumours by avian leukosis virus subgroups A and J, respectively," *The Journal of General Virology*, vol. 83, no. 10, pp. 2553-2561, 2002.
- [29] L. Jiang, X. Zeng, Y. Hua et al., "Genetic diversity and phylogenetic analysis of glycoprotein gp85 of avian leukosis virus subgroup J wild-bird isolates from Northeast China," *Archives of Virology*, vol. 159, pp. 1821-1826, 2014.
- [30] S. M. Opal and V. A. DePalo, "Anti-Inflammatory Cytokines," *CHEST*, vol. 117, no. 4, pp. 1162-1172, 2000.
- [31] A. M. Kestra, M. R. de Zoete, L. I. Bouwman, M. M. Vaezirad, and J. P. van Putten, "Unique features of chicken Toll-like receptors," *Developmental and Comparative Immunology*, vol. 41, no. 3, pp. 316-323, 2013.
- [32] M. A. Brown and J. Hural, "Functions of IL-4 and control of its expression," *Critical Reviews in Immunology*, vol. 17, no. 1, pp. 1-32, 1997.
- [33] I. Tepler, L. Elias, J. W. Smith, M. N. Hussein, and J. A. Kaye, "A randomized placebo-controlled trial of recombinant human interleukin-11 in cancer patients with severe thrombocytopenia due to chemotherapy," *Blood*, vol. 87, pp. 3607-3614, 1996.
- [34] L. M. Smith, A. A. Toye, K. Howes, N. Bumstead, L. N. Payne, and K. Venugopal, "Novel endogenous retroviral sequences in the chicken genome closely related to HPRS-103 (subgroup J) avian leukosis virus," *The Journal of General Virology*, vol. 1317, pp. 261-268, 1999.
- [35] Z. Cui, S. Sun, Z. Zhang, and S. Meng, "Simultaneous endemic infections with subgroup J avian leukosis virus and reticuloendotheliosis virus in commercial and local breeds of chickens," *Avian Pathology*, vol. 38, no. 6, pp. 443-448, 2009.
- [36] P. Wang, Y. Yang, L. Lin, H. Li, and P. Wei, "Complete genome sequencing and characterization revealed a recombinant subgroup B isolate of avian leukosis virus with a subgroup J-like U3 region," *Virus Genes*, vol. 53, no. 6, pp. 927-930, 2017.

Research Article

Yeast Fermentate Prebiotic Ameliorates Allergic Asthma, Associating with Inhibiting Inflammation and Reducing Oxidative Stress Level through Suppressing Autophagy

Subo Gong,¹ Xiaoying Ji,² Jing Su,¹ Yina Wang,¹ Xianghong Yan,³ Guyi Wang,¹ Bin Xiao,¹ Haiyun Dong,¹ Xudong Xiang,¹ and Shaokun Liu¹ 

¹Second Xiangya Hospital of Central South University, No. 139 Middle Renmin Road, Changsha City, Hunan Province, China

²Pulmonary and Critical Care Medicine, The Seventh Affiliated Hospital, Sun Yat-sen University, No. 628, Zhenyuan Road, Xihu Street, Guangming District, Shenzhen City, China

³Department of Laboratory Medicine, Changsha Central Hospital, Nanhua University, Changsha City, Hunan Province, China

Correspondence should be addressed to Shaokun Liu; shaokunliu228@csu.edu.cn

Received 30 July 2020; Revised 24 November 2020; Accepted 30 November 2020; Published 20 January 2021

Academic Editor: Shuai Chen

Copyright © 2021 Subo Gong et al. This is an open access article distributed under the Creative Commons Attribution License, which permits unrestricted use, distribution, and reproduction in any medium, provided the original work is properly cited.

Background and Purpose. Allergic asthma, a respiratory disease with high morbidity and mortality, is reported to be related to the airway allergic inflammation and autophagy-induced oxidative stress. Although the therapeutic effects of fermentate prebiotic (YFP) on allergic asthma have been widely claimed, the underlying mechanism is still unclear. This study is aimed at investigating the possible mechanism for the antiasthma property of YFP in a mouse model. **Methods.** Ovalbumin was used to induce allergic asthma following administration of YFP for one week in mice, to collect the lung tissues, bronchoalveolar lavage fluid (BLFA), and feces. The pathological state, tight-junction proteins, inflammatory and oxidative stress-associated biomarkers, and TLRs/NF- κ B signaling pathway of the lung tissues were evaluated by HE staining, immunofluorescence, ELISA, and WB, separately. RT-PCR was used to test oxidative stress-associated genes. Leukocyte counts of BLFA and intestinal microbiota were also analyzed using a hemocytometer and 16S rDNA-sequencing, separately. **Result.** YFP ameliorated the lung injury of the mouse asthma model by inhibiting peribronchial and perivascular infiltrations of eosinophils and increasing tight-junction protein expression. YFP inhibited the decrease in the number of BALF leukocytes and expression of inflammatory-related genes and reversed OVA-induced TLRs/NF- κ B signaling pathway activation. YFP ameliorated the level of oxidative stress in the lung of the mouse asthma model by inhibiting MDA and promoting the protein level of GSH-PX, SOD, CAT, and oxidative-related genes. ATG5, Beclin1, and LC3BII/I were significantly upregulated in asthma mice, which were greatly suppressed by the introduction of YFP, indicating that YFP ameliorated the autophagy in the lung of the mouse asthma model. Lastly, the distribution of bacterial species was slightly changed by YFP in asthma mice, with a significant difference in the relative abundance of 6 major bacterial species between the asthma and YFP groups. **Conclusion.** Our research showed that YFP might exert antiasthmatic effects by inhibiting airway allergic inflammation and oxidative stress level through suppressing autophagy.

1. Introduction

Allergic asthma is a common chronic inflammatory respiratory disease with high morbidity and mortality all over the world. According to the World Health Organization (WHO) report in 2015 [1], approximately 0.3 billion patients are diagnosed with allergic asthma. Allergic asthma is mainly clinically characterized by discontinuous reversible airway obstruction

and bronchial hyperresponsiveness [2]. Although numerous investigations have explored allergic asthma's pathogenesis in the past decades, allergic asthma's aetiology and pathogenesis remain unknown, which prevents pharmaceutical companies from developing effective targeted drugs and the clinicians from diagnosing accurately [3].

Airway allergic inflammation is regarded as one of the leading theories on allergic asthma [4]. As allergic asthma

develops, large amounts of inflammatory cells infiltrate into the lung tissues in the pathological biopsy of both clinical allergic asthma patients and the experimental animal models, including granulocytes [5], mastocytes [6], macrophages [7], dendritic cells [8], and T cells and B cells [9]. The NF- κ B signal pathway is reported to be both involved in inflammatory activation, including TLR4/NF- κ B [10], CX3CR1/NF- κ B [11], p120/NF- κ B [12], and TRAF6/NF- κ B [13] signal pathways. Hong et al. [14] reported that bromodomain-containing protein 4 inhibition alleviated matrix degradation by enhancing autophagy and suppressing NLRP3 inflammasome activity through regulating NF- κ B signaling in nucleus pulposus cells. Besides, Qi et al. [15] reported that MSTN attenuated cardiac hypertrophy through the inhibition of excessive cardiac autophagy by blocking AMPK/mTOR and miR-128/PPAR γ /NF- κ B signal pathways. These studies reveal the critical roles of NF- κ B for the regulation of inflammations.

Furthermore, the mice with knockout of autophagy gene ATG5 in dendritic cells are more susceptible to sterol-tolerant neutrophilic airway inflammation [16], indicating that autophagy might be involved in the development and progressing of allergic asthma. Autophagy is a relatively conservative degradation of cellular materials, such as damaged organelles or reactive oxygen species (ROS) [17]. Recent studies reveal the high correlation of the nucleotide polymorphism of ATG5/7 and the development of asthma in pediatrics [18] and adults [19]. Besides, more autophagic vacuoles are observed in the clinical-pathological biopsy of allergic asthma patients [20]. Excessive production of ROS induced by the aggravation of autophagy in the tissues further contributes to oxidative stress, while oxidative stress could be suppressed by 3-MA, an autophagy inhibitor, in a murine allergic asthma mouse model [21]. Poon et al. also reported an important role of autophagy-regulated oxidative stress in the developing and processing of asthma [20]. Therefore, investigations on oxidative stress induced by autophagy should help understand allergic asthma's pathogenesis better.

Yeast Fermentate Prebiotics (YFP), a group of live microorganisms, have benefit roles in maintaining the health of the host [22], which could be associated with balancing the microbial community structure, inducing the degradation of antigens [23], and regulating immunity [24]. Recently, YFP was reported to exert therapeutic effects on the treatment of allergic asthma [25–29]. Besides, prebiotic was reported to regulate the NF- κ B signal pathway in colitis [30] and diabetes [31] by modulating gut microbiota. In the present study, the antiasthma effects of YFP and the underlying mechanism will be investigated to provide the fundamental basis for the potential therapeutic application of YFP against allergic asthma.

2. Materials and Methods

2.1. Animals and Allergic Asthma Model. Twenty-four 6-week old BABL/c male mice were purchased from Beijing Vital River Laboratory Animal Technology Co., Ltd. The mice were divided into three groups: the control group, the asthma group, and the asthma+YFP group. The mice in the

asthma+YFP group were orally administrated with YFP (1×10^9 CFU/day) from day 0 to day 6, while the other mice received oral administration of normal saline. Ovalbumin (OVA) was used to establish the murine asthma model according to a modification of the methods proposed by Yu et al. [29]. Briefly, the mice in the asthma group and the asthma+YFP group were administrated with an intraperitoneal injection of 20 μ g OVA emulsified in 2.25 mg alum hydroxide in a total volume of 100 μ L at day 7 and day 14 and inhaled with 1% OVA through an ultrasonic sprayer (Nescosonic UN-511, Alfresa, Osaka, Japan) for three days from day 21. Normal saline was administered orally instead of OVA to the control mice. On day 23, all the mice were sacrificed for the collection of lung and feces. The lungs were flushed twice with cold 0.5% fetal bovine serum in 1 mL PBS, and bronchoalveolar lavage fluid (BALF) was obtained for leukocyte counts using a hemocytometer (Thermo) after lavage and centrifuged at 2000 g at 4°C for 5 min. We declare that all animal experiments involved in this manuscript were authorized by the ethical committee of The Second Xiangya Hospital of Central South University and carried out according to the guidelines for care and use of laboratory animals as well as to the principles of laboratory animal care and protection.

2.2. Enzyme-Linked Immunosorbent Assay (ELISA). Inflammatory or oxidative stress biomarkers, including tumor necrosis factor- α (TNF- α), interleukin- (IL-) 1 β , IL-6, transforming growth factor- (TGF-) β , interferon- (IFN-) γ , malondialdehyde (MDA), glutathione peroxidase (GSH-Px), superoxide dismutase (SOD), and catalase (CAT), in BALF were detected by ELISA according to the instruction of the manufacturer (Sigma-Aldrich, Missouri, USA). The samples were firstly incubated with 1% BSA and then incubated with the primary antibodies for one hour. Subsequently, the samples were mixed with streptavidin-horseradish peroxidase (HRP) conjugated secondary antibodies for 20 mins at room temperature; then, the absorption at 450 nm was analyzed using a microplate spectrophotometer (Thermo Fisher, Massachusetts, USA).

2.3. Hematoxylin and Eosin (HE) Staining. The lungs were washed over by sterile water for three hours, dehydrated by 70%, 80%, and 90% ethanol solution successively, and mixed with equal quality of ethanol and xylene. After 15 min incubation, the tissues were mixed with equal quality of xylene for 15 min. Repeat the steps until the tissues looked transparent. Subsequently, the tissues were embedded in paraffin, sectioned, and stained with hematoxylin and eosin (HE). H&E-stained tissue sections were analyzed under a microscope (Olympus).

2.4. Real-Time Polymerase Chain Reaction (RT-PCR). Total RNA of the lungs was extracted using a TaKaRa MiniBEST Universal RNA Extraction Kit (TaKaRa, Dalian, China), according to the manufacturer's instructions, and quantified with a NanoDrop spectrophotometer (NanoDrop Technologies, Wilmington, DE). Complementary DNA was generated with a specific RT primer. RT-PCR was performed with SYBR Premix Ex TaqTM (Tli RNaseH plus) (TaKaRa,

Dalian, China) by the Applied Bio-Rad CFX96 Sequence Detection System (Applied Biosystems). The expression level of GPX1-4, CAT, SOD1, SOD2, and UCP2 was defined from the threshold cycle (Ct), and relative expression levels were calculated using the $2^{-\Delta\Delta Ct}$ method after normalization regarding the expression of U6 small nuclear RNA. The expression level of GAPDH in the tissues was taken as the negative control. Three independent assays were performed. The information of the primers is shown in Table 1.

2.5. Immunofluorescence. The BALF cells were incubated with primary rabbit anti-ZO-1, anti-Claudin1, anti-Claudin4, and anti-Occludin (OmnimAbs, 1:1000) antibody overnight at 4°C. Following washed three times with PBS, cells were incubated with secondary Cy3-conjugated anti-rabbit IgG (Abcam, 1:200) for 30 min at room temperature. The DAPI was added to dye the nuclear for 5 min, and 50% glycerin was used to block the medium. Stained cells were photographed under a fluorescence microscope (Olympus, Tokyo, Japan).

2.6. Western Blot. Inflammatory and autophagy-related proteins were evaluated by Western blot. Proteins were extracted from the lung tissues using the Nuclear and Cytoplasmic Protein Extraction Kit (Beyotime, China). Approximately 40 µg of protein was loaded and separated with the 12% SDS-polyacrylamide gel (SDS-PAGE) and then transferred to polyvinylidene difluoride (PVDF) membrane (Millipore, MIT, USA). The membrane was incubated with 5% nonfat dry milk in TBST (Tris-buffered saline/0.1% Tween-20, pH 7.4) for 1 h at room temperature, followed by incubation overnight with primary rabbit anti-mouse antibodies to NF-κB (1:1000, Abcam, USA), p-NF-κB (1:1000, Abcam, USA), TLR1 (1:1000, Abcam, USA), TLR2 (1:1000, Abcam, USA), TLR3 (1:1000, Abcam, USA), TLR4 (1:1000, Abcam, USA), Myd88 (1:1000, Abcam, USA), ATG5 (1:1000, Abcam, USA), LC3I/II (1:1000, Abcam, USA), Beclin1 (1:1000, Abcam, USA), and GAPDH (1:1000, Abcam, USA). A horseradish peroxidase-conjugated antibody against rabbit IgG (1:5000, Abcam, USA) was used as a secondary antibody. Blots were incubated with the ECL reagents (Beyotime, Jiangsu Province, China) and exposed to Tanon 5200-multi to detect protein expression. Three independent assays were performed.

2.6.1. 16S rDNA-Sequencing Analysis. Three feces were collected from each group for the microbiome analysis. Bacterial genomic DNA was extracted from feces using the Qiagen DNA Mini Kit (Qiagen, Valencia, California) according to manufacturer's protocols, and the V4-V5 hypervariable regions of the 16S rDNA gene were PCR-amplified with the appropriate controls against reagent contamination. Amplified DNA fragments were sequenced using the 454 Genome Sequencer FLX platform (454 Life Sciences, Roche Diagnostics, Burgess Hill, United Kingdom). The raw data were processed using quantitative insights into microbial ecology (QIIME) pipeline version 1.7. Stringent criteria were used to remove low quality and chimeric reads. The remaining rarified reads were subject to open reference operational

TABLE 1: The primers used in this study.

Primer name	Primer sequence (5' -3')
GPX1 forward	CAGTTGCAGTGCTGCTGTCTC
GPX1 reverse	GCTGACACCCGGCACTTTATTAG
GPX2 forward	GACACGAGGAAACCGAAGCA
GPX2 reverse	GGCCCT TCACAACGTCT
GPX3 forward	CTTCCTA CCCTCAAGTATGTCCG
GPX3 reverse	GAGGTGGGAGGACAGGAGTT CTT
GPX4 forward	GCAACCAGTTTGGGAGGCAGGAG
GPX4 reverse	CCTCCATGGGACCATAGCGC TTC
CAT forward	GGTCATGCATTTAATCAGGCAGAA
CAT reverse	TTGCTTGGGTCTGAAGGCTATC
SOD1 forward	GAAGGTGTGGGGAAGCATT
SOD1 reverse	ACATTGCCCAAGTCTCCAAC
SOD2 forward	CCAAATCAGGATCCACTGCAA
SOD2 reverse	CAGCATAACGATCGTGGTTTACTT
UCP2 forward	CTACAAGACCATTGCACGAGAGG
UCP2 reverse	AGCTGCTCATAGGTGACAAACAT
GAPDH forward	CAATGACCCCTTCATTGACC
GAPDH reverse	GAGAAGCTTCCCGTTCTCAG

taxonomic unit (OTU) picking (97% identity cutoff). The mean sequencing depth used for analysis was 31615. There is no sample drop-off. The sequence data were deposited to NCBI SRA (Sequence Read Archive) (SRP065072).

2.7. Statistical Analysis. GraphPad Prism 7.0 (GraphPad Software, USA) was employed to perform statistical analysis. Results were statistically analyzed with Student's *t*-test for two-group comparisons. Data are presented as mean ± SEM. *P* values < 0.05 were considered significant.

3. Results

3.1. YFP Ameliorated the Lung Injury of the Mouse Asthma Model. HE staining was used to check the pathological state of the lung tissues, and the immunofluorescence assay was used to determine the expression level of tight junction-related proteins. As shown in Figure 1(a), significant peribronchial and perivascular infiltrations of eosinophils were observed in the asthma group, compared to the control, which were significantly suppressed by YFP. ZO-1, Claudin1, Claudin4, and Occludin were significantly downregulated in the asthma group, compared to the control, the expression of which was significantly promoted by the treatment of YFP (Figures 1(b)–1(d)).

3.2. YFP Inhibited the Inflammation in the Lung of the Mouse Asthma Model. YFP inhibited the decrease in the number of BALF leukocytes induced by OVA (Figure 2(a)). As shown in Figures 2(b)–2(f), the concentration of TNF-α, IL-1β, IL-6, TGF-β, and IFN-γ was significantly elevated in the asthma group compared to the control group, which was suppressed by the introduction of YFP. To further evaluate the effects of

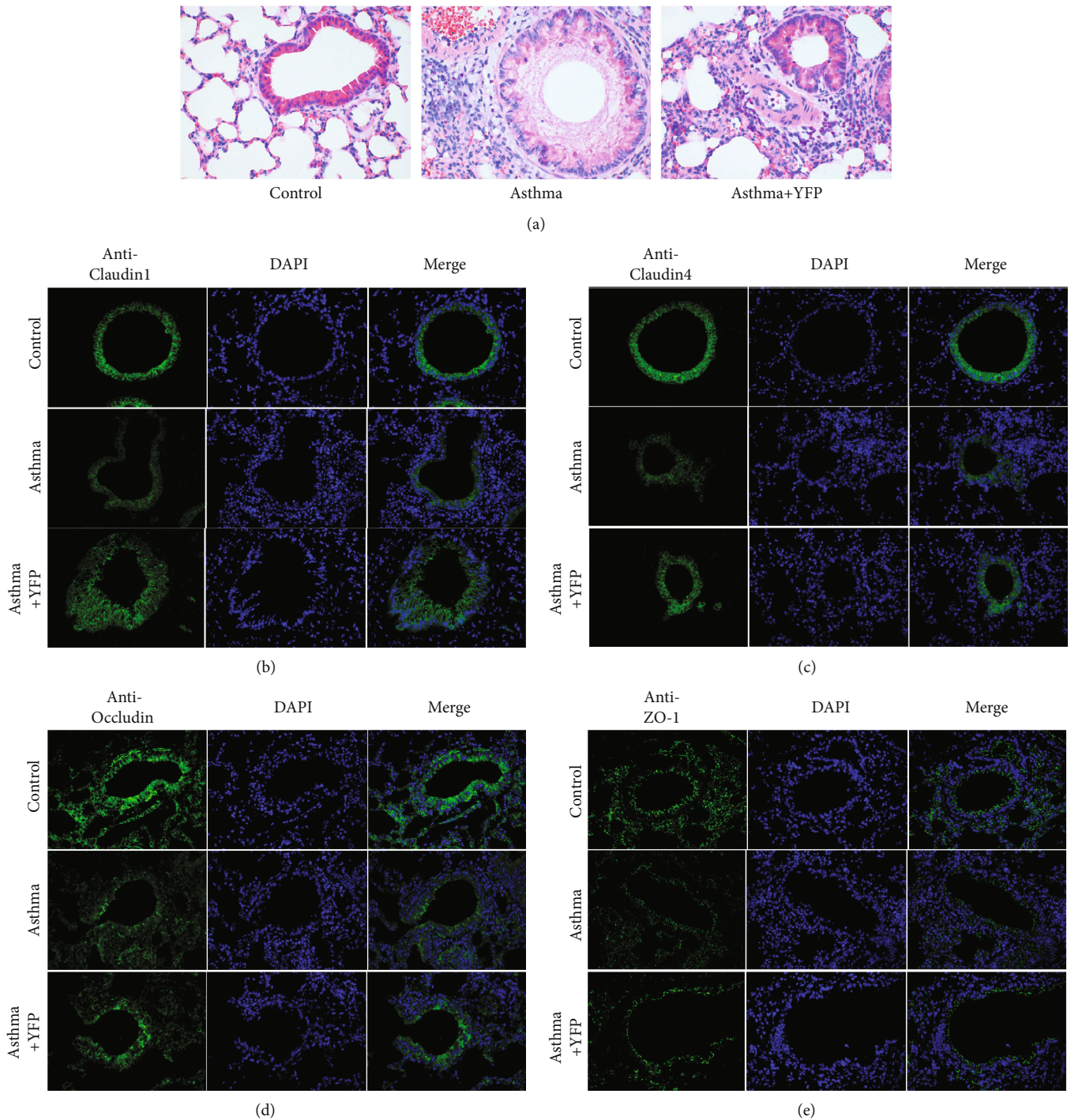


FIGURE 1: YFP ameliorated the injury of lung tissue of the mouse asthma model. HE staining of the lung tissue from each mouse (a). The expression of Claudin1 (b), Claudin4 (c), Occludin (d), and ZO-1 (e) was detected by immunofluorescence.

YFP on the inflammation, the expression of related proteins in the lung tissue was detected by Western blot. As shown in Figures 2(g) and 2(h), the expression level of NF- κ B, p-NF- κ B, TLR1, TLR, TLR3, TLR4, and Myd88 was significantly promoted in the asthma group, compared with the control group, which was also inhibited by the treatment with YFP (** $P < 0.01$ vs. control, *** $P < 0.001$ vs. control, and ### $P < 0.001$ vs. asthma).

3.3. YFP Ameliorated the Level of Oxidative Stress in the Lung of the Mouse Asthma Model. Oxidative stress-related factors were detected in the BALF by ELISA to evaluate the effect of YFP on oxidative stress. Compared to the controls, MDA was significantly improved in the asthma group, which was inhibited by the introduction of YFP (Figure 3(a)), while the decreased production of GSH-PX, SOD, and CAT in the asthma group was significantly elevated by the treatment

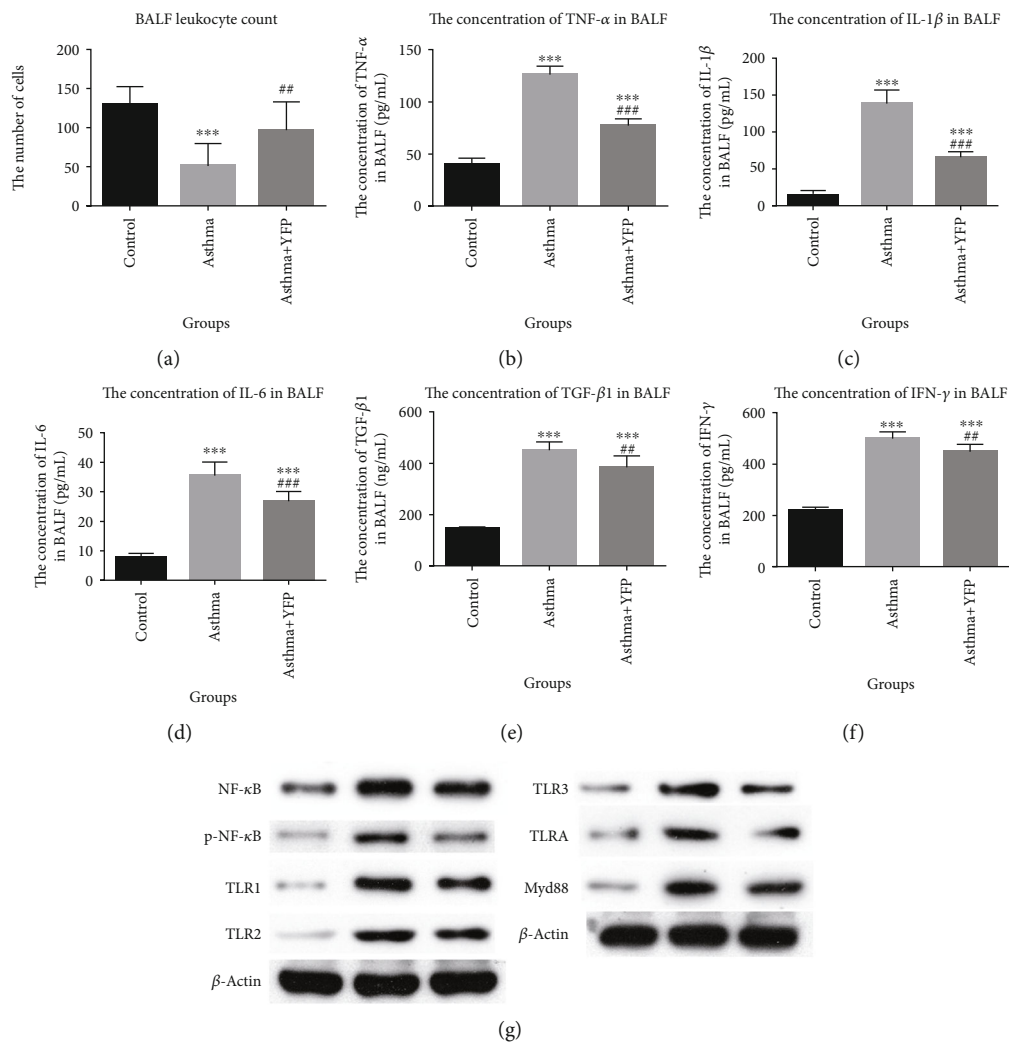


FIGURE 2: Continued.

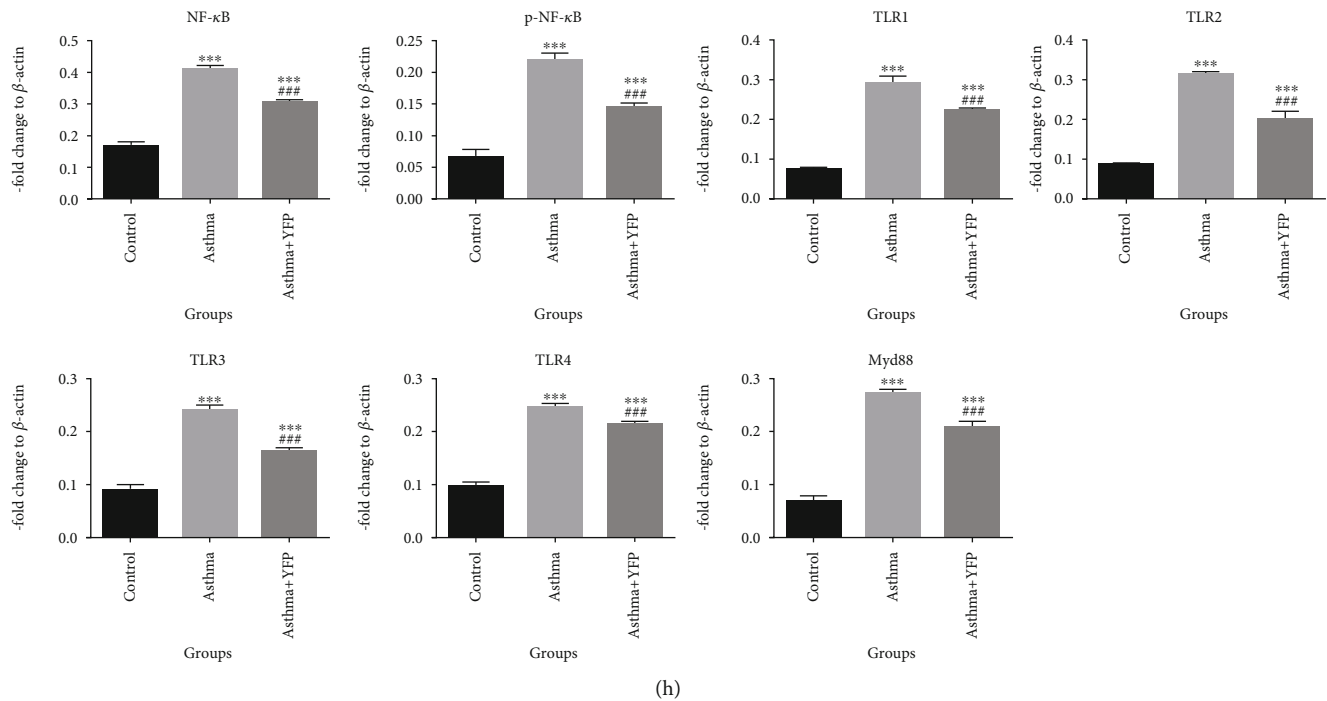


FIGURE 2: YFP promoted the inflammation in the lung of the mouse asthma model. (a) The BALF leukocyte count was checked by a hemocytometer. (b–f) The expression of $\text{TNF-}\alpha$, $\text{IL-1}\beta$, IL-6 , $\text{TGF-}\beta$, and $\text{IFN-}\gamma$ was determined by ELISA. (g, h) The expression of $\text{NF-}\kappa\text{B}$, $\text{p-NF-}\kappa\text{B}$, TLR1 , TLR2 , TLR3 , TLR4 , and Myd88 was evaluated by Western blot. Data are presented as mean \pm SEM. *** $P < 0.001$ vs. control, ** $P < 0.01$ vs. asthma, and ### $P < 0.001$ vs. asthma.

of YFP (Figures 3(b)–3(d)). Besides, the expression of oxidative stress-related genes in the lung tissue was detected by qRT-PCR. The results are shown in Figures 3(e)–3(j). The gene expression level of GPX1 , GPX4 , CAT , SOD1 , SOD2 and UCP2 was significantly suppressed in the asthma group, compared to the control group, and was promoted comparing with that by the asthma+YFP group (** $P < 0.01$ vs. control, *** $P < 0.001$ vs. control, and ### $P < 0.001$ vs. asthma).

3.4. YFP Ameliorated the Autophagy in the Lung of the Mouse Asthma Model. To evaluate the effects of YFP on autophagy in the lung tissues induced by asthma modeling, Western blot was used to determine the expression level of autophagy-related proteins. As shown in Figure 4, ATG5 , Beclin1 , and LC3BII/I were significantly upregulated in asthma mice compared to control, which were greatly suppressed by the introduction of YFP (** $P < 0.01$ vs. control, *** $P < 0.001$ vs. control, and ### $P < 0.001$ vs. asthma).

3.5. The Distribution of Bacteria Species Was Slightly Changed by YFP in Asthma Mice. 16S rDNA sequencing analysis was performed to explore the effect of YFP on the gut microbiota of allergic asthma mice. As shown in Figure 5(a), the Venn diagram revealed that a total of 1045 distinct genera were identified upon YFP treatment. These observations indicated that the YFP treatment increased the bacterial diversity in the gut of the animal, although not statistically significant. Figures 5(b)–5(d) showed the microbial richness (Chao1) analysis, alpha diversity (Shannon) analysis, and PCoA analysis, respectively. However, no significant difference was

observed between the asthma group and the YFP-treated group. As shown in Figure 5(e) and Table 2, the major difference in the relative abundance of the bacteria species in the feces of mice was observed between the control group and the asthma group, of which the top 15 species with the highest abundance were listed. Interestingly, except for *Akkermansia* (higher in the control group), the relative abundance of *Prevotella*, *Oscillospira*, *Helicobacter*, *Coprococcus*, *Ruminococcus*, *Bacteroides*, *Flexispira*, *Odoribacter*, and *Turicibacter* in the asthma mice was significantly elevated, compared to control (* $P < 0.05$ vs. control). By the treatment of YFP, the relative abundance of *Oscillospira*, *Helicobacter*, *Coprococcus*, *Ruminococcus*, *Flexispira*, and *Odoribacter* was greatly decreased (# $P < 0.05$ vs. asthma).

4. Discussion

Airway allergic inflammation is reported to be one of the pathological basis of allergic asthma [32]. Large amounts of inflammatory immune cells are recruited into the lung tissues when allergic occurs and release inflammatory cytokines to accelerate airway allergic inflammation, promoting aggravate allergic asthma process [33]. Therefore, it is of great importance to inhibiting airway inflammation in allergic asthma. In the present study, the antiasthma effect of YFP was investigated. HE staining showed that YFP ameliorated the lung injury caused by asthma modeling in mice. The tight-junction protein of lung tissues is closely related to the pathological state of allergic asthma, which is represented by the expression level of ZO-1 , Claudin1 , Claudin4 , and Occludin

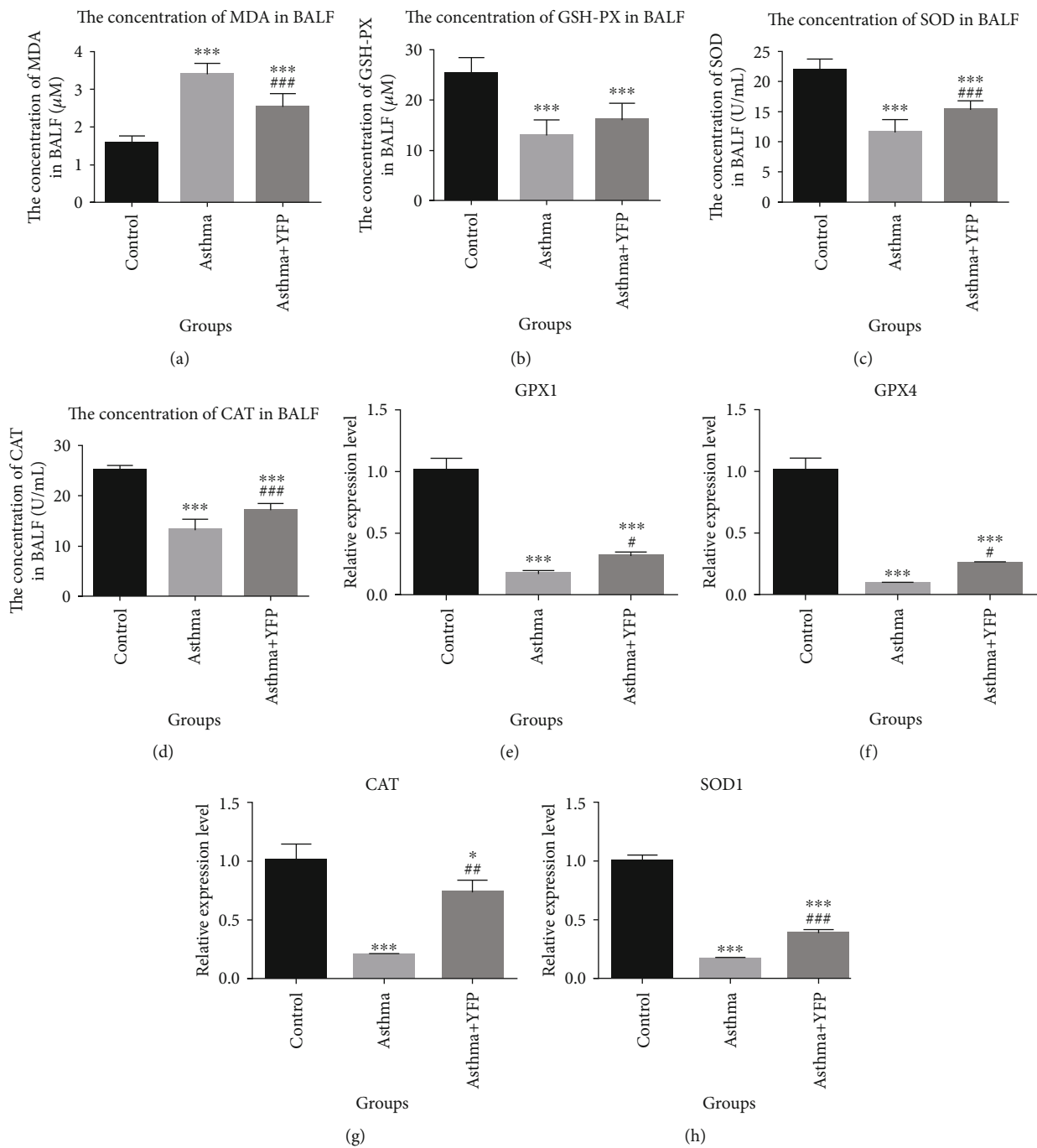


FIGURE 3: Continued.

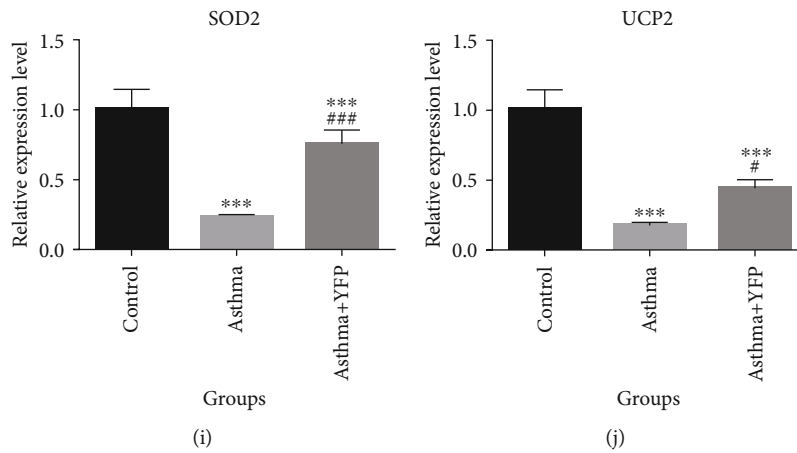


FIGURE 3: YFP ameliorated the level of oxidative stress in the lung of the mouse asthma model. (a–d) The concentration of MDA, GSH-Px, SOD, and CAT was determined by ELISA. (e–j) The gene expression level of GPX1, GPX4, CAT, SOD1, SOD2, and UCP2 was detected by qRT-PCR. Data are presented as mean ± SEM. * $P < 0.05$ vs. control, *** $P < 0.001$ vs. control, # $P < 0.05$ vs. asthma, ## $P < 0.01$ vs. asthma, and ### $P < 0.001$ vs. asthma.

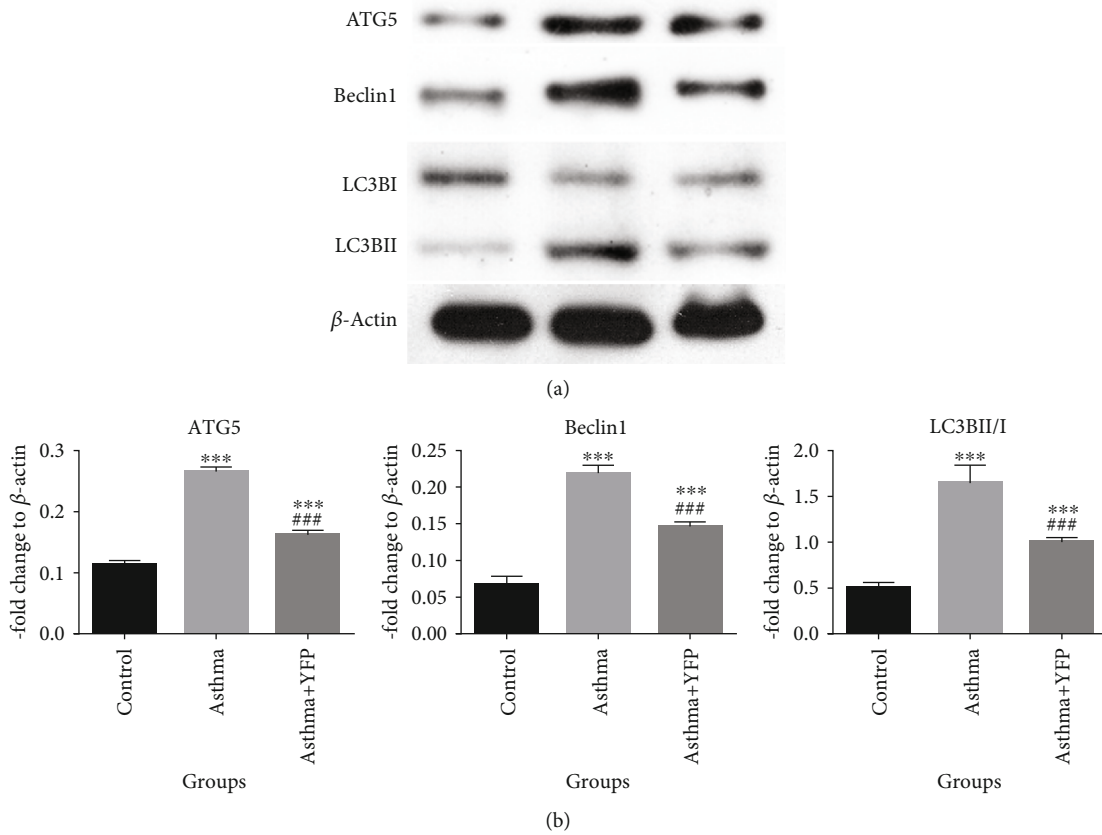


FIGURE 4: YFP ameliorated the level of oxidative stress in the lung of the mouse asthma model. (a) The expression level of ATG5, Beclin1, and LC3I/II detected by Western blot. (b) The quantitative results of the protein expression. Data are presented as mean ± SEM. ** $P < 0.01$ vs. control, *** $P < 0.001$ vs. control, and ### $P < 0.001$ vs. asthma.

[34, 35]. After the administration of YFP, the tight junction of lung tissue was greatly improved. The results indicated that the symptom of allergic asthma in mice was significantly improved by the administration of YFP. Besides, YFP pro-

moted inflammation in the lung. By exploring the state of the inflammatory signal pathways in the lung tissues following treatments with YFP, we found that YFP greatly inhibited the TLR/NF-κB signal pathway in the lung tissue. These data

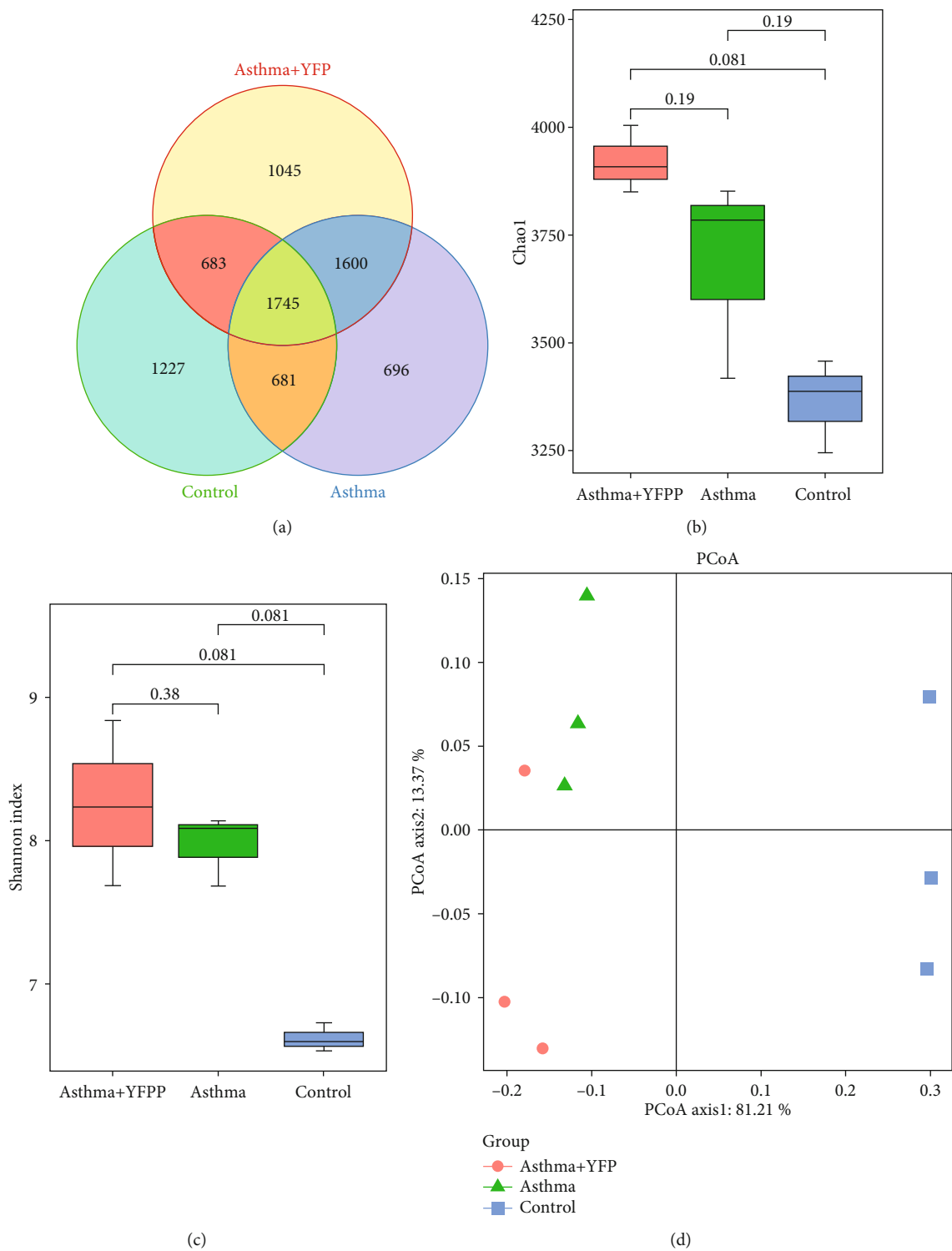
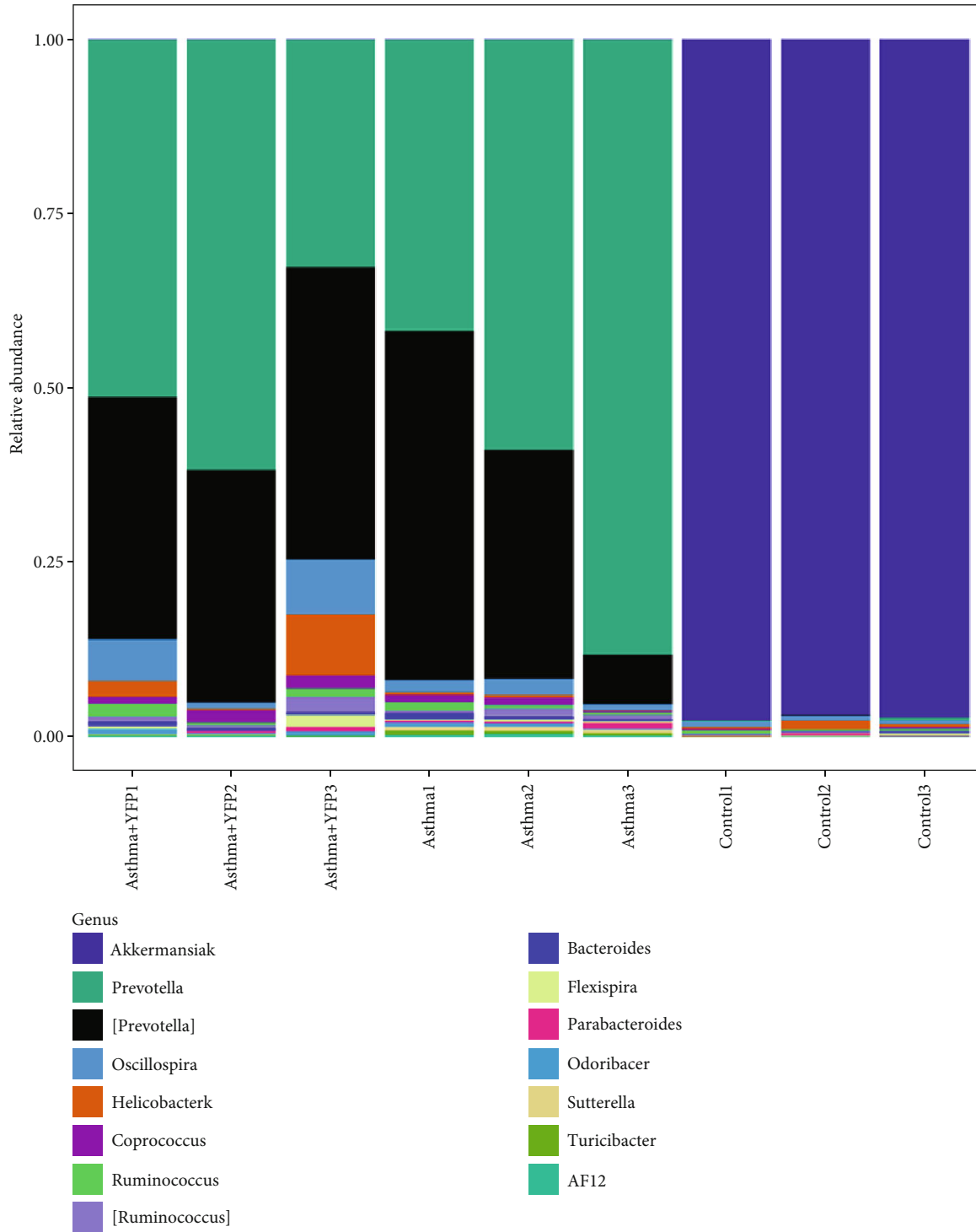


FIGURE 5: Continued.



(e)

FIGURE 5: The distribution of gut microbiota was regulated by YFP. (a) Venn diagram of shared genus observed in the feces samples. (b) The microbial richness (Chao1) analysis in each group. (c) Alpha diversity (Shannon) analysis in each group. (d) The PCoA analysis in each group. (e) The histogram of species distribution of the top 15 with the highest relative abundance.

implied that the symptom of allergic asthma in the mouse model had been greatly improved by YFP, accompanied by suppression of the airway allergic inflammation.

To further investigate the possible mechanism underlying the inflammation inhibitory effects of YFP, the distribu-

tion of gut microbiota in the feces of mice was explored. Salameh et al. [36] reported that gut microbiota plays a great role in the pathogenesis of allergic asthma, to which the inflammatory factors might be the mediators. In the present study, we found that although the relative abundance of the

TABLE 2: The relative abundance of the top 15 bacteria species in the control, asthma, and YFP groups (* $P < 0.05$ vs. control, # $P < 0.05$ vs. asthma).

Name of genus	Relative abundance in the control group	Relative abundance in the asthma group	Relative abundance in the YFP group
Akkermansia	0.376830 ± 0.018474	4.042394 ± 1.664278*	7.308090 ± 3.401218
Prevotella	0.000692 ± 0.000574	0.151322 ± 0.065380*	0.153308 ± 0.083194
[Prevotella]	7.146626 ± 1.974750	0.108791 ± 0.008467*	0.066855 ± 0.048877
Oscillospira	0.002609 ± 0.000602	0.013902 ± 0.009423*	0.003553 ± 0.001185#
Helicobacter	0.002436 ± 0.001818	0.010009 ± 0.010251*	0.000643 ± 0.000375#
Coprococcus	0.000674 ± 0.000434	0.004445 ± 0.001347*	0.001724 ± 0.000896#
Ruminococcus	0.001198 ± 0.000623	0.003315 ± 0.002597*	0.001678 ± 0.001107#
[Ruminococcus]	0.000406 ± 9.398833	0.003168 ± 0.001985*	0.001569 ± 0.000606#
Bacteroides	0.000609 ± 0.000204	0.001355 ± 0.000624*	0.001191 ± 0.000658
Flexispira	0.000674 ± 0.000652	0.001800 ± 0.002127*	0.000515 ± 0.000160#
Parabacteroides	0.000714 ± 0.000509	0.000943 ± 0.000621	0.001299 ± 0.001236
Odoribacter	0 ± 0	0.001427 ± 0.000976*	0.000848 ± 0.000512#
Sutterella	0.000279 ± 0.000132	0.000289 ± 0.000168	0.001239 ± 0.000139
Turicibacter	0 ± 0	0.000369 ± 0.000155*	0.001182 ± 0.000549#
AF12	0.000279 ± 0.000139	0.000472 ± 0.000161	0.000693 ± 0.000180

top 3 bacteria species was not reversed by YFP in the asthma mice, a significant inhibitory effect on the relative abundance of the top 4-8 bacteria species was achieved by the treatment of YFP, indicating a minor impact of YFP on the distribution of gut microbiota of the asthma mice. However, more evidence of the positive correlation between the antiasthma property of YFP and the change of gut microbiota distribution should be provided in our future work. In the present study, only one dosage of YFP was applied and we suspected that the change of gut microbiota distribution, such as the relative abundance of the bacteria species, α -diversity index, and β -diversity index, might be enlarged if we increased the dosage, which will be verified in our subsequent work. Besides, in our future work, the inflammation profile both in the central nervous system and in the peripheral region will also be described to analyze the change of inflammation state before and after the treatment of YFP, which might bring direct evidence to explain the antiasthma property of YFP.

Oxidative stress is also a pathological manifestation of allergic asthma, the representative indexes of which are MDA, GSH-PX, SOD, and CAT [37]. In the present study, the oxidative stress level in the asthmatic mice was significantly inhibited by the treatment of YFP. Silveira et al. [21] reported that autophagy could induce eosinophil extracellular trap formation and allergic airway inflammation in a murine asthma model by activating oxidative stress. Tsai et al. [38] also reported that autophagy against oxidative stress-mediated apoptosis in normal and asthmatic airway epithelium is induced by complement regulatory protein CD46. In the present study, the expression level of autophagy-related proteins (ATG5, Beclin1, and LC3BII/I) was significantly suppressed by YFP. These data indicated that YFP might exert antiasthmatic effects by inhibiting oxidative stress through suppressing autophagy.

According to the data achieved in the present study, on the one hand, the inflammation induced in the murine asthma model could be alleviated by the treatment of YFP, which might be related to the regulatory effect of YFP on the TLR4/NF- κ B signaling pathway. In our future work, the specific inhibitor against the TLR4/NF- κ B signaling pathway will be introduced to verify the mechanism underlying the inhibitory effect of YFP against inflammation. On the other hand, oxidative stress in the lung tissues was ameliorated by YFP by regulating autophagy, which should also be verified by introducing the agonist of autophagy in our future work. As a result, the symptom of asthma in the murine model was significantly alleviated.

Collectively, our research showed that YFP might exert antiasthmatic effects by inhibiting airway allergic inflammation through regulating gut microbiota distribution and inhibiting oxidative stress levels through suppressing autophagy.

Data Availability

The data can be available if requested by the editor.

Conflicts of Interest

The authors declare there are no conflicts of interest regarding the publication of this paper.

Acknowledgments

This work was supported by the National Natural Scientific Fund of PR China (no. 81100059), the Natural Science Foundation of Hunan Province of China (2019JJ50849), and the Scientific Research Project of Science and Technology Office of Hunan Province (2018SK52505).

References

- [1] S. Hadebe and F. Brombacher, "Environment and host-genetic determinants in early development of allergic asthma: contribution of fungi," *Frontiers in Immunology*, vol. 10, p. 2696, 2019.
- [2] W. Eder, M. J. Ege, and E. von Mutius, "The asthma epidemic," *The New England Journal of Medicine*, vol. 355, no. 21, pp. 2226–2235, 2006.
- [3] M. M. Stein, C. L. Hrusch, J. Gozdz et al., "Innate immunity and asthma risk in Amish and Hutterite farm children," *The New England Journal of Medicine*, vol. 375, no. 5, pp. 411–421, 2016.
- [4] F. Hoffmann, F. Ender, I. Schmutte et al., "Origin, localization, and immunoregulatory properties of pulmonary phagocytes in allergic asthma," *Frontiers in Immunology*, vol. 7, p. 107, 2016.
- [5] H. Vroman, I. M. Bergen, B. W. Li et al., "Development of eosinophilic inflammation is independent of B-T cell interaction in a chronic house dust mite-driven asthma model," *Clinical and Experimental Allergy*, vol. 47, no. 4, pp. 551–564, 2017.
- [6] L. Fleming, S. Saglani, and A. Bush, "Asthma attacks: should we nail our colours to the mast (cell)?," *The European Respiratory Journal*, vol. 48, no. 5, pp. 1261–1264, 2016.
- [7] C. Z. Han, I. J. Juncadella, J. M. Kinchen et al., "Macrophages redirect phagocytosis by non-professional phagocytes and influence inflammation," *Nature*, vol. 539, no. 7630, pp. 570–574, 2016.
- [8] Y. Zhang, Y. Xu, S. Liu et al., "Scaffolding protein Gab1 regulates myeloid dendritic cell migration in allergic asthma," *Cell Research*, vol. 26, no. 11, pp. 1226–1241, 2016.
- [9] R. Divekar and W. J. Calhoun, "Heterogeneity of asthma in society," *Advances in Experimental Medicine and Biology*, vol. 795, pp. 31–41, 2014.
- [10] Q. Ma, W. Huang, J. Zhao, and Z. Yang, "Liu Shen Wan inhibits influenza A virus and excessive virus-induced inflammatory response via suppression of TLR4/NF- κ B signaling pathway in vitro and in vivo," *Journal of Ethnopharmacology*, vol. 252, p. 112584, 2020.
- [11] Y. W. Yu, M. X. Li, Z. Y. Zhang, and H. Yu, "The deficiency of CX3CL1/CX3CR1 system ameliorates high fructose diet-induced kidney injury by regulating NF- κ B pathways in CX3CR1-knock out mice," *International Journal of Molecular Medicine*, vol. 41, no. 6, pp. 3577–3585, 2018.
- [12] R. Li, Y. Liu, L. Li, R. Zhang, and Y. Tang, "p120 inhibits LPS/TNF α -induced endothelial Ang2 synthesis and release in an NF- κ B independent fashion," *Cytokine*, vol. 123, p. 154786, 2019.
- [13] X. Tian, H. Zhao, Z. Zhang, Z. Guo, and W. Li, "Correction: intestinal mucosal injury induced by obstructive jaundice is associated with activation of TLR4/TRAF6/NF- κ B pathways," *PLoS One*, vol. 14, no. 12, 2019.
- [14] J. Hong, S. Li, D. Z. Markova et al., "Bromodomain-containing protein 4 inhibition alleviates matrix degradation by enhancing autophagy and suppressing NLRP3 inflammasome activity in NP cells," *Journal of Cellular Physiology*, vol. 235, no. 7-8, pp. 5736–5749, 2020.
- [15] H. Qi, J. Ren, L. Ba et al., "MSTN attenuates cardiac hypertrophy through inhibition of excessive cardiac autophagy by blocking AMPK/mTOR and miR-128/PPAR γ /NF- κ B," *Molecular Therapy-Nucleic Acids*, vol. 19, pp. 507–522, 2019.
- [16] Y. Suzuki, H. Maazi, I. Sankaranarayanan et al., "Lack of autophagy induces steroid-resistant airway inflammation," *The Journal of Allergy and Clinical Immunology*, vol. 137, no. 5, pp. 1382–1389.e9, 2016.
- [17] P. Kuballa, W. M. Nolte, A. B. Castoreno, and R. J. Xavier, "Autophagy and the immune system," *Annual Review of Immunology*, vol. 30, no. 1, pp. 611–646, 2012.
- [18] L. J. Martin, J. Gupta, S. S. Jyothula et al., "Functional variant in the autophagy-related 5 gene promoter is associated with childhood asthma," *PLoS One*, vol. 7, no. 4, 2012.
- [19] D. L. Pham, S. H. Kim, P. Losol et al., "Association of autophagy related gene polymorphisms with neutrophilic airway inflammation in adult asthma," *The Korean Journal of Internal Medicine*, vol. 31, no. 2, pp. 375–385, 2016.
- [20] A. Poon, D. Eidelman, C. Laprise, and Q. Hamid, "ATG5, autophagy and lung function in asthma," *Autophagy*, vol. 8, pp. 694–695, 2012.
- [21] J. S. Silveira, G. L. Antunes, D. B. Kaiber et al., "Autophagy induces eosinophil extracellular traps formation and allergic airway inflammation in a murine asthma model," *Journal of Cellular Physiology*, vol. 235, pp. 267–280, 2020.
- [22] I. Pinheiro, L. Robinson, A. Verhelst et al., "A yeast fermentate improves gastrointestinal discomfort and constipation by modulation of the gut microbiome: results from a randomized double-blind placebo-controlled pilot trial," *BMC Complementary and Alternative Medicine*, vol. 17, no. 1, p. 441, 2017.
- [23] T. Pessi, Y. Sutas, A. Martinen, and E. Isolauri, "Probiotics reinforce mucosal degradation of antigens in rats: implications for therapeutic use of probiotics," *The Journal of Nutrition*, vol. 128, no. 12, pp. 2313–2318, 1998.
- [24] T. R. Klaenhammer, M. Kleerebezem, M. V. Kopp, and M. Rescigno, "The impact of probiotics and prebiotics on the immune system," *Nature Reviews. Immunology*, vol. 12, no. 10, pp. 728–734, 2012.
- [25] C. A. Cuello-Garcia, J. L. Brozek, A. Fiocchi et al., "Probiotics for the prevention of allergy: a systematic review and meta-analysis of randomized controlled trials," *The Journal of Allergy and Clinical Immunology*, vol. 136, no. 4, pp. 952–961, 2015.
- [26] S. O. Jang, H. J. Kim, Y. J. Kim et al., "Asthma prevention by Lactobacillus rhamnosus in a mouse model is associated with CD4(+)CD25(+)Foxp3(+) T cells," *Allergy, Asthma and Immunology Research*, vol. 4, no. 3, pp. 150–156, 2012.
- [27] S. Sagar, M. E. Morgan, S. Chen et al., "Bifidobacterium breve and Lactobacillus rhamnosus treatment is as effective as budesonide at reducing inflammation in a murine model for chronic asthma," *Respiratory Research*, vol. 15, no. 1, p. 46, 2014.
- [28] X. Wang, Y. Hui, L. Zhao, Y. Hao, H. Guo, and F. Ren, "Oral administration of Lactobacillus paracasei L9 attenuates PM2.5-induced enhancement of airway hyperresponsiveness and allergic airway response in murine model of asthma," *PLoS One*, vol. 12, no. 2, 2017.
- [29] J. Yu, S. O. Jang, B. J. Kim et al., "The effects of Lactobacillus rhamnosus on the prevention of asthma in a murine model," *Allergy, Asthma and Immunology Research*, vol. 2, no. 3, pp. 199–205, 2010.
- [30] H. Wang, S. Li, H. Li, F. Du, J. Guan, and Y. Wu, "Mechanism of probiotic VSL#3 inhibiting NF- κ B and TNF- α on colitis through TLR4-NF- κ B signal pathway," *Iranian Journal of Public Health*, vol. 48, no. 7, pp. 1292–1300, 2019.

- [31] R. Bhardwaj, B. P. Singh, N. Sandhu et al., "Probiotic mediated NF-kappaB regulation for prospective management of type 2 diabetes," *Molecular Biology Reports*, vol. 47, no. 3, pp. 2301–2313, 2020.
- [32] G. Liu, M. A. Cooley, P. M. Nair et al., "Airway remodelling and inflammation in asthma are dependent on the extracellular matrix protein fibulin-1c," *The Journal of Pathology*, vol. 243, no. 4, pp. 510–523, 2017.
- [33] Q. Zhang, L. Wang, B. Chen, Q. Zhuo, C. Bao, and L. Lin, "Propofol inhibits NF- κ B activation to ameliorate airway inflammation in ovalbumin (OVA)-induced allergic asthma mice," *International Immunopharmacology*, vol. 51, pp. 158–164, 2017.
- [34] H. J. Kim, S. H. Lee, S. Jeong, and S. J. Hong, "Protease-activated receptors 2-antagonist suppresses asthma by inhibiting reactive oxygen species-thymic stromal lymphopoietin inflammation and epithelial tight junction degradation," *Allergy, Asthma & Immunology Research*, vol. 11, no. 4, pp. 560–571, 2019.
- [35] H. T. Tan, S. Hagner, F. Ruchti et al., "Tight junction, mucin, and inflammasome-related molecules are differentially expressed in eosinophilic, mixed, and neutrophilic experimental asthma in mice," *Allergy*, vol. 74, no. 2, pp. 294–307, 2019.
- [36] M. Salameh, Z. Burney, N. Mhaimed et al., "The role of gut microbiota in atopic asthma and allergy, implications in the understanding of disease pathogenesis," *Scandinavian Journal of Immunology*, vol. 91, no. 3, 2019.
- [37] S. Samarghandian, M. Azimi-Nezhad, T. Farkhondeh, and F. Samini, "Anti-oxidative effects of curcumin on immobilization-induced oxidative stress in rat brain, liver and kidney," *Biomedicine & Pharmacotherapy*, vol. 87, pp. 223–229, 2017.
- [38] Y. G. Tsai, Y. S. Wen, J. Y. Wang et al., "Complement regulatory protein CD46 induces autophagy against oxidative stress-mediated apoptosis in normal and asthmatic airway epithelium," *Scientific Reports*, vol. 8, no. 1, p. 12973, 2018.

Research Article

Effect of Oral Administration with *Lactobacillus plantarum* CAM6 Strain on Sows during Gestation-Lactation and the Derived Impact on Their Progeny Performance

César Betancur ¹, Yordan Martínez ², Guillermo Tellez-Isaias ³, Rogel Castillo ²,
and Xinghua Ding ⁴

¹Departamento de Ciencias Pecuarias, Facultad de Medicina Veterinaria y Zootecnia, Universidad de Córdoba, Montería 230002, Colombia

²Departamento de Ciencia y Producción Agropecuaria, Escuela Agrícola Panamericana Zamorano, Valle de Yeguare, San Antonio de Oriente, Francisco Morazán 96, Honduras

³Department of Poultry Science, University of Arkansas, Fayetteville, AR 72701, USA

⁴School of Biological Sciences, The University of Hong Kong, Pokfulam Road, Hong Kong SAR, China

Correspondence should be addressed to Xinghua Ding; u3005522@connect.hku.hk

Received 30 October 2020; Revised 13 December 2020; Accepted 21 December 2020; Published 8 January 2021

Academic Editor: Shuai Chen

Copyright © 2021 César Betancur et al. This is an open access article distributed under the Creative Commons Attribution License, which permits unrestricted use, distribution, and reproduction in any medium, provided the original work is properly cited.

Background. To evaluate the biological response of the sows and their offspring with oral administration of *Lactobacillus plantarum* CAM6 in breeding sows, a total of 20 Pietrain breeding sows with three farrowings and their descendants were used, randomly divided into two groups of 10 sows each. Treatments included a basal diet (T0) and basal diet +10 mL biological agent containing 10^9 CFU/mL *L. plantarum* CAM6 (T1). No antibiotics were used throughout the entire experimental process of this study. **Results.** The *L. Plantarum* CAM6 supplementation in sows' feeding did not affect ($P > 0.05$) the reproductive performance of the sows; however, the number of deaths for their offspring before weaning ($P \leq 0.05$) decreased. In addition, the oral administration of *Lactobacillus plantarum* CAM6 in sows increased ($P \leq 0.05$) the content of lactose, nonfat solids, mineral salts, and the density of sows' milk, with a decrease in milk fat. Moreover, the probiotic feed orally to the sows improved the body weight ($P \leq 0.05$) and reduced the diarrhea incidence of their offspring ($P \leq 0.05$). Also, the probiotic administration of sows changed ($P \leq 0.05$) the serum concentration of Na^+ , pCO_2 , and D- β -hydroxybutyrate and increased ($P \leq 0.05$) the leukocytes, lymphocytes, and platelets in their piglets. **Conclusion.** Oral administration of *Lactobacillus plantarum* CAM6 in breeding sows improved body weight, physiological status, and the health of their offspring. And preparing the neonatal piglets physiologically is of great importance to the pig farming industry which could decrease the operational cost and medication (especially antibiotics) consumption of the pig producers.

1. Introduction

In the first few days after birth, the piglets are less stable and more susceptible to disturbances and microbial pathogens, because newborn pigs are immunodeficient at birth, and there is no transfer of antibodies through the uterus [1]. They have to acquire passive immunity from colostrum and breast milk for their survival [2]. Therefore, to minimize the use of antibiotics in piglets, one of the strategies is to prepare the

offspring physiologically and microbiologically by administering functional feed orally during the perinatal period of the sows [3].

Among the verities of functional feeds taken orally, probiotics are one of them which are live microbial feed supplements with the capability to beneficially affect the host animal by improving its intestinal microbial balance [4]. Probiotics have been explored as feed additives in swine production by considering their beneficial effects on intestinal

microbial homeostasis of the sows and indirectly benefiting the progeny and helping to minimize the use of subtherapeutic antibiotics [5, 6].

There are several studies reported that the performance of nutrient absorption of the sows during gestation and lactation influences the litter size and body weight of suckling pigs at birth and livability at weaning [7]. And the better utilization of nutrients during lactation is reflected in high-quality milk, which would indirectly improve the growth performance of their piglets [8].

Lactic acid bacteria (LAB) have been the main microorganisms that have been used as potential probiotics in swine production for their beneficial role in the gastrointestinal tract [9]. Few studies have been elucidated on the effect of the supplementation of *Lactobacillus* spp. in sow nutrition can extend to their offspring. Previous studies showed that the isolated *Lactobacillus plantarum* CAM6 can ferment a wide spectrum of plant carbohydrates and tolerant to bile salts and low pH; and it is antagonistic against the common Enterobacteriaceae in swine production [10, 11]. Therefore, the objective of this study was to evaluate the efficacy of *Lactobacillus plantarum* CAM6 in sows during the gestation and lactation and its influence on their milk as well as on the blood parameters and productive performance of their descendants.

2. Materials and Methods

The study was carried out in accordance with the National Institutes of Health guide for the care and use of laboratory animals (NIH publications No. 8023, revised 1978), and the experiment was approved by the Animal Care and Use Committee of Córdoba University and Research (Resolution No. 1 of January 26, 2016).

2.1. Experimental Location. The research in the swine experimental areas of the University of Córdoba, Berástegui campus, Córdoba, Colombia, located between the coordinates 7°23'9"26' north latitude and 74°52'76"32' west longitude meridian of Greenwich was developed. The average annual temperature is 28°C, and the average rainfall is 1400 mm per year.

2.2. Probiotic, Animals, and Treatments. The *L. plantarum* CAM6 strain (access number 4MK523644.1) was isolated from Creole pigs (Zungo Pelado) from the north coast of Colombia [11]. This bacterial strain grew under conditions of pH (3.0), bile salt (0.3%), NaCl (10%), and high temperatures and showed antagonistic activity against bacterial pathogens that frequently infect piglets [10, 11].

This strain was inoculated in pine, apple, banana, and papaya peel juice. Growth kinetics was performed to determine the most appropriate fruit peel concentration and optimize the substrate to the inoculum ratio and pH. The best medium consisted of 40% fruit peels and 60% water. The optimal substrate to inoculum ratio was 6.81, and the best pH was 5.29. Under these conditions, a bacterial density of 10⁹ CFU/mL was obtained, and this concentration was used as a probiotic treatment.

A total of 20 apparently healthy Pietrain sows with three farrowing were used in the last third of gestation (75 days of gestation) and throughout suckling period according to a completely randomized design with two treatments and 10 replicates. Farrowings were synchronized, and no anomalies were found in the first two-thirds of the gestation.

The treatments consisted of T0—basal diet (BD) feeding group—and T1—BD+10 mL biological agent containing 10⁹ CFU/mL *L. plantarum* CAM6 feeding group. No antibiotics were added in either group. It is noted important that the probiotic was not offered to suckling piglets. The diets were formulated according to the recommendations described by NCR (2012) to satisfy the nutritional requirements of the pig category. The ingredients of the diets are shown in Table 1.

2.3. Experimental Conditions. The pregnant sows were placed individually in metal pens of 2.10 m × 0.80 m × 1 m. Three days prior to the expected date, farrowing sows were allocated into metallic farrowing crates of 2.10 m × 1 m × 1 m, inside of an area of 1 m × 1.50 m for their offspring. Feeding for pregnant and lactating sows was restricted at a rate of 2 kg/animal/day. The feed was supplied twice a day (8:00 am and 3:00 pm) in tubular feeders of 52 cm × 16 cm, and the water was available *ad libitum* in nipple-type automatic drinkers. From 8 days old, a prestarter diet in the form of pellets at a rate of 10 grams per animal/day was offered to the piglets, which was increased consecutively until reaching 300 grams per animal/day in two frequencies (8:00 a.m. and 3:00 p.m.) Heater lamps to manage the temperature of the suckling piglets ranged from 30°C (at input) with progressive reduction to 26°C (at output) were used.

2.4. Productive and Reproductive Indicators of the Sow. The individual body weight of the sows was determined at 75 days of gestation (beginning of the experiment), at farrowing and at weaning (Mettler Toledo, Digital Scale, Ohio, USA). Using these data, weight loss during farrowing and weaning was calculated. Also, the days of gestation and weaning-estrus interval were determined per sow. The following data for each litter were recorded: the number of piglets born alive and dead and specific time of death during the lactation period and weight of the piglets at 1, 7, 14, 21, and 28 days old using a precision digital ±0.1 g, scale (OSBORNE®, model 37473®, Kansas, Missouri, USA).

2.5. Chemical Composition of the Milk. Milk was collected in the morning prior to the suction of the piglets (7:00 a.m.), within 4 days after the initiation of farrow. The milk samples were placed in sterile bottles, previously labeled and kept refrigerated (4°C). Proteins, fats, lactose, nonfat solids, total solids, mineral salts, and density were determined using an ultrasonic milk analyzer (Biolac 60, Bogotá, Colombia). The milk tests were performed at the Laboratory of the University of Córdoba.

2.6. Diarrhea Index of Lactating Piglets. Diarrhea incidence (DI) in suckling piglets was determined during the experimental period using the following formula: DI = number of diarrhea/(number of animals × total days) × 100 [12].

TABLE 1: Ingredients for sows in pregnancy and lactation and suckling piglets.

Ingredients (%)	Pregnancy	Lactation	Prestarter
Cornmeal	53.40	63.00	36.00
Soymeal	12.60	26.00	20.00
Wheat bran	30.00	4.00	—
Soybean oil	—	3.00	2.00
Sugar	—	—	2.00
Gestation nucleus ¹	4.00	—	—
Lactation nucleus ²	—	4.00	—
Prestarter nucleus ³	—	—	40.00

¹Gestation nucleus per kg of product: folic acid 39 mg; pantothenic acid 300 mg; biotin 5 mg; Ca 175500 mg; Co 5 mg; Cu 250 mg; choline 10520 mg; Fe 2150 mg; P 12000 mg; I 25 mg; Mn 1,250 mg; niacin 800 mg; Se 9 mg; Na 48,000 mg; vit. A 250000; vit. B1 60 mg; vit. B12 600 mcg; vit. B2 150 mg; vit. B6 80 mg; vit. C 1250 mg; vit. D3 50000 IU; vit. E 1250 mg; vit. K3 100 mg; and Zn 3125 mg. ²Lactation nucleus per kg of product: folic acid 37.5 mg; pantothenic acid 300 mg; BHT 3,750 mg; biotin 5 mg; Ca 205000 mg; Co 6 mg; Cu 250; choline 10000 mg; Fe 2000 mg; P 51000 mg; I 25 mg; Mn 1250 mg; niacin 800 mg; Se 9 mg; Na 44000 mg; vit. A 250000 IU; vit. B1 60 mg; vit. B12 600 mcg; vit. B2 150 mg; vit. B6 80 mg; vit. C 1250 mg; vit. D3 50000 IU; vit. E 1250 mg; vit. K3 100 mg; and Zn 3125 mg. ³Pre-starter nucleus: whey powder, milk powder, skim milk powder, choline, extruded soybeans, corn, sugar, fumaric acid, vegetable oil, dicalcium phosphate, threonine, tryptophan, calcite, mineral premix, L-lysine, vitamin premix, sodium chloride, DL-methionine, butylhydroxytoluene (BHT); levels per kg of product: vit. A 360,000 IU; vit. D3 7,500 IU; vit. E 450 mg; vit. K3 18 mg; B1 12 mg; B2 29.5 mg; B6 13.5 mg; vit. B12 0.01 mg; niacin 118 mg; pantothenic acid 47.5 mg; folic acid 3.25 mg; biotin 0.75 mg; vit. C 300 mg; choline 1,800 mg; Fe 875 mg; Cu 625 mg; Mn 180 mg; Zn 625 mg; and Co 3.25 mg.

2.7. Basic Acid State (BAS) and D- β -Hydroxybutyric Acid (BHB). For this study and hematological profile, five 28-day-old piglets were randomized for treatment, which were identified (marked on the ear). 10 mL of blood samples was collected from the jugular vein with 21G x 1.5 needles, previous disinfection of the area, and adequate restraint. To obtain blood, serum tubes with vacutainer red cap without anticoagulant (Vacutainer®; BD, Franklin Lakes, New Jersey, USA) were used, which were centrifuged at 3000 rpm (Eppendorf centrifuge AG, New York, USA) for 15 min at room temperature. Samples were placed on ice and analyzed after 2 hours of collection.

For the analysis of the BAS, 1 mL of plasma was taken and pH, pCO₂, Na, K, Cl, HCO₃⁻, and anion gap were determined by means of an electrolyte and blood gas analyzer (VetSat, IDEXX, USA). In the blood serum, BHB by optical reflectometry with commercial kits (kit Rambut® D-3-Hydroxybutyrate-RB 1007, Randox Laboratories, Crumlin, County Atrium, UK) in an ultraviolet spectrophotometer (Metrolab 1600, USA) was analyzed.

2.8. Hematological Profile. In blood plasma, the following hematological variables were evaluated in a semiautomatic analyzer (Horiba ABX Micros ESV 60®; Paris, France): hemoglobin, hemogram, hematocrit, mean corpuscular volume (MCV), mean corpuscular hemoglobin concentration (CMCH), mean corpuscular hemoglobin (MCH), and mean platelet volume (MPV). All the samples were processed in

the Veterinary Clinical Laboratory of the Faculty of Veterinary Medicine and Zootechnics, University of Córdoba.

2.9. Statistical Analysis. Sow and its litter were considered the experimental units. The data were expressed as the mean, SD, and EE \pm . Means were compared using Student's *t*-test; mortality and the newborn index were analyzed for comparison of proportions in SPSS 21.0 (SPSS Inc., Chicago, IL, USA).

3. Results

3.1. Effect of *Lactobacillus plantarum* CAM6 on Reproductive Indicators of the Sows. The oral administration of *Lactobacillus plantarum* CAM6 for sows did not affect ($P > 0.05$) the body weight (BW) of the sows in the third part of the pregnancy (Table 2), at the time of parturition or at the end of lactation, and notable difference was found for sow weight loss ($P > 0.05$). In addition, these probiotic treatments for sows did not indicate significant differences ($P > 0.05$) between treatments for the days of gestation, live piglets at birth/litter, piglets dead at birth/litter, weaned piglets/litter, and weaning-estrus interval. However, the probiotic feeding for sows decreased ($P \leq 0.05$) the number of dead piglets prior to weaning per litter (Table 2).

The chemical composition and density of the milk of lactating sows with oral administration treatment of *Lactobacillus plantarum* CAM6 are shown in Figure 1. The concentration of lactose, nonfat solids, mineral salts, and milk density increased ($P \leq 0.05$) with the probiotic treatment group (T1) compared to the control group (T0). However, T1 decreased ($P \leq 0.05$) fat by 2.53% with relation to T0. The level of protein and total solids did not differ significantly between the experimental groups ($P > 0.05$). These values were within normal limits according to Boyce et al. [13].

3.2. Healthy Indicators of the Piglets. The inclusion of a probiotic with *Lactobacillus plantarum* CAM6 in sows before farrowing and during lactation improved the body weight of the piglets from 7 days until weaning (28 days) with significant differences between the control (T0) and probiotic (T1) groups ($P \leq 0.05$; Figure 2(a)). This is an important issue because the overall performance of growing-finishing pigs is determined by the performance of the first days after weaning, and this depends on the weaning weight [14]. And the oral administration with *Lactobacillus plantarum* CAM6 for sows significantly reduced the incidence of diarrhea in lactating piglets (Figure 2(b); $P \leq 0.05$).

The *Lactobacillus plantarum* CAM6 treatment on sows did not modify ($P > 0.05$) some parameters of the basic-acid state (BAS) such as pH, K, Cl⁻, HCO₃⁻, and anion gap in piglets. However, some parameters increased ($P \leq 0.05$) such as Na⁺, pCO₂, and D- β -hydroxybutyrate (BHB) in the T1 group (Table 3).

Supplementation of *Lactobacillus plantarum* CAM6 in sows did not change significantly ($P > 0.05$) the monocytes, granulocytes, eosinophils, erythrocytes, hemoglobin (Hb), hematocrit (Hto), mean corpuscular volume (MCV), mean corpuscular hemoglobin (MCH), and concentration of mean

TABLE 2: Effect of oral supplementation of *Lactobacillus plantarum* CAM6 on lactating sows.

Items	<i>L. plantarum</i> CAM6		SEM±	P value
	T0	T1		
BW 75 days of pregnancy (kg)	229.67	221.00	6.748	0.130
BW at farrowing (kg)	214.97	212.25	5.529	0.201
BW at weaning (kg)	200.00	196.82	3.909	0.690
Weight loss (kg)	14.97	15.43	1.441	0.789
Days of gestation (days)	114.5	115.0	0.360	0.239
Live pigs at birth/litter	12.50	12.00	0.963	0.797
Pigs dead at birth/litter	0.75	1.00	0.126	0.941
Pigs weaned/litter	9.50	9.75	0.381	0.394
Dead pigs before weaning/litter	3.00	2.25	0.226	0.041
Weaning-estrus interval	7.3	6.9	0.417	0.872

BW: body weight; T0: basal diet (BD); T1: BD + 10 mL biological agent containing 10^9 CFU/mL *L. plantarum* CAM6.

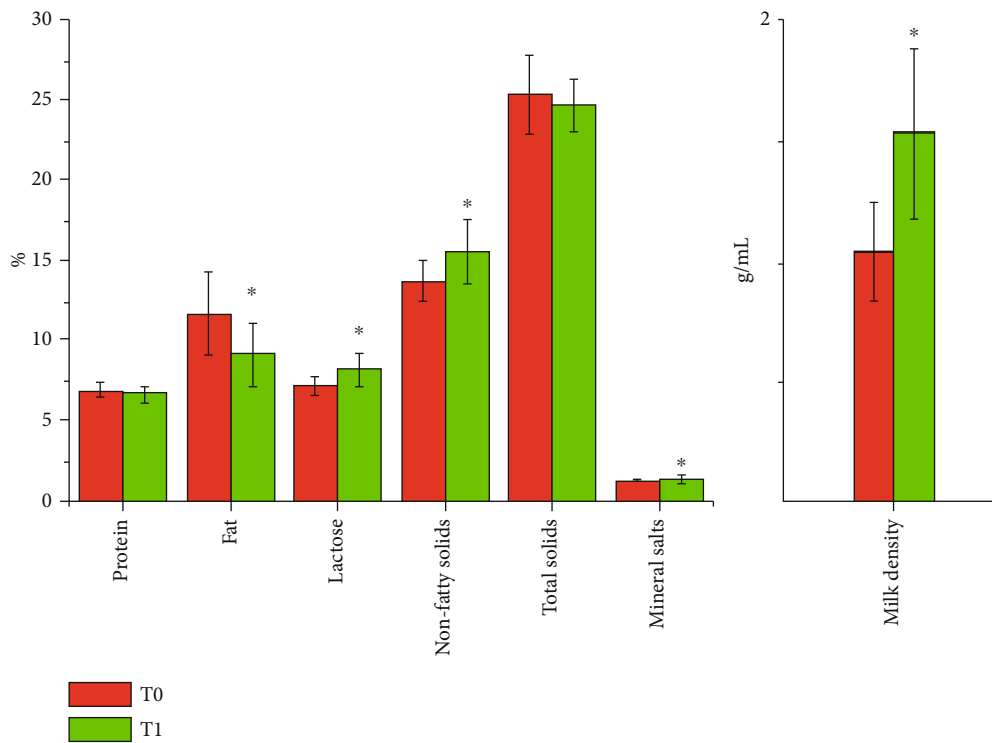


FIGURE 1: Effect of the oral administration of *Lactobacillus plantarum* CAM6 for sows on the chemical composition and density of milk produced by them. T0: basal diet (BD); T1: BD + 10 mL biological agent containing 10^9 CFU/mL *L. plantarum* CAM6. * $P \leq 0.05$.

corpuseular hemoglobin (CMCH) in their piglets. Nevertheless, the bacterial product modified ($P \leq 0.05$) leukocytes, lymphocytes, and platelets (Table 4). And it is also worth mentioning that all these values were within normal ranges according to Friendship et al. and Cooper et al. [15, 16].

4. Discussion

4.1. Effect of *Lactobacillus plantarum* CAM6 Supplementation on Reproductive Indicators of the Sows. In this study, the oral administration of *Lactobacillus plantarum* CAM6 for sows did not affect ($P > 0.05$) the body weight (BW) of the sows in the third part of the pregnancy (Table 2), at the time of

parturition or at the end of lactation, and no notable difference was found for sow weight loss ($P > 0.05$). Similar results were reported by Wang et al. and Hayakawa et al. when they used different probiotics in sow nutrition [5, 17]. But, in our study, the chemical composition and density of the milk secreted by the sows were found changed. Lactation performance may be associated with lactose levels [18], because this sugar is the main source of energy in milk, which is essential for lactating piglets [19]. The higher concentration of lactose in the T1 group ($P \leq 0.05$) compared with those in the T0 group can reflect better utilization of energy used by this group of sows. This may be due to the symbiotic relationship between *L. plantarum* and intestinal microorganisms that

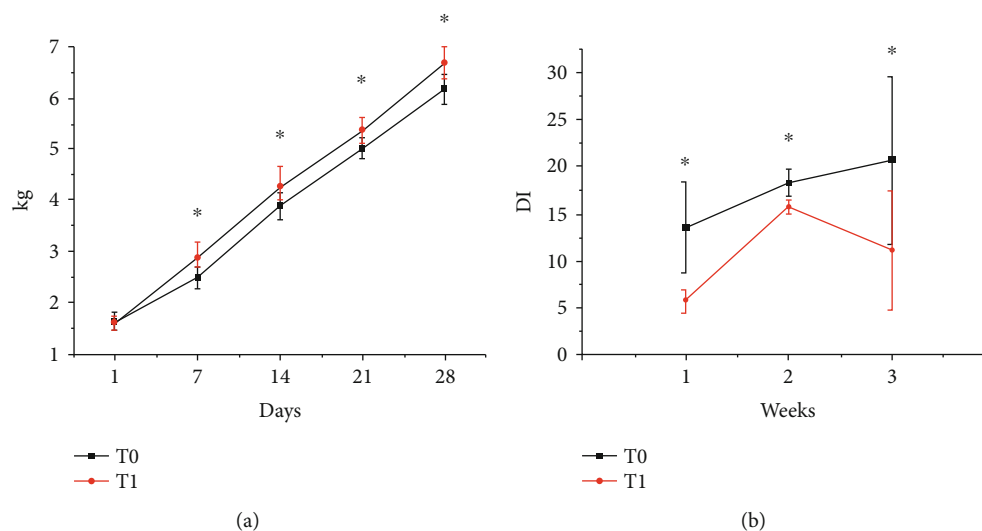


FIGURE 2: Derived impact of *Lactobacillus plantarum* CAM6 supplementation for sows to their progeny performance: (a) the derived impact of the probiotic supplementation for sows to the body weight of their progeny and (b) the derived impact of the probiotic supplementation for sows to reducing the diarrhea incidence (DI) of their progeny. T0: basal diet (BD); T1: BD + 10 mL biological agent containing 10^9 CFU/mL *L. plantarum* CAM6. * $P \leq 0.05$.

TABLE 3: The derived influence of *Lactobacillus plantarum* CAM6 supplementation in sows' feeding on the BAS and serum BHB of the lactating piglets (28 days of lactation).

Items	<i>L. plantarum</i> CAM6		SEM \pm	<i>P</i> value
	T0	T1		
pH	7.34	7.32	0.044	0.819
pCO ₂ (mm/Hg)	44.75	52.50	2.581	0.027
Na (mmol/L)	143.75	147.50	1.325	0.039
K (mmol/L)	4.925	5.350	0.347	0.420
Cl (mmol/L)	106.25	107.00	1.717	0.768
HCO ₃ ⁻ (mEq/L)	21.98	23.63	1.078	0.321
Anion gap	20.75	22.25	1.216	0.417
D- β -Hydroxybutyrate	1.50	2.02	0.154	0.038

T0: basal diet (BD); T1: BD + 10 mL biological agent containing 10^9 CFU/mL *L. plantarum* CAM6; pCO₂: CO₂ pressure; HCO₃⁻: bicarbonate ion.

promotes homeostasis of the intestinal microbiome, which in turn indirectly enhances the absorption of nutrients such as polysaccharides, proteins, and lipids, thereby enhancing the gluconeogenesis in the sow [9]. Current studies suggested that gut microbiota plays a significant role in maternal metabolism [3, 20]; in this way, consumption of probiotic bacteria by lactating sows can improve the absorptive capacity of the intestinal mucosa which may increase milk concentration of certain nutrients [8], such as a higher percentage of minerals and nonfatty solids. In addition, the oral administration of *L. plantarum* for the sows decreased the fat in their lactating milk. The lower percentage of fat of milk in T1 ($P \leq 0.05$) compared to that in the T0 group indicated the potential of *Lactobacillus plantarum* CAM6 for reducing fat in lactating milk. Certain probiotic bacteria with bile salt hydrolase (BSH) activity can lower cholesterol by enzymati-

cally deconjugating bile acids [21]. Genes for BSH on *L. plantarum* Lp9 has been identified, which allows to reduce the absorption of cholesterol and saturated fatty acids [22].

4.2. Effect of *Lactobacillus plantarum* CAM6 Extended to the Piglets. In this study, the oral administration with *Lactobacillus plantarum* CAM6 in sows reduced their piglet mortality before weaning; perhaps the improvements in preweaning performance of the suckling piglets may have been attributed to beneficial effects of probiotics supplementation on sows' milk composition and benign microbial homeostasis in the sows' guts [19, 23]. According to Rodriguez and Chen et al., sows can exert a modulation of the intestinal microbiota of the progeny via modifying the chemical composition of the milk consumed by their descendants [24, 25]. And in our study, the beneficial effects of probiotics supplementation on sows' performance included improving the quality of milk composition. Merrifield et al. and Dou et al. reported that the establishment of a healthy intestinal microbiota in early life might be essential to promote piglets' immunity and health, with a considerable decrease in mortality [26, 27]. In addition, Martin et al. reported that orally supplying probiotics in lactating sows increased the presence of the lactic acid bacteria in the biological fluid (milk), which caused favorable changes in the gut and improved the production of antipathogenic compounds, viability, and body weight of the piglets [28]. In our study, the oral administration with *Lactobacillus plantarum* CAM6 in sows indeed significantly reduced the incidence of diarrhea of their progenies (Figure 2(b); $P \leq 0.05$). The low incidence of diarrhea in the T1 group could possibly be due to the fact that the lactic acid bacteria produce lactic acid which are toxic to the pathogens in the gut of pigs [29]. Perhaps, our probiotic was also incorporated into breast milk; however, other studies are necessary to verify this hypothesis.

TABLE 4: The derived influence of oral administration with *Lactobacillus plantarum* CAM6 in sows towards the hematological parameters of their lactating piglets (28 days of lactation).

Items	<i>L. plantarum</i> CAM6		SEM±	P-value	Normal parameters*
	T0	T1			
Leukocytes (10 ³ /mm ³)	20.73	24.03	0.804	0.046	5.4-25
Lymphocytes (10 ³ /mm ³)	3.98	5.30	0.420	0.038	3.8-14
Monocytes (10 ³ /mm ³)	1.40	1.78	0.172	0.173	0.001-5.0
Granulocytes (10 ³ /mm ³)	15.35	16.95	3.502	0.758	2.5-23
Eosinophils (10 ³ /mm ³)	0.61	0.66	0.204	0.868	0.0-1.8
Erythrocytes (10 ⁶ /mm ³)	5.77	5.88	0.473	0.869	4.8-7.3
Hb (g/dL)	8.75	9.23	0.421	0.456	8.8-12.7
Hto (%)	28.78	30.93	1.787	0.428	28-42.7
MCV (μm ³)	50.00	53.00	1.414	0.184	38-59
MCH (pg)	15.28	15.86	0.620	0.519	11-18
CMCH (g/dL)	30.45	29.98	0.480	0.513	27-32
Platelet (10 ³ /mm ³)	872.52	761.75	28.385	0.041	208-873
MPV (μm ³)	11.15	10.85	0.792	0.798	7.4-16.5

*Friendship et al. [14]; Cooper et al. [15]. T0: basal diet (BD); T1: BD + 10 mL biological agent containing 10⁹ CFU/mL *L. plantarum* CAM6; Hb: hemoglobin; Hto: hematocrit; MCV: mean corpuscular volume MCH: mean corpuscular hemoglobin; CMCH: concentration of mean corpuscular hemoglobin; MPV: mean platelet volume.

Improvement of pig performance is theoretically linked to pig gut health [30]. The diarrheal syndrome is characterized by the loss of electrolytes and water in liquid and semi-liquid stools [31]. And the sodium is the main extracellular ion in the body and influences the electrolytic balance of animals [32]. Thus, in our study, there was a higher diarrheal incidence of piglets in the T0 group (Figure 2(b)), and there was a decrease in the serum concentration of Na⁺ of piglets (Table 3) in this group, correspondingly. On the other hand, the oral administration with *Lactobacillus plantarum* CAM6 in sows decreased the diarrheal incidence of their piglets indicating the benign intestinal ecosystem and healthy gut physiology in this group (T1) which could benefit the maintenance of the electrolyte balance in the piglets' bodies [33]. In the meantime, the significant higher pCO₂ and BHB in the serum of piglets in the T1 group were observed. Although the increase of CO₂ pressure in piglets may indicate possible metabolic acidosis which could increase β-hydroxybutyrate [34], it does not imply an alteration in acid-base balance since gap anion which was within the range biologically expected for the healthy piglets [16]. In this study, all the hematological parameters of lactating piglets were within normal ranges [15, 16], but it is still worth noting that the leukocytes, lymphocytes, and platelets increased in the piglets of the T1 group ($P \leq 0.05$) compared to T0. A significant increase in leukocytes and lymphocytes in piglets in the T1 group ($P \leq 0.05$) could indicate that probiotics supplied with *Lactobacillus plantarum* CAM6 in sows might increase the immune response of their piglets. The peptidoglycans and lipopolysaccharides attached to the cell wall of the lactic acid bacteria (LAB) play an important role in the immune system, which increases the number of the precursor cells of the humoral immunity [35]. Liu et al. and Xin et al. reported an increase in endogenous antioxidant enzymes and sIgA when evaluating the effect of yeasts and LAB in piglets [36, 37]. The results in the hematological indicators related to

the blood immunological parameters of the present study (Table 4) could be associated with the probiotic microorganisms introduced in the diet of sows which may favor the physiological changes in piglets possibly owing to the homeostasis of the autochthonous microbiota of the gastrointestinal tract and benefiting their healthy and productive performance [38, 39].

5. Conclusions

The oral administration of *Lactobacillus plantarum* CAM6 in sows from the last third of gestation until weaning did not affect the behavior of the sow; it decreased the number of death of the piglets before weaning and the diarrheal syndrome and improved the weight gaining performance of their offspring weekly. Furthermore, this probiotic improved the nutritional value of the breast milk consumed by their descendants. Likewise, the group of oral administration of *Lactobacillus plantarum* CAM6 in sows increased Na⁺, D-β-hydroxybutyrate, leukocytes, and lymphocytes in their offspring's blood. Oral administration of *Lactobacillus plantarum* CAM6 in breeding sows improved body weight, physiological status, and the health of their offspring.

Abbreviations

BAS:	Basic acid state
BD:	Basal diet
BHB:	D-β-Hydroxybutyric acid
BHT:	Butyl-hydroxytoluene
BSH:	Bile salt hydrolase
BW:	Body weight
DI:	Diarrhea incidence
CMCH:	Concentration of mean corpuscular hemoglobin
Hb:	Hemoglobin
Hto:	Hematocrit

LAB: Lactic acid bacteria
 MCH: Mean corpuscular hemoglobin
 MCV: Mean corpuscular volume
 MPV: Mean platelet volume
 pCO₂: CO₂ pressure.

Data Availability

The data are all included in the manuscript.

Conflicts of Interest

The authors declare that there is no conflict of interest.

Acknowledgments

The authors thank the dairy unit crew of the University of Córdoba for their input to this study. This study was made possible by a grant from the University of Córdoba.


References

- [1] B. Morissette, G. Talbot, C. Beaulieu, and M. Lessard, "Growth performance of piglets during the first two weeks of lactation affects the development of the intestinal microbiota," *Journal of Animal Physiology and Animal Nutrition*, vol. 102, no. 2, pp. 525–532, 2018.
- [2] C. J. Hedegaard, C. Lauridsen, and P. M. H. Heegaard, "Purified natural pig immunoglobulins can substitute dietary zinc in reducing piglet post weaning diarrhoea," *Veterinary Immunology and Immunopathology*, vol. 186, pp. 9–14, 2017.
- [3] P. Zhou, Y. Zhao, P. Zhang et al., "Microbial mechanistic insight into the role of inulin in improving maternal health in a pregnant sow model," *Frontiers in Microbiology*, vol. 8, 2017.
- [4] L. J. Fooks, R. Fuller, and G. R. Gibson, "Prebiotics, probiotics and human gut microbiology," *International Dairy Journal*, vol. 9, no. 1, pp. 53–61, 1999.
- [5] T. Hayakawa, T. Masuda, D. Kurosawa, and T. Tsukahara, "Dietary administration of probiotics to sows and/or their neonates improves the reproductive performance, incidence of post-weaning diarrhea and histopathological parameters in the intestine of weaned piglets," *Animal Science Journal*, vol. 87, no. 12, pp. 1501–1510, 2016.
- [6] S. F. Liao and M. Nyachoti, "Using probiotics to improve swine gut health and nutrient utilization," *Animal Nutrition*, vol. 3, no. 4, pp. 331–343, 2017.
- [7] H. Wang, C. Zhang, G. Wu et al., "Glutamine enhances tight junction protein expression and modulates corticotropin-releasing factor signaling in the jejunum of Weanling piglets," *The Journal of Nutrition*, vol. 145, no. 1, pp. 25–31, 2015.
- [8] L. Scharek-Tedin, S. Kreuzer-Redmer, S. O. Twardziok et al., "Probiotic treatment decreases the number of CD14-expressing cells in porcine milk which correlates with several intestinal immune parameters in the piglets," *Frontiers in Immunology*, vol. 6, 2015.
- [9] R. Dowarah, A. K. Verma, and N. Agarwal, "The use of *Lactobacillus* as an alternative of antibiotic growth promoters in pigs: A review," *Animal Nutrition*, vol. 3, no. 1, pp. 1–6, 2017.
- [10] C. Betancur, Y. Martínez, R. Merino-Guzman et al., "Evaluation of Oral Administration of *Lactobacillus plantarum* CAM6 Strain as an Alternative to Antibiotics in Weaned Pigs," *Animals*, vol. 10, no. 7, p. 1218, 2020.
- [11] C. Betancur, Y. Martínez, G. Tellez-Isaias, M. C. Avellaneda, and B. Velázquez-Martí, "In vitro characterization of indigenous probiotic strains isolated from Colombian Creole pigs," *Animals*, vol. 10, no. 7, p. 1204, 2020.
- [12] W.-C. Liu, H.-M. Yun, S.-H. Pi, and I.-H. Kim, "Supplementing lactation diets with herbal extract mixture during summer improves the performance of sows and nursing piglets," *Annals of Animal Science*, vol. 17, no. 3, pp. 835–847, 2017.
- [13] C. Boyce, M. Watson, G. Lazidis et al., "Preterm human milk composition: a systematic literature review," *British Journal of Nutrition*, vol. 116, no. 6, pp. 1033–1045, 2016.
- [14] X. Ding, W. Lan, G. Liu, H. Ni, and J.-D. Gu, "Exploring possible associations of the intestine bacterial microbiome with the pre-weaned weight gaining performance of piglets in intensive pig production," *Scientific Reports*, vol. 9, no. 1, article 15534, 2019.
- [15] R. M. Friendship, J. H. Lumsden, I. Mcmillan, and M. R. Wilson, "Hematology and Biochemistry Reference Values for Ontario Swine," *Canadian Journal of Comparative Medicine*, vol. 48, no. 4, pp. 390–393, 1984.
- [16] C. A. Cooper, L. E. Moraes, J. D. Murray, and S. D. Owens, "Hematologic and biochemical reference intervals for specific pathogen free 6-week-old Hampshire-Yorkshire crossbred pigs," *Journal of Animal Science and Biotechnology*, vol. 5, no. 1, p. 5, 2014.
- [17] J. Wang, H. F. Ji, C. L. Hou et al., "Effects of *Lactobacillus johnsonii* XS4 supplementation on reproductive performance, gut environment, and blood biochemical and immunological index in lactating sows," *Livestock Science*, vol. 164, pp. 96–101, 2014.
- [18] C. Tan, Z. Zhai, X. Ni et al., "Metabolomic profiles reveal potential factors that correlate with lactation performance in sow milk," *Scientific Reports*, vol. 8, no. 1, p. 10712, 2018.
- [19] S. W. Kim, A. C. Weaver, Y. B. Shen, and Y. Zhao, "Improving efficiency of sow productivity: nutrition and health," *Journal of Animal Science and Biotechnology*, vol. 4, no. 1, 2013.
- [20] C. Q. Tan, H. K. Wei, J. T. Ao, G. Long, and J. Peng, "Inclusion of konjac flour in the gestation diet changes the gut microbiota, alleviates oxidative stress, and improves insulin sensitivity in sows," *Applied and Environmental Microbiology*, vol. 82, no. 19, pp. 5899–5909, 2016.
- [21] Z. C. Dlamini, R. L. S. Langa, O. A. Aiyegoro, and A. I. Okoh, "Effects of probiotics on growth performance, blood parameters, and antibody stimulation in piglets," *South African Journal of Animal Science*, vol. 47, no. 6, pp. 765–775, 2017.
- [22] L. Alonso, J. Fontecha, and P. Cuesta, "Combined effect of *Lactobacillus acidophilus* and β -cyclodextrin on serum cholesterol in pigs," *The British Journal of Nutrition*, vol. 115, no. 1, pp. 1–5, 2016.
- [23] I. C. Starke, R. Pieper, K. Neumann, J. Zentek, and W. Vahjen, "Individual responses of mother sows to a probiotic *Enterococcus faecium* strain lead to different microbiota composition in their offspring," *Beneficial Microbes*, vol. 4, no. 4, pp. 345–356, 2013.
- [24] J. M. Rodríguez, "The origin of human milk bacteria: is there a bacterial entero-mammary pathway during late pregnancy and lactation?," *Advances in Nutrition*, vol. 5, no. 6, pp. 779–784, 2014.

- [25] W. Chen, J. Mi, N. Lv et al., "Lactation stage-dependency of the sow milk microbiota," *Frontiers in Microbiology*, vol. 9, 2018.
- [26] C. A. Merrifield, M. C. Lewis, B. Berger et al., "Neonatal environment exerts a sustained influence on the development of the intestinal microbiota and metabolic phenotype," *The ISME Journal*, vol. 10, no. 1, pp. 145–157, 2016.
- [27] S. Dou, P. Gadonna-Widehem, V. Rome et al., "Characterisation of early-life fecal microbiota in susceptible and healthy pigs to post-weaning diarrhoea," *PLoS One*, vol. 12, no. 1, 2017.
- [28] R. Martín, S. Delgado, A. Maldonado et al., "Isolation of lactobacilli from sow milk and evaluation of their probiotic potential," *Journal of Dairy Research*, vol. 76, no. 4, pp. 418–425, 2009.
- [29] S. Ammor, G. Tauveron, E. Dufour, and I. Chevallier, "Antibacterial activity of lactic acid bacteria against spoilage and pathogenic bacteria isolated from the same meat small-scale facility: 2—Behaviour of pathogenic and spoilage bacteria in dual species biofilms including a bacteriocin-like-producing lactic acid bacteria," *Food Control*, vol. 17, no. 6, pp. 462–468, 2006.
- [30] H. Sayan, P. Assavacheep, K. Angkanaporn, and A. Assavacheep, "Effect of *Lactobacillus salivarius* on growth performance, diarrhea incidence, fecal bacterial population and intestinal morphology of suckling pigs challenged with F4+ enterotoxigenic *Escherichia coli*," *Asian-Australasian Journal of Animal Sciences*, vol. 31, no. 8, pp. 1308–1314, 2018.
- [31] J. Wang, H. Ji, S. Wang et al., "Probiotic *Lactobacillus plantarum* promotes intestinal barrier function by strengthening the epithelium and modulating gut microbiota," *Frontiers in Microbiology*, vol. 9, 2018.
- [32] H. Wiig, F. C. Luft, and J. M. Titze, "The interstitium conducts extrarenal storage of sodium and represents a third compartment essential for extracellular volume and blood pressure homeostasis," *Acta Physiologica*, vol. 222, no. 3, 2018.
- [33] Q. W. Meng, L. Yan, X. Ao et al., "Influence of probiotics in different energy and nutrient density diets on growth performance, nutrient digestibility, meat quality, and blood characteristics in growing-finishing pigs," *Journal of Animal Science*, vol. 88, no. 10, pp. 3320–3326, 2010.
- [34] C. R. Dove and K. D. Haydon, "The effect of various diet nutrient densities and electrolyte balances on sow and litter performance during two seasons of the year," *Journal of Animal Science*, vol. 72, no. 5, pp. 1101–1106, 1994.
- [35] F. Guarner and J.-R. Malagelada, "Gut flora in health and disease," *The Lancet*, vol. 361, no. 9356, pp. 512–519, 2003.
- [36] G. Liu, L. Yu, Y. Martínez et al., "Dietary *Saccharomyces cerevisiae* cell wall extract supplementation alleviates oxidative stress and modulates serum amino acids profiles in weaned piglets," *Oxidative Medicine and Cellular Longevity*, vol. 2017, Article ID 3967439, 7 pages, 2017.
- [37] J. Xin, D. Zeng, H. Wang et al., "Probiotic *Lactobacillus johnsonii* BS15 promotes growth performance, intestinal immunity, and gut microbiota in piglets," *Probiotics and Antimicrobial Proteins*, vol. 12, no. 1, pp. 184–193, 2020.
- [38] P. Trevisi, M. Colombo, D. Priori et al., "Comparison of three patterns of feed supplementation with live *Saccharomyces cerevisiae* yeast on postweaning diarrhea, health status, and blood metabolic profile of susceptible weaning pigs orally challenged with *Escherichia coli* F4ac1," *Journal of Animal Science*, vol. 93, no. 5, pp. 2225–2233, 2015.
- [39] R. Gresse, F. Chaucheyras-Durand, M. A. Fleury, T. Van de Wiele, E. Forano, and S. Blanquet-Diot, "Gut microbiota dysbiosis in postweaning piglets: understanding the keys to health," *Trends in Microbiology*, vol. 25, no. 10, pp. 851–873, 2017.

Research Article

circRNA circ_102049 Implicates in Pancreatic Ductal Adenocarcinoma Progression through Activating CD80 by Targeting miR-455-3p

Jie Zhu,¹ Yong Zhou,¹ Shanshan Zhu,¹ Fei Li,¹ Jiajia Xu,¹ Liming Zhang,¹
and Hairong Shu² 

¹Medical Laboratory, Taizhou Central Hospital (Taizhou University Hospital), Taizhou, Zhejiang, China

²Department of Medical Service, Taizhou Central Hospital (Taizhou University Hospital), Taizhou, Zhejiang, China

Correspondence should be addressed to Hairong Shu; shuhr@tzzxyy.com

Received 30 September 2020; Revised 27 November 2020; Accepted 13 December 2020; Published 7 January 2021

Academic Editor: Xiaolu Jin

Copyright © 2021 Jie Zhu et al. This is an open access article distributed under the Creative Commons Attribution License, which permits unrestricted use, distribution, and reproduction in any medium, provided the original work is properly cited.

Emerging evidence has shown that circular RNAs (circRNAs) and DNA methylation play important roles in the causation and progression of cancers. However, the roles of circRNAs and abnormal methylation genes in the tumorigenesis of pancreatic ductal adenocarcinoma (PDAC) are still largely unknown. Expression profiles of circRNA, gene methylation, and mRNA were downloaded from the GEO database, and differentially expressed genes were obtained via GEO2R, and a ceRNA network was constructed based on circRNA-miRNA pairs and miRNA-mRNA pairs. Inflammation-associated genes were collected from the GeneCards database. Then, functional enrichment analysis and protein-protein interaction (PPI) networks of inflammation-associated methylated expressed genes were investigated using Metascape and STRING databases, respectively, and visualized in Cytoscape. Hub genes of PPI networks were identified using the NetworkAnalyzer plugin. Also, we analyzed the methylation, protein expression levels, and prognostic value of hub genes in PDAC patients through the UALCAN, Human Protein Atlas (HPA), and Kaplan-Meier plotter databases, respectively. The circRNA_102049/miR-455-3p/CD80 axis was identified by the ceRNA network and hub genes. In vitro and in vivo experiments were performed to evaluate the functions of circRNA_102049. The regulatory mechanisms of circRNA_102049 and miR-455-3p were explored by RT-PCR, western blot, and dual-luciferase assays. In the present study, twelve hub genes (STAT1, CCND1, KRAS, CD80, ICAM1, ESR1, RAF1, RPS6KA2, KDM6B, TNRC6A, FOSB, and DNMT1) were determined from the PPI networks. Additionally, the circRNA_102049 was upregulated in PDAC cell lines. Functionally, the knockdown of circRNA_102049 by siRNAs inhibited cell growth, inflammatory factors, and migratory and invasive potential and promoted cell apoptosis. Mechanistically, circRNA_102049 functioned as a sponge of miR-455-3p and partially reversed the effect of miR-455-3p and consequently upregulated CD80 expression. Our findings showed that circRNA_102049 and methylated hub genes play an important role in the proliferation, apoptosis, migration, invasion, and inflammatory response of PDAC, which might be selected as a promising prognostic marker and therapeutic target for PDAC.

1. Introduction

Pancreatic cancer is the seventh leading cause of global cancer-associated death, with an estimated 432,242 deaths in 2018 [1], and is predicted to become in 2030 the second leading cause of cancer-related death [2, 3]. Pancreatic ductal adenocarcinoma (PDAC) is the most common class of aggressive malignancies in the exocrine pancreas, accounting for approximately 90% of cases, with an unsatisfactory prog-

nosis [4]. This fatal disease is characterized by a few obvious clinical presentation, metastasis, and recurrence that contribute to the poor quality of life of patients [5]. At present, curative resection, classical chemotherapy, and radiotherapy are the main therapeutic strategies [6]. Despite the great advances of clinical technology, the outcomes remain unsatisfactory and the five-year survival rate of PDAC patients remains below 5% [5]. Therefore, there is an urgent need to increase the understanding of underlying molecular

mechanisms of PDAC that might result in discovering distinct diagnostic and therapeutic targets for PDAC treatment.

Accumulating studies demonstrated that the inflammatory microenvironment plays a significant role in the development of various cancers, including PDAC [7, 8]. Additionally, the inflammatory cytokines widely participate in various biological processes such as cell growth, differentiation, and metabolism by directly affecting cancer cells [9]. Moreover, previous research studies have reported that cancer cells are also produced and secrete many different kinds of cytokines, including IL-6, IL-1 β , IL-8, IL-17, and TNF- α [8, 10]. However, the pathogenesis of PDAC patients has not been fully investigated. Recently, it has been reported that abnormal DNA methylation, one of the epigenetic modifications, is an important mechanism helping the initiation and development of cancers [11, 12]. Besides, a study by Yang et al. demonstrated that DNA methylation frequently appears in early cancers and might be used as the biological marker for early diagnosis and screening of tumors [13]. The clinical potential of DNA methylation in the pathogenesis of cancer has gradually been valued. Significantly, recent studies show that chronic inflammation promotes the genetic and epigenetic disturbances with external stimuli [14], and PDAC is an epigenetic disease characterized by widespread and profound alterations in DNA methylation [15]. According to the finding above, potential therapeutic strategies associated with inflammation and DNA methylation are urgently needed.

Currently, noncoding RNAs, including circular RNAs (circRNAs), long noncoding RNAs (lncRNAs), and microRNAs (miRNAs), all have an important role in physiological and pathological events, and some of which have emerged as promising novel biomarkers for the detection of PDAC [16–18]. circRNAs are formed by the linking of the 3' end of the exon back to its 5' end, forming a covalently closed loop with no or limited protein-coding potential [19]. miRNAs are a class of small endogenous noncoding RNAs that consisted of 18~22 nucleotides, which mainly regulate the expression of the target genes posttranscriptionally to affect the PDAC progression [20]. Mechanistically, the competing endogenous RNA (ceRNA) mechanism is identified as one of the vital mechanisms of circRNAs to function as a “sponge” by binding the miRNA response elements (MREs) for mediating the pathological processes in PDAC. For instance, upregulated circ_0030235 facilitates PDAC cell growth and migratory and invasive potential, partly by inhibiting and sponging miR-1253 and miR-1294 [21]. Highly expressed circBFAR is also correlated with the poorer prognosis of patients with PDAC and promoted the progression of PDAC cells by sponging miR-34b-5p to activate the mesenchymal-epithelial transition factor (MET)/PI3K/Akt signaling pathway [22]. Hence, the evidence has been obtained to support the clinical significance of investigating the functional roles of circRNAs in PDAC and many circRNAs remain to be discovered.

With the great advances of high-throughput sequencing technologies and highly developed bioinformatics tools, the differentially expressed genes (DEGs) or differentially methylated genes (DMGs) in cancers have laid a favorable foundation for personalized target therapy. In this study, we integrated and analyzed the circRNA profiling microarrays

(GSE69362, GSE79634), gene methylation profiling microarray (GSE49149), and seven microarray datasets (GSE14245, GSE27890, GSE32676, GSE41372, GSE62165, GSE62452, and GSE71989) to identify the circRNA biomarkers and the abnormal inflammation-associated methylation target genes of PDAC patients. Subsequently, we screened the hub genes in the protein-protein interaction (PPI) networks. Moreover, we estimated the promoter methylation level and protein expression level of hub genes by using the UALCAN platform and the Human Protein Atlas database, respectively. And the prognostic value of hub genes was assessed through the Kaplan-Meier plotter. After that, we focused on an oncogenic circRNA (hsa_circRNA_102049, also known as hsa_circ_0043278) generated from exon 16 of the TADA2A gene, termed circTADA2A, located at chromosome 17: 35797838-35800763. In the current study, we measured the expression levels of hsa_circRNA_102049 in PDAC cell lines. Then, loss-of-function experiments were performed in two selected PDAC cells to measure the specific impacts of circRNA_102049 on cell growth, apoptosis, migration, and invasion characteristics. Importantly, we revealed that circRNA_102049 sponged hsa-miR-455-3p to promote CD80 expression and partially reversed the effect of miR-455-3p. Collectively, the results indicated that the circRNA_102049/miR-455-3p/CD80 axis had an important role in the development of PDAC, which suggested that circRNA_102049 might serve as a novel therapeutic target in PDAC.

2. Materials and Methods

2.1. Microarray Datasets and Data Processing. We retrieved the National Center for Biotechnology Information Gene Expression Omnibus (GEO, <https://www.ncbi.nlm.nih.gov/geo/>) database with the keyword “Pancreatic ductal adenocarcinoma.” Then, the circRNA expression profiling datasets (GSE69362, GSE79634), gene methylation profiling microarray (GSE49149), and gene expression datasets (GSE14245, GSE27890, GSE32676, GSE41372, GSE62165, GSE62452, and GSE71989) were downloaded for further analysis. All included datasets met the following criteria: (1) samples consisted of both PDAC tissues and normal control tissues and (2) gene expression profiling of circRNA or mRNA. Subsequently, we employed the GEO2R (<https://www.ncbi.nlm.nih.gov/geo/geo2r/>), an R programming language-based web tool that allows users to compare two or more groups of samples in a GEO series to identify DEGs and DMGs between the PDAC and normal tissue samples. P value < 0.05 and $|\log_2$ fold change (FC)| > 1 were set as the thresholds for screening DEGs. And the criteria for identifying DMGs were $|t| > 2$ and q value < 0.05 (q value is the P value adjusted by FDR (false discovery rate)). To screen the intersectional circRNAs significantly expressed in GSE69362 and GSE79634, an online tool Venny2.1 (<https://bioinfogp.cnb.csic.es/tools/venny/>) was used to plot the Venn diagrams.

2.2. Prediction of MRE and miRNA Targets. The screened differentially expressed circRNA- (DEC-) miRNA interactions were predicted using the Circular RNA Interactome

(CircInteractome, <https://circinteractome.nia.nih.gov/>) [23], which predicts the miRNAs which can potentially target the circRNAs using the TargetScan prediction tool [24]. Additionally, the genes targeted by miRNAs were predicted using TargetScanHuman (http://www.targetscan.org/vert_72/) [25] and miRDB (<http://mirdb.org/>) [26] online databases. The target genes of miRNAs identified simultaneously by both the TargetScan and miRDB databases were chosen. According to these selected DEC-miRNA and miRNA-mRNA interactions, we constructed a circRNA-miRNA-mRNA regulatory network, which was visualized using Cytoscape (version 3.8.0, <https://cytoscape.org/>), an open-source software platform for visualizing molecular interaction networks.

2.3. Identification of Inflammation-Associated Methylation Genes. In this study, we collected different genes associated with inflammation according to GeneCards (version 5.0; <https://www.genecards.org/>), which is a searchable, integrative online platform that provides comprehensive, user-friendly information on all annotated and predicted human genes [27]. The performing keyword “inflammation” was input into GeneCards to obtain targets associated with PDAC. Finally, we obtained inflammation-associated hypomethylation-high expression genes after overlapping of upregulated DEGs and hypomethylation genes and obtained hypermethylation-low expression genes after overlapping of downregulated DEGs and hypermethylation genes through drawing a Venn diagram.

2.4. Functional Enrichment Analysis. The Metascape database (<http://metascape.org/gp/index.html#/main/step1>) was used to perform functional enrichment analysis of the hypomethylation-high expression genes and hypermethylation-low expression genes, respectively. Metascape is an integrated and user-friendly web tool that combines functional enrichment, interactome analysis, and gene annotation to aid in revealing the biological meaning of the offered gene list, including the Gene Ontology (GO) and Kyoto Encyclopedia of Genes and Genomes (KEGG) pathway terms [28]. The inflammation-associated hypomethylation-high expression genes and hypermethylation-low expression genes of PDAC were input into Metascape for GO-biological processes (BP) and KEGG analysis, and the species was selected as “*Homo sapiens*.” $P < 0.05$ was considered statistically significant.

2.5. Protein-Protein Interaction (PPI) Network of Inflammation-Associated Methylation Genes. The inflammation-associated hypomethylation-high expression genes and hypermethylation-low expression genes of PDAC were imported into Search Tool for the Retrieval of Interacting Genes (STRING) (version 11.0, <https://string-db.org/>) to construct the PPI networks, respectively. STRING is an online tool that is aimed at collecting, scoring, and integrating the direct and indirect interaction between proteins and proteins [29], and interaction associations with a combined score of ≥ 0.7 were retained. In search of hub genes in the two networks, Cytoscape was utilized to analyze the degree value of nodes. Using Cytoscape’s plugin NetworkAnalyzer, we selected a total of 12 DEGs with high connectivity in

the inflammation-associated methylation DEG networks as the hub genes based on the degree algorithm.

2.6. Methylation, Immunohistochemical, and Survival Analyses of Hub Genes. To further confirm the bioinformatics results of the hub genes, we used UALCAN (<http://ualcan.path.uab.edu/index.html>) for methylation level analysis. UALCAN is a comprehensive, user-friendly, and interactive web portal that is extremely helpful in gene-level querying of The Cancer Genome Atlas (TCGA) data [30]. The gene symbol of hub genes was imported into the UALCAN, and TCGA dataset was selected as “Pancreatic adenocarcinoma.” The beta value indicates the level of DNA methylation ranging from 0 (unmethylated) to 1 (fully methylated). Different cutoff beta values have been considered to indicate hypermethylation (beta value: 0.7-0.5) or hypomethylation (beta value: 0.3-0.25) [31, 32], and differences were regarded as significant with P value less than 0.05.

For immunohistochemical analysis, Human Protein Atlas (HPA) (version 19.3, <https://www.proteinatlas.org/>), which is aimed at mapping all the human proteins in cells, tissues, and organs using an integration of various omics technologies [33], was used to assess the protein expressions of hub genes in normal tissues and pancreatic cancer tissues. To further elucidate the relationship between DEC targets and hub gene expression and PDAC prognosis, the web server Kaplan-Meier (KM) plotter (<http://kmplot.com/analysis/>) was utilized for overall survival (OS) analyses using the log-rank test [34]. $P < 0.05$ was considered statistically significant.

2.7. Cell Culture and Transfection. The human PDAC cell lines AsPC-1, CFPAC-1, BxPC-3, SW1990, and Panc-1 were purchased from the cell bank of the Chinese Academy of Science, Shanghai, and maintained in Dulbecco’s Modified Eagle’s Medium (DMEM, Thermo Fisher Scientific, USA) supplemented with 10% FBS, 100 units/mL penicillin, and 100 $\mu\text{g}/\text{mL}$ streptomycin in a humidified incubator with 5% CO_2 at 37°C. HPDE cells, the immortalized pancreatic duct cells, are used as the normal control subject in this study. Two siRNAs against circRNA_102049 (si-circ_102049_#1 and si-circ_102049_#2) were constructed to block the expression of circRNA_102049 in SW1990 and Panc-1 cells, respectively. Negative control siRNA (si-NC) was utilized as a control. The target sequence of si-circ_102049_#1 and si-circ_102049_#2 was 5’-ATTCCATTTCACTACT TCAGA-3’ and 5’-TCCATTTCACTACTTCAGATT-3’, respectively. In addition, the miR-455-3p inhibitor and mimic were utilized to silence and enhance the expression of miR-455-3p, respectively. For transfection, SW1990 and Panc-1 cells were placed in 6-well plates with DMEM. After growth to 80% confluence, SW1990 and Panc-1 cells were transfected with 50 nM si-circ_102049_#1 or si-circ_102049_#2 and 100 nM miR-455-3p inhibitor or mimic by using Lipofectamine 3000 (Thermo Fisher Scientific, USA). The circ_102049 expression in the transfected cells was measured by real-time quantitative PCR (RT-qPCR) with specially appointed primers.

2.8. RNA Isolation, Treatment with RNase R, and RT-qPCR. Total RNA was extracted from the PDAC cell lines using the TRIzol reagent (Beyotime, Shanghai, China) following the manufacturer's protocol. The quality of RNA was assessed by NanoDrop 2000 spectrophotometry (Thermo Fisher Scientific, USA). RNase R treatment was performed for 20 min at 37°C using 3 U/ μ g RNase R (Sigma-Aldrich, St. Louis, MO, USA). Then, total RNAs were reverse transcribed into cDNA through PrimeScript RT Master Mix (Takara, Japan). Reverse transcription of miRNA was performed using the Mir-X™ miRNA First-Strand Synthesis Kit (Clontech Laboratories, Inc.), and RT-qPCR analysis was performed using the SYBR Green qPCR Kit (Takara Biotechnology Co., Dalian, China) on an ABI 7300 Real-Time PCR System (Applied Biosystems, Thermo Fisher Scientific). Primers used in the current study were all obtained from Sangon Biotech (Shanghai, China). The sequence of primers was as follows: circ_102049, F: 5'-ACCCTGCTGAACCTGAACA-3'; R: 5'-TCCTGCCAATTTCCAAAGCC-3'; miR-455-3p, F: 5'-TGCGCCAAACCACACTGTGGTG-3'; R: 5'-CCAGTGCAGGGTCCGAGGTATT-3'; TADA2A, F: 5'-CCTTTTTTCTCTGCTTGCA-3'; R: 5'-ATCCTGCCAATTTCCAAAGC-3'; CD80, F: 5'-CCTCTCCATTGTGATCCTGG-3'; R: 5'-GGCGTACACTTCCCTTCTC-3'; TNF- α , F: 5'-GTGACAAGCCTGTAGCCCAT-3'; R: 5'-CAGACTCGGCAAAGTCGAGA-3'; IL-6, F: 5'-TGAACCTCTTCTCCACAAGCG-3'; R: 5'-ATTTGTGGTTGGGT CAGGGG-3'; IL-1 β , F: 5'-CTTTCCCGTGGACCTTC CAG-3'; R: 5'-AATGGGAACGTACACACCA-3'; IL-8, F: 5'-AAGGTGCAGTTTTGCCAAGG-3'; R: 5'-CAACCC TCTGCACCCAGTTT-3'; IL-17, F: 5'-CTGTCCCCATC CAGCAAGAG-3'; R: 5'-AGCCACATGGTGGACAAT C-3'; GAPDH, F: 5'-GAAGGTGAAGGTCGGAGTC-3'; R: 5'-GAAGATGGTGATGGGATTTC-3'; and U6, F: 5'-CTCGCTTCGGCAGCACA-3'; R: 5'-AACGCTTCACGA ATT TGCCT-3'. The expression of circ_102049, TADA2A, CD80, TNF- α , IL-6, IL-1 β , IL-8, and IL-17 were normalized to GAPDH, and miR-455-3p expression was normalized to U6, using the $2^{-\Delta\Delta Ct}$ method [35].

2.9. circRNA Localization. For circRNA localization, the nuclear and cytoplasmic RNAs of SW1990 and Panc-1 cells were isolated and extracted using the Cytoplasmic & Nuclear RNA Purification Kit (Ambion, Austin, TX, USA), and the expression of circ_102049 in nuclear and cytoplasmic RNAs was detected by qRT-PCR. GAPDH and U6 served as the cytoplasm and nuclear controls, respectively.

2.10. Actinomycin D Assay. To assess the stability of circ_102049 and its linear isoform, SW1990 and Panc-1 cells were seeded at 5×10^4 cells per well in 24-well plates. After 24 h, the cells were treated with 2 mg/L actinomycin D (Sigma-Aldrich, St. Louis, MO, USA) for 0 h, 6 h, 12 h, and 24 h. After treatment with actinomycin D, qRT-PCR was performed to determine the expression levels of circ_102049 and TADA2A mRNA.

2.11. Cell Viability and Colony Formation Assay. After transfection, SW1990 and Panc-1 cells were seeded at 4×10^3 cells per well in a 96-well plate and incubated for 24 h, 48 h, 72 h, and 96 h, and then, 10 μ L of Cell Counting Kit- (CCK-) 8 (Beyotime, China) was added to each well. The plates were then incubated at 37°C for 2 hours. A microplate reader (Tecan, Mannedorf, Switzerland) was used to measure the OD value of each well at 450 nm. For colony formation assay, SW1990 and Panc-1 cells were seeded into 6-well plates. After transfection, cells were cultured for 2 weeks until most colonies were visible to the naked eye. Then, SW1990 and Panc-1 cells were fixed with 4% paraformaldehyde for 20 minutes and stained with 0.1% crystal violet to observe and count the number of colonies.

2.12. Flow Cytometry Assay. For the cell apoptosis analysis, the cell apoptosis was assessed with the Annexin V Apoptosis Detection Kit (BD Biosciences, NJ, USA). SW1990 and Panc-1 cells were collected and washed with ice-cold PBS, followed by staining with 5 μ L fluorescein isothiocyanate (FITC) and 5 μ L propidium iodide (PI), and then incubated for 15 min in the dark at room temperature. Subsequently, a BD FACS-Calibur (Beckman Coulter, USA) was utilized to measure the cell apoptotic rate.

2.13. Wound Healing and Invasion Assays. Transfected SW1990 and Panc-1 cells were cultured in 6-well plates, and the cell monolayer was scratched with a 200 μ L pipette tip when cells were grown to approximately 80% confluence, and PBS was used to remove the detached cells. Representative images of cell migration were captured at 0 h and 24 h after injury using an Olympus light microscope (Olympus Optical Co., Ltd., Tokyo, Japan), and the wound width was calculated using ImageJ software (National Institutes of Health, USA). For the invasion assay, the chambers were coated with Matrigel. SW1990 and Panc-1 cells were seeded into the upper chamber (4×10^3 cells) with a serum-free medium, while a medium containing 10% FBS was added into the lower chamber. After incubation for 24 h, cotton wool was used to remove the cells in the upper chamber, and cells on the lower side of the filter were fixed with 4% paraformaldehyde for 30 min and then stained with 0.5% crystal violet for 10 min. The PDAC cells of the invasion were counted and photographed in at least five random fields under a light microscope.

2.14. Tumor Xenograft Assay. Six-week-old female BALB/c male nude mice were purchased from Shanghai Slac Laboratory Animals, Ltd., and randomly divided into two groups ($n = 3$ for each group). Control cells and circ_102049 knock-down Panc-1 cells (1×10^7) were suspended in 100 μ L DMEM without FBS and then subcutaneously inoculated into the right flank of the mice, respectively. Mice were monitored every 5 days for tumor growth, and tumor size was measured using a caliper and calculated as follows: volume = (length \times width²)/2. After 25 days, mice were sacrificed, and then, the primary tumors were removed and harvested and weighed. All experiments were performed in accordance with the *Guide for the Care and Use of Laboratory Animals*

(NIH publication 80-23, revised 1996), with the approval of the Animal Care and Welfare Committee of Zhejiang Chinese Medical University.

2.15. Dual-Luciferase Reporter Assay. The constructs containing wild-type (wt) or mutant (mut) circ_102049-miR-455-3p and CD80-miR-455-3p were subcloned into the luciferase gene by the psiCHECK2 Vector (Promega Corporation, Madison, WI, USA) or the pmirGLO Vector (Promega Corporation, Madison, WI, USA), respectively. The above reporter vectors were cotransfected with miR-455-3p mimic or miR-455-3p NC into SW1990 and Panc-1 cells using Lipofectamine 3000. After 24 h of transfection, activities were analyzed using a dual-luciferase reporter assay system (Promega Corporation, Madison, WI) according to the manufacturer's instructions. Relative firefly luciferase activity was normalized to Renilla luciferase activity.

2.16. Western Blot. The total protein of transfected SW1990 and Panc-1 cells was lysed with ice-cold RIPA buffer (Beyotime, Shanghai, China). And the protein concentration was quantified by the bicinchoninic acid (BCA) kit (Beyotime, Shanghai, China) according to the manufacturer's instructions. Afterward, equal amounts of protein (30 μ g) were separated via sodium dodecyl sulfate-polyacrylamide gel electrophoresis (SDS-PAGE) gel and transferred onto polyvinylidene fluoride (PVDF) membranes (Millipore). After blocking with 5% nonfat milk in TBST, the membranes were incubated with primary antibodies against CD80 (1:1000, #54521, Cell Signaling Technology, Inc., USA) and GAPDH (1:5000, P04406, Sangon Biotech, China) at 4°C overnight. Then, the membranes were incubated with the horseradish peroxidase-labeled IgG goat anti-rabbit or goat anti-mouse antibody (1:5000, Invitrogen, USA) for 1 h at room temperature. Finally, the membranes were treated with enhanced chemiluminescence (ECL) solution (Beyotime, China) to detect the protein blots.

2.17. Statistical Analysis. All statistical data were expressed as the mean \pm standard deviation. Two-tailed Student's *t*-test was utilized to make a comparison in two groups, and one-way ANOVA was used to compare multiple groups, respectively. All analyses were performed using SPSS 22.0 (SPSS Inc., Chicago). $P < 0.05$ was considered statistically significant.

3. Results

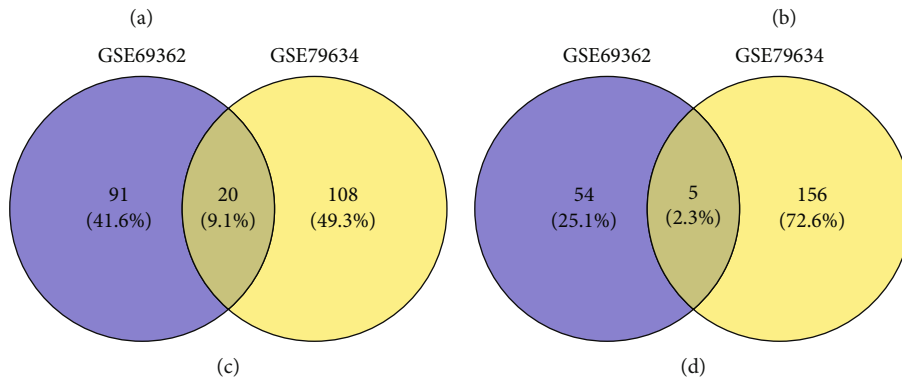
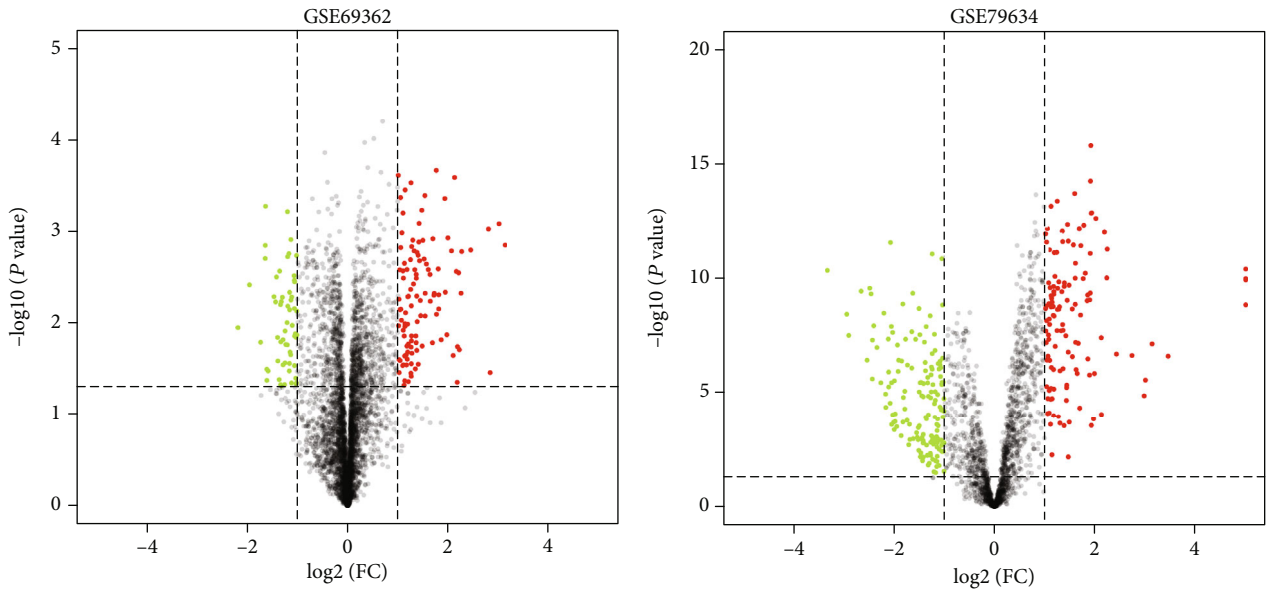
3.1. Identification of DEGs and DMGs in PDAC. To identify the DEGs between PDAC tissue samples and normal tissue samples, we obtained the publicly available microarray datasets GSE69362 and GSE79634 from the GEO database. There were 170 DECs (111 upregulated and 59 downregulated) in GSE69362 and 289 DECs (128 upregulated and 161 downregulated) in GSE79634, which were differentially expressed between PDAC tissues and noncancerous tissues as shown by volcano plots in Figures 1(a) and 1(b) (Supplementary Table S1 and Table S2). Among them, 25 DECs overlapped, and 20 were upregulated (Figure 1(c)), and 5 were downregulated (Figure 1(d)). The DECs from each of the

two datasets were ranked and are shown by a heatmap in Figure 1(e). Further, we found that hsa_circRNA_102049 (circ_0043278) was the most significantly upregulated circRNA in GSE69362 and GSE79634, respectively (Figures 1(f) and 1(g)).

3.2. Construction of the circRNA-miRNA-mRNA Network in PDAC. To better explore the role of overlapped DECs and miRNAs in the ceRNA mechanism of PDAC, we established a circRNA-miRNA-mRNA network. The CircInteractome database was used for overlapped circRNA-miRNA prediction, and a total of 372 target miRNAs were obtained (Supplementary Table S3). Furthermore, we conducted an overall survival analysis to detect the potential prognostic value. The results are shown in Supplementary Figure S1 and Table S4. The 53 highly expressed miRNAs and 38 lowly expressed miRNAs in the KM plotter may be associated with poor survival of PDAC patients. Besides, we then identified mRNAs targeted by these 91 miRNAs in TargetScan and miRDB databases. These results indicated that 7871 mRNAs were involved in the ceRNA network (Supplementary Table S5 and Table S6). Finally, we used 22 overlapped DECs, 91 miRNAs, and 7871 mRNAs in Cytoscape 3.6.1 to construct a circRNA-miRNA-mRNA network (Figure 2). Significantly, we found that hsa-miR-455-3p and hsa-miR-342-3p were predicted to be the downstream of hsa_circRNA_102049, which suggested that there could be some biological relationships between them in the development of PDAC.

3.3. Identification of Inflammation-Associated Methylated Expressed Genes. We used the GEO2R to identify the data of each microarray separately and screened the DEGs and DMGs. The detailed platform and number of samples for microarray datasets are shown in Table 1, respectively. A total of 65,535 DMGs were extracted from GSE49149 (Supplementary Table S7). And a total of 1981, 2375, 864, 1948, 817, 321, and 1375 DEGs were extracted from GSE14245, GSE27890, GSE32676, GSE41372, GSE62165, GSE62452, and GSE71989, respectively (Supplementary Table S8). Also, a total of 10,272 potential inflammation-associated genes were collected in the GeneCards database (Supplementary Table S9). Finally, we further identified 183 overlapping inflammation-associated hypomethylation-high expression genes by intersecting the results of integrated microarray and the predicted target genes of lowly expressed miRNAs in the KM plotter (Figure 3(a)). Similarly, 75 overlapping inflammation-associated hypermethylation-low expression genes were selected by intersecting the results of integrated microarray and the predicted target genes of highly expressed miRNAs in the KM plotter (Figure 3(b)).

3.4. Functional Enrichment Analysis. To further investigate the biological functions of the abovementioned potential overlapping inflammation-associated methylated expressed genes, GO-BP terms and KEGG pathway enrichment analysis were conducted via the Metascape platform. As shown in Figure 4(a), the upregulated DEGs with low methylation were significantly enriched in GO:0048514~blood vessel



GSE69362	GSE79634	hsa_circRNA	Count
1.25	2.43	hsa_circRNA_101226	6
1.07	1.13	hsa_circRNA_103089	5
1.99	1.93	hsa_circRNA_103390	4
1.27	1.39	hsa_circRNA_103076	3
2.26	1.09	hsa_circRNA_100117	2
1.37	1.28	hsa_circRNA_104759	1
1.40	1.09	hsa_circRNA_102465	0
1.24	1.36	hsa_circRNA_400091	-1
1.42	2.02	hsa_circRNA_102984	-2
1.30	1.47	hsa_circRNA_104003	-3
1.37	1.45	hsa_circRNA_103285	-4
1.45	1.72	hsa_circRNA_100904	-5
1.07	1.60	hsa_circRNA_102359	-6
1.14	1.29	hsa_circRNA_104313	
1.10	1.44	hsa_circRNA_100790	
1.26	1.04	hsa_circRNA_103655	
2.09	1.97	hsa_circRNA_400068	
1.02	1.62	hsa_circRNA_101798	
1.11	1.13	hsa_circRNA_101656	
1.26	5.70	hsa_circRNA_102049	
-2.17	-2.10	hsa_circRNA_100302	
-1.15	-1.27	hsa_circRNA_102741	
-1.60	-1.86	hsa_circRNA_104310	
-1.58	-2.04	hsa_circRNA_400027	
-1.33	-1.21	hsa_circRNA_000274	

(e)

FIGURE 1: Continued.

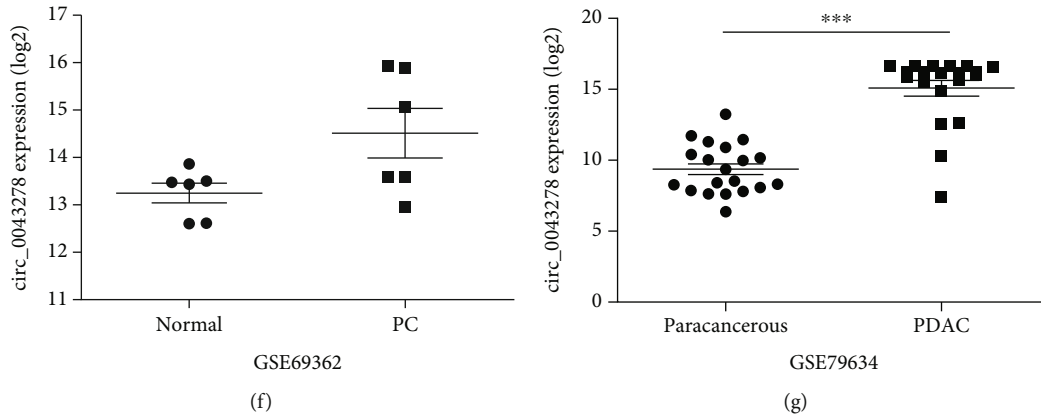


FIGURE 1: Identification of differentially expressed circRNAs (DECs) between the PDAC and nonmalignant tissues. The volcano plots of DECs for GSE69362 (a) and GSE79634 (b) datasets. The Venn diagrams of the overlapping DECs, including 20 upregulated (c) and 5 downregulated (d), among the two datasets. (e) Heatmap of the twenty-five DECs in the two microarray datasets. The expression levels of hsa_circRNA_102049 (circ_0043278) in GSE69362 (f) and GSE79634 (g) datasets, respectively.

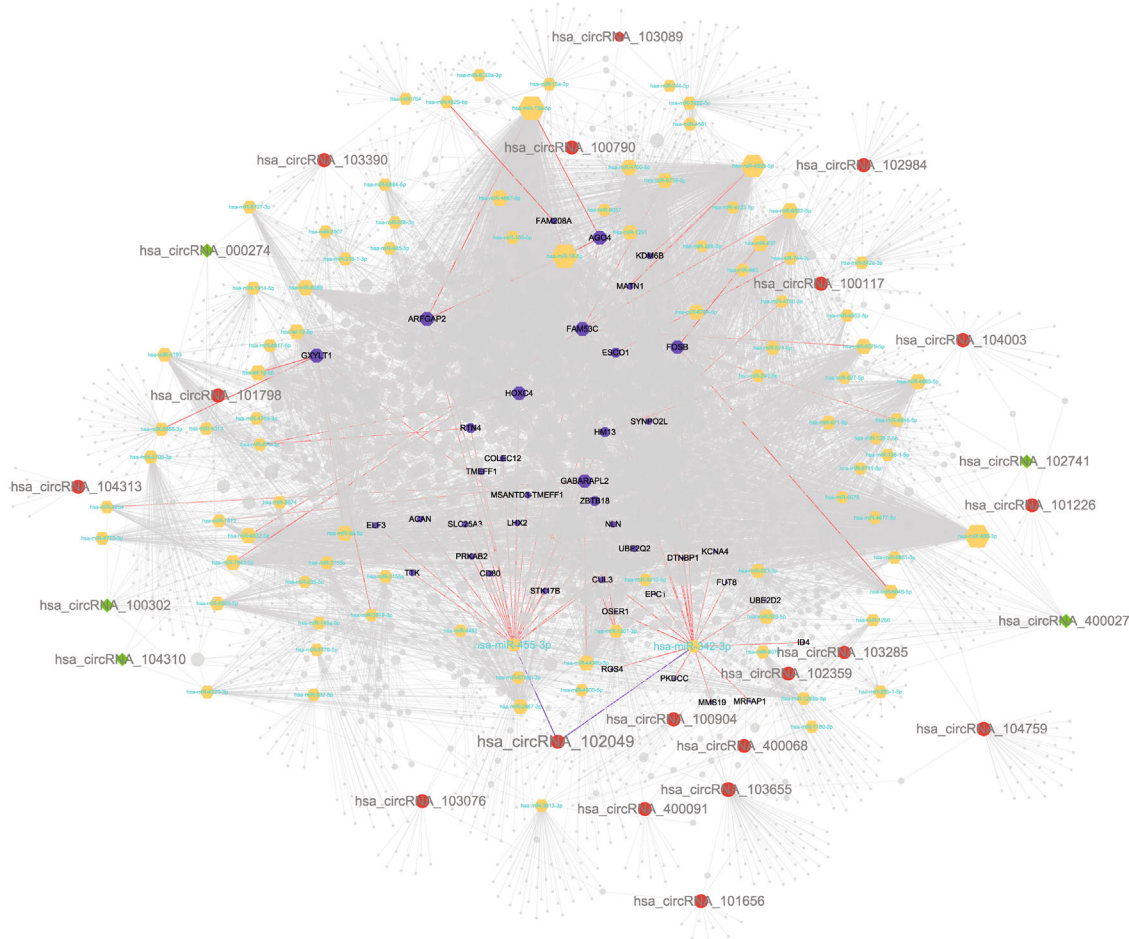


FIGURE 2: The circRNA-miRNA-mRNA network in PDAC. Red ellipse indicates upregulated circRNAs, green diamond indicates downregulated circRNAs, yellow hexagon indicates predicted miRNAs, and purple hexagon indicates target genes of hsa-miR-455-3p, as well as hsa-miR-342-3p.

morphogenesis, GO:0019221~cytokine-mediated signaling pathway, and GO:0030155~regulation of cell adhesion; additionally, KEGG analysis proved that the upregulated DEGs

were significantly enriched in hsa05200~pathways in cancer (Figure 4(a)). And again, Metascape was used to analyze the roles of identified downregulated DEGs with high

TABLE 1: Information of the microarray datasets in GEO for integrated analysis in this study.

Dataset	PMID	Platform	Number of samples (tumor/control)	circRNA/mRNA	Number of DEGs/DMGs
GSE69362	27997903	GPL19978 Agilent-069978 Arraystar Human CircRNA microarray V1	12 (6/6)	circRNA	170
GSE79634	29620241	GPL19978 Agilent-069978 Arraystar Human CircRNA microarray V1	40 (20/20)	circRNA	289
GSE49149	24500968	GPL13534 Illumina Human Methylation450 BeadChip (HumanMethylation450_15017482)	196 (167/29)	mRNA	65,531
GSE14245	19931263	GPL570 [HG-U133_Plus_2] Affymetrix Human Genome U133 Plus 2.0 Array	24 (12/12)	mRNA	1981
GSE27890	—	GPL570 [HG-U133_Plus_2] Affymetrix Human Genome U133 Plus 2.0 Array	8 (4/4)	mRNA	2375
GSE32676	25846727	GPL570 [HG-U133_Plus_2] Affymetrix Human Genome U133 Plus 2.0 Array	32 (25/7)	mRNA	864
GSE41372	24120476	GPL6244 [HuGene-1_0-st] Affymetrix Human Gene 1.0 ST Array [transcript (gene) version]	30 (15/15)	mRNA	1948
GSE62165	27520560	GPL13667 [HG-U219] Affymetrix Human Genome U219 Array	131 (118/13)	mRNA	817
GSE62452	27197190	GPL6244 [HuGene-1_0-st] Affymetrix Human Gene 1.0 ST Array [transcript (gene) version]	130 (69/61)	mRNA	321
GSE71989	27363020	GPL570 [HG-U133_Plus_2] Affymetrix Human Genome U133 Plus 2.0 Array	21 (13/8)	mRNA	1375

methylation. Downregulated DEGs with high methylation were mainly involved in BP: GO:0032870~cellular response to hormone stimulus, GO:0006367~transcription initiation from RNA polymerase II promoter, and GO:0007169~transmembrane receptor protein tyrosine kinase signaling pathway. Based on the KEGG pathway enrichment analysis, the specific downregulated DEGs mainly participated in hsa04961~endocrine and other factor-regulated calcium reabsorption and hsa04915~estrogen signaling pathway (Figure 4(b)).

3.5. PPI Network of Inflammation-Associated Methylated Expressed Genes. The PPI network was built to analyze interactions between the 183 upregulated DEGs with low methylation, as well as 75 downregulated DEGs with high methylation, respectively. After removing the isolated nodes, 146 nodes and 320 edges remained in the upregulated DEG PPI network (Figure 5(a)). Similarly, the PPI network of downregulated DEGs with 37 nodes and 39 edges was constructed using the Cytoscape software (Figure 5(b)). To identify hub genes associated with the pathogenesis of PDAC, the NetworkAnalyzer plugin was used to analyze the degree value of nodes. Five genes with degree > 16 were chosen as hub genes in the upregulated DEG PPI network, and seven genes with degree > 3 were selected as hub genes in the downregulated DEG PPI network also, including signal transducer and activator of transcription 1 (STAT1); cyclin D1 (CCND1); KRAS proto-oncogene, GTPase (KRAS); CD80 molecule (CD80); intercellular adhesion molecule 1 (ICAM1); estrogen receptor 1 (ESR1); Raf-1 proto-oncogene, serine/threonine kinase (RAF1); ribosomal protein S6 kinase A2 (RPS6KA2); lysine demethylase 6B

(KDM6B); trinucleotide repeat-containing adaptor 6A (TNRC6A); FosB proto-oncogene, AP-1 transcription factor subunit (FOSB); and dynamin 1 (DNM1).

3.6. Validation of Hub Genes according to Various Pathophysiological Characteristics. Next, UALCAN was used to validate the methylation levels of 12 hub genes in pancreatic adenocarcinoma. The methylation levels of KRAS, ESR1, RAF1, RPS6KA2, and TNRC6A were significantly higher in primary tumor tissues compared with those in normal tissues, while the methylation levels of CD80 and DNM1 were significantly decreased in tumor samples than adjacent normal samples; but, there is no statistical difference in methylation levels of STAT1, CCND1, ICAM1, KDM6B, and FOSB (Figures 6(a)–6(l)). Additionally, the clinical stage analysis of hub genes was investigated by using the GEPIA2 database (<http://gepia2.cancer-pku.cn/#index>), and the results suggest that the expression levels of CD80 and ICAM1 were significantly increased in various tumor stages (Supplementary Figure S2). Further analysis of hub genes in the HPA database showed that the protein expression levels of STAT1, CCND1, KRAS, CD80, ICAM1, ESR1, RAF1, FOSB, and DNM1 were upregulated in PDAC tissues compared with normal tissues, and the RPS6KA2 protein level was significantly decreased in PDAC tissues; however, the expression of RPS6KA2, KDM6B, and TNRC6A was not significantly different between pancreatic cancer samples and normal control tissues (Figures 7(a)–7(l)). Additionally, we used the KM plotter to analyze the correlation between hub gene expression and PDAC prognosis. We found that high mRNA expression of STAT1, CCND1, KRAS, CD80, and RAF1 and low mRNA expression of KDM6B, TNRC6A,

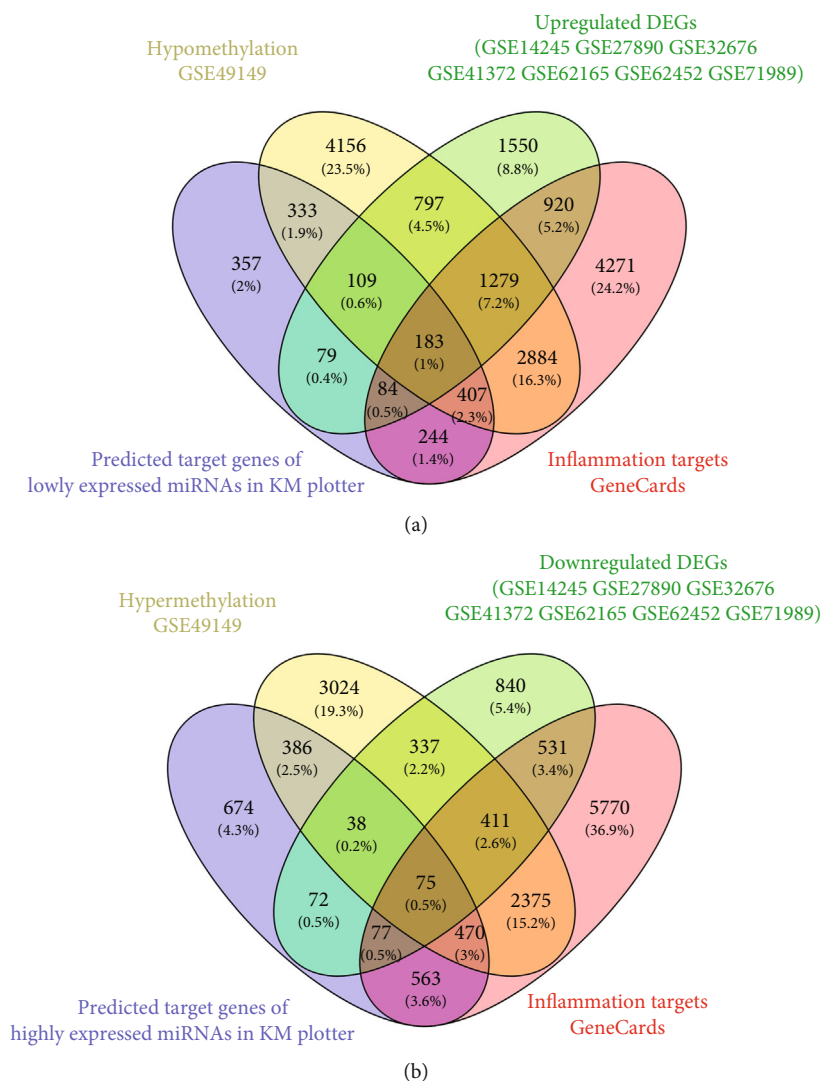


FIGURE 3: Identification of overlapping inflammation-associated methylated expressed genes. (a) Highly expressed inflammation-associated genes with low methylation. (b) Lowly expressed inflammation-associated genes with high methylation.

and DNMT1 were associated with worse overall survival (Figures 8(a)–8(h)). There was no significant association between ICAM1, ESR1, RPS6KA2, and FOSB expression and overall survival (Figures 8(i)–8(l)). Considering the ceRNA mechanisms and the signature value of hub genes, the circ_102049/miR-455-3p/CD80 axis was selected for further circRNA functional verification in PDAC cell lines.

3.7. Characteristics of circ_102049 in PDAC. The basic structural molds of hsa_circ_102049 (alias: hsa_circ_0043278) are displayed in Figure 9(a). circ_102049 originates from exons 5 and 6 of the transcriptional adaptor 2A (TADA2A) gene, and its mature length after splicing is 250 nt. RT-qPCR results confirmed that Panc-1 cells had the highest circ_102049 expression, followed by SW1990 cells (Figure 9(b)). Therefore, the SW1990 and Panc-1 cell lines were selected for subsequent experiments in this study. To confirm the stability of circ_102049, RNase R was used in the current study. As illustrated in Figure 9(c), circ_102049 was resistant to RNase R, whereas the linear forms of TADA2A were digested by

RNase R treatment. Moreover, we also determined that circ_102049 is mainly located in the cytoplasm by performing nuclear and cytoplasmic separation RT-PCR in SW1990 and Panc-1 cells, respectively (Figure 9(d)). Additionally, we further found that circ_102049 was more stable than the linear forms of TADA2A in SW1990 and Panc-1 cells under treatment with the transcription inhibitor actinomycin D (Figure 9(e)). Taken together, these results indicated that circ_102049 is a stable cytoplasmic circRNA.

3.8. hsa_circ_102049 Exerts Oncogenic Effects in the SW1990 and Panc-1 Cells. Due to a high expression of circ_102049 in the SW1990 and Panc-1 cells, we depleted the expression of circ_102049 in the SW1990 and Panc-1 cell lines by treating cells with specific circ_102049 siRNAs (si-circ_102049_#1, si-circ_102049_#2) and si-NC as a control. Results showed that circ_102049 was apparently decreased in si-circ_102049_#1- and si-circ_102049_#2-treated PDAC cells compared to those cells treated with si-NC; in particular, si-circ_102049_#1-treated cells are more obvious

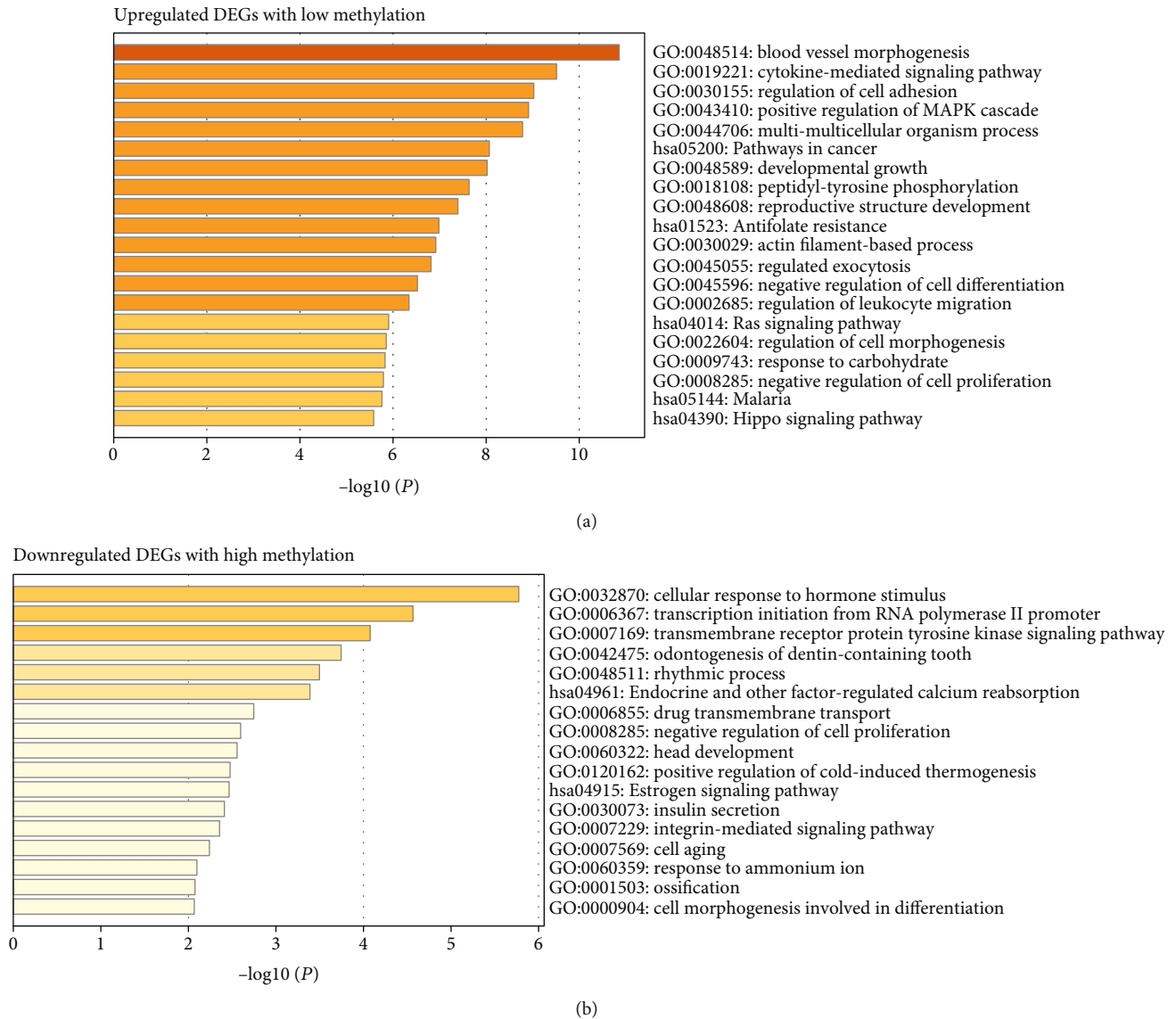
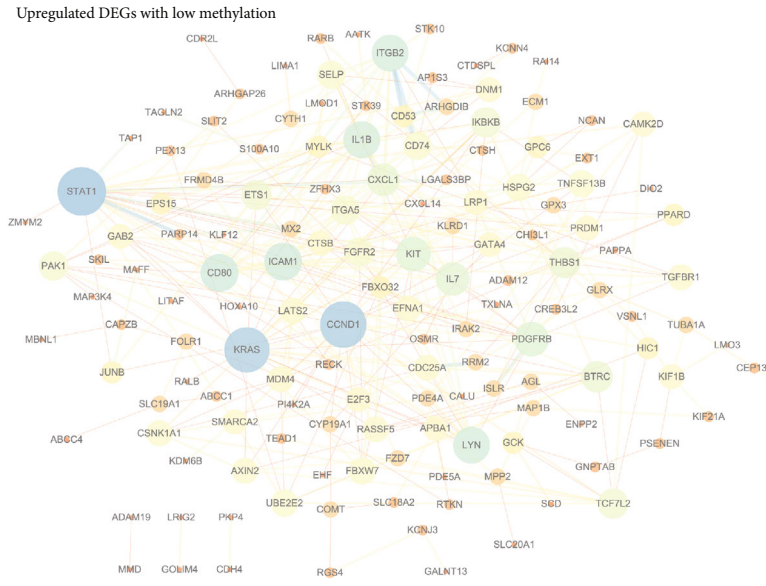


FIGURE 4: GO and KEGG pathway enrichment analysis for the inflammation-associated methylated expressed genes. GO-BP terms and KEGG pathway enrichment analysis of upregulated DEGs with low methylation (a) and downregulated DEGs with high methylation (b).

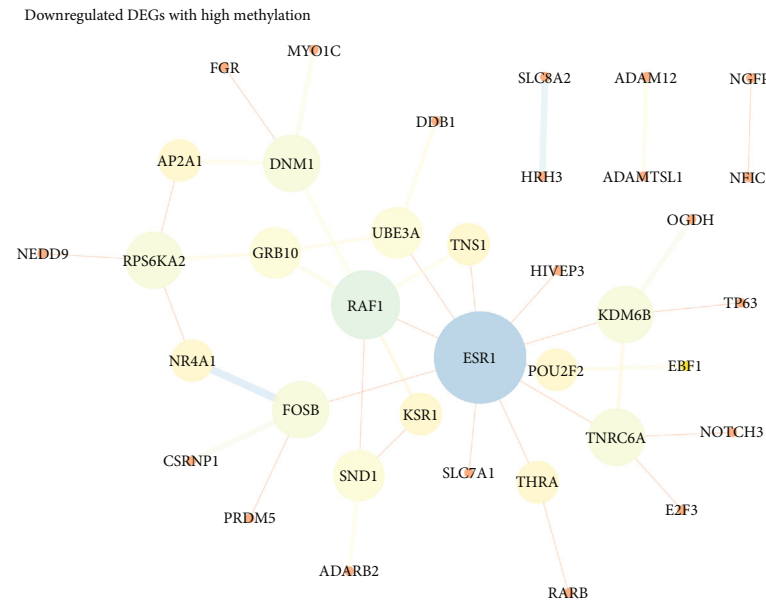
(Figure 10(a)). Then, we selected the siRNA, si-circ_102049_#1, for further functional experiments. CCK-8 assay showed that cell viability was significantly reduced in circ_102049 knockdown SW1990 and Panc-1 cells (Figure 10(b)), and the colony formation assay showed a decrease of the colony number in si-circ_102049_#1-treated SW1990 and Panc-1 cells (Figure 10(c)). Also, as shown in Figure 10(d), after the knockdown of circ_102049 in SW1990 and Panc-1 cells, the cell apoptotic rate significantly increased, respectively. Moreover, the wound healing assay demonstrated that circ_102049 knockdown led to decreased migration ability in PDAC cells (Figure 10(e)), and transwell analysis also demonstrated that circ_102049 knockdown dramatically inhibited the invasion of SW1990 and Panc-1 cells (Figure 10(f)). Meanwhile, RT-qPCR results demonstrated that circ_102049 knockdown significantly inhibited the mRNA expression levels of TNF- α , IL-6, IL-1 β , IL-8, and

IL-17 in the PDAC cell lines (Figure 10(g)). To further assess the effect of circ_102049 knockdown in vivo, we inoculated stable circ_102049 knockdown with Panc-1 cells subcutaneously into 6-week-old nude mice. Our results indicate that the silencing of circ_102049 decreased the weight and sizes of PDAC tumors (Figure 10(h)). These results demonstrated that blocking circ_102049 inhibited PDAC progression in vitro and in vivo.

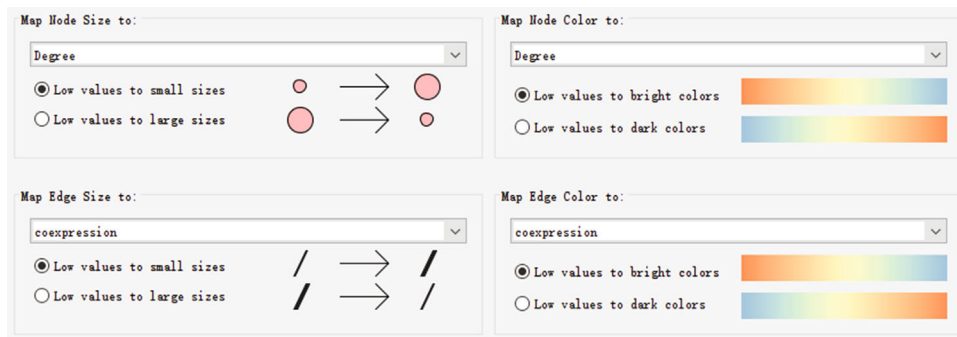
3.9. Identification of miR-455-3p as a circ_102049 Target Gene. Increasingly, circRNAs have been reported to function as a miRNA sponge. To confirm the ability of hsa_circ_102049 to regulate the expression of miR-455-3p, the CircInteractome database was used to predict the miRNAs with potential circ_102049 binding sites (Figures 11(a) and 11(b)). Luciferase assays confirmed that miR-455-3p overexpression inhibited the luciferase of wild-type circ_102049 in



(a)



(b)



(c)

FIGURE 5: Identification of hub genes in the PPI network of inflammation-associated methylated expressed genes. (a) PPI network of upregulated DEGs with low methylation. (b) PPI network of downregulated DEGs with high methylation. (c) The node size and color were mapped with the degree value. And the edge size and color were mapped with the coexpression value.

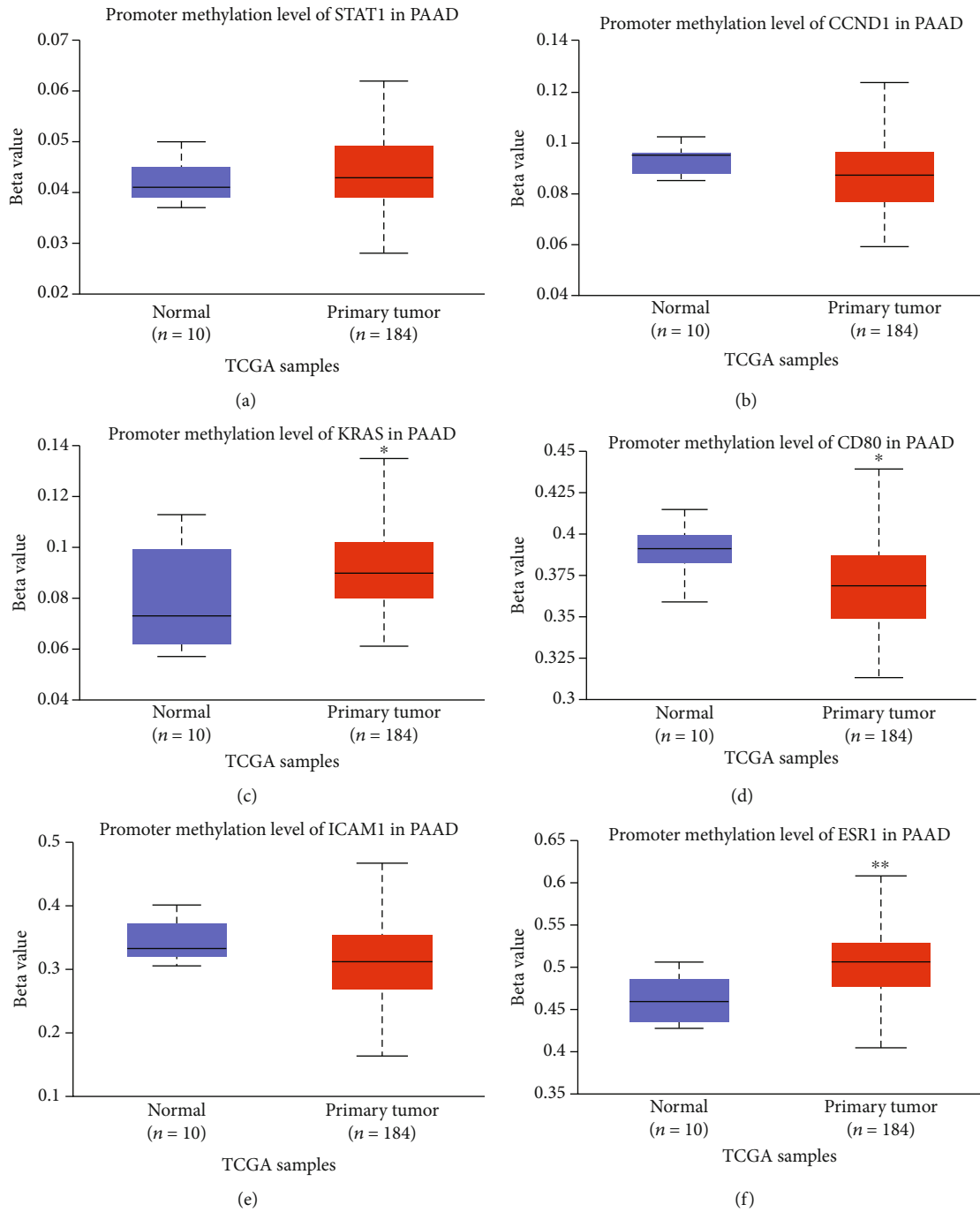


FIGURE 6: Continued.

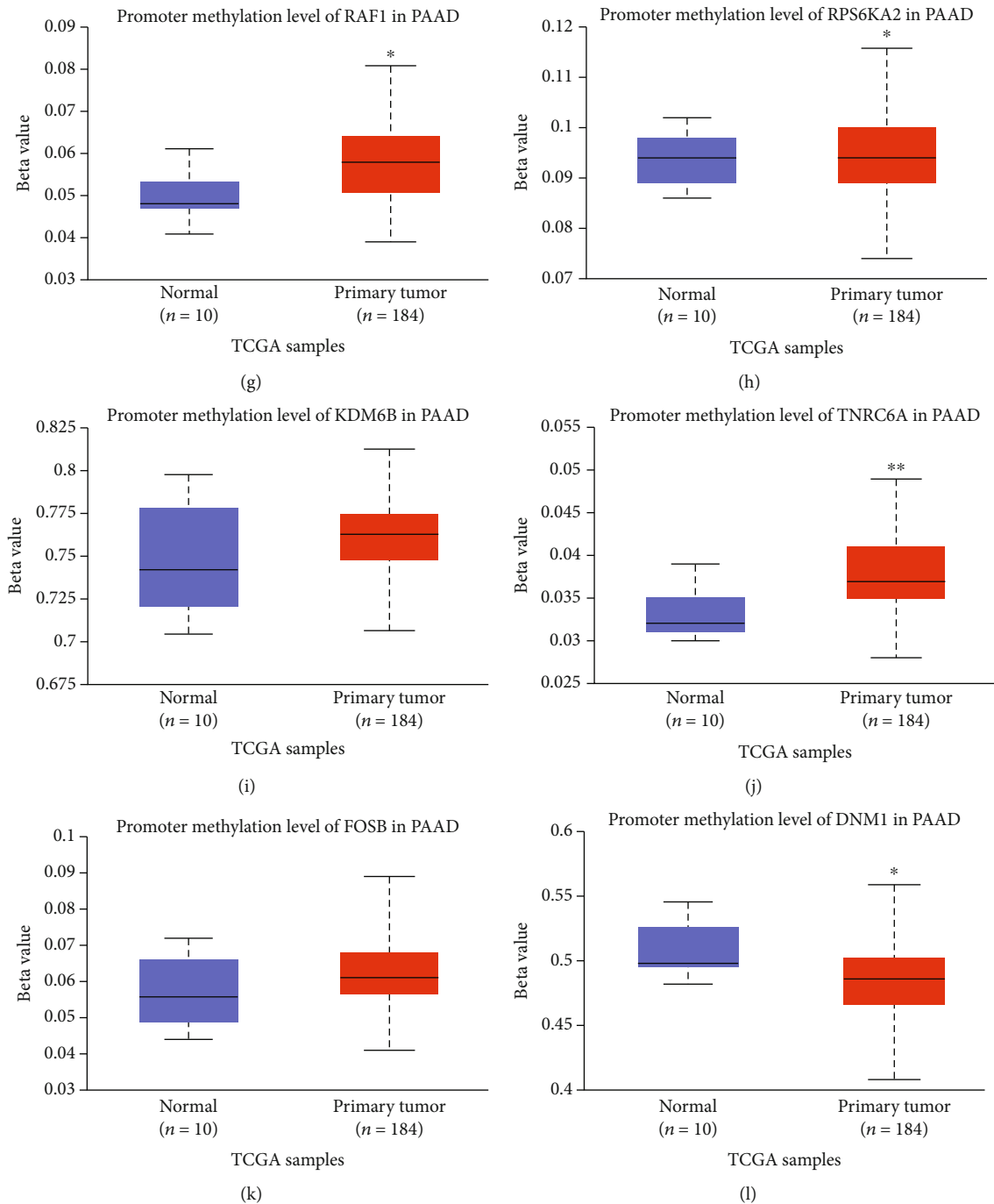


FIGURE 6: Verification of methylation levels of hub genes in pancreatic adenocarcinoma (PAAD). Promoter methylation level of STAT1 (a), CCND1 (b), KRAS (c), CD80 (d), ICAM1 (e), ESR1 (f), RAF1 (g), RPS6KA2 (h), KDM6B (i), TNRC6A (j), FOSB (k), and DNMI (l) in PAAD. * $P < 0.05$, ** $P < 0.01$. Primary tumor tissues vs. normal tissues.

SW1990 and Panc-1 cells, respectively (Figure 11(c)). In addition, the mRNA expression level of miR-455-3p was observably lower in SW1990 and Panc-1 cells than in HPDE6c7 cells (Figure 11(d)). Furthermore, SW1990 and Panc-1 cell lines were transfected with miR-455-3p mimic or miR-455-3p inhibitor to regulate miR-455-3p expression, as confirmed using RT-PCR (Figure 11(e)). Interestingly enough, the expression of circ_102049 was negatively regulated by miR-455-3p in both PDAC cell lines (Figure 11(f)).

Similarly, circ_102049 knockdown significantly increased miR-455-3p expression (Figure 11(g)). From the results above, we can confirm that miR-455-3p acts as a downstream target of circ_102049 in PDAC.

3.10. circ_102049 Regulates CD80 Expression in PDAC Cells by Sponging miR-455-3p. Based on the theory of ceRNA, there should be a positive correlation between the circ_102049 expression and the expression of its potential target

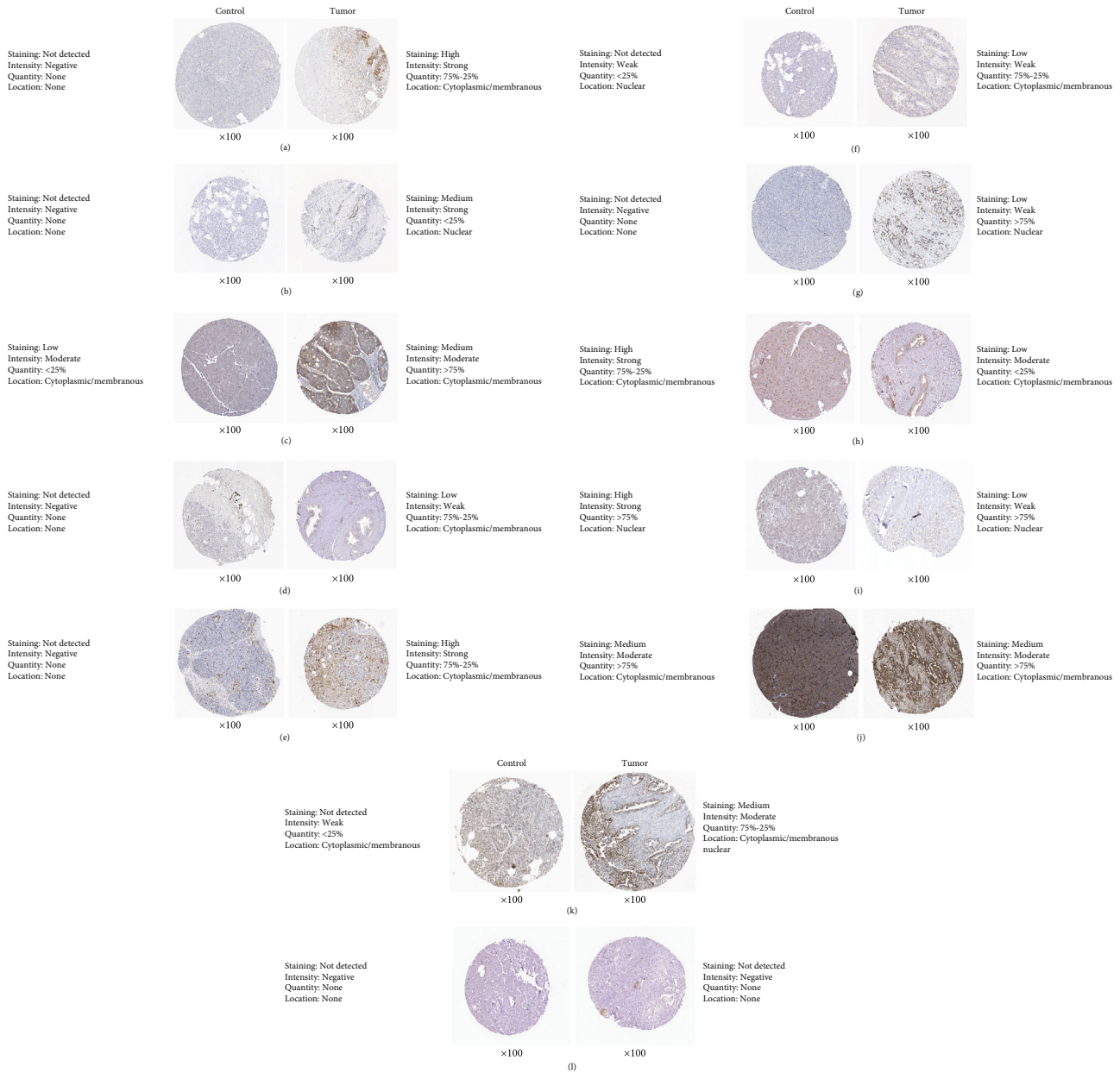
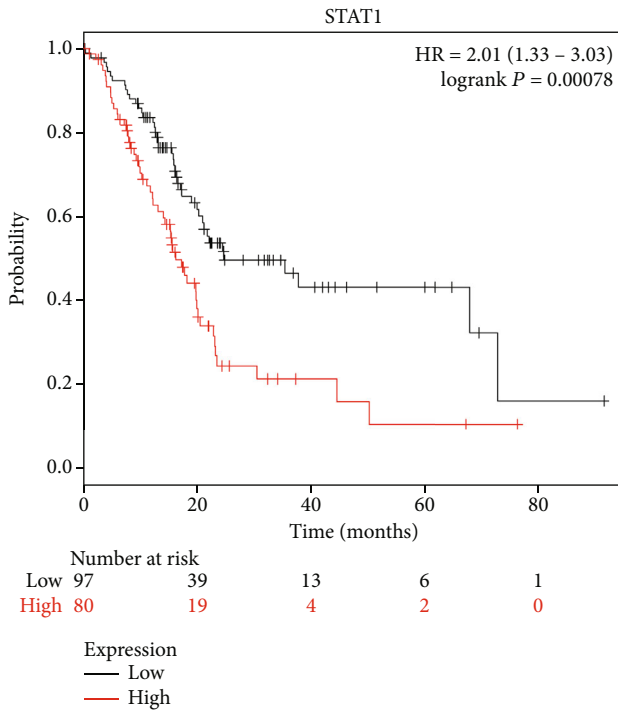


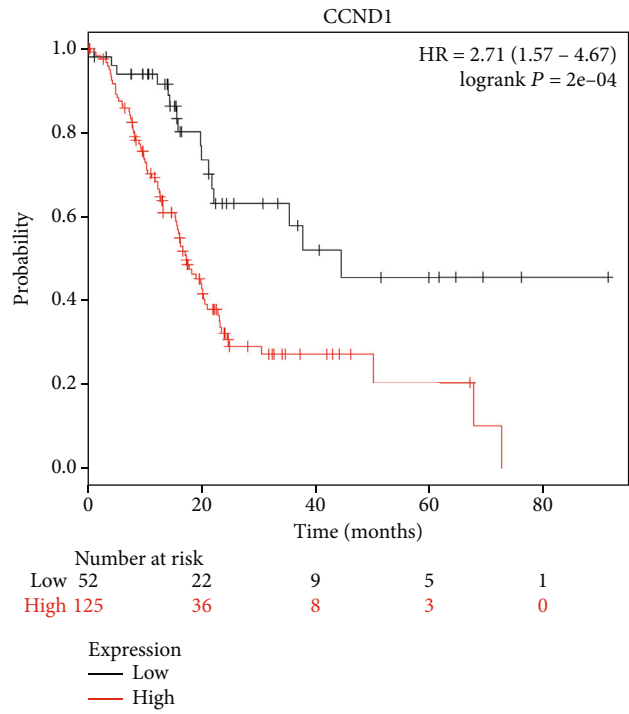
FIGURE 7: Comparison of protein expression of hub genes between normal pancreatic tissues and pancreatic cancer tissues. (a) STAT1, (b) CCND1, (c) KRAS, (d) CD80, (e) ICAM, (f) ESRI, (g) RAF1, (h) RPS6KA2, (i) KDM6B, (j) TNRC6A, (k) FOSB, and (l) DNMI1.

genes. In the circRNA-miRNA-mRNA network of circ_102049 within miR-455-3p and the hub genes, we found that miR-455-3p could target CD80. Also, bioinformatics analysis showed there are putative binding sites between miR-455-3p and CD80, and it is conserved among species (Figure 12(a)). Hence, we selected CD80 for further validation. Then, luciferase assays confirmed the binding activity of miR-455-3p to CD80, and miR-455-3p mimic significantly attenuated the luciferase activity of SW1990 and Panc-1 cells driven by psiCHECK2 CD80 wt, but not that driven by psiCHECK2 CD80 mut, compared to the miR-455-3p NC group (Figure 12(b)). Notably, the results of western blot assay indicate that circ_102049 knockdown and miR-455-3p overex-

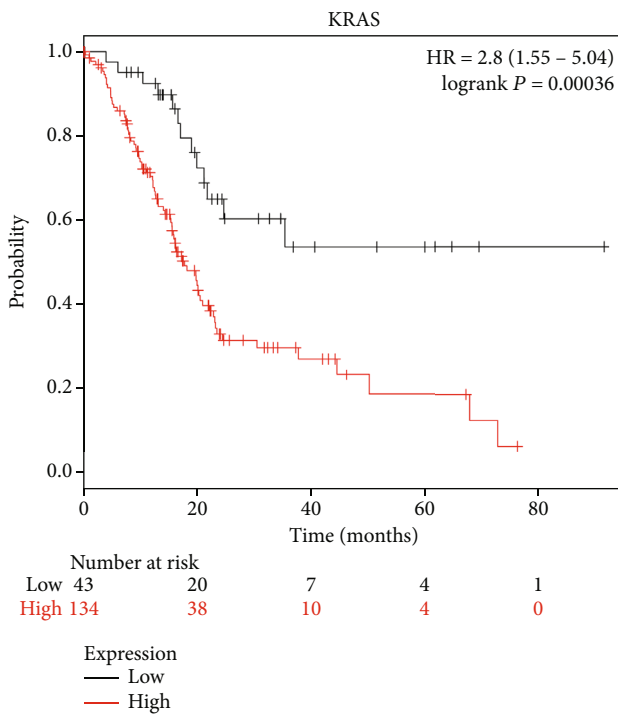
pression resulted in a decrease of CD80 protein expression in SW1990 and Panc-1 cells (Figure 12(c)). Then, we investigated the roles of circ_102049 in the miR-455-3p/CD80 axis, and relative mRNA expression of CD80; TNF- α , IL-6, IL-1 β , IL-8, and IL-17 expression; and invasion cell number were estimated in SW1990 and Panc-1 cells treated with si-circ_102049_#1 and miR-455-3p inhibitor. Our results showed that miR-455-3p knockdown significantly increased the mRNA expression of CD80; TNF- α , IL-6, IL-1 β , IL-8, and IL-17 expression; and invasion ability of PDAC cells, while cotransfection of si-circ_102049_#1 and miR-455-3p inhibitor could partially reverse the suppressive role of circ_102049 deficiency in CD80; TNF- α , IL-6, IL-1 β , IL-8, and IL-17



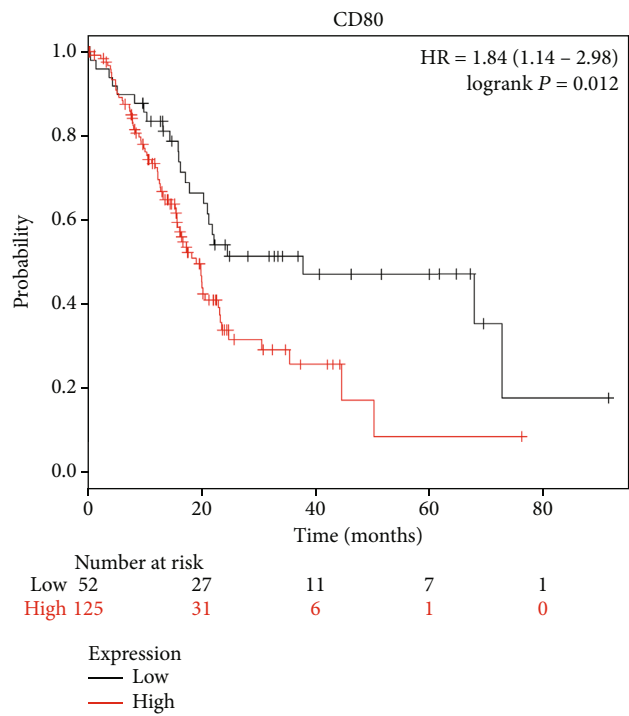
(a)



(b)

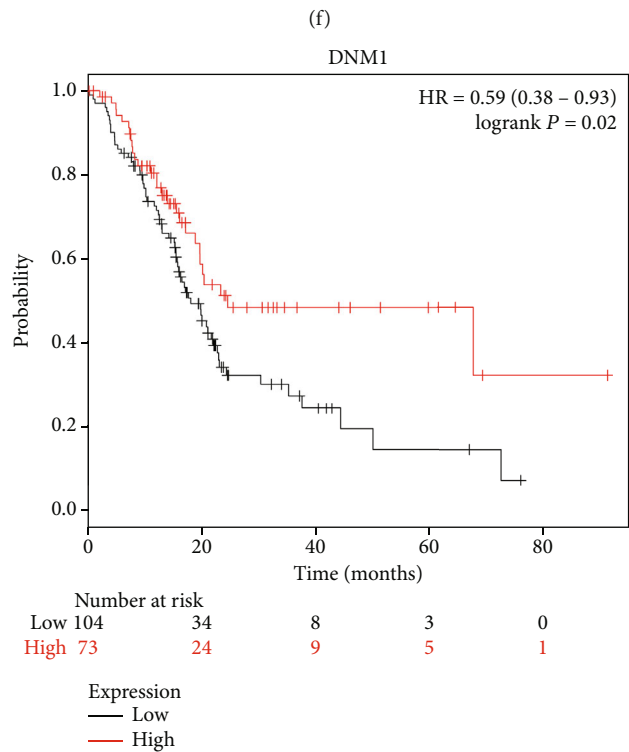
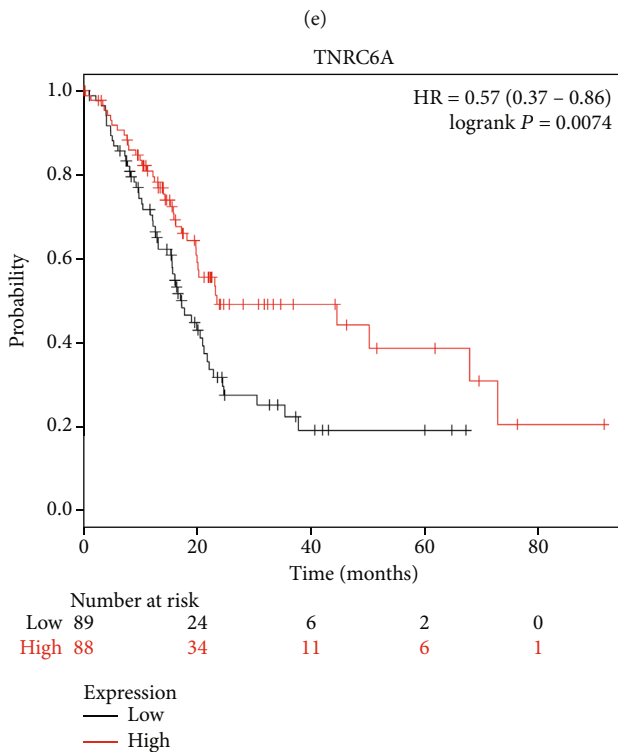
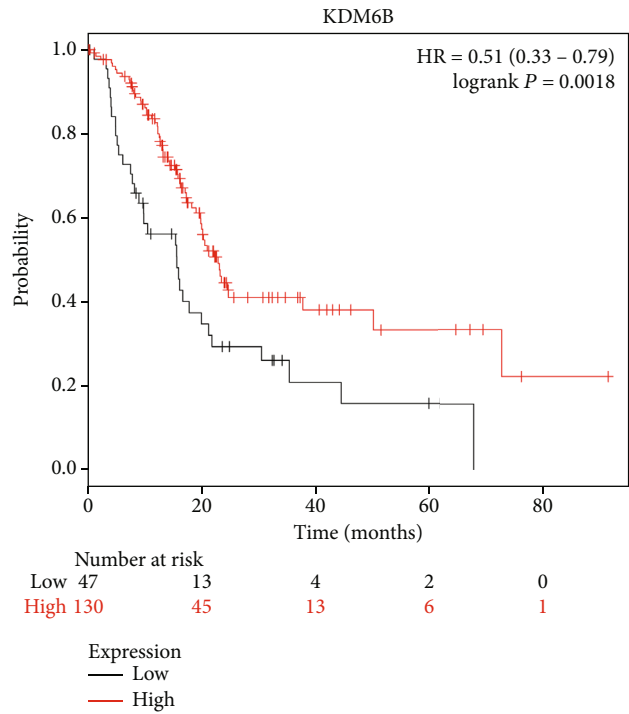
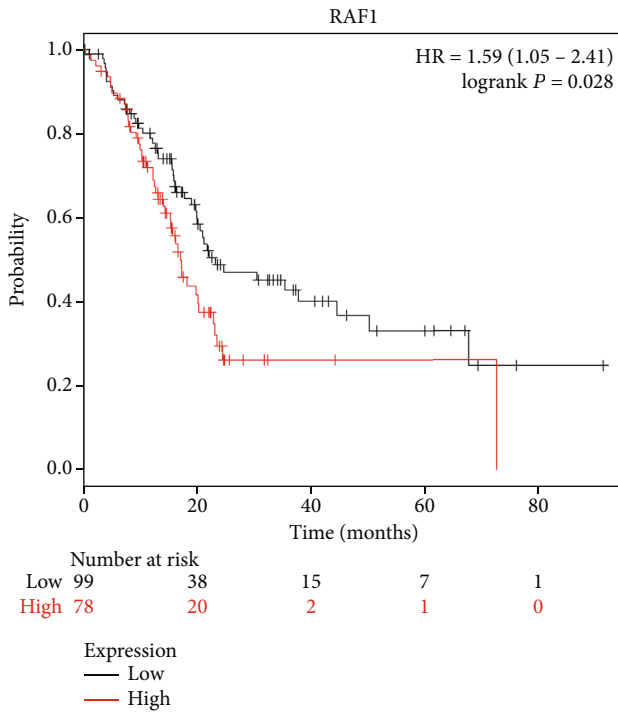


(c)



(d)

FIGURE 8: Continued.



(e)

(f)

(g)

(h)

FIGURE 8: Continued.

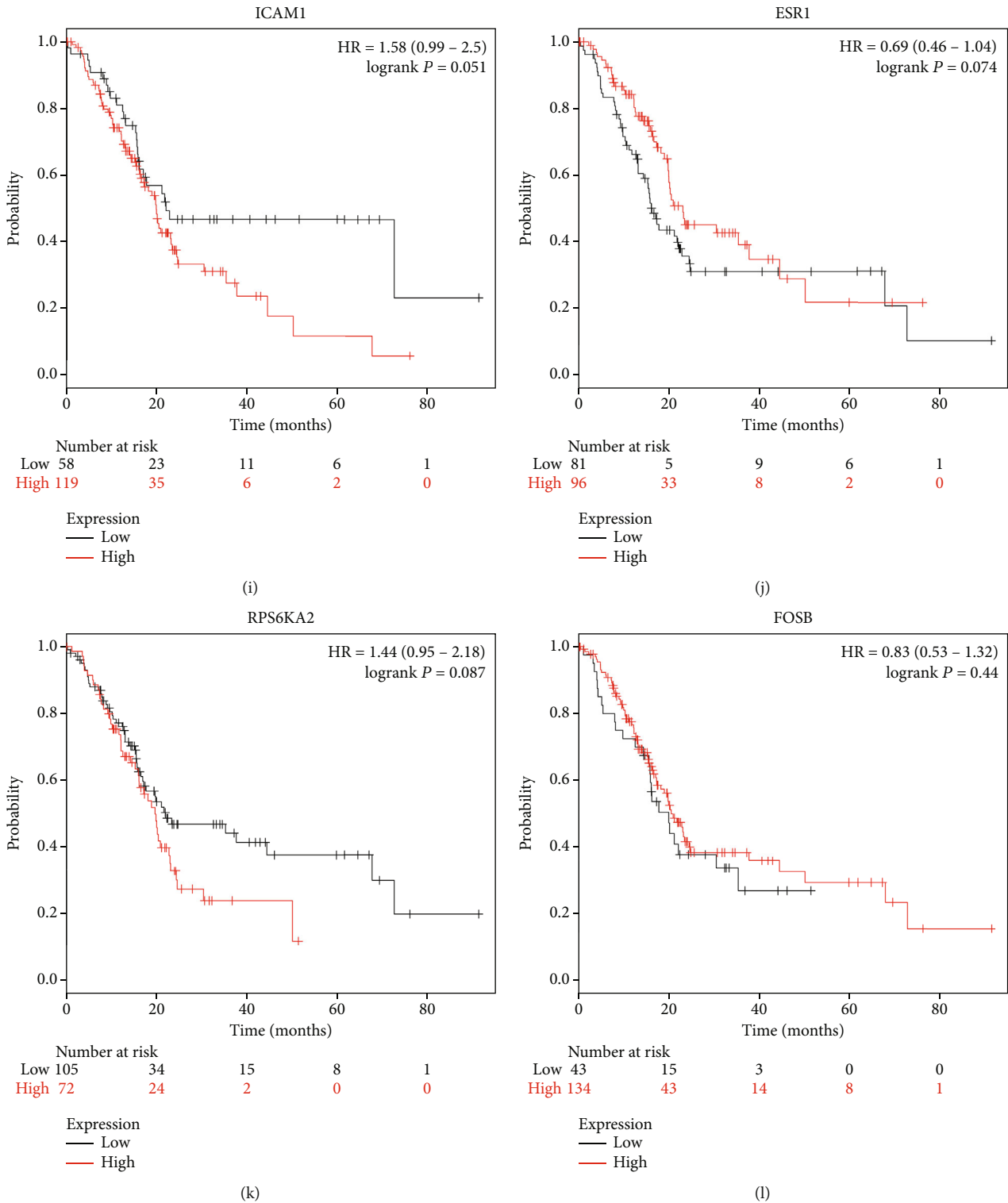
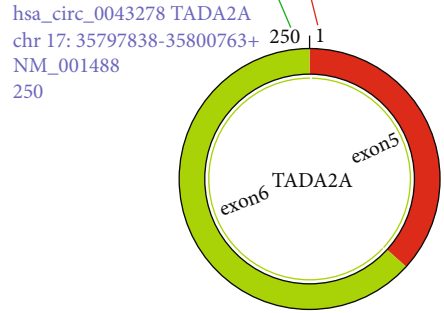
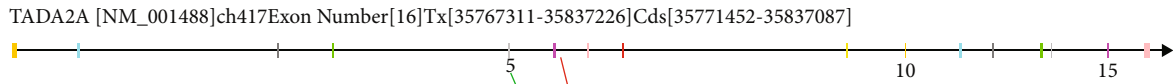


FIGURE 8: Kaplan-Meier survival curves of twelve hub genes in pancreatic adenocarcinoma patients. Overall survival by low and high (a) STAT1, (b) CCND1, (c) KRAS, (d) CD80, (e) RAF1, (f) KDM6B, (g) TNRC6A, (h) DNMT1, (i) ICAM1, (j) ESR1, (k) RPS6KA2, and (l) FOSB expression.

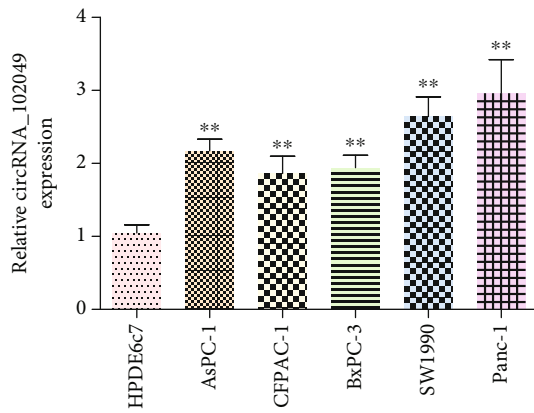
expression; and invasion of SW1990 and Panc-1 cells (Figures 12(d)–12(f)). These results indicate that circ_102049 promoted the tumorigenesis of PDAC by increasing the expression of CD80 via miR-455-3p.

4. Discussion

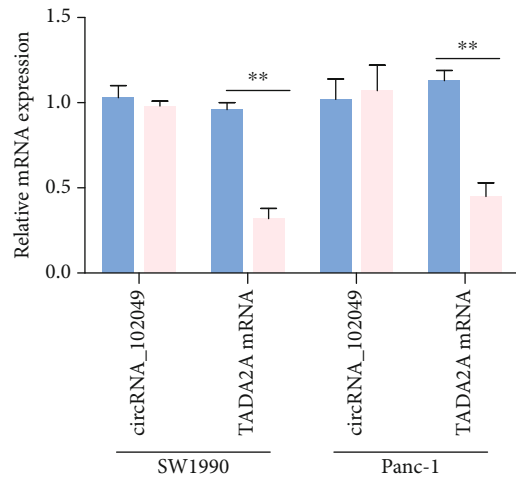
Pancreatic ductal adenocarcinoma (PDAC) is a typically malignant tumor of the digestive system, with a 5-year



(a)



(b)



(c)

FIGURE 9: Continued.

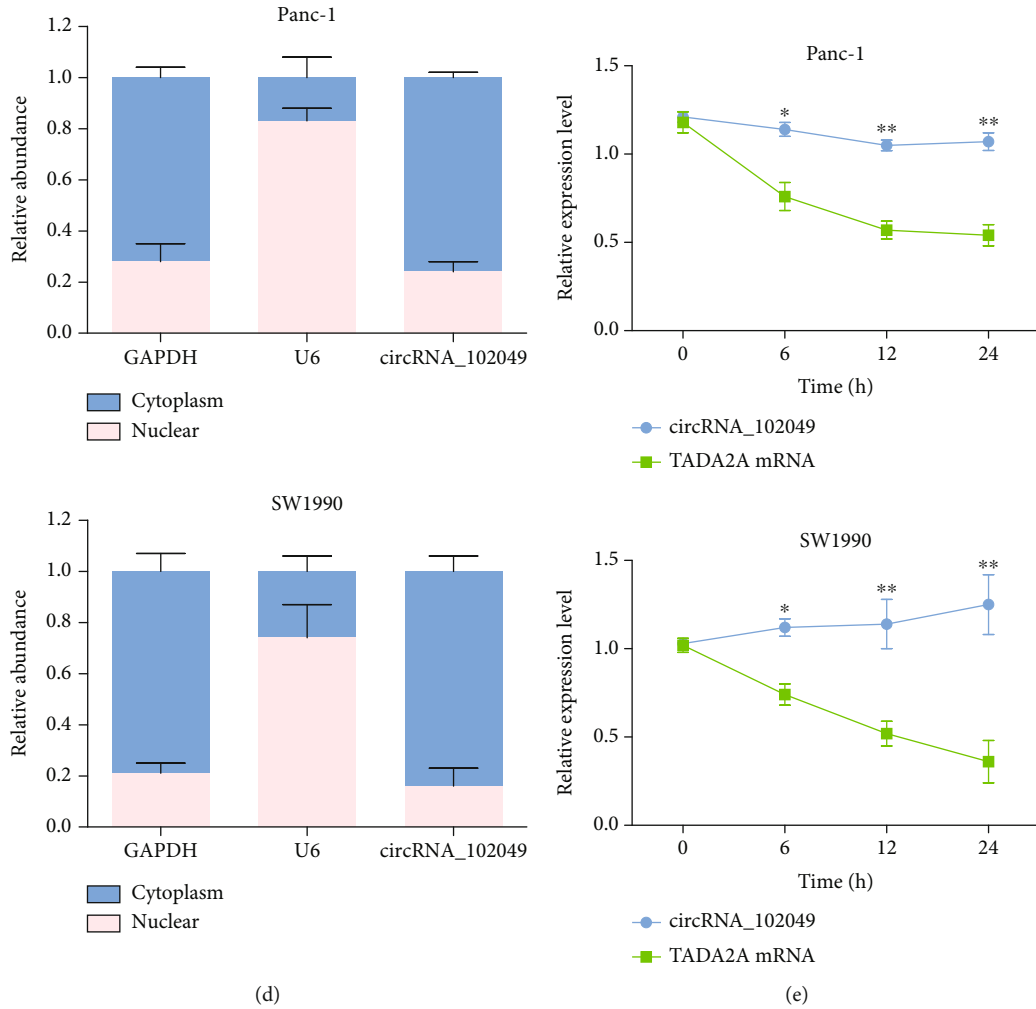


FIGURE 9: hsa_circRNA_102049 is upregulated in PDAC cell lines. (a) Schematic illustration showed that the circularization of TADA2A exons 5 and 6 formed circ_102049. (b) Measurement of circ_102049 expression in HPDE6c7 cells and PDAC cell lines. (c) RT-PCR analysis of circ_102049, liner TADA2A in SW1990 and Panc-1 cells treated with RNase R. (d) qPCR for the abundance of circ_102049 in the cytoplasm of SW1990 and Panc-1 cells. GAPDH and U6 were endogenous controls. (e) RT-PCR analysis of circ_102049 and TADA2A RNA after treatment with actinomycin D at the indicated time points in SW1990 and Panc-1 cells. * $P < 0.05$, ** $P < 0.01$.

overall survival rate of less than 6% [36]. It is reported that approximately 80% of patients have lost the chance for surgical resection because of its complexity and invisibility [36, 37]. Hence, it is imperative to promote the development of early biomarkers and novel therapeutic methods according to the molecular mechanisms for the prognosis of PDAC. Great advances in high-throughput gene expression profiling and the development of integrated bioinformatics analysis are providing remarkable perspectives for us to perform methylation research that is associated with the pathogenesis of cancers. Also, aberrations of methylation are extremely common in the cancer genome. It is widely accepted that high methylation of tumor suppressor genes and low methylation of cancer genes play significant roles in the occurrence and development of cancers [38]. Recently, a number of studies have elucidated that circRNAs, a type of covalent closed circular noncoding RNAs, are strongly implicated in tumor growth, metastasis, and proliferation through the circRNA-miRNA-mRNA axis in a wide variety of tumors [39, 40]. cir-

crNAs are highly stable and tissue-specific compared with linear RNAs that might be used as promising biomarkers for the detection of clinicopathological status in PDAC. Meanwhile, systemic inflammation is a hallmark of PDAC, which is associated with poor clinical outcomes by supporting malignant cells escape from immune elimination [41]. Thus, exploring further strategies to ameliorate inflammatory reaction is necessary for increasing the effectiveness of cancer immunotherapy in PDAC.

In the current study, the circRNA expression profiling datasets (GSE69362, GSE79634), gene methylation profiling microarray (GSE49149), and gene expression datasets (GSE14245, GSE27890, GSE32676, GSE41372, GSE62165, GSE62452, and GSE71989) were downloaded from the GEO database to identify DECs and DMGs with GEO2R, and P value < 0.05 was considered statistically significant. Then, we comprehensively analyzed the ceRNA regulatory network consisting of circRNAs, miRNAs, and mRNAs in PDAC. Twenty upregulated and five downregulated DECs

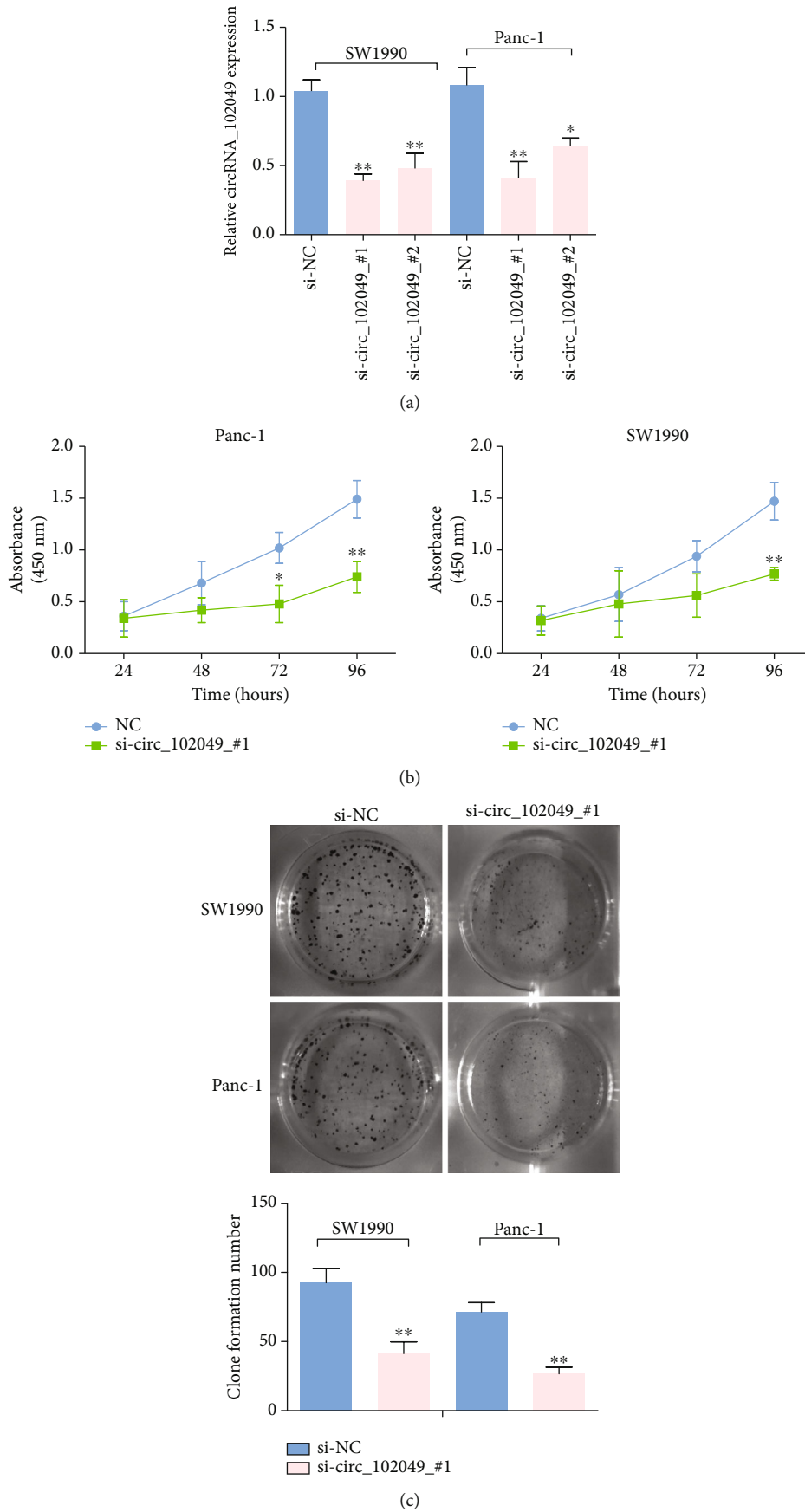
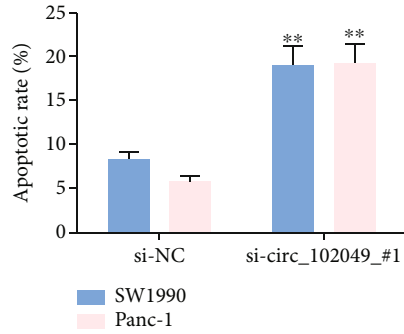
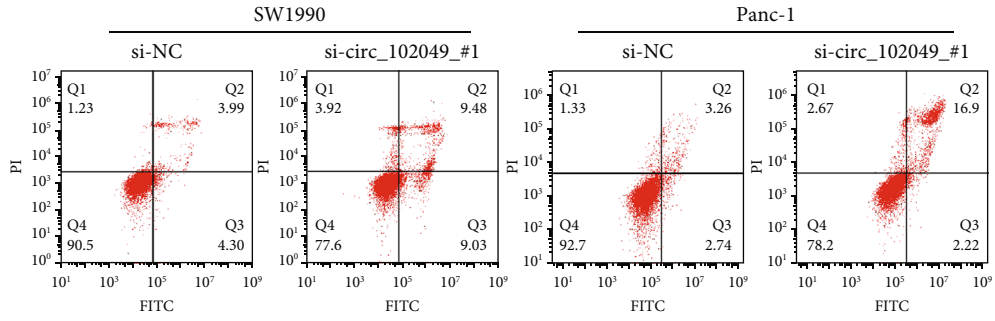
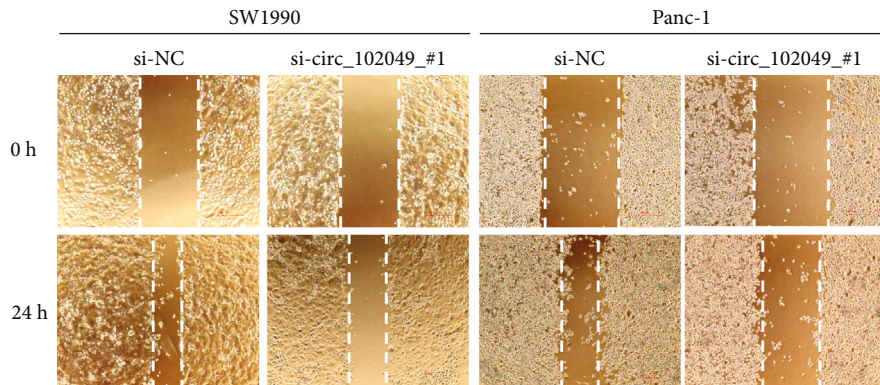
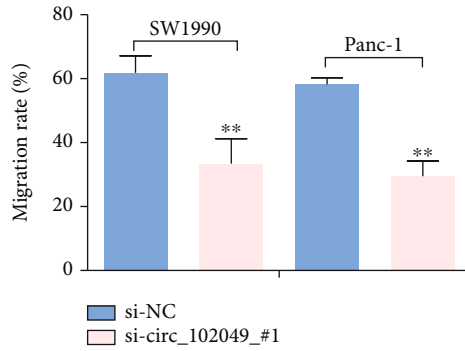


FIGURE 10: Continued.

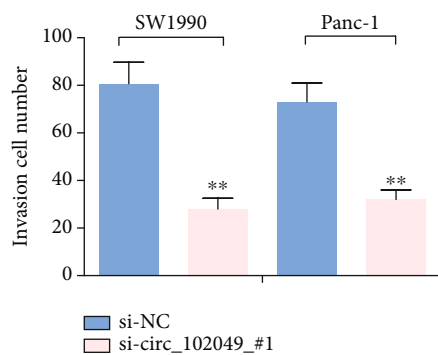
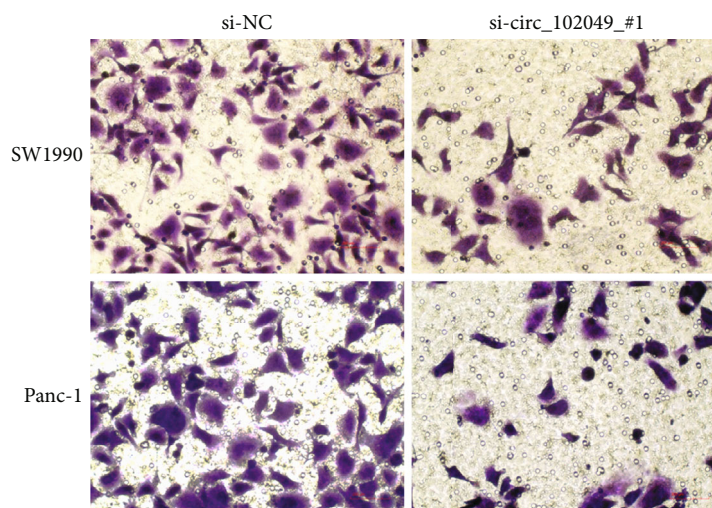


(d)

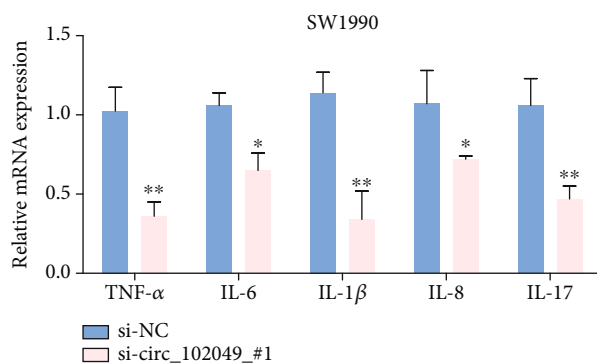
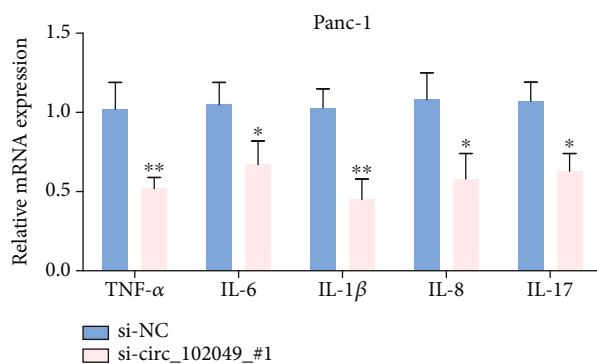


(e)

FIGURE 10: Continued.



(f)



(g)

FIGURE 10: Continued.

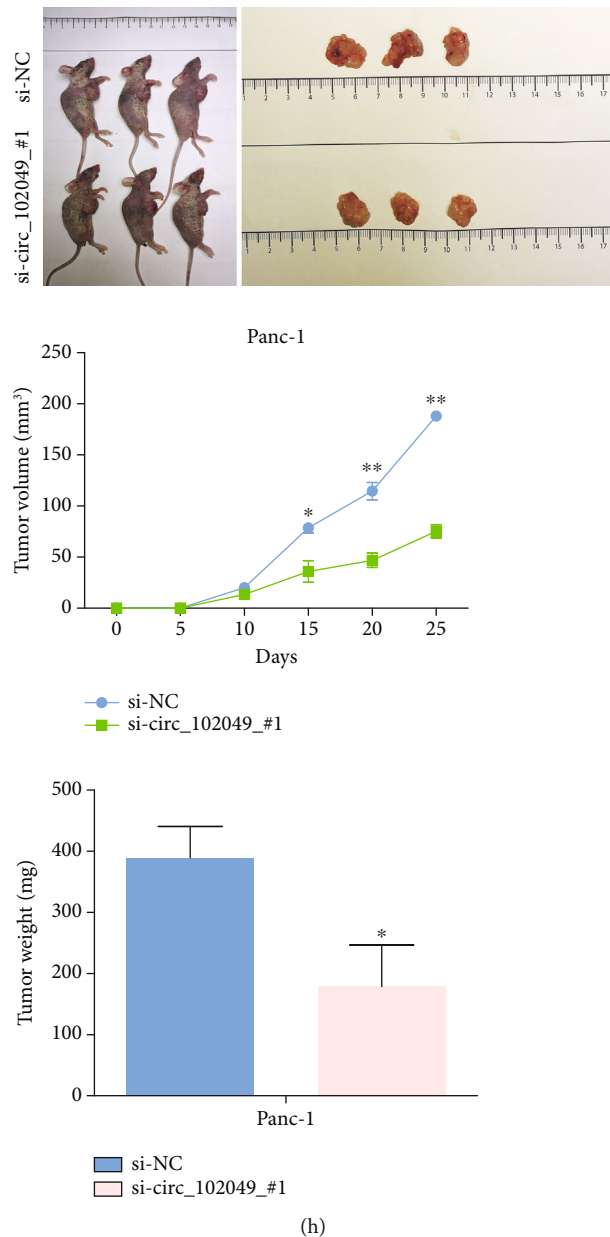
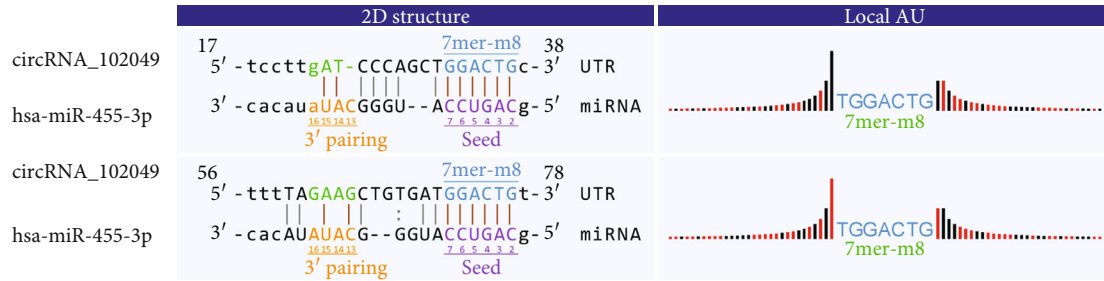


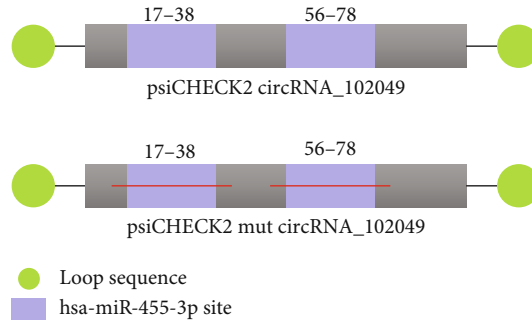
FIGURE 10: The role of circ_102049 knockdown in cell growth, apoptosis, inflammation, invasion, and migration in PDAC cells. (a) circ_102049 expression was measured after transfection in SW1990 and Panc-1 cells by RT-PCR. (b) CCK-8 assays were used to detect cell viability of SW1990 and Panc-1 cells after transfection. (c) Numbers of clone formation were decreased when transfected with si-circ_102049_#1. (d) The apoptosis of SW1990 and Panc-1 cells examined by flow cytometry after transfection. (e) Wound healing assays were performed in SW1990 and Panc-1 cells treated with si-NC or si-circ_102049_#1. (f) Cell invasion ability of SW1990 and Panc-1 cells transfected with si-NC or si-circ_102049_#1 was evaluated by the transwell assays. (g) mRNA expression levels of TNF- α , IL-6, IL-1 β , IL-8, and IL-17 were detected in SW1990 and Panc-1 cells transfected with si-NC or si-circ_102049_#1 by RT-PCR. (h) circ_102049 knockdown inhibited tumor growth in vivo. Tumor weight and volumes were significantly reduced in the si-circ_102049_#1 group compared with the si-NC group. * $P < 0.05$, ** $P < 0.01$.

were screened for further research. Particularly, hsa_circ_102049 was significantly upregulated in GSE69362 and GSE79634 datasets. We predicted potential circRNA-miRNA via the CircInteractome database, and TargetScan and miRDB databases were used to identify miRNA-mRNA pairs. Finally, we confirmed 53 highly expressed miRNAs and 38 lowly expressed miRNAs in the KM plotter, associated with poor survival of PDAC patients, and 7871 mRNAs

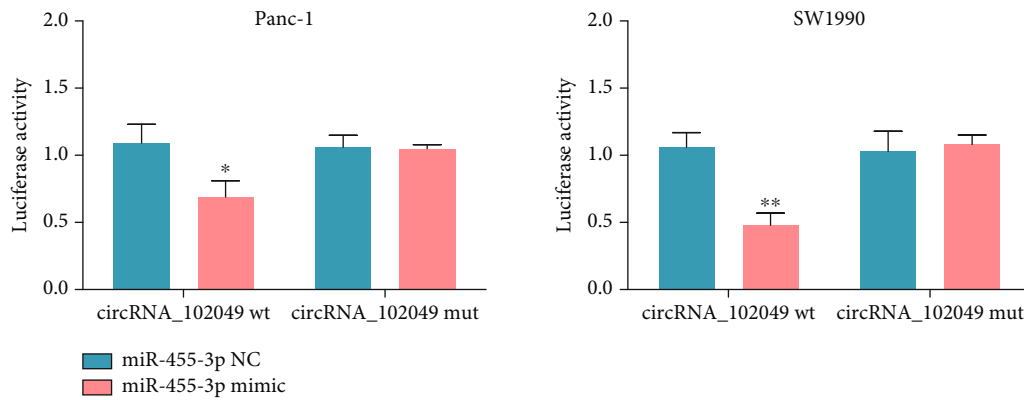
to construct a circRNA-miRNA-mRNA regulatory network preliminarily. In addition, we also found that hsa-miR-455-3p and hsa-miR-342-3p may be the target genes of circ_102049. Next, we identified and investigated the inflammation-associated hypomethylation-high expression genes and hypermethylation-low expression genes and their potential upstream regulatory mechanisms in PDAC, respectively. Functional enrichment analysis showed that



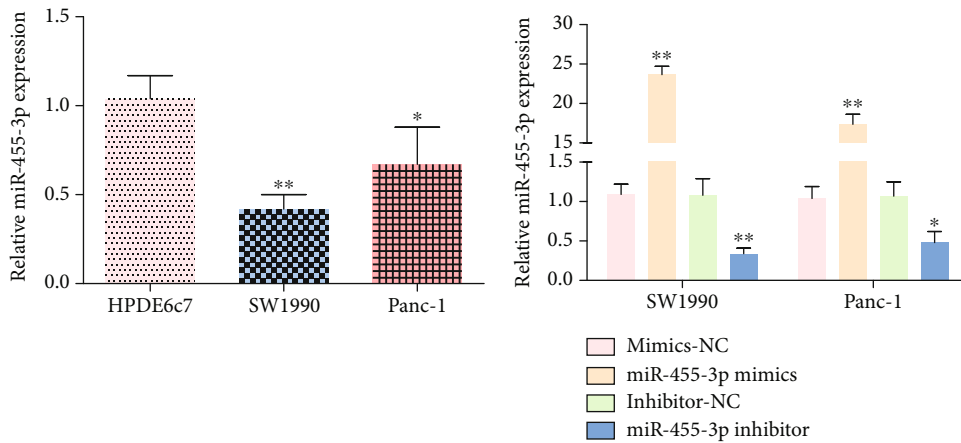
(a)



(b)



(c)



(d)

(e)

FIGURE 11: Continued.

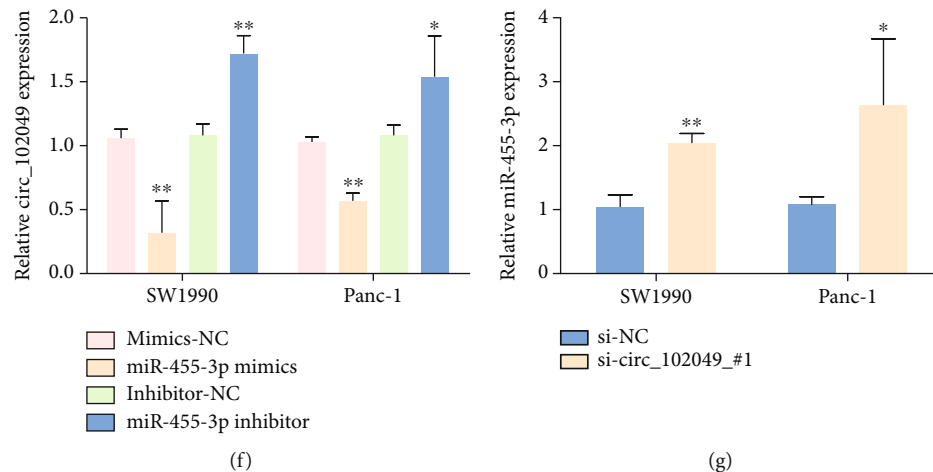


FIGURE 11: circ_102049 functions as a miRNA sponge for miR-455-3p. (a) The binding site for miR-455-3p and circ_102049 was analyzed with the bioinformatics tool. (b) Schematic outlining the wild-type and mutant circ_102049 luciferase plasmid. (c) Luciferase reporter assay was performed to analyze the interaction between circ_102049 and miR-455-3p in PDAC cells. (d) miR-455-3p expression was confirmed by using RT-PCR in PDAC cells. (e) Overexpression and silencing of miR-455-3p in SW1990 and Panc-1 cells via miR-455-3p mimic or miR-455-3p inhibitor, respectively. (f) circ_102049 expression was detected in transfected PDAC cells with miR-455-3p mimic or miR-455-3p inhibitor, respectively. (g) miR-455-3p expression was measured in SW1990 and Panc-1 cells that were transfected with si-NC or si-circ_102049_#1. * $P < 0.05$, ** $P < 0.01$.

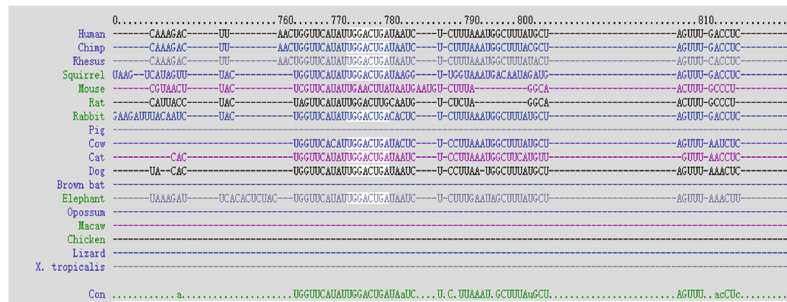
these hypomethylation-high expression genes were involved in blood vessel morphogenesis, cytokine-mediated signaling pathway, regulation of cell adhesion, and pathways in cancer, which are well known in regulating the progression of PDAC [42, 43].

The PPI network revealed the intercommunication of the hypomethylation-high expression genes/hypermethylation-low expression genes, among which the hub genes were STAT1, CCND1, KRAS, CD80, ICAM1, ESR1, RAF1, RPS6KA2, KDM6B, TNRC6A, FOSB, and DNMT1. Among them, KRAS, ESR1, RAF1, RPS6KA2, and TNRC6A have higher methylation levels, and in particular, CD80 and DNMT1 have low methylation levels; furthermore, the results of the Kaplan-Meier analyses demonstrate that the STAT1, CCND1, KRAS, CD80, ICAM1, KDM6B, TNRC6A, and DNMT1 were associated with the prognostic outcomes of patients with PDAC. STAT1 is activated by interferon- γ (IFN γ) in pancreatic stellate cells (PSCs), which plays an important role in chronic pancreatitis and pancreatic cancer [44]. Besides, a recent study showed that STAT1 inhibition significantly suppressed the upregulation of PD-L1 in stimulated B cells for the immunology regulation of PDAC patients [45]. Radulovich et al. uncovered that the overexpression of CCND1 is most common in PDAC and occurred mainly in late-stage pancreatic intraepithelial neoplastic (PanIN) lesions [46]. In addition, Chen et al. revealed that CCND1 was targeted by miR-193a-3p, and overexpression of miR-193a-3p significantly decreased CCND1 expression to inhibit the tumor growth in PDAC cells [47]. CCND1 may be one of the abnormally methylated genes, which have been indicated as proto-oncogenes that are positively associated with lymph node metastasis, regulating G1-to-S phase progression in human tumors [48–50]. KRAS is the predominant mutated RAS gene in human cancer and the initiating genetic event for PDAC [51]. CD80 (also known as B7-1) encodes a mem-

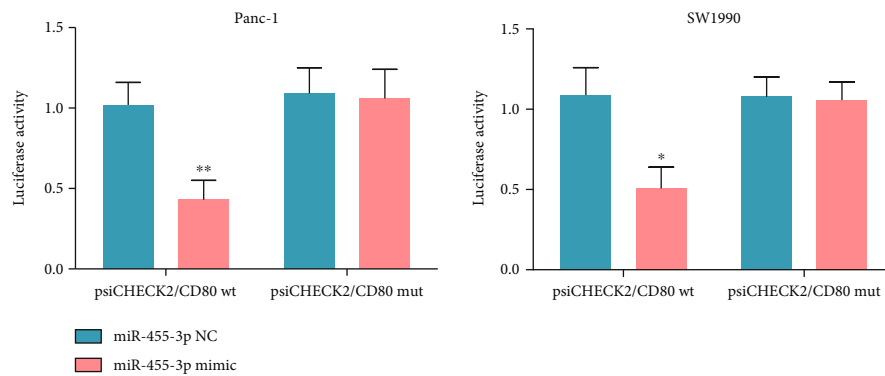
brane receptor that is activated by the binding of CD28 or CTLA-4, then further induces T cell proliferation and cytokine production [52]. Additionally, Bengsch et al. found that the CTLA-4/CD80 pathway was implicated in T cell immunotherapy in PDAC [53]. Moreover, Das et al. reported that the potential immunosuppressive effect in gingivobuccal oral squamous cell carcinoma (OSCC-GB) may be associated with promoter hypomethylation, which was driven by the upregulation of CD80 [54]. To our knowledge, cytokines have a vital function in angiogenesis, tumor carcinogenesis, and metastasis in the tumor microenvironment. A study by Huang et al. found that interleukin 35 (IL-35) promotes PDAC metastasis by mediating ICAM1 expression [55]. KDM6B, also known as JMJD3, is a histone demethylase and located on the short arm of chromosome 17 (17p13.1) that removes the H3K27me3 methyl marks [56]. Also, the loss of KDM6B enhances the aggressiveness of PDAC cells by inhibiting the expression of C/EBP α [57]. TNRC6A, an essential mRNA-binding protein in miRISC, is inducing the DDRNA expression and functionality; and miR-30 promotes cancer by suppressing TNRC6A [58]. Shukla et al. discussed DNMT1 may participate in driving long-term radiation toxicity in the brain [59]. Even though the results of hub genes were according to computational biology, in vitro and in vivo biological and molecular experiments need to be performed to further verify our hypothesis. Generally, the identification of the above hub genes could improve the understanding of the pathogenesis and also provide prognostic markers and therapeutic targets for PDAC.

Herein, circ_102049, also known as hsa_circ_0043278 according to circBase, was found to be the common circRNA in the GSE69362 and GSE79634 datasets and was upregulated in PDAC cell lines. The expression of circ_102049 was resistant to RNase R degradation, and the subcellular distribution of circ_102049 was overwhelming in the cytoplasm.

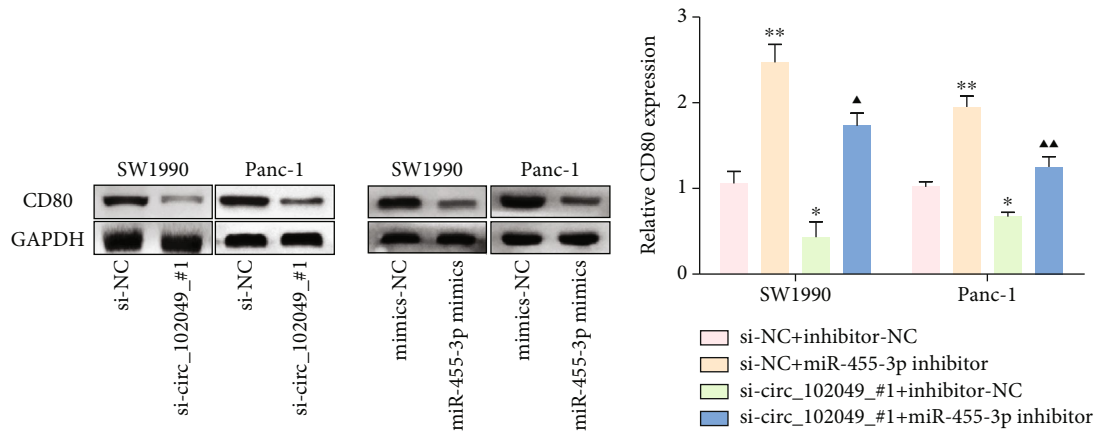
Position 773-780 of CD80 3' UTR wt 5' ...UUAACUGGUUCAUUAUUGGACUGA... 3'
 hsa-miR-455-3p 3' CACAUAUACGGGUACCUGACG 5'
 Position 773-780 of CD80 3' UTR mut 5' ...UUAACUGGUUCAUUAU**ACCUGACA**... 3'



(a)

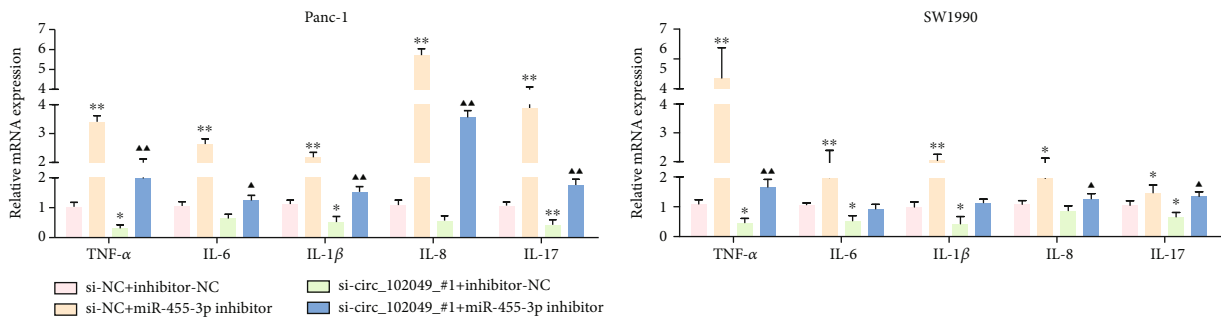


(b)



(c)

(d)



(e)

FIGURE 12: Continued.

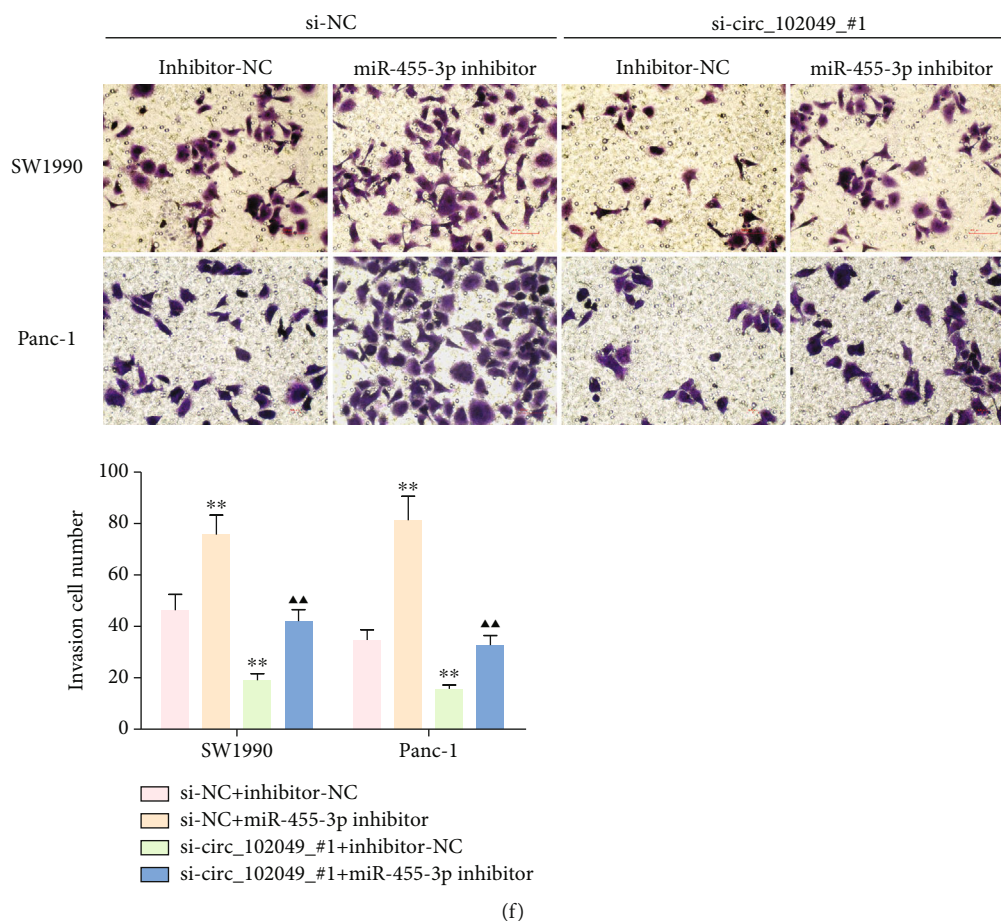


FIGURE 12: circ_102049 regulates CD80 expression in PDAC cells by sponging miR-455-3p. (a) A predicted binding site of miR-455-3p within the CD80 3'-UTR. (b) Luciferase reporter assays were employed to assess the interaction between CD80 3'-UTR and miR-455-3p. (c) circ_102049 knockdown and miR-455-3p overexpression suppressed CD80 protein expression in SW1990 and Panc-1 cells. Knockdown of circ_102049 reduced (d) CD80; (e) TNF- α , IL-6, IL-1 β , IL-8, and IL-17 expression; and (f) invasion ability in SW1990 and Panc-1 cells while inhibition of miR-455-3p in the meantime reversed it. The results were measured and expressed as mean \pm SD. * P < 0.05, ** P < 0.01 vs. the si-NC+inhibitor-NC group. ▲ P < 0.05, ▲▲ P < 0.01 vs. the si-circ_102049_#1+inhibitor-NC group.

All these results suggested an important role of circ_102049 in PDAC cell progression. Functionally, circ_102049 knockdown significantly decreased the growth, inflammatory factors, and migratory and invasive potential and promoted cell apoptosis in SW1990 and Panc-1 cells, whereas these effects could be reversed by downregulation of miR-455-3p. Importantly, we found that miR-455-3p was sponged by circ_102049, leading to the increased CD80 expression and the inflammatory reaction and invasion of PDAC. Therefore, the identification of the circ_102049/miR-455-3p/CD80 axis increases our understanding of the regulatory mechanism underlying PDAC progression.

5. Conclusion

In conclusion, twelve hub genes (STAT1, CCND1, KRAS, CD80, ICAM1, ESR1, RAF1, RPS6KA2, KDM6B, TNRC6A, FOSB, and DNMT1) were identified as abnormal methylation genes in PDAC with integrated bioinformatics analysis. We further indicated that circ_102049 knockdown could effectively inhibit cell growth, inflammatory state, migration,

and invasion of PDAC cells in vivo and in vitro via the miR-455-3p/CD80 axis. Our results suggest that the circ_102049/miR-455-3p/CD80 axis may potentially be used as a promising prognostic biomarker for PDAC.

Data Availability

The data used to support the findings of this study are available from the corresponding author upon request.

Conflicts of Interest

The authors declare that they have no conflict of interest.

Acknowledgments

This work was supported by research grants from the Taizhou Science and Technology Bureau (1901ky38), Zhejiang Provincial Health Commission (2020ky1054), and Zhejiang Science and Technology Department (LGC20H200004).

Supplementary Materials

Supplementary 1. Figure S1 The survival analysis of target miRNAs of selected DECs.

Supplementary 2. Figure S2 The clinical stage analysis of hub genes by using the GEPIA database.

Supplementary 3. Table S1 The differentially expressed circRNAs in the GSE69362 dataset.

Supplementary 4. Table S2 The differentially expressed circRNAs in the GSE79634 dataset.

Supplementary 5. Table S3 The target miRNAs of overlapped DECs according to the CircInteractome database.

Supplementary 6. Table S4 The target miRNAs of overlapped DECs according to the KM plotter analysis.

Supplementary 7. Table S5 The potential target genes of 53 highly expressed miRNAs with poor survival of PDAC patients.

Supplementary 8. Table S6 The potential target genes of 38 lowly expressed miRNAs with poor survival of PDAC patients.

Supplementary 9. Table S7 The differentially methylated genes in the GSE14245 dataset.

Supplementary 10. Table S8 The differentially expressed genes of GSE14245, GSE27890, GSE32676, GSE41372, GSE62165, GSE62452, and GSE71989.

Supplementary 11. Table S9 The inflammation-associated genes in the GeneCards database.

References

- [1] F. Bray, J. Ferlay, I. Soerjomataram, R. L. Siegel, L. A. Torre, and A. Jemal, "Global cancer statistics 2018: GLOBOCAN estimates of incidence and mortality worldwide for 36 cancers in 185 countries," *CA: a Cancer Journal for Clinicians*, vol. 68, no. 6, pp. 394–424, 2018.
- [2] S. Paternoster and M. Falasca, "The intricate relationship between diabetes, obesity and pancreatic cancer," *Biochimica et Biophysica Acta (BBA) - Reviews on Cancer*, vol. 1873, no. 1, article 188326, 2020.
- [3] A. P. Klein, B. M. Wolpin, H. A. Risch et al., "Genome-wide meta-analysis identifies five new susceptibility loci for pancreatic cancer," *Nature Communications*, vol. 9, no. 1, p. 556, 2018.
- [4] E. S. Christenson, E. Jaffee, and N. S. Azad, "Current and emerging therapies for patients with advanced pancreatic ductal adenocarcinoma: a bright future," *The Lancet Oncology*, vol. 21, no. 3, pp. e135–e145, 2020.
- [5] R. L. Siegel, K. D. Miller, and A. Jemal, "Cancer statistics, 2019," *CA: a Cancer Journal for Clinicians*, vol. 69, no. 1, pp. 7–34, 2018.
- [6] E. Lai, M. Puzzone, P. Ziranu et al., "New therapeutic targets in pancreatic cancer," *Cancer Treatment Reviews*, vol. 81, p. 101926, 2019.
- [7] J. Shi and J. Xue, "Inflammation and development of pancreatic ductal adenocarcinoma," *Chinese Clinical Oncology*, vol. 8, no. 2, p. 19, 2019.
- [8] A. Padoan, M. Plebani, and D. Basso, "Inflammation and pancreatic cancer: focus on metabolism, cytokines, and immunity," *International Journal of Molecular Sciences*, vol. 20, no. 3, p. 676, 2019.
- [9] R. Roshani, F. McCarthy, and T. Hagemann, "Inflammatory cytokines in human pancreatic cancer," *Cancer Letters*, vol. 345, no. 2, pp. 157–163, 2014.
- [10] Y. Y. Yako, D. Kruger, M. Smith, and M. Brand, "Cytokines as biomarkers of pancreatic ductal adenocarcinoma: a systematic review," *PLoS One*, vol. 11, no. 5, article e0154016, 2016.
- [11] N. Singh, S. Rashid, S. Rashid, N. R. Dash, S. Gupta, and A. Saraya, "Clinical significance of promoter methylation status of tumor suppressor genes in circulating DNA of pancreatic cancer patients," *Journal of Cancer Research and Clinical Oncology*, vol. 146, no. 4, pp. 897–907, 2020.
- [12] A. Bararia, S. Dey, S. Gulati et al., "Differential methylation landscape of pancreatic ductal adenocarcinoma and its precancerous lesions," *Hepatobiliary & Pancreatic Diseases International*, vol. 19, no. 3, pp. 205–217, 2020.
- [13] X. Yang, L. Gao, and S. Zhang, "Comparative pan-cancer DNA methylation analysis reveals cancer common and specific patterns," *Briefings in Bioinformatics*, vol. 18, no. 5, pp. 761–773, 2017.
- [14] M. Murata, "Inflammation and cancer," *Environmental Health and Preventive Medicine*, vol. 23, no. 1, p. 50, 2018.
- [15] A. Lukosiute-Urboniene, A. Mazeike, M. Kazokaite et al., "Epigenetic regulation of APAF-1 through DNA methylation in pancreatic cancer," *Anticancer Research*, vol. 40, no. 7, pp. 3765–3779, 2020.
- [16] K. Takahashi, Y. Ota, T. Kogure et al., "Circulating extracellular vesicle-encapsulated HULC is a potential biomarker for human pancreatic cancer," *Cancer Science*, vol. 111, no. 1, pp. 98–111, 2019.
- [17] N. Li, G. Yang, L. Luo et al., "lncRNA THAP9-AS1 promotes pancreatic ductal adenocarcinoma growth and leads to a poor clinical outcome via sponging miR-484 and interacting with YAP," *Clinical Cancer Research*, vol. 26, no. 7, pp. 1736–1748, 2020.
- [18] C. H. Wong, U. K. Lou, Y. Li et al., "CircFOXK2 promotes growth and metastasis of pancreatic ductal adenocarcinoma by complexing with RNA-binding proteins and sponging MiR-942," *Cancer Research*, vol. 80, no. 11, pp. 2138–2149, 2020.
- [19] S. Memczak, M. Jens, A. Elefsinioti et al., "Circular RNAs are a large class of animal RNAs with regulatory potency," *Nature*, vol. 495, no. 7441, pp. 333–338, 2013.
- [20] M. I. Qadir and A. Faheem, "miRNA: a diagnostic and therapeutic tool for pancreatic cancer," *Critical Reviews in Eukaryotic Gene Expression*, vol. 27, no. 3, pp. 197–204, 2017.
- [21] Y. Xu, Y. Yao, P. Gao, and Y. Cui, "Upregulated circular RNA circ_0030235 predicts unfavorable prognosis in pancreatic ductal adenocarcinoma and facilitates cell progression by sponging miR-1253 and miR-1294," *Biochemical and Biophysical Research Communications*, vol. 509, no. 1, pp. 138–142, 2019.
- [22] X. Guo, Q. Zhou, D. Su et al., "Circular RNA circBFAR promotes the progression of pancreatic ductal adenocarcinoma via the miR-34b-5p/MET/Akt axis," *Molecular Cancer*, vol. 19, no. 1, p. 83, 2020.
- [23] D. B. Dudekula, A. C. Panda, I. Grammatikakis, S. De, K. Abdelmohsen, and M. Gorospe, "CircInteractome: a web

- tool for exploring circular RNAs and their interacting proteins and microRNAs,” *RNA Biology*, vol. 13, no. 1, pp. 34–42, 2015.
- [24] A. Grimson, K. K. Farh, W. K. Johnston, P. Garrett-Engele, L. P. Lim, and D. P. Bartel, “MicroRNA targeting specificity in mammals: determinants beyond seed pairing,” *Molecular Cell*, vol. 27, no. 1, pp. 91–105, 2007.
- [25] V. Agarwal, G. W. Bell, J. W. Nam, and D. P. Bartel, “Predicting effective microRNA target sites in mammalian mRNAs,” *eLife*, vol. 4, article e05005, 2015.
- [26] Y. Chen and X. Wang, “miRDB: an online database for prediction of functional microRNA targets,” *Nucleic Acids Research*, vol. 48, no. D1, pp. D127–D131, 2020.
- [27] G. Stelzer, N. Rosen, I. Plaschkes et al., “The GeneCards suite: from gene data mining to disease genome sequence analyses,” *Current Protocols in Bioinformatics*, vol. 54, no. 1, pp. 1.30.1–1.30.33, 2016.
- [28] Y. Zhou, B. Zhou, L. Pache et al., “Metascape provides a biologist-oriented resource for the analysis of systems-level datasets,” *Nature Communications*, vol. 10, no. 1, p. 1523, 2019.
- [29] D. Szklarczyk, A. L. Gable, D. Lyon et al., “STRING v11: protein-protein association networks with increased coverage, supporting functional discovery in genome-wide experimental datasets,” *Nucleic Acids Research*, vol. 47, no. D1, pp. D607–D613, 2019.
- [30] D. S. Chandrashekar, B. Bashel, S. A. H. Balasubramanya et al., “UALCAN: a portal for facilitating tumor subgroup gene expression and survival analyses,” *Neoplasia*, vol. 19, no. 8, pp. 649–658, 2017.
- [31] C. Men, H. Chai, X. Song, Y. Li, H. Du, and Q. Ren, “Identification of DNA methylation associated gene signatures in endometrial cancer via integrated analysis of DNA methylation and gene expression systematically,” *Journal of Gynecologic Oncology*, vol. 28, no. 6, article e83, 2017.
- [32] T. Shinawi, V. K. Hill, D. Krex et al., “DNA methylation profiles of long- and short-term glioblastoma survivors,” *Epigenetics*, vol. 8, no. 2, pp. 149–156, 2014.
- [33] M. Uhlén, L. Fagerberg, B. M. Hallström et al., “Tissue-based map of the human proteome,” *Science*, vol. 347, no. 6220, p. 1260419, 2015.
- [34] Á. Nagy, A. Lánckzy, O. Menyhárt, and B. Györfy, “Validation of miRNA prognostic power in hepatocellular carcinoma using expression data of independent datasets,” *Scientific Reports*, vol. 8, no. 1, p. 9227, 2018.
- [35] K. J. Livak and T. D. Schmittgen, “Analysis of relative gene expression data using real-time quantitative PCR and the 2^{-ΔΔCT} method,” *Methods*, vol. 25, no. 4, pp. 402–408, 2001.
- [36] W. Guo, L. Zhao, G. Wei, P. Liu, Y. Zhang, and L. Fu, “Blocking circ_0013912 suppressed cell growth, migration and invasion of pancreatic ductal adenocarcinoma cells in vitro and in vivo partially through sponging miR-7-5p,” *Cancer Management and Research*, vol. 12, pp. 7291–7303, 2020.
- [37] Y. Chen, Z. Li, M. Zhang et al., “Circ-ASH2L promotes tumor progression by sponging miR-34a to regulate Notch1 in pancreatic ductal adenocarcinoma,” *Journal of Experimental & Clinical Cancer Research*, vol. 38, no. 1, p. 466, 2019.
- [38] X. Zhang, C. Gao, L. Liu et al., “DNA methylation-based diagnostic and prognostic biomarkers of nonsmoking lung adenocarcinoma patients,” *Journal of Cellular Biochemistry*, vol. 120, no. 8, pp. 13520–13530, 2019.
- [39] Y. Kong, Y. Li, Y. Luo et al., “circNFIB1 inhibits lymphangiogenesis and lymphatic metastasis via the miR-486-5p/PIK3R1/VEGF-C axis in pancreatic cancer,” *Molecular Cancer*, vol. 19, no. 1, p. 82, 2020.
- [40] L. Liu, F. B. Liu, M. Huang et al., “Circular RNA ciRS-7 promotes the proliferation and metastasis of pancreatic cancer by regulating miR-7-mediated EGFR/STAT3 signaling pathway,” *Hepatobiliary & Pancreatic Diseases International*, vol. 18, no. 6, pp. 580–586, 2019.
- [41] M. L. Stone and G. L. Beatty, “Cellular determinants and therapeutic implications of inflammation in pancreatic cancer,” *Pharmacology & Therapeutics*, vol. 201, pp. 202–213, 2019.
- [42] J. Okazaki, T. Tanahashi, Y. Sato et al., “MicroRNA-296-5p promotes cell invasion and drug resistance by targeting Bcl2-related ovarian killer, leading to a poor prognosis in pancreatic cancer,” *Digestion*, vol. 101, no. 6, pp. 794–806, 2020.
- [43] B. Aguilar, D. L. Gibbs, D. J. Reiss et al., “A generalizable data-driven multicellular model of pancreatic ductal adenocarcinoma,” *GigaScience*, vol. 9, no. 7, p. gaa075, 2020.
- [44] K. Rateitschak, A. Karger, B. Fitzner, F. Lange, O. Wolkenhauer, and R. Jaster, “Mathematical modelling of interferon-γ signaling in pancreatic stellate cells reflects and predicts the dynamics of STAT1 pathway activity,” *Cellular Signalling*, vol. 22, no. 1, pp. 97–105, 2010.
- [45] D. N. Tong, J. Guan, J. H. Sun et al., “Characterization of B cell-mediated PD-1/PD-L1 interaction in pancreatic cancer patients,” *Clinical and Experimental Pharmacology & Physiology*, vol. 47, no. 8, pp. 1342–1349, 2020.
- [46] N. Radulovich, N. A. Pham, D. Strumpf et al., “Differential roles of cyclin D1 and D3 in pancreatic ductal adenocarcinoma,” *Molecular Cancer*, vol. 9, no. 1, p. 24, 2010.
- [47] Z. M. Chen, Q. Yu, G. Chen et al., “MiR-193a-3p inhibits pancreatic ductal adenocarcinoma cell proliferation by targeting CCND1,” *Cancer Management and Research*, vol. 11, pp. 4825–4837, 2019.
- [48] G. Fan, Y. Tu, C. Chen, H. Sun, C. Wan, and X. Cai, “DNA methylation biomarkers for hepatocellular carcinoma,” *Cancer Cell International*, vol. 18, no. 1, pp. 1–13, 2018.
- [49] N. Shen, J. du, H. Zhou et al., “A diagnostic panel of DNA methylation biomarkers for lung adenocarcinoma,” *Frontiers in Oncology*, vol. 9, p. 1281, 2019.
- [50] Y. Tong, Y. Song, and S. Deng, “Combined analysis and validation for DNA methylation and gene expression profiles associated with prostate cancer,” *Cancer Cell International*, vol. 19, no. 1, p. 50, 2019.
- [51] A. M. Waters and C. J. der, “KRAS: the critical driver and therapeutic target for pancreatic cancer,” *Cold Spring Harbor Perspectives in Medicine*, vol. 8, no. 9, p. a031435, 2018.
- [52] Y. Li, W. Bai, and L. Zhang, “The overexpression of CD80 and ISG15 are associated with the progression and metastasis of breast cancer by a meta-analysis integrating three microarray datasets,” *Pathology Oncology Research*, vol. 26, no. 1, pp. 443–452, 2020.
- [53] F. Bengsch, D. M. Knoblock, A. Liu, F. McAllister, and G. L. Beatty, “CTLA-4/CD80 pathway regulates T cell infiltration into pancreatic cancer,” *Cancer Immunology, Immunotherapy*, vol. 66, no. 12, pp. 1609–1617, 2017.
- [54] D. Das, S. Ghosh, A. Maitra et al., “Epigenomic dysregulation-mediated alterations of key biological pathways and tumor immune evasion are hallmarks of gingivo-buccal oral cancer,” *Clinical Epigenetics*, vol. 11, no. 1, p. 178, 2019.

- [55] C. Huang, N. Li, Z. Li et al., "Tumour-derived interleukin 35 promotes pancreatic ductal adenocarcinoma cell extravasation and metastasis by inducing ICAM1 expression," *Nature Communications*, vol. 8, no. 1, p. 14035, 2017.
- [56] K. Agger, P. A. Cloos, J. Christensen et al., "UTX and JMJD3 are histone H3K27 demethylases involved in *_HOX_* gene regulation and development," *Nature*, vol. 449, no. 7163, pp. 731–734, 2007.
- [57] K. Yamamoto, K. Tateishi, Y. Kudo et al., "Loss of histone demethylase KDM6B enhances aggressiveness of pancreatic cancer through downregulation of *C/EBP α* ," *Carcinogenesis*, vol. 35, no. 11, pp. 2404–2414, 2014.
- [58] W. Su, L. Hong, X. Xu et al., "miR-30 disrupts senescence and promotes cancer by targeting both p16INK4A and DNA damage pathways," *Oncogene*, vol. 37, no. 42, pp. 5618–5632, 2018.
- [59] S. Shukla, U. T. Shankavaram, P. Nguyen, B. A. Stanley, and D. D. K. Smart, "Radiation-induced alteration of the brain proteome: understanding the role of the sirtuin 2 deacetylase in a murine model," *Journal of Proteome Research*, vol. 14, no. 10, pp. 4104–4117, 2015.

Review Article

Associations among Dietary Omega-3 Polyunsaturated Fatty Acids, the Gut Microbiota, and Intestinal Immunity

Yawei Fu ^{1,2}, Yadong Wang ^{1,2}, Hu Gao,² DongHua Li,¹ RuiRui Jiang,¹ Lingrui Ge,³ Chao Tong,¹ and Kang Xu ^{2,4}

¹College of Animal Science and Technology, Henan Agricultural University, Zhengzhou, Henan, China

²Key Laboratory of Agro-ecological Processes in Subtropical Region, Institute of Subtropical Agriculture, Chinese Academy of Sciences, Changsha, Hunan, China

³Hunan Biological and Electromechanical Polytechnic, Changsha, Hunan, China

⁴State Key Laboratory of Developmental Biology of Freshwater Fish, College of Life Sciences, Hunan Normal University, Changsha, Hunan, China

Correspondence should be addressed to Kang Xu; xukang2020@163.com

Received 24 September 2020; Revised 2 December 2020; Accepted 18 December 2020; Published 4 January 2021

Academic Editor: Miaomiao Wu

Copyright © 2021 Yawei Fu et al. This is an open access article distributed under the Creative Commons Attribution License, which permits unrestricted use, distribution, and reproduction in any medium, provided the original work is properly cited.

Omega-3 polyunsaturated fatty acids (omega-3 PUFAs), which are essential fatty acids that humans should obtain from diet, have potential benefits for human health. In addition to altering the structure and function of cell membranes, omega-3 PUFAs (docosahexaenoic acid (DHA), eicosapentaenoic acid (EPA), alpha-linolenic acid (ALA), and docosapentaenoic acid (DPA)) exert different effects on intestinal immune tolerance and gut microbiota maintenance. Firstly, we review the effect of omega-3 PUFAs on gut microbiota. And the effects of omega-3 PUFAs on intestinal immunity and inflammation were described. Furthermore, the important roles of omega-3 PUFAs in maintaining the balance between gut immunity and the gut microbiota were discussed. Additional factors, such as obesity and diseases (NAFLD, gastrointestinal malignancies or cancer, bacterial and viral infections), which are associated with variability in omega-3 PUFA metabolism, can influence omega-3 PUFAs-microbiome-immune system interactions in the intestinal tract and also play roles in regulating gut immunity. This review identifies several pathways by which the microbiota modulates the gut immune system through omega-3 PUFAs. Omega-3 supplementation can be targeted to specific pathways to prevent and alleviate intestinal diseases, which may help researchers identify innovative diagnostic methods.

1. Introduction

Gut microbes play vital roles in maintaining intestinal health [1]. Nutrients exert profound effects on gut microbes and intestinal immunity. Nutrients and intestinal immunity are mediated by gut microbes, and there is a strong correlation between these factors. Omega-3 PUFAs, particularly DHA, are widely used, as they promote the intellectual development of children [2]. As essential fatty acids, dietary omega-3 PUFAs participated in regulating gut immunity and the maintenance of gut homeostasis, which are associated with the gut microbiota, fatty acid metabolism, and intestinal health [3]. In this review, we discuss how omega-3 PUFAs

interact with the gut microbiota, how omega-3 PUFAs modulate gut immunity, and the relationship between gut microbes and intestinal immunity. The factors that alter the interaction among omega-3 PUFAs, gut microbes, and intestinal immunity will be discussed. These discussions might provide new insights into the prevention or treatment of diseases related to disorders of omega-3 PUFA metabolism or intestinal microbes.

2. Omega-3 Polyunsaturated Fatty Acids

Omega-3 PUFAs including EPA, DHA, and ALA are essential fatty acids for animals [4]. DPA is an intermediate

between EPA and DHA. EPA and DHA are mainly derived from marine organisms or deep-sea fish, such as salmon, sardines, and mackerel [5]. Omega-3 PUFAs cannot be synthesized by the human body and must be directly supplied by diet or converted from ingested ALA. Only a small fraction of ALA can be converted to EPA, DPA, or DHA (Figure 1), so dietary supplements or pharmaceutical preparations are essential to provide sufficient unsaturated fatty acids [6]. In addition to being an energy source for body, omega-3 PUFAs play important roles in infant brain development and relieving inflammation [7]. The addition of omega-3 PUFAs to the diet could decrease LDL-cholesterol, prevent myocardial infarction, and reduce the morbidity and mortality of cardiovascular disease [8–10]. Omega-3 PUFAs are widely ingested through food or supplements, which was considered to exert additional beneficial effects throughout the whole body, so the effect of omega-3 PUFAs on gut microbes is a topic worth exploring. The abundance of human gut microbes is positively correlated with the concentration of omega-3 PUFAs in the blood [11]. Currently, omega-3 PUFAs have become one of the hotspots in nutritional biochemistry research and play important roles in regulating gut microbes and gut immunity [12].

3. Omega-3 PUFAs and the Gut Microbiota

Accumulating evidence implicates the correlation between omega-3 PUFAs and gut microbiota. Omega-3 PUFAs can influence the gut microbial community; in turn, gut microbiota can also affect the metabolism and absorption of omega-3 PUFAs. However, the knowledge about the connections between omega-3 PUFAs and gut microbiota is limited. In adults, changes in the gut microbiota were observed after omega-3 PUFA supplementation [3]. Coincidentally, changes in gut microbiota were observed in patients with intestinal inflammation. The connections between omega-3 PUFAs and gut microbiota will be discussed in the following sections.

3.1. Omega-3 PUFAs Could Affect Gut Microbiota. Omega-3 PUFAs affect the gut microbiome in three main ways: (1) modulating the type and abundance of gut microbes; (2) altering the levels of proinflammatory mediators, such as endotoxins (lipopolysaccharides) and IL17; and (3) regulating the levels of short-chain fatty acids or short-chain fatty acid salts.

Omega-3 PUFAs could directly modulate the diversity and abundance of the gut microbiota. Compared with sunflower oil, the dietary intake of fish oil exerted the greatest effect on the diversity of the intestinal flora [13]. High levels of omega-3 PUFAs in fish oil cause significant changes in the gut microbiota, which might explain the health benefits of its use [14]. In addition, fish oil exerts an inhibitory effect on a variety of bacteria. Omega-3 PUFAs could exert beneficial effects on the gut microbiota through decreasing the growth of *Enterobacteria*, increasing the growth of *Bifidobacteria*, and subsequently inhibiting the inflammatory response associated with metabolic endotoxemia [15].

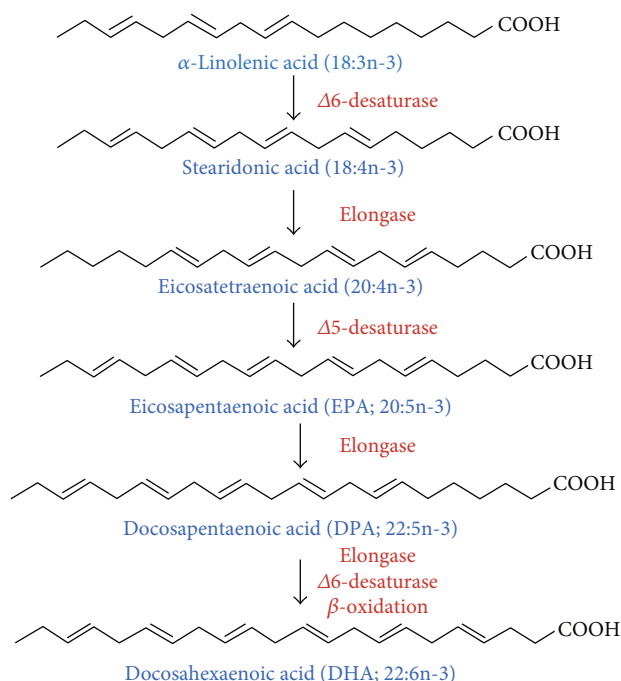


FIGURE 1: Synthetic pathway of omega-3 polyunsaturated fatty acids.

Studies using animal models show the association between fatty acid ingestion and changes in gut microbiota [16]. Omega-3 PUFAs, obtained from the diet, are partially metabolized by anaerobic bacteria, such as *Bifidobacteria* and *Lactobacilli*, in the distal intestine, thus affecting the distribution of the intestinal flora [17]. In addition, omega-3 PUFAs can also increase the number and abundance of beneficial bacteria, such as *Bifidobacterium* [18]. Dietary addition of omega-3 PUFAs increases the abundance and percentage of *Bifidobacteria* in the gut of male Sprague-Dawley rats [19]. EPA and DHA treatment could prevent gut microbiota dysregulation in mice [20] and increase the number of potentially beneficial lactic acid-producing bacteria and *Bifidobacteria* in the gut of the mice fed a high-fat diet [21, 22]. Omega-3 PUFAs alter the abundance of beneficial intestinal bacteria, particularly *Akkermansia*, improve the intestinal microenvironment, increase the intestinal mucosal thickness, improve the barrier function of the intestinal mucosa, and achieve weight loss by controlling the expression of genes related to fat metabolism [23].

Omega-3 PUFAs could directly or indirectly alter the balance of gut microbes, contributing to the occurrence and development of multiple diseases [24]. Omega-3 PUFAs modulate the content of the gut microbiota [25, 26]. Firmicutes and Bacteroidetes are two major bacterial phyla that dominate the human gut microbiota. The Firmicutes-to-Bacteroidetes ratio (F/B ratio) is associated with obesity, non-alcoholic fatty liver disease (NAFLD), and other diseases. An imbalanced intake of omega-3/omega-6 PUFAs may lead to gut microbe dysbiosis, particularly a significant increase of the F/B ratio, which eventually leads to overweight and obesity [27]. Dietary omega-3 PUFAs are able to attenuate the decrease of the F/B ratio observed in high-fat diet-fed mice

[28]. Furthermore, omega-3 PUFAs could improve the condition of patients with IBD by reverting the microbiota to a healthier composition [29]. The increase of the abundance of the *Escherichia*, *Faecalibacterium*, *Streptococcus*, *Sutterella*, and *Veillonella* genera and the decrease of the abundance of the *Bacteroides*, *Flavobacterium*, and *Oscillospira* genera were detected in the IBD group after supplementation with omega-3 PUFAs, presenting the decreased F/B ratio [30]. Furthermore, omega-3 PUFA supplementation may attenuate early life stress-induced perturbations in the gut microbiota [31]. In summary, omega-3 PUFAs directly alter the diversity and abundance of gut microbes, particularly the F/B ratio.

Omega-3 PUFAs also can modulate gut microbes through inhibiting the production of proinflammatory mediators or promoting the production of anti-inflammatory mediators. In some cases, LPS passes through the intestinal wall, particularly when the barrier is destroyed, causing further damage [32]. The increased intestinal permeability will in turn result in the accumulation of toxic bacterial products such as LPS and bacterial DNA in the hepatic portal circulation [33]. Even small amounts of LPS in the systemic circulation, measured in picogram, have the potential to cause an inflammatory response in humans [34].

The consumption of omega-3 PUFAs inhibits the LPS-induced production of proinflammatory cytokines in human blood monocytes [35], relieves intestinal inflammation, and maintains a steady state of gut microbes. Omega-3 PUFAs inhibit all NF- κ B pathways induced by LPS. Incubation of macrophages with omega-3 PUFAs reduces MAPK kinase activity induced by LPS and decreases the expression of proinflammatory mediators, such as TNF- α [36]. Omega-3 PUFAs promote the release of large amounts of anti-inflammatory factors such as IL-10 from resident macrophages, promote the induction of regulatory T cells (Tregs), and prevent the overdevelopment of T helper 17 (Th17) cells [37]. Interleukin 17 (IL-17), a proinflammatory cytokine produced primarily by Th17 cells, causes tissue inflammation. Omega-3 PUFAs may reduce gut inflammation by increasing Treg differentiation and decreasing IL-17 production [38].

Omega-3 PUFAs can also affect gut microbes through increasing the content of SCFAs. Omega-3 PUFAs exert a positive effect through restoring the microbiota composition in individuals with various diseases and increasing the production of anti-inflammatory compounds, such as SCFAs [39]. Butyric acid-producing bacteria play an important role in maintaining human gut health by degrading nonfermentable dietary fibers into SCFAs, such as butyrate [40]. Butyrate is considered an essential energy source for the colonic mucosa that controls gene expression, inflammation, differentiation, and apoptosis in host cells [41]. The addition of omega-3 PUFAs to *Salmonella*-infected mice significantly increased the SCFA content, thereby altering the gut microbiota and favoring host resistance to pathogens [42]. In one case report of the effect of an omega-3 PUFA-rich diet on human intestinal microbiota, a significant increase in several SCFA (butyrate)-producing genera, including *Blautia*, *Bacterioides*, *Roseburia*, and *Coprococcus*, was observed [43].

Increased daily intake of 4g of mixed omega-3 PUFAs (DHA and EPA) significantly increased the density of bacteria that are known to produce butyrate. Butyrate-producing bacteria play a key role in maintaining human gut health by degrading nonfermentable dietary transfer into short-chain fatty acids (SCFAs), such as butyrate [44, 45].

The effect of omega-3 PUFAs on the gut microbiota may be a main contributor to the health benefits of omega-3 PUFAs. Omega-3 PUFAs are mainly absorbed in the gut, where some microorganisms can directly utilize omega-3 PUFAs and produce numerous small molecules. Studies have highlighted the changes in the gut microbiota after omega-3 PUFAs supplementation [22]. Further studies should provide additional insights into the associations among the gut microbiota, omega-3 PUFAs, and intestine health [46].

3.2. Effect of Intestinal Microbes on the Metabolism and Absorption of Omega-3 PUFAs. Omega-3 PUFAs could directly affect the gut microbiota, and correspondingly, the gut microbiota could directly or indirectly modulate the absorption, bioavailability, and biotransformation of omega-3 PUFAs and further influence the imbalance of PUFA intake and its function. Gut microbes produce PUFA-derived metabolites, which may be novel active metabolites [47]. As shown in animal models, microorganisms play an essential role in the biotransformation of PUFAs. Some microbial species, such as *Bacillus proteus* or *Lactobacillus plantarum*, convert the omega-3/omega-6 PUFA precursors ALA and LA into CLA (conjugated linoleic acids) and CALA (conjugated α -linolenic acids), respectively, which are then further hydrogenated to saturated fatty acids (stearic acid, C18:0), thereby reducing PUFA composition [48]. PUFA-derived intermediate metabolites are produced by a wide range of bacteria, including lactic acid-producing bacteria. In addition, the in vitro stimulation and in vivo administration of PUFA-derived bacterial metabolites results in antiobesity and anti-inflammatory effects [49].

The intestinal flora affects host health or nutrition-related diseases through regulating the digestion and absorption of PUFAs [50]. The main source of omega-3 PUFAs is the diet, and some microorganisms in the intestine directly alter the availability of omega-3 PUFAs. *Bifidobacterium* modulates fatty acid metabolism or fatty acid uptake by the intestinal epithelium, but the mechanism underlying the association between *Bifidobacterium* and the absorption of omega-3 PUFAs was not elucidated [51]. Interactively, dietary intake of omega-3 PUFAs may increase the abundance of *Bifidobacterium* in the gut. An increase in the relative abundance of *Bifidobacterium* in the gut via the administration of probiotics or prebiotics also increases the blood omega-3 PUFA levels, which is beneficial to our health, such as preventive and therapeutic effects on cardiovascular diseases and affective disorders.

The effects of gut microbes on the metabolism and absorption of omega-3 PUFAs may be mediated by SCFAs. Omega-3 PUFA supplementation induces a reversible increase in the abundance of several SCFA-producing bacteria, containing *Bifidobacterium*, *Roseburia*, and *Lactobacillus* in the mouse intestinal tract [52]. In mice, high levels of omega-3 PUFAs in tissue are associated with differences in

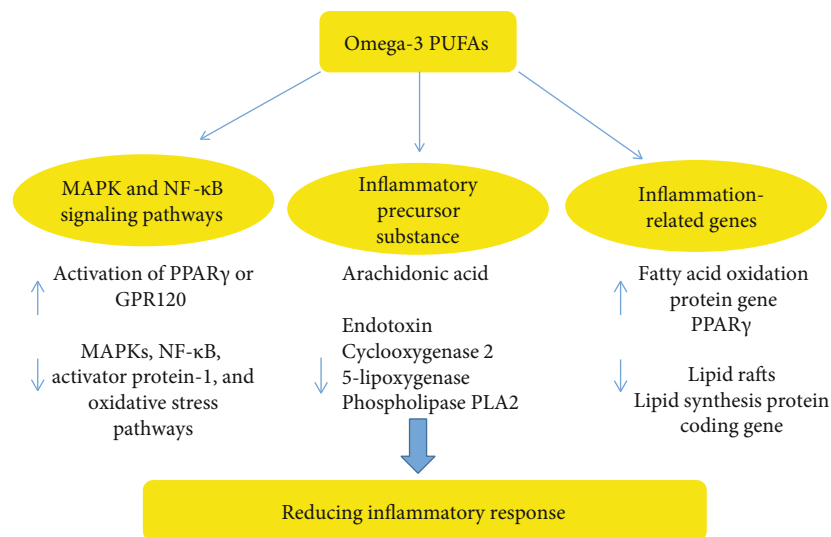


FIGURE 2: Omega-3 PUFAs reduce inflammation through three main pathways.

intestinal microbiota, such as *Bifidobacterium* and *Lactobacillus* [53]. Based on studies, *Bifidobacterium* may be the main genus of bacteria that modulates the utilization of omega-3 PUFAs by microorganisms. Further studies are needed to explore the relationship between *Bifidobacterium* and omega-3 PUFAs.

4. Omega-3 PUFAs and Inflammation

4.1. Omega-3 PUFAs Affect Intestinal Immunity. Omega-3 PUFAs can improve intestinal immunity. Omega-3 PUFAs could reduce intestinal epithelial cell damage caused by LPS, sodium dextran sulfate, or hydrogen peroxide and increase intracellular mitochondrial activity and cell membrane integrity [54]. Stress exposure increases intestinal dysfunction and decreases intestinal immunity. Chronic stress causes a series of anomalies in the intestine, including a decreased fecal water content, increased production of proinflammatory cytokines (TNF- α , IL-1 β , IFN- γ , and IL-6), and aberrant changes in the microbiota composition (particularly *Bifidobacterium*, *Lactobacillus*, and *Roseburia* and *Prevotella* spp.). Omega-3 PUFAs have been shown to effectively counteract these adverse effects [15].

Omega-3 PUFAs modulate intestinal immunity through three main mechanisms. First, omega-3 PUFAs reduce the release of membrane phospholipid arachidonic acid (AA) by reducing the intracellular AA content or by inhibiting phospholipase activity [55]. Second, omega-3 PUFAs inhibit NF- κ B-mediated inflammation or attenuate the phosphorylation of MAPKs, subsequently reducing the transcription of inflammatory molecules [56]. Finally, the intake of omega-3 PUFA modifies the gut microbiome and ameliorates dysbiosis by increasing the abundance of lactic acid-producing bacterial species and reducing the abundance of *Bacillus* species. The ingestion of omega-3 PUFAs inhibits LPS-induced proinflammatory cytokine production in human blood monocytes [57]. Omega-3 PUFAs modulate intestinal immunity in many ways, and the studies described

above have provided some avenues and evidence, but further studies are needed.

4.2. Omega-3 PUFAs on Inflammation. Accumulating evidences revealed omega-3 PUFAs, primarily EPA and DHA, suppress inflammation and exert a beneficial effect on a variety of inflammation-related diseases, such as inflammatory bowel disease, rheumatoid arthritis, asthma, cancer, and cardiovascular diseases [58]. PUFAs suppress immune responses and are used as adjuvant immunosuppressive agents in the clinic to treat inflammatory diseases (rheumatoid arthritis and IBD) or after organ transplantation [59]. Omega-3 PUFAs are known to interfere with the synthesis of proinflammatory eicosanoids [22]. However, PUFA-mediated inhibition of T lymphocyte activation and function has been repeatedly shown to be independent of eicosanoid synthesis.

Omega-3 PUFAs may reduce inflammation through three main pathways: (1) mediating immune cell activation through the MAPK and NF- κ B signaling pathways, (2) reducing the production of precursors that cause inflammation, and (3) altering the mechanism regulating the expression of inflammation-related genes (Figure 2).

Omega-3 PUFAs reduce inflammation by decreasing the activation of proinflammatory MAPK, NF- κ B, activator protein-1, and oxidative stress pathways or through increasing the activation of PPAR γ or GPR120. Given the proinflammatory effects of several MAPKs, particularly extracellular signal-related kinases and c-Jun N-terminal kinase (JNK), the inhibition of specific MAPKs is a prospective mechanism by which omega-3 PUFAs block or reduce intestinal inflammation. Omega-3 PUFAs maintain intestinal health by reducing oxidative stress and NF- κ B-mediated inflammation in immune cells and intestinal cells [60]. Omega-3 PUFAs inhibit NF- κ B signaling by activating peroxisome proliferator-activated receptor (PPAR)- γ [61, 62].

Another possible mechanism is the suppression of inflammation through the activation of GPR120, an omega-3 fatty acid-activated receptor expressed in white adipose

tissue (WAT) and bone marrow-derived dendritic cells and macrophages [63, 64]. For example, in the Sprague-Dawley rat model, supplementation with an equal mixture of EPA and DHA reduced intestinal barrier dysfunction and reversed the decrease in PPAR- γ levels in the intestine due to ischemia and reperfusion injury [15]. Thus, the amount of evidence has confirmed the anti-inflammatory effects of supplementation with long-chain omega-3 PUFAs. Among the components of a healthy diet, the intake of omega-3 fatty acids is associated with reduced inflammation [65].

The consumption of a diet rich in omega-3 PUFAs has been reported to protect intestinal cells from inflammatory damage that leads to IBD and to activate immune cells by reducing the production of proinflammatory eicosanoids. Omega-3 PUFAs may also exert their anti-inflammatory effects through incorporation into the plasma or phospholipid membranes of immune cells or intestinal mucosal tissues in human and rodent models [66]. Furthermore, studies using omega-3 desaturase transgenic mice enriched in endogenous omega-3 PUFAs strongly support the hypothesis that omega-3 PUFAs exert a protective effect on inflammatory pathology [67]. Omega-3 PUFAs serve as alternative substrates for cyclooxygenase (COX) or lipoxygenase (LOX), preventing the conversion of arachidonic acid (AA) to the proinflammatory eicosanoid and reducing the production of inflammatory factors [68]. In summary, omega-3 PUFAs reduce inflammation by incorporating into phospholipid membranes, where they inhibit the production of proinflammatory eicosanoids and reduce the immune cell activation and the release of proinflammatory cytokines [69, 70].

Some of the beneficial effects of PUFAs are attributed to changes in the fatty acid composition of the membrane and subsequent alterations in hormone signaling. Omega-3 PUFAs disrupt lipid rafts and inhibit the activation of the proinflammatory transcription factor NF- κ B, thereby reducing the expression of inflammatory genes and activating the anti-inflammatory transcription factor PPAR γ [71]. The fatty acids themselves exert direct, membrane-independent effects on the molecular events that control gene expression. The regulation of gene expression by dietary fat exerts the greatest effect on the development of insulin resistance and its associated pathophysiology. PUFAs exert their beneficial effects by upregulating the expression of genes involved in fatty acid oxidation while downregulating genes encoding proteins involved in lipid synthesis [72]. PUFAs regulate the expression of oxidative stress-related genes by activating the transcription factor peroxisome proliferator-activated receptor. PUFAs inhibit the expression of lipogenic genes by decreasing the nuclear abundance and DNA-binding affinity of transcription factors responsible for inducing the expression of lipogenic and glycolytic genes to control insulin and carbohydrate levels [73, 74].

Omega-3 PUFAs also alleviate alcoholic steatosis and alcohol-induced liver injury through various mechanisms, including reducing adipose tissue lipogenesis and lipid mobilization, enhancing mitochondrial fatty acid β -oxidation, reducing hepatic inflammation and oxidative stress, and promoting intestinal homeostasis, suggesting that omega-3 PUFAs may be promising treatments in the management of

alcoholic liver disease (ALD) [75]. EPA and DHA maintain the integrity of the intestinal barrier by reducing the permeability-induced increases in the levels of inflammatory cytokines, such as tumor necrosis factor α (TNF α), interferon γ (IFN γ), and IL-4. In addition, dietary omega-3 PUFAs, which affect intestinal integrity, have been shown to reduce clinical colitis and colonic immunopathology by improving epithelial barrier function in animal models [76]. In addition, as mentioned above, several lines of evidence support roles for both the microbiota and omega-3 PUFAs in the regulation of inflammation and the immune system. In particular, omega-3 PUFAs share an important immune system activation/inhibition pathway with gut microbes that modulate the profiles of proinflammatory factors [77].

4.3. The Host Immune-Microbiome Interaction Mediated by Omega-3 PUFAs. PUFAs simultaneously modulate the gut microbiota and immunity. Piglets fed omega-3 PUFA-enriched diets exhibit an increase in systemic and intestinal immunity, as evidenced by increased plasma concentrations of immunoglobulin G, decreased numbers of CD3+CD8+ T lymphocytes, and downregulated expression of intestinal genes (MyD88, NF- κ B, TNF- α , and IL-10). This diet also increased the amount of omega-3 PUFAs in the mucosa and decreased the ratio of omega-6/omega-3 PUFAs. In addition, the omega-3 PUFA-enriched diet decreased the abundance of pathogenic spirochaetes in the colonic digestive tract and increased the abundance of *Actinomycetes*, *Blautia* spp., and *Bifidobacteria* [78]. Omega-3 fatty acids inhibit the growth of gut microbiota associated with obesity and peptic ulcer disease and increase the proliferation of beneficial bacteria. The key to maintaining the steady state is a good ratio of omega-3 to omega-6 PUFAs, the former are anti-inflammatory molecules and the latter are proinflammatory molecules [79]. High saturated fat and omega-6 intake by stud rats induced alterations in the microbiota of their offspring, exacerbating inflammatory responses and conferring increased susceptibility to autoimmune, allergic, and infectious diseases [80]. Omega-3 PUFAs reduce the inflammatory response associated with metabolic endotoxemia, which has been shown to affect the gut microbiota, by promoting the growth of *Bifidobacteria* [51]. In addition, supplementation with omega-3 PUFAs relieves gut microbial dysbiosis caused by early life stress [50]. Based on these results, omega-3 PUFAs potentially alter gut immunity, which may be associated with altering the type and abundance of gut microbiota.

Omega-3 PUFAs also maintain host immunity by maintaining the balance between beneficial and harmful bacteria. A decrease in beneficial bacteria leads to a weakened intestinal resistance to harmful bacteria, resulting in a strong activation of proinflammatory signaling pathways, such as LPS-producing bacteria activate the NF- κ B signaling pathway by binding to TLR-4 on intestinal epithelial cells, which subsequently leads to the secretion of proinflammatory cytokines [81]. Various studies have found that omega-3 PUFAs can reverse gut microbial dysbiosis by increasing probiotic species (including *Lactobacillus* and *Bifidobacterium*) and butyric acid-producing bacteria [52].

Omega-3 PUFAs may modulate immune responses through several potential mechanisms. Primarily, omega-3 PUFAs directly modulate systemic immunity by altering the phospholipid membranes of immune cells, inhibiting omega-6-induced inflammation, downregulating inflammatory transcription factors, or serving as precursors of anti-inflammatory lipid mediators. The intestinal microbiota in the offspring of mice fed high-omega-3 diets was altered, with a moderate increase in the levels of the anti-inflammatory cytokine IL-10 in both the colon and spleen [82]. Increased levels of omega-3 PUFAs alter the phospholipid membrane composition of immune cells, thereby affecting proinflammatory signaling pathways. Alterations in regulatory T cell (Treg) function may be another potential explanation for omega-3 PUFA-mediated changes in host immunity and gut microbes. Omega-3 PUFAs prevent allergic diseases and reduce inflammatory responses by increasing the number of Treg cells. However, our findings from methicillin-resistant *Staphylococcus aureus* (*S. aureus*) skin infections are inconsistent with the findings from human studies suggesting a protective effect of enhanced Treg function on *S. aureus* infection [38]. Finally, current knowledge of how dietary fats alter the microbiome includes the TLR4-dependent induction of local inflammation that leads to alterations in the host environment, shifts in immune cell membrane function, and changes in nutrient availability that favor some organisms over others. Overall, these studies prompted researchers to propose associations among omega-3 PUFAs intake, alterations in the gut microbiome, and the regulation of the immune system, which may prevent associated inflammatory diseases [34].

5. Factors Associated with Omega-3 PUFA-Microbiome-Host Immunity Interactions

Many factors can affect omega-3 PUFA-microbiome-host immunity interactions, containing obesity, cancer, genetic disorders, and metabolic diseases. Omega-3 PUFAs may interfere with the development of obesity by modulating the gut microbiota and influencing the function of white adipose tissue [83]. Supplementation with omega-3 PUFAs can decrease blood lipids, and a meta-analysis included 2,630 showed that ALA significantly decreased triglycerides, LDL-cholesterol, and VLDL-cholesterol [84]. Evidence suggests that omega-3 PUFAs have anticancer activity, modulating cancer development by maintaining cell proliferation signals, inhibiting growth inhibitors and cell death, promoting angiogenesis, and reducing inflammation [85]. In genetic diseases such as epilepsy, although there are studies suggesting that omega-3 PUFAs may be beneficial, but the current research is insufficient to support this conclusion [86, 87].

5.1. Obesity. Obesity is associated with low-grade systemic inflammation. The consumption of a high-fat diet modulates the gut microbiota to substantially increase intestinal permeability, leading to LPS absorption and metabolic endotoxemia that triggers inflammation and metabolic disorders [88]. In particular, a high-fat diet is implicated in enteric dysbacteriosis, including a decrease in the abundance of Bacter-

oidetes, an increase in the abundance of both Firmicutes and Proteobacteria in the murine model, a reduction in the microbiota richness in terms of the number of species per sample, an increase in the abundance of LPS-producing bacteria such as Enterobacteriaceae, and/or a decrease in the abundance LPS-suppressing bacteria (species that decrease the numbers of LPS-producing bacteria, such as *Bifidobacterium*).

Obese patients exhibit impaired intestinal immunity due to a reduced gut microbial diversity, and metabolic pathway alteration leads to the level of DHA and EPA decreased, which can be alleviated by supplementation with omega-3 PUFAs [89]. In addition, obese patients usually present low levels of inflammation, which is often associated with metabolic syndrome. Oral administration of omega-3 PUFAs alleviates inflammation in fat mice, thereby enhancing the function of the immune system [90]. As the role of omega-3 PUFAs in treating obesity, preserving gut microbial diversity, and maintaining gut health, this may provide us a possible new approach to improve obesity by modulating omega-3 PUFAs, gut microbes, and gut health.

5.2. Nonalcoholic Fatty Liver Disease (NAFLD). Increased lipogenesis, hyperlipidemia, and increased fat deposition contribute to NAFLD development. NAFLD is characterized by triacylglycerol accumulation in hepatocytes (steatosis), which may progress to inflammation, fibrosis, and cirrhosis (steatohepatitis). Numerous studies have implicated the gut microbiota in the development of NAFLD (Figure 3), as it specifically mediates the interaction between nutrient intake and gut-liver function. The administration of *Lactobacillus rhamnosus* to NAFLD mice for 8 weeks increases the abundance of beneficial bacteria in the distal small intestine and decreases portal alanine aminotransferase activity, thereby reducing the symptoms of NAFLD [91].

Meanwhile, omega-3 and omega-6 PUFAs (omega-3/omega-6 PUFAs) have been linked to NAFLD [75, 92]. The omega-3/omega-6 balance is important for maintaining human health. In recent years, the percentage of omega-6 PUFAs in Western diets has increased significantly, disrupting this balance and increasing the incidence of various inflammatory diseases, such as obesity, NAFLD, and insulin resistance [93]. Currently, many clinical studies have reported that supplementation with fish oil, seal oil, and purified omega-3 PUFAs can reduce hepatic lipid content in individuals with NAFLD. Hepatic steatosis is alleviated by omega-3 PUFAs in individuals with NAFLD. In patients with NAFLD, administration of high concentrations of omega-3 significantly increased the omega-3 index and absolute values of EPA and DHA in red blood cells (RBC) and reduced the RBC omega-6/omega-3 fatty acid ratio ($P < 0.0001$) [94]. In rats fed a high-fat diet, combined omega-3 PUFA supplementation protected the animals from the development of severe NAFLD [95].

5.3. Gastrointestinal Malignancies or Cancer. Omega-3 PUFAs are important lipids that participate in many pathological processes related to tumor occurrence and development by relieving inflammation [4]. Omega-3 PUFAs may

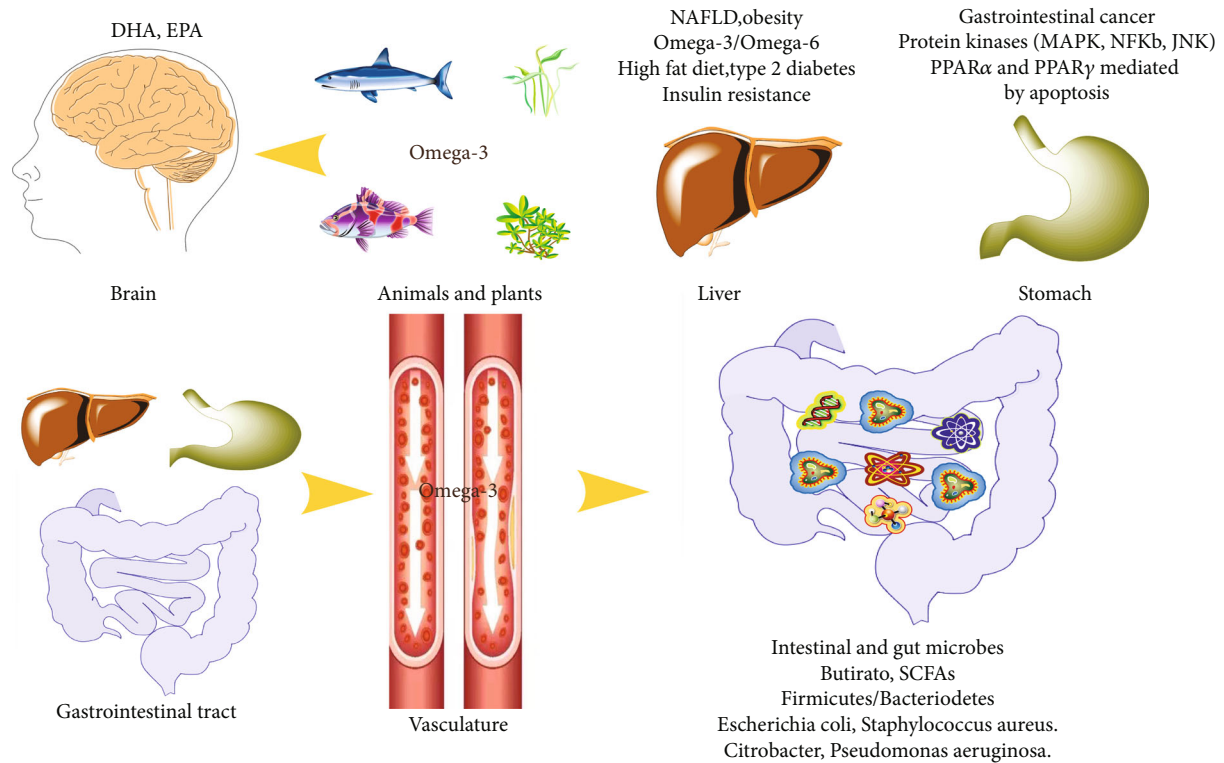


FIGURE 3: Factors associated with omega-3 PUFAs-microbiome-host immunity interactions.

protect against cancers, including colorectal, breast, and prostate cancer (Figure 3). A study of 68,109 Washington residents found that omega-3 PUFAs reduced the risk of colon cancer in men, but had no significant effect on women or on rectal cancer [96]. Another meta-analysis showed an inverse relationship between EPA and DHA levels and colorectal cancer [97]. However, the relationship between omega-3 PUFA intake and colorectal cancer remains controversial, as a meta-analysis of 8,875 patients showed that omega-3 PUFAs tended to reduce the risk of cancer in the proximal colon but increased the risk of distal colon cancer [98]. Studies using a mouse model have shown that EPA supplementation decreases the number and size of tumors and increases body weight, changes that are associated with inhibition of COX-2 and reduced β -catenin nuclear translocation [99]. While omega-3 PUFAs inhibit tumor growth and relieve inflammation, they do not prevent the damage caused by cancer.

One possible explanation is that the modulation of the intestinal microbiota may contribute to the cancer-preventative properties of omega-3 PUFAs. Free feeding of EPA on mice with colon cancer increased the abundance of lactic acid-producing bacterial species in the gut [100]. Patients with colorectal cancer exhibit significant intestinal dysbiosis, including reduced microbial diversity and richness and impaired intestinal immunity [101]. In patients with severe cases, symptoms such as diarrhea, intestinal bleeding, and localized ulceration may occur, weakening the immune system. Colorectal cancer significantly decreases immunity and gut microbial diversity, and although omega-3 PUFAs reduce inflammation, the effect is not significant.

5.4. Bacterial and Viral Infections. Omega-3 PUFAs may play a key role in the host defense against infections by limiting excess inflammation and enhancing the immune response [35], but bacterial and viral infections compromise the effectiveness of omega-3 PUFAs. Omega-3 PUFA-enriched diets promote the colonization of beneficial bacteria and protect against the growth of pathogenic bacteria [62], thereby maintaining gut microbes in a healthy physiological environment and enhancing gut immunity. *Staphylococcus aureus* produces enterotoxins in the human intestinal tract that wreak havoc on the human gut, causing symptoms such as vomiting and diarrhea [102]. Omega-3 PUFAs inhibit *Staphylococcus aureus*, and DHA and EPA have been used clinically as topical agents to treat skin lesions caused by *Staphylococcus aureus* [102]. *Citrobacter* is a bacterium present in the intestinal tract of mice that promotes the proliferation of other pathogenic bacteria in the intestinal tract and causes gastrointestinal disease. An experiment conducted using mice with colitis showed that the administration of omega-3 PUFA-rich diet for 3 weeks altered the phospholipid composition of the intestinal cell membrane, reduced local inflammation, and reduced the production of proinflammatory cytokines and chemokines, thereby reducing colonic damage [103]. The consumption of omega-3 PUFA-rich foods for 5 weeks affected the intestinal microbiota, reducing the amount of *Clostridium perfringens* (a bacterium associated with IBD) and increasing the amount of *Lactobacillus* spp. and *Bifidobacterium* spp. with anti-inflammatory properties [104, 105]. The intake of 500 mg/d omega-3 PUFAs by adults reduced infections caused by *Escherichia coli*, *Staphylococcus aureus*, *Pseudomonas aeruginosa*, and *Streptococcus*

pneumoniae and reduced the incidence of pneumococcal infections in the elderly [35]. The species and functions of gut microbes are complex, and a large number of microbes that are potentially influenced by omega-3 PUFAs will be gradually identified.

6. Summary and Perspectives

We reviewed the interactions among PUFAs, gut microbes, and host immunity. Based on accumulating evidence, omega-3 PUFAs (DHA, EPA, and ALA) exert profound effects on the intestinal microbiota, the host-microbiome interaction, and interactions between the host immune system and gut microbiota. Accordingly, the gut microbiota modulates the absorption and metabolism of omega-3 PUFAs and directly or indirectly modulates subsequent physiological and immune responses in the host. In previous studies, researchers focused on the trends in the host digestion and absorption of omega-3 PUFAs, while the effects of gut microbes on omega-3 PUFAs have often been neglected. Therefore, further comprehensive studies about the effects of omega-3 PUFAs on gut microbes and gut immunity will be meaningful. Likewise, we also must determine which gut microbes, which type of omega-3 PUFAs, or which pathways affect gut microbial homeostasis and host immunity.

Factors such as obesity and diseases are associated with host gut microbes, gut immunity, and omega-3 PUFAs. Omega-3 PUFAs modulate gut immunity by acting on gut microbes. In addition, omega-3 PUFAs are a feasible approach to maintain gut health. However, the composition of the gut microbes is complex, and simply using one substance will not be an effective method to solve these problems; individualized treatments for patients should be developed.

Conflicts of Interest

The authors declared that there are no conflicts of interest.

Authors' Contributions

Yawei Fu and Yadong Wang contributed equally to this work.

Acknowledgments

This work was supported by the Special Funds for the Construction of Innovative Provinces in Hunan (2020JJ5635, 2019RS1068, 2019NK2193, and 2020WK2030), the State Key Laboratory of Developmental Biology of Freshwater Fish, the National Natural Science Foundation of China (31601953), and Open Fund of Key Laboratory of Agroecological Processes in Subtropical Region, Chinese Academy of Sciences (ISA2019304).

References

- [1] C. L. Gentile and T. L. Weir, "The gut microbiota at the intersection of diet and human health," *Science*, vol. 362, no. 6416, pp. 776–780, 2018.
- [2] M. Healy-Stoffel and B. Levant, "N-3 (omega-3) fatty acids: effects on brain dopamine systems and potential role in the etiology and treatment of neuropsychiatric disorders," *CNS & Neurological Disorders Drug Targets*, vol. 17, no. 3, pp. 216–232, 2018.
- [3] L. Costantini, R. Molinari, B. Farinon, and N. Merendino, "Impact of omega-3 fatty acids on the gut microbiota," *International Journal of Molecular Sciences*, vol. 18, no. 12, p. 2645, 2017.
- [4] D. Swanson, R. Block, and S. A. Mousa, "Omega-3 fatty acids EPA and DHA: health benefits throughout life," *Advances in Nutrition*, vol. 3, no. 1, pp. 1–7, 2012.
- [5] I. de Bus, R. Witkamp, H. Zuillhof, B. Albada, and M. Balvers, "The role of n-3 PUFA-derived fatty acid derivatives and their oxygenated metabolites in the modulation of inflammation," *Prostaglandins & Other Lipid Mediators*, vol. 144, p. 106351, 2019.
- [6] P. Yang, Y. Jiang, and S. M. Fischer, "Prostaglandin E₃ metabolism and cancer," *Cancer Letters*, vol. 348, no. 1–2, pp. 1–11, 2014.
- [7] H. Chappus-McCendie, L. Chevalier, C. Roberge, and M. Plourde, "Omega-3 PUFA metabolism and brain modifications during aging," *Progress in Neuro-Psychopharmacology & Biological Psychiatry*, vol. 94, p. 109662, 2019.
- [8] J. E. Manson, N. R. Cook, I. M. Lee et al., "Marine n-3 fatty acids and prevention of cardiovascular disease and cancer," *The New England Journal of Medicine*, vol. 380, no. 1, pp. 23–32, 2019.
- [9] E. C. Rizos, G. Markozannes, A. Tsapas, C. S. Mantzoros, and E. E. Ntzani, "Omega-3 supplementation and cardiovascular disease: formulation-based systematic review and meta-analysis with trial sequential analysis," *Heart*, p. heartjnl-2020-316780, 2020.
- [10] T. A. Jacobson, M. K. Ito, K. C. Maki et al., "National lipid association recommendations for patient-centered management of dyslipidemia: part 1—full report," *Journal of Clinical Lipidology*, vol. 9, no. 2, pp. 129–169, 2015.
- [11] A. Horigome, R. Okubo, K. Hamazaki et al., "Association between blood omega-3 polyunsaturated fatty acids and the gut microbiota among breast cancer survivors," *Beneficial Microbes*, vol. 10, no. 7, pp. 751–758, 2019.
- [12] P. C. Calder, "Omega-3 fatty acids and inflammatory processes: from molecules to man," *Biochemical Society Transactions*, vol. 45, no. 5, pp. 1105–1115, 2017.
- [13] M. P. A. Wijekoon, C. C. Parrish, and A. Mansour, "Reprint of "Effect of dietary substitution of fish oil with flaxseed or sunflower oil on muscle fatty acid composition in juvenile steelhead trout (*Oncorhynchus mykiss*) reared at varying temperatures,"" *Aquaculture*, vol. 447, pp. 108–115, 2015.
- [14] C. Quin, D. M. Vollman, S. Ghosh et al., "Fish oil supplementation reduces maternal defensive inflammation and predicts a gut bacteriome with reduced immune priming capacity in infants," *The ISME Journal*, vol. 14, no. 8, pp. 2090–2104, 2020.
- [15] W. Cao, C. Wang, Y. Chin et al., "DHA-phospholipids (DHA-PL) and EPA-phospholipids (EPA-PL) prevent intestinal dysfunction induced by chronic stress," *Food & Function*, vol. 10, no. 1, pp. 277–288, 2019.
- [16] C. Druart, A. M. Neyrinck, B. Vlaeminck, V. Fievez, P. D. Cani, and N. M. Delzenne, "Role of the lower and upper




- intestine in the production and absorption of gut microbiota-derived PUFA metabolites," *PLoS One*, vol. 9, no. 1, article e87560, 2014.
- [17] C. Lauridsen, "Effects of dietary fatty acids on gut health and function of pigs pre- and post-weaning," *Journal of Animal Science*, vol. 98, no. 4, 2020.
- [18] K. Kaliannan, B. Wang, X. Y. Li, K. J. Kim, and J. X. Kang, "A host-microbiome interaction mediates the opposing effects of omega-6 and omega-3 fatty acids on metabolic endotoxemia," *Scientific Reports*, vol. 5, no. 1, article 11276, 2015.
- [19] C. M. Guinane and P. D. Cotter, "Role of the gut microbiota in health and chronic gastrointestinal disease: understanding a hidden metabolic organ," *Therapeutic Advances in Gastroenterology*, vol. 6, no. 4, pp. 295–308, 2013.
- [20] R. Feng, L. J. Ma, M. Wang et al., "Oxidation of fish oil exacerbates alcoholic liver disease by enhancing intestinal dysbiosis in mice," *Communications Biology*, vol. 3, no. 1, p. 481, 2020.
- [21] J. R. Mujico, G. C. Bacchan, A. Gheorghie, L. E. Diaz, and A. Marcos, "Changes in gut microbiota due to supplemented fatty acids in diet-induced obese mice," *The British Journal of Nutrition*, vol. 110, no. 4, pp. 711–720, 2013.
- [22] R. C. Robertson, C. Seira Oriach, K. Murphy et al., "Omega-3 polyunsaturated fatty acids critically regulate behaviour and gut microbiota development in adolescence and adulthood," *Brain, Behavior, and Immunity*, vol. 59, pp. 21–37, 2017.
- [23] D. R. Warner, J. B. Warner, J. E. Hardesty et al., "Decreased ω -6: ω -3 PUFA ratio attenuates ethanol-induced alterations in intestinal homeostasis, microbiota, and liver injury," *Journal of Lipid Research*, vol. 60, no. 12, pp. 2034–2049, 2019.
- [24] G. Wang, S. Huang, Y. Wang et al., "Bridging intestinal immunity and gut microbiota by metabolites," *Cellular and Molecular Life Sciences*, vol. 76, no. 20, pp. 3917–3937, 2019.
- [25] H. N. Yu, J. Zhu, W. S. Pan, S. R. Shen, W. G. Shan, and U. N. Das, "Effects of fish oil with a high content of n-3 polyunsaturated fatty acids on mouse gut microbiota," *Archives of Medical Research*, vol. 45, no. 3, pp. 195–202, 2014.
- [26] Z. J. Cao, J. C. Yu, W. M. Kang, Z. Q. Ma, X. Ye, and S. B. Tian, "Effect of n-3 polyunsaturated fatty acids on gut microbiota and endotoxin levels in portal vein of rats fed with high-fat diet," *Zhongguo Yi Xue Ke Xue Yuan Yuan Bao Acta Academiae Medicinae Sinicae*, vol. 36, no. 5, pp. 496–500, 2014.
- [27] H.-Q. Liu, Y. Qiu, Y. Mu et al., "A high ratio of dietary n-3/n-6 polyunsaturated fatty acids improves obesity-linked inflammation and insulin resistance through suppressing activation of TLR4 in SD rats," *Nutrition Research*, vol. 33, no. 10, pp. 849–858, 2013.
- [28] J. C. Onishi, S. Campbell, M. Moreau et al., "Bacterial communities in the small intestine respond differently to those in the caecum and colon in mice fed low- and high-fat diets," *Microbiology*, vol. 163, no. 8, pp. 1189–1197, 2017.
- [29] A. Belluzzi, "Polyunsaturated fatty acids (n-3 PUFAs) and inflammatory bowel disease (IBD): pathogenesis and treatment," *European Review for Medical & Pharmacological Ence*, vol. 8, no. 5, p. 225, 2004.
- [30] M. L. Santoru, C. Piras, A. Murgia et al., "Cross sectional evaluation of the gut-microbiome metabolome axis in an Italian cohort of IBD patients," *Scientific Reports*, vol. 7, no. 1, p. 9523, 2017.
- [31] S. Egerton, F. Donoso, P. Fitzgerald et al., "Investigating the potential of fish oil as a nutraceutical in an animal model of early life stress," *Nutritional Neuroscience*, pp. 1–23, 2020.
- [32] M. Schoeler and R. Caesar, "Dietary lipids, gut microbiota and lipid metabolism," *Reviews in Endocrine & Metabolic Disorders*, vol. 20, no. 4, pp. 461–472, 2019.
- [33] A. Hutchinson, L. Tingö, and R. J. N. Brummer, "The potential effects of probiotics and ω -3 fatty acids on chronic low-grade inflammation," *Nutrients*, vol. 12, no. 8, p. 2402, 2020.
- [34] C. Parolini, "Effects of fish n-3 PUFAs on intestinal microbiota and immune system," *Marine Drugs*, vol. 17, no. 6, p. 374, 2019.
- [35] M. O. Husson, D. Ley, C. Portal et al., "Modulation of host defence against bacterial and viral infections by omega-3 polyunsaturated fatty acids," *The Journal of Infection*, vol. 73, no. 6, pp. 523–535, 2016.
- [36] T. A. Babcock, A. Kurland, W. S. Helton, A. Rahman, K. N. Anwar, and N. J. Espat, "Inhibition of activator protein-1 transcription factor activation by omega-3 fatty acid modulation of mitogen-activated protein kinase signaling kinases," *Journal of Parenteral and Enteral Nutrition*, vol. 27, no. 3, pp. 176–180, 2016.
- [37] M. Zeyda, G. Staffler, V. Hořejší, W. Waldhäusl, and T. M. Stulnig, "LAT displacement from lipid rafts as a molecular mechanism for the inhibition of T cell signaling by polyunsaturated fatty acids," *The Journal of Biological Chemistry*, vol. 277, no. 32, pp. 28418–28423, 2002.
- [38] J. Kim, K. Lim, K. H. Kim, J. H. Kim, J. S. Choi, and S. C. Shim, "N-3 polyunsaturated fatty acids restore Th17 and Treg balance in collagen antibody-induced arthritis," *PLOS ONE*, vol. 13, no. 3, article e0194331, 2018.
- [39] A. Awoyemi, M. Trøseid, H. Arnesen, S. Solheim, and I. Seljelot, "Effects of dietary intervention and n-3 PUFA supplementation on markers of gut-related inflammation and their association with cardiovascular events in a high-risk population," *Atherosclerosis*, vol. 286, pp. 53–59, 2019.
- [40] S. Fang, X. Chen, X. Ye, L. Zhou, S. Xue, and Q. Gan, "Effects of gut microbiome and short-chain fatty acids (SCFAs) on finishing weight of meat rabbits," *Frontiers in Microbiology*, vol. 11, p. 1835, 2020.
- [41] S. J. O'Keefe, "Diet, microorganisms and their metabolites, and colon cancer," *Nature Reviews Gastroenterology & Hepatology*, vol. 13, no. 12, pp. 691–706, 2016.
- [42] D. J. Machate, P. S. Figueiredo, G. Marcelino et al., "Fatty acid diets: regulation of gut microbiota composition and obesity and its related metabolic dysbiosis," *International Journal of Molecular Sciences*, vol. 21, no. 11, p. 4093, 2020.
- [43] J. Ochoa-Repáraz and L. H. Kasper, "The second brain: is the gut microbiota a link between obesity and central nervous system disorders?," *Current Obesity Reports*, vol. 5, no. 1, pp. 51–64, 2016.
- [44] J. Hofmanová, A. Vaculová, Z. Koubková, M. Hýžd'alová, and A. Kozubík, "Human fetal colon cells and colon cancer cells respond differently to butyrate and PUFAs," *Molecular Nutrition & Food Research*, vol. 53, no. S1, pp. S102–S113, 2009.
- [45] J. Chen, Q. Xu, Y. Li et al., "Comparative effects of dietary supplementations with sodium butyrate, medium-chain fatty acids, and n-3 polyunsaturated fatty acids in late pregnancy and lactation on the reproductive performance of sows and growth performance of suckling piglets," *Journal of Animal Ence*, vol. 97, no. 10, pp. 4256–4267, 2019.

- [46] V. H. Telle-Hansen, K. B. Holven, and S. M. Ulven, "Impact of a healthy dietary pattern on gut microbiota and systemic inflammation in humans," *Nutrients*, vol. 10, no. 11, p. 1783, 2018.
- [47] C. Druart, L. B. Bindels, R. Schmaltz et al., "Ability of the gut microbiota to produce PUFA-derived bacterial metabolites: proof of concept in germ-free versus conventionalized mice," *Molecular Nutrition & Food Research*, vol. 59, no. 8, pp. 1603–1613, 2015.
- [48] H. Blanchard, F. Pédrone, N. Boulrier-Monthéan, D. Catheline, V. Rioux, and P. Legrand, "Comparative effects of well-balanced diets enriched in α -linolenic or linoleic acids on LC-PUFA metabolism in rat tissues," *Prostaglandins, Leukotrienes and Essential Fatty Acids*, vol. 88, no. 5, pp. 383–389, 2013.
- [49] P. C. Calder, "Mechanisms of action of (n-3) fatty acids," *The Journal of Nutrition*, vol. 142, no. 3, pp. 592s–599s, 2012.
- [50] M. M. Pusceddu, S. el Aidy, F. Crispie et al., "N-3 polyunsaturated fatty acids (PUFAs) reverse the impact of early-life stress on the gut microbiota," *Plos One*, vol. 10, no. 10, p. e0139721, 2015.
- [51] R. Wall, R. P. Ross, F. Shanahan et al., "Impact of administered bifidobacterium on murine host fatty acid composition," *Lipids*, vol. 45, no. 5, pp. 429–436, 2010.
- [52] H. Watson, S. Mitra, F. C. Croden et al., "A randomised trial of the effect of omega-3 polyunsaturated fatty acid supplements on the human intestinal microbiota," *Gut*, vol. 67, no. 11, pp. 1974–1983, 2018.
- [53] A. Kumar, S. S. Mastana, and M. R. Lindley, "n-3 Fatty acids and asthma," *Nutrition Research Reviews*, vol. 29, no. 1, pp. 1–16, 2016.
- [54] T. Sundaram, C. Giromini, R. Rebutti, and A. Baldi, "Omega-3 polyunsaturated fatty acids counteract inflammatory and oxidative damage of non-transformed porcine enterocytes," *Animals*, vol. 10, no. 6, p. 956, 2020.
- [55] A. Denys, A. Hichami, and N. A. Khan, "N-3 PUFAs modulate T-cell activation via protein kinase C- α and - ϵ and the NF- κ B signaling pathway," *Journal of Lipid Research*, vol. 46, no. 4, pp. 752–758, 2005.
- [56] Y. Adkins and D. S. Kelley, "Mechanisms underlying the cardioprotective effects of omega-3 polyunsaturated fatty acids," *The Journal of Nutritional Biochemistry*, vol. 21, no. 9, pp. 781–792, 2010.
- [57] B. Michaeli, M. M. Berger, L. Tappy, J. P. Revely, M. C. Cayeux, and R. Chiolo'ro, "Effects of N-3 pufas on metabolic, inflammatory and systemic responses to single LPS-injection in healthy volunteers," *Clinical Nutrition*, vol. 22, pp. S17–S17, 2003.
- [58] J. Liu, X. Li, J. Hou, J. Sun, N. Guo, and Z. Wang, "Dietary intake of N-3 and N-6 polyunsaturated fatty acids and risk of cancer: meta-analysis of data from 32 studies," *Nutrition and Cancer*, no. 8, pp. 1–13, 2020.
- [59] R. Marion-Letellier, G. Savoye, and S. Ghosh, "Polyunsaturated fatty acids and inflammation," *IUBMB Life*, vol. 67, no. 9, pp. 659–667, 2015.
- [60] L. U. Yuan-Yuan, K. S. Yan, C. N. Fan et al., "Effect of Dietary N-3 Polyunsaturated Fatty Acids on the Gut Microbiota in Diet-Induced Obese Mice," *Chinese Journal of Child Health Care*, vol. 22, no. 11, pp. 1157–1160, 2014.
- [61] S. Gutiérrez, S. L. Svahn, and M. E. Johansson, "Effects of omega-3 fatty acids on immune cells," *International Journal of Molecular Sciences*, vol. 20, no. 20, p. 5028, 2019.
- [62] O. Kuda, M. Rossmeisl, and J. Kopecky, "Omega-3 fatty acids and adipose tissue biology," *Molecular Aspects of Medicine*, vol. 64, pp. 147–160, 2018.
- [63] D. S. Im, "Functions of omega-3 fatty acids and FFA4 (GPR120) in macrophages," *European Journal of Pharmacology*, vol. 785, pp. 36–43, 2016.
- [64] P. Liang, S. M. Henning, J. Guan et al., "Role of host GPR120 in mediating dietary omega-3 fatty acid inhibition of prostate cancer," *Journal of the National Cancer Institute*, vol. 111, no. 1, pp. 52–59, 2019.
- [65] P. C. Calder, N. Ahluwalia, F. Brouns et al., "Dietary factors and low-grade inflammation in relation to overweight and obesity," *The British Journal of Nutrition*, vol. 106, Suppl 3, pp. S5–78, 2011.
- [66] P. C. Calder, "n-3 polyunsaturated fatty acids, inflammation, and inflammatory diseases," *American Journal of Clinical Nutrition*, vol. 83, no. 6, pp. 1505s–1519s, 2006.
- [67] Q. Jia, J. R. Lupton, R. Smith et al., "Reduced colitis-associated colon cancer in Fat-1 (n-3 fatty acid desaturase) transgenic mice," *Cancer Research*, vol. 68, no. 10, pp. 3985–3991, 2008.
- [68] M. Igarashi, F. Gao, H. W. Kim, K. Ma, J. M. Bell, and S. I. Rapoport, "Dietary n-6 PUFA deprivation for 15 weeks reduces arachidonic acid concentrations while increasing n-3 PUFA concentrations in organs of post-weaning male rats," *Biochimica et Biophysica Acta (BBA) - Molecular and Cell Biology of Lipids*, vol. 1791, no. 2, pp. 132–139, 2009.
- [69] Y. Williams-Bey, C. Boularan, A. Vural et al., "Omega-3 free fatty acids suppress macrophage inflammasome activation by inhibiting NF- κ B activation and enhancing autophagy," *PLoS One*, vol. 9, no. 6, article e97957, 2014.
- [70] D. Y. Oh, S. Talukdar, E. J. Bae et al., "GPR120 is an omega-3 fatty acid receptor mediating potent anti-inflammatory and insulin-sensitizing effects," *Cell*, vol. 142, no. 5, pp. 687–698, 2010.
- [71] P. C. Calder, "Marine omega-3 fatty acids and inflammatory processes: effects, mechanisms and clinical relevance," *Biochimica et Biophysica Acta*, vol. 1851, no. 4, pp. 469–484, 2015.
- [72] L. Hou, K. Lian, M. Yao et al., "Reduction of n-3 PUFAs, specifically DHA and EPA, and enhancement of peroxisomal beta-oxidation in type 2 diabetic rat heart," *Cardiovascular Diabetology*, vol. 11, no. 1, p. 126, 2012.
- [73] K. M. Appleton, H. M. Sallis, R. Perry, A. R. Ness, R. Churchill, and Cochrane Common Mental Disorders Group, "Omega-3 fatty acids for depression in adults," *Cochrane Database of Systematic Reviews*, vol. 2015, no. 11, article Cd004692, 2015.
- [74] V. Ciappolino, G. Delvecchio, C. Agostoni, A. Mazzocchi, A. C. Altamura, and P. Brambilla, "The role of n-3 polyunsaturated fatty acids (n-3PUFAs) in affective disorders," *Journal of Affective Disorders*, vol. 224, pp. 32–47, 2017.
- [75] M. Wang, L. J. Ma, Y. Yang, Z. Xiao, and J. B. Wan, "n-3 Polyunsaturated fatty acids for the management of alcoholic liver disease: a critical review," *Critical Reviews in Food Science and Nutrition*, vol. 59, no. sup1, pp. S116–S129, 2019.
- [76] C. M. Yates, P. C. Calder, and G. Ed Rainger, "Pharmacology and therapeutics of omega-3 polyunsaturated fatty acids in chronic inflammatory disease," *Pharmacology & Therapeutics*, vol. 141, no. 3, pp. 272–282, 2014.
- [77] C. Madore, A. Nadjar, J. C. Delpech et al., "Nutritional n-3 PUFAs deficiency during perinatal periods alters brain innate

- immune system and neuronal plasticity-associated genes,” *Brain, Behavior, and Immunity*, vol. 41, pp. 22–31, 2014.
- [78] T. Wang, L. Sha, Y. Li et al., “Dietary α -Linolenic acid-rich flaxseed oil exerts beneficial effects on polycystic ovary syndrome through sex steroid hormones—microbiota—inflammation axis in rats,” *Frontiers in Endocrinology*, vol. 11, p. 284, 2020.
- [79] M. Li, H. Ouyang, H. Yuan et al., “Site-specific Fat-1 knock-in enables significant decrease of n-6PUFAs/n-3PUFAs ratio in pigs,” *G3*, vol. 8, no. 5, pp. 1747–1754, 2018.
- [80] K. L. Fritsche, “The science of fatty acids and inflammation,” *Advances in Nutrition*, vol. 6, no. 3, pp. 293s–301s, 2015.
- [81] Y. Zhang, B. Zhang, L. Dong, and P. Chang, “Potential of omega-3 polyunsaturated fatty acids in managing chemotherapy- or radiotherapy-related intestinal microbial dysbiosis,” *Advances in Nutrition*, vol. 10, no. 1, pp. 133–147, 2019.
- [82] R. C. Robertson, K. Kaliannan, C. R. Strain, R. P. Ross, C. Stanton, and J. X. Kang, “Maternal omega-3 fatty acids regulate offspring obesity through persistent modulation of gut microbiota,” *Microbiome*, vol. 6, no. 1, p. 95, 2018.
- [83] N. S. Kalupahana, B. L. Goonapienuwala, and N. Moustaid-Moussa, “Omega-3 fatty acids and adipose tissue: inflammation and browning,” *Annual Review of Nutrition*, vol. 40, no. 1, pp. 25–49, 2020.
- [84] H. Yue, B. Qiu, M. Jia et al., “Effects of α -linolenic acid intake on blood lipid profiles: a systematic review and meta-analysis of randomized controlled trials,” *Critical Reviews in Food Science and Nutrition*, pp. 1–17, 2020.
- [85] K. Jing, T. Wu, and K. Lim, “Omega-3 polyunsaturated fatty acids and cancer,” *Anti-Cancer Agents in Medicinal Chemistry*, vol. 13, no. 8, pp. 1162–1177, 2013.
- [86] M. Pourmasoumi, N. Vosoughi, S. M. Derakhshandeh-Rishehri, M. Assaroudi, and M. Heidari-Beni, “Association of omega-3 fatty acid and epileptic seizure in epileptic patients: a systematic review,” *International Journal of Preventive Medicine*, vol. 9, p. 36, 2018.
- [87] C. M. DeGiorgio and A. Y. Taha, “Omega-3 fatty acids (ω -3 fatty acids) in epilepsy: animal models and human clinical trials,” *Expert Review of Neurotherapeutics*, vol. 16, no. 10, pp. 1141–1145, 2016.
- [88] J. Bellenger, S. Bellenger, Q. Escoula, C. Bidu, and M. Narce, “N-3 polyunsaturated fatty acids: an innovative strategy against obesity and related metabolic disorders, intestinal alteration and gut microbiota dysbiosis,” *Biochimie*, vol. 159, pp. 66–71, 2019.
- [89] H. Tilg, “Obesity, Metabolic Syndrome, and Microbiota: Multiple Interactions,” *Journal of Clinical Gastroenterology*, vol. 44, no. 1, pp. S16–S18, 2010.
- [90] J. C. Delpuch, A. Thomazeau, C. Madore et al., “Dietary n-3 PUFAs Deficiency Increases Vulnerability to Inflammation-Induced Spatial Memory Impairment,” *Neuropsychopharmacology*, vol. 40, no. 12, pp. 2774–2787, 2015.
- [91] Y. Ritze, G. Bárdos, A. Claus et al., “Lactobacillus rhamnosus GG protects against non-alcoholic fatty liver disease in mice,” *PLoS One*, vol. 9, no. 1, article e80169, 2014.
- [92] D. Vauzour, I. Rodriguez-Ramiro, S. Rushbrook et al., “n-3 Fatty acids combined with flavan-3-ols prevent steatosis and liver injury in a murine model of NAFLD,” *Biochimica et Biophysica Acta - Molecular Basis of Disease*, vol. 1864, no. 1, pp. 69–78, 2018.
- [93] E. Patterson, R. Wall, G. F. Fitzgerald, R. P. Ross, and C. Stanton, “Health implications of high dietary omega-6 polyunsaturated fatty acids,” *J Nutr Metab*, vol. 2012, article 539426, pp. 1–16, 2012.
- [94] J. Araya, R. Rodrigo, L. A. Videla et al., “Increase in long-chain polyunsaturated fatty acid n-6/n-3 ratio in relation to hepatic steatosis in patients with non-alcoholic fatty liver disease,” *Clinical Science*, vol. 106, no. 6, pp. 635–643, 2004.
- [95] J. S. Bae, J. M. Park, J. Lee et al., “Amelioration of non-alcoholic fatty liver disease with NPC1L1-targeted IgY or n-3 polyunsaturated fatty acids in mice,” *Metabolism*, vol. 66, pp. 32–44, 2017.
- [96] M. A. Straus and D. A. Donnelly, “Corporal punishment of adolescents by American Parents,” *Youth & Society*, vol. 24, no. 4, pp. 419–442, 2016.
- [97] Y. Kim and J. Kim, “Prevention: a publication of the American Association for Cancer Research, Intake or blood levels of n-3 polyunsaturated fatty acids and risk of colorectal cancer: a systematic review and meta-analysis of prospective studies,” *Cancer Epidemiology and Prevention Biomarkers*, vol. 29, no. 2, pp. 288–299, 2020.
- [98] B. Yang, F. L. Wang, X. L. Ren, and D. Li, “Biospecimen long-chain N-3 PUFA and risk of colorectal cancer: a meta-analysis of data from 60,627 individuals,” *PLoS One*, vol. 9, no. 11, article e110574, 2014.
- [99] L. Fini, G. Piazzzi, C. Ceccarelli et al., “Highly purified eicosapentaenoic acid as free fatty acids strongly suppresses polyps in Apc(Min/+) mice,” *Clinical Cancer Research*, vol. 16, no. 23, pp. 5703–5711, 2010.
- [100] G. Piazzzi, G. D’Argenio, A. Prossomariti et al., “Eicosapentaenoic acid free fatty acid prevents and suppresses colonic neoplasia in colitis-associated colorectal cancer acting on Notch signaling and gut microbiota,” *International Journal of Cancer*, vol. 135, no. 9, pp. 2004–2013, 2014.
- [101] G. C. Chen, L. Q. Qin, D. B. Lu et al., “N-3 polyunsaturated fatty acids intake and risk of colorectal cancer: meta-analysis of prospective studies,” *Cancer Causes & Control*, vol. 26, no. 1, pp. 133–141, 2015.
- [102] A. Desbois and K. Lawlor, “Antibacterial activity of long-chain polyunsaturated fatty acids against *Propionibacterium acnes* and *Staphylococcus aureus*,” *Marine Drugs*, vol. 11, no. 11, pp. 4544–4557, 2013.
- [103] A. Hekmatdoost, X. Wu, V. Morampudi, S. M. Innis, and K. Jacobson, “Dietary oils modify the host immune response and colonic tissue damage following *Citrobacter rodentium* infection in mice,” *American Journal of Physiology-Gastrointestinal and Liver Physiology*, vol. 304, no. 10, pp. G917–G928, 2013.
- [104] H. Takaishi, T. Matsuki, A. Nakazawa et al., “Imbalance in intestinal microflora constitution could be involved in the pathogenesis of inflammatory bowel disease,” *International Journal of Medical Microbiology*, vol. 298, no. 5-6, pp. 463–472, 2008.
- [105] S. Ghosh, D. DeCoffe, K. Brown et al., “Fish oil attenuates omega-6 polyunsaturated fatty acid-induced dysbiosis and infectious colitis but impairs LPS dephosphorylation activity causing sepsis,” *PLoS One*, vol. 8, no. 2, article e55468, 2013.

Research Article

Early T-Cell Precursor Leukemia Has a Higher Risk of Induction-Related Infection among T-Cell Acute Lymphoblastic Leukemia in Adult

Kangyu Huang ¹, Min Dai,¹ Qiuli Li,² Nannan Liu,¹ Dainan Lin,¹ Qiang Wang,¹ Xuan Zhou,¹ Zhixiang Wang,¹ Ya Gao,¹ Hua Jin,¹ Xiaoli Liu,¹ Qifa Liu ¹, and Hongsheng Zhou ¹

¹Department of Hematology, Nanfang Hospital, Southern Medical University, Rd 1838 North Guangzhou Avenue, Guangzhou 510515, China

²Department of Hematology, The People's Hospital of Guangxi Zhuang Autonomous Region, Nanning, China

Correspondence should be addressed to Qifa Liu; liuqifa628@163.com and Hongsheng Zhou; hanson_tcm@126.com

Received 24 September 2020; Revised 10 November 2020; Accepted 10 December 2020; Published 24 December 2020

Academic Editor: Mingliang Jin

Copyright © 2020 Kangyu Huang et al. This is an open access article distributed under the Creative Commons Attribution License, which permits unrestricted use, distribution, and reproduction in any medium, provided the original work is properly cited.

Background. Infections are an important cause of morbidity and mortality for acute lymphoblastic leukemia (ALL). However, the reports regarding risk factors of induction-related infection are roughly unknown/limited in adult T-ALL during induction chemotherapy. **Methods.** We performed a retrospective cohort study for the prevalence and risk predictors of induction-related infection among consecutive T-ALL patients ($N = 97$) enrolled in a PDT-ALL-LBL clinical trial. Of 97 patients with T-ALL enrolled in the trial, 46 were early T-cell precursor (ETP) ALL and 51 were non-ETP ALL. **Results.** When compared with non-ETP, ETP ALL subtype was characterized with lower neutrophil count ($1.35 \times 10^9/L$ vs. $8.7 \times 10^9/L$, $P < 0.001$) and lower myeloid percentage in the bone marrow (13.35% vs. 35.31%, $P = 0.007$). Additionally, ETP ALL had longer neutropenia before diagnosis ($P < 0.001$), as well as during induction chemotherapy ($P < 0.001$). Notably, the ETP cohort experienced higher cumulative incidence of clinically documented infections (CDI; 33.33%, $P = 0.001$), microbiologically documented infections (MDI; 45.24%, $P = 0.006$), resistant infection (11.9%, $P = 0.013$), and mixed infection (21.43%, $P = 0.003$), respectively, than those of the non-ETP cohort. Furthermore, multivariable analysis revealed that T-ALL mixed infection was more likely related to chemotherapy response (OR, 0.025; 95% CI 0.127-0.64; $P = 0.012$) and identified myeloid percentage as a predictor associated with ETP-ALL mixed infection (OR, 0.915; 95% CI 0.843-0.993; $P = 0.033$), with ROC-defined cut-off value of 2.24% in ETP cohorts. **Conclusions.** Our data for the first time demonstrated that ETP-ALL characterized with impaired myelopoiesis were more susceptible to induction-related infection among T-ALL populations.

1. Introduction

Infections are important causes on morbidity and mortality of children and adults with acute leukemia [1–7]. These patients are at a high risk of infection, particularly in induction therapy, likely related to the intensive therapy resulting in profound neutropenia and lymphopenia. [1–3] Infections contribute to not only mortality but also pro-

longed hospitalization, compromised chemotherapy delivery, and increased health care utilization. Furthermore, empiric and preemptive treatments with broad-spectrum antibiotics may lead to the emergence of multidrug resistance microbiological flora.

Although it is well known that invasive infections are common, little is known about predictors of infections in acute lymphoblastic leukemia (ALL). A report from the

Medical Research Council in UK found that Down syndrome was the most significant risk factor for infection-related mortality (IRM) of childhood ALL [1]. Recently, early T-cell precursor ALL (ETP-ALL) was recognized as a form of T-cell ALL with poor prognosis [8–10]. ETP-ALL is characterized with a unique immunophenotype of early arrest in T-cell differentiation, accompanied by markers of stem cells and myeloid progenitors [11–17]. It is less documented about the epidemiology and risk factors of invasive infection in adult ALL, particularly in ETP-ALL, undergoing induction chemotherapy. [18, 19]

To address the current lack of clinical evidence, we performed a retrospective cohort analysis based on a consecutive T-ALL patient trial enrolled onto pediatric-inspired, PEG-L-asparaginase-intensified, and MRD-directed precision-classification-directed-target-total-therapy (PDT-ALL-LBL). The objectives of this study were to explore the incidence of morbidity and mortality, the relationship of disease-related variables with infections, and potential clinical risk factors.

2. Patients and Methods

2.1. Patients and Induction Chemotherapy. A total of 97 adult T-ALL patients were enrolled in pediatric-inspired, PEG-L-asparaginase-intensified, and MRD-directed PDT-ALL-LBL protocol (Clinical Trials ID: NCT03564704). The study was conducted in accordance with the Declaration of Helsinki and approved by Institutional Review Board (IRB)/Ethical Committee (EC) according to institutional guidelines. ETP patients were diagnosed by WHO immunophenotypic criteria: [1] absent (<5% positive cells) CD1a, CD8 expression; [2] absent or dim (<75% positive cells) CD5 expression; and [3] expression (>25% positive cells) of 1 or more myeloid (CD11b, CD13, CD33, and CD117) or stem cell (CD34, HLA-DR) markers [20]. An intensive chemotherapy regimen for induction consists of VICLD (vincristine/VCR: 1.4 mg/m² for day 1, 8, 15, and 22; idarubicin/IDA: 10 mg/m² for day 1, 8; cyclophosphamide/CTX: 1 g/m² for day 1; pegaspargase/PEG-asp: 2000 IU/m² for day 1, 15; dexamethasone: day 1 to 24 as continuous infusion; and chidamide: 10 mg from day 1 to 24) (Supplemental Table 1). Bone marrow test and flow-based MRD-assessment were performed on day 15, day 24, and day 45 during the induction phase. The definitions of infections were based on the European Organization for Research and Treatment of Cancer (Supplemental Table 2) [21]. Mixed infection was defined as more than one microbiologically documented infection during induction therapy. Episodes of infections recorded during induction therapy within a time span of 24 days were analytically reviewed. Echinocandins, a class of antifungal drugs used for prophylaxis, were administered during neutropenia during the induction phase. Patients received no prophylaxis for antibacterial. Infection-related mortality (IRM) was defined by any CDI/MDI-related death during the induction treatment. Myeloid percentage in the bone marrow was determined by flow cytometry and aspirate smear by Wright-Giemsa stain on bone marrow samples at diagnosis and measured as the mean plus/minus the standard deviation.

2.2. Potential Predictors. Potential predictors of infection complications included age, gender, leukemia subtype (ETP, non-ETP), immunophenotype (CD4, CD8, CD13, CD33, CD34, CD38, CD11b, CD65, and HLA-DR), WBC count (0- <4, 4-30, and >30 × 10⁹/L), neutrophil count (0- <0.5, 0.5-1.5, and >1.5 × 10⁹/L), LDH level (<600, ≥600 U/L), duration of neutropenia, and myeloid-percentage in the bone marrow at diagnosis.

2.3. Statistical Analysis. Associations and distinctions among clinical factors, including age, gender, leukemia subtype, immunotype (CD4, CD8, CD13, CD33, CD34, CD38, CD11b, CD65, and HLA-DR), WBC (0- <4, 4-30, and >30 × 10⁹/L), neutrophil (0- <0.5, 0.5-1.5, and >1.5 × 10⁹/L), LDH (<600, ≥600 U/L), duration of neutropenia, and myeloid percentage in the bone marrow at diagnosis and infection events were evaluated. Data were analyzed by using SPSS 20. Variables were compared with the χ -squared test or Fisher's exact test and continuous variables with an appropriate nonparametric test. The relationships between the potential predictors and binary outcome, sepsis death, and other variables were examined using multivariate logistic regression. A *P* value (two tailed) of < 0.05 was statistically significant.

3. Results

3.1. Study Diagram of Induction-Related Infections. From Feb 2016 to Dec 2019, 100 adult patients with newly diagnosed T-ALL were enrolled in this study. Three patients were excluded for lacking clinical raw data as shown in Figure 1. A total of 97 patients received intensive induction chemotherapy according to the PDT-ALL-LBL protocol and experienced 92 episodes of infections within first 24 days of induction phase (Figure 1). As shown in Figure 1, induction-related infections included fever of uncertain origin (FOU) 22.83% (21/92), 35.87% (33/92) clinically documented infections (CDI), and 41.3% (38/92) microbiologically documented infections (MDI). Noteworthy, the majority of FOU (57.14%), CDI (90.91%), and MDI (71.05%) occurred in ETP cohort (Figure 1).

3.2. Clinical Characteristics. Overall, 46 out of 97 patients enrolled in the PDT-ALL-LBL trial were diagnosed as ETP ALL. Basic clinical characteristics are presented in Table 1. When compared with non-ETP, ETP patients had lower WBC, neutrophil, and LDH (*P* < 0.001) and higher platelet count (*P* < 0.001). Notably, myeloid percentage at diagnosis in ETP leukemia was lower than that of non-ETP ALL (median, 13.35% vs. 35.31%, *P* = 0.007). ETP cohort presented a higher incidence (34.78% vs. 1.96%) and longer duration (18 days vs. 1 day) of neutropenia at prediagnosis phase and during induction chemotherapy (Figures 2(a)–2(c)). A negative linear relationship was identified between the duration of neutropenia in induction treatment and BM myeloid percentage (*r* = -0.4, *P* < 0.001) in the T-ALL group (Figure 2(d)), but there was no relationship of this kind observed in the ETP and non-ETP cohorts. As shown in Figure 2(d), most cases with ETP were located above the line fitting, while non-ETP were below the line, indicating more

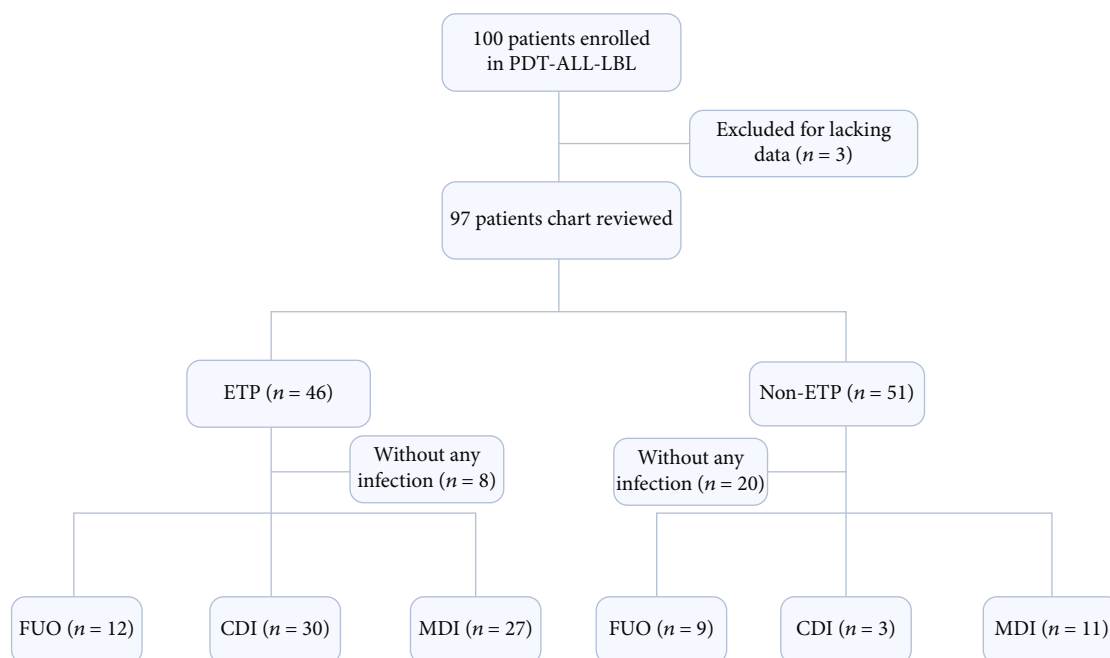


FIGURE 1: Flow diagram of induction-related infections. Forty-six patients in the ETP cohort experienced 69 episodes of induction-related infection, while 51 cases in non-ETP cohort had 23 episodes of infections in 24 days of induction phase. ETP: early T-cell progenitor ALL; non-ETP: non-early T-cell progenitor ALL; FOU: fever of uncertain origin; CDI: clinically documented infection; MDI: microbiologically documented infection.

TABLE 1: Clinical characteristics of T-ALL adult patients.

Characteristics	ETP <i>n</i> = 46	Non-ETP <i>n</i> = 51	<i>P</i> value
Age	25 (19-33)	24 (17-32)	0.131
Median (IQR)			
Gender			
Female	15	12	
Male	31	39	0.442
Laboratory values			
Median (IQR)			
WBC count ($\times 10^9/L$)	8.15 (3.13-66.07)	92.84 (13.36-187.29)	<0.001
Neutrophil count ($\times 10^9/L$)	1.35 (0.73-5.03)	8.70 (4.13-14.38)	<0.001
Platelet count ($\times 10^9/L$)	145 (76.76-198.5)	42 (24-147.5)	<0.001
Hemoglobin (g/dL)	102 (68.75-124.5)	116 (92.5-131.5)	0.117
LDH (IU/L)	270 (176.75-417.75)	1229 (425-2154.25)	<0.001
Duration of neutropenia	13 (9.25-18.75)	5 (0-10)	<0.001
BM myeloid percentage	13.35 (2.87-38.8)	35.31 (9.28-62.25)	0.007
Response to induction	<i>n</i> = 46	<i>n</i> = 51	
CR*	21	40	0.001
PR/failure*	25	11	0.001
Death in induction	4	3	0.593

Quantitative variables are expressed as median (IQR range). IQR: interquartile range; WBC: white blood cell; LDH: lactate dehydrogenase; BM: bone marrow; BM myeloid percentage: identified by flow cytometry and aspirate smear by Wright-Giemsa stain on bone marrow samples at diagnosis and measured as the mean plus or minus the standard deviation; CR*: complete response after the first treatment; PR*: partial response after the first treatment.

impaired myelopoiesis in the ETP cohort than that in non-ETP ALL. The CR rate after first induction treatment in patients with ETP was significantly lower than that of non-

ETP patients ($P = 0.001$) as expected. However, the death rate during induction treatment between the ETP and non-ETP patients was similar ($P = 0.593$, Table 1).

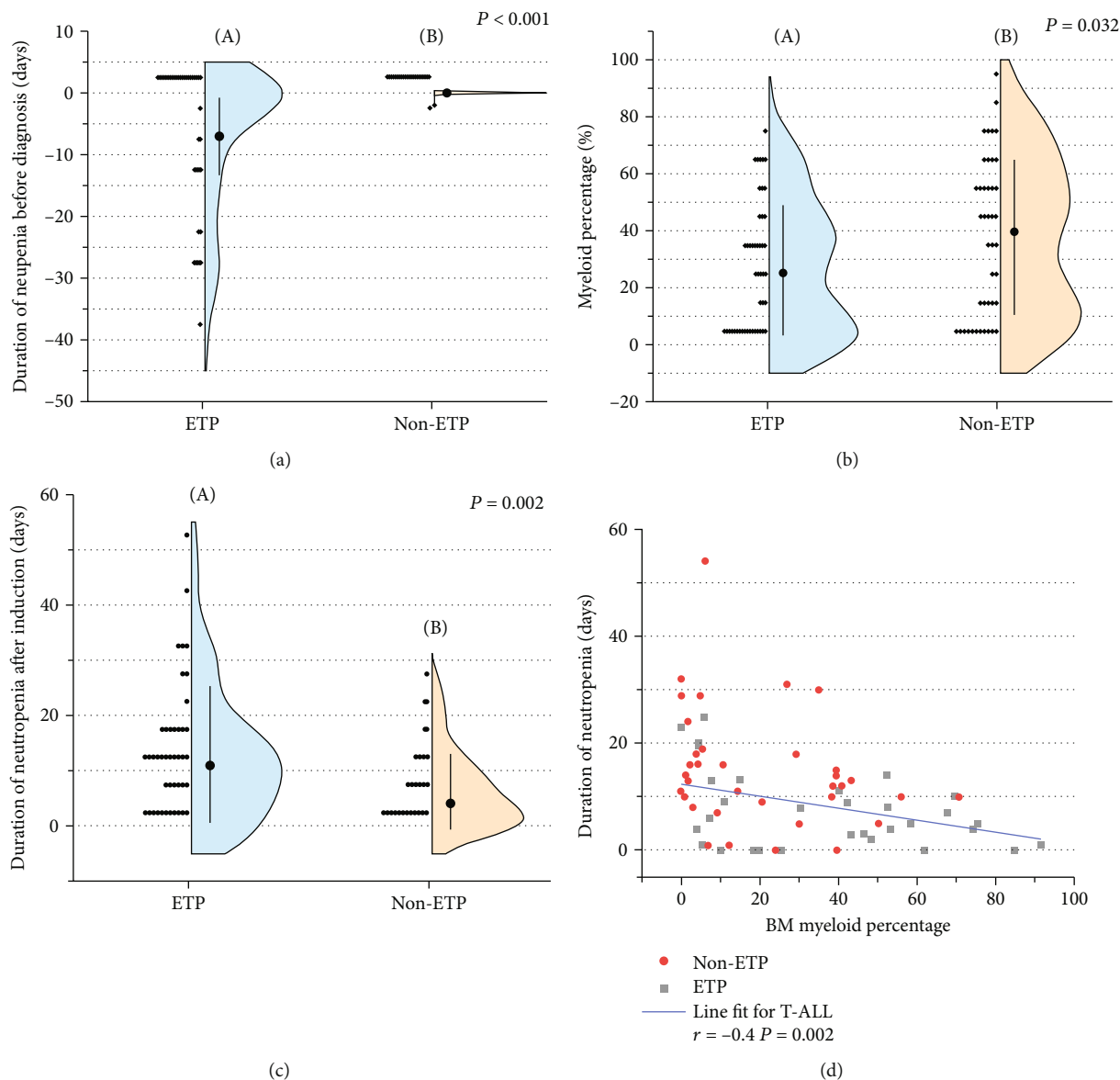


FIGURE 2: Clinical characteristics of the ETP and non-ETP cohorts. (a) Comparison of neutropenia at prediagnosis between the ETP (A) and non-ETP (B) patients. (b) Analysis of myeloid percentage in the bone marrow in the ETP (A) and non-ETP (B) cohorts. (c) Comparison of neutropenia duration during induction in the ETP (A) and non-ETP (B). (d) Linear relationship analysis between the myeloid percentage and neutropenia duration during induction, ETP is shown as red-dot and non-ETP as solid black square. Quantitative variables are expressed as mean (a) or median (b, c).

3.3. Clinical-Biological Features of Induction-Related Infections. During the first 24 days of intensive treatment, 97 patients experienced a total of 92 infectious episodes, consisting of 21 episodes of fever of unknown origin (FUO, 22.83%), 33 episodes of CDI (35.87%), and 38 episodes of MDI (41.3%). Firstly, we compared the CDI and MDI between the ETP and non-ETP cohorts. Log-rank tests demonstrated that the ETP cohort had a higher cumulative incidence of both CDI (30.43% vs. 5.88%, $P = 0.001$) and MDI (41.3% vs. 19.6%, $P = 0.006$), compared with the non-ETP cohort. In terms of pathogens, we further analyzed infections caused by Gram-negative and Gram-positive organisms and fungi between the ETP and non-ETP cohorts and found that there was no significant difference observed

(Supplemental Figure 1). On the other hand, the ETP cohort had a higher incidence of drug resistant (10.87% vs. 0%, $P = 0.013$) and mixed infection (19.57% vs. 1.96%, $P = 0.003$) (Figure 3).

Cumulative incidence with first 24 days as indicated as incidence rate plus or minus two standard errors. Resistant infection: Diagnosed resistant bacterial infection with supportive microbiological evidence, such as a positive culture, antigen or PCR test results, or characteristic histopathological findings. Mixed infection: Identified more than one microbiologically documented infection during the first induction therapy [21].

Next, we analyzed infection sites and pathogen types in induction-related infection. As shown in Table 2,

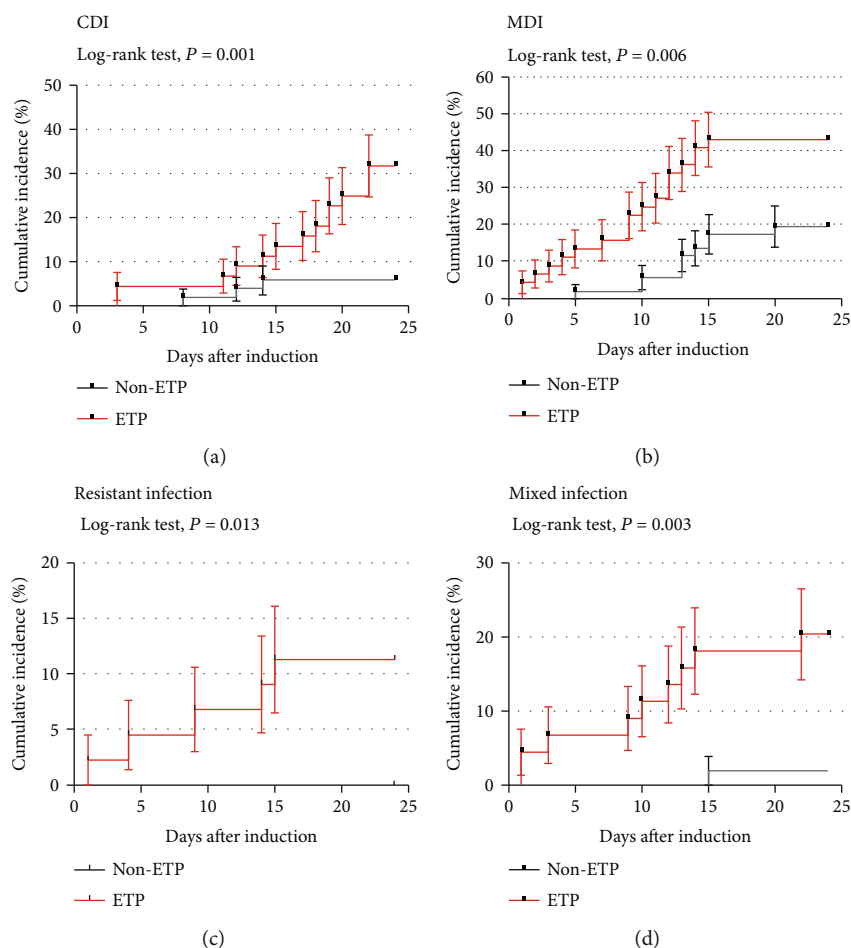


FIGURE 3: Kaplan-Meier analysis of induction-related infections in the ETP and non-ETP cohort.

bloodstream and pulmonary infections were the most prominent sites of infection in the T-ALL group. Of note, both the bloodstream and pulmonary infections were more common in the ETP cohort than in the non-ETP cohort (Table 2(a), $P = 0.057$, $P = 0.01$). In the context of disseminated infections, 19 cases occurred in the ETP-ALL cohort and only 4 cases in the non-ETP cohort. The fascia, perianal, intestinal tract, endocardium, and bone marrow were involved in infections of the ETP cohort, while limited sites in the skin and gastrointestinal tract in the non-ETP cohort (Table 2(a)). Therefore, an increased awareness of disseminated infection potential for ETP patients is required during the induction period. Actually, infection sites of ETP ALL are also more scattered than the non-ETP patients in the prediagnosis phase and clinical lesions involved in the gastrointestinal tract, central nervous system, cardiovascular system, skin, and soft tissue (Supplemental Table 3).

Besides, we further reviewed the pathogens of MDI in the ETP and non-ETP cohorts. As shown previously, the ETP cohort presented a markedly higher incidence of MDI than non-ETP. Gram-negative bacteria (26/38, 68.42%) predominated among the pathogens were isolated from both cohorts, followed by fungi (6/38, 15.79%) and Gram-positive bacteria (6/38, 15.79%). *Klebsiella* spp. and *Pseudomonas aeruginosa* accounted for most Gram-negative infections (Table 2(b)).

Nonfermenting Gram-negative bacilli is frequently related to intrinsic antibiotic resistance. In our study, 7 of 9 nonfermenting bacterial episodes, including *Acinetobacter* spp., *Stenotrophomonas maltophilia*, and *Sphingomonas paucimobilis*, were detected in only the ETP cohort. Particularly, 10 out of 97 patients (10.31%) were infected with more than one pathogen, including 9 ETP and 1 non-ETP patients (OR 9.978; 95% CI 1.314-75.761; $P = 0.005$), indicating that the ETP cohort had a higher risk of mixed infection during induction chemotherapy. Furthermore, antimicrobial resistance was only found in 5 ETP patients (5/46, 10.87%), including carbapenem-resistant *Klebsiella pneumoniae* (CRKP), pan-drug-resistant *Acinetobacter baumannii* (PDRAB), methicillin-resistant *Staphylococcus aureus*- (MRSA-) resistant *Aeromonas hydrophila* and ESBLs-producing *Escherichia coli* (Supplemental Table 4).

Taken together, our data showed that ETP leukemia was associated with a higher incidence of CDI and MDI, and severe and complicated infections, compared with the non-ETP subset.

3.4. Infection-Related Mortality (IRM). In our study, IRMs of induction therapy were 7.2% (7/97) in T-ALL, and 8.7% (4/46) in the ETP cohort and 5.88% (3/51) in the non-ETP cohort, respectively. Four patients with ETP ALL died of

TABLE 2: Infection sites and causative agents of induction-related infections in PDT-ALL-LBL.

(a)

Infection sites	Total	ETP	Non-ETP	P
Bloodstream	27	17	10	0.057
Pulmonary	9	8	1	0.01
Disseminated	23	19	4	
Crissum and mucosa	8	7	1	
Gastrointestinal tract	5	4	1	
Skin and soft tissue	5	4	1	
Central nervous system	2	1	1	
Tonsil	1	1	0	
Bone marrow	1	1	0	
Cardiovascular system	1	1	0	

(b)

Causative agents	Total	ETP	Non-ETP
	38 (100%)	27 (71.05)	11 (28.95)
Gram-positive organisms	6 (15.79)	4 (10.53)	2 (5.26)
<i>Staphylococcus</i>	3 (7.89)	2 (5.26)	2 (5.26)
<i>Staphylococcus aureus</i>		1 (2.60)	1 (2.60)
MRSA		1 (2.60)	0
<i>Bacillus cereus</i>	2 (5.26)	1 (2.60)	1 (2.60)
<i>Enterococcus faecium</i>	1 (2.60)	1 (2.60)	0
Gram-negative organisms	26 (68.42)	18 (47.37)	8 (21.05)
<i>Klebsiella</i> spp.	11 (28.95)	7 (18.42)	4 (10.53)
<i>Klebsiella Pneumoniae</i>		4 (10.53)	3 (7.89)
CRKP		1 (2.60)	0
<i>Klebsiella ozaenae</i>		1 (2.60)	0
Resistant <i>K. ozaenae</i>		1 (2.60)	0
<i>Acinetobacter</i> spp.	2 (5.26)	2 (5.26)	0
ACB complex		1 (2.60)	0
PDRAB		1 (2.60)	0
<i>Pseudomonas aeruginosa</i>	5 (13.16)	2 (5.26)	3 (7.89)
<i>Escherichia</i>	3 (7.89)	3 (7.89)	0
<i>Escherichia coli</i>		2 (5.26)	0
ESBLs-producing <i>Escherichia coli</i>		1 (2.60)	0
<i>Salmonella choleraesuis</i>	1 (2.60)	0	1 (2.60)
<i>Aeromonas hydrophila</i>	2 (5.26)	1 (2.60)	1 (2.60)
<i>Aeromonas hydrophila</i>		0	1 (2.60)
Resistant <i>Aeromonas hydrophila</i>		1 (2.60)	0
<i>Sphingomonas paucimobilis</i>	1 (2.60)	1 (2.60)	0
<i>Stenotrophomonas maltophilia</i>	2 (5.26)	2 (5.26)	0
Fungus	6 (15.79)	5 (13.16)	1 (2.60)

MRSA: methicillin-resistant *Staphylococcus aureus*; CRKP: carbapenem-resistant *Klebsiella pneumoniae*, ACB complex: *A. calcoaceticus*-*A. baumannii* complex, PDRAB: pan-drug-resistant *Acinetobacter baumannii*.

severe and complicated infections induced by CRE, PDRAB, and nonfermenting bacteria (Supplemental Table 5). To identify the potential risk factor associated with IRM during induction, we performed univariate and multivariate analy-

ses. In univariate regression analysis, Gram-negative bacteria and mixed infection were associated with higher risk of IRM in T-ALL patients (OR, 20.4; 95% CI 2.318-179.55; $P = 0.007$ and OR, 10.25; 95% CI 1.852-56.736; $P = 0.008$) (Table 3).

TABLE 3: Univariate analysis identifying factors associated with IRM.

Causative agent	T-ALL			ETP		
	OR	95% CI	P	OR	95% CI	P
G-positive infection	1.929	0.203-18.36	0.568	4.222	0.33-54.085	0.268
G-negative infection	20.4	2.318-179.55	0.007	0	0	0.999
Fungal infection	0	0	0.999	0	0	0.999
Resistant infection	3.5	0.336-36.429	0.295	9.25	1.01-84.732	0.049
Mixed infection	10.25	1.852-56.736	0.008	21.6	1.866-250.025	0.014

G-negative MDI and mixed infection were critical risk factors associated with IRM in the T-ALL population. Mixed infection and resistant infection was identified factors associated with IRM in the ETP-ALL cohort. IRM: infection-related mortality.

TABLE 4: T-ALL and ETP ALL regression analyses of induction infection.

Characteristic	T-ALL			ETP		
	OR	95% CI	P	OR	95% CI	P
Univariate regression analysis of mixed infection in the induction phase						
Characteristic						
WBC			0.555			0.819
WBC [1]	0.4	0.049-3.243	0.391	1.5	0.164-13.749	0.72
WBC [2]	1.071	0.15-7.642	0.945	1.929	0.25-14.887	0.529
NEU			0.323			0.843
NEU [1]	0.221	0.029-1.664	0.143	0.938	0.114-7.728	0.952
NEU [2]	0.5	0.054-4.672	0.543	0.556	0.059-5.241	0.608
BM myeloid percentage	0.975	0.94-1.01	0.156	0.915	0.843-0.993	0.033
CR	0.025	0.127-0.64	0.012	0.6	0.014-1.354	0.323
Multiple regression analysis of mixed infection in induction phase						
Characteristic						
WBC			0.146			0.388
WBC [1]	0.059	0.001-4.03	0.189	0.119	0.002-8.306	0.326
WBC [2]	2.25	0.072-69.965	0.644	1.434	0.045-45.853	0.838
NEU			0.823			0.512
NEU [1]	1.45	0.039-54.431	0.841	2.057	0.057-74.632	0.694
NEU [2]	0.472	0.012-19.311	0.692	0.211	0.003-13.712	0.465
BM myeloid percentage	0.895	0.807-0.992	0.035	0.864	0.75-0.995	0.043
CR	0.019	0.001-0.557	0.022	0.012	0-1.092	0.055

Collectively, our study indicated that mixed infections contributed to IRM in T-ALL (data not shown) and ETP-ALL cohorts.

3.5. Risk Factors Associated with Infections. To identify the potential risk factors associated with induction-related infection, univariate and multivariable analyses were performed. BM myeloid percentage was related to prediagnosed infections in T-ALL (univariate model $P = 0.003$, multiple model $P = 0.005$) and ETP cohorts (univariate model $P = 0.009$, multiple model $P = 0.011$) (Supplemental Table 6). During remission induction in the first 24 days, WBC count, NEU count, phenotype, and myeloid percentage did not significantly influence the development of CDI and MDI among T-ALL/LBL, ETP, or non-ETP patients (data not shown). In terms of mixed infection in the T-ALL cohort and ETP cohort, potential clinical risk factors would be different. In univariate regression analysis, for the T-ALL group, induction treatment responses (CR or not) ($P = 0.012$) were related

to mixed infection, while in the ETP cohort, myeloid percentage was the only clinical risk factor ($P = 0.033$) (Table 4). Multivariable regression analysis demonstrated that induction treatment response (CR or not) and myeloid percentage was significantly associated with mixed infection in T-ALL ($P = 0.022$, $P = 0.035$, $AUC = 0.962$), with an ROC defined cut-off value of 12.27%. And myeloid percentage was the only infection risk factor related to the ETP cohort ($P = 0.043$, $AUC = 0.961$), and ROC defined cut-off value was set as 2.24% (Figure 4). Overall, these data unearthed the relationship between impaired myelopoiesis, i.e., reduced myeloid percentage and susceptibility to serious and complicated infection during induction chemotherapy.

4. Discussion

In this study, we investigated the prevalence of infection-related complications during induction therapy among T-

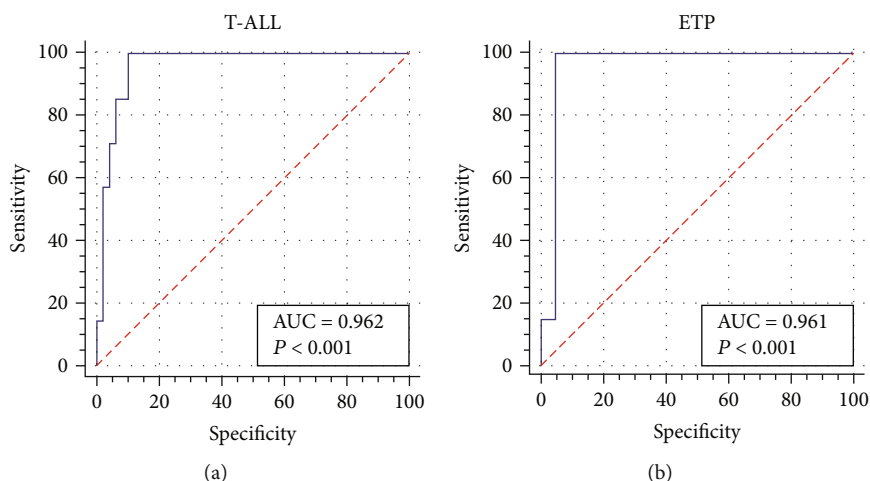


FIGURE 4: Receiver operating characteristic (ROC) curve for the multivariate model of mixed infection in the T-ALL (a) and ETP-ALL (b) cohorts.

ALL population and compared the clinical features between the ETP and non-ETP cohorts. It has been documented that intensive induction chemotherapy yielded serious neutropenia and high incidence of infection in ALL, but little has been reported about risk factors implicated in T-ALL population. [9, 19, 22] Our study revealed that ETP ALL was characterized with markedly impaired myelopoiesis at diagnosis, presenting with lower neutrophil and reduced myeloid percentage, when compared with non-ETP ALL. Notably, ETP experienced a significantly higher incidence of CDI, MDI, antimicrobial resistance, and mixed infection, which were 2-10-folds higher than that in the non-ETP cohort. Furthermore, our study confirmed the association between reduced myeloid percentage and the risk of mixed infection. Additionally, identified myeloid percentage as a predictor was highly associated with mixed infection in both the T-ALL and ETP-ALL cohorts. Collectively, our data provided evidences, for the first time, about the relationship between clinical features of ETP subtype and susceptibility to infection among T-ALL population during induction chemotherapy. [14, 15, 17, 23–25]

Induction-related infections account for most of the morbidity and mortality of acute leukemia. In the present study, among 92 infection episodes occurred in T-ALL population, consisting of around 80% CDI and MDI. With the same regimen of induction chemotherapy, the ETP cohort experienced three-quarters of CDI and MDI episodes among the T-ALL cohort. Furthermore, our study demonstrated that ETP patients were significantly more vulnerable to complicated infection, compared to other T-ALL patients. In addition, among the episodes of Gram-negative bacteremia, nonfermenting Gram-negative bacilli were present in one-third of episodes and predominant in the ETP cohort (7/9). Infection with resistant bacteria, including CRE, MRSA, PDRAB, and *Aeromonas hydrophila*, were only found in the ETP cohort. These data highlighted higher susceptibility to induction-related infection in ETP leukemia, in contrast to non-ETP T-ALL, which was not well addressed yet. In our study, patients received echinocandins prophylaxis for antifungi, which might contribute to the low incidence of fungal infection and no fungus-related IRM. Antibacterial

prophylaxis was still controversial in ALL, and accumulating evidences indicated that levofloxacin prophylaxis reduces odds of febrile neutropenia and bacterial infection during induction in pediatric ALL [6]. Therefore, an increased awareness of infection is required for the T-ALL and ETP patients.

Our data revealed that the clinical features and chemotherapy responses might contribute to the increased risk of infection during induction chemotherapy in T-ALL. Regarding infection management of T-ALL patients, poor chemotherapy responses increased the unacceptably heightened risk induced by mixed infection. These patients would undergo a period of profound and prolonged immunosuppression so that opportunistic infections might occur. However, myelosuppression is more likely to contribute to febrile neutropenia and severe infections in the ETP subgroup. In this regard, ETP leukemia is defined by gene expression profiling and immunophenotype, representing a novel high-risk subtype of ALL.^(8,9,17,18) Our data showed that ETP leukemia had distinct clinical features presenting with significantly lower WBC and neutrophil count and reduced myeloid percentage at diagnosis when compared with other T-ALL. ETP leukemia is postulated to derive from a subset of early thymus-cell progenitor and transcriptionally related to hematopoietic stem cells and myeloid progenitors. [10, 24] It is reported that the earliest thymic T-cell progenitors sustain B and myeloid lineage potential and ETPs are major granulocyte precursors in mouse thymus [24]. We speculate that the origin of ETP leukemia harbors impairment in both T lymphopoiesis and myelopoiesis, resulting in persistent neutropenia. This hypothesis might partly explain more prolonged neutropenia in prediagnosis and induction in the ETP cohort than in the non-ETP cohort. In addition, high-frequency genomic mutation in ETP patients might be another potential factor for T lymphopoiesis and myelopoiesis [19]. Elucidating genetic profile and comparing the mutational genotypes of adult T-ALL might provide more valuable information in terms of the disease control and prevention. Unfortunately, we are not able to perform a comprehensive analysis due to lack of enough genomic mutation data on adult T-ALL in our center.

Therefore, the exact relationship of persistent febrile neutropenia and long-term exposure to broad-spectrum antibiotics which induce drug resistance and mixed infection is uncertain, but this could be the reasons of the high prevalence of MDR and mixed infection in ETP-ALL.

Defining the potential predictors for infection will be valuable to reduce treatment-related toxicity. Previous studies have recognized Down syndrome, microbiome diversity, and severe neutropenia as preexisting risk factors for infection-associated adverse events [1–3, 9, 18, 26]. In this study, we identified myeloid percentage as a risk factor for mixed infection, with about 12.27% and 2.24% cut-off value defined by ROC analysis in the T-ALL and ETP-cohorts, indicating that the most of ETP ALL had a high risk of mixed infection during induction chemotherapy. These results also suggest us to reassess the intensive regimen during induction chemotherapy for T-ALL, particularly, for ETP-ALL. Because of the high incidence of infection-related complications in ETP patients, we recommended that more intensive monitoring and early antibiotic combination treatment should be applied. It is critical to the logistics management for ETP patients. To avoid severe infections, it is of importance that utilizing conventional and contemporary diagnostic tools identify pathogens and spectrum of infections to optimize antimicrobial therapy. Although being classified as a high risk with poor outcome, accumulating evidences indicate that pediatric-inspired protocols, such as Berlin-Frankfurt-Münster (BFM) backbone and GRALL-2003 Trials, have improved the outcome of ETP-ALL similar with other T-ALL [27]. Preliminary results of the PDT-ALL-LBL trial also showed promising outcomes for both ETP and other T-LBL/ALL. An optimal regimen for ETP-ALL might be based on reduced intensity of chemotherapy and reveal risk predictors to reduce induction-related infection and mortality to improve the outcome. [3, 4, 28–30]

In conclusion, our findings demonstrated that ETP ALL, a novel high-risk subtype, is more susceptible to induction-related infection. BM myeloid percentage is identified as a major risk factor for a poor outcome of infection-related complications. Due to limited sample size and lack of enough genomic mutation data, our dataset failed to identify more specific population(s) and other potential responsible risk factors. In addition, these results were just derived from a single-center data. A larger, multicenter, prospective cohort studies are needed to develop and validate an optimal scoring system for the risk of infection in the T-ALL and ALL populations.

Data Availability

The datasets during and/or analyzed during the current study are available from the corresponding author on reasonable request.

Conflicts of Interest

The authors declare that they have no conflicts of interest.

Authors' Contributions

Kangyu Huang performed the data analyses and prepared the manuscript. Min Dai collected data and helped perform the analyses with constructive discussions. Qiuli Li significantly contribute to the analysis and manuscript preparation. Nannan Liu, Dainan Lin, Qiang Wang, Xuan Zhou, Zhixiang Wang, Ya Gao, and Hua Jin Xiaoli Liu contributed to conceiving the ideas, carrying out related analyses, and finalizing this paper. Qifa Liu contributed to the conception of the research. Hongsheng Zhou conceived of the research, designed the research, and revised the manuscript. Kangyu Huang, Min Dai, and Qiuli Li are joint first authors.

Acknowledgments

This study was supported by the Natural Science Foundation of Guangdong Province (Nos. 81770170, 81970147 to HSZ), the Science and Technology Planning Project of Guangdong Province (No. 2017A030313601 to HSZ), the Clinical Trial Funding of SMU (2016A020215112 to HSZ), and Nanfang Hospital (LC2016ZD009/2019CR012).

Supplementary Materials

Supplemental Figure 1 Kaplan-Meier analysis of induction-related infections in ETP and non-ETP cohort. Supplemental Table 1: treatment protocol PDT-ALL-LBL. Supplemental Table 2: definitions related to infections. Supplemental Table 3: sites infections in prediagnosed phase. Supplemental Table 4: resistant infection characteristics of ETP patients. Supplemental Table 5: infection characteristics of infection-related mortality (IRM) T-ALL patients. Supplemental Table 6: T-ALL and ETP CDI risk factor regression analysis in prediagnosed phase. (*Supplementary Materials*)

References

- [1] D. O'Connor, J. Bate, R. Wade et al., "Infection-related mortality in children with acute lymphoblastic leukemia: an analysis of infectious deaths on UKALL2003," *Blood*, vol. 124, no. 7, pp. 1056–1061, 2014.
- [2] H. Inaba, D. Pei, J. Wolf et al., "Infection-related complications during treatment for childhood acute lymphoblastic leukemia," *Annals of Oncology*, vol. 28, no. 2, pp. 386–392, 2017.
- [3] L. Sung, B. J. Lange, R. B. Gerbing, T. A. Alonzo, and J. Feusner, "Microbiologically documented infections and infection-related mortality in children with acute myeloid leukemia," *Blood*, vol. 110, no. 10, pp. 3532–3539, 2007.
- [4] K. Bochennek, A. Hassler, C. Perner et al., "Infectious complications in children with acute myeloid leukemia: decreased mortality in multicenter trial AML-BFM 2004," *Blood Cancer Journal*, vol. 6, no. 1, pp. e382–e382, 2016.
- [5] D. Dix, S. Cellot, V. Price et al., "Association between corticosteroids and infection, sepsis, and infectious death in pediatric acute myeloid leukemia (AML): results from the Canadian infections in AML Research Group," *Clinical Infectious Diseases*, vol. 55, pp. 1608–1614, 2012.
- [6] J. Wolf, L. Tang, P. M. Flynn et al., "Levofloxacin prophylaxis during induction therapy for pediatric acute lymphoblastic

- leukemia," *Clinical Infectious Diseases*, vol. 65, no. 11, pp. 1790–1798, 2017.
- [7] C. Even, S. Bastuji-Garin, Y. Hicheri et al., "Impact of invasive fungal disease on the chemotherapy schedule and event-free survival in acute leukemia patients who survived fungal disease: a case-control study," *Haematologica*, vol. 96, no. 2, pp. 337–341, 2011.
- [8] N. Jain, A. V. Lamb, S. O'Brien et al., "Early T-cell precursor acute lymphoblastic leukemia/lymphoma (ETP-ALL/LBL) in adolescents and adults: a high-risk subtype," *Blood*, vol. 127, no. 15, pp. 1863–1869, 2016.
- [9] V. Conter, M. G. Valsecchi, B. Buldini et al., "Early T-cell precursor acute lymphoblastic leukaemia in children treated in AIEOP centres with AIEOP-BFM protocols: a retrospective analysis," *Lancet Haematol*, vol. 3, no. 2, pp. e80–e86, 2016.
- [10] J. E. Haydu and A. A. Ferrando, "Early T-cell precursor acute lymphoblastic leukaemia," *Current Opinion in Hematology*, vol. 20, no. 4, pp. 369–373, 2013.
- [11] L. M. Treanor, S. Zhou, L. Janke et al., "Interleukin-7 receptor mutants initiate early T cell precursor leukemia in murine thymocyte progenitors with multipotent potential," *Journal of Experimental Medicine*, vol. 211, no. 4, pp. 701–713, 2014.
- [12] M. Neumann, S. Heesch, C. Schlee et al., "Whole-exome sequencing in adult ETP-ALL reveals a high rate of DNMT3A mutations," *Blood*, vol. 121, no. 23, pp. 4749–4752, 2013.
- [13] M. Tesio, "On the origin of ETP leukemias," *HemaSphere*, vol. 2, p. e48, 2018.
- [14] L. Belver and A. Ferrando, "The genetics and mechanisms of T cell acute lymphoblastic leukaemia," *Nature Reviews. Cancer*, vol. 16, no. 8, pp. 494–507, 2016.
- [15] J. De Bie, S. Demeyer, L. Alberti-Servera et al., "Single-cell sequencing reveals the origin and the order of mutation acquisition in T-cell acute lymphoblastic leukemia," *Leukemia*, vol. 32, no. 6, pp. 1358–1369, 2018.
- [16] T. Inukai, N. Kiyokawa, D. Campana et al., "Clinical significance of early T-cell precursor acute lymphoblastic leukaemia: results of the Tokyo Children's Cancer Study Group Study L99-15," *British Journal of Haematology*, vol. 156, no. 3, pp. 358–365, 2012.
- [17] J. Zhang, L. Ding, L. Holmfeldt et al., "The genetic basis of early T-cell precursor acute lymphoblastic leukaemia," *Nature*, vol. 481, no. 7380, pp. 157–163, 2012.
- [18] A. Vitale, A. Guarini, C. Ariola et al., "Adult T-cell acute lymphoblastic leukemia: biologic profile at presentation and correlation with response to induction treatment in patients enrolled in the GIMEMA LAL 0496 protocol," *Blood*, vol. 107, no. 2, pp. 473–479, 2006.
- [19] J. Bond, C. Graux, L. Lhermitte et al., "Early response-based therapy stratification improves survival in adult early Thymic precursor acute lymphoblastic leukemia: a group for research on adult acute lymphoblastic leukemia study," *Journal of Clinical Oncology*, vol. 35, pp. 2683–2691, 2017.
- [20] M. J. Borowitz and C. JKC, "T lymphoblastic leukaemia/lymphoma," in *World Health Organization Classification of Tumors of Haematopoietic and Lymphoid Tissues*, S. H. Swerdlow, E. Campo, and N. L. Harris, Eds., pp. 176–178, IARC, Lyon, France, 4th edition, 2008.
- [21] The EORTC International Antimicrobial Therapy Cooperative Group, "Ceftazidime combined with a short or long course of amikacin for empirical therapy of Gram-negative bacteremia in cancer patients with granulocytopenia," *New England Journal of Medicine*, vol. 317, no. 27, pp. 1692–1698, 1987.
- [22] A. Vitale, A. Guarini, C. Ariola et al., "Adult T-cell acute lymphoblastic leukemia: biologic profile at presentation and correlation with response to induction treatment in patients enrolled in the GIMEMA LAL 0496 protocol," *Blood*, vol. 107, no. 2, pp. 473–479, 2016.
- [23] M. Neumann, S. Heesch, N. Gökbuget et al., "Clinical and molecular characterization of early T-cell precursor leukemia: a high-risk subgroup in adult T-ALL with a high frequency of FLT3 mutations," *Blood Cancer Journal*, vol. 2, no. 1, p. e55, 2012.
- [24] M. E. De Obaldia, J. J. Bell, and A. Bhandoola, "Early T-cell progenitors are the major granulocyte precursors in the adult mouse thymus," *Blood*, vol. 121, no. 1, pp. 64–71, 2013.
- [25] S. L. Maude, S. Dolai, C. Delgado-Martin et al., "Efficacy of JAK/STAT pathway inhibition in murine xenograft models of early T-cell precursor (ETP) acute lymphoblastic leukemia," *Blood*, vol. 125, no. 11, pp. 1759–1767, 2015.
- [26] J.-H. Yoo, S. M. Choi, D.-G. Lee et al., "Prognostic factors influencing infection-related mortality in patients with acute leukemia in Korea," *Journal of Korean Medical Science*, vol. 20, no. 1, pp. 31–35, 2005.
- [27] H. Zhou, Y. Gao, Q. Wang et al., "A novel oral histone deacetylase inhibitor chidamide is highly effective and well-tolerated in adult early T-cell precursor and Ph-like acute lymphoblastic leukemia," *Blood*, vol. 132, Supplement 1, p. 4011, 2018.
- [28] R. Zhang, J. Chen, H. Huang et al., "Primary fungal prophylaxis in acute leukemia patients with different risk factors: retrospective analysis from the CAESAR study," *International Journal of Hematology*, vol. 106, no. 2, pp. 221–228, 2017.
- [29] M. Caira, A. Candoni, L. Verga et al., "Pre-chemotherapy risk factors for invasive fungal diseases: prospective analysis of 1,192 patients with newly diagnosed acute myeloid leukemia (SEIFEM 2010-a multicenter study)," *Haematologica*, vol. 100, no. 2, pp. 284–292, 2015.
- [30] M. Nucci and E. Anaissie, "Infections in patients with multiple myeloma in the era of high-dose therapy and novel agents," *Clinical Infectious Diseases*, vol. 49, no. 8, pp. 1211–1225, 2009.

Research Article

Therapeutic Effect of Ginsenoside Rd on Experimental Autoimmune Encephalomyelitis Model Mice: Regulation of Inflammation and Treg/Th17 Cell Balance

Bo Jin,¹ Chixiao Zhang,² Yu Geng,¹ and Mei Liu ¹

¹Department of Neurology, Zhejiang Provincial People's Hospital, People's Hospital of Hangzhou Medical College, Hangzhou 310014, China

²Key Laboratory of Neuropsychiatric Drug Research of Zhejiang Province, Hangzhou Medical College, Hangzhou 310013, China

Correspondence should be addressed to Mei Liu; 2020020041@hmc.edu.cn

Received 30 September 2020; Revised 17 November 2020; Accepted 24 November 2020; Published 18 December 2020

Academic Editor: Xiaolu Jin

Copyright © 2020 Bo Jin et al. This is an open access article distributed under the Creative Commons Attribution License, which permits unrestricted use, distribution, and reproduction in any medium, provided the original work is properly cited.

Multiple sclerosis (MS) is an autoimmune inflammatory disease. Inflammatory infiltrates and demyelination of the CNS are the major characteristics of MS and its related animal model-experimental autoimmune encephalomyelitis (EAE). Immoderate autoimmune responses of Th17 cells and dysfunction of Treg cells critically contribute to the pathogenesis of MS and EAE. Our previous study showed that Ginsenoside Rd effectively ameliorated the clinical severity in EAE mice, but the mechanism remains unclear. In this study, we investigated the therapeutic effect of Ginsenoside Rd on EAE *in vivo* and *in vitro* and also explored the potential mechanisms for alleviating the injury of EAE. The results indicated that Ginsenoside Rd was effective for the treatment of EAE in mice and splenocytes. Ginsenoside Rd treatment on EAE mice ameliorated the severity of EAE and attenuated the characteristic signs of disease. Ginsenoside Rd displayed the therapeutic function to EAE by modulating inflammation and autoimmunity, via the downregulation of related proinflammatory cytokines IL-6 and IL-17, upregulation of inhibitory cytokines TGF- β and IL-10, and modulation of Treg/Th17 imbalance. And the Foxp3/ROR γ t/JAK2/STAT3 signaling was found to be associated with this protective function. In addition, analysis of gut microbiota showed that Ginsenoside Rd also had modulation potential on gut microbiota in EAE mice. Based on this study, we hypothesize that Ginsenoside Rd could be a potential and promising agent for the treatment of MS.

1. Introduction

Multiple sclerosis (MS) is an autoimmune inflammatory disease affecting the central nervous system (CNS) of the body [1]. The clinical features of MS are diverse and mainly include limb weakness, paresthesia, fatigue, blurred vision, ataxia, and cognitive deficits [2]. The etiology of MS is thought to result from the interaction of genetic and environment factors, but this remains to be partially understood. CD4⁺ T cells regulated autoimmune/inflammatory response is thought to critically associate with this disease. T cells enter into the CNS through the damaged blood-brain barrier (BBB), initiate a series chain-type inflammatory response, to induce inflammation, demyelization, oligodendrocyte loss, and subsequent axonal and neuronal damage [3]. Treatment

options of MS have become increasingly multifaceted and multiselective, but in long-term prognosis, the relapses of MS still cause substantial disability in many patients; a meta-analysis also shows that suicide is significantly associated with MS [4, 5]. Thus, therapeutic strategy that reducing the occurrence and severity of MS to improve prognosis is worthy to be explored. For the study of MS, rat experimental autoimmune encephalomyelitis (EAE) is the most widely used animal model. While it is not a so perfect set of animal model, it can mimic mainly pathological features of MS and can be used for pathophysiology and therapy study [6].

T helper 1 (Th1), T helper 2 (Th2), T helper 17 (Th17) cells, and regulatory T (Treg) cells are critical subsets of CD4⁺ T cells which are central elements in immune homeostasis. Many previous studies show that the imbalance of T

cell responses, such as proinflammatory Th1 and Th17 cells, and anti-inflammatory Th2 and Treg cells, is crucial for the pathogenesis and progression of MS and EAE [7–10]. The immoderate immunoreaction of Th17 cells and dysfunction of Treg cells is responsible to dysregulated immunity, inflammatory response, oxidative stress, attack on self-myelin basic protein (MBP) of the MS. Thereby, upregulation of anti-inflammatory Th2 and Treg cells and inhibition of proinflammatory Th1 and Th17 cells, to restore the balance of T cell response, are an ideal strategy for EAE therapy. In addition, for Th17 cells, ROR- γ t is the essential transcription factor of it. ROR- γ t could be activated by JAK2/STAT3 signaling and thereby promotes the CD4⁺ T cells differentiating into Th17 cells [11, 12]. Foxp3 is a key regulator of Treg cells; stable expression of Foxp3 is important for the cell development and function of Treg cells [10]. Foxp3 can inhibit the differentiation of Th17 cells through the direct interaction with ROR- γ t. Other study also shows that modulation of JAK2/STAT3 signaling activity could regulate the balance of Th17 and Treg cells [13, 14].

Ginsenoside Rd is a dammarane-type steroid glycoside extracted from a traditional Chinese herbal medicine, Panax notoginseng (*Panax notoginseng* (Burk.) F.H.Chen). Accumulation studies evidence the multiple pharmacological effects of Ginsenoside Rd, including the application in inflammatory diseases, metabolic diseases, immune regulation, and CNS [15–17]. Particularly, Ginsenoside Rd is a promising neuroprotective agent. It can attenuate the cerebral ischemia-induced BBB damage and spinal cord injury-induced secondary injury through reversing the redox-state imbalance, inhibiting the inflammatory response and apoptosis in the spinal cord tissue of rat model [18, 19]. Other study shows that Ginsenoside Rd has the ability to regulate the Th1/Th2 immune responses [20]. Our previous study of Ginsenoside Rd on EAE animal model shows that Ginsenoside Rd effectively ameliorated the clinical severity in EAE mice, reduced the permeability of the BBB, regulated the secretion of IFN- γ and IL-4, and promoted the Th2 shift in cerebral cortex and splenocytes [21]. It indicated the potential of Ginsenoside Rd in inhibiting the clinical course of EAE, but the underlying mechanism remains unclear. Therefore, in this study, we further investigate the therapeutic effect of Ginsenoside Rd in EAE *in vivo* and *in vitro* and also hope to clarify the potential mechanisms underlying the efficacy of Ginsenoside Rd in alleviating the injury of EAE. Based on this study, we hypothesize that Ginsenoside Rd could be a potential and promising agent for MS treatment.

2. Materials and Methods

2.1. Animals and Regents. C57BL/6 mice, 6–8 weeks of age, were purchased from the Shanghai SLAC Laboratory Animal Co. Ltd. (Certificate No. SCXK (Hu) 2013-0018; Shanghai, China) and housed under specific pathogen-free conditions with a 12 h light/dark cycle. The mice have free access to food and water, and all experimental procedures were conducted in accordance with the Institutional Animal Care and Use Committee Guidelines of Zhejiang Chinese Medical University (Hangzhou, China).

Ginsenoside Rd with a purity of 98% was purchased from Nanjing Zelang Medical Technology (Nanjing, China). Myelin oligodendrocyte glycoprotein (MOG)_{35–55} peptide was synthesized by Meilian Biotechnological Co., Ltd. (Xi'an, China), and the purity of the peptide was greater than 95%. *Mycobacterium tuberculosis* H37RA was obtained from Difco (Germany). Pertussis toxin (PTX) was purchased from Alexis (San Diego, CA). Complete Freund's adjuvant (CFA) was purchased from Sigma-Aldrich (St. Louis, USA).

2.2. EAE Induction and Treatment. The induction of EAE was performed by C57BL/6 mice immunized with a MOG peptide, and the protocols were referenced to the published study [20]. Briefly, 200 μ g MOG_{35–55} peptide was emulsified in CFA containing 500 μ g *Mycobacterium tuberculosis* H37RA and percutaneous injected to C57BL/6 mice. This protocol was repeat at 7 days later. At the same time, mice were also i.p. injected with 0.1 ml PBS containing 300 ng PTX, and this protocol was repeat after 48 h. At day 13 of immunization, Ginsenoside Rd was dissolved into PBS and i.p. injected to the EAE mice at a dosage of 40 mg/kg/d. The dosage of Ginsenoside Rd was referenced to our previous study [21]. Mice in control group ($n = 10$) were percutaneous and injected with same volume of PBS (i.p.). During the day of 0 to 35 of the experiment, mice in EAE group ($n = 10$) and EAE + Ginsenoside Rd group ($n = 10$) were examined daily for disease signs by clinical scores. Researchers were blinded to experimental conditions and assigned scores on a scale of 0–5 as follows [22]: 0, no signs; 1, loss of tail tonicity; 2, flaccid tail; 3, ataxia and/or paresis of hind limbs; 4, complete paralysis of hind limbs; and 5, moribund or death.

2.3. Tissue Preparation and Splenocyte Isolation. On the day 20 postimmunization, 6 mice in each group were euthanized; the blood was collected from the abdominal cavity and centrifuged at 2,500 rpm for 15 min to obtain the serum sample. The lumbar spinal cords were harvested after PBS perfusion and immediately frozen in liquid nitrogen and stored at -80°C. Splenic cells were also isolated from the spleen tissues of different groups on day 20 postimmunization. Briefly, spleen tissues in each group were removed and ground; then, the chopped spleen tissues were passed through a 70 μ m nylon mesh cell strainer, washed with RPMI-1640, to obtain a splenocytes suspension. Then, the cells (2×10^6 /well) in each group were incubated in RPMI 1640 medium containing 10% FBS. 10 μ g/ml of MOG_{35–55} was added for immunization, and cell supernatants were collected after 48 h for further ELISA and flow cytometry assay.

2.4. Histopathological Assessment. The spinal cord tissues were fixed in 4% paraformaldehyde and embedded in paraffin to cut into 5 μ m sections. Then, the spinal cord sections were stained with hematoxylin and eosin (H&E) for routine evaluation of histopathological changes and inflammation and were stained with luxol fast blue (LFB) for the evaluation of demyelination. In addition, semiquantitative analysis was also used to assess the degree of inflammation and demyelination. A 0–3 scale was used to assess the HE stained sections for inflammation [23]: 0, no inflammatory cells; 1, a few

TABLE 1: Primers for qRT-PCR.

Target bacteria	Forward	Reverse
Total gut bacteria	5'-TCCTACGGGAGGCAGCAGT-3'	5'-GGACTACCAGGGTATCTAATCCTGTT-3'
<i>Escherichia</i>	5'-GTTAATACCTTTGCTCATTGA-3'	5'-ACTCGTTTCTACTTCCCATTGT-3'
<i>Bacteroid</i>	5'-CACGAAGAACTCCGATTG-3'	5'-CACTTAAGCCGACACCT-3'
<i>Saccharomycetes</i>	5'-GAAGAGTCGAGTTGTTGGGAA-3'	5'-TCCTTCCCTTTCAACAATTTAC-3'
<i>Streptococcus</i>	5'-AGCAGTAGGGAATCTTCCA-3'	5'-CGCCACTGGTGTTCYTCCATATA-3'
<i>Lactobacillus</i>	5'-AGCAGTAGGGAATCTTCCA-3'	5'-CGCCACTGGTGTTCYTCCATATA-3'

scattered inflammatory cells; 2, organisation of perivascular inflammatory infiltrates; and 3, extensive perivascular cuffing with extension into adjacent parenchyma or parenchymal infiltration without obvious cuffing. Demyelination in the LFB stained spinal cords was scored according to the following [24]: 1, traces of subpial demyelination; 2, marked subpial and perivascular demyelination; 3, confluent perivascular or subpial demyelination; 4, massive perivascular and subpial demyelination involving one half of the spinal cord with presence of cellular infiltrates in the CNS parenchyma; and 5, extensive perivascular and subpial demyelination involving the whole cord section with presence of cellular infiltrates in the CNS parenchyma.

2.5. Immunofluorescence Staining. The expression of MBP in spinal cord tissues was also evaluated using immunofluorescence staining. The spinal cord sections in each group were firstly incubated in blocking solution (3% donkey serum, 0.3% Triton X-100 in PBS) for 30 min and stained with primary antibodies anti-MBP (dilution ratio, 1:200; Abcam, UK) at 4°C overnight. Then, the sections were further incubated with secondary antibody to goat anti-rabbit. DAPI was used to stain the DNA in the nucleus. Sections were imaged by a Nikon Eclipse Ti-SR inverted fluorescence microscopy (Nikon, Japan), and the quantification of the fluorescence intensity was analyzed by the ImageJ software.

2.6. Quantitative Real-Time PCR Analysis (qRT-PCR). Total DNA was isolated from the collected feces using QIAamp kit (QIAGEN, Germany) according to the manufacturer's instructions. qRT-PCR was performed using the Applied Biosystems 7500 Real-Time PCR System with LightCycler® 96 Real-time PCR (Roche, Switzerland). The reaction condition was 95°C, 15 s, 60°C, 60 s, and 40 circles. The sequences of the primers are listed in Table 1.

2.7. Treatment in Splenocytes. The isolated splenocytes from the EAE group were cultured in RPMI-1640 medium supplemented with 10% FBS in a 5% CO₂ incubator at 37°C. Then, the splenocytes were divided into two groups: vehicle group and Ginsenoside Rd group. The vehicle group splenic cells were incubated with 10 µg/ml of MOG₃₃₋₃₅ for 48 h. The Ginsenoside Rd group splenic cells were incubated with 10 µg/ml of MOG₃₃₋₃₅ and Ginsenoside Rd (50 µM) for 48 h.

2.8. ELISA Assay. The concentrations of IL-17, IL-6, TGF-β, and IL-10 in the serum samples and the supernatants of sple-

nocytes were determined using ELISA assay with the corresponding cytokine-specific detection kits, following the manufacturer's instructions.

2.9. Flow Cytometry Assay. Splenocytes were used to analyze the CD4⁺ T cells. First, splenocytes were incubated with fluorochrome-conjugated antibodies (Abs) to CD4, CD25 (BioLegend, USA), or isotype control Abs for 30 min on ice to make surface-marker stain. Splenocytes were then stimulated with 50 ng/ml phorbol myristate acetate (PMA) and 500 ng/l ionomycin in the presence of Golgi-Plug for 5 h. After cell surface-stained, fixed, and permeabilized, intracellular cytokines staining was conducted, and cells were stained with Abs to IL-17A (BioLegend, USA) for Th17 cells and Foxp3 (BioLegend, USA) for Treg cells, respectively. Then, followed by flow cytometry analysis using a flow cytometer (C6, BD, USA) and data were analyzed with the FlowJo software Vision 10 (Beckman).

2.10. Western Blotting Analysis. To investigate the expressions of ROR-γt/Fox3/JAK2/STAT3 signaling in the lumbar spinal cord and splenocytes of differently treated groups, western blot analysis was performed. The spinal cord tissues or splenic cells were lysed with RIPA lysis buffer (Beyotime, China) in ice-cold, and the concentrations of proteins in tissues or cells were measured using a BCA protein assay reagent kit (Solarbio, China). Then, equal amounts of protein samples were loaded on 10% gradient sodium dodecyl sulfate-polyacrylamide gels (SDS-PAGE) for electrophoresing and transferred onto polyvinylidene fluoride (PVDF) membrane. The membranes were blocked with 5% nonfat milk, washed with TBST buffer three times, and then followed by incubation overnight with primary antibodies (anti-JAK1 antibody: 1:5000, anti-JAK2 antibody: 1:5000, anti-FOXP3 antibody: 1:1000, anti-RORγt antibody: 1:2000, anti-STAT3 antibody: 1:1000, anti-GAPDH antibody: 1:5000; Abcam, UK; anti-phospho-JAK1 (Tyr1125) antibody: 1:1000, anti-phospho-JAK2 (Tyr931) antibody: 1:1000, anti-phospho-STAT3 (Tyr705) antibody: 1:1000; Affinity, USA) at 4°C. After the incubation and washed with TBST buffer three times, the membranes were incubated with goat anti-rabbit-HRP for 30 min. Then, the enhanced chemiluminescence reagents were employed to detect chemiluminescence signals; the protein bands were quantified using the ImageJ software. The experiment was repeated in triplicate and used GAPDH as internal control.

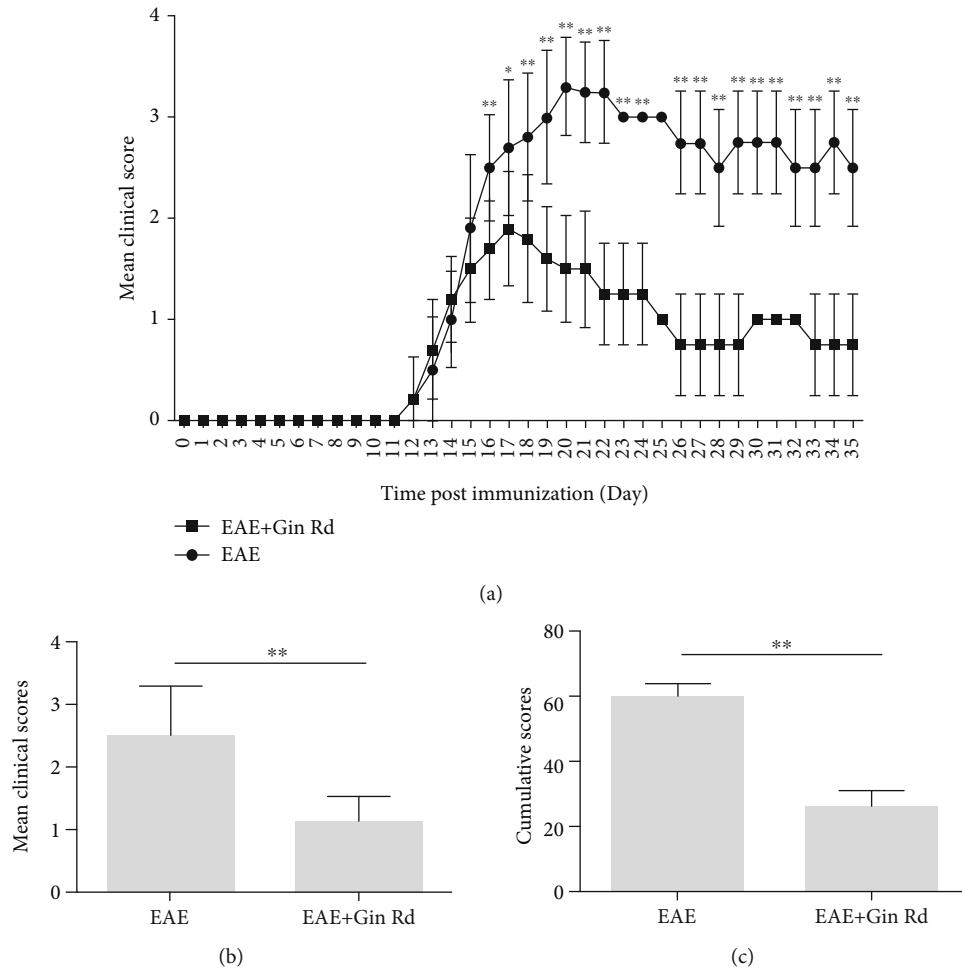


FIGURE 1: Treatment with Ginsenoside Rd ameliorated the clinical severity of experimental autoimmune encephalomyelitis (EAE) mice. Following immunization and treatment with Ginsenoside Rd, daily clinical scores of EAE mice with or without Ginsenoside Rd treatment were recorded over the course of the 35-day experiment: (a) daily clinical scores of EAE mice with or without Ginsenoside Rd treatment; (b) mean clinical scores of EAE mice with or without Ginsenoside Rd treatment; (c) cumulative clinical scores of EAE mice with or without Ginsenoside Rd treatment. * $P < 0.05$, ** $P < 0.01$ vs. EAE group. Gin Rd: Ginsenoside Rd.

2.11. Statistical Analysis. Data are expressed as the means \pm standard deviation (SD). Differences between the two groups were analyzed using Student t -test; differences among the more than two groups were analyzed by conducting one-way ANOVA followed by analysis followed by SNK test using the SPSS 18.0 software (SPSS, USA). P values < 0.05 were considered statistically significant.

3. Results

3.1. Treatment with Ginsenoside Rd Ameliorated the Clinical Severity of EAE Mice. First, the potential effect of Ginsenoside Rd on clinical course of EAE was assessed. Following immunization and with Ginsenoside Rd treatment or vehicle alone, daily clinical scores of EAE mice were recorded over the course of the 35-day experiment. As showed in Figure 1(a), the EAE model group and EAE + Gin Rd group of mice began to develop clinical signs of EAE about on day 11 postimmunization, and the scores were increased continuously for several days, maintained for several days, and then decreased. As

a result, the daily clinical scores in the EAE + Gin Rd group were lower than those in the EAE model group mice. Moreover, the mean clinical score and cumulative score in the EAE + Gin Rd group were all significantly lower than those in the EAE model group of mice (Figures 1(b) and 1(c)).

3.2. Treatment with Ginsenoside Rd Improved the Histopathology Outcomes of EAE Mice. The histopathology changes of spinal cord from different groups of mice were also examined on day 20 postimmunization. H&E and LBP staining were performed to detect the spinal cord inflammatory infiltrates and demyelination in mice, respectively. H&E staining (Figure 2(a)) showed that there were numerous inflammatory cells infiltrated in the spinal cord tissue sections of the EAE group compared to the normal control group; semiquantitative analysis also showed that the inflammation degree was significantly increased. While in the Ginsenoside Rd-treated group, the infiltration of inflammatory cells was alleviated; the histopathology score of inflammation was also significantly lower compared to the EAE group. LBP

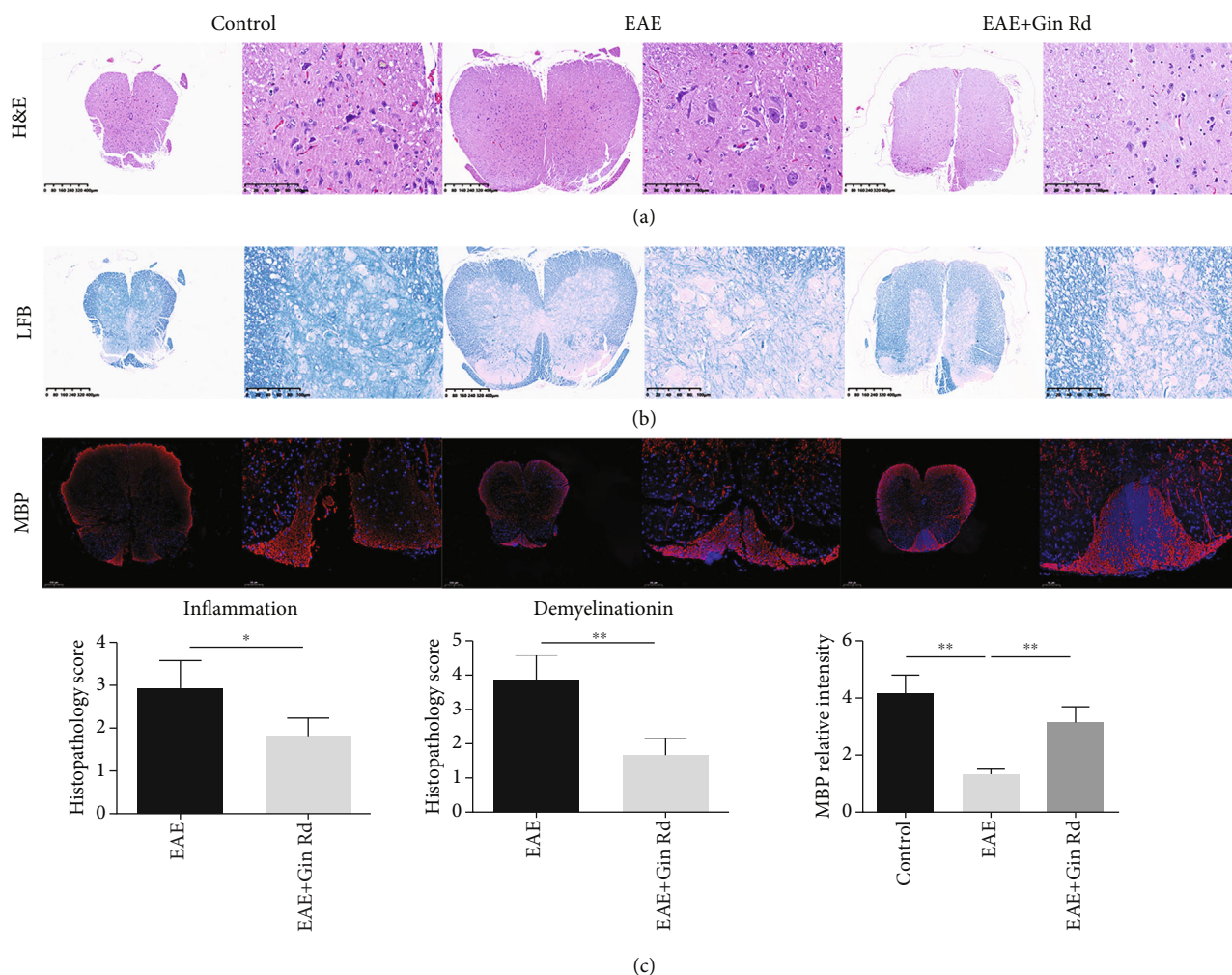


FIGURE 2: Ginsenoside Rd treatment ameliorated the severity of EAE via inhibiting spinal cord inflammation and demyelination. Following immunization and treatment with Ginsenoside Rd, some mice from the control, EAE, and Ginsenoside Rd-treated EAE groups were subjected to histopathological assay at day 20 postimmunization. Spinal cord tissue sections were stained with H&E or LBP, respectively. In addition, the degrees of inflammatory infiltrates and demyelination were semiquantitatively analyzed. Data are expressed as the mean \pm SD for each group ($n = 3$). (a) H&E analysis of the spinal cord sections. Magnification $\times 40$, 200. (b) LBP analysis of the spinal cord sections. Magnification $\times 40$, 200. (c) MBP immunofluorescence staining of the spinal cord sections. Tissue sections of spinal cord from each group mice were stained with antibodies against MBP (red) and DAPI (blue, nucleus). Magnification $\times 50$, 200. * $P < 0.05$, ** $P < 0.01$ vs. EAE group. Gin Rd: Ginsenoside Rd.

staining (Figure 2(b)) showed that there was demyelination in the spinal cord tissues of EAE mice; semiquantitative analysis revealed that the demyelination score was significantly increased compared to the control mice. With the treatment of Ginsenoside Rd, the degree of demyelination was alleviated; the pathological scores of demyelination were also lower than that in the EAE mice. MBP staining also showed that the relative expression of MBP was decreased in the EAE group of mice, and Ginsenoside Rd treatment increased the MBP expression and blocked myelin loss compared to the EAE group.

3.3. Ginsenoside Rd Treatment Suppressed the Production of Inflammatory Cytokines in EAE Mice. The concentrations of IL-6, IL-10, IL-17, and TGF- β in serum and splenocyte supernatants of mice were detected with ELISA assay, and the results were showed in Figure 3. As the results indicated,

compared to the control group, the concentrations of serum IL-6, IL-10, and IL-17 were increased significantly; TGF- β was decreased significantly (Figure 3(a)). With the treatment of Ginsenoside Rd and compared to the EAE group, it could be found that the concentrations of serum IL-6 and IL-17 were lowered significantly, but TGF- β was increased significantly. For the inflammatory cytokine levels in the splenocyte supernatants of mice, as shown in Figure 3(b), compared to the control group, the IL-6, IL-10, and IL-17 levels were increased significantly, but TGF- β was decreased significantly, while Ginsenoside Rd treatment significantly lowered the levels of IL-6 and IL-17 and increased the levels of IL-10 and TGF- β significantly compared to those in the EAE group.

3.4. Effect of Ginsenoside Rd Treatment on Treg/Th17 Cell Imbalance in EAE Mice. Further, we examined the effect of Ginsenoside Rd on T cell immunity and inflammation in

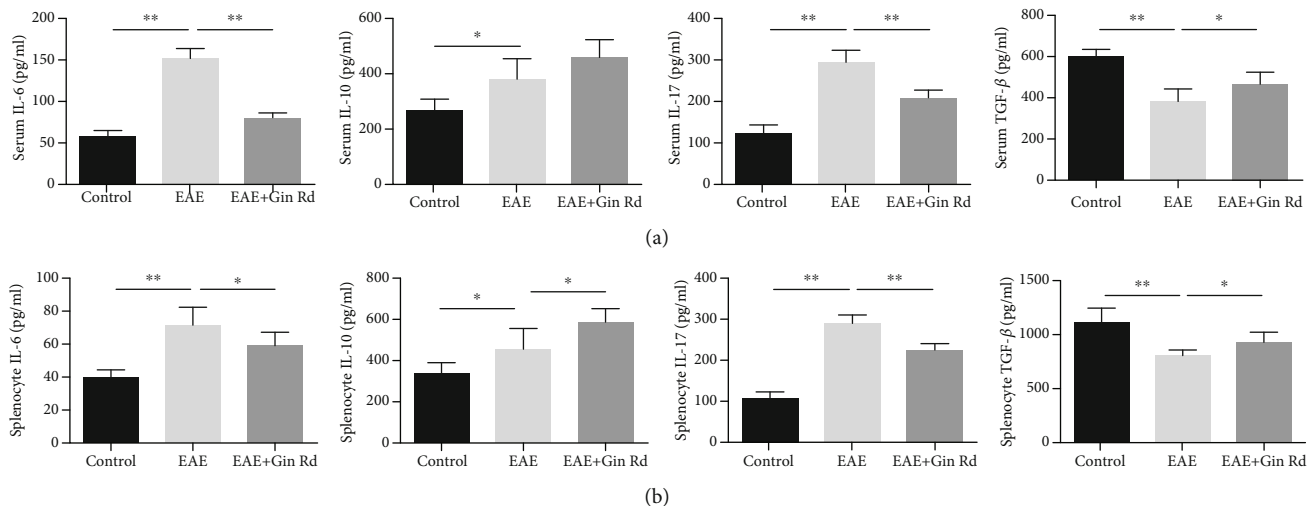


FIGURE 3: The concentrations of IL-6, IL-10, IL-17, and TGF- β in serum and splenocyte supernatants of mice ($n = 6$). Following immunization and treatment with Ginsenoside Rd, some mice from the control, EAE, and Ginsenoside Rd-treated EAE groups were sacrificed at day 20 postimmunization. Serum was collected, and splenocytes were isolated, for ELISA assay to detect the concentrations of IL-6, IL-10, IL-17, and TGF- β . Data are expressed as mean \pm SD for each group ($n = 3$). (a) ELISA analysis for the levels of IL-6, IL-10, IL-17, and TGF- β in serum of mice. (b) ELISA analysis for the levels of IL-6, IL-10, IL-17, and TGF- β in splenocyte supernatants of mice. * $P < 0.05$, ** $P < 0.01$ vs. EAE group. Gin Rd: Ginsenoside Rd.

EAE mice. Flow cytometry analysis revealed that the percentages of CD4⁺ IL-17⁺ Th17 cells in splenocytes of EAE mice were significantly increased than that in normal controls, but in the Ginsenoside Rd treatment group, the Th17 cell percentage was significantly lowered (Figure 4(a)). For Treg cells, flow cytometry analysis showed that in splenocytes of EAE mice, the percentages of CD4⁺ CD25⁺ Foxp3⁺ Treg cells were significantly increased, but in the Ginsenoside Rd treatment group, the Treg cell percentage was increased significantly (Figure 4(b)).

3.5. Gut Microbiota Changes in EAE Mice. The changes of gut microbiota in EAE mice were also detected. As showed in Figure 5, compared to the control mice, the relative contents of total gut microbiota, *bacteroid*, and *lactobacillus* were significantly decreased; *streptococcus* was significantly increased in the EAE group of mice. In the EAE + Gin Rd group treated with Ginsenoside Rd, the relative contents of total gut microbiota, *bacteroid*, and *lactobacillus* were significantly increased; *streptococcus* was decreased compared to those in the EAE group.

3.6. The Effect of Ginsenoside Rd Treatment on the Foxp3/ROR γ t/JAK2/STAT3 Signaling Pathway in EAE Mice. As the above results suggested that Ginsenoside Rd could regulate inflammation and immune responses in EAE mice, we further investigated the effect of Ginsenoside Rd on the Foxp3/ROR γ t/JAK2/STAT3 signaling pathway. Western blot assay was used to detect the protein expression levels of Foxp3, ROR γ t, p-JAK1, JAK1, p-JAK2, JAK2, p-STAT3, and STAT3 in the spinal cord of mice (Figure 6). As the results showed, the relative protein expression level of Foxp3 was significantly decreased, while ROR γ t was significantly increased in the EAE model group compared to those in

the control group. However, Ginsenoside Rd treatment significantly activated the level of Foxp3 and suppressed the level of ROR γ t compared to those in the EAE group. Furthermore, the relative expression levels of p-JAK1/JAK1, p-JAK2/JAK2, and p-STAT3/STAT3 in the spinal cord of EAE mice were significantly increased compared to those in the control group, while Ginsenoside Rd treatment inhibited the levels of p-JAK1/JAK1, p-JAK2/JAK2, and p-STAT3/STAT3 significantly.

3.7. Treatment with Ginsenoside Rd Inhibited the Inflammation and Improved Treg/Th17 Cell Imbalance in Splenocytes with EAE. ELISA assay results showed that compared to the EAE splenocytes induced with MOG₃₅₋₅₅, the concentrations of IL-17 and IL-6 were significantly lowered, and the concentrations of TGF- β and IL-10 were significantly higher in Ginsenoside Rd-treated and MOG₃₅₋₅₅-induced EAE splenocytes (Figure 7(a)). Flow cytometry analysis showed that the percentages of CD4⁺ IL-17⁺ Th17 cells were significantly lower, and the percentages of CD4⁺ Foxp3⁺ Treg cells were significantly higher in Ginsenoside Rd-treated splenocytes than those in vehicle-treated splenocytes of EAE (Figure 7(b)).

3.8. Ginsenoside Rd Treatment Regulated the Foxp3/ROR γ t/JAK2/STAT3 Signaling Pathway in Splenocytes with EAE. As the above results suggested that Ginsenoside Rd could also regulate the inflammation and Treg/Th17 cell imbalance in splenocytes with EAE, we further investigated the effect of Ginsenoside Rd on the Foxp3/ROR γ t/JAK2/STAT3 signaling pathway. Western blot assay was used to detect the protein expression levels of Foxp3, ROR γ t, p-JAK1, JAK1, p-JAK2, JAK2, p-STAT3, and STAT3 in splenocytes (Figure 8). As the results showed, the relative protein

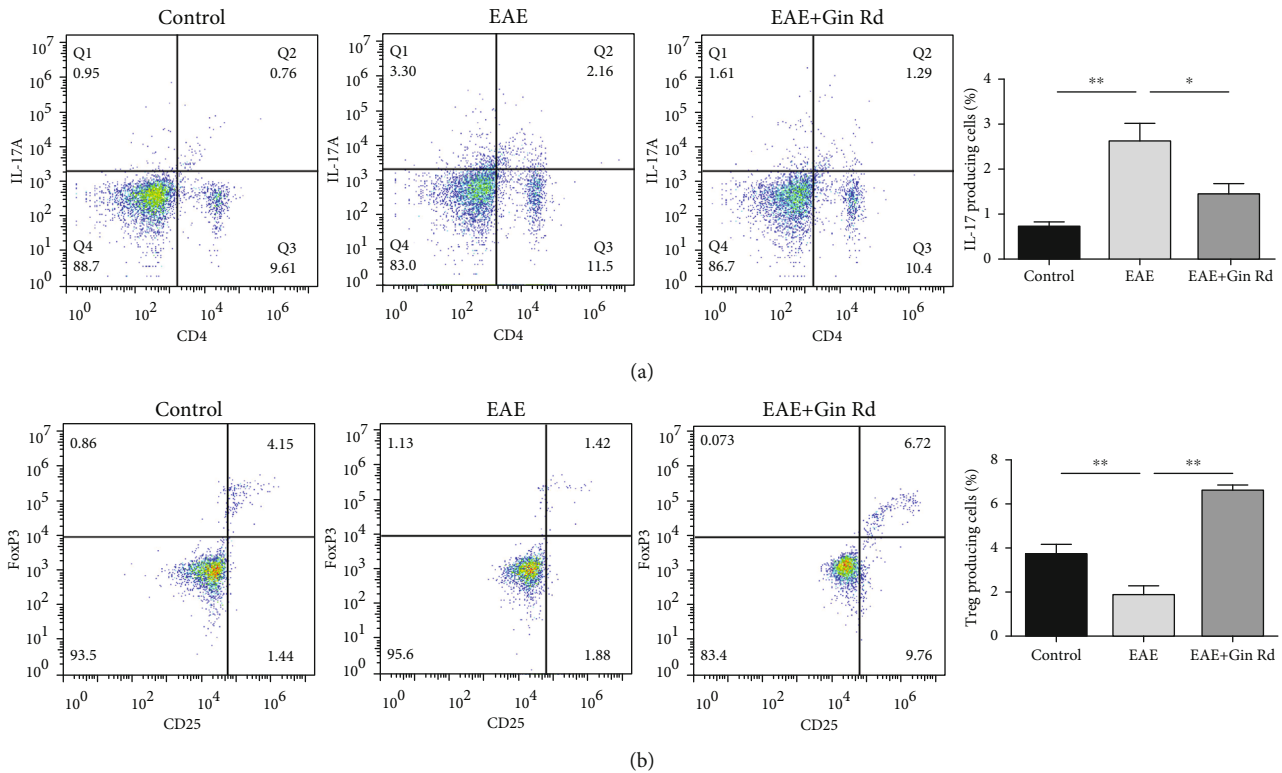


FIGURE 4: Ginsenoside Rd treatment modulates Treg/Th17 cell imbalance in EAE mice. Following immunization and treatment with Ginsenoside Rd, some mice from the control, EAE, and Ginsenoside Rd-treated EAE groups were sacrificed at day 20 postimmunization; splenocytes were isolated. The percentages of CD4+ IL-17+ Th17 cell (a) and CD4+ CD25+ Foxp3+ Treg cells (b) in each group were determined by flow cytometry ($n = 3$). Data are expressed as the mean \pm SD for each group ($n = 3$). * $P < 0.05$, ** $P < 0.01$ vs. EAE group. Gin Rd: Ginsenoside Rd.

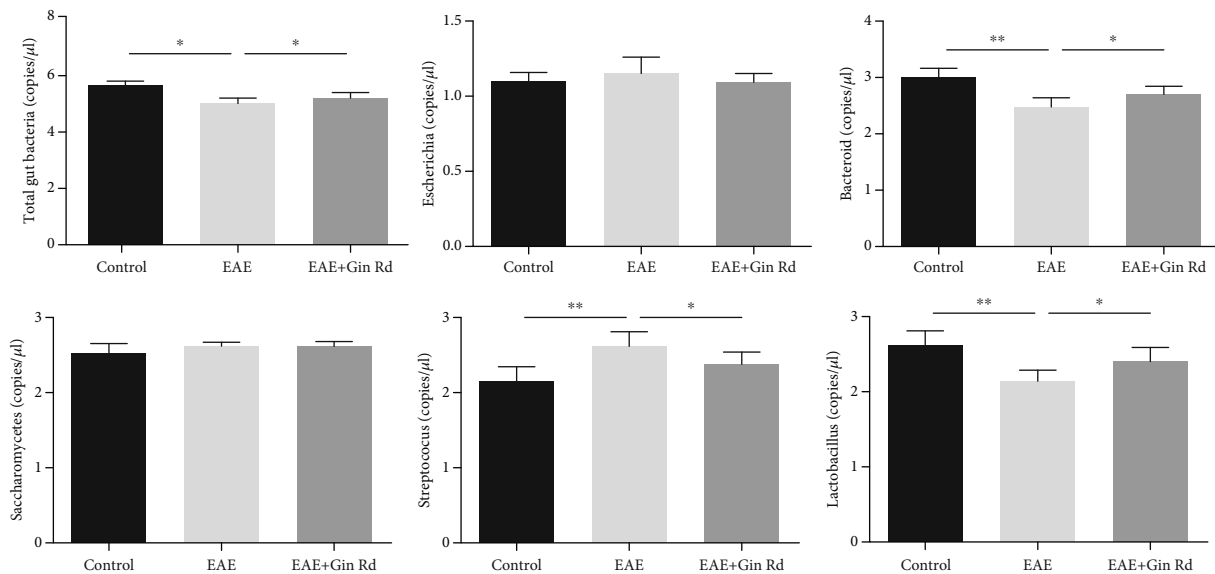


FIGURE 5: Relative content of gut bacteria in different groups by qRT-PCR analysis. Data are expressed as the mean \pm SEM of each group ($n = 3$). * $P < 0.05$, ** $P < 0.01$ vs. EAE group. Gin Rd: Ginsenoside Rd.

expression level of Foxp3 was significantly increased, while ROR γ t was significantly decreased in Gin Rd group splenocytes compared to those in vehicle group splenocytes. In addition, the relative expression levels of p-

JAK1/JAK1, p-JAK2/JAK2, and p-STAT3/STAT3 in splenocytes of the Gin Rd group were significantly suppressed compared to those in the vehicle group without Ginsenoside Rd treatment.

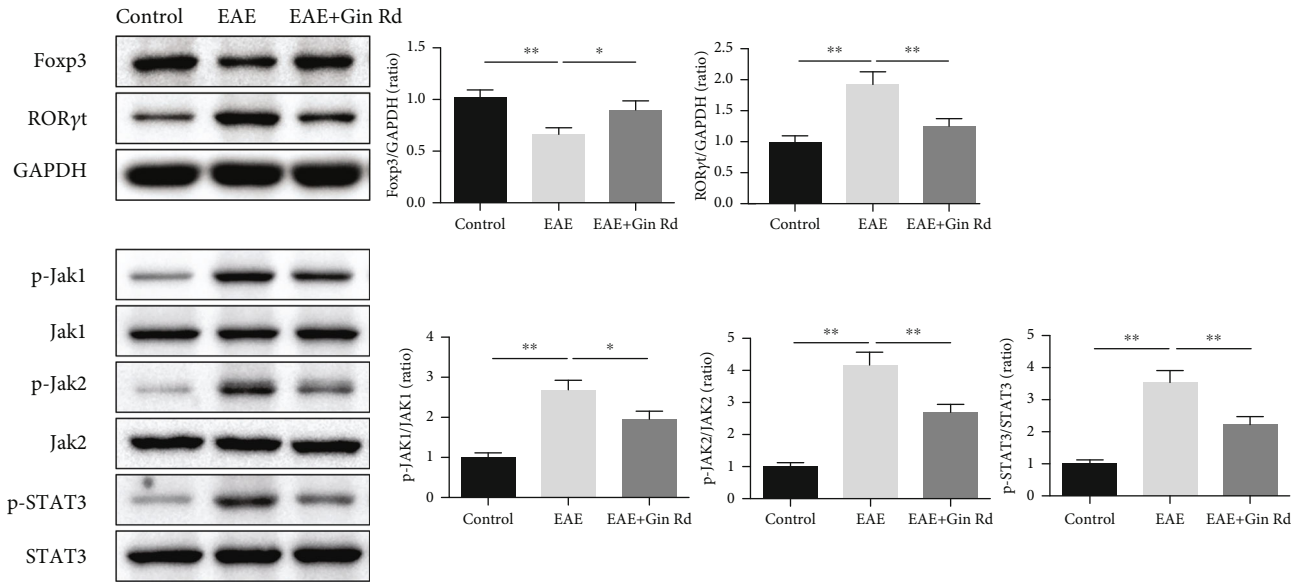


FIGURE 6: Relative protein expressions of Foxp3, ROR γ t, p-JAK1, JAK1, p-JAK2, JAK2, p-STAT3, and STAT3 in the spinal cord of EAE mice using western blotting assay ($n = 3$). GAPDH was used as the internal control. Data are expressed as the mean \pm SD for each group ($n = 3$). * $P < 0.05$, ** $P < 0.01$ vs. EAE group. Gin Rd: Ginsenoside Rd.

4. Discussion

As an autoimmune inflammatory disease, MS typically occurs in young adults and has a high risk of disability in most patients. Treatments for MS are not only costly but also have the risk of side effects. In this study, based on a widely used MS animal model-EAE, we reported that Ginsenoside Rd was effective for the treatment of EAE *in vivo* and *in vitro*. Ginsenoside Rd treatment of EAE ameliorated the severity of EAE and attenuated the characteristic signs of disease. In addition, Ginsenoside Rd displayed the therapeutic function to EAE specifically by modulating inflammation and immunity, via the inhibition of related inflammatory cytokine secretion and regulation of Treg/Th17 cell imbalance. And the Foxp3/ROR γ t/JAK2/STAT3 signaling was associated to this function in EAE.

As well acknowledged, inflammatory infiltrates and demyelination of the CNS are the major characteristics of MS and EAE animal model [1, 25]. In this study, histopathological assay by H&E and LBP staining showed that the spinal cord tissues of EAE group mice have significant inflammatory infiltrates and demyelination. And MBP is a major component of myelin sheath in CNS, with the ability of maintaining structure and function of myelin sheath [26, 27]. In particular, MBP is correlated with the severity of MS. MBP immunofluorescence staining intensity in this study was also weakened in spinal cord of EAE mice, which were consisted with the major characteristics of EAE. While in Ginsenoside Rd-treated group mice, the degrees of inflammatory infiltrates and demyelination as well as the MBP expression in spinal cord tissues were restored. These results suggested the therapeutic potential of Ginsenoside Rd to EAE. The clinical scores of EAE mice were also in accordance with these improvements in the Ginsenoside Rd-treated

group. As a natural agent, except for the various pharmacological activities, Ginsenoside Rd is also a promising anti-inflammation and neuroprotective agent [15, 28]. Clinical studies in healthy volunteers and in patients with neurological disease or deficit showed that ginsenosides, including Ginsenoside Rd, can affect neurotransmission and neuroprotection [29]. López et al. reported that ginsenosides induce neuroprotection effect on astrocytes mainly through the activation of antioxidant enzymes [30]. In addition, our previous study of Ginsenoside Rd on EAE mice also showed that Ginsenoside Rd effectively ameliorated the clinical severity of EAE mice and reduced the permeability of BBB, which also proved the neuroprotective and therapeutic potential of Ginsenoside Rd on MS [20].

The immoderate autoimmune responses of Th17 cells and dysfunction of Treg cells critically contribute to the pathogenesis of MS and EAE [31]. Th17 cell is a proinflammatory subset of Th cells and contributes to autoimmunity, inflammatory response, and tissue damage; in contrast, Treg cell has anti-inflammatory properties and confers protective effects on CNS [32]. Therefore, modulation of Th17/Treg balance is an ideal strategy for EAE therapy. In this study, except for the amelioration effect of Ginsenoside Rd on clinical severity of EAE, the regulation potentiality on Th17 and Treg cells as well as associated proinflammatory and anti-inflammatory cytokines by Ginsenoside Rd was investigated. As the flow cytometry results indicated, Ginsenoside Rd modulated the percentages of Treg and Th17 cells in splenocytes of EAE and thus improved the Treg/Th17 cell imbalance. Furthermore, Treg and Th17 cell characteristic cytokines, IL-17 and TGF- β , as well as IL-6 and IL-10, the characteristic cytokines of Th1/2 cells, their concentrations in serum and splenocytes were also restored with the treatment of Ginsenoside Rd.

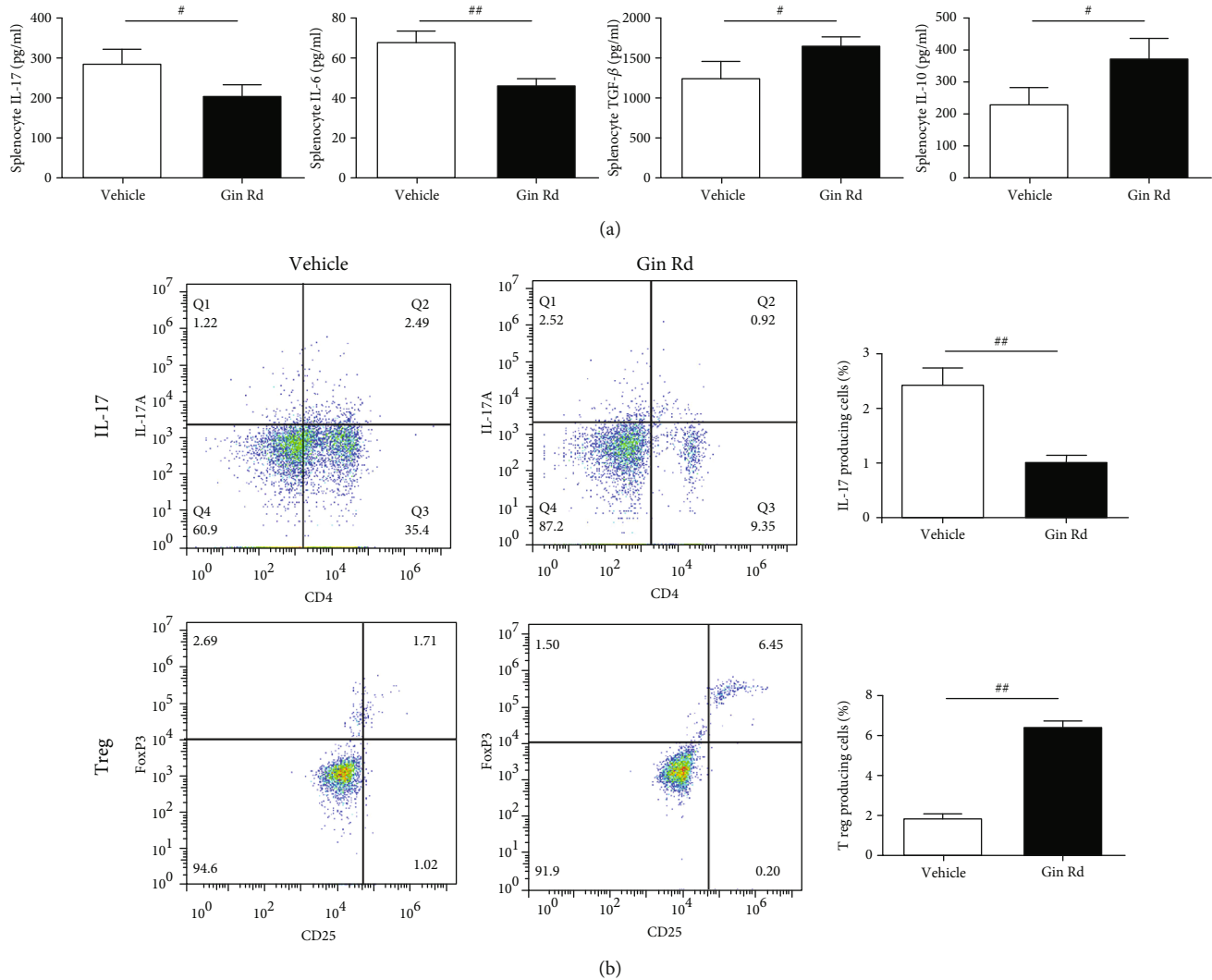


FIGURE 7: The effect of Ginsenoside Rd on inflammatory cytokine levels and Treg/Th17 cell percentages in splenocytes of EAE. Splenocytes were isolated from EAE mice and further treated with 10 $\mu\text{g/ml}$ of MOG₃₃₋₃₅ for 48 h, with or without Ginsenoside Rd (50 μM). (a) ELISA assay for detection of the levels of IL-6, IL-10, IL-17, and TGF- β in splenocyte supernatants ($n = 3$). (b) Flow cytometry assay for detection the percentages of CD4⁺ IL-17⁺ Th17 and CD4⁺ Foxp3⁺ Treg cells in splenocytes ($n = 3$). Data are expressed as the mean \pm SEM of each group ($n = 3$). [#] $P < 0.05$, ^{##} $P < 0.01$ vs. vehicle group. Gin Rd: Ginsenoside Rd.

The integrity of BBR is an important prerequisite for normal function of CNS, but Th17 cells could disrupt BBR by the action of IL-17. IL-17 can act on endothelial cells directly, sequentially disrupts the BBR tight junctions and integrity, and promotes inflammatory infiltrates and tissue damage of CNS via Th17 lymphocytes recruitment [33, 34]. IL-17 also induces the production of cytokines, such as IFN- γ , IL-1, and IL-6 that facilitating inflammatory cell infiltration into the CNS [35]. Thereby, the lower levels of IL-17 production may inhibit the functional development of Th17 cells in EAE. Besides, as a crucial transcriptional regulator of Th17 cell differentiation, the suppression on ROR γt transcription could result in the inhibition on Th17 cell differentiation and function [36]. In present study, we evaluated the differentiation of Th17 cells by examining the percentage of Th17 cells, as well as the production of IL-17 in activated

splenocytes of mice with EAE. As a result, Ginsenoside Rd treatment modulated the population of Th17 cells and production of IL-17; the protein expressions of ROR γt in the spinal cord and splenocytes of EAE mice were also decreased, indicated that Ginsenoside Rd inhibited the antigen-specific Th17 responses in EAE via the inhibition of IL-17, IL-6, and ROR γt expression. As a subset of ginsenosides, Park et al. study showed that Ginsenoside Rg3 alleviated the onset and severity of EAE by significantly inhibited the Th17 differentiation and Th17-mediated neuro-inflammation and hampered the expression of IL-17A and ROR γt in T cells [37].

In contrast, Treg cells are negative regulators of autoimmune diseases and play a critical role in the maintenance of self-tolerance. Treg cells induce to the production of inhibitory cytokines TGF- β and IL-10, protect against inflammatory infiltrates and tissues damage [38]. A disturbance in

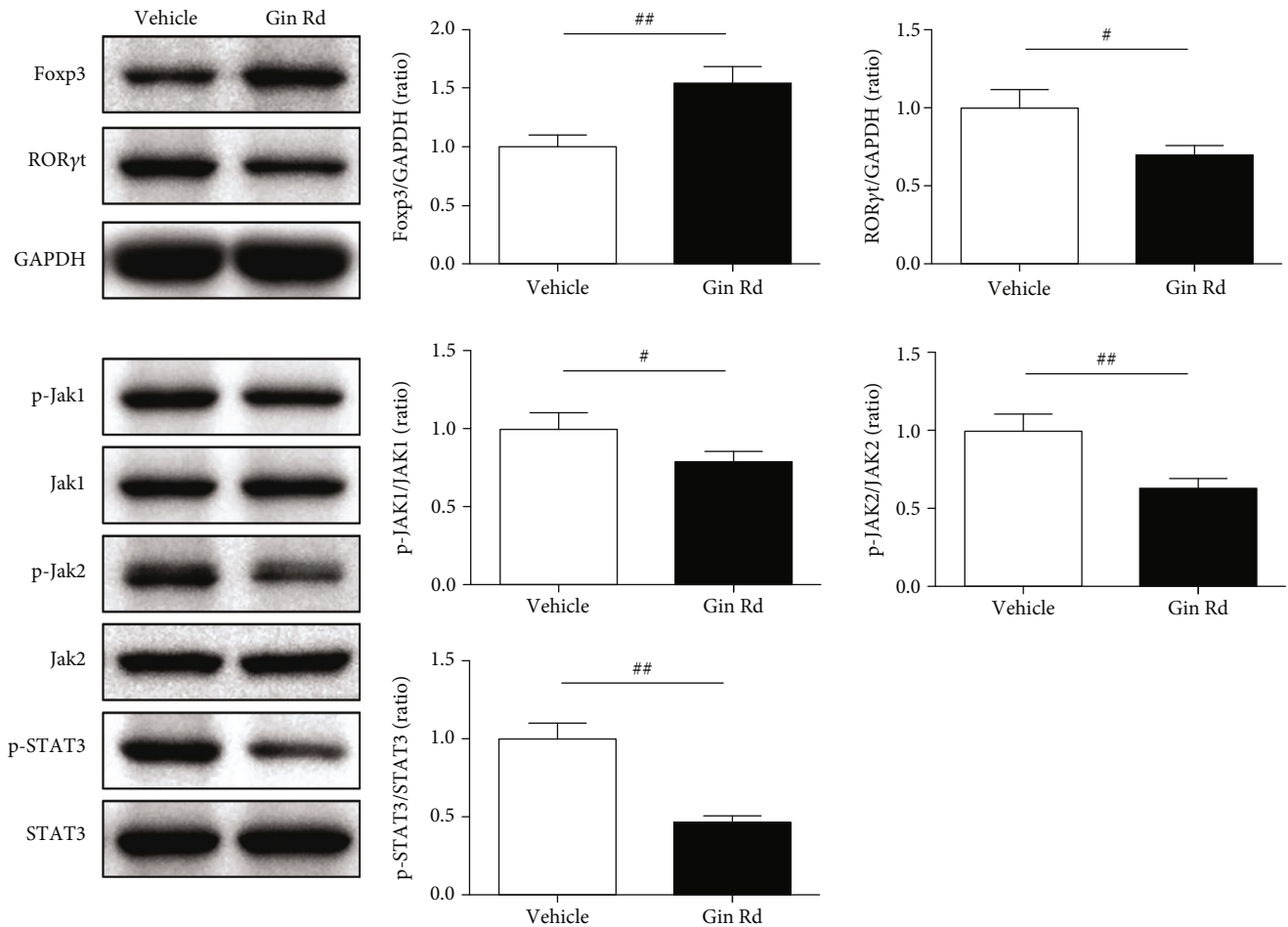


FIGURE 8: Relative protein expression of Foxp3, ROR γ t, p-JAK1, JAK1, p-JAK2, JAK2, p-STAT3, and STAT3 in splenocytes of EAE using western blotting assay ($n = 3$). GAPDH was used as the internal control. Data are expressed as the mean \pm SEM of each group ($n = 3$). * $P < 0.05$, ** $P < 0.01$ vs. vehicle group. Gin Rd: Ginsenoside Rd.

the function and percentage of the Treg cells is associated with the severity of disease in relapsing MS [39]. Korean red ginseng extract, which is abundant with ginsenosides, was demonstrated to significantly reduce the population of CD4+, CD4+/IFN- γ +, and CD4+IL-17+ T cells, increase the population of Treg cells in the spinal cord and lymph nodes, corresponding to the downregulation of the mRNA expression of IFN- γ , IL-17, and IL-23 and upregulation of the mRNA expression of Foxp3 in the spinal cord of EAE [40]. Kim et al. reported that Ginsenoside Rd could induce Treg cell differentiation by upregulating the Foxp3 expression and increasing the generation of TGF- β 1, IL-10, and IL-35 [41]. In this study, we found that Ginsenoside Rd treatment modulated the population of Treg cells in activated splenocytes, and productions of TGF- β 1 and IL-10 were also increased. As a key regulator of Treg cells, the protein expressions of Fox3 in the spinal cord and splenocytes of EAE mice were also activated. Furthermore, the protein expressions of JAK2/STAT2 signaling that is proved to rectify the imbalance of Th17/Treg cells were also regulated with the treatment of Ginsenoside Rd. These results indicated that Ginsenoside

Rd upregulated the levels of TGF- β 1, IL-10, and Fox3; down-regulated the levels of IL-17A, IL-6, and ROR γ t; and changed the percentage of Th17 and Treg cells in EAE and thus improving Treg/Th17 cell imbalance in EAE.

Furthermore, the present study also investigated the gut microbiota changes in EAE mice. The results showed that the gut microbiota was changed in EAE mice, and Ginsenoside Rd treatment restored partly. The gut microbiota plays an essential role in the occurrence and development of the immune system in EAE; it appears to be involved in modulating the host's immune system, altering the integrity and function of the BBB, triggering autoimmune demyelination, expressing myelin genes, and interacting directly with different cell types in the CNS [42, 43]. Our study showed that the *bacteroid* and *lactobacillus* were decreased in EAE mice, which was consisted with the previous studies [44, 45]. Ginsenoside Rd treatment restored the decreased content of *bacteroid*, *lactobacillus*, and total gut bacteria, indicated a potential regulation effect of on EAE mice. In addition, this indicated that microbiota therapy restoration of the microbial population in patients with MS also provides possibility for MS treatment.

5. Conclusions

In summary, based on EAE model induced by MOG₃₅₋₅₅, this study indicated that Ginsenoside Rd was effective for the treatment of EAE *in vivo* and *in vitro*. Ginsenoside Rd treatment of EAE ameliorated the severity of EAE and attenuated the characteristic signs of disease. In addition, Ginsenoside Rd displayed the therapeutic function to EAE specifically by modulating inflammation and autoimmunity, via the down-regulation of related proinflammatory cytokines IL-6 and IL-17, upregulation of inhibitory cytokines TGF- β and IL-10, and regulation of Treg/Th17 imbalance. And the Foxp3/ROR γ t/JAK2/STAT3 signaling was associated to this protective function of Ginsenoside Rd in EAE. According to this finding, we hypothesized that Ginsenoside Rd could be a potential and promising agent for the treatment of MS.

Data Availability

The data used to support the findings of this study are included within the article.

Conflicts of Interest

The authors declare that there is no conflict of interest regarding the publication of this paper.

Authors' Contributions

Bo Jin and Chixiao Zhang contributed equality to this work.

Acknowledgments

This work was supported by the Zhejiang Natural Science Foundation Youth Project, China (LQ19H090013), and the Key Laboratory of Neuropsychiatric Drug Research of Zhejiang Province, China (2019E10021), the National Natural Science Foundation of China (82001366) and the Natural Science Foundation of Zhejiang Province, China (LQ20H090019).

References

- [1] I. K. Sand, "Classification, diagnosis, and differential diagnosis of multiple sclerosis," *Current Opinion in Neurology*, vol. 28, no. 3, pp. 193–205, 2015.
- [2] C. Gu, "KIR4.1: K⁺ channel illusion or reality in the autoimmune pathogenesis of multiple sclerosis," *Frontiers in Molecular Neuroscience*, vol. 9, p. 90, 2016.
- [3] M. Sospedra and R. Martin, "Immunology of multiple sclerosis," *Annual Review of Immunology*, vol. 23, no. 1, pp. 683–747, 2005.
- [4] D. S. Goodin, A. T. Reder, R. A. Bermel et al., "Relapses in multiple sclerosis: relationship to disability," *Multiple Sclerosis and Related Disorders*, vol. 6, pp. 10–20, 2016.
- [5] Q. Shen, H. Lu, D. Xie, H. Wang, Q. Zhao, and Y. Xu, "Association between suicide and multiple sclerosis: an updated meta-analysis," *Multiple Sclerosis and Related Disorders*, vol. 34, pp. 83–90, 2019.
- [6] C. S. Constantinescu, N. Farooqi, K. O'Brien, and B. Gran, "Experimental autoimmune encephalomyelitis (EAE) as a model for multiple sclerosis (MS)," *British Journal of Pharmacology*, vol. 164, no. 4, pp. 1079–1106, 2011.
- [7] A. L. Zozulya and H. Wiendl, "The role of regulatory T cells in multiple sclerosis," *Nature Clinical Practice Neurology*, vol. 4, no. 7, pp. 384–398, 2008.
- [8] J. Zepp, L. Wu, and X. Li, "IL-17 receptor signaling and T helper 17-mediated autoimmune demyelinating disease," *Trends in Immunology*, vol. 32, no. 5, pp. 232–239, 2011.
- [9] G. Ntolkeras, C. Barba, A. Mavropoulos et al., "On the immunoregulatory role of statins in multiple sclerosis: the effects on Th17 cells," *Immunologic Research*, vol. 67, no. 4-5, pp. 310–324, 2019.
- [10] K. Venken, N. Hellings, R. Liblau, and P. Stinissen, "Disturbed regulatory T cell homeostasis in multiple sclerosis," *Trends in Molecular Medicine*, vol. 16, no. 2, pp. 58–68, 2010.
- [11] Z. Chen, F. Lin, Y. Gao et al., "FOXP3 and ROR γ t: transcriptional regulation of Treg and Th17," *International Immunopharmacology*, vol. 11, no. 5, pp. 536–542, 2011.
- [12] I. I. Ivanov, B. S. McKenzie, L. Zhou et al., "The orphan nuclear receptor ROR γ t directs the differentiation program of proinflammatory IL-17⁺ T helper cells," *Cell*, vol. 126, no. 6, pp. 1121–1133, 2006.
- [13] J.-S. Park, J. Lee, M.-A. Lim et al., "JAK2-STAT3 blockade by AG490 suppresses autoimmune arthritis in mice via reciprocal regulation of regulatory T cells and Th17 cells," *Journal of Immunology*, vol. 192, no. 9, pp. 4417–4424, 2014.
- [14] Y. Zheng, Z. Wang, L. Deng et al., "Modulation of STAT3 and STAT5 activity rectifies the imbalance of Th17 and Treg cells in patients with acute coronary syndrome," *Clinical Immunology*, vol. 157, no. 1, pp. 65–77, 2015.
- [15] J. H. Kim, Y.-S. Yi, M.-Y. Kim, and J. Y. Cho, "Role of ginsenosides, the main active components of Panax ginseng, in inflammatory responses and diseases," *Journal of Ginseng Research*, vol. 41, no. 4, pp. 435–443, 2017.
- [16] S. F. Nabavi, A. Sureda, S. Habtemariam, and S. M. Nabavi, "Ginsenoside Rd and ischemic stroke; a short review of literatures," *Journal of Ginseng Research*, vol. 39, no. 4, pp. 299–303, 2015.
- [17] L. Yao, Z. Han, G. Zhao et al., "Ginsenoside Rd ameliorates high fat diet-induced obesity by enhancing adaptive thermogenesis in a cAMP-dependent manner," *Obesity*, vol. 28, no. 4, pp. 783–792, 2020.
- [18] X. Zhang, X. Liu, G. Hu, G. Zhang, G. Zhao, and M. Shi, "Ginsenoside Rd attenuates blood-brain barrier damage by suppressing proteasome-mediated signaling after transient forebrain ischemia," *NeuroReport*, vol. 31, no. 6, pp. 466–472, 2020.
- [19] L. Cong and W. Chen, "Neuroprotective effect of Ginsenoside Rd in spinal cord injury rats," *Basic & Clinical Pharmacology & Toxicology*, vol. 119, no. 2, pp. 193–201, 2016.
- [20] Z. Yang, A. Chen, H. Sun, Y. Ye, and W. Fang, "Ginsenoside Rd elicits Th1 and Th2 immune responses to ovalbumin in mice," *Vaccine*, vol. 25, no. 1, pp. 161–169, 2007.
- [21] D. Zhu, M. Liu, Y. Yang et al., "Ginsenoside Rd ameliorates experimental autoimmune encephalomyelitis in C57BL/6 mice," *Journal of Neuroscience Research*, vol. 92, no. 9, pp. 1217–1226, 2014.
- [22] X. Chen, R. Pi, M. Liu et al., "Combination of methylprednisolone and minocycline synergistically improves experimental autoimmune encephalomyelitis in C57 BL/6 mice," *Journal of Neuroimmunology*, vol. 226, no. 1-2, pp. 104–109, 2010.

- [23] E. J. O'Neill, M. J. Day, and D. C. Wraith, "IL-10 is essential for disease protection following intranasal peptide administration in the C57BL/6 model of EAE," *Journal of Neuroimmunology*, vol. 178, no. 1-2, pp. 1-8, 2006.
- [24] S. Kuerten, D. Kostovabales, L. Frenzel et al., "MP4- and MOG:35-55-induced EAE in C57BL/6 mice differentially targets brain, spinal cord and cerebellum," *Journal of Neuroimmunology*, vol. 189, no. 1-2, pp. 31-40, 2007.
- [25] C. F. Lucchinetti, B. F. G. Popescu, R. F. Bunyan et al., "Inflammatory cortical demyelination in early multiple sclerosis," *The New England Journal of Medicine*, vol. 365, no. 23, pp. 2188-2197, 2011.
- [26] A. A. Musse and G. Harauz, "Molecular "negativity" may underlie multiple sclerosis: role of the myelin basic protein family in the pathogenesis of MS," *International Review of Neurobiology*, vol. 79, pp. 149-172, 2007.
- [27] G. Harauz and A. A. Musse, "A tale of two citrullines—structural and functional aspects of myelin basic protein deimination in health and disease," *Neurochemical Research*, vol. 32, no. 2, pp. 137-158, 2007.
- [28] J. M. Lü, Q. Yao, and C. Chen, "Ginseng compounds: an update on their molecular mechanisms and medical applications," *Current Vascular Pharmacology*, vol. 7, no. 3, pp. 293-302, 2009.
- [29] I. Smith, E. M. Williamson, S. Putnam, J. Farrimond, and B. J. Whalley, "Effects and mechanisms of ginseng and ginsenosides on cognition," *Nutrition Reviews*, vol. 72, no. 5, pp. 319-333, 2014.
- [30] M. V. N. López, M. P. G.-S. Cuadrado, O. M. Palomino Ruiz-Poveda, A. M. Villar Del Fresno, and M. E. C. Accame, "Neuroprotective effect of individual ginsenosides on astrocytes primary culture," *Biochimica et Biophysica Acta (BBA) - General Subjects*, vol. 1770, no. 9, pp. 1308-1316, 2007.
- [31] M. Kleinewietfeld and D. A. Hafler, "The plasticity of human Treg and Th17 cells and its role in autoimmunity," *Seminars in Immunology*, vol. 25, no. 4, pp. 305-312, 2013.
- [32] Y. Sun, T. Tian, J. Gao et al., "Metformin ameliorates the development of experimental autoimmune encephalomyelitis by regulating T helper 17 and regulatory T cells in mice," *Journal of Neuroimmunology*, vol. 292, pp. 58-67, 2016.
- [33] J. Huppert, D. Closhen, A. Croxford et al., "Cellular mechanisms of IL-17-induced blood-brain barrier disruption," *The FASEB Journal*, vol. 24, no. 4, pp. 1023-1034, 2009.
- [34] A. Waisman, J. Hauptmann, and T. Regen, "The role of IL-17 in CNS diseases," *Acta Neuropathologica*, vol. 129, no. 5, pp. 625-637, 2015.
- [35] H. Ogura, M. Murakami, Y. Okuyama et al., "Interleukin-17 promotes autoimmunity by triggering a positive-feedback loop via interleukin-6 induction," *Immunity*, vol. 29, no. 4, pp. 628-636, 2008.
- [36] S. Liu, Y. Liu, Z. Xiao, S. Pan, Q. Gong, and Z. Lu, "Th17 cells and their cytokines serve as potential therapeutic target in experimental autoimmune neuritis," *Brain and Behavior*, vol. 9, no. 12, article e01478, 2019.
- [37] Y.-J. Park, M. Cho, G. Choi, H. Na, and Y. Chung, "A critical regulation of Th17 cell responses and autoimmune neuroinflammation by Ginsenoside Rg3," *Biomolecules*, vol. 10, no. 1, p. 122, 2020.
- [38] P. W. Lee, M. E. Severin, and A. E. Lovett-Racke, "TGF- β regulation of encephalitogenic and regulatory T cells in multiple sclerosis," *European Journal of Immunology*, vol. 47, no. 3, pp. 446-453, 2017.
- [39] L. Bjerg, A. Brosbøl-Ravnborg, C. Tørring et al., "Altered frequency of T regulatory cells is associated with disability status in relapsing-remitting multiple sclerosis patients," *Journal of Neuroimmunology*, vol. 249, no. 1-2, pp. 76-82, 2012.
- [40] M. J. Lee, M. Jang, J. Choi et al., "Korean red ginseng and Ginsenoside-Rb1/-Rg1 alleviate experimental autoimmune encephalomyelitis by suppressing Th1 and Th17 cells and upregulating regulatory T cells," *Molecular Neurobiology*, vol. 53, no. 3, pp. 1977-2002, 2016.
- [41] J. Kim, H. Byeon, K. Im, and H. Min, "Effects of ginsenosides on regulatory T cell differentiation," *Food Science and Biotechnology*, vol. 27, no. 1, pp. 227-232, 2018.
- [42] F. Chu, M. Shi, Y. Lang et al., "Gut microbiota in multiple sclerosis and experimental autoimmune encephalomyelitis: current applications and future perspectives," *Mediators Inflamm*, vol. 2018, article 8168717, 17 pages, 2018.
- [43] L. Calvo-Barreiro, H. Eixarch, X. Montalban, and C. Espejo, "Combined therapies to treat complex diseases: the role of the gut microbiota in multiple sclerosis," *Autoimmunity Reviews*, vol. 17, no. 2, pp. 165-174, 2018.
- [44] G. Schepici, S. Silvestro, P. Bramanti, and E. Mazzon, "The gut microbiota in multiple sclerosis: an overview of clinical trials," *Cell Transplantation*, vol. 28, no. 12, pp. 1507-1527, 2019.
- [45] B. He, T. K. Hoang, X. Tian et al., "Lactobacillus reuteri reduces the severity of experimental autoimmune encephalomyelitis in mice by modulating gut microbiota," *Frontiers in Immunology*, vol. 10, p. 385, 2019.

Research Article

High-Fructose Diet Increases Inflammatory Cytokines and Alters Gut Microbiota Composition in Rats

Yong Wang ¹, Wentao Qi ¹, Ge Song,^{1,2} Shaojie Pang,¹ Zhenzhen Peng,¹ Yong Li,² and Panli Wang¹

¹Academy of National Food and Strategic Reserves Administration, Beijing 100037, China

²Department of Nutrition and Food Hygiene, School of Public Health, Peking University, Beijing 100191, China

Correspondence should be addressed to Wentao Qi; qwt@ags.ac.cn

Received 14 October 2020; Revised 1 November 2020; Accepted 17 November 2020; Published 30 November 2020

Academic Editor: Shuai Chen

Copyright © 2020 Yong Wang et al. This is an open access article distributed under the Creative Commons Attribution License, which permits unrestricted use, distribution, and reproduction in any medium, provided the original work is properly cited.

High-fructose diet induced changes in gut microbiota structure and function, which have been linked to inflammatory response. However, the effect of small or appropriate doses of fructose on gut microbiota and inflammatory cytokines is not fully understood. Hence, the abundance changes of gut microbiota in fructose-treated Sprague-Dawley rats were analyzed by 16S rRNA sequencing. The effects of fructose diet on metabolic disorders were evaluated by blood biochemical parameter test, histological analysis, short-chain fatty acid (SCFA) analysis, ELISA analysis, and Western blot. Rats were intragastrically administered with pure fructose at the dose of 0 (Con), 2.6 (Fru-L), 5.3 (Fru-M), and 10.5 g/kg/day (Fru-H) for 20 weeks. The results showed that there were 36.5% increase of uric acid level in the Fru-H group when compared with the Con group. The serum proinflammatory cytokines (IL-6, TNF- α , and MIP-2) were significantly increased ($P < 0.05$), and the anti-inflammatory cytokine IL-10 was significantly decreased ($P < 0.05$) with fructose treatment. A higher fructose intake induced lipid accumulation in the liver and inflammatory cell infiltration in the pancreas and colon and increased the abundances of *Lachnospira*, *Parasutterella*, *Marvinbryantia*, and *Blantia* in colonic contents. Fructose intake increased the expressions of lipid accumulation proteins including perilipin-1, ADRP, and Tip-47 in the colon. Moreover, the higher level intake of fructose impaired intestinal barrier function due to the decrease of the expression of tight junction proteins (ZO-1 and occludin). In summary, there were no negative effects on body weight, fasting blood glucose, gut microbiota, and SCFAs in colonic contents of rats when fructose intake is in small or appropriate doses. High intake of fructose can increase uric acid, proinflammatory cytokines, intestinal permeability, and lipid accumulation in the liver and induce inflammatory response in the pancreas and colon.

1. Introduction

Fructose consumption is part of Western diets but is on the rise elsewhere, due to the introduction and generalized use of high-fructose corn syrup (HFCS) in the food industry [1, 2]. A review showed that fructose increased energy intake, reduced insulin sensitivity, increased circulating triglyceride (TG) and visceral fat stores, and depressed energy metabolism compared with glucose or starch [3]. In patients administered with sugary beverages containing high fructose, increasing fat in the liver was detected within the sixth month [4]. Evidence showed that consumption of HFCS in beverages and processed foods induced development of nonalcoholic fatty liver disease (NAFLD) and chronic inflammation

[5]. A research suggested that fructose overconsumption-induced inflammation in the visceral adipose tissue *in vivo* could be involved in the development of obesity [6].

Most of the researchers agreed that fructose diet contributed to the risks of obesity, metabolic syndrome, and diabetes mellitus due to excessive consumption [7]. However, Chiu et al. showed that fructose in isocaloric exchange for other carbohydrates had no adverse effects, especially at small or appropriate doses [8]. For example, small doses of fructose (≤ 50 g/day or $\leq 10\%$ of total energy intake/day) might improve glycemic control over the long term [9]. Acute clinical evidence demonstrated that small doses (≤ 10 g/meal) of fructose decreased the postprandial glycemic response in type 2 diabetes patients [10].

The intestinal microbial community has been related to many kinds of metabolic diseases, such as obesity, diabetes, and NAFLD [11–13]. It was reported that high-fructose diet altered the gut microbiota and induced intestinal barrier deterioration *in vivo* [14, 15]. The intestinal metabolite profile is associated with fructose feeding outcomes in reducing bacterial diversity and seems to have more potential in terms of inducing host metabolic disturbances [16]. Results also showed that high-fructose diets induced inflammation and metabolic disorders owing to changes in gut microbiota composition and enhancing intestinal permeability [11]. Mice fed with a 60% fructose diet had alterations of the gut microbiota and intestinal mucosa integrity [17]. However, there is only limited research on the influence of low-dose fructose on gut microbial community and the subsequent effects on inflammatory response and intestinal barrier function.

It appears that the effects of fructose on health are controversial and closely related to intake dose. More physiologically relevant experiments should be designed to generate evidence to better understand the role of fructose on human health. Therefore, different dosages of pure fructose were intragastrically administered to healthy rats over a 20-week period to evaluate the effects of fructose on blood inflammatory cytokines, intestinal barrier function, and gut microbiota in this study.

2. Materials and Methods

2.1. Materials. Standard substances of acetic, propionic, isobutyric, and butyrate acid were obtained from Sigma-Aldrich (St. Louis, MO, USA). The antibodies perilipin-1, occludin, adipose differentiation-related protein (ADRP), and β -actin and secondary antibodies were purchased from Abcam (Cambridge, MA, USA). ZO-1 was obtained from Millipore (Billerica, MA, USA). Tail-interacting protein (Tip-47) was purchased from Santa Cruz (Texas, CA, USA).

2.2. Animals. Six-week-old male Sprague-Dawley (SD) rats weighing approximately 220 g were purchased from Beijing Vital River Laboratory Animal Technology (Beijing, China) and acclimatized for 1 week before the experiment. Two rats were in each cage, and they were housed with a 12 h/12 h light/dark cycle at 22°C–25°C and 55%–60% humidity.

2.3. Experimental Design. The rats were randomly divided into four groups ($n = 10$): Con group (administration of saline solution), Fru-L group (low dose of fructose, 2.6 g/kg/day), Fru-M group (moderate dose of fructose, 5.3 g/kg/day), and Fru-H group (high dose of fructose, 10.5 g/kg/day). The rats were treated with fructose for 20 weeks until sacrifice. Rats were kept under SPF conditions and were fed with a standard chow diet (Beijing Keao Xieli Feed Co., Ltd., Beijing, China). The energy supply (%) in maintenance diet is as follows: protein 23.07%, fat 11.85%, and carbohydrate 65.08%.

The WHO proposed to halve free sugar intake to 5% of daily calories, which is about 0.83 g/kg/day [18]. Therefore, rats in the Fru-M group were treated with a dose of 5.3 g/kg/day fructose based on the suggested equivalent dose

conversion [19]. And the rats in the Fru-L and Fru-H groups were treated with a dose of 2.6 and 10.5 g/kg/day fructose, respectively. A same volume of saline solution was intragastrically administered to the rats in the Con group. Blood glucose levels were measured with a glucometer (LifeScan Inc., Milpitas, CA, USA) every two weeks, and weight were recorded every week. Food consumption was recorded every two days until the end of this study.

2.4. Biochemical Parameters. After 20 weeks, the rats were fasted for 12 h and euthanized using CO₂. The blood samples were collected by cardiac puncture and centrifuged as our previous study [20] and stored at 4°C. The levels of total TG, total cholesterol (TC), low-density lipoprotein cholesterol (LDL-C), high-density lipoprotein cholesterol (HDL-C), aspartate transaminase (AST), alanine aminotransferase (ALT), superoxide dismutase (SOD), malondialdehyde (MDA), lipase, free fatty acid (FFA), and uric acid in serum were determined with the corresponding diagnostic kits (Zhongsheng Beikong Bioengineering Institute, Beijing, China) on a Mindray BS-420 Automatic Analyzer (Shenzhen, China).

2.5. Histopathological Examination. Liver, pancreas, and colon tissues were fixed in 10% formalin and then embedded in paraffin. The tissue sections were stained with hematoxylin-eosin and observed by using a BA-9000L microscope (Osaka, Japan). All experiments and scores were performed in a blinded manner by a pathologist in Peking University [21].

2.6. Western Blotting. The total protein concentration of colonic mucosal samples was determined using the BCA protein assay kit (Tiangen Biotech, Beijing, China). Western blot analysis was performed according to our previous study [22]. In brief, an equal amount of protein from each group was separated by sodium dodecyl sulfate-polyacrylamide gel electrophoresis and transferred to nitrocellulose (NC) membranes (Millipore, Bedford, MA, USA). Thereafter, the NC membranes were blocked with 5% nonfat dry milk and then were probed with the corresponding primary and secondary antibodies. Finally, proteins were detected and quantified using the ODYSSEY FC imaging system (Gene Company Limited, NE, USA).

2.7. Short-Chain Fatty Acid (SCFA) Analysis. Colonic contents were diluted, mixed, and centrifuged, and then, 25% (w/v) metaphosphoric acid solution was added to the supernatant to extract SCFA. SCFA analysis was performed according to the method previously described using gas chromatography (Agilent 6890, CA, USA) with a DB-FFAP chromatographic capillary column (30 m \times 0.25 mm \times 0.5 μ m; Agilent) [20].

2.8. ELISA Analysis. IL-6, TNF- α , MIP-2, and IL-10 levels in serum were measured using ELISA kits (R&D Systems, Minneapolis, MN, USA) and a 2300 EnSpire Multimode Plate Reader (PerkinElmer, Waltham, MA, USA) according to the manufacturer's instructions.

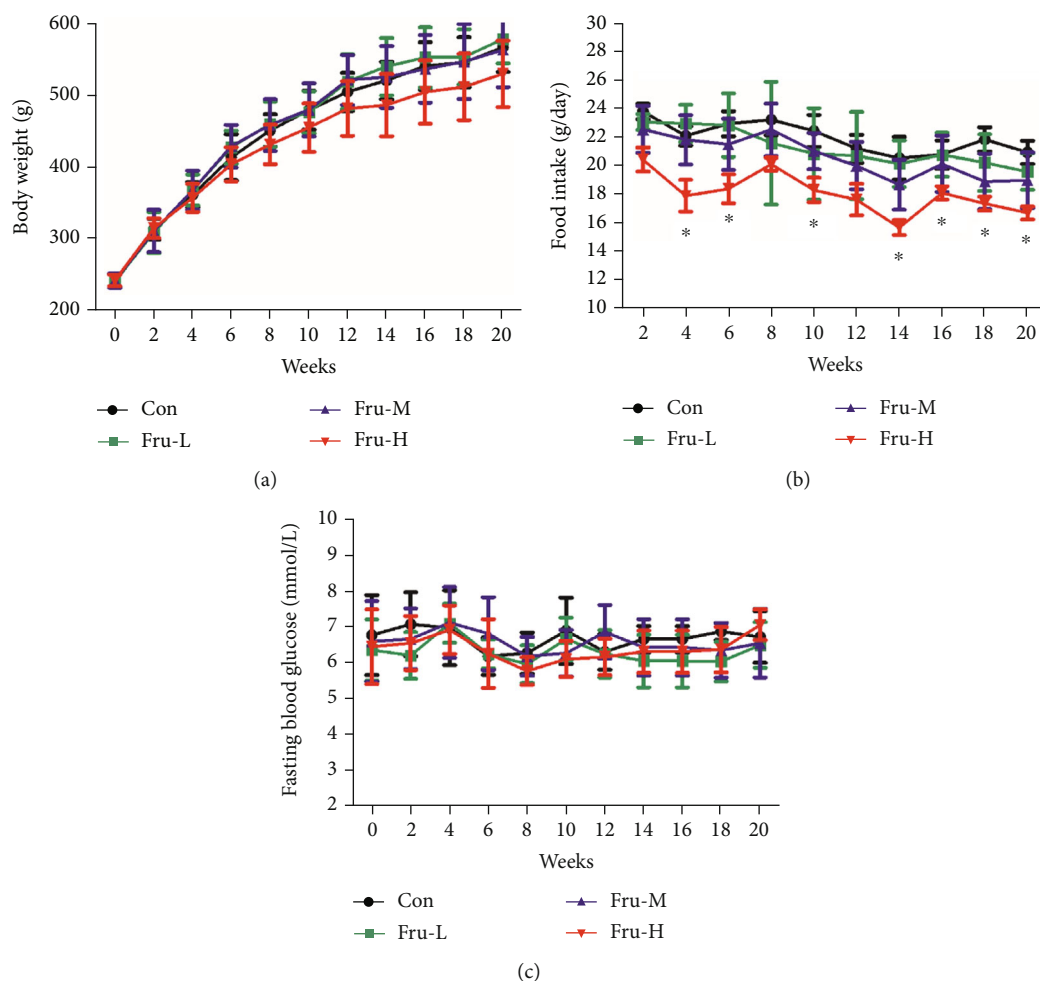


FIGURE 1: (a) Body weight, (b) food intake, and (c) fasting blood glucose of rats with different doses of fructose during 20 weeks. Con group, administration of saline solution; Fru-L group, administration of a low dosage of fructose (2.6 g/kg/day); Fru-M group, administration of a moderate dosage of fructose (5.3 g/kg/day); Fru-H group, administration of a high dosage of fructose (10.5 g/kg/day). Data are presented as the mean \pm SD ($n = 10$). * $P < 0.05$ means significantly different from the Con group.

TABLE 1: Blood biochemical parameters of rats at the end of 20 weeks.

	Con	Fru-L	Fru-M	Fru-H
TG (mmol/L)	1.31 \pm 0.26 ^a	1.56 \pm 0.83 ^a	1.67 \pm 0.71 ^a	0.99 \pm 0.12 ^a
TC (mmol/L)	2.84 \pm 0.48 ^a	2.36 \pm 0.30 ^b	2.42 \pm 0.41 ^b	2.18 \pm 0.28 ^b
HDL-C (mmol/L)	1.68 \pm 0.23 ^a	1.49 \pm 0.14 ^a	1.62 \pm 0.21 ^a	1.49 \pm 0.19 ^a
LDL-C (mmol/L)	0.65 \pm 0.11 ^a	0.52 \pm 0.15 ^a	0.57 \pm 0.20 ^a	0.47 \pm 0.14 ^a
AST (U/L)	110.40 \pm 24.80 ^a	93.01 \pm 18.81 ^a	104.64 \pm 73.97 ^a	110.66 \pm 37.71 ^a
ALT (U/L)	51.90 \pm 9.50 ^a	49.57 \pm 8.65 ^a	60.19 \pm 38.72 ^a	44.96 \pm 12.53 ^a
SOD (U/mL)	72.80 \pm 12.57 ^a	70.13 \pm 9.99 ^a	77.43 \pm 11.05 ^a	78.72 \pm 9.55 ^a
MDA (nmol/mL)	4.39 \pm 1.03 ^a	4.64 \pm 0.99 ^a	4.15 \pm 0.57 ^a	3.61 \pm 0.82 ^a
Lipase (U/mL)	67.32 \pm 10.90 ^a	68.50 \pm 12.00 ^a	63.25 \pm 6.92 ^a	59.52 \pm 10.95 ^a
FFA (mmol/L)	0.45 \pm 0.07 ^a	0.50 \pm 0.08 ^a	0.50 \pm 0.09 ^a	0.47 \pm 0.04 ^a
Uric acid (μ mol/L)	242.27 \pm 94.63 ^a	213.04 \pm 131.31 ^{ab}	167.98 \pm 64.49 ^a	330.81 \pm 71.48 ^b

Con group, administration of saline solution; Fru-L group, administration of a low dosage of fructose (2.6 g/kg/day); Fru-M group, administration of a moderate dosage of fructose (5.3 g/kg/day); Fru-H group, administration of a high dosage of fructose (10.5 g/kg/day). Data are expressed as the mean \pm standard deviation ($n = 6$). Values in the same row that do not share the same lowercase letter are significantly different ($P < 0.05$).

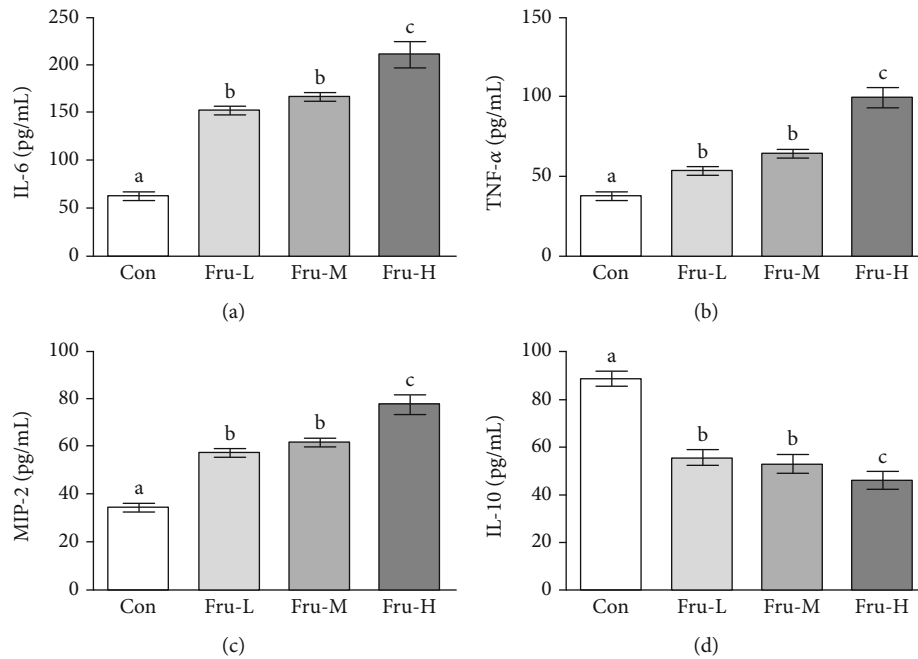


FIGURE 2: Concentrations of inflammatory cytokines including (a) IL-6, (b) TNF- α , (c) MIP-2, and (d) IL-10 in the serum. Con group, administration of saline solution; Fru-L group, administration of a low dosage of fructose (2.6 g/kg/day); Fru-M group, administration of a moderate dosage of fructose (5.3 g/kg/day); Fru-H group, administration of a high dosage of fructose (10.5 g/kg/day). Data are presented as the mean \pm SD ($n = 5$). Values that do not share the same lowercase letter are significantly different ($P < 0.05$).

2.9. Gut Microbiota Analysis. Colonic contents were collected at week 20 and stored at -80°C until analysis. The microbiomes were analyzed at the Novogene Bioinformatics Technology Co., Ltd. (Beijing, China) on an Illumina MiSeq platform. DNA was amplified by using the 515f/806r primer set (515f: 5'-GTGCCAGCMGCCGCGGTAA-3', 806r: 5'-XXXXXXXXGGACTACHVGGGTWTCTAAT-3'), which targets the V4 region of bacterial 16S rRNA. Sequencing libraries were generated and analyzed as previously described [20]. Paired-end reads from the original DNA fragments are merged by using FLASH. Sequences were analyzed using QIIME software package, and in-house Perl scripts were used to analyze alpha (Observed_species and Shannon index) and beta diversity.

2.10. Statistical Analysis. Data are expressed as the mean \pm standard deviation (SD). Statistical analyses were performed using GraphPad Prism Software 5.0 (La Jolla, CA, USA). Differences were analyzed by one-way analysis of variance (ANOVA) with Dunnett's contrast for multiple group comparisons. P value < 0.05 was considered significant.

3. Results

3.1. Effect of Fructose on Body Weight, Feed Intake, and Fasting Blood Glucose. Rats treated with fructose in different dosages had similar weight gains to those in the Con group over the 20-week period (Figure 1(a)). The weight gain of rats in the Fru-H group had a lower trend than that in the other groups, although there were no significant differences ($P > 0.05$) during the whole period. It was interesting that

the food intake of rats in the Fru-H group was significantly lower than that in the Con, Fru-L, and Fru-M groups in almost the whole period ($P < 0.05$) (Figure 1(b)). There were no significant differences ($P > 0.05$) on fasting blood glucose levels between different groups during 20 weeks (Figure 1(c)).

3.2. Effect of Fructose on Serum Biochemical Parameters. TC levels in serum in all the fructose groups were found significantly lower than those in the Con group ($P < 0.05$) (Table 1). The uric acid level in both the Fru-L and Fru-M groups had no significant difference ($P > 0.05$) compared with that in the Con group, while the uric acid level was increased 36.5% in the Fru-H group when compared with the Con group ($P < 0.05$). There were no significant differences on other blood parameters including TG, HDL-C, LDL-C, AST, ALT, SOD, MDA, lipase, and FFA ($P > 0.05$).

3.3. Effect of Fructose on Inflammatory Cytokines in Serum. The inflammatory cytokines (IL-6, TNF- α , MIP-2, and IL-10) in serum were further determined (Figure 2). The concentrations of IL-6, TNF- α , and MIP-2 were all significantly higher in the Fru-L, Fru-M, and Fru-H groups than in the Con group ($P < 0.05$). The levels of IL-6, TNF- α , and MIP-2 increased along with fructose dosage, whereas the concentrations of IL-10 were significantly lower in the Fru-L, Fru-M, and Fru-H groups than in the Con group ($P < 0.05$). The levels of IL-10 were decreased as the fructose dosage increases.

3.4. Effect of Fructose on Liver and Pancreas Histology. In the Fru-H group, 10% hepatic microvesicular steatosis was

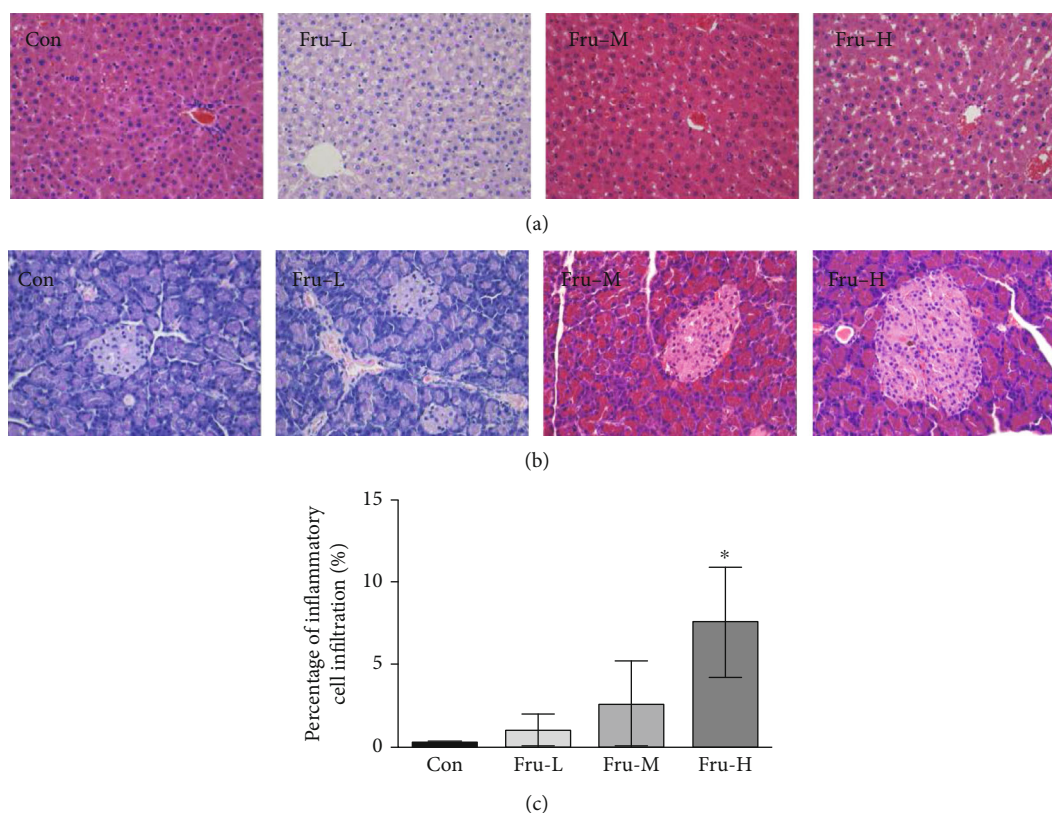


FIGURE 3: Effect of fructose in different dosages on the liver and pancreas of rats. (a) Representative micrographs of HE-stained sections of the liver ($\times 40$); (b) representative micrographs of HE-stained sections of the pancreas ($\times 40$); (c) scores based on inflammatory cell infiltration in the pancreas. Con group, administration of saline solution; Fru-L group, administration of a low dosage of fructose (2.6 g/kg/day); Fru-M group, administration of a moderate dosage of fructose (5.3 g/kg/day); Fru-H group, administration of a high dosage of fructose (10.5 g/kg/day). Data are presented as the mean \pm SD ($n = 5$). * $P < 0.05$ means significantly different from the Con group.

observed, while no obvious microvesicular steatosis was observed in the other groups (Figure 3(a)). Tissue necrosis and inflammatory cell infiltration could be found in the pancreas of rats in the Fru-M and Fru-H groups, while the pancreatic constructions of rats in the Con and Fru-L groups were very clear and no obvious pathology damage (Figure 3(b)). The score based on the inflammatory cell infiltration in the pancreas of the Fru-H group was significantly higher than that of the Con group ($P < 0.05$), while the Fru-L and Fru-M groups showed no significant difference compared with the Con group ($P > 0.05$, Figure 3(c)).

3.5. Effect of Fructose on Colon Histology. Inflammatory cell infiltration can be observed in the mucoderm and submucosa in the Fru-H group, while no obvious inflammatory cell infiltration was observed in those of other groups (Figure 4(a)). The percentage of inflammatory cell infiltration in the colon of the Fru-H group was significantly higher than that of the Con group ($P < 0.05$, Figure 4(b)), while there were no significant differences among the Con, Fru-L, and Fru-M groups ($P > 0.05$).

3.6. Effect of Fructose on the Expressions of Lipid Accumulation and Tight Junction (TJ) Proteins. Proteins related to lipid accumulation and TJ were further examined by Western blot. The results showed that the expressions of

lipid accumulation proteins including perilipin-1, ADRP, and Tip-47 were increased obviously, while the expressions of TJ proteins including ZO-1 and occludin were decreased especially in the Fru-H group (Figure 4(c)).

3.7. Effect of Fructose on Gut Microbiota and SCFAs in Colonic Contents. To compare community structure and similarity of gut microbiota, 16S rRNA analysis was carried out in this research. The shared OTUs for different groups were determined via the Venn diagram (Figure 5(a)). A total of 382 OTUs (67.3%) could be detected in all groups. The Con group had more unique OTUs (28) than the other groups including Fru-L (22), Fru-M (13), and Fru-H (9). The different OTUs between Con and Fru-L, Con and Fru-M, and Con and Fru-H were 86, 118, and 118, respectively. No significant differences were found at the phylum level among these four groups (Figure 5(b)). *Lachnospira*, *Intestinimonas*, *Parasutterella*, *Marvinbryantia*, *Blantia*, and *Oscilibacter* abundances at the genus level were significantly differential under the effect of fructose (Figures 5(c) and 5(d)). *Lachnospira* and *Marvinbryantia* were significantly enriched in the Fru-M and Fru-H groups compared with the Con group ($P < 0.05$). *Parasutterella* and *Blantia* were significantly increased in the Fru-H group compared with the Con group ($P < 0.05$), but *Blantia* was significantly decreased in the Fru-M group compared with the Con group

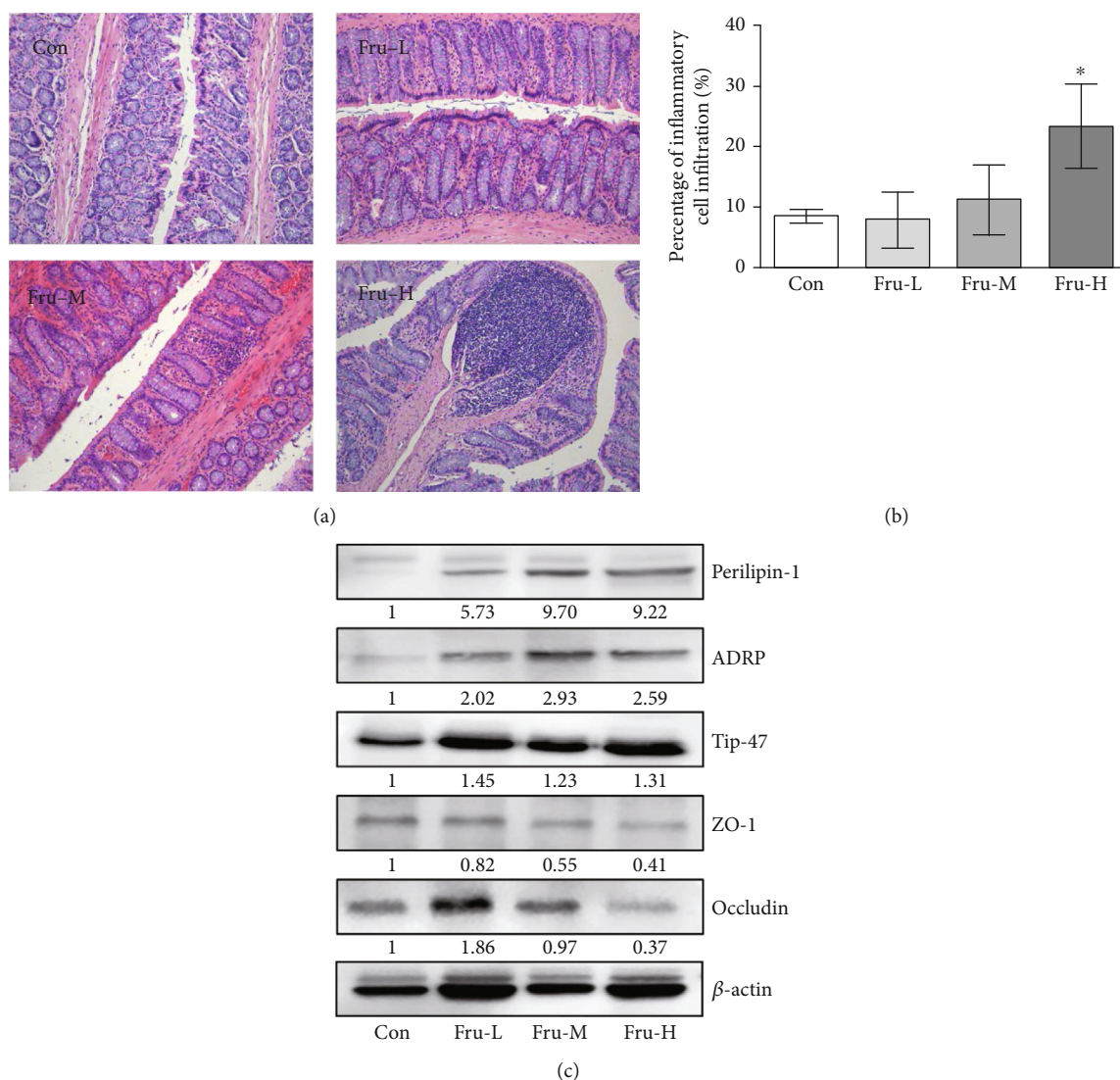


FIGURE 4: Effect of fructose in different dosages on the colon of rats. (a) Representative micrographs of HE-stained sections of rat colon (×40); (b) scores based on inflammatory cell infiltration in the colon. Data are presented as the mean ± SD ($n = 5$). * $P < 0.05$ means significantly different from the Con group; (c) Western blot bands of perilipin-1, ADRP, Tip-47, ZO-1, and occludin in the colon. Con group, administration of saline solution; Fru-L group, administration of a low dosage of fructose (2.6 g/kg/day); Fru-M group, administration of a moderate dosage of fructose (5.3 g/kg/day); Fru-H group, administration of a high dosage of fructose (10.5 g/kg/day).

($P < 0.05$). *Intestinimonas* was significantly decreased in the Fru-M and Fru-H groups compared with the Con group ($P < 0.05$). *Oscilibacter* was significantly decreased in the Fru-L group compared with the Con group ($P < 0.05$).

SCFAs in colonic contents of rats were further examined. There were no significant differences ($P > 0.05$) on acetic, propionic, and butyric acid and total SCFAs in all groups (Table 2). However, the concentration of isobutyric acid was relatively lower in all the fructose-treated groups than the Con group ($P < 0.05$).

4. Discussion

The effect of fructose on health has been controversial and closely related to its intake dosage. In this study, rats were intragastrically administered with fructose at the dosages of

2.6, 5.3, and 10.5 g/kg/day, respectively. It was found that the diet consumption of rats significantly decreased in the Fru-H group. As for the reason, we supposed that high fructose intake provided energy to those rats and decreased diet consumption. The body weight and epididymal fat index (data not shown) of rats in the Fru-H group were lower than those in the Con group. This could be the reason why TC levels were decreased with the treatment of fructose. Nevertheless, this related mechanism needs to be investigated in future works. Our data also showed that there were no changes on fasting blood glucose of rats after fructose intake during the whole feeding period.

A previous study showed that long-term fructose consumption increased serum uric acid concentration [23]. In the present study, a 36.5% increase of serum uric acid level was found in high fructose intake rats compared with

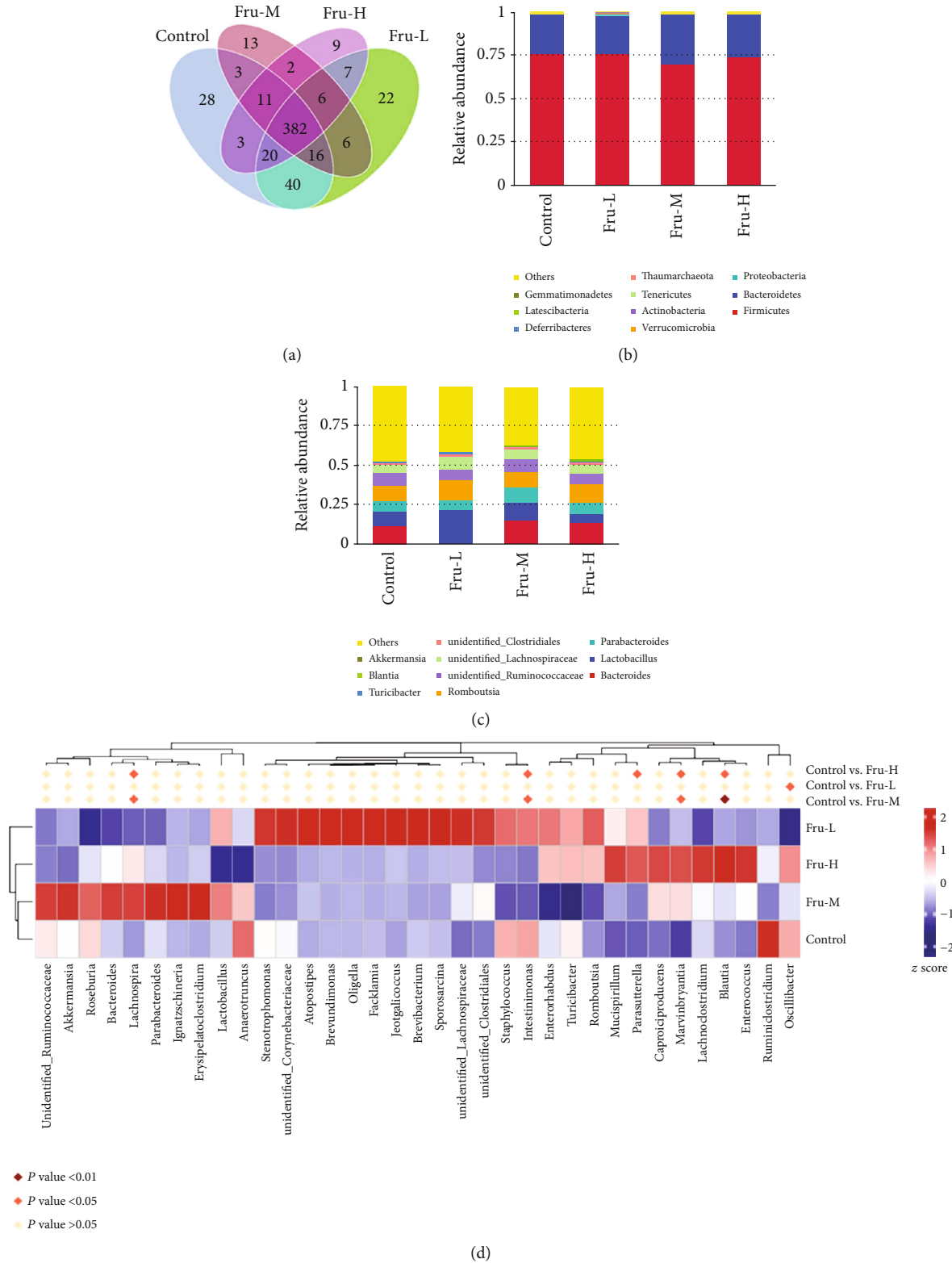


FIGURE 5: Effect of fructose in different dosages on gut microbiota of rats. (a) Venn diagram displays OTUs among the four groups in colonic contents ($n = 6$ per group); (b) analysis of relative abundance of microbiota at the phylum level in colonic contents; (c) analysis of relative abundance of microbiota at the genus level in colonic contents; (d) heatmaps of genus. Control, administration of saline solution; Fru-L group, administration of a low dosage of fructose (2.6 g/kg/day); Fru-M group, administration of a moderate dosage of fructose (5.3 g/kg/day); Fru-H group, administration of a high dosage of fructose (10.5 g/kg/day).

TABLE 2: Effects of fructose on SCFA concentrations in the colon of rats at the end of 20 weeks.

	Con	Fru-L	Fru-M	Fru-H
Acetic acid ($\mu\text{g/g}$)	147.02 \pm 39.60 ^a	157.52 \pm 36.14 ^a	126.70 \pm 17.20 ^a	145.33 \pm 28.62 ^a
Propionic acid ($\mu\text{g/g}$)	34.25 \pm 9.27 ^a	41.92 \pm 8.75 ^a	29.38 \pm 3.74 ^a	39.27 \pm 6.03 ^a
Butyric acid ($\mu\text{g/g}$)	22.81 \pm 8.63 ^a	40.49 \pm 9.08 ^a	38.70 \pm 5.28 ^a	41.37 \pm 5.11 ^a
Isobutyric acid ($\mu\text{g/g}$)	56.33 \pm 23.99 ^a	15.12 \pm 7.61 ^b	6.06 \pm 1.20 ^b	6.40 \pm 0.91 ^b
Total SCFAs ($\mu\text{g/g}$)	260.41 \pm 56.49 ^a	255.05 \pm 52.26 ^a	200.84 \pm 25.71 ^a	232.36 \pm 39.91 ^a

Con group, administration of saline solution; Fru-L group, administration of a low dosage of fructose (2.6 g/kg/day); Fru-M group, administration of a moderate dosage of fructose (5.3 g/kg/day); Fru-H group, administration of a high dosage of fructose (10.5 g/kg/day). Data are expressed as the mean \pm standard deviation ($n = 10$). Values in the same row that do not share the same lowercase letter are significantly different ($P < 0.05$).

control rats. Here, we found that there were no significant differences in serum levels of uric acid between control rats and small or mild fructose-fed rats which means the risk of hyperuricemia with appropriate fructose intake is not high. Meta-analysis showed that “catalytic” small fructose doses might improve glycemic control without adverse effects on body weight and uric acid [9, 24].

Many factors such as uric acid generation and high sugar exposure may accelerate the fructose-induced NAFLD [25]. Our results showed that there was no obvious inflammatory response in the liver after intake of fructose. However, mild microvesicular steatosis was detected at the highest dose of fructose, which indicated a higher risk of fatty liver induced by high fructose, even though the function of the liver has not been affected at that time.

It has been demonstrated that fructose-induced metabolic syndrome is closely related to inflammation, characterized by increased proinflammatory cytokine concentration and inflammation signaling activation in the organs (liver, pancreatic islet, and intestine) [26]. Superabundant fructose alters the gut microbiota composition and impairs intestinal barrier function via decreased expression of TJ proteins, therefore initiating inflammatory process [11, 27]. High fructose has been found with the capability to induce inflammation chemokine overproduction, such as IL-1 β , TNF- α , and IL-6 [28]. In the present study, we discovered that fructose significantly increased the levels of plasma proinflammatory markers IL-6, TNF- α , and MIP-2 in a dose-dependent manner and decreased the level of anti-inflammatory marker IL-10 in rats. In addition, some organs including the pancreas and colon showed significant inflammatory symptoms at the highest doses of fructose in this study.

In this research, we found significant inflammatory symptoms in the colon of rats with the highest fructose intake. Li et al. revealed high-fructose diet-induced intestinal epithelial barrier dysfunction in mice, and SCFAs could improve intestinal barrier function [27]. SCFAs are the end products of microbial fermentation of nondegradable carbohydrates and can inhibit intestinal inflammation [29, 30]. A high-sugar diet could reduce SCFA production in mice, decrease microbial diversity, and thus enhance susceptibility to colitis [31]. In our study, the isobutyric acid and total SCFAs showed a decreased trend in the fructose intake group.

PAT proteins, such as perilipin, ADRP and Tip-47, could induce cellular lipid stores [32]. In this paper, we

found that the expressions of perilipin, ADRP, and Tip-47 were all induced by high levels of fructose intake which means a potential increase of lipid droplets in the colon. We also confirmed that high fructose intake rats exhibited increased gut permeability, characterized by disruption of the TJ proteins (ZO-1 and occludin) in the colon. Increased gut permeability was closely related to obesity and causes inflammation [33]. Therefore, these results indicated that high-level fructose intake induces the extension of the colon, which further leads to increased gut permeability and inflammation.

A previous study has proved that elevated luminal fructose could induce proinflammatory effects via initiating changes in gut microbiota [15]. Higher abundance of proinflammatory taxa *Marvinbryantia* which was associated with intestinal inflammation and bowel dysfunction [34, 35] was observed in the Fru-M and Fru-H groups. Increased abundances of *Lachnospira*, *Parasutterella*, and *Blantia* in colonic contents were detected, while *Lachnospira*, an acetate-producing bacteria, was related to increasing blood glucose levels [36], and *Parasutterella*, known as the saccharolytic strain, was increased by carbohydrate consumption with a potential role on bile acid maintenance and intestinal mucosal homeostasis [37, 38]. *Blantia* had positive anti-inflammatory effects and had the ability to produce SCFAs [39]. While high-fructose diet altered the abundance of certain taxa, both overall alpha diversity (Observed_species and Shannon index) and beta diversity of colonic content samples among the four groups were not significantly different in this study (data not shown).

In summary, we demonstrated a potential connection between fructose-rich diet, gut microbiota profile, and inflammatory process in the liver, pancreas, and colon. There were no negative effects on body weight, fasting blood glucose, histological analysis, gut microbiota, and SCFAs in the colon when fructose intake was in small or appropriate doses. High fructose intake could induce uric acid increase, lipid accumulation in the liver, and an inflammatory response in the pancreas and colon and increase the abundances of *Lachnospira*, *Parasutterella*, *Marvinbryantia*, and *Blantia* in colonic contents. All doses of fructose dysregulated the inflammatory cytokine production in serum and the expressions of lipid accumulation and TJ proteins in the colon. Further studies should be undertaken to explore more details and mechanisms of fructose intake on health effects.

Data Availability

The data used to support the findings of this study are available from the corresponding author upon request.

Ethical Approval

The procedures were approved by the Ethical Committee for Animal Experimentation of the Academy of National Food and Strategic Reserves Administration with utilization permission from Beijing Municipal Science & Technology Commission (No. SYXK (Jing) 2019-0015).

Conflicts of Interest

The authors declare that they have no competing interests.

Authors' Contributions

Wentao Qi conceived and designed the experiments. Yong Wang, Wentao Qi, Ge Song, Shaojie Pang, Zhenzhen Peng, Yong Li, and Panli Wang performed the experiments. Yong Wang and Wentao Qi wrote the paper. All authors have read and agreed to the published version of the manuscript.

Acknowledgments

This work was funded by the Special Funds of Basic Research of Central Public Welfare Institute (No. ZX1902), the National Natural Science Foundation of China (Grant No. 31901698), and the Young Elite Scientists Sponsorship Program by the China Association for Science and Technology (No. 2019QNR001).


References

- [1] K. ter Horst and M. Serlie, "Fructose consumption, lipogenesis, and non-alcoholic fatty liver disease," *Nutrients*, vol. 9, no. 9, p. 981, 2017.
- [2] L. Liu, T. Li, Y. Liao et al., "Triose kinase controls the lipogenic potential of fructose and dietary tolerance," *Cell Metabolism*, vol. 32, no. 4, pp. 605–618.e7, 2020.
- [3] R. J. Johnson, L. G. Sánchez-Lozada, P. Andrews, and M. A. Lanaspá, "Perspective: a historical and scientific perspective of sugar and its relation with obesity and diabetes," *Advances in Nutrition*, vol. 8, no. 3, pp. 412–422, 2017.
- [4] T. Jensen, M. F. Abdelmalek, S. Sullivan et al., "Fructose and sugar: a major mediator of non-alcoholic fatty liver disease," *Journal of Hepatology*, vol. 68, no. 5, pp. 1063–1075, 2018.
- [5] S. Zhao, C. Jang, J. Liu et al., "Dietary fructose feeds hepatic lipogenesis via microbiota-derived acetate," *Nature*, vol. 579, no. 7800, pp. 586–591, 2020.
- [6] S. Kovačević, J. Nestorov, G. Matić, and I. Elaković, "Fructose-enriched diet induces inflammation and reduces antioxidative defense in visceral adipose tissue of young female rats," *European Journal of Nutrition*, vol. 56, no. 1, pp. 151–160, 2017.
- [7] J. S. Lim, M. Mietus-Snyder, A. Valente, J.-M. Schwarz, and R. H. Lustig, "The role of fructose in the pathogenesis of NAFLD and the metabolic syndrome," *Nature Reviews Gastroenterology & Hepatology*, vol. 7, no. 5, pp. 251–264, 2010.
- [8] S. Chiu, J. L. Sievenpiper, R. J. de Souza et al., "Effect of fructose on markers of non-alcoholic fatty liver disease (NAFLD): a systematic review and meta-analysis of controlled feeding trials," *European Journal of Clinical Nutrition*, vol. 68, no. 4, pp. 416–423, 2014.
- [9] J. Noronha, C. Braunstein, S. B. Mejia et al., "The effect of small doses of fructose and its epimers on glycemic control: a systematic review and meta-analysis of controlled feeding trials," *Nutrients*, vol. 10, no. 11, p. 1805, 2018.
- [10] J. C. Noronha, C. R. Braunstein, A. J. Glenn et al., "The effect of small doses of fructose and allulose on postprandial glucose metabolism in type 2 diabetes: a double-blind, randomized, controlled, acute feeding, equivalence trial," *Diabetes Obesity & Metabolism*, vol. 20, no. 10, pp. 2361–2370, 2018.
- [11] M. Do, E. Lee, M.-J. Oh, Y. Kim, and H.-Y. Park, "High-glucose or -fructose diet cause changes of the gut microbiota and metabolic disorders in mice without body weight change," *Nutrients*, vol. 10, no. 6, p. 761, 2018.
- [12] S. Bibbò, G. Ianaro, M. P. Dore, C. Simonelli, E. E. Newton, and G. Cammarota, "Gut microbiota as a driver of inflammation in nonalcoholic fatty liver disease," *Mediators of Inflammation*, vol. 2018, Article ID 9321643, 7 pages, 2018.
- [13] D. Pagliari, A. Saviano, E. E. Newton et al., "Gut microbiota-immune system crosstalk and pancreatic disorders," *Mediators of Inflammation*, vol. 2018, Article ID 7946431, 13 pages, 2018.
- [14] G. E. Townsend, W. Han, N. D. Schwalm et al., "Dietary sugar silences a colonization factor in a mammalian gut symbiont," *Proceedings of the National Academy of Sciences of the United States of America*, vol. 116, no. 1, pp. 233–238, 2019.
- [15] J. Todoric, G. Di Caro, S. Reibe et al., "Fructose stimulated de novo lipogenesis is promoted by inflammation," *Nature metabolism*, vol. 2, no. 10, pp. 1034–1045, 2020.
- [16] A. N. Payne, C. Chassard, and C. Lacroix, "Gut microbial adaptation to dietary consumption of fructose, artificial sweeteners and sugar alcohols: implications for host-microbe interactions contributing to obesity," *Obesity Reviews*, vol. 13, no. 9, pp. 799–809, 2012.
- [17] R. Mastrocola, I. Ferrocino, E. Liberto et al., "Fructose liquid and solid formulations differently affect gut integrity, microbiota composition and related liver toxicity: a comparative in vivo study," *Journal of Nutritional Biochemistry*, vol. 55, pp. 185–199, 2018.
- [18] World Health Organization, *Guideline: sugars intake for adults and children*, WHO, 2015.
- [19] S. Reagan-Shaw, M. Nihal, and N. Ahmad, "Dose translation from animal to human studies revisited," *FASEB Journal*, vol. 22, no. 3, pp. 659–661, 2007.
- [20] F. Han, Y. Wang, Y. Han et al., "Effects of whole-grain rice and wheat on composition of gut microbiota and short-chain fatty acids in rats," *Journal of Agricultural and Food Chemistry*, vol. 66, no. 25, pp. 6326–6335, 2018.
- [21] M. Yan, L. Ye, S. Yin et al., "Glycycomarin protects mice against acetaminophen-induced liver injury predominantly via activating sustained autophagy," *British Journal of Pharmacology*, vol. 175, no. 19, pp. 3747–3757, 2018.
- [22] W. Qi, Y. Wang, J. Yao et al., "Genistein inhibits AOM/DSS-induced colon cancer by regulating lipid droplet accumulation and the SIRT1/FOXO3a pathway in high-fat diet-fed female mice," *Food and Agricultural Immunology*, vol. 30, no. 1, pp. 1271–1285, 2019.

- [23] C. Kaneko, J. Ogura, S. Sasaki et al., "Fructose suppresses uric acid excretion to the intestinal lumen as a result of the induction of oxidative stress by NADPH oxidase activation," *Biochimica et Biophysica Acta-General Subjects*, vol. 1861, no. 3, pp. 559–566, 2017.
- [24] J. L. Sievenpiper, L. Chiavaroli, R. J. de Souza et al., "Catalytic doses of fructose may benefit glycaemic control without harming cardiometabolic risk factors: a small meta-analysis of randomised controlled feeding trials," *British Journal of Nutrition*, vol. 108, no. 3, pp. 418–423, 2012.
- [25] M. A. Lanaspá, L. G. Sánchez-Lozada, Y. J. Choi et al., "Uric acid induces hepatic steatosis by generation of mitochondrial oxidative stress," *Journal of Biological Chemistry*, vol. 287, no. 48, pp. 40732–40744, 2012.
- [26] D.-M. Zhang, R.-Q. Jiao, and L.-D. Kong, "High dietary fructose: direct or indirect dangerous factors disturbing tissue and organ functions," *Nutrients*, vol. 9, no. 4, p. 335, 2017.
- [27] J.-M. Li, R. Yu, L.-P. Zhang et al., "Dietary fructose-induced gut dysbiosis promotes mouse hippocampal neuroinflammation: a benefit of short-chain fatty acids," *Microbiome*, vol. 7, no. 1, p. 98, 2019.
- [28] P. D. Prince, C. R. Lanzi, J. E. Toblli et al., "Dietary (-)-epicatechin mitigates oxidative stress, NO metabolism alterations, and inflammation in renal cortex from fructose-fed rats," *Free Radical Biology and Medicine*, vol. 90, pp. 35–46, 2016.
- [29] P. M. Smith, M. R. Howitt, N. Panikov et al., "The microbial metabolites, short-chain fatty acids, regulate colonic Treg cell homeostasis," *Science*, vol. 341, no. 6145, pp. 569–573, 2013.
- [30] V. P. N. Miranda, P. R. dos Santos Amorim, R. R. Bastos et al., "Abundance of gut microbiota, concentration of short-chain fatty acids, and inflammatory markers associated with elevated body fat, overweight, and obesity in female adolescents," *Mediators of Inflammation*, vol. 2019, Article ID 7346863, 11 pages, 2019.
- [31] M. Laffin, R. Fedorak, A. Zalasky et al., "A high-sugar diet rapidly enhances susceptibility to colitis via depletion of luminal short-chain fatty acids in mice," *Scientific Reports*, vol. 9, no. 1, article 12294, 2019.
- [32] P. E. Bickel, J. T. Tansey, and M. A. Welte, "PAT proteins, an ancient family of lipid droplet proteins that regulate cellular lipid stores," *Biochimica et Biophysica Acta-Molecular and Cell Biology of Lipids*, vol. 1791, no. 6, pp. 419–440, 2009.
- [33] F. F. Anhê, D. Roy, G. Pilon et al., "A polyphenol-rich cranberry extract protects from diet-induced obesity, insulin resistance and intestinal inflammation in association with increased *Akkermansia* spp. population in the gut microbiota of mice," *Gut*, vol. 64, no. 6, pp. 872–883, 2015.
- [34] Y. Zhang, L. Chen, M. Hu et al., "Dietary type 2 resistant starch improves systemic inflammation and intestinal permeability by modulating microbiota and metabolites in aged mice on high-fat diet," *Aging*, vol. 12, no. 10, pp. 9173–9187, 2020.
- [35] B. Gungor, E. Adiguzel, I. Gursel, B. Yilmaz, and M. Gursel, "Intestinal microbiota in patients with spinal cord injury," *PLoS One*, vol. 11, no. 1, article e0145878, 2016.
- [36] Q. Luo, D. Cheng, C. Huang et al., "Improvement of colonic immune function with soy isoflavones in high-fat diet-induced obese rats," *Molecules*, vol. 24, no. 6, p. 1139, 2019.
- [37] T. Ju, J. Y. Kong, P. Stothard, and B. P. Willing, "Defining the role of *Parasutterella*, a previously uncharacterized member of the core gut microbiota," *ISME Journal*, vol. 13, no. 6, pp. 1520–1534, 2019.
- [38] E. E. Noble, T. M. Hsu, R. B. Jones, A. A. Fodor, M. I. Goran, and S. E. Kanoski, "Early-life sugar consumption affects the rat microbiome independently of obesity," *Journal of Nutrition*, vol. 147, no. 1, pp. 20–28, 2017.
- [39] L. Hou, J. Wang, W. Zhang et al., "Dynamic alterations of gut microbiota in porcine circovirus type 3-infected piglets," *Frontiers in Microbiology*, vol. 11, article 1360, 2020.

Research Article

Effects of Dietary Histidine on Growth Performance, Serum Amino Acids, and Intestinal Morphology and Microbiota Communities in Low Protein Diet-Fed Piglets

Meng Kang,¹ Jie Yin ,¹ Jie Ma,¹ Xin Wu,¹ Ke Huang,¹ Tiejun Li,² and Long Ouyang³

¹College of Animal Science and Technology, Hunan Agricultural University, Changsha, China

²Key Laboratory of Agro-ecological Processes in Subtropical Region, Institute of Subtropical Agriculture, Chinese Academy of Sciences; Scientific Observing and Experimental Station of Animal Nutrition and Feed Science in South-Central, Ministry of Agriculture; Hunan Provincial Engineering Research Center for Healthy Livestock and Poultry Production, Hunan, China

³Hunan Provincial Veterinary Drug and Feed Supervision Institute, Changsha, China

Correspondence should be addressed to Jie Yin; yinjie2014@126.com

Received 13 June 2020; Revised 8 October 2020; Accepted 19 October 2020; Published 28 November 2020

Academic Editor: Miaomiao Wu

Copyright © 2020 Meng Kang et al. This is an open access article distributed under the Creative Commons Attribution License, which permits unrestricted use, distribution, and reproduction in any medium, provided the original work is properly cited.

Previous study showed that low protein diet-fed pigs are characterized by lower histidine concentration in the serum and muscle, suggesting that histidine may involve in protein-restricted response. Thus, the current study mainly investigated the effects of dietary histidine on growth performance, blood biochemical parameters and amino acids, intestinal morphology, and microbiota communities in low protein diet-challenged-piglets. The results showed that protein restriction inhibited growth performance, blood biochemical parameters and amino acids, and gut microbiota but had little effect on intestinal morphology. Dietary supplementation with histidine markedly enhanced serum histidine level and restored tryptophan concentration in low protein diet-fed piglets, while growth performance and intestinal morphology were not markedly altered in histidine-treated piglets. In addition, histidine exposure failed to affect bacterial diversity (observed species, Shannon, Simpson, Chao1, ACE, and phylogenetic diversity), but histidine-treated piglets exhibited higher abundances of *Butyrivibrio* and *Bacteroides* compared with the control and protein-restricted piglets. In conclusion, dietary histidine in low protein diet enhanced histidine concentration and affected gut microbiota (*Butyrivibrio* and *Bacteroides*) but failed to improve growth performance and intestinal morphology.

1. Introduction

Low protein diet has been widely used in pig industry to save protein sources and alleviate the nitrogen excretion [1]. Covering amino acid requirements maintains the growth performance in proper low protein diet-fed pigs [2]. For example, we found that reducing 3% dietary crude protein and balancing lysine, methionine, threonine, and tryptophan fails to markedly affect feed intake and weight gain from weaning piglets to finishing pigs, while 6% protein limitation causes a significant reduction in growth performance [3]. Also, low protein diet has been reported to enhance meat quality of growing and finishing pigs by targeting lipid metabolism, fiber characteristics, and amino acid metabolism in the muscle tissue [4]. Meanwhile, protein restriction in other animal models also

shows many merits, such as improving healthy lifespan and reducing tumor incidence [5, 6]. The potential mechanism may be associated with amino acid metabolic programming, while amino acid metabolic response and the requirement in protein-restricted models have not been fully study.

Our previous study revealed a marked change in amino acid metabolism in low protein diet-fed pigs, especially for reduction in histidine and branched-chain amino acids [3]. Zhang et al. reported that dietary supplementation with branched-chain amino acids increases growth performance and muscle mass in low protein diet-challenged piglets [7]. However, little study has focused on the role of histidine in protein-restricted piglets. In addition, histidine deficiency in diet shows a negative relationship with lactational performance in dairy cows [8]. Furthermore, dietary 0.18%

TABLE 1: Effect of dietary histidine on growth performance in low protein diet-fed piglets.

Item	Control group	Low protein group	Histidine group	Sem	P value
Initial body weight (kg)	7.69	7.64	7.68	0.17	0.99
Final body weight (kg)	21.53 ^a	16.86 ^b	16.51 ^b	0.69	<0.01
Average daily weight gain (kg)	0.39 ^a	0.26 ^b	0.25 ^b	0.02	<0.01
Average daily feed intake (kg)					
Week 1	0.42	0.41	0.39	0.01	0.18
Week 2	0.66	0.64	0.53	0.03	0.16
Week 3	0.61	0.51	0.54	0.04	0.51
Week 4	0.63 ^a	0.47 ^b	0.45 ^b	0.03	<0.01
Week 5	0.94 ^a	0.64 ^b	0.63 ^b	0.04	<0.01
Week 6	0.85 ^{ab}	0.69 ^b	0.87 ^a	0.04	0.08
Week 7	1.11 ^a	0.75 ^b	0.80 ^b	0.05	<0.01

^{a,b}Within a row means the difference was significant with different superscripts ($P < 0.05$).

histidine improves muscle and blood 1,1-diphenyl-2-picrylhydrazyl radical scavenging capacity in turkey [9]. Thus, this study mainly investigated the effect of histidine on low protein diet-fed piglets with focuses on growth performance, serum amino acid profiles, and gut microbiota communities.

2. Materials and Methods

2.1. Animals and Groups. 24 piglets (Landrace×large white, gibbed male, and 7.678 ± 0.17 kg body weight) were randomly divided into 3 groups ($n = 8$): a control group (17% CP), a low protein group (14% CP), and a low protein group supplemented with 0.1% histidine to keep the same concentration compared with the control diet. Data from the control and low protein groups shared with our previous study [10]. Animals were housed individually and given fresh feed 3 times per day for 35 days. At the end of each period, all piglets were killed for sample collection. Experimental protocol of piglet study was approved by the Animal Care and Use Committee of Institute of Subtropical Agriculture, Chinese Academy of Sciences.

2.2. Growth Performance. Feed intake and body weight from each animal were recorded. The liver, kidney, and spleen indexes were also calculated according to the ratio to the body weight of piglet.

2.3. Blood Biochemical Parameters. Blood samples were harvested from anterior vena cava and centrifugated (3000 rpm, 10 min, and 4°C) for serum collection. Biochemical kits for total protein (TP), albumin (ALB), alanine aminotransferase (ALT), aspartate aminotransferase (AST), alkaline phosphatase (ALP), urea nitrogen (BUN), creatinine (CREA), glucose (Glu), C-reactive protein (CERL3), bile acid (BILT3), and immunoglobulin G (IGG) were purchased from Roche (Shanghai, China) and tested by the Cobas c-311 coulter chemistry analyzer [3].

2.4. Blood Sample Preparation and Amino Acid Determination. 18 amino acids in the serum were determined via a High-speed Amino Acid Analyzer L-8900 (Japan).

2.5. Intestinal Histological Examination. Middle sections of the jejunum and ileum from all animals were fixed with 4% paraformaldehyde-PBS and then dehydrated and embedded in paraffin blocks for H&E dyeing. Villus length, crypt depth, and villus surface area were measured.

2.6. Gut Microbiota Sequencing. Total genome DNA from distal intestinal digesta samples was extracted for amplification using specific primer with the barcode (16S V3+4). Sequencing libraries were generated and analyzed according to our previous study [11]. Subsequent analysis of alpha diversity (Observed-species, Chao1, Shannon, and Simpson) was performed basing on this output normalized data.

2.7. Statistical Analysis. Statistical analysis of all data was performed using the one-way analysis of variance (ANOVA) to test homogeneity of variances via Levene's test and followed with Duncan's test (IBM SPSS 23 software). Data are expressed as the mean. Values in the same row with different superscripts are significant ($P < 0.05$).

3. Results

3.1. Effect of Dietary Histidine on Growth Performance in Low Protein Diet-Fed Piglets. Final body weight, average daily weight gain, and average daily feed intake in each week during the experiment were analyzed, and the results showed that reducing dietary CP markedly reduced final body weight and average daily weight gain ($P < 0.05$), while dietary supplementation with histidine failed to improve body weight gain ($P > 0.05$). Feed intake was not altered at weeks 1-3, but low protein diet reduced feed intake from week 4 to week 7 ($P < 0.05$). Interestingly, dietary histidine markedly improved average feed intake at week 6 ($P < 0.05$) but had no effect in other weeks (Table 1).

3.2. Effect of Dietary Histidine on Relative Organ Weight in Low Protein Diet-Fed Piglets. The relative weights of the liver, kidney, and spleen were calculated, and the results showed that the liver relative weight was markedly increased and the kidney relative weight was reduced in the low protein group ($P < 0.05$), while histidine supplementation failed to

TABLE 2: Effect of dietary histidine on relative organ weight in low protein diet-fed piglets.

Item	Control group	Low protein group	Histidine group	Sem	P value
Liver	2.71 ^b	3.00 ^a	3.05 ^a	0.06	0.05
Kidney	0.53 ^a	0.45 ^b	0.49 ^b	0.01	<0.01
Spleen	0.19	0.20	0.21	0.01	0.55

^{a,b}Within a row means the difference was significant with different superscripts ($P < 0.05$).

TABLE 3: Effect of dietary histidine on serum biochemical indexes in low protein diet-fed piglets.

Item	Control group	Low protein group	Histidine group	Sem	P value
Total protein	55.43	54.59	52.95	0.89	0.52
Albumin	39.69 ^a	37.23 ^{ab}	33.99 ^b	0.82	0.01
Alanine aminotransferase	60.44 ^b	78.60 ^a	75.20 ^a	2.90	0.02
Aspartate aminotransferase	72.43	62.25	69.13	3.28	0.46
Alkaline phosphatase	291.86	263.50	269.00	8.97	0.43
Gamma glutamyl transpeptidase	46.50	40.00	44.63	1.79	0.34
Lactate dehydrogenase	923.38 ^a	722.38 ^b	733.50 ^b	34.76	0.02
Acid phosphatase	18.52	20.15	18.28	1.61	0.89
NH ₃ L	287.80	295.36	275.86	16.56	0.89
Immunoglobulin M	0.31	0.26	0.29	0.01	0.26
Cholinesterase	711.75	727.50	672.75	20.22	0.54

^{a,b}Within a row means the difference was significant with different superscripts ($P < 0.05$).

affect the liver and kidney weights ($P > 0.05$). Meanwhile, the relative weight of the spleen was not significantly affected in this study (Table 2).

3.3. Effect of Dietary Histidine on Serum Biochemical Indexes in Low Protein Diet-Fed Piglets. Results of serum biochemical indexes were shown in Table 3. Compared with the control group, serum alanine aminotransferase activity was markedly enhanced, and lactate dehydrogenase activity was reduced in the low protein group ($P < 0.05$). Although histidine exposure failed to alleviate the changes of alanine aminotransferase and lactate dehydrogenase activities, albumin abundance was markedly reduced in the histidine-supplemented group compared with that in the control ($P < 0.05$).

3.4. Effect of Dietary Histidine on Serum Amino Acid Pool in Low Protein Diet-Fed Piglets. Compared with the control group, serine, threonine, alanine, lysine, methionine, and tryptophan were markedly increased, and valine and isoleucine abundances were reduced in low protein diet-fed piglets ($P < 0.05$) (Table 4). Histidine supplementation markedly enhanced histidine and reversed tryptophan concentration ($P < 0.05$). Meanwhile, histidine tended to reversed the changes of methionine and valine, but the difference was insignificant ($P > 0.05$).

3.5. Effect of Dietary Histidine on Intestinal Morphology in Low Protein Diet-Fed Piglets. In the jejunum, piglets from the low protein group showed impaired intestinal morphology evidenced by the decreased trend of villus length, the ratio of villus to crypt depth, and villus surface area, which

were slightly improved in the histidine treated group, but all these indexes were insignificant ($P > 0.05$) (Table 5).

In the ileum, villus length was significantly reduced in low protein diet-fed piglets ($P < 0.05$), while dietary supplementation with histidine failed to affect villus length and other morphologic indexes ($P > 0.05$) (Table 5).

3.6. Effect of Dietary Histidine on α -Diversity and Gut Microbiota Compositions in Low Protein Diet-Fed Piglets. Observed species, Shannon, Simpson, Chao1, ACE, and phylogenetic diversity were analyzed to evaluate the α -diversity of gut microbiota, while all of them were not markedly differentiated between three groups (Table 6), indicating that protein restriction and histidine treatment had little effect on α -diversity of gut microbiota in the current study.

Microbiota compositions at the phylum and genus levels were analyzed (Table 7). At the phylum level, *Firmicutes* and *Bacteroidetes* were two major bacteria and occupied up to 40%, but all of them were not markedly changed in response to low protein diet and histidine supplementation ($P > 0.05$). The relative abundance of *Spirochaetes* was markedly increased in low protein diet-fed piglets ($P < 0.05$) but not altered at the histidine group ($P > 0.05$). In addition, *Proteobacteria*, *Melainabacteria*, and *Tenericutes* were also tested at the ileum, but we failed to notice any significant difference between three groups.

At the genus level, *Succinivibrio*, *Anaerovibrio*, *Faecalibacterium*, *Alloprevotella*, *Lactobacillus*, *Butyrivibrio*, *Roseburia*, *Parabacteroides*, *Subdoligranulum*, *Oribacterium*, *Oscillospira*, *Streptococcus*, *Fournierella*, *Bacteroides*, and *Sphaerochaeta* were identified. Compared with the control group, the relative abundances of *Subdoligranulum* and

TABLE 4: Effect of dietary histidine on serum amino acid pool in low protein diet-fed piglets.

Item	Control group	Low protein group	Histidine group	Sem	P value
Histidine	2.32 ^{ab}	2.04 ^b	2.82 ^a	0.13	0.05
Serine	15.21 ^b	20.59 ^a	19.61 ^a	0.74	<0.01
Arginine	29.77	28.10	27.47	0.99	0.64
Glycine	115.42	103.13	100.51	3.64	0.20
Aspartic acid	3.46	2.76	2.65	0.18	0.14
Glutamic acid	66.34	61.76	57.20	2.73	0.41
Threonine	22.90 ^b	95.46 ^a	94.13 ^a	9.61	<0.01
Alanine	80.23 ^b	109.29 ^a	104.04 ^a	5.15	0.04
Proline	34.44	37.20	37.87	1.53	0.63
Cysteine	0.79	0.59	0.74	0.08	0.56
Lysine	42.97 ^b	81.43 ^a	77.76 ^a	5.61	<0.01
Tyrosine	15.40	14.42	14.43	0.51	0.70
Methionine	15.22 ^b	21.83 ^a	17.06 ^{ab}	1.30	0.09
Valine	10.95 ^a	8.51 ^b	9.52 ^{ab}	0.41	0.05
Isoleucine	12.44 ^a	4.30 ^b	5.21 ^b	0.85	<0.01
Leucine	19.80	18.19	18.04	0.63	0.47
Phenylalanine	10.47	10.85	11.13	0.28	0.64
Tryptophan	11.47 ^b	14.6 ^a	11.81 ^b	0.58	0.05

^{a,b}Within a row means the difference was significant with different superscripts ($P < 0.05$).

TABLE 5: Effect of dietary histidine on intestinal morphology in low protein diet-fed piglets.

Item	Control group	Low protein group	Histidine group	Sem	P value
Jejunum					
Villus length	513.52	469.42	542.06	14.52	0.11
Villus width	139.61	142.18	135.31	3.77	0.76
Crypt depth	202.84	194.10	201.17	5.40	0.80
Villus length/crypt depth	2.67	2.37	2.73	0.11	0.35
Villus surface area (mm ²)	0.24	0.21	0.23	0.01	0.23
Ileum					
Villus length	361.30 ^a	307.13 ^b	313.07 ^b	7.72	<0.01
Villus width	104.52	109.24	95.82	2.73	0.08
Crypt depth	121.09	111.34	109.65	3.95	0.52
Villus length/crypt depth	2.75	2.81	2.86	0.10	0.91
Villus surface area (mm ²)	0.11	0.10	0.10	0.00	0.27

^{a,b}Within a row means the difference was significant with different superscripts ($P < 0.05$).

Oscillospira were markedly reduced in response to dietary low protein diet ($P < 0.05$), while histidine exposure failed to alleviate the changes of *Subdoligranulum* and *Oscillospira* ($P > 0.05$). Interestingly, histidine-treated piglets exhibited higher abundances of *Butyrivibrio* and *Bacteroides* compared with the control and protein-restricted subjects ($P < 0.05$).

4. Discussion

Previous studies showed that dietary supplementation with amino acids improves growth performance in low protein diet-fed pigs. For example, supplementation of leucine in low protein diet improves protein deposition and meat quality in finishing pigs [12]. Also, the minimum standardized

ileal digestible histidine to lysine ratio is suggested to be 28% in piglets to maintain growth performance by using the curvilinear-plateau model [13]. However, in this study, balancing dietary histidine compared with the control diet failed to affect final body weight and weight gain in pigs, while feed intake at week 6 was markedly enhanced in the histidine group. Furthermore, relative weight of organ and serum biochemical indexes were not altered in response to dietary histidine. The reason may be caused by the dietary dosage and time of histidine, and further studies are suggested to confirm the high histidine and long-term effect on the growth performance in low protein diet-fed piglets.

Our previous study revealed a marked reduction of muscle and serum histidine in low protein diet-fed pigs [3, 14].

TABLE 6: Effect of dietary histidine on α -diversity of gut microbiota in low protein diet-fed piglets.

Item	Control group	Low protein group	Histidine group	Sem	<i>P</i> value
Observed species	594.88	595.75	589.00	9.43	0.96
Shannon	6.60	6.66	6.64	0.09	0.97
Simpson	0.97	0.97	0.98	0.00	0.46
Chao1	657.03	663.29	636.86	12.81	0.70
ACE	658.76	662.57	628.47	12.07	0.47
Phylogenetic diversity	45.76	45.15	45.37	0.67	0.40

^{a,b}Within a row means the difference was significant with different superscripts ($P < 0.05$).

TABLE 7: Effect of dietary histidine on gut microbiota compositions in low protein diet-fed piglets.

Item	Control group	Low protein group	Histidine group	Sem	<i>P</i> value
Phylum level (%)					
Firmicutes	50.53	47.44	53.30	1.26	0.17
Bacteroidetes	43.52	41.88	38.71	1.08	0.19
Proteobacteria	2.45	4.38	3.72	0.61	0.44
Spirochaetes	0.63 ^b	2.86 ^a	2.63 ^a	0.39	0.03
Melainabacteria	0.85	0.41	0.28	0.12	0.15
Tenericutes	0.44	0.51	0.43	0.06	0.88
Genus level (%)					
Succinivibrio	1.61	0.52	1.85	0.42	0.56
Anaerovibrio	1.72	2.20	3.98	0.75	0.45
Faecalibacterium	2.41	1.25	1.84	0.28	0.26
Alloprevotella	1.84	2.38	1.55	0.31	0.54
Lactobacillus	2.58	1.06	1.59	0.40	0.31
Butyrivibrio	0.01 ^b	0.05 ^b	0.56 ^a	0.11	0.06
Roseburia	0.66	1.19	0.94	0.20	0.56
Parabacteroides	0.52	0.83	1.05	0.11	0.11
Subdoligranulum	1.13 ^a	0.29 ^b	0.31 ^b	0.13	<0.01
Oribacterium	0.31	0.24	0.02	0.07	0.22
Oscillospira	1.56 ^a	0.92 ^b	0.96 ^b	0.13	0.06
Streptococcus	0.24	0.15	0.06	0.04	0.18
Fournierella	0.83	0.40	0.39	0.10	0.10
Bacteroides	0.09 ^b	0.27 ^b	0.74 ^a	0.10	0.02
Sphaerochaeta	0.39	0.84	0.50	0.11	0.24

^{a,b}Within a row means the difference was significant with different superscripts ($P < 0.05$).

Similarly, serum histidine concentration also tended to decrease in protein-restricted piglets, while balancing histidine in the diet markedly enhanced serum histidine, indicating that dietary supplementation with histidine enhanced intestinal absorption and circulating of histidine. Our previous studies reported that histidine and lysine exhibit competitive inhibitory association in transport and metabolism [11, 15], while dietary histidine in low protein diet failed to markedly inhibit lysine metabolism in the current study. Meanwhile, histidine supplementation markedly reversed tryptophan increase in low protein diet-fed piglets. Dietary tryptophan in pigs has been widely reported to improve growth performance and gut barrier [16, 17]; thus, we speculated the serum tryptophan concentration failed to correlate to growth performance in this study. Together, dietary

supplementation with histidine enhanced serum histidine concentration and affected tryptophan metabolism in low protein diet-fed piglets, but the detailed mechanism should be further studied.

Growth performance of piglet is highly associated with intestinal functions (i.e., nutrient digestibility, absorption, and barrier function). Dietary amino acids are mainly used by intestinal epithelial cells to provide energy and form protein molecules [18, 19]. For example, our previous study showed that dietary supplementation with glutamate markedly improved intestinal morphological structure, intestinal barrier function, and antioxidant system in mycotoxin-challenged pigs [18]. However, dietary histidine slightly improved villus length, the ratio of villus to crypt depth, and villus surface area in the jejunum. Jiang et al. reported

that histidine supplementation in diets (3.7 up to 12.2 g/kg) blocked Cu-induced decreases in intestinal tight junction proteins and mRNA levels of antioxidant genes [20]. Thus, the effect of histidine on intestinal morphology should be further investigated in different dosages and models.

Dietary changes and supplements are highly associated with gut microbiota, which further affect host metabolism. For example, intestinal bacterial diversity and the relative abundances of *Actinobacteria*, *Saccharibacteria*, and *Synergistetes* at the phylum level were increased in a pig model when feeding a low diet [11]. In addition, gut microbiota alteration contributed to host metabolism, such as energy metabolism, lipid metabolism, and carbohydrate metabolism [21]. In this study, we found that histidine affected tryptophan metabolism, while tryptophan metabolite (melatonin) markedly improved gut microbiota evidenced by increasing bacterial diversity and affecting the relative abundances of *Bacteroides* and *Alistipes* in murine model [21]. The current results showed that dietary histidine failed to affect bacterial diversity, but histidine-treated piglets exhibited higher abundances of *Butyrivibrio* and *Bacteroides* compared with the control and protein-restricted subjects. *Butyrivibrio* has been identified in pigs with high residual feed intake [22], indicating that *Butyrivibrio* may involve in feed intake regulation. *Bacteroides* species are significant clinical pathogens and are found in most anaerobic infections [23]. However, the mechanism of histidine-mediated *Bacteroides* proliferation and its role in piglet were not understood in the current study.

In conclusion, low protein diet reduced growth performance and affected serum amino acids and gut microbiota. Dietary supplementation with histidine markedly enhanced serum histidine concentration in low protein diet-fed piglets and restored tryptophan level. In addition, histidine-treated piglets exhibited higher abundances of *Butyrivibrio* and *Bacteroides*.

Data Availability

The data used to support to the findings of this study are available from the corresponding author upon request.

Conflicts of Interest

The authors declare that they have no competing interests.

Authors' Contributions

Meng Kang and Jie Yin contributed equally in this work.

Acknowledgments

This study was supported by the Hunan Science Foundation for Outstanding Young Scholars (2020JJ3023) and the R&D Program of China (2016YFD0501201).

References

- [1] L. T. Wu, X. Zhang, Z. Tang et al., "Low-protein diets decrease porcine nitrogen excretion but with restrictive effects on amino acid utilization," *Journal of Agricultural and Food Chemistry*, vol. 66, no. 31, pp. 8262–8271, 2018.
- [2] M. Gloaguen, N. le Floch, Y. Primot, E. Corrent, and J. van Milgen, "Performance of piglets in response to the standardized ileal digestible phenylalanine and tyrosine supply in low-protein diets," *Animal*, vol. 8, no. 9, pp. 1412–1419, 2014.
- [3] J. Yin, Y. Li, X. Zhu et al., "Effects of long-term protein restriction on meat quality, muscle amino acids, and amino acid transporters in Pigs," *Journal of Agricultural and Food Chemistry*, vol. 65, no. 42, pp. 9297–9304, 2017.
- [4] Y. H. Li, F. N. Li, Y. H. Duan et al., "Low-protein diet improves meat quality of growing and finishing pigs through changing lipid metabolism, fiber characteristics, and free amino acid profile of the muscle," *Journal of Animal Science*, vol. 96, no. 8, pp. 3221–3232, 2018.
- [5] J. Yin, W. Ren, X. Huang, T. Li, and Y. Yin, "Protein restriction and cancer," *Biochimica et Biophysica Acta (BBA) - Reviews on Cancer*, vol. 1869, no. 2, pp. 256–262, 2018.
- [6] H. Mirzaei, J. A. Suarez, and V. D. Longo, "Protein and amino acid restriction, aging and disease: from yeast to humans," *Trends in Endocrinology and Metabolism*, vol. 25, no. 11, pp. 558–566, 2014.
- [7] L. Zheng, H. Wei, C. Cheng, Q. Xiang, J. Pang, and J. Peng, "Supplementation of branched-chain amino acids to a reduced-protein diet improves growth performance in piglets: involvement of increased feed intake and direct muscle growth-promoting effect," *The British Journal of Nutrition*, vol. 115, no. 12, pp. 2236–2245, 2016.
- [8] F. Giallongo, M. T. Harper, J. Oh, C. Parys, I. Shinzato, and A. N. Hristov, "Histidine deficiency has a negative effect on lactational performance of dairy cows," *Journal of Dairy Science*, vol. 100, no. 4, pp. 2784–2800, 2017.
- [9] W. Kopec, A. Wiliczkiwicz, D. Jamroz et al., "Antioxidant status of turkey breast meat and blood after feeding a diet enriched with histidine," *Poultry Science*, vol. 95, no. 1, pp. 53–61, 2016.
- [10] J. Yin, J. Ma, Y. Y. Li et al., "Branched-chain amino acids, especially of leucine and valine, mediate the protein restricted response in a piglet model," *Food & Function*, vol. 11, no. 2, pp. 1304–1311, 2020.
- [11] J. Yin, H. Han, Y. Li et al., "Lysine restriction affects feed intake and amino acid metabolism via gut microbiome in piglets," *Cellular Physiology and Biochemistry*, vol. 44, no. 5, pp. 1749–1761, 2018.
- [12] S. Zhang, L. Chu, S. Qiao, X. Mao, and X. Zeng, "Effects of dietary leucine supplementation in low crude protein diets on performance, nitrogen balance, whole-body protein turnover, carcass characteristics and meat quality of finishing pigs," *Animal Science Journal*, vol. 87, no. 7, pp. 911–920, 2016.
- [13] A. G. Wessels, H. Kluge, N. Mielenz, E. Corrent, J. Bartelt, and G. I. Stangl, "Estimation of the leucine and histidine requirements for piglets fed a low-protein diet," *Animal*, vol. 10, no. 11, pp. 1803–1811, 2016.
- [14] Y. Li, J. Yin, H. Han et al., "Metabolic and proteomic responses to long-term protein restriction in a pig model," *Journal of Agricultural and Food Chemistry*, vol. 66, no. 47, pp. 12571–12579, 2018.
- [15] J. Yin, Y. Li, H. Han et al., "Long-term effects of lysine concentration on growth performance, intestinal microbiome, and metabolic profiles in a pig model," *Food & Function*, vol. 9, no. 8, pp. 4153–4163, 2018.

- [16] M. C. B. Tossou, H. Liu, M. Bai et al., "Effect of high dietary tryptophan on intestinal morphology and tight junction protein of weaned pig," *BioMed Research International*, vol. 2016, Article ID 2912418, 6 pages, 2016.
- [17] H. N. Liu, C. A. A. Hu, M. M. Bai et al., "Short-term supplementation of isocaloric meals with L-tryptophan affects pig growth," *Amino Acids*, vol. 49, no. 12, pp. 2009–2014, 2017.
- [18] J. Yin, M. Liu, W. Ren et al., "Effects of dietary supplementation with glutamate and aspartate on diquat-induced oxidative stress in piglets," *PLoS One*, vol. 10, no. 4, article e0122893, 2015.
- [19] J. Yin, W. Ren, J. Duan et al., "Dietary arginine supplementation enhances intestinal expression of SLC7A7 and SLC7A1 and ameliorates growth depression in mycotoxin-challenged pigs," *Amino Acids*, vol. 46, no. 4, pp. 883–892, 2014.
- [20] W. D. Jiang, B. Qu, L. Feng et al., "Histidine prevents Cu-induced oxidative stress and the associated decreases in mRNA from encoding tight junction proteins in the intestine of grass carp (*Ctenopharyngodon idella*)," *PLoS One*, vol. 11, no. 6, article e0157001, 2016.
- [21] J. Yin, Y. Li, H. Han et al., "Melatonin reprogramming of gut microbiota improves lipid dysmetabolism in high-fat diet-fed mice," *Journal of Pineal Research*, vol. 65, no. 4, article e12524, 2018.
- [22] T. Kubasova, L. Davidova-Gerzova, V. Babak et al., "Effects of host genetics and environmental conditions on fecal microbiota composition of pigs," *PLoS One*, vol. 13, no. 8, article e0201901, 2018.
- [23] H. M. Wexler, "Bacteroides: the good, the bad, and the nitty-gritty," *Clinical Microbiology Reviews*, vol. 20, no. 4, pp. 593–621, 2007.

Research Article

Cangfudaotan Decoction Alleviates Insulin Resistance and Improves Follicular Development in Rats with Polycystic Ovary Syndrome via IGF-1-PI3K/Akt-Bax/Bcl-2 Pathway

Chenye Wang , Caifei Ding, Zhoujia Hua, Chunyue Chen, and Jia Yu 

Department of Reproductive Medicine, Zhejiang Chinese Medicine and Western Medicine Integrated Hospital, Hangzhou, 310003 Zhejiang, China

Correspondence should be addressed to Jia Yu; cruzjia@163.com

Received 19 September 2020; Revised 26 October 2020; Accepted 2 November 2020; Published 24 November 2020

Academic Editor: Xiaolu Jin

Copyright © 2020 Chenye Wang et al. This is an open access article distributed under the Creative Commons Attribution License, which permits unrestricted use, distribution, and reproduction in any medium, provided the original work is properly cited.

Polycystic ovary syndrome (PCOS) is the most common endocrine and metabolic disorder prevalent in females of reproductive age; insulin resistance (IR) is the major pathogenic driver. Pharmacology is a basic option for PCOS therapy; traditional Chinese medicine (TCM), as a significant part of complementary and alternative medicine, has a long history in the clinical management of PCOS. Cangfudaotan decoction (CFD) has been used clinically for gynaecological diseases especially PCOS. In this study, first, chemical components in CFD were clarified using UPLC-Q/TOF-MS analysis. Then, an animal model of PCOS was established, granular cells were also isolated from the rats with PCOS, and CFD was administrated at different dosages in PCOS rats and granular cells, to investigate the therapeutic effect and mechanisms of CFD for PCOS treatment. The result showed that CFD treatment is effective in PCOS rats and granulosa cells. CFD was able to improve IR, restore the serum hormone levels, inhibit the inflammatory cytokines in PCOS rat, and alleviate ovary morphological injury and apoptosis in PCOS rats. In granulosa cells of PCOS, the result showed that the cell viability was improved, and cell apoptosis was inhibited after CFD administration. Further experiments suggested that CFD improves IR, follicular development, cell apoptosis, and inflammatory microenvironment, and this was associated to the regulation of IGF-1-PI3K/Akt-Bax/Bcl-2 pathway-mediated gene expression. Given that CFD sufficiently suppresses insulin resistance and improves follicular development in this study, exploring these mechanisms might help to optimize the therapeutic treatment of CFD in PCOS patients.

1. Introduction

Polycystic ovary syndrome (PCOS) is the most common endocrine and metabolic disorder prevalent in females of reproductive age. Usually, PCOS is characterized by hyperandrogenism, irregular menstrual cycle, abnormal ovarian function, follicular dysplasia (with multiple cystic ovarian follicles), and insulin resistance (IR) [1]. IR is the major pathogenic driver of PCOS; approximately 75% of PCOS patients have an impairment of insulin action [2]. In PCOS patients, ovarian cells are hyperresponsive to the stimulatory effects of insulin, thus causing ovarian hyperplasia; IR also amplifies hyperandrogenism, resulting in a disruption in the hypothalamic-pituitary-ovarian axis and aggravating PCOS [3]. Under the impairment of IR, abnormal apoptosis and

dysregulation of granulosa cells are also observed [4]. In addition, systemic low-grade chronic inflammation also appears in women with PCOS, with some parameters at hypo- or hyperlevels [5]. Case-control studies show that PCOS is associated with lower life quality and increased psychological distress; both PCOS and thereby induced infertility have negative impact on reproductive age women [6, 7]. Moreover, in a female with PCOS, except for the great probability of infertility, the risks of endometrial carcinoma, diabetes mellitus, and cardiovascular diseases also seem to be higher than the normal populations [8, 9]. Hence, it is necessary for PCOS patients to be cured of reproductive disorders.

Pharmacology management is the major therapeutic option of PCOS patients. Metformin hydrochloride (MH) is commonly used as an insulin sensitizer to restore the elevated

insulin and androgens levels and BMI; clomiphene citrate, developed as antiandrogens, is another way to resolve hyperandrogenism [10, 11]. Oral contraceptive pill (OCP) is focused on regularizing menstrual cycles and sex hormone levels [12]. Pharmacological therapies are useful to a certain extent, but we have to admit that these therapeutic medications are not totally effective and side effect-free. Long-term usage of these hormone manipulators can cause some side problems, including obesity, cancer, lactic acidosis, liver toxicity, ovarian hyperstimulation syndrome (OHSS), or miscarriage, even at low risk [13, 14]. Therefore, complementary treatments can be proper alternatives. Traditional Chinese medicine (TCM), as a significant part of complementary and alternative medicine, has a long history of usage in PCOS management. Various TCM herbs and prescriptions, which contain multiple active compounds without major adverse effects, are proposed in the treatment of clinical and laboratory symptoms of PCOS [15].

Cangfudaotan decoction (CFD), also known as Changbudodam-tang, is a TCM prescription which originates from a classic TCM book of gynecology. Several randomized controlled clinical trials show that CFD administration or combination with Western medications has the efficacy and safety on patients with PCOS [16, 17]. Although CFD has been used clinically for gynaecological diseases especially PCOS for a long time, its mechanism of action remains unclear because of its complex composition. A network pharmacology analysis that focuses on exploring the active ingredients and related pathways of CFD for treating PCOS shows that the PI3K-Akt, IR, Toll-like receptor, MAPK, and HIF-1 signaling pathways are related to the treatment of PCOS [18]. This preliminary analysis provides a possible clue for the pharmacodynamic mechanism research of CFD. In the present study, an animal model of PCOS was established, granular cells were also isolated from the rats with PCOS, and CFD was administrated at different dosages *in vivo* and *in vitro*, to investigate the therapeutic mechanisms of CFD for PCOS treatment.

2. Materials and Methods

2.1. Preparation and Identification of CFD. CFD was prepared by the Zhejiang Jingyuetang Pharmaceutical Co., Ltd (Shaoxing, China) from the same batch. CFD contains Rhizoma Atractylodis (Chinese pinyin name Cangzhu, 15 g), Rhizoma Cyperi (Chinese pinyin name Xiangfu, 10 g), Pinellia ternata (Chinese pinyin name Banxia, 9 g), Pericarpium Citri Reticulatae (Chinese pinyin name Chenpi, 6 g), Poria Cocos (Chinese pinyin name Fuling, 12 g), Arisaematis Rhizoma (Chinese pinyin name Tiannanxing, 6 g), Astragalus membranaceus (Chinese pinyin name Huangqi, 15 g), Fructus Aurantii (Chinese pinyin name Zhike, 10 g), Codonopsis Radix (Chinese pinyin name Dangshen, 15 g), Herba Epimr-dii (Chinese pinyin name Yinyanghuo, 15 g), Crataegus pinnatifida Bge (Chinese pinyin name Shanzha, 30 g), Radix Salviae (Chinese pinyin name Danshen, 20 g), licorice (Chinese pinyin name Gancao, 5 g), white mustard (Chinese pinyin name Baijiezi, 10 g), Endothelium Corneum Gigeriae Galli (Chinese pinyin name Jineijin, 30 g), and Gleditsiae

Spina (Chinese pinyin name Zaojiaoci, 10 g). In order to analyze the main phytochemicals in CFD, an UPLC-Q/TOF-MS technology was applied. UPLC-Q/TOF-MS analysis was performed on a Waters ACQUITY I-Class Plus UPLC system (Waters, USA) coupled to a SCIEX X-500R Q/TOF-MS (AB SCIEX, USA). The operation was conducted in both positive and negative ionization modes. The data was analyzed using SCIEX OS software, and the compounds were identified according to the MS data and matched to the TCM MS/MS Library.

2.2. Animals and PCOS Animal Models. The female SD rats (180 ± 20 g) were purchased from the Shanghai Sippr-BK Laboratory Animal Co. Ltd. (Certificate No. SCXK (Hu) 2018-0006; Shanghai, China) and housed in Zhejiang Chinese Medical University Animal Experiment Center (Certificate No. SYXK (Zhe) 2013-0184) in temperature 23 ± 2°C and humidity 60 ± 10% under 12 h light-dark cycles; water and food were available *ad libitum*. All animal experiments were approved by the Zhejiang Chinese Medical University Committee on Laboratory Animals, and the experiments were performed in strict accordance with the guidelines of the Chinese Council on Animal Care. After a week of adaptation to the laboratory conditions, rats were randomly divided into the control and experiment groups ($n = 10$ in each group). Control group rats were fed with normal diet during all the period of the experiments and intraperitoneally injected with 0.5% carboxymethyl cellulose (CMC, 1 ml/kg/d) for 21 days and then were orally administered with saline (1 ml/kg/d) for the next 4 weeks. For the experiment groups, rats were fed with high-fat diet (HFD) and intraperitoneally injected with 1.0 mg/kg of letrozole (1 ml/kg/d, dissolved in 0.5% CMC) for 21 days [19]. During this period, body weight and estrous cycle of rats were recorded; vaginal smears were performed to assess whether the PCOS model was successfully established. After the PCOS animal model was successfully established, the model rats were further randomly divided into the PCOS group (saline), the PCOS+L-CFD group (intragastrically administered with CFD at a dosage of 15 g/kg/d), the PCOS+H-CFD group (intragastrically administered with CFD at a dosage of 30 g/kg/d), and the PCOS+MH group (intragastrically administered with MH at a dosage of 50 mg/kg/d). Animals were treated for 4 weeks.

2.3. Sample Collection and IR Calculation. After 12 h fasting after the last administration, all rats were weighed, and then, blood samples were obtained from the tail vein to assess fasting blood glucose (FBG) and fasting insulin (FINS) levels. HOMA-IR was calculated according to the following formula: $IR = FBG \text{ (mmol/l)} \times FINS \text{ (m U/l)} / 22.5$. Then, all rats were euthanized, blood samples were collected from the abdominal aorta, and serum samples were isolated by centrifugation at 3000 rpm for 15 min and then stored at -80°C for further experiments. The left and right ovaries were dissected and weighed; the diameter of both ovaries was also detected.

2.4. ELISA. Serum follicle-stimulating hormone (FSH), luteinizing hormone (LH), testosterone (T), estradiol (E2),

TNF- α , IL-1 β , IL-6, and CRP levels were determined using commercially available ELISA kits (MEIMIAN, China). All procedures were performed according to the manufacturer's instructions. All samples were analyzed in duplicate.

2.5. Histological Analysis. Then, ovarian tissues were fixed in 4% paraformaldehyde, embedded in paraffin, sectioned at 4 μ m thickness, and stained with hematoxylin and eosin (H&E). Then, sections were viewed and photographed using a Leica DM3000 microscope (Leica, Germany). TUNEL staining was performed to assess the cell apoptosis in ovarian tissues. Briefly, ovarian tissue sections were incubated with the TUNEL reaction mixture in a humidified chamber at 37°C for 1 h (Beyotime Biotechnology Co., Ltd., Shanghai) and further incubated with peroxidase-conjugated HRP antibody at 37°C for 30 min. Then, immunoreactivity was visualized using 3,3'-diaminobenzidine (DBA), and the TUNEL-positive cells in ovarian tissue sections were observed and photographed using a Leica DM3000 microscope (Leica, Germany).

2.6. Immunohistochemical (IHC) Analysis. IHC staining was performed to assess the expression of Bax and Bcl-2 in ovarian tissues. First, ovarian tissue sections were subjected to 0.1 M citrate buffer (pH 6.0) at 95~100°C for 1 h. After blocking with 3% BSA, sections were incubated with primary antibody (Bax: 1:200 dilution, ab32503, Abcam, USA; Bcl-2: 1:200 dilution, ab182858, Abcam, USA) at 4°C overnight. After washing with PBS for three times, the section was further incubated with horseradish peroxidase- (HRP-) conjugated secondary antibody for 20 min at room temperature. Then, immunoreactivity was visualized using DBA and examined using a Leica DM3000 microscope (Leica, Germany).

2.7. Preparation of CFD-Containing Serum. Female SD rats were intragastrically administrated with normal saline (control) or CFD (15 g/kg/d and 30 g/kg/d) once daily for seven consecutive days. Two hours after the last administration, blood samples were collected from the aorta ventralis of each group's rats, saved at 4°C for 1 h, and then centrifuged at 3000 rpm/min for 15 min. The obtained blood samples from the same group were mixed together, inactivated by incubating in a water bath at 56°C for 30 min for, and sterilized through microporous membrane filtration. Then, the CFD-containing serum samples were stored at -80°C for subsequent *in vitro* experiments.

2.8. Granular Cell Isolation and Identification. Granular cell isolation was conducted according to the protocol previously described [20]. Briefly, normal and PCOS rat ovaries were removed and placed in serum-free high-glucose DMEM; adipose and connective tissues were removed. Then, the ovaries were washed and suspended in DMEM/F12. Then, follicle puncture was performed with fine needles under microscopic visualization, and granular cells were released into the medium. Then, cells were filtered through 200 μ m nylon meshes, allowing granular cells to pass through. The collected granular cells were centrifuged, and the supernatant was thereupon cultured in fresh 10% FBS-DMEM/F12 at 37°C

in a 5% CO₂ atmosphere. Cell morphology was observed under a Ts2-FC inverted fluorescence microscope (Nikon, Japan); HE assay was performed to identify the isolated granular cells.

2.9. Cell Treatment and CCK-8 Cell Viability Assay. Cell viability was detected with CCK-8 assay. Briefly, granular cells were seeded in 96-well plates for 24 h and further treated with CFD (CFD-containing serum, 0.1 mg/ml, 0.2 mg/ml), MK-2206 (PI3K inhibitor, 20 μ M), LY294002 (Akt inhibitor, 20 μ M), or 20 μ M IGF-1 for 12 h, 24 h, 48 h, and 72 h, respectively. Then, 10 μ l of CCK-8 solution was added and further incubated at 37°C for 1.5 h. The optical density (OD) of each was detected 490 nm with a CMax Plus microplate reader (MD, USA). The cell viability with different treatment conditions was then calculated from their corresponding OD values.

2.10. Flow Cytometry Analysis. Cell apoptosis was assessed using the Annexin V/fluorescein isothiocyanate (FITC)/propidium iodide (PI) apoptosis detection kit (BD Pharmingen, USA). Generally, granular cells in logarithmic phase were seeded in 6-well plates at a density of 1.2×10^6 . Then, cells were washed by binding buffer, centrifuged, and resuspended in 100 μ l binding buffer. 5 μ l Annexin V-FITC and 10 μ l PI solution were added to the suspension under dark room for 15 min. 400 μ l binding buffer was added, and cell apoptosis was analyzed using a FC500 flow cytometer (Beckman, USA). The percentage of early and late phase of apoptotic cells was calculated as cell apoptotic rate (%).

2.11. Western Blotting Assay. Granular cells from each group were homogenized in ice-cold RIPA lysis buffer (Beyotime Biotechnology Co., Ltd., China) for 30 min, and the supernatants were isolated after centrifugation at 12,000 g for 5 min at 4°C. The total protein concentration was determined using BCA kit (Solarbio, China). After that, 50 μ g of protein samples was separated on 10% SDS-PAGE gels in Tris-glycine and 0.1% SDS buffer and transferred to PVDF membranes. After blocking with 5% nonfat milk and washing with TBST for three times, the membranes were incubated with the primary antibodies (BAD, Bax, and Bcl-2: CST, USA; IGF-1, Akt, p-Akt, and GAPDH: Abcam, UK; PI3K, p-PI3K: Affinity Biosciences, USA) at 4°C overnight. Then, after blocking with 5% nonfat milk and washing with TBST for three times, the membranes were further incubated with the HRP-conjugated goat anti-rabbit IgG secondary antibody (Abcam, UK) for 1 h at room temperature. The protein bands were detected using ECL reagents and visualized by a chemiluminescence capture system. The quantification was carried out using ImageJ software, and GAPDH was used as the internal control.

2.12. Statistical Analysis. The data are presented as mean \pm SD. Differences between the two groups were analyzed using the Student *t* test; differences among more than two groups were analyzed by conducting one-way ANOVA followed by LSD comparison test using SPSS 18.0 software (SPSS, USA). *P* < 0.05 was considered as statistically significant.

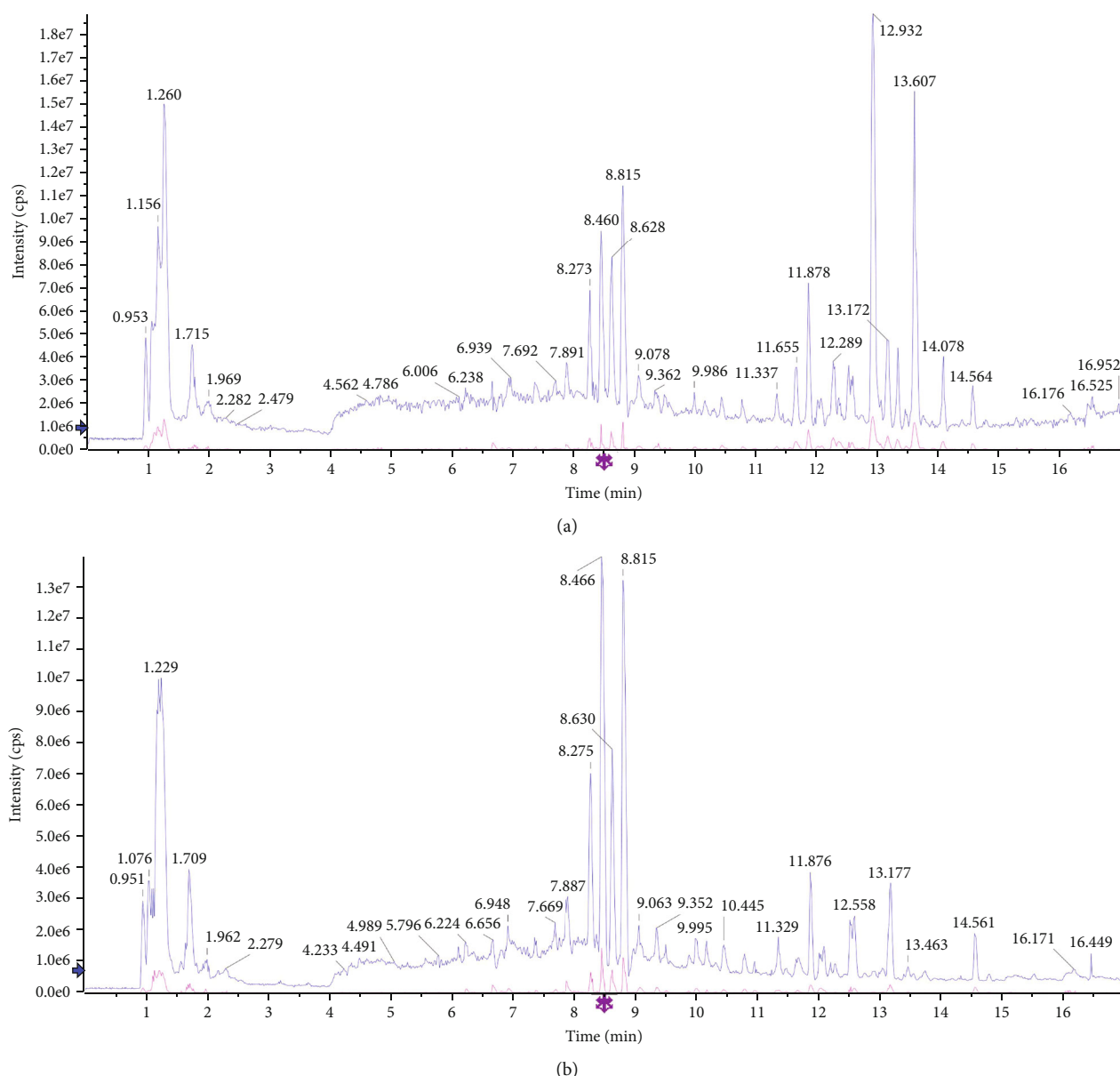


FIGURE 1: Characteristics of chemical components in CFD by UHPLC-Q/TOF/MS analysis in the (a) positive ion mode and (b) negative ion mode.

3. Results and Discussion

3.1. Determination of Chemical Components in CFD. Characteristics of chemical components in CFD were analyzed by UHPLC-Q/TOF-MS under positive ion mode and negative ion mode. As shown in Figure 1 and Table 1, UHPLC-Q/TOF/MS analysis in positive ion mode identified 43 compounds in CFD, including betaine, stachydrine, narirutin, hesperetin, and nobiletin. UHPLC-Q/TOF-MS analysis in negative ion mode also identified 43 compounds in CFD; some of them were the same with the compounds in the positive mode.

3.2. Changes of Estrous Cycle in PCOS Rat Models. The vaginal smears of the rats in the normal control and PCOS groups are presented in Figure 2(a). Rats in controls had nor-

mal 4-5 days estrous cycles, comprising proestrus, estrus, metestrus, and diestrus. Nucleated epithelial cells were observed in proestrus; keratinocytes with irregular shape that interconnected into pieces were observed in estrus; nucleated epithelial cells, irregular epithelial keratinocytes, and leukocytes were observed in metestrus; and a large number of leukocytes were observed in diestrus. But with letrozole administration, there was an irregular estrous cycle in PCOS group rats, with prolonged diestrus phase, and a large number of leukocytes were observed.

3.3. Effect of CFD on Ovary Weights and Diameter and Ovary Index of PCOS Rat Model. At the end of the experiments, rat body weight and left and right ovary weight and diameter were detected. It could be observed that with HFD feeding,

TABLE 1: Characteristics of chemical components in CFD by UHPLC-Q-TOF/MS analysis.

No.	Component name	Retention time	Formula	Precursor mass	Found at mass	Mass error (ppm)	Library score	Isotope ratio difference
1	L(+)-Arginine	1.08	C ₆ H ₁₄ N ₄ O ₂	175.119	175.1191	0.7	89.8	1.0
2	Betaine	1.16	C ₅ H ₁₁ NO ₂	118.086	118.0865	2.0	100.0	0.4
3	Trigonelline	1.20	C ₇ H ₇ NO ₂	138.055	138.0552	2.1	95.8	0.2
4	Proline	1.23	C ₅ H ₉ NO ₂	116.071	116.0709	2.3	97.8	0.6
5	Stachydrine	1.26	C ₇ H ₁₃ NO ₂	144.102	144.1019	-0.3	96.4	1.3
6	Nicotinic acid	1.73	C ₆ H ₅ NO ₂	124.039	124.0396	2.4	99.5	0.1
7	Adenosine	3.68	C ₁₀ H ₁₃ N ₅ O ₄	268.104	268.1044	1.4	100.0	1.8
8	Guanosine	4.12	C ₁₀ H ₁₃ N ₅ O ₅	284.099	284.0995	2.0	100.0	2.2
9	Phenprobamate	4.78	C ₉ H ₁₁ NO ₂	166.086	166.0865	1.3	95.7	0.8
10	Esculin hydrate	5.88	C ₁₅ H ₁₆ O ₉	341.087	341.0881	4.0	92.4	2.8
11	Chlorogenic acid	6.24	C ₁₆ H ₁₈ O ₉	355.102	355.1027	0.9	99.5	0.4
12	Fraxetin	7.25	C ₁₀ H ₈ O ₅	209.044	209.0449	2.3	75.6	0.8
13	Eriodictyol	7.88	C ₁₅ H ₁₂ O ₆	289.071	289.0713	2.1	84.4	1.7
14	Polygalaxanthone IV	7.88	C ₂₇ H ₃₂ O ₁₅	597.181	597.1823	1.4	74.6	3.8
15	Liquiritigenin	7.94	C ₁₅ H ₁₂ O ₄	257.081	257.0814	2.3	95.3	4.3
16	Scopoletin	8.07	C ₁₀ H ₈ O ₄	193.050	193.0500	2.6	91.4	2.5
17	Isoferulic acid	8.09	C ₁₀ H ₁₀ O ₄	195.065	195.0657	2.6	97.0	1.1
18	Isorhamnetin	8.17	C ₁₆ H ₁₂ O ₇	317.066	317.0664	2.6	70.4	2.9
19	Narirutin	8.47	C ₂₇ H ₃₂ O ₁₄	581.186	581.1872	1.2	97.6	0.9
20	Naringenin	8.48	C ₁₅ H ₁₂ O ₅	273.076	273.0762	1.6	100.0	0.2
21	Hesperetin	8.82	C ₁₆ H ₁₄ O ₆	303.086	303.0865	0.6	99.4	0.9
22	Hesperidin	8.82	C ₂₈ H ₃₄ O ₁₅	611.197	611.1975	0.7	84.1	1.8
23	Apigenin 7-O-beta-D-glucuronide	9.37	C ₂₁ H ₁₈ O ₁₁	447.092	447.0928	1.4	100.0	2.6
24	6,7-Dimethoxycoumarin	9.40	C ₁₁ H ₁₀ O ₄	207.065	207.0656	2.2	96.5	1.5
25	Xanthotoxol	10.13	C ₁₁ H ₆ O ₄	203.034	203.0344	2.4	74.6	1.5
26	Wogonin 7-O-glucuronide	10.45	C ₂₂ H ₂₀ O ₁₁	461.108	461.1087	1.9	100.0	1.0
27	Glycocholic acid	11.34	C ₂₆ H ₄₃ NO ₆	466.316	466.3168	1.1	79.8	2.7
28	Sodium glycocholate	11.34	C ₂₆ H ₄₂ NNaO ₆	488.298	488.2987	0.9	97.0	3.3
29	Baicalein	11.64	C ₁₅ H ₁₀ O ₅	271.060	271.0604	1.1	89.1	0.8
30	Glycyrrhetic acid	12.04	C ₃₀ H ₄₆ O ₄	471.347	471.3474	1.0	83.7	2.8
31	Formononetin	12.06	C ₁₆ H ₁₂ O ₄	269.081	269.0812	1.4	91.2	1.1
32	Bergapten	12.10	C ₁₂ H ₈ O ₄	217.050	217.0500	2.1	96.3	3.6
33	Limonin	12.54	C ₂₆ H ₃₀ O ₈	471.201	471.2020	1.4	97.0	0.4
34	Patchouli alcohol	12.61	C ₁₅ H ₂₄	205.195	205.1955	2.0	85.5	3.9
35	Wogonin	12.90	C ₁₆ H ₁₂ O ₅	285.076	285.0762	1.7	93.6	2.1
36	Nobiletin	12.93	C ₂₁ H ₂₂ O ₈	403.139	403.1387	-0.2	94.7	1.6
37	Chrysin	12.99	C ₁₅ H ₁₀ O ₄	255.065	255.0660	3.2	84.7	2.1
38	Nomilin	13.07	C ₂₈ H ₃₄ O ₉	515.228	515.2286	2.0	89.6	0.2
39	Tangeretin	13.62	C ₂₀ H ₂₀ O ₇	373.128	373.1280	-0.5	98.3	1.6
40	Curdione	13.65	C ₁₅ H ₂₄ O ₂	237.185	237.1853	1.8	92.1	2.0
41	Obacunone	13.67	C ₂₆ H ₃₀ O ₇	455.206	455.2075	2.3	76.3	0.4
42	Costunolide	15.09	C ₁₅ H ₂₀ O ₂	233.154	233.1542	2.5	91.1	1.5
43	α -Cyperone	15.41	C ₁₅ H ₂₂ O	219.174	219.1748	1.9	87.8	1.3
1	L(+)-Arginine	1.06	C ₆ H ₁₄ N ₄ O ₂	173.104	173.1043	-0.6	95.9	0.7
2	Aspartic acid	1.09	C ₄ H ₇ NO ₄	132.030	132.0302	-0.5	84.0	0.8
3	D-(+)-Glucose	1.18	C ₆ H ₁₂ O ₆	179.056	179.0559	-0.9	78.3	0.1

TABLE 1: Continued.

No.	Component name	Retention time	Formula	Precursor mass	Found at mass	Mass error (ppm)	Library score	Isotope ratio difference
4	Quinic acid	1.23	C ₇ H ₁₂ O ₆	191.056	191.0559	-1.1	91.3	1.1
5	Maltopentaose	1.27	C ₃₀ H ₅₂ O ₂₆	827.267	827.2664	-1.3	97.4	1.6
6	L-Malic acid	1.30	C ₄ H ₆ O ₅	133.014	133.0141	-1.0	86.4	0.2
7	Citric acid	1.98	C ₆ H ₈ O ₇	191.020	191.0196	-0.4	99.4	0.3
8	Uridine	2.52	C ₉ H ₁₂ N ₂ O ₆	243.062	243.0621	-0.8	78.5	1.2
9	Guanosine	4.10	C ₁₀ H ₁₃ N ₅ O ₅	282.084	282.0841	-0.9	98.2	2.1
10	Phenprobamate	4.77	C ₉ H ₁₁ NO ₂	164.072	164.0714	-1.7	98.4	1.7
11	Protocatechuic acid	5.23	C ₇ H ₆ O ₄	153.019	153.0191	-1.7	96.0	0.8
12	Vanillic acid	5.52	C ₈ H ₈ O ₄	167.035	167.0348	-1.3	81.2	2.3
13	L-Tryptophan	5.82	C ₁₁ H ₁₂ N ₂ O ₂	203.083	203.0823	-1.7	93.1	0.6
14	Protocatechuic aldehyde	6.14	C ₇ H ₆ O ₃	137.024	137.0243	-0.7	97.2	0.3
15	Chlorogenic acid	6.23	C ₁₆ H ₁₈ O ₉	353.088	353.0876	-0.5	100.0	0.4
16	A3-N-butyl-4,5-Dihydrophthalide	6.53	C ₁₂ H ₁₆ O ₂	191.108	191.1076	-0.6	77.2	3.3
17	Caffeic acid	6.72	C ₉ H ₈ O ₄	179.035	179.0349	-0.5	83.5	1.6
18	Rutin	7.61	C ₂₇ H ₃₀ O ₁₆	609.146	609.1455	-1.0	96.6	1.1
19	p-Coumaric acid	7.66	C ₉ H ₈ O ₃	163.040	163.0400	-0.7	99.0	0.3
20	Hyperin	7.85	C ₂₁ H ₂₀ O ₁₂	463.088	463.0878	-0.9	87.3	4.0
21	Neorientocitrin	7.88	C ₂₇ H ₃₂ O ₁₅	595.167	595.1663	-0.9	95.1	0.7
22	Liquiritin	7.93	C ₂₁ H ₂₂ O ₉	417.119	417.1187	-1.0	98.1	1.7
23	Isoferulic acid	8.08	C ₁₀ H ₁₀ O ₄	193.051	193.0505	-0.8	97.6	0.3
24	Naringin	8.47	C ₂₇ H ₃₂ O ₁₄	579.172	579.1712	-1.2	96.2	2.0
25	Isochlorogenic acid C	8.62	C ₂₅ H ₂₄ O ₁₂	515.119	515.1190	-1.0	98.5	0.1
26	Baicalin	9.36	C ₂₁ H ₁₈ O ₁₁	445.078	445.0772	-1.0	99.4	1.2
27	Cistanoside D	9.73	C ₃₁ H ₄₀ O ₁₅	651.229	651.2284	-1.7	88.6	4.5
28	Isoliquiritigenin	9.87	C ₁₅ H ₁₂ O ₄	255.066	255.0660	-1.0	92.7	0.8
29	Eriodictyol	9.96	C ₁₅ H ₁₂ O ₆	287.056	287.0556	-1.7	98.9	2.9
30	Xanthotoxol	10.12	C ₁₁ H ₆ O ₄	201.019	201.0190	-1.6	91.2	0.9
31	Wogonin 7-O-glucuronide	10.44	C ₂₂ H ₂₀ O ₁₁	459.093	459.0928	-1.1	98.1	0.9
32	Naringenin	10.95	C ₁₅ H ₁₂ O ₅	271.061	271.0610	-0.9	99.4	0.5
33	Hesperetin	11.30	C ₁₆ H ₁₄ O ₆	301.072	301.0715	-1.0	95.7	0.7
34	Glycocholic acid	11.34	C ₂₆ H ₄₃ NO ₆	464.302	464.3010	-1.6	78.0	0.3
35	Baicalein	11.64	C ₁₅ H ₁₀ O ₅	269.046	269.0454	-0.6	94.0	2.4
36	Glycoursodeoxycholic acid	11.88	C ₂₆ H ₄₃ NO ₅	448.307	448.3067	-0.3	95.2	0.8
37	Glycyrrhizic acid	12.03	C ₄₂ H ₆₂ O ₁₆	821.397	821.3955	-1.2	92.1	2.3
38	Eupatilin	12.45	C ₁₈ H ₁₆ O ₇	343.082	343.0819	-1.1	98.1	3.2
39	Chrysin	12.99	C ₁₅ H ₁₀ O ₄	253.051	253.0503	-1.4	78.2	1.2
40	Chrysosplenetin B	13.05	C ₁₉ H ₁₈ O ₈	373.093	373.0924	-1.3	94.3	0.9
41	Ursodeoxycholic acid	13.19	C ₂₄ H ₄₀ O ₄	391.285	391.2848	-1.4	96.4	2.3
42	Asiatic acid	13.77	C ₃₀ H ₄₈ O ₅	487.343	487.3419	-2.1	73.2	2.9
43	Dioscin	14.97	C ₄₅ H ₇₂ O ₁₆ COOH ⁻	913.480	913.4789	-1.5	76.9	2.2

the body weight was significantly increased in PCOS rats. As shown in Table 2, compared to the control group, rat ovary diameter and organ index in the PCOS group were significantly increased ($P < 0.01$). Compared to the PCOS model

group, in the CFD low-dose group, the ovary index was significantly decreased ($P < 0.05$); in the CFD high-dose group, the ovary diameter and ovary index were significantly decreased ($P < 0.05$).

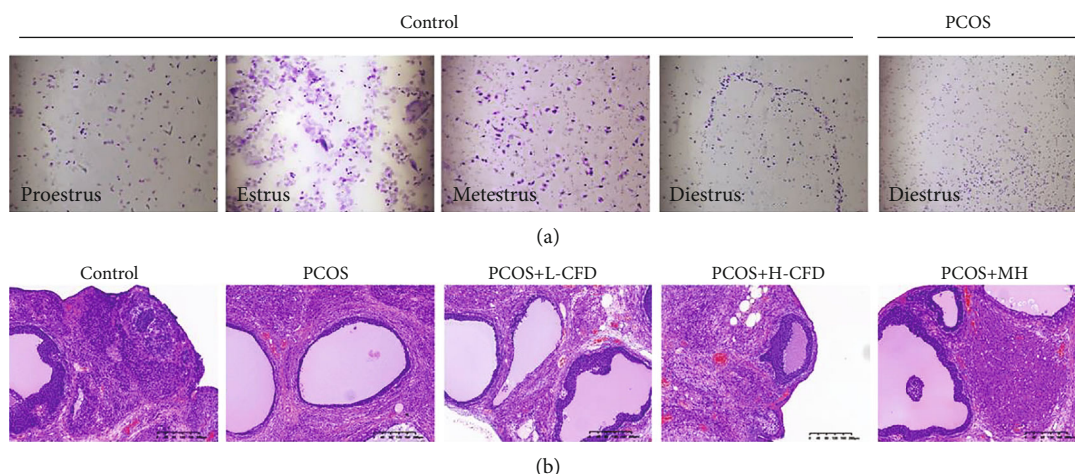


FIGURE 2: Effect of CFD on estrous cycle and ovary morphological alterations of PCOS rat model: (a) changes of estrous cycle in rats; (b) H&E staining (magnification $\times 200$).

TABLE 2: Effect of CFD on PCOS rat ovary weights and diameter and organ index ($n = 10$).

	Weight (g)	Weight of left ovary (mg)	Weight of right ovary (mg)	Ovary organ index	Diameter of left ovary (mm)	Diameter of left ovary (mm)
Control	312.52 ± 17.14	69.2 ± 8.66	70.02 ± 7.89	44.72 ± 5.14	5.89 ± 0.68	6.0 ± 0.68
PCOS	393.74 ± 18.1 ▲▲	157.09 ± 17.61 ▲▲	162.1 ± 19.9 ▲▲	81.06 ± 7.31 ▲▲	7.87 ± 0.75 ▲▲	7.86 ± 0.64 ▲▲
PCOS+L-CFD	383.25 ± 18.36	139.55 ± 11.99 *	145.76 ± 15.89	74.65 ± 6.11 *	7.52 ± 0.63	7.58 ± 0.33
PCOS+H-CFD	366.73 ± 12.06 *	117.5 ± 26.96 **	122.8 ± 19.52 *	65.67 ± 9.4 *	7.12 ± 0.67 *	7.05 ± 0.72 *
PCOS+MH	331.81 ± 11.14 **	94.98 ± 19.27 **	97.78 ± 8.52 **	58.23 ± 8.18 **	6.43 ± 0.73 **	6.69 ± 0.91 **

Compared to the control group, ▲ $P < 0.05$ and ▲▲ $P < 0.01$; compared to the PCOS group, * $P < 0.05$ and ** $P < 0.01$.

3.4. Effect of CFD on Ovary Morphological Recovery of PCOS Rat Model. H&E staining (Figure 2(b)) showed that the structure in the control group ovarian tissues exhibited a normal morphology, with multiple luteal and follicles, as well as normal oocytes, and multiple layers of granular cells within the follicles were observed. But the ovary in the PCOS group showed multiple follicles with apparent cystic dilatation, and the layers of the granular cells were decreased, and the oocytes within the follicles also seemed to disappear. Upon treatment with CFD, it showed that the morphological alterations in PCOS rat ovary were recovered partly, the oocytes appeared, the layers of the granular cells increased, and the cystic follicles also decreased.

3.5. Effect of CFD on IR, Serum Hormone, and Proinflammatory Cytokine Levels of PCOS Rat Model. The FPG and FNS levels were detected; the HOMA-IR was also calculated in each group's rats. It could be observed that the levels of FPG and FNS and HOMA-IR were increased in PCOS model rats, but these increases were restored with CFD or MH treatment, especially in the H-CFD and MH groups with significant differences compared with the PCOS group ($P < 0.05$, $P < 0.01$; Figure 3(a)). Serum hormone

levels including FSH, LH, P, and T were also detected to assess the effect of CFD on serum hormone (Figure 3(b)). The results showed that there are no significant changes of the FSH levels among the groups, while LH, T, and E2 levels in the PCOS group were significantly increased compared with those in the control group ($P < 0.01$). Compared with the PCOS model group, the levels of LH and T were significantly decreased in the CFD-treated groups ($P < 0.05$). As shown in Figure 3(c), serum levels of proinflammatory cytokines, including TNF- α , IL-1 β , IL-6, and CRP, were also detected. In the PCOS group, the levels of TNF- α , IL-1 β , IL-6, and CRP were significantly elevated compared with those in the control group, but these elevated levels were significantly inhibited in the CFD treatment groups ($P < 0.05$).

3.6. Effect of CFD on Cell Apoptosis and Bax and Bcl-2 Expression in Ovarian Tissues of PCOS Rat Model. TUNEL staining was used to assess the effect of CFD on cell apoptosis in ovarian tissues (Figure 4(a)). The result showed that the PCOS group exhibited a significant high rate of cell apoptosis compared with the control group. CFD treatment had an inhibition effect on the cell apoptosis in PCOS rat ovarian tissues, especially in high dosage. Since the TUNEL staining

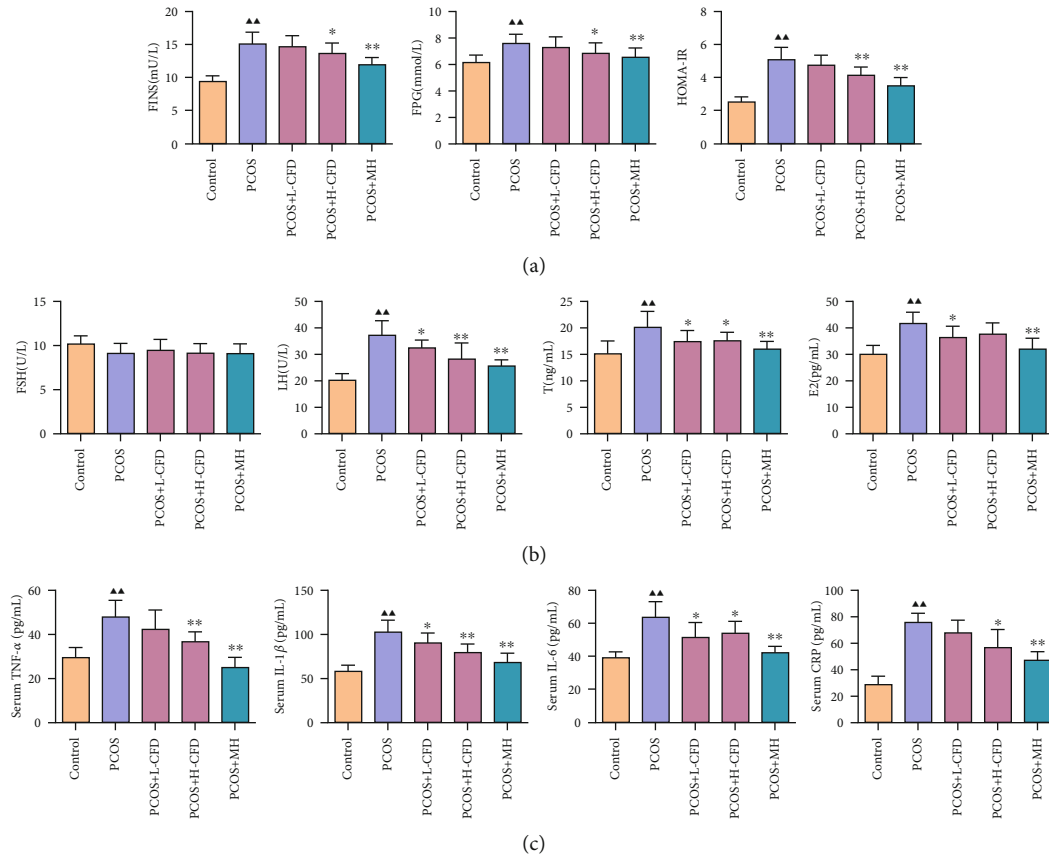


FIGURE 3: Effect of CFD on PCOS rat (a) insulin resistance, (b) serum hormone levels, and (c) proinflammatory cytokine levels ($n = 10$). Compared to the control group, ▲ $P < 0.05$ and ▲▲ $P < 0.01$; compared to the PCOS group, * $P < 0.05$ and ** $P < 0.01$.

showed that CFD could inhibit cell apoptosis in PCOS model rats, IHC staining was further performed to determine the expression of Bax and Bcl-2 in ovarian tissues. As the results indicated in Figure 4(b), the relative expression of Bax was significantly increased; Bcl-2 was significantly decreased in the PCOS model group compared to the control group, while in CFD-treated groups the relative expression of Bax was decreased, and Bcl-2 was increased, with statistical significance in the L-CFD group for Bax and in the H-CFD group for Bax and Bcl-2 ($P < 0.05$).

3.7. Identification of the Isolated Granular Cells. Normal and PCOS model granular cells were isolated from the control and PCOS rat ovary, respectively. It could be observed that the granular cells in the control group had a pleomorphic or fusiform shape, and the cells were connected together by their pseudopodia; the cells in the PCOS group had a pleomorphic or fiber shape (Figure 5(a)). H&E staining showed that the granular cells in the control group had dark blue-stained cell nuclei, reddish-stained cytoplasm, and nucleolus were easy observed; the granular cell nuclei in the PCOS group were dark blue in stained color, oval in shape, with some cell nuclei enlarged (Figure 5(b)).

3.8. Effect of CFD on Cell Viability and Apoptosis in Granular Cells of PCOS Rat Model. CCK-8 assay was used to analyze the granular cell viability with or without CFD treatment

for 0 h, 12 h, 24 h, 48 h, and 72 h. As the result indicated, the cell viability rate in the PCOS group was significantly inhibited compared to that in the control group in 0 h, 12 h, 24 h, 48 h, and 72 h ($P < 0.01$; Figure 5(c)). After incubation with CFD at different dosages, the results showed that the cell viability rates were increased compared with those of the PCOS group. In 24 h and 48 h, statistical differences were observed between the CFD groups and the PCOS group. Cell apoptosis was also evaluated using the flow cytometry assay (Figure 5(d)). After incubation with CFD for 24 h, it showed that the cell apoptosis rates were significantly increased in the PCOS group granular cells ($P < 0.01$), but upon CFD treatment, the apoptotic rate was decreased significantly ($P < 0.01$).

3.9. Effect of CFD on IGF-1-PI3K/Akt-Bax/Bcl-2 Pathway in Granular Cells of PCOS. As shown in Figure 6(a), the relative protein expression levels of Bax and Bad were significantly increased, and Bcl-2 was significantly decreased in the PCOS model granular cells compared to the control granular cells ($P < 0.01$). Upon CFD administration, the expression level of Bcl-2 was significantly increased in the L-CFD group ($P < 0.05$), the expression levels of Bax and Bad were significantly decreased, and Bcl-2 was significantly increased in the H-CFD group ($P < 0.05$). As shown in Figure 6(b), the relative expression levels of IGF-1 were significantly increased, and p-Akt/Akt and p-PI3K/PI3K were significantly

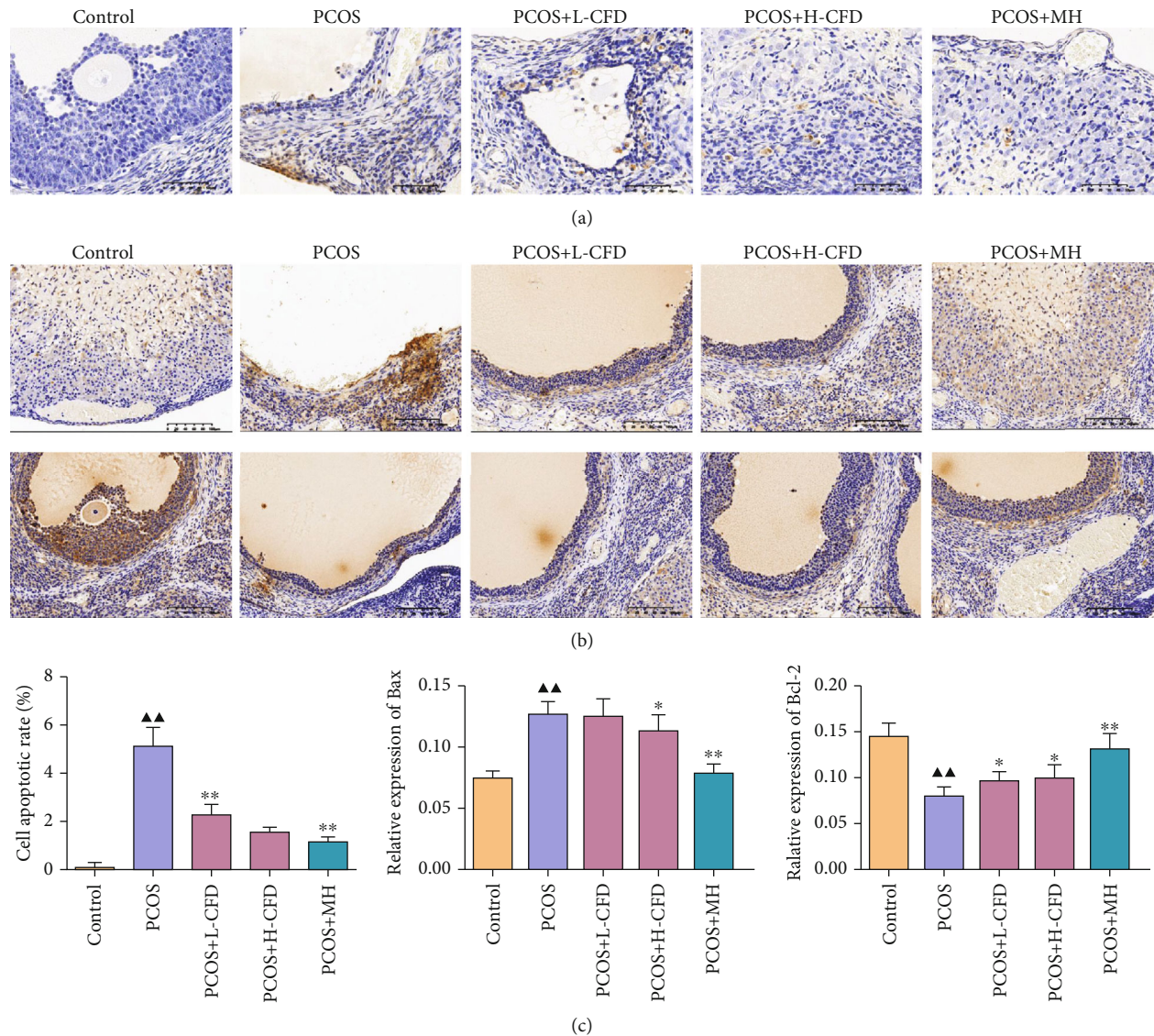


FIGURE 4: Effect of CFD on cell apoptosis and Bax and Bcl-2 expression in PCOS rat ovarian tissues ($n = 3$). (a) TUNEL staining; (b) immunohistochemistry staining of Bax and Bcl-2; (c) semi-quantification of cell apoptosis and relative expression of Bax and Bcl-2. Magnification $\times 200$.

decreased in the PCOS model cells ($P < 0.05$). Upon CFD administration, the expression levels of p-Akt/Akt and p-PI3K/PI3K were significantly increased in the CFD groups ($P < 0.05$).

3.10. IGF-1-PI3K/Akt-Bax/Bcl-2 Pathway Involved in the Attenuation of CFD on PCOS Model Granular Cells. To explore the role of the IGF-1-PI3K/Akt-Bax/Bcl-2 pathway in the attenuation of CFD on PCOS, PCOS model granular cells were incubated with CFD (0.2 mg/ml), together with 20 μ M MK-2206 (PI3K inhibitor), 20 μ M LY294002 (Akt inhibitor), or 20 μ M IGF-1. CCK-8 assay showed that compared to the PCOS group cells, the cell viability rates were significantly increased in the treatment groups ($P < 0.01$; Figure 7(a)). Furthermore, compared with the H-CFD group, the cell viability was significantly increased in the H-CFD+IGF-1 group; the cell viability was significantly

increased in the H-CFD+MK-2206 group and the H-CFD+LY294002 group after 24 h, 48 h, and 72 h treatment ($P < 0.05$). Cell apoptosis results also showed that the apoptosis rates in the treatment groups were significantly decreased compared to those in the PCOS group ($P < 0.01$; Figure 7(b)). Compared to the H-CFD group, cell apoptosis was significantly increased in the H-CFD+MK-2206 group and the H-CFD+LY294002 group, and it was significantly increased in the H-CFD+IGF-1 group ($P < 0.05$).

As shown in Figure 8(a), the relative protein expression levels of Bax and Bad were significantly decreased, and Bcl-2 was significantly increased in the H-CFD granular cells compared to the PCOS model granular cells ($P < 0.01$). Compared to the H-CFD group, the expression levels of Bax and Bad were increased, and Bcl-2 was decreased in the H-CFD+MK-2206 group and the H-CFD+LY294002 group ($P < 0.05$); the expression level of Bad was significantly

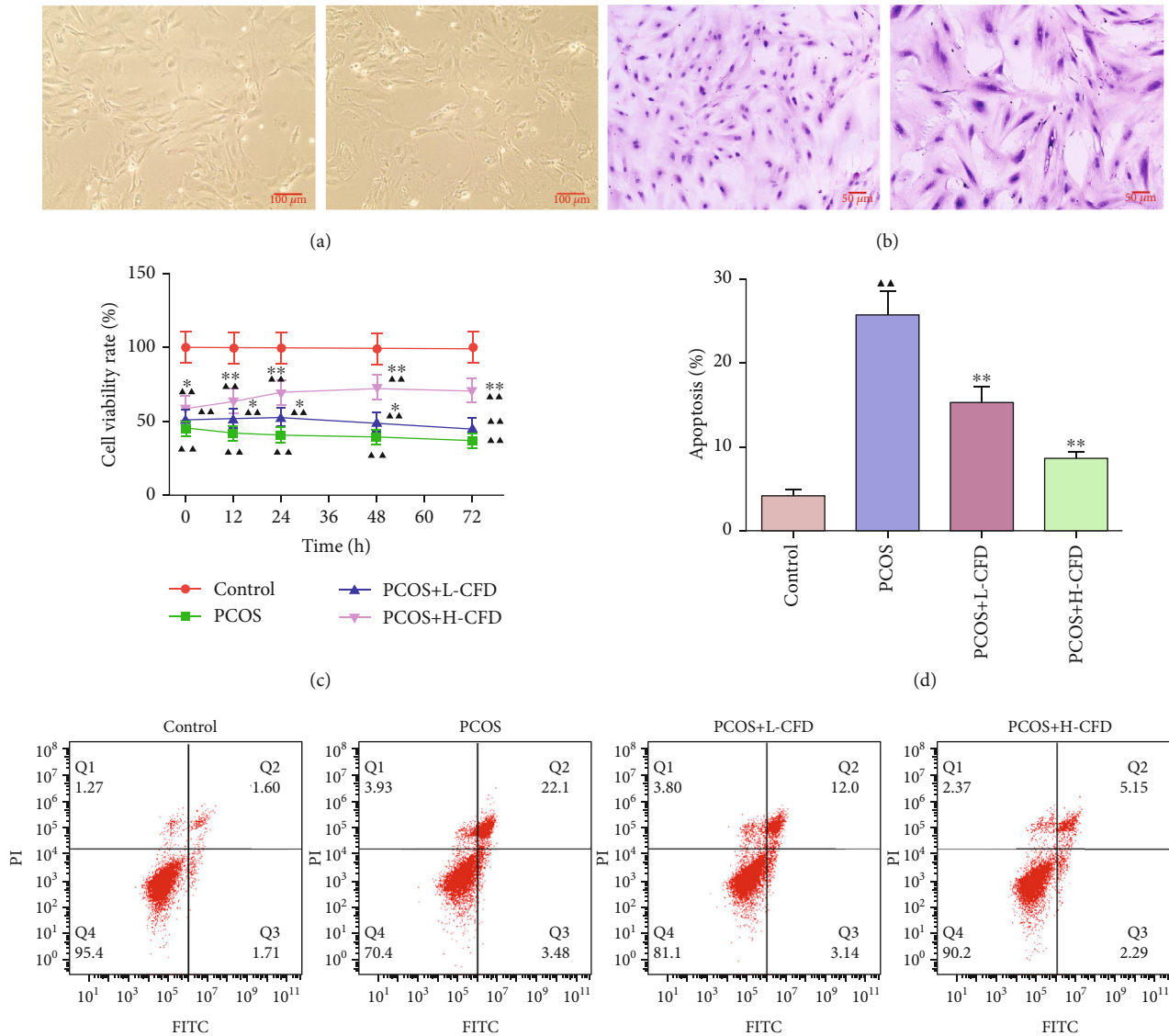


FIGURE 5: CFD ameliorates cell viability, inhibiting cell apoptosis in granular cells with PCOS ($n = 3$). (a) Cell morphology identification of the normal and PCOS model granular cells (magnification $\times 100$); (b) H&E staining of the normal and PCOS model granular cells (magnification $\times 200$); (c) granular cells were treated with CFD (0.1 mg/ml, 0.2 mg/ml) for 12 h, 24 h, 48 h, and 72 h, and then, CCK-8 assay was used to assess cell viability; (d) cell apoptosis was assessed using Annexin V/FITC/PI flow cytometry analysis.

decreased in the H-CFD+IGF-1 group ($P < 0.05$). As shown in Figure 8(b), compared to the H-CFD group, the relative expression levels of IGF-1 were decreased; p-Akt/Akt and p-PI3K/PI3K were decreased in the H-CFD+MK-2206 group and the H-CFD+LY294002 group cells ($P < 0.05$). The expression levels of IGF-1, p-Akt/Akt, and p-PI3K/PI3K were increased in the H-CFD+IGF-1 group.

4. Discussion

Given to the conditions that PCOS continues to increase and has a negative impact on reproductive age females, it is necessary for PCOS patients to be cured of reproductive disorders. Based on a PCOS model in rat and granulosa cells, in this study, we found that CFD treatment for a period is effective *in vivo* and *in vitro*. It showed that CFD is able to

improve IR, restore the serum hormone levels in PCOS rats, and alleviate ovary morphological injury and apoptosis in PCOS rats. In granulosa cells of PCOS, the result showed that the cell viability was improved, and cell apoptosis was inhibited after CFD administration. Further experiments suggested that CFD alleviated PCOS which contributed to the regulation of the IGF-1-PI3K/Akt-Bax/Bcl-2 pathway. In addition, characteristics of the chemical components in CFD were clarified using UPLC-Q/TOF-MS analysis; 43 compounds were identified under positive ion mode and negative ion mode.

The pathogenesis of PCOS remains complicated and not clear yet. But more and more studies evidence that IR regulates multiple mediators and pathways and is critically involved in the pathogenesis and development of PCOS [2, 21]. Insulin is the key regulatory hormone in the processes

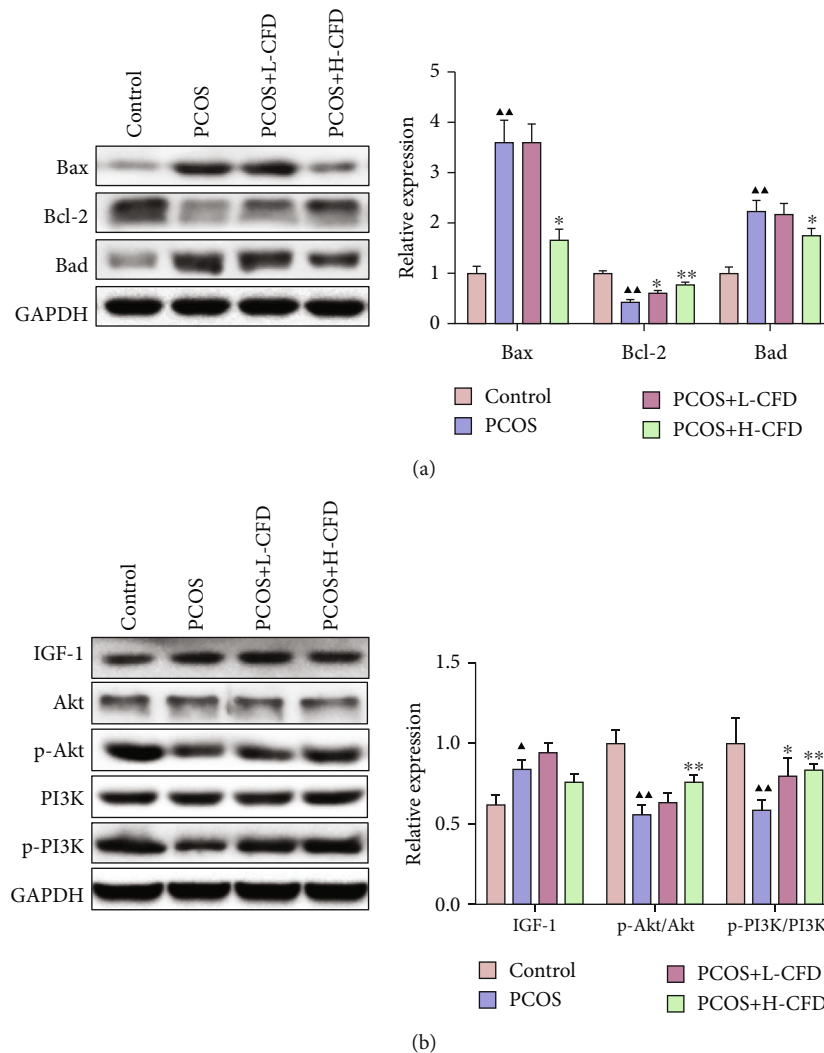


FIGURE 6: CFD ameliorates follicular development and insulin resistance via the IGF-1-PI3K/Akt-Bax/Bcl-2 pathway ($n = 3$). (a) Expression of Bax, Bcl-2, and Bad was measured by western blotting. (b) Expression of IGF-1, p-PI3K/PI3K, and p-Akt/Akt was measured by western blotting. GAPDH was used as control.

of glucose and lipid energy metabolism. In the present study, except for the significantly increased HOMA-IR in PCOS rats, the serum level of T and LH/FSH ratio were also significantly increased compared to those in normal rats, which corresponded with the previous studies. The abnormal increase of insulin could stimulate the oversecretion of androgen, thus inducing hyperandrogenism. A recent study published in "Lancet" demonstrated that insulin could drive adipose androgen generation in PCOS female subcutaneous adipose tissue, and this improvement is worked by increasing AKR1C3 activity [22]. Furthermore, an irregular estrous cycle, with a prolonged diestrus phase in PCOS rats, was observed via vaginal smears in this study. At the same time, HE staining showed that the ovary morphology in PCOS rats was different from the controls, characterized by multiple follicles with apparent cystic dilatation and the decrease of the granular cell layers and oocytes within the follicles. The excessive androgen in PCOS can cause early luteinization of ovarian granular layer cells, stop follicular development and

growth, and lead to follicle atresia and eventually anovulation or poor ovulation [19]. Thereby, irregular menstrual cycle or estrous cycle also occurred. After CFD treatment, our result found that HOMA-IR was decreased. It seems that CFD could regulate the FPG and FINS levels to inhibit IR in PCOS rats, which was consistent with the clinical study of CFD [17]. In CFD-treated groups, the serum LH and T levels were restored, the injury on ovary morphology was recovered, and cell apoptosis was also inhibited, especially in the high-dosage group.

Chronic inflammation is accompanied with the occurrence and progression of PCOS. Continuous release of inflammatory mediators could perpetuate the inflammatory condition in women with PCOS, possibly associated with IR and other long-term clinical manifestations [23, 24]. Multiple mediators of inflammation, such as TNF- α , IL-1, IL-6, IL-8, CCL2, CRP, and MCP, as well as inflammatory-immune cells and increased oxidative stress contributed to the low-grade systemic inflammation of PCOS. A prospective

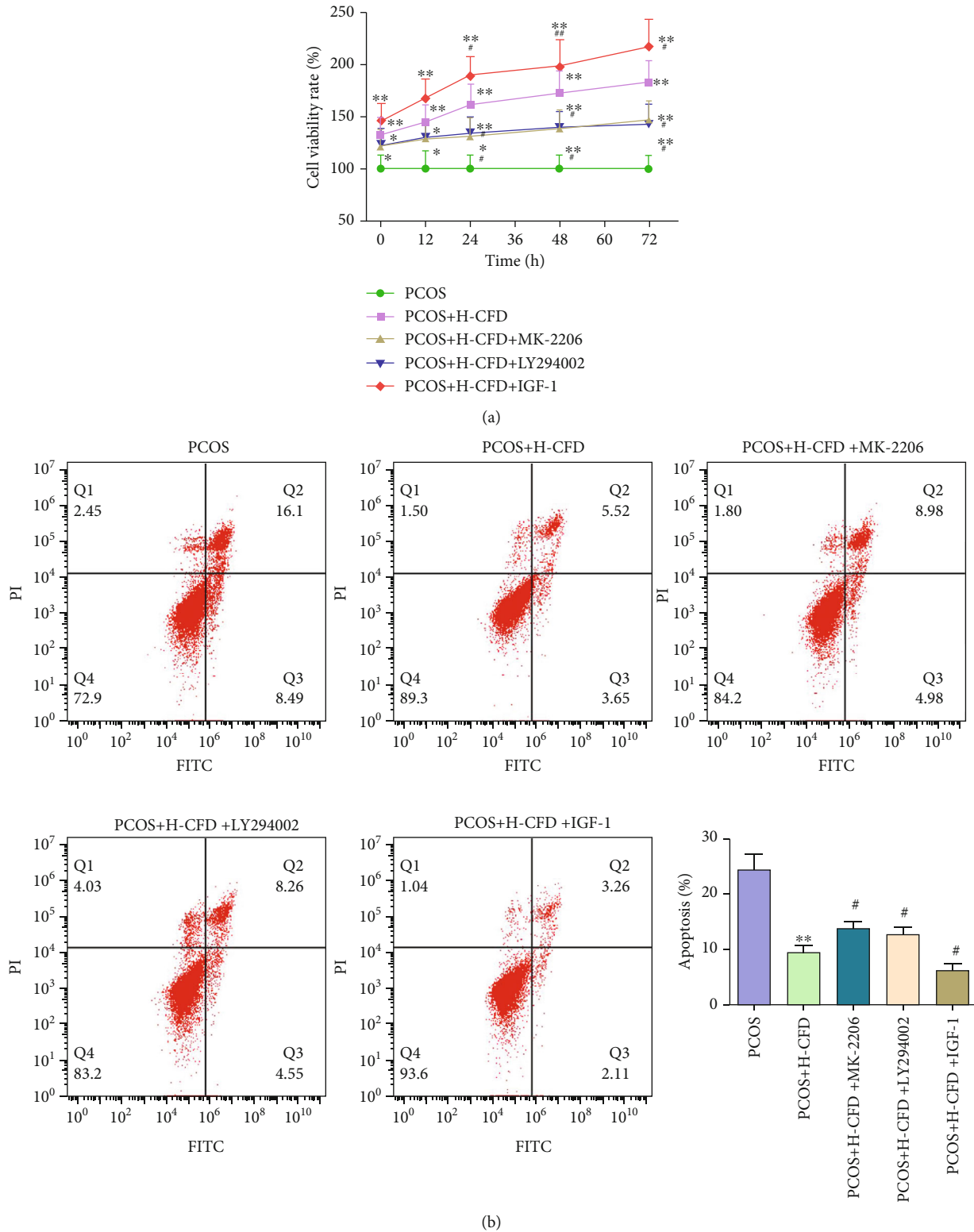


FIGURE 7: CFD ameliorates cell viability, inhibiting cell apoptosis in granular cells of PCOS rat model ($n = 3$). (a) Granular cells were treated with CFD (0.2 mg/ml), MK-2206 (20 μ M), LY294002 (20 μ M), or IGF-1 (20 μ M) for 12 h, 24 h, 48 h, and 72 h, and then, CCK-8 assay was used to assess cell viability. (b) Cell apoptosis was assessed using Annexin V/FITC/PI flow cytometry analysis.

case-control study shows that the serum TGF- β 1 and NF- κ B were significantly higher and TSP-1 was significantly lower in the PCOS groups than those in the control group, which sup-

port the association between PCOS and chronic inflammation [5]. Hence, strategies focused on ameliorating inflammation may be possible management of PCOS [25,

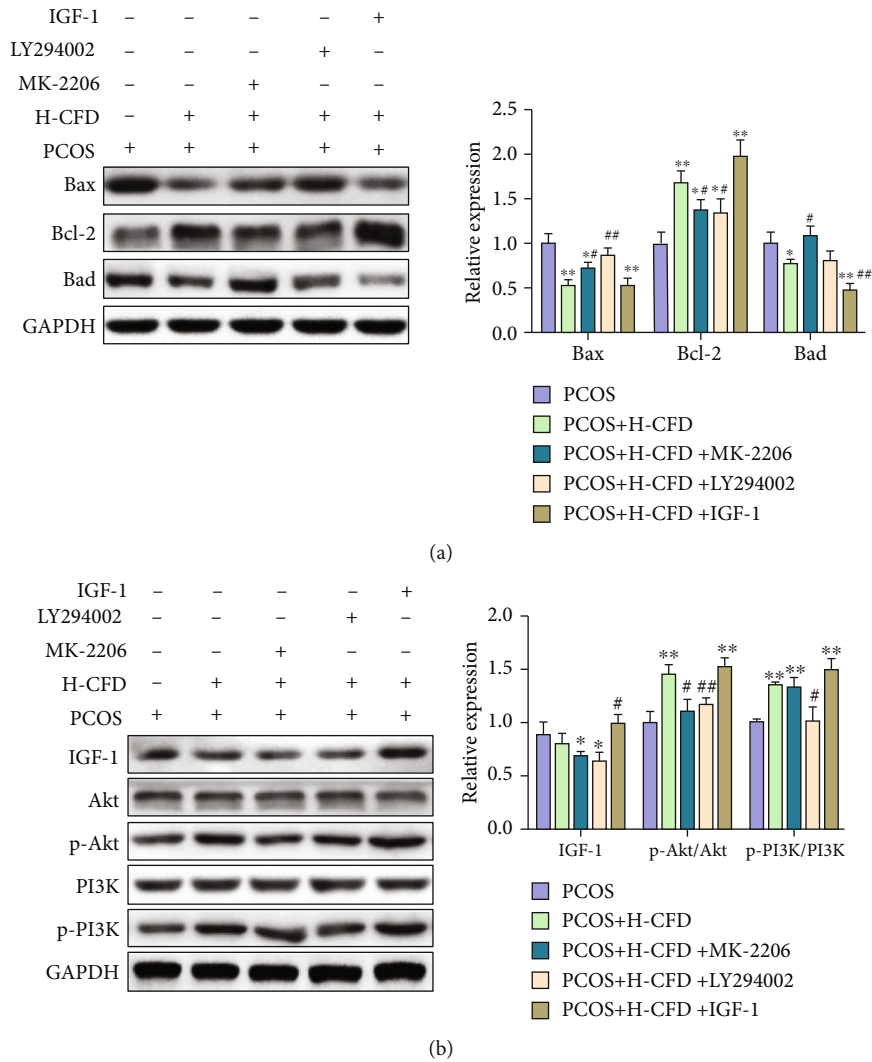


FIGURE 8: CFD ameliorates follicular development and insulin resistance via the regulation of the IGF-1-PI3K/Akt-Bax/Bcl-2 pathway ($n = 3$). (a) The expression of Bax, Bcl-2, and Bad was measured by western blotting. (b) The expression of IGF-1, p-PI3K/PI3K, and p-Akt/Akt was measured by western blotting. GAPDH was used as control.

26]. In our study, we detected the inflammatory cytokines, including TNF- α , IL-1 β , IL-6, and CRP in PCOS; the result showed that the elevated serum levels of TNF- α , IL-1, IL-6, and CRP in PCOS model rats were significantly decreased with CFD treatment.

As a guarder of ovum, granulosa cells produce steroidal hormones and growth factors, interact with the oocyte, create a highly specialized microenvironment, and play an essential role in normal follicular development and maturation process [27]. Follicular dysplasia is a basic characteristic of PCOS, and accumulation studies show that the follicular dysplasia in PCOS is critically associated with the abnormal apoptosis of granulosa cells [20, 28]. The Bcl-2 family has a key role in the mitochondrial apoptosis pathway; the abnormal expression of proteins in the Bcl-2 family, such as Bcl-2, Bcl-XL, Bax, and Bad, is involved in the abnormal increased apoptosis in PCOS [29, 30]. In our study, TUNEL staining and flow cytometry analysis showed that cell apoptosis was significantly increased in PCOS rat ovary tissues and granu-

losa cells. In addition, it seemed that there is abnormal expression of Bcl-2 family proteins in PCOS, the expressions of Bax and Bad were increased, and Bcl-2 was decreased compared to the normal controls. But in the CFD treatment groups, inhibition effects on cell apoptosis *in vivo* and *in vitro* were observed, and the protein expression of the Bcl-2 family was also restored. It indicated that CFD might improve follicular development in PCOS rats by regulating apoptosis.

PI3K/Akt signaling is one of the classic insulin signaling pathways; insulin mainly regulates the PI3K/Akt signaling to mediate its metabolic regulation effect. Insulin receptor (INSR), as a receptor of insulin, usually combines with insulin receptor substrate (IRS) to activate two signaling pathways: PI3K and MAPK. The PI3K/Akt pathway could be induced via insulin and acts as an important effector; Akt/PKB is capable of translocating glucose transporters, like GLUT4, to the cell membrane thus increasing glucose uptake [31]. Cho et al.'s study published in "Science" showed that

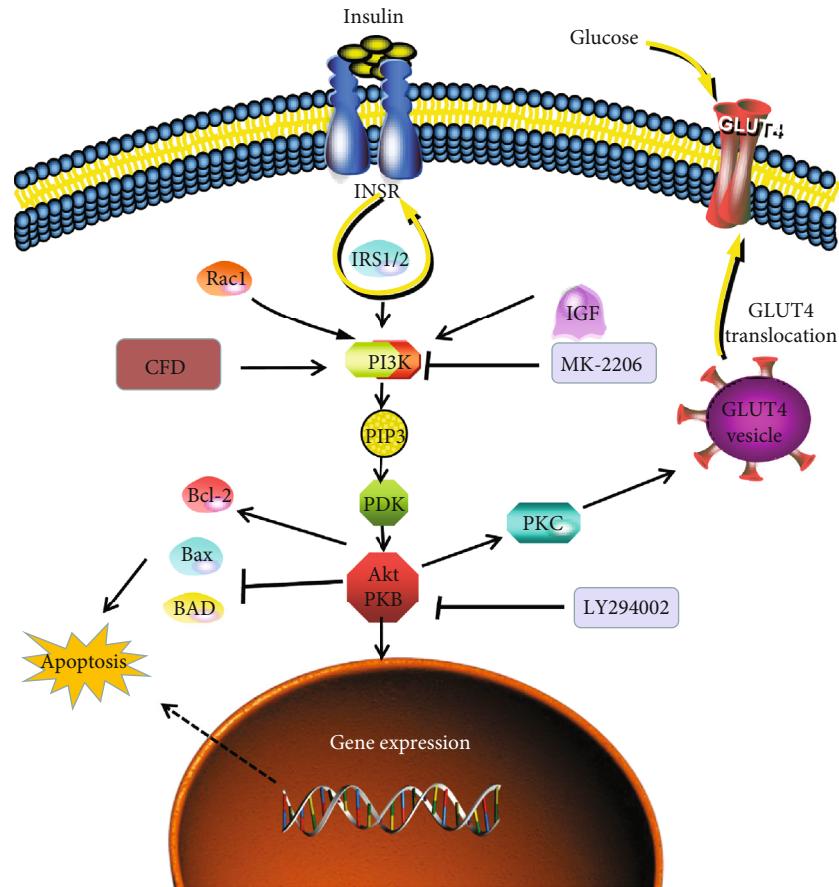


FIGURE 9: CFD ameliorates insulin resistance and improves follicular development in rats with polycystic ovary syndrome via the IGF-1-PI3K/Akt-Bax/Bcl-2 pathway.

mice deficient in AKT2 are impaired in the ability of insulin to lower blood glucose [32]. Zhang et al. showed that in PCOS rats, the therapy effect of berberine in reducing PCOS pathology and IR values is associated with a mechanism linked to GLUT4 upregulation via PI3K/Akt activation and MAPK pathway suppression [33]. The aforementioned network pharmacology of CFD shows that CFD could regulate the IR and PI3K/Akt pathway for PCOS treatment, which suggested that the therapy effect of CFD in PCOS was related to the improvement of IR and might be via the PI3K/Akt pathway [18]. In this study, in PCOS rats with IR, the inhibition on PI3K/Akt signaling was also observed using western blotting. And CFD could restore this inhibition effect, which was enhanced with IGF-1 (PI3K activator) cotreatment but was counteracted with MK-2206 (PI3K inhibitor) or LY294002 (Akt inhibitor) cotreatment. Based on this, we suggested that CFD ameliorates ovary function and IR via the IGF-1-PI3K/Akt pathway. PI3K/Akt signaling is not only critically associated with IR but also involved in the regulation of cell survival, autophagy, and inflammatory microenvironment. Zhao et al. show that regulation of PI3K/Akt signaling is associated to the inflammation and oxidative stress in granulosa cells of PCOS patients [34]. In this study, the improvement on inflammatory microenvironment with CFD administration indicated that CFD might regulate PI3K/Akt signaling to suppress the production of proinflam-

matory cytokines, thus improving the inflammatory microenvironment in PCOS rats.

5. Conclusions

In conclusion, based on a PCOS model, we found that CFD treatment had a therapeutic effect in PCOS rats and granulosa cells. It showed that CFD is able to improve IR, restore the serum hormone levels, inhibit the inflammatory cytokines, and alleviate ovary morphological injury and apoptosis in PCOS rats. In granulosa cells with PCOS, the result showed that cell viability was improved, and cell apoptosis was inhibited after CFD administration. Further experiments suggested that CFD improves follicular development and IR, inhibits apoptosis and inflammatory microenvironment, and contributes to the regulation of the IGF-1-PI3K/Akt-Bax/Bcl-2 pathway (Figure 9). Given that CFD sufficiently suppresses IR and improves follicular development, exploring these mechanisms might help to optimize the therapeutic treatment of CFD in PCOS patients.

Data Availability

The data used to support the findings of this study are included in this manuscript.

Conflicts of Interest

The authors have declared no conflicts of interest.

Acknowledgments

This work was supported by the Natural Science Foundation of Zhejiang Province (Grant Number LQ19H270005) and Hangzhou medical and health science and technology project (Grant Numbers 20190114 and 20190089).

References

- [1] N. F. Goodman, R. H. Cobin, W. Futterweit, J. S. Glueck, R. S. Legro, and E. Carmina, "American Association of Clinical Endocrinologists, American College of Endocrinology, and Androgen Excess and PCOS Society disease state clinical review: guide to the best practices in the evaluation and treatment of polycystic ovary syndrome part 2," *Endocrine Practice*, vol. 21, no. 12, pp. 1415–1426, 2015.
- [2] P. Moghetti and F. Tosi, "Insulin resistance and PCOS: chicken or egg?," *Journal of Endocrinological Investigation*, 2020.
- [3] S. Patel, "Polycystic ovary syndrome (PCOS), an inflammatory, systemic, lifestyle endocrinopathy," *The Journal of Steroid Biochemistry and Molecular Biology*, vol. 182, pp. 27–36, 2018.
- [4] X. R. Ni, Z. J. Sun, G. H. Hu, and R. H. Wang, "High concentration of insulin promotes apoptosis of primary cultured rat ovarian granulosa cells via its increase in extracellular HMGB1," *Reproductive Sciences*, vol. 22, no. 3, pp. 271–277, 2014.
- [5] M. Liu, J. Gao, Y. Zhang et al., "Serum levels of TSP-1, NF- κ B and TGF- β 1 in polycystic ovarian syndrome (PCOS) patients in northern China suggest PCOS is associated with chronic inflammation," *Clinical Endocrinology*, vol. 83, no. 6, pp. 913–922, 2015.
- [6] P. Angin, T. Yoldemir, and K. Atasayan, "Quality of life among infertile PCOS patients," *Archives of Gynecology and Obstetrics*, vol. 300, no. 2, pp. 461–467, 2019.
- [7] A. L. Damone, A. E. Joham, D. Loxton, A. Earnest, H. J. Teede, and L. J. Moran, "Depression, anxiety and perceived stress in women with and without PCOS: a community-based study," *Psychological Medicine*, vol. 49, no. 9, pp. 1510–1520, 2019.
- [8] E. J. Fearnley, L. Marquart, and A. B. Spurdle, "Polycystic ovary syndrome increases the risk of endometrial cancer in women aged less than 50 years: an Australian case-control study," *Cancer Causes & Control*, vol. 21, no. 12, pp. 2303–2308, 2010.
- [9] L. C. Torchen, "Cardiometabolic risk in PCOS: more than a reproductive disorder," *Current Diabetes Reports*, vol. 17, no. 12, 2017.
- [10] R. S. Legro, H. X. Barnhart, W. D. Schlaff et al., "Clomiphene, metformin, or both for infertility in the polycystic ovary syndrome," *The New England Journal of Medicine*, vol. 356, no. 6, pp. 551–566, 2007.
- [11] R. Dumitrescu, C. Mehedintu, I. Briceag, V. L. Purcărea, and D. Hudita, "Metformin-clinical pharmacology in PCOs," *Journal of Medicine and Life*, vol. 8, no. 2, pp. 187–192, 2015.
- [12] H. Teede, E. C. Tassone, T. Piltonen et al., "Effect of the combined oral contraceptive pill and/or metformin in the management of polycystic ovary syndrome: a systematic review with meta-analyses," *Clinical Endocrinology*, vol. 91, no. 4, pp. 479–489, 2019.
- [13] C. C. Huang, R. Q. He, S. W. Li et al., "Efficacy of liraglutide in treating polycystic ovary syndrome: a systematic review and meta-analysis," *Chinese Journal of Modern Applied Pharmacy*, vol. 37, no. 16, pp. 1986–1992, 2020.
- [14] J. P. Domecq, G. Prutsky, R. J. Mullan et al., "Adverse effects of the common treatments for polycystic ovary syndrome: a systematic review and meta-analysis," *The Journal of Clinical Endocrinology and Metabolism*, vol. 98, no. 12, pp. 4646–4654, 2013.
- [15] A. Moini Jazani, H. Nasimi Doost Azgomi, A. Nasimi Doost Azgomi, and R. Nasimi Doost Azgomi, "A comprehensive review of clinical studies with herbal medicine on polycystic ovary syndrome (PCOS)," *Daru*, vol. 27, no. 2, pp. 863–877, 2019.
- [16] P. Xie, "Meta-analysis and trial sequential analysis of therapeutic efficacy of modified Cangfu Daotan decoction combined with chemical medicine versus chemical medicine alone in the treatment of polycystic ovarian syndrome," *China Pharmacy*, vol. 30, pp. 698–703, 2019.
- [17] L. I. Xingying, Y. Qin, and W. Qi, "Effects of Cangfu Daotan decoction combined with clomiphene on serum hormone level and endometri-al receptivity in patients with polycystic ovary syndrome combined with infertility," *China Pharmacy*, vol. 2826, pp. 3698–3701, 2017.
- [18] W. Xu, M. Tang, J. Wang, and L. Wang, "Identification of the active constituents and significant pathways of Cangfu Daotan decoction for the treatment of PCOS based on network pharmacology," *Evidence-Based Complementary and Alternative Medicine*, vol. 2020, Article ID 4086864, 15 pages, 2020.
- [19] J. Sun, C. Jin, H. Wu et al., "Effects of electro-acupuncture on ovarian P450arom, P450c17 α and mRNA expression induced by letrozole in PCOS rats," *PLoS One*, vol. 8, no. 11, article e7938218, 2013.
- [20] H. Shen and Y. Wang, "Activation of TGF- β 1/Smad3 signaling pathway inhibits the development of ovarian follicle in polycystic ovary syndrome by promoting apoptosis of granulosa cells," *Journal of Cellular Physiology*, vol. 234, no. 7, pp. 11976–11985, 2019.
- [21] E. Diamanti-Kandarakis and A. Dunaif, "Insulin resistance and the polycystic ovary syndrome revisited: an update on mechanisms and implications," *Endocrine Reviews*, vol. 33, no. 6, pp. 981–1030, 2012.
- [22] M. O'Reilly, L. Gathercole, F. Capper, W. Arlt, and J. Tomlinson, "Effect of insulin on AKR1C3 expression in female adipose tissue: in-vivo and in-vitro study of adipose androgen generation in polycystic ovary syndrome," *The Lancet*, vol. 385, p. S16, 2015.
- [23] M. Ojeda-Ojeda, M. Murri, M. Insenser, and H. Escobar-Morreale, "Mediators of low-grade chronic inflammation in polycystic ovary syndrome (PCOS)," *Current Pharmaceutical Design*, vol. 19, no. 32, pp. 5775–5791, 2013.
- [24] A. J. Duleba and A. Dokras, "Is PCOS an inflammatory process?," *Fertility and sterility*, vol. 97, no. 1, pp. 7–12, 2012.
- [25] B. J. Wang, L. Qian, J. Li et al., "sRAGE plays a role as a protective factor in the development of PCOS by inhibiting inflammation," *Gynecological Endocrinology*, vol. 36, no. 2, pp. 148–151, 2020.
- [26] Q. Lang, X. Yidong, Z. Xueguang, W. Sixian, X. Wenming, and Z. Tao, "ETA-mediated anti-TNF- α therapy ameliorates the

- phenotype of PCOS model induced by letrozole,” *PLoS One*, vol. 14, no. 6, article e02174956, 2019.
- [27] C. P. Almeida, M. C. F. Ferreira, C. O. Silveira et al., “Clinical correlation of apoptosis in human granulosa cells—a review,” *Cell Biology International*, vol. 42, no. 10, pp. 1276–1281, 2018.
- [28] R. J. Chang and H. Cook-Andersen, “Disordered follicle development,” *Molecular and Cellular Endocrinology*, vol. 373, no. 1–2, pp. 51–60, 2013.
- [29] D. Bas, D. Abramovich, F. Hernandez, and M. Tesone, “Altered expression of Bcl-2 and Bax in follicles within dehydroepiandrosterone-induced polycystic ovaries in rats,” *Cell Biology International*, vol. 35, no. 5, pp. 423–429, 2011.
- [30] X. X. Chi, T. Zhang, X. L. Chu, J. L. Zhen, and D. J. Zhang, “The regulatory effect of Genistein on granulosa cell in ovary of rat with PCOS through Bcl-2 and Bax signaling pathways,” *The Journal of Veterinary Medical Science*, vol. 80, no. 8, pp. 1348–1355, 2018.
- [31] Z. Zhang, H. Liu, and J. Liu, “Akt activation: a potential strategy to ameliorate insulin resistance,” *Diabetes Research and Clinical Practice*, vol. 156, article 107092, 2019.
- [32] H. Cho, “Insulin resistance and a diabetes mellitus-like syndrome in mice lacking the protein kinase Akt 2 (PKBbeta),” *Science*, vol. 292, no. 5522, pp. 1728–1731, 2001.
- [33] N. Zhang, X. Liu, L. Zhuang et al., “Berberine decreases insulin resistance in a PCOS rats by improving GLUT4: dual regulation of the PI3K/AKT and MAPK pathways,” *Regulatory Toxicology and Pharmacology*, vol. 110, article 104544, 2020.
- [34] Y. Zhao, C. Zhang, Y. Huang et al., “Up-regulated expression of WNT5a increases inflammation and oxidative stress via PI3K/AKT/NF- κ B signaling in the granulosa cells of PCOS patients,” *The Journal of Clinical Endocrinology and Metabolism*, vol. 100, no. 1, pp. 201–211, 2015.

Research Article

The Association of Fecal Microbiota in Ankylosing Spondylitis Cases with C-Reactive Protein and Erythrocyte Sedimentation Rate

Gang Liu, Yonghong Hao, Qiang Yang, and Shucaï Deng 

Tianjin Hospital, 406 Jiefangnan Road, Tianjin 300210, China

Correspondence should be addressed to Shucaï Deng; shucaideng2005@163.com

Received 6 September 2020; Revised 9 October 2020; Accepted 14 October 2020; Published 7 November 2020

Academic Editor: Xiaolu Jin

Copyright © 2020 Gang Liu et al. This is an open access article distributed under the Creative Commons Attribution License, which permits unrestricted use, distribution, and reproduction in any medium, provided the original work is properly cited.

The purpose of this work was to identify the features of the gut microbiome in cases of ankylosing spondylitis (AS) testing positive for human leukocyte antigen- (HLA-) B27 and healthy controls (HCs) as well as to determine how bacterial populations were correlated with C-reactive protein (CRP) and erythrocyte sedimentation rate (ESR). Fecal DNA extracted from fecal samples from 10 AS cases and 12 HCs was subjected to 16S rRNA gene sequencing. The two research groups did not differ significantly regarding alpha diversity. By comparison to HCs, AS cases displayed a lower relative level of Bacteroidetes ($P < 0.05$), but a higher level of Firmicutes and Verrucomicrobia ($P < 0.05$). Furthermore, the correlation between the specific gut bacteria and ESR or CRP was investigated. At the phylum level, Firmicutes and Verrucomicrobia had a positive association with ESR and CRP, while Bacteroidetes exhibited an inverse correlation with ESR and CRP. Meanwhile, in terms of genus, *Bacteroides* had a positive association with ESR and CRP, whereas *Ruminococcus* and *Parasutterella* had an inverse correlation with ESR and CRP, and *Helicobacter* also displayed an inverse correlation with CRP. Such findings indicated dissimilarities between AS cases and HCs regarding the gut microbiome, as well as the existence of correlations between bacterial populations and both ESR and CRP.

1. Introduction

The series of chronic inflammatory joint conditions impacting mainly the spinal, pelvic, and thoracic wall joints of the axial skeleton are known as spondyloarthritis (SpA) [1]. However, it often affects the upper and lower extremities as well, taking the form of arthritis, enthesitis, or dactylitis. Besides its effects on the joints, SpA can manifest as anterior uveitis, psoriasis, inflammatory bowel disease (IBD), such as Crohn's disease (CD) or ulcerative colitis (UC), and urethritis. SpA ranks among the chronic inflammatory rheumatic conditions of greatest frequency as it affects 0.2-1.61% of people [2].

The genes with the greatest predisposition towards ankylosing spondylitis (AS), with more than 90% heritability for AS, are the human leukocyte antigen (HLA) alleles [3]. SpA is often transmitted from one generation to the next, with the risk of acquiring this condition being determined by a number of genetic polymorphisms, especially the HLA-B27

allele belonging to the MHC class I [4]. A close correlation has been established between HLA-B27 and SpA. AS is the radiographic axial subset of SpA, and HLA-B27 is carried by 80-85% of individuals with AS, although the condition evolves in just 5% of those [5]. AS heritability depends on HLA-B27 in a proportion of 20.1%, while an additional 7.38% of the genetic risk is due to a further 113 loci [6].

In cases of genetic predisposition, the condition is also precipitated by the contribution of environmental factors. There is ample proof that the gut microbiome is pathogenically correlated with inflammatory arthritis including SpA [7, 8]. One study on HLA-B27 transgenic rats reported that colitis development was ameliorated when antibiotics targeting anaerobic bacteria, such as metronidazole, or antibiotics with broad action range, such as vancomycin and imipenem, were administered early on [9]. A different study found that caecal inflammation was aggravated when a caecal self-filling blind loop was generated to promote excessive growth of bacteria, while general intestinal inflammation was

reduced when the caecum was eliminated from the fecal stream [10]. On the other hand, no significant colon alterations of an inflammatory nature were induced by *E. coli* recolonization, and the progression of colitis was slowed down when probiotic *Lactobacillus rhamnosus* GG was given to HLA-B27 transgenic rats following the administration of antibiotics [11]. A wide range of metabolic activities with direct or indirect connections to the commensal microbiota is susceptible to changes by microbial dysbiosis [12]. It is argued that disease pathogenesis may hinge more on such modifications instead of on differences between species of bacteria.

As suggested above, the microbiota may be involved in SpA pathogenesis. Therefore, a hypothesis can be formulated that the microbiome composition in at-risk individuals might be impacted by HLA-B27. In this work, 16S rRNA analysis was undertaken, with a comparison of fecal samples from adult individuals with AS and healthy controls, to gain more insight into the potential correlation of specific gut dysbiosis and HLA-B27 in AS cases. Another research aim was to determine how the microbiota correlated with C-reactive protein (CRP) and erythrocyte sedimentation rate (ESR), since both CRP and ESR tend to be elevated in AS cases carrying HLA-B27.

2. Materials and Methods

The research sample comprised of 22 subjects (Table 1), of whom ten were AS cases and twelve were controls. The modified New York classification criteria for AS informed the employed definition of AS [13]. Informed consent was obtained in writing from all subjects, and the research ethics committee of Tianjin Hospital granted approval for the research procedure. No AS case was on a medication regime of nonsteroidal anti-inflammatory drugs (NSAIDs) or acetaminophen and/or tramadol.

2.1. Analysis of CRP, ESR, and HLA-B27. The Boster enzyme-linked immunosorbent assay kit was employed to measure the level of CRP in the blood plasma of the research subjects, while the Westergren technique was applied in keeping with the International Council for Standardization in Hematology to determine ESR (ml/hr) [14]. The HLA-B27 was tested with flow cytometry according to the methods described by Albrecht and Muller [15].

2.2. 16S rRNA Gene Sequencing and Analysis. Feces were sampled from each of the 22 research subjects to enable DNA analysis. The Qiagen QIAamp DNA Stool Mini Kit was employed for the extraction of total genomic DNA from the fecal samples, while the primers 338 F 5'-ACTCCTACGGGAGGCA GCA-3' and 806 R 5'-GGACTACHVGGGTWTCTAAT-3' were used for amplification of the V3-V4 hypervariable region of the bacterial 16S rRNA gene. The Qiagen Gel Extraction Kit (Qiagen, Germany) facilitated the mixing in ratios of identical density and the purification of PCR products. The TruSeq® DNA PCR-Free Sample Preparation Kit (Illumina, USA) was used to produce sequence libraries, with the addition of index codes. The Qubit® 2.0 Fluorometer (Thermo Scientific) and

TABLE 1: The traits of the AS cases and HCs at the point of biopsy*.

Subject ID	Age, years	Sex	Disease duration, years	ESR, mm/hour	CRP, mg/liter	HLA-B27
AS-01	44	M	7	23	27.25	Positive
AS-02	45	F	5	33	24.65	Positive
AS-03	59	F	4	30	20.52	Positive
AS-04	46	F	2	22	25.75	Positive
AS-05	48	M	6	25	20.80	Positive
AS-06	52	M	7	36	17.02	Positive
AS-07	48	F	5	36	29.96	Positive
AS-08	57	M	6	29	27.14	Positive
AS-09	40	M	3	34	15.85	Positive
AS-10	53	M	7	28	15.98	Positive
HC-01	35	F	—	12	0.45	Negative
HC-02	47	M	—	6	2.43	Negative
HC-03	39	F	—	9	2.26	Negative
HC-04	54	M	—	10	1.38	Negative
HC-05	52	M	—	1	1.67	Negative
HC-06	43	F	—	2	0.23	Negative
HC-07	51	M	—	9	0.52	Negative
HC-08	47	F	—	5	1.80	Negative
HC-09	47	F	—	3	2.95	Negative
HC-10	44	F	—	12	1.56	Negative
HC-11	46	M	—	7	1.22	Negative
HC-12	43	M	—	8	2.33	Negative

the Agilent Bioanalyzer 2100 system permitted evaluation of the quality of the libraries. The Illumina HiSeq2500 platform was employed for library sequencing, with production of 250-bp paired-end reads, which were allocated to samples according to their singular barcode, followed by truncation through excision of the barcode and primer sequences. The integration of paired-end reads was achieved via FLASH51, which was geared towards fusing paired-end reads in response to the overlapping of at least a few of the reads with the read produced from the other end of an identical DNA fragment. The name given to the trimmed sequences was raw tags. The QIIME quality control process was applied for filtering those tags to yield uncontaminated tags of high quality [16]. The UCHIME algorithm allowed a comparison between the tags and the reference database for the purpose of identifying chimeric sequences that were subsequently eliminated [17, 18]. This procedure eventually generated the effective tags.

Uparse software (Uparse v7.0.1001) was employed to analyze the sequences. The sequences that were similar in proportion greater than 97% were allocated to identical OTUs [19], and a sequence representative for every OUT was chosen for additional annotation. The RDP classifier algorithm was applied to extract taxonomic information from the GreenGene Database regarding the representative sequences [20]. Normalization of OUT abundance was done according to the sequence count in the sample with the lowest number of sequences. The normalized data were then

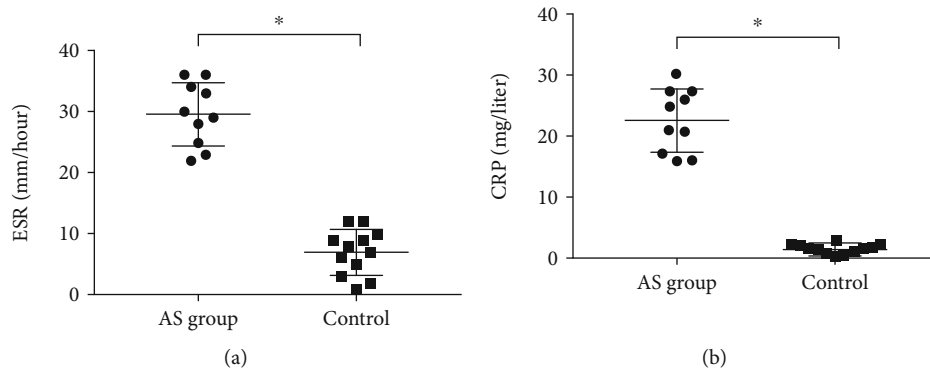


FIGURE 1: The ESR and CRP levels in the AS and control groups. * $P < 0.05$.

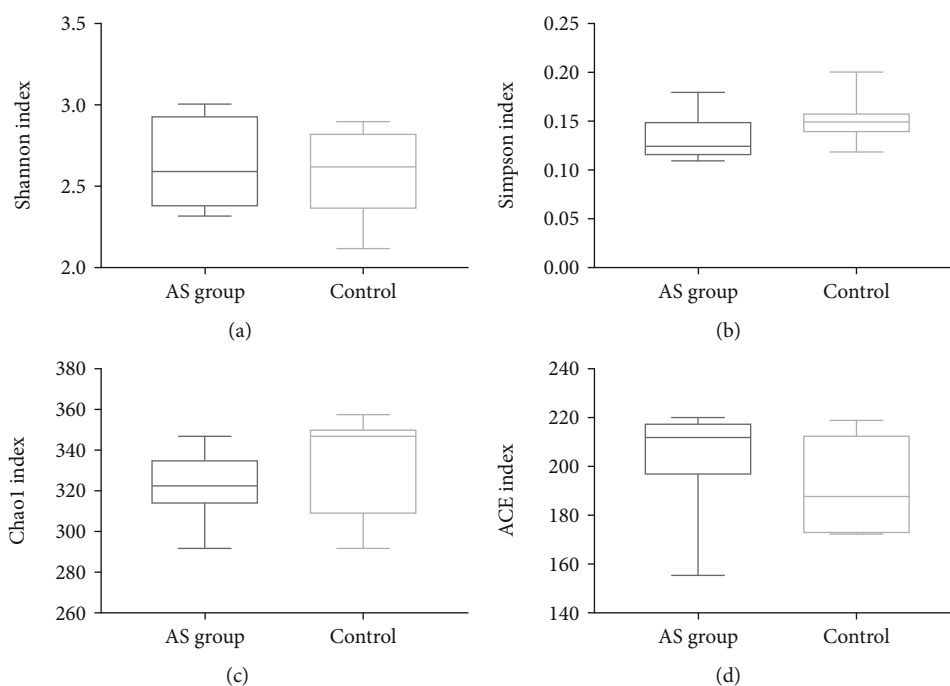


FIGURE 2: The diversity indices associated with populations of bacteria present in feces. Box plots reflect microbiome diversity discrepancies between the AS cases and HCs as revealed by the Shannon index (a), Simpson index (b), Chao1 index (c), and ACE index (d).

employed to analyze alpha and beta diversity. Observed-species, Chao1, Shannon, Simpson, ACE, and Good-coverage were the alpha diversity indices that were used for the analysis of the complexity of species diversity. QIIME (version 1.7.0) and R software (version 2.15.3) were, respectively, employed for calculation and visualization of each index.

2.3. Statistical Analysis. SPSS (version 22.0, IBM SPSS Inc., USA) was employed for statistical analysis, with the expression of the generated values taking the form of mean \pm SD. The intergroup statistical analysis was performed via Student's t -test, while Spearman's rank correlation analysis was performed to determine how gut microbiota and CRP or ESR were correlated. Differences of statistical significance were reflected by a P value of less than 0.05.

3. Results

3.1. Elevated CPR and ESR in AS Cases. Figure 1 provides details about the research sample. Compared to the HCs, the AS cases had significantly higher levels of both CRP (Figure 1(a)) and ESR (Figure 1(b)) ($P < 0.05$).

3.2. Phylum-Level Microbiota Differences. Diversity indices were applied to assess how diverse the fecal microbes were. The AS cases and HCs did not differ in terms of the Shannon, Simpson, Chao1, and ACE indices (Figure 2).

At the level of phylum, Firmicutes (44.08% in AS cases and 34.62% in HCs), Bacteroidetes (42.62% in AS cases and 50.10% in HCs), Proteobacteria (4.10% in AS cases and 4.01% in HCs), Verrucomicrobia (3.35% in AS cases and 2.65% in HCs), and Actinobacteria (1.01% in AS cases and

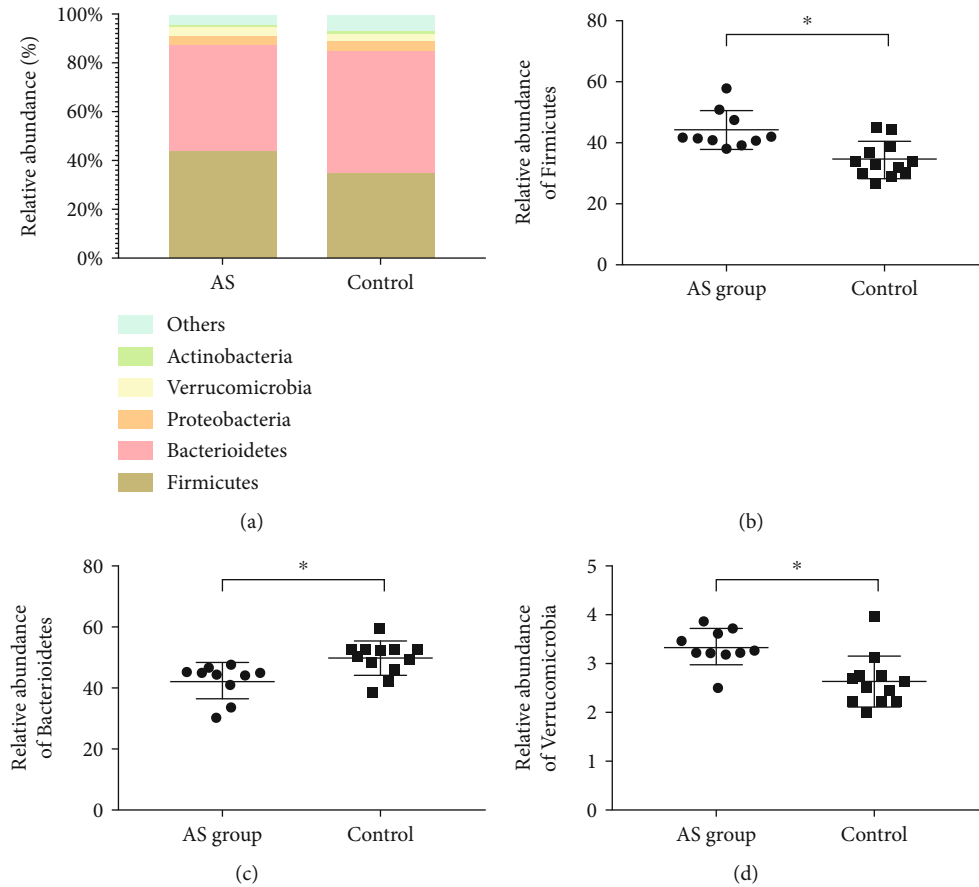


FIGURE 3: Phylum-level examination of microbiome composition. (a) The relative abundance of fecal microbes at the phylum level. Intergroup comparison of relative abundance of (b) Bacteroidetes, (c) Firmicutes, and (d) Verrucomicrobia. * $P < 0.05$.

0.94% in HCs) were the main bacterial populations in feces (Figure 3). Furthermore, by comparison to HCs, AS cases showed a reduction in Bacteroidetes relative abundance, but an increase in the relative abundance of Firmicutes and Verrucomicrobia ($P < 0.05$).

3.3. Genus-Level Microbiota Discrepancies. Figure 4 illustrates the genus-level abundance of eight major microbes. At the genus level, *Bacteroides* (18.14% in AS cases and 14.40% in HCs), *Ruminococcus* (0.63% in AS cases and 0.86% in HCs), *Lactobacillus* (1.19% in AS cases and 1.30% in HCs), *Desulfovibrio* (3.16% in AS cases and 2.93% in HCs), *Ruminiclostridium* (1.22% in AS cases and 1.19% in HCs), *Helicobacter* (2.52% in AS cases and 2.99% in HCs), *Parasutterella* (3.03% in AS cases and 4.75% in HCs), and *Facklamia* (0.66% in AS cases and 0.59% in HCs) were the main bacterial genus in feces (Figure 3). Furthermore, by comparison to HCs, AS cases showed a reduction in relative abundance of *Ruminococcus*, *Helicobacter*, and *Parasutterella* genus, but an increase in the relative abundance of *Bacteroides* ($P < 0.05$).

3.4. Microbiota Associations with CPR and ESR. To determine how the microbiota and ESR were correlated at the level of phylum and genus, Spearman's correlation analysis was carried out, revealing a positive correlation of Firmicutes

(Figure 5(a)) and Verrucomicrobia (Figure 5(c)) with ESR at phylum level and direct correlation between *Bacteroides* (Figure 5(d)) and ESR, but inverse correlation of *Ruminococcus* (Figure 5(e)) and *Parasutterella* (Figure 5(f)) with ESR at genus level.

To determine how the microbiota and CRP were correlated at the level of phylum and genus, Spearman's correlation analysis was carried out, revealing a positive correlation of Firmicutes (Figure 6(a)) and Verrucomicrobia (Figure 6(c)) with CRP at phylum level and positive correlation between *Bacteroides* (Figure 6(d)) and CRP, but inverse correlation of *Ruminococcus* (Figure 6(e)), *Helicobacter* (Figure 6(f)), and *Parasutterella* (Figure 6(g)) with CRP at genus level.

4. Discussion

Classified as SpA "prototype", AS represents a chronic, progressive inflammatory autoimmune condition that affects primarily the sacroiliac joints and the vertebral column [21]. The present work conducted 16S rRNA sequence analysis of fecal samples to detect the profile intestinal dysbiosis in the microbiome of individuals with AS.

The contribution of the gut microbiota to AS is widely acknowledged, but knowledge remains limited as to the exact

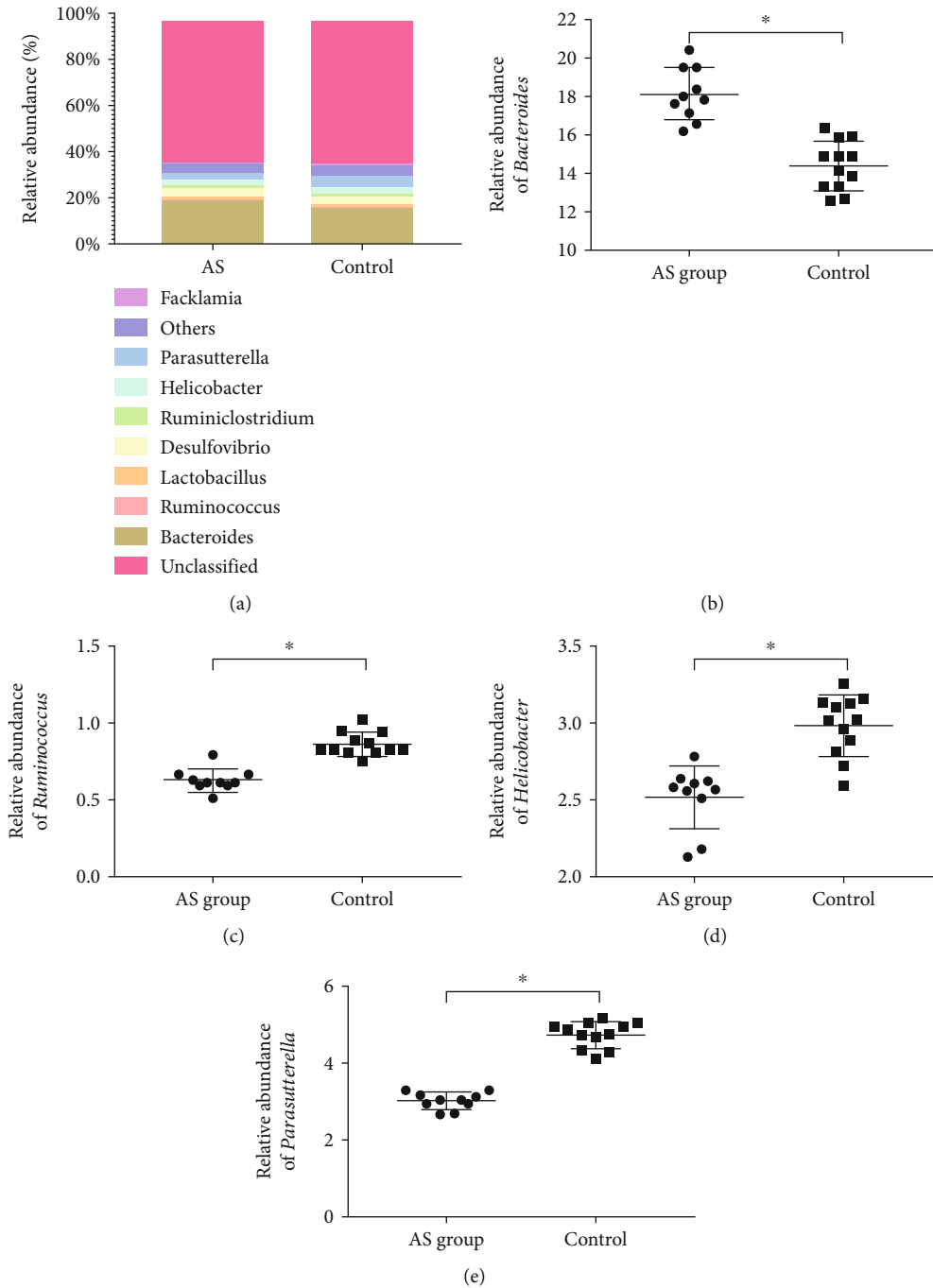


FIGURE 4: Genus-level examination of microbiota composition. (a) The relative abundance of fecal microbes at the genus level. Intergroup comparison of relative abundance of (b) *Bacteroides*, (c) *Ruminococcus*, (d) *Helicobacter*, and (e) *Parasutterella*. * $P < 0.05$.

form taken by that contribution [8]. The general consensus is that both genetic and environmental factors underpin AS development [22]. In the context of investigations of disease etiology, the human gut microbiome should be afforded due consideration, given the likely correlation between indigenous gut bacterial populations and AS. Nevertheless, a comprehensive explanation of AS etiology is yet to be formulated, and the identification of potential causative factors is ongoing. Interest in human microbiome mapping has risen con-

siderably in the recent ten years [23], and it has become possible to determine the exact species making up the microbiota owing to the introduction of molecular-based techniques (e.g., metagenomics), which are more advanced than standard culture-based techniques. In spite of this, there are still several important aspects that need to be addressed, including the involvement of the microbiota in AS and the mechanism of microbiome impact on immune response as well as local and systemic inflammation.

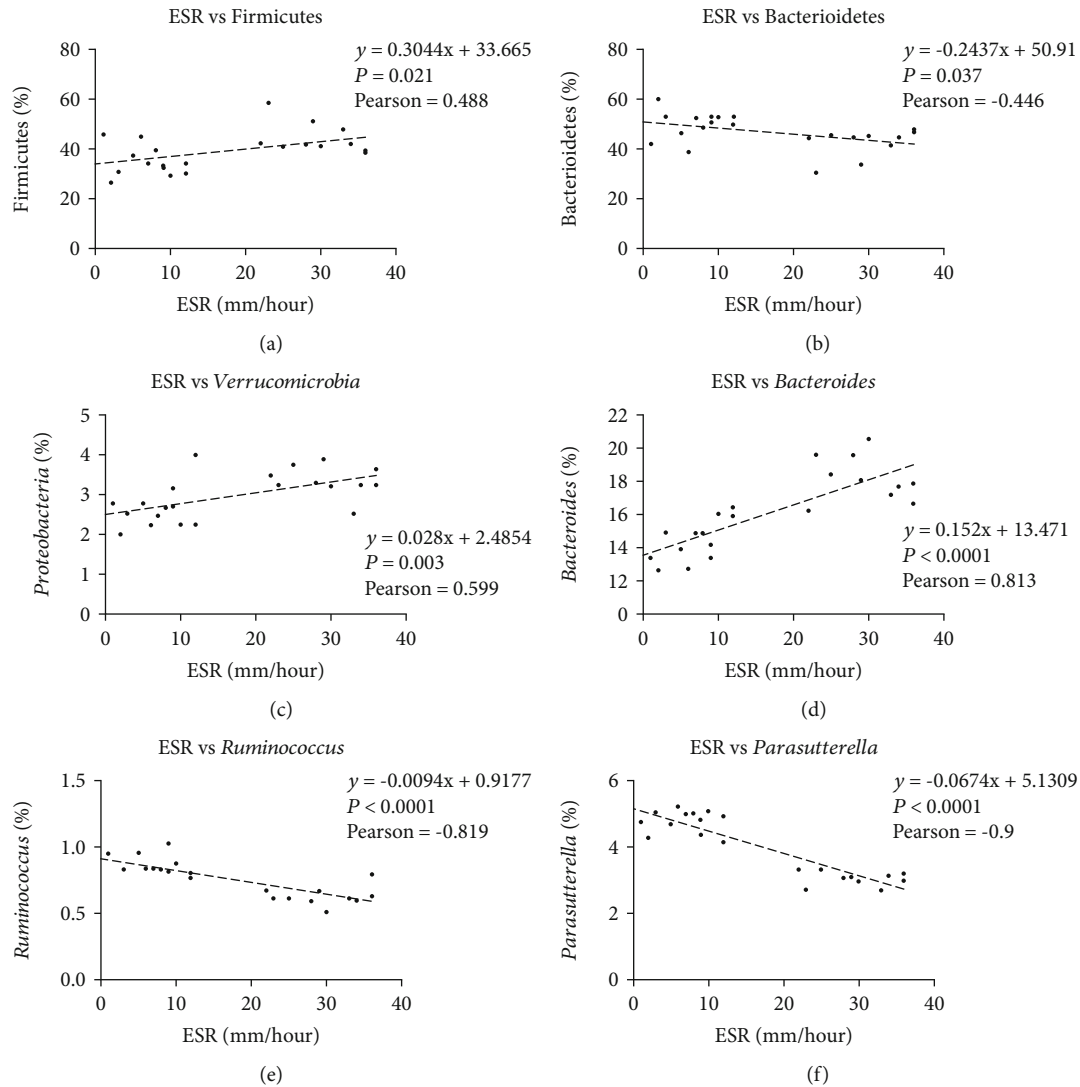


FIGURE 5: The association of microbiota with ESR. (a) Positive correlation between Bacteroidetes abundance and ESR; (b) Inverse correlation between Firmicutes and ESR; (c) Positive correlation between Verrucomicrobia and ESR; (d) Positive correlation between *Bacteroides* and ESR; (e) Inverse correlation between *Ruminococcus* and ESR; (f) Positive correlation between *Parasutterella* and ESR.

The present work provides convincing proof that there are differences in gut microbiome among cases with and without AS. AS cases were found to have a markedly greater abundance of *Bacteroides*, but a lower abundance of *Ruminococcus*, *Helicobacter*, and *Parasutterella*. Such changes might have a regulating effect on innate and adaptive immunity, thus contributing to AS development [24]. This work compared cases with and without AS in terms of microbiome density and abundance to improve knowledge of how the gut microbiome varied between different populations as well as how the microbiota-host cross-talk occurred. *Klebsiella pneumoniae* and *Bacteroides vulgatus* are among the bacteria that have been identified to be essential for AS pathogenesis [25]. Nevertheless, the amount of bacteria is typically associated with causal immune response rather than infection. According to research conducted on animal models, *Bacteroides* contribute to the occurrence of inflammation in peripheral joint or intestinal conditions. In line with earlier studies

[8, 26], this work confirmed that *Bacteroides* abundance was greater in AS cases than in HCs. Furthermore, studies have demonstrated that both IBD and arthritis developed as a result of a rise in the level of HLA-B27 in transgenic rat gut that reflected the presence of *Bacteroides vulgatus* [26, 27].

The existence of a correlation between some constituents of the microbiota and ESR or CRP was confirmed by correlation analysis. It was thus deduced that AS pathogenesis depends significantly on the gut microbiota. Hence, future studies should profile the species constituting the AS-related microbiota and shed light on how the gut microbiome contributes to AS progression.

Additional aspects worth researching include the extent to which genetic factors underpin alterations in gut microbiota and what implications this has for the general microbiome functionality in AS cases and its impact on immune response and inflammation. Further attention should also be given to the hypothesis that AS is triggered by HLA-B27

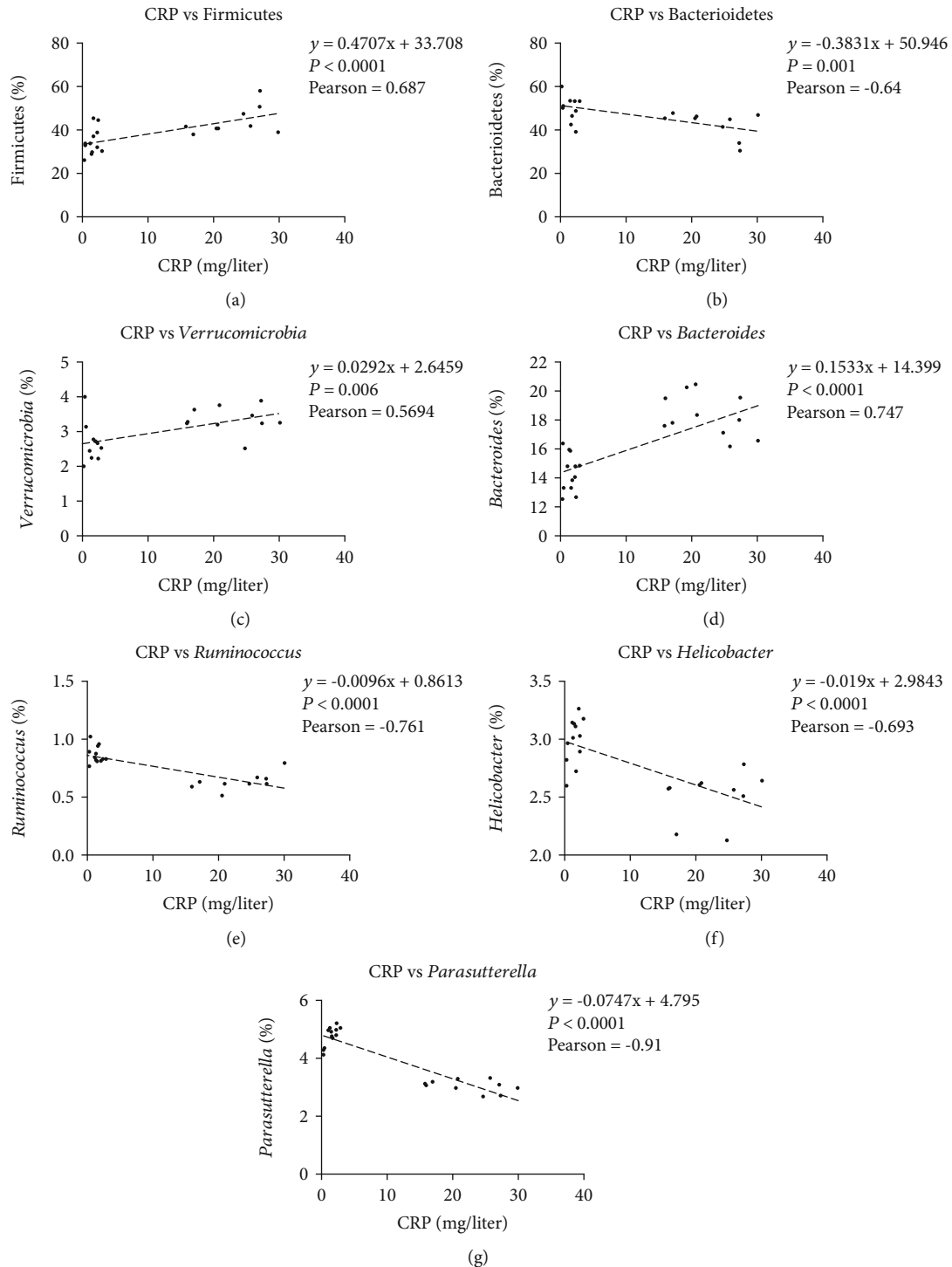


FIGURE 6: The association of microbiota with CRP. (a) Positive correlation between Bacteroidetes abundance and CRP; (b) Inverse correlation between Firmicutes and CRP; (c) Positive correlation between Verrucomicrobia and CRP; (d) Positive correlation between *Bacteroides* and CRP; (e) Inverse correlation between *Ruminococcus* and CRP; (f) Inverse correlation between *Helicobacter* and CRP; (g) Positive correlation between *Parasutterella* and CRP.

through its impact on the gut microbiome, which was formulated in light of the identified correlation between HLA-B27 and AS. By expanding knowledge about such aspects, comprehension of AS development can be improved.

Data Availability

The original data used to support the findings of this study are available from the corresponding author upon request.

Conflicts of Interest

The authors declare no competing interests.

Acknowledgments

This work was supported by a grant from Tianjin Health Bureau Technology Fund (No. 2012KZ052).

References

- [1] J. D. Taurog, A. Chhabra, and R. A. Colbert, "Ankylosing spondylitis and axial spondyloarthritis," *The New England Journal of Medicine*, vol. 374, no. 26, pp. 2563–2574, 2016.
- [2] C. Stolwijk, M. van Onna, A. Boonen, and A. van Tubergen, "Global prevalence of spondyloarthritis: a systematic review and meta-regression analysis," *Arthritis Care & Research (Hoboken)*, vol. 68, no. 9, pp. 1320–1331, 2016.
- [3] O. B. Pedersen, A. J. Svendsen, L. Ejstrup, A. Skytthe, J. R. Harris, and P. Junker, "Ankylosing spondylitis in Danish and Norwegian twins: occurrence and the relative importance of genetic vs. environmental effectors in disease causation," *Scandinavian Journal of Rheumatology*, vol. 37, no. 2, pp. 120–126, 2008.
- [4] M. Breban, F. Costantino, C. André, G. Chiochia, and H. J. Garchon, "Revisiting MHC genes in spondyloarthritis," *Current Rheumatology Reports*, vol. 17, no. 6, p. 516, 2015.
- [5] Y. Liu, L. Jiang, Q. Cai et al., "Predominant association of HLA-B*2704 with ankylosing spondylitis in Chinese Han patients," *Tissue Antigens*, vol. 75, no. 1, pp. 61–64, 2010.
- [6] D. Ellinghaus, The International IBD Genetics Consortium (IBDGC), L. Jostins et al., "Analysis of five chronic inflammatory diseases identifies 27 new associations and highlights disease-specific patterns at shared loci," *Nature Genetics*, vol. 48, no. 5, pp. 510–518, 2016.
- [7] J. U. Scher, C. Ubeda, A. Artacho et al., "Decreased bacterial diversity characterizes the altered gut microbiota in patients with psoriatic arthritis, resembling dysbiosis in inflammatory bowel disease," *Arthritis & Rheumatology*, vol. 67, no. 1, pp. 128–139, 2015.
- [8] G. Liu, Y. Ma, Q. Yang, and S. Deng, "Modulation of inflammatory response and gut microbiota in ankylosing spondylitis mouse model by bioactive peptide IQW," *Journal of Applied Microbiology*, vol. 128, no. 6, pp. 1669–1677, 2020.
- [9] H. C. Rath, M. Schultz, R. Freitag et al., "Different subsets of enteric bacteria induce and perpetuate experimental colitis in rats and mice," *Infection and Immunity*, vol. 69, no. 4, pp. 2277–2285, 2001.
- [10] H. C. Rath, J. S. Ikeda, H. J. Linde, J. Schölmerich, K. H. Wilson, and R. B. Sartor, "Varying cecal bacterial loads influences colitis and gastritis in HLA-B27 transgenic rats," *Gastroenterology*, vol. 116, no. 2, pp. 310–319, 1999.
- [11] L. A. Dieleman, M. S. Goerres, A. Arends et al., "Lactobacillus GG prevents recurrence of colitis in HLA-B27 transgenic rats after antibiotic treatment," *Gut*, vol. 52, no. 3, pp. 370–376, 2003.
- [12] K. Wang, X. Jin, Q. Li et al., "Propolis from different geographic origins decreases intestinal inflammation and Bacteroides spp. populations in a model of DSS-induced colitis," *Molecular Nutrition & Food Research*, vol. 62, no. 17, article 1800080, 2018.
- [13] J. M. Moll and V. Wright, "New York clinical criteria for ankylosing spondylitis. A statistical evaluation," *Annals of the Rheumatic Diseases*, vol. 32, no. 4, pp. 354–363, 1973.
- [14] R. D. Thomas, J. C. Westengard, K. L. Hay, and B. S. Bull, "Calibration and validation for erythrocyte sedimentation tests. Role of the International Committee on Standardization in Hematology reference procedure," *Archives of Pathology & Laboratory Medicine*, vol. 117, no. 7, pp. 719–723, 1993.
- [15] J. Albrecht and H. A. Muller, "HLA-B27 typing by use of flow cytometry," *Clinical Chemistry*, vol. 33, no. 9, pp. 1619–1623, 1987.
- [16] N. Mancuso, B. Tork, P. Skums, L. Ganova-Raeva, I. Mandoiu, and A. Zelikovsky, "Reconstructing viral quasispecies from NGS amplicon reads," *In Silico Biology*, vol. 11, no. 5-6, pp. 237–249, 2012.
- [17] R. C. Edgar, B. J. Haas, J. C. Clemente, C. Quince, and R. Knight, "UCHIME improves sensitivity and speed of chimera detection," *Bioinformatics*, vol. 27, no. 16, pp. 2194–2200, 2011.
- [18] B. J. Haas, D. Gevers, A. M. Earl et al., "Chimeric 16S rRNA sequence formation and detection in Sanger and 454-pyrosequenced PCR amplicons," *Genome Research*, vol. 21, no. 3, pp. 494–504, 2011.
- [19] R. C. Edgar, "UPARSE: highly accurate OTU sequences from microbial amplicon reads," *Nature Methods*, vol. 10, no. 10, pp. 996–998, 2013.
- [20] Q. Wang, G. M. Garrity, J. M. Tiedje, and J. R. Cole, "Naive Bayesian classifier for rapid assignment of rRNA sequences into the new bacterial taxonomy," *Applied and Environmental Microbiology*, vol. 73, no. 16, pp. 5261–5267, 2007.
- [21] M. Ronneberger and G. Schett, "Pathophysiology of spondyloarthritis," *Current Rheumatology Reports*, vol. 13, no. 5, pp. 416–420, 2011.
- [22] A. Verwoerd, N. M. Ter Haar, S. de Rook, S. J. Vastert, and D. Bogaert, "The human microbiome and juvenile idiopathic arthritis," *Pediatric Rheumatology Online Journal*, vol. 14, no. 1, p. 55, 2016.
- [23] M. Dave, P. D. Higgins, S. Middha, and K. P. Rioux, "The human gut microbiome: current knowledge, challenges, and future directions," *Translational Research*, vol. 160, no. 4, pp. 246–257, 2012.
- [24] M. Salio, D. J. Puleston, T. S. M. Mathan et al., "Essential role for autophagy during invariant NKT cell development," *Proceedings of the National Academy of Sciences of the United States of America*, vol. 111, no. 52, pp. E5678–E5687, 2014.
- [25] H. C. Rath, K. H. Wilson, and R. B. Sartor, "Differential induction of colitis and gastritis in HLA-B27 transgenic rats selectively colonized with *Bacteroides vulgatus* or *Escherichia coli*," *Infection and Immunity*, vol. 67, no. 6, pp. 2969–2974, 1999.
- [26] P. Lin, M. Bach, M. Asquith et al., "HLA-B27 and human β 2-Microglobulin affect the gut microbiota of transgenic rats," *PLoS One*, vol. 9, no. 8, article e105684, 2014.
- [27] F. Hoentjen, S. L. Tonkonogy, B. F. Qian, B. Liu, L. A. Dieleman, and R. B. Sartor, "CD4(+) T lymphocytes mediate colitis in HLA-B27 transgenic rats monoassociated with nonpathogenic *Bacteroides vulgatus*," *Inflammatory Bowel Diseases*, vol. 13, no. 3, pp. 317–324, 2007.

Research Article

Alterations in the Blood Parameters and Fecal Microbiota and Metabolites during Pregnant and Lactating Stages in Bama Mini Pigs as a Model

Cui Ma,^{1,2} QianKun Gao,¹ WangHong Zhang,^{1,2} Md. Abul Kalam Azad¹ ,¹
and XiangFeng Kong¹ 

¹CAS Key Laboratory of Agro-ecological Processes in Subtropical Region, Hunan Provincial Key Laboratory of Animal Nutritional Physiology and Metabolic Process, National Engineering Laboratory for Pollution Control and Waste Utilization in Livestock and Poultry Production, Institute of Subtropical Agriculture, Chinese Academy of Sciences, Changsha, 410125 Hunan, China

²University of Chinese Academy of Sciences, Beijing 100008, China

Correspondence should be addressed to XiangFeng Kong; nnkxf@isa.ac.cn

Received 21 August 2020; Revised 17 September 2020; Accepted 27 September 2020; Published 26 October 2020

Academic Editor: Yaoyao Xia

Copyright © 2020 Cui Ma et al. This is an open access article distributed under the Creative Commons Attribution License, which permits unrestricted use, distribution, and reproduction in any medium, provided the original work is properly cited.

This study was conducted to analyze plasma reproductive hormone and biochemical parameter changes, as well as fecal microbiota composition and metabolites in sows, at different pregnancy and lactation stages, using Bama mini pig as an experimental animal model. We found that plasma prolactin (PRL), progesterone, follicle-stimulating hormone (FSH), and estrogen levels decreased from day 45 to day 105 of pregnancy. Plasma total protein and albumin levels were lower in pregnant sows, while glucose, urea nitrogen, total cholesterol, and high-density lipoprotein-cholesterol, as well as fecal acetate, butyrate, valerate, total short-chain fatty acids, skatole, and tyramine levels, were higher in lactating sows. Interestingly, the lactating sows showed lower α -diversity and *Spirochaetes* and *Verrucomicrobia* relative abundances, while pregnant sows showed a higher *Proteobacteria* relative abundance. Notably, the *Akkermansia* relative abundance was highest on day 7 of lactation. Spearman analysis showed a positive correlation between plasma triglyceride and cholinesterase levels and *Akkermansia* and *Streptococcus* relative abundances. Moreover, *Oscillospira* and *Desulfovibrio* relative abundances were also positively correlated with plasma FSH, LH, and E₂ levels, as well as PRL and LH with *Bacteroides*. Collectively, plasma reproductive hormones, biochemical parameters, and fecal microbiota composition and metabolite levels could alter along with pregnancy and lactation, which might contribute to the growth and development demands of fetuses and newborns.

1. Introduction

Pregnancy and lactation are extremely complex physiological processes during which a variety of systemic changes occur, including body weight, blood hormones, and fecal metabolites fluctuations, as well as immune conditions [1, 2]. Previous study showed that the host's hormones could shape the gut microbial structure and function, and the gut microbiota also altered the production and regulation of hormones in turn [3]. Thus, it is not surprising that the maternal intestinal microbiota shifts dramatically during pregnancy and lactation. Accumulating evidences demonstrate that gut microbiota governs host metabolism, and its composition varies in hosts

in different physiological states [4, 5]. Indeed, it has been well established that the gut microbiota composition is inconsistent in mammals during pregnancy [4, 6]. For example, the gut microbiota changes dramatically from the first to the third trimesters of pregnancy (e.g., the increased *Actinobacteria* and *Proteobacteria* relative abundances and beta diversity and reduced individual richness) [4]; the intestinal microbiota composition is also dynamic in lactating mammals [7]. However, the intestinal microbiota variation or difference in the composition during pregnancy and lactation remains poorly understood.

Notably, maternal physiological changes during pregnancy could highly influence growth and/or development

of fetus, which might be influenced by gut microbes [4]. Indeed, maternal microbes (e.g., *Firmicutes* and *Proteobacteria*) could colonize the fetal/neonatal gut during pregnancy (via placenta) or lactation (via maternal milk and mother's feces), affecting the offspring's growth and development (e.g., fetal programming) [7, 8]. Because the gut microbiota is involved in regulating various host functions (e.g., nutrient absorption and body pathological or physiologic metabolism) [9] and the offspring's growth and development largely depends on maternal physiological changes during pregnancy and lactation. Therefore, it is urgent to fully understand how maternal gut microbiota composition changes and the relationship between intestinal microbiota and maternal metabolism during pregnancy and lactation.

Bama mini pig is genetically stable and size small and shares higher blood biochemical parameter, as well as internal organ shape and size similarities with humans [10]. Moreover, their gut microbiota structure and function are similar to human's [11]. Bama mini pig is the preferred experimental animal for studying how the gut microbiota changes and interacts with their host during pregnancy and lactation. Therefore, we analyzed the fecal microbiota composition and their metabolites, as well as plasma reproductive hormone and biochemical parameter levels during pregnancy and lactation. Then, correlation analyses were conducted to find the relationships between the aforementioned indexes.

2. Materials and Methods

2.1. Animals and Experimental Design. In this study, a total of 16 Bama mini pigs with 3-5 parity were herd in a mini pig farm of Goat Chong located in Shimen Town, Changde City, Hunan Province, China. After insemination, the sows were housed individually in crates (2.2 m × 0.6 m) from day 1 to day 105 of pregnancy and then housed in farrowing crates (2.2 m × 1.8 m) until weaning. Throughout the experimental period, there was no antibiotic or probiotic use, and diet intake changed with sow body condition (fed at 8:00 and 17:00 each day), and water was drunk freely. The sows were fed 0.8, 1.0, 1.2, 1.5, and 2.0 kg of the pregnant diets during 1-15, 16-30, 31-75, 76-90, and 91-105 days of pregnancy, respectively, fed 1.0 kg pregnant diets before a week of parturition and *ad libitum* after three days of parturition, and fed 2.4 kg lactation diets until weaning. The sows' nutrition met the Chinese conventional diet- (GB diet-) recommended requirements (NY-T, 2004) (Table 1).

2.2. Sample Collection. According to Kong et al. [12], the early, middle, and later stages of pregnancy in mini pigs are from days 1 to 45, days 46 to 75, and days 76 to delivery, respectively. During the trial period, there were four sows returned to estrus in the early pregnancy and two sows returned to estrus in the middle pregnancy. In order to minimize abortion caused by sampling stress and to ensure that the same gilts were sampled at each time point, 6-8 blood samples and feces samples of sows per stage were chosen for subsequent analysis. The litter sizes used for the experiment were 8-12.

TABLE 1: Composition and nutrient levels of the basal diets (air-dry basis; %).

Items	Pregnant sows' diet	Lactating sows' diet
Ingredients		
Corn	37.50	66.00
Soybean meal	9.50	25.00
Wheat bran	14.00	5.00
Barley	25.00	
Soybean hull	10.00	
Pregnant sows' premix ¹	4.00	
Lactating sows' premix ²		4.00
Total	100.00	100.00
Nutrient levels ³		
DE (MJ/kg)	12.55	13.87
CP	12.82	16.30
CF	4.56	2.87
SID Lys	0.48	0.75
SID met+Cys	0.43	0.51
SID Thr	0.37	0.53
SID Trp	0.13	0.17
Ca	0.62	0.65
P	0.47	0.50

Note: ¹Pregnant sows' premix provided the following per kg of diets: CaHPO₄·2H₂O 10 g, NaCl 4 g, CuSO₄·5H₂O 80 mg, FeSO₄·H₂O 360 mg, ZnSO₄·H₂O 240 mg, MnSO₄·H₂O 100 mg, MgSO₄·7H₂O 1 g, 1% ICl 50 mg, 1% Na₂SeO₃ 36 mg, 1% CoCl₂ 16 mg, NaHCO₃ 1.4 g, VA 10000 IU, VD₃ 1800 IU, VE 20 mg, VK₃ 2.4 mg, VB₁ 1.6 mg, VB₂ 6 mg, VB₆ 1.6 mg, VB₁₂ 0.024 mg, folic acid 1.2 mg, nicotinamide 20 mg, pantothenic acid 12 mg, biotin 0.12 mg, ferrous glycinate 100 mg, choline chloride 1 g, phytase 200 mg, fruity 80 mg, and limestone 12 g. ²Lactating sows' premix provided the following per kg of the diet: CaHPO₄·2H₂O 10 g, NaCl 4 g, CuSO₄·5H₂O 80 mg, FeSO₄·H₂O 360 mg, ZnSO₄·H₂O 240 mg, MnSO₄·H₂O 100 mg, 1% ICl 50 mg, 1% Na₂SeO₃ 36 mg, 1% CoCl₂ 16 mg, NaHCO₃ 1.4 g, VA 10000 IU, VD₃ 1800 IU, VE 20 mg, VK₃ 2.4 mg, VB₁ 1.6 mg, VB₂ 6 mg, VB₆ 1.6 mg, VB₁₂ 0.024 mg, folic acid 1.2 mg, nicotinamide 20 mg, pantothenic acid 12 mg, biotin 0.12 mg, lysine 1.5 g, ferrous glycinate 100 mg, choline chloride 1 g, phytase 200 mg, fruity 80 mg, and limestone 12 g. ³Nutrient levels were calculated values. Ca: calcium; CF: crude fiber; CP: crude protein; DE: digestible energy; P: phosphorus; SID: standard ileum digestible.

On days 45, 75, and 105 of pregnancy and 7 and 21 of lactation, fresh sow feces were collected in 10 mL sterile centrifuge tubes and stored immediately at -20°C until processing. Meanwhile, precaval vein blood samples were collected in 10 mL heparinized tubes, centrifuged at 3500 g and 4°C for 10 min, and stored at -20°C for further analysis.

2.3. Determination of Plasma Reproductive Hormones and Biochemical Parameters. Plasma reproductive hormones, including prolactin (PRL), luteinizing hormones (LH), follicle-stimulating hormones (FSH), progesterone (PROG), and estradiol (E₂), were determined using enzyme linked immunosorbent assay (ELISA) kit (Suzhou keming Co., Ltd, China), following the manufacturer's instructions.

Plasma biochemical parameters, including total protein (TP), albumin (ALB), alanine aminotransferase (ALT), aspartate aminotransferase (AST), alkaline phosphatase (ALP), urea nitrogen (UN), ammonia (AMM), glucose (GLU), triglyceride (TG), total cholesterol (TC), high-density lipoprotein-cholesterol (HDL-C), low-density lipoprotein-cholesterol (LDL-C), and cholinesterase (CHE), were determined using commercially available kits (F. Hoffmann-La Roche Ltd, Basel, Switzerland) and Roche automatic biochemical analyzer (Cobas c311, F. Hoffmann-La Roche Ltd, Basel, Switzerland).

2.4. DNA Extraction, PCR Amplification, and MiSeq Sequencing. Fecal microbial DNA was extracted using the Fast DNA SPIN extraction kit (MP Biomedicals, Santa Ana, CA, USA), following the manufacturer's introductions. Final DNA concentration and purity were determined using a NanoDrop ND-1000 spectrophotometer (Thermo Fisher Scientific, Waltham, MA, USA).

The bacteria 16S rRNA gene V3-V4 hypervariable region amplification was performed using the forward primer 338F (5'-GCACCTAAYTGGGYDTAAAGNG-3') and reverse primer 806R (5'-TACNVGGGTATCTAATCC-3') [13]. The PCR thermal cycle conditions comprised 2 min initial denaturation at 98°C; 25 cycles of 15 s at 98°C, 30 s annealing at 55°C, and 30 s elongation at 72°C; and a final extension at 72°C for 5 min. The PCR components include 5 μ L of Q5 reaction buffer (5 \times), 5 μ L of Q5 High-Fidelity GC buffer (5 \times), 0.25 μ L of Q5 High-Fidelity DNA Polymerase (5 U/ μ L), 2 μ L (2.5 mM) of dNTPs, 1 μ L (10 μ M) each of forward and reverse primers, 2 μ L of DNA template, and 8.75 μ L of ddH₂O. The PCR amplicons were further purified with AgencourtAMPure Beads (Beckman Coulter, Indianapolis, IN) and quantified with the PicoGreen dsDNA Assay Kit (Invitrogen, Carlsbad, CA, USA), following the manufacturer's protocols. The resulting PCR products were successfully separated using 1.2% agarose gel electrophoresis.

The equimolar purified amplicons were pooled and paired (2 \times 300) sequenced using the MiSeq Reagent Kit v3 (600 cycles) on an Illumina MiSeq platform (Illumina, San Diego, USA), following the standard protocols by Shanghai Personal Biotechnology Co. Ltd. (Shanghai, China). Raw 16S gene data are available in the NCBI Sequence Read Archive with accession number PRJNA595474.

2.5. Determination of Fecal Metabolites. Fecal short-chain fatty acid (SCFA) levels were determined by gas chromatography, as previously detailed [14]. Fecal indole, skatole, and bioamine levels were determined by the reverse-phase high-performance liquid chromatography (Agilent 1290, Santa Clara, CA, USA), as previously described [14].

2.6. Statistical Analyses. Data analyses and graph preparation were performed using SPSS 22, Excel 2010, R package ggplot2 [15], and GraphPad Prism ver7.0 (San Diego, CA, USA). Plasma biochemical parameters, reproductive hormones, fecal metabolites, and microbiota alpha diversity were analyzed by one-way analysis of variance (ANOVA) and Duncan's multiple range post hoc test. The structural

variation of microbial community among samples was analyzed with the beta diversity analysis (PERMANOVA) [16]. The relative abundance of gut microbiota at phyla and genera levels during pregnancy and lactation was analyzed via Metastats analysis (<http://metastats.cbcb.umd.edu/>) [17]. Spearman's correlation between the fecal metabolites, plasma indexes, and relative abundance of different microbial genera was performed using the R package [18]. All data were presented as means \pm standard error of mean (SEM) and considered statistically significant when $P < 0.05$.

3. Results

3.1. Changes in Plasma Levels of Reproductive Hormone and Biochemical Parameter in Sows During Pregnancy and Lactation. Plasma reproductive hormone levels changed dramatically during pregnancy (Figure 1). The PRL and FSH levels on pregnancy 105 d were significantly decreased ($P < 0.05$), compared with days 45 and 75 of pregnancy. The PROG level on days 75 and 105 of pregnancy was significantly decreased ($P < 0.05$) compared with day 45 of pregnancy. In addition, the LH level was higher ($P < 0.05$) on day 45, while E₂ level was lower ($P < 0.05$) on day 105, compared with the day 75 of pregnancy. The plasma levels of biochemical parameters associated with protein and gluco-lipid metabolism in sows also changed differently from pregnancy to lactation (Figure 2). Plasma TP and ALB levels were significantly lower ($P < 0.05$) in all pregnant stages, whereas UN and GLU were higher ($P < 0.05$) during lactation. Notably, ALP activity on lactation 21 d was higher ($P < 0.05$) than on pregnancy 75 d and lactation 7 d. Both AST and ALT activities on pregnancy 105 d were higher ($P < 0.05$) than on 45 d. In addition, plasma biochemical parameters associated with nitrogen metabolism changed with pregnancy and lactation. On lactation 21 d, TC and HDL-C levels were higher ($P < 0.05$) than those of other pregnant stages and the TG level highest ($P < 0.05$) on pregnancy 105 d.

3.2. The Fecal Microbiota Community Profile in Sows during Pregnancy and Lactation. A total of 1,465,181 sequences were obtained from 37 samples after size filtering, quality control, and chimera removal, with an average of 39,600 sequences per fecal sample. Based on a 97% similarity, 48,615 operational taxonomic units (OTUs) were obtained with an average of 1,314 OTUs per sample (Supplementary Table S1). The diversity and richness of the observed_species of fecal microbiota in gestating and lactating sows were measured by the Chao1 and Shannon indexes, respectively (Figure 3). Observed_species between pregnancy and lactation were significantly different, with highest Chao1 index ($P < 0.05$) on pregnancy 75 d. However, the Shannon index on pregnancy 105 d was lowest ($P < 0.05$) among the different stages.

Nonmetric multidimensional scaling (NMDS) can assess the between group distance in the sow fecal bacteria community structure. Microbial community profiles were clustered more closely to each other from pregnancy days 45 to 105, while clearly separated between gestation and lactation

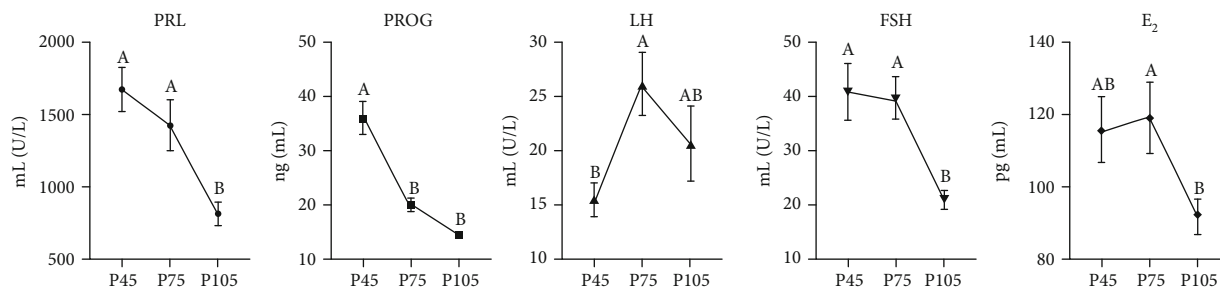


FIGURE 1: The changes of plasma reproductive hormone levels in sows at different stages of pregnancy. PRL: prolactin; PROG: progesterone; LH: luteinizing hormone; FSH: follicle-stimulating hormone; E₂: estradiol. P45, P75, and P105 mean days 45, 75, and 105 of pregnancy, respectively. The same as below. Data show the means ± SEM. ^{A,B} indicates statistically significant differences ($P < 0.05$). $n = 6-8$ per group.

(Figure 3(d)), indicating that the β -bacterial diversity of samples between gestation and lactation differed significantly.

3.3. Change of Fecal Microbial Community and Composition in Sows During Pregnancy and Lactation. The microbial community compositions of all fecal samples were analyzed at phylum and genus levels. Based on 97% 16S rRNA gene sequence identity, 15 microbial phyla and top 20 microbial genera, with a clear classification status, were identified in all pregnancy and lactation stages. Firmicutes (69.58%, 66.15%, 63.69%, and 74%), Bacteroidetes (18.4%, 22.75%, 20.71%, and 17.1%), and Spirochaetes (7.88%, 7.13%, 12.40%, and 3.74%) were the top three dominant phyla on pregnancy 45, 75, and 105 d and on lactation 21 d, respectively; whereas Firmicutes (67.11%), Bacteroidetes (18.08%), and Proteobacteria (5.17%) were the top three dominant phyla on lactation 7 d (Figure 4(a)). Aside from these dominant phyla, there were other dominant phyla with >1% relative abundances of the total microbial composition, including Proteobacteria (1.39%), on pregnancy 45 d; Proteobacteria (1.27%), 105 d; Spirochaetes (3.27%), Actinobacteria (2.85%), and Fibrobacteres (1.85%) on lactation 7 d; and Fibrobacteres (1.54%), Proteobacteria (1.39%), and Actinobacteria (1.17%) on lactation 21 d (Figure 4(a)). At the genus level, 20 bacterial taxa distributions were clearly and visually presented (Figure 4(b)), indicating the varied relative abundances of bacterial genera from pregnancy to lactation, with the top three dominant genera, including Streptococcus (9.66%), Treponema (6.75%), and Prevotella (3.86%).

3.4. Differences in Microbial Communities during Pregnancy and Lactation. The different fecal microbial phylum abundances between pregnancy and lactation are shown in Figure 4(c). Verrucomicrobia and Spirochaetes relative abundances increased ($P < 0.05$) during pregnancy but decreased ($P < 0.05$) during lactation. Further, TM7 relative abundance was the highest ($P < 0.05$) on lactation 7 d among all the groups.

Fecal microbial relative abundance at the genus level varied greatly among different stages of pregnancy and lactation (Figure 4(d)). The relative abundances of *Streptococcus* and *Treponema* during lactation were significantly lower ($P < 0.05$) than those during pregnancy. Interestingly, *Akkermansia*, *Bacteroides*, and *Desulfovibrio* relative abundances were higher ($P < 0.05$) during lactation than pregnancy.

3.5. Changes in Fecal Metabolite Abundances in Sows During Pregnancy and Lactation. The changes in sow fecal metabolites during pregnancy and lactation are shown in Figure 5. Acetate, propionate, butyrate, valerate, straight-chain fatty acids, and SCFAs levels were higher ($P < 0.05$) during lactation than pregnancy. Interestingly, isobutyrate, isovalerate, and branched-chain fatty acids (BCFAs) levels on day 105 of pregnancy, were the lowest ($P < 0.05$) compared to other stages. Putrescine, cadaverine, and spermidine levels were lower ($P < 0.05$) during lactation, whereas tyramine, indole, and skatole levels were higher ($P < 0.05$), compared with those during pregnancy.

3.6. Correlation between Fecal Microbiota Relative Abundances and Plasma Parameters. The correlation between fecal microbiota and plasma reproductive hormones or biochemical parameters is presented in Figure 6(a). There were positive correlations ($P < 0.05$) between microbial relative abundances and plasma indexes levels, including Cupriavidus, Proteobacteria, and Oscillospira and E₂, LH, and FSH; Bacteroides and LH and PRL; Desulfovibrio and E₂, LH, FSH, and PRL; Streptococcus and CHE, TG, and ALB; and Akkermansia and CHE. There were negative correlations ($P < 0.05$) between Bacteroides and ALP; Desulfovibrio and CHE; Streptococcus and UN and LH; Akkermansia and LH, FSH, and PRL; and Verrucomicrobia and GLU.

3.7. Correlation between Fecal Metabolite Levels and the Relative Abundances. The Spearman correlation between the fecal metabolites and microbial genera abundances in the sows is shown in Figure 6(b). The relative abundances of Spirochaetes and Treponema were negatively correlated with valerate, butyrate, BCFAs, isovalerate, isobutyrate, and skatole levels and were positively with spermidine level ($P < 0.05$). Moreover, Spirochaetes was negatively correlated ($P < 0.05$) with acetate level, but Treponema was positively correlated ($P < 0.05$) with putrescine level. Verrucomicrobia was negatively correlated ($P < 0.05$) with indole level; Streptococcus was negatively with butyrate level and positively ($P < 0.05$) with spermidine level; Akkermansia was negatively ($P < 0.05$) with butyrate and skatole levels and positively ($P < 0.05$) with spermidine level; Cupriavidus was positively ($P < 0.05$) with valerate, butyrate, BCFAs, isovalerate, isobutyrate, and indole levels and negatively ($P < 0.05$)

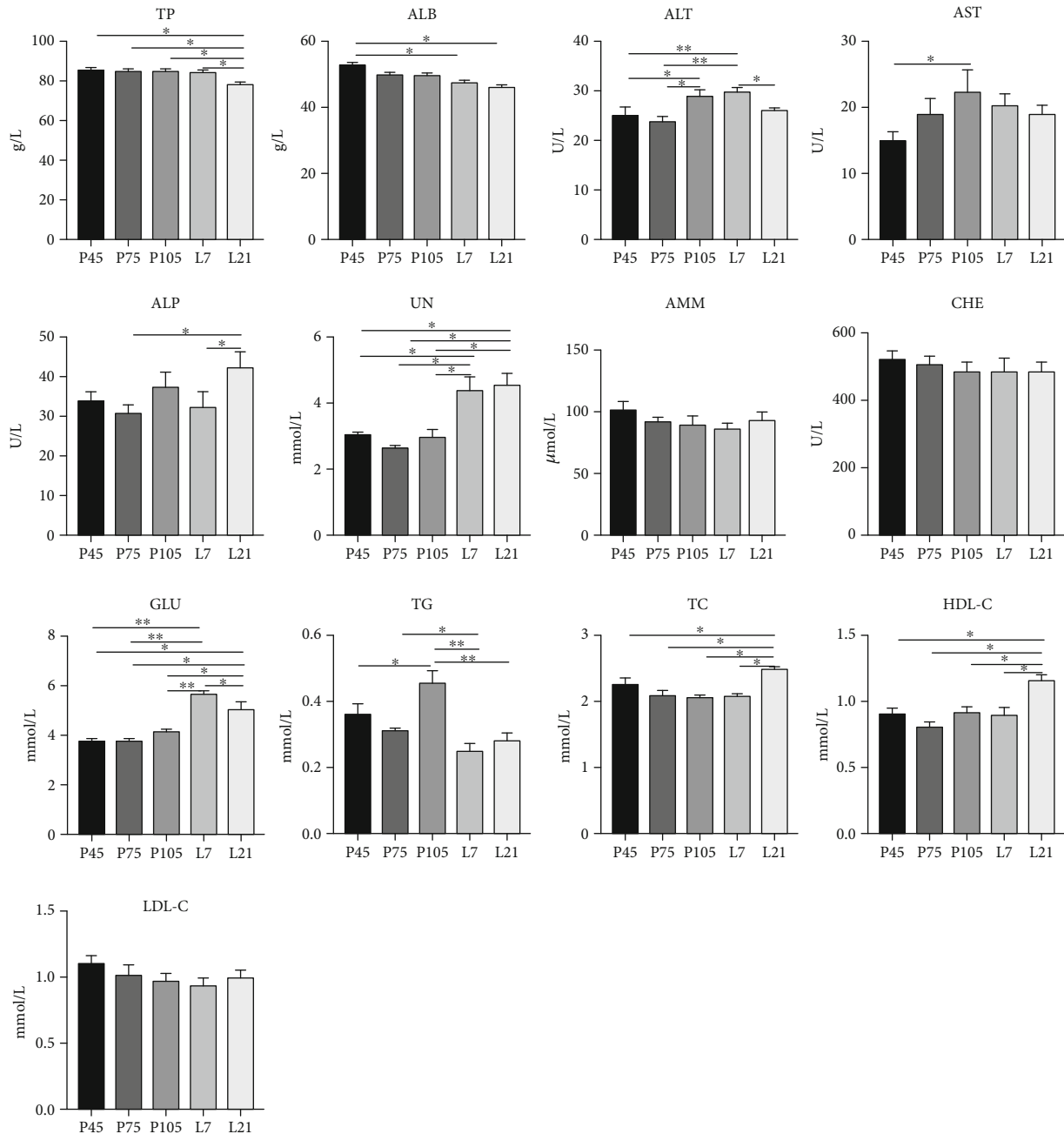


FIGURE 2: The changes of plasma biochemical parameters in sows at different stages of pregnancy and lactation. TP: total protein; ALB: albumin; ALT: alanine aminotransferase; AST: aspartate aminotransferase; ALP: alkaline phosphatase; UN: urea nitrogen; AMM: ammonia; CHE: cholinesterase; GLU: glucose; TG: triglyceride; TC: total cholesterol; HDL-C: high-density lipoprotein-cholesterol; LDL-C: low-density lipoprotein-cholesterol. L7 and L21 mean day 7 and day 21 of lactation, respectively. The same as below. Data show the means \pm SEM. * $P < 0.05$, ** $P < 0.01$. $n = 6-8$ per group.

with spermidine level; and *Desulfovibrio* was positively ($P < 0.05$) with tyramine level.

4. Discussion

Many intricate and comprehensive physiology and metabolism alterations occur in sows during pregnancy and lactation, accompanied with hormonal and metabolic changes to meet maternal nutrient needs and support growth and development of offspring. In this study, changes in fecal microbi-

ota composition and metabolites, as well as protein and gluco-lipid metabolisms, were analyzed at pregnancy (from day 45 to day 105) to lactation (from day 7 to day 21) stages. Our data showed that maternal fecal microbiota composition and metabolite alterations changed during pregnancy and lactation to meet the growth and development demands of their fetuses and/or newborns.

The nutrient metabolism status of sows during pregnancy and lactation are crucial for modulating body health and offspring growth. Generally, plasma TP and ALB levels

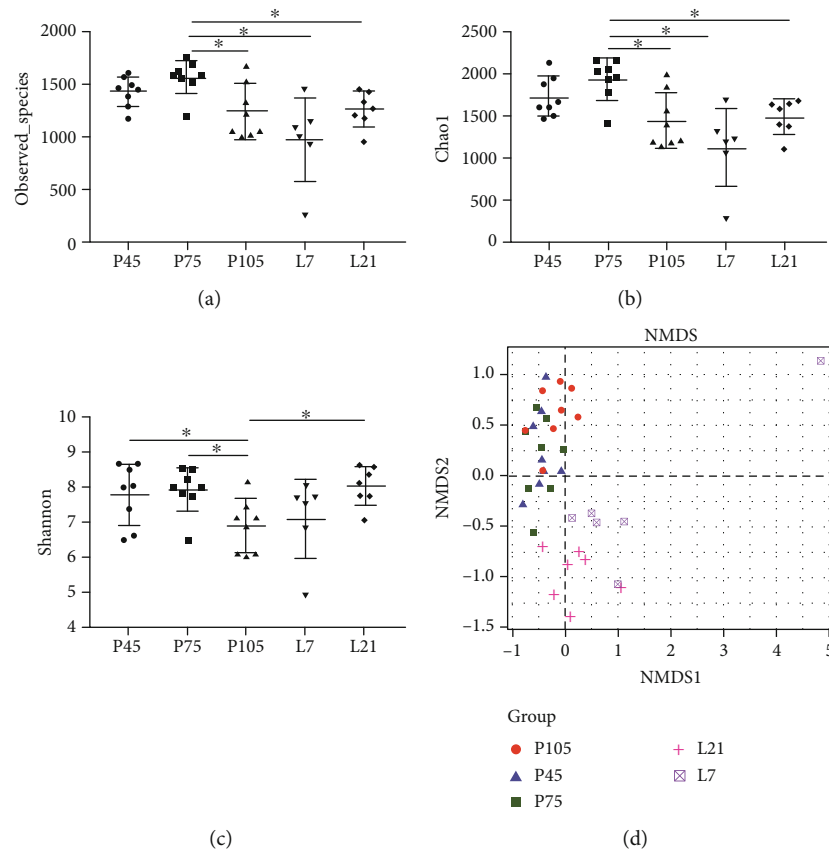


FIGURE 3: Fecal microbiota diversity of sows at different stages of pregnancy and lactation. The bacterial diversity was estimated by observed species (a), Chao1 (b), Shannon index (c), and nonmetric multidimensional scaling (NMDS) of bacterial community (d). Data show the means \pm SEM. $n = 6-8$ per group.

reflect the absorption and metabolism of protein in sows [19]. Plasma UN level can evaluate the body protein and amino acid catabolism status, and a decrease in plasma UN level reflects that the amino acid composition in body is well balanced [20]. In this study, plasma TP and ALB levels were higher, and the UN level was lower during pregnancy stage than lactation, implying that protein utilization was increased in sows during pregnancy, which could benefit sows to favor growth and development of their fetuses. The higher plasma UN level during lactation might be induced by higher crude protein (16.30%) level in lactating diets. The lactating sows were fed 2.4 kg diets with a 16.30% CP level while the pregnant sows were fed 0.8-2.0 kg diets with 12.82% CP level. The higher plasma UN level might cause an increase of milk UN level, which is positively correlated with blood UN level [21], suggesting that it can facilitate fat deposition and growth and development of suckling piglets [22].

Blood TG, TC, HDL-C, and LDL-C levels reflect the lipid utilization and absorption [12]. HDL-C can transport TC to the liver for metabolizing to be other substances, thereby maintaining a stable TC level in the body [23]. The plasma TC and HDL-C levels were higher on day 21 of lactation than other stages in the present study, consistent with a previous report [6], suggesting that lipoprotein metabolism was enhanced in sows to offset the nutrient loss induced by lacta-

tion. Previous studies demonstrated that there is a diabetogenic status in late pregnancy, including high TG level, insulin resistance, and/or hyperglycemia, which could provide adequate nutrients to the fetuses, as well as fulfill the energy demands of infants during lactation [24, 25]. Koren found that the reduced insulin sensitivity and increased blood glucose level in pregnant women are beneficial in the context of a normal pregnancy [4]. Interestingly, we found that plasma TG level was the highest on day 105 of pregnancy, while GLU level presented an increasing trend during pregnancy, suggesting that metabolic syndrome in sows is existed during late pregnancy to favor the availability of glucose and other nutrients for growth and development of fetuses.

Reproductive hormones change regularly during the reproductive cycle. FSH can promote follicular development and act synergistically with LH to promote the secretion of E_2 by host, which roughly complied with our findings that a synergistic relationship between FSH, LH, and E_2 . Additionally, proliferation of some bacterial species (e.g., *Lactobacillus*, *Streptococcus*, and *Escherichia coli*) was enhanced by female hormones [26]. There was a similar changed trend between PROG, E_2 , and PRL during different pregnancy stages, which were the lowest on pregnancy 105 d. Indeed, several bacteria (e.g., *Bacteroides*, unclassified *Lachnospiraceae*, *Clostridiales*, and *Akkermansia*) could metabolize E_2 and PROG [27],

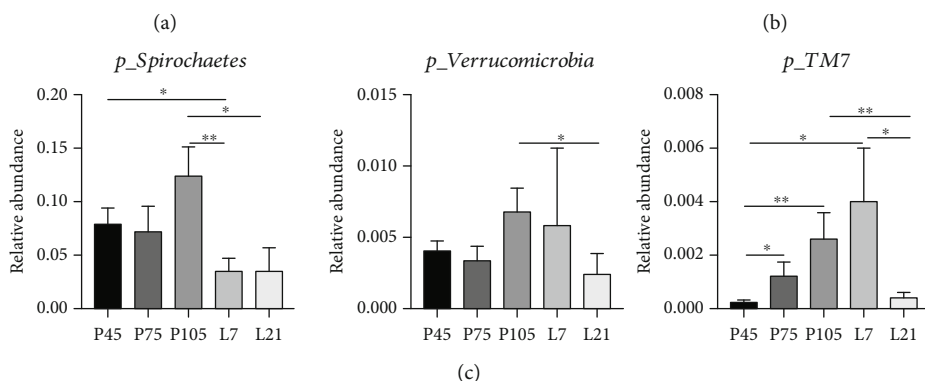
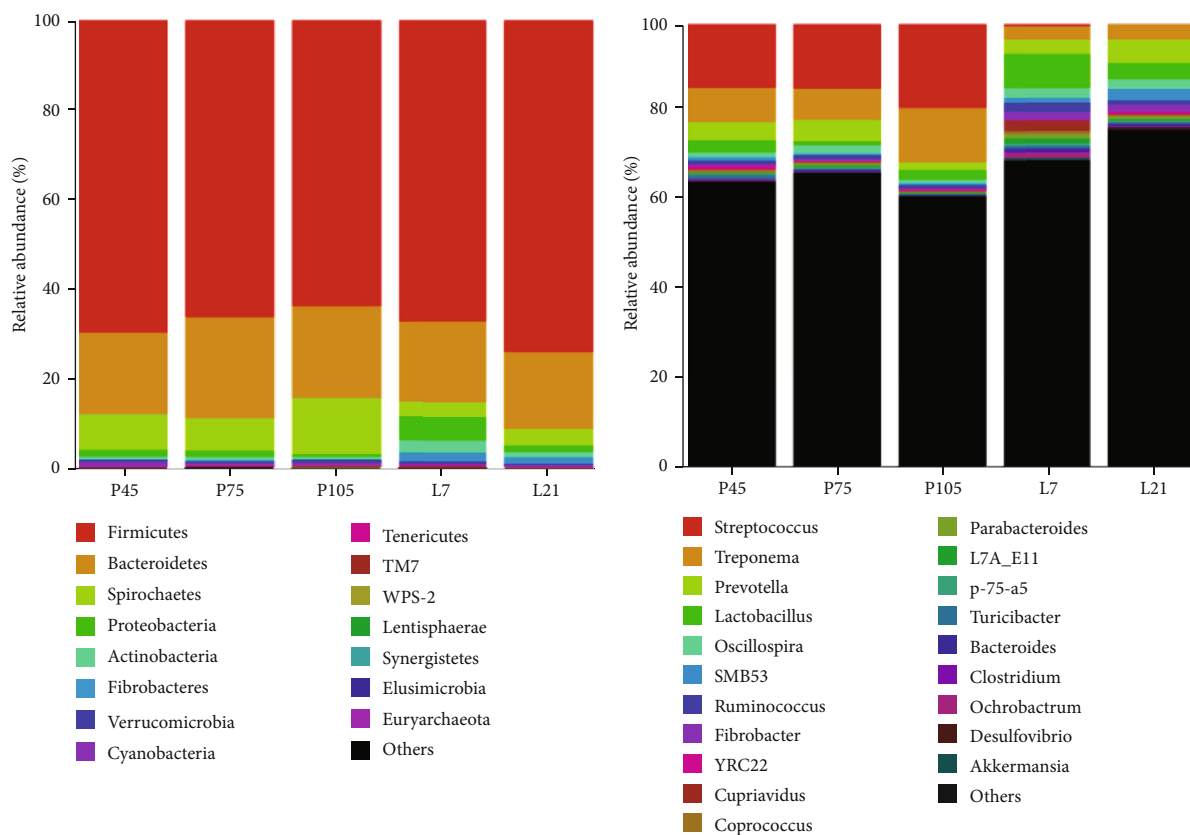


FIGURE 4: Continued.

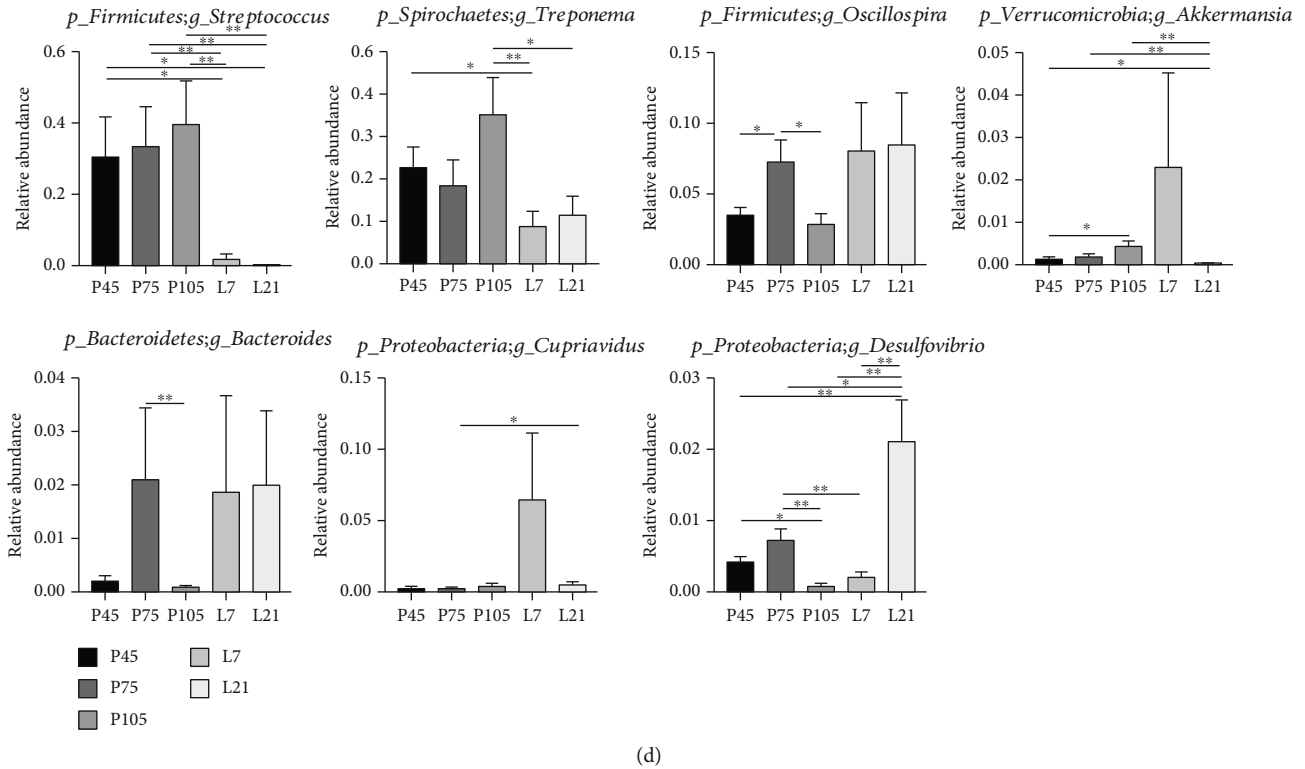


FIGURE 4: Fecal microbiota community structure of sows at different stages of pregnancy and lactation. Fecal microbiota distributed at phylum (a) and genera (b) levels. All of the phyla were listed, and only the top twenty genera were listed. Comparison of relative abundances at the phylum (c) and genera (d) levels, and discrepancy of the top ten fecal microbiota was listed. $n = 6-8$ per group.

suggesting that there is an association between hormones and gut microbiota. Moreover, Adlercreutz reported that there was a correlation between E_2 level and fecal microbiota composition and abundance [28], and Kornman and Loesche found E_2 and PROG could foster the growth of *Bacteroides* (including *Prevotella intermedius*) by taking up E_2 and PROG [27]. The mechanism might be that gut microbiota composition was affected by the changes of hormones receptor [29], and some bacteria have also been found to involve in the secretion or modification of hormone [30]. SCFAs (including acetate, propionate, and butyrate) produced by gut microbiota could inhibit PRL gene transcription, thus reducing the PRL production [31]. These findings suggested that gut microbiota played an important role in hormones metabolism of host.

Gut microbiota structure and composition shift dramatically during pregnancy and lactation. The alpha diversity of gut microbiota is closely related to host health [32], and low alpha diversity is expected to mirror the adverse metabolic conditions (e.g., increased gut permeability) [33]. In the present study, the Shannon index increased on day 21 of lactation compared with on day 105 of pregnancy, which is consistent with previous studies [12, 34]. These findings suggested that the gut microbiota might have a positive effect on sow's metabolism during lactation. In addition, bacterial community composition analysis (β -diversity) showed that the gut microbial composition of sows was significantly altered during pregnancy and lactation, which

might be caused by delivery, different diets, or the change of feeding environment.

The dominant phyla were *Firmicutes* and *Bacteroides* in animal gut [35] and the relative abundances of which were higher than other microbiota in our study, though *Firmicutes* and *Bacteroidetes* relative abundances were not significantly different during pregnancy and lactation. Interestingly, we also found that several gut microbiota composition varied from pregnancy to lactation stages. *Streptococcus* (*Firmicutes* phylum), *Treponema* (*Spirochaetes* phylum), and *Spirochaetes* relative abundances were significantly reduced, but *Desulfovibrio* relative abundance was increased during lactation, relative to several pregnancy stages in this study. These alterations might be influenced by dietary fiber from feed ingredients in the present study. Previous study found that *Streptococcus* decreased while *Desulfovibrio* increased in overweight and obese pregnant women after ingested high fiber diets, though the changed fiber had no effects on microbial alpha diversity [36], which is not consistent with our findings. In addition, *Streptococcus*, the dominant human milk bacteria [37], was thought to induce lactation mastitis [38]. Previous studies showed that decreased *Spirochaetes* abundance relieved constipation in mini sows [39] and that *Spirochaetes* abundance was higher in obese pigs compared with lean pigs [40]. Thus, these findings suggested that sows at different pregnancy and lactation stages show varied intestinal microbiota composition, which may depend on host metabolism at disparate physiological states.

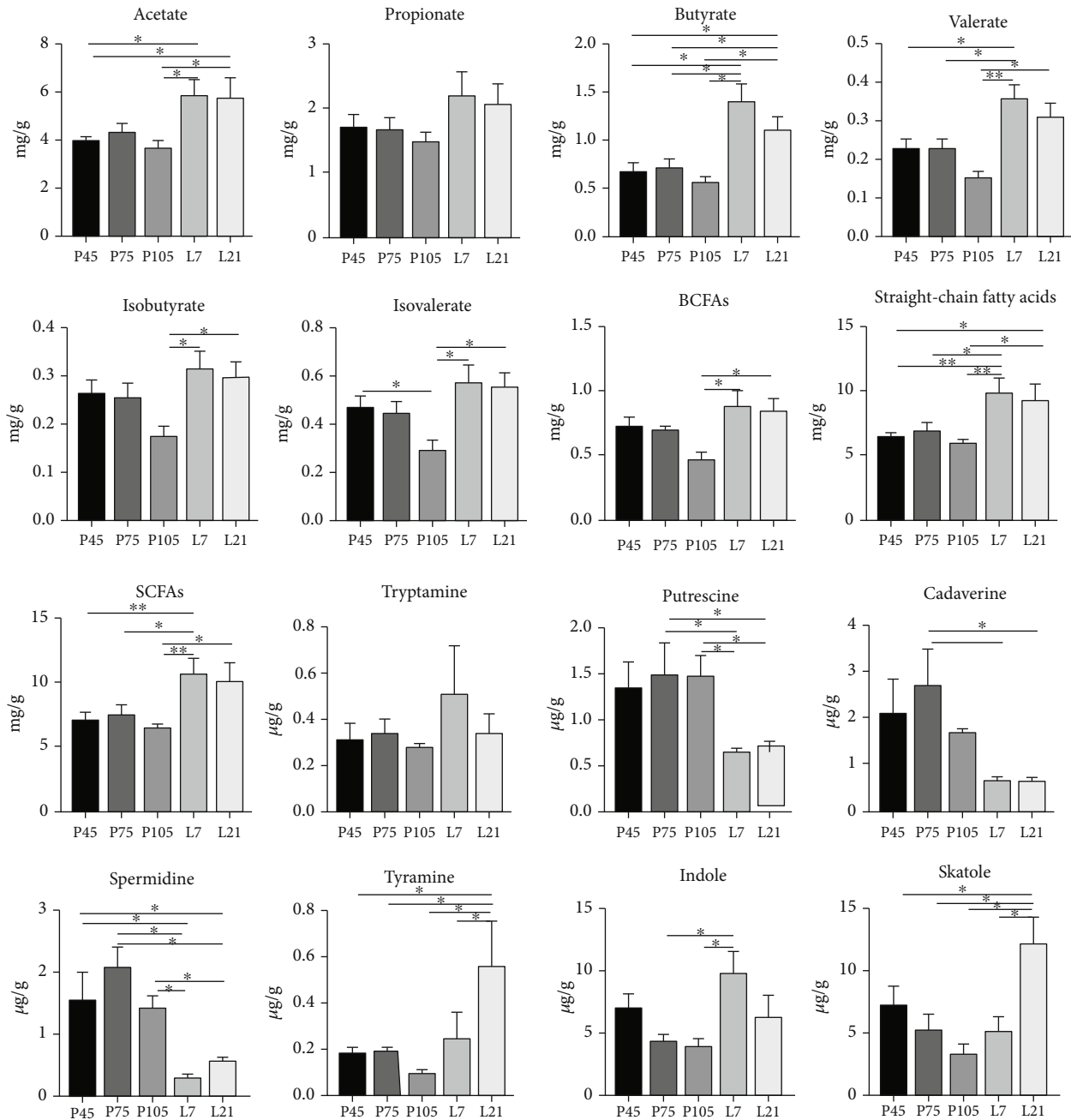


FIGURE 5: The levels of short-chain fatty acids (SCFAs), bioamines, indole, and skatole of sows at different stages of pregnancy and lactation. BCFAs: branched-chain fatty acids. Data show the means ± SEM. $n = 6-8$ per group.

Metabolites produced by gut microbiota govern host metabolism and health [41]. Several studies have shown that SCFAs, particularly butyrate, produced by the *Firmicutes* using dietary fiber and resistant starch as the substrates, mainly provide energy for host colonic epithelium cells [42], exert relieving metabolic syndrome effects (e.g., anti-Type 2 diabetes during pregnancy) [43], and prevent hypertension occurrence and/or development during pregnancy [44]. In the present study, the SCFAs (including acetate, butyrate, and valerate) levels decreased during pregnancy than those during lactation and presented a decreasing trend

from early pregnancy to late pregnancy, suggesting that the SCFAs not only favored maternal energy requirement but were absorbed to benefit fetuses' growth and development [45]. These alterations in intestine SCFA levels might be due to the stronger absorption capacity in Bama mini pigs during late pregnancy, and the specific reasons remain to be further investigated. Besides, the BCFAs are mainly derived from the catabolism of proteins in the intestinal lumen, which are the products of oxidative deamination of leucine, isoleucine, and valine [46]. The present study showed that isobutyrate, isovalerate, and total BCFA levels

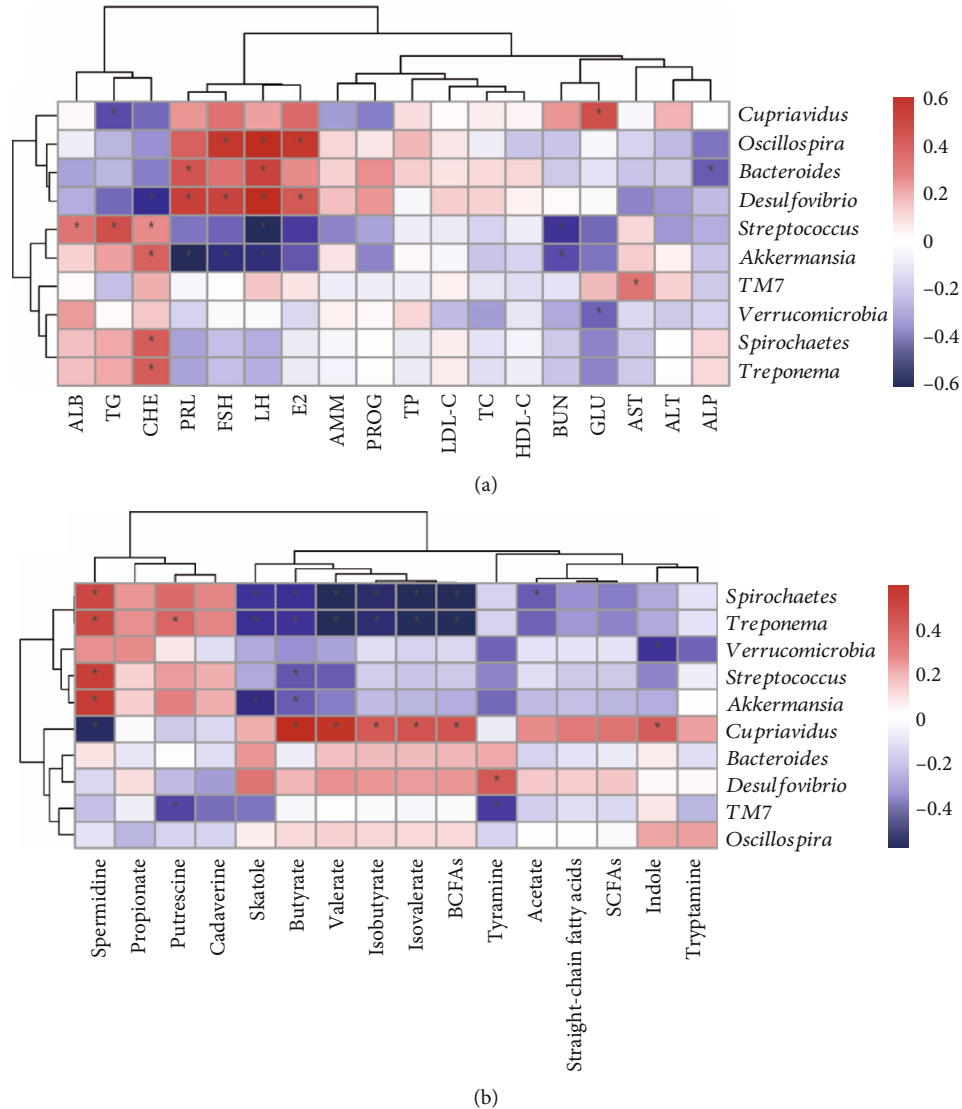


FIGURE 6: Correlations between the discrepant fecal microbiota and metabolite levels of sows. The plasma parameters (a) and fecal metabolites (b) are presented to be correlated with gut microbiota, respectively. Spearman correlations were used, and * means the correlation significant. PRL: prolactin; LH: luteinizing hormone; FSH: follicle-stimulating hormone; PROG: progesterone; E₂: estradiol; TP: total protein; ALB: albumin; ALT: alanine aminotransferase; AST: aspartate aminotransferase; ALP: alkaline phosphatase; UN: urea nitrogen; AMM: ammonia; GLU: glucose; TG: triglyceride; TC: total cholesterol; HDL-C: high-density lipoprotein-cholesterol; LDL-C: low-density lipoprotein-cholesterol; CHE: cholinesterase; BCFAs: branched-chain fatty acids; SCFAs: short-chain fatty acids.

were higher during lactation than pregnancy, which might be due to the increased feed intake (2.4 kg per day) and CP level (16.30%) in lactation diets, thus increasing the catabolism of these amino acids in the hindgut [12]. However, the physiological significance of which remains to be further explored.

In addition, polyamines, including putrescine, spermine, and spermidine, present functions in gene expression regulation, DNA and protein synthesis, and cell proliferation and differentiation [47]. In the present study, both putrescine and spermidine levels increased during pregnancy compared with lactation, indicating that they are made available for rapid fetus growth in the second and third trimesters, since polyamines play a key regulatory role in angiogenesis, as well as placental and fetal growth and development [48]. Indole

and skatole in the hindgut are produced by the decomposition of proteins undigested in the small intestine [49]. However, the present study showed that indole and skatole levels were decreased during pregnancy but were increased during lactation, which might result from undigested protein metabolites in lactation sows, because the dietary crude protein level during lactation (16.30%) was higher than pregnancy (12.82%). A previous study also showed that high wheat bran-containing diets could affect gut microbiota structure in pregnant sows [50], suggesting that maternal dietary composition might influence gut microbial metabolites by altering microbiota composition.

Metabolic syndromes, including hyperglycemia and excess energy intake, can be induced by the high plasma

TG, TC, LDL-C, or GLU levels [51]. Previous study showed that *Akkermansia muciniphila* could enhance the glucose tolerance, regulating host's metabolism [52]. In the present study, the GLU level and *Akkermansia* abundance were the highest on day 7 of lactation, which is consistent with previous findings [53]. Recent studies showed that *Akkermansia* abundance reduced in host with type 2 diabetes [25, 54], which was negatively correlated with the metabolic syndromes, obesity, type 2 diabetes, and hypertension [55]. It was also reported that *Akkermansia* could play an immunomodulatory role by interacting with host intestinal epithelial cells [56]. Hence, it is interesting to investigate the relationship between intestinal microbiota and hormones or metabolites levels in pregnant and lactating sows. Here, we showed a positive correlation between TG and CHE levels, and *Akkermansia* and *Streptococcus* relative abundances. *Akkermansia* abundance was also positively correlated with spermidine level but negatively with LH, FSH, PRL, butyrate, or skatole levels. These relationships implied that there might be a synergistic effect or negative feedback mechanism between fecal microbiota and their metabolites and/or plasma metabolites.

In conclusion, gut microbiota was mainly dominated by the *Firmicutes*, *Bacteroidetes*, and *Spirochaetes* phyla, though the *Firmicutes* and *Bacteroidetes* phyla showed no significant differences during pregnancy and lactation. Compared with pregnancy, the fecal microbial alpha diversity and relative abundances of *Spirochaetes*, *Streptococcus*, and *Treponema* decreased during lactation. *Akkermansia* relative abundance was the highest on day 7 of lactation. In addition, there is a tight cross-talk between gut microbial remodeling and host physiological status, including plasma biochemical parameter and reproductive hormone changes, as well as fecal metabolite changes. Further, it will be interesting to explore whether and how *Akkermansia* influences pregnancy and lactation in mammals.

Data Availability

The data used to support the findings of this study are available from the corresponding author upon request.

Ethical Approval

Animal use and animal trials in this study have been approved by the Animal Care and Use Committee of the Institute of Subtropical Agriculture, Chinese Academy of Sciences, No. ISA-2018-071.

Conflicts of Interest

The authors declare no conflict of interest.

Authors' Contributions

XK designed the experiment; CM, QG, WZ, MA, and XK carried out the animal experience, sample collection, and sample analysis; CM and WZ performed the statistical anal-

yses; CM wrote the manuscript; XK revised the manuscript. All authors read and approved the final manuscript.

Acknowledgments

The present study was jointly supported by National Key Research and Development Project (2018YFD0500404-4), National Natural Science Foundation of China (31772613), STS regional key project of the Chinese Academy of Sciences (KFJ-STQZ-052), Special Funds for Construction of Innovative Provinces in Hunan Province (2019RS3022), and Talent Projects of Guangxi Science and Technology Department (AD17195043). We thank the staff and post-graduate students of Hunan Provincial Key Laboratory of Animal Nutritional Physiology and Metabolic Process for collecting samples and technicians from CAS Key Laboratory of Agro-ecological Processes in Subtropical Region for providing technical assistance. We would like to thank Editage (<https://www.editage.cn/>) for English language editing.

Supplementary Materials

Table S1: mean count of clean sequences and OTUs among five stages of gestation and lactation. (*Supplementary Materials*)

References

- [1] D. Newbern and M. Freemark, "Placental hormones and the control of maternal metabolism and fetal growth," *Current Opinion in Endocrinology Diabetes and Obesity*, vol. 18, no. 6, pp. 409–416, 2011.
- [2] G. Mor and I. Cardenas, "The immune system in pregnancy: a unique complexity," *American Journal of Reproductive Immunology*, vol. 63, no. 6, pp. 425–433, 2010.
- [3] J. M. Evans, L. S. Morris, and J. R. Marchesi, "The gut microbiome: the role of a virtual organ in the endocrinology of the host," *The Journal of Endocrinology*, vol. 218, no. 3, pp. R37–R47, 2013.
- [4] O. Koren, J. K. Goodrich, T. C. Cullender et al., "Host remodeling of the gut microbiome and metabolic changes during pregnancy," *Cell*, vol. 150, no. 3, pp. 470–480, 2012.
- [5] Q. H. Mu, X. Cabana-Puig, J. Mao et al., "Pregnancy and lactation interfere with the response of autoimmunity to modulation of gut microbiota," *Microbiome*, vol. 7, Article ID 105, 2019.
- [6] Y. J. Ji, H. Li, P. F. Xie et al., "Stages of pregnancy and weaning influence the gut microbiota diversity and function in sows," *Journal of Applied Microbiology*, vol. 127, no. 3, pp. 867–879, 2019.
- [7] W. Chen, J. Mi, N. Lv et al., "Lactation stage-dependency of the sow milk microbiota," *Frontiers in Microbiology*, vol. 9, Article ID 945, 2018.
- [8] M. Wang, M. Li, S. Wu et al., "Fecal microbiota composition of breast-fed infants is correlated with human milk oligosaccharides consumed," *Journal of Pediatric Gastroenterology and Nutrition*, vol. 60, no. 6, pp. 825–833, 2015.
- [9] C. M. Rath and P. C. Dorrestein, "The bacterial chemical repertoire mediates metabolic exchange within gut microbiomes," *Current Opinion in Microbiology*, vol. 15, no. 2, pp. 147–154, 2012.

- [10] J. Yang, L. Dai, Q. Yu, and Q. Yang, "Histological and anatomical structure of the nasal cavity of Bama minipigs," *PLoS One*, vol. 12, no. 3, Article ID e0173902, 2017.
- [11] E. M. Walters and R. S. Prather, "Advancing swine models for human health and diseases," *Molecular Medicine*, vol. 110, no. 3, pp. 212–215, 2013.
- [12] X. F. Kong, Y. J. Ji, H. W. Li et al., "Colonic luminal microbiota and bacterial metabolite composition in pregnant Huanjiang mini-pigs: effects of food composition at different times of pregnancy," *Scientific Reports*, vol. 6, no. 1, Article ID 37224, 2016.
- [13] J. G. Caporaso, C. L. Lauber, W. A. Walters et al., "Global patterns of 16S rRNA diversity at a depth of millions of sequences per sample," *Proceedings of the National Academy of Sciences*, vol. 108, Supplement 1, pp. 4516–4522, 2011.
- [14] C. Hu, F. Li, Y. Duan, Y. Yin, and X. Kong, "Glutamic acid supplementation reduces body fat weight in finishing pigs when provided solely or in combination with arginine and it is associated with colonic propionate and butyrate concentrations," *Food & Function*, vol. 10, no. 8, pp. 4693–4704, 2019.
- [15] J. L. V. Maag, "ganatogram: An R package for modular visualisation of anatograms and tissues based on ggplot 2," *F1000Research*, vol. 7, p. 1576, 2018.
- [16] B. H. McArdle and M. J. Anderson, "Fitting multivariate models to community data: a comment on distance-based redundancy analysis," *Ecology*, vol. 82, no. 1, pp. 290–297, 2001.
- [17] J. R. White, N. Nagarajan, and M. Pop, "Statistical methods for detecting differentially abundant features in clinical metagenomic samples," *PLoS Computational Biology*, vol. 5, no. 4, article ID e1000352, 2009.
- [18] W. Zhang, C. Ma, P. Xie et al., "Gut microbiota of newborn piglets with intrauterine growth restriction have lower diversity and different taxonomic abundances," *Journal of Applied Microbiology*, vol. 127, no. 2, pp. 354–369, 2019.
- [19] A. J. Verheyen, D. G. Maes, B. Mateusen et al., "Serum biochemical reference values for gestating and lactating sows," *Veterinary Journal*, vol. 174, no. 1, pp. 92–98, 2007.
- [20] M. M. Gadhia, A. M. Maliszewski, M. C. O'Meara et al., "Increased amino acid supply potentiates glucose-stimulated insulin secretion but does not increase β -cell mass in fetal sheep," *American Journal of Physiology-Endocrinology and Metabolism*, vol. 304, no. 4, pp. E352–E362, 2013.
- [21] J. W. Spek, A. Bannink, G. Gort, W. H. Hendriks, and J. Dijkstra, "Effect of sodium chloride intake on urine volume, urinary urea excretion, and milk urea concentration in lactating dairy cattle," *Journal of Dairy Science*, vol. 95, no. 12, pp. 7288–7298, 2012.
- [22] C. Alexopoulos, A. Karagiannidis, S. K. Kritas et al., "Field evaluation of a bioregulator containing live *Bacillus cereus* spores on health status and performance of sows and their litters," *Journal of Veterinary Medicine. A-Physiology Pathology Clinical Medicine*, vol. 48, no. 3, pp. 137–145, 2001.
- [23] L. Tian, Y. Xu, M. Fu, T. Peng, Y. Liu, and S. Long, "The impact of plasma triglyceride and apolipoproteins concentrations on high-density lipoprotein subclasses distribution," *Lipids in Health and Disease*, vol. 10, no. 1, 2011.
- [24] S. M. Nelson, P. Matthews, and L. Poston, "Maternal metabolism and obesity: modifiable determinants of pregnancy outcome," *Human Reproduction Update*, vol. 16, no. 3, pp. 255–275, 2010.
- [25] X. Zhang, D. Shen, Z. Fang et al., "Human gut microbiota changes reveal the progression of glucose intolerance," *PLoS One*, vol. 8, no. 8, article e71108, 2013.
- [26] E. S. Pelzer, J. A. Allan, C. Theodoropoulos, T. Ross, K. W. Beagley, and C. L. Knox, "Hormone-dependent bacterial growth, persistence and biofilm formation—a pilot study investigating human follicular fluid collected during IVF cycles," *PLoS One*, vol. 7, no. 12, article e49965, 2012.
- [27] K. S. Kornman and W. J. Loesche, "Effects of estradiol and progesterone on bacteroides-melaninogenicus and bacteroides-gingivalis," *Infection and Immunity*, vol. 35, no. 1, pp. 256–263, 1982.
- [28] H. Adlercreutz, M. O. Pulkkinen, E. K. Hamalainen, and J. T. Korpela, "Studies on the role of intestinal bacteria in metabolism of synthetic and natural steroid hormones," *Journal of Steroid Biochemistry*, vol. 20, no. 1, pp. 217–229, 1984.
- [29] R. Menon, S. E. Watson, L. N. Thomas et al., "Diet complexity and estrogen receptor β status affect the composition of the murine intestinal microbiota," *Applied and environmental microbiology*, vol. 79, no. 18, pp. 5763–5773, 2013.
- [30] J. M. Ridlon, S. Ikegawa, J. M. Alves et al., "Clostridium scindens: a human gut microbe with a high potential to convert glucocorticoids into androgens," *Journal of Lipid Research*, vol. 54, no. 9, pp. 2437–2449, 2013.
- [31] J. F. Wang, S. P. Fu, S. N. Li et al., "Short-chain fatty acids inhibit growth hormone and prolactin gene transcription via cAMP/PKA/CREB signaling pathway in dairy cow anterior pituitary cells," *International Journal of Molecular Sciences*, vol. 14, no. 11, pp. 21474–21488, 2013.
- [32] F. A. Duca, Y. Sakar, P. Lepage et al., "Replication of obesity and associated signaling pathways through transfer of microbiota from obese-prone rats," *Diabetes*, vol. 63, no. 5, pp. 1624–1636, 2014.
- [33] K. Mokkala, H. R oyti o, E. Munukka et al., "Gut microbiota richness and composition and dietary intake of overweight pregnant women are related to serum zonulin concentration, a marker for intestinal permeability," *The Journal of Nutrition*, vol. 146, no. 9, pp. 1694–1700, 2016.
- [34] L. Chen, Y. Xu, X. Chen, C. Fang, L. Zhao, and F. Chen, "The maturing development of gut microbiota in commercial piglets during the weaning transition," *Frontiers in Microbiology*, vol. 8, 2017.
- [35] G. L. Jiang, Y. Y. Liu, A. O. Oso et al., "The differences of bacteria and bacteria metabolites in the colon between fatty and lean pigs1," *Journal of Animal Science*, vol. 94, Supplement 3, pp. 349–353, 2016.
- [36] L. Gomez-Arango, H. L. Barrett, S. A. Wilkinson et al., "Low dietary fiber intake increases *Collinsella* abundance in the gut microbiota of overweight and obese pregnant women," *Gut Microbes*, vol. 9, no. 3, pp. 189–201, 2018.
- [37] L. Fern andez, R. Arroyo, I. Espinosa, M. Mar ın, E. Jim enez, and J. M. Rodr ıguez, "Probiotics for human lactational mastitis," *Beneficial microbes*, vol. 5, no. 2, pp. 169–183, 2014.
- [38] D. Tena, C. Fern andez, B. L opez-Garrido et al., "Lactational mastitis caused by *Streptococcus lactarius*," *Diagnostic Microbiology and Infectious Disease*, vol. 85, no. 4, pp. 490–492, 2016.
- [39] Y. Zhang, T. Lu, L. Han, L. Zhao, Y. Niu, and H. Chen, "L-glutamine supplementation alleviates constipation during late gestation of mini sows by modifying the microbiota

- composition in feces,” *BioMed Research International*, vol. 2017, Article ID 4862861, 9 pages, 2017.
- [40] R. B. Guevarra, J. Kim, S. G. Nguyen, and T. Unno, “Comparison of fecal microbial communities between white and black pigs,” *Journal of Applied Biological Chemistry*, vol. 58, no. 4, pp. 369–375, 2015.
- [41] W. R. Wikoff, A. T. Anfora, J. Liu et al., “Metabolomics analysis reveals large effects of gut microflora on mammalian blood metabolites,” *Proceedings of the National Academy of Sciences of the United States of America*, vol. 106, no. 10, pp. 3698–3703, 2009.
- [42] H. M. Hamer, D. Jonkers, K. Venema, S. Vanhoutvin, F. J. Troost, and R. J. Brummer, “Review article: the role of butyrate on colonic function,” *Alimentary Pharmacology & Therapeutics*, vol. 27, no. 2, pp. 104–119, 2008.
- [43] M. Nuriel-Ohayon, H. Neuman, O. Ziv et al., “Progesterone increases *Bifidobacterium* relative abundance during late pregnancy,” *Cell reports*, vol. 27, no. 3, pp. 730–736.e3, 2019.
- [44] Y. L. Tain, W. C. Lee, K. L. H. Wu, S. Leu, and J. Y. H. Chan, “Resveratrol prevents the development of hypertension programmed by maternal plus post-weaning high-fructose consumption through modulation of oxidative stress, nutrient-sensing signals, and gut microbiota,” *Molecular Nutrition & Food Research*, vol. 62, no. 15, article e1800066, 2018.
- [45] Y. Chen, X. Gong, G. Li et al., “Effects of dietary alfalfa flavonoids extraction on growth performance, organ development and blood biochemical indexes of Yangzhou geese aged from 28 to 70 days,” *Animal Nutrition*, vol. 2, no. 4, pp. 318–322, 2016.
- [46] X. F. Kong, X. L. Zhou, G. Q. Lian et al., “Dietary supplementation with chitoooligosaccharides alters gut microbiota and modifies intestinal luminal metabolites in weaned Huanjiang mini-piglets,” *Livestock Science*, vol. 160, pp. 97–101, 2014.
- [47] DK. Igarashi and K. Kashiwagi, “Polyamines: mysterious modulators of cellular functions,” *Biochemical and Biophysical Research Communications*, vol. 271, no. 3, pp. 559–564, 2000.
- [48] R. D. Pereira, N. E. de Long, R. C. Wang, F. T. Yazdi, A. C. Holloway, and S. Raha, “Angiogenesis in the placenta: the role of reactive oxygen species signaling,” *BioMed Research International*, vol. 2015, Article ID 814543, 12 pages, 2015.
- [49] Q. K. Sheng, Z. J. Yang, H. B. Zhao, X. L. Wang, and J. F. Guo, “Effects of L-tryptophan, fructan, and casein on reducing ammonia, hydrogen sulfide, and skatole in fermented swine manure,” *Asian-Australasian Journal of Animal Sciences*, vol. 28, no. 8, pp. 1202–1208, 2015.
- [50] M. Kraler, M. Ghanbari, K. J. Domig, K. Schedle, and W. Kneifel, “The intestinal microbiota of piglets fed with wheat bran variants as characterised by 16S rRNA next-generation amplicon sequencing,” *Archives of Animal Nutrition*, vol. 70, no. 3, pp. 173–189, 2016.
- [51] F. Qian, A. A. Korat, V. Malik, and F. B. Hu, “Metabolic effects of monounsaturated fatty acid-enriched diets compared with carbohydrate or polyunsaturated fatty acid-enriched diets in patients with type 2 diabetes: a systematic review and meta-analysis of randomized controlled trials,” *Diabetes Care*, vol. 39, no. 8, pp. 1448–1457, 2016.
- [52] R. L. Greer, X. Dong, A. C. Moraes et al., “*Akkermansia muciniphila* mediates negative effects of IFN γ on glucose metabolism,” *Nature Communications*, vol. 7, no. 1, article ID 13329, 2016.
- [53] G. Di Cianni, R. Miccoli, L. Volpe, C. Lencioni, and S. Del Prato, “Intermediate metabolism in normal pregnancy and in gestational diabetes,” *Diabetes/Metabolism Research and Reviews*, vol. 19, no. 4, pp. 259–270, 2003.
- [54] C. Chelakkot, Y. Choi, D. K. Kim et al., “*Akkermansia muciniphila*-derived extracellular vesicles influence gut permeability through the regulation of tight junctions,” *Experimental & Molecular Medicine*, vol. 50, no. 2, article e450, 2018.
- [55] C. Depommier, A. Everard, C. Druart et al., “Supplementation with *Akkermansia muciniphila* in overweight and obese human volunteers: a proof-of-concept exploratory study,” *Nature Medicine*, vol. 25, no. 7, pp. 1096–1103, 2019.
- [56] J. Reunanen, V. Kainulainen, L. Huuskonen et al., “*Akkermansia muciniphila* adheres to enterocytes and strengthens the integrity of the epithelial cell layer,” *Applied and Environmental Microbiology*, vol. 81, no. 11, pp. 3655–3662, 2015.

Research Article

Crude Radix Aconiti Lateralis Preparata (Fuzi) with *Glycyrrhiza* Reduces Inflammation and Ventricular Remodeling in Mice through the TLR4/NF- κ B Pathway

Ping Yan,¹ Wen Mao,² Lushuai Jin,³ Mingsun Fang,³ Xia Liu,³ Jiali Lang,³ Lu Jin,³ Beibei Cao,³ Qiyang Shou ³, and Huiying Fu ³

¹Department of Internal Medicine, University Hospital, Qufu Normal University, Qufu, China

²School of Basic Medicine, Zhejiang Chinese Medical University, Hangzhou, China

³The Second Clinical Medical College, Zhejiang Chinese Medical University, Hangzhou, China

Correspondence should be addressed to Qiyang Shou; sqy133@126.com and Huiying Fu; fhy131@126.com

Ping Yan and Wen Mao contributed equally to this work.

Received 20 July 2020; Revised 8 September 2020; Accepted 22 September 2020; Published 20 October 2020

Academic Editor: Xiaolu Jin

Copyright © 2020 Ping Yan et al. This is an open access article distributed under the Creative Commons Attribution License, which permits unrestricted use, distribution, and reproduction in any medium, provided the original work is properly cited.

Radix *Aconiti Lateralis Preparata* (Fuzi) is a traditional Chinese medicine. Its alkaloids are both cardiotoxic and cardioprotective; however, the underlying mechanisms are unclear. Compatibility testing and processing are the primary approaches used to reduce the toxicity of aconite preparations. The purpose of this study was to compare the effects of crude Fuzi (CFZ), CFZ combined with *Glycyrrhiza* (Gancao) (CFZ+GC), and prepared materials of CFZ (PFZ) on heart failure (HF) in C57BL/6J mice and explore the potential mechanisms of action of CFZ. Transverse aortic constriction (TAC) was used to generate the HF state, and CFZ (1.5 g·mL⁻¹), PFZ (1.5 g·mL⁻¹), or CFZ+GC (1.8 g·mL⁻¹) was orally administered to the HF-induced mice daily. For the subsequent 8 weeks, hemodynamic indicators, ventricular pressure indices, and mass indices were evaluated, and histopathological imaging was performed. CFZ, CFZ+GC, and PFZ significantly improved left ventricular function and structure and reduced myocardial damage. CFZ+GC was more effective than CFZ and PFZ, whereas CFZ had higher toxicity than CFZ+GC and PFZ. CFZ and CFZ+GC attenuated ischemia-induced inflammatory responses and also inhibited Toll-like receptor-4 (TLR4) and nuclear factor kappa beta (NF- κ B) action in the heart. Moreover, mass spectrometry analysis revealed a decrease in the levels of toxic components of CFZ+GC, whereas those of the protective components were increased. This study suggested that GC reduces the toxicity and increases the efficacy of CFZ on HF induced by TAC. Furthermore, GC+CFZ reduces the risk of HF by ameliorating the inflammation response, which might be partially related to the inhibition of the TLR4/NF- κ B pathway.

1. Introduction

Heart failure (HF) is a clinical syndrome characterized by ventricular filling or ejection impairment that might be accompanied by signs of structural and functional cardiac abnormalities [1]. The main pathological mechanisms that lead to HF include increased hemodynamic overload, ventricular remodeling, ischemia-related dysfunction, neuro-humoral stimulation, abnormal cardiac calcium circulation, and accelerated apoptosis [2, 3]. There are approximately 38 million patients with HF worldwide, and the number is

increasing as the population ages [4]. Although medicine and device-based therapy improve survival in patients with HF, they have been unable to prevent this disease from progressing and cannot restore the quality of life for patients; the 5-year mortality rate remains at 50% [5]. Owing to the significant morbidity and mortality of HF, it has become a huge challenge in terms of socioeconomics and medical resources [6]. Therefore, it is important to develop effective treatments.

Traditional Chinese medicine (TCM) plays an indispensable role in the prevention and treatment of many diseases,

including HF [7–9]. Almost all patients in China with HF are administered Chinese herbs or proprietary Chinese medicines combined with Western medicines because TCM can not only enhance heart function but also reduce the side effects of Western medicine [10, 11]. *Radix Aconiti Lateralis Preparata* (Fuzi), the lateral root of *Aconitum carmichaelii* Debx, has already been used in Asia for 2,000 years [12]. The alkaloids contained in Fuzi have widespread pharmacological activities, such as cardiotoxic, antiarrhythmic, analgesic, anti-inflammatory, antiaging, immunomodulatory, and antitumor effects; however, they are also cardiotoxic [13], which leads to a conundrum regarding the use of Fuzi. Compatibility and processing are the primary methods to reduce the toxicity of Fuzi. For example, combination with *Glycyrrhizae Radix et Rhizoma* (Gancao, GC), another frequently used Chinese herb, attenuates the toxicity of Fuzi and is used as a compatible ingredient for Fuzi as a classic herb pair [14]. However, there are no modern standards for the use of crude Fuzi (CFZ), prepared materials of Fuzi (PFZ), and CFZ with a compatible ingredient because of the lack of in-depth research. This hinders the application of Fuzi in the treatment of HF in contemporary clinical settings.

In this study, a mouse HF model was used to investigate the effects of processing and compatibility on the pharmacological activity and toxicity of CFZ and explore the underlying mechanism. In addition, the composition of CFZ with enhanced activity and reduced toxicity was analyzed before and after compatibility to provide references for the proper use of CFZ in clinical practice.

2. Methods

2.1. Preparation of Extracts. After CFZ (purchased from Jiangyou Sichuan Zhongba Fuzi Technology Development Co., Ltd., Sichuan, China) extraction with 20x pure water three times, the extracts were combined and concentrated via rotary evaporation to $1.5 \text{ g}\cdot\text{mL}^{-1}$. PFZ (purchased from Jiangyou Sichuan Zhongba Fuzi Technology Development Co., Ltd., Sichuan, China) at 100 g was immersed 10 times in water for 30 min and boiled for 1 h. The supernatant was filtered and concentrated to $1.5 \text{ g}\cdot\text{mL}^{-1}$. CFZ (100 g) and GC (20 g; purchased from the TCM Clinic of Zhejiang University of Traditional Chinese Medicine, Hangzhou, China) were immersed in deionized water (1,200 mL, 1:10w/v) for 30 min and decocted by boiling for 1 h. The two liquids were combined and concentrated to $1.8 \text{ g}\cdot\text{mL}^{-1}$.

2.2. Identification of Extracts. Based on previous methodology [15], the components in the water extracts of CFZ and CFZ+GC were determined by ultrahigh performance liquid chromatography-quadrupole time-of-flight mass spectrometry (UPLC-Q/TOF MS). The chromatographic conditions were as follows: the chromatographic column was a ZORBAX Eclipse Plus C18 column ($2.1 \times 100 \text{ mm}$, $1.8 \mu\text{m}$, Agilent 1290-6545 UPLC-Q/TOF MS, Santa Clara, CA, USA); mobile phase: A solvent (0.1% formic acid solution), B solvent (0.1% acetonitrile); flow rate: 0.3 mL/min; elution procedure: 2 min, 95% A, 5% B; 20 min, 100% B; 25 min, 100% B;

column temperature: 40°C ; sample and standard sample injection volume: $2 \mu\text{L}$.

The mass spectrometry experimental conditions were as follows: ion source mode: electrospray ionization, negative ion mode; drying gas temperature: 325°C ; drying gas flow rate: 1012 L/min; sheath gas temperature: 370°C ; sheath gas flow rate: 12 L/min; nebulizer pressure: 35 psi; capillary voltage: 3000 V; nozzle voltage: 1500 V; acquisition mode: full scan, m/z : 100–1700.

2.3. Experimental Groups. All animal protocols were approved by the Zhejiang Chinese Medical University Laboratory Animal Research Center, and the experiments were performed in compliance with the “Guide for the Care and Use of Laboratory Animals” from the US National Institute of Health. We used 50 healthy, male, 10-week-old, clean CFZ-grade C57BL/6J mice (purchased from Shanghai Lingchang Biotechnology Co., Ltd., Shanghai, China) that weighed $22 \pm 2 \text{ g}$. The mice were randomly divided into five experimental groups as follows: (1) sham operation group ($n = 7$), (2) model group ($n = 10$), (3) CFZ group ($n = 10$, $\text{CFZ } 1.5 \text{ g}\cdot\text{mL}^{-1}$), (4) CFZ+GC group ($n = 10$, $\text{CFZ+GC } 1.8 \text{ g}\cdot\text{mL}^{-1}$), and (5) PFZ group ($n = 10$, $\text{PFZ } 1.5 \text{ g}\cdot\text{mL}^{-1}$). HF was induced in all groups, except the sham group, by transverse aortic constriction (TAC). After 4 weeks, the sham and model groups were administered distilled water intragastrically and the treatment groups were administered different treatments for 8 weeks.

2.4. Establishment of a Mouse Model of HF Induced by TAC. Based on a previous study [16], the mice were anesthetized with 0.3% sodium pentobarbital ($75 \text{ mg}\cdot\text{kg}^{-1}$) intraperitoneally and ophthalmic scissors were used to make a longitudinal incision of 0.5–1 cm at the midline of the neck and chest of the mouse. After the separation of the two thymus halves using microforceps, the aortic arch and two carotid arteries were observed. Microtweezers were used to pass a 6-0 nylon suture gently between the left common carotid artery and the right innominate artery. A homemade L-shaped 26G cushion needle was used to ligate the aortic arch, and the cushion needle was carefully removed after ligation. A significant increase in the right common carotid artery pulsation was observed after successful aortic arch stenosis. Penicillin sodium (5000 U/head) was injected intramuscularly 3 days after the operation.

2.5. Measurement of Hemodynamic Indicators and Ventricular Pressure Indicators. Eight weeks after dosing, we performed an ultrasound examination of mouse hearts to obtain M-mode echocardiographic images using a Vevo 1100 ultra-high-resolution small animal ultrasound imaging system and an MS400 ultrasound probe (VisualSonics, Toronto, Canada). The images were analyzed to measure the hemodynamic indicators. Three consecutive cardiac cycles were analyzed, and the average value was used to calculate ventricular pressure indicators.

2.6. Measurement of Mass Indices. Mass indices were measured using the methods reported in a previous study [16]. Having measured hemodynamic parameters after 8 weeks,

TABLE 1: The primer sequences used in this study.

Gene ¹	Forward primer (5'-3')	Reverse primer (5'-3')
CCL2	GATCCCAATGAGTAGGCTGG	CGGGTCAACTTCACATTCAAAG
CCL4	AAACCTAACCCCGAGCAAC	CTGTCTGCCTCTTTTGGTCA
CCL7	TCTCTCACTCTCTTTCTCCACC	GGTGATCCTTCTGTAGCTCTTG
TLR4	ATGGCATGGCTTACACCACC	GAGGCCAATTTTGTCTCCACA
TLR2	CTCTTCAGCAAACGCTGTTCT	GGCGTCTCCCTCTATTGTATTG
Cox2	TGCATTCTTTGCCAGCACT	AAAGGCGCAGTTTACGCTGT
TNF- α	CAGGCGGTGCCTATGTCTC	CGATCACCCCGAAGTTTCAGTAG
IL-6	TGAGCAGGATGGAGAATTACAGG	GTCCAAGTTCATCTTCTAGGCAC
IL-2	TGAGCAGGATGGAGAATTACAGG	GTCCAAGTTCATCTTCTAGGCAC
β -Actin	GTGACGTTGACATCCGTAAAGA	GCCGACTCATCGTACTCC

the mice were sacrificed by placing them in a sealed chamber containing CO₂. Briefly, the time expected for mice to lose consciousness is typically within 2 to 3 min. Each mouse was observed for a lack of respiration and faded eye color, and the flow of CO₂ was maintained for a minimum of 1 min after respiration had ceased. If both signs were observed, the mouse was removed from the cage. After euthanasia, the chest was rapidly opened to remove the heart, thymus, and spleen to calculate the weight index.

2.7. Histopathological Examination. The heart was cut transversely into two parts from the median plane. The apical part was fixed with neutral formaldehyde and conventional paraffin embedding, and hematoxylin and eosin (HE) staining was performed. The pathological sections were scanned using the NanoZoomer 2.0 RS digital slice scanning device to observe the pathological changes in the heart.

2.8. Detection of Serum Inflammatory Markers. From each mouse, 1 mL of blood was extracted from the abdominal aorta and stored at room temperature for 30 min. Then, the sample was centrifuged at 3,500 rpm for 10 min and the supernatant was used to detect the levels of inflammatory factors, tumor necrosis factor- (TNF-) α , interleukin- (IL-) 6, interferon- (IFN-) γ , and monocyte chemoattractant protein-1 (MCP-1), in serum. BD™ Cytometric Bead Array mouse inflammation kits were used according to the manufacturer's instructions (BD Biosciences, San Jose, CA, USA).

2.9. Quantitative RT-PCR (qRT-PCR) Assay to Monitor the Gene Expression Levels of Inflammatory Factor, Chemokine, Toll-Like Receptor (TLR) 2, and TLR4 Genes. Total RNA was extracted from heart tissue using Trizol® total RNA isolation reagent (Shanghai Yubo Biotechnology Co., Ltd., Shanghai, China) according to the manufacturer's protocol and reverse transcribed to cDNA. Quantitative PCR was performed in duplicate using a TB Green Master Mix (Takara Bio Co., Ltd., Beijing, China) and a Bio-Rad C1000 thermal cycler. Genes were amplified using the following primer pairs (Sangon Biotech, Shanghai, China) (Table 1); the expression of β -actin was simultaneously analyzed as the endogenous control (Table 1).

2.10. Western Blotting Analysis of Nuclear Factor-Kappa Beta (NF- κ B). Total protein was extracted from heart tissue using a radioimmunoprecipitation assay buffer (Biyuntian Biotechnology Co., Ltd., Shanghai, China) containing phenylmethanesulfonyl fluoride. The extract was homogenized (Bertin Technologies, France) and lysed on ice for 15 min. Then, the sample was centrifuged at 12,000 rpm for 10 min and the supernatant was used to determine the total protein in the heart tissue. Protein concentrations were determined using a bicinchoninic acid protein-determination kit (Biyuntian Biotechnology Co., Ltd.). Protein samples were separated using 10% sodium dodecyl sulfate gel electrophoresis, transferred onto polyvinylidene fluoride membranes, and blocked for 2 h with a solution containing 5% skim milk powder (Sangon Biotech, Shanghai, China) in Tris buffer. The membrane was incubated overnight at 4°C with primary antibodies for NF- κ B, TLR4, and β -actin (Cell Signaling Technology, Beverly, MA, USA), which were diluted at the concentration recommended by the manufacturer. Then, the membrane was incubated with horseradish peroxidase-labeled secondary antibody in Tris-buffered saline containing 5% skim milk at room temperature for 2 h. Proteins were visualized using an ultrasensitive chemiluminescence imaging system (Jingtan Biotechnology (Shanghai) Co., Ltd., Shanghai, China), and the AlphaView FluorChem FC3 3.4.0.0 software (ProteinSimple, San Jose, CA, USA) was used for the quantitative analysis of the ribbons and normalized to β -actin.

2.11. Statistical Methods. SPSS 26.0 was used for statistical analysis. Quantitative data are presented as the mean \pm standard deviation. ANOVA was used for the comparison of normal distribution data, and a nonparametric test was used for the comparison of nonnormal distribution continuous data. A chi-square test was used to compare survival time. $P < 0.05$ was considered statistically significant.

3. Results

3.1. CFZ+GC and PFZ Increased Survival Rate of Mice with HF. The survival rate was lower in the model group than that in the sham group (from 100% to 70%) with the progression

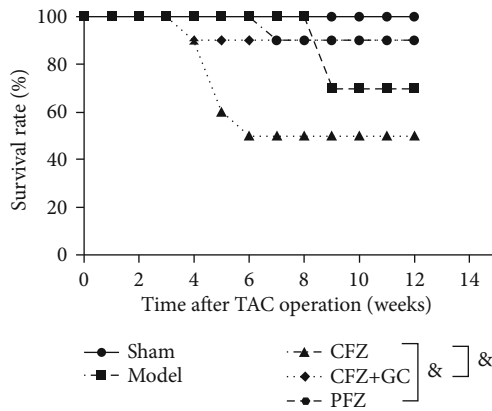


FIGURE 1: Survival rate of heart failure (HF) with different treatments. $^{\&}P < 0.05$ versus the crude Fuzi (CFZ) group.

of HF (Figure 1). However, CFZ treatment decreased the survival rate of mice to 50% lower than that in the model group, but in the CFZ+GC and PFZ treatment group, the survival rate was significantly higher than that in the CFZ group (from 50% to 90%) ($P < 0.05$).

3.2. CFZ+GC Improved Hemodynamic Indicators of Mice with HF. Most hemodynamic indicators, except stroke volume and cardiac output, were significantly changed in mice subjected to TAC compared with the sham group based on the cardiac ultrasound ($P < 0.05$; Figure 2). In the CFZ+GC treatment group, the left ventricular end-diastolic diameter (IVS; d), left ventricular end-systolic diameter (IVS; s), left ventricular end-diastolic volume (LV Vold; d), left ventricular end-systolic volume (LV Vol; s), and left ventricular-corrected weight (LV mass corrected) were significantly lower and the fractional shortening (FS) and ejection fraction (EF) were significantly higher than those in the model group ($P < 0.01$). In addition, the indicators of EF and FS in the CFZ and PFZ groups were both noticeably higher than those in the model group ($P < 0.05$). The hemodynamic indicators with CFZ+GC treatment were improved more than those with the other treatments.

3.3. CFZ, CFZ+GC, and PFZ Improved Ventricular Pressure Indicators in Mice with HF. Most ventricular pressure indicators were significantly different between the model group and the sham group ($P < 0.05$ or $P < 0.01$; Figure 3). However, the indices of left ventricular end-diastolic pressure (LVEDP), systolic pressure (SYS), minimum intracardiac pressure (MIN), diastolic pressure (DP), cardiac index (CI), and tension time index (TTI) in all treatment groups were significantly lower ($P < 0.01$), whereas the maximum rate of the left ventricular pressure decline indicator ($-dp/dt$ max) was significantly higher ($P < 0.01$) than that in the model group. The maximum rate of increase of left ventricular pressure ($+dp/dt$ max) was significantly higher in the CFZ and CFZ+GC groups ($P < 0.01$) than that in the model group, whereas the PFZ group did not show a statistically significant difference.

3.4. CFZ, CFZ+GC, and PFZ Improved Mass Indices of Mice with HF. Spleen weight (SW) and spleen weight index (SPI) were significantly lower ($P < 0.01$), and heart weight (HW), left ventricle weight (LVW), heart weight index (HWI), and left ventricle weight index (LVWI) were significantly higher in the model group than those in the sham group ($P < 0.01$; Figure 4). However, LVW, LVWI, and HWI in the CFZ+GC group ($P < 0.01$), LVW, SW, and LVWI in the PFZ group ($P < 0.05$), and LVW and LVWI in the CFZ group ($P < 0.05$) were significantly lower than those in the model group.

3.5. CFZ, CFZ+GC, and PFZ Improved Histopathological Results of Mice with HF. The heart volume in the model group was significantly higher than that in the sham group, and treatments with CFZ, CFZ+GC, and PFZ reduced cardiac hypertrophy to varying degrees (Figure 5(a)). The HE staining showed that the myocardial fibers were arranged neatly and there was no interstitial edema or myocardial fiber rupture in the sham group, whereas the histopathological structure of the heart in the model group had widened and broken myocardial tissue gaps, vascular degeneration, edema, necrosis, atrophy, and other pathological changes in myocardial cells. However, these pathological changes were alleviated to varying degrees in the treatment, especially the CFZ+GC, groups, in which the cardiac pathology of mice was notably improved compared with that of the model group mice (Figures 5(b) and 5(c)).

3.6. CFZ, CFZ+GC, and PFZ Inhibited Inflammation and Chemokine Levels of Mice with HF. The protein levels of TNF- α , IL-6, IFN- γ , and MCP-1 in the serum of mice in the HF groups were higher than those in the sham group ($P < 0.05$; Figure 6). IL-12 and IL-10 levels were also higher, but this was not statistically significant ($P > 0.05$). CFZ treatment had significantly lower TNF- α , IL-6, IFN- γ , IL-12, and IL-10 levels than the other HF groups ($P < 0.05$ or $P < 0.01$). However, only TNF- α , IL-6, and IL-10 levels in the CFZ+GC treatment group were significantly lower than those in the other HF groups ($P < 0.05$ or $P < 0.01$). There was no significant difference in protein levels between PFZ treatment and any other group ($P < 0.05$) (Figure 6).

In addition, the expression of inflammation factors, TNF- α , IL-6, and chemokine ligand (CCL) 4 mRNA, in the heart tissue of mice in the HF groups, was higher than that in the sham group ($P < 0.05$ or $P < 0.01$; Figures 7(b), 7(c), and 7(e)). In the CFZ, CFZ+GC, and PFZ groups, the mRNA levels of IL-2, TNF- α , IL-6, and CCL7 were significantly lower than those in the model group ($P < 0.05$ or $P < 0.01$; Figures 7(a)–7(c) and 7(f)). In the CFZ+GC and PFZ groups, the mRNA level of CCL4 was significantly lower than that in the model group ($P < 0.05$; Figure 7(d)). However, the mRNA levels of IL-2, TNF- α , and IL-6 in the CFZ group were significantly lower than those in the sham group ($P < 0.05$ or $P < 0.01$; Figures 7(a)–7(c)).

3.7. CFZ, CFZ+GC, and PFZ Improved the Inflammation Pathway in Mice with HF. TLR4 and NF- κ B signaling pathways were involved in the inflammatory response to TAC-

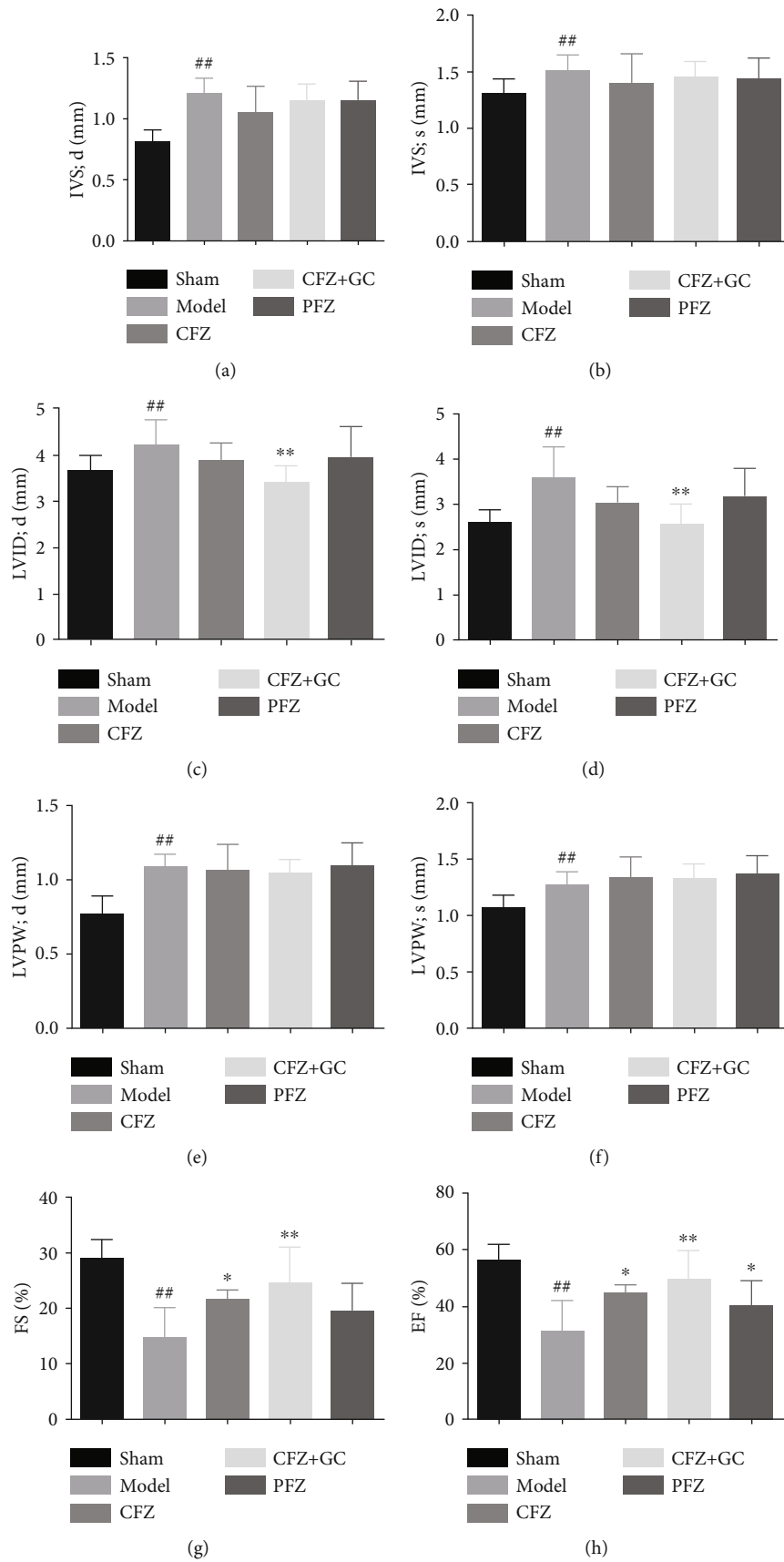


FIGURE 2: Continued.

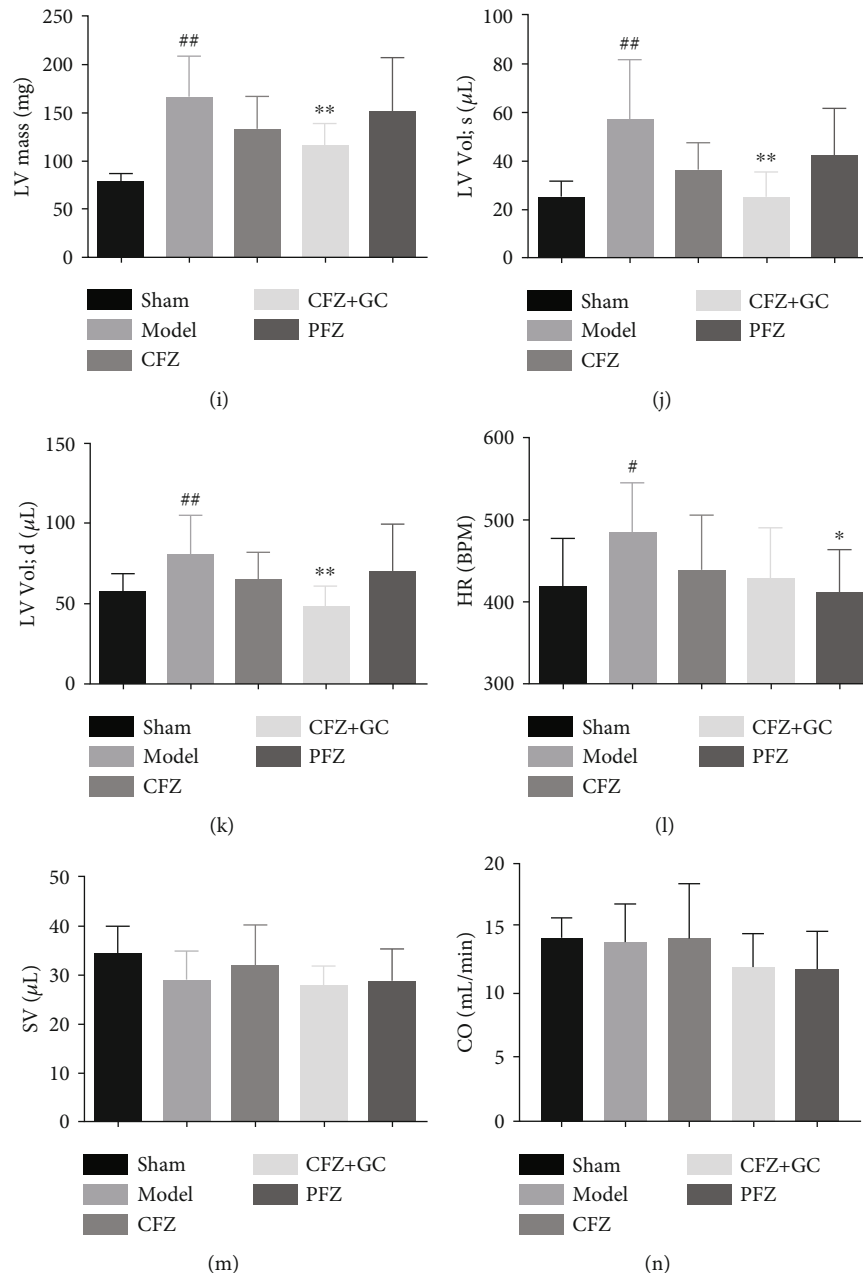


FIGURE 2: Hemodynamic indicators in mice of each group: (a) IVS; d: left ventricular end-diastolic anterior wall thickness; (b) IVS; s: left ventricular end-systolic anterior wall thickness; (c) LVID; d: left ventricular end-diastolic diameter; (d) LVID; s: left ventricular end-systolic diameter; (e) LVPW; d: left ventricular end-diastolic wall thickness; (f) LVPW; s: left ventricular end-systolic posterior wall thickness; (g) EF: ejection fraction; (h) LV mass corrected: left ventricular-corrected weight; (i) FS: fractional shortening; (j) HR: heart rate; (k) SV: stroke volume; (l) LV Vol; s: left ventricular end-systolic volume; (m) LV Vol; d: left ventricular end-diastolic volume; (n) CO: cardiac output. Sham group ($n=7$), model group ($n=7$), crude Fuzi (CFZ) group ($n=5$), CFZ combined with *Glycyrrhiza* (CFZ+GC) group ($n=9$), and prepared materials of Fuzi (PFZ) group ($n=9$). All data are presented as the mean \pm SD. [#] $P < 0.05$ and ^{##} $P < 0.01$ versus model group; ^{*} $P < 0.05$ and ^{**} $P < 0.01$ versus model group.

induced HF (Figure 8). HF significantly upregulated the protein expression of TLR4 and NF- κ B compared with the sham group, whereas CFZ, CFZ+GC, and PFZ downregulated the expression of these proteins.

In addition, the mRNA expression of TLR4 and cyclooxygenase-2 (COX-2) in heart tissues significantly increased after TAC induction, whereas CFZ and PFZ treat-

ment resulted in a significant decrease in their expression, to lower than that in the sham group. Moreover, CFZ had a significant inhibitory effect on the expression of TLR2.

3.8. Analysis of CFZ and CFZ+GC Water Extracts by UPLC-Q/TOF MS. Forty-seven components in the CFZ water extract (SI Table 1) and 49 components in the CFZ+GC

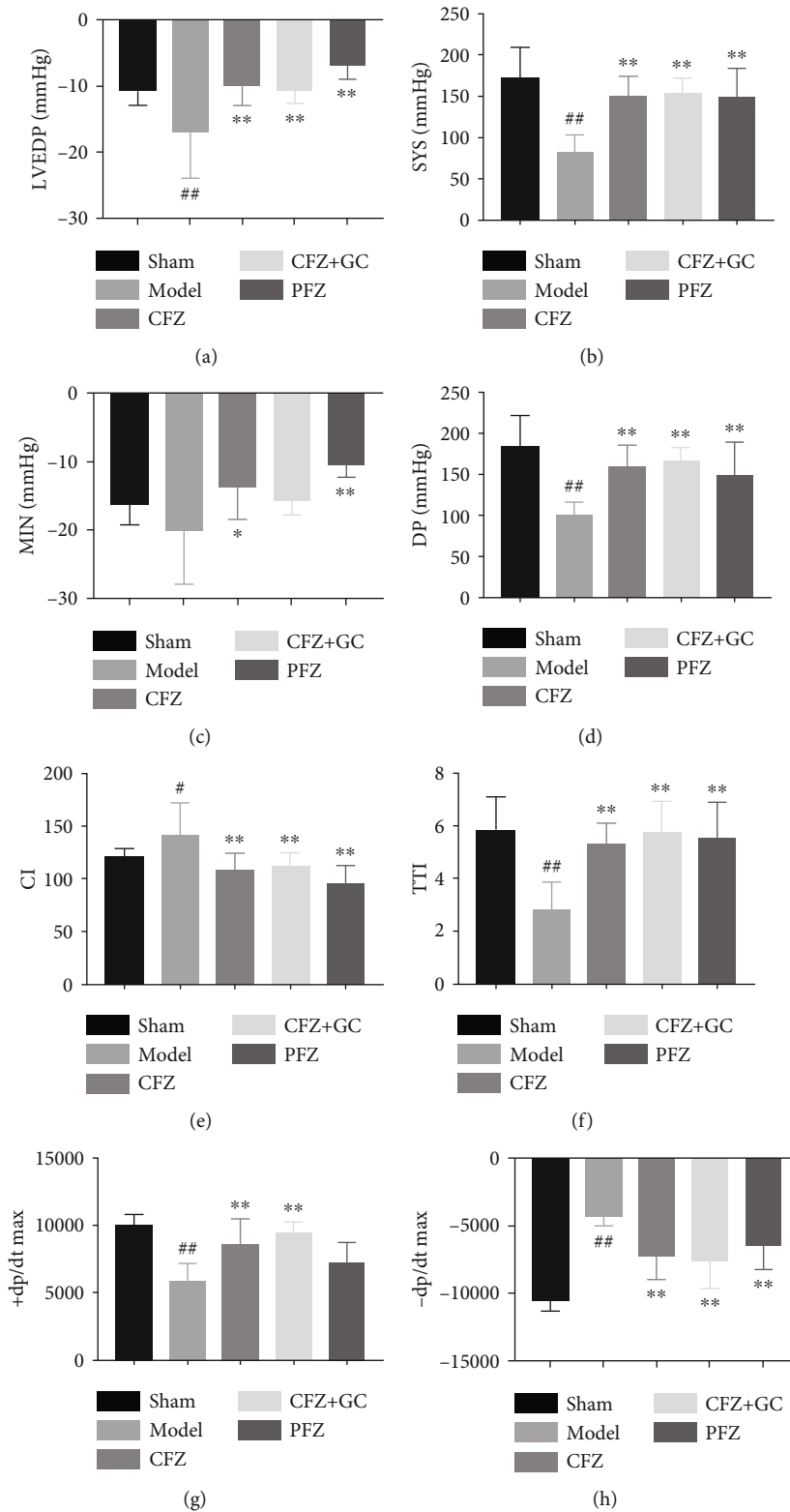


FIGURE 3: Ventricular pressure indicators in mice of each group: (a) LVEDP: left ventricular end-diastolic pressure; (b) SYS: systolic pressure; (c) MIN: minimum intracardiac pressure; (d) DP: diastolic pressure; (e) CI: cardiac index; (f) TTI: tension time index; (g) +dp/dt max: maximum rate of increase of left ventricular pressure; (h) -dp/dt max: maximum rate of left ventricular pressure decline. Sham group ($n = 7$), model group ($n = 7$), crude Fuzi (CFZ) group ($n = 5$), CFZ combined with *Glycyrrhiza* (CFZ+GC) group ($n = 9$), and prepared materials of Fuzi (PFZ) group ($n = 9$). All data are presented as the mean \pm SD. # $P < 0.01$ versus the sham group; * $P < 0.05$ and ** $P < 0.01$ versus the model group.

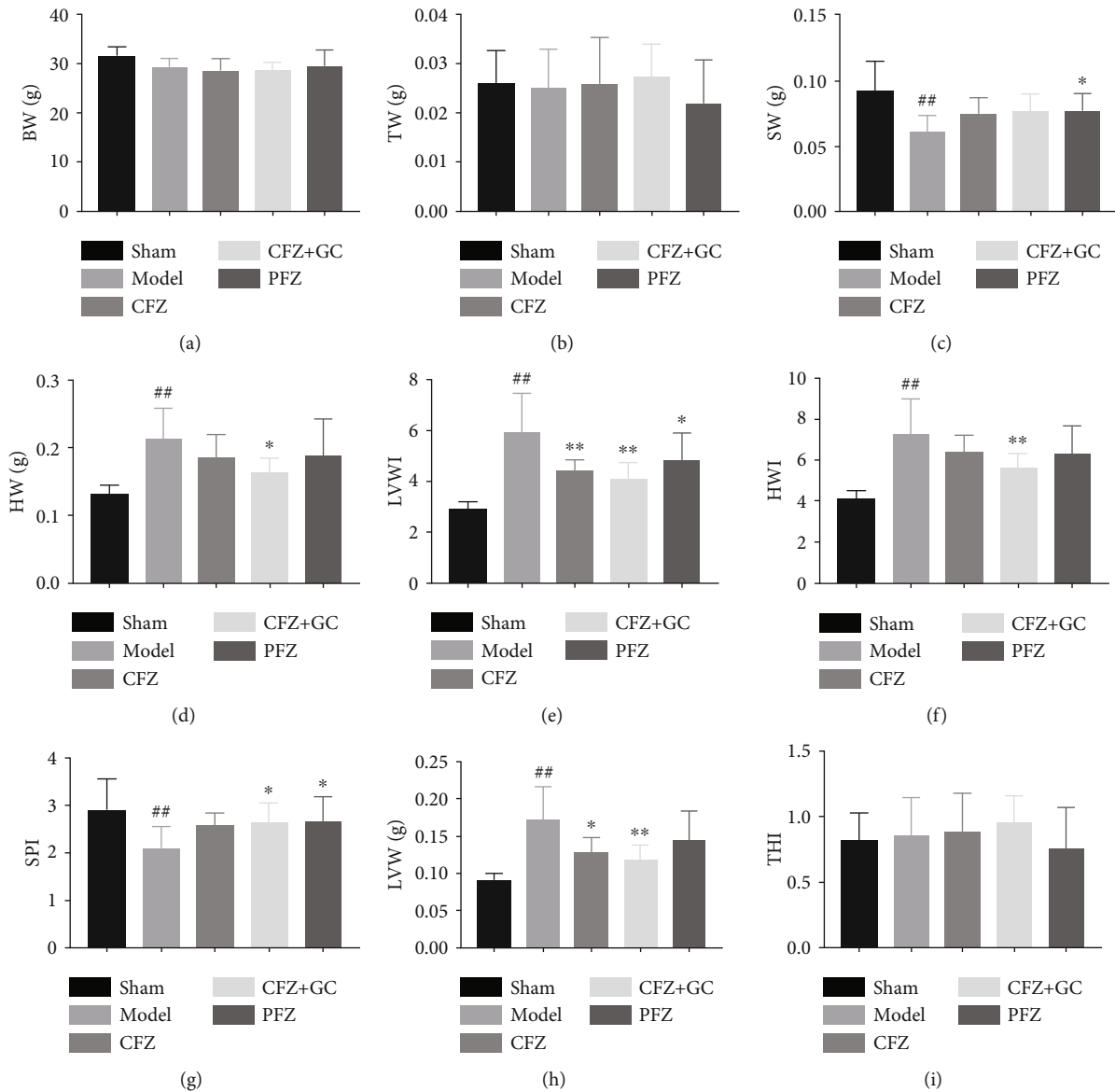


FIGURE 4: Mass indices in mice of each group: (a) BW: body weight; (b) TW: thymus weight; (c) SW: spleen weight; (d) HW: heart weight; (e) LVW: left ventricle weight; (f) THI: thymus weight index; (g) SPI: spleen weight index; (h) HWI: heart weight index; (i) LVWI: left ventricle weight index. Sham group ($n = 7$), model group ($n = 7$), crude Fuzi (CFZ) group ($n = 5$), CFZ combined with *Glycyrrhiza* (CFZ+GC) group ($n = 9$), and prepared materials of Fuzi (PFZ) group ($n = 9$). All data are presented as the mean \pm SD. ^{##} $P < 0.01$ versus the sham group; ^{*} $P < 0.05$ and ^{**} $P < 0.01$ versus the model group.

water extract (SI Table 2) were identified. Comparing the composition of the two groups, there were some differences between the active components (Figure 9(a)). For example, the peak area of benzoylmesaconine and benzoylhypaconine, which considered the key toxic components of CFZ [17, 18], was reduced by half and isoscopoletin, detected in CFZ, was not detected in CFZ+GC, whereas some of the heart-protective components of GC, such as isoliquiritin, were detected (Figure 9(b)).

4. Discussion

HF is a complex clinical syndrome and represents the final stage of numerous heart diseases. This study showed that

Fuzi significantly inhibited TAC-induced HF, improved the pathological changes of myocardial structure and cardiac function, and reduced the mortality rate when combined with GC, which suggested that the combination of CFZ and GC has great potential in the development of a treatment for HF in the future.

The $+dp/dt$ max is highly sensitive to variable force factors and reflects the maximum shortening rate of myocardial contractile components. Therefore, $+dp/dt$ max is a good indicator of the acute changes in contractile performance. The $-dp/dt$ max reflects the maximum rate of myocardial fiber elongation during myocardial diastole [19, 20]. Both are common indicators to evaluate myocardial contraction and diastolic performance. CFZ, CFZ+GC, and PFZ groups

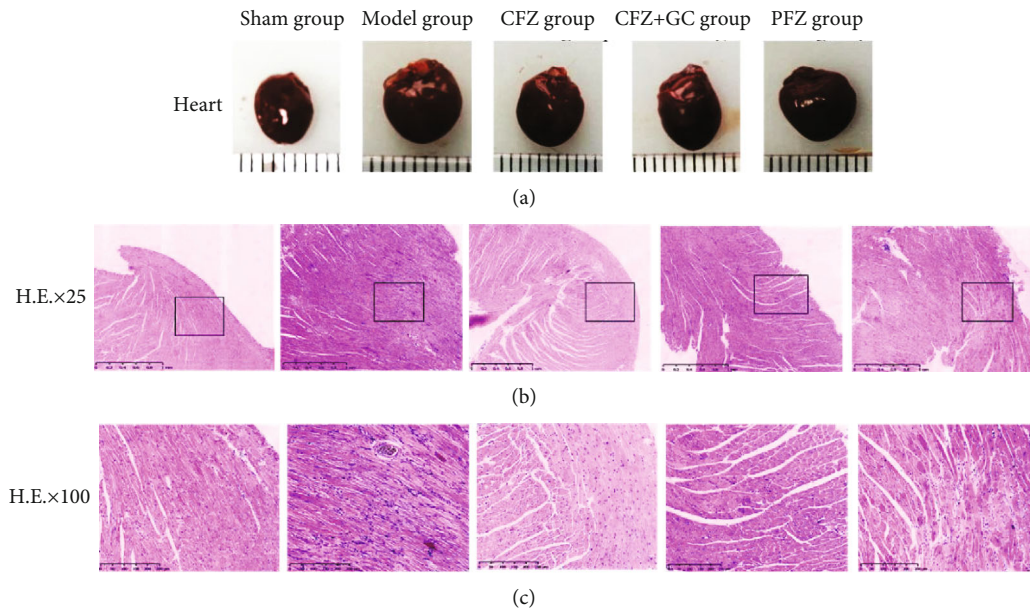


FIGURE 5: Heart morphologies and myocardial hematoxylin and eosin (HE) staining in each group. (a) Representative images of the heart. (b) Representative images for the pathological changes of the heart, scale bar = 1 mm. (c) Representative images for the pathological changes of the heart, scale bar = 250 μ m.

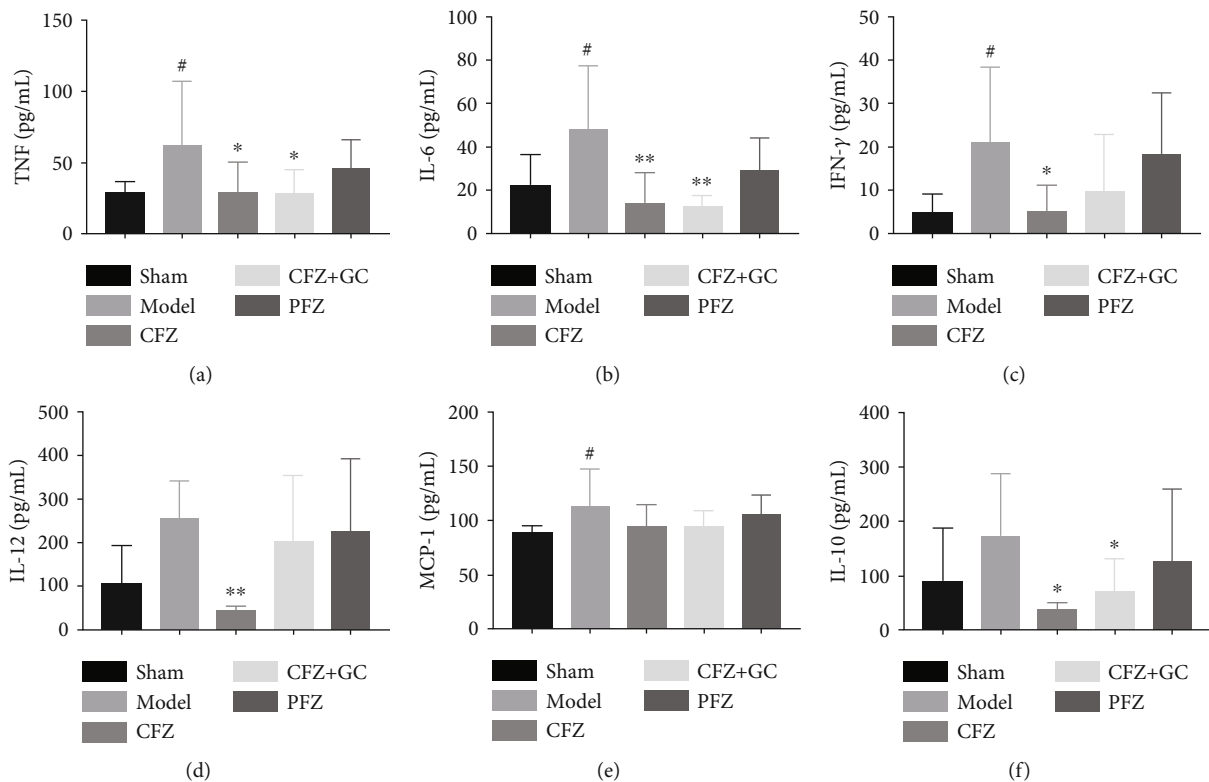


FIGURE 6: Inflammation and chemokine levels in mice of each group: (a–f) tumor necrosis factor- (TNF-) α , interleukin- (IL-) 6, interferon- (IFN-) γ , IL-12, and monocyte chemoattractant protein- (MCP-) 1 levels, respectively. All data are presented as mean \pm SD ($n \geq 5$ /group). [#] $P < 0.05$ and ^{**} $P < 0.01$ versus the sham group; ^{*} $P < 0.05$ and ^{**} $P < 0.01$ versus the model group.

all significantly improved these indicators, as well as other ventricular pressure indicators, such as LVEDP, SYS, MIN, DP, CI, and TTI. In addition, the CFZ+GC group partly

improved the hemodynamic indicators and mass indices of mice with HF. Therefore, GC not only reduced the toxicity of CFZ but also increased the effects of CFZ on HF.

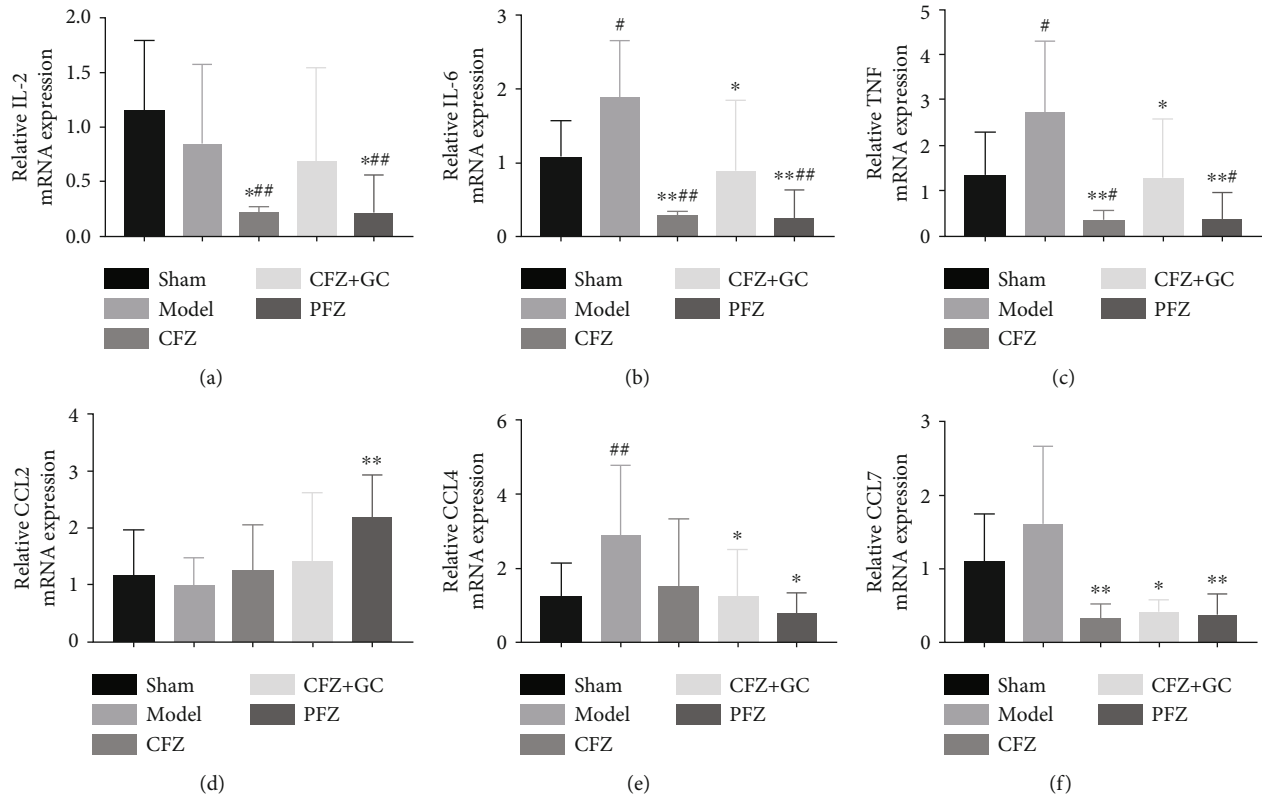


FIGURE 7: The mRNA expression of inflammatory factors and chemokines in heart of each group: (a–f) inflammation factors interleukin- (IL-) 2, tumor necrosis factor- (TNF-) α , IL-6, and chemokine ligand (CCL) 2, CCL4, and CCL7 mRNA levels, respectively. All data are presented as mean \pm SD ($n \geq 5$ /group). # $P < 0.05$ and ## $P < 0.01$ versus the sham group; * $P < 0.05$ and ** $P < 0.01$ versus the model group.

HF is associated with systemic inflammation [21–23]. The hemodynamic stress of HF induces sterile inflammation, and the resulting increased wall tension and mechanical stretch trigger the release of a range of proinflammatory cytokines, including TNF- α , IL-6, and IL-1 β , as shown in our results. The TNF- α signaling pathway is associated with impaired systolic and diastolic function and poor cardiac remodeling [24]. However, clinical evidence suggests that the inhibition of TNF- α does not improve HF, rather increases the hospitalization rate for HF [25], suggesting the double-edged sword effect of TNF- α signaling. CFZ and CFZ+GC significantly reduced the serum levels of inflammatory factors such as TNF- α and IL-6. In addition, CFZ, CFZ+GC, and PFZ also can significantly reduce the mRNA levels of macrophage-related chemokines CCL7 and CCL4 in heart tissue [26, 27]. However, the mRNA levels of cardiac inflammatory factors in the CFZ group were significantly lower than those in the sham group, but not those in the CFZ+GC group. These showed CFZ has a strong inhibitory effect on inflammation.

TLR4 is most expressed in the heart and is involved in myocardial inflammation. TLR4 activation increases the production of IL-6 and TNF- α . NF- κ B is a transcriptional regulator that is activated by TNF- α and mediates inflammation, apoptosis, and extracellular matrix remodeling. However, NF- κ B has also been reported to have cardioprotective effects, such as reducing mitochondrial dysfunction and mitochondrial autophagy, inhibiting cell death, and inducing

antioxidant effects [24]. CFZ significantly inhibited the mRNA levels of TLR4 and COX2 compared to those in the sham group. However, CFZ+GC treatment had no significant effect on mRNA expression in relation to inflammatory signaling pathways. This beneficial effect of NF- κ B may be lost owing to excessive inhibition of TNF- α , leading to progressive HF and death. Therefore, the toxicity of CFZ may be owing to a high-intensity blockade of TNF- α , which contributes to HF.

The clinical symptoms of Fuzi poisoning include dizziness, vomiting, hypotension, arrhythmia, chest tightness, palpitations, dyspnea, and coma [28]. In this study, we observed that GC significantly reduced the mortality associated with CFZ. In addition, the content of alkaloids, including monoester alkaloids of benzoylmesaconine and benzoylhypaconine that are associated with cardiotoxicity [17, 18] in CFZ+GC is significantly lower than that in CFZ alone. Moreover, the GC in the CFZ+GC group added some heart-protective components, such as flavonoids [29]. The changes in these components indicated that GC can alleviate the toxicity of CFZ and increase the protective effect of Fuzi on the heart.

5. Conclusions

CFZ, CFZ+GC, and PFZ exert protective effects on the heart by inhibiting the inflammatory response through the

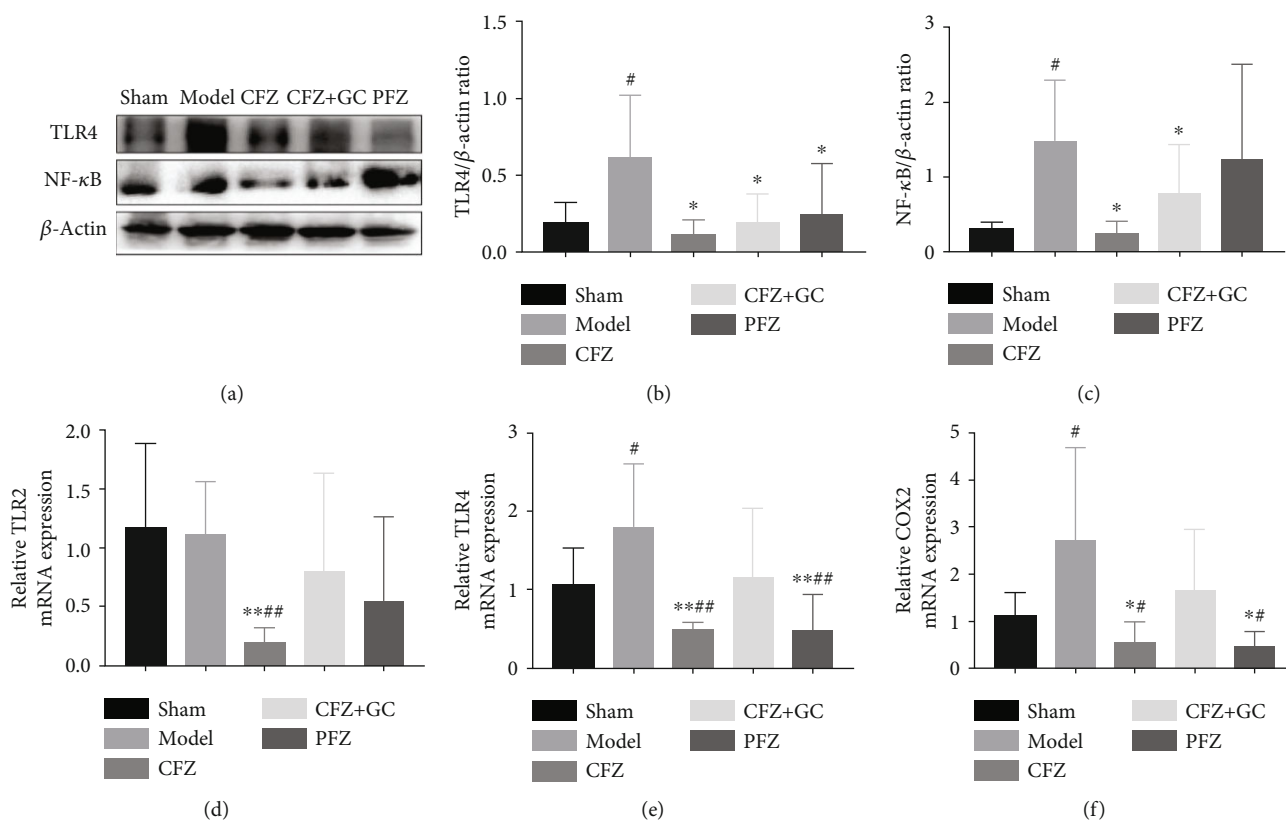


FIGURE 8: Toll-like receptor-4 (TLR4)/nuclear factor kappa beta (NF-κB) pathway detection in the heart among mice in all groups. (a) Representative images for TLR4 and NF-κB protein detection by western blotting. (b–c) TLR4 and NF-κB protein expression in the heart of mice, respectively. (d–f) mRNA expression of TLR2, TLR4, and cyclooxygenase-2 (COX2) in the heart of mice, respectively. #*P* < 0.05 and ###*P* < 0.01 versus the sham group, **P* < 0.05 and ***P* < 0.01 versus the model group.

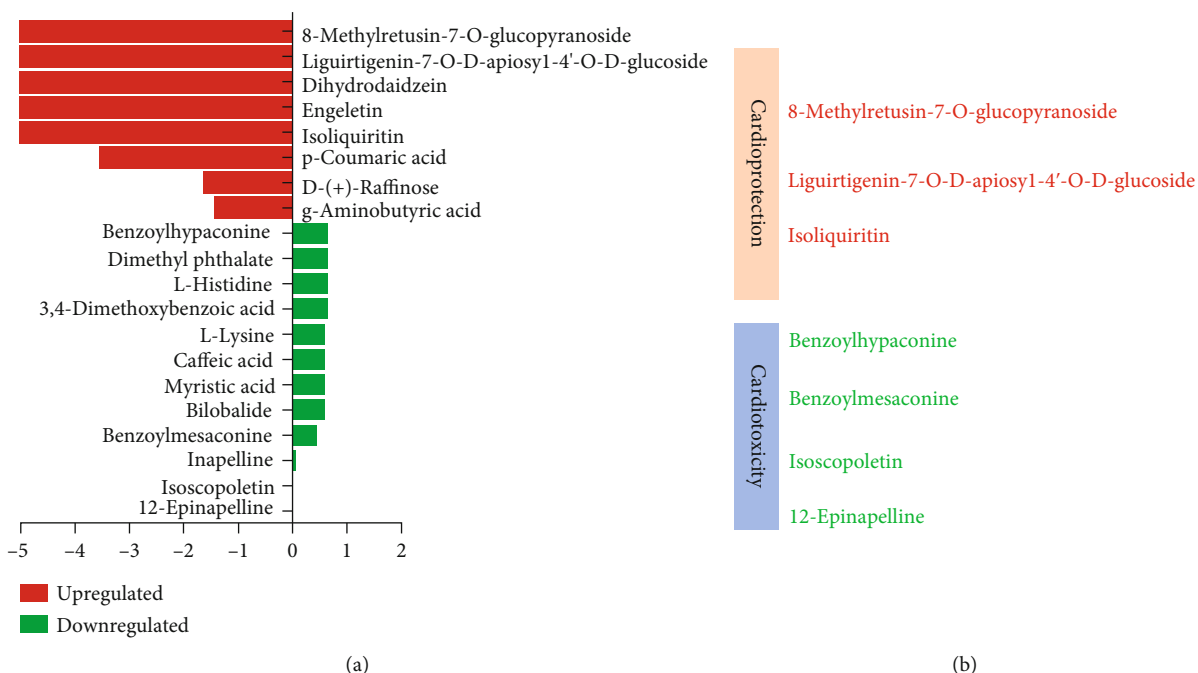


FIGURE 9: Component comparison of crude Fuzi (CFZ) and CFZ combined with *Glycyrrhiza* (CFZ+GC) related to function. (a) Significantly changed composition in CFZ+GC water extract compared with CFZ water extract. (b) Effects of changed ingredients on the heart.

TLR4/NF- κ B pathway. However, CFZ is more toxic and PFZ has less efficacy than CFZ+GC. The combination of CFZ and GC is more effective for the treatment of HF in mice than CFZ or PFZ alone.

Abbreviations

BW:	Body weight
CFZ:	Crude Fuzi
CFZ+GC:	Crude Fuzi with Glycyrrhiza
+dp/dt max:	Maximum rate of increase of left ventricular pressure
EF:	Ejection fraction
FS:	Fractional shortening
HF:	Heart failure
HR:	Heart rate
HW:	Heart weight
HWI:	Heart weight index
IVS; d:	Left ventricular end-diastolic anterior wall thickness
IVS; s:	Left ventricular end-systolic anterior wall thickness
LVPW; d:	Left ventricular end-diastolic wall thickness
LVPW; s:	Left ventricular end-systolic posterior wall thickness
LVW:	Left ventricle weight
LVWI:	Left ventricle weight index
PFZ:	Prepared materials of Fuzi
SPI:	Spleen weight index
SW:	Spleen weight
THI:	Thymus weight index
TW:	Thymus weight.

Data Availability

The data used to support the findings of the study is available in the supplementary materials.

Conflicts of Interest

The authors declare that they have no competing interests.

Authors' Contributions

MSF, JLL, BBC, and XL carried out the animal experiments. LJ and JLL participated in the hemodynamic indicator, ventricular pressure indices, mass indices, and histopathological imaging experiments. LSJ, LJ, and HYF completed molecular detection. QYS and HYF participated in the design of the study and participated in its coordination. PY and WM performed the statistical analysis and drafted the manuscript. All authors have read and approved the manuscript. Ping Yan and Wen Mao contributed equally to this work.

Acknowledgments

This study was funded by the National Natural Science Foundation of China (Nos. 81673645, 81873047 to QYS, and 81573677 to HYF), the Natural Science Foundation of

Zhejiang Province (No. LQ17H030006 to LX), and the Research Fund of Zhejiang University of Traditional Chinese Medicine (2017ZY19 to MSF). The funders also participated in the experimental design, operation, and writing of the article (see Authors' Contributions for details).

Supplementary Materials

SI Table 1: chemical information for identified compounds of CFZ. SI Table 2: chemical information for identified compounds of CFZ+GC. (*Supplementary materials*)

References

- [1] S. V. Konstantinides, G. Meyer, C. Becattini et al., "2019 ESC guidelines for the diagnosis and management of acute pulmonary embolism developed in collaboration with the European Respiratory Society (ERS)," *European Heart Journal*, vol. 41, no. 4, pp. 543–603, 2020.
- [2] S. Dassanayaka and S. P. Jones, "Recent developments in heart failure," *Circulation Research*, vol. 117, no. 7, pp. e58–e63, 2015.
- [3] B. R. Pagliaro, F. Cannata, G. G. Stefanini, and L. Bolognese, "Myocardial ischemia and coronary disease in heart failure," *Heart Failure Reviews*, vol. 25, no. 1, pp. 53–65, 2020.
- [4] E. Braunwald, "The war against heart failure: the Lancet lecture," *Lancet*, vol. 385, no. 9970, pp. 812–824, 2015.
- [5] P. T. O' Gara, F. G. Kushner, D. D. Ascheim et al., "2013 ACCF/AHA Guideline for the Management of ST-Elevation Myocardial Infarction: Executive Summary: A Report of the American College of Cardiology Foundation/American Heart Association Task Force on Practice Guidelines," *Catheterization and Cardiovascular Interventions*, vol. 82, no. 1, pp. E1–E27, 2013.
- [6] WRITING GROUP MEMBERS, D. Lloyd-Jones, R. Adams et al., "Heart Disease and Stroke Statistics—2009 Update," *Circulation*, vol. 119, no. 3, pp. 480–486, 2009.
- [7] Y. Li, X. Zhang, X. Chen et al., "Chinese herbal preparations for chronic heart failure: study protocol for an umbrella review of systematic reviews and meta-analyses," *Medicine*, vol. 99, no. 7, p. e18966, 2020.
- [8] J. Wen, W. Zou, R. Wang et al., "Cardioprotective effects of Aconiti Lateralis Radix Praeparata combined with Zingiberis Rhizoma on doxorubicin-induced chronic heart failure in rats and potential mechanisms," *Journal of Ethnopharmacology*, vol. 238, p. 111880, 2019.
- [9] Y. Wang, Q. Wang, C. Li et al., "A review of Chinese herbal medicine for the treatment of chronic heart failure," *Current Pharmaceutical Design*, vol. 23, no. 34, pp. 5115–5124, 2017.
- [10] L. Wang, Y. He, Y. Zhang et al., "Effects of Active Components of Fuzi and Gancao Compatibility on Bax, Bcl-2, and Caspase-3 in Chronic Heart Failure Rats," *Evidence-Based Complementary and Alternative Medicine*, vol. 2016, Article ID 7686045, 12 pages, 2016.
- [11] P. Hao, F. Jiang, J. Cheng, L. Ma, Y. Zhang, and Y. Zhao, "Traditional Chinese medicine for cardiovascular disease: evidence and potential mechanisms," *Journal of the American College of Cardiology*, vol. 69, no. 24, pp. 2952–2966, 2017.
- [12] X. X. Liu, X. X. Jian, X. F. Cai et al., "Cardioactive C₁₅-diterpenoid alkaloids from the lateral roots of *Aconitum carmichaeli*

- "Fu Zi", *Chem Pharm Bull (Tokyo)*, vol. 60, no. 1, pp. 144–149, 2012.
- [13] G. Zhou, L. Tang, X. Zhou, T. Wang, Z. Kou, and Z. Wang, "A review on phytochemistry and pharmacological activities of the processed lateral root of *Aconitum carmichaelii* Debeaux," *Journal of Ethnopharmacology*, vol. 160, pp. 173–193, 2015.
- [14] Q. T. Gao, X. H. Chen, and K. S. Bi, "Comparative pharmacokinetic behavior of glycyrrhetic acid after oral administration of glycyrrhizic acid and Gancao-Fuzi-Tang," *Biological & Pharmaceutical Bulletin*, vol. 27, no. 2, pp. 226–228, 2004.
- [15] K. Wang, X. Jin, Q. Li et al., "Propolis from Different Geographic Origins Decreases Intestinal Inflammation and *Bacteroides* spp. Populations in a Model of DSS-Induced Colitis," *Molecular Nutrition & Food Research*, vol. 62, no. 17, 2018.
- [16] M. S. Fang, L. S. Jin, L. Z. Zhang et al., "Construction and evaluation of a model of heart failure in mice with non-thoracic aortic arch stenosis," *Chinese Journal of Comparative Medicine*, vol. 30, no. 3, pp. 14–19, 2020.
- [17] J. Yoo, V. Chepurko, R. J. Hajjar, and D. Jeong, "Conventional Method of Transverse Aortic Constriction in Mice," *Methods in Molecular Biology*, vol. 1816, pp. 183–193, 2018.
- [18] A. C. de Almeida, R. J. van Oort, and X. H. T. Wehrens, "Transverse Aortic Constriction in Mice," *Journal of Visualized Experiments*, no. 38, 2010.
- [19] S. P. Murphy, R. Kakkar, C. P. McCarthy, and J. L. Januzzi Jr., "Inflammation in Heart Failure," *Journal of the American College of Cardiology*, vol. 75, no. 11, pp. 1324–1340, 2020.
- [20] L. Adamo, C. Rocha-Resende, S. D. Prabhu, and D. L. Mann, "Reappraising the role of inflammation in heart failure," *Nature Reviews. Cardiology*, vol. 17, no. 5, pp. 269–285, 2020.
- [21] A. Glasenapp, K. Derlin, Y. Wang et al., "Multimodality imaging of inflammation and ventricular remodeling in pressure-overload heart failure," *Journal of Nuclear Medicine*, vol. 61, no. 4, pp. 590–596, 2020.
- [22] M. Hori and O. Yamaguchi, "Is tumor necrosis factor- α friend or foe for chronic heart failure?," *Circulation Research*, vol. 113, no. 5, pp. 492–494, 2013.
- [23] D. L. Mann, J. J. V. McMurray, M. Packer et al., "Targeted Anticytokine Therapy in Patients With Chronic Heart Failure," *Circulation*, vol. 109, no. 13, pp. 1594–1602, 2004.
- [24] T. Y. K. Chan, "Aconitum alkaloid content and the high toxicity of aconite tincture," *Forensic Science International*, vol. 222, no. 1–3, pp. 1–3, 2012.
- [25] T. Q. C. Nguyen, T. Duy Binh, T. L. A. Pham et al., "Anti-Inflammatory Effects of *Lasia spinosa* Leaf Extract in Lipopolysaccharide-Induced RAW 264.7 Macrophages," *International Journal of Molecular Sciences*, vol. 21, no. 10, p. 3439, 2020.
- [26] A. Inaba, Z. K. Tuong, A. M. Riding et al., "B Lymphocyte-Derived CCL7 Augments Neutrophil and Monocyte Recruitment, Exacerbating Acute Kidney Injury," *The Journal of Immunology*, vol. 205, no. 5, pp. 1376–1384, 2020.
- [27] D. Qi, M. Wei, S. Jiao et al., "Hypoxia inducible factor 1 α in vascular smooth muscle cells promotes angiotensin II-induced vascular remodeling via activation of CCL7-mediated macrophage recruitment," *Cell Death & Disease*, vol. 10, no. 8, 2019.
- [28] Y. Yang, X.-J. Yin, H.-M. Guo et al., "Identification and comparative analysis of the major chemical constituents in the extracts of single Fuzi herb and Fuzi-Gancao herb-pair by UFLC-IT-TOF/MS," *Chinese Journal of Natural Medicines*, vol. 12, no. 7, pp. 542–553, 2014.
- [29] B. Ji, L. Zhuo, B. Yang et al., "Development and validation of a sensitive and fast UPLC-MS/MS method for simultaneous determination of seven bioactive compounds in rat plasma after oral administration of Guizhi-gancao decoction," *Journal of Pharmaceutical and Biomedical Analysis*, vol. 137, pp. 23–32, 2017.

Research Article

Inhibitory Effects of Apigenin on Tumor Carcinogenesis by Altering the Gut Microbiota

Shichang Bian , Hongjuan Wan, Xinyan Liao, and Weisheng Wang 

Tianjin Fourth Central Hospital, The Fourth Central Hospital Affiliated to Nankai University, The Fourth Central Clinical College, Tianjin Medical University, Tianjin, China

Correspondence should be addressed to Weisheng Wang; tjdszxyygcw@126.com

Received 3 August 2020; Revised 11 September 2020; Accepted 19 September 2020; Published 6 October 2020

Academic Editor: Xiaolu Jin

Copyright © 2020 Shichang Bian et al. This is an open access article distributed under the Creative Commons Attribution License, which permits unrestricted use, distribution, and reproduction in any medium, provided the original work is properly cited.

The flavonoid apigenin is common to many plants. Although the responsible mechanisms have yet to be elucidated, apigenin demonstrates tumor suppression *in vitro* and *in vivo*. This study uses an azoxymethane (AOM)/dextran sodium sulfate- (DSS-) induced colon cancer mouse model to investigate apigenin's potential mechanism of action exerted through its effects upon gut microbiota. The size and quantity of tumors were reduced significantly in the apigenin treatment group. Using 16S rRNA high-throughput sequencing of fecal samples, the composition of gut microbiota was significantly affected by apigenin. Further experiments in which gut microbiota were reduced and feces were transplanted provided further evidence of apigenin-modulated gut microbiota exerting antitumor effects. Apigenin was unable to reduce the number or size of tumors when gut microbiota were depleted. Moreover, tumor inhibition effects were initiated following the transplant of feces from mice treated with apigenin. Our findings suggest that the effect of apigenin on the composition of gut microbiota can suppress tumors.

1. Introduction

In 2012, it was estimated that there were 14.1 million new cancer cases worldwide, and by 2032, this figure is projected to increase to 25 million [1]. The incidence rate of malignant tumors was 199.4/10 million in 2012; 8.22 million deaths were attributed to malignant tumors, with a mortality rate of 116.3/10 million [1]. There is an urgent need to undertake more cancer prevention and treatment research to address this serious situation.

The number of symbiotic bacteria in the human gut is calculated to be approximately 100 trillion, weighing 1–2 kg. These symbionts are made up of more than 7,000 strains representing approximately 800 bacterial genera. The microbiota can be considered an immune organism contributing to the human host's health [2, 3]. The importance of gut flora to host health is highlighted by their critical functions of breaking down indigestible carbohydrates, inhibiting pathogenic bacterial infections, synthesizing vitamins, exerting antitumor effects, and modifying host immune reaction [4, 5].

Studies that compare the intestinal flora of tumor patients with that of healthy people reveal significant differences in the microbiota [6, 7]. Gut microbiota are an important factor in treating tumors [8].

Over the past 20 years, many researchers have focused on the anticancer properties of plant-derived polyphenols [9]. Polyphenolic compounds possess one or more aromatic rings and hydroxyl functional groups and are potential anticancer drug candidates [10]. Polyphenols are naturally occurring compounds present in fruit, nuts, vegetables, and plant-based products such as spices, tea, and wine [11]. There is considerable diversity among these plant secondary metabolites, with the compounds extending from simple small molecules to complex, highly polymeric compounds [12–14]. Natural polyphenols exhibit antioxidant and anti-inflammatory activities. They also have the capacity to influence molecular targets and signaling pathways, thereby modulating various processes, including angiogenesis, cell differentiation, migration, proliferation and survival, detoxification enzymes, hormone activities, and immune responses.

It is these impressive qualities that are deemed responsible for the anticancer effects of natural polyphenols [15, 16].

Among other plant foods, the common flavonoid apigenin is found in oranges, onions, parsley, tea, and wheat sprouts [17]. The administration of 40–160 μM of apigenin to H460 lung cancer cells resulted in damaged DNA and a concomitant increase in the production of reactive oxygen species (ROS) and Ca^{2+} [18]. Apoptosis was induced in gastric cancer cells by apigenin (20 $\mu\text{g}/\text{mL}$); while normal gastric cells exhibited minimal cytotoxicity, undifferentiated gastric cancer cells were especially vulnerable [19]. Apigenin treatment (50 mg/kg) has been shown to be effective in inhibiting tumor growth and metastasis in the orthotopic colorectal cancer (CRC) model. At lower doses (20–120 μM), cell proliferation, invasion, and migration have been reduced in a number of CRC cell lines [20].

The morbidity of CRC in rats fed a high-fat diet may be reduced by apigenin modulating gut microbiota; apigenin might also modulate the microbiota-gut-brain axis. The bacteria *Helicobacter pylori* responsible for stomach ulcers are also implicated in gastric cancer. Atrophic gastritis has been proposed as being a key precursor condition in stomach cancer induced by *Helicobacter pylori*. In a study of Mongolian gerbils, administering apigenin (30–60 mg/kg/week) successfully prevented the development of *Helicobacter pylori*-induced atrophic gastritis and subsequent gastric cancer [21]. The *in vivo* mechanisms responsible for the effects of apigenin have yet to be fully characterized; however, we hypothesize that the antitumor effects of apigenin are determined by its effect upon gut microbiota.

To explore the *in vivo* effects of apigenin on the composition of intestinal microbiota composition, carcinogenesis, and tumors in tumor-bearing mice, this study used high-throughput sequencing of 16S rRNA to refine the antitumor effects of apigenin on intestinal microbiota, and a fecal transplant experiment was conducted.

2. Materials and Methods

2.1. Animals. This research was approved by the animal use and welfare committee of Tianjin Fourth Central Hospital. All the experiments were performed according to the committee's animal welfare guidelines. Four-week-old female-specific pathogen-free (SPF) BALB/c mice were acquired from the Tianjin Laboratory Animal Center (Tianjin, China). Prior to experimentation, the mice were given 5 d to acclimatize to the laboratory environment. All animals were kept in an air-conditioned room (temperature $23^{\circ}\text{C} \pm 3^{\circ}\text{C}$; relative humidity, $50\% \pm 20\%$; ventilated fresh air > 17 times/h; 12 h light/dark cycle).

Dextran sulfate sodium (DSS) (MW 36–50 kDa) (Cat. No. 160110) was obtained from MP Biomedicals, LLC (Aurora, OH, USA). Mice were randomly allocated to two groups, a control group and an intervention (AP) group ($n = 8$ per group). Azoxymethane (Sigma-Aldrich) (10 mg/kg) was injected intraperitoneally to induce colon cancer. One week later, DSS (2.5%) was added to drinking water to last for 5 d, and then, plain drinking water was provided for the next 14 d. This 19 d cycle was repeated three

times. The mice in the AP group received a 30 mg/kg apigenin supplement in their diet. All mice were sacrificed 4 weeks after DSS treatment via cervical dislocation.

Cephadrine (cephalosporin) and gentamicin (aminoglycoside) broad-spectrum antibiotics were administered to deplete gut flora for the commensal microbe-depleted (CMD) experiment [22]. Cephadrine was prepared at a concentration of 67 mg/kg, and gentamicin was prepared at a concentration of 2 mg/kg with a sterile saline solution. Antibiotics were administered by oral gavage b.i.d. for 30 d. To evaluate the efficiency of depletion, bacterial DNA was extracted. The mice were then randomly segregated into a CMD group and a CMD-AP group ($n = 8$ per group). The same protocol was applied to the groups treated with azoxymethane (AOM) and DSS. The diet of the mice in the CMD-AP group was supplemented with 30 mg/kg apigenin.

The surgical procedure for the fecal microbiota transplantation (FMT) experiment is as follows. Stools were collected from mice fed a 30 mg/kg apigenin-supplemented diet and normal SPF mice (control donor mice). The feces were collected daily under sterile conditions in laminar flow fume hoods, and the same group of feces was combined. Next, 100 mg of feces was resuspended in 1 mL sterile saline and then mixed using a benchtop vortex for 10 s. The solution was centrifuged at 800 g for 3 min, and the supernatant was collected to transplant microbiota. Fresh transplant microbiota was prepared 10 min before use to prevent changes in bacterial composition. The mice were separated into an FMT-AP group and an FMT control group ($n = 8$). The same AOM and DSS protocol that has been described previously was applied. The FMT control group mice received 0.1 mL transplant microbiota from control donor mice each day, and the FMT-AP mice received 0.1 mL transplant material from apigenin donor mice each day [23]. Throughout the experiment, each mouse was monitored individually.

2.2. Fecal Microbiological Determination by 16S rRNA Gene Sequencing. Prior to sacrifice, approximately 200 mg of fecal matter was collected from each rodent. Following the manufacturer's instructions, a commercial E.Z.N.A Stool DNA Kit (Omega Bio-Tek, Inc., Norcross, GA, USA) was used to isolate the higher-quality total microbial DNA. The 20 μL reaction mixture for PCR comprised 10 ng template DNA, 1 μL each of forward and reverse primers, 2 μL dNTPs (2.5 mM), 4 μL FastPfu buffer, and 0.5 μL FastPfu polymerase; the mixture was supplemented with phosphate-buffered saline (PBS; Beyotime Biotech, Shanghai, China). The following PCR amplification process was applied: 95°C for 2 min, then 30 cycles at 94°C for 30 s, at 50°C for 30 s, at 72°C for 45 s, and at 72°C for 10 min. Using a DNA gel-extracting kit (Cat. No. AP-GX-250, Axygen Biosciences, Union City, CA, USA), the amplified PCR products were mixed and purified in accordance with the manufacturer's instructions. Using a DNA PCR-Free Sample Preparation Kit (Cat. No. FC-121-3003, Illumina, San Diego, CA, USA) combined with the pooled PCR products as templates, the gene library was built. To sequence the PCR products, equimolar amounts were pooled and then sequenced using the Illumina High-Throughput Sequencing Platform (mode: Hiseq2500; Illumina, San Diego, CA, USA).

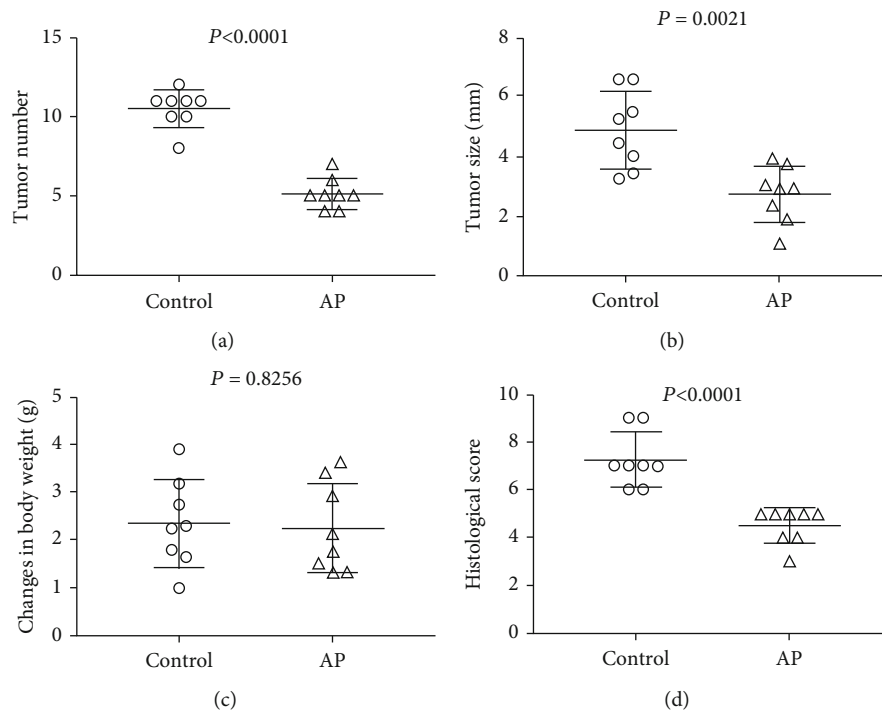


FIGURE 1: Apigenin decreased tumor morbidity in a CRC model related to colitis: the number (a) and size (b) of colon tumors in the control and AP groups, (c) change in body weight in the control and AP groups, and (d) histological score for the control and AP groups; $n = 8$.

2.3. Colon Inflammatory Index. Colons and tumors were harvested for histology. Samples were processed and fixed on slides before applying hematoxylin and eosin stains. The inflammatory index was analyzed according to a previous study [24]. The inflammatory index recorded the areas of epithelial degeneration and the severity, the presence of ulcers, epithelial erosions, tissue hyperplasia, the size of the affected area, and whether the areas were focal or multifocal.

2.4. Statistical Analysis. SPSS statistical software was used to analyze the results. To assess differences involving two groups, Student's t -test or one-way ANOVA was used. The data are expressed as mean \pm standard deviation (SD), with $P < 0.05$ indicating statistical significance.

3. Results

3.1. Depressor Effect of Apigenin on Tumor Growth and Metastasis In Vivo. A comparison was made of the weight and volume of tumors and the change in body weight between the AP mice and the controls (Figures 1(a)–1(c)). Although there were no changes in body weight, the control mice exhibited heavier and larger tumors ($P < 0.05$). Figure 1(d) presents the histological scores, which are higher for the control mice ($P < 0.05$). This suggests that apigenin treatment might have helped the tumor-bearing mice to maintain some level of physical condition.

3.2. The Influence of Apigenin on Gut Microbiota in Tumor-Bearing Mice. To investigate apigenin-altered gut microbiota, the gut bacterial populations were determined using high-throughput sequencing. Figures 2(a) and 2(b) present the dif-

ferences in the abundance of operational taxonomic units (OTUs) and the diversity index of the gut microbiota of the control and AP groups. Changes in the abundance of microbiota are illustrated in phylum-level heat maps of the community following the administration of apigenin (Figure 2(c)). There was a trend of decrease in Firmicutes (Figure 2(d)) and a significant increase in Actinobacteria (Figure 2(e)) in the AP group. Apigenin may exert antitumor effects that are responsible for changes to the phylum.

3.3. The Influence of Gut Microbiota on the Antitumor Effects of Apigenin. To examine the effect of gut microbiota on the antitumor effects of apigenin, gut microbiota were reduced using cephaloridine and gentamicin. No significant difference in the antitumor role as determined by tumor size and volume was identified between the CMD group and the CMD-AP group (Figures 3(a) and 3(b)). This indicates that after depleting the gut microbiota, apigenin did not have any benefit on the general health of the mice (Figures 3(a) and 3(b)). Furthermore, there were no significant differences in the change in body weight or histological scores (Figures 3(c) and 3(d)). However, as Figures 3(d) and 3(e) depict, the amount of OTU and bacterial 1diversity was significantly decreased in the CMD groups relative to the controls. This confirms that the antibiotics had effectively depleted gut microbiota. The relative abundance of the microbiota is shown in Figure 3(g); we did not detect any microbial difference at the phylum level among the groups.

3.4. Regaining Antitumor Effects Using Fecal Microbiota from the Apigenin Treatment. Freshly extracted supernatant from control donor and apigenin-fed (30 mg/kg) donor mice was

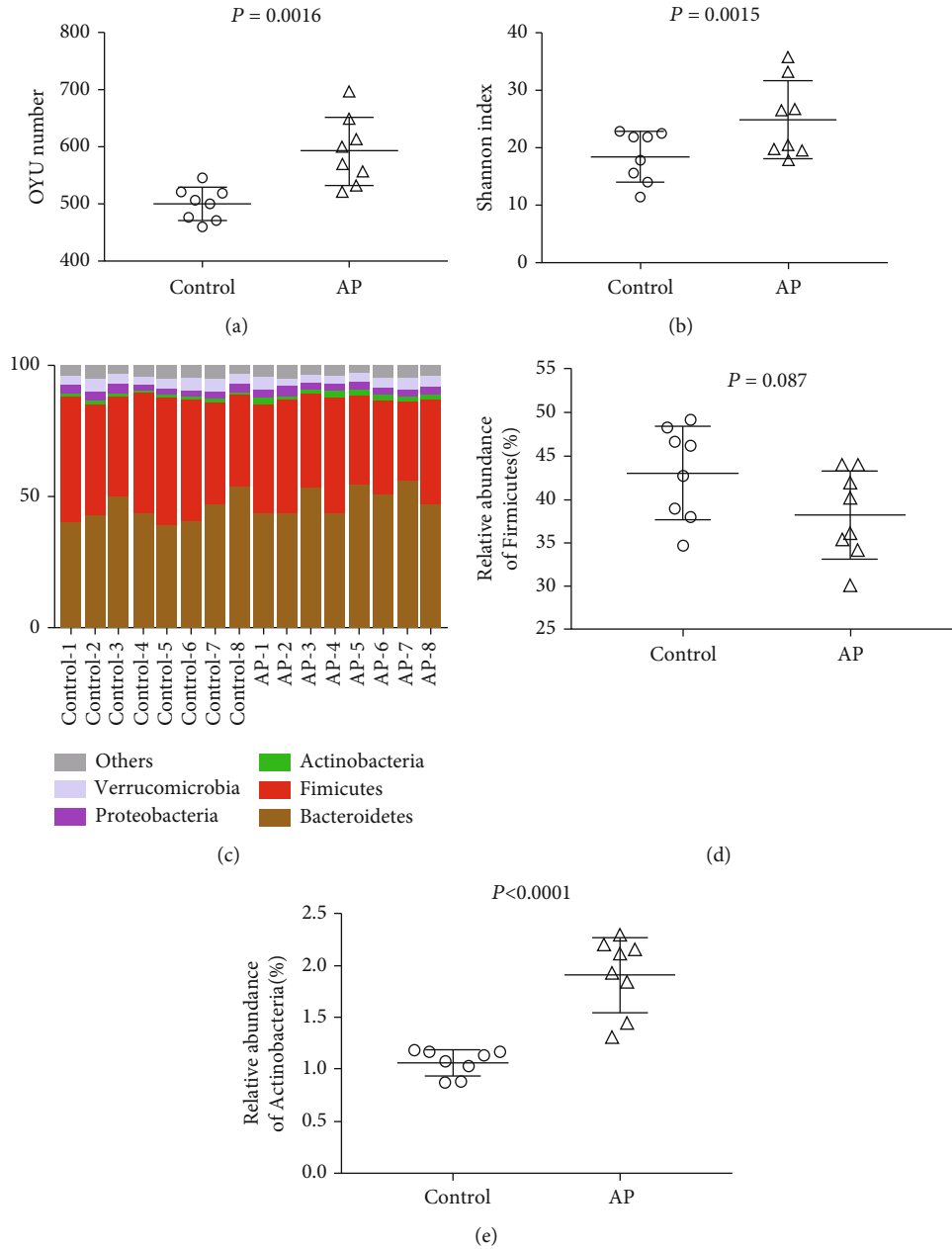


FIGURE 2: Results of 16S rRNA high-throughput sequencing: (a) OTU number and (b) Shannon index in the control ($n = 8$) and AP ($n = 8$) groups. (c) The heat map and the relative abundance of (d) Firmicutes and (e) Actinobacteria showing differences in the abundance of gut microbiota in the different groups at the phylum level.

intragastrically administered to the FMT model and FMT-AP groups over 14 d. The number and size of tumors in the FMT group of mice were significantly greater ($P < 0.05$) than in the FMT-AP model group (Figures 4(a) and 4(b)), whereas no difference in the change of body weight was detected (Figure 4(c)). Similarly, the histological score of the colon in the latter group was significantly lower ($P < 0.05$) (Figure 4(d)). Meanwhile, the amount of OTU and bacterial diversity was significantly increased in the FMT-AP group relative to the control and FMT groups ($P < 0.05$) (Figures 4(e) and 4(f)). The relative abundance of the microbiota is shown in Figure 4(g). The relative abundance of Bacteroidetes (Figure 4(h)) and Actinobacteria (Figure 4(j)) in

the FMT group of mice was significantly lower ($P < 0.05$) than that in the FMT-AP model group, and the relative abundance of Firmicutes (Figure 4(i)) in the FMT group of mice was significantly greater ($P < 0.05$) than that in the FMT-AP model group.

4. Discussion

Each year, approximately 1.2 million people are diagnosed with CRC, which is the third most prevalent cancer. There is a high incidence of CRC in developed countries [25, 26]. There are approximately 1,000 different kinds of bacteria in the human body, amounting to 10^{14} individual bacteria.

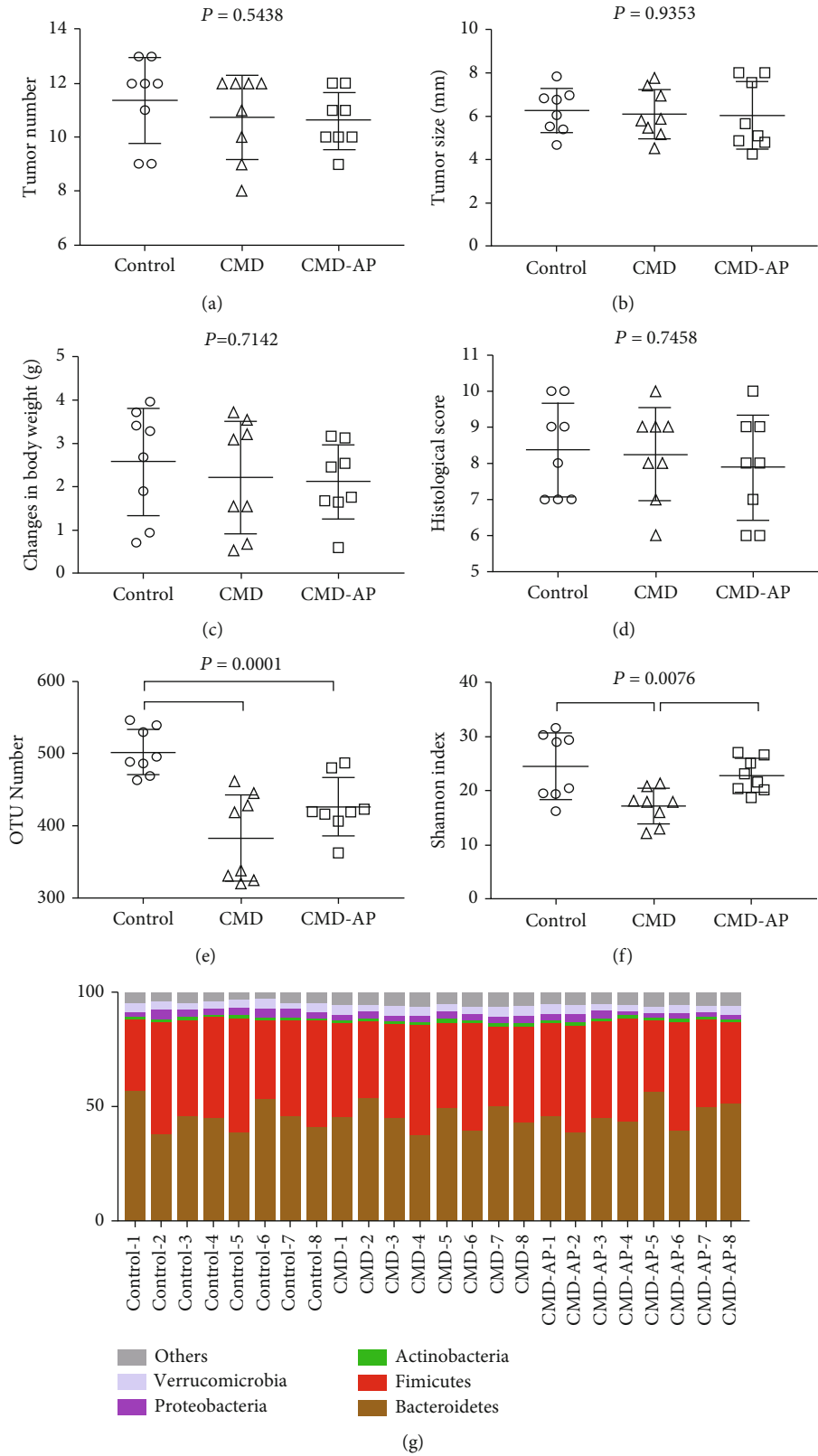


FIGURE 3: Influence of gut microbiota depletion on the antitumor effects of apigenin. The number (a) and size (b) of colon tumors in the CMD and CMD-AP groups; (c) change in body weight, (d) histological scores, (e) OTU number, (f) diversity indexes, and (g) the abundance of gut microbiota at the phylum level in the commensal microbe-depleted (CMD) experiment; $n = 8$.

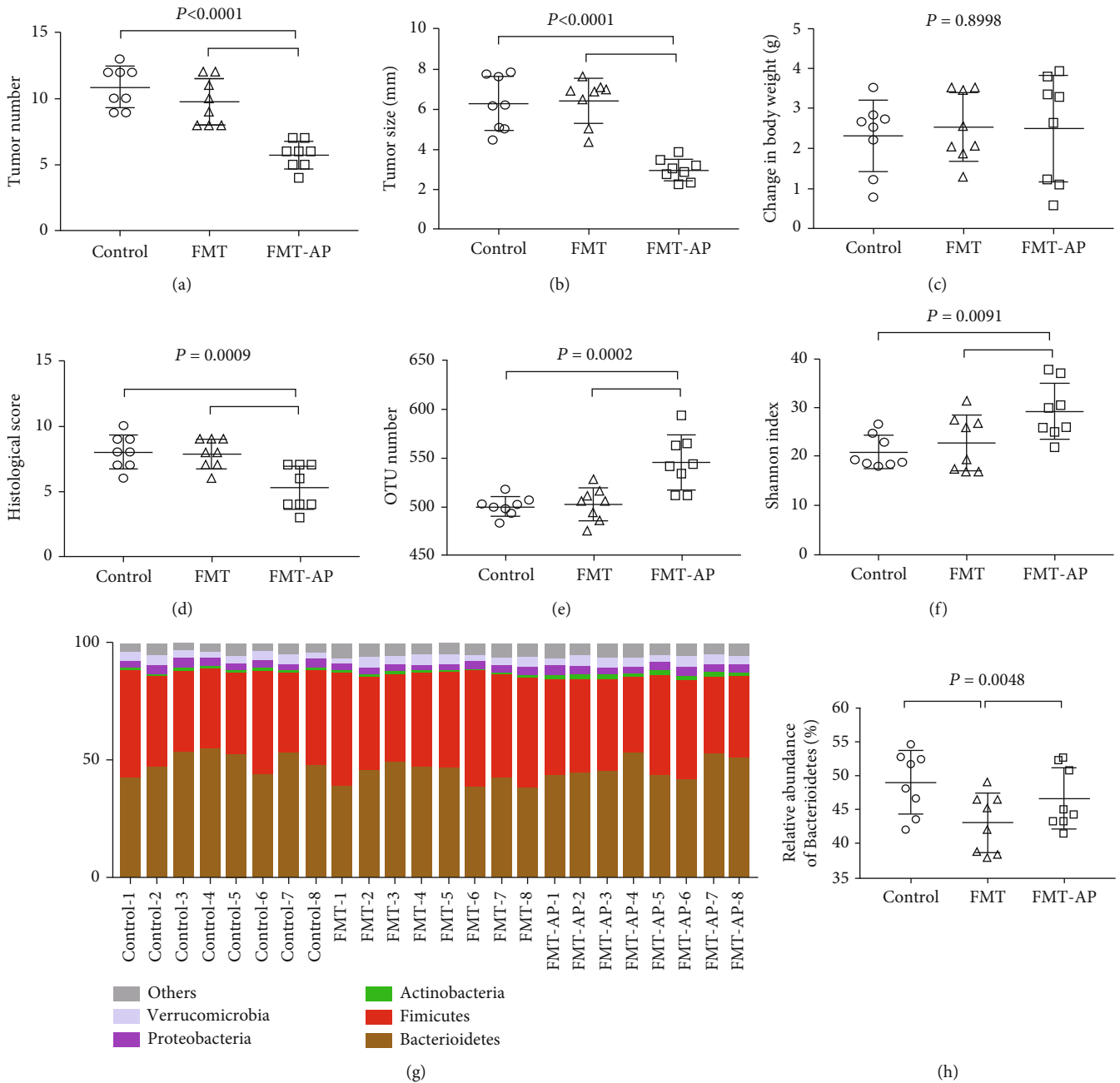


FIGURE 4: Continued.

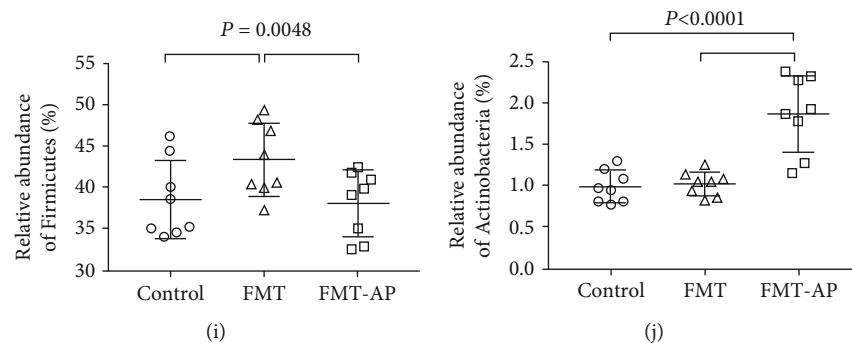


FIGURE 4: *In vivo* inhibition of tumor growth following fecal transplants. Number (a) and size (b) of colon tumors in the FMT ($n = 8$) and FMT-AP ($n = 8$) groups; (c) change in body weight, (d) histological scores, (e) OTU number, (f) diversity indexes, (g) the abundance of gut microbiota at the phylum level, and the relative abundance of (h) Bacteroidetes, (i) Firmicutes, and (j) Actinobacteria in the fecal microbiota transplantation (FMT) experiment; $n = 8$.

The sum of microbial genes is calculated to be at least 150 times more than the number of human host genes [27]. Gut microbiota are symbionts, contributing to host health and to the biological barrier that aids nutrient absorption, immune regulation, and energy metabolism [28]. Studies reveal that cancer patients present with gut microbiota disorders; therefore, the rationale is that by modifying gut flora, tumor-ameliorating effects may ensue. This study administered apigenin that moderated the antitumor effects of the microbiota.

Apigenin is one of the most bioactive flavonoids and is present in many fruits and vegetables [29]. Research into apigenin started in the 1960s; by the 1980s, it was postulated that the compound had cancer-preventing properties [29, 30]. The low intrinsic toxicity of apigenin has attracted the interest of many researchers [31]. Different types of cancer and normal cell types respond differently to apigenin, influencing cancer cell growth, survival, and apoptosis [29, 30]. Although apigenin is degraded by gut microbiota, this polyphenol and its metabolites may in turn modulate the structure and function of the gut microbiota. As yet, these modulatory effects on the microbiota remain largely uncharacterized [32].

Even though there has been considerable progress in understanding cancer over the decades, there are still details relating to cancer initiation, development, metastasis, and recurrence that have yet to be elucidated. A significant challenge to acquiring a comprehensive understanding is that multiple factors are in play in tumor microenvironments. Understanding the role of the host's microbiota has been overlooked in the past but has recently become of increasing interest [33, 34]. According to the findings of Vétizou et al., specific species of *Bacteroides* exert an effect upon the antitumor capacity of immune checkpoint inhibitors [35]. The effectiveness of antitumor medicine is reduced in germ-free mice with sterilized gut microbiota compared to SPF mice; when particular *Bacteroides* species were implanted into the intestines of mice, effectiveness was restored. Sivan et al. found that using immune checkpoint inhibitors in conjunction with a transplant of gut microbiota could significantly improve their antitumor efficacy [36].

Many symbiotic bacteria, such as *Lactobacillus* and *Lachnospiraceae*, are found in the intestines. These important

species help with host digestion, maintain the intestinal environment by preventing intestinal colonization by oral bacterial clades, and exert anti-inflammatory effects. The importance of these bacteria is highlighted by studies that show microbiota dysbiosis can occur when these beneficial bacteria are absent, contributing to diabetes, inflammatory bowel disease, intestinal cancers, and obesity and adversely affecting the immune system [28, 37]. Insights into the development, metastasis, and recurrence of CRC can be increased by detailing features of dysbiosis in intestinal microbiota, especially of the large intestine. By developing a better understanding of host-microbiota interactions in CRC, the treatment of CRC patients can become more targeted. The tumor location in the intestines influences the severity of CRC [38] and the level of resistance to chemotherapy [39] in different patients. More than any other factors, diet and lifestyle are regarded as determining the probability of developing CRC. Ingesting polyphenols, such as apigenin, benefits gut microbiota and helps to protect against CRC [40, 41]. We explored the antitumor relationship between gut microbiota and apigenin through fecal bacteria transplantation experiments. Transplanting feces from apigenin donor mice into FMT-AP mice inhibited tumor carcinogenesis in the recipient mice.

As this study has shown, *in vivo* tumor carcinogenesis is inhibited by apigenin by influencing the gut microbiota. However, the precise mechanism by which apigenin affects the gut microbiota and exerts its antitumor effects have yet to be determined.

Data Availability

The datasets used and/or analyzed during the current study are available from the corresponding author on reasonable request.

Conflicts of Interest

The authors declare that the research was conducted in the absence of any commercial or financial relationships that could be construed as a potential conflict of interest.

Authors' Contributions

Shichang Bian and Hongjuan Wan contributed equally to this manuscript.

Acknowledgments

This work was supported by the National Natural Science Foundation of China (81600509) and the Tianjin Science and Technology Support Key Project Plan (20140109).


References

- [1] M. Todaro, M. D'Asaro, N. Caccamo et al., "Efficient killing of human colon cancer stem cells by $\gamma\delta$ T lymphocytes," *The Journal of Immunology*, vol. 182, no. 11, pp. 7287–7296, 2009.
- [2] W. B. Whitman, D. C. Coleman, and W. J. Wiebe, "Prokaryotes: the unseen majority," *Proceedings of the National Academy of Sciences*, vol. 95, no. 12, pp. 6578–6583, 1998.
- [3] R. E. Ley, D. A. Peterson, and J. I. Gordon, "Ecological and evolutionary forces shaping microbial diversity in the human intestine," *Cell*, vol. 124, no. 4, pp. 837–848, 2006.
- [4] I. Sekirov, S. L. Russell, L. C. Antunes, and B. B. Finlay, "Gut microbiota in health and disease," *Physiological Reviews*, vol. 90, no. 3, pp. 859–904, 2010.
- [5] Q. Li, C. Ding, T. Meng et al., "Butyrate suppresses motility of colorectal cancer cells via deactivating Akt/ERK signaling in histone deacetylase dependent manner," *Journal of Pharmacological Sciences*, vol. 135, no. 4, pp. 148–155, 2017.
- [6] T. T. Wang, G. X. Cai, Y. P. Qiu et al., "Structural segregation of gut microbiota between colorectal cancer patients and healthy volunteers," *The ISME journal*, vol. 6, no. 2, pp. 320–329, 2012.
- [7] J. R. Marchesi, B. E. Dutilh, N. Hall et al., "Towards the human colorectal cancer microbiome," *PLoS One*, vol. 6, no. 5, article e20447, 2011.
- [8] J. Kaiser, "Gut microbes shape response to cancer immunotherapy," *Science*, vol. 358, no. 6363, p. 573, 2017.
- [9] M. Ashrafizadeh, H. Yaribeygi, and A. Sahebkar, "Therapeutic effects of curcumin against bladder cancer: a review of possible molecular pathways," *Anti-Cancer Agents in Medicinal Chemistry (Formerly Current Medicinal Chemistry-Anti-Cancer Agents)*, vol. 20, no. 6, pp. 667–677, 2020.
- [10] C. Manach, A. Scalbert, C. Morand, C. Remesy, and L. Jimenez, "Polyphenols: food sources and bioavailability," *American Journal of Clinical Nutrition*, vol. 79, no. 5, pp. 727–747, 2004.
- [11] S. Ding, S. Xu, J. Fang, and H. Jiang, "The protective effect of polyphenols for colorectal cancer," *Frontiers in Immunology*, vol. 11, p. 1407, 2020.
- [12] Y. Zhou, Y. Li, T. Zhou, J. Zheng, S. Li, and H. B. Li, "Dietary natural products for prevention and treatment of liver cancer," *Nutrients*, vol. 8, no. 3, p. 156, 2016.
- [13] L. Fu, B. T. Xu, X. R. Xu, X. S. Qin, R. Y. Gan, and H. B. Li, "Antioxidant capacities and total phenolic contents of 56 wild fruits from south China," *Molecules*, vol. 15, no. 12, pp. 8602–8617, 2010.
- [14] G. F. Deng, X. Lin, X. R. Xu, L. L. Gao, J. F. Xie, and H. B. Li, "Antioxidant capacities and total phenolic contents of 56 vegetables," *Journal of Functional Foods*, vol. 5, no. 1, pp. 260–266, 2013.
- [15] F. Li, S. Li, H. B. Li, G. F. Deng, W. H. Ling, and X. R. Xu, "Antiproliferative activities of tea and herbal infusions," *Food & Function*, vol. 4, no. 4, pp. 530–538, 2013.
- [16] F. Li, S. Li, H. B. Li et al., "Antiproliferative activity of peels, pulps and seeds of 61 fruits," *Journal of Functional Foods*, vol. 5, no. 3, pp. 1298–1309, 2012.
- [17] Y. Zhu, J. Wu, S. Li et al., "Apigenin inhibits migration and invasion via modulation of epithelial mesenchymal transition in prostate cancer," *Molecular Medicine Reports*, vol. 11, no. 2, pp. 1004–1008, 2015.
- [18] H. F. Lu, Y. J. Chie, M. S. Yang et al., "Apigenin induces apoptosis in human lung cancer H460 cells through caspase- and mitochondria-dependent pathways," *Human & Experimental Toxicology*, vol. 30, no. 8, pp. 1053–1061, 2011.
- [19] J. Chen, J. Chen, Z. Li, C. Liu, and L. Yin, "The apoptotic effect of apigenin on human gastric carcinoma cells through mitochondrial signal pathway," *Tumor Biology*, vol. 35, no. 8, pp. 7719–7726, 2014.
- [20] L. Chunhua, L. Donglan, F. Xiuqiong et al., "Apigenin up-regulates transgelin and inhibits invasion and migration of colorectal cancer through decreased phosphorylation of AKT," *The Journal of Nutritional Biochemistry*, vol. 24, no. 10, pp. 1766–1775, 2013.
- [21] C. H. Kuo, B. C. Weng, C. C. Wu, S. F. Yang, D. C. Wu, and Y. C. Wang, "Apigenin has anti-atrophic gastritis and anti-gastric cancer progression effects in Helicobacter pylori-infected Mongolian gerbils," *Journal of Ethnopharmacology*, vol. 151, no. 3, pp. 1031–1039, 2014.
- [22] Y. Zhao, J. Wu, J. V. Li, N. Y. Zhou, H. Tang, and Y. Wang, "Gut microbiota composition modifies fecal metabolic profiles in mice," *Journal of Proteome Research*, vol. 12, no. 6, pp. 2987–2999, 2013.
- [23] C. J. Chang, C. S. Lin, C. C. Lu et al., "Ganoderma lucidum reduces obesity in mice by modulating the composition of the gut microbiota," *Nature Communications*, vol. 6, no. 1, 2015.
- [24] H. S. Cooper, S. N. Murthy, R. S. Shah, and D. J. Sedergran, "Clinicopathologic study of dextran sulfate sodium experimental murine colitis," *Laboratory Investigation; a Journal of Technical Methods and Pathology*, vol. 69, no. 2, pp. 238–249, 1993.
- [25] H. Brenner, M. Kloor, and C. P. Pox, "Colorectal cancer," *Lancet*, vol. 383, no. 9927, pp. 1490–1502, 2014.
- [26] R. L. Siegel, K. D. Miller, and A. Jemal, "Colorectal cancer statistics, 2017," *CA: a Cancer Journal for Clinicians*, vol. 67, no. 1, pp. 7–30, 2017.
- [27] MetaHIT Consortium, J. Qin, R. Li et al., "A human gut microbial gene catalogue established by metagenomic sequencing," *Nature*, vol. 464, no. 7285, pp. 59–65, 2010.
- [28] V. Tremaroli and F. Backhed, "Functional interactions between the gut microbiota and host metabolism," *Nature*, vol. 489, no. 7415, pp. 242–249, 2012.
- [29] S. Shukla and S. Gupta, "Apigenin: a promising molecule for cancer prevention," *Pharmaceutical Research*, vol. 27, no. 6, pp. 962–978, 2010.
- [30] E. C. Lefort and J. Blay, "Apigenin and its impact on gastrointestinal cancers," *Molecular Nutrition & Food Research*, vol. 57, no. 1, pp. 126–144, 2013.
- [31] D. Tang, K. Chen, L. Huang, and J. Li, "Pharmacokinetic properties and drug interactions of apigenin, a natural flavone," *Expert Opinion on Drug Metabolism & Toxicology*, vol. 13, no. 3, pp. 323–330, 2016.

- [32] F. Cardona, C. Andres-Lacueva, S. Tulipani, F. J. Tinahones, and M. I. Queipo-Ortuno, "Benefits of polyphenols on gut microbiota and implications in human health," *The Journal of Nutritional Biochemistry*, vol. 24, no. 8, pp. 1415–1422, 2013.
- [33] X. Zhang, S. Zhao, X. Song et al., "Inhibition effect of glycyrrhiza polysaccharide (GCP) on tumor growth through regulation of the gut microbiota composition," *Journal of Pharmacological Sciences*, vol. 137, no. 4, pp. 324–332, 2018.
- [34] G. Guan, S. Ding, Y. Yin, V. Duraipandiyar, N. A. Al-Dhabi, and G. Liu, "Macleaya cordata extract alleviated oxidative stress and altered innate immune response in mice challenged with enterotoxigenic *Escherichia coli*," *Science China Life Sciences*, vol. 62, no. 8, pp. 1019–1027, 2019.
- [35] M. Vetizou, J. M. Pitt, R. Daillere et al., "Anticancer immunotherapy by CTLA-4 blockade relies on the gut microbiota," *Science*, vol. 350, no. 6264, pp. 1079–1084, 2015.
- [36] A. Sivan, L. Corrales, N. Hubert et al., "Commensal *Bifidobacterium* promotes antitumor immunity and facilitates anti-PD-L1 efficacy," *Science*, vol. 350, no. 6264, pp. 1084–1089, 2015.
- [37] R. E. Ley, P. J. Turnbaugh, S. Klein, and J. I. Gordon, "Microbial ecology: human gut microbes associated with obesity," *Nature*, vol. 444, no. 7122, pp. 1022–1023, 2006.
- [38] T. Aoyama, K. Kashiwabara, K. Oba et al., "Clinical impact of tumor location on the colon cancer survival and recurrence: analyses of pooled data from three large phase III randomized clinical trials," *Cancer Medicine*, vol. 6, no. 11, pp. 2523–2530, 2017.
- [39] B. Flemer, D. B. Lynch, J. M. Brown et al., "Tumour-associated and non-tumour-associated microbiota in colorectal cancer," *Gut*, vol. 66, no. 4, pp. 633–643, 2017.
- [40] S. J. O'Keefe, "Diet, microorganisms and their metabolites, and colon cancer," *Nature Reviews Gastroenterology & Hepatology*, vol. 13, no. 12, pp. 691–706, 2016.
- [41] M. Arnold, M. S. Sierra, M. Laversanne, I. Soerjomataram, A. Jemal, and F. Bray, "Global patterns and trends in colorectal cancer incidence and mortality," *Gut*, vol. 66, no. 4, pp. 683–691, 2017.

Research Article

Essential Oil and Juice from Bergamot and Sweet Orange Improve Acne Vulgaris Caused by Excessive Androgen Secretion

Peng Sun,¹ Liang Zhao ,² Nanhai Zhang,¹ Chengtao Wang,² Wei Wu,³ Arshad Mehmood,² Liebing Zhang,¹ Baoping Ji,¹ and Feng Zhou ¹

¹Beijing Key Laboratory of Functional Food from Plant Resources, College of Food Science and Nutritional Engineering, China Agricultural University, Beijing 100083, China

²Beijing Advance Innovation Center for Food Nutrition and Human Health, Beijing Engineering and Technology Research Center of Food Additives, Beijing Technology and Business University, Beijing 100048, China

³College of Engineering, China Agricultural University, Beijing 100083, China

Correspondence should be addressed to Feng Zhou; zf@cau.edu.cn

Received 1 September 2020; Revised 11 September 2020; Accepted 24 September 2020; Published 6 October 2020

Academic Editor: Shuai CHEN

Copyright © 2020 Peng Sun et al. This is an open access article distributed under the Creative Commons Attribution License, which permits unrestricted use, distribution, and reproduction in any medium, provided the original work is properly cited.

Acne vulgaris is one of the most common chronic inflammatory skin diseases. Bergamot and sweet orange are rich in nutritional and functional components, which exhibit antioxidant, anti-inflammatory, and antiapoptotic effect. The aim of this study was to evaluate the potential effect of bergamot and sweet orange (juice and essential oil) on acne vulgaris caused by excessive secretion of androgen. Eighty male golden hamsters were randomly divided into 10 groups and received low or high dose of bergamot and sweet orange juice and essential oil, physiological saline, and positive drugs for four weeks, respectively. Results showed that all interventions could improve acne vulgaris by reducing the growth rate of sebaceous gland spots, inhibiting TG accumulation, decreasing the release of inflammatory cytokines (notably reducing IL-1 α levels), promoting apoptosis in the sebaceous gland, and decreasing the ratio of T/E₂. Among them, bergamot and orange essential oil may have better effects (dose dependent) on alleviating acne vulgaris than the corresponding juice. In view of the large population of acne patients and the widespread use of sweet orange and bergamot, this study is likely to exert an extensive and far-reaching influence.

1. Introduction

Acne vulgaris is a prevalent dermatologic disease, mainly distributed in the pilosebaceous units including the face, neck, chest, back, and shoulders. The clinical manifestations of acne vulgaris are mainly seborrheic, noninflammatory skin lesions, inflammatory lesions, and varying degrees of scarring [1, 2]. More than 85% of young individuals are affected by acne vulgaris worldwide and can suffer from the disease into adulthood [3]. Although acne vulgaris is not life-threatening, this disease can have a huge impact on patients' psychosocial and physical health. Acne vulgaris results from the androgen-induced sebum production, altered keratinization, inflammation, and colonization of *Propionibacterium acnes* (*P. acnes*)

on the pilosebaceous follicles [4]. Among them, inflammations are present in all acne vulgaris lesions—including microcomedones, inflammatory lesions, hyperpigmentation, and scarring [5, 6]. Also, acne vulgaris is associated with diet, occupation, climate, and psychological and lifestyle factors [7, 8]. Thus, more and more researchers are getting interested in preventing acne vulgaris. According to recent dermatologic guidelines, the current treatments for acne vulgaris are divided into conventional pharmacological and nonpharmacological therapies. The former therapies include antibiotics, retinoids, hormonal agents, and benzoyl peroxide while laser and light-based therapies, chemical peels, micro-needling, (micro) dermabrasion, and (mechanical) lesion removal are the latter therapies most commonly applied

[9, 10]. Nevertheless, none of these therapies is free of side effect [11]. Furthermore, more investigations are needed to seek alternative and complementary medicine, including medicinal plants.

Bergamot (*Citrus medica* L. var. *sarcodactylis*) has been applied as a medicinal plant just because of its stomachic, antifungal, and bacteriostatic properties [12]. Bergamot, also called finger citron, is one of the species of *Citrus* [13]. The carpels of finger citron split, causing a finger-like fruit shape [14]. The flowers, leaves, and fruits of bergamot can be used as medicine, which play roles in soothing the liver and relieving depression [15]. Bergamot peel is mostly used to distill bergamot essential oil (BEO) while bergamot juice (BJ) is obtained by squeezing the endocarp of the fruits [16]. Evidences indicated that BEO could show some properties like anti-inflammation, immunomodulatory, and wound healing [17]. The flavonoid-rich fraction of BJ could also exhibit anti-inflammatory and antioxidant activities [16]. Sweet orange (*Citrus sinensis* (L.) Osbeck) is another member of the *Citrus* genus fruit which becomes more and more popular in recent years. According to the previous research, sweet orange was widely consumed as fresh fruit and juice, while the peel was also rich in essential oils [18]. Sweet orange juice is one of the natural sources of large amounts of vitamin C, flavonoids, and other bioactive compounds with potential effects on the inflammatory response [19]. Sweet orange essential oil is one of the important natural plant essential oils, with an attractive orange flavor, which was reported to have stress-relief, antifungal, anticarcinogenic, and radical-scavenging properties [20–22]. Moreover, formulations based on orange and sweet basil oils were effective in treating acne vulgaris [23]. Based on the potential physiological activities of bergamot and sweet orange, it is interesting to figure out whether they could show effects on alleviating acne vulgaris. Is it the juice or essential oil that plays roles in improving acne vulgaris? What is the difference between bergamot and sweet orange in ameliorating acne vulgaris?

Therefore, this study was aimed at investigating the effects of different doses of bergamot essential oil, bergamot juice, sweet orange essential oil, and sweet orange juice on acne vulgaris caused by excessive androgen secretion. Since acne vulgaris is associated with elevated levels of androgen, the golden hamster animal model was used in our research, which was frequently used to study acne vulgaris based on the flank sebaceous gland [24–26].

2. Materials and Methods

2.1. Materials and Reagents. Commercial kits of triglyceride (TG) and enzyme-linked immunosorbent assay (ELISA) commercial kits of caspase-3 were obtained from Nanjing Jiancheng Bioengineering Institute (Nanjing, China), while ELISA kits of testosterone (T), estrogen 2 (E₂), interleukin-1 α (IL-1 α), interleukin-6 (IL-6), tumor necrosis factor- α (TNF- α), matrix metalloproteinase-2 (MMP-2), and matrix metalloproteinase-9 (MMP-9) were purchased from Keyingmei Biotechnology and Science Inc. (Beijing, China). Other chemical reagents were purchased from Sinopharm Chemical Reagent Co., Ltd. (Beijing, China). Compound

pearl acne capsules were produced by Shaanxi Dongtai Pharmaceutical Co., Ltd. (Xianyang, China).

2.2. Preparation of Bergamot Juice. After fresh bergamot was cleaned and peeled, peeled bergamot was cut into small pieces of 1 cm \times 1 cm \times 1 cm to be crushed with the juice extractor. Finally, the bergamot juice was obtained by filtering after placing at 4°C overnight.

2.3. Preparation of Bergamot Essential Oil. The peel fractions were diced into small pieces of 8 mm \times 8 mm \times 1 mm, which were mixed with distilled water at a ratio of 1 : 4 (*m/v*). After subjecting small peel fractions to steam distillation for 2 h, the obtained mixtures were dehydrated with anhydrous sodium sulfate. Then, the remaining mixture was strained to remove anhydrous sodium sulfate. Subsequently, the bergamot essential oil was collected after filtration.

2.4. Preparation of Sweet Orange Juice. After fresh sweet oranges were cleaned and peeled, peeled oranges were cut into small pieces of 4 cm \times 4 cm \times 4 cm to be crushed with the juice extractor. Finally, the sweet orange juice was obtained by filtering after placing at 4°C overnight.

2.5. Preparation of Sweet Orange Essential Oil. The peel fractions were diced into small pieces of 8 mm \times 8 mm \times 8 mm, which were mixed with distilled water at a ratio of 1 : 6 (*m/v*). After subjecting small peel fractions to steam distillation for 6 h, the obtained mixtures were dehydrated with anhydrous sodium sulfate. Then, the remaining mixture was strained to remove anhydrous sodium sulfate. Subsequently, the sweet orange essential oil was collected after filtration.

2.6. Preparation of Solution for Gavage. The prepared essential oil was added to an aqueous solution with 0.2% Tween 80 in a ratio of 1 : 7 (*m/v*). Subsequently, the mixtures were ultrasonicated for 30 min to obtain uniform essential oil emulsion. The compound pearl acne capsules were dissolved with distilled water in a ratio of 1 : 6 (*m/v*) to prepare an aqueous solution.

2.7. Animals and Treatments. Eighty male golden hamsters (120 \pm 10 g) were purchased from Beijing Vital River Laboratory Animal Technology Co., Ltd. (Beijing, China) (Certificate SCXK (Beijing) 2012-0001). The hamsters were acclimatized with a daily 12 h light/12 h dark cycle at 23 \pm 1°C room temperature and 50 \pm 2% relative humidity. After 1 week of adaptation, eighty golden hamsters were randomly divided into 10 groups: model group (MG), positive control group (PG), low-dose group of sweet orange juice (LOJ), high-dose group of sweet orange juice (HOJ), low-dose group of sweet orange essential oil (LOO), high-dose group of sweet orange essential oil (HOO), low-dose group of bergamot juice (LBJ), high-dose group of bergamot juice (HBJ), low-dose group of bergamot essential oil (LBO), and high-dose group of bergamot essential oil (HBO). The entire experiment lasted for four weeks. The MG was given physiological saline by oral route. The PG was administered 0.375 mg/kg BW of compound pearl acne capsules. The LOJ and HOJ

were, respectively, orally given 14 and 17.5 mL/kg BW of sweet orange juice. The LOO and HOO received 0.21 and 0.33 mL/kg BW of sweet orange essential oil, respectively. The LBJ and HBJ were, respectively, treated with 14 and 17.5 mL/kg BW of bergamot juice. The LBO and HBO received 0.21 and 0.33 mL/kg BW of sweet bergamot essential oil, respectively. Juice and essential oil that contain a low dose and high dose, respectively, were from fresh fruits in the same weight. The gastric volume of each intervention was 10 mL/kg BW.

At the end of the experiment, the golden hamster was fasted for 12 h (free drinking water) and then deeply comatose with diethyl ether. After taking blood from the eyelids with a capillary tube, hamsters were sacrificed. Blood was stored at 4°C for 4 h and then centrifuged at 4000 g for 10 min in a refrigerated centrifuge. Finally, the supernatant was collected and stored at -80°C for further detection. At the same time, the golden hamsters were dissected and the spleen, testis, and sebaceous gland were taken to weigh them. Part of the sebaceous gland was precooled in liquid nitrogen and then stored in an ultra-low-temperature refrigerator for later detection of related indicators. All experiment procedures in our study involving animals were allowed by the Ethics Committee of the Beijing Key Laboratory of Functional Food from Plant Resources and carried out in accordance with the guidelines for the use and care of laboratory animals of the National Institutes of Health.

2.8. Determination of the Growth Rate of Sebaceous Gland Spots. Before the experiment started, the size of sebaceous gland spots on the lateral abdomen of golden hamsters was measured. And the sebaceous gland spots were measured every 7 days. The sebaceous gland spots were calculated as follows:

$$S = \frac{\pi ab}{4}. \quad (1)$$

The growth rate of sebaceous gland spots on both sides was calculated as follows:

$$R = \frac{S_{n+1} - S_n}{S_n} \times 100\%, \quad (2)$$

where a , b , S_n , and S_{n+1} refer to the maximum transverse diameter of the sebaceous gland, the maximum longitudinal diameter of the sebaceous gland, the sebaceous gland area at the n -th week, and the sebaceous gland area at the $n + 1$ -th week, respectively.

2.9. Determination of the Organ Index. After the golden hamsters were weighed and killed, the spleen and testicle weights were measured. The organ index of golden hamsters was calculated as follows:

$$\text{organ index} = \frac{\text{organ weight (mg)}}{\text{body weight (g)}}. \quad (3)$$

2.10. TG Analysis. About 0.1 g of sebaceous gland was mixed with physiological saline at a ratio of 1:9 (m/v) and then

ground with a homogenizer. The tissue homogenate was prepared in a glass homogenizer and centrifuged at 3000 g for 10 min in a refrigerated centrifuge. The supernatant was taken to detect TG levels following the manufacturer's protocol of the commercial kit.

2.11. ELISA Analysis. The serum T, E_2 , IL-1 α , IL-6, TNF- α , MMP-2, and MMP-9 levels and the activity of caspase-3 in sebaceous gland tissue were detected on a SpectraMax M2e enzyme microplate reader (Thermo Fisher Scientific, USA) using the corresponding ELISA kits following the manufacturer's instructions.

2.12. Statistical Analysis. All diagrams were generated using GraphPad Prism 8.0 (GraphPad Software, San Diego, CA, USA). Statistical data were analyzed by one-way analysis of variance (ANOVA) followed by Tukey's test using SPSS 25.0 software (IBM Corporation, Armonk, NY, USA). Results were expressed as mean \pm standard deviation (SD) with significance accepted at $P < 0.05$.

3. Results

3.1. Effect of Different Treatments on the Growth Rate of Sebaceous Gland Spots in the Golden Hamster. As shown in Figure 1(a), all groups exhibited better inhibitory effect than MG on the growth rate of sebaceous gland spots ($P < 0.05$). The growth rate of the sebaceous gland spots in bergamot essential oil groups was remarkably decreased compared with the corresponding dose of juice groups. HBO, LBO, and HOO could significantly inhibit the growth rate of the left-side sebaceous gland spots of hamsters compared with the PG group ($P < 0.05$). The HBO, LBO, and HBJ groups significantly decreased the growth rate of the right-side sebaceous gland spots in golden hamsters to 2.21%, 1.13%, and 1.09%, respectively ($P < 0.05$). The growth rate of the sebaceous gland spots in bergamot essential oil groups was clearly decreased in contrast with the corresponding dose of sweet orange groups ($P < 0.05$). In Figure 1(b), each intervention group clearly reduced the growth rate of the left-side sebaceous gland spots compared with MG ($P < 0.05$). Only the groups of bergamots, LOO, HOO, and HOJ, could significantly inhibit the growth rate of right-side sebaceous gland spots in comparison with MG ($P < 0.05$). The growth rate of sebaceous gland spots in essential oil groups was lower than that in the corresponding dose of juice groups. According to Figure 1(c), the growth rate of the right-side sebaceous gland of each intervention group was significantly different from that of the MG ($P < 0.05$), while the growth rate of the left-side sebaceous gland of LBO, HBO, HBJ, and sweet orange groups was significantly lower than that of the MG ($P < 0.05$). The growth rate of the sebaceous gland spots in sweet orange essential oil groups was obviously decreased in contrast with the corresponding dose of juice groups ($P < 0.05$). In Figure 1(d), compared with the MG, each intervention group significantly reduced the growth rate of the left-side sebaceous gland spots of the golden hamster ($P < 0.05$). In contrast, only the groups of LBO, HBO, and HBJ could significantly decrease the growth rate of the

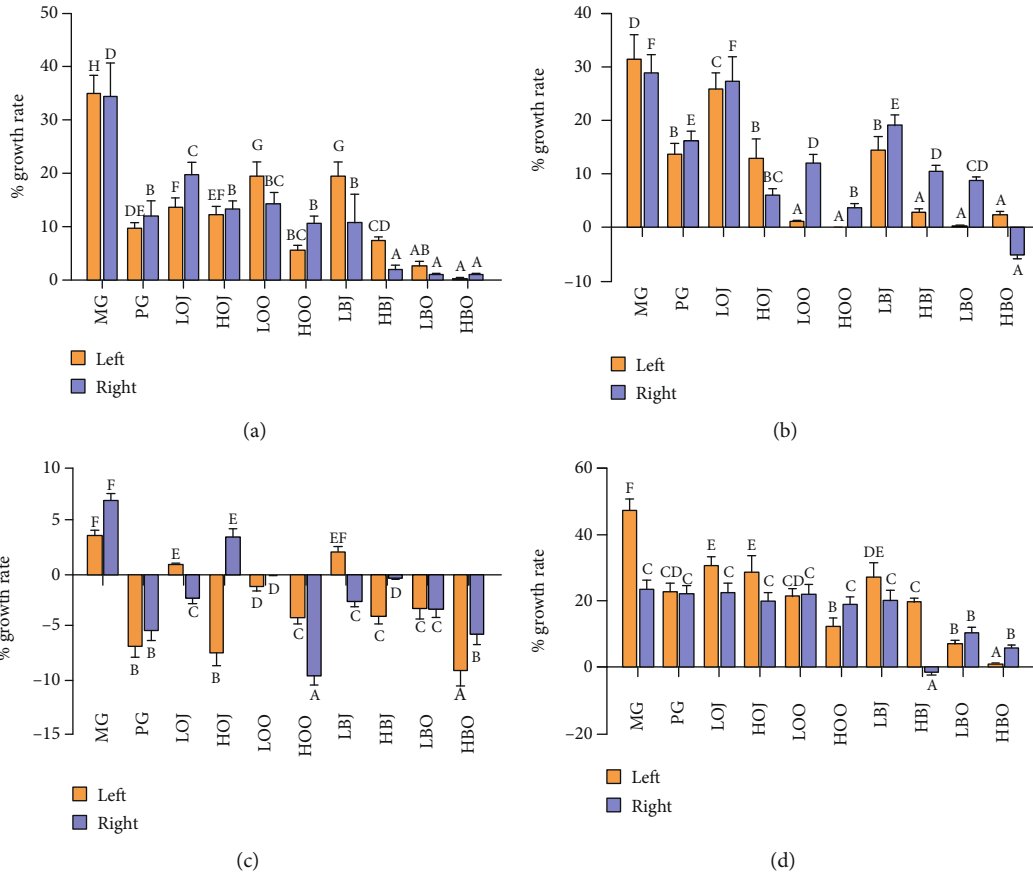


FIGURE 1: Effect of different treatments on the growth rate of sebaceous gland spots: (a) the growth rate of sebaceous gland spots in the first week, (b) the growth rate of sebaceous gland spots in the second week, (c) the growth rate of sebaceous gland spots in the third week, and (d) the growth rate of sebaceous gland spots in the fourth week. Values are expressed as the mean \pm SD ($n = 8$). Data with different letters indicate significant differences ($P < 0.05$).

right-side sebaceous gland spots in contrast with MG ($P < 0.05$). Treatment with sweet orange essential oil could significantly decrease the growth rate of the sebaceous gland spots compared with the corresponding dose of juice groups ($P < 0.05$). Both of bergamot and sweet orange groups exhibited the effect of decreasing the growth rate of sebaceous gland spots with a dose-effect relationship.

3.2. Effect of Different Treatments on the Organ Index in the Golden Hamster. As listed in Table 1, there was no significant difference in the testicular index and spleen index between the intervention groups and MG. These results indicated that the intervention substances did not have adverse effects on the testicular and spleen indexes in golden hamsters.

3.3. Effect of Different Treatments on the Level of Serum T and E_2 in the Golden Hamster. The changes in T level of golden hamsters are shown in Figure 2(a). Compared with the MG, the content of T in each intervention group showed a certain degree of reduction. However, only the bergamot essential oil groups significantly reduced the T level in comparison with MG ($P < 0.05$). Besides, all intervention groups increased the E_2 content compared with MG (shown in Figure 2(b)). But only HOO and HBJ could remarkably

increase the E_2 content compared with MG ($P < 0.05$). These results did not show a statistical difference between the sweet orange groups. In Figure 2(c), data showed that each intervention group lowered the ratio of T/ E_2 in comparison with MG. Among them, the ratio of T/ E_2 in high-dose intervention groups was significantly decreased in comparison with that in MG ($P < 0.05$). The ratio of T/ E_2 in essential oil groups was lower than that in the corresponding dose of juice groups. Both of bergamot and sweet orange groups had shown a dosage-effect relationship.

3.4. Effect of Different Treatments on the Level of TG of Sebaceous Gland Tissue in the Golden Hamster. The results of TG level are shown in Figure 3. Compared with the MG, each intervention group significantly reduced the content of TG in the sebaceous gland of golden hamsters ($P < 0.05$). As can be seen from Figure 3, the TG level in sweet orange essential oil groups was obviously decreased in contrast with the corresponding dose of juice groups ($P < 0.05$). The content of TG in bergamot essential oil groups was lower than that in the corresponding dose of juice groups. Both of bergamot and sweet orange groups exhibited effects on attenuating TG level with a dose-effect relationship.

TABLE 1: Effect of different treatments on the organ index.

Group	Testicular index (mg/g)	Spleen index (mg/g)
MG	34.41 ± 2.09 ^a	0.72 ± 0.05 ^a
PG	32.54 ± 1.33 ^a	0.78 ± 0.09 ^a
LOJ	31.14 ± 2.63 ^a	0.71 ± 0.17 ^a
HOJ	31.87 ± 3.08 ^a	0.78 ± 0.08 ^a
LOO	33.09 ± 2.48 ^a	0.71 ± 0.07 ^a
HOO	34.16 ± 2.39 ^a	0.74 ± 0.08 ^a
LBJ	32.07 ± 2.20 ^a	0.70 ± 0.08 ^a
HBJ	33.57 ± 3.25 ^a	0.71 ± 0.08 ^a
LBO	33.66 ± 2.80 ^a	0.71 ± 0.01 ^a
HBO	34.14 ± 2.60 ^a	0.70 ± 0.11 ^a

Values are expressed as the mean ± SD ($n = 8$). Data with different letters on the same line indicate significant differences ($P < 0.05$).

3.5. Effect of Different Treatments on Inflammatory Factors in the Golden Hamster. In this part, we studied the effect of different treatments in the golden hamster on the level of the serum inflammatory factor (shown in Figure 4). In Figure 4(a), data showed that each intervention group clearly lowered the serum IL-1 α content in comparison with MG ($P < 0.05$). The HBO even lowered the IL-1 α level to about one-fifth of the MG (83 pg/mL and 433 pg/mL, respectively). The IL-1 α level in HOO was obviously reduced relative to that in HOJ. Meanwhile, bergamot groups showed similar results. As shown in Figure 4(b), the content of IL-6 was clearly decreased in HBO, LBO, and HOO groups in contrast with MG ($P < 0.05$). Groups with essential oil could significantly decrease IL-6 level compared with the corresponding dose of juice groups ($P < 0.05$). As shown in Figure 4(c), in addition to LOJ, all other intervention groups significantly reduced TNF- α level ($P < 0.05$). Treatment with low-dose sweet essential oil could significantly reduce TNF- α level relative to that with LOJ ($P < 0.05$). The TNF- α level in essential oil groups was lower than that in the corresponding dose of juice groups. Both of bergamot and sweet orange groups had anti-inflammation effect by a quantity-effect relationship.

3.6. Effect of Different Treatments on the Level of Serum MMPs in the Golden Hamster. We found that each intervention group significantly reduced the MMP-2 content in comparison with the MG ($P < 0.05$). As shown in Figure 5(a), the content of MMP-2 in HOO groups was obviously decreased in contrast with that in HOJ ($P < 0.05$). Groups with bergamot essential oil could significantly decrease MMP-2 level compared with the corresponding dose of juice groups ($P < 0.05$). In Figure 5(b), the content of MMP-9 in the essential oil groups could be reduced to about half of that in the MG. Groups with essential oil could significantly reduce MMP-9 level in contrast with the corresponding dose of juice groups ($P < 0.05$). Both of bergamot and sweet orange groups had attenuating effects on MMP level with a dose-effect relationship.

3.7. Effect of Different Treatments on the Activity of Caspase-3 of Sebaceous Gland Tissue in the Golden Hamster. Caspase-3 levels were determined to assess the effect of different treat-

ments on apoptosis of sebaceous gland cells. As shown in Figure 6, we found that each intervention group significantly increased the relative activity of caspase-3 in comparison with the MG ($P < 0.05$). Groups with essential oil could significantly increase the relative activity in comparison with the corresponding dose of juice groups ($P < 0.05$). Bergamot and sweet orange groups could increase the relative activity of caspase-3 with a dosage-effect relationship.

4. Discussion

Golden hamsters could be used as a model of acne vulgaris caused by the excessive secretion of androgen, which appeared in two sebaceous glands in the lateral abdomen [27]. Therefore, determining the area and thickness of the sebaceous gland can reflect the severity of acne vulgaris in golden hamsters, to a certain extent. It was reported that *Lactobacillus*-fermented *C. obtuse* significantly decreased sebum secretion and size of the sebaceous gland compared with baseline ($0.24 \pm 0.09 \text{ mm}^2$ vs. $0.38 \pm 0.11 \text{ mm}^2$, respectively) [28]. In our study, the size of the sebaceous gland was not reduced with the treatment with bergamot and sweet orange, and the growth rate of sebaceous gland spots decreased instead. It was reported that activating the expression of apoptotic proteins through a series of reactions could ultimately lead to a reduction in the area or thickness of the sebaceous gland [29]. Caspase-3 plays an executing role in the process of apoptosis, and it is also the most important downstream protease of the apoptotic effect and execution process [30]. Inhibition of caspase-3 was reported to attenuate sebaceous gland cell proliferation and organ size [31]. In this study, the growth rate of sebaceous gland spots and caspase-3 activity in golden hamsters with different doses of intervention substances were analyzed. It was found that after 4 weeks of intervention, the growth rate of sebaceous gland spots in each intervention group was significantly decreased compared with that in MG, and caspase-3 activity was significantly increased in comparison with that in MG (Figures 1 and 6). Moreover, the effect of each intervention substance was positively correlated with the dose, and the bergamot essential oil had the best improvement effect. Therefore, it is suggested that bergamot essential oil, bergamot juice, sweet orange essential oil, and sweet orange juice may alleviate acne vulgaris by promoting the apoptosis of sebaceous gland cells in the golden hamster through enhancing the activity of caspase-3.

The secretion of androgen plays an important role in the occurrence and development of acne lesions [11]. Excessive androgen secretion or imbalance of androgen and estrogen levels can lead to sebaceous gland hyperplasia, excessive sebum secretion, and abnormal keratinization of the hair follicle sebaceous gland, resulting in the development and continuous occurrence of acne vulgaris [32]. High-dose estrogen exerted a negative feedback on the gonadal axis, which could result in the reduction of sebum formation [33]. Evidence showed that higher content of free T with lower level of E₂ was significantly in favor of severe acne vulgaris [34]. Thus, balancing the ratio between androgens and estrogens could help alleviate or treat acne vulgaris. In

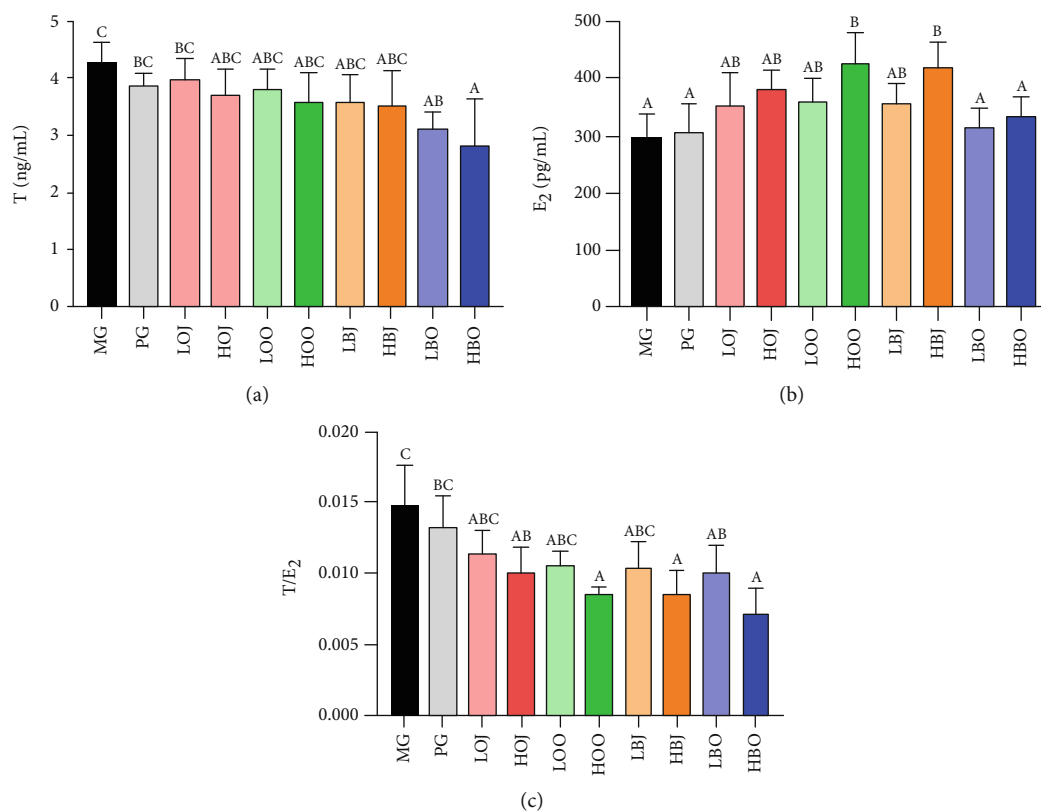


FIGURE 2: Effect of different treatments on serum sex hormone levels: (a) serum T level, (b) serum E₂ level, and (c) the ratio of T/E₂. Values are expressed as the mean \pm SD ($n = 8$). Significance was defined as $P < 0.05$.

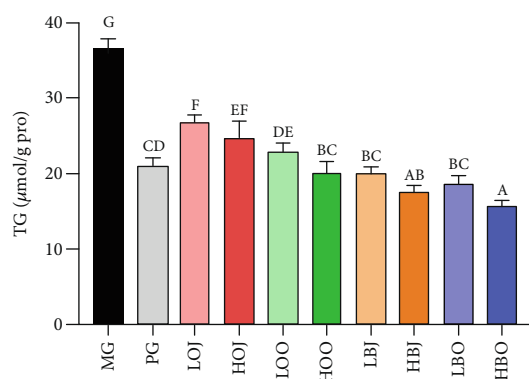


FIGURE 3: Effect of different treatments on the level of TG. Values are expressed as the mean \pm SD ($n = 8$). Data with different letters indicate significant differences ($P < 0.05$).

our study, the bergamot essential oil significantly reduced the serum T content in golden hamsters, while HOO and HOJ groups markedly increased the serum E₂ level (Figures 2(a) and 2(b)). This indicated that sweet orange essential oil and bergamot essential oil could improve acne lesions via directly reducing the androgen level or decreasing the androgen/estrogen ratio (Figure 2(c)).

Sebum is synthesized and secreted by sebaceous gland cells, consisting of TG, nonesterified fatty acid, wax ester, squalene, and cholesterol ester [35]. Since sebum contains

approximately 30% TG, the amount of sebum synthesis and secretion was reflected in the study by measuring the TG content in the sebaceous gland tissue of golden hamsters. The study found that bergamot essential oil, bergamot juice, sweet orange essential oil, and sweet orange juice can significantly reduce the TG content of golden hamsters, indicating that each intervention substance can improve acne vulgaris via restraining TG level to a certain extent (Figure 3). Besides, the bergamot essential oil, bergamot juice, sweet orange juice, and sweet orange essential oil exhibited a dose-dependent effect on inhibiting TG accumulation.

Inflammation is an initial host immune reaction which is mediated by inflammatory factors [36]. The induction of inflammation mediators is associated with *P. acnes* [37]. *P. acnes* and associated cellular membrane lipopolysaccharides could induce the expression of IL-8, TNF, and IL-1 α in cultured sebocytes [38]. The underlying mechanisms are that sebocytes can be recognized and activated by *P. acnes*, which further trigger the release of inflammatory cytokines [39]. TNF- α is an extensively studied cytokine associated with many inflammatory diseases [40]. Evidences indicated that IL-1 α is one of the main inflammatory factors, which could induce the proliferation of keratinocytes and sebaceous gland cells and eventually promote the formation of acne vulgaris [41]. Moreover, increased IL-1 contents could further promote the expression of MMPs and lipid synthesis [42, 43]. MMPs have been suggested to be involved in acne vulgaris, and different levels of MMP expression could contribute to

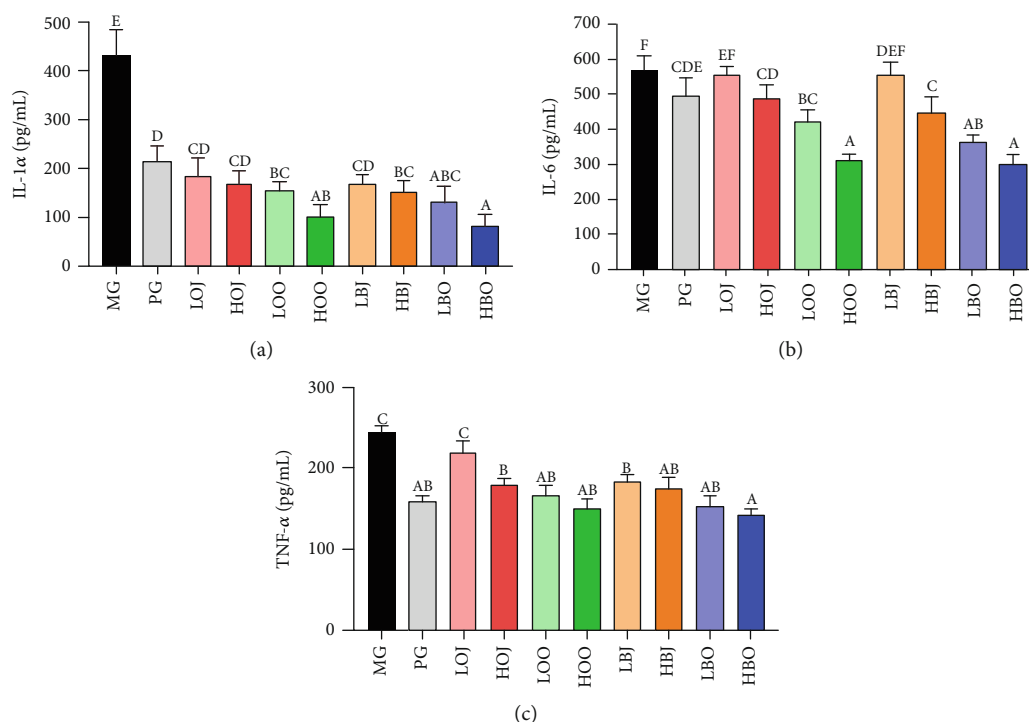


FIGURE 4: Effect of different treatments on the level of serum inflammatory factors in the golden hamster: (a) IL-1 α level, (b) IL-6 level, and (c) TNF- α level. Values are expressed as the mean \pm SD ($n = 8$). Data with different letters indicate significant differences ($P < 0.05$).

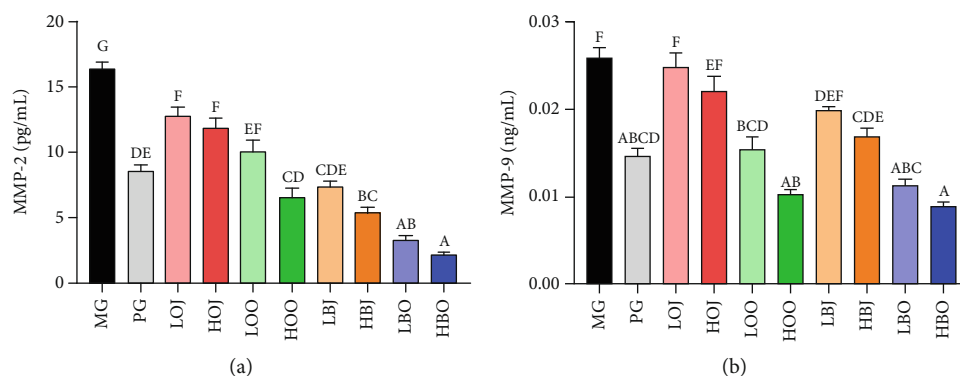


FIGURE 5: Effect of different treatments on the level of serum MMP-2 and MMP-9 in the golden hamster: (a) MMP-2 level and (b) MMP-9 level. Values are expressed as the mean \pm SD ($n = 8$). Significance was defined as $P < 0.05$.

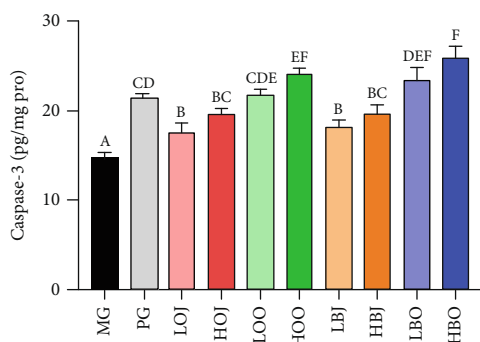


FIGURE 6: Effect of different treatments in the golden hamster on the activity of caspase-3. Values are expressed as the mean \pm SD ($n = 8$). Significance was defined as $P < 0.05$.

the development of different types of acne lesions [44–46]. Keratinocytes are an important source of MMPs in acne vulgaris, and *P. acnes* can induce the expression of several kinds of MMPs, including MMP-2 and MMP-9 [47]. Kim et al. reported that *Citrus obovoides* and *Citrus natsudaidai* essential oils could reduce *P. acnes*-induced secretion of IL-8 and TNF- α [48]. In one study, a *Lactobacillus*-fermented *Chamaecyparis obtusa* leaf extract was reported to have a great effect on inflammatory markers, such as IL-8, IL-1, and NF- κ B [28]. Also, previous studies reported that essential oil and juice could alleviate acne vulgaris based on their antibacterial effect [49, 50]. In our study, results showed that bergamot essential oil, bergamot juice, sweet orange essential oil, and sweet orange juice could reduce the levels of IL-6, TNF- α , MMP-2, MMP-9, and especially IL-1 α , indicating

that bergamot essential oil, bergamot juice, sweet orange essential oil, and sweet orange juice could improve acne vulgaris through alleviating inflammatory response and suppressing *P. acnes* in golden hamsters (Figures 4 and 5).

5. Conclusions

In summary, bergamot essential oil, bergamot juice, sweet orange essential oil, and sweet orange juice could improve acne vulgaris caused by excessive secretion of androgen via reducing the growth rate of the sebaceous gland, inhibiting TG accumulation and inflammatory cytokines release in the sebaceous gland, promoting apoptosis in the sebaceous gland, and decreasing the ratio of T/E₂. In general, bergamot essential oil and sweet orange essential oil may have better effects on alleviating acne vulgaris than the corresponding juice. Among them, the levels of IL-1 α in the sebaceous gland could be best reduced in both bergamot and sweet orange. This implies that bergamot and sweet orange may improve acne lesions via alleviating inflammatory response and suppressing *P. acnes*, but further studies of the mechanism are needed.

Data Availability

The data used to support the findings of this study are available from the corresponding author upon request.

Conflicts of Interest

The authors declare that there is no conflict of interest regarding the publication of this paper.

Authors' Contributions

Liebing Zhang and Baoping Ji designed the experiments. Liang Zhao, Arshad Mehmood, and Peng Sun conducted the research. Chengtao Wang and Nanhai Zhang analyzed the data. Baoping Ji and Wei Wu provided reagents/materials/analysis tools. Peng Sun and Liang Zhao wrote the paper. Feng Zhou had primary responsibility for the final content. All authors read and approved the final manuscript. Peng Sun and Liang Zhao contributed equally to this work.

Acknowledgments

This work was supported by the National Natural Science Foundation of China (grant number 31571831) and the fund of China Postdoctoral Science Foundation (grant number 2019TQ0011).

References

- [1] D. Meixner, S. Schneider, M. Krause, and W. Sterry, "Acne inversa," *JDDG: Journal der Deutschen Dermatologischen Gesellschaft*, vol. 6, no. 3, pp. 189–196, 2008.
- [2] A. R. Shalita, "Acne: clinical presentations," *Clinics in Dermatology*, vol. 22, no. 5, pp. 385–386, 2004.
- [3] F. M. C. de Vries, A. M. Meulendijks, R. J. B. Driessen, A. A. van Dooren, E. P. M. Tjin, and P. C. M. van de Kerkhof, "The efficacy and safety of non-pharmacological therapies for the treatment of acne vulgaris: a systematic review and best-evidence synthesis," *Journal of the European Academy of Dermatology and Venereology*, vol. 32, no. 7, pp. 1195–1203, 2018.
- [4] H. C. Williams, R. P. Dellavalle, and S. Garner, "Acne vulgaris," *The Lancet*, vol. 379, no. 9813, pp. 361–372, 2012.
- [5] J. K. L. Tan, L. F. Stein Gold, A. F. Alexis, and J. C. Harper, "Current concepts in acne pathogenesis: pathways to inflammation," *Seminars in Cutaneous Medicine and Surgery*, vol. 37, no. 3S, pp. S60–S62, 2018.
- [6] B. Dreno, H. Gollnick, S. Kang et al., "Understanding innate immunity and inflammation in acne: implications for management," *Journal of the European Academy of Dermatology and Venereology*, vol. 29, pp. 3–11, 2015.
- [7] M. Aghasi, M. Golzarand, S. Shab-Bidar, A. Aminianfar, M. Omidian, and F. Taheri, "Dairy intake and acne development: a meta-analysis of observational studies," *Clinical Nutrition*, vol. 38, no. 3, pp. 1067–1075, 2019.
- [8] R. Smith, N. Mann, H. Mäkeläinen, J. Roper, A. Braue, and G. Varigos, "A pilot study to determine the short-term effects of a low glycemic load diet on hormonal markers of acne: a nonrandomized, parallel, controlled feeding trial," *Molecular Nutrition & Food Research*, vol. 52, no. 6, pp. 718–726, 2008.
- [9] A. L. Zaenglein, A. L. Pathy, B. J. Schlosser et al., "Guidelines of care for the management of acne vulgaris," *Journal of the American Academy of Dermatology*, vol. 74, no. 5, pp. 945–973.e33, 2016.
- [10] D. Thiboutot, H. Gollnick, V. Bettoli et al., "New insights into the management of acne: an update from the Global Alliance to Improve Outcomes in Acne Group," *Journal of the American Academy of Dermatology*, vol. 60, no. 5, pp. S1–S50, 2009.
- [11] H. Nasri, M. Bahmani, N. Shahinfard, A. Moradi Nafchi, S. Saberianpour, and M. Rafieian Kopaei, "Medicinal plants for the treatment of acne vulgaris: a review of recent evidences," *Jundishapur Journal of Microbiology*, vol. 8, no. 11, article e25580, 2015.
- [12] D. Scuteri, M. Crudo, L. Rombolà et al., "Antinociceptive effect of inhalation of the essential oil of bergamot in mice," *Fitoterapia*, vol. 129, pp. 20–24, 2018.
- [13] X. Wang, Y. Xu, S. Zhang et al., "Genomic analyses of primitive, wild and cultivated citrus provide insights into asexual reproduction," *Nature Genetics*, vol. 49, no. 5, pp. 765–772, 2017.
- [14] F. Liao, Y. Wang, M. Chen et al., "Low transcription of *CmsIAA9* in the basal pistil is related to parthenocarpic fruiting of fingered citron (Foshou)," *Molecular Breeding*, vol. 37, no. 8, 2017.
- [15] S. Song, Y. Tong, T. Feng, and J. Zhu, "Multi-analysis of odorous compounds in finger citron (*Citrus medica* L. var. *sarcodactylis* Swingle) and certification of key compounds," *Journal of Essential Oil Bearing Plants*, vol. 21, no. 3, pp. 600–613, 2018.
- [16] D. Impellizzeri, M. Cordaro, M. Campolo et al., "Anti-inflammatory and antioxidant effects of flavonoid-rich fraction of bergamot juice (BJe) in a mouse model of intestinal ischemia/reperfusion injury," *Frontiers in Pharmacology*, vol. 7, 2016.
- [17] X. Han, C. Beaumont, and N. Stevens, "Chemical composition analysis and *in vitro* biological activities of ten essential oils in human skin cells," *Biochimie Open*, vol. 5, pp. 1–7, 2017.
- [18] M. Shui, T. Feng, Y. Tong et al., "Characterization of key aroma compounds and construction of flavor base module of Chinese sweet oranges," *Molecules*, vol. 24, no. 13, 2019.

- [19] H. Ghanim, C. L. Sia, S. Abuaysheh et al., "An antiinflammatory and reactive oxygen species suppressive effects of an extract of *Polygonum cuspidatum* containing resveratrol," *The Journal of Clinical Endocrinology and Metabolism*, vol. 95, no. 9, pp. E1–E8, 2010.
- [20] T. Hata, I. Sakaguchi, M. Mori et al., "Induction of apoptosis by *Citrus paradisi* essential oil in human leukemic (HL-60) cells," *In Vivo*, vol. 17, no. 6, pp. 553–559, 2003.
- [21] M. Viuda-Martos, Y. Ruiz-Navajas, J. Fernández-López, and J. Pérez-Álvarez, "Antifungal activity of lemon (*Citrus lemon* L.), mandarin (*Citrus reticulata* L.), grapefruit (*Citrus paradisi* L.) and orange (*Citrus sinensis* L.) essential oils," *Food Control*, vol. 19, no. 12, pp. 1130–1138, 2008.
- [22] H. Kawai, S. Tanaka, C. Nakamura, T. Ishibashi, and A. Mitsumoto, "Effects of essential oil inhalation on objective and subjective sleep quality in healthy university students," *Sleep and Biological Rhythms*, vol. 16, no. 1, pp. 37–44, 2018.
- [23] G. Matiz, M. R. Osorio, F. Camacho, M. Atencia, and J. Herazo, "Effectiveness of antimicrobial formulations for acne based on orange (*Citrus sinensis*) and sweet basil (*Ocimum basilicum* L.) essential oils," *Biomédica*, vol. 32, no. 1, pp. 125–133, 2012.
- [24] P. A. Wuest and A. W. Lucky, "Differential effect of testosterone on pigmented spot, sebaceous glands and hair follicles in the Syrian hamster flank organ," *Skin Pharmacology and Physiology*, vol. 2, no. 2, pp. 103–113, 1989.
- [25] L. Zhao, J. Qiu, X. Yin et al., "Blossom and bee pollen from *Rosa rugosa* as potential intervention for acne caused by excessive androgen secretion in golden hamster acne model," *Food and Agricultural Immunology*, vol. 30, no. 1, pp. 1174–1188, 2019.
- [26] L. Li, L. Tang, E. Baranov et al., "Selective induction of apoptosis in the hamster flank sebaceous gland organ by a topical liposome 5- α -reductase inhibitor: a treatment strategy for acne," *The Journal of Dermatology*, vol. 37, no. 2, pp. 156–162, 2010.
- [27] I. Vega-Naredo, C. Tomas-Zapico, and A. Coto-Montes, "Potential role of autophagy in behavioral changes of the flank organ," *Autophagy*, vol. 5, no. 2, pp. 265–267, 2009.
- [28] H. H. Kwon, J. Y. Yoon, S. Y. Park, S. Min, and D. H. Suh, "Comparison of clinical and histological effects between *Lactobacillus*-fermented *Chamaecyparis obtusa* and tea tree oil for the treatment of acne: an eight-week double-blind randomized controlled split-face study," *Dermatology*, vol. 229, no. 2, pp. 102–109, 2014.
- [29] E. C. Gomez, "Hamster flank organ: assessment of drugs modulating sebaceous gland function," *Karger Basle*, vol. 2, pp. 100–111, 1985.
- [30] T. R. van de Water, F. Lallemand, A. Eshraghi et al., "Caspases, the enemy within, and their role in oxidative stress-induced apoptosis of inner ear sensory cells," *Otology & Neurotology*, vol. 25, no. 4, pp. 627–632, 2004.
- [31] Y. Yosefzon, D. Soteriou, A. Feldman et al., "Caspase-3 regulates YAP-dependent cell proliferation and organ size," *Molecular Cell*, vol. 70, no. 4, pp. 573–587.e4, 2018.
- [32] E. Giltay and L. Gooren, "Effects of sex steroid deprivation/administration on hair growth and skin sebum production in transsexual males and females," *The Journal of Clinical Endocrinology and Metabolism*, vol. 85, no. 8, pp. 2913–2921, 2000.
- [33] M. L. Elsaie, "Hormonal treatment of acne vulgaris: an update," *Clinical, Cosmetic and Investigational Dermatology*, vol. 9, pp. 241–248, 2016.
- [34] B. Wei, L. Qu, H. Zhu et al., "Higher 17 α -hydroxyprogesterone levels aggravated the severity of male adolescent acne in Northeast China," *The Journal of Dermatology*, vol. 229, no. 4, pp. 359–362, 2014.
- [35] R. S. Greene, D. T. Downing, P. E. Pochi, and J. S. Strauss, "Anatomical variation in the amount and composition of human skin surface lipid," *The Journal of Investigative Dermatology*, vol. 54, no. 3, pp. 240–247, 1970.
- [36] K.-N. Kim, Y.-J. Ko, H.-M. Yang et al., "Anti-inflammatory effect of essential oil and its constituents from fingered citron (*Citrus medica* L. var. *sarcodactylis*) through blocking JNK, ERK and NF- κ B signaling pathways in LPS-activated RAW 264.7 cells," *Food and Chemical Toxicology*, vol. 57, pp. 126–131, 2013.
- [37] S. M. Tuchayi, E. Makrantonaki, R. Ganceviciene, C. Dessinioti, S. R. Feldman, and C. C. Zouboulis, "Acne vulgaris," *Nature Reviews Disease Primers*, vol. 1, no. 1, article 15029, pp. 1–20, 2015.
- [38] I. Nagy, A. Pivarcsi, K. Kis et al., "Propionibacterium acnes and lipopolysaccharide induce the expression of antimicrobial peptides and proinflammatory cytokines/chemokines in human sebocytes," *Microbes and Infection*, vol. 8, no. 8, pp. 2195–2205, 2006.
- [39] J. L. Selway, T. Kurczab, T. Kealey, and K. Langlands, "Toll-like receptor 2 activation and comedogenesis: implications for the pathogenesis of acne," *BMC Dermatology*, vol. 13, no. 1, 2013.
- [40] K. Wang, Z. Wan, A. Ou et al., "Monofloral honey from a medical plant, *Prunella vulgaris*, protected against dextran sulfate sodium-induced ulcerative colitis via modulating gut microbial populations in rats," *Food & Function*, vol. 10, no. 7, pp. 3828–3838, 2019.
- [41] M. D. Farrar and E. Ingham, "Acne: inflammation," *Clinics in Dermatology*, vol. 22, no. 5, pp. 380–384, 2004.
- [42] A. Lomri, J. Lemonnier, P. Delannoy, and P. Marie, "Increased expression of protein kinase Ca, interleukin-1 α , and RhoA guanosine 5'-triphosphatase in osteoblasts expressing the Ser252Trp fibroblast growth factor 2 Apert mutation: identification by analysis of complementary DNA microarray," *Journal of Bone and Mineral Research*, vol. 16, no. 4, pp. 705–712, 2001.
- [43] K. Wang, X. Jin, Q. Li et al., "Propolis from different geographic origins decreases intestinal inflammation and Bacteroides spp. Populations in a Model of DSS-Induced Colitis," *Molecular Nutrition & Food Research*, vol. 62, no. 17, article 1800080, 2018.
- [44] W. Lee, H. Jung, H. Lim, Y. H. Jang, S. J. Lee, and D. W. Kim, "Serial sections of atrophic acne scars help in the interpretation of microscopic findings and the selection of good therapeutic modalities," *Journal of the European Academy of Dermatology and Venereology*, vol. 27, no. 5, pp. 643–646, 2013.
- [45] M. Saint-Jean, A. Khammari, F. Jasson, J.-M. Nguyen, and B. Dréno, "Different cutaneous innate immunity profiles in acne patients with and without atrophic scars," *European Journal of Dermatology*, vol. 26, no. 1, pp. 68–74, 2016.
- [46] S. Ozkanli, A. S. Karadag, E. Ozlu et al., "A comparative study of MMP-1, MMP-2, and TNF- α expression in different acne vulgaris lesions," *International Journal of Dermatology*, vol. 55, no. 12, pp. 1402–1407, 2016.
- [47] S. E. Lee, J.-M. Kim, S. K. Jeong et al., "Protease-activated receptor-2 mediates the expression of inflammatory cytokines,

- antimicrobial peptides, and matrix metalloproteinases in keratinocytes in response to *Propionibacterium acnes*,” *Archives of Dermatological Research*, vol. 302, no. 10, pp. 745–756, 2010.
- [48] S.-S. Kim, J. S. Baik, T.-H. Oh, W.-J. Yoon, N. H. Lee, and C.-G. Hyun, “Biological activities of Korean *Citrus obovoides* and *Citrus natsudaoides* essential oils against acne-inducing bacteria,” *Bioscience, Biotechnology, and Biochemistry*, vol. 72, no. 10, pp. 2507–2513, 2008.
- [49] M. E. Ahmed, “The study of bacteriocin of *Pseudomonas fluorescens* and *Citrus limon* effects against *Propionibacterium acnes* and *Staphylococcus epidermidis* in acne patients,” *Journal of Physics: Conference Series*, vol. 1003, article 012004, 2018.
- [50] S. Deyno, A. G. Mtewa, A. Abebe et al., “Essential oils as topical anti-infective agents: a systematic review and meta-analysis,” *Complementary Therapies in Medicine*, vol. 47, article 102224, 2019.

Research Article

Metabolic Profiling by UPLC–Orbitrap–MS/MS of Liver from C57BL/6 Mice with DSS-Induced Inflammatory Bowel Disease

Zhongquan Xin,¹ Zhenya Zhai,² Hongrong Long,¹ Fan Zhang,¹ Xiaojun Ni,³ Jinping Deng,¹ Lunzhao Yi^{ID},⁴ and Baichuan Deng^{ID}¹

¹Maoming Branch, Guangdong Laboratory for Lingnan Modern Agriculture, Guangdong Provincial Key Laboratory of Animal Nutrition Control, National Engineering Research Center for Breeding Swine Industry, College of Animal Science, South China Agricultural University, Guangzhou, China

²Institute of Biological Resource, Jiangxi Academy of Sciences, Nanchang 330029, China

³Yunnan Animal Science and Veterinary Institute, Jindian, Panlong County, Kunming City, Yunnan Province, China

⁴Yunnan Food Safety Research Institute, Kunming University of Science and Technology, Kunming 650500, China

Correspondence should be addressed to Lunzhao Yi; yilunzhao@kmust.edu.cn and Baichuan Deng; dengbaichuan@scau.edu.cn

Received 14 July 2020; Revised 28 August 2020; Accepted 31 August 2020; Published 23 September 2020

Academic Editor: Xin Zong

Copyright © 2020 Zhongquan Xin et al. This is an open access article distributed under the Creative Commons Attribution License, which permits unrestricted use, distribution, and reproduction in any medium, provided the original work is properly cited.

Liver disorder often occurs in patients with inflammatory bowel disease (IBD); however, the changes in IBD-induced liver disorder at the intrinsic molecular level (chiefly metabolites) and therapeutic targets are still poorly characterized. First, a refined and translationally relevant model of DSS chronic colitis in C57BL/6 mice was established, and cecropin A and antibiotics were used as interventions. We found that the levels of tumor necrosis factor (TNF)- α , interleukin (IL)-1 β , and IL-6 in the liver tissues of mice were highly increased in the context of DSS treatment but were lowered by cecropin A and antibiotics. Subsequently, an untargeted metabolomics analysis was performed by UPLC–Orbitrap–MS/MS to reveal the metabolic profile and attempt to find the potential therapeutic targets of the liver disorders that occur in IBD. Notably, 133 metabolites were identified by an integrated database. Metabolism network and pathway analyses demonstrated that the metabolic disturbance of the liver in IBD mice was mainly enriched in bile acid metabolism, arachidonic acid metabolism, amino acid metabolism, and steroid hormone biosynthesis, while those disturbances were regulated or reversed through cecropin A and antibiotic treatment. Furthermore, the top 20 metabolites, such as glutathione, maltose, arachidonic acid, and thiamine, were screened as biomarkers via one-way analysis of variance (one-way ANOVA, $p < 0.05$) coupled with variable importance for project values (VIP > 1) of orthogonal partial least-squares discriminant analysis (OPLS-DA), which could be upregulated or downregulated with the cecropin A and antibiotics treatment. Spearman correlation analysis showed that the majority of the biomarkers have a significant correlation with cytokines (TNF- α , IL-1 β , IL-6, and IL-10), indicating that those biomarkers may act as potential targets to interact directly or indirectly with cecropin A and antibiotics to affect liver inflammation. Collectively, our results extend the understanding of the molecular alteration of liver disorders occurring in IBD and offer an opportunity for discovering potential therapeutic targets in the IBD process.

1. Introduction

Inflammatory bowel disease (IBD) is a complex chronic disease of the gastrointestinal tract, including Crohn's disease (CD) and ulcerative colitis (UC) [1]. As a systemic disorder, IBD has been associated with many extraintestinal manifestations (EIMs) involving almost all organ systems, including the musculoskeletal, dermatologic, renal, hepatobiliary, pul-

monary, and ocular systems [2]. The liver is the main metabolic organ that could interact with the intestinal tract directly through the hepatic hilum and/or bile secretion system; therefore, liver disorder is frequently observed in IBD and along with various hepatobiliary diseases, including fatty liver, autoimmune hepatitis, and cirrhosis [3]. It has been estimated that approximately 5% of patients with IBD develop serious liver diseases [4].

The invasion of pernicious bacteria such as *Escherichia coli* (*E. coli*) and *Salmonella* and/or the destruction of intestinal microbial structure is the main trigger of IBD [5]. Recent studies have found that intestinal metabolome disorders in patients with IBD are characterized by metabolic disorders of short-chain fatty acids, bile acids, and tryptophan [6], which are often correlated with liver metabolism [7–9]. It has been well accepted that antibiotics are commonly used to relieve IBD through the elimination of harmful bacteria and reduction of inflammation [10, 11]. Moreover, we also found that an antimicrobial peptide (cecropin A) can alleviate IBD [12]. Despite scientific advances in pathology studies on liver disorders associated with IBD, its metabolic and potential therapeutic targets are still obscure.

There are numerous ways (e.g., RT-qPCR and ELISA) to detect the liver response to exogenous stimuli; however, these methods only partially illustrate the changes in liver, and are thus limited and not comprehensive to evaluate the liver response to stimuli. Metabolomics is a popular technology and powerful high-throughput platform that can identify and quantify metabolites in organisms and find the relationship between metabolites and physiological/pathological changes [13, 14]. Ultrahigh-performance liquid chromatography coupled with high-resolution mass spectrometry (UPLC-HRMS) is one of the most efficient and robust methods of generating metabolite profiles for biological samples because of its high throughput, resolution, and sensitivity [15, 16]. To further understand the biological basis of the responses of the liver, it is necessary to explore the metabolic biology of IBD mice induced by DSS.

In the present study, an IBD model was established in C57BL/6 mice to induce liver inflammation, and cecropin A and antibiotics were used as interventions. ELISA was used to evaluate the inflammation of the liver based on the concentration of cytokines (TNF- α , IL-1 β , and IL-6). The control group, the DSS group, the CA group (DSS + cecropin A treatment), and the GA group (DSS + antibiotics treatment) were used for untargeted metabolic analysis performed on a UPLC-Orbitrap-MS/MS. We aimed to reveal the metabolic profile of the liver in IBD and acquire biomarkers and potential therapeutic targets by metabolic pathway analysis.

2. Methods

2.1. Animals. Thirty-six C57BL/6 mice (7 ~ 8 weeks old) were kept in a mouse room without specific pathogens with a relative humidity of 45~60% and a 12 h/day lighting cycle (7:00 AM~7:00 PM for light) at $25 \pm 1^\circ\text{C}$ and divided into four groups ($n = 9$ mice per group). The refined and translationally relevant model of DSS chronic colitis in C57BL/6 mice was established by giving water containing 2.5% DSS for 5 days. After that, mice were intraperitoneally injected with or without cecropin A (15 mg/kg) or gentamicin (5 mg/kg) for 5 days. All mice were weighed every day and permitted ad libitum access to feed and water. All mice were sacrificed with CO₂ inhalation (1 L/min, 5 min) followed by cervical dislocation to ensure death on the eighth day. The colon and liver of each mouse were collected for further processing.

The experimental design and procedures in this study were reviewed and approved by the Animal Care and Use Committee of the Institute of Subtropical Agriculture, Chinese Academy of Science (No.ISA-2018-035).

2.2. Chemicals and Reagents. Acetonitrile (LC-MS grade) and methanol (LC-MS grade) were purchased from Merck. Formic acid (LC-MS grade), gentamicin and dextran sulfate sodium (DSS, Mw 36,000~50,000) were purchased from J&K Scientific Limited. Cecropin A was synthesized by a peptide company (DgPeptides Co., Ltd., Hangzhou, China). Ultra-pure water was prepared from the ELGA system (RIGHTLEDER International Holding Group Limited).

2.3. Histopathological Examination. Tissue histological analysis was performed with hematoxylin and eosin (H&E). Fragments of the liver and colon were fixed in 4% neutral polyformaldehyde fixative, followed by dehydration, embedding in paraffin, cutting into 5- μm slices, deparaffinization, hydration and staining. Thereafter, all tissue sections were examined by microscopy.

2.4. Elisa. To verify the liver disorder caused by IBD and the recovery effect of cecropin A and gentamicin, the levels of the cytokines TNF- α , IL-1 β , IL-6, and IL-10 in the liver were detected by enzyme-linked immunosorbent assay (ELISA). Briefly, the liver tissues were weighed and homogenized in cold saline containing 0.1 mM phenylmethyl sulfonyl fluoride (PMSF), and the levels of cytokines were measured by commercial kits following the protocols (CUSABIO, Wuhan, China). The total protein was adjusted by the BCA assay kit (Thermo, Waltham, MA, USA).

2.5. Metabolite Extraction and Quality Control Sample. All of the tested liver samples were cut on dry ice and weighed. Liver tissue (~40 mg) was homogenized with a freeze tissue grinder, and homogenate (200 μL) was moved to 1.5-mL EP tubes and mixed with 800 μL of methanol/acetonitrile (1 : 1, v/v). The samples were vortexed for 30 s and centrifuged at 14,500 rpm for 15 min at 4°C . The supernatant was evaporated to dryness using nitrogen blowing followed by reconstitution with 100 μL of acetonitrile/water (1 : 1, v/v). Finally, the solution was filtered with a 0.22- μm membrane and used for UPLC-HRMS analysis.

The quality control (QC) sample was prepared by mixing equal volumes of different individual liver samples. A QC sample was inserted into every five samples during UPLC-HRMS analysis. The reproducibility and reliability of the method were assessed by the coefficients of variation (CV%) of metabolites from QC samples.

2.6. HRMS Analysis. The UPLC system was combined with a Q-Orbitrap mass spectrometer (Thermo Fisher Scientific, Q-Exactive Focus). A total of 2 μL of sample solution was separated using a C18 column at 35°C with a linear gradient elution with 0.2% (v/v) formic acid solution (eluent A) and acetonitrile (eluent B) at a flow rate of 0.2 mL/min. A total 20-minute gradient program was set as follows: 0–8 min, 5–75% B; 8–11 min, 75–90% B; 11–15 min, 90–95% B, equilibration time of 5 min at 5% B. Xcalibur (version

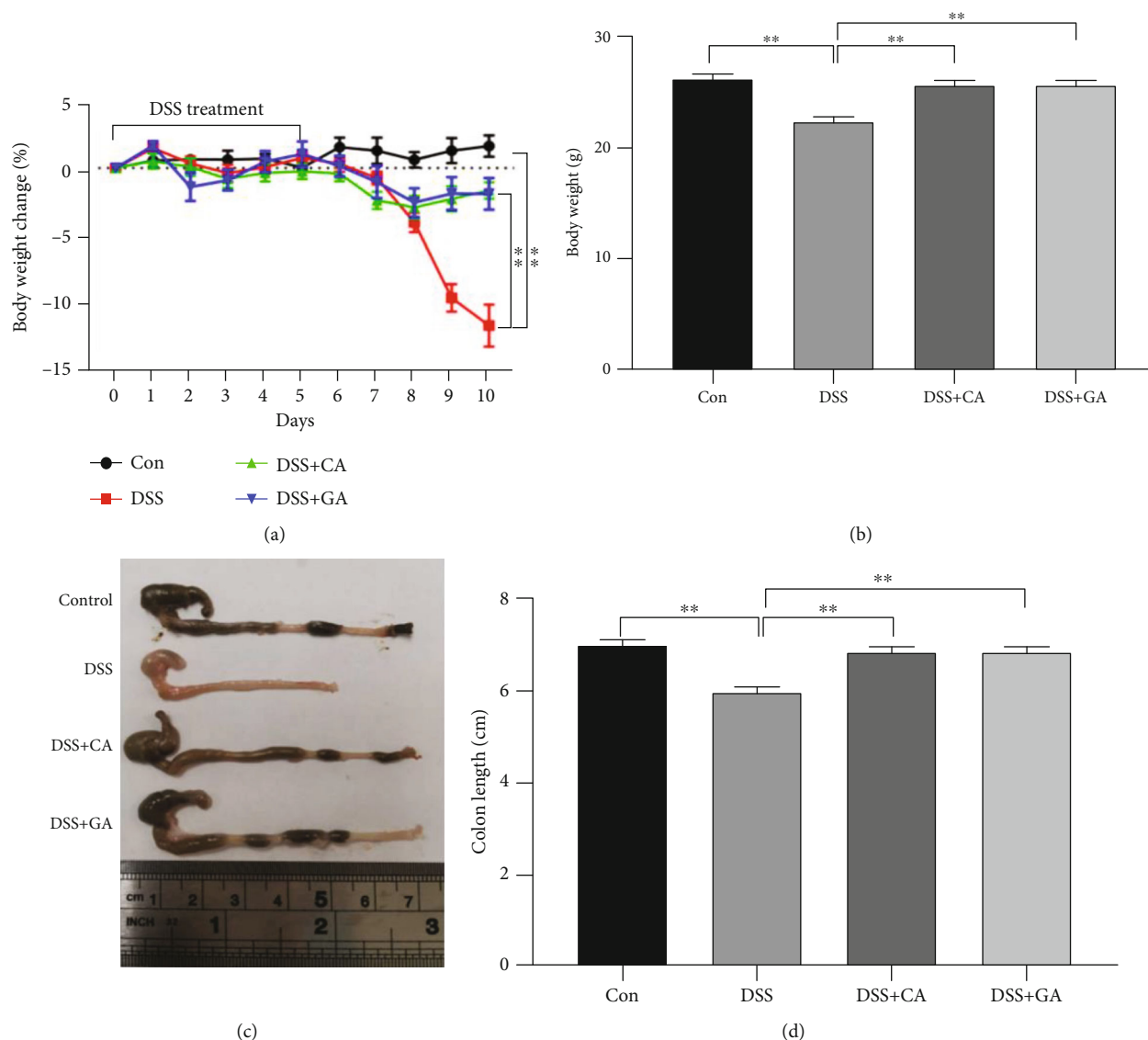


FIGURE 1: The effect of cecropin A and antibiotic treatment in 2.5% DSS-treated mice on body weight (a and b) and colon length (c and d). The data were analyzed by one-way ANOVA ($n = 9$) and are shown as the mean \pm SEM with $*P < 0.05$, $**P < 0.01$, $***P < 0.001$ versus DSS.

3.0) was utilized for instrument control, data acquisition, and data analysis.

The MS analyses were conducted using electrospray ionization (ESI) modes and a full MS (m/z 70 to 1000) scan in positive ionization at a resolution of 35000. The ion spray voltage and heater temperature were kept at 3.5 kV and 300°C. MS/MS data were acquired using a data-dependent ms^2 scan (dd- ms^2) at a resolution of 17,000, and high collision-induced dissociation voltage (HCD) was set as a normalization stepped mode of 10, 30, 50.

2.7. Data Preprocessing and Metabolite Identification. Analytical instruments usually do not supply clean and visualized information on metabolites. Raw data must be processed to produce a workable data matrix through series preprocessing. These experiments were performed on the Compound Discoverer 2.1 (CD, Thermo Fisher Scientific) data analysis

tool, which is flexible and able to automate complete preprocessing according to presupposed parameters. The CD has integrated various tools to identify small molecule metabolites, including search mzCloud (online spectral library >2 million spectra), ChemSpider (chemical structure database with >500 data sources, 58 million structures), mzVault (local spectral libraries), and Masslist (local databases). Data preprocessing and metabolite identification were completed by one-stop.

2.8. Statistical Analysis. Data in the current study were analyzed by one-way ANOVA using GraphPad Prism 6 (GraphPad Software LLC, San Diego, CA, USA) and SPSS 22.0 (SPSS Inc., Chicago, IL, USA) software, and all the data are shown as the mean \pm standard error of the mean (SEM). Principal component analysis (PCA) and hierarchical cluster analysis (HCA) coupled with orthogonal partial least-squares

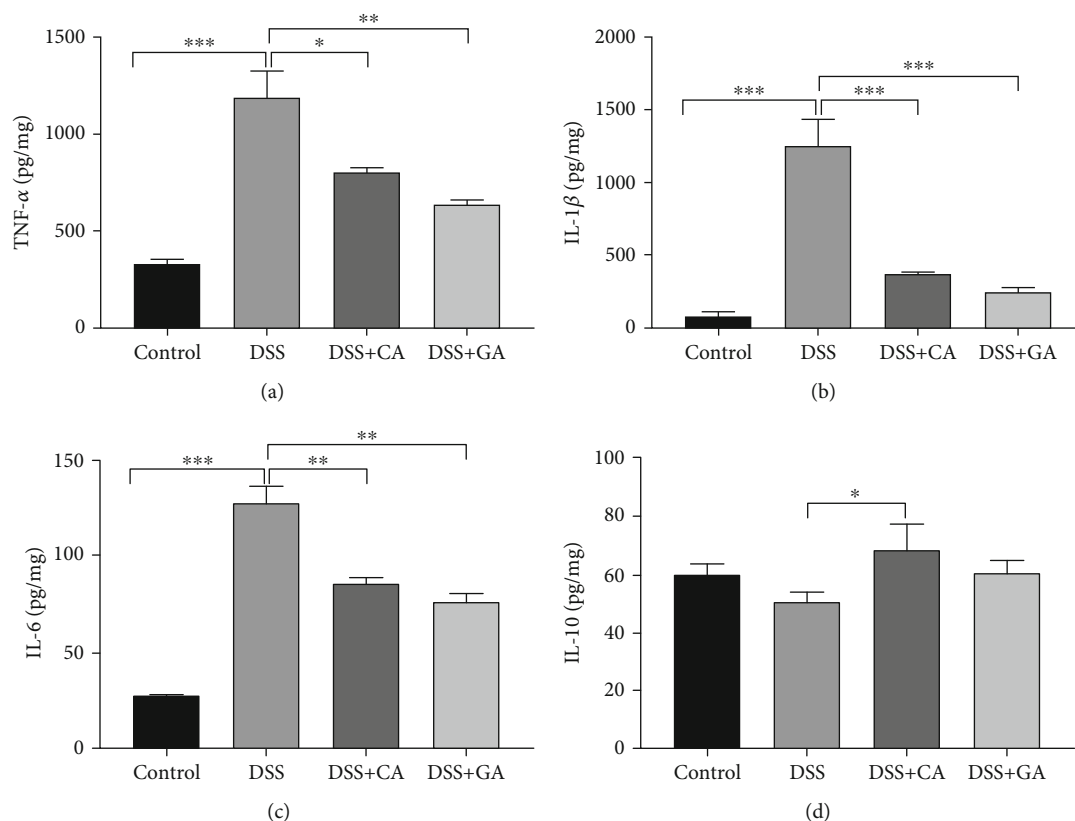


FIGURE 2: Local liver cytokine production in IBD mice and the effect of cecropin A and antibiotic treatment in DSS-treated mice. Protein concentrations of TNF- α , IL-1 β , IL-6, and IL-10 per milligram of liver tissue by ELISA in the DSS group ($n = 9$), control group ($n = 9$), cecropin A group (CA, $n = 9$), and gentamicin group (GA, $n = 9$). The data were analyzed by one-way ANOVA and presented as the mean \pm SEM with * $P < 0.05$, ** $P < 0.01$, *** $P < 0.001$ versus DSS.

discriminant analysis (OPLS-DA) were performed to investigate the data of liver metabolites, and biomarkers were selected by S-plot of OPLS-DA. The methods mentioned above were performed on SIMCA-14.1, R program, and Metaboanalyst 4.0 (<http://www.metaboanalyst.ca>). The values at $P < 0.05$ (*), $P < 0.01$ (**), and $P < 0.001$ (***) were considered statistically significant.

3. Results

3.1. Evaluation of DSS-Induced IBD Mice and the Therapeutic Effects of Cecropin a and Gentamicin. The body weight and colon length of mice in the DSS group were both substantially reduced in comparison to those in the control group ($P < 0.01$, Figures 1(a)–1(d)). Besides In addition, the colon became less noticeable or even disappeared in the context of DSS treatment (Fig. S1a and b). These aforementioned findings vividly demonstrated that the refined and translationally relevant model of DSS chronic colitis in C57BL/6 mice was successfully established. Intriguingly, CA and GA both alleviated IBD symptoms, as evidenced by the increased body weight and colon length of IBD mice ($P < 0.01$, Figures 1(a)–1(d)).

3.2. Cecropin a and Gentamicin Both Attenuate DSS-Induced Liver Inflammation in Mice. Based on the H&E staining anal-

ysis, the liver morphology of mice in the DSS group showed hepatic cell swelling, cytoplasmic loosening, reticular structure and large numbers of apoptotic hepatocytes surrounding the vein (Fig. S1c and d), indicating the possible development of liver inflammation during IBD progression. ELISA was performed to detect the levels of inflammatory cytokines in livers, and DSS treatment was found to significantly increase TNF- α , IL-1 β , and IL-6 levels ($P < 0.001$, Figure 2(a)–2(c)), while the levels of those proinflammatory cytokines were highly decreased after CA and GA treatment ($P < 0.05$, $P < 0.01$ or $P < 0.001$, Figures 2(a)–2(c)). Additionally, although DSS had little effect on its production, CA improved the level of IL-10 ($P < 0.05$, Figure 2(d)).

3.3. Evaluation of Analytical Performance. We conducted PCA on all samples, and the QC samples were tightly clustered in the middle of all samples in the PCA score plot, as shown in Figure 3(b). The coefficients of variation (CV %) of 133 metabolites from QC samples ranged from 2.74% to 17.83% (Supplementary Materials, Table S1). The results show that the method has good repeatability, stability and reliability for metabolomics analysis.

3.4. Qualitative Analysis of Liver Metabolites. Liver samples were analyzed by UPLC-Orbitrap-MS/MS, and the details of this process are shown in Figure 3(a). Complicated

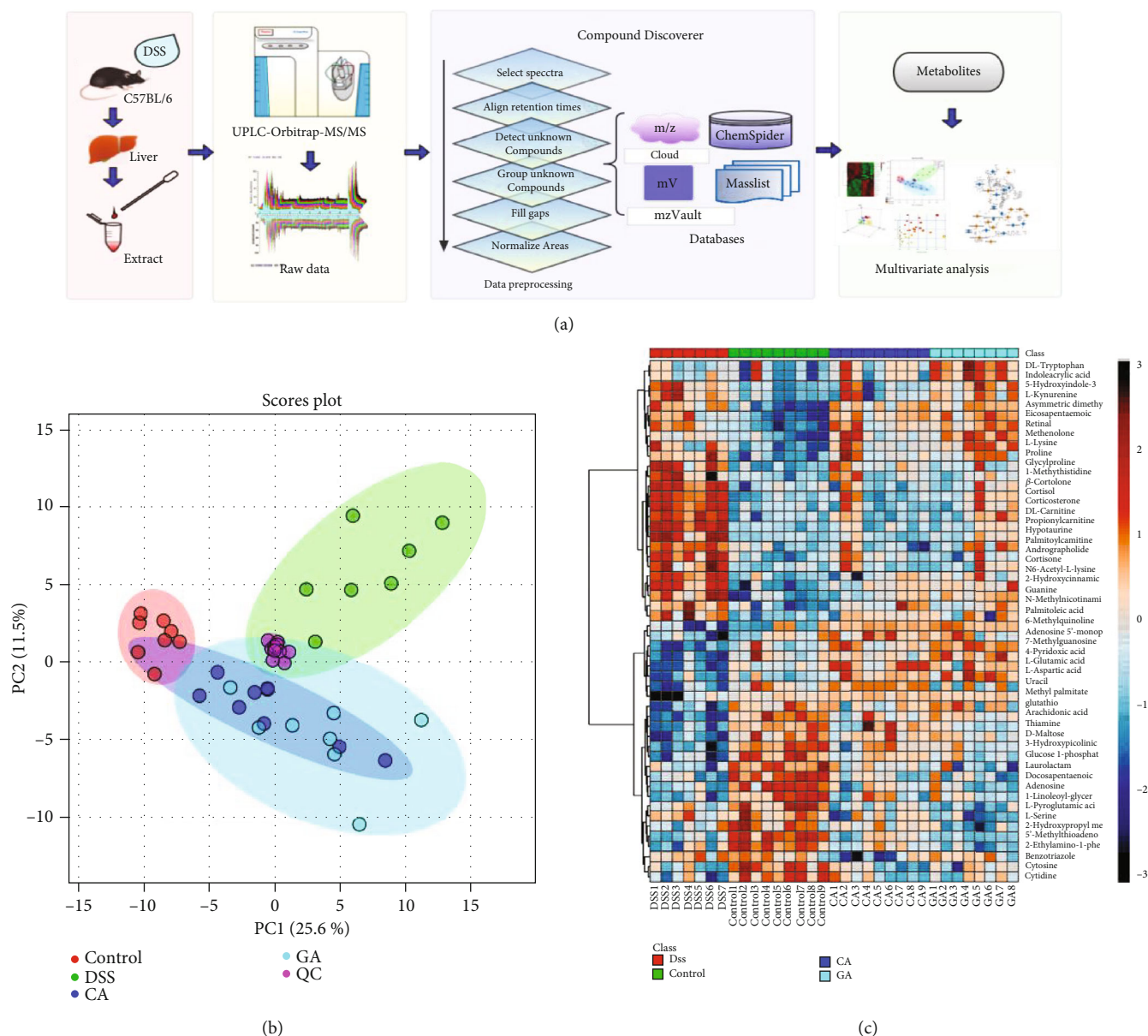


FIGURE 3: Metabolomics analysis flowchart and multivariate statistical analysis. (a) The study process diagram includes sample preprocessing, instrumental analysis, data preprocessing and qualitative analysis, multivariate screening and differential metabolite screening. (b) PCA of the DSS group, control group, cecropin A group (CA), gentamicin group (GA), and QC. (c) Heatmap analysis of the metabolites ($P < 0.05$) based on one-way ANOVA.

raw data were obtained and displayed as the total ion chromatogram (TIC) shown in Fig. S2. Effective mass spectra of peaks were extracted by CD software and matched with accurate mass data, isotope patterns, and mass databases. For example, taurocholic acid $[M+H]^+$ at m/z 516.2969 and m/z 517.3000 and m/z 518.2989 of its isotope were found in MS1 (Fig. S3a). Then, the MS/MS of taurocholic acid was matched to the mzCloud library, and a score was given to indicate the similarity (Fig. S3b). In this research, we chose the mzCloud score of peaks greater than 75 and could match ChemSpider, mzVault, or Masslist. Finally, a total of 133 peaks were identified in each sample, and the Human Metabolome Database (HMDB) and Kyoto Encyclopedia of Genes

and Genomes (KEGG) were used for further confirmation of metabolites. Detailed information on the metabolites is presented in Table S1. In addition, the chromatographic peak area of those metabolites was normalized before multivariate analysis.

3.5. Multivariate Statistical Analysis and Potential Metabolites. Based on the qualitative and semiquantitative results of liver metabolites, chemometric methods were utilized to provide more in-depth information about them. The PCA results (Figure 3(b)) revealed that metabolites in the different groups were separated into distinct clusters, and dots of two treatment groups were scattered in the

TABLE 1: The twenty significant metabolites in liver of control group, DSS group, CA group, and GA group.

No.	Name	t_R (min)	HMDB	KEGG	VIP>1	Relative intensity			
						Control	DSS	CA	GA
1	Propionyl carnitine	2.31	HMDB0000824	C03017	Δ^a	384.21 \pm 98.64	5700.72 \pm 2028.84 ^c	588.66 \pm 375.78	847.76 \pm 530.07
2	Arachidonic acid	14.09	HMDB0001043	C00219	Δ	5997.26 \pm 1389.78	2527.74 \pm 396.91 ^c	3919.27 \pm 744.50 ^e	4579.15 \pm 951.61
3	Hypotaurine	1.23	HMDB0000965	C00519	Δ	284.55 \pm 70.53	4235.41 \pm 2659.97 ^c	358.70 \pm 289.65	606.52 \pm 428.58 ^f
4	D-maltose	1.21	HMDB0000163	C00208	Δ	1779.42 \pm 483.21	1155.87 \pm 283.50 ^b	1747.31 \pm 317.29	1807.18 \pm 343.14
5	4-Pyridoxic acid	2.02	HMDB0000017	C00847	Δ	144.45 \pm 66.08	65.88 \pm 29.11 ^b	131.24 \pm 19.31	164.84 \pm 46.90
6	Cortisol	8.62	HMDB0000063	C00735	Δ	11.69 \pm 9.99	506.20 \pm 352.53 ^c	21.59 \pm 20.54	73.07 \pm 52.63 ^g
7	Guanine	1.34	HMDB0000132	C00242	Δ	187.17 \pm 47.36	336.74 \pm 109.82 ^c	245.23 \pm 58.58	263.57 \pm 57.07 ^f
8	Uracil	1.35	HMDB0000300	C00106	Δ	4359.67 \pm 764.58	2963.04 \pm 608.96 ^b	5243.61 \pm 1162.11	3965.74 \pm 1520.60
9	L-Carnitine	1.24	HMDB0000062	C00318	Δ	17807.48 \pm 3512.00	38793.25 \pm 6811.27 ^c	20469.79 \pm 5089.24	23672.54 \pm 7816.16
10	β -Cortolone	8.32	HMDB0013221	C05481	Δ	18.50 \pm 12.94	234.38 \pm 106.55 ^c	5.97 \pm 4.67	28.75 \pm 24.15 ^f
11	Corticosterone	8.08	HMDB0001547	C02140	Δ	3.72 \pm 2.15	73.06 \pm 37.02 ^c	2.27 \pm 0.84	37.94 \pm 30.86
12	Andrographolide	9.62	Na*	NA	Δ	2.31 \pm 0.62	42.36 \pm 22.28 ^c	4.05 \pm 3.04	8.07 \pm 5.67
13	Glycylproline	1.70	HMDB0000721	NA	Δ	116.59 \pm 19.36	213.04 \pm 45.74 ^c	164.62 \pm 29.84 ^d	154.76 \pm 49.39
14	Thiamine	1.18	HMDB0000235	C00378	Δ	1213.24 \pm 172.57	721.46 \pm 104.90 ^c	1244.25 \pm 330.44	936.37 \pm 77.03 ^g
15	Glutathione	1.33	HMDB0000125	C00051	—	39617.25 \pm 6036.10	22513.56 \pm 4980.63 ^c	34831.89 \pm 6374.22	34240.51 \pm 8982.61
16	N6-acetyl-L-lysine	1.28	HMDB0000206	C02727	Δ	265.83 \pm 37.06	507.29 \pm 141.26 ^c	309.20 \pm 95.39	350.36 \pm 83.69 ^f
17	L-Kynurenine	3.25	HMDB0000684	C00328	Δ	654.22 \pm 129.20	2302.36 \pm 1173.26 ^c	1233.12 \pm 1104.86	1653.55 \pm 699.91 ^g
18	2-Hydroxypropyl methacrylate	6.68	NA	NA	—	13422.12 \pm 3602.44	10060.25 \pm 2172.58 ^c	11174.65 \pm 1769.03	8035.20 \pm 2318.02 ^g
19	Palmitoyl carnitine	11.76	HMDB0000222	C02990	Δ	39.64 \pm 15.63	131.29 \pm 32.20 ^c	39.09 \pm 24.66	87.65 \pm 56.63
20	Cortisone	8.38	HMDB0002802	C00762	Δ	1.81 \pm 0.46	33.18 \pm 27.09 ^b	2.02 \pm 0.92	10.02 \pm 8.24 ^f

*NA means not available. ^a Δ means VIP>1 in OPLS-DA. ^bDSS group compared with control group, $p < 0.05$. ^cDSS group compared with control group, $p < 0.01$. ^dCA group compared with control group, $p < 0.05$. ^eCA group compared with control group, $p < 0.01$. ^fGA group compared with control group, $p < 0.05$. ^gGA group compared with control group, $p < 0.01$.

middle between the DSS and control groups. The differential metabolites among diverse groups with $p < 0.05$ were selected by one-way analysis of variance (one-way ANOVA), as shown in Fig. S4a and Table S2. Heatmap analysis was performed to represent the differences and similarities among the four groups, as shown in Figure 3(c). The results suggested that some metabolite levels may be reversed by the cecropin A or gentamicin treatment. Then, the OPLS-DA model and S-plot were established to screen potential metabolites using restrictions including VIP>1 and the absolute value of the correlation coefficient (Corr) >0.80. Finally, 20 compounds were selected by this limiting condition and were tagged using red dots in the S-plot

shown in Fig. S4b–d. These potential metabolites were considered biomarkers, and the details of those metabolites are listed in Table 1. The relative concentration changes in the 4 groups are shown in Figure 4. Overall, components related to glutathione metabolism, energy metabolism and inflammation, such as glutathione, maltose and arachidonic acid, as well as thiamine and 4-pyridoxic acid, which are metabolites of the liver, were downregulated in the DSS group and upregulated in the CA and GA group. Conversely, steroid hormones metabolites such as cortisol and cortisone were upregulated because of the long-term stress resulting from IBD and were alleviated by treatment with CA and GA.

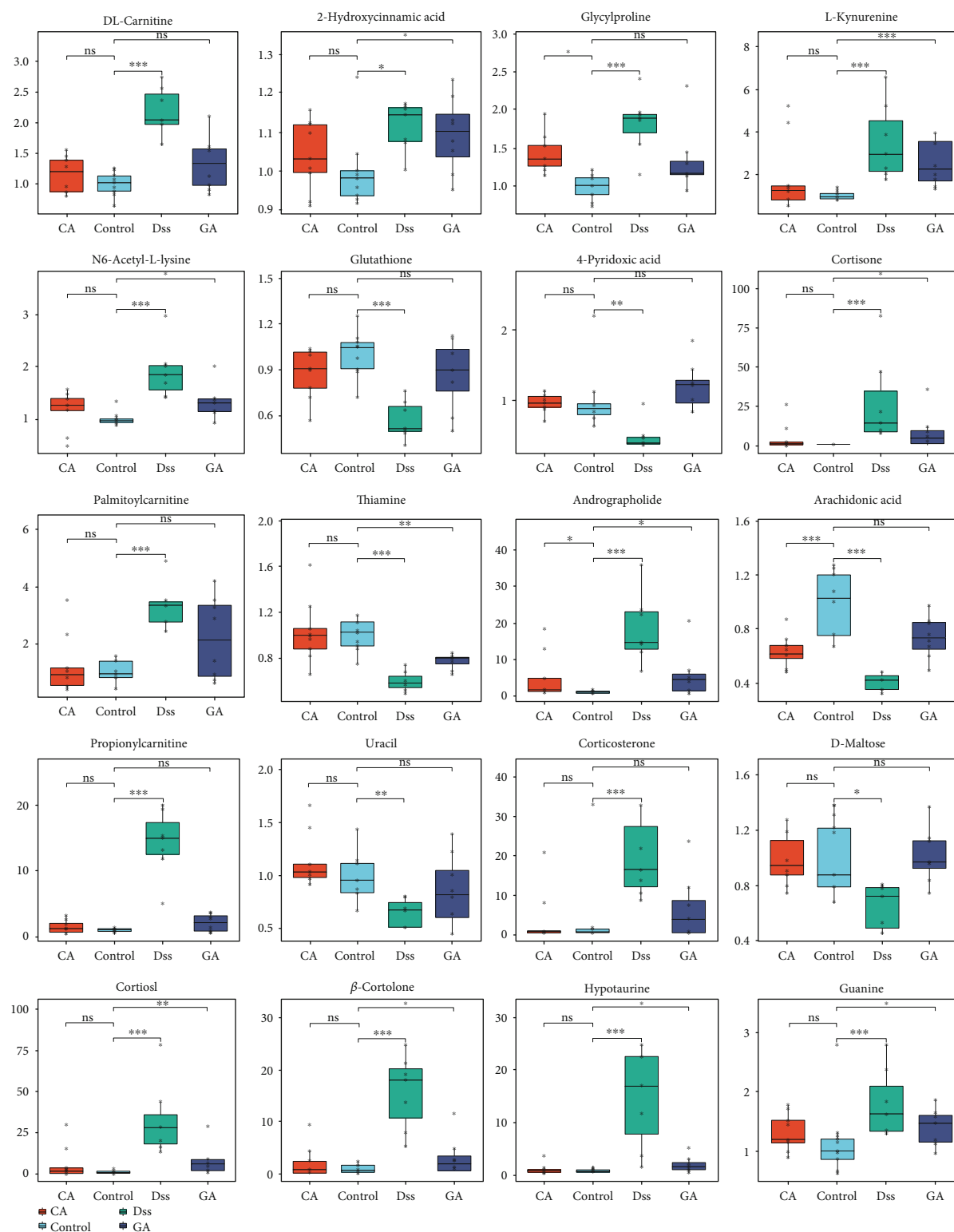
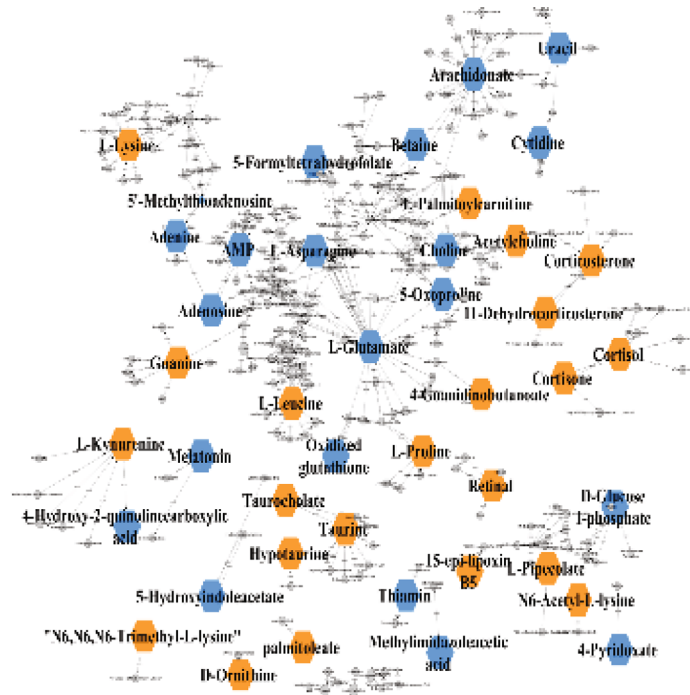


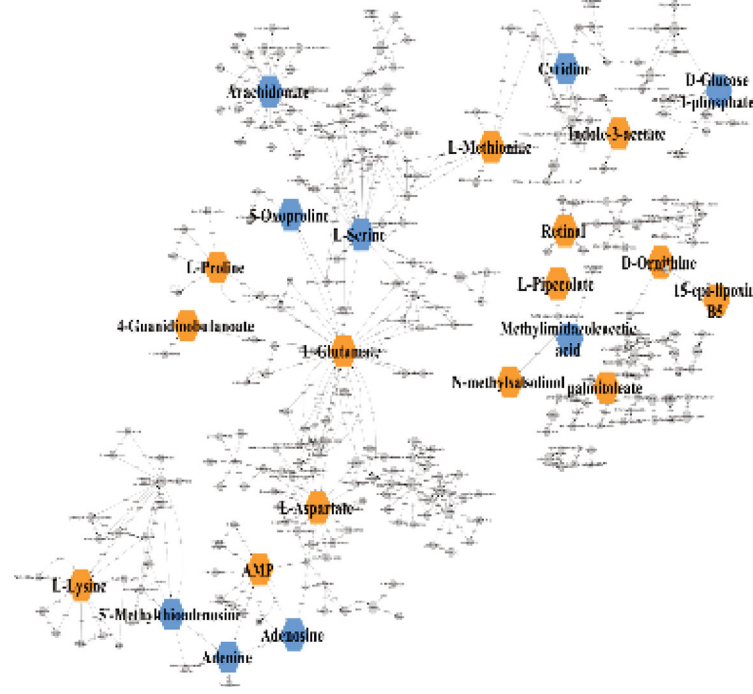
FIGURE 4: Box-plot of potential metabolites in the four groups: control, DSS, CA and GA group (* $P < 0.05$, ** $P < 0.01$, *** $P < 0.001$, ns means not significant).

3.6. *Metabolic Pathway and Potential Therapeutic Targets.* In this research, a metabolic network analysis was established based on the p-value and fold-change among the different groups. There were 21 downregulated compounds and 22

upregulated compounds in the metabolic network of the DSS group (Figure 5(a)). In the GA group (Figure 5(b)), 11 compounds were downregulated and 27 compounds were upregulated, whereas only 9 compounds were downregulated



(a)



(b)

FIGURE 5: Continued.

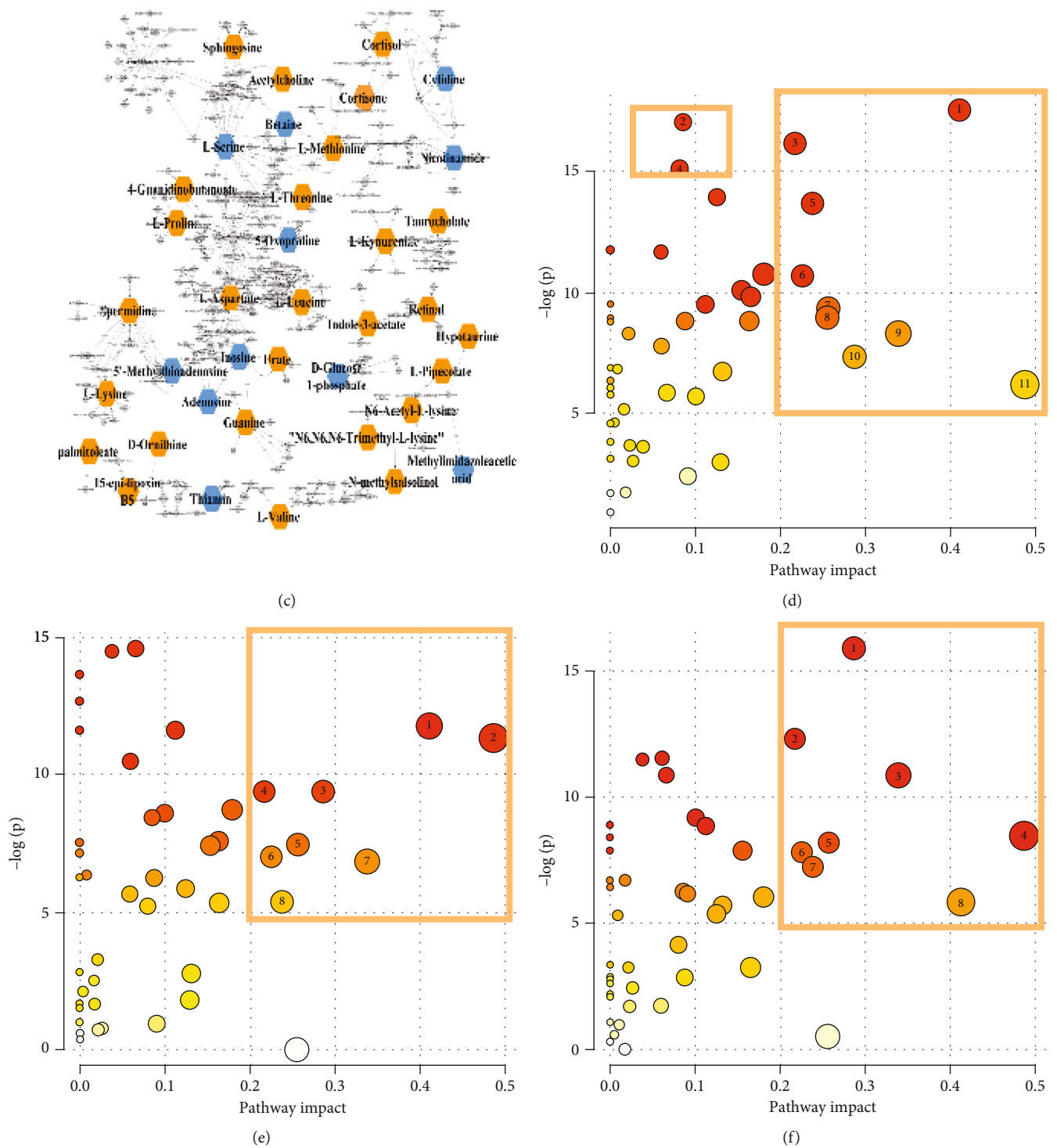


FIGURE 5: Metabolism network analysis of three treatment groups: (a) DSS group vs control group. (b) CA group vs control group. (c) GA group vs control group. Blue indicates downregulated metabolites, and red indicates upregulated metabolites. Metabolism pathway analysis of the four groups. The x-axis and the y-axis represent the pathway impact and enrichment, respectively. The critical pathways are framed by yellow boxes. (d) DSS vs control, 1-taurine and hypotaurine metabolism; 2-steroid hormone biosynthesis; 3-arachidonic acid metabolism; 4-tryptophan metabolism; 5-cysteine and methionine metabolism; 6-aminoacyl-tRNA biosynthesis; 7-glycine, serine and threonine metabolism; 8-retinol metabolism; 9-glutathione metabolism; 10-arginine and proline metabolism; 11-alanine, aspartate and glutamate metabolism. (e) DSS vs CA, 1-taurine and hypotaurine metabolism; 2-alanine, aspartate and glutamate metabolism; 3-glutathione metabolism; 4-arachidonic acid metabolism; 5-glycine, serine and threonine metabolism; 6-aminoacyl-tRNA biosynthesis; 7-arginine and proline metabolism; 8-cysteine and methionine metabolism. (f) DSS vs GA, 1-glutathione metabolism; 2-arachidonic acid metabolism; 3-arginine and proline metabolism; 4-alanine, aspartate and glutamate metabolism; 5-glycine, serine and threonine metabolism; 6-aminoacyl-tRNA biosynthesis; 7-taurine and hypotaurine metabolism; 8-cysteine and methionine metabolism.

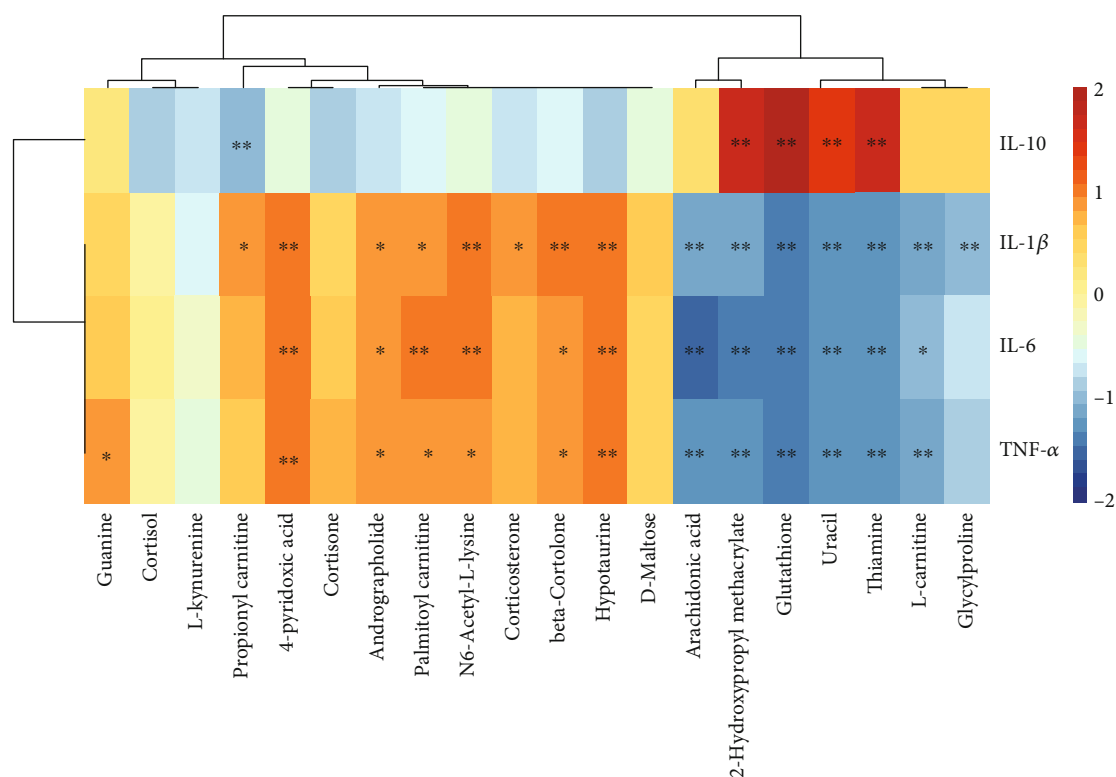


FIGURE 6: The Spearman correlation analysis among cytokines and biomarkers, and clustering is shown as a heat map. Color from red to blue indicates a positive correlation to a negative correlation, and the asterisk represents the significance of the correlation, * $P < 0.05$, ** $P < 0.01$.

and 16 were upregulated in the CA group (Figure 5(c)). Additionally, corresponding to the metabolic network, the metabolic pathway was analyzed on the Metaboanalyst 4.0 platform. Figures 5(d)–5(f) shows the pathway analysis between the DSS and control group, DSS and CA group, and the DSS and GA group. There were extensive changes in the pathways of liver metabolism influenced by IBD. On the basis of an impact >0.2 and $-\log(p) > 5$, Figure 5(d) shows that the pathways with significant impacts were taurine and hypotaurine metabolism; arachidonic acid metabolism; cysteine and methionine metabolism; aminoacyl-tRNA biosynthesis; glycine, serine and threonine metabolism; arginine and proline metabolism; glutathione metabolism; and alanine, aspartate and glutamate metabolism. Additionally, steroid hormone biosynthesis and tryptophan metabolism were impacted. Figures 5(e) and 5(f) shows that the predominant pathway of liver metabolism with the CA and GA treatment is through its effects on amino acid metabolism, aminoacyl-tRNA biosynthesis, and especially a regulating effect on taurine and hypotaurine metabolism, glutathione metabolism, and arachidonic acid metabolism. In addition, a Spearman correlation analysis showed the correlation between cytokines and biomarkers, as shown in Figure 6. Most of the 20 biomarkers were positively or negatively correlated with four cytokines, among which thiamine, uracil, glutathione, and 2-hydroxypropyl methacrylate were significantly correlated with proinflammatory (TNF- α , IL-1 β , and IL-6) and anti-inflammatory (IL-10) cytokines, and those metabolites also belong to the pathway regulated by CA and GA, implying

that those biomarkers may act as potential therapeutic targets of liver disorder resulting from IBD.

4. Discussion

IBD has a complex pathology and easily causes systemic inflammatory responses. In our results, we established a refined and translationally relevant model of DSS chronic colitis in C57BL/6 mice and found morbidity in liver morphology and significant increases in proinflammatory cytokines (TNF- α , IL-1 β , and IL-6) in the liver tissue of IBD mice. Metabolomics revealed 20 potential metabolites closely related to inflammatory cytokines, mainly involved in the following aspects: (a) bile acid metabolism disorder (taurine, taurocholate, hypotaurine); (b) arachidonic acid metabolism disorder; (c) amino acid and protein metabolism (guanine, glutathione, glutamate acid, glycylproline, kynurenine); and (d) steroid hormone biosynthesis (cortisol, cortisone, corticosterone).

Bile acids are liver-derived cholesterol derivatives that control digestion and modulate lipid metabolism [17]. Many published studies have suggested the importance of appropriately maintaining bile acid homeostasis to liver metabolism, and bile acid overload will cause inflammation and impair the liver [18–20]. Furthermore, recent research has shown that the gut microbiota plays a key role in various disorders within and beyond the gastrointestinal tract [21, 22]. The gut microbiota affects intestinal signaling and enterohepatic circulation of bile acids via a “liver-microbiome axis” [7,

23]. In this research, bile acid metabolism disorders may result from disturbances of the gut microbiota due to IBD.

Arachidonic acid is a polyunsaturated fatty acid that is essential for normal health and is a component of the biological cell membrane, which can maintain the normal permeability and flexibility of cells [24]. Notably, during inflammation, arachidonic acid reacts with enzymes to form prostaglandins, leukotrienes, and thromboxanes, which are considered predominantly proinflammatory molecules [25]. Additionally, the arachidonic acid metabolic pathway was changed because phospholipase has been shown to be decreased in patients with IBD [26]. Therefore, arachidonic acid was downregulated in the liver during the course of IBD.

The liver is the major metabolic organ for amino acids and proteins. The DSS group was altered in amino acid and protein metabolism, and amino acid-related compounds such as pyroglutamic acid, glutamic acid, and glutathione were involved in glutathione metabolism and downregulated in the DSS group. The glutathione pathway is a key hepatic defense mechanism and deactivates reactive metabolites before they have an opportunity to damage cellular proteins [27]. In addition, we found that tryptophan metabolism was influenced considerably by IBD in our research. Tryptophan is an essential amino acid involved in various biological processes, and its metabolites play a crucial role in the regulation of immunity [28]. Recently published studies have shown that gut microbiota can affect host physiology and pathology by interfering with tryptophan metabolism [29]. Therefore, in the process of IBD, the disorder of tryptophan metabolism in the liver may be caused by the intervention mechanism of gut microbiota on tryptophan metabolism.

IBD also caused the disarray of steroid hormone biosynthesis. Glucocorticoids are the primary steroid hormones, including cortisol and cortisone, which are related factors that indicate stress and pain and play a decisive role in metabolism, maintaining energy balance and animal survival in adversity [30]. An appropriate stress response is conducive to the body's short-term adaptation to the environment; however, long-term stress or strong stimulation and a high level of glucocorticoids are bound to cause energy metabolism and hormone secretion disorder, thereby affecting health [31]. Published research has found that excessive cortisol secretion will promote the catabolism of proteins in extrahepatic tissues, resulting in negative nitrogen balance [32]. In our study, IBD exposed mice to long-term stress and promoted excessive glucocorticoid secretion (cortisol and cortisone, as shown in Figure 4), which may induce liver injury.

The gut microflora is an important factor in regulating gastrointestinal homeostasis, affecting the immune system and host metabolism [33]. In recent studies, the gut microflora has been closely related to the development of hepatopathy [34]. In our studies, we found that cecropin A has better effectiveness than gentamicin, and CA reversed bile acid metabolism and amino acid and protein and steroid hormone biosynthesis disarray caused by IBD. The concentrations of taurine, taurocholate, hypotaurine, cortisol, cortisone, and corticosterone were downregulated in the CA group. Glutathione and metabolites of tryptophan metabolism returned to normal levels. Compared to CA, the reverse

ability of the GA group was weak, and only glutathione and arachidonic acid levels were reversed. The possible reasons for these results were that cecropin A can improve the abundance of beneficial bacteria and reduce the adhesion of harmful bacteria to cells [35], which may benefit intestinal epithelium recovery and regulate gut microbiota, thereby alleviating IBD and liver metabolism disturbance. On the other hand, cecropin A and gentamicin showed different effects on their microbiota populations, which may lead to different degrees of recovery from intestinal injury.

5. Conclusion

This study concentrates on revealing the metabolic profiles of the liver in mice with DSS-induced IBD. Metabolomics analysis was performed on UPLC-HRMS combined with effective untargeted qualitative tools, and 20 potential metabolites were screened as biomarkers to represent the characteristics of liver disorder in IBD. Metabolic pathway analysis and metabolite network analysis indicated that bile acid metabolism, arachidonic acid metabolism, amino acid and protein metabolism, and steroid hormone biosynthesis were changed in the liver caused by IBD. Additionally, the correlation analysis between cytokines (TNF- α , IL-1 β , IL-6, and IL-10) and biomarkers indicated that CA and GA may be able to regulate those metabolites and metabolic pathways by regulating the structure of gut microflora in the treatment of IBD, thereby assisting in alleviating liver inflammation. We hope that our efforts may serve as a reference in the study of IBD and its associated molecular mechanisms in the liver.

Data Availability

The data used to support the findings of this study are available from the corresponding author upon request.

Additional Points

Preprint. This work has a preprint online, preprint link: <https://www.researchsquare.com/article/rs-7302/v1>, DOI: 10.21203/rs.2.16664/v1.

Conflicts of Interest

The authors declare that they have no conflict of interest.

Acknowledgments

This project was supported by the National Key R&D Program of China (Grant No. 2018YFD0500600), National Natural Science Foundation of China (Grant No.31790411), Natural Science Foundation of Guangdong Province (Grant No. 2020A1515010322), Innovation Team Project in Universities of Guangdong Province (2017KCXTD002) and Guangdong Provincial Promotion Project on Preservation and Utilization of Local Breed of Livestock and Poultry. The studies meet with the approval of the university's review board.

Supplementary Materials

Supplementary Figure 1 Histopathological results of colon and liver stained with H&E of the control group (a and b) and DSS group (c and d). Supplementary Figure 2: The total ion chromatograms (TICs) of the control group, DSS group, CA group and GA group. Supplementary Figure 3: Two steps used for metabolite identification: (a) isotope pattern matching and (b) MS/MS spectral library matching. Supplementary Figure 4: Selection of potential metabolites based on one-way ANOVA and OPLS-DA. (a) One-way ANOVA of metabolites in the four groups; red dots represent metabolites with $p < 0.05$, and the green dot represents $p > 0.05$. (b) OPLS-DA between the DSS group and the control group. (c) Permutation test to evaluate OPLS-DA. (d) S-plot showing the OPLS-DA analysis of the DSS group and control group. Potential biomarkers (red dots) were chosen according to $p < 0.05$ in the one-way ANOVA, $VIP > 1$ in OPLS-DA, and the absolute value of the correlation coefficient (Corr) > 0.80 of the S-plot. Supplementary Table 1: List of metabolites identified in the liver. Supplementary Table 2: List of the 52 metabolites that were screened by one-way analysis of variance of metabolites in the control group, DSS group, CA group and GA group. (Supplementary Materials)

References

- [1] D. H. Kerman and A. R. Deshpande, "Gut microbiota and inflammatory bowel disease: the role of antibiotics in disease management," *Postgraduate Medicine*, vol. 126, no. 4, pp. 7–19, 2015.
- [2] V. Annese, "A review of Extraintestinal manifestations and complications of inflammatory bowel disease," *Saudi Journal of Medicine & Medical Sciences*, vol. 7, no. 2, pp. 66–73, 2019.
- [3] V. Uko, S. Thangada, and K. Radhakrishnan, "Liver disorders in inflammatory bowel disease," *Gastroenterology Research and Practice*, vol. 2012, Article ID 642923, 7 pages, 2012.
- [4] F. D. Mendes, C. Levy, F. B. Enders, E. V. Loftus Jr., P. Angulo, and K. D. Lindor, "Abnormal hepatic biochemistries in patients with inflammatory bowel disease," *The American Journal of Gastroenterology*, vol. 102, no. 2, pp. 344–350, 2007.
- [5] D. Sheehan and F. Shanahan, "The gut microbiota in inflammatory bowel disease," *Gastroenterology Clinics of North America*, vol. 46, no. 1, pp. 143–154, 2017.
- [6] E. A. Franzosa, A. Sirota-Madi, J. Avila-Pacheco et al., "Gut microbiome structure and metabolic activity in inflammatory bowel disease," *Nature Microbiology*, vol. 4, no. 2, pp. 293–305, 2019.
- [7] T. E. Adolph, C. Grandner, A. R. Moschen, and H. Tilg, "Liver-microbiome Axis in health and disease," *Trends in Immunology*, vol. 39, no. 9, pp. 712–723, 2018.
- [8] C. Acharya, S. E. Sahingur, and J. S. Bajaj, "Microbiota, cirrhosis, and the emerging oral-gut-liver axis," *JCI Insight*, vol. 2, no. 19, p. 11, 2017.
- [9] A. R. Moschen, S. Kaser, and H. Tilg, "Non-alcoholic steatohepatitis: a microbiota-driven disease," *Trends in Endocrinology and Metabolism*, vol. 24, no. 11, pp. 537–545, 2013.
- [10] O. Ledder, "Antibiotics in inflammatory bowel diseases: do we know what we're doing?," *Translational Pediatrics*, vol. 8, no. 1, pp. 42–55, 2019.
- [11] G. Ianiro, H. Tilg, and A. Gasbarrini, "Antibiotics as deep modulators of gut microbiota: between good and evil," *Gut*, vol. 65, no. 11, pp. 1906–1915, 2016.
- [12] Z. Y. Zhai, F. Zhang, R. H. Cao et al., "Cecropin a alleviates inflammation through modulating the gut microbiota of C57BL/6 mice with DSS-induced IBD," *Frontiers in Microbiology*, vol. 10, p. 13, 2019.
- [13] A. Zhang, H. Sun, P. Wang, Y. Han, and X. Wang, "Modern analytical techniques in metabolomics analysis," *The Analyst*, vol. 137, no. 2, pp. 293–300, 2012.
- [14] Z. Xin, S. Ma, D. Ren et al., "UPLC–Orbitrap–MS/MS combined with chemometrics establishes variations in chemical components in green tea from Yunnan and Hunan origins," *Food Chemistry*, vol. 266, pp. 534–544, 2018.
- [15] B. Kluger, C. Bueschl, N. Neumann et al., "Untargeted Profiling of Tracer-Derived Metabolites Using Stable Isotopic Labeling and Fast Polarity-Switching LC–ESI–HRMS," *Analytical Chemistry*, vol. 86, no. 23, pp. 11533–11537, 2014.
- [16] D. Ren, L. Ran, C. Yang, M. Xu, and L. Yi, "Integrated strategy for identifying minor components in complex samples combining mass defect, diagnostic ions and neutral loss information based on ultra-performance liquid chromatography-high resolution mass spectrometry platform: folium Artemisiae Argyi as a case study," *Journal of Chromatography A*, vol. 1550, pp. 35–44, 2018.
- [17] W. Chen, Y. Wei, A. Xiong et al., "Comprehensive analysis of serum and Fecal bile acid profiles and interaction with gut microbiota in primary biliary cholangitis," *Clinical Reviews in Allergy & Immunology*, vol. 58, no. 1, pp. 25–38, 2020.
- [18] N. Péan, I. Doignon, I. Garcin et al., "The receptor TGR5 protects the liver from bile acid overload during liver regeneration in mice," *Hepatology*, vol. 58, no. 4, pp. 1451–1460, 2013.
- [19] W. D. Huang, K. Ma, J. Zhang et al., "Nuclear receptor-dependent bile acid signaling is required for normal liver regeneration," *Science*, vol. 312, no. 5771, pp. 233–236, 2006.
- [20] H. X. Liu, R. Keane, L. Sheng, and Y. J. Wan, "Implications of microbiota and bile acid in liver injury and regeneration," *Journal of Hepatology*, vol. 63, no. 6, pp. 1502–1510, 2015.
- [21] S. V. Lynch and O. Pedersen, "The human intestinal microbiome in health and disease," *The New England Journal of Medicine*, vol. 375, no. 24, pp. 2369–2379, 2016.
- [22] P. I. Costea, F. Hildebrand, M. Arumugam et al., "Enterotypes in the landscape of gut microbial community composition," *Nature Microbiology*, vol. 3, no. 1, pp. 8–16, 2018.
- [23] A. Wahlström, S. I. Sayin, H. U. Marschall, and F. Bäckhed, "Intestinal crosstalk between bile acids and microbiota and its impact on host metabolism," *Cell Metabolism*, vol. 24, no. 1, pp. 41–50, 2016.
- [24] H. Tallima and R. El Ridi, "Arachidonic acid: physiological roles and potential health benefits - a review," *Journal of Advanced Research*, vol. 11, pp. 33–41, 2018.
- [25] R. Poorani, A. N. Bhatt, B. S. Dwarakanath, and U. N. Das, "COX-2, aspirin and metabolism of arachidonic, eicosapentaenoic and docosahexaenoic acids and their physiological and clinical significance," *European Journal of Pharmacology*, vol. 785, pp. 116–132, 2016.
- [26] A. Murgia, C. Hinz, S. Liggi et al., "Italian cohort of patients affected by inflammatory bowel disease is characterised by variation in glycerophospholipid, free fatty acids and amino acid levels," *Metabolomics*, vol. 14, no. 10, p. 140, 2018.

- [27] R. L. Gould, Y. Zhou, C. L. Yakaitis et al., "Heritability of the aged glutathione phenotype is dependent on tissue of origin," *Mammalian Genome*, vol. 29, no. 9-10, pp. 619–631, 2018.
- [28] H. M. Roager and T. R. Licht, "Microbial tryptophan catabolites in health and disease," *Nature Communications*, vol. 9, no. 1, article 3294, 2018.
- [29] A. Agus, J. Planchais, and H. Sokol, "Gut microbiota regulation of tryptophan metabolism in health and disease," *Cell Host & Microbe*, vol. 23, no. 6, pp. 716–724, 2018.
- [30] L. Magomedova and C. L. Cummins, "Glucocorticoids and Metabolic Control," in *Metabolic Control. Handbook of Experimental Pharmacology*, S. Herzig, Ed., vol. 233, pp. 73–93, Springer, Cham, 2015.
- [31] K. Dedovic, A. Duchesne, J. Andrews, V. Engert, and J. C. Pruessner, "The brain and the stress axis: the neural correlates of cortisol regulation in response to stress," *NeuroImage*, vol. 47, no. 3, pp. 864–871, 2009.
- [32] G. A. Rinard, G. Okuno, and R. C. Haynes JR., "Stimulation of gluconeogenesis in rat liver slices by epinephrine and glucocorticoids," *Endocrinology*, vol. 84, no. 3, pp. 622–631, 1969.
- [33] T. Sunkara, P. Rawla, A. Ofori, and V. Gaduputi, "Fecal microbiota transplant — a new frontier in inflammatory bowel disease," *Journal of Inflammation Research*, vol. 11, pp. 321–328, 2018.
- [34] W. W. Jiang, N. Wu, X. M. Wang et al., "Dysbiosis gut microbiota associated with inflammation and impaired mucosal immune function in intestine of humans with non-alcoholic fatty liver disease," *Scientific Reports*, vol. 5, no. 1, article 8096, 2015.
- [35] Z. Y. Zhai, X. Ni, C. Jin et al., "Cecropin a modulates tight junction-related protein expression and enhances the barrier function of porcine intestinal epithelial cells by suppressing the MEK/ERK pathway," *International Journal of Molecular Sciences*, vol. 19, no. 7, p. 1941, 2018.

Research Article

miRNA-10a-5p Alleviates Insulin Resistance and Maintains Diurnal Patterns of Triglycerides and Gut Microbiota in High-Fat Diet-Fed Mice

Yawei Guo ¹, Xiaohui Zhu,¹ Sha Zeng,² Mingyi He,¹ Xiurong Xing,¹ and Changyuan Wang ¹

¹Xuanwu Hospital Capital Medical University, Beijing 100053, China

²Xiangtan Central Hospital, Xiangtan 411100, China

Correspondence should be addressed to Changyuan Wang; wangchangyuan73@xwhosp.org

Received 27 June 2020; Revised 18 July 2020; Accepted 24 July 2020; Published 17 August 2020

Academic Editor: Shuai Chen

Copyright © 2020 Yawei Guo et al. This is an open access article distributed under the Creative Commons Attribution License, which permits unrestricted use, distribution, and reproduction in any medium, provided the original work is properly cited.

miRNA-10a is rhythmically expressed and regulates genes involved in lipid and glucose metabolism. However, the effects of miRNA-10a on obesity and glucose intolerance, as well as on the diurnal pattern of expression of circadian clock genes, remain unknown. We explored the effects of miRNA-10a-5p on insulin resistance and on the diurnal patterns of serum triglycerides and gut microbiota in high-fat diet- (HFD-) fed mice. The results showed that oral administration of miRNA-10a-5p significantly prevented body weight gain and improved glucose tolerance and insulin sensitivity in HFD-fed mice. Administration of miRNA-10a-5p also maintained the diurnal rhythm of *Clock*, *Per2*, and *Cry1* expression, as well as serum glucose and triglyceride levels. Surprisingly, the diurnal oscillations of three genera of microbes, *Oscillospira*, *Ruminococcus*, and *Lachnospiraceae*, disrupted by HFD feeding, maintained by administration of miRNA-10a-5p. Moreover, a strong positive correlation was found between hepatic *Clock* expression and relative abundance of *Lachnospiraceae*, both in control mice ($r = 0.877$) and in mice administered miRNA-10a-5p ($r = 0.853$). Furthermore, we found that along with changes in *Lachnospiraceae* abundance, butyrate content in the feces maintained a diurnal rhythm after miRNA-10a-5p administration in HFD-fed mice. In conclusion, we suggest that miRNA-10a-5p may improve HFD-induced glucose intolerance and insulin resistance through the modulation of the diurnal rhythm of *Lachnospiraceae* and its metabolite butyrate. Therefore, miRNA-10a-5p may have preventative properties in subjects with metabolic disorders.

1. Introduction

The spiraling rates of obesity and type 2 diabetes mellitus are a worldwide health problem affecting millions of people. Overeating and reduced physical exercise are the primary reasons for these worrisome phenomena. Among the many factors proven to be involved in the development of obesity, hyperglycemia, and insulin resistance, gut microbiota plays important roles. Long-term high-fat-diet (HFD) intake can result in dysbiosis of gut microbiota and obese subjects are often characterized by low microbial diversity and impairment of microbiota composition [1–3].

Circadian rhythmicity plays critical roles in maintaining physiological homeostasis and overall health. Disruption of the circadian rhythm is often related to the onset and development of obesity, type 2 diabetes, and other metabolic syndromes [4]. Previous studies using rodent models of circadian disruptions showed that HFD feeding adversely modulated circadian signaling, suggesting a bi-directional regulation between circadian signaling and diet [5]. However, the related mechanisms need further elucidation. Recently, the gut microbiome, a vital mediator for dietary composition entrainment, was found to be involved in the maintenance of circadian rhythm [6]. Importantly, the gut

microbiome exhibits diurnal rhythm and produces oscillations in its metabolites, and these diurnal variations can be disrupted by HFD intake [6, 7].

MicroRNAs (miRNAs), a class of endogenously small noncoding RNAs consisting of 19–25 nucleotides, can exert inhibitory or promoting effects on the expression of target genes posttranscriptionally. Recently, these important gene-regulatory units have been shown to modulate circadian locomotor rhythm and output pathways [8, 9]. For instance, miRNA-276a and let-7 can regulate the expression of the pacemaker gene *timeless* [10, 11], while miRNA-276b can control circadian locomotor rhythm by repressing *Beadex* expression [12]. Additionally, it has been suggested that miRNAs can modulate gene expression in their target bacteria and promote their growth, consequently shaping the gut microbiota [13]. Therefore, we speculate that miRNA-10a, which is rhythmically expressed and regulates genes involved in lipid and glucose metabolism [14], may have an effect on gut microbiota and insulin sensitivity. In this study, we found that miRNA-10a-5p alleviated HFD-induced obesity, glucose intolerance, and insulin resistance. Moreover, miRNA-10a-5p maintained diurnal patterns of triglyceride and gut microbiota that were disrupted by HFD intake.

2. Materials and Methods

2.1. Animals and Experimental Design. A total of 126 male C57BL/6J mice (8 weeks old) were purchased from Huabukang Biotech Company (Beijing, China). After an acclimatization of 1 week, all mice were randomly grouped into 3 groups ($n = 42$): Control treatment, mice fed a low-fat diet and gavaged with saline; HFD treatment, mice fed an HFD and gavaged with saline; miRNA treatment, mice fed an HFD and gavaged with miRNA-10a-5p (100 pmol/mice per day). The low-fat (10%) and high-fat diet (45%) were purchased from Research Diets (New Brunswick, NJ, USA). miRNA-10a-5p mimics were purchased from Guangzhou RiboBio, Co., Ltd (Guangzhou, China). All mice were maintained on a 12:12 Light/Dark cycle (Zeitgeber time (ZT) 0 = 6:00), in plastic cages under standard conditions and were free to access feed and water. During the experiment, body weight (BW) was recorded every two weeks. After eight weeks of treatment, six mice in each group were randomly sacrificed at 6:00 (Zeitgeber time 0 [ZT0], lights on), 10:00 (ZT4), 14:00 (ZT8), 18:00 (ZT12, lights off), 22:00 (ZT16), and 2:00 (ZT20), and 6:00 (ZT0) ($n = 6$). Blood samples were collected by orbital bleeding, and serum was separated and maintained at -20°C . After the abdominal cavity opened, liver and colonic digesta samples were collected and immediately frozen in liquid nitrogen. The experimental protocol was approved by the Protocol Management and Review Committee of Xuanwu Hospital Capital Medical University, and mice were treated according to the animal care guidelines of Xuanwu Hospital Capital Medical University (Beijing, China).

2.2. Intraperitoneal Glucose and Insulin Tolerance Test. Intraperitoneal glucose test (IGTT) and insulin tolerance test (ITT) were performed after seven weeks of treatment. Animals

TABLE 1: Primers for RT-qPCR.

Gene	5'-3' primer sequence
<i>Clock</i>	F: ACCACAGCAACAGCAACAAC
	R: GGCTGCTGAACTGAAGGAAG
<i>Per2</i>	F: TGTGCGATGATGATTCGTGA
	R: GGTGAAGGTACGTTTGGTTTGC
<i>Cry1</i>	F: CACTGGTCCGAAAGGGACTC
	R: CTGAAGCAAAAATCGCCACCT
β -Actin	F: TGTCCACCTTCCAGCAGATGT
	R: AGCTCAGTAACAGTCCGCCTAGA
<i>But</i>	F: TCAAATCMGGIGACTGGGTWGA
	R1: TCGATACCGGACATATGCCAKGAG
16s	R2: TCATAACCGCCCATATGCCATGAG
	F: TCCTACGGGAGGCAGCAGT
	R: GGACTACCAGGTATCTAATCCTGTT

were intraperitoneally injected with 1.0 g glucose or 0.65 U insulin per kg BW after a six-hour fasting period. After glucose or insulin injection, blood from the tail vein was used for the measurement of glucose concentration at 0, 30, 60, and 120 min, using a One Touch Ultra Easy glucometer.

2.3. Gene Expression Analysis. Total RNA was extracted from the liver as previously described [15]. cDNA was synthesized using SuperScript II (Invitrogen, Shanghai, China). Primers were mixed with SYBR Green PCR mix (Invitrogen) to amplify *Clock*, *Per2*, and *Cry1* by Real-time quantitative PCR analysis. Results of gene expression were calculated using the comparative CT method normalizing target mRNA to β -actin. Primers are used as previously described [6] and listed in Table 1.

2.4. Determination of Serum Concentration of Glucose, Triglyceride, and Cholesterol. Glucose concentration was analyzed with the commercially available kit (Nanjing Jiancheng Bioengineering Institute, Nanjing, China), and triglyceride (TG) and cholesterol (Chol) contents were determined with commercially available kits (Beijing Strong Biotechnologies, Inc. Beijing, China).

2.5. Microbiota Profiling. Samples of colonic digesta were used for the extraction of total genome DNA and amplification was done using a specific primer with a barcode (16S V3+V4). Sequencing libraries were generated and analyzed as previously described [16]. Operational taxonomic units (OTUs) were performed for genomic prediction of microbial communities by Tax4Fun analysis as previously described [17].

2.6. Determination of SCFA Concentrations. After the addition of deionized precold water, samples of colonic digesta were put intermittently on a vortex mixer for 2 min. Then, the samples were maintained at 4°C for 15 min and centrifuged at 5 000 g for 15 min at 4°C . The supernatant was determined by injection onto the chromatographic system as previously described [18].

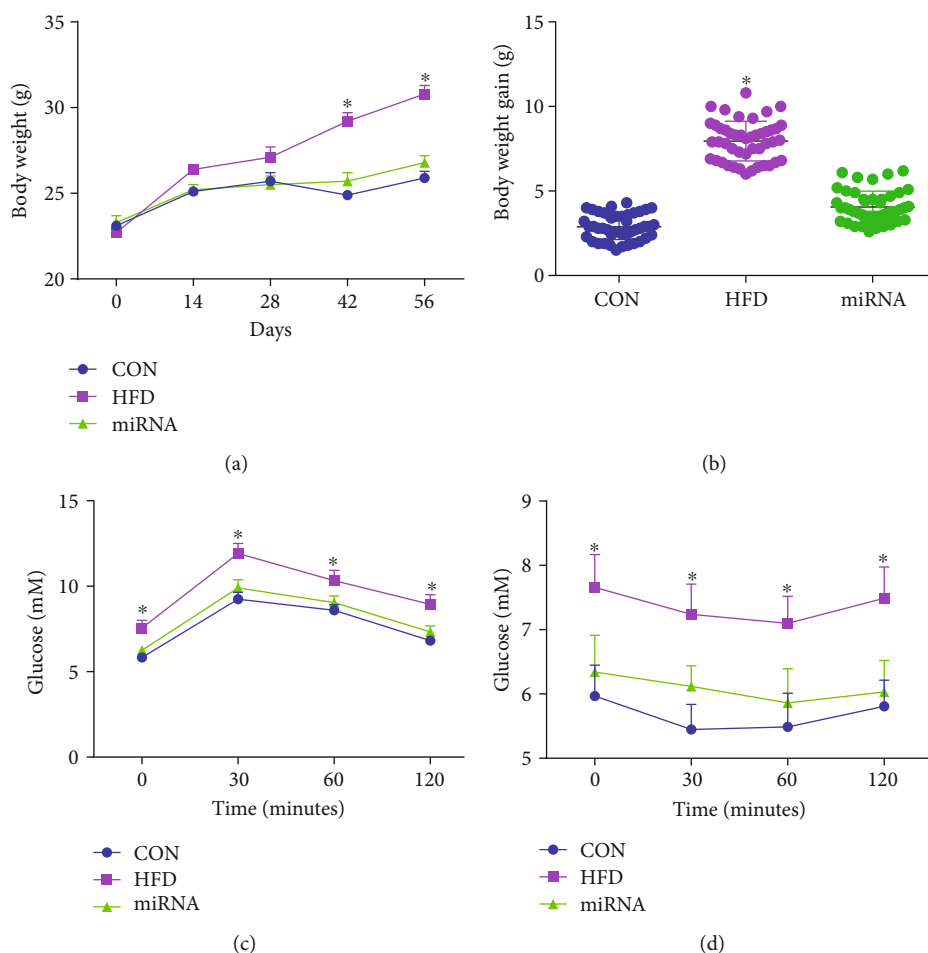


FIGURE 1: Effects of miRNA-10a-5p on body weight gain, IGTT, and ITT in high-fat diet-fed mice. (a) body weight; (b) body weight gain; (c) intraperitoneal glucose test; (d) insulin tolerance test. Data were expressed as Mean \pm SEM. * $P < 0.05$.

2.7. Bacterial Gene Quantification. Samples of colonic digesta were used for the determination of butyryl-CoA: acetate CoA-transferase (*But*) gene copy number. Genes were quantified by determining a standard curve and primers are used as previously described [6] and listed in Table 1.

2.8. Statistical Analysis. Statistical analyses were performed using ANOVA and followed by multiple comparisons using Bonferroni analysis (SPSS 18 software). For the time series, multivariate analysis of variance was performed by Duncan's test. Data are presented as means \pm SEM. Significance was accepted at $P < 0.05$. Matrices for Pearson's r correlation coefficients were generated in GraphPad Prism (7.03) software. Rhythmicity was detected by CircWave v1.4 software (<https://www.euclock.org/>).

3. Results

3.1. Effects of miRNA-10a-5p on Body Weight Gain, IGTT, and ITT in HFD-Fed Mice. As shown in Figure 1(a), body weight significantly increased after HFD intake for 8 weeks, while the administration of miRNA-10a-5p prevented this change. The body weight gain of control mice during the experiment was significantly lower than that of HFD-fed

mice, while no significant difference in body weight was observed between control mice and HFD-fed mice administered with miRNA-10a-5p (Figure 1(b)). The results of IGTT (Figure 1(c)) and ITT (Figure 1(d)) showed that HFD-fed mice had decreased glucose tolerance and insulin sensitivity, while miRNA-10a-5p administration improved these parameters in HFD-fed mice.

3.2. Effects of miRNA-10a-5p on Diurnal Rhythms of Hepatic Clock Gene and Serum Lipids in HFD-Fed Mice. As shown in Figures 2(a)–2(c), the HFD altered circadian clock pattern of hepatic *Clock*, *Per2*, and *Cry1* mRNA expression as shown in previous studies [6, 7]. *Clock*, *Per2*, and *Cry1* mRNA expression in mice administered with miRNA-10a-5p showed daily rhythms similar to those in control mice (Table 2). We found that HFD significantly increased glucose, triglycerides, and cholesterol levels in the sera of mice compared with those in the sera of mice on a low-fat diet, while there was no significant difference in these parameters between the control mice and HFD-fed mice administered with miRNA-10a-5p (Figures 2(d)–2(f)). However, serum glucose level only showed rhythmicity in control mice, while serum triglyceride content showed rhythmicity

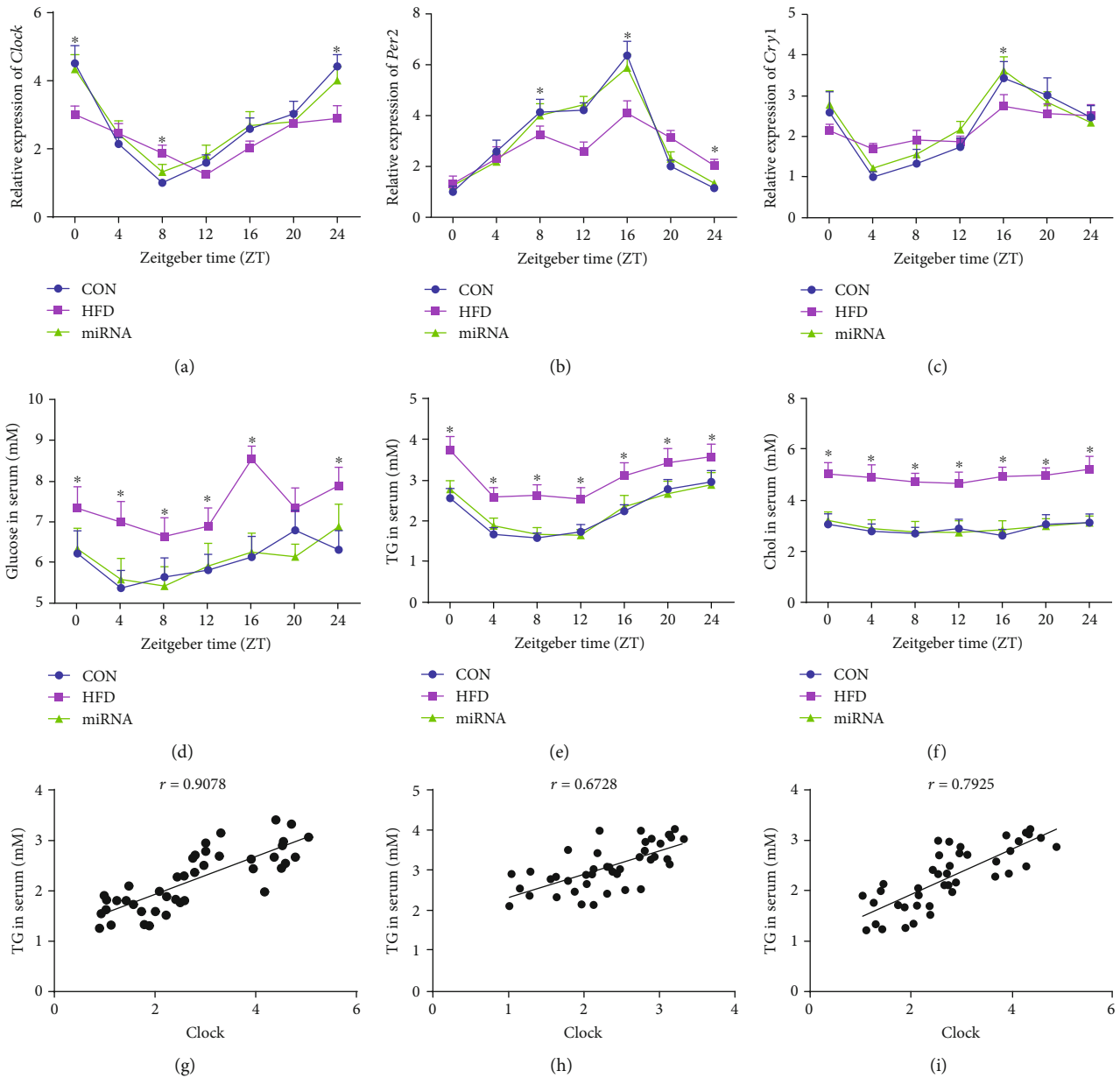


FIGURE 2: Effects of miRNA-10a-5p on diurnal rhythms of the hepatic clock gene and serum lipids in high-fat diet-fed mice. (a) Relative expression of *Clock*; (b) relative expression of *Per2*; (c) relative expression of *Cyr1*; (d) glucose content in serum; (e) triglyceride content in serum; (f) cholesterol content in serum; correlation between triglyceride content and *Clock* expression in CON group (g), HFD group (h), and miRNA group (i). Data were expressed as Mean \pm SEM. * $P < 0.05$.

both in control mice and HFD-fed mice administered with miRNA-10a-5p (Table 3).

To determine whether rhythmicity of serum triglycerides was related to hepatic clock gene expression, we conducted Pearson correlation analysis between triglyceride levels and circadian clock gene expressions. A strong positive correlation was observed between serum triglyceride content and hepatic *Clock* expression in control mice ($r = 0.9078$) (Figure 2(g)). Meanwhile, there was a less positive correlation between serum triglyceride levels and hepatic *Clock* expression in both control mice ($r = 0.6728$) (Figure 2(h)) and HFD-fed mice administered with miRNA-10a-5p ($r = 0.7925$) (Figure 2(i)).

3.3. Effects of miRNA-10a-5p on Diurnal Rhythms of Gut Microbiota in HFD-Fed Mice. The circadian rhythms of gut microbiota and the disturbing effects of HFD have been previously reported [6, 19]. Our results further confirmed that three genera of microbes, *Oscillospira*, *Ruminococcus*, and *Lachnospiraceae*, undergo diurnal oscillations (Table 4; Figures 3(a)–3(c)). However, as previously described [6, 7], HFD disrupted their diurnal rhythms. Importantly, HFD decreased *Lachnospiraceae* abundance at ZT0, while it increased *Ruminococcus* abundance in all the time points. The administration of miRNA-10a-5p maintained the diurnal rhythms of the aforementioned microbes.

TABLE 2: Mesor, amplitude, and acrophase of mRNA levels of clock genes in the liver of mice.

Gene	Group	Acrophase	Mesor	Amplitude	P value
<i>Clock</i>	CON	23.01	2.75	0.72	<0.05
	HFD				NS*
	miRNA	23.21	2.77	0.50	<0.05
<i>Per2</i>	CON	13.05	3.07	0.47	<0.05
	HFD				NS
	miRNA	13.39	3.06	0.57	<0.05
<i>Cry1</i>	CON	20.64	2.22	1.19	<0.01
	HFD				NS
	miRNA	20.46	2.36	1.06	<0.05

*NS: not significant.

TABLE 3: Mesor, amplitude, and acrophase of glucose and triglycerides in the serum of mice.

Item	Group	Acrophase	Mesor	Amplitude	P value
Glucose	CON	23.10	6.04	0.22	<0.01
	HFD				NS*
	miRNA				NS
Triglycerides	CON	22.63	2.22	0.51	<0.05
	HFD				NS
	miRNA	22.90	2.27	0.42	<0.01

*NS: not significant.

TABLE 4: Mesor, amplitude, and acrophase of gut microbiota, butyrate content, and *But* expression.

Item	Group	Acrophase	Mesor	Amplitude	P value
<i>Oscillospira</i>	CON	5.92	0.021	0.008	<0.05
	HFD				NS*
	miRNA	5.72	0.021	0.011	<0.05
<i>Ruminococcus</i>	CON	5.33	0.005	0.002	<0.05
	HFD				NS
	miRNA	4.48	0.005	0.002	<0.05
<i>Lachnospiraceae</i>	CON	23.95	0.040	0.004	<0.05
	HFD				NS
	miRNA	23.97	0.041	0.002	<0.05
Butyrate	CON	23.73	99.00	6.35	<0.05
	HFD				NS
	miRNA	23.94	102.71	1.15	<0.05
<i>But</i>	CON	23.74	1.62	0.09	<0.05
	HFD				NS
	miRNA				NS

*NS: not significant.

Pearson's r coefficient indicated positive correlations between hepatic *Clock* expression and relative abundance of *Lachnospiraceae*, both in control mice ($r = 0.877$) (Figure 3(d)) and in HFD-fed mice administered with miRNA-10a-5p ($r = 0.853$) (Figure 3(f)). However, only a

marginal negative correlation was observed between hepatic *Clock* expression and the relative abundance of *Lachnospiraceae* in HFD-fed mice ($r = -0.03935$) (Figure 3(e)).

3.4. Effects of miRNA-10a-5p on Diurnal Rhythms of Butyrate Content and *But* Gene Expression in HFD-Fed Mice. As shown in Figure 4(a), we observed diurnal oscillation in fecal butyrate and disruption of its daily rhythm by HFD. Administration of miRNA-10a-5p maintained the diurnal rhythm of the butyrate level. Additionally, administration of miRNA-10a-5p restored the diurnal oscillation of abundant expression of the microbial gene *But*, which encodes the enzyme involved in butyrate synthesis, after the disruption caused by HFD intake (Table 4; Figure 4(b)).

4. Discussion

Long-term HFD intake can lead to dysfunction of glucose and lipid metabolism and dysbiosis of gut microbiota, furthering the development of metabolic diseases. Overexpression of miRNA-10a has been proven to inhibit genes involved in lipid synthesis and gluconeogenesis. We found that oral administration of miRNA-10a-5p prevented HFD-induced body weight gain and improved glucose tolerance and insulin sensitivity in mice. These results suggest that miRNA-10a-5p may have preventive effects against obesity and type 2 diabetes. Surprisingly, miRNA-10a-5p maintained the diurnal rhythms of serum triglyceride levels and expression of the hepatic clock genes *Clock*, *Per2*, and *Cry1* that were disrupted by HFD intake. Moreover, the diurnal rhythms of the bacterium *Lachnospiraceae* and its metabolite butyrate were maintained by miRNA-10a-5p administration. As expected, we found that *Lachnospiraceae* abundance showed a strong correlation with the expression of the *Clock* gene. Based on these results, we suggest that miRNA-10a-5p may alleviate HFD-induced insulin resistance through the regulation of the diurnal rhythm of *Lachnospiraceae* and its metabolite butyrate.

HFD-induced disorders of glucose and lipid metabolism are characterized by abnormally high glucose and triglyceride levels in the serum. In the present study, the decreased glucose and triglyceride levels may have resulted from the inhibitory effects of miRNA-10a-5p on hepatic expression of the genes involved in lipid synthesis and gluconeogenesis [14]. Furthermore, we confirmed that glucose and triglyceride levels in the serum of mice showed daily variations, as reported in previous studies [7, 20], and miRNA-10a-5p reestablished the triglyceride diurnal rhythm that was disrupted by HFD intake. However, the glucose diurnal rhythm was altered by HFD, in contrast to that in a previous study [7], and miRNA-10a-5p did not restore the diurnal rhythm of glucose level. We speculate that these contradictory results were because of the time of HFD feeding. Based on these results, we suggest that miRNA-10a-5p has an important effect on the maintenance of both the circadian clock pattern of triglyceride and glucose. These effects were further corroborated by the strong positive correlation between serum triglyceride levels and hepatic *Clock* expression in mice administered with miRNA-10a-5p as well as in control mice.

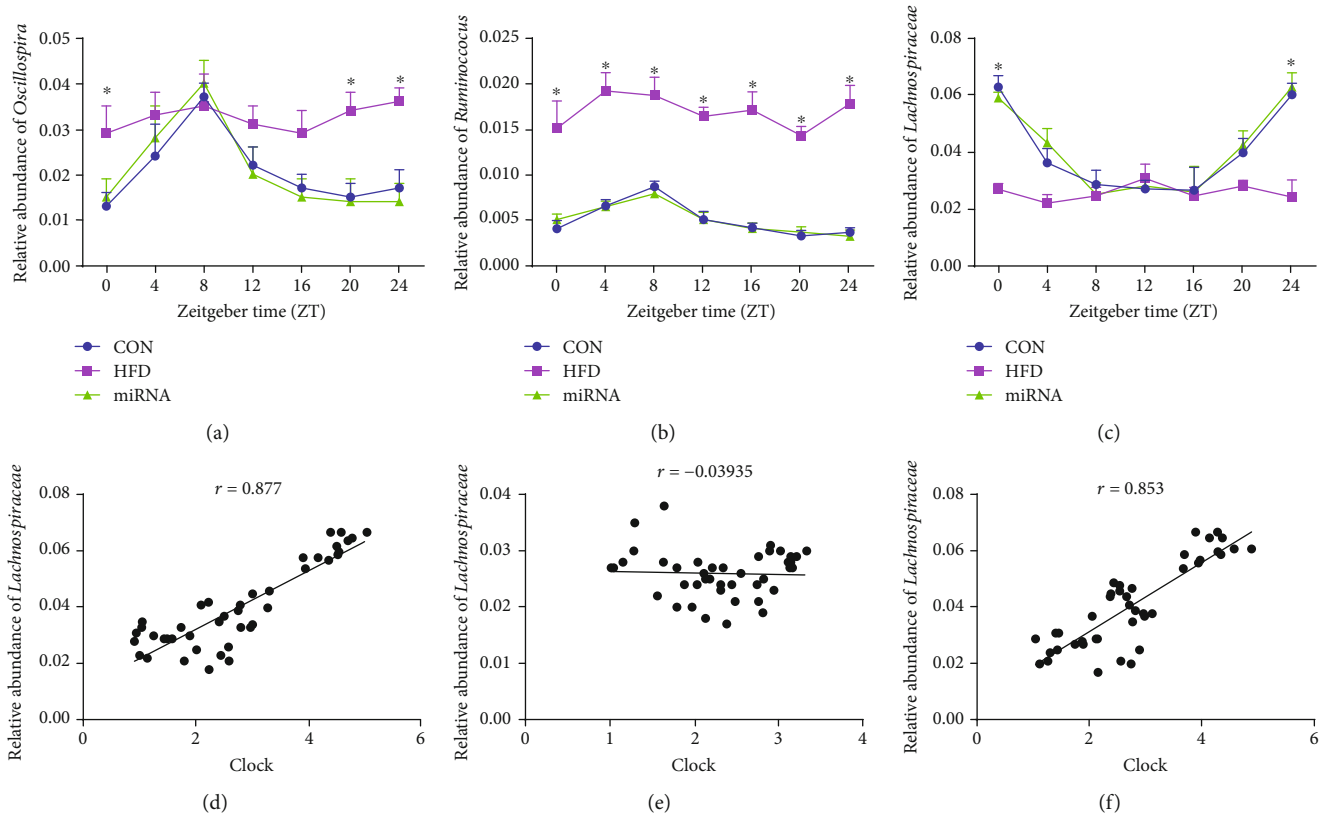


FIGURE 3: Effects of miRNA-10a-5p on diurnal rhythms of gut microbiota in high-fat diet-fed mice. (a) Relative abundance of *Oscillospira*; (b) relative abundance of *Ruminococcus*; (c) relative abundance of *Lachnospiraceae*; correlation between triglyceride content and Clock expression in CON group (d), HFD group (e), and miRNA group (f). TG: glycerides; Chlo: cholesterol. Data were expressed as Mean \pm SEM. * $P < 0.05$.

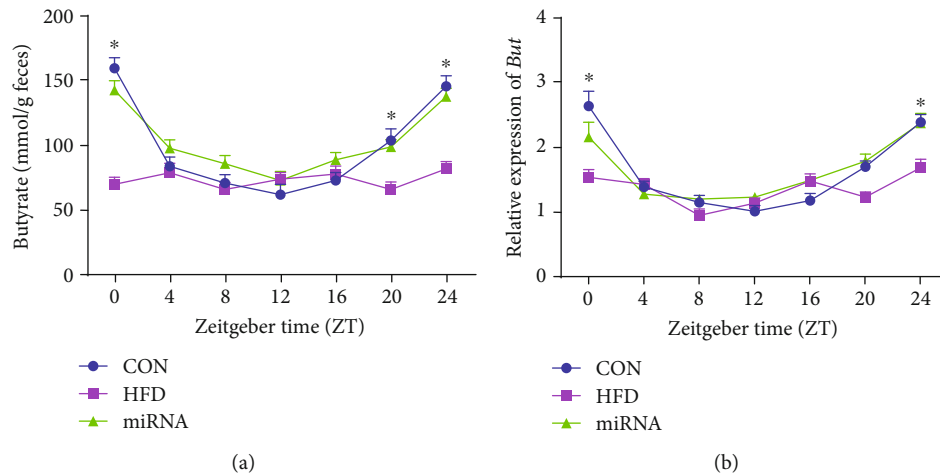


FIGURE 4: Effects of miRNA-10a-5p on diurnal rhythms of butyrate content and gene expression of *But* in high-fat diet-fed mice. (a) Relative abundance of Butyrate in feces; (b) relative expression of *But*. Data were expressed as Mean \pm SEM. * $P < 0.05$.

It is suggested that gut microbes undergo diurnal variations [6]. Moreover, the composition and function of gut microbes can be influenced by dietary factors [6]. As expected, we found that three genera of microbes—*Oscillospira*, *Ruminococcus*, and *Lachnospiraceae*—showed diurnal rhythms. However, their diurnal oscillations were disturbed by HFD intake, in line with the results of previous studies

showing that HFD disrupted the diurnal pattern of gut microbiota composition and their functions [6, 7]. MiRNAs play vital roles in the process by which the host shapes the gut microbes. Notably, miRNAs are not only critical for the homeostasis of gut microbiota in normal conditions but also provide preventative and therapeutic benefits in diseased subjects by maintaining gut microbiota. Since miRNA-10a-

5p is rhythmically expressed and can regulate the expression of circadian rhythm genes, it is reasonable that miRNA-10a-5p can affect the diurnal rhythm of gut microbes. The restoration of the diurnal rhythms of *Oscillospira*, *Ruminococcus*, and *Lachnospiraceae* by the administration of miRNA-10a-5p in HFD-fed mice confirmed this theory. Moreover, the strong correlation between hepatic *Clock* expression and relative abundance of *Lachnospiraceae* in mice administered with miRNA-10a-5p suggested that miRNA-10a-5p alleviated HFD-induced dysbiosis of gut microbiota by promoting diurnal rhythms. However, the mechanisms by which miRNA-10a-5p affects the growth of *Oscillospira*, *Ruminococcus*, and *Lachnospiraceae* have not been explored and need to be elucidated in future studies.

Lachnospiraceae is characterized by its ability to synthesize butyrate [21, 22]. We found that the changes in butyrate content in feces were accompanied by changes in *Lachnospiraceae* count. The beneficial effects of butyrate on the alleviation of HFD-induced metabolic disorders have been widely reported. Butyrate supplementation prevents obesity, alleviates insulin resistance, improves glucose tolerance, and decreases fat accumulation in HFD-fed mice [23–25]. Consequently, we theorize that miRNA-10a-5p alleviates insulin resistance mainly through the modulation of the diurnal rhythm of *Lachnospiraceae* and its metabolite butyrate. The effects of miRNA-10a-5p on butyrate content were further confirmed by its effects on the gene expression of *But*, which encodes the enzyme involved in butyrate production.

In conclusion, our results suggest that oral administration of miRNA-10a-5p protected against obesity, glucose intolerance, and insulin resistance in HFD-fed mice. Additionally, miRNA-10a-5p maintained the diurnal rhythms of hepatic clock genes, serum triglyceride levels, and *Lachnospiraceae* abundance in feces. Moreover, a strong positive correlation was observed between the hepatic expression of the *Clock* gene and serum triglyceride levels and *Lachnospiraceae* abundance. Along with the increase in *Lachnospiraceae* numbers, butyrate content in feces also resumed a diurnal rhythm after miRNA-10a-5p administration in HFD-fed mice. In summary, we suggest that miRNA-10a-5p may improve HFD-induced metabolic disorders through the modulation of the diurnal rhythm of *Lachnospiraceae* and its metabolite butyrate.

Data Availability

The data used to support the findings of this study are included within the article.

Conflicts of Interest

The authors declared that there are no conflicts of interest.

Acknowledgments

This work was supported by the National Natural Science Foundation of China (81801313).

References

- [1] R. K. Singh, H. W. Chang, D. Yan et al., "Influence of diet on the gut microbiome and implications for human health," *Journal of Translational Medicine*, vol. 15, no. 1, p. 73, 2017.
- [2] A. P. B. Moreira, T. F. S. Texeira, A. B. Ferreira, M. do Carmo Gouveia Peluzio, and R. de Cássia Gonçalves Alfenas, "Influence of a high-fat diet on gut microbiota, intestinal permeability and metabolic endotoxaemia," *The British Journal of Nutrition*, vol. 108, no. 5, pp. 801–809, 2012.
- [3] S. Lacroix, F. Pechereau, N. Leblanc et al., "Rapid and concomitant gut microbiota and endocannabinoidome response to diet-induced obesity in mice," *mSystems*, vol. 4, no. 6, article e00407-19, 2019.
- [4] S. Q. Shi, T. S. Ansari, O. P. McGuinness, D. H. Wasserman, and C. H. Johnson, "Circadian disruption leads to insulin resistance and obesity," *Current Biology*, vol. 23, no. 5, pp. 372–381, 2013.
- [5] A. Kohsaka, A. D. Laposky, K. M. Ramsey et al., "High-fat diet disrupts behavioral and molecular circadian rhythms in mice," *Cell Metabolism*, vol. 6, no. 5, pp. 414–421, 2007.
- [6] V. Leone, S. M. Gibbons, K. Martinez et al., "Effects of diurnal variation of gut microbes and high-fat feeding on host circadian clock function and metabolism," *Cell Host & Microbe*, vol. 17, no. 5, pp. 681–689, 2015.
- [7] J. Yin, Y. Li, H. Han et al., "Administration of exogenous melatonin improves the diurnal rhythms of the gut microbiota in mice fed a high-fat diet," *mSystems*, vol. 5, no. 3, article e00002-20, 2020.
- [8] L. Mendoza-Viveros, C. K. Chiang, J. L. K. Ong et al., "miR-132/212 modulates seasonal adaptation and dendritic morphology of the central circadian clock," *Cell Reports*, vol. 19, no. 3, pp. 505–520, 2017.
- [9] Y. Xue and Y. Zhang, "Emerging roles for microRNA in the regulation of *Drosophila* circadian clock," *BMC Neuroscience*, vol. 19, no. 1, pp. 1–9, 2018.
- [10] W. Chen, Z. Liu, T. Li et al., "Regulation of *Drosophila* circadian rhythms by miRNA let-7 is mediated by a regulatory cycle," *Nature Communications*, vol. 5, no. 1, p. 5549, 2014.
- [11] X. Chen and M. Rosbash, "Mir-276a strengthens *Drosophila* circadian rhythms by regulating timeless expression," *Proceedings of the National Academy of Sciences of the United States of America*, vol. 113, no. 21, pp. E2965–E2972, 2016.
- [12] X. Nian, W. Chen, W. Bai, Z. Zhao, and Y. Zhang, "miR-263b controls circadian behavior and the structural plasticity of pacemaker neurons by regulating the LIM-only protein Beadex," *Cells*, vol. 8, no. 8, p. 923, 2019.
- [13] S. Liu, A. P. da Cunha, R. M. Rezende et al., "The host shapes the gut microbiota via fecal microRNA," *Cell Host & Microbe*, vol. 19, no. 1, pp. 32–43, 2016.
- [14] R. Horii, M. Honda, T. Shirasaki et al., "MicroRNA-10a impairs liver metabolism in hepatitis C virus-related cirrhosis through deregulation of the circadian clock gene brain and muscle aryl hydrocarbon receptor nuclear translocator-like 1," *Hepatology*, vol. 3, no. 12, pp. 1687–1703, 2019.
- [15] X. Zhou, L. He, C. Wu, Y. Zhang, X. Wu, and Y. Yin, "Serine alleviates oxidative stress via supporting glutathione synthesis and methionine cycle in mice," *Molecular Nutrition & Food Research*, vol. 61, no. 11, article 1700262, 2017.
- [16] S. Chen, B. Tan, Y. Xia et al., "Effects of dietary gamma-aminobutyric acid supplementation on the intestinal functions

- in weaning piglets,” *Food & Function*, vol. 10, no. 1, pp. 366–378, 2019.
- [17] S. Chen, M. Wang, L. Yin et al., “Effects of dietary tryptophan supplementation in the acetic acid-induced colitis mouse model,” *Food & Function*, vol. 9, no. 8, pp. 4143–4152, 2018.
- [18] F. Wang, H. Zhou, L. Deng, L. Wang, J. Chen, and X. Zhou, “Serine deficiency exacerbates inflammation and oxidative stress via microbiota-gut-brain Axis in D-galactose-induced aging mice,” *Mediators of Inflammation*, vol. 2020, Article ID 5821428, 7 pages, 2020.
- [19] Y. Wang, Z. Kuang, X. Yu, K. A. Ruhn, M. Kubo, and L. V. Hooper, “The intestinal microbiota regulates body composition through NFIL3 and the circadian clock,” *Science*, vol. 357, no. 6354, pp. 912–916, 2017.
- [20] X. Zhou, D. Wan, Y. Zhang et al., “Diurnal variations in polyunsaturated fatty acid contents and expression of genes involved in their de novo synthesis in pigs,” *Biochemical and Biophysical Research Communications*, vol. 483, no. 1, pp. 430–434, 2017.
- [21] P. Louis, P. Young, G. Holtrop, and H. J. Flint, “Diversity of human colonic butyrate-producing bacteria revealed by analysis of the butyryl-CoA:acetate CoA-transferase gene,” *Environmental Microbiology*, vol. 12, no. 2, pp. 304–314, 2010.
- [22] M. Vital, C. R. Penton, Q. Wang et al., “A gene-targeted approach to investigate the intestinal butyrate-producing bacterial community,” *Microbiome*, vol. 1, no. 1, p. 8, 2013.
- [23] G. M. Raso, R. Simeoli, R. Russo et al., “Effects of sodium butyrate and its synthetic amide derivative on liver inflammation and glucose tolerance in an animal model of steatosis induced by high fat diet,” *PLoS One*, vol. 8, no. 7, article e68626, 2013.
- [24] T. M. Henagan, B. Stefanska, Z. Fang et al., “Sodium butyrate epigenetically modulates high-fat diet-induced skeletal muscle mitochondrial adaptation, obesity and insulin resistance through nucleosome positioning,” *British Journal of Pharmacology*, vol. 172, no. 11, pp. 2782–2798, 2015.
- [25] S. Khan and G. Jena, “Sodium butyrate reduces insulin-resistance, fat accumulation and dyslipidemia in type-2 diabetic rat: a comparative study with metformin,” *Chemico-Biological Interactions*, vol. 254, pp. 124–134, 2016.